

MICROBEAM ANALYSIS

1989

Phillip E. Russell, *Editor*

Proceedings of the 24th Annual Conference
of the
Microbeam Analysis Society
Asheville, N.C., 16-21 July 1989



San Francisco Press, Inc.

Box 6800, San Francisco, CA 94101-6800

PUBLISHER'S NOTICE

The Microbeam Analysis Society (MAS) and San Francisco Press, Inc., are not responsible for the information and views presented in this volume by the several contributors.

Permission to reprint portions of this volume in professional journals published by scientific or technical societies (with suitable acknowledgment) will be given free of charge on application to the publisher; a nominal fee may be charged for reprint rights given to book publishers, commercial journals, company publications, and other media.

Copies of this volume are available to members of the Microbeam Analysis Society (MAS) and of the Electron Microscopy Society of America (EMSA) *who send prepayment by personal check* at a 20% discount from the list price. (Californians add tax.) The same discount is available to members of both societies for the MAS triennial *Analytical Electron Microscopy*, and for the *Proceedings* of the annual EMSA meeting. The following books are available (most back issues at reduced prices):

Microbeam Analysis

1975, 1977 (8th ICXOM), 1979, 1980, 1981, 1982, \$25 each

1986, 1987, \$50 each

1988, \$60

1989, \$65

Analytical Electron Microscopy

1981, \$25

1984, \$40

1987,* \$50

Proceedings EMSA

1982, 1985, 1986, \$45 each

1987, 1988, \$65 each

1989, \$72.50

Electron Microscopy Safety Handbook, \$15

Electron Microscopy and Alzheimer's Disease (J. Metuzals, Ed.), \$10

Early History of the Electron Microscope (L. Marton), \$5

Electricity and Medicine: History of Their Interaction (M. Rowbottom and C. Susskind), \$30

*AEM—1987 also contains the MAS—1987 papers on surface analysis.

TABLE OF CONTENTS*

	<i>Page</i>
Officers of the Microbeam Analysis Society	ix
1989 MAS paper awards	x
1989 MAS presidential awards	x
Sustaining members' information	xii
TUTORIAL (P. E. Russell, D. B. Williams)	
Van Vaeck, L., Gijbels, R., Overview of laser mass spectrometry techniques	xvii
1. PRESIDENTIAL SYMPOSIUM: SPECTROSCOPY IN MICROSCOPY & MICROANALYSIS (D. B. Wittry)	
Hillier, J., Electron microscopy to electron microprobe analysis: The early days	1
Batson, P. E., Spatially resolved EELS	5
Batstone, J. L., Determination of electronic properties of defects in semiconductors by cathodoluminescence	11
Levi-Setti, R., Chabala, J. M., Girod, C., Hallégot, P., Wang, Y. L., The use of focused heavy ion beams for submicrometer imaging analysis	17
2. MICROPROBE ANALYSIS IN MEDICINE (J. Shelburne, V. Roggli)	
Roomans, G. M., X-ray microanalysis in the study of cystic fibrosis	23
LoPachin, R. M., Lowery, J., Eichberg, J., LoPachin, V. R., Saubermann, A. J., Effects of injury on distribution of elements in peripheral nerve axons	26
Kirk, R. G., Reasor, M. K. J., Lee, P., Drug distribution in cells using x-ray microanalysis	31
Kaufmann, R. L., Rechmann, P., Tourmann, J. L., Schnatz, H., LAMMS in biomedical research: Achievements, shortcomings, and promises	35
Perl, D. P., Good, P. F., Trace element analysis in neurodegenerative disease	43
Lee, J. J., Linton, R. W., Hunter, J. L., Shelburne, J. D., Burchette, J. L., Jr., Sanfilippo, A. P., Voyksner, R. E., Correlative ion and electron microscopy for immunocytochemistry	45
Schmidt, P. F., Zunkley, H., Barckhaus, R., Winterberg, B., Distribution patterns of aluminum accumulations in bone tissue from patients with dialysis osteomalacia determined by LAMMA	50
Abraham, J. L., In situ microprobe quantitation of inorganic particle burden in paraffin sections of lung tissue	55
Roggli, V. L., Nonasbestos mineral fibers in human lungs	57
Klintworth, G. K., Ocular applications of energy-dispersive microprobe analysis	60
Kusy, R. P., Buchanan, J. W., Quality control of cardiovascular wire plunge electrodes	63
3. BIOLOGICAL MICROANALYSIS (P. Ingram, D. E. Johnson, A. LeFurgey)	
Lechene, C., Cantello, H., Crabos, M., Cohen, B. J., Role of the (Na,K)-pump in intracellular Na homeostasis	65
LeFurgey, A., Mandel, L. J., Ingram, P., Alteration of Ca and S compartmentation during anoxia in proximal renal tubules	69
Cantino, M. E., Izutsu, K. T., Johnson, D. E., Wilkinson, L. E., Kayton, R. J., Chen, S. W., Heterogeneity in elemental images of cells and tissues	73
Spencer, A. J., Osborne, M. P., Stephen, J., X-ray microanalysis of normal and Edim rotavirus-infected mouse intestine	75
Echlin, P., Cryomicroscopy and analysis: Procedures, problems, and prospects	79
Andrews, S. B., Leapman, R. D., Performance of a cryotransfer/cold stage system for a VG Microscopes HB501 STEM	85
Leapman, R. D., Swyt, C. R., Parallel EELS microanalysis of cells	89
Wong, J. G., Johnson, D. E., Cantino, M. E., Semi-automated selection of objects from digital STEM images	94
Strain, J. J., Kopf, D. A., Hawkey, L. A., Ingram, P., LeFurgey, A., Computer-assisted bright-field signal measurement of water content in frozen hydrated and dehydrated cryosections of gelatin	97
Roomans, G. M., Zglinicki, T. von, Spencer, A. J., Ion distribution in epithelial cells studied by x-ray microanalysis	103
Zglinicki, T. von, Roomans, G. M., Sodium, potassium, and chlorine in electrolyte secreting cells	105
Pavenstädt-Grupp, I., Grupp, C. T., Franz, H. E., Kinne, R. K. H., Evidence for a barium-sensitive potassium channel in rat papillary collecting duct (PCD) cells: Evaluation by x-ray microanalysis in SEM	107
Zierold, K., Cryotechniques for biological microanalysis	109
Saubermann, A. J., Quantitative x-ray imaging of frozen hydrated cryosections	112

*An author index begins on p. 609.

Torney, J. McD., Walsh, L. G., Strategies for spatial deconvolution of calcium stores in cardiac muscle	115
Wendt-Gallitelli, M. F., Isenberg, G., Voltage-clamp as a tool for gradation of Ca-influx, Ca-load, and contractility	117
Warley, A., X-ray microanalysis of isolated cardia myocytes	118
Carney, M., Lehman, J., Ingram, P., LeFurgey, A., Lieberman, M., An electron probe x-ray microanalysis comparison of Na detection within cultured heart cells using Be window and windowless Si detectors	119
Bond, M., Jaraki, A.-R., Rapid freezing of hamster hearts in vivo at defined timepoints of the cardiac cycle	122
Wittry, D. B., Golijanin, D. M., Sun, S., Comparison of damage produced by photon and electron excitation	125
Dunlap, J. R., Lus, S., Bunn, R. D., Joy, D. C., An electron spectroscopic study of ice	127
Zhang, X., Joy, D. C., Buchanan, R. A., EM study of microbially influenced corrosion	129
Armstrong, D. A., Joy, D. C., Comparative ultrastructure and x-ray microanalysis of <i>Salmonella</i> <i>typhimurium</i> by CTEM, cryofixation, and EM	131
Wurster, R., Lehner, S., EDX and EELS measurements of Ca-doped thin sections	135
Foster, M. C., Effective use of a TN5500 x-ray analyzer together with a personal computer for microanalysis of biological sections	137
 4. OPTICAL MICROANALYSIS (M. A. Paesler, R. Messerschmidt)	
Nemanich, R. J., Interference-enhanced Raman scattering from thin films and interfaces	141
Morris, M. D., Treado, P. J., Hadamard transform Raman microscopy	146
Sparks, R. G., Enloe, W. S., Paesler, M. A., Development of a high-axial-resolution micro-Raman technique for studying the effects of machine parameters in machined semiconductors	148
Musselman, R. L., Polarized specular reflectance UV-visible spectroscopy of charge-transfer transitions in bioinorganic and one-dimensional systems	151
Adar, F., Weinlaender, M., Investigation of the mineral phases on the surfaces of dental implants by the Raman microprobe MOLE	159
Carl, R. T., Applications of infrared microimaging to coatings	163
Darmon, L. S., Pierce, D. L., A microextraction technique for the direct isolation of liquid droplets contained within a matrix	166
Reffner, J. A., Infrared spectral mapping of polymers by FT-IR microscopy	167
Humphreys, T. P., Posthill, J. B., Das, K., Sukow, C. A., Parikh, N. R., Nemanich, R. J., Raman characterization of strain in GaAs epitaxial films grown on sapphire and silicon-on-sapphire substrates	171
Burrus, R. C., Ging, T., Carlson, D., Raman microprobe observations of carbon and oxygen stable isotopes in geologic materials	173
Russ, J. C., Internal and surface measurements using the confocal scanning laser microscope	176
 5. NEW OR EMERGING MICROPROBES (A. D. Romig Jr.)	
Arlinghous, H. F., Thonnard, N., Schmitt, H. W., Ultratrace element microcharacterization of surfaces and solids with SIRIS	180
Golijanin, D. M., Wittry, D. B., Sun, S., Further developments in instrumentation for microprobe x-ray fluorescence analysis	186
Jones, K. W., Gordon, B. M., Hanson, A. L., Pounds, J. G., Rivers, M. L., Schidlovsky, G., Smith, J. V., Spanne, P., Sutton, S. R., X-ray microscopy using synchrotron radiation	191
Barbour, J. C., Doyle, B. L., Materials analysis with nuclear microprobes: Superconductors and buried conductors	196
Kellog, G. L., Novel applications of the field ion microscope and atom probe	201
 6. QUANTITATIVE ANALYSIS (J. R. Armstrong, K. F. J. Heinrich)	
Bastin, G. F., Heijligers, H. J. M., Quantitative EPMA of oxygen	207
Packwood, R., Boore, V., Thomas, S., Analyses of layered specimens in the electronprobe microanalyzer	211
Newbury, D. E., Steel, E. B., Mass concentration vs atomic concentration in EPMA	216
Myklebust, R. L., Fiori, C. E., The application of a numerical procedure in the calculation of the atomic number correction in EPMA	219
Small, J. A., Myklebust, R. L., An evaluation of x-ray absorption expressions for pure and multielement targets	223
Wells, O. C., Escape area of singly and plurally backscattered electrons in the SEM	227
Bostrom, T. E., and Nockolds, C. E., Filtered least-squares fitting of EDS spectra using derivative references: Problems and limitations imposed by counting statistics	233
Fiori, C. E., Swyt, C. R., The use of theoretically generated spectra to estimate detectability limits and concentration variance in energy-dispersive x-ray microanalysis	236
Abo-Namous, S. A., On the peak-to-background ratio in microprobe analysis of porous materials	239
Heinrich, K. F. J., A binary alloy data set for comparison of quantitative electron probe correction procedures	242
Lifshin, E., Peluso, L. A., Mogro-Campero, A., Turner, L., Microprobe analysis of thin $\text{YBa}_2\text{Cu}_3\text{O}_{6+x}$ superconducting films	243

Yang, V., Wagstaff, J., McKay, G., A case study of temperature-related peak shift in WDS microprobe analysis	247
Anderhalt, R. W., Sandborg, A. O., Quantitative compositional mapping in an SEM with an energy-dispersive spectrometer	249
Marinenko, R. B., Small, J. A., Blackburn, D. H., Retorick, D. R., Shire, N. J., Preparation and preliminary analysis of K-411 glass microspheres	254
Newbury, D. E., Marinenko, R. B., Design for an electron probe microanalyzer k-value round robin	257
7A. LAMMS: FUNDAMENTALS & ION FORMATION PROCESSES (R. L. Kaufmann)	
Dreyfus, R. W., Are laser-ablated monolayers accurately characterized by their ion emission?	261
Matthews, L. J., Baxter, C. S., Leake, J. A., Electron-optical examination of LAMMS craters in transverse section	264
Housden, J., Hutt, K. W., Wallach, E. R., Evolution of ion energy distributions with increasing ion yields in LAMMS ...	269
Vertes, A., Juhasz, P., Balazs, L., Gijbels, R., Target heating, plasma formation, and expansion processes during laser ionization	273
Hillenkamp, F., Ion formation by desorption for LAMMS	277
Becker, C. H., Tingle, T. N., Hochella, M. F., General laser post-ionization	281
7B. LAMMS: PATTERN RECOGNITION & CLUSTER IONS (R. A. Fletcher, R. W. Linton)	
Odom, R. W., Radicati di Brozolo, F., Harrington, P. B., Voorhees, K. J., Polymer characterization and classification with LAMMS and principal-component analysis	283
Lindner, B., Sydel, U., Pattern recognition as a complementary tool for the evaluation of complex LAMMS data	286
Ro, C.-U., Musselman, I. H., Linton, R. W., Molecular speciation of particles: Application of pattern recognition techniques to LAMMS data	293
Lineman, D. N., Viswanadham, S. K., Sharkey, A. G., Hercules, D. M., Observation of carbon clusters from polycyclic aromatic hydrocarbons	297
Mele, A., Stranges, D., Giardini-Guidoni, A., Teghil, R., Cluster ion formation by laser-induced evaporation of Group IV oxide elements	299
Tsugoshi, T., Kikuchi, T., Furuya, K., Ino, Y., Hayashi, Y., Structural interpretation of silicate network from various silicate rock-forming minerals in LAMMS analysis	301
Fletcher, R. A., Currie, L. A., Utility of laser microprobe for source identification	303
7C. LAMMS: INSTRUMENTATION (R. L. Kaufmann)	
Brenna, J. T., Laser microprobe Fourier transform ion cyclotron resonance mass spectrometry: Instrumentation and results of polymer studies	306
Muller, J. F., Pelletier, M., Krier, G., Weil, D., Campana, J., A new generation of microprobe: Laser ionization and FT/ICR mass spectrometry	311
Yamamoto, T., Ishimori, A., LAMMS for the analysis of high-vapor-pressure materials	317
Thompson, S. P., Dingle, T., Griffiths, B. W., Analysis by laser microprobe and related techniques	319
Nicholas, M., Pruett, J. G., Havrilla, G. J., Bryan, S. R., Laser post-ionization time-of-flight mass spectrometry with a laser-ablation carrier-gas transport source	323
7D. LAMMS: APPLICATIONS IN MATERIALS SCIENCE (R. W. Linton)	
Holm, R., Holtkamp, D., Industrial applications of LAMMA	325
Schmidt, P. F., Brinkmann, B., Investigation on the identification and discrimination of indigo-dyed cotton fibers by means of LAMMA	330
Evans, B., LAMMS applied to processing problems in the glass industry	333
Heimbrook, L. A., Moyers, K. W., Hillenius, S. J., Application of LAMMS to lateral diffusion in semiconductor devices	335
Bahr, U., Karas, M., Hillenkamp, F., Depth profiling by LAMMA	337
Pelletier, M., Krier, G., Muller, J. F., Campana, J., Weil, D., Laser microprobe FTMS and materials science	339
Hercules, D. M., Solid-state mass spectrometry with a laser microprobe	343
Scanlan, F. P., Study of polymer degradation by laser mass spectrometry	345
Krier, G., Pelletier, M., Muller, J. F., Lazare, S., Granier, V., Lutgen, P., Laser ionization and photoablation of polymers with LAMMA and FTMS microprobes	347
7E. LAMMS: BIOMEDICAL & ENVIRONMENTAL APPLICATIONS (R. A. Fletcher)	
Mathey, A., Van Vaeck, L., Ricci, P., In situ analysis of carnation phytoalexins by LAMMS	350
Karas, M., Hillenkamp, F., Prospects for laser molecular microprobing	353
Reichmann, P., Tourmann, J. L., Kaufmann, R. L., LAMMS detection of dental metallic compounds in the human oral mucosa	355
Tourmann, J. L., Kaufmann, R. L., LAMMS studies of silica dusts: Chemical characterization and cytotoxicity correlation	359

Kubis, A. J., Viswanadham, S. K., Sharkey, A. G., Hercules, D. M., In situ analysis of compounds separated by thin-layer chromatography using laser mass spectrometry	364
Güçer, S., Van Vaeck, L., Adams, F., Characterization of graphite furnace-produced aerosols by LAMMS	366
Radicati di Brozolo, F., Meeker, G. P., Fleming, R. H., Microanalytical characterization of prebiological components in interplanetary dust	370
Good, P. F., Roboz, J. S., Perl, D. P., Laser microprobe studies of neuropeptides	373
8. COMPUTER-AIDED MICROANALYSIS AND IMAGING (D. S. Bright)	
Bright, D. S., Steel, E. B., Newbury, D. E., The problem of visibility in SEM images	377
McCarthy, J. J., Walker, J. S., Dillon, C. E., Techniques for 3-D image presentation from confocal scanning microscopy	381
Kelley, M. H., Unguris, J., Scheinfein, M. R., Pierce, D. T., Celotta, R. J., Vector imaging of magnetic microstructure ...	391
Czyzewski, Z., Joy, D. C., Elastic scattering cross section for electron energy above 1 keV	396
Bumgarner, S. D., Hoffmeister, S., Griffis, D. P., Russell, P. E., Automated qualitative analysis of Auger electron spectra	399
Chen, J. H., Johnson, P. F., Computer simulation of initial stage sintering in two-dimensional particulate systems	405
Radzimski, Z. J., Russ, J. C., Backscattered electron imaging of subsurface structures	410
9. ASBESTOS ANALYSIS (W. E. Longo, R. J. Lee)	
Millette, J. R., Burris, S. B., Krewer, J. A., An in-house training program for the TEM laboratory	413
Steel, E. B., Asbestos analytical techniques: Capabilities and limitations	414
Clark, B. H., Collection, preparation, and analysis of surface samples	421
Spurny, K. R., On the characterization of asbestos aerosols	422
Detter, L. D., Vander Wood, T. B., Procedures for the preparation and analysis of bulk asbestos-containing materials by computer-controlled SEM	423
Perkins, R. L., Harvey, B. W., Beard, M. E., Asbestos analysis by polarized light microscopy: Problems and suggestions	425
Davis, J. A., Kalinowski, M. R., Development of LM/SM/TEM methods for the quantitative analysis of airborne glass fiber levels	427
Verkouteren, J. R., Phelps, J. M., Steel, E. B., Guidelines for refractive index measurements of asbestos	433
10. NEW OR EMERGING MICROPROBES (D. B. Wittry)	
Dingley, D. J., Mackenzie, R., Baba-Kishi, K., Application of backscatter Kikuchi diffraction for phase identification and crystal orientation measurement in materials	435
James, M. R., Surface displacement measurements based on digital image processing of micrographs	441
Bourcier, R. J., Micromechanical characterization of near-surface layers	443
Bolon, R. B., Robertson, C. D., Lifshin, E., The environmental SEM: A new way to look at insulating materials	449
11. SEMICONDUCTOR APPLICATIONS (P. Roitman)	
Chevachorenkul, S., Osburn, C. M., McGuire, G. E., Characterization of microstructural defects in semiconductor silicon	453
Radzimski, Z. J., Shou, T., Rozgonyi, G. A., Russell, P. E., Laser beam and electron beam induced current techniques for Si defect analysis: A comparative study	456
Krause, S. J., Mohr, J., Bernstein, G. H., Ferry, D. K., Joy, D. C., A new method for measuring the thickness of thin-film insulators	459
Chapman, R. C., Robers, W. B., Thompson, D. G., Use of SEM and DES to monitor and characterize Al/Cu/Si metallization	463
Kirkendall, T. D., Wilcox, D. B., Materials characterization of alloyed ohmic contacts on GaAs	465
Heyman, R. V., Ross, D. K., Elthon, D., Routine electron microprobe analysis of carbon in high- T_c superconductors: Initial results	468
Rothwell, T., Myers, S., Analysis of metal opens failure in VLSI Al-Si-Cu metallization	471
Cho, S. G., Johnson, P. F., The microstructure and initial magnetic permeability of fast-fired MnZn ferrites	474
12. ANALYTICAL ELECTRON MICROSCOPY (D. B. Williams, K. S. Vecchio, J. Hren)	
Vecchio, K. S., Experimental limitations of CBED HOLZ lines for compositional measurements	477
Ou, H. J., Glaisher, R. W., Cowley, J. M., Morkoc, H., Using the (200) thickness contour to measure the absolute Al concentration of $Al_xGa_{1-x}As$ -GaAs MQWS structures	480
Howe, J. M., Reliability of different symmetry features and procedures for point group determination of thin specimens by CBED	483

Malis, T. S., AEM specimens: Staying one step ahead	487
Kenik, E. A., Loss of grain boundary segregant during ion milling	493
Michael, J. R., The effect of specimen thickness and electron probe characteristics on the x-ray spatial resolution in the AEM	496
Goldstein, J. I., Williams, D. B., Effect of foil thickness on quantification of EDS spectra	501
Lyman, C. E., Ackland, D. W., Williams, D. B., Goldstein, J. I., The hole-count test revisited: Effects of test specimen thickness	507
Romig, A. D., Jr., Headley, T. J., Carr, M. J., Cieslak, M. J., Quantitative thin-film x-ray microanalysis of Nb-modified Ti ₃ Al	511
Lin, Y. J., Mecartney, M. L., Angelini, P., Analytical TEM of yttria-stabilized zirconia with silicate grain boundary phases	515
Batson, P. E., Bruley, J., Experimental difficulties with obtaining electrical properties using spatially resolved electron energy loss spectroscopy	518
Konopka, J. F., Quantitative mapping of thin-film STEM samples with energy-dispersive x-ray spectrometry	523
Gauvin, R., L'Esperance, G., The effect of fast secondary electrons on k factors and spatial resolution ..	527
 13. SCANNING TUNNELING MICROSCOPY & RELATED TECHNIQUES (P. E. Russel)	
Panitz, J., STM imaging of biological structure: Status and prospects	531
Musselman, I. H., Chen, R.-T., Russell, P. E., Platinum thin-film roughness measurements by STM	535
Pellerin, J., Shedd, G., Griffis, D. P., Russell, P. E., Micro- and nanofabrication with a combined focused ion beam/STM	540
Teague, E. C., The NIST Molecular Measuring Machine: A long-range STM for dimensional metrology	545
 14. GEOLOGY APPLICATIONS (G. Jarosevich)	
McKay, G., Analysis of rare earth elements by electron microprobe	549
Fodor, R. V., Malta, D. P., Bauer, G. R., Jacobs, R. S., Microbeam analyses of rare-earth element phosphate in basalt from Kahoolawe Island, Hawaii	554
Smith, D. G. W., Identification of rare earth and yttrium minerals by use of the MinIdent database	559
Harrington, C. D., Raymond, R., Jr., SEM analysis of rock varnish chemistry: A geomorphic age discriminator	563
Stuart, C. J., Liang, L. C., Toney, J. B., A new technique utilizing SEM at low temperature and voltage to analyze native-state reservoir rocks	566
Raymond, R., Jr., Harrington, C. D., Lithologic controls on rock varnish formation as determined with SEM	567
Knight, C. L., Williamson, M. A., Bodnar, R. J., Raman spectroscopy of zeolites: Characterization of natural zeolites with the laser Raman microprobe	571
Williamson, M., Knight, C. L., Characterization of authigenic zeolite phases in vapor-dominated hydrothermal systems with micro-Raman spectroscopy	574
O'Grady, M. R., Bodnar, R. J., Hellgeth, J. R., Conroy, C. M., Taylor, L. T., Knight, C. L., Application of Fourier transform IR microprobe analysis of petroleum fluid inclusions in the geological sciences	579
Vanko, D. A., Knight, C. L., Analysis of fluid inclusions in oceanic rocks by laser Raman microprobe techniques	583
 15. SECONDARY ION MASS SPECTROMETRY (D. S. Simons)	
Chabala, J. M., Levi-Setti, R., Yang, Y. L., Advanced imaging and analysis techniques with a scanning ion microprobe	586
Vander Wood, T. B., Bowers, C., Interpretation of SIMS spectra by linear programming techniques	591
Michiels, F. P., Vanhoolst, W. K., Van Espen, P. E., Adams, F. C., Aspects of quantification of ion microscope images recorded with a camera-based detection system	594
Hunter, J. L., Jr., Corcoran, S. F., Linton, R. W., Griffis, D. P., A high-sensitivity, high dynamic range SIMS digital image acquisition and processing system	597
Simons, D. S., Fassett, J. D., Kelly, W. R., Determination of uranium and thorium in oyster tissue by isotope-dilution SIMS	600
Corcoran, S., Parikh, N., Griffis, D. P., Linton, R. W., Characterization of a fast atom source for SIMS	605
Author index	609

NOTE. Because of last-minute changes in the order of papers, some page numbers had to be adjusted, as follows:

Page 130 is followed by pp. 130A-D
Page 206 is followed by pp. 206A-B
Page 226 is followed by pp. 226A-B
Pages 375-376 and 387-390 have been omitted

Officers of the Microbeam Analysis Society

MAS Executive Council

President: D. B. Wittry, University of Southern California, Los Angeles, Calif.
President Elect: Alton D. Romig Jr., Sandia National Laboratories, Albuquerque, N.M.
Past President: W. F. Chambers, Sandia National Laboratories, Albuquerque, N.M.
Treasurer: Harvey Freeman, Dow Corning Corp., Midland, Mich.
Secretary: J. T. Armstrong, California Institute of Technology, Pasadena, CA 91125
(818) 356-6253

Directors

Serge Cvikevich, IBM GTD, Hopewell Junction, N.Y.
Peter Ingram, Research Triangle Institute, N.C.
Rich Lee, ETC, Monroeville, Pa.
Rich Linton, University of North Carolina, Chapel Hill, N.C.
Jon McCarthy, Tracor Northern, Middleton, Wis.
John Small, National Institute of Standards and Technology, Gaithersburg, Md.

Honorary Members

L. S. Birks, Naval Research Laboratory, USA
Raymond Castaign, University of Paris (Orsay), France
A. A. Chodos, Monrovia, Calif., USA
V. E. Cosslett, University of Cambridge, Great Britain
Peter Duncumb, Tube Investment Research Laboratories, Great Britain
T. A. Hall, University of Cambridge, Great Britain
K. F. J. Heinrich, National Institute of Standards and Technology, USA
R. E. Ogilvie, Massachusetts Institute of Technology, USA
S. J. B. Reed, University of Cambridge, Great Britain
Gunji Shinoda, Osaka University, Japan
D. B. Wittry, University of Southern California, USA

1988 MAS Paper Awards

Birks Award: W. Rehbach and P. Karduck, "Verification of the Gaussian $\phi(\rho z)$ approach and the determination of the limits of validity by trace experiments and Monte Carlo calculations"

Macres Award: J. A. Small, D. E. Newbury, R. L. Myklebust, C. E. Fiori, A. A. Bell, and K. F. J. Heinrich, "An electron/x-ray optical bench for the measurement of fundamental parameters for electron-probe microanalysis"

Castaign Award: J. S. Hepburn, H. G. Stenger, and C. E. Lyman, "Rh and Pt distributions in Rh/Al₂O₃ and Pt/Al₂O₃ catalysts"

Procter & Gamble Award: K. N. Colonna and G. Oliphant, "Capacitation and decapacitation: Ionically distinct physiological states of the mammalian sperm"

1989 MAS Presidential Awards

Outstanding contributions to microanalysis: James Hillier

Outstanding service to the Society: William F. Chambers

Special service award: Ron Gooley

K. F. J. Heinrich Award for outstanding young MAS scientist: Richard Leapman

Sustaining Members' Information

AMRAY, INC.
160 Middlesex Turnpike
Bedford, MA 10730

Product Contacts:

Technical Data:	Dr. Sheldon Moll	(617) 275-1400
Delivery & Prices:	Gerald Cameron, Jr.	(617) 275-1400

Product Line: Manufacturer of scanning electron microscopes

Regional Sales Offices:

George Bruno	New England	(617) 275-8310
Ed Griffith	Mid-Atlantic North	(609) 662-3922
Tom Richards	Mid-Atlantic South	(609) 662-3922
Ken Lindberg	Southeast	(305) 767-4220
Rich Lantz	Southwest	(214) 247-3542
Gerry O'Loughlin	Northern California	(408) 748-1300
Don Brayton	Southern California	(408) 748-1300
Fred Feuerstein	Mid-West	(312) 695-6117
Matt Gohlke	Mid-East	(216) 579-0035

BIO-RAD, MICROSCIENCE DIVISION

19 Blackstone Street
Cambridge, MA 02139

Product Contact: Robert Schoonhoven (617) 864-5809

Product Line: Laser confocal fluorescent imaging systems, vacuum evaporators, SEM/TEM consumables, SEM/TEM processing equipment.

Regional Sales Offices:

James Steele, 780 Montecue Expressway, San Jose, CA 95131 (408) 435-5530

CAMBRIDGE INSTRUMENTS, INC.

P.O. Box 123
Buffalo, NY 14240

Product Contact: Peter W. Boutell (716) 891-3009

Product Line: Scanning electron microscopes - EDX and WDX x-ray systems.

CAMECA INSTRUMENTS, INC.

2001 West Main Street
Stamford, CT 06902

Product Contact: Thomas C. Fisher (203) 348-5252

Product Line: Scanning electron microprobes and secondary ion mass spectrometers.

DAPPLE SYSTEMS

355 West Olive, Suite 100
Sunnyvale, CA 94086

Product Contact: Bill Stewart (408) 733-3283

Product Line: Microcomputer-based analytical instrumentation including automatic image analysis and energy-dispersive x-ray microanalysis.

THE DIRECTORATE, INC.

1418 Upfield Dr.
Carrollton, TX 75006

Product Contact: Joseph Bartush (214) 466-6465

Product Line: Remarket and lease: Test, lab, and inspection equipment.

Regional Sales Office:

Jim George, 624 Evelyn Ave., Sunnyvale, CA 94086

ELECTROSCAN CORPORATION

100 Rosewood Drive
Danvers, MA 01923

Product Contacts:

Technical Data: Dick Harniman (617) 777-9280
Delivery and Prices: Barry A. Weavers (617) 777-9280

Product Line: Multi-environmental electron microscopes - operating up to 20 torr specimen chamber pressure. Secondary and backscattered high-resolution imaging is available throughout this pressure range (from 10 to minus 5 torr to 20 torr). Dynamic imaging provided by variable specimen chamber control and real-time (TV) imaging of any experiment irrespective of specimen's physical state.

Regional Sales Offices:

San Francisco: Rick Kanishak (415) 831-9986
North East: early 1988
Middle Atlantic: early 1988
Southern California: early 1988

EMTEK (Electron Microprobe Technologies Corp.)

24932 Avenue Kearny, Suite 1
Valencia, CA 91355

Product Contacts: D.J. Bleu, President

Technical Data: Bob Matchett (805) 257-1215
Delivery & Prices: Ed North (805) 257-1215

Product Line: Service and provision of parts and upgrades for SEMQ scanning electron microprobes.

Regional Sales Offices:

Donald P. Leshner	Warren, Ohio	(216) 856-4830
Roland T. Henry	Morton, Pennsylvania	(215) 544-0924
Gernot Winkler	Langen, West Germany	49-6103-24064

GATAN, INC.

6678 Owens Drive
Pleasanton, CA 94566

Product Contact: Kevin Scudder (412) 776-5260

Product Line: Specimen preparation equipment for material science, specialized TEM specimen holders, parallel-detection electron energy loss spectrometers.

Regional Sales Office:

Kevin Scudder, 780 Commonwealth Dr., Warrendale, PA 15086 (412) 776-5260

GW ELECTRONICS, INC.

6981 Peachtree Industrial Boulevard
Norcross, GA 30092

Product Contact: Robert A. Lewis (404) 449-0707

Product Line: Electronic accessories for scanning electron microscopes and microprobes.

INSTRUMENTS SA, INC.

6 Olsen Ave.
Edison, NJ 08820

Product Contact:

Bruce D. Perrulli (201) 494-8660
Susan Maher (201) 494-8660

Product Line: MOLE - Raman molecular microprobes, contact Bruce D. Perrulli; Surface analysis microprobes, contact Susan Maher.

INTERNATIONAL SCIENTIFIC INSTRUMENTS, INC.

1457 McCarthy Blvd.
Milpitas, CA 95035

Product Contact: Dr. Robert Buchanan (408) 945-2233

Product Line: Scanning electron microscopes and transmission electron microscopes.

JEOL USA, INC.

11 Dearborn Road
Peabody, MA 01960

Product Contacts: Charles Nielsen, Steve Hamilton (617) 535-5900

Product Line: EPMA, Auger, SEM, TEM, NMR, mass spectrometers.

Regional Sales Offices:

Thayer Brickman, Jack Francis, JEOL USA, Inc., 3500 Bayshore Road,
Palo Alto, CA 94303 (415) 493-2600

KEVEX INSTRUMENTS, INC.

355 Shoreway Road
San Carlos, CA 94070-1308

Product Contacts:

Technical Data:	Tom Stark/Nancy Wolfe	(415) 591-3600
Delivery & Prices:	Helen J. Barker	(415) 591-3600

Product Line: Energy-dispersive x-ray spectrometers for materials analysis including instrumentation for EDS, WDS, EELS, and digital image processing.

Regional Sales Offices:

Frank Mannino, 9989 Windsor Way, San Ramon, CA 94583 (415) 828-2188
Home: (415) 828-1655

Rick Cumby, P.O. Box 850820, Mesquite, TX 75185-0820 (214) 226-0182
Ans. Serv.: (214) 699-1944 Home: (214) 240-4095

Dan Polakowski, 9918 Scots Circle, Crystal Lake, IL 60014 (815) 455-8448
Home: (815) 455-8444

Vic Balmer, 7600 Primavera Way, La Costa, CA 92009 (619) 436-2932
Home: (619) 944-1063

Joe Piersante, 16 Barberry Hill Dr., Gainesville, GA 30506 (404) 887-9965
Home: (404) 889-1363

Robert Fucci, 60-C Charles Dr., Manchester, CT 06040 (203) 646-6325
Home: (203) 645-6373

Rich Fiore, Rd. 3 Box 99, Harvey's Lake, PA 18618, (717) 639-2330
Home: (717) 639-2021

Karen McGranahan, 19635 Cottonwood Trail, Strongsville, OH 44136
(216) 238-8666 Home: (216) 572-3606

Barry Weavers, 7 Valley Forge Dr., North East, MD 21901 (301) 287-3955
Home: (301) 287-5285

Rod Palmberg, P.O. Box 200, Mercer Island, WA 98040 (206) 232-3444
Home: (206) 232-6097 FAX: (206) 232-8323

Karl L.R. Mahler, P.O. Box 505, Thornhill, Ontario, Canada L3T 4A2
(416) 731-2161 Home: (416) 889-8907 FAX: (416) 731-2162

Kevex East Application Lab, 50 Valley Stream Parkway, Suite 180, Great
Valley Corporate Center, Malvern PA 19355
Office: (215) 647-4866 FAX: (215) 889-9050

R.J. LEE GROUP, INC.

350 Hochberg Road
Monroeville, PA 15146

Product Contact: Ed Bollinger (412) 325-1776

Product Line: Analytical services, consulting, contract research, materials characterization, TEM, SEM, PC-based microimaging.

LINK ANALYTICAL INC.

Microscope Products
8017 Excelsior Drive
Madison, WI 53717

Product Contacts:

Technical Data: Helen Correy (608) 836-3200
Delivery & Prices: Donald Grimes (608) 836-3200

Product Line: Advanced energy-dispersive x-ray microanalysis and imaging systems.

Regional Sales Offices:

Paul Smith, 790 Turnpike St., North Andover, MA 01845 (508) 682-4323
Pat Campos, 240 Twin Dolphin Dr, Suite D, Redwood City, CA 94065

(415) 595-5465

Richard Bonney, 1010 Huntcliff, Suite 1350, Atlanta, GA 30352 (414) 642-7666
Graham Bird, 5300 Hollister, Suite 230, Houston, TX 77040 (713) 642-0200

McCRONE ASSOCIATES, INC.

850 Pasquinelli Drive
Westmont, IL 60559

Product Contacts:

Dr. John Gavrilovic (312) 887-7100
Dr. Timothy Vander Wood (404) 368-9600

Product Line: Materials characterization, surface analysis, particle characterization and identification, forensic contamination, pharmaceuticals, dust, corrosion, semiconductors, wafers, electronics. Instruments available to apply: EMA, SIMS, ESCA, Auger, Raman, SEM, AEM, ultramicrotomy, class 100 cleanroom.

Regional Sales Offices:

McCrone Associates/Atlanta, Dr. Timothy Vander Wood, 1412 Oakbrook Drive, Norcross, GA 30093 (404) 368-9600

MICRON, INC.

3815 Lancaster Pike
Wilmington, DE 19805

Product Contact: James F. Ficca, Jr. (302) 998-1184

Product Line: Analytical services including SEM, EPA, TEM, XRF, XRD, OES, DSC, FTIR, ESCA.

MICROSPEC CORPORATION

45950 Hotchkiss Street
Fremont, CA 94539

Product Contact: H.S. Culver (415) 656-8820

Product Line: WDX-3PC wavelength-dispersive x-ray spectrometer system for use on SEMs.

NISSEI SANGYO AMERICA, LTD.

HITACHI SCIENTIFIC INSTRUMENT DIVISION

460 Middlefield Road
Mountain View, CA 94043

Product Contact: Hideo Naito (415) 961-0461

Product Line: Scanning electron microscopes, transmission electron microscopes, field emission.

Regional Sales Offices:

Nissei Sangyo America, Ltd., 2096 Gaither Rd., Rockville, MD 20850
Nissei Sangyo America, Ltd., 1701 Golf Rd., Suite 401, Rolling Meadows,
IL 60008

Nissei Sangyo America, Ltd., 89 Galaxy Blvd., Suite 14, Rexdale,
Ontario M9W 6A4, Canada

OVONIC SYNTHETIC MATERIALS, INC.
1788 Northwood
Troy, MI 48084

Product Contact: Steven A. Flessa (313) 362-1290

Product Line: The OVONIX line of multilayer x-ray monochromators are replacing natural crystals and Langmuir-Blodgett pseudocrystals for light-element analysis in WD/XRF and EPMA spectrometers. Increased peak intensities and suppression of higher orders improves analysis of Al-B in XRF and of Na-Be in EPMA.

OXFORD INSTRUMENTS NORTH AMERICA, INC.
3A Alfred Circle
Bedford, MA 01730

Product Contact: Glenn Kinnear (617) 275-4350

Product Line: Accessories for SEM and TEM, including the following: Liquid nitrogen and liquid helium cold stages, cryo-preparation systems, heating stage, tensile stage, automatic and cathodoluminescence systems.

PERKIN-ELMER
6509 Flying Cloud Dr.
Eden Prairie, MN 55344

Product Contacts:
Technical Data: Greg Carpenter (612) 828-1600,
Delivery & Prices: Customer Order Dept. (800) 328-7515
FAX: (612) 828-6322

Product Line: ESCA, Auger, SIMS and MBE instruments, vacuum products.

Regional Sales Offices:
Boston: 5 Medallion Center, Greeley St., Merrimack, NH 03054
(800)523-2310; In NH (603)424-6100, FAX: (603)424-0902

New York: 5 Progress St., Edison, NJ 08820
(201)561-6730, FAX: (201)561-0268
Wash. DC: 7310 Ritchie Hwy., Suite 520, Glen Burnie, MD 21061
(301)761-3053, FAX: (301)761-0479
Cleveland: 24700 Chagrin Blvd., Suite 211, Cleveland, OH 44122
(216)464-2370, FAX: (216)464-5919
Denver: 14818 W. 6th Avenue, PHI Suite, Golden, CO 80401 (303) 271-0040
San Jose: 151 Bernal Road, Suite 5, San Jose, CA 95119
(408)629-4343, FAX: (408)629-7740

PRINCETON GAMMA-TECH
1200 State Rd.
Princeton, NJ 08540

Product Contacts:
Technical Data: Doug Skinner (609) 924-7310
Delivery and Prices: Mark Smith (609) 924-7310

Product Line: Princeton Gamma-Tech's product line consists of the PGT System 4+ microanalysis system with complete EDS x-ray analysis capabilities for SEM, TEM, and STEM. Also highlighted in our product line is PGT Imagecraft, digital image processing, enhancement, and quantitative image analysis for light microscopy as well as electron microscopy.

QBI INTERNATIONAL
2034 Golden Gate Avenue
San Francisco, CA 94115-4399

Product Contact: Quentin A. Brown (415) 929-1622

Product Line: The SEMSCAN, a wavelength dispersive spectrometer with optimum performance for the analysis of light elements and resolution of peak overlaps. SEMSCAN control and data collection are accomplished with a personal computer system.

SPECTRA-TECH, INC.
652 Glenbrook Road
P.O. Box 2190-G
Stamford, CT 06906

Product Contacts:

Technical Data:	Cindy Friedman	3 University Plaza
Delivery & Prices:	Faith Cornick	Hackensack, NJ 07601
		(201)646-0351

Product Line: FT-IR microscopes and accessories

Regional Sales Offices:

Tom Driscoll, Spectra-Tech, 3 University Plaza, Hackensack, NJ 07601

SPI SUPPLIES

DIVISION OF STRUCTURE PROBE, INC.

P.O. Box 656
West Chester PA 19381-0656

Product Contact:

Technical Data:	Ms. Sue Morris	(215) 436-5400, FAX (215) 436-5755
Delivery & Prices:	Ms Rose Singleton	(Tel. and FAX as above)

Product Line: Sample preparation equipment and consumable supplies for electron microanalytical laboratories, including standards, carbon coaters, plasma etchers, table-top vacuum evaporators. Laboratory services include SEM/EDS, TEM/STEM/SAED, WDS, LM, XRD, on metals, ceramics, refractories, polymers, electron devices, and other materials science systems.

Laboratories (Structure Probe, Inc.):

Mr. A. Jabbar, 230 Forrest St., Metuchen, NJ 08840 (201) 549-9350

Dr. A. Blackwood, 63 Unquowa Rd., Fairfield, CT 06430 (203) 254-0000

Mr. Ronald Bucari, 1015 Merrick Rd., Copiague, L.I., NY (516) 789-0100

Regional Sales Offices:

SPI Supplies/Canada, Mrs. Pnina Rosenberg, PO Box 187, Station "T", Toronto, Ontario, Canada M6B 4A1 (416) 787-9193

Microsource EM Supplies, Ms. Hilary Constable, 10 Combe End, Crowborough,

E. Sussex, TN6 1NH United Kingdom 892-663375

Rontgenanalytik Vertriebs GmbH, Mr. Ulrich Theis, Rosenweg 18,

6204 Taunusstein-Neuhof, F.R. Germany 06128/7 10 80

Techno Chemical Co., Mr. Yasu Ueki, Kobayashi Building 302, Honkomagome 1 Chome,

Bunk-ku, Tokyo 113, Japan 03-947-7310

M.E. TAYLOR ENGINEERING, INC.

21604 Gentry Lane
Brookeville MD 20833

Product Contact: M.E. (Gene) Taylor

Product Line: Scintillators, SEM supplies, secondary and backscatter electron detectors, vacuum foreline traps, specimen stubs, filaments and related items. Precision machine work and scientific glass blowing. Repair most EDS detectors.

Regional Sales Office:

Dave Ballard, 15817 Crabbs Branch Way, Rockville, MD 20855 (301) 330-0077

TRACOR NORTHERN, INC.

2551 W. Beltline Hwy.
Middleton, WI 53562

Product Contacts:

Technical Data:	Jerry Shattuck	(608) 831-6511
Delivery & Prices:	John Santroch	(608) 813-6511

Product Line: Scanning electron microscopes, energy-dispersive x-ray microanalysis systems, image analysis systems for microscopy, confocal light microscopes.

Regional Sales Offices:

TN-East: Don Dunkin, 4001 G, Greentree Executive Campus,

Marton, NJ 08053 (609)596-6335

TN-South: Tom Levesque, 4270 Kellway Circle, Dallas, TX (214) 380-1942

TN-Midwest: Dennis Masaki, 6313 Odana Rd., Suite 2N, Madison, WI 53719
(608) 274-1666

TN-West: Mike Ivey, 70 Whitney Place, Fremont, CA 93539 (415) 656-9898

VG INSTRUMENTS, INC.
32 Commerce Center
Cherry Hill Drive
Danvers, MA 01923

Product Contact: Bob Michaels (508) 777-8034
Product Line: UHV analytical instrumentation; those pertinent to MAS include high-resolution Auger, UHV dedicated STEM, imaging SIMS.

Regional Sales Offices:
Howard Danaceau, 966 Hungerford Dr., Rockville, MD 20850
Randy Aramburn, 1128 Sunset Dr., Roanoke TX 76262

CARL ZEISS, INC.
One Zeiss Drive
Thornwood, NY 10594

Product Contact: Dr. Dieter K. Kurz (914) 747-1800

Product Line: Transmission and scanning electron microscopes.

Regional Sales Offices:
Dietrich Voss, PO Box 2025, Willis, TX 77378 (409) 856-7678
Virginia Hanchett, 14870 Marie Court, San Martin, CA 95046 (408) 779-0100

OVERVIEW OF LASER MICROPROBE MASS SPECTROMETRY TECHNIQUES

L. Van Vaeck and R. Gijbels

During the past decades, the rate of growing of methods becoming available or even routinely applied for micro- and/or surface analysis of solids has been absolutely breathtaking. As a convenient way to survey these techniques, Fig. 1 gives schematically the fundamental basis of most techniques in terms of input probes and outcoming fluxes.¹ Excitation involves eight major mechanisms: particle beams (electrons, ions, neutrals, photons) as well as electric and magnetic fields, sonic waves, and thermal energy. With the exception of magnetic fields, these probes can give rise to the emission of one or more particle beams. During analysis, four types of information are aimed at: particle identification [e.g., in mass spectrometry (MS) polarity and m/z of ions], spatial distribution (e.g., imaging), energy distribution, and number or intensity. So at least 32 links between incoming and outgoing arrows in Fig. 1 can be made. Screening of

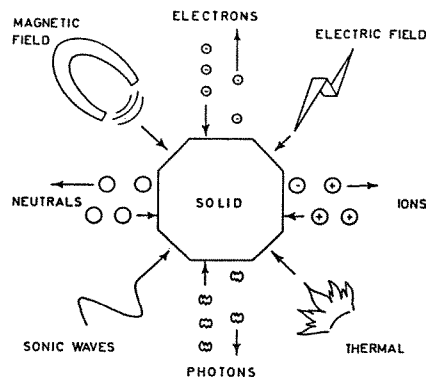


FIG. 1.--Pictorial representation of micro- and surface-analytical techniques as a function of combinations between probes in and particles out.¹

The authors are at the Department of Chemistry, University of Antwerp, B-2610 Wilrijk, Belgium. L. Van Vaeck is indebted to NFWO Belgium as a Research Associate.

TABLE 1.--Survey of some micro- and surface-analytical techniques.

Probe		Method + acronym
In	Out	
electrons	electrons	Auger electron spectroscopy (Auger) electron energy loss spectroscopy (EELS)
	photons	electron probe X-ray micro-analysis (EPXMA)
	ions	spark source mass spectrometry (SSMS)
ions	ions	secondary ion mass spectrometry (SIMS)
	neutrals	sputtered neutrals mass spectrometry (SNMS)
	photons	proton induced X-ray emission (PIXE)
neutral	ions	fast atom bombardment mass spectrometry (FABMS)
photons	photons	Raman microprobe Fourier transform infrared spectroscopy (FTIR) X-ray fluorescence (XRF)
	ions	laser (microprobe) mass spectrometry
	electrons	electron spectroscopy for chemical analysis (ESCA) X-ray or UV photoelectron spectroscopy (XPS, UPS)
	neutrals	laser ablation based techniques (see text)
electric field	ions	field ionisation mass spectrometry
thermal energy	ions	direct insertion probe mass spectrometry (Curie point) pyrolysis mass spectrometry thermal ionisation mass spectrometry

Laser microprobe mass spectrometry (LMMS) employs the photons-in and ions-out route. But LMMS is only one step in a 20-year tradition of use of lasers in MS. Before, the applications in inorganic analysis, where emphasis has traditionally been on element quantitation, have been elaborated separately from those in organic chemistry, where the prime interest has concerned structural characterization of molecules. The spectrum of techniques that has emerged in both fields will be addressed in the first two sections of this paper.

LMMS has introduced the aspect of analysis with high spatial resolution. Moreover, the remarkable flexibility of the instrument, permitting operation under largely different local conditions, has made it possible to overcome the traditional gap between organic and inorganic analysis. So the third section will deal with LMMS in the context of other recent techniques for microanalysis of solids and surfaces.

Finally, emission of ions is inevitably combined with generation of neutrals. Post-ionization techniques offer promising prospects here. A fourth section is dedicated to laser ablation based techniques.

Lasers in Inorganic Mass Spectrometry

Several review papers are available²⁻⁴. In fact a lot of work in this area is concerned with the possible application of lasers as an alternative for spark source mass spectrometry (SSMS) for very low amounts of sample (less than 10^{-8} g) and/or insulating materials.

One of the first attempts was reported by Honig and Woolston on a double-focusing magnetic instrument.⁵ A crater 150 μm in diameter and 125 μm deep was produced, yielding $2 \cdot 10^{14}$ ions from $2 \cdot 10^{17}$ atoms. Pulse duration was 50 μs . The high ion current has given rise to space charge broadening problems. Hence, Fenner and Daly presented a combination of a Q-switched ruby laser with time-of-flight (TOF) analysis.⁶ Nonconducting samples, such as glass, ceramic whiskers, and human hair, in the range 10^{-8} to 10^{-10} g could be handled, but mass resolution was problematic. Research has then continued along these two main directions. On the one hand, double-focusing Mattauch-Herzog instruments have been equipped with more or less focused lasers. The low transmission has required repetitive irradiation (Fig. 2a). In fact, these instruments primarily try to exploit the inherent advantages of laser ionization of solids for quantitation. On the other hand, Eloy worked on the microprobe idea (Fig. 2b).⁷ With a single magnetic sector, equipped with a specially designed panoramic electro-optic detector, TOF measurements have been achieved on a variety of dielectric samples, e.g., biological and geological materials. Finally, the LMMS instruments have been developed with a short single pulse laser irradiation combined with a TOF analyzer with ion reflector to compensate for the initial energy spread

(Fig. 2c). Table 2 compares the major characteristics from different in-house developed instruments with the commercial versions, both for the modified SSMS (EMAL, USSR) and the microprobes (LAMMA, FRG, and LIMA, U.K.).⁸⁻¹⁸

Besides the obvious advantages for dielectric samples or materials hard to convert into electrodes, interest in laser ionization as an alternative to SSMS arises from the quite narrow range in which the relative sensitivity factors (RSF) lie. Matus et al.¹⁹ compared results from SSMS and laser ionization for a geological standard (ocean island basalt). More than 80% of the RSFs for laser ionization are within a factor of 2, which is significantly better than in SSMS.

The hopes of early investigators for straightforward quantitation by LMMS have not been generally fulfilled. RSFs remain within roughly an order of magnitude but strongly depend on the matrix, which makes even semiquantitative results within a factor 5 not feasible for different materials. Hence, the applicability of the local thermal equilibrium model derived for SIMS to LMMS remains a matter of debate. It is based on the assumption that the ion yield can be assessed by use of realistic assumptions for electron density and plasma temperature. Results have been described previously and sustained by other authors.^{20,21}

Another interesting application is reported by Furman et al.²² A laser has been mounted on a Cameca 3f secondary ion mass spectrometer (SIMS) instrument. Laser irradiation has allowed direct imaging of (for example) Na, K, and Rb distributions on the surface of insulators. This experiment corresponds to a photons-in and ions-out route but the generated particles are now characterized by mass and *spatial distribution*. Other areas of interest include the processing of materials in the sample chamber of the ion microanalyzer, e.g., monitoring of the dopant redistribution during irradiation as an alternative to the SIMS study of samples after laser annealing. Also, the problem of residual vacuum contamination (deposition of oxygen, for example) is successfully dealt with.²³

Lasers in Organic Mass Spectrometry

The report of Mumma et al.²⁴ on sodium hexylsulfonates is generally considered as the start of laser desorption (LD) MS, a soft ionization method for nonvolatile polar compounds and ionic salts. In spite of the highly destructive power of the laser beam, thermolabiles are detected as intact molecules under the cationized form in the virtual absence of decomposition or fragmentation. Another milestone has been the publication of Posthumus et al. on LDMS of thermolabile biomolecules such as oligosaccharides, peptides, digitonine, etc.²⁷ Conceived within the context of organic MS, instruments have been developed on the basis of double-focusing magnetic analyzers and quadrupole filters. Virtually all pos-

TABLE 2.--Laser ionization in elemental mass spectrometry.

	Modified spark source instruments					Microprobes			
	Conzemius et al. Iowa 1978 [8]	Janssen et al. Eindhoven 1982 [9]	Dietze et al. Leipzig 1988 [10]	Matus et al. Mainz 1988 [11]	EMAL USSR [12]	Eloy et al. Grenoble 1983 [13]	Brenna et al. Endicot 1988 [14]	LAMMA 1000 (FRG) LIMA (UK) [15-17]	LAMMA 500 (FRG) LIMA (UK) [18]
Mode	reflection					reflection			
Sample	bulk					bulk			
Laser	Nd YAG					Nd YAG			
Wavelength (μm)	1.06					.266			
Pulse duration (ns)	200	15	100	15	15	.355	3-4	15	
Repetition frequency(Hz)	1-24 K	1-50	5-50 K	1-50	1-50	1	n.r	single shot	
Energy per pulse (mJ)	1	10-100	60	15	3-5	1-3	n.r	2	
Power density (W/cm ²)	2.10 ⁹	n.r	5 10 ⁹	2.10 ¹⁰	n.r	10 ⁸ -10 ¹⁰	n.r.	10 ¹¹	
Geometry ¹	90/60	45/45	45/45	45/45	60/90	90/60	33/90	45/90 90/90	-90/90
Crater diameter (μm)	25	20	10-500	50	50	5-100	10	2-3	1
Crater depth (μm)	3	1-10	1-300	3	1	.2	n.r.	1	n.a.
Mass spectrometer type	Mattauch Herzog double focussing MS					TOF/magnet 2			
Transmission	n.r	n.r	n.r	10 ⁻⁶	n.r	1-5 %	n.r	1-10 %	
Mass resolution	2,000	3,000	3,000	10,000	2,000	100	105	500-800	
Mass range	7-250	7-250	7-250	7-250	≤ 500	7-250	n.r.	"unlimited" ⁴	
Detection photoplate	yes	yes	yes	yes	yes	converter ³	n.a.	not	
SEM	yes	not	not	not	not	yes	yes	yes	
Ions polarity	+	+	+	+	+	+	+	+/	+/
s/m charged	5	s/m	s	s	s/m	s/m	s	s/m	s
Absolute detection limit (g)	10 ⁻¹⁰ (photo) 10 ⁻¹³ (SEM)	10 ⁻¹²	n.r	n.r	n.r	10 ⁻¹⁶	n.r	10 ⁻²⁰	

1 geometry according to conventions of Conzemius et al [3] given in angles (°) of laser and ion beam vs. sample surface

2 TOF measured within magnetic sector (cf figure 2)

3 electro-optical panoramic converter - SEM (cf figure 2)

4 mass range unlimited unless by mass resolution

5 singly or multiply charged ions

Abbreviations

FTMS Fourier transform MS
TOF time of flight
SEM secondary electron multiplier
n.r not reported
n.a. not applicable

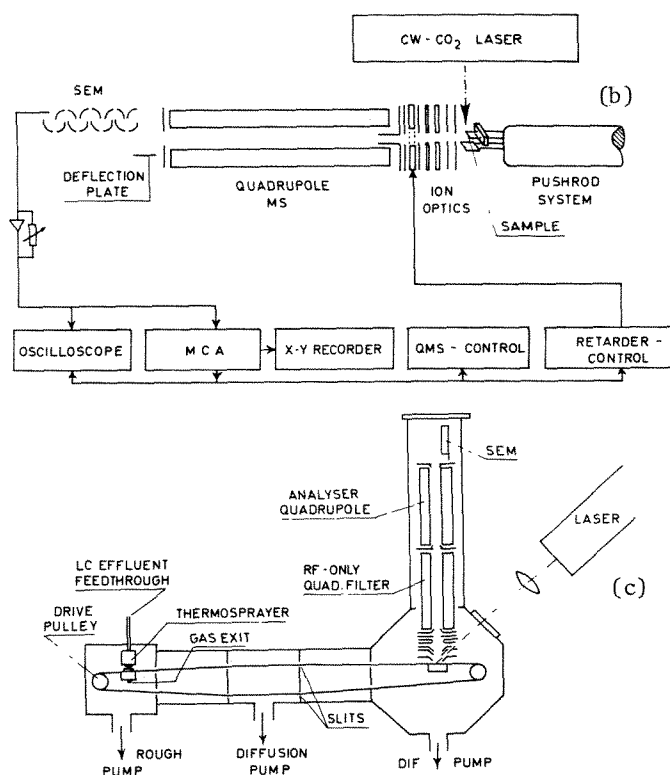
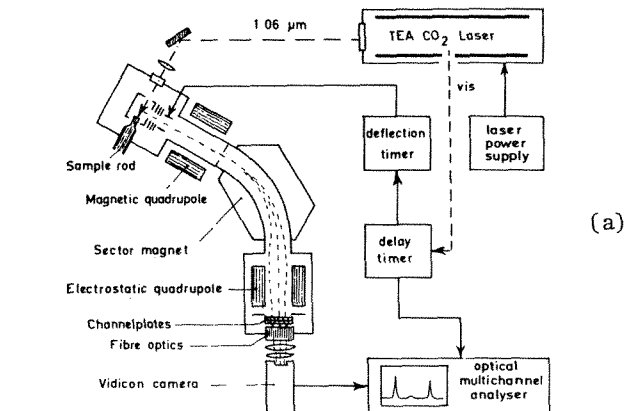
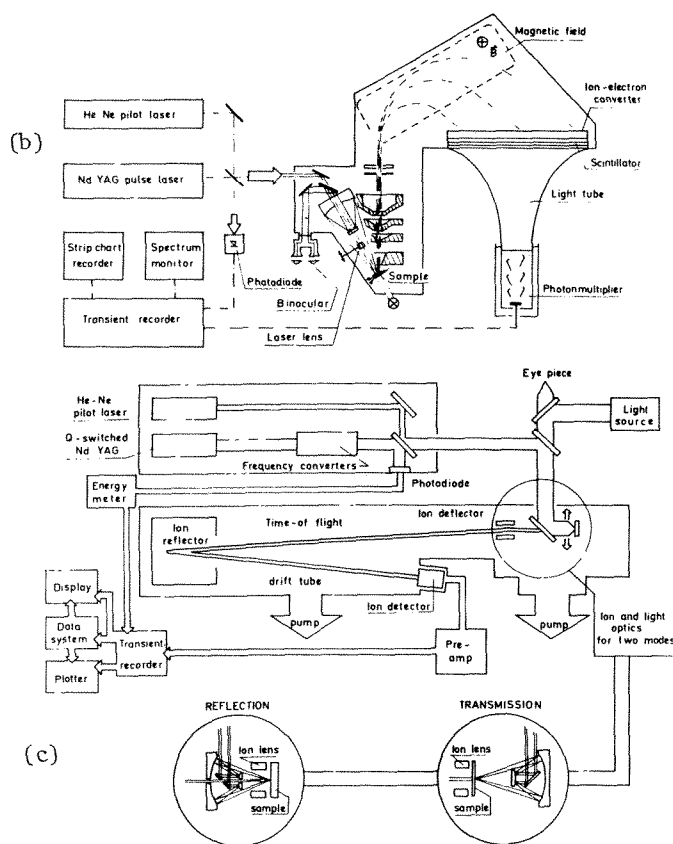
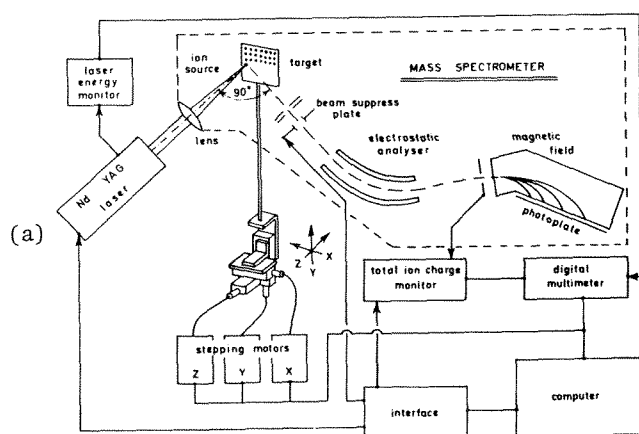


FIG. 2.--Typical examples for laser ionization in elemental mass spectrometry with (a) modified spark source instrument,¹¹ (b) experimental microprobe with magnetic sector,²⁴ (c) commercial LIMA 2A microprobe with time-of-flight MS and reflector.²⁵

FIG. 3.--Typical examples for laser ionization in organic mass spectrometry with experimental set-ups based on (a) magnetic sector instrument,²⁷ (b) quadrupole,³⁷ (c) moving-belt LC-MS interface.³⁴

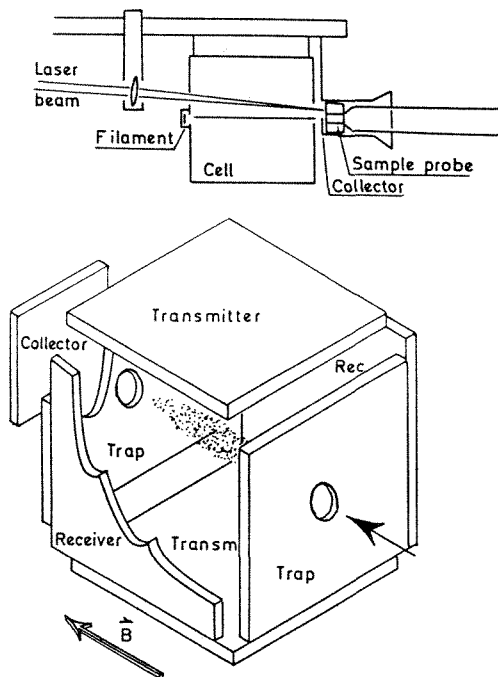
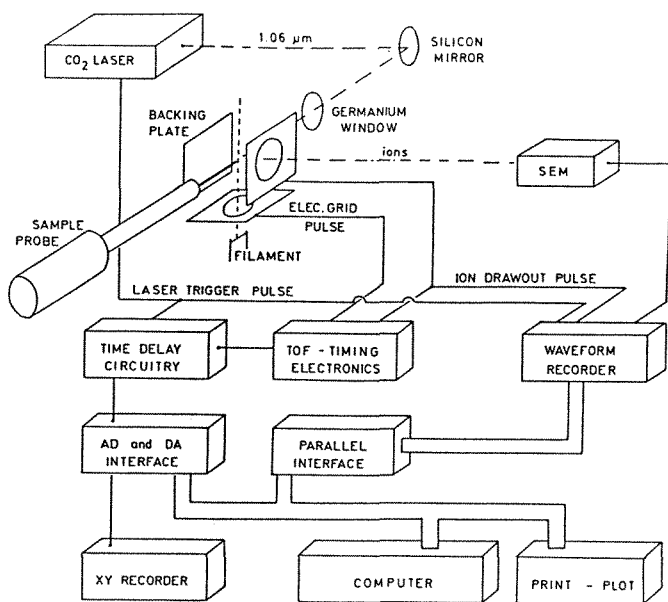


FIG. 3. (Cont'd): Experimental set-ups based on (d) time-of-flight with draw-out pulse,³⁰ (e) Fourier-transform MS.³⁵ (For more details, see Table 3).

sible types of lasers, continuous and repetitively pulsed, with various wavelengths, pulse duration, etc., and several sample geometries, including a modified moving-belt liquid chromatography (LC) MS interface, have been tried (cf. survey in Table 3 and representative examples in Fig. 3). Here again, the commercial LMMS equipment deserves an appropriate place, though the focusing into a micrometer spot is not required for purely mass spectrometric studies.

In fact, all LDMS results for organic compounds are largely comparable. Laser wavelength, pulse duration, power density, etc., do not seem to be critical. Initial instruments for rather bulky samples normally use power densities in the range up to 10^7 W/cm², mostly in the reflection geometry. In contrast, LMMS results show unexpected features, i.e., extensive fragmentation, more protonation instead of cationization, thermal degradation, and electron (capture) ionization. The relative abundance of these processes may depend on the local analyzing conditions. Also, wavelength has a pronounced effect on the kind of information, as evidenced by work at 532 nm instead of 266 nm. This disagreement can be partly related to the higher power density in LMMS (10^8 - 10^{11} W/cm²) and the use of thin samples, at least in the transmission mode. It has been shown that the contribution of prompt vs delayed ion formation may depend on the configuration. In fact, the actual LMMS equipment requires prompt ionization to achieve reasonable mass resolution and calibration. The experiments with draw-out pulses in time-of-flight (TOF) LDMS³⁸ sustain the idea that the incompatibility between the delayed ion formation and the specific requirements for detection in LMMS may explain the different results.

The continued research toward high masses

gives LMMS a distinct advantage. The TOF system is transparent for heavy species. Ions up to 270 000 daltons are already generated by laser microbeam irradiation but then mass resolution of the instrument becomes inadequate.³⁹ A promising alternative is offered by combination with Fourier transform (FT) MS, for which purpose the pulsed nature of laser ionization and the very limited material consumption are definite assets (Fig. 3e). The ultimate MS resolution thus achieved, extended mass range, and the possibility of fundamental studies on ion chemistry hold a great deal of promise in this field.

Comparison of LMMS with Current Microanalytical Techniques

Table 4 summarizes the major characteristics of current methods as to spatial resolution, depth profiling, obtained information, etc.

Prime assets of LMMS concern the ability to analyze conducting or insulating samples as well as the versatility to allow characterization of elemental composition, inorganic speciation, or even organic structural information. Whereas techniques as electron spectroscopy for chemical analysis (ESCA) and SIMS describe more or less indirectly the chemical environment, LMMS enables detailed identification of inorganic substances, virtually in the same way that organic chemists are used to. So far, there is no other technique by which such a wide range of information is made available from a single instrument. Moreover, sample preparation gives the possibility of rapid sputtering. Erosion of layers of the order of several micrometers is more easily achieved than with ion bombardment in (for instance) Auger electron spectroscopy, ESCA, or SIMS.

TABLE 3.--Laser ionization in organic mass spectrometry.

Laser type	Kistemaker et al Amsterdam 1978 [27]	Stoll et al Bonn 1979 [28]	Cotter et al Baltimore 1980 [29]	Heresch et al Vienna 1980 [31]	Cooks et al Lafayette 1981 [32]	Hardin et al Houston 1981 [33]	Wilkins et al Riverside 1985 [35]	BRUKER	LMMS
	TEA-CO ₂	CO ₂	TEA-CO ₂	Nd:YAG	Nd:YAG	dye	TEA-CO ₂	abl Nd:YAG ins. dye	Nd:YAG
Mode	pulsed	cont.	pulsed	pulsed	Q-switch	pulsed	pulsed	pulsed	Q-switch
Wavelength (μm)	1.06	1.06	1.06	1.06	1.06	483	1.06	abl 1.06 ins. .27-.3	.266
Pulse duration (ns)	150	10 ⁵	40	8 10 ⁴	10	5-7	40	5	15
Energy (W)	n.a.	n.a.	n.a.	n.a.	n.a.	n.a.	n.a.	n.a.	n.a.
Energy per pulse (J)	.1	n.a.	7	.1	.1	10 ⁻⁴	10 ⁻⁴	ins 2.10 ⁻³	2.10 ⁻³
Spot diameter (μm)	≥102	10 ²	10 ³	5 10 ²	10 ³	10 ³	10 ³	10 ³	.5-.5
Typical power density (W/cm ²)	10 ⁶	10 ⁷ -10 ⁸	5.10 ⁶	10 ⁴ -10 ⁶	10 ⁸	10 ⁷	10 ⁸	n.r	10 ¹⁰ 10 ¹¹
Geometry ¹	90/0	90/0	70/0	45/45	0/90	30/90	45/90	n.a.	()90/90 45/90
Sample and support	thin layer on metal quartz	thick on metal	thin layer on polymer	thin on glass	thin on metal	thin layer on moving belt LCMS interface	thin on metal	thin on metal	thin layer or bulk
Mass spectrometer description	magnetic sector	quadrup. scan. 1 s full sp.	double foc. MS CI source	double foc MS	double foc. reversed geometry (MIKES)	quadrupole scan rate 1 p/m 5 p/m + TOF	FTMS 3T magnet	TOF + reflector	TOF reflector
Mass range	1-500	800	500	n.r	500	500	7,000	(?) ²	(?) ²
Mass resolution at m/z	300 600	20 365	500	1,000	n.r n.r	500	10 ⁴ 1,000	6,500 100	500-800 500-208
Detector type	OMA	SEM + MCA	SEM + MCA	SEM	integrat. electro- meter	SEM + box car integr. SEM + MCA	n.a.	SEM + MCA	SEM + MCA
Ions	+/-	-/-	+	+	+	+	+/-	+/-	+/-
Applications	Am.Acids, peptides nucleos, glucosides	oligosaccharides NAD R ₄ N ⁺	high MW R ₄ N ⁺	sucrose Am.Acids nucleos	sucrose	Am.Ac, peptides, nucleot. ol sac	peptides polymers	variety of peptides, biomolec.	variety of peptides, polyfunc- tionals

1 geometry angles(°) between laser and ion beam versus sample surface according to Conzemius et al [3]

2 mass range unlimited unless by mass resolution

Abbreviations

OMA optical multichannel analyser (channelplate + vidicon + multichannel analyser), MCA multichannel analyser; SEM secondary electron multiplier;
 TOF time-of-flight mass spectrometer; Am.Ac amino acids; nucleos. nucleosides, nucleot. nucleotides; NAD nicotinamide dinucleotide;
 MW molecular weight, R₄N⁺ quaternary ammonium salts, p/m pulse per mass; foc. focussing.
 abl ablation, ins. ionisation, ol sac oligosaccharides, n.a. not applicable; n.r not reported

Major problems at this moment are the poor visual resolution during sample observation, which is definitely inferior to EPMA: the confined depth-profiling capabilities, since consecutive shots do not allow the same thin-layer erosion as for example ion sputtering; the confined mass resolution, limiting the inherent possibilities of laser microbeam irradiation for analysis of very heavy ions. Quantification remains difficult, excepted for well-defined homogeneous systems analyzed under strict protocols, applicable to selected cases only. Finally, an often underestimated problem is the extreme dependency between results and local experimental conditions, i.e., at the position of laser impact, which are often hard to describe. As a result, interlaboratory comparisons tend to yield disappointing results.

In conclusion, LMMS is often quoted as a unique tool for problem solving. Usually, the combination of several techniques is required. The laser microprobe delivers rapidly complete but qualitative information on a variety of micro-objects with often negligible sample pretreatment. Indeed, the presence of organics and/or inorganics can be traced in local spots on surfaces, in the near surface region, in micrometer-size particles. Applications are found in almost all industrial and scientific research: analysis of biological materials, polymers, ceramics, metal alloys, aerosols, organic compounds, explosives, etc.

Laser Ablation

Generation of ions is inevitably accompanied by the release of neutrals (Fig. 1). Laser-ablation techniques are employed to volatilize solid samples prior to gas phase ionization. Applications are again found in elemental analysis, organic MS, and further developments of the actual LMMS instruments.

The inductively coupled plasma (ICP) source is developed for nebulized solution samples but accepts other sources so long as the material is entrained in the sample flow gas as a vapor or aerosol of solid particles or liquid droplets. Particularly attractive is the use of a pulsed laser to ablate a sample directly from the solid into the injector flow to the ICP ion source (Fig. 4a).⁴⁰ This procedure removes the need for dissolution and makes ICP directly compatible with the analysis of glasses, ceramics, geological samples, semiconductors, metals, etc.

A commercial TOF MS with a dual laser system has been available for several years now. First, organics are desorbed by IR and the gas phase is cooled by a supersonic jet pulse to insure a narrow energy distribution (Fig. 4b). Next, ionization is performed with a tunable dye laser, which enables selective ion formation and at the same time controlled fragmentation. Sensitivity is lower than in LMMS but this is a promising tool for structural characterization. Attempts in the same direction are currently under development for the microprobes.

A tempting idea concerns the combination of

two lasers in LMMS: one primarily to ablate the sample, the second for postionization of the desorbed neutrals. Schueler et al. reported a significant gain by 100-1,000 in sensitivity for GaAs.⁴² Verdun et al. complemented the LAMMA 500 with a tunable dye laser and observed a noticeably increased ion yield for copper-doped resins at two wavelengths, which are associated with the matrix absorption and the real resonance ionization of copper.⁴³

Conclusion

The fast progress in the field of laser technology permits us to forecast implementation on a variety of MS instruments, providing microprobe facilities or not, with high (10 000) or even ultimate mass resolution (FTMS). Moreover, there is a renewed interest in the use of TOF analyzers as a result of the continuing efforts to apply MS on very high molecular weight compounds, for example in the life sciences. The resulting feedback will allow further refinement of the actual LMMS and strengthen its position within the range of micro-analytical instruments.

References

1. D. Lichtman, "A comparison of the methods of surface analysis and their applications," in A. W. Czanderna, Ed., *Methods of Surface Analysis*, Amsterdam: Elsevier, 1975, 40.
2. I. Kovalev, G. Maksimov, A. Suckhov, and N. Larin, *Int. J. Mass Spectrom. Ion Phys.* 27: 101-137, 1978.
3. R. J. Conzemius and J. M. Capellen, *Int. J. Mass Spectrom. Ion Phys.* 34: 197-271, 1980.
4. R. J. Conzemius, D. S. Simons, Z. Shangkai, and G. D. Byrd, "Laser mass spectrometry of solids: A bibliography 1963-1982," *Microbeam Analysis--1983*, 301-328.
5. R. E. Honig and J. R. Woolston, *Appl. Phys. Lett.* 2: 138-139, 1963.
6. N. C. Fenner and N. R. Daly, *Rev. Sci. Instrum.* 37: 1067-1070, 1966.
7. J. F. Eloy, *Int. J. Mass Spectrom. Ion Physics* 6: 101-115, 1971.
8. R. J. Conzemius and H. J. Svec, *Anal. Chem.* 50: 1854-1860, 1978.
9. J. A. J. Janssen and A. W. Witmer, *Spectrochim. Acta* 37B: 483-491, 1982.
10. H. J. Dietze, S. Becker, I. Opausky, L. Matus, I. Nyary, and J. Frecska, *Mikrochim. Acta* 3: 263-270, 1983.
11. K. P. Jochum, L. Matus, and H. M. Suefert, *Fresenius Z. anal. Chem.* 331: 136-139, 1988.
12. *EMAL Technical Information*, Moscow: V/O Sojuzzagranpribor, 1982.
13. A. Chamel and J. F. Eloy, *SEM/1983 II*, 841-851.
14. J. T. Brenna and W. R. Creasy, "Laser microprobe Fourier transform ion cyclotron resonance mass spectrometry," *Microbeam Analysis--1988*, 377-378.
15. H. J. Heinen, S. Meier, H. Vogt, and R. Wechsung, *Int. J. Mass Spectrom. Ion Phys.*

TABLE 4.--Survey of some current microanalytical techniques.

	EPMA	Auger	ESCA (XPS, UPS)	Raman	FTIR (DRIFT, PAS, μ IR)	SIMS direct ion micro- imaging	SIMS scanning ion microprobe + liquid metal	IMMS
Probe input beam energy	electrons 20 keV	electrons ≤ 3 keV	photons X-ray, UV	photons visible	photons infrared	ions ≤ 20 keV	ions 40-60 keV	photons UV, few eV
Detected beam parameter	X-rays WDS (λ) EDS (En)	electrons energy	electrons energy	photons wavelength	photons wavelength	ions +/- m/z	ions +/- m/z	ions +/- m/z
Resolution of detector	WDS 20 eV EDS 150 eV	1-15 eV	.3-1 eV	$7\text{ cm}^{-1}(\text{sp})$ $8\text{ cm}^{-1}(\text{im.})$	$7\text{ cm}^{-1}(\text{IR})$ $2\text{ cm}^{-1}(\mu\text{IR})$	M/ Δ M 400-10 ⁴	M/ Δ M 250-500	M/ Δ M 500-800
Typically analysed area	$\sim 1\text{ }\mu\text{m}$.2 μm	$\geq 150\text{ }\mu\text{m}$ 5 μm (μESCA)	1 μm	5-10 μm	2-250 μm	$\geq 20\text{ nm}$	1 μm
Depth of information	$\leq 1\text{ }\mu\text{m}$	1-3 nm	1-10 nm	10 μm 5-50nm(PAS)	10 μm	.5 nm	1 nm	(0 1-1 μm)
Image resolution	SEM 7 nm STEM 1.5nm SEM/X STEM/X $<1\text{ }\mu\text{m}$	50-100 nm	not yes(μESCA)	μm	n.a. 1 $\mu\text{m}(\mu\text{IR})$.5 μm	20 nm	$> 1\text{ }\mu\text{m}$
Detection limit	WDS 100 ppm EDS 1,000 ppm	$\geq 1\%$	$\geq 1\%$	major	ppm	\leq ppm	10-100 ppm	? ppm
Element coverage	WDS $Z\geq 4$ EDS $Z\geq 11$	all but H, He	all but H, He	n.a.	n.a.	H-U	H-U	H-U
Direct isotope information	not	not	not	not	not	yes	yes	yes
Compound speciation	not	not	yes	yes	yes	not	not	yes
Versatile organic characterisation	not	not	not	yes	yes	yes	yes	yes
Destructive with sputtering	(not) n.a.	not yes	not yes	not n.a.	not n.a.	yes n.a.	yes n.a.	yes n.a.
In-depth profiling with sputtering	not n.a.	not yes	not yes	not n.a.	not n.a.	yes n.a.	yes n.a.	yes n.a.
Quantitation	yes	yes	yes	(yes)	yes	difficult		very difficult
Easy analysis of insulating samples	not	not	yes	yes	yes	not	not	yes
Sample in vacuum required	yes	yes	yes	not	not	yes	yes	yes

1 EDS ranges to lower elements with windowless detector

Abbreviations

DRIFT diffuse reflectance FTIR: PAS photoacoustic single detection, XPS X-ray photoelectron spectroscopy; UPS UV-photoelectron spectroscopy;
WDS wavelength dispersive spectrometry; EDS energy dispersive spectrometry; SEM scanning electron microscope; STEM scanning transmission
electron microscope; sp. spectrum; im. imaging mode; μ IR microscope FT-IR, μESCA micro ESCA, n.a. not applicable

47: 19-22, 1983.

16. T. Dingle, B. W. Griffiths, and J. C. Ruckman, *Vacuum* 31: 571-577, 1981.

17. M. J. Southon, M. C. Witt, A. Harris, and E. R. Wallach, *Vacuum* 34: 903-909, 1984.

18. H. Vogt, H. J. Heinen, S. Meier, and R. Wechsung, *Fresenius Z. anal. Chemie* 308: 195-200, 1981.

19. L. Matus, M. Seufert, and K. P. Jochum, *Int. J. Mass Spectrom. Ion Phys.* 84: 101-111, 1988.

20. E. Michiels, L. Van Vaeck, and R. Gijbels, *SEM/1984 III*, 1111-1128.

21. A. Harris and E. R. Wallach, "The application of simple statistics to the LMMS analysis of binary and ternary compounds," *Proc. Third Intern. Laser Microprobe Mass Spectrometry Workshop*, University of Antwerpen, 1986, 83-85.

22. B. K. Furman and C. A. Evans Jr., "Direct-imaging laser mass analyzer," *Microbeam Analysis--1981*, 336-338.

23. B. K. Furman and C. A. Evans Jr., "Applications of combined direct imaging laser ionization mass spectrometer to materials analysis," *Microbeam Analysis--1982*, 222-228.

24. R. Stefani, *Analysis* 16: 147-156, 1988.

25. LIMA Technical documentation, Cambridge Mass Spectrometry, Cambridge, England, 1985.

26. R. O. Mumma and F. J. Vastola, *Org. Mass Spectrom.* 6: 1373-1376, 1972.

27. M. A. Posthumus, P. G. Kistemaker, H. L. C. Meuzelaar, and M. C. Ten Noever de Brauw, *Anal. Chem.* 50: 985-991, 1978.

28. R. Stoll and F. W. Rollgen, *Org. Mass Spectrom.* 14: 642-645, 1979.

29. R. J. Cotter, *Anal. Chem.* 52: 1770-1771, 1980.

30. R. Van Breemen, M. Snow, and R. J. Cotter, *Int. J. Mass Spectrom. Ion Phys.* 49: 35-50, 1983.

31. F. Heresch, E. R. Schmid, and J. F. K. Huber, *Anal. Chem.* 52: 1803-1807, 1980.

32. D. Zakett, A. E. Schoen, and R. G. Cooks, *J. Am. Chem. Soc.* 103: 1295-1297, 1981.

33. E. D. Hardin and M. L. Vestal, *Anal. Chem.* 53: 1492-1497, 1981.

34. E. D. Hardin, T. P. Fan, C. R. Backley, and M. L. Vestal, *Anal. Chem.* 56: 2-7, 1984.

35. C. L. Wilkins, D. A. Weil, C. L. C. Yang, and C. F. Ijames, *Anal. Chem.* 57: 520-524, 1985.

36. J. Grotemeyer, U. Boesl, K. Walter, and E. W. Schlag, *Org. Mass Spectrom.* 21: 645-653, 1986.

37. R. Stoll and F. W. Rollgen, *Z. Naturforsch.* 37a: 9-14, 1982.

38. R. J. Cotter, *Anal. Chim. Acta* 159: 45-59, 1987.

39. M. Karas and F. Hillenkamp, "Ultraviolet laser desorption of ions above 10 kDa," in P. Longieville, Ed., *Advances in Mass Spectrometry*, London: Heyden and Sons, vol. 11 (in press).

40. A. L. Gray, *Analyst* 110: 551-556, 1985.

41. Bruker-Franzen Analytik GmbH., Bremen, Technical information, 1987.

42. B. Schueler, R. W. Odom, and C. A. Evans Jr., "Nonresonant multiphoton ionisation of neutrals ablated by the laser microprobe technique," *Proc. Third Intern. Laser Microprobe*

Mass Spectrometry Workshop, University of Antwerpen, 1986, 171-173.

43. F. R. Verdun, G. Krier, and J. F. Muller, *Anal. Chem.* 59: 1383-1387, 1987.

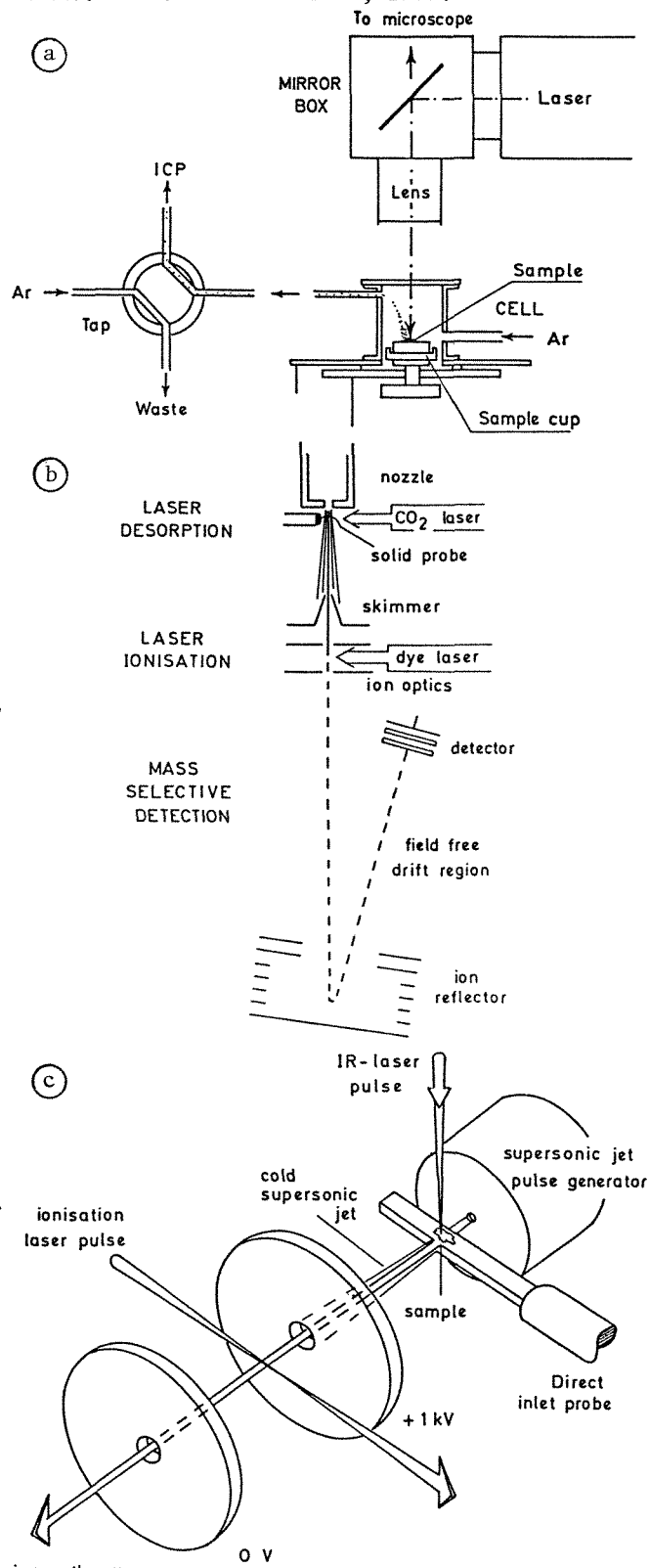


FIG. 4.--Selected examples for laser ablation exploited (a) in combination with inductively coupled plasma MS,⁴⁰ (b) in Bruker commercial two-stage laser ablation-ionization instrument.^{36,41}

Presidential Symposium: Spectroscopy in Microscopy & Microanalysis

ELECTRON MICROSCOPY TO ELECTRON MICROPROBE ANALYSIS; THE EARLY DAYS

James Hillier

The period I shall describe is the decade from 1935 to 1945. That is from 44 to 54 years ago and safely beyond the reach of most my readers' memories. Looking back, it was a most exciting, even spectacular, decade during which a remarkably small group of researchers scattered around Europe and North America took the magnetic transmission electron microscope (TEM) from a rather quiescent, theoretical concept to a reasonably reliable, practical instrument that was in serial production. By the end of the decade it had a routine resolving power of better than 10 nm, and in expert hands was reaching 1 nm. In that same period, the first attempt to build a scanning electron microscope was made and the basic principles of microprobe analysis were demonstrated. The fields of application of the TEM were expanded from essentially zero to the full range of the light microscope, with two exceptions. There was not yet any way of cutting sufficiently thin sections of biological materials. That came a few years later. Color, so valuable in light microscopy, seemed to have no counterpart in electron microscopy.

It seems almost incomprehensible in today's world that, in the middle 1930s, a few individuals were putting enormous effort into developing a high-resolution electron microscope when the only type of specimen we were sure we could examine was no more exotic than the edge of a razor blade. It was generally assumed that the electron intensity required to make a highly magnified image useful would immediately destroy any but the most refractory specimen. In 1937 Marton published his paper in which he demonstrated that a sufficiently thin suspended film of collodion could be the counterpart of the microscope slide. Immediately the entire field of very fine solid particles -- paint pigments, colloids, bacteria, viruses, etc., was opened up, followed rapidly by replicas of metallurgical specimens and shadowing techniques. Although beam-induced contamination of the specimen was recognized early, it was several years before it was recognized that the electron beam did cause some radiation damage even in the thinnest specimens. It was also several years before it was recognized that specimens sufficiently thin to avoid beam heating could still be too thick to permit the extraction of intelligence from the images because of a plethora of overlapping structures.

Why did the TEM come into being in that particular decade? My view is that the technological infrastructure of the electronics industry was coming together. Suddenly we had 50-liter/s oil-diffusion pumps instead of frac-

tional liter/s mercury pumps. We had continuously reading electronic vacuum gauges instead of McLeod gauges; rapid demountability with synthetic-rubber O-rings and gaskets instead of ground grease joints; vacuum-tight, flexible metal bellows that gave us new opportunities for designing means of manipulating within a vacuum chamber. I am sure some high-vacuum technologists may blanch as I list these developments. I understand; but to us, in 1940, they were miracles. On the electronic circuitry side, we had regulated high-voltage supplies instead of expensive and dangerous capacitor-resistor filter chains, and regulated current supplies instead of water-cooled lens coils and banks of automobile batteries. These developments, and others, speeded our work by an order of magnitude or two. Such numbers practically guarantee the historical coincidence of the development of an enabling technology and the emergence of a major new development.

Unfortunately, although the technological infrastructure that supported the design and construction of TEMs was becoming available, the instrumentation needed to study their limiting performance did not exist. Before 1940 few of us appreciated how many external and internal factors were capable of disturbing the TEM image, or the sensitivity of the images to these factors. Ultimately, the instruments themselves, being the only devices with sufficient sensitivity, had to become the means for detecting and measuring the effects of the myriads of technical problems that existed in those early instruments. The read-out was, of course, the nature and degree of blurring of the recorded image. It was because of the low intensity of the visual images in those days that the sensitivity was achievable only in the recorded image and not in real time. Not only was the read-out very ambiguous, but it related only to events that occurred during the exposure interval. For example, the effect of a thermal drift of the specimen on the image was indistinguishable from the effect of an insulating particle, somewhere near the imaging beam, that was being charged by scattered electrons and was slowly deflecting the image. Similarly, the effect of a minute mechanical vibration of the column could be indistinguishable from the two just mentioned.

Thus, the development of the TEM became an unending repetitive series of proposed hypotheses, followed by the design of an experimental test and then by the actual test. Because of the variability of many of the defects and of their large number, the successful identification and removal of one defect did not necessarily lead to an observable improvement. However, as it turned out, it was that same variability that prevented the process from being

The author's address is 22 Arreton Road,
Princeton, NJ 08540.

completely discouraging. As we were struggling to achieve consistent results, at, say, 10 nm and making thousands of exposures, there was always the unexpected exposure that showed resolving power several times better. Those were the micrographs that were published but, more important, they were the teasers that persuaded the early workers to keep trying.

By 1943 the number of defects still present had been whittled down to the point where identifying and removing the remaining ones became relatively easy. As a result, some spectacular improvements in resolving power were made quickly and easily. It was this phenomenon that allowed the implicit astigmatism of the magnetic objective to emerge from the masking effect of other problems and to be corrected by the development of the stigmator.

If I have a message in this part of my account, it is to note that the great bulk of the work that brought the TEM into being as a most useful tool for science had nothing to do with the basic theory of the electron microscope. That also leads to a small complaint that, through some form of accepted snobbery (of which I was as guilty as anyone), no reports of any of this work were ever published. Although there was much word-of-mouth exchange of information among the early workers, I fear that our behavior condemned many newcomers here and overseas to repeating many of our mistakes.

Despite our problems, the TEM did begin to be useful and started providing essential information to an expanding universe of research, sometimes in spectacular and unexpected ways. One such incident sticks in my memory as a particularly significant demonstration of the role of the early TEM and as a cornerstone of my own understanding.

The time was the fall of 1940. We had the first developmental model of the RCA EMB microscope working in my laboratory in Camden, N.J. We received a call from Dr. Wendell Stanley asking if it would be possible to take a look at one of his tobacco mosaic virus (TMV) preparations. Dr. Stanley was working at the Rockefeller Institute Laboratories in Princeton, N.J. (In 1946 he received the Nobel Prize in chemistry for his work on plant viruses.) We made a date and within an hour after he arrived, we had a spectacular picture of the characteristic rods of his virus. In minutes, we had confirmed what had taken Dr. Stanley's group many years to determine, indirectly, by means of such techniques as low-angle x-ray scattering, the ultracentrifuge, birefringence optical studies, plus all the necessary biological tests. Note that I used the word "confirmed."

It is illuminating to consider what the scenario might have been if the TEM had been available when Dr. Stanley started his work. He would have doubtless compared micrographs of juices from healthy and from the infected plants, and his attention would have been attracted by the presence of the TMV rods as

alien structures present only in the juices from the infected plants. Please note that the presence of the rods would have been strongly suggestive but would have proved nothing. However, supported by the TEM results, showing that the rods were indeed the infectious agent, would have been a rather straightforward and relative simple procedure.

The spectacular confirmation of Dr. Stanley's work is only one indicator of the value of the TEM. My alternative scenario presents another measure and shows that a more important, but less appreciated, value of the TEM was in the enormous improvement in the efficiency that would have occurred in Dr. Stanley's research on the basis of what the TEM did *not* show! Without the TEM, the possible presence of each of all the particle sizes and shapes that the virus could have had would have had to be postulated and tested.

This little anecdote shows that, in those days, the TEM had two functions. The first was to illuminate "submicroscopic" geometric structures relevant to ongoing research programs. The second was to increase the efficiency of research by greatly reducing the number of possible geometric structures and thus eliminating the need to test the relevant hypotheses.

As we struggled to appreciate the significance of the electron microscope images in research, it became quite clear that geometric information, in isolation, had relatively little value. It did assume importance when taken in conjunction with information from related research. Around 1940 most of the early workers recognized how valuable it would be to be able to identify the chemistry of the structures that the TEM was making visible. Staining with heavy-metal compounds became useful for enhancing the contrast in images of organic materials, but that was a very blunt probe for identifying the chemistry of the specimen.

There was a flurry of activity in our laboratory to explore the potential of electron diffraction as a means of identifying the chemical structure of small particles and structures. The effort fizzled for a number of reasons. It was essentially worthless for small organic structures. Very small inorganic particles tended to be single or near single crystal structures with indeterminate orientation. Given the cumbersome facilities for image intensity measurements available to us at that period, it became clear that the limited results obtained did not justify the effort required. Nevertheless, the research had a payoff. We obtained invaluable experience in the design and operation of an electron-probe type of instrumentation.

The probe system used in the electron-diffraction experiments was a stationary probe that produced a transmission shadow image of the specimen. As the probe was focused closer to the specimen, the magnification in the shadow image increased. Ultimately, the part of

the specimen that covered the entire field was the area being bombarded by the probe, and therefore the area subject to analysis. Moving the specimen enabled the operator to select any point for examination.

In 1941 we had tried to build a scanning microscope. It was primarily an effort to apply high-resolution electron microscopy to metallurgical and other solid specimens. (This was prior to the development of replica techniques.) We did succeed in building such an instrument and obtaining a few pictures. However, it became painfully clear that the technology of 1940 was not up to our objectives and that we could do much more good by continuing the development of the TEM.

Early in 1943 I was browsing in the library and ran across an article by G. Ruthemann in *Naturwissenschaften*. Ruthemann had investigated the electron velocity distribution in the electrons transmitted by thin films of collo-dion. He showed that the discrete energy losses caused by the excitation of the K-levels of C, N, and O produced observable peaks in the distribution of electrons that had suffered energy losses due to inelastic collisions. Reading that article was an interesting experience in how the human mind works. In seconds my mind recognized the possibility of using the phenomenon for microanalysis and provided me with essentially the complete design of our first instrument! I finally truly understood what the patent attorneys meant when they talked about the "flash of inspiration."

We quickly modified one of our probe instruments and confirmed Ruthemann's results. We also extended them to include levels for some other light elements. We even did some work on the detection of the x rays emitted from a very small area of the specimen. All of this was very good research that we pursued very enthusiastically. Unfortunately, our enthusiasm began to turn to discouragement as we began to realize that, once again, our concepts were running far ahead of the technologies needed for their routine application. It was almost three decades before all the technologies needed to make microprobe analysis reasonably practical came together. Among them were some very major developments, such as very-high-resolution scanning transmission electron microscopes and very powerful small computers, as well as a broad range of very sensitive sensors. The stories of those developments will have to be told by the individuals involved.

For my part, the exercise of reexamining our activities from a vantage point of a half a century later has been a most interesting one and I appreciate the opportunity to do it. It also presents the opportunity to appreciate once again how valuable the inexperience and naivety of youth can be.

SPATIALLY RESOLVED ELECTRON ENERGY LOSS SPECTROSCOPY

P. E. Batson

It has been apparent since the first work of Hillier and Baker in 1944¹ that electron energy loss spectroscopy can provide information which is characteristic of the elemental content of small areas in thin specimens. In the time since then, advances in equipment and understanding have produced a technique that promises to be routinely applicable in any modern electron microscope on a spatial scale of a few nanometers. With the new field-emission-equipped instruments, we can determine the elemental content in areas as small as 0.5 nm in diameter in 5nm thick specimens--i.e., as few as 50 atoms in silicon. It has also been apparent that energy loss structure should be characteristic of the elemental bonding environment and electronic structure, as well as reflecting the absolute numbers of atoms. The gross variation of the shape of the carbon K-edge (1s→CB) in amorphous carbon, graphite, and diamond is a good example of this behavior. The work reported here has been undertaken to show the feasibility of obtaining detailed shapes of energy loss scattering from very small areas, to provide information about the local bonding and electronic structure. Some surprising results have been obtained. For instance, the shape of the carbon K-edge can be used to infer the presence of carbonate at grain boundaries in the high- T_c material $YBa_2Cu_3O_{7-\delta}$. With care, this identification can be taken further to choose between $BaCO_3$ and $CuCO_3$. Thus the environment of the carbon can be deduced without reference to other energy loss edges. In conduction bandstructure determination, it turns out to be possible to observe changes in the silicon bandstructure caused by the nearby presence of a single dislocation.

The Instrument

The energy loss system is shown in Fig. 1, reproduced from Ref. 2. It includes a VG Microscopes HB501 Scanning Transmission Electron Microscope (STEM), a Wien filter electron spectrometer,³ and a Princeton Applied Research diode array and acquisition system.⁴ The three instruments are controlled via a Series/1 computer through extensive digital links.⁵ The microscope can routinely form a sub-1nm diameter probe of 100 keV electrons with a beam current greater than 1 nA. The spectrometer is situated within an electrode which is connected to the microscope high voltage to eliminate problems of microscope instability. With pre-spectrometer electron transfer optics, which

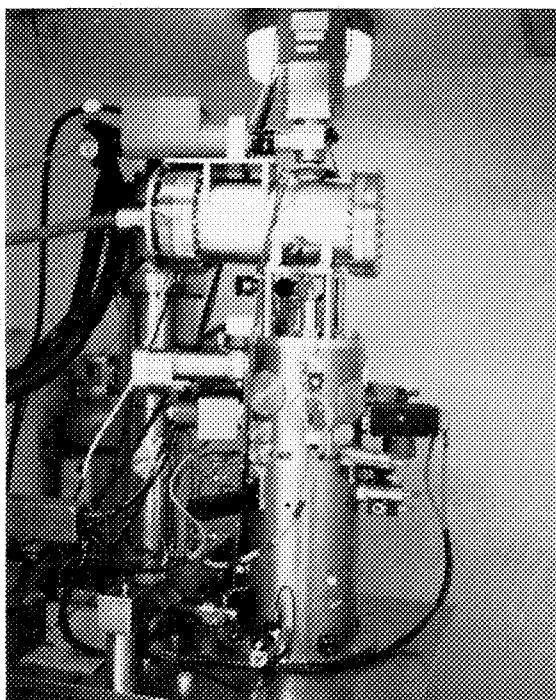


FIG. 1.--High-energy resolution EELS-STEM system.² Wien filter is mounted within horizontal chamber above microscope. Single-slit counting and diode array parallel detection are located above Wien filter chamber.

consist of a doublet quadrupole and a sextupole, the Wien filter is operated in a double-focusing configuration with partial second-order angular correction. The spectroscopic energy resolution is routinely between 0.35 and 0.40 eV, dominated by the 0.28eV contribution from the room-temperature field-emission source. This is obtainable out to about a 20mR half-angle of collection. At present, the second largest contribution (150 meV) comes from blurring in the diode array detector system.⁴ The contribution from the spectrometer optics is about 70 meV at a 10mR collection half angle, worsening to about 120 meV at a 20mR collection half angle. The stability and accuracy of the energy scale of this device is ± 30 meV. This performance is unrelated to the probe-forming optical configuration of the STEM. Thus it is entirely feasible to equip a modern instrument capable of a 0.3nm probe diameter.

Physical Basis

When a fast electron passes through a thin film of material, there is a high probability that it will give up some energy to the material. The various ways that a material can

The author is at the IBM Thomas J. Watson Research Center, Yorktown Heights, NY 10598.

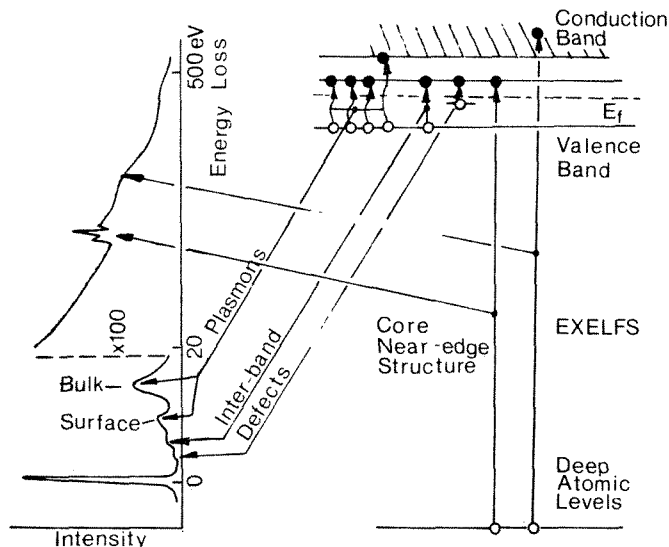


FIG. 2.--Energy level diagram and its relationship with energy loss spectrum for a simple semiconductor.⁶ Single electron transitions from filled to empty states are denoted by vertical arrows. Various transitions give rise to characteristic features in energy loss spectrum as indicated.

take up energy are then reflected in the energy change of the fast electron. Figure 2 shows possible single electron energy states for a typical semiconducting material.⁶ Below the maximum occupied energy, the Fermi level, we find deep atomic levels, the valence band, and defect levels within a semiconductor gap. Above the Fermi level, unoccupied levels include defect levels in the gap, the conduction band edge with possible structure, and a continuum of free-electron-like states extending to high energies. A typical energy loss spectrum is displayed on the left in the figure. Features at various energies in the energy loss spectrum are related to transitions between filled and empty single electron states in the material. The simplest of them is the promotion of an atomic core electron to the continuum of states above the Fermi level. This effect produces a step-like edge in the energy loss spectrum at an energy which is characteristic of the element whose core is excited. The edge is featureless in this model, and a continuum of intensity extends hundreds of electron volts beyond the step onset. These excitations are particularly useful for microanalysis, because the intrinsic spatial resolution is high--usually limited only by the electron beam size. In the low-energy region, resonance structures occur. These are the bulk- and surface-related plasmons. They reflect correlated motion of all the valence and conduction electrons in the material. On the single electron state model in Fig. 2, this type of excitation is indicated by transitions of many electrons together by small amounts of energy. Since the energy lost is given up to motion of many electrons, the spatial resolution of this process is not very high. In fact, the detailed morphology of the specimen

material determines the spatial range of the plasmon scattering. These losses are therefore not of much use for elemental microanalysis, but they can provide insight into the optical behavior of complicated submicron structures.⁷

Transitions from the valence band to unfilled defect levels, or to the conduction band edge, appear as absorption edges in the sub-5eV range. The spatial resolution of these excitations can be fairly good for defect-related scattering, because the scattering range can be dominated by the small size of the defect. In addition, the defect scattering can be large with respect to the direct valence to conduction-band scattering that occurs at a similar energy. However, the magnitude of scattering in both cases is very small--similar in size to a core absorption.⁸ Since this intensity occurs fairly close to the very intense unscattered beam, it is very difficult to obtain.

Transitions from the core levels to defect and low-energy conduction band states modify the shape of the core-level absorption onset. Like the direct defect to conduction band transitions, they can be unexpectedly large with respect to the associated core-level absorption.⁹ They are easier to obtain than the losses in the low-energy region because the background--due to the unscattered beam and due to the strong collective excitations--is relatively weak at the large energy losses associated with the core edges. Several kinds of variations in the shape of the core losses occur. Transitions to states near the conduction band edge are sensitive to the number and types of near neighbors of the excited atom. As will be apparent below, it is possible to identify near neighbors in Si with reference to the Si $L_{2,3}$ edge alone. Transitions to defect states within the semiconductor gap produce intensity below the absorption onset. This intensity can be used to infer the electrical properties of defects and interfaces. The effect of a single dislocation on the silicon conduction bandstructure can be easily discerned within about 2 nm of the dislocation. Also, the local Fermi level pinning position can be obtained near a metal-semiconductor interface.

Results Using the Carbon K-edge

Figure 3 shows a typical 2eV resolution plot of the energy loss scattering for $\text{YBa}_2\text{Cu}_3\text{O}_{7-\delta}$. This is the kind of result that generally gives the elemental content fairly well. The core to continuum transitions for Ba, O, and Cu are fairly obvious, although the Cu signal is difficult to obtain due to the background from the Ba $M_{4,5}$ edge near 785 eV. Also, the Y signal is very weak in this example. Therefore, in the region below 1000 eV for this material, electron energy loss scattering is not very useful for quantitative elemental analysis. On the other hand, if we want to have detailed information on the local environment of oxygen in this material, we may look at the detailed

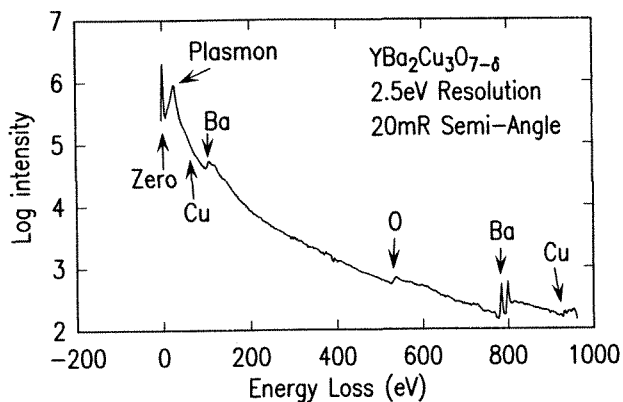


FIG. 3.--Wide energy scan of $\text{YBa}_2\text{Cu}_3\text{O}_{7-\delta}$ with 2.5eV resolution. Most major constituents are visible, but in this energy regime, Y is not evident. Also, Cu is difficult to obtain due to large background caused by Ba signal. This figure is combination of several spectra taken under varying conditions.

shape of the oxygen K-edge. The oxygen edge is low enough in energy (530 eV) and well enough separated from other edges to permit a careful look at its shape and absolute position. Figure 4 shows the oxygen K-edge obtained from CuO compared with results from two orientations of $\text{YBa}_2\text{Cu}_3\text{O}_{7-\delta}$.¹⁰ We see immediately, first, that the oxygen environment is very different for these two materials, since their absorption profiles are entirely different. Second, there is a pronounced orientation dependence of the $\text{YBa}_2\text{Cu}_3\text{O}_{7-\delta}$ results. It turns out that the conduction band edge in the superconductor has a pronounced electrical anisotropy: the material has a high conductivity in directions parallel to the a-b plane and a low conductivity in the c-axis direction. The energy loss experiments show nicely that the conduction band has p_{xy} symmetry with very little p_z character near the Fermi level.

Under some circumstances, carbon is observable at grain boundaries in $\text{YBa}_2\text{Cu}_3\text{O}_{7-\delta}$. This result should not be surprising, since the materials preparation includes BaCO_3 as an early constituent. It would be difficult to identify the chemical nature of this carbon if we were forced to use quantitative core loss analysis only, because isolated pockets of the grain boundary material are scarce, so it is difficult to obtain a clear-cut signal. Figure 5 shows high-resolution results for carbon in various forms (diamond, graphite, amorphous, CuCO_3 , and BaCO_3) compared with the carbon signal obtained from the $\text{YBa}_2\text{Cu}_3\text{O}_{7-\delta}$ grain boundary.¹¹ The gross variations of the carbon K-edge structure for the various forms are striking in these results. The edge position varies by as much as 5 eV, and the detailed shape variations depend strongly on whether the carbon is sp^2 or sp^3 bonded. On a finer scale, the mainly sp^2 bonded amorphous carbon is still clearly distinguishable from the graphite results. In fact, others have shown that the carbon K-edge shape varies in a re-

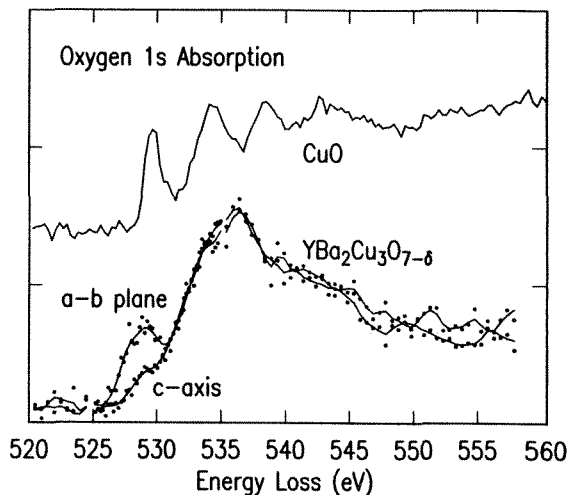


FIG. 4.--Oxygen K-edge obtained for CuO and two orientations of $\text{YBa}_2\text{Cu}_3\text{O}_{7-\delta}$. It is evident that 528eV peak on O edge is strongest when scattering momentum is largely confined to a-b plane of material. This is an indication of p_{xy} character of holes near Fermi level in $\text{YBa}_2\text{Cu}_3\text{O}_{7-\delta}$.

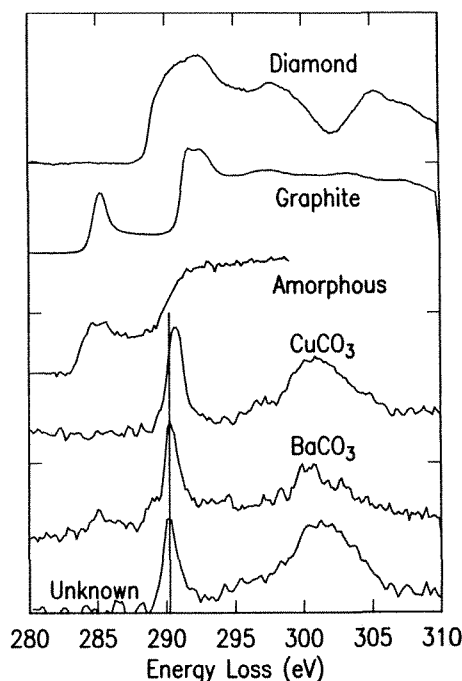


FIG. 5.--Near-edge structure for various types of carbon, compared with unknown spectrum acquired from grain boundary in $\text{YBa}_2\text{Cu}_3\text{O}_{7-\delta}$. Shape is characteristic of local environment of carbon. BaCO_3 result appears to have some amorphous carbon, probably surface contamination. Unknown can be identified as BaCO_3 from good registry of 290.25eV peaks. Graphite result was obtained with parallel recording system in ~1 min; amorphous result was obtained with serial recording for >1 h.

producable manner in amorphous carbon grown in gas decomposition reactions that leave varying

amounts of hydrogen within the material.¹² In this example, we can compare with the observed grain boundary signal and quickly eliminate an amorphous carbon layer in favor of a carbonate structure as the source of the observed signal. In addition, the precise position of the sharp resonance at 290.25 eV identifies this as BaCO₃ rather than CuCO₃, whose first peak occurs at 290.6 eV. The ability to measure the absolute position of the grain boundary loss to the accuracy ± 30 meV is crucial to making the final identification of BaCO₃. In passing, it should be mentioned that it is also crucial to have a parallel recording capability, particularly for the problem concerning the radiation-sensitive YBa₂Cu₃O_{7- δ} . Even with a very good resolution and stability, a serial collection system would not produce an adequate statistical accuracy.

Results at the Silicon L_{2,3} Edge

Silicon provides many interesting examples of the utility of fine details at the core edge. Figure 6 shows the bulk Si L_{2,3} edge which occurs at 99.84 eV. This onset energy is the point of maximum slope at the initial absorption onset, and is reproducible within the accuracy quoted above of ± 30 meV. It is possible to extract the 2p^{3/2} part of the scattering to eliminate structure due to the spin-orbit splitting of the core state. This result is compared with known positions of critical points in the Si Brillouin zone. Also included in the figure is a result from a calculation of the s- and d-projected density of states.¹³ Prior work has concentrated on comparisons of the shape of the onset with the total density of states in the conduction band. Agreement was not very good, and attempts were made to account for the differences using core excitons, as discussed in Ref. 13. It appears from the good comparison in Fig. 6 that excitonic interactions are not necessary to an understanding of the scattering in silicon.

The precise shape and position of the L_{2,3} edge reflects the local bonding environment of silicon in the material. Figure 7 shows a set of silicon spectra obtained for Si, Si₃N₄, Si₂N₂O, SiO, and SiO₂. The edges shift toward higher binding energy from the least oxidized (Si) to the most oxidized (SiO₂). Examination of the oxygen signal for these compounds reveals that no major differences exist¹⁴ for that edge. This result is explained by the realization that oxygen makes a bridge between silicon atoms in each of the oxygen-bearing compounds, so that near-neighbor environment is unchanged for the oxygen. The near-edge structure therefore provides a sensitive probe of the local atomic environment. The SiO results are interesting in this context in that they are very similar to the results for SiO₂, leading one to wonder whether the material actually consists of regions of SiO₂ surrounding silicon. Examination of the expanded pre-edge signal in Fig. 7 shows that this is not the case. There it is apparent that the onset energy of the ramp-like structure is 100.15 eV

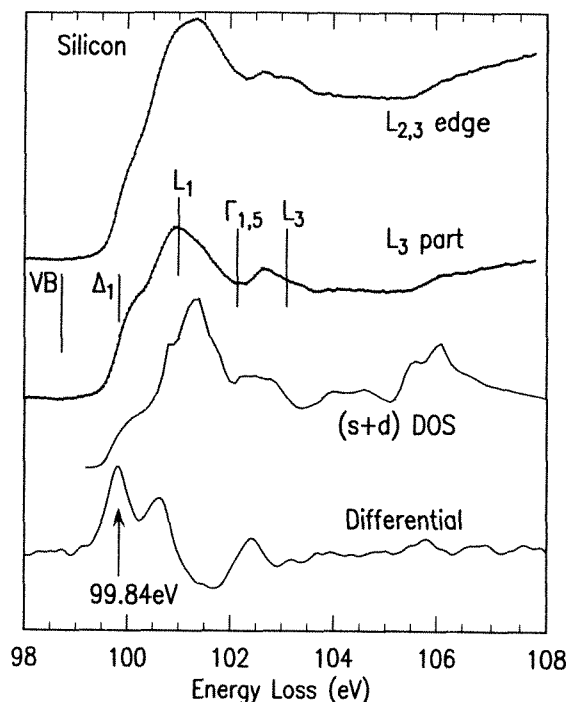


FIG. 6.--Si 2p^{3/2} edge obtained for bulk crystal. L₃ part has been extracted to show structure that reflects structure in conduction bands. Probable positions of various critical points from the Si bandstructure are indicated. Also, results of a calculation of s- and d-projected density of final states are shown.¹³

rather than 99.84 eV as in bulk Si. Thus the material appears to be homogeneous on an atomic scale. There are ways of assembling random networks of Si and O in such a way as to have most Si four-fold coordinated by O with a minority of Si having three O neighbors and one Si neighbor. This arrangement would likely give the observed behavior, but bandstructure calculations need to be attempted to be sure of this configuration. These edge structures were utilized to identify Si₂N₂O in a 5nm layer of material between Si₃N₄ and Si.¹⁴

Results from the Metal/Silicon Interface

As should be apparent from the above discussion, the shape of the silicon L_{2,3} edge can be obtained with sufficient accuracy to highlight features of the conduction bandstructure. If empty electronic states occur within the silicon band gap, they should produce scattering intensity within 1 eV below the onset of the L_{2,3} edge. Surprisingly, the differential scattering at the onset in silicon corresponds to only about 0.1 electron states per eV per atom, due partly to the centrifugal barrier, which forces most of the scattering intensity to higher energies. A slice of scattering within the 0.35eV resolution of the spectrometer thus arises from 0.035 states per atom. Consider then a single, sharply defined localized defect state at an interface. All the scattering associated with this state occurs within the energy resolution of the spec-

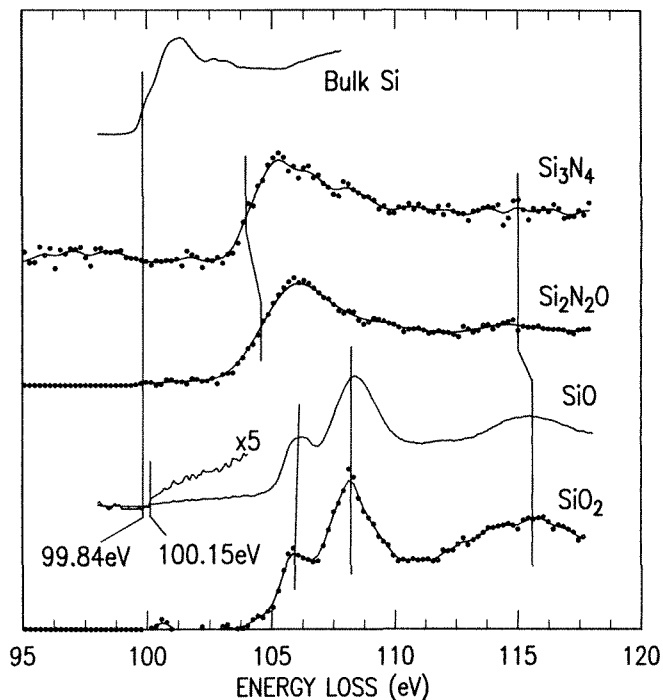


FIG. 7.-- $L_{2,3}$ results for Si in various compounds. Edge shifts to higher energies for stronger oxidation of Si. In SiO result, pre-edge ramp of intensity is expanded to show that onset energy is not the same as that for bulk Si. Thus SiO material in this example did not contain islands of bulk Si. These spectra were used to deduce identity of 5nm layer of Si_2N_2O between Si and Si_3N_4 in device-related structure.

trometer, giving essentially 1 electronic state per "atom." For the conditions quoted above, of a 0.5nm probe incident on a 5nm specimen, only 50 Si atoms are illuminated. Thus the differential bulk signal consists of scattering involving $50 \times 0.035 = 1.75$ electronic states. The defect scattering involving one state will therefore be 50% as large as the bulk signal. Therefore a single defect state should be observable in the energy loss scattering.

Figure 8 shows an example of this behavior for the Al/Si(111) interface. Two results for the Si L_3 edge are shown: in the bulk Si and as close as possible to the interface in a cross-section sample originally made for high-resolution microscopy of the interface structure.¹⁵ There are two differences between the spectra. First, intensity is present below the onset of the absorption edge. This intensity extends down to about 99.20 eV in energy. Second, the peak at 102.6 eV in the bulk material has shifted down to about 102.1 eV. These results can be interpreted in terms of the metal induced gap states theory for Schottky barrier formation. That model predicts that near the interface, electronic states are pulled down out of the Si conduction band to form gap states that are capable of pinning the

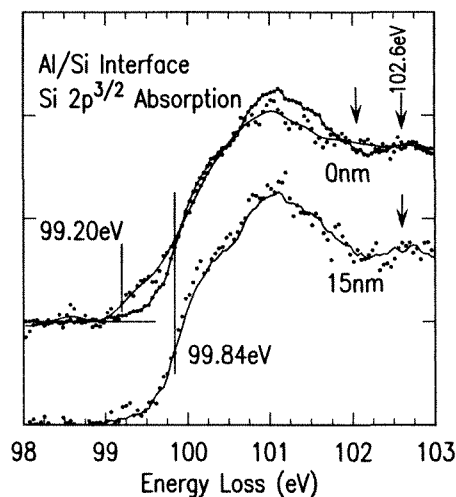


FIG. 8.--Comparison of Si $2p_{3/2}$ edge obtained at Al/Si(111) interface with bulk Si signal. Extra scattering intensity below edge is signature of electronic states within gap. Onset of scattering may be identified with Fermi level pinning point. Local Schottky barrier may be deduced from this measurement.

Fermi level. The onset of scattering in the energy loss experiment should be a measure of the new position of the Fermi level in this case. The "robbing" of the Si conduction band for the new gap states results in the observed modification of the 102.6eV peak. The difference between the bulk onset of the scattering at 99.84 eV and the interface onset at 99.20 eV should give the Schottky barrier height for a metal on a p-type Si substrate. The measured value is thus 0.64 eV, which agrees nicely with the bulk measurements which lie in the range 0.55-0.70 eV. A detailed account of this work will be published.⁹

Prospects for the Future

These results are still preliminary. To a large extent, the statistical accuracy and energy resolution are still improving. The above spectra were acquired over a space of about 5 years, with the statistical accuracy being a fairly good gauge of the age of the result. Spectra obtained in 1984 with several hours of serial acquisition (e.g., the amorphous carbon example in Fig. 5) may be obtained today in minutes with a better energy resolution (e.g., the graphite spectrum, also in Fig. 5). At the same time, analyses of the possible scattering intensities and instrumental capabilities suggest that another factor of 100 in performance should be achievable. Thus we may expect to be able, in the future, to obtain sub-0.1eV resolution spectra in seconds. This performance would allow many spectra within 0.1-10 nm of interesting structures. These spectra would be of sufficient quality to rival optical absorption spectra obtained today in bulk specimens. Truly atomic resolution probes of the electronic properties of buried structures will be the result.

References

1. J. Hillier and R. F. Baker, "Microanalysis by means of electrons," *J. Appl. Phys.* 15: 663, 1944.
2. P. E. Batson, "High resolution energy loss spectroscopy," *Ultramicroscopy* (in press).
3. P. E. Batson, "High resolution electron energy loss spectrometer for the scanning transmission electron microscope," *Rev. Sci. Inst.* 57: 43, 1986.
4. P. E. Batson, "Parallel detection for high resolution electron energy loss studies in the scanning transmission electron microscope," *Rev. Sci. Inst.* 59: 1132, 1988.
5. P. E. Batson and G. Trafas, "The IBM computer STEM system," *Ultramicroscopy* 8: 293, 1982.
6. P. E. Batson, "Analytical techniques for thin films: STEM" in K. N. Tu and R. Rosenberg, Eds., *Treatise on Materials Science and Technology*, New York: Academic Press, 1988, vol. 27, p. 337.
7. P. E. Batson, "Inelastic scattering of fast electrons in clusters of small spectra," *Surface Science* 156: 720, 1985.
8. P. E. Batson, K. L. Kavanagh, J. M. Woodall, and J. W. Mayer, "Observation of defect electronic states associated with misfit dislocations at the GaAs/GaInAs interface," *Phys. Rev. Lett.* 57: 2729, 1986.
9. P. E. Batson, "Local electronic structure at the Al/Si interface obtained with spatially resolved electron energy loss spectroscopy," *Phys. Rev. Lett.* (submitted).
10. P. E. Batson and M. F. Chisholm, "Anisotropy in the near edge fine structure of $\text{YBa}_2\text{Cu}_3\text{O}_{7-\delta}$," *Phys. Rev.* B37: 635, 1988.
11. P. E. Batson and M. F. Chisholm, "Carbon content of grain boundaries in $\text{YBa}_2\text{Cu}_3\text{O}_{7-\delta}$," (in preparation).
12. J. Fink, T. Muller-Heinzerling, J. Pfluger, A. Bubenzer, P. Koidl, and G. Creclius, "Structure and bonding of hydrocarbon plasma generated carbon films: An electron energy loss study," *Sol. S. Comm.* 47: 687, 1983.
13. X. Weng, P. Rez, and P. E. Batson, "The Si $L_{2,3}$ near edge structure: Single electron or many electron effects?" *Phys. Rev. Lett.* (submitted).
14. P. E. Batson, K. L. Kavanagh, C. Y. Wong, and J. M. Woodall, "Local bonding and electronic structure obtained from electron energy loss scattering," *Ultramicroscopy* 22: 89, 1987.
15. F. LeGoues, W. Krakow, and P. S. Ho, "Atomic structure of the epitaxial Al-Si interface," *Phil. Mag.* A53: 833, 1986.

DETERMINATION OF ELECTRONIC PROPERTIES OF DEFECTS IN SEMICONDUCTORS BY CATHODOLUMINESCENCE

J. L. Batstone

Electron-beam excitation of carriers across the band gap in semiconductors can be performed within the electron microscope. Detailed spectroscopic information can be obtained from defect states related to both impurity species and crystallographic defects such as dislocations. Results are presented from an in situ transmission electron microscope and cathodoluminescence study of epitaxial films of ZnSe grown on GaAs. Low-temperature (< 100 K) luminescence at 2.60 eV, and quenching of exciton luminescence (2.79 eV), have been correlated with the presence of dislocations. The dependence of spectral line-shapes and intensities on temperature and excitation energies is described.

Generation of electron-hole pairs with an electron beam results in carrier recombination that can occur either nonradiatively via phonon mechanisms or radiatively with the emission of a photon, resulting in cathodoluminescence (CL). Spectral analysis of CL can yield information about characteristic energy levels present in the material. Radiative transitions in semiconductors can be divided into two classes, (i) intrinsic and (ii) extrinsic. In the absence of defect states in the band gap E_g , intrinsic recombination is dominated by forming Mott-Wannier type free excitons (FE) via coulombic attraction.¹ The subsequent radiative emission can be expressed as

$$h\nu = E_g - E_x \quad (1)$$

where E_x is the exciton ionization energy.

In general, CL from real materials is dominated by extrinsic recombination mechanisms as a result of states associated with donors, acceptors, and native defects. Information about these impurity states is of prime importance for the optoelectronic device industry. Extrinsic states are classified as shallow or deep, where shallow levels have transition energies close to E_g and can be described by effective mass theory with reference to the hydrogen atom. Deep levels are frequently highly localized with ionization energies in excess of 200 meV below E_g .

In the presence of impurities, bound excitons (BE) can be formed with recombination characterized by narrow emission lines of energy

The author is in the Department of Materials Science and Engineering, University of Liverpool, P.O. Box 147, Liverpool, England L69 3BX. (Present address: IBM Thomas J. Watson Research Center, Yorktown Heights, NY 10598). Valuable discussions with J. W. Steeds are gratefully acknowledged.

$$h\nu = E_g - E_x - E_b \quad (2)$$

where E_b is the binding energy of the exciton to the impurity atom. In addition, excitons can bind to crystallographic defects such as dislocations. Exciton coupling to the crystal lattice can occur via electron-phonon interaction. Clearly resolved spectral peaks can be observed with energy

$$h\nu = E_g - E_x - E_b - mE_p \quad (3)$$

where E_p is the energy of the emitted phonons and m is the number of phonons emitted. An understanding of exciton behavior in semiconductors is crucial for the identification of CL spectra. The above brief introduction allows identification of many luminescence features observed in ZnSe, a II-VI semiconductor.

Interest in the II-VI compounds can be roughly classified into two separate areas. Wide-band gap II-VI materials (e.g., ZnS, ZnSe) are of use as the active optoelectronic medium in thin-film electroluminescent displays, where control of dopants can allow blue room temperature emission to be realized. Narrow-band gap II-VI materials (e.g., CdTe, CdHgTe) are of interest for infrared detector devices and are not considered in detail here.

Epitaxial thin films of ZnSe can be grown on a variety of substrates by low-temperature epitaxial techniques such as molecular beam epitaxy and metal organic chemical vapor deposition (MOCVD). Examination of MOCVD ZnSe layers grown on glass, GaAs, Ge, and ZnSe revealed GaAs as the best choice of substrate.² Radiative recombination in ZnSe/GaAs(100) was dominated by donor-bound exciton transitions, denoted in this paper by D^0X . Growth of ZnSe on GaAs occurs with a lattice mismatch of 0.028%. Heteroepitaxial systems frequently contain high densities of crystallographic defects such as grain boundaries, stacking faults, and twins. Previous work has shown that relief of lattice strain in ZnSe/GaAs films occurs via misfit dislocations in Al-doped layers and via stacking faults in undoped layers.³

Excellent spectroscopic analysis of semiconductors can be performed by photoluminescence (PL) with laser excitation used for carrier excitation. However, PL is performed on bulk samples and can yield only limited information about the spatial distributions of luminescent features. A clear advantage of CL is the ability to obtain microscopic information about defect distributions by conventional electron microscopy techniques in conjunction with in situ CL collection optics. CL is used in the SEM (as extensively reviewed⁴) where

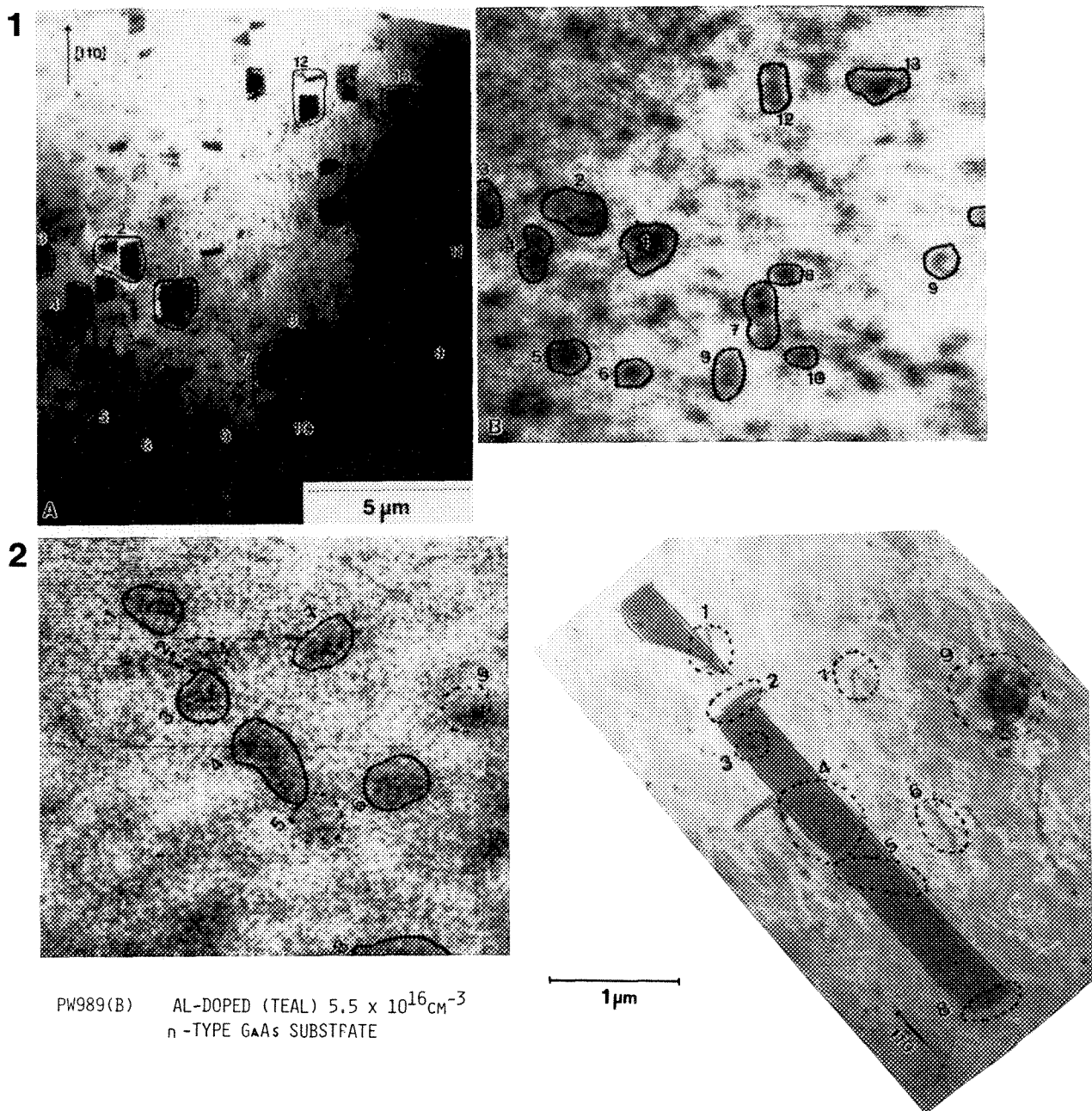


FIG. 1.--(a) Bright-field image ($g = 220$) of stacking faults in Al-doped ZnSe; (b) CL image at 300 K at 2.69 eV showing quenching.
FIG. 2.--(a) CL image at 300 K at 2.69 eV; (b) bright-field image ($g = 220$) of extended stacking fault.

large specimen chambers provide space for efficient light-collection optics and allow liquid helium cooling of specimens to <10 K. Disadvantages of SEM-CL include no direct imaging of defects which affects CL contrast and yields poor spatial resolution. Resolution in a CL image can be expressed as

$$d = (d_p^2 + d_g^2 + d_l^2)^{1/2} \quad (4)$$

where d_p is the electron probe diameter, d_g is the generation volume, and d_l is the minority carrier diffusion length.⁵ In thin foils suitable for TEM, both d_g and d_l are reduced; d_g

is truncated and d_l is restricted to the thickness of the foil. Significant improvements in resolution are observed in the TEM but surface recombination becomes an increasingly dominant parameter. For high surface recombination velocities, excess carrier recombination processes can be limited by carrier diffusion to surfaces where nonradiative recombination due to band-bending and surface states can occur. This limitation results in an effective diffusion length proportional to the film thickness t and an improvement in spatial resolution. This improvement must be balanced against an overall decrease in CL intensity, which can

vary as t^n with $n = 2$ for surface-recombination-limited emission. Thus TEM-CL involves a compromise between optimum spatial resolution and high CL intensities. The use of a TEM-CL system to determine electronic properties of dislocations are described next.

Experimental

Epitaxial films ($\sim 2 \mu\text{m}$ thick) of ZnSe/GaAs(100) grown by MOCVD with use of dimethyl zinc and hydrogen selenide were examined in a CL system implemented on a Philips EM400 in the H. H. Wills Physics Laboratory, University of Bristol. Specimens suitable for TEM analysis were prepared by chemical polishing in $\text{Cl}_2/\text{CH}_3\text{OH}$ to remove the GaAs substrate locally.

The design and construction of the CL system has been described previously.⁵ A small retractable ellipsoidal mirror is inserted above the specimen in the TEM to collect CL excited by the electron beam. The light is focused by a series of mirrors and quartz lenses onto the entrance points of a Bentham M300 monochromator, modified⁷ to direct light onto (a) a S20 photomultiplier (PM) for integrated CL, imaging and linescans, (b) a RCA PM with GaAs photocathode operated in single photon counting mode for spectrum acquisition and wavelength selective imaging in the range 300-900 nm, or (c) a cooled North Coast germanium photodiode for analysis in the range 0.9-1.8 μm . A Link Systems 860 Series II dedicated minicomputer is used for software control of the spectrometer drive, TEM scan coils, and data storage. A continuously pumped liquid He specimen stage allows CL measurements to be performed between 30 and 300 K.⁸

Results

Room-temperature CL. The quality of wide-band gap materials can be assessed by measurement of the ratio of intensities of shallow (band edge) to radiative deep level emission R. For Al-doped ZnSe ($n = 2 \times 10^{16}$ - $4 \times 10^{17} \text{ cm}^{-3}$) band edge emission dominates and a single broad emission line is observed at 2.69 eV, which shows excitonic character⁹ resulting in blue room temperature emission of promise for electroluminescent displays. However, CL imaging of ZnSe specimens frequently revealed black spots. Electrically and optically active defects are obviously undesirable in device material.

Figure 1(a) shows a TEM image of stacking faults and dislocations in Al-doped ($n = 3 \times 10^{15} \text{ cm}^{-3}$) ZnSe of thickness $\sim 0.5 \mu\text{m}$ (after etching). The corresponding CL image (Fig. 1(b)) corresponds to monochromatic imaging by use of the 2.69 eV spectral line at 300 K. Black contrast due to stacking faults and dislocations is seen and examples of correlations between black spots and defects have been marked. The majority of the stacking faults show bright-field diffraction contrast indicative of overlapping faults and multiple partial dislocations. In order to distinguish between the effects of partial dislocations and the

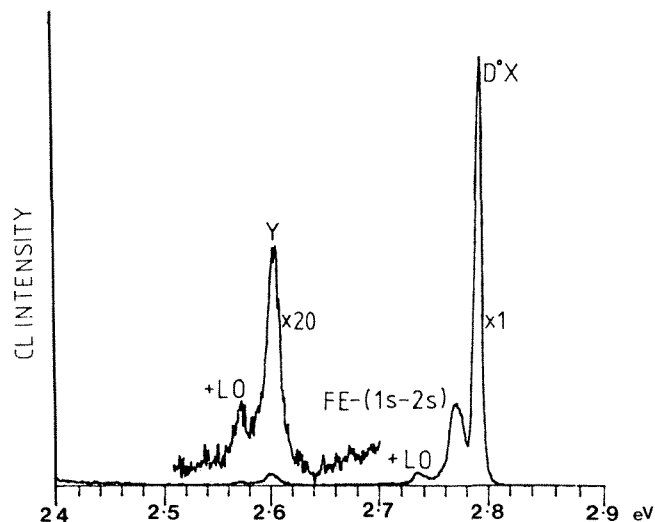


FIG. 3.--Spectrum at 35 K and 120 kV from Al-doped MOCVD ZnSe/GaAs.

stacking faults on CL contrast (quenching at defects), a long extended stacking fault was studied. Figure 2(a) shows the CL image at 300 K associated with the fault shown in Fig. 2(b). The magnifications of the two images are approximately equal and the dislocations labeled (1-9) are correlated with darker regions in the CL image. No variation in CL contrast was observed from the stacking fault ribbon alone indicating only the partial dislocations were electrically alive. This result is in agreement with electron-beam-induced current observations of stacking faults in silicon.¹⁰

Low-temperature CL. Low-temperature CL and PL measurements reveal information about discrete defect energy levels in the band gap which are normally thermalized at 300 K. Whereas PL measurements can be obtained at 4.2 K, CL measurements depend on the temperature T which can be obtained in the electron microscope by use of a specially designed He stage. In this work, CL measurements were performed in the range 30-300 K. The lower limit (30-35 K) was determined from parallel PL studies on vapor-phase epitaxy InP in the temperature range 5-75 K.¹¹ The variation in full width half maximum (FWHM) of the D°X transition as a function of T was used. Confirmation of the lower limit was obtained from CL from Si and a determination of the excess carrier distribution effective temperature yielded $T_e = 33 \text{ K}$.¹¹

Figure 3 shows a spectrum obtained from Al-doped MOCVD ZnSe/GaAs at 35 K and 120 V. The peak at $\sim 2.795 \text{ eV}$ is due to recombination of the Al D°X . The peak appears broad, FWHM = 9 meV, presumably as a result of inter-impurity interactions. A lower energy peak at 2.779 eV, FE (1s-2s) was identified as radiative recombination of free excitons (FE) with simultaneous inelastic scattering of shallow neutral donors.¹² The line lies close to (1s-2s,p) below the FE energy gap for Cl and represents relaxation from the FE bottleneck with inelastic scattering at neutral Cl donors relaxing momentum selection rules. Longitudinal optical (LO)

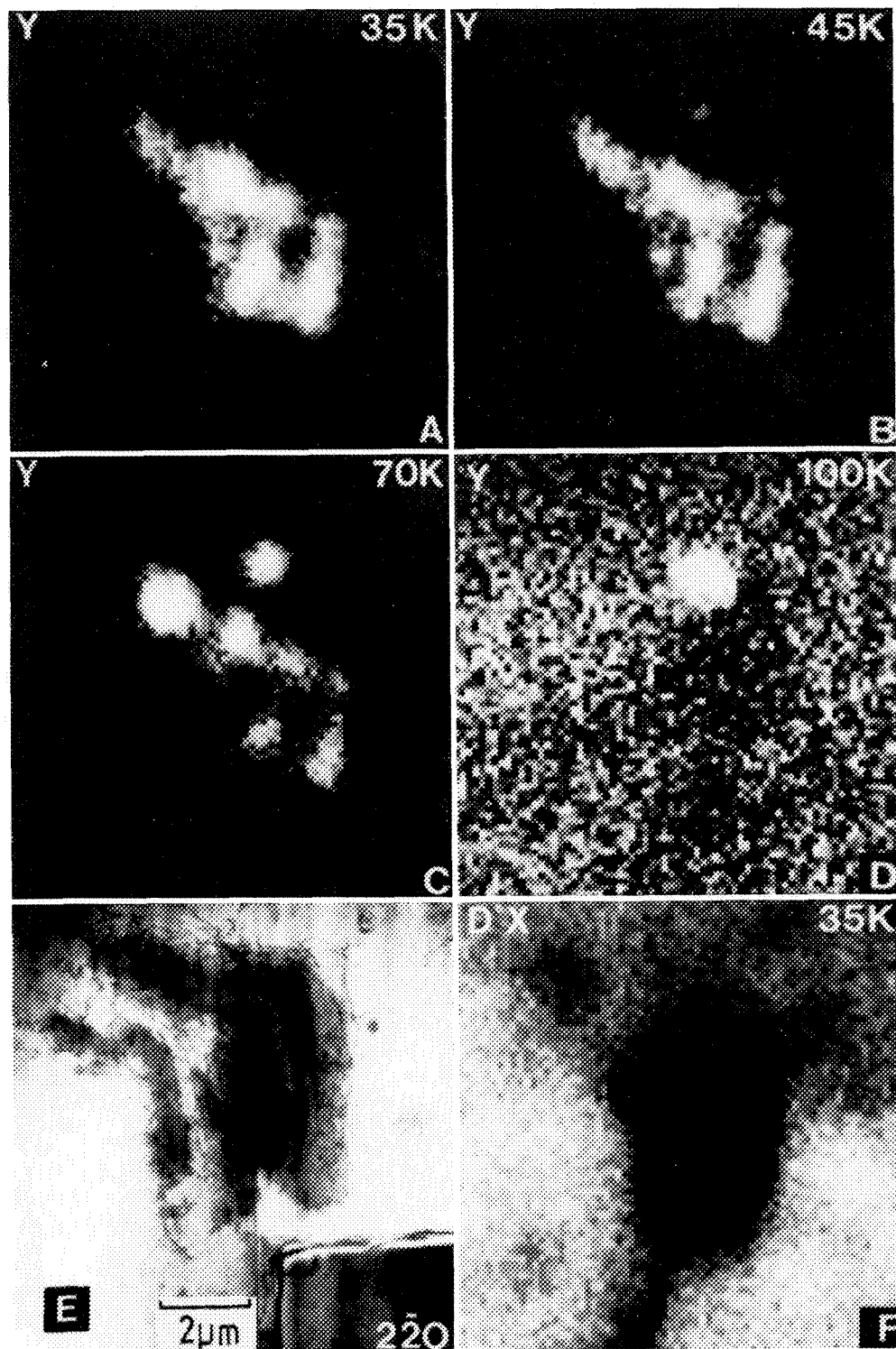


FIG. 4.--Monochromatic CL images at 2.69 eV; (a) 35 K; (b) 45 K; (c) 70 K; (d) 100 K; (e) TEM image of dislocations at crack tip; (f) CL image at 2.79 eV.

phonon coupling is observed with a peak occurring at 2.742 eV, 35 meV below the FE (1s-2s) transition. The line at 2.602 eV, labeled Y, is particularly characteristic of epitaxial ZnSe. Previous work^{3,11} has shown correlations between regions of Y emission and dense dislocation networks. A particularly valuable feature of in situ TEM-CL is the ability to

obtain both CL and TEM information from exactly the same region of the specimen simultaneously. Figure 4 shows monochromatic CL images from ZnSe; at 35 K, local exciton quenching is observed at 2.79 eV (Fig. 4f), which corresponds to a tangle of dislocations occurring at a crack tip (Fig. 4e). CL images obtained at 2.6 eV show localized regions of Y emission in

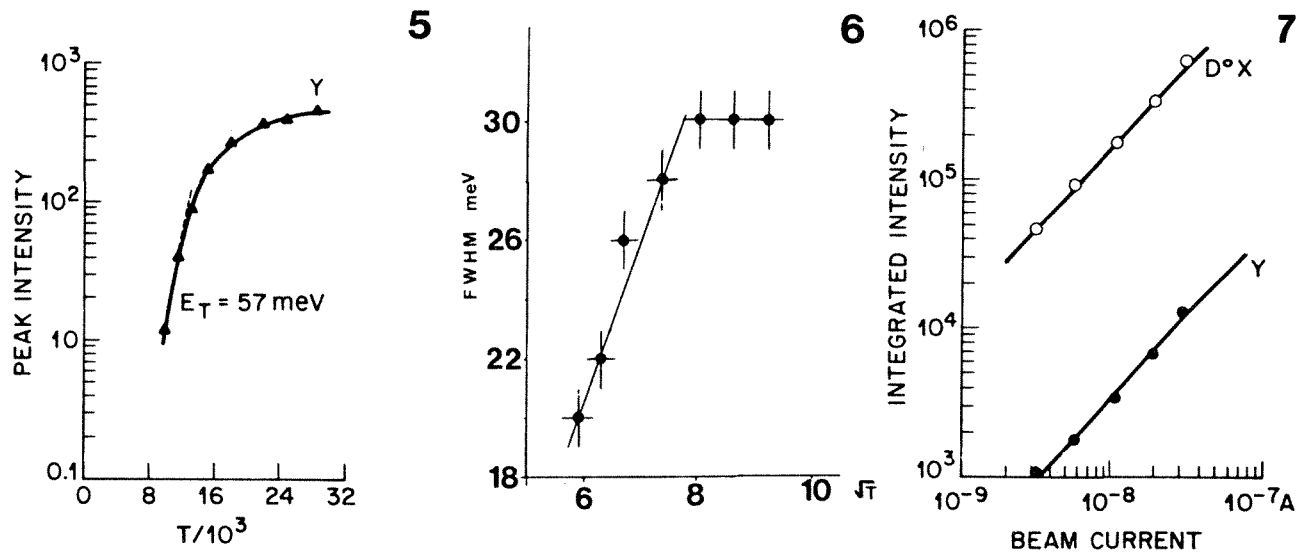


FIG. 5.--Temperature dependence of Y emission.
 FIG. 6.--FWHM dependence with T of Y emission.
 FIG. 7.--Excitation dependence for Y and D⁰X emission.

the vicinity of the dislocations, Fig. 4(a)-(d). The spatial distribution of this emission varies markedly with increasing T, until at ~100 K, the radiative transition Y is thermally quenched. From an analysis of spectral peak intensities, it is possible to extract activation energies E_a for thermal dissociation, from empirical expressions of the form

$$I = A \exp (E_a/k_B T) \quad (5)$$

where I is the peak intensity and A is a constant. Figure 5 shows a plot of intensity against $10^3/T$ for Y emission from which an activation energy of 57 meV is obtained. Data from the temperature dependence of a spectral feature can enable the identification of a particular transition species. Y emission lies ~220 meV below E_g . It has been suggested¹³ that Y emission arises from FE recombinations in the vicinity of an impurity or defect, which experience simultaneous excitation in an inelastic scattering event, in a manner analogous to FE-(1s-2s). If this interpretation is correct, a spectral analysis of T dependence, lineshapes, and excitation dependences should reveal excitonic behavior. FE lines occur at ~20 meV below E_g , which means that an impurity/defect localization energy of 200 meV is involved if Y is an excitonic complex.

For strongly localized centers the FWHM temperature dependence of a spectral line can be expressed as¹⁴

$$\text{FWHM} = 4(\ln 2)^{1/2} (S\hbar\omega/k_B T)^{1/2} \quad (6)$$

where S is the Huang-Rhys factor obtained from a configurational coordinate model and $\hbar\omega$ is the vibrational energy associated with the excited state of the luminescence center. Figure 6 shows the FWHM behavior as a function of \sqrt{T} for

Y emission. At 70-100 K, saturation of the FWHM broadening occurs which is not characteristic of a "deep" configurational coordinate center and suggests that Y emission is consistent with shallow band edge recombination.

Another method for determination of recombination mechanisms available in the TEM is the measurement of CL excitation dependences. Experimentally, the steady state CL intensity I_{CL} varies as

$$I_{CL} \propto i_b^n \quad (7)$$

where i_b is the beam current. Values of n can vary from n = 0 (saturation) to n = 1-2. For high injected current densities, high values of n can be obtained indicating the onset of stimulated emission. Different recombination routes have different lifetimes; hence the excitation dependence is expected to be different for different mechanisms. Figure 7 shows variations in integrated CL intensities as a function of beam current for D⁰X and Y emission bands, so that n can be obtained from the gradients. Both D⁰X and Y show very similar excitation dependences with n = 1.1 suggesting that Y may be excitonic in nature.

Discussion

The above results have illustrated some of the complex features of CL recombination in the vicinity of crystal defects. Exciton quenching is commonly observed (e.g., Figs. 1, 2 and 4e) and can be explained in terms of exciton dissociation in the presence of dislocation electric fields. Local electric fields arise at dislocations due to (i) core effects and (ii) long-range strain effects. The former are due to states within E_g that can be occupied by car-

riers from E_V or E_C . An electron (or hole) is localized in [2-D] in the dislocation band and ionization turns the dislocations into charged lines. A Coulomb field is produced that is screened within a cylinder of radius λ_D , which is the characteristic Debye screening length

$$\lambda_D = \left(\frac{\epsilon \epsilon_0 k_B T}{q^2 N_D - N_A} \right)^{1/2} \quad (8)$$

where $\epsilon = 8.84$ for ZnSe. For the Al-doped sample shown in Figs. 1 and 2 ($n = 3 \times 10^{15} \text{ cm}^{-3}$), $\lambda_D = 650 \text{ \AA}$ at 300 K, compared with the Fe radius $\sim 40 \text{ \AA}$. Dislocations in ZnSe are known to be charged¹⁵ and the electric fields due to both core effects and long-range strain fields due to deformation potentials and piezoelectric effects influence recombination. In addition to electric field dissociation of excitons at dislocations, attraction of excitons to charged crystal defects could occur followed by non-radiative recombination and thus apparent exciton quenching.

In addition to nonradiative behavior at defects, characteristic dislocation emission at 2.6 eV is observed in ZnSe that appears to be excitonic in nature. Radiative emission from dislocations has previously been observed by PL in bulk plastically deformed crystals of Si,¹⁶ CdS,¹⁷ and ZnS.¹⁸ Radiative emission has also been observed from dislocation loops in ZnTe,¹⁹ from point defects in mechanically damaged GaAs and InP,²⁰ and from individual dislocations in diamond.⁵ In ZnSe, Y emission is observed from both individual dislocations and complex tangles;¹¹ however, not all dislocations are luminescent and there is strong evidence that an association of impurities with the dislocations results in Y emission. The 2.6 eV emission line lies relatively deep in the band gap but exhibits anomalously low phonon coupling. Phonon coupling is usually expected to increase with increasing localization of the center. The model¹³ proposed for recombination at extended defects explains some features of Y emission. Transitions involving electronic states on dislocation loops with N nearly equivalent binding sites per loop due to kinks, jogs, points of dissociation, precipitation, or other form of dislocation perturbation were proposed. Small changes in environment between sites within a loop or between loops could lead to the observed inhomogeneous broadening of no-phonon lines. Recombination can thus involve centers with binding potentials distributed on extended defects enabling the center to become delocalized even though 2.6 eV lies relatively deep in the gap. Exciton emission in the vicinity of dislocation is affected by the presence of clouds of impurities and precipitates. The elastic strain around dislocation produces a Cottrell atmosphere where the total energy of the crystal may be reduced by an impurity smaller than the host lattice constituents occupying an atomic site in the compression region around a dislocation. Clouds of impurities can thus accumulate around dislocations. Electrically and optically active point defects and impurity

clouds affect the dislocation elastic strain field and result in perturbations in the luminescence around the dislocation.

Conclusion

The optical activity of dislocations in epitaxial films of ZnSe/GaAs has been demonstrated with in situ TEM-CL. Dislocation luminescence has been observed at 2.60 eV that appears to be excitonic in nature. Exciton quenching is frequently observed in the vicinity of dislocations and stacking fault partial dislocations.

References

1. C. Kittel, *Introduction to Solid State Physics*, New York: Wiley, 1976, 5th ed., chap. 11.
2. P. J. Dean, *Phys. Stat. Sol.* B98: 439, 1980.
3. J. L. Batstone and J. W. Steeds, *Inst. Phys. Conf. Ser.* No. 76: 383, 1985.
4. S. Davidson, *J. Microscopy* 110: 177, 1977.
5. S. J. Pennycook, *Ultramicroscopy* 7: 99, 1981.
6. S. J. Roberts, *Inst. Phys. Conf. Ser.* No. 61: 51, 1981.
7. P. Aplin, private communication.
8. J. A. Eades, *J. Phys.* E15: 184, 1982.
9. J. L. Batstone, Ph.D. Thesis, University of Bristol, 1985.
10. A. Ourmazd, *Contemp. Phys.* 25: 251, 1984.
11. S. Myhajlenko, J. L. Batstone, H. J. Hutchinson, and J. W. Steeds, *J. Phys.* C17: 6477, 1984.
12. P. J. Dean, P. J. Wright, and B. Cockayne, *J. Phys.* C16: 3493, 1983.
13. P. J. Dean, *Phys. Stat. Sol.* A81: 625, 1984.
14. K. Huang and A. Rhys, *Proc. Roy. Soc.* A204, 406, 1950.
15. Y. A. Ossipyan and V. F. Petrenko, *Sov. Phys. JETP* 48: 147, 1983.
16. M. Sueza and K. Sumino, *J. Physique Coll.* 4: C4-133, 1983.
17. V. D. Negryi and Y. A. Ossipyan, *Phys. Stat. Sol.* A55: 583, 1979.
18. S. I. Bredikhin and S. Z. Shmurak, *Sov. Phys. JETP* 49: 520, 1979.
19. V. A. Ivanov, G. P. Yablonskii, and V. P. Gribkovskii, *Sov. Phys. Solid State* 26: 455, 1984.
20. V. Swaminathan, M. S. Young, and R. Caruso, *J. Appl. Phys.* 57: 1387, 1985.

THE USE OF FOCUSED HEAVY-ION BEAMS FOR SUBMICROMETER IMAGING MICROANALYSIS

R. Levi-Setti, J. M. Chabala, C. Girod, P. Hallégot, and Y. L. Wang

We have repeatedly reported in this forum updates about the development of a high-resolution scanning ion microprobe (UC SIM) and its application to the imaging microanalysis of materials.^{1,2} This instrument, which used the method of secondary ion mass spectrometry (SIMS) to obtain chemical information of a sample surface, is capable of focusing a 40keV heavy-ion probe (typically Ga⁺ extracted from a liquid metal ion source) to a spot as small as 20 nm in diameter. In addition to the above references, our progress in micro-SIMS over the past five years has been described in over 21 topical publications and 14 review articles that cover instrumental aspects, methods, and numerous interdisciplinary studies. A few of the most comprehensive papers are referenced here.³⁻⁷ They also contain appropriate mention of the relevant literature on the subject. It would be repetitious and inadequate to undertake within these confines an exhaustive discussion of the many aspects that the present topic entails. Instead, we limit this presentation to gain some perspective on the utilization of ultrafine heavy ion probes and to discuss some of the issues of current concern in imaging microanalysis at high lateral resolution. Not to default on tradition, we also present several of our micrographs.

Finely Focused Heavy Ion Probes and Their Utilization

Point-like liquid metal ion sources and conventional electrostatic lens systems enable the extraction and focusing of heavy metal ion probes to diameters in the submicrometer range, approaching a practical limit estimated at 10-20 nm.³ In spite of the high brightness of these sources, such fine probes carry feeble currents (in the pA range at the smallest probe sizes)

The authors are at the Enrico Fermi Institute and Department of Physics, The University of Chicago, Chicago, IL 60637. This material is based on work supported by the National Science Foundation under grants DMR-8612254 and BBS-8610518. Additional support was obtained from Ilford Ltd. We thank Dr. E. Olsen of Field Museum of Natural History, Chicago, for lending us the Chainpur meteorite sample. The biological samples shown in Figs. 2(c) and (d), and 3(a) and (b), were obtained through courtesy of Prof. P. Galle of the University of Paris, Creteil; that shown in Fig. 3(c), through courtesy of Dr. C. Chassard-Bouchaud of the University Pierre et Marie Curie, Paris. We are indebted to our colleagues at Ilford Ltd. and Dr. Kriebel of Ilford AG for the expert preparation and loan of the photoemulsion sample.

of probe-size independent current density (about 1 A/cm²), resulting from the energy spread of the emitted ions and consequent chromatic aberration of the optical system.⁶ Probes with these characteristics are generally adequate for scanning ion microscopy, via detection of the ion-induced secondary electrons.⁸ A wide range of other applications is accessible to these probes in systems where the time spent by the probe (dwell time) on a given location can be varied at will and its location addressed in a controlled manner, by means of a digital sweep or pattern generator. In this manner, sputter erosion by the probe can be used for the fabrication of microstructures (maskless focused ion beam lithography), and the emission of secondary ions can be exploited for imaging purposes (as for secondary electrons) or to perform chemical analysis of surfaces by SIMS. In the latter mode, mass spectra, depth profiles, or high-resolution images of the surface elemental distribution (elemental maps) can be obtained, where the depth of material being probed in a given time (and by a given probe current) is proportional to the area over which the probe is swept. For example, a typical analytical scan (500 s) with a 40keV, 10pA Ga⁺ probe 35 nm in diameter (as with the UC SIM) may remove on the order of one monolayer of surface material when scanning an area of say, 100 × 100 μm², or some 100 monolayers for an area 10 × 10 μm², corresponding to a volume of about 1 μm³ containing approximately 10¹¹ atoms. These figures set the stage for the discussions to follow, concerning the limits of sensitivity and lateral resolution of SIMS imaging microanalysis and the problems associated with quantitation in the submicrometer domain.

Analytical Lateral Image Resolution

With a scanning probe, analytical image resolution (edge definition) can, in principle, be made to match the probe size, provided sufficient statistics of detected counts are available. As previously shown,^{4,5} this proviso is met for partially overlapping probe spacings, when the change in signal across a compositional step is imaged with statistics in excess of one count/probe setting. However, several sample-dependent factors, of instrumental and physical origin, sometimes prevent this best case condition from occurring.⁶ Instrumental limitations arise from the behavior of chromatic-aberration-limited probes, as mentioned above, and from the overall imperfect collection and transmission efficiency of the SIMS system. These factors constrain the use of the smallest probes, which lead to sputter

rates that are inadequate for the generation and collection of sufficient count statistics. Physical limitations include the ion yield, which is strongly species-dependent; the elemental concentration; and ultimately the size (10-20 nm) of the lateral spread of the collisional cascade responsible for secondary ion emission.¹⁰ Attainable analytical image resolution is inextricably related to analytical sensitivity, a well-known trade-off. With reference to the above numerical example, and assuming a SIMS detection efficiency of 2×10^{-3} (a realistic estimate for the quadrupole system of the UC SIM) combined with an ion yield of 0.1 (a relatively high figure) and unity concentration, out of the originally sputtered 10^{11} atoms only 2×10^7 ions would be counted. In a typical map with 2.5×10^5 pixels (512×512) picture elements (pixels), on average approximately 80 counts/pixel would be available. This figure implies that only elemental concentration steps in excess of 1% could be detected with probe-size resolution, and that the edge definition would have already degraded to four times the probe size for a 0.1% step.⁵ Of course, this is still an optimistic estimate: relatively few elements (the alkali, the halogens, and a few others) have ion yields in excess of 0.1 (unless special measures are taken to enhance the ion yield). In many cases, the ion yield may be as low as 10^{-3} - 10^{-4} , in which case, even for major components, it may be difficult to attain probe-size resolution at the 35nm level considered in this example. If the probe diameter were increased to 100 nm, the sensitivity limits for probe-size resolution would improve by a factor of ten.

What emerges from the above considerations is an important, unconventional concept: SIMS image resolution is not a constant of the instrument, but may vary over a wide range, depending on the ion yield and concentration of a particular element or molecular species, and the time spent on acquiring an image. Only in particular circumstances may the *limiting image resolution* approach the probe size. This conclusion also implies that, on a species-dependent basis, it may be advantageous in terms of attainable image resolution to operate the microprobe with a spot size larger than the minimum possible for the instrument.

In this context, nature sometimes may come to the rescue by providing an incentive for the use of the smallest probes: elemental segregation may cause local concentrations, otherwise too diluted in the bulk, to exceed the threshold for maximal image resolution. Two examples of this kind of occurrence are presented in a later section.

Microquantitation

The extraction of quantitative microanalytical information from submicrometer areas with a heavy-ion probe presents novel problems whose solution rests heavily on computer-aided methods of probe positioning and image analysis. Point analysis is impractical: with a stationary 35nm

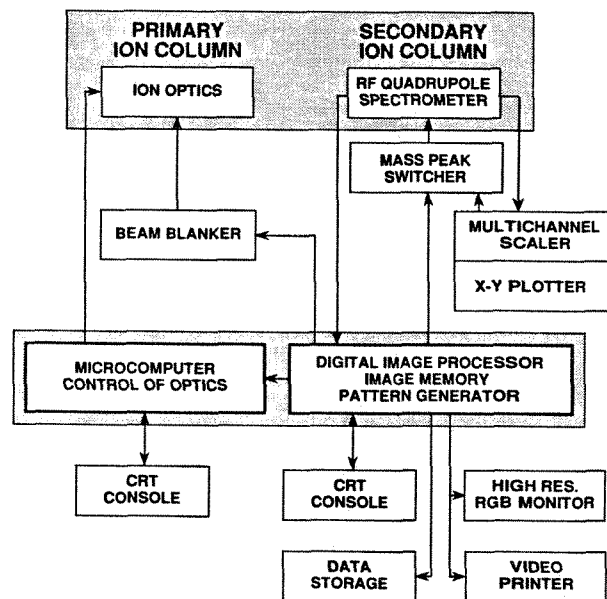


FIG. 1.--Schematics of data acquisition and control instrumentation interfaced with University of Chicago Scanning Ion Microprobe.

probe as in the previous example, a microhole would be drilled into a sample at a rate of several microns per second, and its aspect ratio would rapidly prevent the escape of the secondary ions. In addition, the positioning of the probe to submicrometer precision (an operation that necessitates some form of electronic beam control) would alone require the pre-existence of a digitized image of the region of interest. Therefore, imaging microanalysis (the acquisition of chemical maps) and the subsequent analysis of the acquired images are essential for submicrometer chemical characterization. Two procedures can be adopted for this task, based on the use of an image-processing system capable of both acquiring digitized image information and controlling the probe positioning. In one approach, intensity data for a submicrometer detail can simply be read out of the image matrix acquired over a much larger sample area. When that is done, problems of secondary-ion escape from deep craters are avoided, and the retrieved information is known to originate from a well-defined depth of erosion in the sample. In the second approach, a preliminary map is rapidly acquired, and the probe is then directed (vector or region scan) to complete the analysis of preselected details over a depth controlled by an appropriate dwell time. This procedure is more fully described in an accompanying contribution in this volume.¹¹

The above functions are performed with the UC SIM by use of the auxiliary instrumentation and computer facilities schematized in the block diagram of Fig. 1. The beam blanker, consisting of a deflection octupole inserted in the primary optical column upstream of a beam crossover, is used in conjunction with the region scan function. The digital image processor is a Kontron IBAS system supplemented

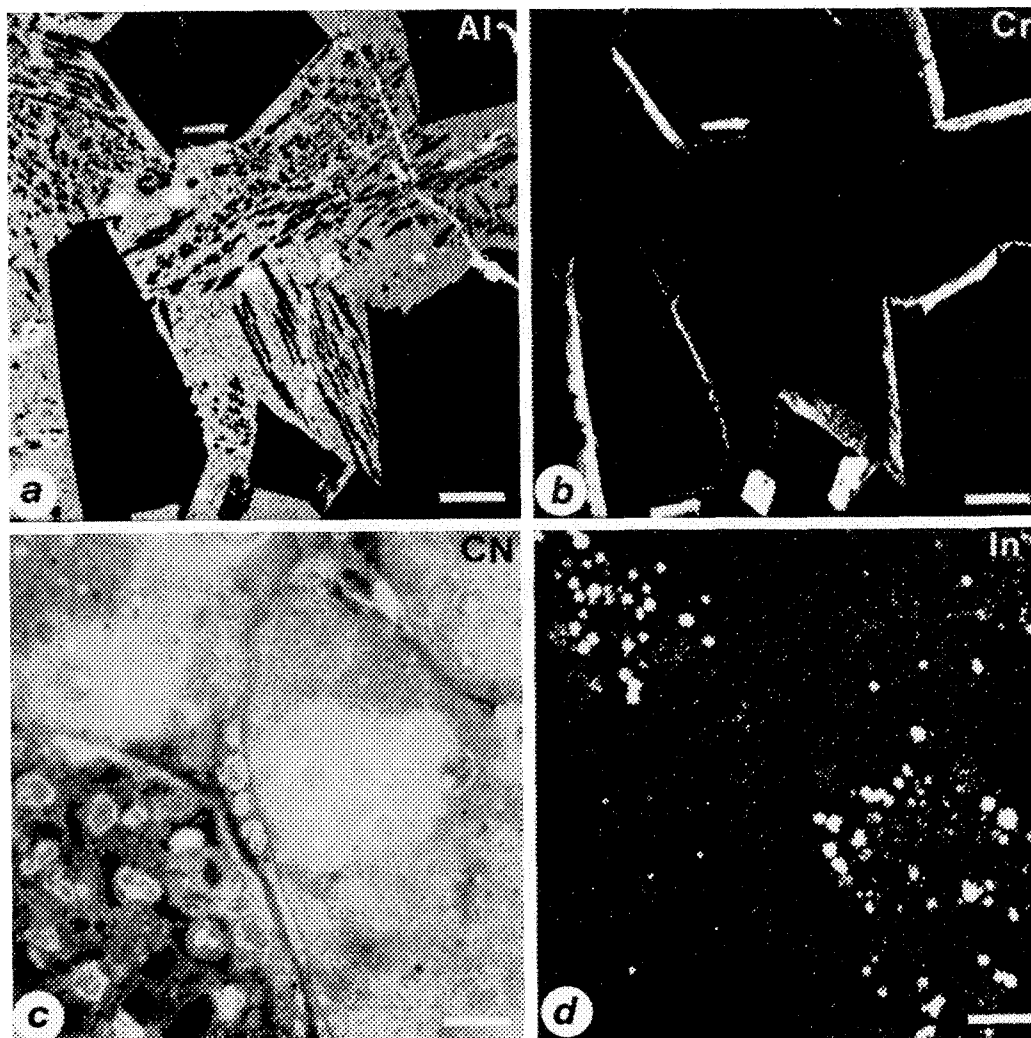


FIG. 2.--SIMS elemental distribution images of interior of Chainpur meteorite chondrule, 40 keV Ga^+ probe, scale bar 20 μm , (a) $^{27}\text{Al}^+$, (b) $^{52}\text{Cr}^+$; and SIMS images of fixed, resin-embedded thin section of rat kidney, after in vivo administration of In in soluble form, scale bar 10 μm , (c) $^{26}\text{CN}^-$, (d) $^{115}\text{In}^+$.

with a microprobe scan interface.¹²

Parallel Multielement Analytical Imaging

A shortcoming of RF quadrupole mass filters, which becomes particularly vexing in the analysis of submicrometer structures, is their inability to yield parallel multielement mass information, as time of flight or magnetic spectrometers can. Thus, correlative mass-resolved imaging generally requires sequential scans. Unfortunately, submicrometer structures or precipitates in a complex matrix, and particulate matter, may be sputtered away after just one scan. Some form of parallel readout of more than one mass-resolved image during the first scan is highly desirable. Further motivation for this requirement stems from two more concerns. Highly insulating samples, even if coated with a layer of gold, sometimes prevent sequential acquisition of SIMS images due to charging effects. Furthermore, multielement parallel image readout always provides perfect registration of images to be superposed for

correlative purposes, even when systematic difficulties such as stage drift would render such registration problematic. In view of these requirements, a scheme for RF quadrupole control during image acquisition was devised for the UC SIM, which effectively permits the simultaneous acquisition of more than one mass-resolved image during a single scan. This innovation is also described in detail, with examples, in our accompanying contribution.¹¹

By means of a "mass peak switcher," controlled by the image processor as indicated in Fig. 1, the quadrupole is retuned ($<100 \mu\text{s}$) during each raster line retrace. The result is an interlaced image for two or more distinct SIMS species, which is then unscrambled into separate mass-resolved images by image processing. These images, of reduced line resolution (raster size 526×256 for two masses), have the advantage, over those generated by sequential scans, of having originated from the same depth in the sample. By careful dosage of the dwell time, it is then possible to derive

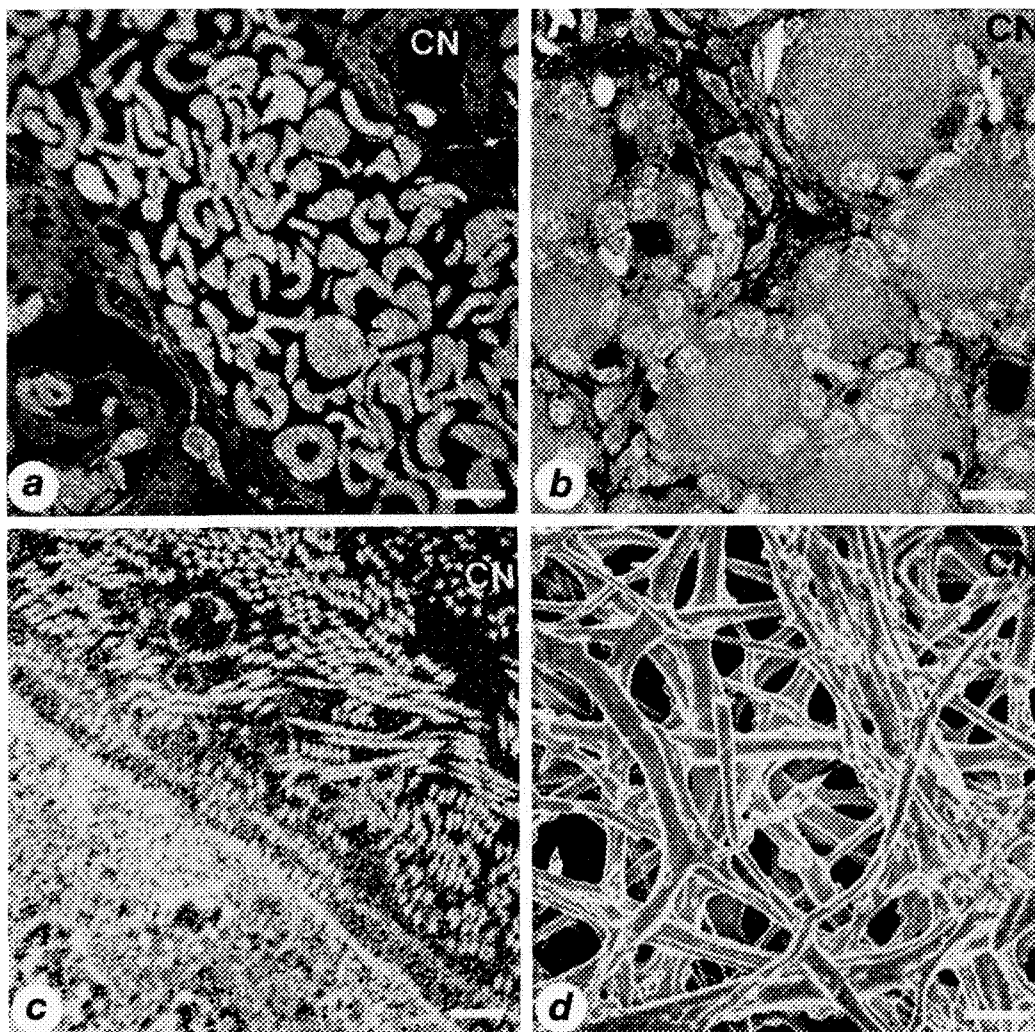


FIG. 3.--SIMS distribution maps of $^{26}\text{CN}^-$ in various biological tissues. (a) Resin-embedded thin section of rat lung blood vessel, scale bar 10 μm ; (b) resin-embedded thin section of rat thyroid, scale bar 10 μm ; (c) resin-embedded thin section through labial palp of *Mytilus edulis*, scale bar 2 μm ; (d) interior surface of ethanol-dried egg shell, scale bar 5 μm .

multielement mass information even from shallow, minute sample structures.

Examples of Analytical Imaging

After the preceding discussion, advocating the use of computer-aided techniques in SIMS imaging, it is somewhat of an anticlimax to present images in black and white. In fact, the bulk of our SIMS imaging work over the past two years has relied on image processor analysis and is best presented through color-coded images, much as described in a recent publication by Newbury et al.¹³ However, until the publishing trade finds the means to upgrade its standards, to keep pace on a routine basis with recent trends in microbeam analysis, we must revert to the conventional methods of presentation of analytical images.

Two examples from disparate fields (Fig. 2) illustrate the concept, discussed above, that elemental segregation may help bring low elemental bulk concentrations to levels sufficient for high-lateral-resolution imaging. In one

glassy matrix that cements together large olivine crystals, as well as dendritic pyrocerite precipitates, which appear black in this image. A matching map of $^{52}\text{Cr}^+$ is shown in Fig. 2(b). The Cr appears concentrated in a few crystal inclusions at the bottom of the map, and what is more interesting, at the rim of several of the olivine crystals, within the glass matrix. The definition of these Cr rims is extremely sharp, in particular where the intensity is highest, and the advantage of using a small probe size, even of low intensity, if fully exploited, in a situation where the average Cr concentration would not allow the attainment of good edge definition.

The second example of Fig. 2 (Fig. 2c and d), stems from biological microanalysis and is part of an investigation of the absorption of toxic metals by test animals. In this case the case (Figs. 2a and b), the sample is the same stone meteorite (Chainpur) whose origins and composition were described in our 1988 MAS presentation.² Here the interior of a chondrule is summarily described by the $^{27}\text{Al}^+$ map of Fig. 1(a), where the Al-rich areas represent a

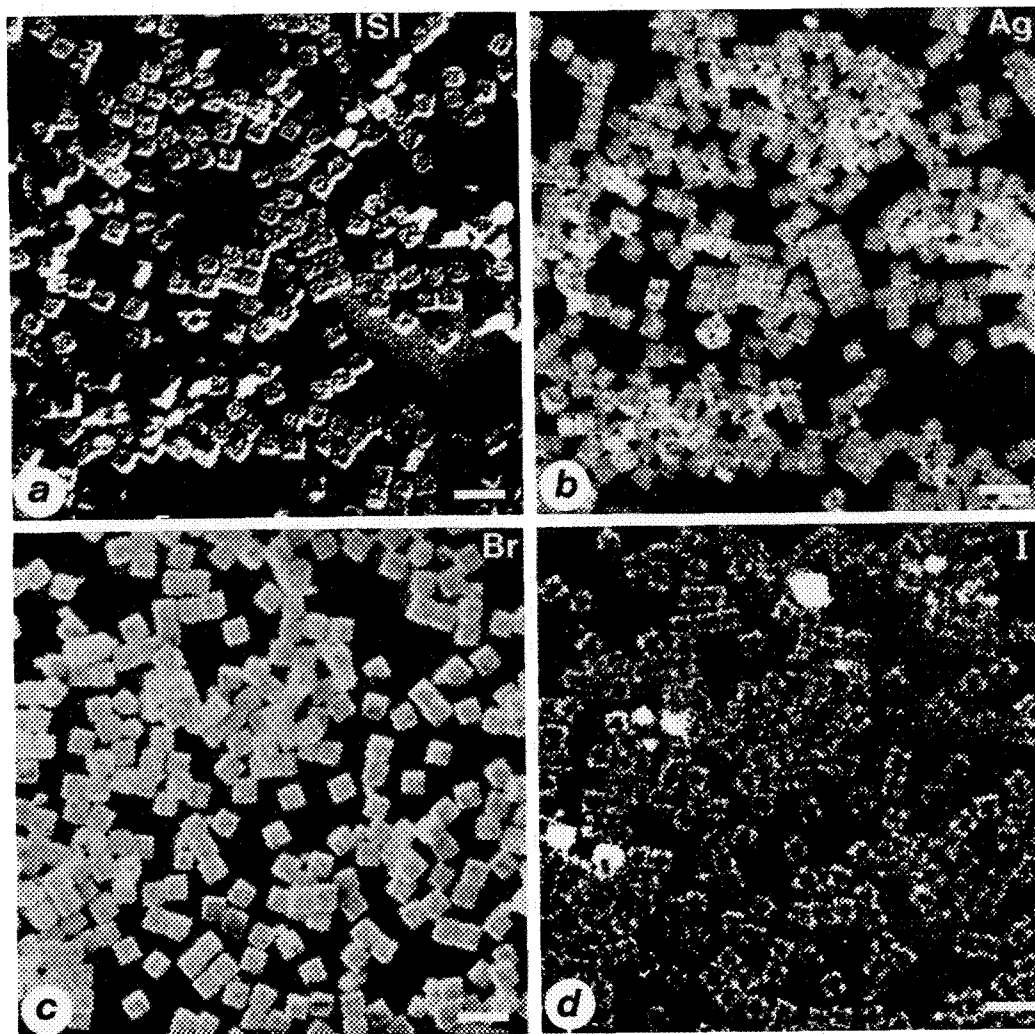


FIG. 4.--Cubic monosize AgBr photoemulsion crystals, with AgIBr layer buried beneath surface, scale bar 5 μm . (a),(b) corresponding, sequential images of surface topography (secondary ions) and of Ag distribution; (c),(d) corresponding, sequential distribution images of $^{79}\text{Br}^-$ and $^{137}\text{I}^-$.

tissue is a conventionally fixed, resin-embedded section of rat kidney, following administration to the animal of In in soluble form. The two corresponding maps show the distributions of CN and In, respectively. The copious CN-signal originates dominantly from proteins and provides detailed information of tissue histology. In this case (Fig. 2c), the morphology of part of a glomerulus is clearly outlined in the lower left corner, surrounded by proximal tubules, several cell nuclei of which are discernible. The In map (Fig. 2d) shows well-defined rounded inclusions, 0.5-3 μm in size, which correlate with the cytoplasm of the tubule cells. Their location in the CN map is indicated by a slight intensity enhancement. In praise of the black-and-white reproduction, we note that such detail would be lost in a color-coded superposition. To dwell further on the value of CN mapping in the description of the protein distribution in soft biological tissue, Fig. 3 contains an assortment of tissues viewed in rather stunning detail through

this approach. The selective, often pinpoint concentration of foreign elements such as Be, F, Cr, Ag, I, as well as of tracers such as ^{14}C , ^{15}N , and ^{44}Ca in a number of tissues can be easily detected and localized.

Finally, we present in Fig. 4 images of two spreads of photoemulsion silver halide grains, from a systematic study of model engineered crystal structures.¹⁴ These cubic monosize AgBr grains, 0.8 μm in size, contain a layer of AgIBr buried at a shallow depth beneath the surface. It is a challenge to map the distribution of several elements by sequential scans in these fragile structures: this task calls for the use of the parallel mass imaging capability implemented in our instrument by the peak-switching technique, to obtain isodepth multielement images prior to the destruction of the object. Results obtained by this approach for the same sample are shown in our accompanying contribution.¹¹ In any case, by carefully adjusting dwell time dosage, we were able to obtain the two sets of sequential images of

Fig. 4, representing respectively the topography (Fig. 4a) with the corresponding Ag distribution (Fig. 4b) for one set, and the Br (4c) and I (4d) distributions for another. The existence of a buried I layer is proved by the square rings, tentatively outlined in the low-statistics image of Fig. 4(d). This set of sequential images could only be obtained thanks to the low probe-current of our high-resolution scanning ion microprobe, which proves that the trade-off of sensitivity for resolution occasionally has its rewards.

References

1. R. Levi-Setti, G. Crow, and Y. L. Wang, "High-resolution topographic and isotopic imaging with a 40 keV Ga⁺ scanning ion microprobe," *Microbeam Analysis--1985*, 209-218.
2. R. Levi-Setti, Y. M. Chabala, Y. L. Wang, and P. Hallégot, "High-resolution ion probe imaging and analysis," *Microbeam Analysis--1988*, 93-101.
3. R. Levi-Setti, Y. L. Wang, and G. Crow, "Scanning ion microscopy: Elemental maps at high lateral resolution," *Appl. Surf. Sci.* 26: 249-264, 1986.
4. R. Levi-Setti, J. M. Chabala and Y. L. Wang, "Micro-secondary ion mass spectrometry: Physical and instrumental factors affecting image resolution," *Scanning Microscopy Suppl.* 1: 13-22, 1987.
5. R. Levi-Setti, J. M. Chabala, and Y. L. Wang, "Aspects of high resolution imaging with a scanning ion microprobe," *Ultramicroscopy* 24: 97-114, 1988.
6. J. M. Chabala, R. Levi-Setti, and Y. L. Wang, "Practical resolution limits of imaging microanalysis with a scanning ion microprobe," *Appl. Surf. Sci.* 32: 10-32, 1988.
7. R. Levi-Setti, "Structural and microanalytical imaging of biological materials by scanning microscopy with heavy-ion probes," *Ann. Rev. Biophys. Biophys. Chem.* 17: 325-347, 1988.
8. R. Levi-Setti, "Secondary electron and ion imaging in scanning ion microscopy," *SEM/1983 I*, 1-22.
9. P. H. La Marche, K. Lam, T. H. Shields, and Y. L. Wang, "Secondary ion imaging in the scanning ion microscope," *Nucl. Instr. Methods* 218: 368-374, 1983.
10. J. P. Biersack, "Computer simulations of sputtering," *Nucl. Instr. Methods Phys. Res.* B27: 21-36, 1987.
11. J. M. Chabala, R. Levi-Setti, and Y. L. Wang, "Advanced imaging and analysis techniques with a scanning ion microprobe," this volume.
12. Kontron Bildanalyse GMBH, Eching/Munich, Federal Republic of Germany.
13. D. E. Newbury, R. B. Marinenko, D. S. Bright, and R. L. Myklebust, "Computer-aided imaging: Quantitative compositional mapping with the electron probe microanalyzer," *Scanning*, 213-225, 1988.
14. T. J. Maternaghan, J. M. Chabala, C. J. Falder, and R. Levi-Setti, "Elemental mapping of silver halide emulsion microcrystals by high resolution imaging SIMS," *Proc. Int. East-West Symp. II on Factors Influencing the Efficiency of Photographic Sensitivity*, C41-46, 1988.

X-RAY MICROANALYSIS IN THE STUDY OF CYSTIC FIBROSIS

G. M. Roomans

Cystic fibrosis (CF) is the most common congenital hereditary disease among Caucasians. The main clinical symptoms are chronic obstructive lung disease and pancreatic insufficiency. Although the basic defect underlying the disease is not known, there is strong evidence that an error in the regulation of transepithelial chloride transport is of primary importance for the etiology of the disease. Also, many cell types and secretory products in CF patients show abnormally high levels of calcium. It is not clear whether this abnormality is secondary to the abnormal chloride transport, or whether the reverse holds. Since abnormal ion transport and ion distribution clearly play a central role in CF, electron-probe x-ray microanalysis appears a suitable technique to elucidate a number of questions related to the disease. X-ray microanalysis has been used in the diagnosis of CF, in the analysis of cells and tissues from CF patients, and in the analysis of cells and tissues from "animal models" for CF.

Diagnosis of CF by Electron-probe X-ray Microanalysis

The conventional way to diagnose CF is a sweat test, in which pilocarpine-stimulated sweat from the forearm is collected and its chloride content determined titrimetrically. However, in some countries, neutron activation analysis of nail clippings is used. Analysis of nail clippings can also be carried out by electron probe x-ray microanalysis:¹ abnormally high levels of sodium and chloride are indicative of CF. We have found this method suitable for diagnosis in cases where patients lack easy access to a hospital with experience in the conventional sweat test.

X-ray Microanalysis of Cells and Tissues from CF Patients

Bronchial epithelium was studied by x-ray microanalysis of sections of freeze-substituted plastic-embedded bronchial biopsies. In comparison to a control group of patients with chronic bronchitis, the goblet cells of the CF patients contained abnormally high concentration of calcium.² Also, sulfur concentrations were increased, whereas potassium levels were

relatively low. Increased calcium and sulfur levels in the secretory granules of the goblet cells of the respiratory epithelium of CF patients were also demonstrated in a study on cryosectioned nasal scrapings.³

We have studied chloride transport in cultured respiratory cells from CF patients.⁴ Cell cultures were initiated from nasal polyps from CF patients or atopic controls. The cells were cultured on membrane filters, which were mounted in an Ussing chamber and exposed to a variety of stimulants and inhibitors of ion transport. The filters were washed with isotonic mannitol to remove the culture medium, rapidly frozen, freeze-dried, and coated with a conductive carbon layer. Analysis was carried out in the scanning electron microscope. Under unstimulated conditions, there is no significant difference in elemental composition of CF cells and normal cells. However, whereas normal cells react to stimulation with beta-adrenergic agonists (isoproterenol or cAMP-analogue) with a loss of cellular chloride, the chloride content of CF cells increased after stimulation. This finding would agree with the notion that after stimulation, CF cells take up chloride ions via the $\text{Na}^+\text{-K}^+\text{-2Cl}^-$ cotransport mechanism in the basolateral membrane, but do not secrete chloride via the apical chloride channel. Whether the chloride channel itself or only its regulation is defective cannot be ascertained in this type of experiment. In addition, the CF cells appear to be more sensitive to apical application of amiloride, which inhibits the influx of Na^+ ions. On the other hand, the CF cells do not appear to be more sensitive to inhibition of the basolateral $\text{Na}^+\text{-K}^+\text{-ATPase}$ with ouabain than the controls.

Cultured fibroblasts of CF patients have significantly higher calcium levels than control cells, as was found both by x-ray microanalysis^{5,6} and other analytical techniques.⁷ Fibroblasts are not epithelial cells, but recent results showing a defective chloride channel also in lymphocytes from CF patients⁸ points to the possibility that the basic defect in CF is not restricted to epithelial cells but also occurs in cells of mesodermal origin. The subcellular distribution of the calcium in the CF fibroblasts has not been determined with certainty, but there are indications that most of the calcium is associated with the secretory proteins,⁹ which would be in line with the findings of high calcium in the secretory granules of goblet cells from CF nasal epithelium.⁴

The author is in the Department of Human Anatomy, University of Uppsala, Box 571, S-75123 Uppsala, Sweden. This study was supported by grants from the Swedish Medical Research Council (Project 07125), the Swedish National Association against Heart and Chest Diseases, and the Swedish Association for Cystic Fibrosis.

Because of the difficulties in obtaining relevant human tissue, and the ethical problems associated with experiments on patients, attempts have been made to produce an "animal model" for CF. The chronically reserpinized rat was introduced as an animal model for CF by Martinez et al.¹⁰ because it showed certain changes in exocrine gland structure function that resembled the pathological changes in the CF patients, e.g., an increased calcium content of the submandibular gland and of submandibular saliva. In our studies with x-ray microanalysis on the reserpinized rat, we observed that the local calcium content of the intracellular mucus in the acinar cells of the submandibular gland of rats had increased after treatment for 1 to 7 days with reserpine.¹¹ This change explained the increased calcium content of the submandibular saliva. In addition, the relative amount of mucus in the acinar cells has increased, which also contributed to the increase of calcium in the gland. The increase in calcium binding by the mucus may be due to reserpine-induced changes in glycoprotein composition of the intracellular mucus.¹² Changes in the total calcium content of the acinar cells of the submandibular gland were also found in other suggested animal models for CF, such as the chronically isoproterenol-treated rat, the chronically pilocarpine-treated rat, and the acidotic rat.^{11,13} Accumulation of intracellular mucus, which is the reason for the increased calcium levels, can be induced by a variety of treatments; no specific mechanism has yet been demonstrated.¹³

More recently, we have introduced a different kind of "animal model" for CF. If CF is due to an inhibition of transepithelial chloride transport, it should be possible to induce symptoms resembling CF in experimental animals by treatment with drugs that inhibit transepithelial chloride and water transport. In short-term experiments, chloride efflux through cAMP-controlled chloride channels can be inhibited by alloxan, an inhibitor of adenylate cyclase.¹⁴ Chronic treatment of rats with furosemide (1 month) causes a significant decrease in salivary flow rate after pilocarpine stimulation.¹⁵ The treatment also causes accumulation of mucus in the submandibular gland acinar cells with concurrent increase in the cellular calcium concentration. There is some indication of increased obstruction of the gland duct with mucus. Also, the calcium concentration in pilocarpine-stimulated submandibular saliva is slightly increased. This result could imply that secondary changes in calcium transport and localization in exocrine cells can be evoked by inhibition of chloride and water transport. On the other hand, one has to take into account that obstruction of the gland duct in itself could lead to some of the effects observed.¹⁶ Chronic treatment with combinations of diuretics (furosemide, bumetanide, acetazolamide, amiloride) that should further reduce fluid transport gave a similar or even more pronounced increase of the calcium

concentration in submandibular gland acinar cells compared to a furosemide alone. However, as yet we have not been able to produce the severe changes in pancreatic structure and function that are typical in CF patients. Therefore, long-term (up to three months) treatments with diuretics are now being carried out. A failure of chronic inhibition of chloride and fluid transport to induce CF-like symptoms in experimental animals might point to the possibility that the defective chloride transport could be secondary to another, more basic defect of CF cells.

Conclusion

X-ray microanalysis has been useful not only as a diagnostic method for CF, but it has also produced valuable information about ion distribution in CF epithelial cells. It has been shown by x-ray microanalysis that CF is associated with a defective chloride transport, and that in addition some CF cells have abnormally high calcium levels. Work on experimental animal models has shown that these two abnormalities may in fact be coupled. However, neither the basic defect, nor the sequence of events leading from the basic defect to the clinical symptoms, has been fully elucidated.

References

1. G. M. Roomans et al., "Electrolytes in nails analyzed by x-ray microanalysis in electron microscopy: Considerations on a new method for the diagnosis of cystic fibrosis," *Acta Paediatr. Scand.* 67: 89, 1978.
2. G. M. Roomans et al., "X-ray microanalysis of goblet cells in bronchial epithelium of cystic fibrosis patients," *J. Submicrosc. Cytol.* 18: 613, 1986.
3. J. R. Herlong et al., "Quantitative x-ray imaging of human cystic fibrosis nasal epithelium," *Microbeam Analysis--1988*, 447.
4. G. M. Roomans et al., "X-ray microanalysis of respiratory epithelial cells in cystic fibrosis," *Proc. 40th Ann. Meeting SCANDEM*, Aarhus, 1988, 38.
5. G. M. Roomans et al., "Electrolyte redistribution in cystic fibrosis fibroblasts studied by electron probe x-ray microanalysis," *Ultrastruct. Pathol.* 2: 53, 1981.
6. O. Ceder and G. M. Roomans, "Effects of culture medium on cystic fibrosis and normal fibroblasts studied by x-ray microanalysis," *Ultrastruct. Pathol.* 4: 305, 1982.
7. S. Katz et al., "The calcium hypothesis of cystic fibrosis," *Cell Calcium* 5: 421, 1984.
8. J. H. Chen et al., "A cAMP-regulated chloride channel in lymphocytes that is affected in cystic fibrosis," *Science* 243: 657, 1989.
9. G. M. Roomans et al., "Ultrastructural studies on cultured fibroblasts from patients with cystic fibrosis," *J. Submicrosc. Cytol.* 13: 445, 1981.
10. J. R. Martinez et al., "The chronically

reserpinized rat as a possible model for cystic fibrosis," *Pediatr. Res.* 9: 463, 1974; see also *Animal Models for Cystic Fibrosis*, San Francisco: San Francisco Press, 1985.

11. R. M. Müller and G. M. Roomans, "X-ray microanalysis of exocrine glands in animal models for cystic fibrosis," *SEM/1985* IV: 1583, 1985.

12. P. Versura et al., "Changes in glycoconjugates in rat submandibular gland after chronic treatment with reserpine and isoproterenol," *Histochemistry* 90: 285, 1988.

13. G. M. Roomans, "Calcium and cystic fibrosis," *SEM/1986* I: 165, 1986.

14. S. Sagström et al., "Early effects of alloxan on rat submandibular gland," *J. Submicrosc. Cytol.* 19: 555, 1987.

15. S. M. Scarlett et al., "Effects of chronic furosemide treatment on rat exocrine glands," *Exp. Mol. Pathol.* 48: 206, 1988.

16. S. Sagström et al., "Effect of duct obstruction on structure, elemental composition, and function of rat submandibular glands," *Scanning Microsc.* (in press).

EFFECTS OF INJURY ON DISTRIBUTION OF ELEMENTS IN PERIPHERAL NERVE AXONS

R. M. LoPachin, Joan Lowery, Joseph Eichberg, V. R. LoPachin, and A. J. Saubermann

The morphological changes in peripheral sciatic nerve associated with Wallerian degeneration and diabetic neuropathy are well characterized. Yet the mechanisms by which these neurotoxic processes cause structural and functional deficits remains to be determined. Several research groups using electron probe microanalysis have shown that characteristic distributions of elements and water exist in parenchymal cells.^{1,2} Accumulating evidence from studies of non-neuronal cells indicates that following physical or chemical injury these distinct patterns of distribution are lost and that this decompartmentalization mediates the consequences of injury.¹⁻³ Microprobe studies have also shown that nerve cell bodies and axons exhibit distinct patterns of elemental distribution and water content, but how this compartmentalization is altered following injury has not been examined.⁴ Therefore, in the present study, microprobe analysis was used to determine the distribution of elements (Na, K, Cl, and Ca) and water in frozen, hydrated, and dehydrated sections of sciatic nerves from diabetic rats and of sections from nerves undergoing Wallerian degeneration.

Experimental

Sciatic Nerve Injury. Unilateral sciatic nerve transection was performed on male Sprague-Dawley rats. Animals were anesthetized with ether and a midthigh incision was made. The exposed sciatic nerve was cut with a scalpel and the entry wound sutured. For induction of diabetes, rats were given intraperitoneal injections of streptozocin (60 mg/kg) to kill pancreatic beta cells.

Cryopreparation of Nervous Tissue. At 8 (n = 4 rats), 16 (n = 6) and 48 (n = 4) h post axotomy, rats were sacrificed by decapitation and incisions were made to expose the transected sciatic nerve. The distal stumps of axotomized nerves were rapidly frozen in situ by means of a pair of liquid nitrogen cooled copiers.⁴ The control group consisted of sham operated (n = 2) and nonoperated (n = 6) rats from which frozen midthigh sciatic nerve

sections were removed.⁴ At 10 (n = 6 rats) weeks following induction of diabetes, rats were sacrificed and frozen samples of distal sciatic nerve were removed. After 20 (n = 6 rats) weeks of diabetes, frozen samples were removed from proximal and distal sciatic nerve as well as from tibial nerve. Comparable regions were removed from control rats (n = 6). All frozen samples of sciatic nerve were stored in liquid nitrogen until analyzed.

Cryosectioning and Analysis. Detailed descriptions of the methods used for preparation, handling and analysis of frozen sections have been published.⁴⁻⁷ Frozen sections of control, transected, and diabetic nerve were cut at -55 C with a Sorvall MT2B microtome equipped with a cryochamber. For frozen samples of transected nerves, sections were cut at a point approximately 4 mm behind the transected face of distal stumps. An evacuated transfer device was used to transport frozen, hydrated sections from the microtome to the cold stage of an AMRay 1400T scanning electron microscope equipped with a Tracor Northern 2100 energy-dispersive system and computerized digital beam control.

In frozen sciatic nerve sections from control, axotomized and diabetic rats, myelinated axons were classified as either small (<3 μ m), medium (3 - 7 μ m) or large (\geq 7 μ m) diameter fibers. For each type of nerve fiber, elemental content and distribution were determined in four morphological compartments: mitochondria, axoplasm, myelin, and extra-axonal space. Schwann cell cytoplasm was also analyzed. Morphological compartments were visualized by scanning transmission electron microscopy (STEM): the anatomical criteria used to identify them have been described and confirmed in a previous study.⁴ Elemental content of morphological compartments such as mitochondria was determined by selected compartment analysis of 200nm-thick frozen sections. Wet weight mass was determined from continuum generation rates for hydrated samples. Sections were then dehydrated in the column vacuum of the microscope. A specially written computer program based on the Hall method⁸ for continuum normalization was used to determine elemental mass fractions.⁶⁻⁹ Data are expressed as mmol element/kg dry or wet weight (wt); for each anatomical compartment 40-60 analyses were performed.

Digital x-ray imaging was employed to generate quantitative maps of elemental distribution in nerves from 500nm-thick frozen cryosections.^{9,10} A region of section chosen for digital imaging was analyzed point by point according to a 64 \times 64 pixel matrix. Movement of the electron beam across the chosen region

R. M. LoPachin and A. J. Saubermann are at the Department of Anesthesiology, State University of New York Medical School, Stony Brook, NY 11794; Joan Lowery and Joseph Eichberg are at the Department of Biochemical and Biophysical Sciences, University of Houston, Houston, TX 77004; and V. R. LoPachin is affiliated with the College of Pharmacy, University of Houston, Houston, TX 77004. This research was supported by NIH grants ES 03830 (RML), NS 21455 (AJS) and DK 30577 (JE).

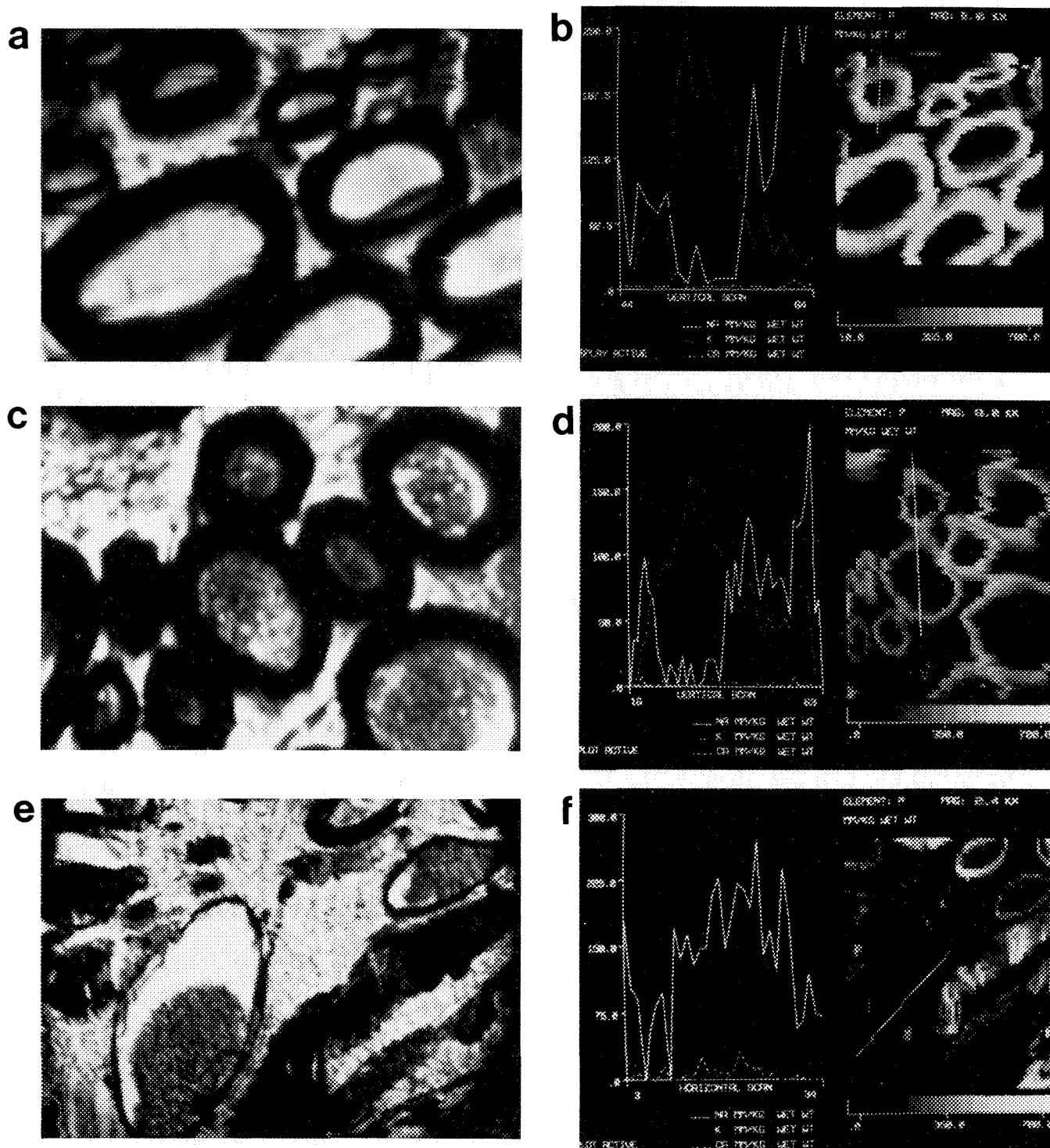


FIG. 1.--Scanning transmission electron micrographs (STEM; 1a, c, e) of frozen, unfixed, dehydrated sections from control and transected sciatic nerves. Corresponding quantitative digital x-ray images for P (1b, d and f) and comparative graphs for Na, K, Ca are also shown. Each digital image is superimposable on the appropriate STEM. Line transecting axons in each digital image represents points (pixels) from which comparative data were derived.

Data are expressed as mmol element/kg wet weight. Figures 1(c), (d) show a field of myelinated axons (8000x) from frozen section of sciatic nerve 16 h after transection. Line transects medium and small myelinated axons. Figures 1(e), (f) show large swollen axon and two smaller axons (2400x) from section of sciatic nerve 48 h after axotomy. Large fiber is transected by comparative line.

was controlled by computer. In Figs. 1(b), (d), and (f) the P digital image is displayed and each point or pixel of this image is fully quantitative. P is most often associated with structure and therefore acts as a background for comparisons of Na, K, and Ca distributions. The line transecting axons in each digital image represents points (pixels) from which comparative data were derived. Values for Na, K, Ca, and P in these images are expressed as mmol element/kg wet wt. One- and two-way analyses of variance were used and where appropriate, Dunnett's test and a least-significant-difference method of multiple comparisons were used to determine differences among means ($p < 0.05$). In the following section, only statistically significant changes in the concentration of individual elements are described for injured nerve.

Results

Normal Nerves. Figure 1(a) shows a field of small-, medium-, and large-diameter myelinated axons from a frozen section of normal sciatic nerve. The corresponding digital image for P indicates the predominant association of this element with myelin (Fig. 1b). In addition, the line graph of this figure compares the distribution of Na, K, and Ca in a small-diameter fiber. The high intracellular wet weight levels of K and low concentrations of Na and Ca are clearly evident. Although not shown, axoplasmic concentrations of Cl averaged 44 ± 3 mmol/kg wet wt. Our observations indicate that regardless of size, all axons exhibit comparable wet-weight levels of intra-axonal elements. Moreover, our results show that axoplasm and mitochondria have similar elemental compositions. When elemental distributions in axoplasm and mitochondria of proximal and distal sciatic nerve sections and of tibial sections were compared, a proximo-distal decreasing concentration gradient was revealed for Na, K, and Cl contents (Table 1). In extra-axonal space, Na (115 ± 10 mmol/kg wet wt) and Cl (100 ± 9 mmol/kg wet wt) were the predominant elements, whereas in Schwann cell cytoplasm, wet weight concentrations of P (153 ± 10 mmol/kg) and K (109 ± 8 mmol/kg) were highest.

Transected Nerves. In this study, frozen sections of transected sciatic nerve revealed progressive, degenerative changes in axonal morphology (Figs. 1c and e). These changes were similar to those reported in previous studies of axotomy in which chemically fixed tissues were examined.¹¹ Changes in elemental distribution associated with axotomy were observed first in small axons. During the

TABLE 1.--Microprobe analysis of axoplasm from frozen dehydrated sections of proximal and distal sciatic nerve and of tibial nerve from normal and diabetic rats. Also shown is the proximal to tibial decreasing concentration gradient in diabetic rats. Data represent mean values \pm SEM and are expressed as mmol element/kg dry weight. Number (n) of scans per region of sciatic nerve is presented in parenthesis.

	Element			
	K	Cl	Ca	P
Proximal Axoplasm				
control (n=47)	2342 \pm 95	803 \pm 42	1.9 \pm 0.1	409 \pm 16
diabetic (n=31)	1681 \pm 137**	594 \pm 54**	2.4 \pm 0.2	422 \pm 32
Distal Axoplasm				
control (n=89)	1914 \pm 54	688 \pm 18	1.2 \pm 0.1	402 \pm 10
diabetic (n=89)	1850 \pm 78	735 \pm 35	2.4 \pm 0.5**	423 \pm 18
Tibial Axoplasm				
control (n=75)	1570 \pm 41	617 \pm 19	1.9 \pm 0.3	319 \pm 10
diabetic (n=114)	2234 \pm 62**	794 \pm 23**	1.8 \pm 0.1	468 \pm 12**

** $p < 0.01$.

initial 16 h post-transection, small axons and their respective mitochondria lost approximately 32% of axoplasmic K and Cl, whereas Na levels increased nearly three-fold. This finding is illustrated in Fig. 1(d); the comparative line transects a medium and a small fiber and the respective data show normal wet weight concentrations of elements in the larger fiber, whereas the smaller axon exhibits decreased K and increased Na levels. Although axoplasmic Ca did not change during the first 16 h post axotomy (Fig. 1, line graph), mitochondrial concentrations of this element rose 4.5 fold. In contrast, medium- and large-diameter fibers exhibited increases in dry weight concentration of axoplasmic K with no other changes in elemental content noted. At 48 h post transection (Figs. 1e, f), axoplasm and mitochondria from all axons exhibited large gains in both dry and wet weight concentrations of Na, Cl, and Ca, whereas K levels declined to 20-30% of control. Figure 1(f) shows the elemental distribution for a large, possibly swollen axon. The comparative line graph of this figure shows the remarkable intra-axonal increase in wet weight concentrations of Na and Ca coupled with substantial loss of K.

Microprobe analysis of myelin revealed an increase in Ca content only, which persisted during the 48h experimental period. In Schwann cell cytoplasm, dry weight concentrations of K, Na, and Cl increased within the first 8 h after axotomy and remained elevated throughout the experimental period. The extra-axonal space exhibited graded increases in the dry weight levels of K, Na, and Cl over the 48h experimental period.

Diabetic Nerves. At 10 and 20 weeks after induction of diabetes with streptozocin, few morphological changes were evident in frozen sections of rat sciatic nerve. Moreover, changes in the elemental composition of axonal compartments of diabetic nerves were not

related to fiber size. After 10 weeks of diabetes, axoplasm from frozen sections of distal sciatic nerve showed increases in dry weight concentration of P (25%) and Ca (42%), whereas K levels decreased slightly (14%). In mitochondria, dry-weight K concentration fell 35%, and Na and Ca content nearly doubled.

At 20 weeks after induction of diabetes, the proximodistal decreasing concentration gradient for Cl and K observed in axoplasm and mitochondria of normal sciatic nerve was reversed; e.g., in proximal nerve sections axoplasmic K and Cl concentrations were reduced, whereas in tibial sections, the levels of these elements were increased (Table 1). These changes in elemental distribution were evident on both a dry and wet weight basis. Increases in mitochondrial P and Ca were also noted. Changes in myelin were confined mainly to proximal sections, where Na and P levels were raised and K levels decreased slightly. Elemental content of Schwann cell cytoplasm from distal sciatic nerve sections was not altered in diabetic rats. However, in proximal sciatic and tibial nerve sections, Schwann cell cytoplasm showed increased dry and wet weight concentrations of P and K.

Conclusions

Electron probe microanalysis has demonstrated the highly compartmentalized nature of elements and water in normal rat sciatic nerve.⁴ Each morphological compartment of nerve exhibits a characteristic distribution of elements that not only reflects the chemical anatomy of that region but also, possibly, its function. Further studies with microprobe analysis have shown that, following injury, the compartmentalization of elements in sciatic nerve is lost and that normal elemental distribution is perturbed according to an injury specific pattern.

Transection of rat sciatic nerve caused a sequential change in intra-axonal elemental distribution characterized by initial reductions in the levels of K and Cl followed by increases in Na and, much later, Ca. These changes in elemental composition developed prior to morphological alterations and occurred first in small axons. This latter finding correlates well with previous studies, which demonstrated a predisposition of small fibers to morphological changes following axotomy.^{12,13} How transection of sciatic nerve results in disturbed subcellular elemental distribution is unknown. The temporal nature of our results do not suggest a nonspecific increase in membrane permeability which would lead to simultaneous changes in elemental content. Rather, our data are consistent with a progressive decrease in the activity of membrane ion pump secondary to diminished neuronal energy production.^{14,15} Although previous research suggests an important role for altered elemental distribution, further studies are necessary to determine whether such changes are directly involved in mediating the structural

and functional consequences of transection.³

Induction of diabetes in rats produced subtle time-dependent changes in elemental distribution of axoplasm and mitochondria. Regionally specific alterations in K and Cl were manifest collectively as a reversal of the proximodistal decreasing gradient present along normal nerve. In addition, Schwann cell cytoplasm exhibited changes in elemental content that were related to the region of sciatic nerve examined. The mechanism by which elemental composition of axons is disrupted has not been identified. Biochemical studies of peripheral nerve from diabetic animals have shown that phosphoprotein and membrane phospholipid metabolism is disrupted, and energy utilization and (Na + K)-ATPase activity are reduced.¹⁶⁻¹⁹ These effects, either separately or in concert, might be responsible for altered elemental regulation. The consequences of disrupted homeostasis have not been determined, but might be related to characteristic alterations in morphology as well as decreased axonal transport and other functional deficits associated with diabetic neuropathy.

The present study of injured nerve cells has shown that electron-probe microanalysis can be used to measure elemental distribution and water content in peripheral nerve axons. Thin cryosections can be cut from samples of nerve that were frozen in situ. The morphology of these sections is well preserved and cellular compartments can be reliably identified. Microprobe analysis not only measures total concentration (bound and free), but also provides detailed chemical maps of elemental distribution. Such information complements studies of ion composition in nerve cells and is therefore necessary for a complete understanding of neurophysiology. For each type of nerve cell injury examined, microprobe analysis identified a characteristic, temporally dependent change in elemental distribution. Careful consideration of these distinct patterns of altered elemental distribution can suggest appropriate biochemical studies. Thus, use of both microanalytical and complementary biochemical methods can provide a rational approach to identifying the mechanisms of certain neuropathological conditions.

References

1. A. LeFurgey et al., "Heterogeneity of calcium compartmentation: Electron probe analysis of renal tubules," *J. Membrane Biol.* 94: 191, 1986.
2. L. M. Buja et al., "Alterations of ultrastructure and elemental composition in cultured neonatal rat cardiac myocytes after metabolic inhibition with iodoacetic acid," *Lab Invest.* 53: 397, 1985.
3. B. F. Trump et al., "The role of ion shifts in cell injury," *SEM/1979* III, 1.
4. R. M. LoPachin et al., "Distribution of elements in rat peripheral axons and nerve cell bodies determined by x-ray microprobe analysis," *J. Neurochem.* 51: 764, 1988.

5. A. J. Saubermann et al., "Application of scanning electron microscopy to x-ray analysis of frozen-hydrated sections: I. Specimen handling techniques," *J. Cell Biol.* 88: 257, 1981.
6. A. J. Saubermann et al., "Application of scanning electron microscopy to x-ray analysis of frozen-hydrated sections: II. Analysis of standard solutions and artificial electrolyte gradients," *J. Cell Biol.* 88: 268, 1981.
7. A. J. Saubermann et al., "Elemental composition and water content of neuron and glial cells in the central nervous system of the North American medicinal leech (*Macrobdella decora*)," *J. Neurochem.* 44: 825, 1985.
8. T. A. Hall et al., "The use of thin specimens for x-ray microanalysis in biology," *J. Microsc.* 99: 177, 1973.
9. A. J. Saubermann and R. V. Heyman, "Quantitative digital x-ray imaging using frozen hydrated and frozen dried tissue sections," *J. Microsc.* 146: 169, 1987.
10. A. J. Saubermann, "X-ray mapping of frozen hydrated and frozen dried cryosections using electron microprobe analysis," *Scanning* 10: 239, 1988.
11. J. R. Donat and H. M. Wisneiwski, "The spatio-temporal pattern of Wallerian degeneration in mammalian peripheral nerves," *Brain Res.* 53: 41, 1973.
12. R. L. Friede and A. J. Martinez, "Analysis of axon-sheath relations during early Wallerian degeneration," *Brain Res.* 19: 199, 1970.
13. L. Lubinska, "Early course of Wallerian degeneration in myelinated fibers of the rat phrenic nerve," *Brain Res.* 130: 47, 1977.
14. H. S. Bachelard and G. D. Silva, "The (Na-K) activated ATPase in degenerating peripheral nerve," *Arch. Biochem. Biophys.* 117: 98, 1966.
15. G. Majno and M. L. Karnofsky, "A biochemical and morphologic study of myelination and demyelination: II. Lipogenesis in vitro by rat nerves following transection," *J. Exp. Med.* 108: 197, 1958.
16. L. H. Schrama et al., "Altered protein phosphorylation in sciatic nerve from rats with streptozocin-induced diabetes," *Diabetes* 36: 1254, 1987.
17. L. Berti-Mattera et al., "Effect of hyperglycemia and its prevention by insulin treatment on the incorporation of ^{32}P into polyphosphoinositides and other phospholipids in peripheral nerve of the streptozotocin diabetic rat," *J. Neurochem.* 45: 1692, 1985.
18. D. A. Greene and A. L. Winegrad, "Effects of acute experimental diabetes on composite energy metabolism in peripheral nerve axons and Schwann cells," *Diabetes* 30: 967, 1981.
19. R. J. Green et al., "Sodium-potassium-ATPase activity in the dorsal root ganglia of rats with streptozotocin-induced diabetes," *Diabetologia* 28: 104, 1985.

DRUG DISTRIBUTIONS IN CELLS MEASURED BY X-RAY MICROANALYSIS

R. G. Kirk, M. J. Reasor, and Ping Lee

X-ray microanalysis can be used to study transport, quantitative distributions, and target locations of drugs in tissues. To do so the drug has to be labeled with an element not normally present in cells. The iodine-containing antiarrhythmic drug, amiodarone, is ideal for this type of study. Both amiodarone and its metabolite, desethylamiodarone, contain two atoms of iodine per molecule of drug. Long-term treatment with this drug causes pulmonary toxicity. Alveolar macrophages of amiodarone-treated animals are particularly susceptible to forming lipid-rich lamellar bodies. In experimental animals it has been shown that the toxicity caused by amiodarone is associated with a generalized induction of phospholipid accumulation in many cell types of the body.¹⁻⁵ In alveolar macrophages, the presence of numerous lysosomal lamellar bodies is a distinct characteristic of amiodarone toxicity. We have shown by electron microscopy that such abnormal alveolar macrophages developed in Fisher 344 rats treated with amiodarone.⁶ The levels of phospholipid and amiodarone as well as its principal metabolite, desethylamiodarone, have been quantified in the cells by high-pressure liquid chromatography (HPLC).⁷

In our studies we have used a combination of rapid freezing, cryosectioning, and x-ray microanalysis to measure quantitatively the intracellular distribution of iodine. Previously, we examined quantitatively distributions of the iodine-containing drug and its metabolites 24 h following the administration of a single dose.⁶ It was found that with a single dose the majority of the iodine-containing species appeared in the lysosomal granular structures and amorphous bodies. We have now extended our study to longer exposure times of 1 week and 9 weeks and have found high concentrations of iodine-containing species in the nuclei, not observed in the single-dose experiments.

Methods

Drug Treatment. Male Fisher 344 rats (Hilltop Labs., Scottsdale, Pa.) were given amio-

darone orally for periods of 1 or 9 weeks (150 mg/kg/day, 5 days/week). Controls received only the water vehicle. These animals were kept in wire mesh cages and were given water and food (standard rat lab chow) ad libitum. Alveolar macrophages were then collected after 1 week or 9 weeks of drug administration. In previous experiments, where a single dose was given, the experimental group was given orally 400 mg of the drug per kilogram of body weight.⁶

Collection of Alveolar Macrophages

To prepare rats for collection of alveolar macrophages, rats were anesthetized with sodium pentobarbital (100 mg/kg), and exsanguinated by severing of the abdominal aorta. Alveolar macrophages were recovered from the lungs by means of 5 ml lavages of warm calcium and magnesium-free Hanks' Balanced Salt Solution (HBSS) through a polyethylene tubing (PE 160) cannulated to the trachea. Cells were centrifuged at 500 G for 10 min at 4 C, washed once with HBSS, and resuspended in plasma collected from control rats. The cells were then warmed at 37 C for 15 min to allow recovery of their cellular potassium, following which they were centrifuged again to obtain a packed pellet for freeze preservation. A portion of the cell suspension was fixed in glutaraldehyde for conventional electron microscopy.⁶

Preparation of Cells for Conventional Electron Microscopy. The procedure used was similar to that reported in Reasor et al.⁷ Cells were fixed for 1 h at 4 C in 3% glutaraldehyde in Dulbecco's phosphate buffered saline (PBS) (pH = 7.4). After having been in PBS, the cells were postfixed in 1% OSO_4 in PBS for 1 h at room temperature. To preserve the lipid lamellar structure of the cells, they were treated with 0.5% tannic acid in PBS for another hour. The cells were then dehydrated with a series of ethanol solutions of increasing concentrations, infiltrated in propylene oxide, and embedded in Epon 812. Thin sections were cut with an Ultracut E41 microtome (Reichert, Vienna) and stained with 3% uranyl acetate for 20 min followed by Reynolds' lead citrate for 5 min. Sections were examined on a JEOL 100 CX electron microscope (JEOL, Tokyo).

Preparation of Cells for X-ray Microanalysis. The procedures are similar to those published previously.⁶ Small drops of packed cells were deposited on wooden dowels (4 mm long, 1.5 mm in diameter) and rapidly frozen in stirred precooled liquid propane (-190 C). Thin sections were cut with an Ultracut E41 microtome equipped with a low-temperature

R. G. Kirk is in the Department of Anatomy; M. J. Reasor, the Department of Pharmacology and Toxicology; and Ping Lee, the Department of Physiology, West Virginia University Health Sciences Center, Morgantown, WV 26506. This research was supported by a grant-in-aid from the American Heart Association and Grant DCB 88-18863 from the National Science Foundation. The authors are grateful to Laura Knoff and Candace Ogle for expert technical assistance, and to Sanofi Recherches Centre and Wyeth Laboratories for their generous gifts of drugs.

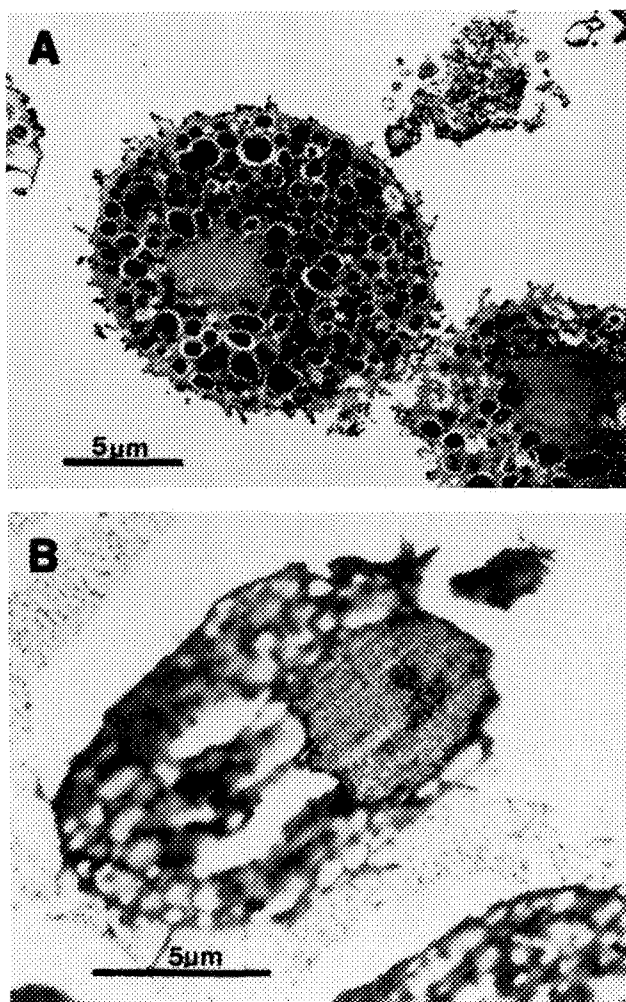


FIG. 1.--Transmission electron micrographs of rat alveolar macrophages from rat treated with amiodarone for 9 weeks. (A) Plastic section, chemically fixed and stained. Cells are engorged with lamellar bodies appearing here as dark-stained inclusions. (B) Freeze-dried cryosection without chemical fixation or stains. Lighter inclusions (amorphous bodies) correspond to "dark stained" inclusions in (A).

sectioning system (FC4C, Reichert). Sections were cut at -110°C with glass knives. Thin sections were sandwiched between two nitrocellulose films on nickel grids (100 mesh), freeze-dried in a vacuum evaporator (Denton Vacuum, Cherry Hill, N.J.) equipped with a turbo molecular pump (Balzers, Asslar, Germany). Samples were protected during freeze-drying in cold small brass containers. These containers were placed in the evaporator and allowed to warm to room temperature and then coated with a thin film of carbon. Dry nitrogen was vented into the evaporator.

X-Ray Microanalysis. A 30mm^2 energy dispersive detector (Kevex Corp., San Carlos, Calif.) and an x-ray spectrometer (Kevex 7000 series) interfaced to a PDP 1123 (DEC, Maynard, Mass.) were used to collect x-ray data. This spectrometer was used in conjunction with a JEOL 100CX electron microscope in the scanning mode.

Samples were transferred to the microscope carbon sample holder in the dry-nitrogen atmosphere of the desiccator. Spectra were acquired at an accelerating voltage of 80 kV and a beam current of 1 nA for 50 s. The method of quantification of the data has been described by Schamber⁸ and Shuman et al.⁹ The Hall method was used to calculate concentrations from the peak/continuum ratios.¹⁰

Results and Discussion

In Fig. 1 alveolar macrophages from a rat treated for 9 weeks with amiodarone are shown. It is seen that the 9-week treatment with amiodarone causes severe lipodosis in the alveolar macrophage with the appearance of numerous lamellar bodies. This appearance is similar to that previously reported following 1 week of treatment by Reasor et al.⁷

Figure 2 shows the spectra of the nucleus and amorphous bodies of cells from control animals. It is seen that there is no significant iodine in these structures. However, iodine is found in the spectra of both the nuclei and amorphous bodies in cells of 9-week treated animals as shown in Fig. 3. When iodine values obtained from long-term treated animals are compared with those obtained from 1-day treated animals, the iodine levels in both the nuclei and amorphous bodies are higher as the exposure time to the drug is extended. The relative iodine values of the nuclei and amorphous bodies are compared in Table 1. In the earlier single-dose study, the nuclear iodine concentration is very low. The majority of the cellular iodine occurs in the amorphous bodies. When drug treatment is continued for longer periods, there is a trend for the nuclear concentrations to approach those of the amorphous bodies.

In our previous study, x-ray microanalysis was used to measure the intracellular distribution of the iodine-containing amiodarone in alveolar macrophages from rats 1 day after a single dose administration of the drug.⁶ The major sites of iodine accumulation were the dense granules and amorphous bodies. Although x-ray microanalysis measures the elements present, it does not distinguish among the chemical forms in which each element may occur. It is possible to suggest the origin of the characteristic x rays from a knowledge of the intracellular chemical composition. The iodine doubtless originates from the amiodarone and its metabolites, since the control cells contain no detectable iodine. Which drug-derived species gives rise to the iodine signal is not known, since treatment with amiodarone results in accumulation of desethylamiodarone, bis-desethylamiodarone, and other unidentified polar metabolites in the cell (Fig. 4). The phosphorus in the nucleus is derived from nucleic acids; that in the lamellar bodies, from the phospholipids. Sulfur is probably derived from protein. From this kind of deduction one can arrive at certain conclusions regarding the distributions of the drug and its metabo-

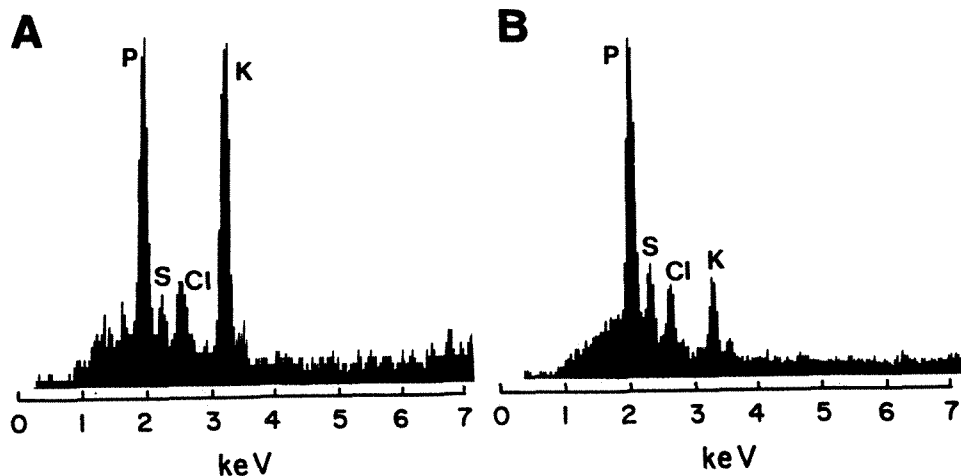


FIG. 2.--X-ray spectra of (A) nucleus, (B) amorphous body of control rat alveolar macrophage. Rat is of same age and kept in same environment as rats treated with amiodarone for 9 weeks.

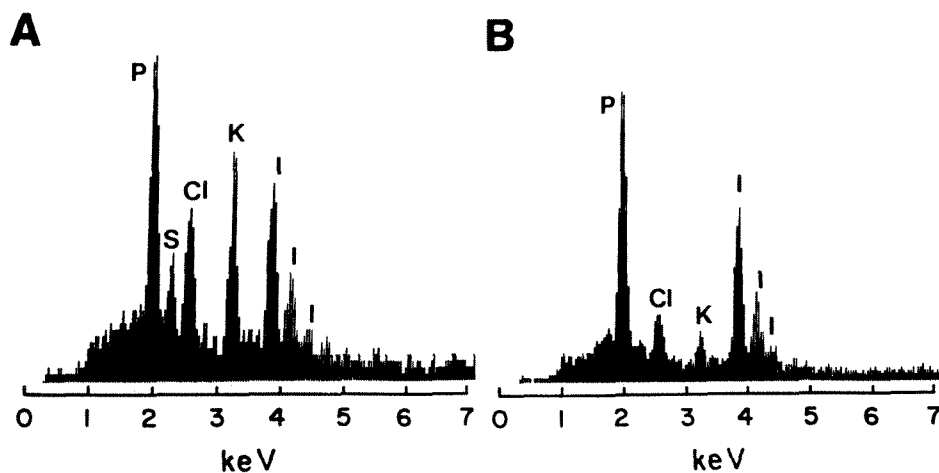


Fig. 3.--X-ray spectra of (A) nucleus, (B) amorphous body of alveolar macrophage from rat treated with amiodarone for 9 weeks.

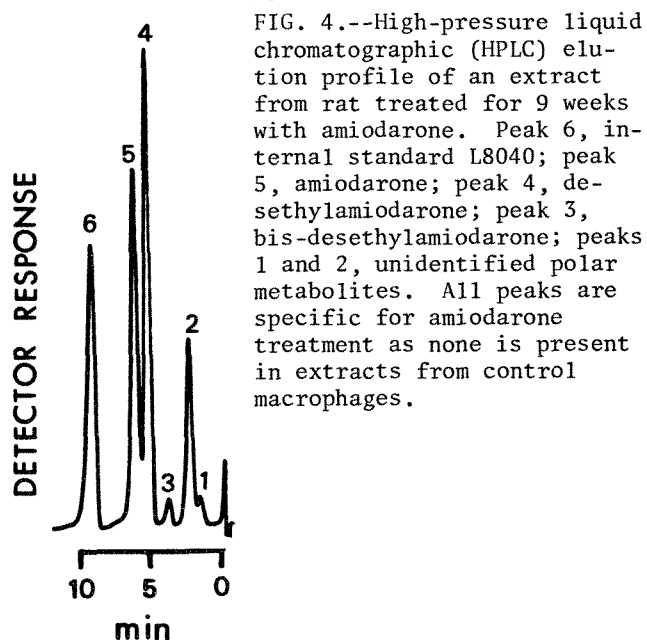


FIG. 4.--High-pressure liquid chromatographic (HPLC) elution profile of an extract from rat treated for 9 weeks with amiodarone. Peak 6, internal standard L8040; peak 5, amiodarone; peak 4, desethylamiodarone; peak 3, bis-desethylamiodarone; peaks 1 and 2, unidentified polar metabolites. All peaks are specific for amiodarone treatment as none is present in extracts from control macrophages.

tron density that they appear empty (Fig. 1). This appearance is a result of the high contrast found in freeze-dried cryosections even when no stains are used. However, x-ray microanalysis of these structures of low electron density measures high concentrations of phosphorus and iodine. The phosphorus indicates the presence of phospholipid; the iodine, the binding of amiodarone and its metabolites.

Iodine in the nucleus is negligible after 1 day but it becomes significant relative to the lamellar bodies after 1 week of treatment. After 9 weeks it is almost equal to the lamellar concentration (Table 1). In the 1-day treated rats there were two distinct groups of amorphous bodies, those with high and those with low iodine concentrations. In the 1-week and 9-week treated animals, iodine concentrations continued to rise in the amorphous bodies of the macrophages and there were no longer two distinct types, only a high-iodine group. From the amphiphilic nature of amiodarone, the preferential binding to the lipid lamellar bodies is expected. The accumulation of iodine in the nuclei of the long-term study was unexpected. Our preliminary HPLC results on isolated nuclei indicate that the iodine signal is primarily associated with the polar metabolites of peaks 1 and 2 in Fig. 4. The chemical structures and biological activities

lites and their effect on ionic composition.

In amiodarone-treated rats, the iodine was found to be highest in the amorphous bodies which are the lamellar bodies seen in plastic sections. In freeze-dried cryosections these amorphous bodies appear as vacuolar structures that are pale and sometimes of such low elec-

TABLE 1.--Comparison of iodine concentrations in the nuclei and amorphous bodies of macrophages of amiodarone-treated rats. (Data given as means \pm SEM.)

Treatment period	Iodine (mmole/kg dry wt)		
	Nuclei (N)	Amorphous bodies (AB)	N/AB
Control	0	0	
24 h ^a	10 \pm 2	90 \pm 10 (High) ^b	0.11
24 h	10 \pm 2	26 \pm 2 (Low) ^b	0.38
1 week	62 \pm 3	116 \pm 6	0.53
9 week	142 \pm 10	168 \pm 11	0.85

^aThe 24h data are taken from our previously published study.⁶

^bAmorphous bodies containing 12-40 mmoles/kg dry wt iodine are grouped as "low iodine"; those containing 52-146 mmoles/kg dry wt are grouped as "high iodine."

of these peaks have not been identified.

In conclusion, x-ray microanalysis has been used in this study to investigate the distribution and accumulation of amiodarone- and metabolite-derived iodine in single alveolar macrophages. We have shown that the technique is sensitive enough to quantify drug species in organelles and to quantify time-dependent changes. This approach can also be extended to studies of other suitable drugs in complex tissues without a need to separate the various cell types.

References

1. F. E. Marchlinski, T. S. Gansler, H. L. Waxman, and M. E. Josephson, "Amiodarone pulmonary toxicity," *Ann. Intern. Med.* 97: 839, 1982.
2. J. B. Simon, P. N. Manley, J. F. Brien, and P. W. Armstrong, "Amiodarone hepatotoxicity simulating alcoholic liver disease," *New Engl. J. Med.* 311: 167, 1984.
3. S. A. Gross and P. Somani, "Amiodarone-induced ultrastructural changes in canine myocardial fibers," *American Heart J.* 112: 771, 1986.
4. C. B. Zachary, D. N. Slater, D. W. Holt, G. C. Storey, and D. M. MacDonald, "The pathogenesis of amiodarone-induced pigmentation and photosensitivity," *Brit. J. Dermatol.* 110: 451, 1984.
5. J. F. Lemaire, A. Autret, K. Biziere, J. L. Romet-Lemone, and F. Gray, "Amiodarone neuropathy: Further arguments for human drug-induced neuropilidosis," *Eur. Neurol.* 21: 65, 1982.
6. R. G. Kirk, M. J. Reasor, and Ping Lee, "Iodine in rat alveolar macrophages following amiodarone treatment: Quantitative x-ray microanalysis," *Experimental and Molecular Pathology* 49: 339, 1988.
7. M. J. Reasor, C. L. Ogle, E. R. Walker,

and S. Kacew, "Amiodarone-induced phospholipidosis in rat alveolar macrophages," *Amer. Rev. Respir. Dis.* 137: 510, 1988.

8. F. H. Chamber, "A modification of the linear least-squares fitting method which provides continuum suppression," in T. G. Dzuby, Ed., *X-ray Fluorescence Analysis of Environmental Samples*, Ann Arbor: Ann Arbor Science, 1977, 241.

9. H. Schuman, A. V. Somlyo, and A. P. Somlyo, "Quantitative electron probe microanalysis of biological thin sections: Method and validity," *Ultramicroscopy* 1: 317, 1976.

10. T. A. Hall, "The microprobe assay of chemical elements," in G. Oster, Ed., *Physical Techniques in Biological Research*, New York: Academic Press, 1A: 157, 1971.

LAMMS IN BIOMEDICAL RESEARCH: ACHIEVEMENTS, SHORTCOMINGS, PROMISES

R. L. Kaufmann, Peter Rechmann, J. L. Tourmann, and Harald Schnatz

Ten years after the advent of the first commercially available instrument for laser microprobe mass analysis (the LAMMA 500 of Leybold-Heraeus), this technique has matured into an established alternative tool in microprobe analysis.

Although other configurations of laser microprobe mass analyzers have meanwhile emerged (LAMMA 1000, LIMA-2A, DILMA, LARIS), aiming primarily at microprobe analysis in material sciences and organic mass spectrometry, the LAMMA 500 is still the instrument by which more than 90% of the published data has been obtained. Detailed descriptions of the instrument can be found in Refs. 1-3; excellent reviews for biomedical applications in Refs. 4-6. For further information, including related topics such as specimen preparation, the reader is referred to the proceedings of previous LAMMA symposia.⁷⁻⁹

In the past, the designation of the technique and the trade name LAMMA have been used as synonyms. After the advent of instruments from various manufacturers it appears fair and appropriate to acronymize technique and instruments differently. Therefore, LAMMS will be used to designate the technique as such; LAMMA, LIMA, etc., will stand for the instruments employed.

At the present time the number of original papers related to LAMMS amounts to over 600. Roughly 30% of them are related to the life sciences. Figure 1 gives an overview of the sorts of specific problems to which the LAMMS technique has been applied. Some conclusions can already be drawn from this compilation as to the specific figures of merit that the LAMMS appears to offer users in its present state of the art.

It is the intention of the present paper to summarize the relevant achievements and limitations of the LAMMS technique, with special emphasis on biomedical samples; and to provide a look at its as yet unexploited promises.

Some General Remarks on Biomedical Microprobe Analysis

Throughout the history of microprobe analysis in the life sciences, the pioneers have faced the argument that they use much too expensive techniques under obsolete conditions to produce doubtful results and data that are con-

R. L. Kaufmann, J. L. Tourmann, and H. Schnatz are at the Institute of Laser Medicine, University of Düsseldorf, Moorenstr. 5, D-4000 Düsseldorf, Federal Republic of Germany; P. Rechmann is at the ZMK-Klinik of the University of Düsseldorf.

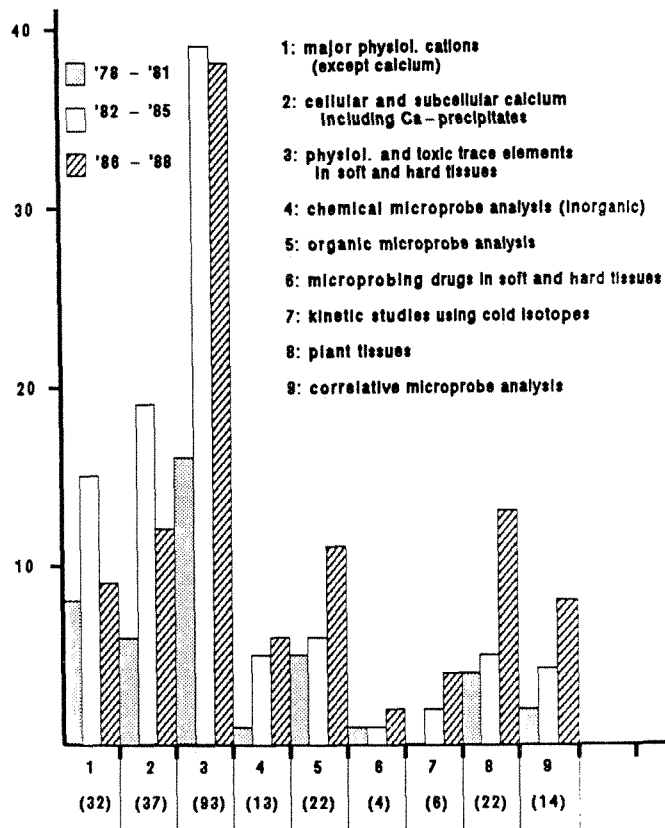


FIG. 1.--Statistical evaluation of published LAMMS work related to various fields of biomedical microprobe analysis.

sidered to be either artifacts or vague replications of what is already known. At the present state of the art, in the hands of experienced researchers, this argument no longer holds. Nevertheless, we must steadily reevaluate the true figure of merit of each technique with regard to the analytical problem under consideration.

In hunting for something known, suspected, or unknown distributed in the complex fine or ultrastructure of a biological specimen, microprobe analysis is far from the only approach available, and in most instances not even the most obvious. Histo- and cytochemistry, and particularly immunohistochemistry, are rapidly evolving disciplines that provide numerous tools to localize organic compounds in an histological section. Autoradiography is a complementary tool. Where, then, do microprobe techniques really excel in doing a job other approaches cannot provide?

The true figures of merit with special emphasis on LAMMS come into play only under the

following circumstances:

- if cyto- or histochemistry are neither sensitive nor selective enough (e.g., toxic and physiological trace metals)
- if one screens for unknowns (atomic or inorganic) constituents
- if no appropriate radioactive isotope is available for autoradiography
- if one wishes access to exchange kinetics in not disintegrated tissues or subcellular compartments by means of cold isotopes
- if basic chemical information on hitherto unidentified microstructures (inorganic or organic) is required

Some of the above conditions require MS detection techniques in combination with "soft ionization microbeam" or "soft ionization-secondary ion imaging" facilities and therefore are the domain of either the LAMMS or the SIMS approach. It can be deduced from Fig. 1 that the number of applications that use (for example) LAMMS for molecular microprobing has steadily increased in recent years, which reflects its inherent capability for providing useful information beyond merely the atomic composition.

Trends in Recent Biomedical LAMMS Application

As shown in Fig. 1, most biomedical LAMMS applications by far are related to the microprobe analysis of trace metals in soft and hard tissues. Here, the special figures of merit of the LAMMS technique converge. They are:

- the low detection limits for many of the heavy metals
- the high selectivity (isotopic discrimination)
- the simultaneous detection of all potential trace and major contaminants
- the ease and speed of operation (under screening or searching conditions)

A rather large fraction of investigations are related to aluminum and lead.¹⁰⁻¹⁴ These elements are good examples for such trace elements, for which histochemistry provides no appropriate method that is sensitive and selective enough for practical purposes. Further interesting and successful investigations refer to platinum¹⁵ (in cisplatin exposed tissues) and the uptake of Ti from dental materials^{16,17} or bone implants.¹⁸

The second largest group of papers (N = 37) concerns calcium, which for obvious reasons has always been a main target element in biomedical microprobe analysis. A special aspect of Ca-related LAMMS analyses is the evaluation of the chemical nature of small Ca concretions or microcrystallites (apatite, oxalate, carbonate)¹⁹⁻²² and the use of cold Ca isotope for kinetic studies of Ca exchange between cellular and subcellular compartments.²³⁻²⁵

Figure 1 further reveals the increasing tendency to use LAMMA as an approach to organic microprobe analysis. This may be indeed considered as a very unique feature of the LAMMS

technique. With the large body of evidence showing laser ionization to be a very powerful and exciting tool in organic mass spectrometry (see also elsewhere in this proceedings), organic laser microprobe mass analysis has rather unexpectedly gained momentum. Among recent successful demonstrations of such capabilities are the localization of lupanin and spartein in lupinus plant tissues,²⁶ the demonstration of organophosphorus on the surface of plant specimen²⁷ analyzed under atmospheric pressure conditions,²⁸ the identification of rather complex organic compounds such as phospholipids in cell organelles,^{29,30} and the microlocalization of drugs by appropriate labels or substitutes.^{31,32}

The rather steeply increasing number of papers related to plant tissue presumably reflects the rapid awareness of the life sciences of environmental and pollutional problems. Here, the recent work of Schroeder (see also elsewhere in this proceedings) on ionic transport processes in the fine roots of conifers^{33,34} may be taken as an excellent example of the specific strengths of the LAMMS technique in life sciences.

The rapidly increasing use of correlative microprobe strategies by the use of cross-checking complementary or concurrent methods (for example checking by LAMMS for the specificity of histochemical precipitation techniques³⁵) clearly fits into the present trends of cyto- and histochemistry toward analytical microscopy³⁶⁻³⁸ (see also this proceedings).

Shortcomings and Deficiencies

The issues to be discussed in this section are divided into three groups: (1) problems the LAMMS approach more or less shares with other microprobe techniques, (2) problems related to the physical principle of LAMMS analysis, and (3) instrumental insufficiencies.

The major point of concern in biomedical microprobe analysis with respect to (1) is specimen preparation. Under (2) we discuss the problem of quantification (although that is not a LAMMS-specific issue); and in (3) we address shortcomings due to nonoptimal engineering realizations (imaging, data readout, and data processing).

Specimen Preparation. It is generally agreed that quick-freezing of a highly hydrated specimen is the only way of preventing intolerable leaching or redistribution of diffusible compounds. With the few exceptions of element-specific precipitation techniques, any wet technique, even a mild glutaraldehyde fixation preceding cryo-preparation, induces disastrous effects, for example on trace element distributions (Fig. 2).

Since neither LAMMA nor LIMA instruments currently in use provide for a cryostage equipment, further specimen processing usually includes freeze drying, plastic embedding, and cutting dry sections; each of these steps features its own nasty pitfalls that one might encounter rather unexpectedly. For example,

LAMMA Analysis

Cr-UPTAKE IN CULTIVATED KIDNEY CELLS

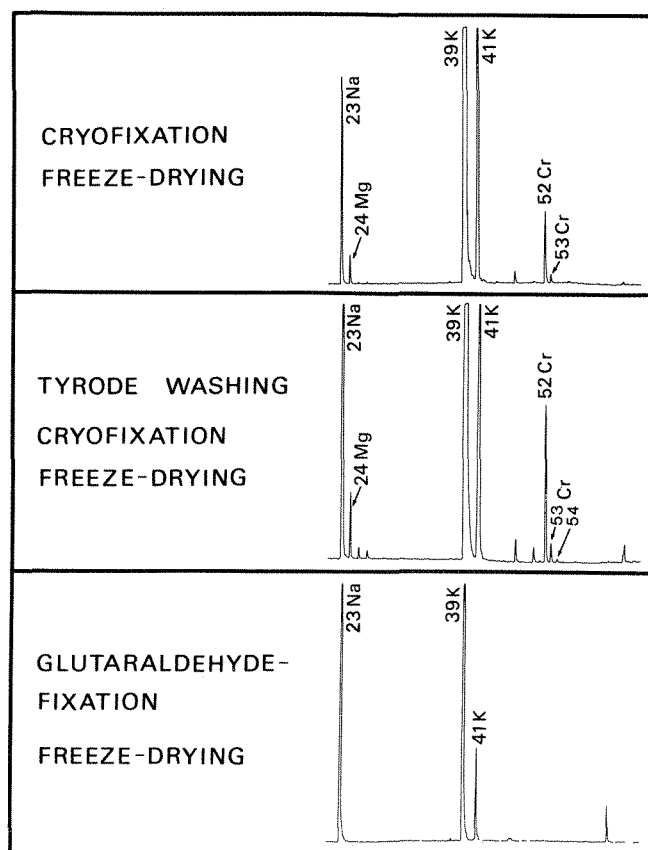


FIG. 2.--Demonstration of the effect of 1min glutaraldehyde fixation prior to shock freezing on Cr content of cultivated kidney cells exposed over 24 h to a Cr-contaminated (10^{-6} M) incubation medium.

it had been tacitly assumed that plastic embedding of freeze-dried specimens should not be a critical step with respect to element redistribution. However, a recent investigation by one of us (P.R.) revealed a rather unexpected "solubility" of metals in Spurr's low-viscosity medium, which is in wide use for tissue embedding. This result in turn led us to a systematic investigation of a larger number of polymers actually employed for plastic embedding. This investigation included other properties of such resins relevant to LAMMS analysis as for example light absorption in the UV, the content of trace impurities, and the contribution of organic fragment ions to background spectra during LAMMS analysis. A summary of the results is given in Table 1.

An embedding material ideally suited for LAMMS analysis should fulfill the following conditions: (1) UV-transparent up to at least 250 nm, (2) virtual absence of inorganic trace contaminants, (3) low MS-background from organic fragments, and, most important, (4) must neither solvate metals nor form soluble metal-organic compounds. The results obtained in 25 different brands of the most common embed-

ding materials based on either epoxy, acrylic, or polyester resins (see also Table 1) indicate that none of the materials tested were fully satisfactory. Unfortunately, the resins with the lowest "solubility" for metals (Araldite D, LR-White) are not transparent at 250 nm, which excludes UV-microscopy at this wavelength. On the other hand, the few matrices in which the UV transparency is sufficient for UV transmission microscopy (Spurr's medium, Technovit) exhibit either rather large "solvation" effects on metals or heavy background interferences from organic fragments or trace impurities.

Plastic embedding may create another problem (particularly en route to a more quantitative approach in LAMMS analysis): matrix effects on ion yield. It is true that in general matrix effects under usual operational conditions in LAMMS do not exceed an order of magnitude (in most cases, less than a factor of 2-3). However, recent observations of Verdun et al.⁴⁰ indicate that under conditions of primary (two-photon) resonant ionization, matrix effects may become much more severe.

It appears, then, that freeze drying/plastic embedding--although widely used--is far from being an optimal preparation technique for biomedical LAMMS analysis. This conclusion clearly points to frozen hydrated specimens (bulk or section) as most probably the only condition for preventing uncontrollable preparation artifacts.

Quantification. The problem of quantification in microprobe analysis has always been a matter of debate. Practically all microprobe techniques more or less share the blemish that quantification is theoretically possible but difficult to achieve in practice. Usually, the notion of "semiquantitative" analysis is chosen to characterize the situation, although to the best of our knowledge there is no general consensus about the borderline between quantitative and semiquantitative analysis. The point cannot be discussed without some conceptual reasoning.

In biomedical microprobe analysis the requirements for accuracy and precision vary widely depending on the analytical problem. In many instances one is dealing with rather large concentration gradients of elements ranging over orders of magnitude rather than over percent differences. More often than not, one is not so much interested in absolute as in relative quantification, which is easier to achieve within certain limits. Finally, with the rapidly improving sensitivity of recent microprobe analytical techniques (especially LAMMS), which have pushed detection limits (for example for toxic trace elements) below the 1ppmw level, the primary concern for using microprobe analysis in many instances is to know "what" and "where" rather than "how much."

That is not to say that the search for better quantification in microprobe analysis is no longer an important issue. With respect to

TABLE 1.--Some properties of plastic embedding materials relevant for LAMMS microprobe analysis of biomedical specimens. "UV transparency" refers to the transmission through a 2 μ m-thick section: (1) $T \geq 90\%$; (2) $90\% > T > 50\%$; (3) $50\% > T > 10\%$; (4) $10\% > T > 1\%$; (5) $T < 1\%$. "Solubility" refers to the area around an embedded metal particle in which LAMMS could detect metal traces at signal intensities twice above background level. (0) = no metal traces detected, (1) = diameter of contaminated area $\approx 20 \mu\text{m}$, (2) = diameter of contaminated area $\approx 35 \mu\text{m}$, (3) homogeneous contamination over the field of view ($\geq 800 \mu\text{m}$).

Embedding resin (trade name)	UV transparency ($\lambda=250 \text{ nm}$)	Contaminants (trace)	Major organic fragment signals (amu)	Solubility of metals				
				Dental amalgam		Wood's metal		
				Sn	Ag	Sn	Cd	Pb
Spurr's Medium	1	Na, (K)		3	2	3	3	3
Araldite M Y 753	5	Na, K		2	2	1	1	3
Araldite D	5	n.d.		0	0	0	0	0
Epon	3	Na, (K)	(53, 55, 58)	1	1	1	1	3
Bone Resin	1	Na, K	53, 55, 58	2	2	1	1	3
Lowicryl HM 20	3	(Na), K, Al	37, 113	2	2	3	3	3
Lowicryl K 11 M	2	(Na), K, P, Al	53, 55, 69, (113)	1	1	1	1	3
Plexit 55	1	Na, K, (P), Al	29, 31, 33, 53, 55, 52, 116, 156	0	0	0	0	1
LR White	5	(Na), K, (Al)	113	0	0	0	1	3
Technovit 7100	1	Na, K	29	1	1	3	3	3
Vestopal	5	Ca, (K)	91	0	0	3	3	3

LAMMS, the specific limitations have been repeatedly and extensively reviewed^{1-4,5} and are not to be reconsidered here. As a general statement one may note that at the present state of the art and with the lack of a theory to unify all physical effects of ion formation under the extremely variable operational conditions, quantification in LAMMS is anything but straightforward. Although some investigators, by careful control of all parameters (including instrumental conditions as well as target properties) have achieved accuracies of $\pm 6-8\%$ S.D. in some reference standard specimens, this is certainly not a realistic figure for practical work with LAMMS, in which (with the possibility of some statistical averaging of the shot-to-shot variability) one may reach a $\pm 30-40\%$ S.D. as a rule of thumb. Reflection-type instruments (LAMMA 1000, LIMA-2A), for some unknown reasons, appear to do better with respect to quantification than the transmission-type LAMMA 500.

Instrument Insufficiencies. In the LAMMA 500 instrument imaging of unstained plastic-embedded tissue sections usually does not permit the identification of cellular and subcellular structures. Therefore, unequivocal correlation of analytical data requires time-consuming subsequent procedures of optical and/or electron optical microscopy.

This shortcoming has been partly overcome by the incorporation of a UV-microscope in the LAMMA 500,^{3,9} which yields an absorption contrast at $\lambda = 250 \text{ nm}$ and in most cases permits an easy orientation in the texture of the specimen. However, for biomedical LAMMS analysis, an improvement of the microscopic facilities remains highly desirable (see also next section), especially for the compromised optics of present-day reflection-type instruments (LAMMA 1000, LIMA-2A).

Other engineering weaknesses of the present instruments relate to the ion optical design (spherical and chromatic aberrations, acceptance angle and off-axis transmission losses, ion detector nonlinearities, and, last but not least, signal digitizing and data processing, all contributing more or less to the problem of quantification.

Another point of concern, widely neglected so far, is the intensity profile of the focused laser beam. Under essentially the same irradiance (as controlled by the incorporated power meter), ion yield and fragmentation pattern can vary largely depending on the intensity (irradiance) distribution in the focus. With well-designed diffraction-limited optics, a laser beam with TEM₀₀ characteristics should theoretically produce either a Gaussian profile or an Aery pattern in the focus; however, the actual conditions encountered in LAMMA instruments (diffraction optics) and even more so in LIMA instruments (reflection optics) are a long way from the ideal situation. In most instances, one is dealing with a rather irregular intensity distribution (spatial and from shot to shot). Even under optimal conditions of a laser running in the TEM₀₀ mode, Cassegrainian optics (in contrast to refraction optics) produce rather complex interference patterns in the laser focus (Fig. 3).

It is obvious that results obtained even with instruments of the same type (let alone with different types of instruments) cannot be easily compared as long as the laser focusing conditions are not carefully controlled.

New Directions and Future Trends

Some recent modifications of the LAMMS technique offer promise with respect to increased sensitivity and selectivity and, in

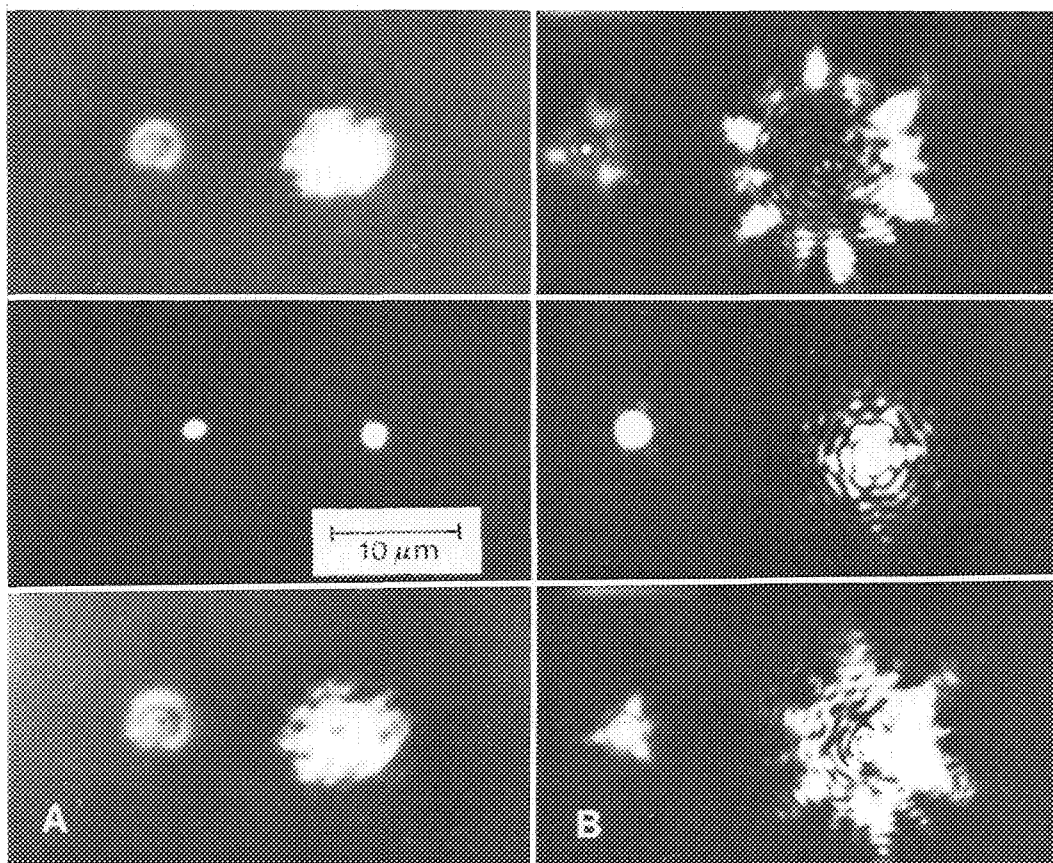


FIG. 3.--Intensity patterns in the focus of (a) UV transmitting refractive microscope objective (Zeiss $\times 32/1.05$ Ultrafluor) and (b) Cassegrainian mirror objective (Ealing $\times 52/0.65$). Image plane in each set of photographs is $20\ \mu\text{m}$ above (upper row), $20\ \mu\text{m}$ below (lower row), and in focus (middle row). Note strong differences between incoherent (lefthand) and coherent (righthand) illumination. Light sources: Ar-ion laser ($\lambda = 488\ \text{nm}$) and spectrally selected ($\lambda_{\text{max}} = 480\ \text{nm}$, $10\ \text{nm}$ half width) light of 150W tungsten/halogen bulb. Beam diameters optically adjusted to fill entrance pupil of objective.

some cases, improved conditions for quantitative analysis.

By substituting the frequency-quadrupled ND:Yag laser ($\lambda = 265\ \text{nm}$) for a tunable dye laser with continuously variable wavelength in the near UV, Muller and coworkers⁴⁰ were able to demonstrate an improvement of sensitivity in some plastic-embedded metal samples ($20\text{--}100\ \text{ppmw}$) by a factor of up to 50 when tuning the dye laser to an element-specific optical resonance. This is certainly an important improvement when one is dealing with very low concentrations of physiological (Zn, Se) or toxic (Cd, Hg) trace elements exhibiting rather unfavorable detection limits due to high ionization potential and/or strong background interferences. However, since this approach appears to be more prone to matrix effects on ion yield, the "primary resonant" laser ionization would probably be infected with a deterioration of quantitative capabilities.

Somewhat more promising in this respect is the so-called two-step approach for ion production. The rationale behind it is to separate the laser ablation process (laser probe) from the laser ionization process (post-ionization). This separation can be achieved by use of two separate lasers: one to ablate the desired amount of material from the area of interest (in the form of mainly neutrals at or even below the threshold for ion production); and the other, tunable laser to be focused above and parallel to the sample surface so that the expanding particle cloud of neutrals emerging

from the probed specimen is post-ionized via either a resonant or nonresonant multiphoton process. The idea here is to achieve a highly uniform gas-phase ionization (near saturation) which, of course, would be an improved condition for quantitative analysis. Laboratory versions have been built so far for reflection-type instruments such as the LIMA 2-A⁴⁶ and the LAMMA 1000.^{47,48} Resonant multiphoton positionization (REMPI) as well as nonresonant ionization may each offer its own figures of merit, depending on the analytical task. Whereas resonant MPI would improve sensitivity and selectivity not only for certain elements but also for selected organic compounds by orders of magnitude, nonresonant MPI might be in addition a major step toward quantitative multi-element analysis.

Laser post-ionization is of course not necessarily restricted to laser probe (ions, neutrals). Such instruments are actually under development and also extend the spectrum of future options in biomedical micro- and micro-probe analysis.

With respect to biomedical micro(probe) analysis, laser-induced mass spectrometry has quite recently opened the way to an analytical field hitherto thought to be inaccessible to mass spectrometry: the mass analysis of large proteins (over 10^5 Daltons). As the Hillenkamp group⁴⁹ has first demonstrated in a LAMMA 1000 instrument (see also this LAMMS workshop),

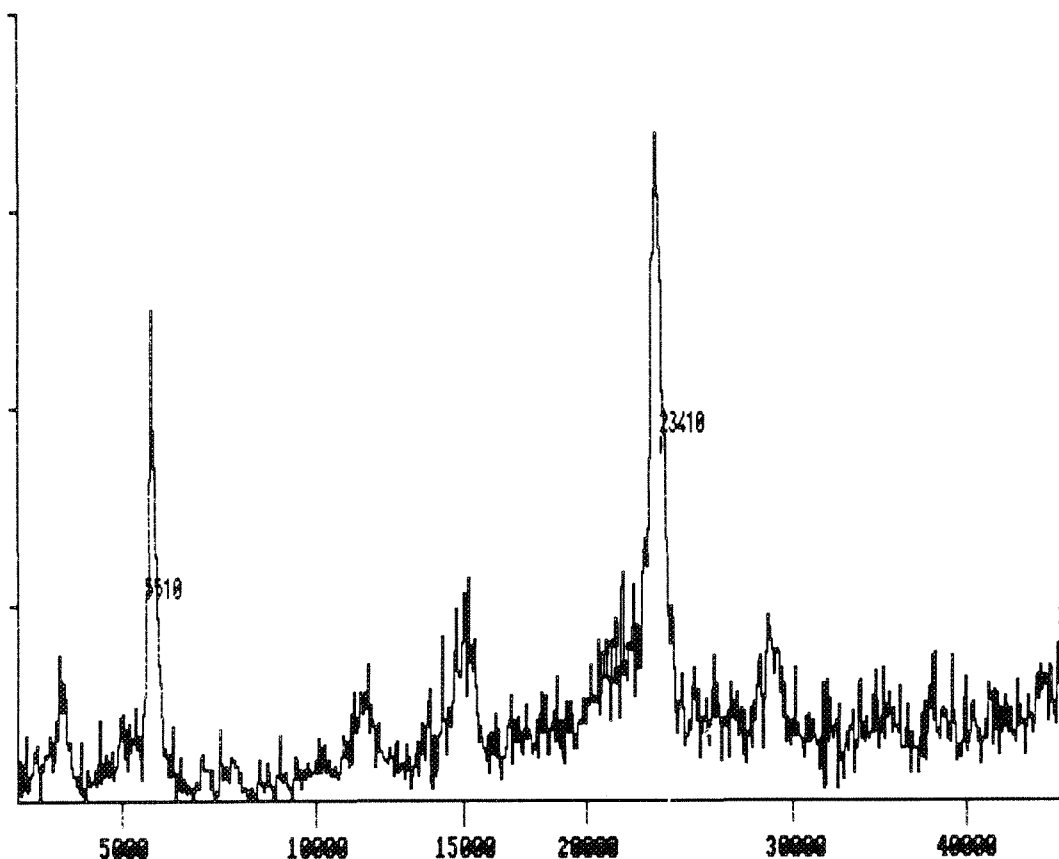


FIG. 4.--LAMMS-spectra recorded by matrix-assisted UV laser desorption from trypsin/insuline mixture, demonstrating capability of LAMMS-technique to extend into the mass spectrometric analysis of very large (protein) molecules. Specimen: air-dried 1 μ l droplet of hydrous solution containing 10^{-5} M insuline/trypsin and 10^{-2} M nicotinic acid (for enhancing laser absorption). Analysis done by reflection-type LAMMA 1000 instrument. Spectra of 10 shots summed. Abscissa in amu.

laser desorption and ionization of intact protein molecules out of their solid-state phase is regularly possible under certain conditions; the heaviest parent molecule ever detected in MS is over 2×10^5 Daltons (catalase monomer).

We have been able to reproduce this exciting achievement (Fig. 4), which in accordance with the present state of the art could develop into an easy and straightforward method for the determination of molecular masses out of minute (femtomolar) amounts of proteins with an accuracy of 0.1%; that is more accurate by nearly two orders of magnitude than the chromatographic techniques currently used in analytical chemistry of proteins in general and biomedicine in particular. Although this is not yet a microprobe capability in the strict sense of the word, one may dare to predict--at least under certain favorable circumstances--that this approach may extend to microprobe analysis, for example of homogeneous cellular or extracellular deposits or inclusions.

Imaging, especially of biomedical specimens, is still unsatisfactory in transmission (and even more so in reflection) of LAMMS instruments. The incorporation of a UV transmission optical microscope in the LAMMA 500 instrument by one of us (R.L.K.) has partly overcome the poor absorption contrast usually encountered in unstained plastic-embedded sections.³⁹ However, with the trend toward deep-frozen hydrated bulk specimen (see the section on specimen preparation above), other imaging techniques must be envisaged. To this end the

principal options are synoptically sketched in Fig. 5. A piezomechanical x-y scanning device acting on the specimen table provides for either electron optical or optical scanning microscopy based on a multiplicity of potentially useful secondary emissions (secondary electrons, photoelectrons, secondary photons, probe current, etc.).

It is obvious that such an arrangement (including the option for laser post-ionization) creates a lot of geometrical conflicts with respect to the various beam axes, at least as long as the ion transfer to the TOF is maintained perpendicular to the specimen surface. However, recent simulations of ion optical extraction geometries indicate that devices can be designed that would permit a 90° deflection of the ions without an intolerable loss of transmission and TOF resolution. That would in turn permit the incorporation of high-N.A. focusing optics for the probing laser beam, so that spot size might be brought down to near the diffraction-limited spot size of, say, 1 μ m or below. (The actual figure is 3-4 μ m in the reflection-type instruments.)

References

1. H. Vogt, H. J. Heinen, S. Meier, and R. Wechsung, "LAMMA 500 principle and technical description of the instrument," *Fresenius Z. Anal. Chem.* 308: 195, 1981.
2. E. Denoyer, R. Van Grieken, F. Adams, and D. F. S. Natusch, "Laser microprobe mass spectrometry: 1. Basic principles and perfor-

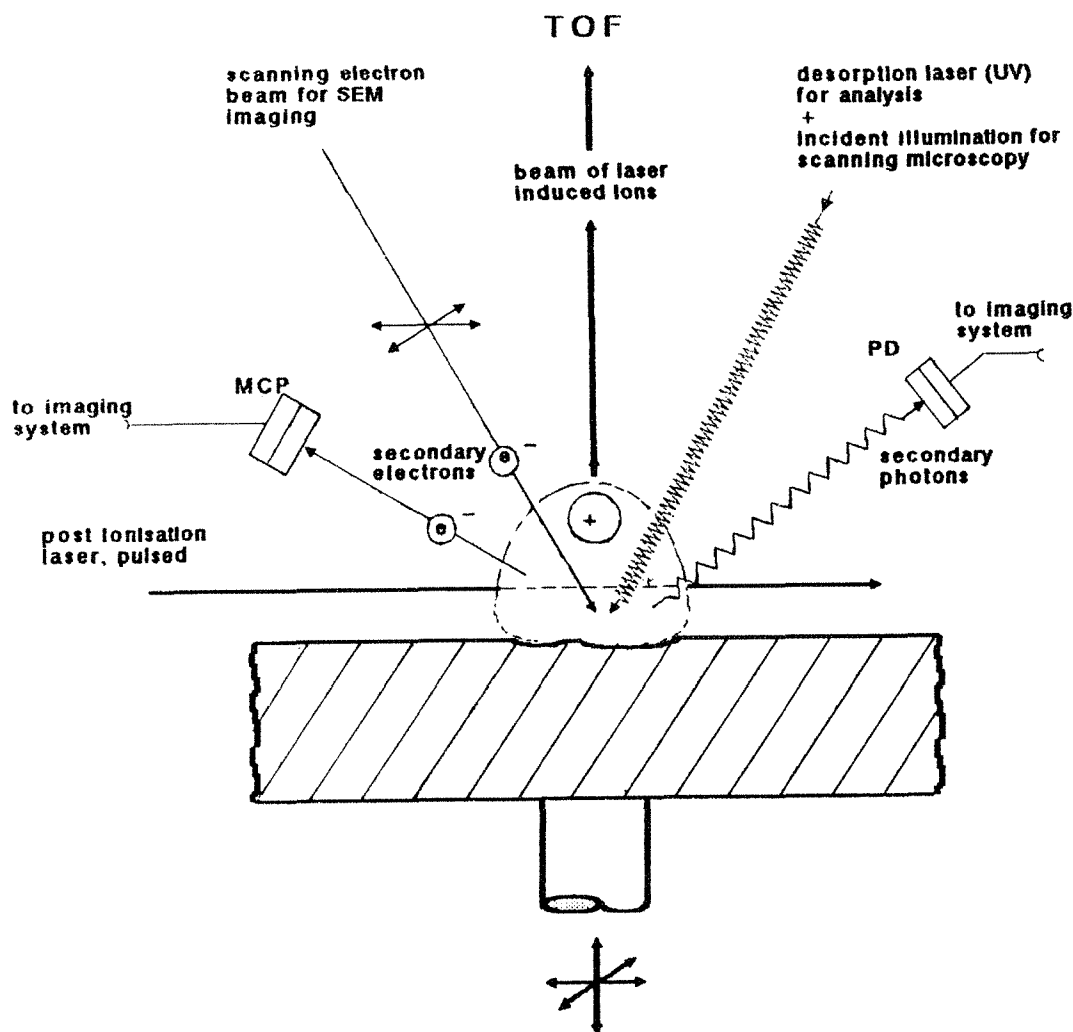


FIG. 5.--Schematic sketch of facilities to be incorporated in future LAMMS instrument with special emphasis on imaging capabilities.

mance characteristics," *Anal. Chem.* 54: 26A, 1982.

3. A. H. Verbueken, F. J. Bruynseels, R. Van Grieken, and F. Adams, Eds., *Laser Microprobe Mass Spectrometry*, New York: Wiley, 1988.

4. A. H. Verbueken, F. Van de Vyver, M. De Broe, and R. Van Grieken, "Applications of laser microprobe mass analysis in medicine," *Clin. Lab. Sci.* 24: 263, 1987.

5. R. Kaufmann, "The present state of laser microprobe mass analysis (LAMMA) as applied to biomedical samples," *Microbeam Analysis--1986*, 177.

6. A. H. Verbueken, F. J. Bruynseels, and R. E. Van Grieken, "laser microprobe mass analysis: A review of applications in the life sciences," *Biomed. Mass Spectrom.* 12: 438, 1985.

7. *Fresenius Z. Anal. Chem.* 308: 193-320, 1981.

8. *Proc. 2nd. LAMMA-Workshop*, Forschungsinstitut Borstel, 1983, 1-159.

9. *Anal. Chim. Acta* 195: 1-361, 1987.

10. F. L. Van de Vyver, A. H. Verbueken, W. J. Visser, R. E. Van Grieken, and M. C. De Broe, "Localization of aluminum and iron by histochemical and laser microprobe mass analytical techniques in bone marrow cells of chronic haemodialysis patients," *J. Clin. Pathol.* 37: 837, 1984.

11. H. Zunkley, P. F. Schmidt, H. P. Bertram,

A. E. Lison, B. Winterberg, K. Spieker, H. Losse, and R. Barckhaus, "Aluminum concentration of bone cells in dialysis osteomalacia," *Trace Elements Med.* 1: 103, 1984.

12. P. F. Schmidt and H. Zunkley, "The use of laser microprobe mass analysis in biomedical research," *J. Phys.* 45: C2-569, 1984.

13. J. F. Muller, M. A. Gelot, P. Netter, and R. Kaufmann, "Detection of aluminum by LAMMA spectrometry in plasma and in synovial liquids of patients on chronic dialysis," *Biomed.* 36: 380, 1982.

14. A. H. Verbueken, F. L. Van de Vyver, R. E. Van Grieken, and M. E. De Broe, "Microanalysis in biology and medicine: Ultrastructural localization of aluminum," *Clin. Nephrol.* 24: S58, 1985.

15. A. H. Verbueken, F. L. Van de Vyver, G. J. Paulus, W. J. Visser, G. A. Verpooten, M. E. De Broe, and R. E. Van Grieken, "Laser microprobe mass analysis (LAMMA) in nephrological investigations," in P. Brätter and P. Schramel, Eds., *Trace Element Analytical Chemistry in Medicine and Biology*, 375, 1984.

16. J. F. Osborn, H. Newesely, C. Werhahn, H. Brückmann, and E. Gabriel, "Doped ceramics: A new approach to the dynamics of osteogenesis following calcium phosphate ceramic implantation?" in A. J. C. Lee, T. Albrektsson and P. I. Branemark, Eds., *Clinical Applications*

- of *Biomaterials*, New York: Wiley, 1982, 219.
17. R. Lehmann, H. Sluka, and P. F. Schmidt, "Unerwartete intrazelluläre Ablagerungen von TiO_2 in Pulpagewebe," *Quintessenz* 3: 613, 1982.
 18. J. F. Osborn and E. Gabriel, "Untersuchung periimplantären Knochengewebes auf Titan mittels Laser-Mikrosonden-Massen-Analysator (LAMMA)," *Dtsch. Zahnärztl. Z.* 37: 769, 1982.
 19. H. Pau and R. Kaufmann, "Laser microprobe analysis (LAMMA) of spherulites in human cataract lenses," *Arch. Ophthalmol.* 101: 1935, 1983.
 20. A. J. Chaplin, P. R. Millard, and P. F. Schmidt, "The use of laser microprobe to identify calcium oxalate in histological material," *Histochem.* 75: 259, 1982.
 21. P. F. Schmidt and H. Zumkley, "The use of laser microprobe mass analysis in biomedical research," *J. Phys.* 45: C2-569, 1984.
 22. J. Pfeiffer, E. Danner, and P. F. Schmidt, "Oxalate-induced encephalitic reactions to polyol-containing infusions during intensive care," *Clin. Neuropathol.* 3: 76, 1984.
 23. H. J. Heinen and W. H. Schröder, "The technique of LAMMA micro mass spectrometry," *Biochem. Soc. Trans.* 9: 591, 1981.
 24. W. H. Schröder, "Tracing the way of Ca from internal stores to the photosensory membrane in crayfish," *Invest. Ophthalmol. Visual Sci.* 22: 276, 1982.
 25. A. M. Meyer zum Gottesberge, "Physiology and pathophysiology of inner ear melanin," *Pigment Cell Res.* 1: 238, 1988.
 26. M. Wink, H. J. Heinen, H. Vogt, and H. M. Schiebel, "Cellular localization of quinolizidine alkaloids by laser desorption mass spectrometry (LAMMA 1000)," *Plant Cell Rep.* 3: 230, 1984.
 27. J. J. Morelli, S. K. Viswanadham, A. G. Sharkey Jr., and D. M. Hercules, "laser mass spectrometry of organophosphorus pesticides and related compounds," *Int. J. Environ. Anal. Chem.* 31: 295, 1987.
 28. J. J. Morelli and D. M. Hercules, "Ambient pressure laser mass spectrometry of organophosphorus pesticides on plant tissues," *Anal. Chem.* 58: 1294, 1986.
 29. B. Lindner and U. Seydel, "Laser desorption mass spectrometry of complex biomolecules at high laser power density," in A. Benninghoven, Ed., *Secondary Ion Mass Spectrometry*, Springer Series in Chemical Physics 36: 370, 1984.
 30. U. Seydel, B. Lindner, U. Zähringer, E. T. Rietschel, S. Kusomoto, and T. Shiba, "Laser desorption mass spectrometry of synthetic lipid alike compounds," *Biomed. Mass Spectrom.* 11: 132, 1984.
 31. S. De Nollin, W. Jacob, L. Van Vaeck, Y. Berger, W. Cautreels, B. Remandet, and P. Vic, "Subcellular localisation of a drug by two independent methods: Laser microprobe mass analysis and autoradiography," *Proc. 3rd Int. Laser Microprobe Mass Spectrom. Workshop*, Antwerp, 1986, 53.
 32. R. Mannhold and R. Kaufmann, "Zur Wirkortanalyse herzkativer Pharmaka," *Arch. Pharm. (Weinheim)* 319: 1028, 1986.
 33. J. Bauch, "Biological alterations in the stem and root of fir and spruce due to pollution influence," in B. Ulrich and J. Pankrath, Eds., *Effects of Accumulation of Air Pollutants in Forest Ecosystems*, D. Reidel Publ. Co., 1983, 377.
 34. W. H. Schröder, A. Einerhand, J. Lauer, H. Eschweiler, R. Langner, G. L. Fain, and J. Bauch, "Multi-isotope multi-element labeling in microbeam analysis of biological tissues," *Microbeam Analysis--1987*, 359.
 35. J. L. Van Reempts, M. Borgers, S. R. De Nollin, T. C. Garrevoet, and W. A. Jacobs, "Identification of calcium in the retina by the combined use of ultrastructural cytochemistry and laser microprobe mass analysis," *J. Histochem. Cytochem.* 32: 788, 1984.
 36. A. H. Verbueken, F. L. Van de Vyver, W. J. Visser, F. Roels, R. E. Van Grieken, and M. E. De Broe, "Use of laser microprobe mass analysis (LAMMA) for localizing multiple elements in soft and hard tissues," *Biol. Trace Element Res.* 13: 397, 1987.
 37. S. De Nollin, M. Borgers, W. Jacob and D. Wellens, "The prevention of Ca^{2+} overload in vascular smooth muscle by flunarizine as detected by laser microprobe mass analysis (LAMMA)," *Angiology* 36: 297, 1985.
 38. F. L. Van de Vyver, A. H. Verbueken, R. E. Van Grieken, and M. E. De Broe, "Laser microprobe mass analysis (LAMMA): Current state of the art with special emphasis on biomedical applications," in K. F. J. Heinrich, Ed., *Microbeam Analysis--1982*, 341.
 40. F. R. Verdun, G. Krier, and J. F. Muller, "Increased sensitivity in laser microprobe mass analysis by using resonant two-photon ionization processes," *Anal. Chem.* 59: 1383, 1987.
 41. P. Wieser, R. Wurster, and R. Wechsung, "Methods for quantification with LAMMA, *Proc. 2nd LAMMA Workshop*, Forschungsinstitut Borstel, 1983.
 42. F. Adams and T. Mauney, "Laser microprobe mass analysis for microscopic characterization," *Adv. Mass Spectrom.*, 1985, 507.
 43. R. W. Odom and I. C. Niemeyer, "Quantitative elemental analysis by laser ionization mass spectrometry (LIMS)," *Proc. 3rd Int. Laser Microprobe Mass Spectrom. Workshop*, Antwerp, 1986, 155.
 44. R. W. Odom, C. J. Hitzman, and B. W. Schueler, "Quantitative materials analysis by laser microprobe mass analysis," *Mat. Res. Soc. Symp. Proc.* 69: 265, 1986.
 45. D. S. Simons, "Laser microprobe mass spectrometry," in A. Benninghoven, I. Okano, R. Shimizu, and H. W. Werner, Eds., *Springer Series in Chemical Physics*, 36: 1984, 158.
 46. R. W. Odom and B. Schueler, "Thin film microanalysis using laser ablation and laser ionization mass spectrometry," *Thin Solid Films* 154: 1, 1987.
 47. U. Bahr, B. Spengler, M. Karas, and F. Hillenkamp, "Multiphotonionization (MPI) mass spectrometry of laserdesorbed molecules," *Proc. 4th Int. Conf. on Ion Formation from Organic Solids*, New York: Wiley, 1988.
 48. U. Bahr, B. Spengler, A. Overberg, and F. Hillenkamp, "UV-multiphoton-ionization of laserdesorbed organic molecules," *11th Int. Mass Spectrom. Conf.*, Bordeaux, 1988.
 49. M. Karas and F. Hillenkamp, "Laser desorption-ionization of proteins with molecular masses exceeding 100 000 Dalton," *Anal. Chem.* 60: 2299, 1988.

TRACE ELEMENT ANALYSIS IN NEURODEGENERATIVE DISEASE

D. P. Perl and P. F. Good

The histological lesions of Alzheimer's Disease (AD) include the neurofibrillary tangle (NFT), granulovacuolar degeneration (GVD), and the senile plaque (SP). In 1965 it was discovered that the intracerebral administration of aluminum salts could initiate the formation of a type of neurofibrillary tangles in the neurons of the rabbit.^{1,2} Brains of AD patients have shown by bulk analysis to contain 2-3 times the amount of aluminum as the brains of age-matched controls.³ With the technique of scanning electron microscopy--x-ray energy spectroscopy (SEM-XES) we demonstrated that neurons from the heavily tangle-bearing region of the hippocampus had an increase of aluminum compared to nontangled cells.⁴

By the use of laser microprobe mass spectrometry we have shown that the aluminum accumulation of AD is specifically localized to the NFT itself and occurs in a concentration of 10-50 ppm.

Methods

Tissue blocks of hippocampus obtained from the brains of patients dying with AD and from those diagnosed as normal aging were fixed in 10% phosphate-buffered formalin, dissected into cubes, postfixed in osmic acid, dehydrated in graded alcohols, and embedded in Spurr's epoxy resin. Sections were cut with glass knives at 0.5 μ m thickness on a Reichert Ultracut ultramicrotome. The sections were mounted on 50-mesh copper grids and stained with 0.01% toluidine blue. Laser microprobe mass analysis was performed with a LAMMA-500 with the 100 \times objective and a laser energy of 8-10 μ J in the positive-ion mode. Mass spectral data from five probe sites in the nucleus, cytoplasm, NFT of tangle-bearing neurons, and adjacent neuropil were collected from each of ten tangle-bearing neurons and ten histologically normal neurons of four AD cases, and ten neurons of two normal aged controls. Integrated peak intensity was calculated at all nominal atomic mass numbers from 1 to 320 and population statistics were obtained for the elements sodium, aluminum, silicon, potassium, calcium, and iron.

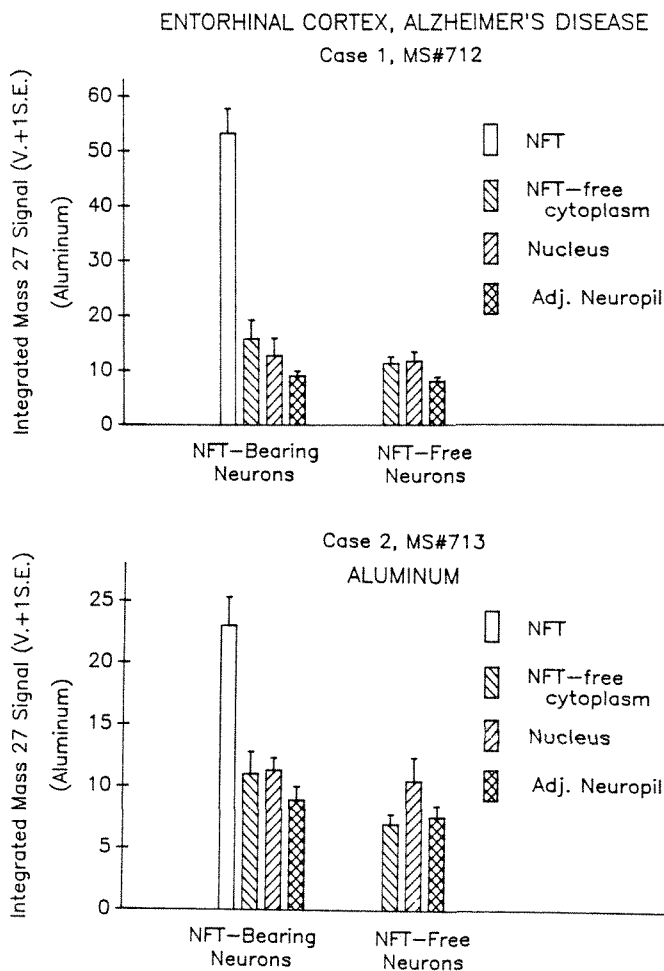
Results

Data for the NFT region of tangle-bearing neurons show a prominent increase in the aluminum-related mass 27 signal when compared with the adjacent cytoplasm and neuropil. The nuclei of these neurons show a mild increase in aluminum-related signal when compared with the

adjacent cytoplasm and neuropil, whereas the normal neurons of the AD cases show only a mild increase in the aluminum-related signal of the nuclei. The neurons of the normal aged controls show no similar increase in aluminum-related signal in any of their cellular compartments.

Discussion

Aluminum toxicity has been considered to be among the candidates for AD etiology. This has been a controversial question among neurologists and neurobiologists concerned with AD. The data presented here suggest that aluminum is selectively bound to the neurofibrillary tangle of AD. This finding must be accounted for in any hypothesis of the etiology and pathogenesis of the disease. These studies also show the power of laser microprobe analysis in addressing these questions.



The authors are at the Division of Neuropathology, Department of Pathology, Mt. Sinai Medical Center, New York, NY 10029-6574.

References

1. I. Klatzo, H. Wisniewski, and E. Streicher, "Experimental production of neurofibrillary degeneration: I. Light microscopic observations," *J. Neuropath. Exptl. Neurol.* 24: 187-199, 1965.
2. R. D. Terry and C. Pena, "Experimental production of neurofibrillary degeneration: 2. Electron microscopy, phosphatase histochemistry and electron probe analysis," *J. Neuropath. Exptl. Neurol.* 24: 200-210, 1965.
3. D. R. Crapper, S. S. Krishnan, and A. J. Dalton, "Brain aluminum distribution in Alzheimer's disease and especially neurofibrillary degeneration," *Science* 180: 511-513, 1973.
4. D. P. Perl and A. R. Brody, "Alzheimer's disease: X-ray spectrometric evidence of aluminum accumulation in neurofibrillary tangle-bearing neurons," *Science* 208: 297-299, 1980.

CORRELATIVE ION AND ELECTRON MICROSCOPY FOR IMMUNOCYTOCHEMISTRY

J. J. Lee, R. W. Linton, J. L. Hunter, J. D. Shelburne, J. L. Burchette Jr.,
A. P. Sanfilippo, and R. D. Voyksner

Colloidal gold probes are widely used for light and electron microscopic immunocytochemistry, for example in cell surface labeling and as markers in histological samples.¹⁻³ One approach for labeling fixed histological sections involves a sequential reaction, first with a primary antibody having specificity for an antigen of interest, followed by treatment with a secondary antibody linked to colloidal gold particles. Small (5nm) gold particles are used to maximize penetration into the sections, which results in greater particle density at the antigenic sites. The signal produced by the gold particles in backscattered electron or light microscopic imaging can be greatly enhanced by a physical silver developer.³ The gold particles grow by silver deposition to diameters as large as 300 nm, thus providing a black stain for light microscopy and an electron-dense deposit for backscattered electron microscopy.

The above approach was utilized in this study to label antigenic sites along the basement membranes (*basal laminae*) of glomeruli in human kidney tissue. The primary antibody used was an anti-human collagen Type IV monoclonal, which binds to an antigen involved in glomerular cell-matrix interactions. An IgG secondary antibody was then used to label the antigenic sites with 5nm gold particles, which were enhanced by subsequent treatment with a silver reagent.

The primary objective of this research was to utilize an established immunocytochemical marking technique to evaluate secondary ion mass spectrometry (SIMS)⁴ as a new approach to image antigen-antibody sites. The SIMS technique is not expected to compete with conventional light and electron microscopic immunocytochemistry. However, imaging mass spec-

trometry eventually may prove useful for direct molecular mapping of antigens and other biomolecules within tissues.⁵ Advances in instrumentation, including high spatial resolution ion microprobes,⁶ post-ionization techniques, and mass spectrometers capable of high mass resolution and high mass range,⁷ will help in pursuit of this objective. The combined limitations of biomolecule concentrations, spatial resolution, and ion transformation probabilities make in situ molecular mapping a very difficult goal for microprobe mass spectrometry at present. Fortunately, chemical tagging techniques can be used for SIMS in a manner analogous to those currently exploited for enhancing image contrast in other microscopies. Exciting possibilities include the use of markers tailored to mass spectrometric detection such as isotopic labels. Such approaches constitute important initial steps in the development of SIMS as a molecular microprobe applicable to biological systems.

This paper provides the first demonstrated use of chemical tags with high ionization efficiency in SIMS to image sites of antigen-antibody interactions in fixed biological tissue. An ion microscope was used to identify antigenic sites by detection of mass selected ions such as Ag⁺ from the bound silver-stained secondary antibody. Results of SIMS were confirmed by light and electron microscopy of identical areas in the same tissue section. An important feature of the ion microscope is that it can generate three-dimensional images by digital image depth profiling.⁸ This analytical mode provides a sensitive measure of the specificity and penetration depth of the antibody reaction, and is conceptually similar to optical sectioning with confocal microscopy or cross-sectional imaging with transmission electron microscopy.

Experimental

Human kidney tissue obtained on autopsy was prepared in 3-5 μ m microtomed sections of formalin-fixed paraffin-embedded tissue. The sections were treated with a two-stage immunogold silver staining (IGSS) process.⁹ Anti-human collagen Type IV monoclonal antibodies (Chemicon International, Inc., Catalog No. MAB 1910) were used to bind to antigenic sites on glomerular basement membranes. Dilutions of the antibody ranged from 1:100 to 1:8000 in pH 8 buffer, and were applied to tissues pretreated with or without a 1% trypsin solution. The higher dilutions generally minimized the extent of nonspecific binding. The secondary

J. J. Lee, R. W. Linton, and J. L. Hunter are with the Department of Chemistry, University of North Carolina, Chapel Hill, NC 27599-3290; J. D. Shelburne, J. L. Burchette, and A. P. Sanfilippo are with the Duke University and V.A. Medical Centers, Durham, NC 27710; R. D. Voyksner is with the Research Triangle Institute, Research Triangle Park, NC 27709. They are grateful to D. P. Griffis and S. F. Corcoran for assistance with ion microscopy experiments conducted at the Analytical Instrumentation Facility at North Carolina State University, and to J. Rickman and D. Wilson at UNC-CH for assistance with electron microscopy and image processing. Research was supported in part by RTI, UNC-CH, Duke University, and NCSU.

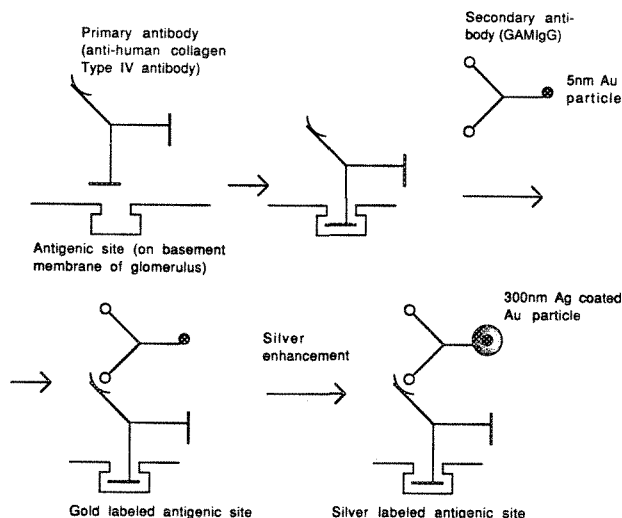


FIG. 1.--Immunocytochemical approach used to stain renal basement membranes of glomeruli with silver particles.

antibody was goat antimouse IgG conjugated with 5nm gold particles (Janssen Life Sciences Products AuroProbe EM No. 23.685.17-GAMIgG). The silver enhancement reaction was then used to enlarge the gold particle size by deposition of silver (Janssen IntenSE M kit). Further details on specimen preparation are found in the product descriptions provided by Chemicon and Janssen. A schematic illustrating the approach to kidney tissue labeling is shown in Fig. 1. Control sections treated in the above manner except for the omission of the primary antibody did not exhibit any detectable silver particles incorporation. Sections that did not utilize silver enhancement provided inadequate labeling for direct imaging of the gold tags by ion microscopy.

The SIMS measurements were made with a Cameca IMS-3f ion microscope equipped with a magnetically filtered primary Cs^+ beam and a custom digital secondary ion imaging system.¹⁰ Negative secondary ion detection was used in conjunction with energy filtering achieved by offsetting of the sample potential (122V). This procedure permitted sensitive detection of Ag^- , confirmed by examination of the isotope ratio of the major Ag isotopes at 107 and 109 Daltons, without significant contributions from polyatomic secondary ions. Sputtering rates of the order of 300 nm/min were achieved with a 100nA, 9.5kV Cs^+ beam rastered over a $250\mu\text{m} \times 250\mu\text{m}$ area. About $0.4\mu\text{m}$ were sputtered in increments between each successive set of image acquisitions. The analytical area was confined within a circle $150\mu\text{m}$ in diameter centered in the sputtered area. Typical image acquisition times required to fill the 8-bit dynamic range of the digital images were 20 s with a 0.1nA primary beam for CN^- and 30 s with a 10nA primary beam for Ag^- . Backscattered electron images were obtained, both before and after ion sputtering, with an ISI DS-130 scanning electron microscope equipped with a Tracor Northern TN5500 imaging system.

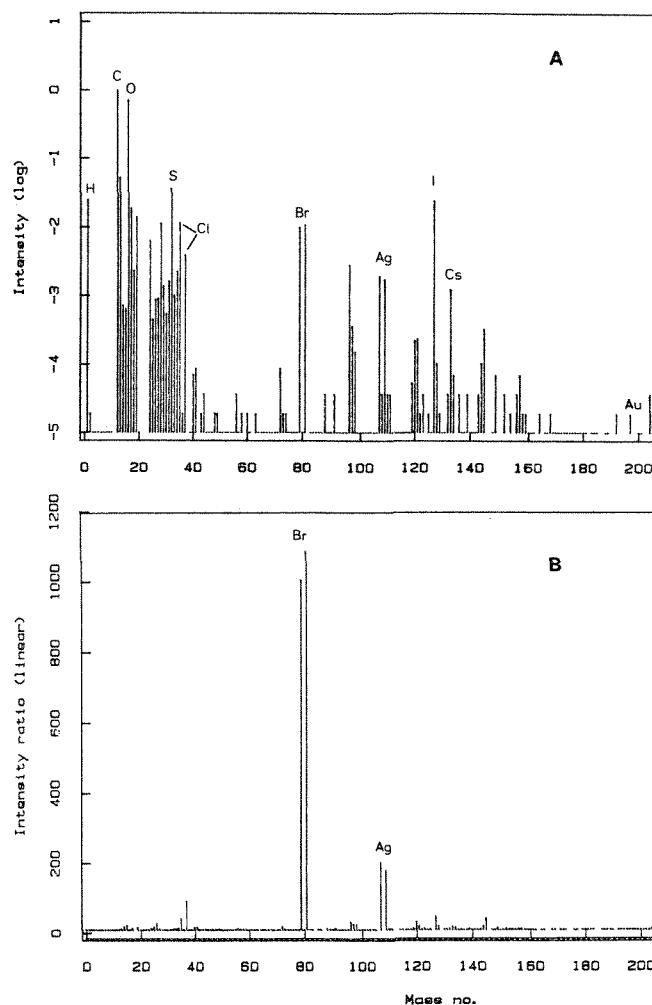


FIG. 2.--SIMS results for kidney glomerulus labeled as shown in Fig. 1. (A) Negative ion mass spectrum of tissue labeled with Ag enhancement step (log intensity scale normalized to carbon intensity at mass 12). (B) Ratioed mass spectrum of tissue labeled with Ag compared to tissue labeled without use of Ag enhancement reagent (linear intensity ratio scale).

Results

Figure 2 illustrates secondary ion mass spectra obtained from areas containing glomeruli from the labeled kidney tissue. In addition to elements characteristic of the organic constituents (H, C, N, O, S), the negative ion spectrum (Fig. 2A) shows high concentrations of the Ag label and halogens with very high secondary ion yields (Cl, Br, I). Energy offsetting was used to minimize polyatomic ion interferences in the spectra at the expense of spectrometer transmission. The Au signal at 197 is barely detectable (of the order of 10 cps) and is difficult to confirm since Au is monoisotopic. The Au^- intensity usually is at least 100 times less than the Ag^- , yet the Au^- ion yield is expected to be about 50 times better than Ag^- based on tabulated relative sensitivity factors for the metals. The lack of Au^- intensity is explained by the difference

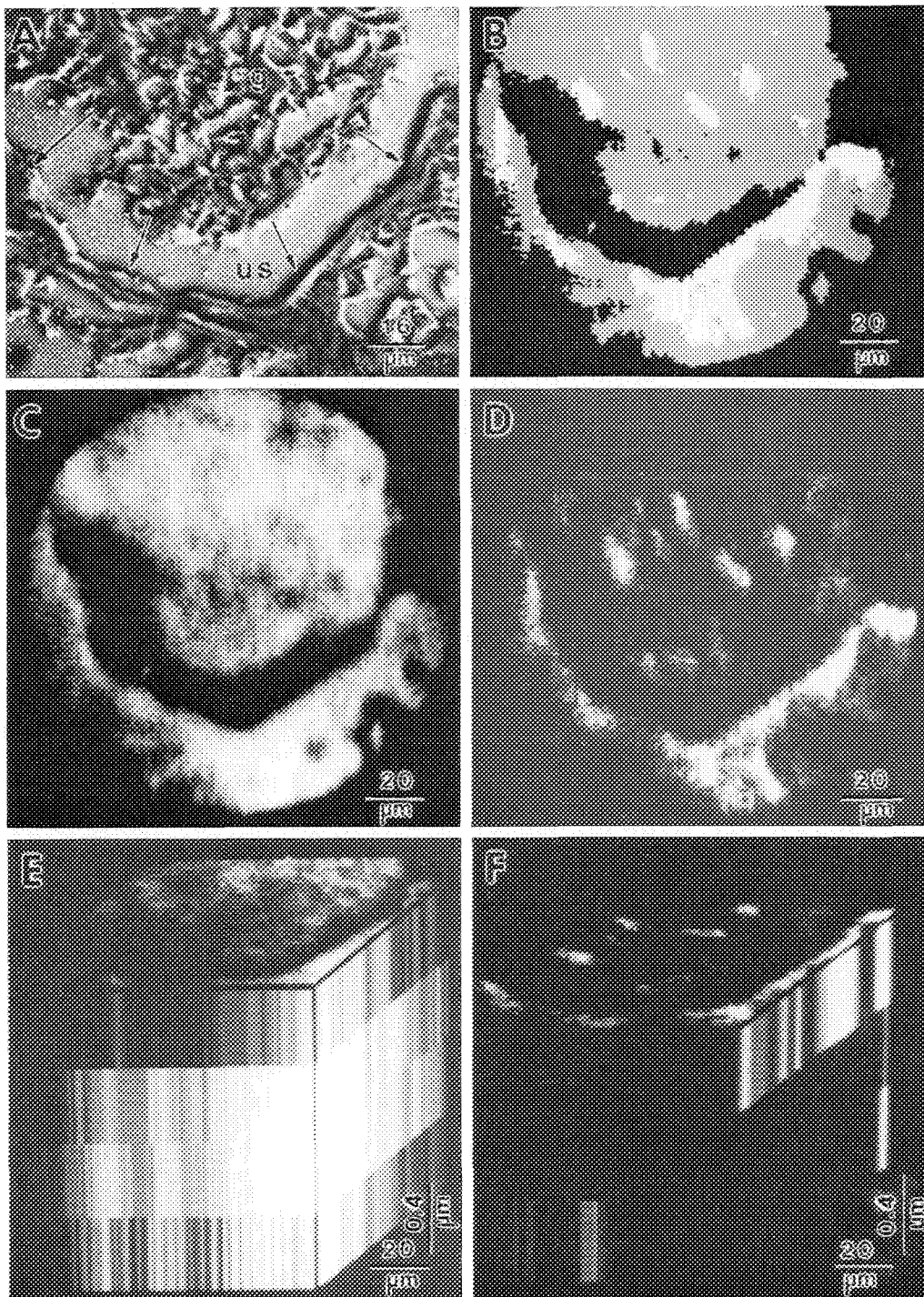


FIG. 3.--SIMS imaging of kidney glomerulus labeled as shown in Fig. 1. (A) Backscattered electron micrograph (after ion sputtering during SIMS measurements): g = glomerulus, us = urinary space, arrows = basement membrane (Bowman's Capsule). (B) Binary overlay of Ag^- and CN^- SIMS images (raw data shown in C and D): black = no Ag^- or CN^- above background; gray = CN^- above background, but no Ag^- ;

white = Ag^- and Ag^- above background. (C) CN^- SIMS image of tissue surface. (D) Ag^- SIMS image of tissue surface. (E) 3-D SIMS image of CN^- (images stacked as a function of depth, approximately 0.4 μm of sputtering between each image acquisition). (F) 3-D SIMS image of Ag^- (images stacked as a function of depth, approximately 0.4 μm of sputtering between each image acquisition).

in relative volumes in the Au cores and Ag overlayers of about 10^5 . Thus, when ion yield differences are considered, the Au⁻ signal should only be about 10^{-3} of the Ag⁻ signal if SIMS intensities are averaged over complete particles. For further substantiation of the unique signals derived from the Ag enhancement step, Fig. 2(B) compares the spectrum in Fig. 2(A) to that obtained for the tissue not exposed to the Ag reagent. The Ag⁻ and Br⁻ signals are several orders of magnitude more intense in the tissue treated with the Ag. The enhanced Br may result from binding to Ag particles during H and E staining subsequent to the Ag enhancement step.

Results of digital ion imaging studies are summarized in Fig. 3 for a selected portion of a single glomerulus with its associated basement membrane (Bowman's Capsule). The tissue morphology is shown in the backscattered electron (Fig. 3A) and is correlated with the surface images of the same feature obtained by SIMS (Fig. 3B-D). The CN⁻ image identifies the regions containing tissue, the dark channel representing the urinary (Bowman's) space (Fig. 3C). The Ag⁻ clearly is located predominantly along the basement membrane (Fig. 3D). Some of the Ag⁻ observed in other areas may reflect labeling of *basal laminae* of tubules, intertubular capillaries, and glomerular mesangial matrix. All these structures are known to be bound by the primary antibody. Some nonspecific staining by the Ag also may occur. The binary SIMS image overlay in Fig. 3(B) illustrates the predominance of Ag in regions associated with the basement membrane (Bowman's Capsule), and is further substantiated by comparison to the backscattered electron image in Fig. 3(A).

Results of 3-D or image depth profiles are shown in Fig. 3(E) and 3(F) for CN⁻ and Ag⁻, respectively. Transaxial slicing¹⁰ of the digital image stack along the basement membrane located in the bottom right of Fig. 3(D) confirms that the Ag is confined to the outer surface of the section. That is, sputtering of the outer 0.4 μ m before the second Ag⁻ was acquired was sufficient to eliminate virtually all detectable Ag (Fig. 3F). In contrast, the CN⁻ signal actually increases somewhat for the second and third data sets (Fig. 3E). This result may reflect attenuation by remnants of a carbon overlayer in the first data set, and progressive ion beam damage effects that may influence the CN⁻ signal. The depth scales (0.4 μ m markers) shown in Fig. 3(E) and (F) are based on cross-sectional TEM studies to estimate the total section thickness. Approximately half the 3 μ m-thick section was sputtered away during the SIMS measurements. SIMS sensitivity is such that less than a 15nm depth normally is consumed to acquire a single Ag⁻ image, and about 0.1 nm for each CN⁻ image.

As a final confirmation of the limited penetration depth of the Ag-enhanced antibodies, Fig. 4 compares a portion of the basement membrane before and after Cs⁺ sputtering of the outer surface of the section. The backscattered electron image of the unsputtered kidney tissue clearly shows the Ag particles along the

basement membrane of a glomerulus, as well as around portions of a few nearby tubular basement membranes (Fig. 4A). After a light sputtering, which has not seriously altered the tissue morphology, the Ag-containing particles appear to have been removed. Indeed, TEM studies of tissue cross sections also indicate that the Au particles are almost exclusively confined to the surface of the section.

Conclusions

The immunogold silver staining process is shown to be useful for the localization of antigen-antibody interactions in fixed biological tissues by SIMS. The 3-D image depth profiling mode provides information on the specificity and penetration of the antibodies used to label antigenic sites. Further improvements are expected in SIMS lateral resolution with the use of focused liquid metal ion sources, in methods to display 3-D information, and in the development of chemical tags for biomolecules tailored to mass spectral detection. These are important early steps in the evolution of imaging mass spectrometry as molecular microprobes with applications to biology and medicine.

References

1. J. Roth, "The colloidal gold marker system for light and electron microscopic cytochemistry," in G. Bullock and P. Petrusz, Eds., *Techniques in Immunocytochemistry*, New York: Academic Press, 1983.
2. M. DeWaele et al., "Immunogold staining method for the light microscopic detection of leukocyte cell surface antigens with monoclonal antibodies," *J. Histochem. Cytochem.* 31: 376, 1983.
3. G. Hacker et al., "The immunogold-silver staining method: A powerful tool in histopathology," *Virchows Archiv (Pathol. Anat.)* 406: 449, 1985.
4. M. S. Burns, "Biological microanalysis by secondary ion mass spectrometry: Status and prospects," *Ultramicroscopy* 24: 269, 1988.
5. R. W. Odom, "SIMS molecular ion imaging of organic molecules on surfaces," *36th ASMS Conference on Mass Spectrometry and Allied Topics*, June, 1988.
6. R. Levi Setti et al., "High-resolution ion probe imaging and analysis," *Microbeam Analysis--1988*, 93.
7. A. Benninghoven, F. G. Rudenauer, and H. W. Werner, *Secondary Ion Mass Spectrometry*, New York: Wiley, 1987.
8. S. R. Bryan, D. P. Griffis, W. S. Woodward, and R. W. Linton, "SIMS/Digital imaging for the three dimensional characterization of solid state devices," *J. Vac. Sci. Technol.* A3: 2102, 1985.
9. J. Polak and I. Varndell, *Immunolabeling for Electron Microscopy*, New York: Elsevier, 1984.
10. S. R. Bryan, W. S. Woodward, D. P. Griffis, and R. W. Linton, "A microcomputer based digital imaging system for ion microanalysis," *J. Microsc.* 138: 15, 1985.

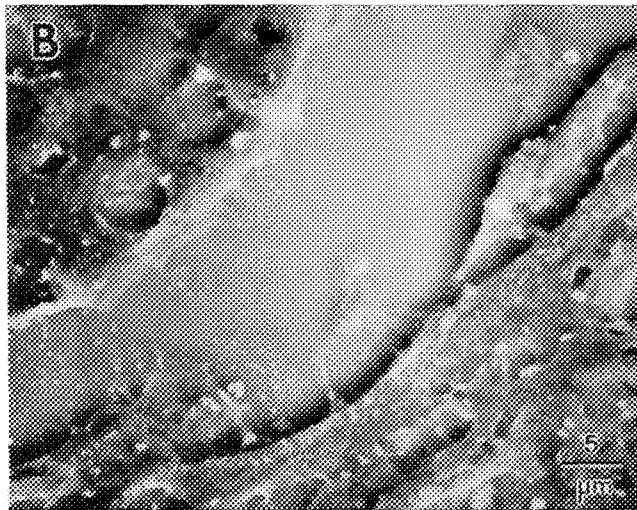
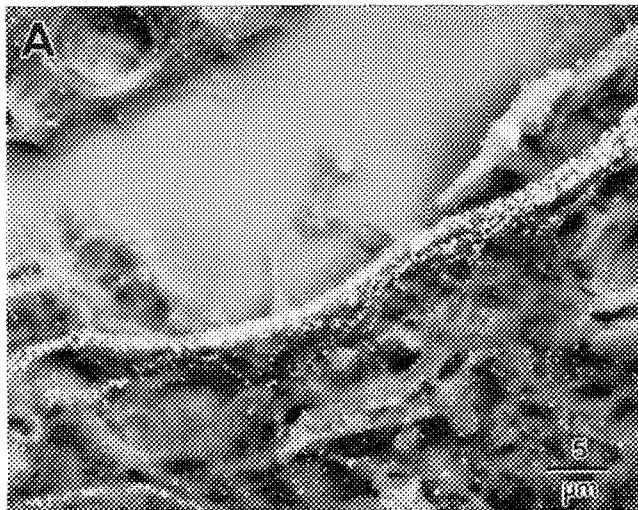


FIG. 4.--Scanning electron micrographs (back-scattered electron images) of basement membrane (Bowman's Capsule) region of glomerulus

labeled as shown in Fig. 1. (A) Before Cs^+ sputtering (note Ag particles). (B) After Cs^+ sputtering (note absence of Ag particles).

DISTRIBUTION PATTERNS OF ALUMINUM ACCUMULATIONS IN BONE TISSUE FROM PATIENTS WITH DIALYSIS OSTEOMALACIA DETERMINED BY LAMMA

P. F. Schmidt, Hernz Zumkley, Rudolf Barckhaus, and Bernd Winterberg

An increased concentration of aluminum in bone has been found in patients with dialysis osteomalacia. To estimate the effects of an elevated aluminum content on the mineralization process, more information on the distribution of aluminum within bone tissue is necessary. Therefore the aluminum content of various structural elements of bone tissue of patients with normal kidney function and of patients with dialysis osteomalacia has been determined by laser microprobe mass analysis (LAMMA). These investigations show that patients with dialysis osteomalacia exhibit an accumulation of aluminum at the junction between osteoid and the mineralized matrix, as well as depositions of aluminum in bone cells (osteocytes, especially in osteoblasts in front of areas of defect bone mineralization).

Increased concentrations of aluminum in blood and tissues are frequently found in patients undergoing intermittent hemodialysis treatment.¹⁻⁴ As early as 1970 hyperaluminemia from Al-containing drugs (antacids) in patients suffering from renal insufficiency was observed by Berlyne et al.² Accumulation of Al in the bone of patients with chronic renal failure was demonstrated by Parsons et al.⁵ Interest in Al toxicity in uremic patients was stimulated when a relation between serum Al concentration and dialysis dementia was found.² Strong evidence that Al is involved in the development of dialysis osteomalacia thereafter accumulated.^{4,6} One of the consequences of this Al intoxication is an accumulation of Al in bone, combined with a defect bone mineralization that results in an increased osteoid volume and a reduced mineralization front (Al-induced osteomalacia).

To obtain more information on the pathogenic mechanisms between Al intoxication and development of dialysis osteomalacia, the Al content of bone cells from patients suffering from dialysis osteomalacia has been determined by laser microprobe mass analysis.⁷ In addition, the integral Al concentration of the tissue has been measured by atomic absorption spectrometry.⁸

Preparation

Bone samples were taken by needle puncture from the pelvic bone. In order to prevent any Al redistribution, the tissue was shock frozen

by immersion into melting N₂, freeze dried in a freeze-drying device at below -80 °C, plastic embedded in an epoxy resin, and sectioned dry on a ultramicrotome. The sections were mounted on 3mm grids used in electron microscopy.

Results

In bone tissue from patients with dialysis osteomalacia, LAMMA revealed an increased Al content in the mineralizing front of the calcified tissue and the osteoid (Fig. 1). Moreover, Fig. 1 demonstrates the high detection sensitivity of LAMMA. Usually the determination of the topochemical distribution of Al within bone tissue is based on histochemical staining by aluminon, the ammonium salt of aurine tricarboxylic acid.^{9,10} It has been shown by staining that Al accumulates at the junction of the mineralized bone and osteoid, in cement lines, in deposits in the osteoid itself, and in reticulum cells of bone marrow.^{11,12} The "detection limit" of this method is about 20-50 µg/g, because no stain is possible when integral bone Al concentration is in this range.¹¹ Figure 1(b) demonstrates that LAMMA can detect Al in concentrations much lower than are necessary for staining. Section A originates from the bone tissue of a patient with an integral Al content of 47 µg/g; section B originates from bone tissue with an Al content of 170 µg/g. By way of comparison with these high Al concentrations, the Al content of bone tissue from patients with normal kidney functions is 4-8 µg/g. Both sections have been stained with aluminon. In section B (Fig. 1b) the dark line at the junction of the mineralized bone and the osteoid produced by the aluminon staining demonstrates the presence of Al, as ascertained by LAMMA measurements. Although no staining could be observed in section A (Fig. 1a), LAMMA revealed an accumulation of Al.

In addition, LAMMA detected an increased Al content in osteocytes of patients with dialysis osteomalacia, especially in osteocytes near the mineralization front.¹³ LAMMA analyses of osteocytes from patients with normal kidney functions and without treatment with Al-containing drugs did not show an elevated Al content. In patients with osteitis fibrosa in fibroblasts, an increased Al content was observed.¹³

Moreover, LAMMA investigations also demonstrated that osteoblasts from patients with dialysis osteomalacia contain an increased concentration of Al. Figure 2(a) shows an histological section from bone tissue of a patient with dialysis osteomalacia. The integral

P. F. Schmidt and R. Barckhaus are at the Institut für Medizinische Physik, Hüfferstrasse 68; H. Zumkley and B. Winterberg are at the Medizinische Universitäts-Poliklinik, Albert Schweitzerstrasse 33, D-44 Münster, Federal Republic of Germany.

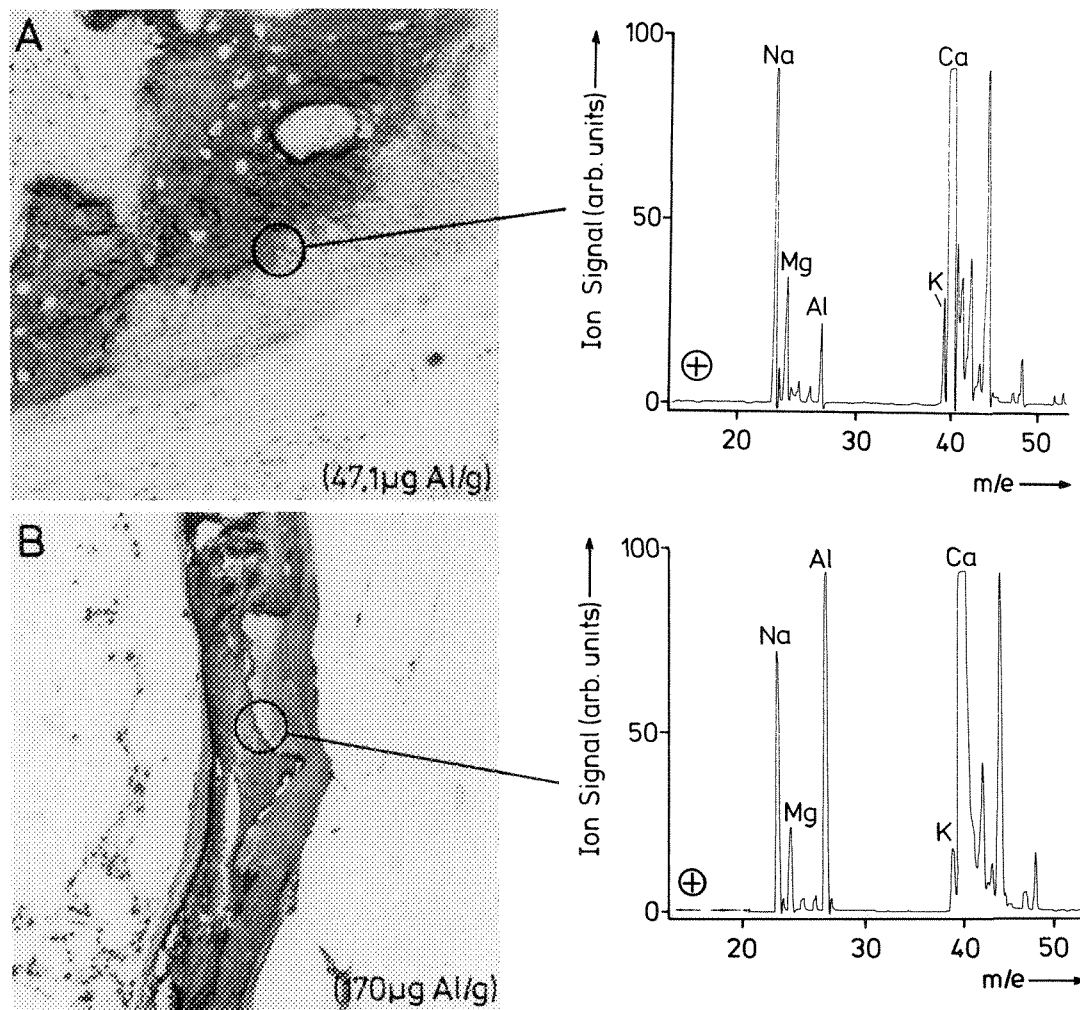


FIG. 1.--LAMMA analyses of aluminum-stained sections of bone tissue from patients with dialysis osteomalacia. Integral aluminum concentrations (AAS): Section A: 47 $\mu\text{g/g}$, section B: 170 $\mu\text{g/g}$.

Al concentration was 47 $\mu\text{g/g}$. This section shows two areas of different mineralization phases: (A) normal mineralized bone with a thin osteoid seam and elongated osteoblasts, (B) an area with a defect mineralization front, a wide osteoid seam, and cubic osteoblasts.

For area A (intact mineralization), no Al was detected by LAMMA measurements in the junction of mineralized bone and osteoid nor in osteoblasts (Fig. 2b).

For area B (defect mineralization), LAMMA analyses indicate a considerable accumulation of Al in the junction of mineralized bone and osteoid seam, and in the cytoplasm of osteoblasts (Fig. 2c). In particular, a comparison of osteoblasts with various Al concentrations indicate that the content of magnesium and calcium may decrease with increasing Al (Fig. 3).

Discussion

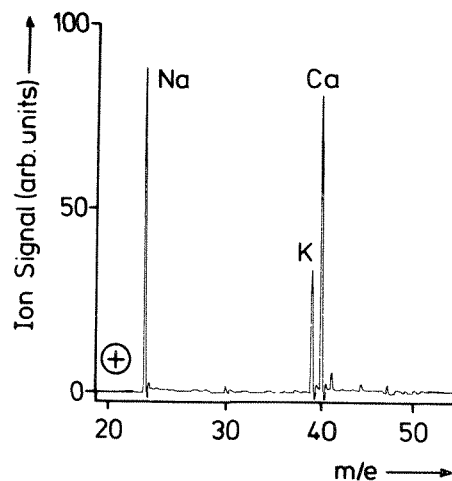
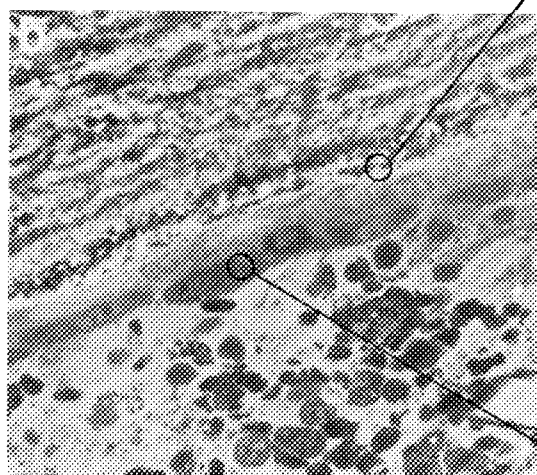
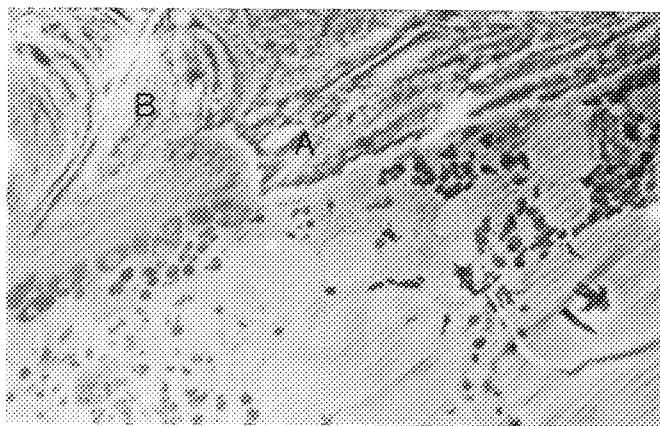
These results have shown that one can obtain indications of Al-induced osteomalacia by means of histomorphologic findings and an estimate of Al concentration of bone tissue by atomic absorption spectrometry, supplemented by an estimate of the Al distribution within bone tissue.

Moreover, by ultrastructural localization of Al, one can get more information on the correlation between Al intoxication and dialysis osteomalacia, in such a manner that the hypothesis of a direct toxic effect of Al on bone cells with consequent development of osteomalacia can be supported.

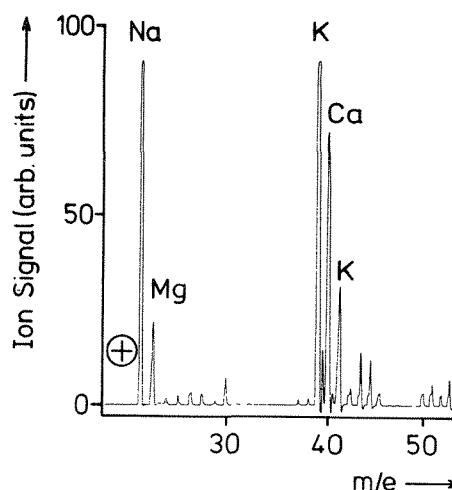
Many investigations made by different methods (such as histochemical staining, x-ray microanalysis, and secondary ion mass spectrometry) have shown that an Al concentration is found at the junction of mineralized bone and osteoid in patients with dialysis osteomalacia.^{9,14,15} This result has been confirmed by LAMMA. In addition, because of the low detection limit of LAMMA, an increased Al content has also been detected in osteocytes, especially near the mineralization front.¹³

The findings on aluminum accumulations in osteoblasts of patients with dialysis osteomalacia are in accord with results obtained by x-ray microanalysis, which demonstrates the presence of Al in the mitochondria of osteoblasts.^{15,16}

Considering that Al ions show phosphate binding properties and that Ca ions can be



mineralization front



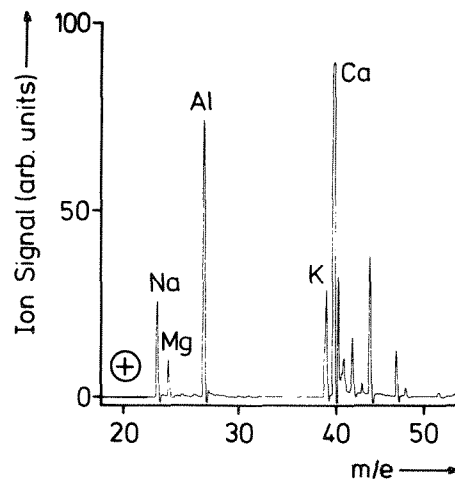
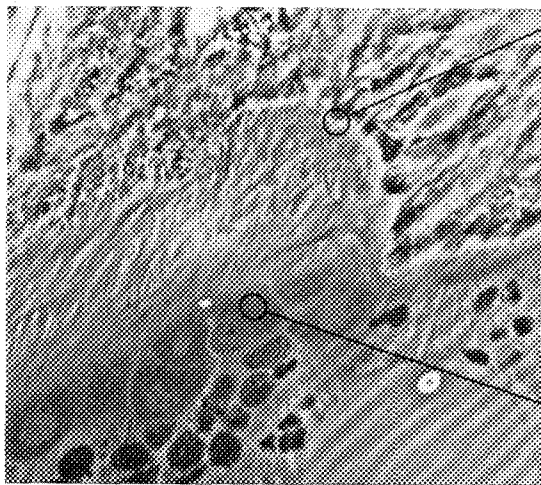
osteoblast

FIG. 2.--(a) Histological section of bone tissue from an aluminum-intoxicated patient with dialysis osteomalacia: Area A intact, area B defect bone mineralization; (b) LAMMA analysis within area of intact bone mineralization.

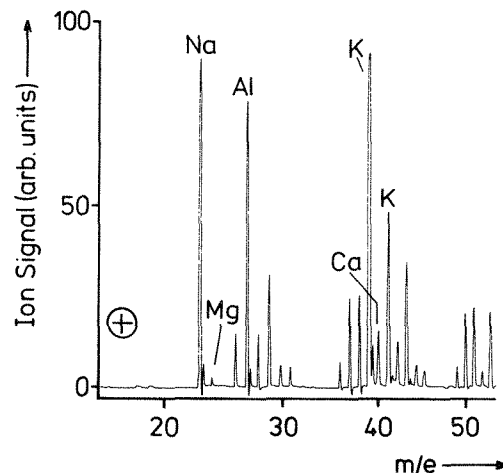
replaced by Al ions in biochemical reactions, the presence of Al at the junction between osteoid and the mineralized matrix suggests that the mineralization of osteoid is inhibited by Al accumulations, so that available Ca cannot be taken up by bone.¹⁷ The findings that osteoblasts in front of areas of defect bone mineralization contain Al (combined with a decreasing Ca content) support the supposition that one of the possible causes of Al-induced osteomalacia is given by Al accumulations that may inhibit the mineralization of the osteoid. The calcification process of bone occurs under the control of osteoblasts. The presence of Ca aggregates in osteoblast mitochondria makes it evident that osteoblasts regulate the transport of Ca ions from the blood vessels toward the calcifying matrix. This regulation takes place through the accumulation of Ca and phosphate ions in mitochondria, followed by their release.¹⁸ The accumulation of Al osteoblasts therefore suggests that Al inhibits the normal mineralization process by interfering with the Ca fluxes.

References

1. A. C. Alfrey, G. R. Le Gendre, and W. D. Kaehny, "The dialysis encephalopathy syndrome," *N. Eng. J. Med.* 294: 184-188, 1976.
2. G. M. Berlyne, "Aluminum toxicity in man," *Min. Elec. Metab.* 2: 71-73, 1979.
3. H. Zumkley, H. P. Bertram, A. Lison, O. Knoll, and H. Losse, "Aluminum, zinc, and copper concentrations in plasma in chronic renal insufficiency," *Clin. Neph.* 12: 18-21, 1979.
4. H. A. Ellis, J. H. McCarthy, and J. Herrington, "Bone aluminum in hemodialysed patients and in rats injected with aluminum chloride: Relationship to impaired bone mineralization," *J. Clin. Pathol.* 32: 832-844, 1979.
5. V. Parsons, C. Davies, C. Goodge, C. Ogg, and J. Siddiwui, "Aluminum in bone from patients with renal failure," *Br. Med. J.*



mineralization front



osteoblast

FIG. 2.--(c) LAMMA analysis within area of defect bone mineralization.

4: 273-275, 1971.

6. T. Drüeke, "Dialysis osteomalacia and aluminum intoxication," *Nephron* 26: 207-210, 1980.

7. P. F. Schmidt, "Localization of trace elements with the laser microprobe mass analyzer (LAMMA)," *Trace Elements in Medicine* 1: 13-20, 1984.

8. H. P. Bertram, "Aluminiumbestimmung in Körperflüssigkeiten," *Nieren- und Hochdruckkrankheiten* 10: 188-191, 1981.

9. M. R. C. Buchanan, B. U. Ihle, and C. M. Dunn, "Haemodialysis related osteomalacia: A staining method to demonstrate aluminum," *J. Clin. Pathol.* 34: 1352-1354, 1981.

10. N. A. Maloney, S. M. Ott, A. C. Alfrey, N. L. Miller, J. W. Coburn, and D. J. Sherrard, "Histological quantitation of aluminum in iliac bone from patients with renal failure," *J. Lab. Clin. Med.* 99: 206-216, 1982.

11. S. M. Ott, N. A. Maloney, J. W. Coburn, A. C. Alfrey, and D. J. Sherrard, "The prevalence of bone aluminum deposition in renal osteodystrophy and its relation to the response to calcitriol therapy," *N. Eng. J. Med.* 307: 709-713, 1982.

12. G. Delling, H.-J. Schäfer, H. Krumme, and W. Schulz, "Renale Osteopathie und Aluminium-Pathomorphologie," *Nieren- und Hochdruckkrankheiten* 12: 207-213, 1983.

13. P. F. Schmidt, H. Zunkley, R. Barckhaus, and B. Winterberg, "Localization of aluminum in bone cells from patients with dialysis osteomalacia," *Trace Elements in Medicine* 1: 167-171, 1984.

14. G. Cournot-Witmer, J. Zingraff, J.-J. Plachot, F. Escaig, R. Lefevre, P. Boumati, A. Bourdeau, M. Garabedian, P. Galle, R. Bourdon, T. Drüeke, and S. Salsan, "Aluminum localization in bone from hemodialyzed patients: Relationship to matrix mineralization," *Kidney International* 20: 375-385, 1981.

15. J.-J. Plachot, G. Cournot-Witmer, S. Halpern, V. Mendez, A. Bourdeau, T. Drüeke, P. Galle, and S. Balsan, "Bone ultrastructure and x-ray microanalysis of aluminum-intoxicated hemodialyzed patients," *Kidney International* 25: 796-803, 1984.

16. G. Cournot-Witmer, J.-J. Plachot, A. Bourdeau, M. Lieberherr, V. Jorgetti, V. Mendes, S. Halpern, J. Hemmerle, T. Drüeke,

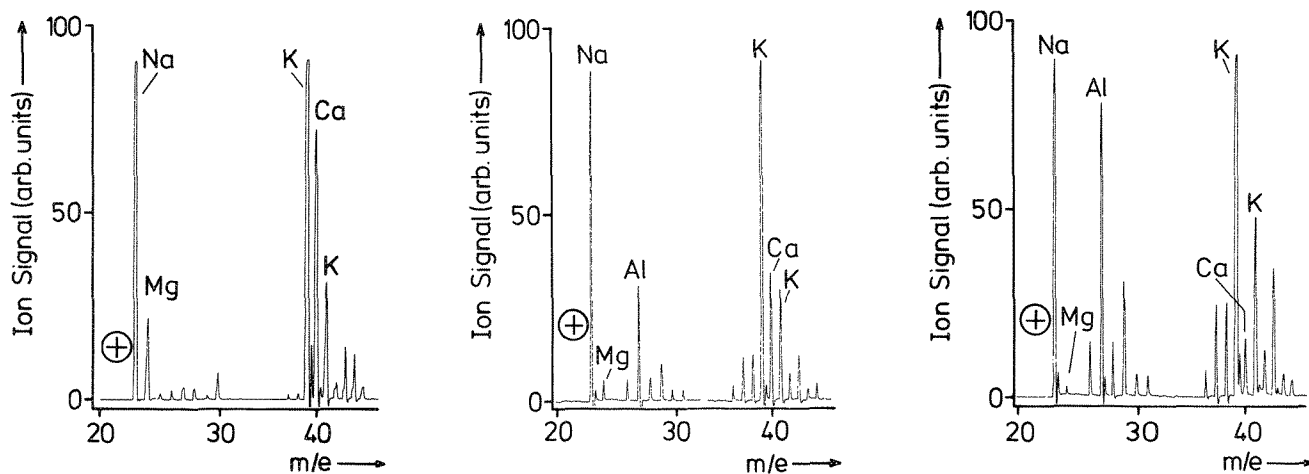


FIG. 3.--LAMMA analyses of three different osteoblasts demonstrating decreasing magnesium and calcium content with increasing aluminum content.

and S. Balsan, "Effect of aluminum on bone and cell localization," *Kidney International* 29 (Suppl. 18): S37-S40, 1986.

17. B. F. Boyce, H. Y. Elder, H. L. Elliot, I. Fogelman, G. S. Fell, B. J. Junors, G. Beastall, and I. T. Boyle, "Hypercalcaemic osteomalacia due to aluminium toxicity," *Lancet* 2: 1009-1012, 1982.

18. E. Bonucci, "The structural basis of calcification," in A. Ruggeri and P. M. Motta, Eds., *Ultrastructure of the Connective Tissue Matrix*, Boston: Martinus Nijhoff, 1984.

IN SITU MICROPROBE QUANTITATION OF INORGANIC PARTICLE BURDEN IN PARAFFIN SECTIONS OF LUNG TISSUE

J. L. Abraham

Inorganic particulate material of diverse types is present in the ambient and occupational environment, and exposure to such materials is a well-recognized cause of some lung disease. To investigate the interaction of inhaled inorganic particulates with the lung, one must obtain quantitative information on the particulate burden of lung tissue in a wide variety of situations. The vast majority of diagnostic and experimental tissue samples (biopsies and autopsies) are fixed with formaldehyde solutions, dehydrated with organic solvents, and embedded in paraffin wax. Over the past 16 years, I have attempted to obtain maximal analytical use of such tissue with minimal preparative steps. Unique diagnostic and research data result from both qualitative and quantitative analyses of sections. Most of the data result from both qualitative and quantitative analyses of sections. Most of the data has been related to inhaled inorganic particulates in lungs, but the basic methods are applicable to any tissues. The preparations are primarily designed for SEM use, but they are stable for storage and transport to other laboratories and several other instruments (e.g., for SIMS techniques).¹

TABLE 1.--Records in master database.

Tissue section	411 analyses
Fibers	285
All particles	21
Reduced area	15
Lavage	6
Nonquantitative	84
Material samples	4
Total	826

Standard paraffin sections of tissue (avoiding contaminating metal fixatives) are cut at 5-8 μm (standard thickness), floated on clean water, and picked up on smooth pure carbon disks. The section is dried as are serial sections mounted on glass slides. Alternatively (and rarely), if the only available tissue is in a section already mounted on a slide, a section or portion of a section may be transferred from a glass slide to a carbon support. Paraffin is removed by soaking in xylene for approximately 30 min, and the preparation is air dried. The specimen is then ready for examination in the SEM; depending on the stub and the

The author is in the Department of Pathology, SUNY Health Science Center, Syracuse, NY 13210. The PC software for this project was largely developed by B. R. Burnett. B. Powell and C. Merritt have also provided invaluable assistance.

instrument to be used, it may be necessary to glue the carbon substrate to another mount of some kind. (Maintaining electrical conductivity is essential.) No conductive coating should be used, as it may obscure features of interest and may introduce contamination. With the 5 μm sections and an accelerating voltage of 20 kV, there should be no need for coating. With thicker sections and lower accelerating voltage, the beam does not fully penetrate the tissue to the conducting carbon substrate, and the insulating properties of the tissue become a problem. Minor charging effects in the secondary electron imaging (SEI) should not interfere with backscatter electron imaging (BEI). The use of a dual screen SEM display greatly facilitates comparison of SEI and BEI. Inorganic material in the organic matrix is easily detected in the BEI. Inorganic material in the organic matrix is easily detected in the BEI. The inverse mode is utilized to protect the viewing CRT from strong signals and for some familiar pattern recognition characteristics, more resembling LM and TEM. Once located, the inorganic material is analyzed by energy-dispersive x-ray analysis (EDXA) or other microprobe techniques as available and necessary. True quantitative analysis of individual particulates of varying size in such specimens is not practical, but quantitation of the tissue particulate burden is readily accomplished by a point-count, morphometric approach.² In brief, fields of standard area (and volume) are searched for inorganic particulates, which are counted, measured, and individually analyzed by EDXA. The resulting data are entered into a PC program using Dbase and better Basic to calculate results and prepare reports. The reports include raw data on each particle analyzed; numbers of particles/field; concentration of particles/ml of tissue; concentrations, sizes, and integral x-ray intensity data for particles by classification. Particles are classified by morphology as fibrous or nonfibrous, and by elemental composition as silica, silicates, metals, asbestos, organic, endogenous, and others. Digestion analysis is strongly recommended for fibrous particulates, which are underrepresented and shortened in sectioned tissue. Reports also include x-ray intensity ratios and data on individual elements and on "alloy"-type particles (metal particles containing more than one element in a single particle, (often useful in providing clues to sources of exposure; e.g., Fe with Cr and Ni suggesting stainless steel)).

Over the past few years, I have collected

quantitative data from analyses of particulates in over 400 lung samples. It is essential to use standardized analytical conditions for comparability of data over time. The data include numerous comparative digestion analyses, in which, in addition to the in situ analysis, tissue is digested and insoluble particulate residue is collected on a membrane filter for SEM analysis.

The results from this in situ method correlate well with other analytic methods, and with comparison of results from other laboratories using similar or other techniques (Tables 2-5).

TABLE 2.--Summary data from 265 tissue section analyses (millions of particles/ml of tissue).

	Median (Range)	Mean (s.e.m.)
Total exogenous particles	94 (1-8413)	314 (47)
Silics	6 (0-1750)	44 (10)
Aluminum silicates	14 (0-7875)	142 (37)
Metals	35 (0-1530)	89 (12)
Talc	0 (0-3469)	21 (13)

TABLE 3.--Frequency of various metal particles in tissue section analyses (of 7429 metal particles in 400 Analyses; or of 267 Cases).

Metal	No. Particles (metal = 1st elem)	No. Analyses (containing metal)	No. Cases
Fe	2331 (31% of 7429)	357 (89% of 400)	186 (70% of 267)
Ti	1581 (22)	336 (84)	229 (86)
Al	932 (13)	211 (53)	193 (72)
W	794 (11)	69 (17)	52 (19)
Sn	330 (4)	120 (30)	82 (31)
Pb	271 (4)	94 (23)	71 (27)
Cr	141 (2)	188 (47)	134 (50)
Ni	134 (2)	120 (30)	86 (32)
Ba	122 (2)	58 (14)	39 (15)
Zn	98 (1)	116 (29)	75 (28)
Au	95 (1)	31 (8)	22 (8)
Hg	80 (1)	23 (6)	19 (7)
Zr	77 (1)	28 (7)	25 (9)
Cu	74 (1)	95 (24)	67 (25)
Ce	59 (1)	38 (9)	29 (11)
Ag	46 (1)	32 (8)	25 (9)
Ta	24	18 (4)	16 (6)
Mo	22	4 (1)	--
Bi	20	15 (4)	13 (5)
Co	13	20 (5)	19 (7)
Sb	8	16 (4)	--
Os	8	1	--
V	7	38 (9)	30 (11)
Cd	6	7 (2)	5 (2)
Mn	6	73 (18)	54 (20)
Br	4	7 (2)	--
Nb	3	4 (1)	--
Se	3	2	--
La	3	4 (1)	4 (1)
Pd	2	1	--
Te	2	1	--
As	1	2	--
Pt	1	1	--
Ru	1	1	--
Nd	1	1	--

TABLE 4.--Comparison of tissue section and digestive analysis for all particles (for 8 cases).

Particle type	Section analyses	Digestion analyses
Silica	26 (7%)	46 (11%)
Aluminum silicates	112 (28)	190 (48)
Metals	237 (60)	147 (37)
Talc	0	7 (2)
Misc. other	20 (5)	12 (2)
Total	395 (100%)	402 (100%)

(Numbers of particles analysed in all 8 cases.)

TABLE 5.--Comparison of types of particles found in sections vs digestion.

	Tissue section	Digestions for fibers
Total particles	17870 (100%)	9852 (100%)
Metals	7352 (41)	685 (7)
Silicates	5301 (30)	2348 (24)
Silics	2202 (12)	485 (5)
Talc	649 (4)	855 (9)
Misc. silicates	1264 (7)	391 (4)
Gypsum	266 (1)	17
Misc.	78	2
Asbestos	278 (2)	4273 (44)

(Numbers of particles in master database.)

One analytical area in which the in situ method may be better than digestive techniques is in the analysis of metal particles. These usually submicrometer particles may be dissolved or disaggregated so as to be lost during filtration procedures, and they may be too small to be counted with the common cutoff threshold values used in some automated particle-analysis systems. Of course, the major disadvantage of the in situ technique is that it has not yet been automated and requires a skilled operator to spend several hours for an average analysis.

A considerable part of this analytical project has been the ongoing development of a PC-based database for data retrieval and analysis. Analytical results on over 14 000 particles are catalogued. Currently, these particles are comprised of 8.8% silica, 28.9% silicates, 25.5% metals, 18.6% endogenous, 3.6% other, and 14.4% asbestos. These results are linked to patient data related to medical and occupational histories, smoking, age, sex, pathologic diagnoses, etc. This database is being queried regarding normal lungs and especially regarding the complex relationships of inorganic particulates to well-recognized pneumoconioses and to diseases of as yet uncertain or less well-documented etiology.

References

1. P. Ingram, J. D. Shelburne, and V. L. Roggli, Eds., *Microbeam Analysis in Medicine*, Washington: Hemisphere, 1989.
2. J. L. Abraham and B. R. Burnett, *SEM/1983 II*, 681.

NONASBESTOS MINERAL FIBERS IN HUMAN LUNGS

V. L. Roggli

Analytical electron microscopy has greatly facilitated the identification of inorganic particulates in human lung tissue. This approach has been particularly effective for the identification of asbestos fibers recovered from lung. However, asbestos fibers are not the only mineral fibers found in human lungs. Indeed, among members of the general population with no more than background exposure to asbestos, nonasbestos mineral fibers outnumber asbestos fibers.¹ In most reported studies, a "fiber" is defined as an inorganic mineral particle with roughly parallel sides and a length-to-width (aspect) ratio of at least 3:1. Evaluation of mineral fiber content of lung tissue is important since there is experimental evidence that the aspect ratio of a mineral particle is an important determinant of its pathogenicity.² The present study is a report on experience with the identification of nonasbestos mineral fibers in more than 200 cases by means of analytical scanning electron microscopy.

Experimental

Wet formalin-fixed lung tissue was obtained for digestion analysis and asbestos quantification in 231 cases. These patients were suspected or known to have been exposed to asbestos, or else had a disease associated with asbestos exposure (e.g., malignant mesothelioma). Samples with wet weights of approximately 0.3 g (range 0.25 to 0.35 g) were digested by the sodium hypochlorite technique,³ and the residue was recovered on 0.4 μ m pore-size Nuclepore filters. Filters were prepared for light microscopy for identification of ferruginous bodies, as well as for scanning electron microscopy for quantification of coated (i.e., ferruginized) and uncoated fibers. Each filter was mounted on a carbon disk with colloidal graphite, sputter-coated with gold, and examined in a JEOL-JSM 35C scanning electron microscope at 20 kV at 1000 \times screen magnification.⁴ At this magnification, primarily fibers 5 μ m or more in length are detected. One hundred consecutive fields or 200 fibers, whichever came first, were evaluated and the number of fibers per square millimeter filter surface determined. From these data, the number of fibers per gram of wet lung tissue may be calculated.³ Energy-dispersive x-ray analysis (EDXA) was performed with a Kevex 7000 detector at an operating voltage of 25 kV. Ten to 25 consecutive fibers were analyzed for elemental composition for each case.

The author is at Durham Veterans Administration and Duke University Medical Centers, Durham, NC 27710.

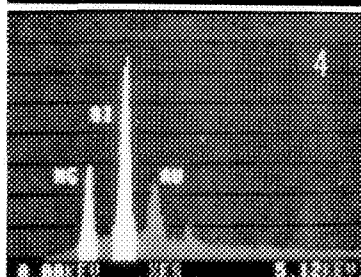
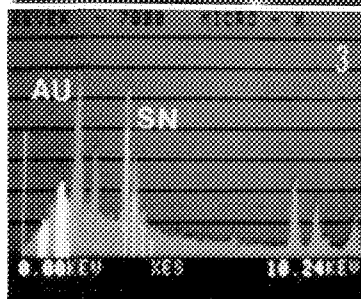
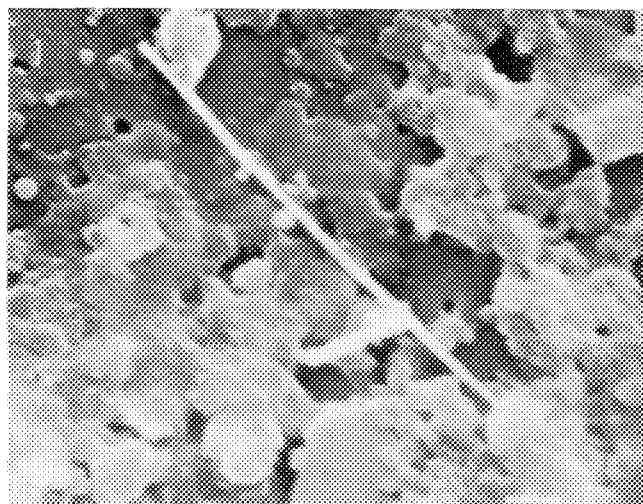


FIG. 1.--Tin fiber from human lung. Bar = 1 μ m.
FIG. 2.--Talc fiber from human lung. Bar = 1 μ m.
FIG. 3.--Energy-dispersive spectrum of fiber from Fig. 1, showing major peak for tin. Au peak is from sputter-coating.
FIG. 4.--Energy-dispersive spectrum of fiber from Fig. 2, showing major peaks for magnesium and silicon. Au peak is from sputter-coating.

TABLE 1.--Summary of EDXA data for 796 nonasbestos mineral fibers isolated from 156 human lung samples.

Mineral Type	No.	(%)	Mineral Type	No.	(%)
Talc	249	(31)	Iron-oxides	34	(4)
Silica	144	(18)	Miscellaneous silicates ^a	76	(10)
Rutile	115	(14)	Other metal oxides ^b	16	(2)
Kaolinite	73	(9)	Endogenous calcium ^c	11	(1)
Mica or feldspar	55	(7)	Fiberglass	23	(3)

^aVarious combinations of Si with Na, Mg, Al, K, Ca and Fe

^bIncludes aluminum (9), iron-chromium (5), iron-aluminum (1), and tin (1)

^cIncludes calcium phosphate (apatite) (10) and calcium-only (carbonate, oxalate, or oxide) (1)

Results

Nonasbestos mineral fibers were identified in 156 of 231 cases (68%). The 32% of cases in which no fibers other than asbestos were identified were among those with the heaviest pulmonary asbestos burdens. In these patients, any background level of nonasbestos mineral fibers is so diluted by the markedly elevated asbestos fiber content that analysis of 25 consecutive fibers is unlikely to detect anything other than asbestos. Among the 156 cases with nonasbestos mineral fibers, these fibers accounted for 5% to as much as 100% of the fiber burden; in general, the higher the percentage of nonasbestos mineral fibers, the lower the total fiber burden. Nonasbestos mineral fibers most often fell in the size range of 5-10 μm in length, with diameters of 0.5-2.0 μm (Figs. 1 and 2). Hence these fibers have a relatively low aspect ratio compared to that of most asbestos fibers. The corresponding spectra are shown in Figs. 3 and 4.

EDXA of more than 3000 fibers showed that 796 were nonasbestos mineral fibers. These are categorized according to their chemical composition in Table 1. The most commonly encountered nonasbestos mineral fibers in decreasing order were talc (31%), silica (18%), rutile (titanium dioxide) (14%), kaolinite (an aluminum silicate) (9%), mica or feldspar (potassium-aluminum-silicates) (7%), and iron-oxides (4%). The remainder were mostly silicates (10%), with various combinations of Si with Na, Mg, Al, K, Ca, and Fe. Metal oxides other than titanium or iron accounted for another 2%, and included aluminum, iron-chromium, iron-aluminum, and tin fibers (in decreasing order). Endogenous calcium fibers (mostly calcium phosphate or apatite) represented 1% of the total. Finally, there were a small number of fibers (3%) with smooth, parallel sides which consisted mostly of silicon with variable small peaks of Al, Mg, and Na. These are tentatively classified as fibrous glass based on their morphology and chemical composition. Carbon fibers (which are occasionally seen in lung tissue⁵) are not shown in the data, since fibers with no detectable elements by EDXA were excluded from the analysis.

Any inhaled fibrous particle of sufficient length ($\geq 20 \mu\text{m}$) and diameter sufficiently thin for the particle to be respirable ($\leq 3 \mu\text{m}$) may become coated with iron, or ferruginized, by alveolar macrophages. Most ferruginous bodies have asbestos fibers at their core and are thus referred to as asbestos bodies. However, nonasbestos mineral fibers may also become coated, and these nonasbestos ferruginous bodies, or pseudoasbestos bodies, can usually be distinguished from true asbestos bodies by light microscopy.⁵ Nonasbestos ferruginous bodies were identified in 24% of cases by light microscopy, and either had broad yellow sheet-like cores or black cores. EDXA showed that most of the former were talc, whereas most of the latter were either pure carbon or metal oxides (titanium, iron, or aluminum). Only a small percentage of nonasbestos mineral fibers examined by SEM ($< 3\%$) were coated.

Conclusions

The observations reported here are quite similar to those reported by Churg in his study of nonasbestos pulmonary mineral fibers in the general population.¹ He used analytical transmission electron microscopy, and found that talc, silica, rutile, kaolinite, micas, feldspar, and other silicates accounted for most nonasbestos mineral fibers recovered from the human lung. The main difference between the present study and that of Churg is the prevalence of calcium phosphate (apatite) fibers, which accounted for 18% of all fibers and were the single most common type found in his study, but accounted for only 1% of the fibers in the present study (Table 1). Both studies employed similar tissue digestion techniques. The distribution of elemental compositions of nonasbestos pulmonary mineral fibers in the present study is also strikingly similar to the distribution of elemental composition of the much more numerous nonfibrous particulates in human lungs, as reported in a study of particulate concentrations in 33 lung samples by Stettler et al.⁶ These authors used analytical scanning electron microscopy with automated imaging/x-ray analysis, and

found that silica, talc, aluminum silicates, rutile, iron oxides, and various other silicates accounted for the vast majority of non-fibrous particles present in human lungs. Although the biologic significance of these non-asbestos mineral fibers and nonfibrous particles is largely unknown, one study has demonstrated a statistically significant increase in the pulmonary content of fibrous and nonfibrous particulates among patients with lung cancer as compared to noncancer controls matched for age, smoking history, and general occupational category.⁷

References

1. A. Churg, "Nonasbestos pulmonary mineral fibers in the general population," *Environ. Res.* 31: 189, 1983.
2. M. F. Stanton et al., "Relation of particle dimensions to carcinogenicity in amphibole asbestos and other fibrous minerals," *J. Natl. Cancer Inst.* 67: 965, 1981.
3. V. L. Roggli, P. C. Pratt, and A. R. Brody, "Asbestos content of lung tissue in asbestos-associated diseases: A study of 110 cases," *Br. J. Ind. Med.* 43: 18, 1986.
4. V. L. Roggli, "Scanning electron microscopic analysis of mineral fibers from human lungs," in P. Ingram, J. D. Shelburne, and V. L. Roggli, Eds., *Microprobe Analysis in Medicine*, New York: Hemisphere, 1989, 97.
5. A. Churg, M. L. Warnock, and N. Green, "Analysis of the cores of ferruginous (asbestos) bodies from the general population: II. True asbestos bodies and pseudoasbestos bodies," *Lab. Invest.* 40: 31, 1979.
6. L. E. Stettler et al., "Particulate concentrations in urban lungs," in Ref. 4, p. 133.
7. A. Churg and B. Wiggs, "Mineral particles, mineral fibers, and lung cancer," *Environ. Res.* 37: 364, 1985.

OCULAR APPLICATIONS OF ENERGY-DISPERSIVE MICROPROBE ANALYSIS

G. K. Klintworth

Since Tousimis and Adler's demonstration of copper in Descemet's membrane in Wilson's disease,¹ energy-dispersive X-ray microanalysis (EDX) has been applied to a variety of ocular situations (Table 1). This review highlights a few of the contributions that EDX has made to ophthalmic pathology and summarizes the applications of this technique in studies of the normal and diseased eye. Because of space restrictions the bibliography is limited to major studies and recent publications. For a fuller discussion and additional references, see Ref. 2.

Ocular Foreign Bodies

EDX has been particularly useful in the elemental analysis of ocular foreign materials. A comparison of the elemental composition of a removed foreign body with its alleged source helps resolve disputes that arise from injuries, such as those that occur at work, in which compensation is sought; or in product liability actions. The following are examples in which EDX helped to identify foreign materials.

Johnson and Zimmerman³ drew attention to unusual golf-ball injuries of the conjunctiva and eyelid caused by tissue penetration of the highly compressed liquid contents (mixture of barium sulfate and zinc sulfate) of certain golfballs.

The identification of titanium, barium, or zinc served to differentiate synthetic fibers from natural fibers or caterpillar hairs in conjunctival lesions.⁴

Silicon has been demonstrated within silica granulomas of the eyelids and periorbital,⁵ and in colorless transparent retinal microemboli that accompanied open heart surgery (presumably derived from an antifoaming agent).⁶

Streeten et al. (see Ref. 2) studied an eye enucleated several months after cyanoacrylate embolization therapy for a post-traumatic carotid-cavernous sinus fistula. Numerous ocular intra-arterial granulomas containing tantalum (included in the injection mixture to allow x-ray visualization of the embolus) were observed within black granular material.

Iron from foreign bodies (siderosis) or repeated intraocular hemorrhage (hem siderosis) deposits preferentially in the sensory retina and other ocular structures and its presence has been detected by SEM.

Silver has been demonstrated within the affected ocular tissues in argyrosis.^{7,8} Several potential pitfalls need to be taken into account in the interpretation of analyses of foreign bodies. The composition of the surgically removed specimen may differ from

the actual source material: (1) elements such as calcium and chloride may deposit on a foreign body that has remained in tissue for some time; (2) specks of extraneous material may contaminate foreign bodies that are not collected under ideal conditions. The latter possibility can be minimized by insuring that the specimen does not lie around unprotected in the operating room or laboratory where it is subject to airborne contamination. Also, in the preparation of the foreign body for microanalysis the surgically removed excised specimen should be kept in a clean container that is not contaminated with foreign particles.

Corneal Disease

Johnson and Campbell⁹ made a noteworthy observation of Descemet's membrane in Wilson's disease. They detected sulfur in copper-rich electron-dense granules. This finding is consistent with the hypothesis that sulfur-rich metallothionein proteins bind and aggregate with copper in Descemet's membrane. Robinson and Streeten¹⁰ found the relative proportions of calcium, phosphorus, and sulfur to be useful in distinguishing calcific band keratopathy from spheroidal degeneration. Deposits in the latter condition contained excess sulfur; and although calcium was often present, phosphorus was lacking.

EDX of corneal tissue with macular dystrophy after tissue exposure to colloidal iron dramatically demonstrates the affinity of the accumulations for colloidal iron. The storage product in macular corneal dystrophy has been found to lack the significant sulfur peak characteristic of normal corneas,¹⁰ which suggests that they are not sulfated.

Other Applications of EDX in Ophthalmic Pathology and in Studies of the Eye

EDX has been used to determine the concentration of calcium in the aqueous humor¹¹ and to characterize a variety of particles found in some solutions infused into the eye.¹² The technique has also been employed to study element concentration, distribution, and transport in the cornea, lens, retina, and retinal pigment epithelium.¹³⁻²⁰

Calcium is localized within the membranous disks (not interdisk spaces) of the rod outer segments in retina.¹⁴ The outer segments of the retina contain phosphorus, potassium, sulfur, chlorine, and calcium.¹⁵ The highest concentration of calcium in frog rods is in the inner segment, where this cation concentrates in the cisternae of the endoplasmic reticulum.¹⁶ The extracellular fluid and the intradisk space of rods have a higher concentration of calcium relative to the cytosol.

In a study of dark-adapted and illuminated frog retinal rods, Somlyo and Walz¹⁶ found that

The author is in the Departments of Pathology and Ophthalmology, Duke University Medical Center, Durham, NC 27705. Supported in part by research grants 1R01-EY00146 and P30-EY05722 from the National Eye Institute.

the total calcium content of the rod outer segment did not change upon prolonged illumination, but the magnesium content of rods diminished significantly after prolonged illumination, a finding consistent with the hypothesis that the dark current is carried by magnesium ions.

Lipofuscin granules contain prominently calcium and zinc, but also sulfur, chlorine, magnesium, potassium, and occasionally copper.¹⁵ Intraocular melanosomes contain more calcium than other cell organelles and the adjacent cytoplasm. Potassium, sulfur, zinc, barium, and other trace metals have also been observed in pigmented ocular tissue.²¹⁻²³

Conclusions

In ophthalmology EDX has proved valuable in the characterization and identification of foreign material in ocular and adnexal tissues as well as on contact and intraocular lenses. In addition the technique has established the elemental composition of lesions in certain pathologic ocular tissues. To date many studies have unfortunately not been performed on ideally prepared tissue and contaminants from fixatives and the embedding media have often complicated interpretations of the data. With the exception of foreign bodies, most conditions analyzed by EDX have merely confirmed observations established by other methods without yielding significant new information.

References

1. A. J. Tousimis and I. Adler, "Electron probe x-ray microanalyzer study of copper within Descemet's membrane of Wilson's disease," *J. Histochem. Cytochem.* 2: 40, 1963.
2. G. K. Klintworth, B. W. Streeten, and R. C. Eagle Jr., "Applications of energy dispersive microprobe analysis in ophthalmic pathology," in P. Ingram, J. Shelbourne, and V. L. Roggli, Eds., *Electron Probe Microanalysis in Human Medicine*, Washington, D.C.: Hemisphere, 1989.
3. F. B. Johnson and L. E. Zimmerman, "Barium sulfate and zinc sulfate deposits resulting from golf-ball injury to the conjunctiva and eyelid," *Am. J. Clin. Pathol.* 44: 533, 1965.
4. J. C. Weinberg et al., "Conjunctival synthetic fiber granuloma: A lesion that resembles conjunctivitis nodosa," *Ophthalmology* 91: 867, 1984.
5. R. J. Riddle et al., "Silica granuloma of eyelid and ocular adnexa," *Arch. Ophthalmol.* 99: 683, 1981.
6. I. M. Williams et al., "Identification of silicon in retinal vessels by electron probe x-ray microanalysis," *J. Histochem. Cytochem.* 23: 149, 1975.
7. W. H. Spencer et al., "Endogenous and exogenous ocular and systemic silver deposition," *Trans. Ophthalmol. Soc. U.K.* 100: 171, 1980.
8. Z. A. Karcioğlu and D. R. Caldwell, "Corneal argyrosis: Histologic, ultrastructural and microanalytic study," *Canad. J. Ophthalmol.* 20: 257, 1985.
9. R. E. Johnson and R. J. Campbell, "Wilson's disease: Electron microscopic, x-ray energy spectroscopic, and atomic absorption spectroscopic studies of corneal copper deposition and distribution," *Lab. Invest.* 46: 564, 1982.
10. M. R. Robinson and B. W. Streeten, "Energy dispersive x-ray analysis of the cornea: Application to paraffin sections of normal and diseased human corneas," *Arch. Ophthalmol.* 102: 1678, 1984.
11. D. J. Doughman, M. J. Ingram, and W. M. Bourne, "Experimental band keratopathy: Electron microprobe x-ray analysis of aqueous and corneal calcium concentrations," *Invest. Ophthalmol.* 9: 471, 1970.
12. O. Winding and E. Gregersen, "Particulate contamination in eye surgery," *Acta Ophthalmol.* 63: 629, 1985.
13. R. Rick et al., "Electron microprobe analysis of chloride secretion in the frog cornea," *Curr. Eye Res.* 4: 377, 1985.
14. M. L. Fishman et al., "Ultrastructural demonstration of calcium in retina, retinal pigment epithelium and choroid," *Exp. Eye Res.* 24: 341, 1977.
15. E. Yamada, "Elemental analysis of frog outer segment and fuscine granule by means of x-ray microanalyzer," *Sensory Processes* 2: 285, 1978.
16. A. P. Somlyo and B. Walz, "Elemental distribution in *Rana pipiens* retinal rods: Quantitative electron probe analysis," *J. Physiol. (London)* 353: 183, 1985.
17. C. V. Harding, S. Susan, and W. Bobrowski, "Elemental profiles in cryosections and frozen-dried bulk specimens of the normal lens," *Ophthalmic Res.* 16: 276, 1984.
18. J. R. Neuringer, J. I. Clark, and G. B. Benedek, "A quantitative microprobe analysis of elements in cortical and nuclear cells of the calf lens," *Anat. Record* 211: 329, 1985.
19. T. Baba, "Study on the lens development in rat embryo: Scanning electron microscopic observation and x-ray microanalysis," *Acta Soc. Ophthalmol. Japan* 85: 530, 1981.
20. I. C. Piscopo, D. D. Kaska, and D. K. Vaughan, "X-ray microanalysis and morphology of retinal Muller cells," *Norelco Rep.* 32: 52, 1985.
21. B. J. Panessa and J. A. Zadunaisky, "Pigment granules: A calcium reservoir in the vertebrate eye," *Exp. Eye Res.* 32: 593, 1981.
22. H. Ripps et al., "Ultrastructural localization and x-ray analysis of calcium-induced electron deposits in the skate retina," *Neuroscience* 4: 1689, 1974.
23. H. Hess, "Trace metals, silicon and calcium in frog rod outer segments, pigment epithelium and retina," *Proc. Assoc. Res. in Vision and Ophthalmology*, p. 86, 1976.
24. J. H. Seland, "The nature of capsular inclusions in lenticular chalcosis: Report of a case," *Acta Ophthalmol.* 54: 99, 1976.
25. K. Olander, A. Kanai, and H. E. Kaufman, "An analytical electron microscopic study of a corneal tattoo," *Ann. Ophthalmol.* 15: 1046, 1983.

26. C. V. Harding et al., "Calcium-containing opacities in the human lens," *Invest. Ophthalmol. Vis. Sci.* 24: 1194, 1983.

27. H. Hoisen et al., "Idiopathic haemochromatosis and eye symptoms: A case report," *Acta Ophthalmol.* 63: 192, 1985.

28. L. K. Garron et al., "A clinical pathologic study of mercuria lentis medicamentosa," *Trans. Am. Ophthalmol. Soc.* 74: 295, 1976.

TABLE 1.--Ophthalmic situations in which EDX has been used.

Foreign Bodies in Ocular Tissues

Golfball injuries: Zn, Ba, S in lesions.³

Intravascular cyanoacrylate granulomas: Identification of Ta.

Silica granulomas: Identification of Si.⁵

Talc granulomas: Presence of Si, Mg in 3:1 ratio.

Silicone/Antifoam retinal emboli: Identification of Si.⁶

Copper foreign body (chalcosis): Cu not detected in anterior lens capsular particles.^{2,4}

Gunshot--casing: Cu, Zn (brass) identified.

Gun powder: Ba, Pb identified.

Glass

Characterization of Ocular Pigmentation

Corneal blood staining: S, P with Fe.

Implanted pigment into eyelid: Identification of Fe, Ti.

Implanted pigment into cornea (corneal tattoo):

Pigments contain various elements including

Al, Co, Si, Pt.^{2,25}

Iron (siderosis bulbi): Fe within retina and other discolored structures.

Pathologic Calcification and Ossification

Calcific band keratopathy (human and experimental): Bowman's layer and the superficial corneal stroma calcified with Ca, P.

Retinoblastoma: Foci of Ca, P.

Phthisis bulbi: Ca, P in bone.

Calcification of Bruch's membrane: Ca, P present.

Proliferative vitreoretinopathy: Ca, P in spicules of one membrane.

Diffuse calcification and senile plaques: Ca, P present.

Primary hyperoxaluria: Ca not associated with P present.

Hyperparathyroidism: Ca, P. in corneal cells.

Optic nerve drusen: Substantial amounts of Ca, P.

Study of Miscellaneous Disorders

Human cataracts: Changes in S, P in opacities; Ca (oxalate) in some deposits.²⁶

Experimental traumatic cataracts: Elemental composition varies with the age of cataract.

Wilson's disease: Copper in Descemet's membrane (Kayser-Fleischer ring).^{1,9}

Hemochromatosis: Ca, P, Mg in Bowman's layer but no Fe.²⁷

Chronic actinic keratopathy (spheroidal degeneration of the cornea): Ca in corneal spheroids in some studies.¹⁰

Macular corneal dystrophy: Diminished S.¹⁰

Asteroid hyalosis: Major detectable element Ca,

P; presence of S disputed.

Subretinal pigment epithelium drusen: Ca, P present in some components; K, Cl in others.

Retinitis pigmentosa: No useful information.

Granular, lattice, and Fuchs's corneal dystrophy: No useful information.

Topical sulfacetamide, atropine sulfate, and tobramycin: Extensive S, Ca in cornea.

Solutions Infused into Eye¹²

Characterization and identification of particles.

Contact and Prosthetic Intraocular Lenses

Characterization of opacities.

Identification of contaminants used in polishing.

Industrial or Medicinal Exposure to Heavy

Metals

Silver (Argyrosis).^{7,8}

Mercury.²⁷

Calcium Determinations in Aqueous¹¹

Studies of elemental concentration and transport in normal cornea, lens, retina, and retinal pigment epithelium.

Chloride transport in cornea.¹⁰

Elemental distribution in normal rat and calf lens.^{17,18}

Elemental distribution in rat fetal and embryonic lenses: Ca, Cl detected during the late embryonic life; S increases as lens fibers become more numerous.¹⁹

Normal retina, retinal pigment epithelium, and choroid: Ca in retina and retinal pigment epithelium; P, Ca concentrated in photoreceptor cells and in nuclei of Müller cells.²⁰

Lipofuscin granules: Contain predominantly Ca, Zn in frog.¹⁵

Melanosomes: Rich in Ca.²¹⁻²³

QUALITY CONTROL OF CARDIOVASCULAR WIRE PLUNGE ELECTRODES

R. P. Kusy and J. W. Buchanan

Potassium (K^+), and hydrogen (pH) and reference (R) wire plunge electrodes are used at present in controlled animal experiments to map the ischemic regions of the heart muscle. During manufacture, transportation, and insertion of these miniature electrodes into the myocardium, as many as 50% fail. Such losses are costly not only because of the time and labor lost

during the fabrication but also because as much as 35% of the electrode array may not function, thereby preventing a decisive experimental conclusion. As a first step to improve the efficiency of the current generation of electrodes, a failure analysis study was initiated. Such quality-control evaluations have not been addressed in the literature previously.

The authors are at the Schools of Dentistry and Medicine, University of North Carolina, Chapel Hill, NC 27599-7455. This research is supported through the NSF's Duke-North Carolina Engineering Research Center by the North Carolina Biotechnology Center. Our thanks to Ms. Connie Engle of the Division of Cardiology for providing the biosensors that were studied during this investigation, and the PPG.

Experimental

Some K^+ , pH, and R electrodes that passed a millivolt potential test and others that failed the same test were investigated by scanning electron microscopy (SEM) and energy-dispersive and x-ray analysis (EDX). Initially, each electrode (0.25 mm in diameter and

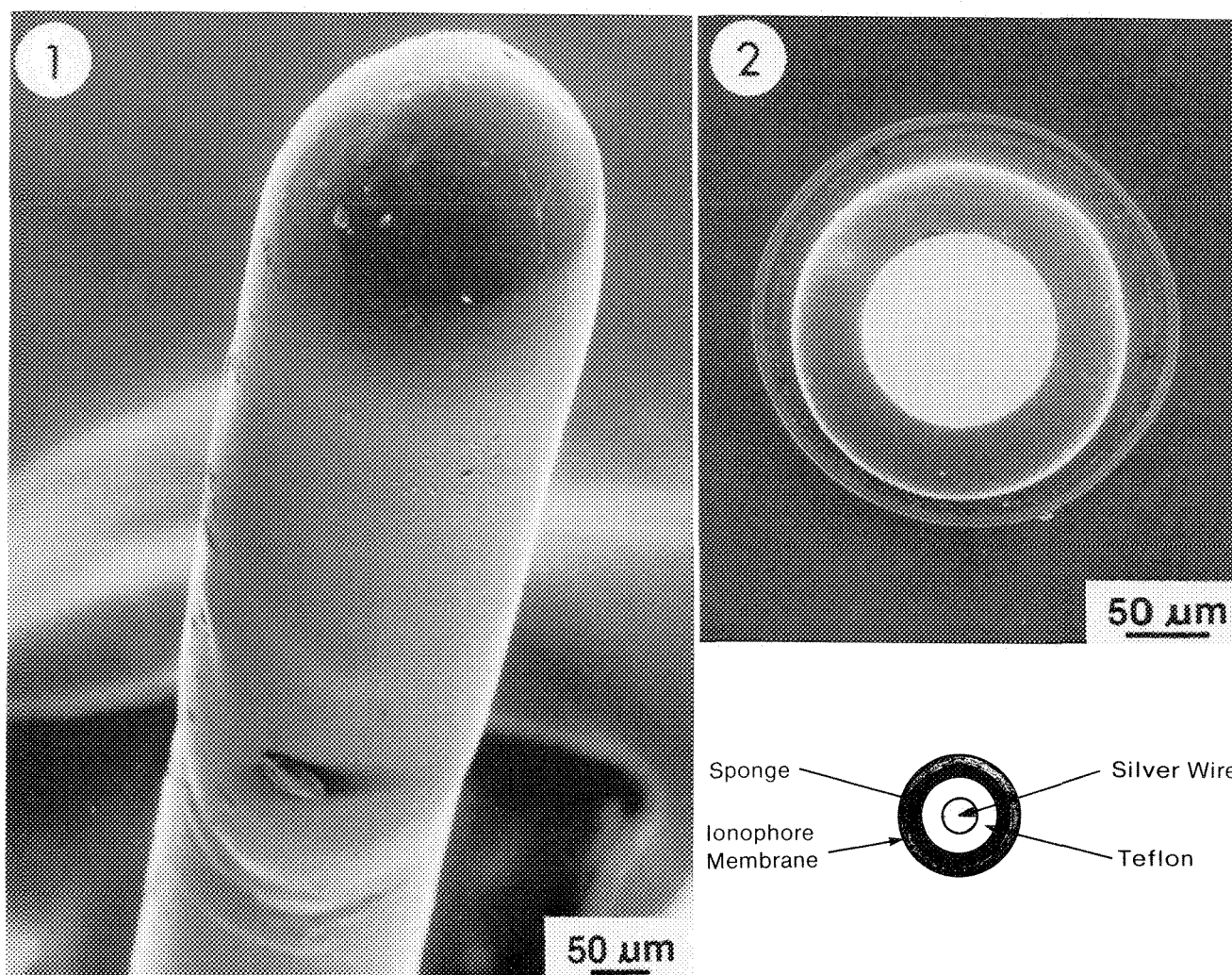


FIG. 1.--Appearance of "good" K^+ electrode.

FIG. 2.--Cross-sectional area of K^+ sensor with asymmetrical sponge layer.

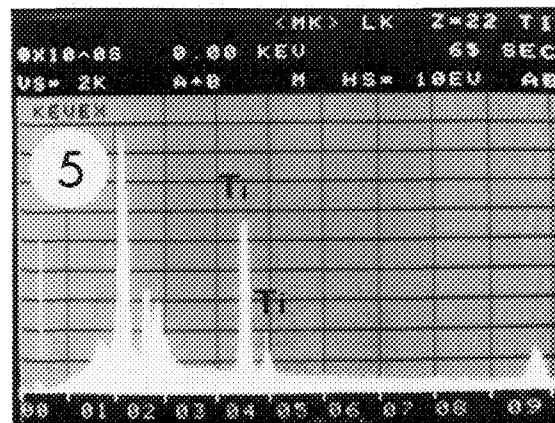
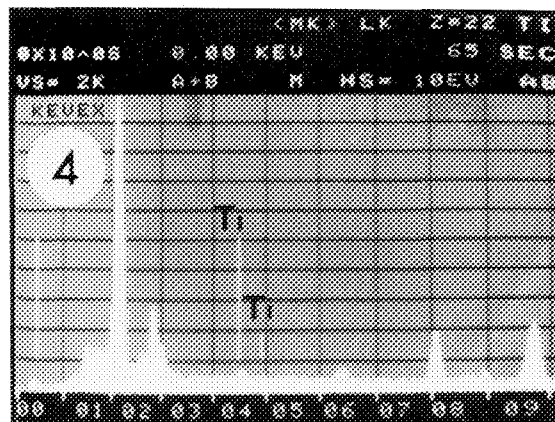
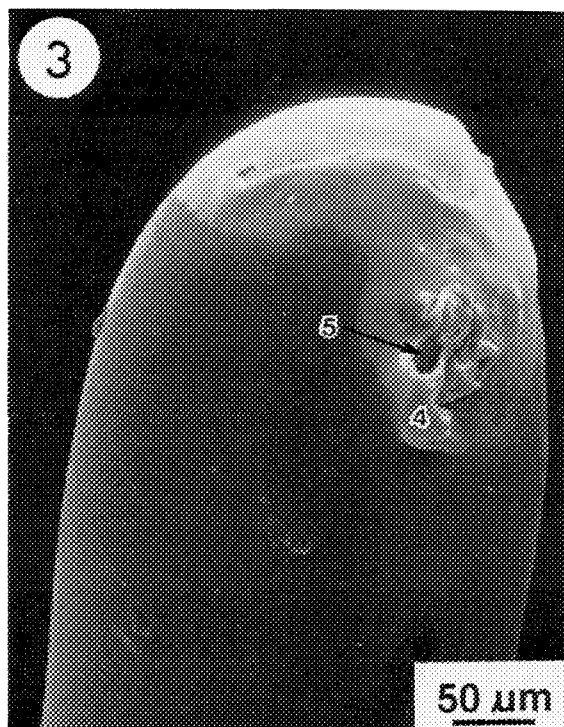


FIG. 3.--SEM of a defective K⁺ electrode with potential drop of only 5 mV.

FIG. 4.--EDX of intact membrane surface of Fig. 3. Note absence of Ti in this x-ray spectrum.

FIG. 5.--EDX within the defect of Fig. 3. Note presence of Ti from sponge layer in this x-ray spectrum.

1 mm long) was sputtered with a 30nm layer of Au-Pd and viewed at 100 \times under the following conditions: gamma-1 mode, 20 kV accelerating voltage, and 2.0 A condenser lens current. Some electrodes were sectioned perpendicular to their wire axes and carefully polished to reveal the geometry of their built up layers. From x-ray analyses at 20 kV, each layer of a K⁺, pH, and R electrode was characterized, thereby permitting the cause of each surface failure to be identified.

Results

On good electrodes the membrane conformed closely to the Teflon (PTFE) coated Ag wire with no cracks in the PTFE layer penetrating to the Ag wire and no tears in the membrane layer penetrating to the Ti sponge layer (Fig. 1). A cross-sectional view showed that the dipping process could form an asymmetrical layer (Fig. 2) that, in the limit, could reduce potential drops in the pH and K⁺ electrodes to below the acceptable 120 and 30mV levels, respectively. In the extreme case, sensors failed because the outermost ionophore layer was too thin, a bubble in the ionophore layer formed and burst, or mechanical abrasion had occurred during some

phase of production, storage, transportation, or insertion. These failures are easy to confirm because x-ray spectra show the presence of Ti, a major constituent in the sponge that is not present in any components of the ionophore membrane layer (Figs. 3-5). By SEM and EDX, fine Al whiskers have been identified as a contaminant, stainless steel debris has been confirmed on insertion needles, and potassium crystals have been observed on electrode surfaces.

Conclusions

Good quality control of wire plunge electrodes requires care during every stage of manufacture; that is, purification and filtering of chemicals, cleanliness of facilities, uniform dipping of layers, and appropriate drying procedures. On pH and K⁺ electrodes that had non-Nernstian responses, x-ray analyses often revealed the presence of Ti atoms on the surface, a clear indication that there was a short circuit through the ion-selective membrane. In the future, x-ray analysis will be a valuable tool to improve electrode design, for example, by the optimization of chloridation conditions.

ROLE OF THE (Na,K)-PUMP IN INTRACELLULAR Na HOMEOSTASIS

Claude Lechene, Horacio Cantiello, Maryse Crabos, and B. J. Cohen

The (Na,K)-pump creates and maintains ionic gradients between intracellular and extracellular milieu that are of fundamental importance for proper function of mammalian cells. Special and general cell processes (e.g., nerve conduction, nutrient transport, pH regulation) are energized by being coupled to the ionic leak pathways that use the potential energy of the ionic gradients. Because the sodium gradient in particular energizes many vital cell processes, alterations in cell activity will often be manifest as changes in rate of sodium entry. The (Na,K)-pump rate varies accordingly and maintains a balance between Na entry and exit thereby maintaining the potential energy of the cell.

The steady-state intracellular concentrations of Na and K of most animal cells are quite similar. This similarity belies the fact that the (Na,K)-pump rate varies by two orders of magnitude among cell types (from several days to a few minutes), and may vary by 3-4 fold within the same cell (see below).¹ This remarkable constancy of intracellular composition despite great variability in ionic traffic in and out of the cell is due to regulatory interactions between the pump and leak pathways. As we shall see, acute changes in sodium influx are rapidly matched by activation of already existing (Na,K)-pumps. This is possible because intracellular sodium is normally poised on the steep limb of the concentration-vs-activity curve for the (Na,K)-pump, at a point well below maximal activity, allowing large increases in (Na,K)-pump rate with only small changes in sodium concentration. However, more chronic changes in sodium entry are followed by insertion of new pumps into the membrane, allowing intracellular sodium concentration to return to its original value.

Methods

Intracellular ionic contents are measured by electron-probe analysis of cultured cells as already described.²⁻⁵ Cells are cultured 2 to 3 days on silicon chips. After an experimental period, cells on silicon chips are washed in cold distilled water (in some cases in isotonic ammonium acetate) for a total of 6 s, followed by immediate quenching in liquid nitrogen. Cells are freeze-dried at -70 °C for 6 h at a

10^{-6} Torr pressure. Cells are analyzed with a 10-15 μ m electron beam, 200 nA beam current, and 11 kV accelerating voltage. Location of individual cell is either selected manually, targeting the cells by means of the optical microscope attached on the electron probe column (Cameca MS46) or automatically by recording of x-ray counts on areas where the phosphorus signal is at least three times higher than the background. Cells are moved under computer control by a specially designed specimen stage allowing an area of 8×5 cm to be explored; locations are retrieved by use of optical encoders with a reproducibility of ± 1 μ m in X and Y; focusing is over 2 mm with a reproducibility of ± 0.1 μ m. A total of 1000 to 2000 cells are measured per experiment. Cells are counted for 10 s. Values of 10 to 50 cells are averaged per experimental time point. K, Cl, and P are selected with a pentathyril crystal, Na with a potassium acid phthalate crystal. Efficiencies of the spectrometers are calibrated by electron probe analysis of dried liquid droplets of known composition. Initial rates of Na (and K) leaks are calculated as the first derivative at time zero of the best fit to the change with time in Na (and K) content measured after inhibition of the (Na,K) pump. (Na,K)-pump rate is measured in three conditions: (1) at functional V_{\max} as the initial rate of ouabain-sensitive K influx and Na efflux, in cells Na loaded by preincubation in a medium lacking K; (a) at steady state, normal low intracellular Na, as the initial rate of ouabain sensitive K influx in cells that had Rb substituted for intracellular K during a preincubation period; and (3) at intermediary levels of intracellular Na in cells that had Rb substituted for intracellular K during a first preincubation period and then had undergone a reversible inhibition of the (Na,K)-pump for different length of time. The apparent V_{\max} and apparent affinity (K_m) of the (Na,K)-pump for Na are calculated from the best fit to a Hill-type equation. Calculations are performed using software programs developed in our laboratory and in the NIH Resource PROPHET.

Short-term Regulation of Changes in Na Influx

Normally intracellular Na concentration is below the K_m of the enzyme for sodium,⁶ so that (Na,K)-pump activity is approximately one-third of its potential maximum (Fig. 1). The (Na,K)-pump can respond immediately to an increase in sodium influx so that a new steady state for sodium movement may be reached with only a small net gain in intra-

The authors are at the Department of Medicine and National Electron Probe Resource for the Analysis of Cells, Brigham and Women's Hospital, and Harvard Medical School, except B. J. Cohen, who is at New England Deaconess Hospital. This work was supported by NIH grant RR02604-04.

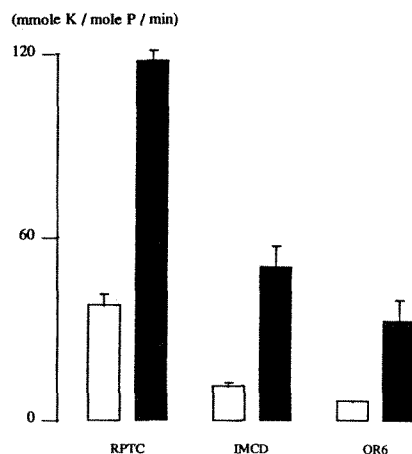


FIG. 1.--(Na,K)-pump rates (ouabain inhibitable K uptake) in normal, low intracellular Na concentration (white bars), and after sodium loading (black bars). RPTC = renal proximal tubule cells.⁴ IMCD = inner medullary collecting duct cells.¹⁷ OR6 = transfected cell line. (J. A. Epstein and C. Lechene, unpublished observations and Ref. 16.)

cellular sodium. The activation of the (Na,K)-pump is likely due to a direct effect of sodium on the enzyme. Because sodium constitutes a small percentage of the total intracellular ionic content, small increases in intracellular sodium content are translated into significant increases in intracellular sodium concentration, and are not blunted by osmotically driven water entry.

In renal proximal tubular cells in short-term primary culture, the effective permeability to sodium is the highest that we have measured among a variety of cell types, and approximately 80% of total sodium entry flux is through Na-H exchange.⁴ Activation of Na-H exchange immediately follows intracellular acidification by NH_4Cl washout, increasing approximately three-fold Na influx, restoring intracellular pH toward normal, but with an increase in intracellular Na content. Immediately after acidification, (Na,K)-pump rate decreases (presumably secondary to the pH change), but in less than 1 min it increases to approximately three-fold its control value. Thus, the activation of Na-H exchange removes the acid load, but at the same time leads to an increase in intracellular sodium concentration. This action stimulates (Na,K)-pump rate, thereby compensating the increase in Na influx and repairing the alteration in intracellular sodium concentration.⁴

Alanine entry into hepatocytes is known to occur primarily through Na-alanine co-transport.⁷ We studied the effects of alanine on ion transport and content in primary cultures of rat hepatocytes 38 h after plating.⁸ The initial rate of Na influx after (Na,K)-pump inhibition with 1 mM ouabain was 5.3 ± 0.5 mmole Na/mole P/min in control Ringer solution, and increased to 19.8 ± 0.4 in Ringer that also contained 10 mM alanine ($p < 0.01$, $n = 4$). Alanine application resulted in a doubling of intracellular sodium content and a nearly

intracellular sodium content and a nearly three-fold increase in ouabain-inhibitable Rb uptake (from 7.6 ± 2.0 mmole Rb/mole P/min in control to 20.0 ± 4.0 in the presence of alanine; $p < 0.5$, $n = 4$). Thus, alanine stimulates passive sodium entry (by an increase in sodium-alanine co-transport) and thereby increases intracellular sodium content. As the percentage increase in sodium content is much greater than the percentage gain in cell water (due to alanine accumulation) measured by others under these conditions,⁹ sodium concentration must rise. An increase in intracellular Na concentration has been confirmed by others.¹⁰ This increase stimulates the (Na,K) pump allowing the pump rate to match the increase in sodium influx with an increase in sodium content which represents no more than a 6% increase in total cation content.

Long-term Regulation of Changes in Na Influx

Intracellular sodium concentration may be an important signal that controls long-term pump regulation. It has been shown that exposing cells to extracellular K concentrations low enough to result in reduced (Na,K)-pump function leads to an initial increase in intracellular Na concentration, but over time the Na concentration returns to normal.¹¹⁻¹³ The cell responds to the reduction in pump activity by synthesizing new pumps. Increased pump mRNA can be detected after 30 min of exposure to low potassium and synthesis of new pumps can be found at 24 h.¹¹

We have studied the development of (Na,K)-ATPase activity in short-term culture of rat proximal tubule cells during terminal differentiation. An increase in Na-H exchange was found in cultured cells from rats between 12 and 15 days of age. This increase in Na-H exchange preceded by two days the well-documented increase in (Na,K)-ATPase synthesis at terminal differentiation. Intracellular Na concentration was elevated at the time of the increase in Na-H exchange [before the increase in (Na,K)-ATPase had occurred], but returned to normal when the number of pumps had increased. It was also found that (Na,K)-ATPase activity in single proximal tubules from 20-day-old rats that received a continuous infusion of amiloride (by mini-pump) for 4 days was significantly lower than that of animals perfused with vehicle alone. Several pieces of evidence indicated that the results were not due to a generalized effect of amiloride on protein synthesis or to a direct effect of amiloride on the (Na,K)-ATPase. We concluded that the increased expression of the sodium-proton exchanger preceded the expression of the (Na,K)-ATPase, and that the increase in sodium influx through the exchanger may be an important signal for the subsequent development of the (Na,K)-ATPase.^{14,15}

Genetic Modulation of (Na,K)-pump and Na and K Leak Rates

In CV-1 cells, a green monkey kidney cell line, transfecting a 6.5-kb genomic fragment from mouse cells that had been chemically muta-

TABLE 1.--Proximal tubular cells from normotensive, MNS and hypertensive rats.

	Na _i	J _{Na}		V _{max}	K _m
		net	amil		
MNS	12.2 ± 0.04 (627)	34.0 ± 3.5 (5)	15.7 ± 1.6 (5)	78.6 ± 1.1 (28)	11.7 ± 0.08 (28)
MHS	17.5 ± 0.05 (534)	30.1 ± 2.6 (6)	14.6 ± 2.3 (6)	82.3 ± 1.5 (23)	18.0 ± 0.10 (23)
p	< 0.0002	< 0.4	< 0.5	< 0.05	< 0.001

TABLE 2.--Inner medullary collecting duct cells from normotensive, MNS and hypertensive, MHS rats.

	Na _i	J _{Na}		V _{max}	K _m
		net	amil		
MNS	7.06 ± 0.07 (96)	15.9 ± 1.3 (2)	7.27 ± 1.45 (2)	57.9 ± 1.12 (23)	23.9 ± 0.4 (23)
MHS	7.60 ± 0.09 (127)	6.66 ± 0.80 (3)	7.98 ± 1.14 (3)	26.8 ± 0.3 (25)	8.9 ± 1.0 (25)
p	< 0.001	< 0.02	< 0.4	< 0.005	< 0.02

Na_i: intracellular Na content, in moles × 100/mole P⁻¹ (number of cells); J_{Na}: initial rate, in mmoles/mole P⁻¹.min⁻¹, under control, net, and in the presence of 1 mM amiloride, amil, (number of rats); V_{max}, apparent maximal velocity of the (Na,K)-pump (in mmoles K/mole P⁻¹.min⁻¹); K_m, apparent affinity for Na of the (Na,K) pump (in mmoles × 100/mole P⁻¹).

genized and selected for ouabain resistance produced a cell line (OR-6) that displayed inducible and reversible ouabain resistance. Strikingly, when the cells are induced to be ouabain resistant, the (Na,K)-pump becomes directly inhibitable by amiloride (K_i of approximately 300 μM). The (Na,K)-pump from OR-6 cells before induction or in cells allowed to revert to the ouabain-sensitive phenotype was not inhibitable by amiloride. The sodium leak pathways in OR-6 cells was not sensitive to amiloride whether or not the cells had been induced.¹⁶

The ouabain-sensitive K uptake rate, a measure of (Na,K)-pump rate, was 20.3 ± 1.53 (SE) mmole K/mole P.min (n = 6) in CV-1 cells and fell to 6.4 ± 0.49 (n = 6) in transfected but noninduced OR-6 cells. At the same time, the potassium leak rate fell from 22.0 mmole K/mole P/min in CV-1 cells to 10.0 in OR-6 cells (J. A. Epstein and C. Lechene, unpublished observations, and Ref. 16). This change may be due to a physiologic coordination between (Na,K)-pump rate and K leak activity, but also suggests the possibility of common genetic regulation.

(Na,K)-pump Activity and Na Leaks in Two Models of Arterial Hypertension

Although total sodium influx rates and amiloride-sensitive influx rates were equal in cultured proximal tubule cells from spontaneously hypertensive rats (SHR) and their nonhypertensive control, Wistar-Kyoto (WKY), the apparent affinity of the (Na,K)-pump for Na was higher in SHR rats (K_m = 14 mM) than in WKY rats (K_m = 20 mM). The apparent affinity of the pump for ouabain was higher in WKY (K_i = 24 μM) than in SHR (K_i = 154 μM). Studies done with K. Sweadner revealed that the α1 isoenzyme was present in both groups with no α2 or α3 detectable. Thus the difference in sodium affinity is not due to detectable structural differences and may be due to an alteration in cytoplasmic or membrane factors in the SHR rats.¹⁷

In Wistar Milano rats, genetically selected for arterial hypertension, we obtained the following results in pilot experiments on primary culture of renal proximal tubular cells (RPTC)

and of renal inner medullary collecting duct cells (IMCD).¹⁸ In RPTC (Table 1), Na content was higher in MHS than MNS. Initial rates of leaks of Na (and K) were equivalents both in total net flux and in their amiloride sensitive component. Apparent V_{max} of the (Na,K) pump were not different but the apparent affinity of the pump for Na (K_m) was lower in MHS than in MNS. Thus in this model of hypertension, an equivalent leak of Na is balanced by (Na,K)-pump rate stimulated by an intracellular concentration of Na higher in hypertensive than in normotensive renal proximal tubule cells. In cells from inner medullary collecting ducts, the results were very different (Table 2). Initial rates of Na (and K) leaks were 3 to 6 times lower than in proximal cells. Intracellular Na content was slightly but highly significantly higher. In experiment performed in Ringer medium, Na influx was 2 times higher in MNS with 50% inhibitable by 10⁻⁶ μM amiloride. The amiloride (10⁻⁶ μM) inhibitable component of Na entry appeared to be lacking in MHS cells. The steady state (Na,K)-pump rates were equivalent, 9.33 ± 2.25 (3) in MNS and 11.2 ± 0.55 (3) in MHS (mmole K/mole P/min). However, the V_{max} and K_m of the (Na,K) pump for Na were lower by a factor of 2 in MHS compared to MNS. Although the cells had an equivalent (Na,K)-pump rate in normal, low intracellular Na concentration, the amplitude of the responses of the pumps to an intracellular load of Na were markedly different. Such a difference may have profound implications for the regulation of whole-animal Na homeostasis and the pathogenesis of systemic hypertension.

References

1. C. Lechene, "Physiological role of the Na-K pump," in J. C. Skou, J. G. Norby, A. B. Maunsbach and M. Esmann, Eds., *The Na⁺, K⁺-Pump, Part B: Cellular Aspects*, New York: Alan Liss, 1988, 171-194.
2. E. H. Abraham, J. L. Brewslow, J. Epstein, P. Chang-Sing, and C. Lechene, "Preparation of individual human diploid fibroblasts and study of ion transport," *Am. J. Physiol.*

248: (Cell Physiol. 17), C154-164, 1985.

3. C. Lechene, "Electron-probe analysis of cultured cells," *Ann. N. Y. Acad. of Sci.* 483: 270-283, 1987.

4. R. C. Harris, J. L. Seifter, and C. Lechene, "Coupling of Na-H exchange and Na-K pump activity in cultured rat proximal tubule cells," *Am. J. Physiol.* 251: C851-824, 1986.

5. C. Lechene, "Electron probe analysis of properties of cultured cells," in H. K. Hagler and K. Zierold, *Springer Series in Biophysics, Electron Probe Microanalysis in Biology and Medicine*, New York: Springer-Verlag (in press).

6. J. C. Skou, "The influence of some cations on an adenosine triphosphate from peripheral nerves," *Biochim. Biophys. Acta* 23: 394-401, 1957.

7. M. S. Kilberg, "Amino acid transport in isolated rat hepatocytes," *J. Membr. Biol.* 69: 1-12, 1982.

8. B. J. Cohen and C. Lechene, "Effects of alanine on ionic fluxes and content in cultured rat hepatocytes," *J. Gen. Physiol.* 92: 28a, 1988.

9. L. O. Kristensen and M. Folke, "Volume-regulatory K^+ efflux during concentrative uptake of alanine in isolated rat hepatocytes," *Biochem. J.* 221: 265-268, 1984.

10. R. W. Van Dyke and B. F. Scharschmidt, "(Na,K)-ATPase-mediated cation pumping in cultured rat hepatocytes: Rapid modulation by alanine and taurocholate transport and characterization of its relationship to intracellular sodium concentration," *J. Biol. Chem.* 258: 12912-12919, 1983.

11. J. Bowen and A. McDonough, "Pretranslational regulation of Na-K-ATPase in cultured canine kidney cells by low K^+ ," *Am. J. Physiol.* 21: C179-189, 1987.

12. T. A. Pressley, "Ion concentration-dependent regulation of Na,K-pump abundance," *J. Membr. Biol.* 105: 187-195, 1988.

13. T. A. Pressley, R. S. Haber, J. N. Loeb, I. S. Edelman, and F. Ismail-Beigi, "Stimulation of Na,K-activated adenosine triphosphate and active transport by low external K^+ in a rat liver cell line," *J. Gen. Physiol.* 87: 591-606, 1986.

14. A. Aperia, Y. Fukuda, and C. Lechene, "Ontogenic increase of Na-H exchange induces Na-K ATPase in rat proximal convoluted tubule (RPCT)," *Kidney Int.* 33: 415a, 1988.

15. S. Rane, Y. Fukuda, S. Larsson, A. Aperia, and C. Lechene, "Developmental increase of Na influx precedes that of (Na,K)-ATPase activity in rat renal proximal tubular cells" (submitted).

16. J. A. Epstein and C. Lechene, "Ouabain-resistant, amiloride-sensitive Na^+-K^+ pumping activity and morphological changes are inducible," *Am. J. Physiol.* 254: C847-854, 1988.

17. M. Crabos, H. F. Cantiello, K. Sweadner, and C. Lechene, "Na-K pump activity in normotensive (WKY) and spontaneously hypertensive (SH) rat renal proximal tubular cells (RPTC)," *J. Gen. Physiol.* 92: 28a, 1988.

18. C. Lechene, M. Crabos, G. Bianchi, and H. Cantiello, "Rôle physiologique de la pompe à

sodium: Implications pour l'étude de l'hypertension artérielle," *Néphrologie* (in press).

ALTERATIONS IN CALCIUM AND SULFUR COMPARTMENTATION DURING ANOXIA IN KIDNEY PROXIMAL TUBULES

Ann LeFurgey, L. J. Mandel, and Peter Ingram

Many investigators have suggested that the movement and redistribution of cellular ion contents, especially calcium, play a key role in the pathophysiology of irreversible cell injury induced by oxygen deprivation.¹⁻⁴ Accumulation of calcium in mitochondria, with associated structural and functional changes, has been postulated as an event leading to irreversibility.⁵⁻⁸ The objective of the current studies was to determine the in situ mitochondrial (and cytoplasmic) calcium content in kidney proximal tubule cells subjected to anoxia. A combination of high-resolution quantitative electron-probe x-ray imaging and static raster probing was employed (a) to obtain an overview of elemental distribution within and between cells, and (b) to achieve the statistical precision necessary for quantitation of calcium.

Methods

Quantitative electron-probe x-ray microanalysis (EPXMA) was performed on rapidly frozen, cryosectioned, and freeze-dried thin sections of a suspension of rabbit proximal tubules as previously described.⁹ The kidney proximal tubule suspension was subjected to anoxia by

allowing the tubules to consume all the oxygen in a sealed chamber; samples for EPXMA and for ultrastructural and biochemical analyses were taken before anoxia and after 40 min of anoxia.¹⁰ All analyses were obtained from freeze-dried cryosections in a transmission electron microscope (JEOL 1200EX TEMSCAN) equipped with a scanning device, additional hard x-ray aperture, collimated 30mm² Si(Li) energy-dispersive x-ray detector and multichannel analyzer (Tracor Northern 5500), and liquid nitrogen-cooled low-background cryotransfer stage (Gatan 626).

Static Raster Probing. X-ray spectra were obtained for 500 s per area from selected cell compartments at ~-119 C by use of a small square raster (0.1-0.06 μm^2) at 100 000 \times magnification with specimen tilt at 35°, accelerating voltage 80 kV, and beam current of ~0.1 nA.

X-ray Mapping. Techniques for obtaining quantitative elemental x-ray images were performed as previously described¹¹ with a multi-element quantitative imaging system (Fig. 1). In this type of analysis, the electron beam of

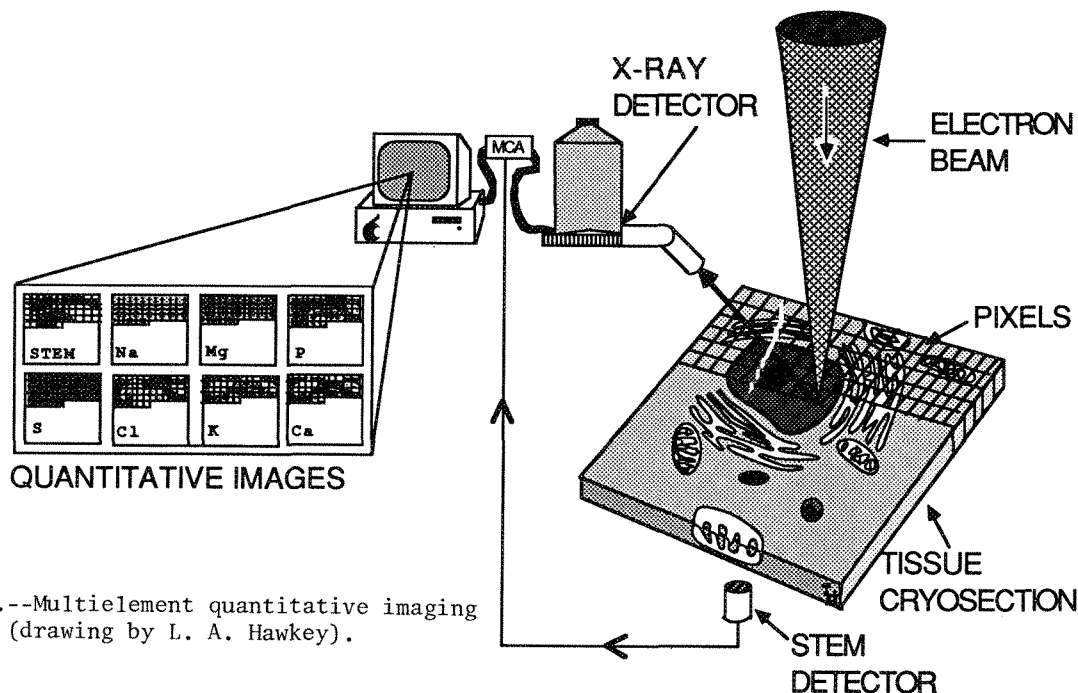


FIG. 1.--Multi-element quantitative imaging system (drawing by L. A. Hawkey).

Ann LeFurgey and L. J. Mandel are with the Division of Physiology, Department of Cell Biology, Duke University School of Medicine, Durham, NC 27710; P. Ingram is with Research Triangle Institute, Research Triangle Park, NC 27709. The expert technical assistance of Mr. L. A. Hawkey and preparation of the manuscript by Ms. K. Byrd are gratefully acknowledged. This work was supported by NIH grants NIDDK37704, NIDDK26816, HL17670, and HL27105.

the microscope was computer-controlled to move sequentially over the sample; at each pixel point an x-ray spectrum was acquired, and quantitation routines were applied. Briefly, 64 \times 64 pixel images were obtained at ~10 000 \times magnification (1 pixel = 0.04 μm^2) for physiologically relevant ions (Na, Mg, P, S, Cl, K, Ca) at a beam current of ~1 nA and dwell times of 1 s per pixel. Thus one can obtain quantitative data from all intracellular compart-

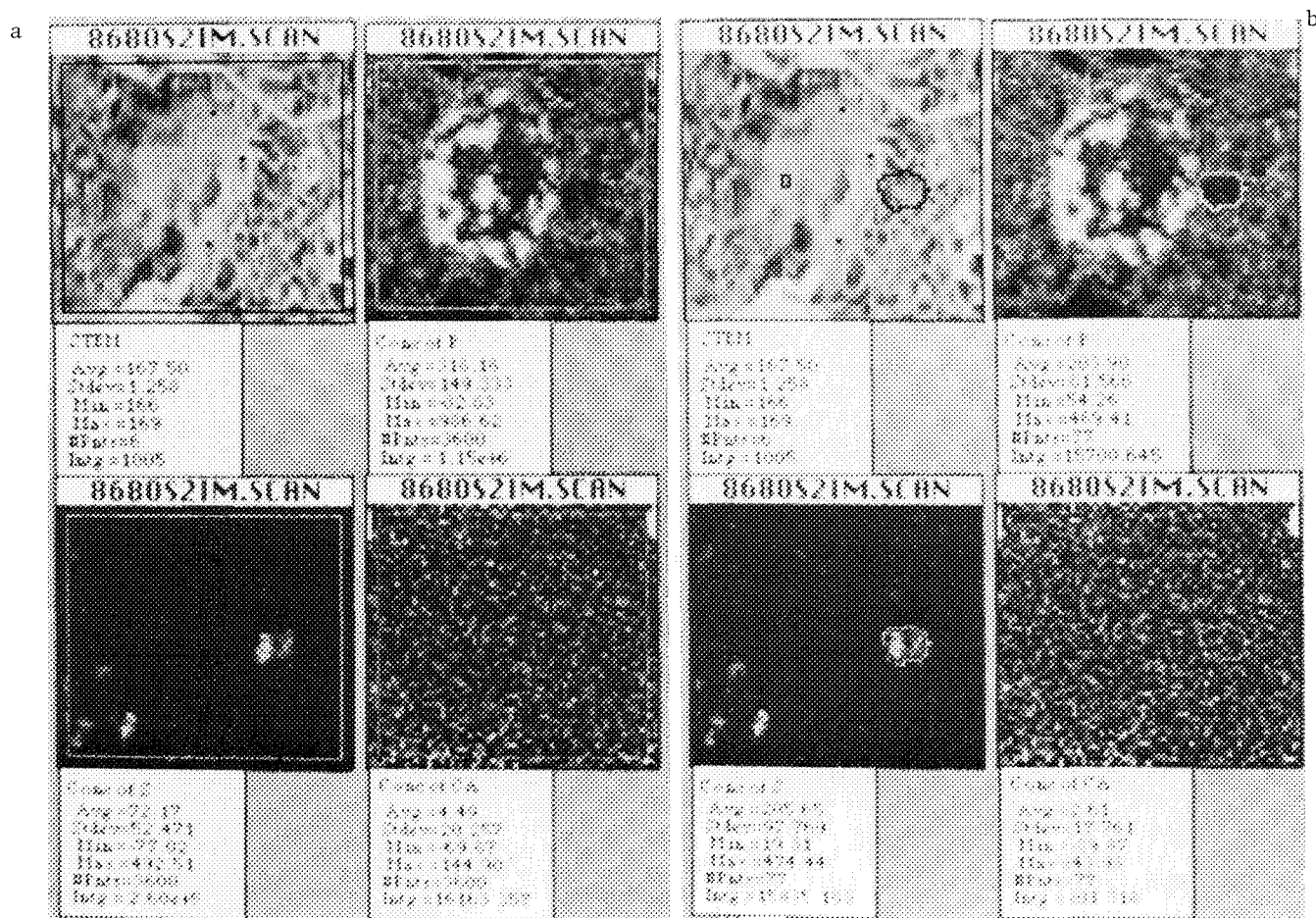


FIG. 2.--Scanning transmission electron micrographs (STEM) and quantitative energy dispersive x-ray images for phosphorus (P), sulfur (S), and calcium (Ca) of control kidney proximal tubule cryosection. (a) Entire area of section (3600 pixels) used in calculation of content values for P, S, Ca. Gray scale relative to quantitative values depicts lowest content as black, highest content as white. Note increased P content in nuclear heterochromatin, increased S content in lysosomes, and uniform distribution of Ca in low amounts throughout. (b) Area circled is lysosome; values displayed are average for this area (77 pixels) only.

ments of a cell or several cells in a fraction of the time required for acquisition of data by manually placing the beam over selected compartments and acquiring spectra from each region independently. All maps were carried out at ambient temperature ($\sim 23^\circ\text{C}$) with no evident specimen contamination. Digital image acquisition and spectral processing were performed with a multitasking graphics workstation (Vaxstation 2000, Digital Equipment Corp.); data storage, image display, processing, and retrieval of quantitative image information were performed with a microcomputer (Macintosh II, Apple Computer).

All spectral data from static probes and maps were processed for real-time quantitative analysis^{11,12} by the Hall continuum normalization method¹³ with the peak centroid shift and broadening corrections of Kitazawa and colleagues¹⁴ and appropriate correction for the carbon support film thickness. Standards were prepared according to the methods of Shuman et al.¹⁵

The accuracy of calcium measurements was confirmed by use of the correlation of Ca K α counts with the first and second derivatives of

K K β counts to identify detector calibration changes in peak centroid position or peak widths.¹⁴ Ca content was also measured (a) in solutions of calcium standards by atomic absorption spectroscopy (AA) and (b) in air dried films of the same solutions by EPXMA. The correlation coefficient for AA-EPXMA was 0.998.

Specimen mass changes due to the electron beam or to shift during static probing were monitored every 50 s by observation of a plot of peak areas and continuum vs time.¹² The microscope and stage temperatures were raised periodically to $\sim 150^\circ\text{C}$ and the stage was left in the instrument at $+70^\circ\text{C}$ when not in use to minimize residual contamination in the region of the specimen; vacuum was monitored with a residual gas analyzer (Ametec Inc.). Following initial mass loss at the high beam currents used,¹⁶ further mass changes were always $<1\%$ and were assumed to be the same for standards and sample.

Results and Discussion

Microchemical cell imaging via quantitative

TABLE 1.--Elemental content of subcellular organelles during basal and anoxic conditions as determined from quantitative x-ray images.

	Control S	Ca (mmol/kg dry wt)	Anoxia S	Ca
Lysosomes	273±17	7.2±2.9	233±44	-1.2±4.9
Mitochondria	173± 9*	2.7±1.0	90± 8*	3.2±1.3
Cytoplasm	181±17*	2.7±0.9	55± 5*	4.7±1.5
Nucleus	119±10*	1.7±2.1	30± 3*	-0.1±2.3

Values are mean ± SEM.

n = number of areas from each intracellular compartment utilized for calculation of average value. An area, 3x3 pixels or 3x4 pixels corresponding to ~0.3 to 0.4 μm^2 , was applied to the specified compartments for obtaining quantitative averages directly from the computer screen display with the mouse function.

*P < 0.01 relative to lysosomes.

electron probe x-ray microanalysis was used to obtain images of the distribution of all physiologically important elements at ultrastructural resolution. These images were used to visualize the alterations in the content of all elements in all subcellular compartments--simultaneously--which occur during oxygen deprivation. With this technique we have obtained images of lysosomes, and organelles not heretofore identified, and have established that after 40 min of anoxia, sulfur-containing enzymes are not released from this organelle.

One could perceive visually from the cell images that potassium was higher in nuclear than in other compartments under control conditions and decreased significantly in all compartments during 40 min of anoxia. Sodium occurred at approximately the same amount in all compartments during control states and decreased throughout the cell during anoxia. An analogous increase occurred in chlorine. This influx of sodium and chlorine, and efflux of potassium suggested that the cells might be swelling during anoxia. In the control cell sulfur maps, one to twelve dense spherical regions were visible, each containing ~50% more sulfur than adjacent cytoplasmic, mitochondrial, or nuclear areas (Fig. 2). The regions coincided with structures visible in correlative scanning transmission electron micrographs (STEM), which resembled lysosomal dense bodies. The high sulfur content of these lysosomal compartments did not change during anoxia, although sulfur in cytoplasm, mitochondria, and nuclei decreased to <50% of control levels. Calcium also occurred in lysosomal structures, at levels comparable to those in other cell areas. Quantitative content data (mmol/kg dry wt) were obtained from multiple images for each intracellular region, as shown in Table 1 for sulfur and calcium. The low content of calcium present in all compartments and the standard errors for calcium as shown in Table 1 indicate the statistical variability obtained with the mapping technique for elements present in low amounts when resolution is only 64 × 64 pixels and dwell time short (1 s).

Because the mapping data were not statistically optimal for calcium, additional data from mitochondrial and cytoplasmic compart-

ments were obtained with static raster probes. A heterogeneity in calcium compartmentation was observed in the anoxic tubules, with two main populations of cells discernible: (1) cells with morphological structures intact but with a decreased ratio of K:Na (~2:1), an elevated cytoplasmic calcium content relative to control (11.3 ± 2.0 [N = 17] vs 4.1 ± 1.4 [N = 23] mmol Ca/kg dry wt), and a mitochondrial calcium content which was unchanged (3.5 ± 0.6 [N = 15] vs 3.1 ± 1.1 [N = 23] mmol Ca/kg dry wt); (2) cells with disrupted brush borders, swollen mitochondria and increased vacuolization in which the ratio of K:Na was reversed (0.4:1), the cytoplasmic calcium content was increased (7.2 ± 1.7 [N = 19] mmol Ca/kg dry wt), and the mitochondrial calcium content was equal to or slightly less than control (1.0 ± 0.9 [N = 20] mmol Ca/kg dry wt). These results with respect to calcium are shown in Fig. 3. This combination of quantitative mapping, together with static raster probing to obtain high statistical accuracy for calcium, has thus yielded comprehensive data on the changes in element distribution that occur during anoxia.

Conclusions

(1) Net accumulation of calcium occurs in the cytoplasm of some of the proximal cells during anoxia; (2) no mitochondrial calcium accumulation is observed; (3) the dominant calcium buffering compartment is in the cytoplasm; (4) calcium accumulation can be found without visible structural cellular damage; (5) lysosomes, which cannot be distinguished from mitochondria in STEM, are immediately discernible via x-ray images of sulfur; and (6) after 40 min of anoxia lysosomes maintain high sulfur content. These data may suggest that sulfur-containing enzymes have not been released from this organelle.

References

1. B. F. Trump, I. K. Berezesky, and R. A. Cowley, "The cellular and subcellular characteristics of acute and chronic injury with emphasis on the role of calcium," in R. A. Cowley and B. F. Trump, Eds., *Pathophysiology of Shock, Anoxia, and Ischemia*, Baltimore: Williams & Wilkins, 1982, 6.

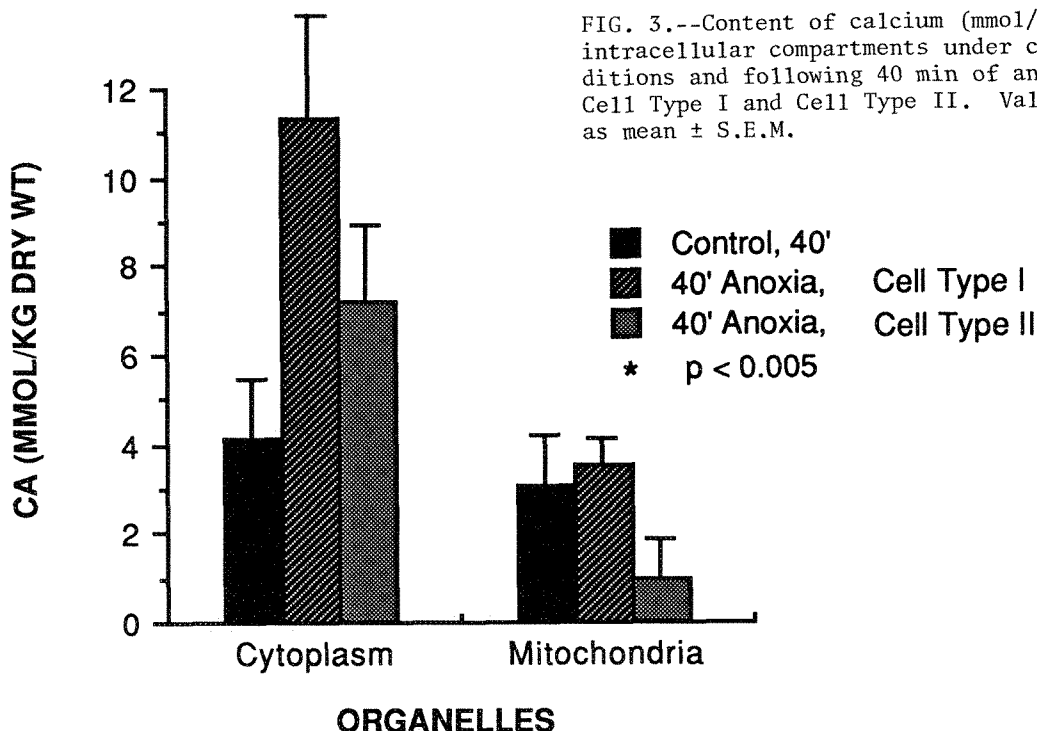


FIG. 3.--Content of calcium (mmol/kg dry wt) in intracellular compartments under control conditions and following 40 min of anoxia for Cell Type I and Cell Type II. Values expressed as mean \pm S.E.M.

2. M. W. Kahng, I. K. Berezsky, and B. F. Trump, "Metabolic and ultrastructural response of rat kidney cortex to *in vitro* ischemia," *Exp. Mol. Pathol.* 29: 183, 1978.

3. J. Mason et al., "Intracellular electrolyte composition following renal ischemia," *Kidney Int.* 20: 61, 1981.

4. J. L. Farber, K. R. Chien, and S. Mittenacht, Jr., "The pathogenesis of irreversible cell injury in ischemia," *Am. J. Pathol.* 102: 271, 1981.

5. D. R. Wilson et al., "Mitochondrial calcium accumulation and respiration in ischemic acute renal failure of the rat," *Kidney Int.* 25: 519, 1984.

6. B. Glauman et al., "Studies on cellular recovery from injury: II. Ultrastructural studies on the recovery of the pars convoluta of the proximal tubule of the rat kidney from temporary ischemia," *Virchows Arch. B. Cell Pathol.* 24: 1, 1977.

7. W. J. Mergner et al., "Studies on the pathogenesis of ischemic cell injury: VII. Proton gradient and respiration of renal tissue cubes, renal mitochondrial and submitochondrial particles following ischemic cell injury," *Beitr. Path.* 161: 230, 1977.

8. M. A. Ventakachalam et al., "Ischemic damage and repair in the rat proximal tubule: Differences among the S₁, S₂, and S₃ segments,"

Kidney Int. 14: 31, 1978.

9. A. LeFurgey, P. Ingram, and L. J. Mandel, "Heterogeneity of calcium compartmentation: Electron probe analysis of renal tubules," *J. Membrane Biol.* 94: 191, 1986.

10. T. Takano et al., "Intracellular respiratory dysfunction and cell injury in short-term anoxia of rabbit renal proximal tubules," *J. Clin. Invest.* 76: 2377, 1985.

11. P. Ingram et al., "Quantitative elemental x-ray imaging of biological cryosections," *Microbeam Analysis--1988*, 433.

12. S. D. Davilla et al., "Real-time graphic display of mass variation or elemental concentration during electron beam microanalysis using a general purpose computer," *J. Microscopy* 149: 153, 1988.

13. T. A. Hall, "Biological x-ray microanalysis," *J. Microscopy* (Oxford) 117: 145, 1979.

14. T. Kitazawa, H. Shuman, and A. P. Somlyo, "Quantitative electron probe analysis: Problems and solutions," *Ultramicroscopy* 11: 251, 1983.

15. H. Shuman, A. V. Somlyo, and A. P. Somlyo, "Quantitative electron probe microanalysis of biological thin sections: Methods and validity," *Ultramicroscopy* 1: 317, 1976.

16. M. E. Cantino et al., "Beam induced mass loss in high resolution biological microanalysis," *J. Microscopy* 144: 317, 1986.

HETEROGENEITY IN ELEMENTAL IMAGES OF CELLS AND TISSUES

M. E. Cantino, K. T. Izutsu, D. E. Johnson, L. E. Wilkinson,
R. J. Kayton, and S. W. Chen

The ability to detect cell-to-cell heterogeneity can be deemed either a shortcoming or an asset in studies in which electron-probe x-ray microanalysis is used. On the one hand, heterogeneity tends to give rise to large standard deviations (and with limited sample sizes, large standard errors) in measurements of average elemental composition. On the other hand, chemical (or biochemical) assays that are insensitive to such heterogeneity may overlook important physiological variation. We have found digital elemental imaging to be an important tool in detecting patterns of heterogeneity within cryosections. The information gained can then be used for developing subsequent sampling strategies that use both imaging and more traditional collection methods.

Experimental

Tissue samples were prepared by immersion in Freon 22 slush. Cryosections were then cut on an MT2B microtome with cryokit, and collected on Formvar- and carbon-coated folding grids. Samples were freeze-dried in an oil-free vacuum system and transferred at slightly above room temperature to a JEOL 1200 combined TEM/STEM. Data were collected and analyzed by means of Link AN10000 and associated software.¹

Two modes of data collection are routinely used in our laboratory. In conventional or "spot" analysis a small analog raster is placed in a given location for several hundred seconds. The location of the small raster and acquisition time are controlled by the operator. In digital imaging, the field is selected by the operator, but a microprocessor positions the beam at points in a prespecified matrix. All analyses described here were done at room temperature in the STEM mode. All elemental images were collected at $128 \times 128 \times 16$ bits. Quantitative data can be extracted from selected areas of the field as described elsewhere.²

Results

Examples of heterogeneity in fields of cells are shown in Fig. 1 through 6. Figures 1 and 2 are STEM and K concentration images of cardiac cells poisoned with acetylthiocholine.

The authors are at the Center for Bioengineering (WD-12) or the Department of Oral Biology, University of Washington, Seattle, WA 98195. They are indebted to Alice Lee and Shellee Cunningham for technical support, and to J. Bassingthwaite for advice in the cardiac muscle studies. This work was supported by NIH grants HL31962, HL19139, DK35975, and DE06373.

The samples were prepared as one step in a sequence designed to produce reversal of the Na:Ca exchanger in cardiac muscle. Under these conditions (with the Na:K ATPase blocked), the K levels are expected to be very low; however, Fig. 2 shows that a small number of cells retain very high K levels. High-potassium cells seem to be characterized by large nuclei surrounded by relatively little cytoplasm, and probably represent a different cell population (although the poor preservation in this case makes cell types difficult to identify).

Figures 3 and 4 are STEM and Ca concentration images of human labial glands. Whereas morphological distinctions based on the electron (STEM) images alone are ambiguous, the calcium concentration images indicate two populations of cells: those with high calcium in their secretory granules (left hand side of field), and those with low calcium. Other elemental images support this conclusion, as do spot analyses on the same samples.³

Figures 5 and 6 show STEM and K concentration images of stimulated rat parotid gland. Both the Na (not shown) and the K concentration images suggest that there may be considerable heterogeneity in the response to stimulation. Several cells in the center of the field show much lower K levels than others around the periphery of the field.

Conclusions

Although these patterns might have been identified by careful collection of randomly selected spot analyses, a less thorough sampling regime could very well fail to detect the cell-to-cell heterogeneity so clearly evident from the digital elemental images. Thus, even if spot analyses are ultimately needed to quantify elements present at low concentration, digital images are invaluable in revealing cell heterogeneity and in developing strategies for collecting subsequent data.

References

1. P. J. Statham, "Quantitative digital mapping with drift compensation," *Analytical Electron Microscopy—1987*, 187.
2. J. G. Wong et al., "Quantitative elemental analysis of digital x-ray images," *ibid.*, p. 191.
3. L. Wilkinson, K. Izutsu, R. Kayton, S. Chen, M. Cantino, and D. Johnson, "Evidence for two acinar cell types in human labial glands," *J. Dental Res.* 68: 279, 1989 (abstract).

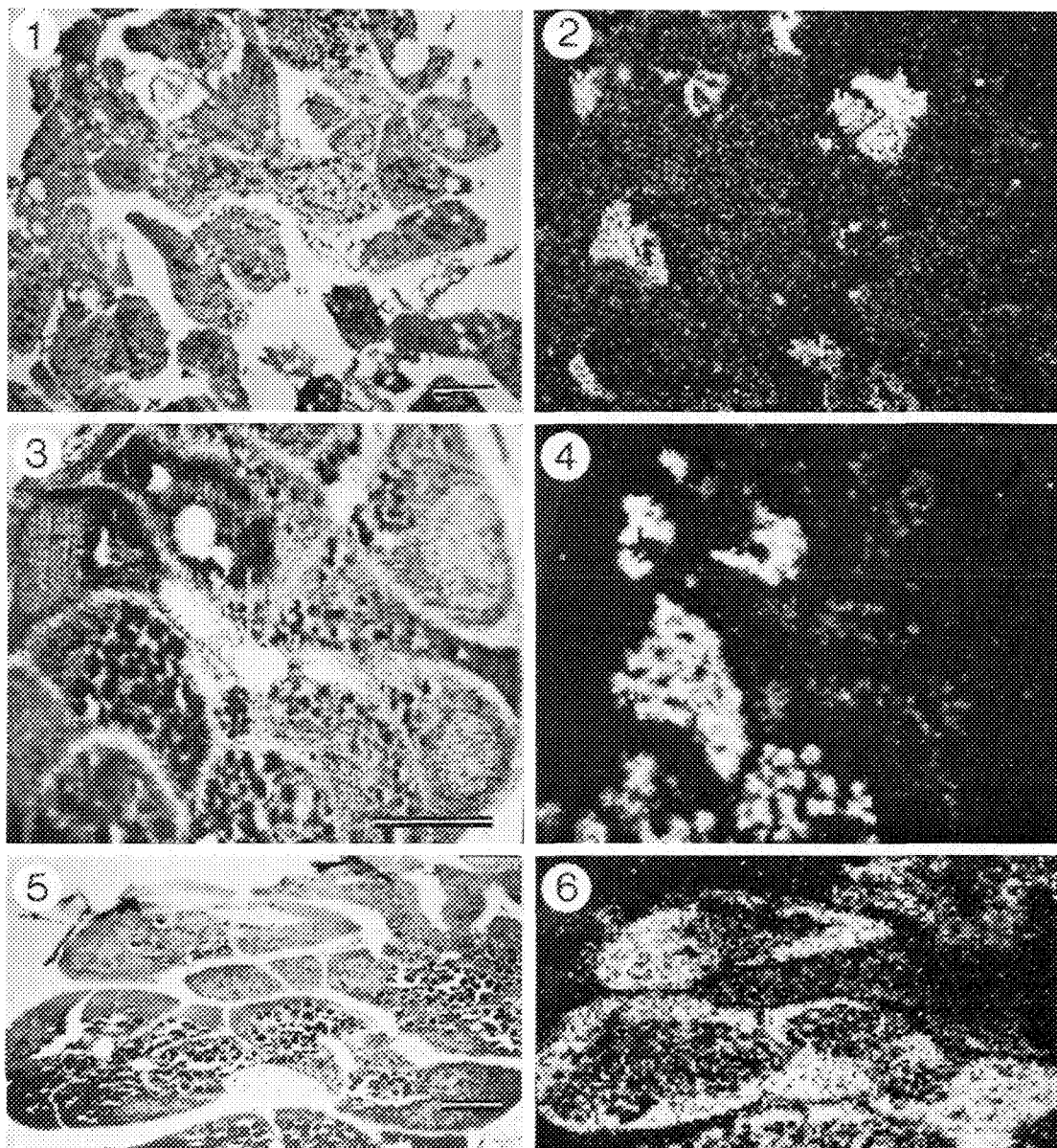


FIG. 1.--Digital STEM image of rabbit papillary muscle bathed for 120 min in Tyrodes solution containing 12 μ M acetylcholinesterase inhibitor. Bar is approximately 5 μ m.
 FIG. 2.--Digital K concentration image (K/Brem) of field in Fig. 1. Several cells have retained high levels of potassium.
 FIG. 3.--Digital STEM image of human labial gland. Bar is approximately 5 μ m.
 FIG. 4.--Digital Ca concentration image (Ca/Brem) of field in Fig. 3.
 FIG. 5.--Digital STEM image of stimulated rat parotid gland. Bar is approximately 5 μ m. Acquisition was terminated after approximately 80 lines in this image.
 FIG. 6.--Digital K concentration image (K/Brem) of field in Fig. 5.

X-RAY MICROANALYSIS OF NORMAL AND EDIM ROTAVIRUS-INFECTED MOUSE INTESTINE

A. J. Spencer, M. P. Osborne, and John Stephen

Rotaviruses are the main cause of virus-induced gastroenteritis in infants, accounting for over 1 million deaths per annum.¹ However, until recently, data on the pathophysiology of the disease were scarce and/or contradictory. Studies of epizootic diarrhea of infant mice (EDIM) infection (an excellent model for human rotavirus gastroenteritis), showed that a dramatic transient shortening of villi occurs, which predictably would lead to a loss of villus absorptive function.² However, diarrhea is not due to lactose intolerance.³ A dramatic reconstruction of villi occurs, involving rapid division of cells in villus base regions.² Here we present x-ray microanalytical data that suggest that stimulation of villus base cells to rapid division is accompanied by transient accumulation of Na and Cl, the exsorption of which into the lumen is the driving force for hypersecretion of fluid.

Methods

Samples of middle small intestine were taken from 9-day-old control mice or mice infected 48 h previously with EDIM rotavirus. The time point 48 h post infection (pi) was chosen for study since this point corresponds to the peak of virus antigen in the middle small intestine.⁴ Tissue was frozen by plunging into liquid propane, sectioned at -140 C, and freeze dried before analysis in a JEOL 120CXII electron microscope fitted with an LaB₆ filament and Link 860 Series 2 analyzer. Quantitation was performed by the Link System QUANTEM program based on the continuum method of Hall,⁵ with reference to gelatin/inorganic salt standards.

Results

By 48 h pi, EDIM-infected mice developed a yellowish watery diarrhea as previously described.^{3,4} No signs of diarrhea were detected in control mice throughout the duration of the study. Figure 1 shows a conventional transmission electron micrograph of mouse small intestine 48 h after infection with EDIM rotavirus. Cellular damage was limited to the upper two thirds of the villi as indicated by extensive cell vacuolation. Cells in the villus base region were relatively electron lucent and

showed signs of cell division, but no signs of vacuolation. At 48 h pi, villi were up to 60% shorter than in age-matched controls and there was evidence of cell shedding from villus tip regions. No morphological changes were seen in the crypt region. Figures 2 and 3 show typical freeze-dried cryosections of mouse small intestine. Concentrations of elements in subcellular regions of villus tip, base, and crypt cells of control and EDIM-infected mice are shown in Tables 1 and 2, respectively. Cytoplasmic data were obtained from core cytoplasm, since preliminary results showed that elements were evenly distributed in the cytoplasm.

In villus tip cells, Na was significantly increased in all subcellular regions, Cl decreased in the cytoplasm and brush border, K decreased in the cytoplasm and nucleus, and Ca increased in the cytoplasm, after EDIM-rotavirus infection. However, the most striking changes occurred in villus base cells, where Na and Cl were increased dramatically in all regions (except brush border for Na), but no significant changes were seen in K or Ca. No obvious pattern of changes were seen in concentrations of elements in crypt cells, apart from the increase in Na and Cl in mitochondria, in line with increases in villus tip and base cell mitochondria.

Discussion

The determination of elemental concentrations in the intestinal mucosa of neonatal mice showed that large changes occur during infection with EDIM rotavirus. In contrast to the study of von Zglinicki and Roomans on intestinal mucosa of adult mice,⁶ no concentration gradients were seen across the cytoplasm of epithelial cells from control animals. Concentrations of Na and Cl were also higher than values obtained from adult mice. It is possible that these differences reflect the fact that tissue was dissected out before freezing and not frozen in situ. However, comparison of concentrations from control and EDIM-infected animals is valid, since all tissues were treated in the same way.

Since infection was limited to the upper parts of the villi, changes in villus tip cells could be directly induced by virus in cells. Permeability changes in cell membranes occur during entry of viruses into cells.⁷ Such changes have been linked to a switch from host cell to virus protein synthesis.⁸ Several groups have shown that rotaviruses inhibit host cell macromolecular synthesis in vitro.^{9,10} The possibility that rotaviruses are mediating a switch from host to virus protein

The authors are at the Departments of Physiology and of Microbiology, University of Birmingham, P.O. Box 363, Birmingham, England, B15 2TT. (A. J. Spencer is now at Department of Cell Biology, Duke University Medical Center, Durham, NC 27710.) The financial support of Janssen Pharmaceutical Ltd. and the Wellcome Trust is gratefully acknowledged.

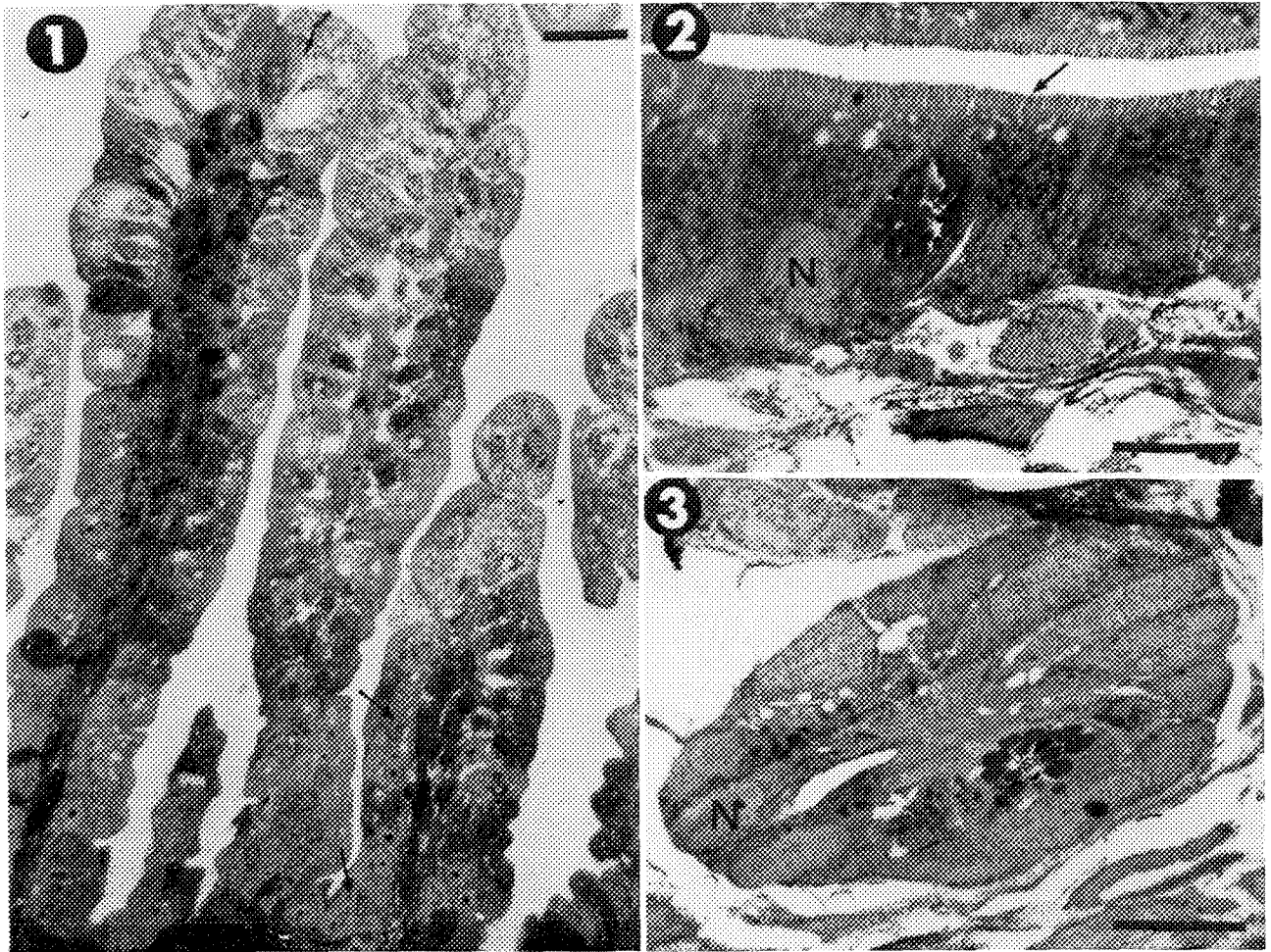


FIG. 1.--Conventional TEM of 9-day-old mouse middle small intestine 48h pi with EDIM rotavirus. Cells in villus tip regions are severely vacuolated. Note electron lucent cells in villus base region, some of which contain mitotic figures (arrows). Scale bar = 25 μ m. FIGS. 2 and 3.--Unstained cryosections of mouse middle small intestine, sectioned through villus tip region (Fig. 2) and crypt region (Fig. 3). Brush border (arrow), goblet cell mucus (*), nuclei (N). Scale bars = 5 μ m.

synthesis, by altering the intracellular ionic milieu, cannot therefore be ruled out. Maturation of bovine rotaviruses in vitro is a calcium-dependent process.¹¹ The high levels of Ca observed in villus tip cells in this study could indicate that maturation of EDIM rotavirus is also a calcium-dependent process.

We have previously proposed that an early virus-induced ischemia occurs.^{2,12} Examination of the vascular system in the villi, using a histochemical technique (M. P. Osborne, personal communication), shows that blood flow was markedly impaired at 48 h pi. Anoxia could result in a fall in intracellular pH and carbon dioxide tension in tip cells, thus affecting Na and Cl absorption by imbalancing of Na^+/H^+ and $\text{Cl}^-/\text{HCO}_3^-$ -coupled antiports.¹³ Increases in intracellular Ca^{2+} decrease neutral NaCl absorption.¹⁴ Since Ca was significantly increased in villus tip cells from 24h pi, the observed decrease in Cl in tip cells may be due to reduced absorption of Cl from the lumen. It is interesting to note that the concentrations of Na and Cl were increased in mitochon-

dria in cells from all regions, including crypt cells. Whether this result indicates that the proposed virus-induced systemic effect also affects villus base and crypt cells, but to a lesser extent than villus tip cells, is not clear.

Since the rise in Na in tip cells was accompanied by a decrease in Cl, whereas the rise in Na in villus base cells was accompanied by a rise in Cl, it is likely that the changes in these two regions were brought about by mechanistically different means. A great deal of evidence has been accumulated to show that the process of cell division involves large changes in monovalent ion fluxes.^{15,16} In light of the evidence for increased cell proliferation in EDIM-infected mice, i.e., the increase in thymidine kinase⁵ and visualization of cell division outside the normal zone of cell proliferation,² it is proposed that the increases in Na and Cl in villus base cells at 48 h pi are consistent with changes associated with cell division. Infection of villus tip cells with EDIM rotavirus results in the stimulation of growth activity

TABLES 1 and 2.--Concentrations of elements in various subcellular regions of (a) villus tip cells, (b) villus base cells, (c) crypt cells from normal 9-day-old mice (Table 1) and 9-day-old mice 48 h pi with EDIM rotavirus (Table 2). Results are mean \pm SEM from 3 animals. n = number of observations. Each observation represents one analysis from a individual cell. *p < 0.05; student's t test (compared with controls).

TABLE 1

		CONCENTRATION [mmol/kg dry weight]						
		Na	Mg	P	S	Cl	K	Ca
a) TIP CELLS								
Cytoplasm	93	183 \pm 6	58 \pm 5	739 \pm 10	370 \pm 7	220 \pm 6	739 \pm 13	7 \pm 1
Nucleus	39	260 \pm 19	65 \pm 10	878 \pm 29	386 \pm 12	245 \pm 14	962 \pm 42	7 \pm 3
Mitochondria	18	101 \pm 9	30 \pm 10	359 \pm 12	412 \pm 20	220 \pm 11	522 \pm 15	5 \pm 2
Brush border	21	170 \pm 19	45 \pm 12	586 \pm 11	443 \pm 14	255 \pm 11	654 \pm 23	10 \pm 1
b) BASE CELLS								
Cytoplasm	80	115 \pm 5	41 \pm 4	672 \pm 13	208 \pm 7	221 \pm 5	773 \pm 13	6 \pm 1
Nucleus	14	172 \pm 14	26 \pm 4	932 \pm 22	209 \pm 16	242 \pm 12	867 \pm 22	6 \pm 2
Mitochondria	20	77 \pm 6	14 \pm 7	427 \pm 25	305 \pm 9	210 \pm 12	540 \pm 25	2 \pm 1
Brush border	20	198 \pm 9	34 \pm 4	495 \pm 23	230 \pm 14	299 \pm 8	758 \pm 32	1 \pm 2
c) CRYPT CELLS								
Cytoplasm	60	130 \pm 8	60 \pm 4	798 \pm 21	207 \pm 9	217 \pm 7	899 \pm 13	5 \pm 1
Nucleus	17	154 \pm 15	50 \pm 9	921 \pm 33	201 \pm 9	261 \pm 12	1008 \pm 25	4 \pm 2
Mitochondria	11	105 \pm 15	41 \pm 7	658 \pm 11	326 \pm 22	155 \pm 9	560 \pm 13	1 \pm 1
Goblet mucus	19	46 \pm 4	25 \pm 6	148 \pm 11	471 \pm 25	149 \pm 14	285 \pm 12	235 \pm 10

TABLE 2

		CONCENTRATION [mmol/kg dry weight]						
		Na	Mg	P	S	Cl	K	Ca
a) TIP CELLS								
Cytoplasm	69	341 \pm 16*	78 \pm 5*	743 \pm 20	296 \pm 9*	110 \pm 9*	600 \pm 18*	25 \pm 2*
Nucleus	17	319 \pm 19*	110 \pm 9*	1121 \pm 28*	387 \pm 12	214 \pm 15	608 \pm 12*	12 \pm 3
Mitochondria	15	289 \pm 18*	46 \pm 10	317 \pm 23	267 \pm 17*	267 \pm 15*	554 \pm 9	10 \pm 2
Brush border	15	471 \pm 17*	91 \pm 10	589 \pm 25	324 \pm 11*	190 \pm 5*	698 \pm 23	19 \pm 5
b) BASE CELLS								
Cytoplasm	71	377 \pm 31*	64 \pm 7	792 \pm 18*	205 \pm 11	426 \pm 15*	817 \pm 19	6 \pm 1
Nucleus	32	347 \pm 19*	54 \pm 5	872 \pm 30	246 \pm 16	400 \pm 10*	947 \pm 15	2 \pm 1
Mitochondria	14	283 \pm 18*	54 \pm 7	612 \pm 13*	326 \pm 19	271 \pm 13*	568 \pm 27	2 \pm 2
Brush border	16	221 \pm 17	42 \pm 7	556 \pm 21	275 \pm 19	346 \pm 7*	679 \pm 23	3 \pm 2
c) CRYPT CELLS								
Cytoplasm	44	128 \pm 10	45 \pm 7	935 \pm 18*	168 \pm 6*	239 \pm 7*	921 \pm 15	4 \pm 2
Nucleus	17	95 \pm 7*	72 \pm 11	1033 \pm 23*	117 \pm 5*	243 \pm 12	991 \pm 47	8 \pm 2
Mitochondria	19	190 \pm 24*	64 \pm 5	736 \pm 10*	288 \pm 15	253 \pm 5*	604 \pm 14*	6 \pm 2*
Goblet mucus	13	89 \pm 10*	47 \pm 7	177 \pm 16	758 \pm 14*	145 \pm 14	241 \pm 8	202 \pm 15

in crypt/villus base regions, giving rise to an increase in intracellular Na⁺; Cl⁻ then follows down a concentration gradient across the basolateral membrane. High intracellular ion concentrations clearly could provide an osmotically assisted mechanism for cell volume expansion, thereby aiding cell division. It is proposed that the high concentrations of Na⁺ then stimulate activity of Na⁺K⁺ATPase and recycle the Na⁺ back across the basolateral membrane. Since there is a considerable excess quantity of Cl⁻ beyond that required for volume expansion, chloride ions are therefore secreted into the lumen to provide the osmotic basis for hypersecretion and hence diarrhea. Examination

of luminal contents showed that concentrations of Na and Cl were significantly increased at 48 h pi (J. Collins, personal communication). Concentrations of Na and Cl in the unstirred fluid layer next to villus base cells, as measured by x-ray microanalysis, were also increased at 48 h pi, from 268 and 163 mmol/kg dry weight to 578 and 387 mmol/kg dry weight, respectively.

It is perhaps surprising that little change was seen in crypt cells. However, this may be because the cryosections were not taken through the normal area of cell division, which is small in neonatal mice, whereas the villus base cells present a relatively large area due

to rapid cell division in the region. Expansion of the normal zone of proliferation has also been documented following ischaemia¹⁷ and in foetal tissue.¹⁸

In conclusion, this paper documents changes in elemental concentration in the small intestine of neonatal mice infected with EDIM rotavirus, which suggest that cell division, required to replace cells lost from upper parts of the villi, may contribute to diarrhea.

References

1. I. DeZoysa and R. G. Feacham, "Interventions for the control of diarrhoeal disease amongst young children: Rotavirus and cholera immunisation," *Bull. WHO* 63: 569, 1985.
2. M. P. Osborne et al., "An electron microscopic investigation of time related changes in the intestine of neonatal mice infected with murine rotavirus," *J. Pediatr. Gastroenterol. Nutr.* 7: 236, 1988.
3. J. Collins et al., "Intestinal enzyme profiles in normal and rotavirus-infected mice," *J. Pediatr. Gastroenterol. Nutr.* 7: 264, 1988.
4. W. G. Starkey et al., "Kinetics, tissue specificity and pathological changes in murine rotavirus infection of mice," *J. Gen. Virol.* 67: 2625, 1986.
5. T. A. Hall and B. L. Gupta, "Quantification for the x-ray microanalysis of cryosections," *J. Microsc.* 126: 333, 1982.
6. T. von Zglinicki and G. M. Roomans, "Element concentrations in the intestinal mucosa of the mouse as measured by x ray microanalysis," *SEM* (in press).
7. C. A. Pasternak, "Virally mediated changes in cellular permeability," in G. Benga, H. Baum, and F. A. Kummerow, Eds., *Membrane Processes: Molecular Biology and Medical Appliances*, 1984, 140-166.
8. A. Lopez-Rivas, J. L. Castrillo, and L. Carrasco, "Cation content in poliovirus-infected HeLa cells," *J. Gen. Virol.* 68: 335, 1987.
9. M. Carpio et al., "Bovine rotavirus-cell interactions: Effects of virus infection on cellular integrity and macromolecular synthesis," *Virology* 114: 86, 1981.
10. M. A. McCrae and G. P. Faulkner-Valle, "Molecular biology of rotaviruses: I. Characterisation of basic growth parameters and pattern of macromolecular synthesis," *J. Virol.* 39: 490, 1981.
11. M. S. Shahrabadi and P. W. K. Lee, "Bovine rotavirus maturation is a calcium-dependent process," *Virology* 152: 298, 1986.
12. J. Stephen and M. P. Osborne, "Pathophysiological mechanisms in diarrhoeal disease," in W. Donachie, E. Griffiths, and J. Stephen, Eds., *Bacterial Infections of Respiratory and Gastrointestinal Mucosae* (Special Publication of the Society for General Microbiology, vol. 24), Oxford: IRL Press, 1988, 149.
13. A. N. Charney and G. M. Feldman, "Systemic acid-base disorder and intestinal electrolyte transport," *Am. J. Physiol.* 247: G1, 1984.
14. M. Donowitz and M. J. Welsh, "Regulation of mammalian small intestinal electrolyte secretion," in L. R. Johnson, Ed., *Physiology of the Gastrointestinal Tract*, New York: Raven Press, 1987, 1351.
15. A. Warley et al., "X-ray microanalysis of He La S3 cells: II. Analysis of elemental levels during the cell cycle," *J. Cell. Sci.* 62: 339, 1983.
16. E. Rozengurt and S. Mendoza, "Monovalent ion fluxes and the control of cell proliferation in cultured fibroblasts," *Ann. N.Y. Acad. Sci.* 339: 175, 1980.
17. H. Menge and J. W. L. Robinson, "Early phase of jejunal regeneration after short term ischaemia in the rat," *Lab. Invest.* 40: 25, 1979.
18. J. A. Hermos, M. Mathan, and J. S. Trier, "DNA synthesis and proliferation by villous epithelial cells in fetal rats," *J. Cell. Biol.* 50: 255, 1971.

CRYOMICROSCOPY AND ANALYSIS: PROCEDURES, PROBLEMS, AND PROSPECTS

Patrick Echlin

Low-temperature microscopy and analysis, and the preparative procedures associated with these techniques, have long held out the promise of providing the only way we may hope to assess the true ultrastructure of cells and hydrated systems together with the in situ local concentration of their diffusible elements. This promise is based on the assumption that the preparative procedures, which revolve around carefully inducing a phase change in the hydrated state of the sample, do not involve any chemical intervention and thus are more likely to preserve structures and materials closer to their natural hydrated state. In addition, it is assumed that by carrying out the ensuing microscopy and analysis at reduced temperatures, the problems associated with beam damage and sample contamination will largely disappear. This paper tests the validity of these assumptions and assesses how far we have progressed in achieving the goal of examining and analyzing specimens at high spatial resolution while still maintaining their unperturbed and natural state.

The Sample and the Instrumentation

It is useful first to set out what would be considered the ideal specimen for the various forms of microscopy and analysis and then consider the constraints the instrumentation might put on the actual form of the sample. Without going into detail, we assume that all the instruments used for cryomicroscopy have cold stages and specimen-transfer devices that meet the following standards.¹

1. Stage temperature of at least 123 K.
2. Stage must have XYZ and tilt movements.
3. Sample must be surrounded by anticontamination devices at least 20 K colder than the stage temperature.
4. The spatial resolution should be 0.3-0.5 nm for high-resolution TEM studies and 0.5-10 nm for analytical studies.
5. The contamination rate should be no more than 1-2 nm/h.
6. The sample must be transferred into the microscope at a temperature of at least 123 K and in a frost-free environment.

The ideal sample for all forms of microscopy and analysis would be one in which the water has been vitrified, i.e., the water has been converted to a high-viscosity glass rather than a crystalline solid. In addition, the organic and inorganic components of the sample have

been preserved in their natural state and location without resort to either chemical fixation or staining. For transmission beam instruments, the specimen must be thin enough to allow the majority of the beam energy to pass through the sample, a constraint that limits specimens to either thin liquid suspensions or thin sections cut from bulk samples.

For reflected-beam instruments, the samples can be either the natural exterior surfaces or interior surfaces artificially exposed by fracturing or sectioning. Nonconductive surfaces rapidly assume an electrical charge unless they are coated with a conductive layer or examined at low voltage. Lower beam energies (ca 1-10 pA) are generally needed to obtain structural information in contrast to the higher beam energies (1-10 nA) needed for microanalysis.

Sample Cooling

For microscopic and analytical studies it is now accepted that optimum sample cryo-preparation is achieved when very small samples are subjected to rapid nonequilibrium cooling. The probability of achieving vitrification increases with the decreased size of the sample and the increased speed of cooling. One of the major reasons for using cryofixation techniques is that they are a very effective way of immobilizing hydrated samples. The average diffusion rate of highly mobile ions such as Na⁺, Cl⁻, and K⁺ in water at 300 K is between 1 and 2 $\mu\text{m}/\text{ms}$ or 10 μm in 30 ms. At a freezing rate of 40 kK/s, the first 10 μm of a hydrated biological sample would be solidified within 0.5 ms; chemical fixation would take between 5-10 s, and even then the sample would not be completely immobilized.² By way of comparison, physiological events take place at 1-5 ms.

Clearly, rapid cooling is a far more effective way of stopping events in cells than chemical fixation, although even rapid cooling may be too slow to arrest all diffusive processes. The situation with ice formation is more complex. The average diffusion rate of water at 300 K is about 1.0 μm 0.5 μs and the time for translational diffusion and re-orientation of the water molecule is of the order of 10^{-12} /s. It is thus necessary to lower the temperature very rapidly if we are to prevent cooling water molecules from moving from the random liquid state to the thermodynamically more stable crystalline state.

Among techniques devised for quench cooling are rapid movement of samples into liquid cryogenics, cryogen jet cooling of stationary samples, and impact cooling of small droplets or bulk samples onto cold surfaces.

The author is at the Botany School, University of Cambridge, Downing St., Cambridge, England CB2 3EA.

A very wide range of cooling rates have been achieved and they run from a near unbelievable 10^6 K/s to a totally unacceptable 10^2 K/s. The numerical hyperbole of the quoted rates is frequently misleading, for what really matters is the state of the specimen following a particular cooling regimen, not some notional idea of how fast it was cooled. We need to ascertain whether the water in the sample has been truly vitrified or has been only converted to a microcrystalline state.

Manipulation of Frozen Samples

There can be no doubt that thin (ca 100-250 nm) liquid suspensions of macromolecules, viruses, particles and polymers, and fine droplet suspensions can be vitrified. Evidence from electron diffraction studies and from the observed temperature-dependent phase changes of $I_V > I_C > I_H$, confirms this view. It is fervently believed that the sample material encapsulated in this near-perfect embedding medium remains unaltered. The final proof is difficult to obtain and is based mainly on the finding that the structural properties of macromolecules prepared by these low-temperature methods bear a close resemblance to the properties obtained either by the more draconian conventional methods or by techniques that are capable of analyzing wet material (i.e., x-ray diffraction). In this respect high-resolution transmission electron microscopy and electron diffraction of vitrified liquid suspensions is now possible and some quite remarkable results have been obtained. However, as we shall see, the constraints of beam damage put a limitation on the ultimate resolution that may be obtained.

The situation with frozen sections is much less promising; there appear to be no recorded examples of vitrified sections having been cut from unfixed, unstained, and noncryoprotected bulk samples. There has been some measure of success in cutting sections of vitreous ice formed by condensing water vapor at reduced pressure onto a metal block maintained at 77 K.³ Many examples exist in the literature of vitrified sections being cut from samples, although unfixed and unstained are nevertheless cryoprotected with glucose, sucrose, or other more exotic antifreeze cocktails. Many of these chemicals generally provide excellent cryoprotection; most cause some tissue shrinkage and we have little definitive knowledge as to what these materials are doing to the hydration shell surrounding many macromolecules. The sheer size of bulk samples militates against them being vitrified in the unprotected state. The following simple calculation shows why that may be the case. A $500 \mu\text{m}^3$ sample of biological tissue when impact cooled on a metal surface held at 25 K might have an initial cooling rate of 5×10^4 K/s. At the very surface of the specimen, in the region where there would be a maximum amount of mechanical damage from sample excision and impact cooling, the sample water might be vitri-

fied. But as one progresses deeper into the sample, crystallization events would begin to occur due to a dramatic decrease in the rate of cooling. For many applications, microcrystalline ice with a cell size below the resolution usually associated with the transmission electron microscopy of sections (2-3 nm) is perfectly acceptable.

One way around the problem of ice-crystal damage in noncryoprotected bulk samples would be to use hyperbaric cooling methods.⁴ The homogeneous nucleation temperature of water T_h , which is c. 233 K at atmospheric pressure, can be reduced to 181 K at a pressure of 200 mPa (2 kBar). The rate of cooling required to achieve microcrystalline ice throughout a 1 mm^3 sample is of the order of 5×10^3 K/s. The quite remarkable quality of the images of plant material preserved by hyperbaric cooling⁵ attests to the efficiency of this cooling procedure.

The problems that beset vitrifying bulk material for subsequent thin sectioning also apply to bulk samples that are to be examined and analyzed by scanning beam instruments. The water in the surface layers of a noncryoprotected bulk sample will at best only be converted to microcrystalline ice when cooled by a liquid cryogen jet at a rate of 30-40 kK/s. (Jet cooling is chosen in preference to impact cooling, for although the latter results in a faster heat removal, it does so at the cost of severe mechanical damage to the surface of the specimen--the very region we wish to investigate.) Heat transfer from below the surface and the latent heat of crystallization conspire to raise the surface temperature above the recrystallization point of water (130 K) and any vitrified material is converted to I_C or I_H .

Even if it were possible to obtain and retain vitrified surface layers on a bulk sample, the processes of transfer into the microscope and subsequent examination are also likely to favor devitrification. Although transfer devices and cold stages are now available that operate well below T_g , less critical attention has been paid in scanning beam instruments to insure low rates of sample contamination. Residual water vapor all too easily lands on the surface of the sample. If the sample temperature is low enough the water vapor condenses to a vitreous solid. However, this material is unlikely to be in good thermal contact and in an inadequately protected systems, thermal energy radiating from warmer parts of the instruments promotes the transition of I_V to I_C and I_H . The newly formed crystallites could in turn promote devitrification in the surface layers. For the present we must be content with microcrystalline ice in the surface layers of bulk samples and resort to cryoprotectants if better-quality cryofixation is required deeper in the sample.

To summarize this section on sample cooling, the current situation is as follows.

1. Thin liquid suspensions (2-300 nm) in which the samples are embedded in a thin layer

of water can be vitrified and examined in the vitrified state in a transmission beam instrument.

2. Although it might be possible to vitrify a few micrometers of an uncryoprotected bulk sample by impact cooling, there are severe problems in cutting and retaining vitrified sections from such material.

3. It is most unlikely that we shall be able to observe vitrified surfaces on bulk materials by scanning beam instruments. At best, the water in the surface layers and the interior will be in the form of microcrystalline ice.

However, we should not become obsessed with always obtaining vitrified specimens or even samples with microcrystalline ice. Vitrification *is* important for high-resolution cryo-TEM, but for all other samples it would be more expedient to aim at obtaining ice crystallites smaller than the spatial resolution needed to solve a particular structural investigation. This same aim would also satisfy most micro-analytical studies. The alternative approach is to explore the usefulness of constructive chemical fixation and cryoprotection coupled, if necessary, with freeze substitution and low-temperature embedding. These combined cryochemical preparative procedures are invaluable for many structural and analytical studies.

Psychrochemical Preparative Procedures

These procedures combine the fast fixation and immobilization that may be obtained by rapid cooling with the comparative ease of processing samples at ambient temperatures. These methods are well documented in the literature and are particularly useful for low to medium resolution (ca 5 nm) TEM studies, immunocytochemical and radiochemical investigations, and many x-ray analytical studies. Space will not permit a detailed discussion of the procedures, but they follow along these general lines. Specimens, unfixed or lightly fixed in glutaraldehyde and/or paraformaldehyde, with or without cryoprotectants, are quenched cooled as effectively as possible. The water in the hydrated samples may be removed either by freeze drying or by low-temperature freeze substitution. The electron scattering (contrast) of low mass density specimens may be enhanced by the addition of heavy metal fixatives such as osmium to the freeze substitution brew. The freeze-dried or freeze-substituted samples may now be infiltrated, at low or ambient temperatures, with hydrophilic resins which are polymerized and subsequently sectioned.

The purist may argue that we have strayed from the straight and narrow path of nonchemical intervention by involving the use of fixatives, desiccants, and polymers, and it is appropriate to ask what advantages we may expect to gain from such methods. It is argued that the structural information from freeze-substituted and low-temperature-embedded material is

at least as good as (or even superior to) that obtained by more conventional ambient temperature procedures. On theoretical grounds the quality of structural information should be better, particularly if no heavy metal fixatives are used and the dehydration/embedding procedure is carried out in a strongly hydrophilic polar environment. However, it is often very difficult to see any improvement in either the quality and/or quantity of structural information when a careful comparison of the images is made. It is unfortunate that too few critically comparative studies have been made to support these claims.

By embedding material in hydrophilic resins such as Lowicryl and LR White we may be able to circumvent the vexing problem of ultracytometry. Only a few people have been able to cut ultrathin frozen sections routinely from a wide variety of samples; plant material continues to provide a major challenge. There is a continuing debate concerning the process of cryosectioning in unfixed and/or unprotected material, although it is now generally agreed that thinner and more complete sections can be obtained from vitrified material. The presence of ice crystals perturbs the cutting process and degrades the quality of the images that may be obtained. Such sections, although of little use for structural studies, remain an important part of many analytical investigations.

The use of light nonmetallic fixation in combination with low-temperature dehydration and embedding has proved to be a boon for immunocytochemical studies on even the most highly diffusible molecules. Difficulties remain, particularly in choosing the correct timing, temperature, and preparative recipe. The resin formulations, embedding schedules, and polymerization procedures are both idiosyncratic and idiopathic. For example, in my own laboratory we have more success with LR White resin than with Lowicryl and have obtained good embedding when we have combined different components from the two types of resin (unpublished data). Low-temperature fixation, dehydration, and embedding have been used to great success with some microanalytical studies, particularly with studies involving the location of heavy metals in tissues. Preliminary studies have also shown that these same procedures may be applicable to investigations involving the low-atomic-weight diffusible elements.

In summary, the psychrochemical methods offer the following advantages.

1. They are the preparative procedure of choice for analytical studies of functional molecules and macromolecules.
2. They appear to offer an alternative to cryomicrotomy, although this method will still probably be necessary for critical analytical studies of diffusible elements.
3. They offer a marginal, but as yet insufficiently well documented, advantages for medium-resolution structural studies.

Low-temperature techniques occupy a central position in the methods available for the localization of diffusible elements such as Na^+ , Cl^- , and K^+ , although the available technology is far from ideal. Chemical intervention is generally proscribed because it seriously affects membrane permeability and hence the natural compartmentation of the elements being analyzed. Cryofixation avoids these problems and, in addition, operates more rapidly than chemical fixation. The major disadvantages is that there is inevitably some ice crystallization in all but the very smallest sample. The consequent structural damage can probably be tolerated in most medium-resolution studies (ca 100 nm) but becomes a problem at higher resolution (25 nm). The phase separation, local concentration changes, and movement of elements by the advancing ice front are a problem for which there seems to be no answer. It is generally assumed that as the cell and tissue water is frozen, the dissolved solutes are moved to the nearest structural component in the cell. These distances are probably quite short because the cytoplasm of most cells is filled with organelles, vesicles, granules, etc., together with the ubiquitous structural components of the cytoskeleton. No precise figures are available but judging from the size of the ice crystal ghosts measured on micrographs the distances might be of the order of 0.1-1.0 μm , depending on the effectiveness of the initial cooling.

This elemental relocation is a measure of the spatial resolution of the analytical system, and although poor in relation to what can be achieved in purely structural studies, still permits accurate microanalysis to be carried out. The problem comes during the analysis of extracellular spaces and the vacuoles of mature plant cells. These large watery spaces are generally devoid of structural components to which the translocated diffusible elements could become attached. For this reason there must be some uncertainty about both the spatial resolution that can be obtained and the exact location and local concentration of any diffusible ions. The ions will presumably be swept to the edge of the growing ice crystals which, in a largely watery environment deep inside a bulk specimen, might be in the size range of 1-3 μm . This patchwork arrangement of ice crystals bordered by abnormally high local concentration of elements would be best analyzed by some sort of averaging technique using a small raster rather than a point source. The extracellular spaces must be analyzed in a frozen hydrated state rather than a frozen dried state because the ice is providing the principal structural component that holds the sorely displaced elements in place.

Contrast and Image Formation

The contrast of frozen hydrated specimens is three to four times lower than that of frozen dried material, which presents problems when

it comes to imaging and photography. Phase contrast, which may be increased by underfocusing the image, is an important part of image formation in fixed-beam instruments. Amplitude contrast is the principal imaging mechanism used in the examination of frozen dried material. In fully vitrified specimens, mass thickness contrast is the dominating contrast mechanism, whereas diffraction contrast dominates where the ice is in a crystalline form. This situation creates a small paradox, as the best contrast would thus appear to be obtained from noncrystalline material (the sample) embedded in a crystalline matrix (ice). In all our preparative procedures, we aim to obtain an unaltered sample composed of ordered and unordered structures embedded in a vitrified ice matrix.

In practice, the process of imaging and photography of thin vitrified specimens is quite complex, as the following example will show.⁶ These workers studied the structure of a protein crystal embedded in ice at 130 K and found it necessary to record four images of each specimen in the following order.

1. An electron diffraction pattern at a dose of $100 \text{ e}^- \text{ nm}^{-2}$.
2. A defocused low-dose image of the protein crystal at 40 000 \times at a dose of 500-1000 $\text{e}^- \text{ nm}^{-2}$.
3. A high-dose image at the same defocus and magnification at a dose of 2000-3000 $\text{e}^- \text{ nm}^{-2}$.
4. A second high-dose image at a slightly higher defocus.

In some cases it has been found necessary to take an additional picture at lower magnification of material which has been frozen dried inside the microscope and cooled back to 130 K. The information from the various micrographs is analyzed by computer-aided image processing.

The processes of contrast and image formation in specimens examined and analyzed at low temperatures by scanning beam instruments are little different from those used at ambient temperatures. Scanning transmission images of unstained and hydrated material generally have low contrast, although with STEM instruments it is possible to form a signal by using the ratio between the elastically scattered and the low-loss electrons. For very thin samples this ratio depends on atomic number only and can be used to provide contrast in thin, unstained sections. Frozen hydrated bulk samples generally need coating with noble metals for structural analysis, or with chromium or beryllium for analytical studies. It would be interesting to find out how much structural information could be obtained from uncoated frozen hydrated samples examined at low (100-1000V) accelerating voltages.

Specimen Damage

Radiation damage has always been a limiting factor to ultrastructural studies with high-

energy beam instrumentation. The processes are relatively well understood, although the problem of protecting specimens remains unsolved. Radiation damage may not prove to be the nemesis of all forms of low-temperature microscopy, but it will put limitations on what can and cannot be achieved. The damage, which is an inevitable consequence of the beam-specimen interaction that yields the image, falls into two main types.

1. Radiation damage where ionizing radiation causes irreversible changes to the microstructure and chemical composition of the specimen and the embedding medium. This type of damage occurs at quite low doses (ca 100 to 1000 $e^- \text{ nm}^{-2}$) and is the principal concern in high-resolution structural studies.

2. Mass loss, where ionizing radiation causes a substantial decrease in the total mass of the specimen and embedding medium. This type of damage becomes a problem at somewhat higher doses (ca 1000-5000 $e^- \text{ nm}^{-2}$) and should be the principal concern with x-ray analytical studies.

Somewhat surprisingly, beam heating of samples at low temperatures is of little concern, unless the sample is in poor thermal contact and/or the cold stage is not cold enough. It has been known for some time that the radiation damage effects are reduced if samples are held at low temperatures. There is a burgeoning literature on the subject and some of the earlier studies suggested the cryoprotection effect could be several hundred fold. Careful cooperative studies⁷ showed that the radiation protection factor is 3-5 fold at 77 K and there may be a further decrease in mass loss at 4 K.⁸ A wide range of results have been obtained, which is to be expected considering the variables of stage temperature, actual sample temperature, specimen chemistry, and dosage. Table 1 gives some idea of the total radiation doses needed to obtain various types of information from a sample and the doses that begin to cause sample damage. The doses, which are cumulative, are given as the number of electrons per square nanometer ($e^- \text{ nm}^{-2}$), which can be converted to Coulombs per square meter (C m^{-2}) by $1 e^- \text{ nm}^{-2} = 0.160 \text{ C m}^{-2}$. (A Coulomb is equivalent to a current of 1 A/s.)

It is now known that ice is an excellent source of the free radicals which cause much of the damage in frozen hydrated specimens.⁹ A dose of ca 1 $\text{ke}^- \text{ nm}^{-2}$ is needed to initiate the production of these free radicals. Depending on the spatial resolution required in the image, low-dose microscopy (100-2000 $e^- \text{ nm}^{-2}$) of frozen hydrated suspensions can be used to give valid structural information. Although high dosages are generally needed for high-resolution studies, most workers get around this problem by taking low-dose photographs followed by extensive computer-aided image analysis. It is useful to remember the general rule of thumb,¹⁰ which states that the spatial resolution that may be obtained is 1/1000th the dose used in $e^- \text{ nm}^{-2}$. This means that the typical

TABLE 1.--Comparative radiation doses (median values at 100 kV and 90 K).

Information sought	Dose ($e^- \text{ nm}^{-2}$)
Low dose searching	50
Diffraction pattern	100
Low dose imaging	200
Loss of crystallinity	1000
Free radical formation	1000
Ice bubbling	1000
Mass loss	2000
Removal of 1 nm ice	3000
Thick section imaging	1000
X-ray microanalysis	7500

low-dose image taken at 90 K does not resolve details much below 1 nm. There is thus every compunction to use the lowest dose possible to obtain the required structural information coupled with computer-aided analysis of the low contrast images. Much lower doses have to be used to obtain high resolution structural information using electron diffraction techniques.

It has been shown⁹ that water is more stable under the electron beam than many organic materials and that I_V is more stable than either I_C or I_H . In this respect these findings confirm that vitreous ice is the best material as an embedding material. But Nature never smiles kindly for too long, for it is now known that radiation damage to organic material is exacerbated in the presence of ice.⁹ This appears to be less of a problem for material completely embedded in ice, but remains a difficulty where an ice contamination layer builds up on specimens during transfer and observation, which creates further difficulties in the examination and x-ray microanalysis of frozen hydrated sections where the frozen section sits on an organic support film. This ice-organic material radiation-induced interaction is less of a problem with frozen thin suspensions that are suspended, unsupported, between the bars of a fine mesh electron microscope grid. An additional dimension arises from studies that show that transitions between ice polymorphs can be induced by electron-beam irradiation.¹¹ The ability to convert I_C to I_V by irradiation at the transition temperature remains an interesting procedure.

Although mass loss from samples at 90 K is generally reduced by a factor of five, this rate of loss is still a matter of some concern for high-resolution analytical studies. Quantitative procedures depend on knowing the local concentration of the element in question in relation to the mass of the sample in the analyzed microvolume. Mass loss changes can affect the organic matrix, the hydrated phases, and even specific elements, and although these losses are reduced at low temperatures, they cannot be entirely avoided. The bubbling phenomena seen in irradiated samples as a large number of bubbles develop, fuse together, and burst to release volatile components is an early manifestation of beam damage and mass

loss. The mass loss from frozen hydrated material is greater than the mass loss from frozen dried material, which is why high-resolution x-ray microanalysis is now confined to frozen-dried specimens analyzed at low temperatures. Experiments have shown¹² that unless great care is taken, residual water vapor in the microscope column can form a volatile surface layer of condensed ice on the specimen. Mass loss measurements can thus either appear reduced due to water absorbance or increased as this layer sublimates and/or contributes to the etching rate of the organic material.

Conclusions

Low-temperature microscopy appears to be the only way we can hope to obtain the highest-resolution structural information about delicate organic and hydrated samples. The limitations to what can and cannot be achieved are becoming more clearly defined. Very low sample temperatures, low-dose imaging, and very high levels of computer-enhanced image analysis of thin hydrated suspensions appear to be the way forward. Frozen hydrated sections and sections of freeze-substituted material do not seem to provide very much more structural information than is available by more conventional ambient-temperature means. However, these types of thin preparations together with low-temperature-embedded material will form the basis of procedures to provide in situ chemical information about specimens. In any event, whatever method is used to prepare the specimen, it is important that it is examined and analyzed at low temperatures. For at 123 K and below, mass loss and radiation damage are reduced, contamination decreases to acceptable levels, and the opportunity exist for using the best embedding material for hydrated sample, Ice. Finally, in case this paper is perceived as representing a somewhat iconoclastic view of the subject, some general references are included that both confirm and counter the views expressed here on low-temperature microscopy and analysis,^{13,14} TEM of thin frozen liquid suspensions,^{10,15} and beam damage to frozen specimens.^{9,16} The dearth of specific textual references should not be construed as not recognizing the important work of many investigators but as an acceptance of the dictum of the notable British scientist, J. B. S. Haldane, who stated that the test of scientific value is that a finding is too true and general and lasting to be ascribable to any individual investigator of the past.

References

1. W. Chui et al., "The EMSA committee on cryoelectron microscopy technology," *EMSA Bulletin* 18: 16, 1988.
2. P. Echlin, "Biological electron-probe x-ray microanalysis: An unfulfilled promise?" *Microbeam Analysis--1988* 451.
3. A. W. McDowell et al., "Electron microscopy of frozen hydrated sections of vitreous ice and vitrified biological samples," *J.*

Microscopy 131: 1, 1983.

4. H. Moor, "Theory and practice of high pressure freezing," in R. A. Steinbrecht and K. Zierold, Eds., *Cryotechniques in Biological Electron Microscopy*, Berlin: Springer, 1987, 175.
5. W. Kaeser et al., "Cryofixation of plant tissues without pretreatment," *J. Microsc.* (in press).
6. R. A. Grant et al., "Alignment and merging of electron microscope images of frozen hydrated crystals of the T4 DNA helix stabilizing protein GP32*1," *Biophys. J.* 49: 251, 1986.
7. International Experimental Study Group, "Cryoprotection in electron microscopy," *J. Microsc.* 141: 385, 1986.
8. M. K. Lamvik et al., "Mass loss in collision is greatly reduced at liquid helium temperatures," *J. Microsc.* 148: 211, 1987.
9. Y. Talmon, "Electron beam radiation damage to organic and biological cryospecimens," in R. A. Steinbrecht and K. Zierold, Eds., *Cryotechniques in Biological Electron Microscopy*, Berlin: Springer, 1987, 64.
10. J. Dubochet et al., "Cryo-electron microscopy of vitrified sections," *Quart. Rev. Biophys.* 21: 129, 1988.
11. H. G. Heide and E. Zeitler, "The physical behavior of solid water at low temperatures and the embedding of electron microscope specimens," *Ultramicroscopy* 16: 151, 1985.
12. M. K. Lamvik and S. C. Davilla, "Dynamic hydration effects in an electron microscope cold stage," *J. Elect. Microsc. Tech.* 8: 349, 1988.
13. R. A. Steinbrecht and K. Zierold, Eds., Ref. 4.
14. P. Echlin, *Low-temperature Microscopy and Analysis*, Cambridge University Press (in press).
15. W. Chui, "Electron microscopy of frozen, hydrated biological specimens," *Ann. Rev. Biophys. Chem.* 15: 237, 1986.
16. R. M. Glaeser and K. A. Taylor, "Radiation damage relative to transmission electron microscopy of biological specimens at low temperatures: A review," *J. Microsc.* 112: 127, 1978.

PERFORMANCE OF A CRYOTRANSFER/COLD STAGE FOR A VG MICROSCOPES HB501 STEM

S. B. Andrews and R. D. Leapman

Biological electron microscopy and microanalysis, particularly at high spatial resolution, often necessitates the use of a cold stage to minimize the effects of radiation damage and mass loss. A cryotransfer capability is also desirable to preserve structures in their "native," hydrated state, and to prevent rehydration artifacts or the loss of labile constituents in specimens freeze-dried in situ.

The authors are at the National Institutes of Health, Bethesda, MD 20892. They are indebted to C. E. Fiori for experimental advice and for interfacing and testing the x-ray spectrometers.

A cryotransfer stage constructed by VG Microscopes, U.K., for a VG HB501 scanning transmission electron microscope (STEM),¹ has been evaluated from micrographs and energy-dispersive x ray (EDX) spectra of hydrated and dehydrated cryosections of protein-embedded, biochemically isolated nerve endings from squid brain. The transfer device and stage were found to perform well with regard to minimum achievable temperature, specimen stability under the electron beam, specimen drift, and EDX spectroscopy.

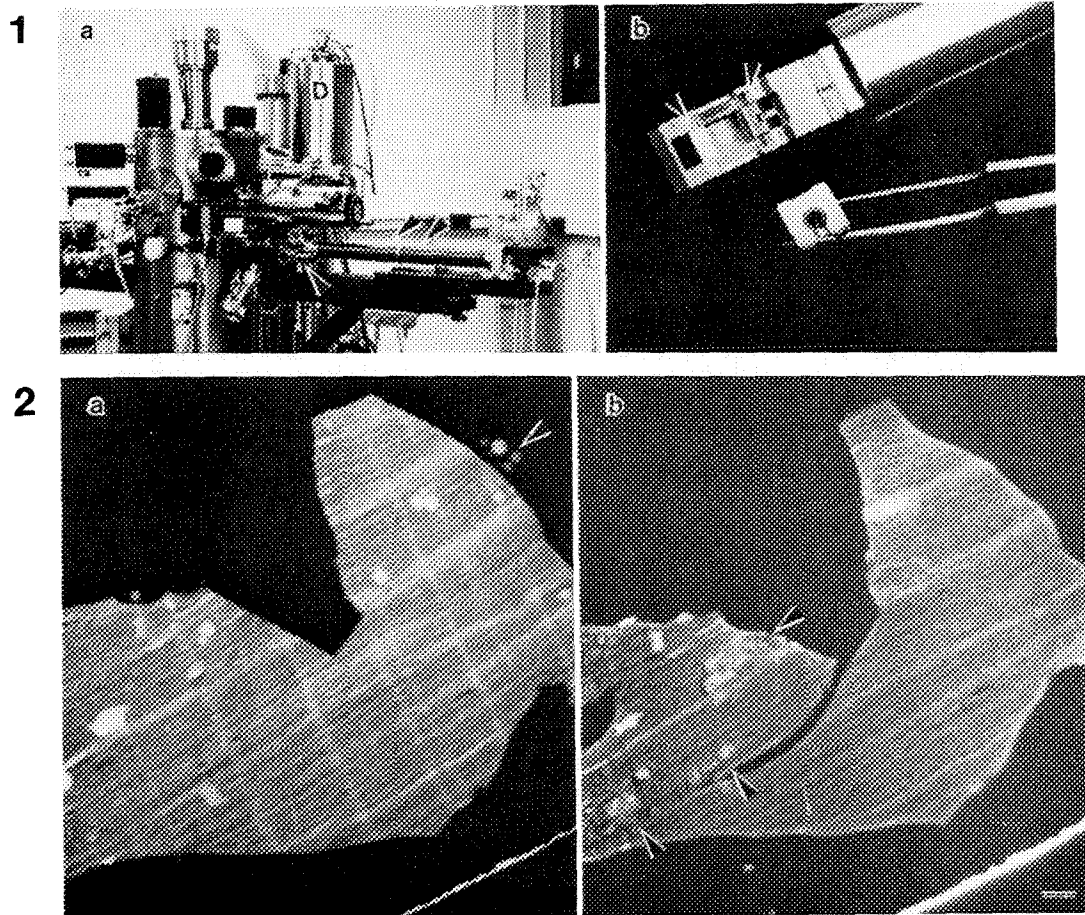


FIG. 1.--Essential components of VG HB501 cryotransfer system. (a) View of right side of microscope illustrating cryotransfer probe with bellows (double arrows) and loading port with viewing windows (arrow). D is pressurized Dewar for cooling specimen stage. (b) Stainless-steel cryotransfer loading tool and beryllium specimen block (resting on forceps). Arrows indicate jaws for clamping specimen block during transfer. Graphite "cir-clip" secures standard 3mm grid to the block.

FIG. 2.--Electron micrographs of cryosection of "synaptosomes" embedded in albumin matrix. (a) Shortly after cryotransfer. Section appears well hydrated; arrow indicates adventitious ice crystals picked up during transfer. (b) Following freeze-drying in situ. Clusters of synaptosomes are evident (arrows). Note difference in overall contrast of sections as indicated by brightness of grid edge (lower right). Micrographs taken at ca. -175 C. Bar = 1 μ m.

Description and Operation of the Cryotransfer System

The design of the cryotransfer stage for the VG HB501 field-emission STEM will be described elsewhere.² Here we only summarize the basic principles of operation as a basis for discussing performance. The actual low-temperature specimen loading device (Fig. 1a) consists of a cold transfer probe with bellows (double arrows) and an airlock chamber with viewing windows (arrow). A removable specimen block, constructed with beryllium to minimize x-ray generation for EDXS, is attached to the tip of the transfer probe within the airlock by means of a stainless steel transfer tool (Fig. 1b). The transfer probe is cooled by liquid nitrogen sucked through a tube along its center by a laboratory vacuum line. A standard 3mm grid is loaded into the block under liquid nitrogen and clamped into position by a graphite "circlip." To optimize x-ray collection, the plane of the grid in the block is tilted 20° and one side of the block is cut away.

The block is delivered to the cold stage by a series of clamp transfers. The block is first clamped in the transfer tool (Fig. 1b) under liquid nitrogen, then inserted into the airlock and attached to the end of the cold probe by a second set of clamps; the transfer tool is then unclamped and withdrawn. After roughing and fine-pumping of the airlock, the probe is inserted into the cold stage, where a third clamp is tightened by means of the x-tilt motor control. After the transfer probe is unclamped, the rod is removed and the airlock gate valve is closed. Sample temperature is controlled by the flow of cold nitrogen gas supplied to passages within the cold stage from a thin stainless-steel tube coiled so as to minimize vibration coupling. An insert heater within the cold stage is available to adjust the temperature above the minimum. The specimen chamber vacuum typically stabilizes at 3×10^{-9} mbar with the cold stage in operation. The cryotransfer stage is incompatible with specimen tilting, but if necessary this stage can be replaced with the standard stage and double-tilt cartridge to permit room temperature tilting.

Performance

Measured Temperature. The temperature of the transfer probe, as measured by means of a calibrated copper-constantan thermocouple attached to a specially fabricated test block, was found to reach below -175 C within 10 min of cooling down. After transfer into the column, the specimen temperature was estimated to be below -180 C by measurement of the output of the chromel-alumel thermocouple that is an integral part of the cold stage and is located close to the specimen. Hydrated samples retained water in the form of loose ice crystals on their surface for 4 h or more. On warming, the free ice was lost at ca. -110 C (according to the cold-stage thermocouple), which is generally consistent with known values.³ "Tissue

water" from the cryosections was lost at slightly higher temperatures (-105 to -100 C).

Mechanical Stability. At room temperature the drift was measured as better than 0.01 nm/s (i.e., essentially undetectable over 15 min). At the lowest temperature (at or below -175 C) the drift was about 0.04 nm/s after a wait of 2 h to reach thermal equilibrium; larger drift rates were observed just after the sample block was inserted into the stage. We could reach significantly lower temperatures (ca. -190 C) by allowing liquid rather than gaseous nitrogen to pass through the stage, but vibration occurred under these conditions.

Contamination and Beam Stability. In general, no detectable ice contamination or etching of a thin carbon film occurred at or below -175 C after several hours of operation at a vacuum of 3×10^{-9} mbar in the sample chamber. (On a few occasions, a small amount of ice contamination was evident after several hours; it is not known how these specimens or conditions differed from the norm.) At this temperature, etching of hydrated sections was not significant at electron doses below $10^6 \text{ e}^- \text{ nm}^{-2}$. In addition, cooling the sample totally eliminated hydrocarbon contamination, even in the case of a "dirty" sample.

Example of Application. The cryotransfer stage was tested by the transfer of hydrated cryosections into the HB501 STEM. The cryosections were cut from a block of directly frozen squid brain "synaptosomes" (i.e., mechanically pinched off, resealed, and isolated nerve endings) suspended in an artificial seawater solution and embedded in a 10% (w/v) bovine serum albumin matrix. The sections were examined in the hydrated state and then dehydrated under controlled conditions. EDX spectra were recorded to test the performance of the stage for microanalytical applications and also to ascertain the success of the cryotransfer and in situ freeze drying for preserving the distributions of diffusible elements in cells. Cryosections of synaptosomes were chosen because they have been previously characterized by analytical electron microscopy.⁴

A dark-field STEM micrograph of a hydrated cryosection, supported on a Formvar- and carbon-coated copper grid at ca. -175 C, shows several small hexagonal ice crystals due to frost carried in during the transfer (Fig. 2a, arrow). Apart from these ice crystals and some compression and knife marks, contrast *within the section* is very low. This lack of visibility of internal structure in the hydrated section, as well as the high contrast relative to the support film, is indicative of ice retention during cryotransfer. Figure 2(b) shows the same section after it was warmed to -100 C for several h and recooled to ca. -175 C. The ice has entirely sublimed and typical section shrinkage has occurred. Overall contrast of the dried section is much lower, but internal structure is now visible; the arrows indicate clusters of synaptosomes.

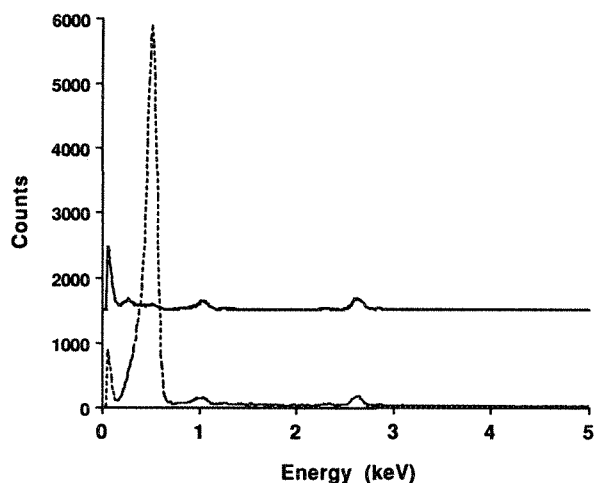


FIG. 3.--EDX spectra (UTW detector) of a cryo-section of synaptosomes in an albumin matrix. Dashed spectrum: $5 \times 5 \mu\text{m}$ area of a frozen-hydrated section at ca. -175°C . Solid spectrum: similar area following freeze-drying at ca. -100°C and recooling to ca. -175°C ; loss of oxygen x rays is major change.

An EDX spectrum (Fig. 3) from a region of the hydrated section containing mainly matrix was recorded by a Tracor Northern Micro-ZHV ultrathin window (UTW) EDX detector and a Tracor TN5500 analyzer. The spectrum is dominated by the $\text{O K}\alpha$ x rays at 0.52 keV due to the ice, although sodium (1.04 keV) and chlorine (2.62 keV) from the seawater solution are evident. After dehydration the oxygen line has almost disappeared and the bremsstrahlung is much lower, but the sodium and chlorine peaks are essentially unchanged; this result is consistent with loss of water but not of diffusible ions on drying. Spectra acquired after dehydration (Fig. 4) show the presence of several elements (Na, Mg, P, S, Cl, K, and Ca, as well as C and O) in amounts typical of biological tissue in general and of this preparation in particular.

Specifically, quantitation (ML fitting) of spectra from the matrix (whose composition is known by chemical assay: $\text{Na} = 405$, $\text{Mg} = 45$, $\text{Cl} = 470$, $\text{K} = 9$, and $\text{Ca} = 9 \text{ mmol/kg}$ wet weight) permits an estimate of relative elemental sensitivities (k-factors) for the UTW detector that reflect a major improvement in the detectability of low-Z elements. By using the matrix as an "internal standard" for quantifying the composition of the nerve endings, we can further demonstrate that the elemental concentrations within tissue compartments are consistent with previous values obtained on traditional AEMs (unpublished data). For example, the average potassium concentration of several synaptosomes measured here was 306 mmol/kg wet weight, as compared with an expected concentration of 300 mmol/kg . The results suggest that established methods of biological microanalysis⁵ can be readily applied on the HB 501 STEM with cryotransfer stage, with the added sensi-

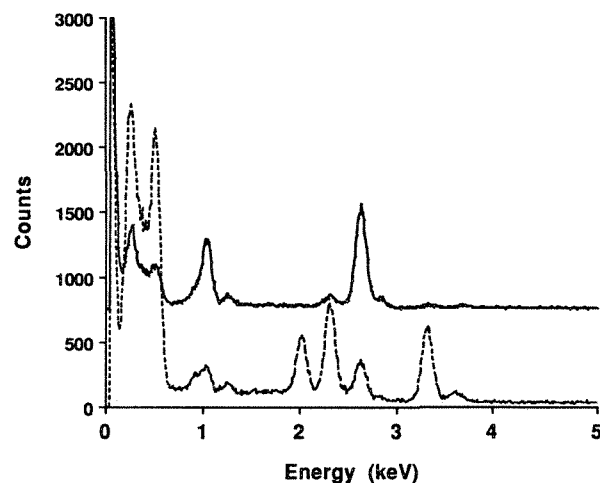


FIG. 4.--EDX spectra and preparation as in Fig. 3, following freeze-drying and recooling to ca. -175°C . Solid spectrum: sum of four spectra from representative $0.5 \times 0.5 \mu\text{m}$ regions of albumin matrix, essentially similar to (and including) solid spectrum in Fig. 3. Dashed spectrum: sum of the contents of four synaptosomes (each analysis area $0.1 \times 0.1 \mu\text{m}$).

tivity advantages of an ultrathin window detector.

Conclusions

The cryotransfer system on the VG HB501 STEM is thermally and mechanically stable at temperatures below -175°C , and provides a very clean specimen environment under these conditions. In combination with a high-brightness field-emission gun, this performance appears to be more than adequate to realize some important advantages for biological electron microscopy:

1. For microanalysis, a stable, low-temperature stage in a very clean environment virtually eliminates the contamination and beam damage that would otherwise accompany the high electron flux delivered by a field-emission gun. This configuration facilitates the measurement of low concentrations of biological elements within small structures in *dried* cryosections, e.g., the determination of calcium at concentrations on the order of 10^{-4} M in organelles only $20\text{--}50 \text{ nm}$ in diameter.

2. The *mechanical* stability of the stage suggests that this instrument should be favorable for x-ray-based elemental imaging, since drift corrections will be less problematical.⁶ Such stability is also desirable for an imaging system that uses parallel electron energy loss detection.

3. Regarding frozen-hydrated preparations, the thermal and mechanical stability of the cold stage recommends this microscope for high-resolution observations of biological structures embedded in thin films of vitreous ice. The performance of the HB501 for low-

dose, high-resolution imaging of hydrated specimens is now being tested.

References

1. I. R. M. Wardell, *Ultramicrosc.* 7: 39, 1982.
2. A. W. Nicholls and P. E. Bovey, *Proc. 47th Ann. Meet. EMSA*, 1989.
3. J. Dubochet, J. Lepault, R. Freeman, J. A. Berriman, and J.-C. Homo, *J. Microsc.* 128: 219, 1982.
4. C. E. Fiori, R. D. Leapman, C. R. Swyt, and S. B. Andrews, *Ultramicrosc.* 24: 237, 1988.
5. T. Kitizawa, H. Shuman, and A. P. Somlyo, *Ultramicrosc.* 11: 251, 1983.
6. P. J. Statham, *Analytical Electron Microscopy--1987*, 187.

PARALLEL EELS MICROANALYSIS OF CELLS

R. D. Leapman and C. R. Swyt

The recent implementation of parallel detectors has greatly improved the signal-to-noise ratio that is attainable in electron energy loss spectra (EELS).¹⁻⁴ It has now become possible to measure physiological concentrations of elements producing extremely weak features in the spectrum.² EELS is not only sensitive to the very low atomic number elements (e.g., carbon, nitrogen, oxygen, and fluorine) through the K-shell excitation, but the technique is also sensitive to other important elements (e.g., phosphorus, sulfur, chlorine, calcium and iron) through the L-shell excitation.⁵ However, certain elements are best detected by energy-dispersive x-ray spectroscopy (EDXS), either because of edge overlap (e.g., potassium) or because of unfavorable ionization cross sections (e.g., sodium and magnesium). For measurement of diffusible ions in dried cryosections EELS should therefore be used in conjunction with EDXS. When elemental concentrations are low, energy-loss spectra can be quantitated by means of reference spectra by similar procedures that are available for x-ray microanalysis. Acquisition of first-difference or second-difference energy-loss spectra is another useful processing technique for detecting and measuring weak core loss signals. This method, which was first applied by Shuman et al.,^{6,7} not only removes channel-to-channel gain variations from the spectrum but also removes the slowly varying background. The purpose of this paper is to demonstrate how a commercially available parallel detection EELS system can be used to analyze a range of elements in cells by application of these processing techniques.

Experimental

Spectra were obtained at 100keV beam energy with a Hitachi H700H analytical electron microscope equipped with a Gatan Model 666 parallel detection electron energy loss spectrometer described previously by Krivanek et al.¹ In this system the energy dispersion is magnified by post-spectrometer quadrupole lenses and the inelastically scattered electrons strike a YAG scintillator. The detector consists of a 1024-channel photodiode array that is read out serially in 12 ms. Spectra were acquired in the scanning transmission (STEM) mode with a dispersion of 0.5 eV per channel and with integration times of the order of 100 ms. A 3mm spectrometer entrance aperture was selected to collect electrons scattered through a semi-

angle of approximately 30 mrad at the specimen. Count rates were sufficiently high for the detective quantum efficiency to be close to unity. The digitized output of the photodiode array was sent over a parallel line to a Tracor Northern TN5500 computer, which controlled data acquisition parameters such as the integration time, the number of read-outs, and the voltage applied to the spectrometer drift tube. Each photodiode count corresponded to approximately 30 incident fast electrons. Spectra were transferred to a DEC PDP11/60 computer in order to apply a multiple least-squares fitting procedure and were transferred to a Macintosh computer for plotting.

Second-difference Reference Spectra and Quantitation

In order to detect very weak core edges it is important to remove from the spectrum the channel-to-channel gain variations of the photodiode array, which in our case typically have a root mean square value of ~0.5%. Several techniques for eliminating the gain variations are available, as described by Shuman and Kruit.⁶ We adopt the second-difference method, which is equivalent to applying a top-hat digital filter, thereby enhancing sharp features while suppressing the slowly varying background. The "filtering" operation is achieved by successively acquiring three spectra with $-\Delta$, $+\Delta$, and zero voltages applied to the electrically isolated drift tube of the spectrometer. If the original spectrum is $I(E)$, the second difference is given by $I''(E) = 2I(E) - I(E + \Delta) - I(E - \Delta)$. The magnitude of the offset Δ should be matched with the width of the sharp peak at the core edge to optimize the signal/noise ratio. We find that the optimum value for Δ is typically around 6 eV.

Figure 1 shows second-difference reference spectra acquired with $\Delta = 6$ eV for the phosphorus L_{23} , sulfur L_{23} , chlorine L_{23} , carbon K, potassium L_{23} , calcium L_{23} , nitrogen K, iron L_{23} , sodium K, and magnesium K edges. They were recorded from thin samples of pure compounds (NaCl, NaH_2PO_4 , MgSO_4 , KCl, CaCl_2 , FeSO_4 , and insulin) supported on carbon films. The near-edge structure is strongly enhanced by the second-difference filtering. For some edges like calcium and iron most of the structure is contained within 20 eV of the edge and we can therefore best utilize this part of the spectrum to detect low elemental concentrations. In fact, the enhancement of the so-called "white-line" intensity by the filtering operation has already been shown to yield excellent detection limits for calcium.^{6,7} The second-difference filter is similar to the top-hat filter commonly used to quantitate energy-dis-

The authors are at the Biomedical Engineering and Instrumentation Branch, DRS, Bldg. 13, Rm. 3W13, National Institutes of Health, Bethesda, MD 20892.

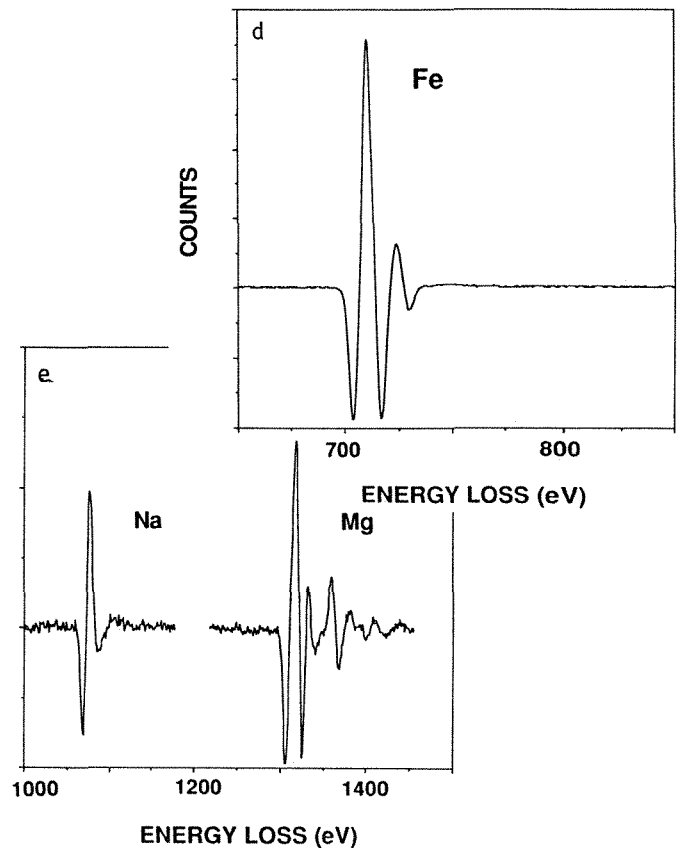
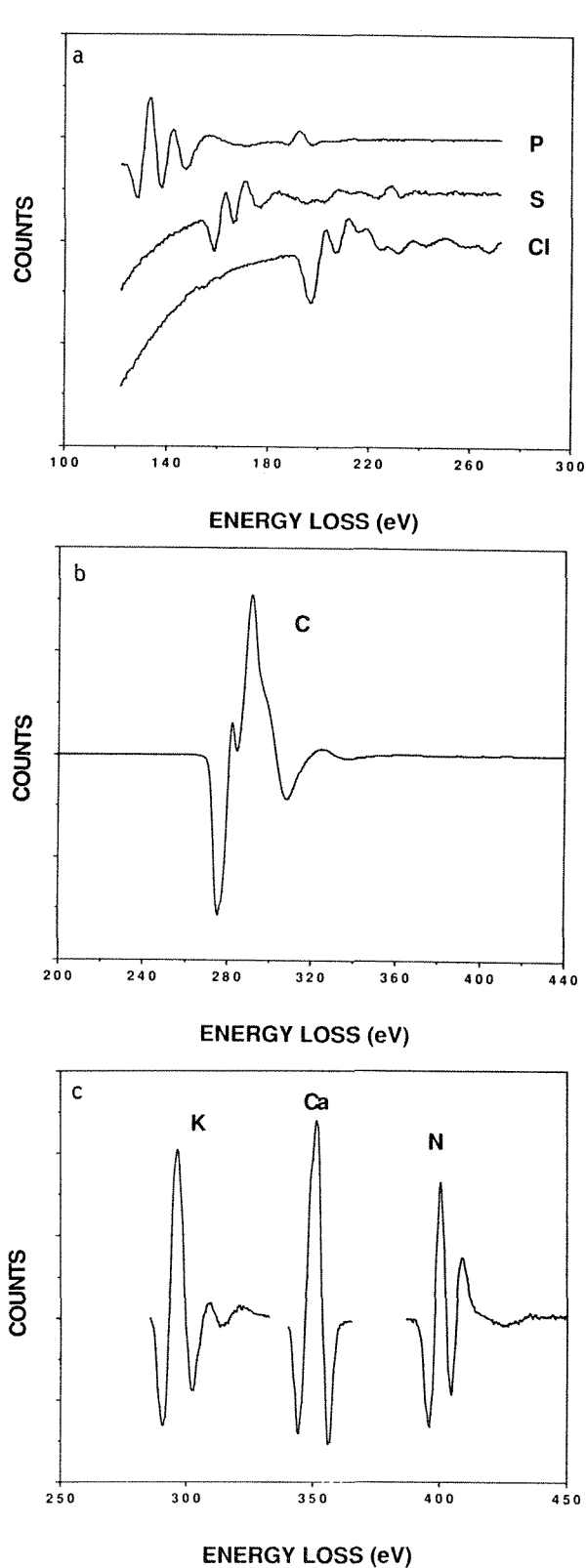


FIG. 1.--Second-difference reference spectra recorded in TEM mode at 100keV beam energy and with $\Delta = 6$ eV; (a) P L₂₃, S L₂₃, and Cl L₂₃; (b) C K; (c) K L₂₃, C L₂₃, and N K; (d) Fe L₂₃; (e) Na K and Mg K. Nitrogen and sulfur reference spectra were obtained from insulin; reference spectra for other elements were obtained from inorganic salts. Note overlap of C K and K L₂₃ edges.

change as a function of incident dose because of radiation damage. Fortunately, for some elements, e.g., calcium and phosphorus, the edge shape and energy remain nearly constant.

Spectra were quantitated by fitting to the second-difference reference spectra (Fig. 1) using a multiple linear least-squares (MLS) procedure. The method is similar to that used to quantitate EDXS spectra. However, for energy loss spectra the method must take into account plural inelastic scattering,^{7,8} which is achieved by generating plural scattering reference spectra from convolution of the carbon low-loss spectrum with the single-scattering core edge spectrum. The fit is performed iteratively by forcing the plural scattering coefficients to be the same at each edge.⁸

Atomic ratios of elements were obtained by use of SIGMAK and SIGMAL cross sections⁹ together with the fitting coefficients produced by the multiple-least-squares fitting procedure.

Examples of Applications

In order to demonstrate the potential of parallel-detection EELS for analyzing a range of elements in cells we present some typical spectra from dried cryosections of rapidly

pervise x-ray spectra, but whereas in EDXS peak widths remain quite constant, energy resolution and natural peak shape can vary in EELS complicating quantitation considerably. In general, near-edge fine structure depends on the chemical bonding environment of a particular atom. Not only can the edge shape change from compound to compound but it can also

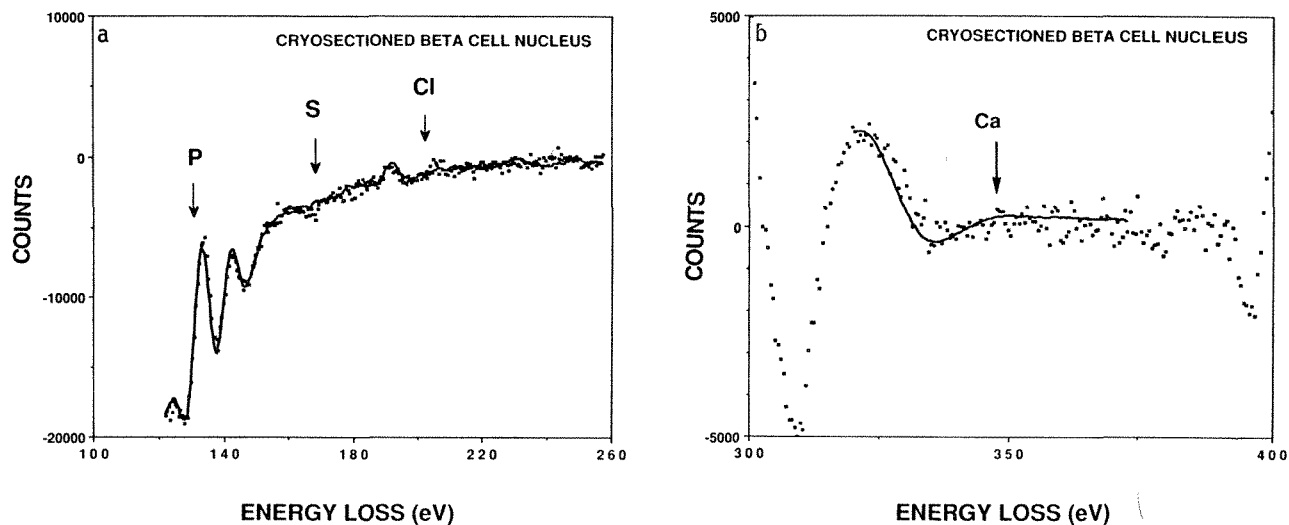


FIG. 2.--Second-difference spectrum from cryosectioned nucleus of pancreatic beta cell (dots) and MLS fit (solid line): (a) in region of phosphorus, sulfur, and chlorine L_{23} edges; (b) in region of calcium L_{23} edge.

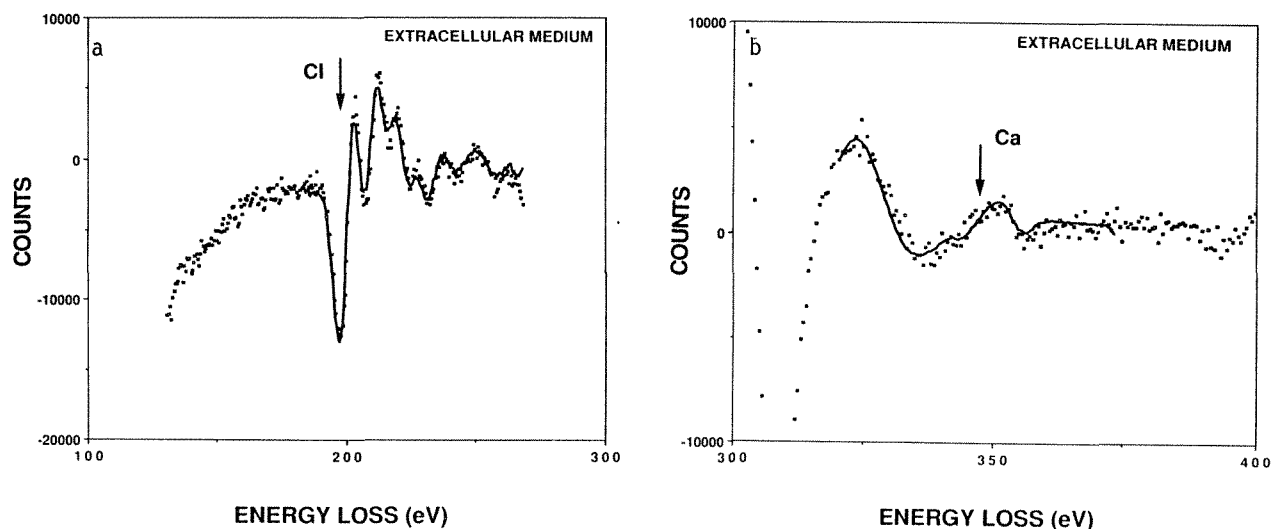


FIG. 3.--Second-difference spectrum from extracellular medium in cryosection of pancreatic islet of Langerhans (dots) and MLS fit (solid line): (a) in region of chlorine L_{23} edge, (b) in region of calcium L_{23} edge.

frozen pancreatic islets of Langerhans.¹⁰ Second-difference spectra were recorded in the STEM mode with a probe current of 0.5 nA.

Figure 2(a) shows such a spectrum (dotted line) from a beta cell nucleus recorded with a total integration time of 120 s. The relative sample thickness was approximately 0.5 inelastic mean free paths. The multiple-least-squares fit for the carbon, phosphorus, sulfur, and chlorine reference spectra (solid line) is seen to follow closely the experimental data for the nucleus. The atomic concentrations of P, S, and Cl are in the ratios $1:0.16 \pm 0.09:0.05 \pm 0.06$, in reasonable agreement with simultaneously recorded EDXS measurements. However, the EELS analysis gave uncertainties in S and Cl concentrations that were a factor of about 5 greater than for the EDXS analysis. These larger uncertainties are attributed to the overlapping fine structures of the P, S, and

Cl L_{23} edges. The calcium L_{23} edge is not detected when Ca and C reference spectra are fitted over the energy range 300-400 eV (Fig. 2b), again consistent with x-ray results showing a low calcium concentration in the nucleus. The fitting procedure gives a Ca/C atomic fraction of $(-0.1 \pm 1.3) \times 10^{-4}$. Potassium is present at a much higher concentration than calcium but it is much more difficult to quantitate because of the overlap of the K L_{23} and C K edges (Fig. 1). If the carbon K edge shape is known, potassium measurement is possible by fitting reference spectra.⁸ However, in this sample the carbon K edge differs significantly from the available reference spectrum and EELS analysis of potassium was not feasible.

Figure 3(a) shows the sum of two spectra from a region of extracellular matrix in the pancreatic islet, recorded with a total integration time of 240 s. The chlorine and car-

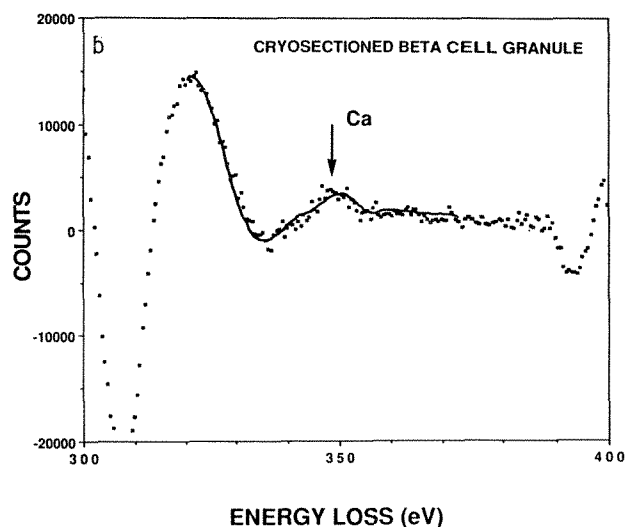
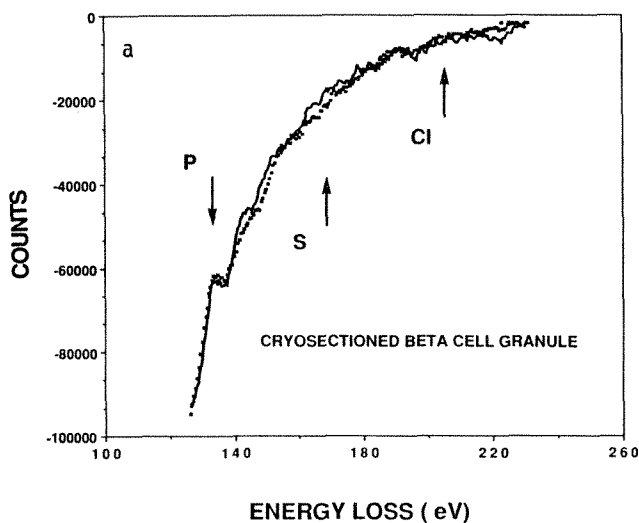


FIG. 4.--Second-difference spectrum from cryosectioned granule of pancreatic beta cell (dots) and MLS fit (solid line): (a) in region of phosphorus, sulfur, and chlorine L_{23} edges; (b) in region of calcium L_{23} edge.

bon reference spectra show a satisfactory fit (solid line) to the experimental data (dots). The chlorine L_{23} edge (200 eV) is easily visible as a series of peaks extending over some 80 eV. The element is present at a dry weight concentration of about 1600 mmol/kg (including the carbon film) which corresponds to a chlorine atomic fraction of 1.9×10^{-2} . Figure 3(b) shows the same spectrum (dotted line) in the region of the calcium L_{23} edge (348 eV). The multiple-least-squares fit (solid line) to the carbon and calcium reference spectra is again satisfactory and yields a Ca/C atomic fraction of $(3.6 \pm 1.8) \times 10^{-4}$ or a dry weight concentration of 30 mmol/kg. Although the sodium L_{23} edge was easily visible at 1080 eV, fitting the reference spectrum in Fig. 1(e) gave significantly larger uncertainties than for EDXS analysis. Neither sodium nor magnesium appear well suited for EELS microanalysis: the K edges are high in energy and therefore have relatively low ionization cross sections, and the L edges cannot be utilized because they are too low in energy and overlap with the valence electron spectrum.

An attempt was made to fit the spectrum from insulin-containing beta cell secretory granules in the same specimen over the range 120-220 eV. Figure 4(a) shows the sum of spectra from three beta granules obtained with a total integration time of 360 s. The phosphorus edge is evident but the least-squares fit is not good in the region of the sulfur edge, perhaps because of differences in near-edge fine structure between the reference compound and the beta granule. Although the granule thickness is relatively high (~ 1.2 inelastic mean free paths) the multiple-least-squares fitting procedure is expected to be valid.⁸ The fit of reference spectra is more satisfactory in the range of 300 to 400 eV (Fig. 4b) where calcium is detected at an atomic fraction Ca/C of $(1.9 \pm 0.5) \times 10^{-4}$, i.e., a dry weight concentration of $\sim 16 \pm 4$ mmol/kg.

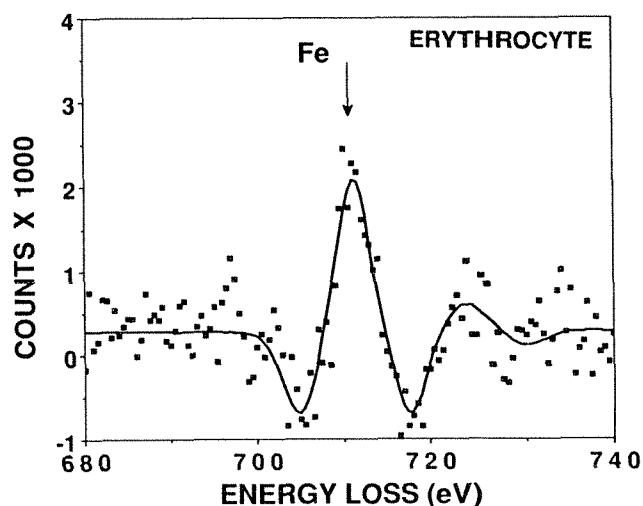


FIG. 5.--Second-difference spectrum from cryosectioned rat erythrocyte in region of Fe L_{23} edge (dots) and MLS fit (solid line).

In order to demonstrate the sensitivity of iron measurement by parallel EELS we have obtained spectra from cryosectioned erythrocytes in rapidly frozen rat liver. Figure 5 shows the second difference spectrum acquired in the STEM mode by scanning the electron probe over a 100nm square region of an erythrocyte ~ 1.2 inelastic mean free paths thick. The total integration time was 40 s and the probe current was 2.0 nA. The Fe L_{23} edge reference spectrum (solid line) closely fits the experimental data. The MLS procedure gives an Fe/C atomic fraction of $(6.7 \pm 0.6) \times 10^{-4}$ in agreement with x-ray measurements. In fact from simultaneously recorded x-ray spectra¹¹ we find that sensitivities for iron detection are about equal for EELS and EDXS.

Conclusions

We have demonstrated how the Gatan parallel detection spectrometer can be used to measure not only low atomic number elements, the major constituents of cells, but also heavier elements that have traditionally been analyzed by EDXS. With EELS such elements are best detected from their $L_{2,3}$ edges and by fitting reference spectra for quantitation. As found by Shuman et al.⁶ application of a second-difference filter removes channel-to-channel gain variations while suppressing the high background and enhancing weak peaks typical in spectra from biological samples. We have also pointed out some problems such as the occurrence of edge overlaps (e.g., carbon K and potassium $L_{2,3}$); the relatively low signals that are generated for some important elements (e.g., sodium and magnesium); and changes in fine structure as a function of chemical bonding that can complicate quantitation.

References

1. O. L. Krivanek, C. C. Ahn, and R. B. Keeney, "Parallel detection electron spectrometer using quadrupole lenses," *Ultramicroscopy* 22: 103-116, 1987.
2. H. Shuman, "Parallel recording of electron energy loss spectra," *Ultramicroscopy* 6: 163-168, 1981.
3. R. F. Egerton, "Parallel recording systems for electron energy loss spectroscopy (EELS)," *J. Electron Microsc. Tech.* 1: 37-52, 1984.
4. D. E. Johnson, K. L. Monson, S. Csillag, and E. A. Stern, "An approach to parallel-detection EELS," *Analytical Electron Microscopy*, 1981, 205-209.
5. R. D. Leapman and R. L. Ornberg, "Quantitative electron energy loss spectroscopy in biology," *Ultramicroscopy* 24: 251-268, 1988.
6. H. Shuman and P. Kruit, "Quantitative data processing of parallel recorded electron energy loss spectra with low signal to background," *Rev. Sci. Instrum.* 56: 231-239, 1985.
7. H. Shuman and A. P. Somlyo, "Electron energy loss analysis of near-trace element concentrations of Ca," *Ultramicroscopy* 21: 23-32, 1987.
8. R. D. Leapman and C. R. Swyt, "Separation of overlapping core edges in electron energy loss spectra by multiple-least-squares fitting," *Ultramicroscopy* 26: 393-404, 1988.
9. R. F. Egerton, *Electron Energy Loss Spectroscopy in the Electron Microscope*, New York: Plenum Press, 1986, 357-362.
10. M. C. Foster, R. D. Leapman, M. X. Li, R. L. Ornberg, and I. Atwater, "Composition of secretory granules by electron probe microanalysis of cryosectioned rat pancreatic islets," *Biophys. J.* 55: 431a, 1989.
11. R. D. Leapman, "Application of parallel-detection electron energy loss spectroscopy in biology," in H. Hagler and K. Zierold, Eds., *Progress of Electron Probe Microanalysis in Biology and Medicine*, Berlin: Springer-Verlag, (in press).

SEMI-AUTOMATED SELECTION OF OBJECTS FROM DIGITAL STEM IMAGES

J. G. Wong, D. E. Johnson, and M. E. Cantino

High-resolution digital elemental images acquired with electron-probe x-ray microanalysis are fast becoming essential components in studies of subcellular elemental localization. Elemental images provide not only excellent visual representations of subcellular elemental distributions, they contain also enormous quantities of data collected essentially without operator bias.¹⁻⁵ Several groups have recently developed methods for quantifying these images from both freeze-dried and hydrated cryosections.^{4,6,7} Approaches for calculating average concentrations for specific objects or subcellular spaces from these images have also been described. These procedures require identification and isolation of objects either manually, with graphics tools, or automatically, by intensity thresholding.^{7,8} Whereas these selection methods are often successful and efficient at defining areas or objects from images, cases such as the isolation of multiple objects, small objects, or objects that have intensities similar to other structures in the image would benefit from more refined selection procedures. This paper describes how simple image processing routines were implemented for selecting and segmenting multiple small objects from a digitized scanning transmission electron microscope (STEM) image. The procedures described work equally well for both STEM and elemental images, but their most useful application is for selecting objects from STEM images, where thresholding methods often include unwanted structures.

Instrumentation and Image Collection Conditions

Digital STEM and elemental images of freeze-dried cryosections were acquired as described elsewhere⁷ in a JEOL 1200 scanning transmission electron microscope fitted with a Link AN10000 Si(Li) drifted x-ray detector. Image resolution was either 512 × 512 pixels for STEM images collected without accompanying x-ray detection, or 128 × 128 pixels when x-ray images were also collected. Routines for carrying out image arithmetic and image convolutions are resident in Link's DIGIPAD suite of programs and routines for segmenting images were written by use of the Link Fortran compiler.

The authors are at the Center for Bioengineering (WD 12), University of Washington, Seattle, WA 98195. They thank Dr. Yongmin Kim, Ms. Linda Wilkinson, Ms. Shellee Cunningham, and Ms. Mary Carney for helpful technical support and advice. This work was supported by NIH grant DE08084.

Feature Selection

The example used in this report is the selection of secretory granules from a digitized STEM image of rat parotid salivary gland (Fig. 1a). The large number of granules present and their uniform electron density suggests that intensity thresholding should be used for their selection. Unwanted structures such as mitochondria, which have intensities similar to granules, were excluded by the formation of three large binary masks corresponding to regions containing only granules and cytoplasm; these masks were then multiplied with the original image to retain only the masked regions (Figs. 1b-d). Although mitochondria were eliminated manually by intentional exclusion from the masks, other descriptors, such as shape factors or elemental content, could have been used to differentiate the organelles.^{7,9,10} The threshold intensity range for selecting granules from this reduced image was chosen by determining which peak in the histogram of intensity levels corresponds to granules (Fig. 1e). Figure 1(f) shows the image that remains when only the pixels with intensities lying in the granule peak are retained. The image is now composed only of granules and points considered to be noise.

Various methods are available for eliminating noise from images.^{9,11} In this example, erosion and dilation matrices¹¹ were applied for sequential stripping and addition of pixel layers from and to the borders of objects. The result of this procedure was to remove the noise while proper shapes for individual granules were maintained (Fig. 1g).

Superimposing the final mask on the original image is the simplest way to assess the success of the selection procedure. Edge enhancement filters applied to masks made from high-resolution (e.g., 512 × 512 pixel) images offer another means for determining the accuracy of mask fit. Only the outlines of the individual granule masks remain after application of a gradient filter (Fig. 1h); superposition on the original image illustrates that the selection procedure was able to retain nearly all of the granules and reproduce most of their individual shapes.

Image Segmentation

Once masks are made, they can be easily applied to the corresponding elemental images and average concentrations calculated over the objects masked.⁷ It may also be of interest to separate each of the objects masked in an image from one another, for example to calculate elemental concentrations for each object, measure each object's dimensions, calculate shape

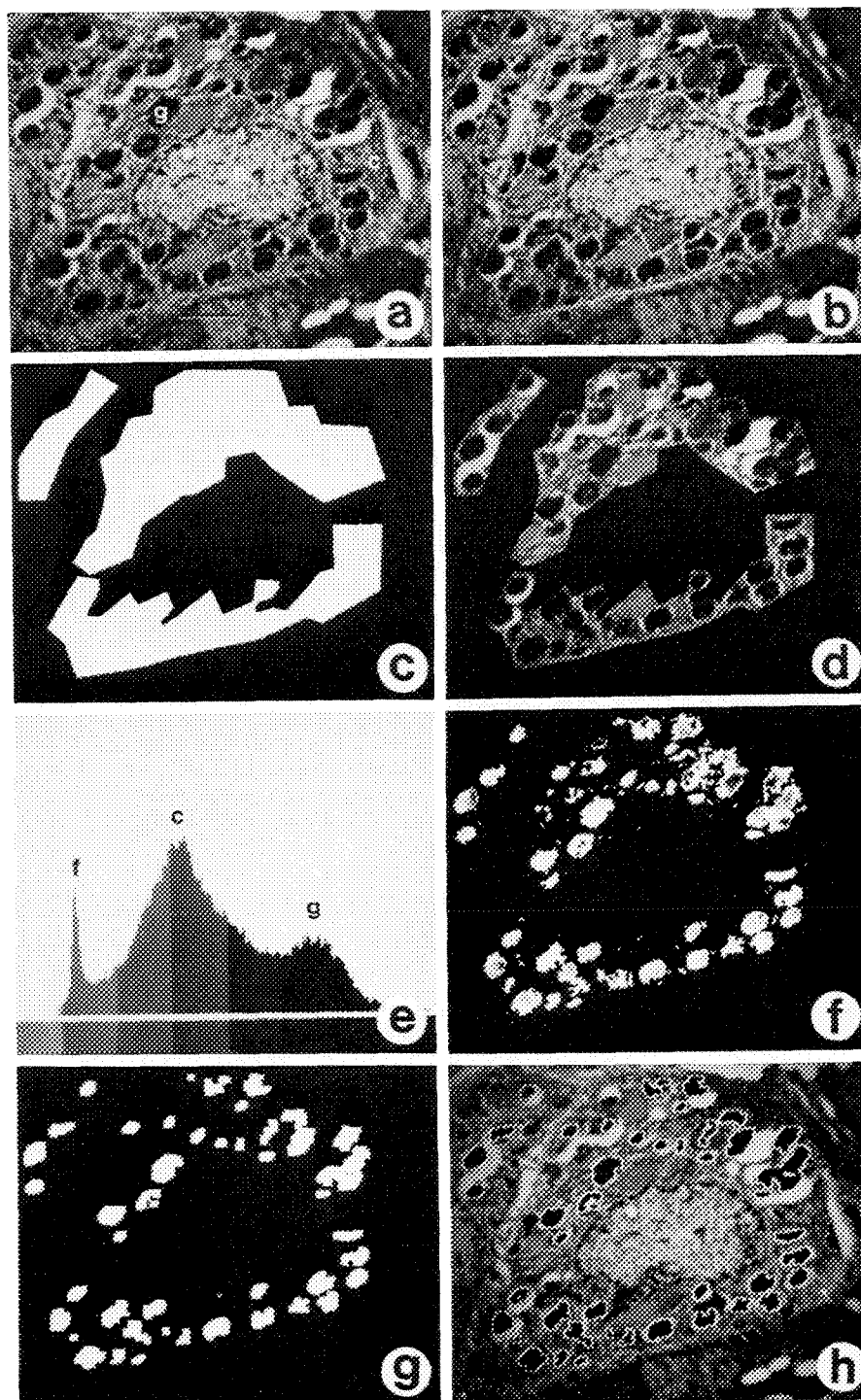


FIG. 1.--Demonstration of feature selection procedure described in text. Resolution = 512×512 pixels for all images shown. (a) Digital STEM image of rat parotid gland cryosection; bar = $2 \mu\text{m}$, c = cytoplasm, g = secretory granule, m = mitochondrion, n = nucleus. (b) Three granule regions outlined to exclude mitochondria and other extraneous structures. (c) Binary mask for (b); white regions have intensity value = 1, black regions have intensity value = 0. (d) Product of (a) and (c) shows that only granule and surrounding cytoplasmic regions remains. (e) Histogram of intensity levels for (d) with each peak corresponding to a different subcellular space; c = cytoplasm, f = film, g = granules. (f) Image resulting from thresholding on the range of intensity values found in the granule peak determined in (e); contrast was increased to allow granule regions to be visible against black background, so that some gray levels within granules have been lost. (g) Binary image resulting from erosion and dilation operations on (f); "noise" pixels have been removed by the process. (h) Gradient filter convolved with (g) caused edge enhancement of granule masks; edge-enhanced mask was superimposed on original image to demonstrate accuracy of mask fit for granules.

descriptors for the objects, or simply count the number of objects masked.

To accomplish this segmentation, various methods are available⁹ to identify and store in a file accessible to the user information concerning locations, shapes, areas, etc., of each of the objects present. One method easily implemented in a user-defined program is entitled "line segment encoding," which involves storing the location and lengths of all line segments comprising the masked objects in one or several files. If x-ray images have also been collected, elemental concentrations

for each object masked can be quickly calculated.

Application of this procedure to a granule mask from another image of rat parotid salivary gland (not shown) was carried out; the results for [Cl] and [K] in each of the granules selected is shown in Fig. 2. The plot indicates a positive correlation for [Cl] with [K] in the granules from this image that agrees with results from several conventional long-lifetime scanning-raster analyses collected from the same tissue (unpublished results). However, two important points must be consid-

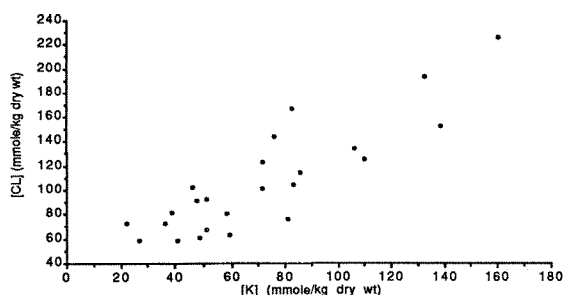


FIG. 2.--Scatterplot of elemental concentration data for granules from single image of rat parotid salivary gland. Resolution of image masked was 128×128 pixels and magnification was 10K. Each point on plot represents [Cl] and [K] concentrations from single granule masked from image. Total number of granules masked was 24.

ered when concentrations for objects composed of as few pixels as these are being determined. Care must be taken during the mask formation procedure to assure that the edges of the individual masks are an adequate distance away from granule borders. This need arises when specimens are tilted to maximize x-ray collection by the x-ray detector; granule borders parallel to the tilt axes will overlap neighboring cytoplasmic regions and cause concentrations in edge pixels to reflect a combination of both granule and cytoplasmic values. In addition, total x-ray collection livetimes for the pixels masked within each granule must be sufficiently long for the particular analysis conditions used to detect the elemental concentrations of interest.^{4,7} Therefore, these requirements (1) of being limited to interior pixels and (2) of total x-ray collection livetimes together dictate that elemental images must have sufficient magnification so that selected objects are composed of a sufficient number of "usable" pixels. The average live-time per granule masked for the data in Fig. 2 was 29 s, which appears sufficient for detecting the illustrated relationship. Thus, results similar to and consistent with those found from a series of conventional raster scan analyses can be gained by use of these procedures for feature selection and image segmentation.

Conclusion

A set of procedures has been described that selects multiple objects of uniform intensity from a digital STEM image. An example shows that elemental concentrations found for the individual objects yield results similar to those gained from conventional raster-scan analyses. These procedures were developed by the application of simple image processing concepts to the particular problems associated with object selection from STEM images and should be helpful in simplifying and extending the types of analyses possible with digital elemental and electron images.

References

1. M. E. Cantino and D. E. Johnson, "Elemental imaging techniques in studies of striated muscle," *Microbeam Analysis--1988*, 427-428.
2. J. R. Herlong, A. LeFurgey, P. Ingram, J. D. Shelburne, L. J. Mandel, and L. A. Hawkey, "Quantitative x-ray imaging of human cystic fibrosis nasal epithelium," *ibid.*, 447-450.
3. P. Ingram, A. LeFurgey, S. D. Davilla, J. R. Sommer, L. J. Mandel, and M. Lieberman, "Quantitative elemental x-ray imaging of biological cryosections," *ibid.*, 433-439.
4. R. D. Leapman and C. E. Fiori, "Biological applications of EELS and EDXS mapping," *Analytical Electron Microscopy--1987*, 184-186.
5. A. P. Somlyo, "Compositional mapping in biology: X rays and electrons," *J. Ultrastruct. Res.* 88: 135-142, 1984.
6. A. J. Saubermann and R. V. Heyman, "Quantitative digital x-ray imaging using frozen hydrated and frozen dried tissue sections," *J. Microsc.* 146: 169-182, 1987.
7. J. G. Wong, L. E. Wilkinson, S. W. Chen, K. T. Izutsu, D. E. Johnson, and M. E. Cantino, "Quantitative elemental imaging in the analytical electron microscope with biological applications," *Scanning* (in press).
8. C. E. Fiori, "Quantitative compositional mapping of biological cryosections," *Microbeam Analysis--1986*, 183-186.
9. K. R. Castleman, *Digital Image Processing*, New Jersey: Prentice-Hall, 1979.
10. D. E. Newbury, R. B. Marinenko, D. S. Bright, and R. L. Myklebust, "Computer-aided imaging: Quantitative compositional mapping with the electron probe microanalyzer," *Scanning* 10: 213-225, 1988.
11. P. J. Statham, "Statistics and wishful thinking in microbeam and image analysis," *Microbeam Analysis--1985*, 230-234.

COMPUTER-ASSISTED BRIGHTFIELD SIGNAL MEASUREMENT OF WATER CONTENT IN FROZEN HYDRATED AND DEHYDRATED GELATIN THIN SECTIONS: A PRELIMINARY REPORT

J. J. Strain, D. A. Kopf, Ann LeFurgey, Peter Ingram,
L. A. Hawkey, and S. D. Davilla

Brightfield signal intensity, an effective and accurate measure of mass thickness, has proved itself to be especially powerful as an adjunct to electron probe x-ray microanalysis (EPXMA).¹ Several other techniques capable of providing mass thickness measurements (e.g., continuum x-ray monitoring and backscatter electron detection) result in destruction of specimen integrity at the levels of irradiation required to obtain a measurable signal; these methods also may require correction factors due to their extreme sensitivity to local variation in specimen composition.² Furthermore, both techniques have been described by investigators as lacking the accuracy of brightfield signal mass determination.² The zero-loss signal of electron energy loss spectroscopy (EELS) has recently become the standard for mass thickness measurement, but requires expensive instrumentation.³ Other factors that may influence the choice of approach to mass thickness measurement include advances in mini- and microcomputer hardware, and new software for data capture, display, and analysis.^{4,5}

Irrespective of measurement technique, intracellular water content and mass thickness determination are required to convert elemental measurements (mmols/kg dry weight) from freeze-dried biological cryosections by EPXMA to more physiologically relevant ones (ion or elemental concentration/unit wet weight). In this paper, we describe one brightfield signal method for estimating changes in the water content of frozen hydrated gelatin sections and tracking hydrated specimen location for later analysis in the dehydrated state.

Materials and Methods

The computer software is a revised version of a general purpose image acquisition and analysis program ("EYESPI") developed by two of the authors (DAK,SSD) for use with a personal computer (Macintosh II, Apple computer) and compatible hardware systems. The specifics of this analysis software have been reported previously.⁶ Hardware requirements for electron microscope-to-minicomputer image transfer include a data acquisition card (National Instruments), enhanced video adaptor for

256 graylevel/color viewing, and 2 megabytes minimum of RAM memory. (Image capture and analysis functions are limited by available memory.) As yet, we have neither an absolute calibration of specimen mass nor the computer software necessary to extract true mass thickness by compensation for local tilt. Consequently, we report here only measurements of relative total section mass between hydrated and dehydrated sections, which are insensitive to these effects.

Images were retrieved from an electron microscope (JEOL 100CX-II) operating in both transmission electron microscope (TEM) and scanning-transmission electron microscope (STEM) modes, utilizing a cold-finger anti-contamination device and a cold stage (Gatan 626). Microscope experimental protocol was identical for both pre cryotransfer and post dehydration image capture: (1) accelerating voltage = 80 keV, (2) LaB₆ filament, (3) starting vacuum = $1-2 \times 10^{-7}$ Torr, (4) default condenser lens current (CL1) adjusted to give a beam current of approximately 10^{-11} A. [The instrument configuration was modified by the installation of an EELS detector prior to analysis of grid #3 and adoption of free-lens control (beam current = 0.2×10^{-11} A) prior to studies of grid #6.]

Gelatin was selected as the object of study because the water content can be varied to mimic that of cells (70-90% dependent on cell and cellular compartment)⁷ and because it is generally available with ease and reproducibility of preparation. Parallels in behavior between biological tissue and gelatin in the uptake of macromolecules (e.g., tannic acid, OsO₄) further support the usage of gelatin as a modeling medium.⁸ Thirty g of gelatin (Matheson, Coleman, and Bell; Gx45 L404) were dissolved in 100 ml of warm, double-distilled, deionized water to generate a 30% solution, then subsequently agitated and heated for 1 h on a hotplate. Gelatin was deposited as a droplet on 12 aluminum stubs and plunge frozen into liquid propane; long-term storage in liquid nitrogen was by laboratory protocol.⁹

Cryomicrotomy yielded thin gelatin sections. (In a previous study using the same cryomicrotometer settings, tissue sections measured by EELS were in the thickness range of 2000-4000 Å.) Multiple sections (15-20) 5-20 were deposited on each fine-bar 200 mesh nickel grid to assure an adequate amount of analyzable material, followed by cryotransfer to the cold stage. Stage thermocouple temperatures ranged from -175 to -163 C at insertion.

After vacuum stabilization, a 256×256

The authors are with the School of Medicine, Division of Physiology, Department of Cell Biology, Duke University, Durham, NC 27710, except Peter Ingram, who is with Research Triangle Institute, Research Triangle Park, NC 27709. This work is supported by NIH grants NIDDK37704, NIDDK26816, HL17670 and HL 27105.

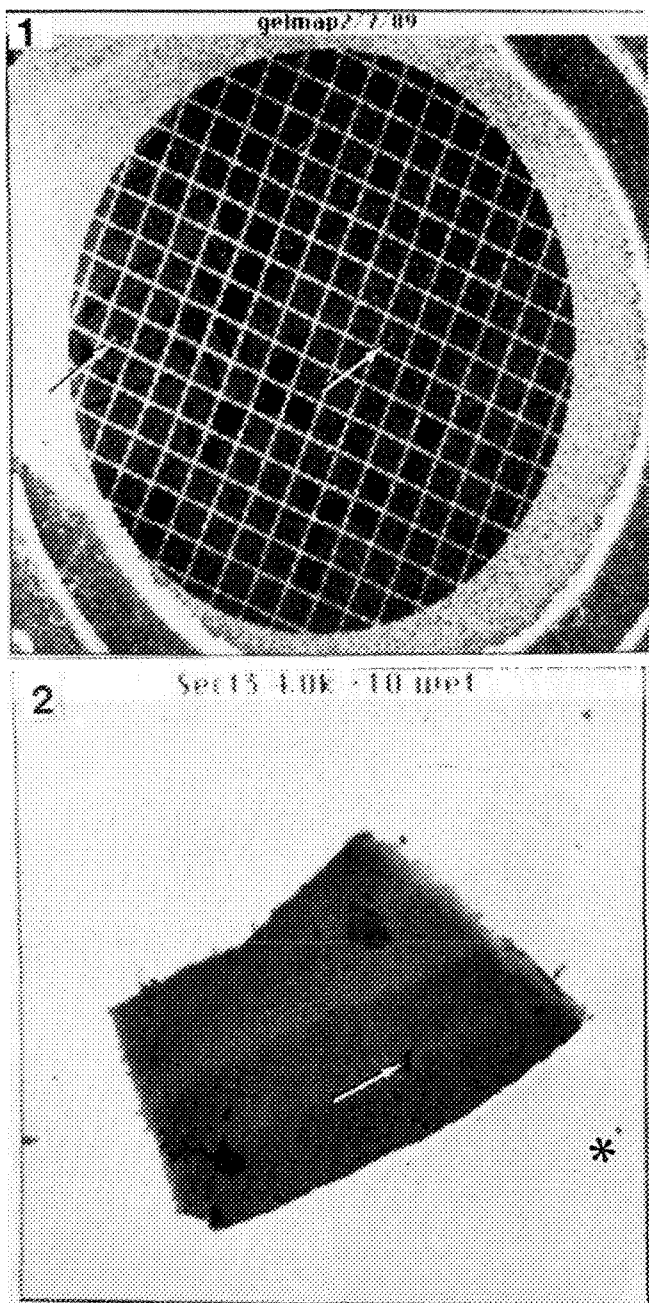


FIG. 1.--256 × 256 pixel "grid-map" (50× magnification in SEM mode) taken of grid #7 with evidence of breaks in carbon film. Sections appear as white objects (arrows) on black background; image can be enlarged in EYESPI to provide more detail.

FIG. 2.--Frozen-hydrated gelatin section at 0.34 μm full scale, inclination +10°. Note evidence of ice on specimen (arrows), ice crystal on dark carbon film (*), and lack of clarity in features.

pixel intensity "map" (Fig. 1) containing gel section locations was made at 50× magnification in secondary electron mode (SEM). Acquisition parameters (including the size of the pixel array) were input into a simple, menu-driven computer system; control of the microscope was relinquished to the computer; and a brightfield

image was obtained. Each image may be altered in size, brightness, and contrast to provide maximal positional information. All scans discussed below were performed in the same manner.

An ideal gel section was considered to be flat, located in the center of the grid square, and distant from the gridbar or any damaged portions of the carbon film (Fig. 2). Hydration state was deemed adequate if multi-sized ice crystals were present on the film, sample, and adjacent gridbars. (Whether the ice was from the initial freezing event or subsequent deposition could not be determined, but its presence did suggest sufficient temperature to maintain a hydrated specimen.) Selected gel fragments were magnified until they occupied a majority of the viewscreen and subsequently were scanned at a cold-stage inclination of +10° and -10° from the horizontal to form a stereo pair (to be used in future analyses). Magnification, contrast, scan tilt angle, and comments were recorded for reference, as was the position of the section on the grid map.

Dehydration protocol for the specimen grid was as follows: (1) increasing the temperature 5 C every 5 min to -90 C, (2) controlled warming for 60 min to -80 C, (3) 10 C every 5 min to -40 C, (4) unimpeded warming to 30 C (approximately 10-15 min). After location via a gridmap, dehydrated sections were scanned at conditions identical to those of their hydrated state (Fig. 3).

Images from both frozen hydrated and dehydrated sections were transferred to 3.5in. floppy diskettes for storage. Individual 256 × 256 pixel image files occupied approximately 256 kilobytes each in EYESPI format (i.e., grayscale range = -2048 to +2048).⁶ Examination of gel section area, gel section mean pixel intensity, and background mean pixel intensity was performed on selected sections using quantitative measurement facilities from the EYESPI analysis menu. Tracing the circumference of the specimen provided average intensity and a summation of pixel points occupied by the region to a statistics window associated with the image (Figs. 4 and 5). The following calculations were used.

$$\frac{(I_s - I_b)_d P_d}{(I_s - I_b)_w P_w} = F_d \quad (1)$$

$$\frac{(P_w - P_d) \times 100}{P_w} = \% \text{ Shrinkage} \quad (2)$$

$$\frac{P_w}{M^2} = SA_w \quad (3)$$

$$\frac{P_d}{M^2} = SA_d \quad (4)$$

where I_s = mean fixed intensity of the sample, I_b = mean fixed intensity of the background, d = dry, w = wet, P_d = dry sample number of

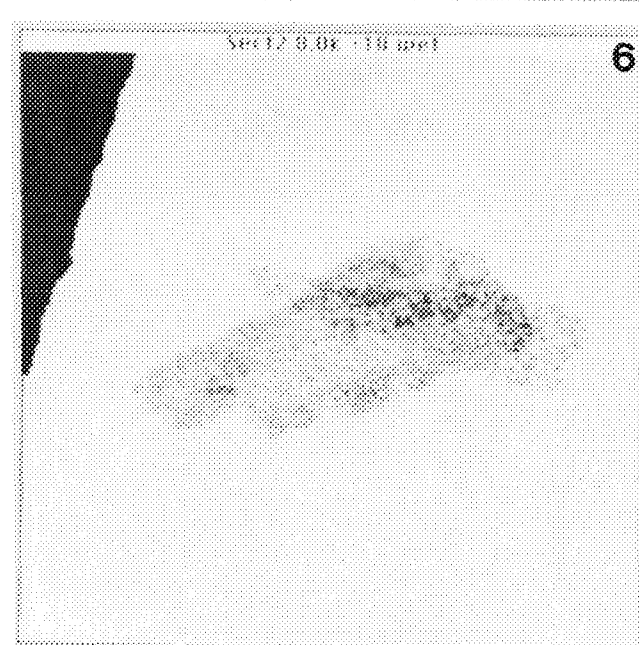
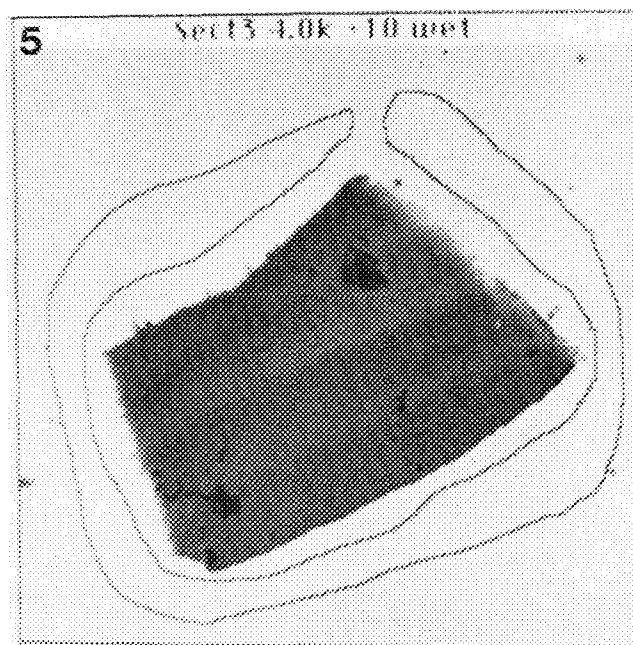
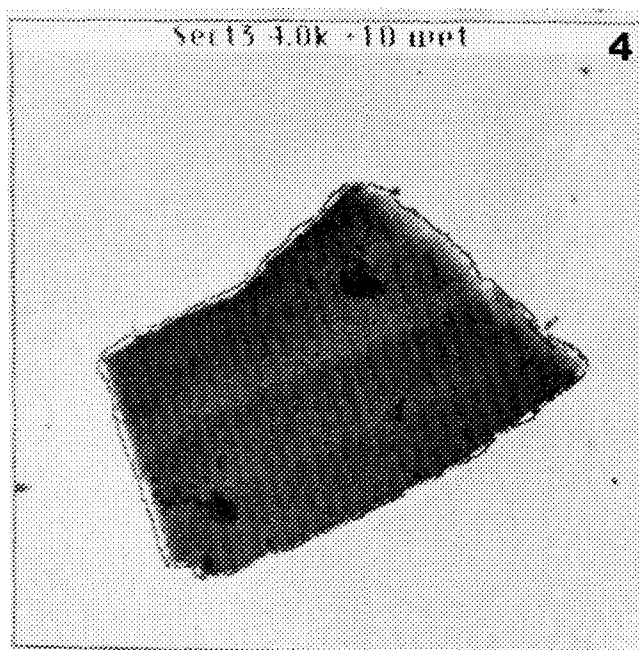
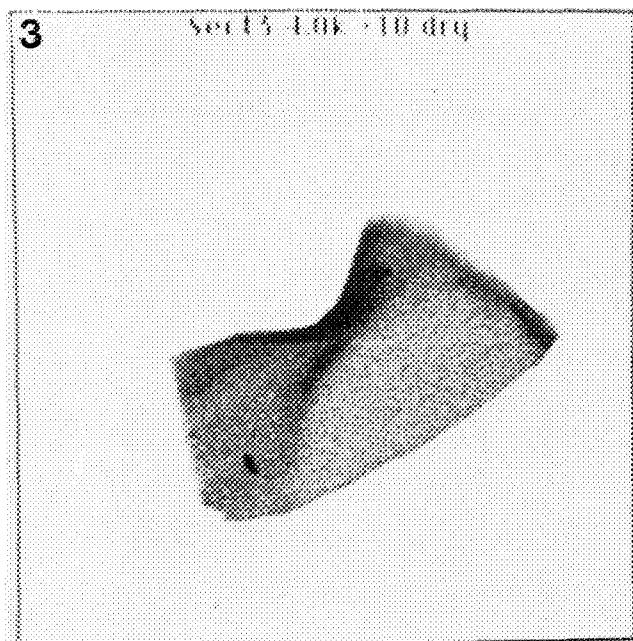


FIG. 3.--Dehydrated gelatin section $0.34 \mu\text{m}$ full scale, inclination $+10^\circ$. Same section as in Fig. 2 after dehydration. Structures of section are more visible, and ice crystals are not visible. Background intensity has increased as would be expected from loss of surface ice.

FIG. 4.--Gel section statistics: circumferential tracing of gelatin provides information about area and average intensity, which is recorded for both frozen hydrated and dehydrated sections.

FIG. 5.--Background statistics: background intensity is measured by marking an arbitrary annulus around sample and measuring average intensity per point for that area. This information is gathered for frozen-hydrated and freeze-dried sections and then applied with results from Fig. 4 into Eq. (1).

FIG. 6.--Irradiation damage to frozen-hydrated gelatin section results in vesicular pattern which at higher magnification demonstrates rings of gelatin with apparent lack of material in center.

pixels, P_w = wet sample number of pixels, F_d = fractional dry weight, SA_d = area of dry gelatin section, and SA_w = sectional area of wet gelatin section. SA_d and SA_w are normalized by division by the magnification M . Graphing and complex statistics were calculated on an external analysis package (SYSTAT, Systat, Inc.).

Results and Discussion

Seventy sections on 8 different grids were analyzed and dehydrated by the techniques described above. As seen in Fig. 1, both positional and structural information is available from these mapping images, even at low magni-

TABLE 1.--General statistics for frozen-hydrated and dehydrated gelatin sections used in the fractional dry weight measurements.

# of Cases	Magnification (x1000)	Gel Sectional Area		% Shrinkage	Fractional Dry Weight
		Wet	Dry		
20					
Min	1.000	204.583	95.240	5.981	0.300
Max	6.000	12240.000	10903.000	71.943	0.444
Mean	2.775	2288.996	1496.534	43.178	0.361
Std. Dev.	1.509	2767.001	2396.169	22.687	0.038

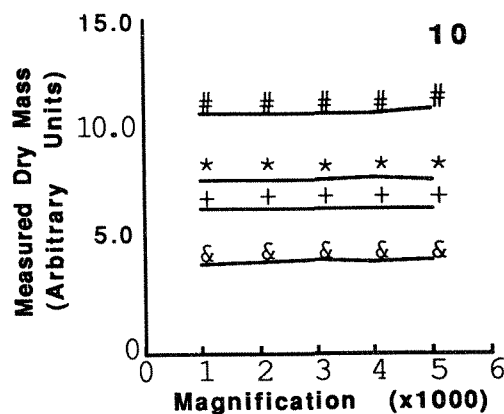
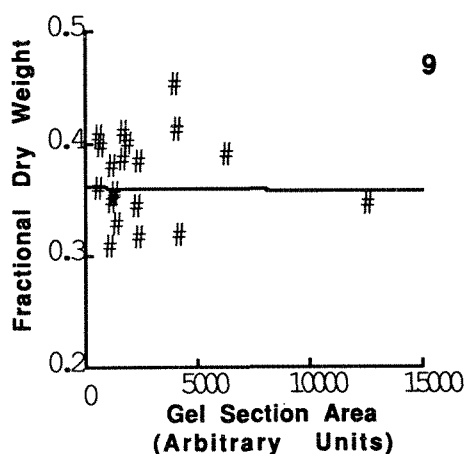
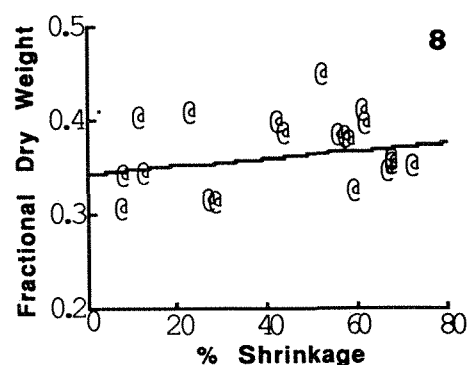
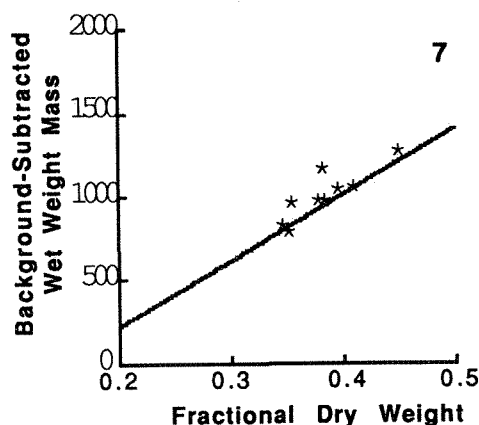


FIG. 7.--Background-subtracted wet weight mass vs fractional dry weight, as calculated from Eq. (1).

FIG. 8.--Fractional dry weight vs % shrinkage, as calculated from Eqs. (1) and (2).

FIG. 9.--Fractional dry weight vs gel section areas, as calculated from Eqs. (1) and (3).

FIG. 10.--Measured dry mass vs magnification.

fication. Sixty-eight of seventy sections, identified and processed by EYESPI grid-mapping, were relocatable post-dehydration. Three more sections were unusable for analysis due to re-orientation, overlap onto neighboring sections, or movement onto a gridbar during dehydration.

Quantitation of water loss in frozen-hydrated and dehydrated sections was limited to selected data from the flattest sections on two grids, a total of 22 sections. Grid 1 was ex-

amined before the addition of a zero-loss EELS system with replacement brightfield detector to the JEOL 100CX-II microscope. Two sections were eliminated from experimental calculations due to excessive manipulation: the first was scanned multiple (>20) times, and was used to find the optimum microscope settings for the subsequent grid analyses, whereas the second was sufficiently small to render it difficult to trace. General statistics for the remaining

twenty sections are shown in Table 1.

Mean fractional dry weight was calculated to be $36.1 \pm 3.8\%$, representing the water loss associated with dehydration, about 20% greater than the initial preparation. Among potential factors contributing to an elevated fractional dry weight would be any form of dehydration before or during the measurement of the frozen-hydrated brightfield signal, for example during the low-magnification SEM mapping image, or incomplete dehydration during freeze-drying. Cryomicrotomy and cryotransfer were suspect, although recent studies show little significant mass loss when sections are correctly prepared.¹¹ However, there were examples in our experiments where elevated stage temperature led to elevated mass loss and visible irradiation damage (Fig. 6). Whether this pattern may be due to ice crystal formation as well has not been determined.¹² To further complicate the issue, Cantino et al. have reported significant radiation-induced mass loss from freeze-dried sections.¹³

Further consideration must be given to the limits inherent in brightfield signal measurement. Measurement of transmission signal intensity is compromised in specimens with mass thickness of greater than $0.6\text{--}1.0 \text{ g}\cdot\text{m}^{-2}$ (3000–5000 Å), depending on accelerating voltage.² Examination of a subset of 9 gelatin sections, imaged at identical contrast, permitted a comparison of background-subtracted wet weight mass vs fractional dry weight (Fig. 7). These values suggested an increasingly nonlinear brightfield transfer characteristic for thicker sections. The increased thickness on a per pixel basis may be secondary to ice (Fig. 3), and, due to insufficient signal transmission in the hydrated specimen, may manifest itself as an apparent lack of dehydration.

Of particular interest is the variation in percent shrinkage. Average percentage change for all sections is greater than 40%, and this change is associated with an eleven-fold difference between the minimum and maximum values. The wide range, as well as the specimen's sectional area, appears to have little correlation with fractional dry weight (Figs. 8 and 9). Possible sources for this result include local folding with shrinkage and discrete changes in the orientation of a specimen with respect to the grid.

Three further analyses were performed to examine reproducibility, variance due to changes in magnification, and the effects on a specimen by irradiation from serial scans. In order to investigate error associated with obtaining an object's circumference, measurements on a single section were repeated 20 times. Mean area in pixels was equal to 6172.70 (standard deviation [s.d.] = 64.542). Measurement of mean background-subtracted mass equaled 1571.71 (s.d. = 16.63). A second study obtained image data from four gelatin sections each at five different magnifications. It was surmised that the larger specimen size (or higher magnification) might result in a proportional decrease in experimenter error. The results are illus-

trated in Fig. 10. As the graph indicates, changes in magnification do not appear to alter the values obtained with this technique. The final experiment examined the effects of repetitive scanning on a dehydrated section. The difference in mass thickness of a section before and after 30 scans was $1.64 \pm 0.02\%$. Changes in the mean sample pixel intensity and fractional dry weight after a similar challenge were $0.8 \pm 0.02\%$ and $1.0 \pm 0.02\%$, respectively.

Future research will focus on more accurate specimen thickness measurements for verification of these findings. If the brightfield signal is to be used, it is necessary to determine the thickness at which nonlinear measurement of the signal begins. Initial studies are under way in this laboratory on folded and tilted carbon films of known thicknesses to estimate the value above which signal loss occurs. Similarly, documentation of the mass thickness via a zero-loss EELS analysis (estimated 3% error) will be used to calibrate measurements from this brightfield signal technique.^{10,14,15} Concurrent projects using stereo pairs to ascertain local tilt and thickness in areas of specimen tilt will also be tested, with the eventual application of this computer-controlled acquisition and brightfield-signal measurement technology to the analysis of intracellular water compartmentation in biological cells and tissues.¹⁰

References

1. P. W. J. Linders et al., "Calibration of transmission electron microscopic mass determination using objects with known mass distribution," *J. Microscopy* 130: 85, 1983.
2. P. W. J. Linders et al., "Mass determination of thin biological specimens for use in quantitative electron probe microanalysis," *SEM/1982 IV*, 1603.
3. P. A. Crozier and R. F. Egerton, "Mass-thickness determination by Bethe-sum-rule normalization of the electron energy-loss spectrum," *Ultramicroscopy* 27: 9, 1989.
4. S. D. Davilla et al., "Real-time graphics display of mass variation or elemental concentration during electron beam microanalysis using a general purpose computer," *J. Microscopy* 149: 153, 1988.
5. P. Ingram et al., "Real-time quantitative elemental analysis and imaging in cells," *Microbeam Analysis--1987*, 179.
6. P. Ingram et al., "Quantitative elemental x-ray imaging of biological cryosections," *Microbeam Analysis--1988*, 433.
7. A. LeFurgey et al., "Electron probe x-ray microanalysis of cultured chick heart cells: In situ calcium content of mitochondria and cytoplasm," *Proc. VIIth Intern. Washington Symposium, Cell Calcium Metabolism '87* (Abstract), 135, 1987.
8. T. Caceci and K. E. Frankum, "Measurement of increased uptake of osmium in skin and in a gelatin model tissue treated with tannic acid," *J. Microscopy* 147: 109, 1987.
9. A. LeFurgey, P. Ingram and M. Lieberman,

"Quantitative microchemical imaging of calcium in Na-K pump inhibited heart cells," *Cell Calcium* 9: 218, 1988.

10. D. A. Kopf et al., "Mass thickness images of frozen hydrated and freeze-dried sections," *Microbeam Analysis--1986*, 241.

11. H. P. Zingheim, "Sublimation rates of ice in a cryoultramicrotome," *J. Microsc. (Oxford)* 133: 307, 1984.

12. Y. Draenert and K. Draenert, "Ice crystal damage in freeze-dried articular cartilage studies by scanning electron microscopy," *SEM/1982* IV, 1799-1804.

13. M. E. Cantino et al., "Beam induced mass loss in high resolution biological microanalysis," *J. Microscopy* 144: 317, 1986.

14. D. E. Johnson, "Post specimen optics for energy loss spectrometry," *SEM/1980* I, 33.

15. R. D. Leapman et al., "Digital processing of electron energy loss spectra and images," *SEM/1985* I, 1.

ION DISTRIBUTION IN EPITHELIAL CELLS STUDIED BY X-RAY MICROANALYSIS

G. M. Roomans, Thomas von Zglinicki, A. J. Spencer

All transport of solutes to and from the body tissues has to pass epithelial cells, which therefore play an important role in regulating this transport. Malfunctioning of the transport of ions and water through epithelia therefore can lead to disease. An example of a disease associated with a defective regulation of transepithelial ion and water transport is cystic fibrosis (CF). In CF patients transport of chloride and water across, for example, the respiratory and intestinal epithelium appears to be defective. In the present paper, studies on ion distribution in these epithelia in experimental animals are reviewed.

X-ray Microanalysis of Intestinal Epithelium

The intestinal epithelium is a complex epithelium, in which several cell types with different functions coexist. It is assumed that the villus cells are mainly absorptive, whereas the crypt cells secrete ions and water. A detailed study of element (ion) concentrations in various compartments of the mouse intestinal mucosa was undertaken to serve as a basis of reference for further studies dealing with changes in ion distribution due to stimulation or inhibition of ion transport.

The study was carried out on mice (male and female, about 20-25 g). The animals were killed by cervical dislocation and samples from the proximal part of the jejunum were punched out and simultaneously frozen with a cryobioptic needle.¹ Thin cryosections were cut at a temperature of about 160-180 K, freeze-dried, and analyzed in a Philips 400T transmission electron microscope equipped with a LINK energy-dispersive analysis system. Quantitative analysis of the spectra was carried out according to the continuum method, by use of cryosections of a gelatin/glycerol matrix containing mineral salts in a known concentration as standards.²

Analysis was carried out in villus cells and in crypt cells. On the basis of their morphology, two types of crypt cells were distinguished: crypt A cells with secretory granules resembling those of Paneth cells, and crypt B cells.

G. M. Roomans and A. J. Spencer are at the Department of Human Anatomy, University of Uppsala, Box 571, S-75123 Uppsala, Sweden. Thomas von Zglinicki was on leave from the Department of Pathology, Charite Hospital, Berlin, German Democratic Republic. This work was supported by grants from the Swedish Medical Research Council (Project 07125), the Swedish National Association against Heart and Chest Diseases, and the Swedish Association for Cystic Fibrosis.

In villus cells, a gradient of sodium from 137 mmol/kg dry weight in the brush border to 68 mmol/kg in the basal cytoplasm was noted. Similarly, a chloride gradient from 154 mmol/kg in the brush border to 48 mmol/kg in the basal cytoplasm was observed. On the other hand, the concentration of potassium slightly increased from 615 mmol/kg in the brush border to 700 mmol/kg in the basal cytoplasm. Similar ion gradients were noted in the crypt B cells: for sodium from 202 (apical) to 90 (basal) mmol/kg, for chloride from 275 (apical) to 1236 (basal) mmol/kg, and for potassium from 708 (apical) to 1010 (basal) mmol/kg dry weight.

Simultaneously, the intracellular water distribution was determined from the measured optical transmission of electron micrographs.³ The water content of absorptive cells was significantly higher than that of crypt B cells. In the villus cells, the luminal cytoplasm had a higher water content in the villus cells, whereas the reverse was the case in the crypt B cells.

Stimulation of secretion was elicited by intraperitoneal injection with isoproterenol (20 mg/kg body weight) or pilocarpine (8 mg/kg body weight). In some of the isoproterenol-injected animals, an attempt was made to inhibit secretion by injection of the adenylate cyclase inhibitor alloxan (175 mg/kg body weight, 1 min after injection of isoproterenol).

Upon stimulation with isoproterenol or pilocarpine, the chloride concentration in the interstitium decreases, most likely as a result of chloride secretion. Crypt A cells react to stimulation as expected for electrolyte secreting cells. The cytoplasmic chloride concentration decreased from 100 ± 9 to 64 ± 10 mmol/kg dry weight after stimulation with isoproterenol. This decrease is prevented by alloxan, and is therefore cAMP-dependent. Pilocarpine produced an even more pronounced decrease of the intracellular chloride concentration (to 24 ± 7 mmol/kg). Crypt B cells as well as Paneth cells, on the other hand, reacted to isoproterenol stimulation with an increase in the intracellular chloride concentration. This increase could be inhibited by cAMP. One may speculate that these cells take up chloride via the basolateral chloride transporter, but do not secrete the chloride via a cAMP-controlled apical chloride channel. Villus cells also react to stimulation by isoproterenol with an increase in intracellular chloride concentration.

Intestinal chloride (and water) transport is known to be inhibited in patients with cystic fibrosis, which may cause or contribute to

meconium ileus in the newborn and meconium ileus equivalent in the older patients. The inhibition of chloride and water transport would be caused by the malfunctioning of a cAMP-regulated chloride channel in the apical cell membrane. It would appear from our data that the crypt A cells possess a cAMP-regulated apical chloride channel.

X-ray Microanalysis of Tracheal Epithelium

In tracheal epithelium it is assumed that chloride, sodium, and potassium enter the cell via a cotransport mechanism in the basolateral membrane. Chloride ions are secreted at the apical side via a cAMP-regulated channel. Water transport follows the flux of chloride through the epithelium.

For studies of ion distribution in tracheal epithelial cells, hamster trachea was used. The animals were anesthetized with sodium pentobarbital, and a small piece of trachea was dissected and frozen in liquid propane cooled by liquid nitrogen. In situ freezing with the cryobioptic needle was attempted but not successful because of the presence of the tracheal cartilage rings. Thin cryosections were cut on a cryoultramicrotome, transferred in the frozen state to the electron microscope, and freeze-dried in the column. Quantitative analysis was carried out as described above.

In contrast to the results obtained in mouse intestinal epithelium, no clear ion gradients across the ciliated epithelial cells could be observed. Chloride concentrations in the tracheal epithelium (250-300 mmol/kg dry weight) were considerably higher than in the intestinal epithelium. That could be due to the fact that the animals were under anesthesia, or that the tissue was not frozen in situ (as was the intestinal epithelium), and that dissection and removal of the tissue would have caused an increase of the intracellular chloride concentrations. However, stimulation with isoproterenol (intraperitoneal, 20 mg/kg body weight) caused a significant decrease in the intracellular chloride channel, similar to what was described above for the intestinal crypt cells. A decrease of the intracellular chloride concentration was also noted in cultured normal human respiratory epithelial cells.⁴ Therefore, the anesthesia does not appear to block chloride secretion in the tracheal epithelium. This finding should make it somewhat easier to carry out similar studies in human respiratory epithelium in situ.

References

1. T. von Zglinicki et al., "Fast cryofixation technique for x-ray microanalysis," *J. Microsc.* 141: 79, 1986.
2. G. M. Roomans, "Quantitative x-ray microanalysis of biological specimens," *J. Electron Microsc. Techn.* 9: 19, 1988.
3. T. von Zglinicki et al., "Estimation of organelle water fractions from frozen-dried cryosections," *J. Microsc.* 146: 67, 1987.

4. G. M. Roomans et al., "X-ray microanalysis of respiratory epithelial cells in cystic fibrosis," *Proc. 40th Ann. Meeting SCANDEM*, Aarhus, 1988, 38.

SODIUM, POTASSIUM, AND CHLORINE IN ELECTROLYTE SECRETING CELLS IN THE INTESTINE

Thomas von Zglinicki and G. M. Roomans

Secretion of salt and water from the intestine can be stimulated *in vitro* by increases in the concentrations of the second messengers cAMP and/or calcium. Whereas villus cells are absorptive, there is evidence that secretion takes place in the crypts.¹ However, intestinal crypts are composed of various cell types including so-called undifferentiated epithelial cells which may or may not contain secretion granula, Paneth cells, Goblet cells, and others.² Therefore, cells actually engaged in electrolyte secretion *in vivo* have not yet been identified.

Experimental

Intestinal secretion in mice was stimulated by injection with either isoproterenol or pilocarpine. In one series of experiments, stimulation by isoproterenol was blocked by alloxane, a potent inhibitor of the adenylate cyclase. Samples of the intestine were taken by a cryobiological method.³ Freeze-dried cryosections about 0.5 μm thick were prepared and measured at 100 kV in the transmission mode in a Phillips EM 400 equipped with a field-emission gun and a Link AN 10 000 microanalyzer. For standardization, frozen-dried cryosections of gelatin containing known amounts of salts were used.⁴

Element concentrations were probed in the cytoplasm of Paneth cells, crypt epithelial cells containing small secretion granula (crypt A cells), crypt epithelial cells without secretion granula (crypt B cells), and, for comparison, also in villus cells.

Results

Concentrations of Cl, Na, and K in the cytoplasm of the respective cells are displayed in Fig. 1. Under stimulation, cytoplasmic Cl concentrations are decreased in crypt A cells only. In these cells, the decrease of Cl due to isoproterenol stimulation is reversed by treatment with alloxane. In contrast to that, isoproterenol treatment leads even to a significant increase of Cl concentrations in the other cells studied, which can be blocked by inhibiting the adenylate cyclase in Paneth and crypt B cells, but not in villus cells. In Paneth and crypt B cells, alloxane treatment decreases cytoplasmic Na and K concentrations below control levels. Pilocarpine does not affect cytoplasmic Cl concentrations in Paneth and crypt B cells but leads to a significant decrease of Cl in villus cells.

T. v. Zglinicki is at the Institut für Pathologie, Humboldt Universität, Postfach 140, Berlin 1040, German Democratic Republic; G. M. Roomans is at the University of Stockholm.

Conclusions

Both crypt B and Paneth cells share a common pattern of ionic changes that is clearly different from that found in crypt A cells. This pattern is characterized by a cAMP-dependent increase of Cl together with a decrease of Na and K by inhibition of the adenylate cyclase. These results are consistent with the existence of a cAMP-dependent Na/K/Cl cotransporter in crypt B and Paneth cells, most probably located in their basolateral membranes as known in a number of cell types.^{5,6}

On the other hand, only those changes measured in crypt A cells are consistent with the opening of apical Cl channels as the main event in stimulated secretion.^{1,7} Pilocarpine seems to be an even more potent stimulator than isoproterenol, depleting crypt A cells of Cl up to a level approximately equal to electrochemical equilibrium. The conclusion is thus that those crypt epithelial cells containing small secretion granula (crypt A cells) are the cell type mainly involved in cAMP-stimulated secretion of salt and water in the intestine.

The pattern of ionic responses in villus cells is also distinctive. The increase of cytoplasmic Cl under isoproterenol treatment is evidently not due to a cAMP increase in these cells. The decrease of Cl and the increase of K under pilocarpine stimulation might be due to a hyperpolarization of the villus cell membrane, taking into account the fact that the Cl concentration in villus cells of controls is already scarcely above electrochemical equilibrium.

References

1. M. Field, "Secretion of electrolytes and water by mammalian small intestine," in L. R. Johnson, Ed., *Physiology of the gastrointestinal tract*, New York: Raven Press, 1981, 963.
2. J. S. Trier and J. L. Madara, "Functional morphology of the mucosa of the small intestine," *ibid.*, 925.
3. T. von Zglinicki, M. Bimmler and H. J. Purz, "Fast cryofixation technique for X-ray microanalysis," *J. Microsc.* 141: 79, 1986.
4. J. Wroblewski et al., "Quantitative X-ray microanalysis of semi-thick cryosections," *Histochemistry* 77: 447, 1983.
5. R. K. H. Kinne, "Sodium cotransport systems in epithelial secretion," *Comp. Biochem. Physiol.* 90A: 721, 1988.
6. R. Rick et al., "Electron-probe X-ray microanalysis of transepithelial ion transport," *Ann. New York Acad. Sci.* 483: 245, 1986.
7. D. R. Halm et al., "Apical membrane chloride channels in a colonic cell line activated by secretory agonists," *Am. J. Physiol.* 254: C505, 1988.

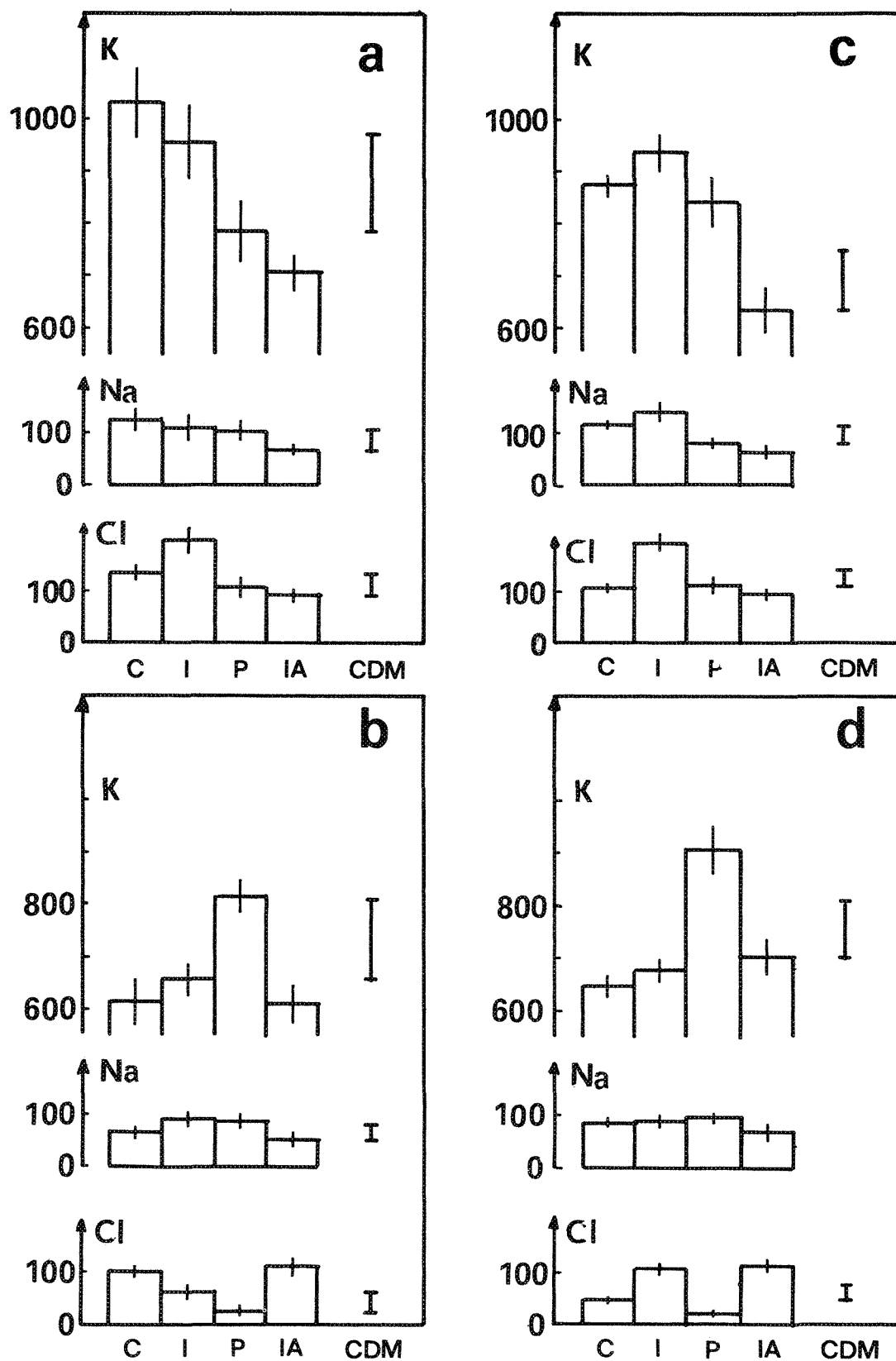


FIG. 1.--Concentrations of K, Na, and Cl (mM/kg dry weight, mean \pm s.e.m.) in the cytoplasm of (a) Paneth cells, (b) crypt A cells, (c) crypt B cells, (d) villus cells of the mouse intestine. C--controls, I--isoproterenol treated group, P--pilocarpine treated group, IA--group treated with isoproterenol and alloxane. CDM--critical difference between means at the 5% significance level. Values are means from at least 10 cells in 3 animals per group.

EVIDENCE FOR A BARIUM-SENSITIVE POTASSIUM CHANNEL IN RAT PAPILLARY COLLECTING DUCT (PCD) CELLS: EVALUATION BY X-RAY MICROANALYSIS IN SCANNING ELECTRON MICROSCOPY (SEM)

Iris Pavenstädt-Grupp, C. T. Grupp, H. E. Franz, and R. K. H. Kinne

Investigation of ion transport processes in papillary collecting duct (PCD) cells is difficult because absolute ion fluxes are low and the cells are inaccessible to experimental manipulations *in situ*. Our aim was therefore to develop a method that permits the detection of transmembrane ion fluxes in a small number of isolated PCD cells. We adapted x-ray microanalysis to the investigation of cellular element content without the time-consuming step of cryosectioning. It was possible to obtain reproducible and reliable measurements from as few as 10 cells, which during the measurement could be clearly identified by their morphology in the SEM.

It thus became possible to characterize sodium influx and potassium efflux in PCD cells in the presence of ouabain¹ and to demonstrate the existence of an amiloride-sensitive sodium entry step¹ and of a bumetanide-sensitive Na-K-Cl cotransport system.² The data presented below suggest the presence of a Ba²⁺-sensitive potassium channel in rat PCD cells.

Experimental

PCD cells were isolated in 285 mosm Hepes-Ringer buffer as described previously.³ Incubation of the cells is described in detail under Results. The cells were then transferred onto a Thermanox disk by sedimentation in a cytocentrifuge (Shandon Cytospin 2, 2 min/32g).¹ The Thermanox disk did not contain any sodium, potassium, chloride, or phosphorus. After removal of the extracellular medium either by washing in distilled water or in ammonium acetate, cells were quickly frozen in liquid propane cooled with liquid nitrogen, freeze-dried at -80 °C, and coated with carbon. The specimen was analyzed in SEM equipped with an energy-dispersive x-ray detector (Link LZ-5, silicon/lithium crystal, ultrathin window) at an accelerating voltage of 12.5 kV. Spectra were evaluated by comparison of the peak area-to-background ratio of the sample with droplet of dextran standards,⁴ which consisted of defined element contents composed in the matrix of 20% dextran and were similar in size to the isolated tubule fragments.⁵ The absolute value of the element content was obtained in mM/kg dry weight (dextran). The values are expressed as element-to-phosphorus ratio and given as means ± standard error of the mean.

The authors are with the Nephrology Section, Medical Clinic of the University of Ulm, Robert-Koch-Str., D-7900 Ulm, Fed. Rep. of Germany.

Results

Effect of Barium on Potassium Efflux After Exposure to Distilled Water. PCD cells were preincubated for 15 min at 37 °C in 285 mosm Hepes-Ringer buffer and centrifuged onto a Thermanox disk. Dipping the cells in distilled water buffered with Tris/Hepes to pH 7.4 for 3 s resulted in a K/P ratio of 0.45 ± 0.025 , whereas in the presence of K⁺ channel blocker Ba(NO₃)₂ (5 mM) the K/P ratio was similar to the ratio normally observed in PCD cells.¹ Substitution of barium by another divalent cation, e.g., Mg²⁺, in the washing solution did not inhibit the potassium efflux (Table 1).

TABLE 1.--Effect of 5 mM Ba²⁺ on potassium content of PCD cells exposed to distilled water.

Washing solution	n	K/P	Na/P
Distilled H ₂ O, pH 7.4	20	0.452±0.036	0.118±0.02
Distilled H ₂ O, + 5 mM Ba(NO ₃) ₂	20	0.650±0.015*	0.108±0.01
Distilled H ₂ O, + 5 mM Mg(NO ₃) ₂	19	0.488±0.043	0.098±0.01

*Significance $p < 0.05$ vs control.

Effect of Barium on Potassium Efflux in Ouabain-treated Cells. Inhibition of Na-K-ATPase by 10 mM ouabain in PCD cells incubated in 285 mosm Hepes-Ringer resulted in a time-dependent significant increase of intracellular Na/P ratio and decrease of the K/P ratio. In the presence of 5 mM BaCl₂ in the ouabain-containing medium K/P ratios nevertheless remained stable (Table 2). In these experiments extracellular medium was removed by dipping the cells into buffered ammonium acetate solution (pH 7.4), a procedure that did not change intracellular ion content and the cell shape.¹

TABLE 2.--Effect of barium on ouabain-induced potassium efflux after 15 min of incubation.

Incubation medium	n	K/P	Na/P
HEPES Ringer (control)	10	0.67±0.037	0.165±0.01
HEPES Ringer + 10 mM ouabain	10	0.514±0.018*	0.465±0.02*
HEPES Ringer + 10 mM ouabain + 5 mM BaCl ₂	10	0.670±0.033	0.343±0.03*

*Significance $p < 0.05$ vs control.

Conclusion

Our data show that potassium efflux in isolated papillary collecting duct cells was reduced in the presence of barium, whereas other divalent cations like magnesium had no effect. Sodium movements were not significantly affected by barium. These results suggest the existence of a Ba^{2+} -sensitive potassium channel in rat PCD cells.

References

1. I. Pavenstädt-Grupp, C. Grupp, and R. K. H. Kinne, "Measurement of element content in isolated papillary collecting duct cells by electron probe microanalysis," *Pflüger's Arch.* 413: 378-384, 1989.
2. C. Grupp, I. Pavenstädt-Grupp, R. W. Grunewald, and R. K. H. Kinne, "A Na-K-Cl cotransporter in isolated papillary collecting duct cells," *Kidney Int.* (submitted).
3. J. B. Stokes, C. Grupp, and R. K. H. Kinne, "Purification of rat papillary collecting duct cells: Functional and metabolic assessment," *Am. J. Physiol.* 253: F251-F262, 1987.
4. P. J. Statham, "Measurement and use of peak-to-background ratios in x-ray analysis," *Mikrochimica Acta* 8: 229-242, 1979.
5. K. Zierold, "The determination of wet weight concentrations of elements in freeze-dried cryosections from biological cells," *SEM/1986 II*, 713-724.

CRYOTECHNIQUES FOR BIOLOGICAL MICROANALYSIS

Karl Zierold

Biological cells are dynamic systems. Structure and elemental composition of cells may vary depending on their functional state. Therefore, cryotechniques are used in biological microanalysis to preserve structure and composition in a defined functional state for identification, localization, and quantitation of elements, in particular of diffusible ions. The most attractive method to achieve this aim with high spatial resolution consists of cryofixation followed by cryoultramicrotomy, cryotransfer including freeze-drying, and cryoelectron microscopy combined with x-ray microanalysis.^{1,2} These preparation and analysis steps are discussed below.

Cryofixation

Cryofixation can be defined as solidification of a biological specimen by cooling with the aim of minimal displacement of its components.³ The basic techniques (plunge freezing, jet freezing, and metal mirror cryofixation) have been extensively reviewed recently.^{4,5} Each of these techniques has its own merits, but they all have to be adapted to the particular biological problem of interest before reliable microanalytical data can be expected, as is illustrated by plunge freezing of liver cells for cryoultramicrotomy and subsequent x-ray microanalysis of freeze-dried cryosections.

Table 1 shows in the left column results obtained from freeze-dried cryosections of dissected tissue samples of approximately 1-2 mm in size. Obviously, the dissection of tissue samples causes severe cell damage, as indicated by high Na and Cl and low K concentrations in the cytoplasm. Isolation of cells by digesting enzymes followed by incubation in a culture medium permits the freezing of small droplets of cell suspension. The middle column shows that the cells have obviously recovered in comparison with the dissected tissue specimen. Liver cells cultured on gas-permeable flexible foil (Petriperm®) show even increased K and decreased Cl levels, as can be seen in the right column.⁶ Cryoultramicrotomy of cells grown on flexible foil was achieved after appropriate modification of the plunge freezing technique, as shown in Fig. 1. This example illustrates that microanalytical results from biological cells depend critically on the choice of specimen sampling and cryofixation. For example, amoebae could not be moved from their culture dish to a plunge freezing device without dis-

TABLE 1.--Element concentrations measured in the cytoplasm of cryosectioned rat liver cells after various preparation procedures (dissected tissue, isolated and cultured cells). Upper values show mMol/kg dry weight, lower values mMol/kg water \pm standard deviation, respectively. Horizontal bars indicate values below the detection limit; n = number of measured cells, d = dry weight portion.

	dissected tissue	isolated cells	cultured cells
n	15	20	12
d	0.26 \pm 0.05	0.32 \pm 0.04	0.30 \pm 0.04
Na	300 \pm 162 105 \pm 57	-	-
Mg	26 \pm 25 9 \pm 8	26 \pm 17 13 \pm 8	41 \pm 14 18 \pm 6
P	387 \pm 158 135 \pm 55	265 \pm 76 125 \pm 36	235 \pm 54 101 \pm 23
S	201 \pm 60 71 \pm 21	211 \pm 17 95 \pm 8	185 \pm 24 80 \pm 10
Cl	403 \pm 194 142 \pm 68	93 \pm 26 44 \pm 12	62 \pm 9 27 \pm 4
K	226 \pm 77 79 \pm 27	137 \pm 26 64 \pm 12	421 \pm 48 181 \pm 21
Ca	-	-	-

turbing cytoplasmic streaming. They were cryofixed in a defined state of locomotion under light microscopical control by a modified jet freezing device.² Specialized freezing devices were developed also for cryofixation of tissue specimens in situ.^{7,8}

Cryoultramicrotomy

Approximately 100nm-thick cryosections are prepared by the use of a dry glass knife at a temperature below 170 K in a cryoultramicrotome. The yield of smooth transparent cryosections requires minimal ice crystal size in the frozen sample to be cut. Large ice crystal damage results in chips and snow instead of clear sections. As a consequence, cells with a water portion <90% are easier to cut than cells with large aqueous compartments, for example plant cells. Although cryosections from most animal tissue cells can be prepared routinely today, typical artifacts such as unidirectional deformations have to be taken into account. Neither these artifacts nor the complete cryosectioning process are understood by a physical theory.⁹

The author is at the Max-Planck-Institut für Systemphysiologie, Rheinlanddamm 201, D-4600 Dortmund 1, Federal Republic of Germany.

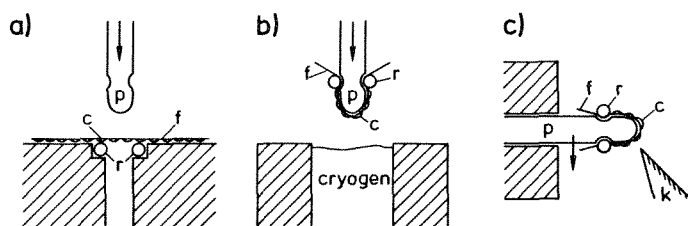


FIG. 1.--Cryofixation of cells cultured on flexible gas-permeable foil for cryoultramicrotomy. Abbreviations: c = cell, f = foil, k = knife, p = plexiglass rod, r - sealing ring. Arrows indicate direction of movement. (a) Punched area (10 mm in diameter) of foil with cells is placed upside down on preparation block with central hole. Plexiglass rod 2mm-thick with a half-sphere-like lower end and indentation above is placed by hand over central hole. Where plexiglass rod is located, foil is stretched over half-sphere-like end and is fixed on rod by sealing ring that comes to rest in indentation. (b) Cells are frozen when plexiglass rod is plunged by air-pressured device into cryogen (liquid propane). (c) Plexiglass rod is mounted in specimen holder of cryoultramicrotome for cryosectioning by dry glass knife. Cells can be seen by light reflected at plexiglass surface. Curved end of plexiglass rod permits approach of knife edge to frozen cell layer from different directions.

Cryotransfer and Freeze-drying

Electron-probe microanalysis of frozen-hydrated specimens is possible only on thick specimens with very limited spatial resolution in the micrometer range. Electron irradiation of thin frozen-hydrated cryosections causes deleterious mass loss, which makes reproducible microanalysis impossible.^{1,10} Therefore, water has to be removed at a temperature below its recrystallization temperature. Sublimation of water by freeze-drying stabilizes cryosections against mass loss by radiation damage. However, slight mass loss occurs in incompletely dried cryosections.

Transfer of freeze-dried cryosections through air causes moisture artifacts.² These sections lose electron optical contrast and brilliance of structures by the contact with wet air and storage in vacuum for days at room temperature. In addition, redistribution of elements was observed in cellular compartments with low dry mass portion.¹¹ Keeping cryosections at low temperature avoids contamination artifacts by lipid melting.¹² Thus, cryotransfer is recommended also for the preparation of freeze-dried cryosections for microanalysis. If cryotransfer is not available, freeze-dried cryosections should be transferred through air slightly warmer than the ambient temperature to minimize elemental redistribution.

Cryo Electron Microscopy and Microanalysis

There are two reasons for microanalysis of freeze-dried cryosections at low temperature

(below 170 K).

1. *Reduction of mass loss.* Sulfur and chlorine in particular are known to escape as volatile molecules by high electron irradiation at room temperature. This effect is not observed in cooled specimens.

2. *Prevention of contamination.* By use of an anticontaminator plate with a temperature below that of the specimen no visible contamination occurs, even at an irradiation dose up to 10^7 e/nm², as necessary for high-resolution microanalysis.

Microanalysis of freeze-dried cryosections provides only dry weight concentrations of elements. Physiologically more relevant element concentrations related to water content are obtained by additional measurement of the water portion in cellular compartments, which can be done by comparison of x-ray spectra¹³ or electron energy loss spectra¹⁴ measured in cryosections in the frozen-hydrated and freeze-dried state. Alternately, dry weight and water portion in 100nm-thick freeze-dried cryosections can be determined by measurement of the relative darkfield intensity in the scanning transmission electron microscope.¹⁰ This aspect is illustrated in Table 1 by element concentration data in terms of mMol/kg dry weight and mMol/kg water, respectively.

Dynamic Processes

One of the most promising applications of biological microanalysis is the detection of ion shifts related to fast processes in cells. This application requires time-controlled cryofixation of cells in defined functional states in the range of milliseconds, as demonstrated by x-ray microanalytical measurements of Ca movements in muscle.¹⁵⁻¹⁷ Recently, fast secretion of specialized organelles such as trichocysts in paramecia and stinging capsules in hydra were studied by x-ray microanalysis of freeze-dried cryosections.¹⁸ In paramecia, exocytosis of trichocysts was found to start 30 ms after chemical triggering. Na accumulated in trichocysts was observed to leave the cell with these organelles. Stinging capsules called nematocysts were triggered to discharge from nematocytes (specialized cells in hydra) by electrical stimulation 1 ms before they were plunged into liquid propane. Although the detailed time course could not be resolved by cryofixation, Ca shifts were found in nematocytes after start of nematocysts discharge.

Conclusion

Cryotechniques such as cryopreparation and cryoelectron microscopy are necessary tools for biological microanalysis in order to get reliable data of element and ion distributions related to various functional states of cells. In particular cryofixation has to be adapted carefully to the particular biological problem to be investigated.

References

1. K. Zierold, "Preparation of biological cryosections for analytical electron microscopy," *Ultramicroscopy* 10: 45, 1982.
2. K. Zierold and D. Schäfer, "Preparation of cultured and isolated cells for X-ray microanalysis," *Scanning Microscopy* 2: 1775, 1988.
3. R. A. Steinbrecht and K. Zierold, Eds., *Cryotechniques in Biological Electron Microscopy*, Heidelberg: Springer-Verlag, 1987, 291.
4. A. W. Robards and U. B. Sleytr, *Low Temperature Methods in Electron Microscopy*, Amsterdam: Elsevier, 1985.
5. H. Sitte, L. Edelmann and K. Neumann, "Cryofixation without pretreatment at ambient pressure," in R. A. Steinbrecht and K. Zierold, Eds., *Cryotechniques in Biological Electron Microscopy*, Heidelberg: Springer-Verlag, 1987, 87.
6. E. Petzinger et al., "Primary liver cell cultures grown on gas permeable membrane as source for the collection of primary bile," *In Vitro Cell. and Dev. Biol.* 24: 491, 1988.
7. H. K. Hagler and L. M. Buja, "New techniques for the preparation of thin freeze-dried cryosections for X-ray microanalysis, in J. P. Revel, T. Barnard, and G. H. Haggis, Eds., *Science of Biological Specimen Preparation for Microscopy and Microanalysis*, Chicago: SEM Inc., 1984, 161.
8. T. von Zglinicki, M. Bimmler, and H.-J. Purz, "Fast cryofixation technique for X-ray microanalysis," *J. Microsc.* 141: 79, 1986.
9. K. Zierold, "Cryoultramicrotomy," in R. A. Steinbrecht and K. Zierold, Eds., *Cryotechniques in Biological Electron Microscopy*, Heidelberg: Springer-Verlag, 1987, 132.
10. K. Zierold, "X-ray microanalysis of freeze-dried and frozen-hydrated cryosections," *J. Electr. Microsc. Techn.* 9: 65, 1988.
11. T. von Zglinicki and K. Zierold, "Element concentrations in air-exposed and vacuum-stored cryosections of rat liver cells," *J. Microsc.* (in press).
12. H. K. Hagler and L. M. Buja, "Effect of specimen preparation and section transfer techniques on the preservation of ultrastructure, lipids and elements in cryosections," *J. Microsc.* 141: 311, 1986.
13. T. A. Hall and B. L. Gupta, "Quantification for the X-ray microanalysis of cryosections," *J. Microsc.* 126: 333, 1982.
14. R. D. Leapman and R. L. Ornberg, "Quantitative electron energy loss spectroscopy in biology," *Ultramicroscopy* 24: 251, 1988.
15. M. F. Wendt-Gallitelli and H. Wolburg, "Rapid freezing, cryosectioning, and X-ray microanalysis on cardiac muscle preparations in defined functional states," *J. Electr. Microsc. Techn.* 1: 151, 1984.
16. A. V. Somlyo et al., "Electron probe X-ray microanalysis of post-tetanic Ca^{2+} and Mg^{2+} movements across the sarcoplasmic reticulum in situ," *J. Biol. Chem.* 260: 6801, 1985.
17. P. Ingram et al., "Quantitative X-ray elemental mapping of dynamic physiological events in skeletal muscle," in K. Zierold and H. K. Hagler, Eds., *Electron Probe Microanalysis: Applications in Biology and Medicine*, Heidelberg: Springer-Verlag (in press).
18. K. Zierold, I. Gerke, and M. Schmitz, "X-ray microanalysis of fast exocytotic processes," in K. Zierold and H. K. Hagler, Eds., *Electron Probe Microanalysis: Applications in Biology and Medicine*, Heidelberg: Springer-Verlag (in press).

QUANTITATIVE X-RAY IMAGING OF FROZEN HYDRATED CRYOSECTIONS

A. J. Saubermann

Computer control of electron beam placement enables collection of energy-dispersive spectra (EDS) according to a predefined pattern.¹ These data can then be used to produce images where each pixel can yield quantitative information on element content.²⁻⁵ Because the image produced provides both morphological information and quantitative elemental values, the resulting images can be a very powerful microscopical tool for elemental analysis in biological specimens. Application of this technology to frozen hydrated cryosections, prepared from biological specimens, involves dealing with a number of specimen preparation and analytical problems including mass loss, poor peak to background ratios, and specimen drift. We have applied methods, previously described for analysis of frozen hydrated cryosections, that largely circumvent many of these problems.^{6,7}

Methods

Currently, electron probe x-ray microanalysis is performed with an AMRay 1400 scanning electron microscope. A specially designed cold stage (E. Fjeld, Co.) provides a low temperature (-185 C) interface for a beryllium holder and beryllium shuttle.⁶ A SiLi detector with a tilted 30mm² detector chip, bias supply, and pulse processor (Tracor Northern) connected to an Accuspec/B data acquisition system and ADC (Nuclear Data, Inc.) in an IBM PC/AT is used for x-ray analysis. To form a quantitative elemental image, the electron beam is driven by a computer-generated voltage sent to the scan generation board (x and y ramp voltage), with a high throughput digital-to-analog converter (Data Translation, Inc. DT2801-A). A computer program written in C (Microsoft C version 5.1), and similar to that previously reported, controls the system and performs the spectral analysis.⁸

Biological specimens (e.g., leech ganglia, sciatic nerve, kidney) are frozen and cryosectioned as previously described. Frozen hydrated cryosections (nominally 0.5µm thick) are then transferred to a cold stage using a specialized vacuum transfer device.⁹ A suitably flat, frozen hydrated cryosection is chosen for analysis and a micrograph of the secondary image is made; the cryosection is then partitioned into compartments according to a superimposed grid pattern and each compartment or area (approximately 60 × 60 µm) is identified and marked on the secondary image. Next the

continuum generation rate (continuum counts measured for 100 s and corrected for extraneous background) is determined over the energy range of 4.6-6.0 keV with a probe current of 0.4 nA measured by a Faraday cup at the level of the specimen. Several measurements are made for each area and averaged, and the value is stored in a data file along with the unique label for the area and section from which the measurement was made. After all suitable areas have been measured, the cryosection is freeze-dried by a raise in the stage temperature to -60 C for 30 min within the column vacuum. Next the stage is re-cooled and an area to be imaged is located by scanning transmission electron microscopy (STEM). The probe current is increased to 1.4 nA and the beam is rastered point by point by use of a computerized signal to the scan coils. Spectra are collected at each point for 4 s live time and the spectra are processed according to methods previously described (Fig. 1).⁵ This processing basically consists of passing the spectrum through a "top hat" digital filter, determining total elemental peak counts, measuring the continuum generation rate, and calculating the elemental mass fraction according to the Hall continuum normalization method.¹⁰

The area to be imaged, which is now visible in the frozen-dried state, is located. Next, the continuum generation rate of the original hydrated area, containing the area to be imaged, is retrieved. That continuum generation rate is then scaled (by use of the known linear relationship between probe current and count rate) in order to calculate the water content based on the difference in continuum generation rates between the hydrated and dried state. Peak-to-background ratios are normalized to standards and the values saved for latter construction of an image.

Results

Mass fraction images can be obtained of frozen hydrated (expressed as mmol/kg wet weight) concentrations, frozen-dried concentrations (expressed as mmol/dg dry weight) of biologically important elements, and water content can be images as percent of total mass (Fig. 2). Values obtained from such images correspond well in both precision and accuracy to values obtained by single point area analysis.⁵ Pixel images (64 × 64) provide reasonably good morphology and sufficient pixel information to provide a suitable sample for statistical analysis of comparable areas (Fig. 3).

The author is with the Department of Anesthesiology, School of Medicine, SUNY at Stony Brook, Stony Brook, NY 11794-8480. This work was supported by NIH grant NS21455.

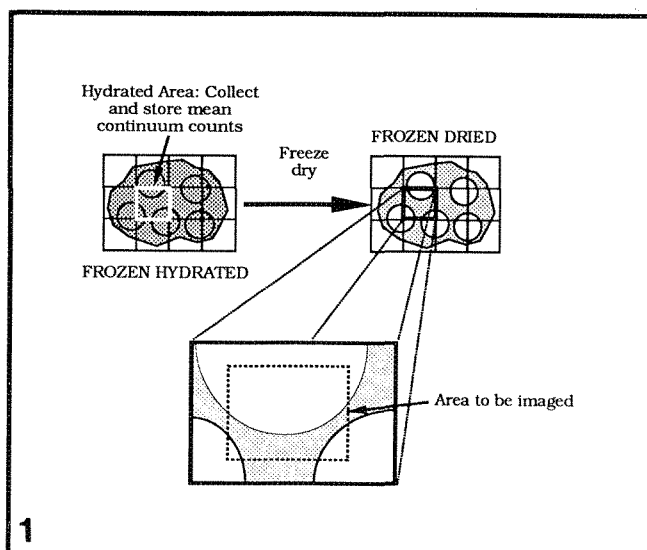


FIG. 1.--General analytical algorithm for analysis of frozen hydrated cryosections. Area to be imaged is subjected to point-by-point analysis by use of computerized beam control according to predefined matrix, usually 64 columns by 64 rows. Hydrated mass fraction is calculated from water fraction obtained by comparison of previously acquired and stored continuum generation rate measured in hydrated state, with continuum generation rate acquired at each location in dried state.

Discussion

X-ray images provide an easily interpretable image that can be of great use to biologists.^{9,11} Use of the frozen-hydrated specimen adds additional information that can provide important and physiologically relevant measurements of cell water and elemental mass fractions as related to water content. Because the eye and brain can do much of the statistical processing, the relationship between elemental distribution and structure is usually intuitively obvious.

The methods described are a relatively simple approach to the problem of electron probe microanalysis of frozen hydrated sections and imaging. By measuring the continuum generation rate in the hydrated specimen with a very low beam induced mass loss to a trivial level in terms of quantification with the Hall method when applied to these relatively thick cryosections. In addition, by reanalyzing in the dehydrated state, both identity and location of the area to be analyzed (prior to its actual analysis) are readily apparent, peak-to-background ratios are greatly improved over those of the hydrated state, and the specimen is less radiation sensitive than the hydrated specimen, which allows higher probe current to be used for analysis. The use of relatively high probe currents and 0.5 μ m-thick sections results in reasonably good counting rates. Under normal circumstances, the major limitation to probe current is the deadtime. Since the deadtime only serves to increase dwell time, efforts are

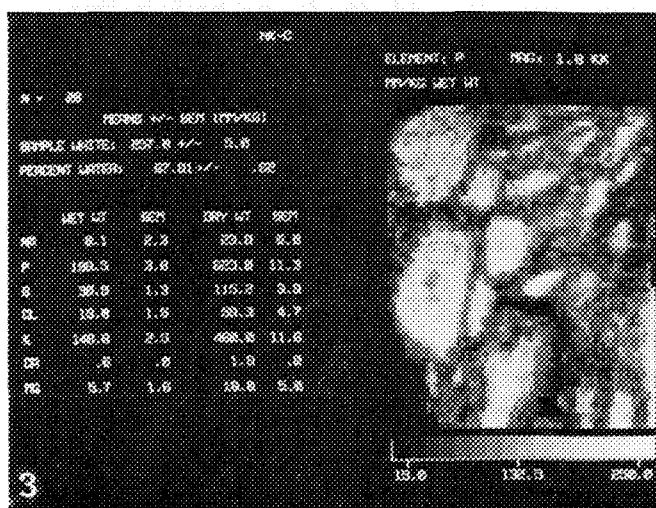
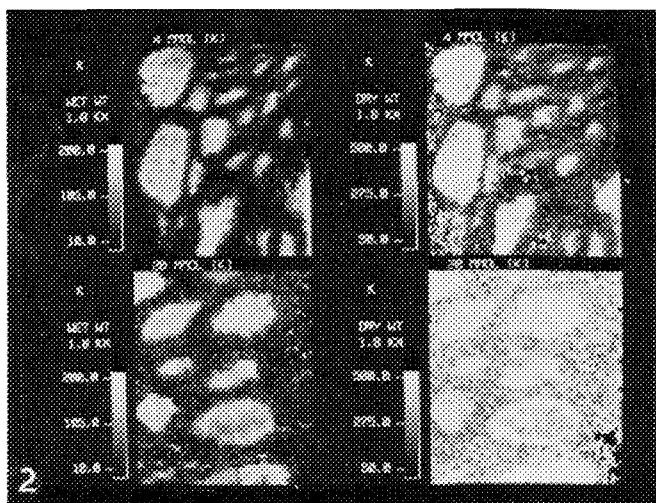


FIG. 2.--Four quantified images of K distribution in leech ganglia. Images on left are displayed as wet weight; those on the right, as dry weight concentrations. Effect of water content on elemental distribution under various experimental conditions demonstrates value of wet weight images in understanding physiological changes which might otherwise be overlooked. (See also Ref. 9.)

FIG. 3.--Specific areas of image can be retrieved and elemental content for important biological elements averaged and displayed. Because of quantitative information available from stored images, rigorous comparisons between anatomic areas can be made.

made to keep maximum deadtime less than 30%.

Use of the above described analytical approach makes two assumptions: (1) the frozen hydrated cryosection, within the area from which the continuum counts are collected, is uniform in thickness; and (2) the frozen hydrated cryosection is uniform in average atomic number. The former assumption can be demonstrated experimentally.⁵ If that assumption should fail, its failure becomes readily apparent in the hydrated images (see, for example, Figs. 4 and 5 in Ref. 5). The latter

assumption, on the other hand, appears to be generally true for biological (nonmineralized) tissue, since water and other biological constituents have nearly the same average atomic number.

One of the major drawbacks of this approach is the long time needed to acquire an image. For example, a 64×64 pixel image requires nearly 6 h. This long period of time can lead to specimen or instrument drift which necessitates correction.¹² However, because of the higher probe current that can be used for analysis in the dried state and the amount of mass present in these relatively thick sections, each pixel has good precision and accuracy.⁵ Thus, a large amount of information is contained in, and easily obtainable from, each image. Since each pixel is in essence a complete analysis, it is possible to extract information from these pixels for experimental purposes, produce line scan histograms, smooth and use other conventional image processing techniques, and superimpose elemental images to provide comparisons between specific elemental distributions.

Since only a few consistent elements are usually analyzed in biological tissue (Na, Mg, P, S, Cl, K, and Ca), the analytical algorithm can be simplified. Consequently, it is possible to use relatively simple and low-cost computer hardware and software to obtain these maps and perform quantitative elemental analysis.

References

1. K. Gorlen et al., "Computerized analytical electron microscope for elemental imaging," *Rev. Sci. Instrum.* 55: 912-921, 1984.
2. D. Johnson et al., "High spatial resolution spectroscopy in the elemental microanalysis and imaging of biological systems," *Ultramicroscopy* 24: 221-236, 1988.
3. P. Ingram et al., "Real-time quantitative elemental analysis and imaging in cells," *Analytical Electron Microscopy--1987*, 179.
4. C. Fiori et al., "Quantitative x-ray mapping of biological cryosections," *Ultramicroscopy* 24: 237-250, 1988.
5. A. Saubermann and R. Heyman, "Quantitative digital x-ray imaging using frozen hydrated and frozen dried tissue sections," *J. Microscop.* 146: 162-182, 1987.
6. A. Saubermann et al., "Application of scanning electron microscopy to x-ray analysis of frozen-hydrated sections: I. Specimen handling techniques," *J. Cell Biol.* 88: 257-267, 1981.
7. A. Saubermann et al., "Application of scanning electron microscopy to x-ray analysis of frozen-hydrated sections. II. Analysis of standard solutions and artificial electrolyte gradients," *J. Cell Biol.* 88: 269-273, 1981.
8. R. Heyman and A. Saubermann, "A multifunctional minicomputer program providing quantitative and digital x-ray microanalysis of cryosectioned biological tissue for the inexperienced analyst," *J. Electron Microsc. Technique* 5: 315-345, 1987.
9. A. Saubermann and J. Stockton, "Effects of increased extracellular K on the elemental composition and water content of neuron and glial cells in leech central nervous system," *J. Neurochem.* 51: 1797-1807, 1988.
10. T. Hall et al., "The use of thin specimens for x-ray microanalysis in biology," *J. Microscop.* 99: 177-182, 1973.
11. R. LoPachin et al., "Distribution of elements in rat peripheral axons and nerve cell bodies determined by x-ray microprobe analysis," *J. Neurochem.* 51: 764-775, 1988.
12. P. Statham, "Quantitative digital mapping with drift compensation," *Analytical Electron Microscopy--1987*, 187.

STRATEGIES FOR SPATIAL DECONVOLUTION OF CALCIUM STORES IN CARDIAC MUSCLE

J. McD. Tormey and L. G. Walsh

The x-ray spectra obtained when thin biological samples are excited by an electron beam commonly include contributions from several adjacent structures. In the past several years, most of the microanalysis carried out in our laboratory has utilized spatial deconvolution techniques that take these contributions into account. The purpose of this presentation is to describe these techniques and to illustrate them by examples from recent studies.

A major goal of our laboratory has been to determine the immediate source of contractile Ca in mammalian cardiac muscle. Our strategy has been to use the electron probe to identify subcellular compartments whose Ca concentration varies as a function of contractility and to estimate whether these compartments contain enough Ca to explain quantitatively measured force development.

All measurements reported here were made on papillary muscles from the ventricles of young adult rabbits. Preparative and analytical techniques were similar to those described previously.^{1,2} A JEOL 100CX was equipped with a W filament and operated at 100 kV with probe currents on the order of 4 nA.

Analysis of Junctional Sarcoplasmic Reticulum (JSR) and Sarcolemma (SL)

When either the JSR or SL of cardiac muscle is probed, the electron beam diameter is so large that x rays from cytosol, sarcolemma, and extracellular fluid are also excited. The contributions arising from these adjacent phases can be evaluated and used to obtain more accurate estimates of concentrations. We have used two different methods to do so.

Deconvolution Based on Electron Beam Geometry. We have previously described how spatial deconvolution can be performed by considering the measured distribution of electrons in the probing beam, the dimensions of adjoining structures, and their measured compositions.³ This approach has been applied to three different experimental conditions in which muscle contractility varied over a wide range.^{4,5}

Before deconvolution, mean calcium concentrations in the JSR varied directly with contractility over a range between 4.0 ± 1.6

mmol/kg dry mass and 13.6 ± 1.5 mmol/kg dry mass. Spatial deconvolution based on estimated electron distribution had a relatively small effect, changing the results to 2.5 mmol/kg dry mass for the lowest contractility and 14.8 mmol/kg dry mass for the highest.

Results with the SL were quantitatively different. Mean calcium concentrations varied between 8.4 ± 1.3 and 17.5 ± 2.7 mmol/kg dry mass, but they correlated inversely with the ionic strength of the bathing solution rather than directly with contractility. Spatial deconvolution caused all SL calcium concentrations to increase by a factor of 2. The large corrections relative to those for the JSR reflect the facts that the measured probe width had a standard deviation of 13.4 nm and that the width of the SL was ca. 8 nm (five-fold narrower than the JSR).

Deconvolution Based on Cobalt EDTA. In a recently completed study,⁶ we employed cobalt EDTA⁷ as an extracellular marker and used it to scale the contributions to JSR and SL measurements that arise from the calcium-rich extracellular fluid. (Cobalt-to-calcium intensity ratios were separately measured for JSR, SL, and extracellular fluid.) Contractility was maximized by use of paired-pulse stimulation, and the redistribution of electrolytes that occurs over a prolonged period of rest was observed. The distributions of Ca after rest periods of 30 and 600 s were compared, during which time contractility declined by 86%. Uncorrected microprobe measurements showed that during the rest period Ca concentrations in the JSR declined from 13.7 ± 0.7 to 5.0 ± 0.5 mmol/kg dry mass. Spatial deconvolution based on cobalt EDTA measurements once again had a small effect but in a direction that emphasized the relative decline in concentration; corrected values were 12.4 ± 1.6 and 3.3 ± 0.9 mmol/kg dry mass, respectively.

Over the same rest period, uncorrected SL calcium concentrations did not change significantly; they were 12.3 ± 1.2 and 10.2 ± 1.0 mmol/kg dry mass, respectively. After cobalt EDTA corrections, these values dropped to 6.7 ± 5.2 and 2.1 ± 1.2 mmol/kg dry mass.

In summary, the two methods of spatial deconvolution produce similar results when applied to JSR but diametrically opposite results when applied to SL calcium measurements. There are several possible explanations for this unexpected discrepancy. The JSR measurements appear relatively reliable, but the ability to obtain reliable microprobe measurements of Ca associated with the SL remains an open issue.

The authors are at the Department of Physiology, UCLA Center for Health Sciences, Los Angeles, CA 90024-1751. The collaboration of JoAnn Hill and of E. S. Wheeler-Clark is gratefully acknowledged. This work was supported in part by NIH Grant HL-31249. L. G. Walsh is recipient of an Advanced Fellowship from the American Heart Association Greater Los Angeles Affiliate.

Deconvolution of the "Third" Compartment

In certain of our earlier studies,^{2,8} sample preparation was not good enough to allow direct measurement of JSR. As a consequence, the only compartments that were directly analyzed were cell, myofibrils, and mitochondria. However, under certain conditions, ouabain contracture² and post-ischemic reperfusion,⁸ cell calcium concentrations increased much more and much less, respectively, than could be accounted for by the concurrent changes in myofibril and mitochondria calcium. It was obvious that a third subcellular compartment (nonmyofibrillar and nonmitochondrial) was convolved in the cell measurements. Of particular interest to us, the principal contents of this compartment should be the T tubules and the total sarcoplasmic reticulum (SR).

We therefore developed a simple approach to deconvoluting the third compartment.⁹ The myocardial cell is treated as three anatomical compartments: myofibrils, mitochondria, and a third compartment that contains the remaining subcellular structures. The intensity of Ca x rays measured when an electron beam rasters a cell is proportional to the amount of Ca present in the cell. In turn, this intensity is the weighted sum of the x-ray intensities that would be generated by each compartment if it alone were irradiated; i.e.,

$$I_{Ca}^{cell} = I_{Ca}^{fibr} F_{fibr} + I_{Ca}^{mito} F_{mito} + I_{Ca}^{iii} F_{iii}$$

where I_{Ca}^{cell} , I_{Ca}^{fibr} , I_{Ca}^{mito} , and I_{Ca}^{iii} are the intensities of Ca x rays that would be measured over cells, myofibrils, mitochondria, and the third compartment, respectively, during separate analyses of each region, and the corresponding values of F are volume fractions that can be obtained by morphometric analysis.

The third compartment includes all components of the SR, plus some T tubules and free sarcoplasm. Additional microprobe measurements of T tubule contents and of T tubule associated sarcolemma, combined with morphometric data, suggested⁹ that under control conditions more than 90% of the Ca in the third compartment is within the SR.

We have now used this approach to measure the change in third compartment calcium content that accompanies prolonged periods of rest.⁶ (This was part of the study employing cobalt EDTA described in the preceding section.) During the interval between 30 and 600 s rest, the cell calcium concentration dropped by 0.9 mmol/kg dry mass (in good agreement with results of wet chemistry¹⁰). Over this time interval, calcium concentrations in the myofibrils, mitochondria, T tubules, and sarcolemma did not change significantly.

Calculations show that in this experiment the drop in third compartment calcium content is 0.7 mmol/kg dry mass of the entire cell. We interpret this as a change in the calcium content of the total SR. When this quantity is compared with biochemical estimates,^{11,12}

it appears quite sufficient to explain the concurrent change in cardiac contractility.

Conclusion

Two strategies of spatial deconvolution have been applied to cardiac muscle and give complementary analytical results, which indicate that, at least under certain conditions, the concentration of calcium in the JSR and the calcium content of the total SR correlate closely with contractility. This correlation in turn indicates a likely source for contractile calcium in the mammalian myocardium.

References

1. J. McD. Tormey, "Improved methods for x-ray microanalysis of cardiac muscle," *Microbeam Analysis--1983*, 221.
2. J. McD. Tormey, "Accuracy and precision of biological x-ray microanalysis: Cardiac muscle," *Microbeam Analysis--1984*, 272.
3. J. McD. Tormey and E.S. Wheeler-Clark, "Spatial resolution of sarcolemma and sarcoplasmic reticulum in electron probe analysis of cardiac muscle," in A. P. Somlyo, Ed., "Recent Advances in Electron and Light Optical Imaging in Biology and Medicine," *Ann. NY Acad. Sci.* 483: 260, 1986.
4. E. S. Wheeler-Clark and J. McD. Tormey, "Electron probe x-ray microanalysis of sarcolemma and junctional sarcoplasmic reticulum in myocardium: Effects of low Na," *Circulation Research* 60: 246, 1987.
5. E. S. Wheeler-Clark and J. McD. Tormey, "Ryanodine accelerates calcium depletion from junctional sarcoplasmic reticulum of resting myocardium: An electron probe study," *Biophysical J.* 51: 198a, 1987.
6. L. G. Walsh and J. McD. Tormey, "Rest-dependent Ca loss from sarcoplasmic reticulum of intact cardiac muscle," *Biophysical J.* 55: 485a, 1989.
7. J. H. B. Bridge et al., "Synthesis and use of radio cobaltic EDTA as an extracellular marker in rabbit heart," *Am. J. Physiol.* 242: H671, 1982.
8. L. G. Walsh and J. McD. Tormey, "Subcellular electrolyte shifts during in vitro myocardial ischemia and reperfusion," *Am. J. Physiol.* 255: H917, 1988.
9. L. G. Walsh and J. McD. Tormey, "Cellular compartmentation in ischemic myocardium: Indirect analysis by electron probe," *Am. J. Physiol.* 255: H929, 1988.
10. J. H. B. Bridge, "Relationships between the sarcoplasmic reticulum and transsarcolemmal Ca transport revealed by rapidly cooling rabbit ventricular muscle," *J. Gen. Physiol.* 88: 437, 1986.
11. R. J. Solaro et al., "Calcium requirements for cardiac myofibrillar activation," *Circulation Research* 34: 525, 1974.
12. A. Fabiato, "Calcium-induced release of calcium from the cardiac sarcoplasmic reticulum," *Am. J. Physiol.* 245: C1, 1983.

X-RAY MICROANALYSIS OF VENTRICULAR MYOCYTES: VOLTAGE-CLAMP AS A TOOL FOR GRADATION OF Ca-INFLUX, Ca-LOAD AND CONTRACTILITY

M. F. Wendt-Gallitelli and G. Isenberg

The Ca-ions entering through the sarcolemma at depolarization into the ventricular myocyte contribute to the Ca load of intracellular compartments such as sarcoplasmic reticulum (SR). It has been shown that this SR Ca load determines the degree of contractile activation.¹ Ventricular myocytes of most species, e.g., from guinea pigs (but not from rats), are depleted of Ca when they remain unstimulated for a period longer than 10 min. Upon resumption of stimulation, Ca influx through channels and via Na,Ca exchanger loads the SR with Ca, and amplitude and rate of contraction increase simultaneously. Here, we use the voltage-clamp technique to grade the amount of Ca influx. In addition, the recorded membrane current is an estimate of the amount of Ca influx. We aim to relate this amount to the total Ca concentration as detected by EPMA in such compartments as sarcolemma, subsarcolemmal SR, junctional SR, corbular SR mitochondria, and cytosol.

During experiments, the isolated myocytes were superfused with a prewarmed (35 C) physiological salt solution containing 3.6 mM CaCl_2 . For the experiment, a cell was transferred by means of a patch pipette into the taper of a silver holder covered by pioloform film. Once the cell was on the film, normal action potentials and contractions were recorded. Then, voltage-clamp pulses were applied at 1 Hz. Starting from the resting potential (-80 mV), a 20ms long pulse to -45 mV (inactivation of fast sodium current) was followed by a 180ms-long depolarization to +5 mV and repolarization back to -80 mV. For paired-pulse stimulation, a second pulse to +50 mV (160 ms) followed the first one after 20 ms. The amount of Ca influx was estimated from the Ca current.

The myocytes were shock frozen after the staircase potentiation had stabilized. Shock freezing was timed as follows: (a) "presystolic," i.e., during diastole immediately before the pulse, and (b) "systolic," i.e., 110 ms after start of the pulse, which is the time to peak of contraction.

Electron micrographs from freeze-substituted cells revealed the good preservation of the intracellular compartments. The myocytes were cut at -150 C and the cryosections were freeze dried. The elemental distribution in the isolated myocytes was analyzed in a Philips CM 12 STEM equipped with a LaB_6 filament, a Gatan cryotransfer stage, and a 30mm² Link energy-dispersive Si(Li) detector. Quantification of elements was carried out according to the Hall continuum-method² by means of the Link "quantem" program (System 860-500). Spectra of cell compartments were collected in the

STEM mode at 100kV acceleration voltage. The analyzed area was set according to the structures to be analyzed. Time of analysis was extended from 100 to more than 1000 s, depending on the instrumental error of the Ca measurements. Variations in the elemental concentration of the groups were tested with analysis of variance for simultaneous control of all groups and followed by an *a posteriori* paired comparison.

The elemental distribution in the isolated myocytes is essentially the same as in corresponding multicellular ventricular thin trabeculae.⁴ In cells that remained unstimulated for 15 min or longer, all compartments did not reveal detectable calcium. In myocytes frozen presystolic after application of voltage-clamp pulses, contractility was enhanced and Ca became detectable in the junctional SR (adjacent to t-tubuli) and at the cell border. In some experiments the period of depolarization was extended, which increased Ca influx. This procedure loaded the compartments to a larger extent. Application of paired pulses was that intervention which potentiated the contractility the most (extent of shortening up to 25%). Under those conditions, Ca accumulation in the compartments was further enhanced, predominantly in the junctional and corbular SR.

When the cells were frozen systolic, i.e., at the peak of contraction, the Ca concentration in the cytosol was elevated. The Ca concentration in compartments fell to a value that was similar to the one in the cytosol. The amount of Ca influx was compared with the subcellular Ca distribution as analyzed by the energy-dispersive x-ray microprobe in the above compartments. The measured Ca load is consistent with the amount estimated from the Ca influx.

References

1. M. F. Wendt-Gallitelli, "Presystolic Ca-loading of the sarcoplasmic reticulum influences time to peak force of contraction: X-ray microanalysis on rapidly frozen guinea-pig ventricular muscle preparations," *Basic Res. Cardiol.* 80: 617-625, 1985.
2. T. A. Hall, "Biological x-ray microanalysis," *J. Microsc.* 117: 145-163, 1979.
3. M. F. Wendt-Gallitelli and G. Isenberg, "Single isolated cardiac myocytes frozen during voltage-clamp pulses: A technique for correlating x-ray microanalysis data on calcium distribution with calcium inward current in the same cell," *Advances in Biological Microanalysis*, Springer Series in Biophysics (in press).
4. M. F. Wendt-Gallitelli and G. Isenberg, "X-ray microanalysis of single isolated myocytes frozen under voltage-clamp conditions," *Am. J. Physiol.* 256: H574-683, 1989.

The authors are at the Physiologisches Institut II, Universität Tübingen, and Institut für Physiologie der Universität Köln, Federal Republic of Germany.

X-RAY MICROANALYSIS OF ISOLATED CARDIAC MYOCYTES

Alice Warley

Cardiac myocytes, isolated from adult animals, have become a useful in vitro model for the study of cardiac function and metabolism. Preparations of isolated myocytes consist of two morphologically distinct cell types, round cells and rod-shaped cells; the rod-shaped cells are viable, the round cells are not. Morphological studies have shown that the structure of the sarcolemma of the rod-shaped cells is not grossly altered during the isolation procedure.¹ Study of the elemental composition of the isolated cells should indicate whether the sarcolemma remains functionally intact, and is able to maintain normal intracellular concentrations of electrolytes.

Methods

Cardiac myocytes were isolated from the hearts of male NZW rabbits by collagenase disaggregation.² The cells were concentrated by centrifugation (500 g, 5 min) and drops of the pellet were placed on silver stubs and frozen in liquefied propane. Cryosections were cut at -130 C collected onto Pioloform-coated Ni grids, transferred to a freeze drier and freeze dried overnight. The sections were carbon coated before analysis. Analysis was carried out on a JEOL 100CX STEM electron microscope at 100 keV and 1.5 nA beam current. Spectra were collected and processed by use of a Link Analytical 800 series EDS detection system.

Results and Discussion

Analysis of the myofibril region of the cells showed that elemental concentrations differed in the round and rod-shaped cells. Round cells showed high concentration of Na coupled with low concentrations of K and the presence of detectable concentrations of Ca. These findings are consistent with the round cells having suffered gross damage to the plasma membrane and are in agreement with functional studies which show that the round cells are nonviable.

Measured mean concentrations of Na, Mg, and K in the myofibrillar region of the rod-shaped cells were Na, 128 mmole/kg dry weight; Mg, 36 mmole/kg dry weight and K, 407 mmole/kg dry weight. The concentration of Na in the freshly isolated cells was higher than that obtained from bulk analysis of rabbit ventricle.³ The high mean concentration of Na in

the isolated cells was due to both the presence of some cells with high Na concentrations, and an overall low K/Na ratio. Incubation of the isolated cells at 37 C for 30 min resulted in an increase in the K/Na ratio.

Myocytes isolated from the hearts of rabbits fed a K-depleted diet showed high K/Na ratios immediately after isolation without the need for incubation. In rabbits, cardiac tissue adapts to K depletion by an increase in Na pump density. The increase in K/Na ratio in the freshly isolated cells from the K-depleted animals reflects this adaptation.

References

1. N. J. Severs and T. Powell, "Sarcolemma structure in isolated rat myocytes," *Electron Microscopy* 2: 134-135, 1980.
2. C. H. Fry et al., "Net calcium exchange in adult ventricular myocytes: An assessment of mitochondrial calcium accumulating capacity," *Proc. Roy. Soc. Lond. B*-223: 223-238, 1984.
3. A. Warley, "X-ray microanalysis of freshly isolated cells in suspension," in K. Zierold and H. K. Hagler, Eds., *Progress of Microprobe Analysis in Biology and Medicine*, Heidelberg: Springer-Verlag (in press).

The author is at The Division of Biochemistry, U.M.D.S. of Guy's and St. Thomas's Hospitals, London, England SE1 7EH. The collaboration of Dr. J. P. T. Ward is gratefully acknowledged. The work was funded by the British Heart Foundation under grant 1 860 892.

AN ELECTRON PROBE X-RAY MICROANALYSIS COMPARISON OF Na DETECTION WITHIN CULTURED HEART CELLS BY USE OF Be WINDOW AND WINDOWLESS Si(Li) DETECTORS

M. C. Carney, J. L. Lehman, Peter Ingram, Ann LeFurgey,
L. A. Hawkey, and Melvyn Lieberman

Quantitative electron probe x-ray microanalysis (EPXMA) has been used extensively in investigations of Na compartmentation within cells from numerous tissues.¹ In myocardium, for example, the ionic content of heart cells under steady-state conditions is maintained by the counterbalancing effects of Na extrusion and the diffusion of other ions and molecules down their electrochemical gradients. Changes in both total and compartmental Na content, via inhibition of Na-K ATPases or alteration of the transmembrane gradients for Na, K, Ca, and Cl, can occur during a variety of physiological conditions or as a result of pathological or pharmacological agents. The role of Na-Ca exchange in maintaining ionic homeostasis has been examined in our laboratory² and by others.³ Such experiments require that the transmembrane Na gradient be reversed; thus total intracellular Na is lowered to levels of <5 mmol Na/mg dry weight. Under such conditions, the measurement of Na by EPXMA is more difficult because Na is decreased to values near the detection limits.⁴ In contrast, the measurement of Ca by EPXMA is made more favorable because Ca is elevated to values above the minimum detection limits.

Spectral measurements have previously been performed with an energy-dispersive x-ray (EDX) detector equipped with a beryllium (Be) window. The Be window strongly absorbs x rays below ~1 keV; removal or replacement of the Be window with an ultrathin window improves prospects of analysis in this region.⁵

Although quantifying low Na amounts within these cells is an ultimate goal, the purpose of this preliminary study is to consider possible advantages of such detectors over Be window detectors in the study of biological specimens. As a first step, we report on the analysis of Na in cryosections of heart cells. We evaluated detector performance using both normal (control) Na preparations and experimental preparations with elevated intracellular Na, prepared by incubation with ouabain.

Sample Preparation

Cell Culture. For x-ray microanalysis, aggregates of heart muscle cells were obtained as previously described.⁶ Briefly, muscle-enriched cells from 11-day-old embryonic chick hearts were used to seed agar-coated culture dishes containing small openings (20 μ m). The cultures were incubated for 3 or 4 days at 37 C in a humidified chamber containing 4% CO₂ and 96% air. Cells cultured under identical conditions for 3-4 days were then incubated for 60 min in either Hepes-Tris balanced salt solution (HT-BSS) or K-free HT-BSS plus 10⁻⁴ M ouabain. The cultures were observed by light microscopy and small, 50-100 μ m spontaneously beating aggregates were chosen for rapid freezing.

Cryopreservation. Individual aggregates of cells were withdrawn from the medium into a pipette attached to a syringe and placed on a cryomicrotome specimen stub precoated with a drop of 20% gelatin solution. The aggregate on the specimen stub was rapidly plunged into liquid nitrogen-cooled liquid propane and then stored under liquid nitrogen. Average time from withdrawal of the aggregates from the culture dish to freezing was <20 s. Frozen aggregates from each experiment were then processed by cryosectioning at -140 C, freeze drying and carbon coating prior to EPXMA.⁷

X-ray Microanalysis

The freeze-dried cryosections were analyzed by use of two similar scanning transmission electron microscopes (STEM) [JEOL JEM1200EX]. One microscope was equipped with a 30mm² Si(Li) beryllium window detector [Tracor Northern] and TN 5500 analyzer, the other with a 30mm² windowless Si(Li) detector [Link Analytical LZ-5] and AN10000 analyzer. The detectors were mounted normal to the beam direction in both instruments (side-entry configuration).

The microscopes were operated with LaB₆ filaments at 80 keV and identical lens and aperture settings in the STEM mode. The condenser lenses were set on each instrument to obtain probe currents of approximately 10⁻⁹ A. The specimens were mounted on nickel grids, within a cryotransfer stage [Gatan 626] operating at -120 C. The stage was eucentrically tilted at 35° from the horizontal toward the EDX detector, which was placed close to the sample such that the solid angle subtended was as large as possible, i.e., approximately 0.13 sr. The pulse processors were set at 10 eV/channel, with approximately 40 μ s processing time.

M. C. Carney, A. LeFurgey, L. A. Hawkey and M. Lieberman are with the Division of Physiology, Duke University Medical Center, Durham, NC 27710; J. L. Lehman is with JEOL USA, Inc., Peabody, MA 01960; and P. Ingram is with the Research Triangle Institute, Chemistry and Life Sciences Division, Research Triangle Park, NC 27709. This work was supported by NIH grants NIDDK37704, HL17670, and HL27105.

TABLE 1.--Peak-to-continuum mean values of Na, K, and Cl in Be window (BeW) and windowless (NoW) detectors. The means are the average of 8 or 9 individual 500s acquisitions. SD = standard deviation of the mean.

	BeW	NoW	BeW	NoW	BeW	NoW
	Na		K		Cl	
Control	0.051	0.146 *	1.104	1.218	0.231	0.257
±SD	0.030	0.097	0.226	0.366	0.109	0.111
Ouabain	0.096	0.254 *	0.255	0.227	0.153	0.205
±SD	0.042	0.112	0.089	0.057	0.051	0.090

*Significant difference between detectors by Student's t-test ($p < 0.01$).

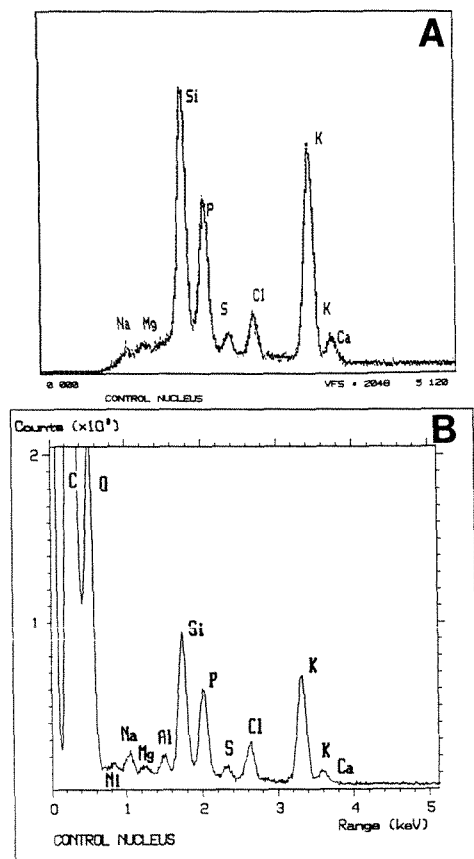


FIG. 1.--Be window (A) and windowless (B) spectrum from nucleus of heart cell under control conditions.

Prior to use, the crystal of the windowless detector and the cryotransfer stage were heated to remove water and hydrocarbon contamination. Organelles were probed on control and on higher Na-containing ouabain-treated samples. The spectra were acquired from a $\sim 1 \mu^2$ raster area within selected organelles for 500 live-time seconds. Adjacent mitochondrial, cytoplasmic, and nuclear regions of the same section were probed on both instruments.

Results

The spectra were evaluated by a peak-to-continuum method.⁸ Peak regions 120 eV wide centered on the peak centroid were established for the elements of interest. The net peak integral was calculated by linear interpolation between the region end points. A 260eV continuum

region was defined in the peak free region between 2.87 and 3.13 keV. This region was selected because the integral continuum counts in this region are unaffected by the presence or absence of the Be window. The effect of a windowless detector on the low energy region of the spectrum can be seen in Fig. 1 where a typical spectrum from each detector is shown. The Na peak using the windowless detector is symmetrical, laying on a relatively flat background. Although there are obvious differences between the detectors at the low energy end of the spectrum, there are no noticeable differences at higher energies. The absence of the Be window enables the detection of the C, N, O K lines and Ni L lines.

The ratio of the peak-to-continuum values are averaged and summarized in Table 1. The Na peak-to-continuum ratio is significantly higher in the windowless mode; there is no significant difference seen in either case in the Cl and K ratios. This observation is made in both the control and ouabain conditions. Similarly with both detectors, intracellular Na is increased and K and Cl are decreased following exposure to ouabain.

Discussion

With the windowless detector, an increased Na peak-to-continuum ratio was seen, but no change was seen in the K and Cl ratios. The known attenuation of low-energy x rays by the Be window predicts this observation.⁹ It is possible for ice and organics within the microscope to build up on the surface of a windowless detector crystal, thus reducing the detector response to low-energy x rays. As noted above, it is necessary to condition the crystal by removing any ice and other contaminants in order to detect low-energy x rays reproducibly.¹⁰

An increase in Na and decrease in K and Cl were noted with ouabain in both detectors, and the magnitude of the ouabain induced elemental change was similar between detectors. For example, the values for Na showed an increase of factors of 1.88 and 1.74, respectively, for the beryllium window and windowless detectors. The Na, Cl, and K response to ouabain follows the same trends as in the quantitative values reported previously for cultured heart cells.⁹

The approximately three-fold increase in the Na peak-to-continuum ratio reflects the sensitivity of a windowless detector to the low-

energy region, which provides better statistical accuracy for cellular Na measurements and may bring the results of low-Na transmembrane manipulations within detection limits. The improved sensitivity should also lower the Na minimum detectable mass (MDM), determined by count rate, and minimum detectable concentration (MDC), determined by peak-to-background ratio. With regard to quantitation, the errors in Na quantitation due to digital filtering of the slowly varying continuum¹¹ should not be a problem with windowless detectors, for the continuum shape is dramatically different.

We are currently preparing suitable standards with which to estimate the MDM and MDC of elements of biological importance in the low-energy region. Future work will include the use of the windowless detector to evaluate quantitatively low-Na transmembrane manipulations.

References

1. A. LeFurgey, M. Bond, and P. Ingram, "Frontiers in electron probe microanalysis: Applications to Cell Physiology," *Ultramicroscopy* 24: 185, 1988.
2. A. LeFurgey et al., "Na-Ca compartmentation in cultured heart cells," *Microbeam Analysis--1987*, 267.
3. E. S. Wheeler-Clark and J. McD. Tormey, "Electron probe x-ray microanalysis of sarcolemma and junctional sarcoplasmic reticulum in rabbit papillary muscles: Low sodium-induced calcium alterations," *Circulation Research* 60: 246, 1987.
4. T. A. Hall and B. L. Gupta, "Quantification for the x-ray microanalysis of cryosections," *J. Microscopy* 126: 333, 1982.
5. L. E. Thomas, "Microanalysis of light elements with an ultrathin window x-ray spectrometer," *Proc. 38th Ann. Meet. EMSA* 1980, 90.
6. L. Ebihara et al., "The initial inward current in spherical clusters of chick embryonic heart cells," *J. Gen. Physiol.* 75: 437, 1980.
7. A. LeFurgey, P. Ingram, and M. Lieberman, "Quantitative microchemical imaging of calcium in Na-K pump inhibited heart cells," *Cell Calcium* 9: 219, 1988.
8. T. A. Hall, "Biological x-ray microanalysis," *J. Microscopy* 117: 145, 1979.
9. J. L. Goldstein et al., *Scanning Electron Microscopy and X-ray Microanalysis*, New York: Plenum Press, 1981.
10. R. G. Musket, "Properties and applications of windowless Si(Li) detectors," in K. F. J. Heinrich et al., Eds., *Energy Dispersive X-Ray Spectrometry*. National Bureau of Standards Special Publication 604, Washington, D.C., 1981, 97.
11. T. Kitazawa, H. Shuman, and A. P. Somlyo, "Quantitative electron probe analysis: Problems and solutions," *Ultramicroscopy* 11: 251, 1983.

RAPID FREEZING OF HAMSTER HEARTS IN VIVO AT DEFINED TIMEPOINTS OF THE CARDIAC CYCLE

M. Bond and A.-R. Jaraki

The technique of electron probe microanalysis (EPMA) is uniquely able to measure subcellular elemental concentrations in situ with nanometer spatial resolution.^{1,2} The majority of EPMA studies have been carried out on isolated tissue preparations rapidly frozen in vitro, e.g., vascular smooth muscle strips,³ bundles of skeletal muscle fibers,⁴ or freshly isolated or cultured cell preparations.^{5,6} In vitro preparations are ideal for rapid freezing for EPMA, since the dissected piece of tissue is sufficiently small not to constitute a significant heat sink and thus freezing rates are optimized.⁷ Nevertheless, as documented by recent EPMA studies performed on rat liver,^{8,9} pancreas,¹⁰ brain cortex,¹¹ lung,¹² and kidney papillae¹³ rapidly frozen in vivo, tissue need not necessarily be excised from the animal for elemental composition to be successfully measured at the subcellular level. For example, in the rat liver rapidly frozen in vivo,⁸ measurements obtained by EPMA demonstrated that the principal subcellular store of Ca^{2+} was localized in the endoplasmic reticulum (ER) and not in the mitochondria, as had previously been proposed.¹⁴ With a similar in vivo freezing protocol, EPMA measurements demonstrated that vasopressin stimulation of the liver in vivo could directly activate release of Ca^{2+} from the ER and stimulate the uptake of Mg^{2+} (but not Ca^{2+}) into the mitochondria.⁹

For the investigation of Ca^{2+} compartmentation in cardiac muscle and Ca^{2+} movements during the cardiac cycle, the measurement of subcellular Ca^{2+} concentrations by EPMA in the intact beating heart in vivo would be a useful corollary to the EPMA measurements of subcellular elemental composition that have previously been obtained in cryosections of rapidly frozen papillary muscle or other in vitro cardiac preparations.¹⁵⁻¹⁸ To achieve this aim, we have recently developed a protocol that permits rapid freezing, with good ultrastructural preservation, of the intact, spontaneously beating hamster heart in vivo at precise timepoints of the cardiac cycle.¹⁹

Experimental

In contrast to other tissues that have been

The authors are at the Cleveland Clinic Foundation, Department of Heart and Hypertension Research, 9500 Euclid Ave., Cleveland, OH 44195-5069. This work was supported in part by a grant from the Northeast Ohio American Heart Association to M.B. We gratefully acknowledge the technical assistance of Candis H. Disch.

rapidly frozen in vivo, cytosolic Ca^{2+} in the heart is known to be constantly cycling. Therefore, in order to know the precise timepoint in the cardiac cycle at which the beating heart is frozen in vivo, left ventricular pressure (LVP) or some other physiological indicator must be continuously monitored, right up to the moment the heart is frozen.

The experimental procedures that we have developed for rapid freezing of the heart in vivo will be described as performed for the hamster heart;¹⁹ however, we have found these methods to be also applicable to rapid freezing of rat or guinea pig heart in vivo (unpublished observations).

Hamsters anesthetized with Inactin (80-90 mg/kg) are tracheotomized and ventilated with room air (80-90 strokes/min; tidal volume: 1-1.2 ml). The femoral and right carotid arteries are then cannulated with PE10 tubing. Blood gases are measured from a 200 μl sample of arterial blood from the femoral artery to insure that blood pH, pO_2 , and pCO_2 are within physiological limits. A cannula is inserted from the right carotid artery into the left ventricle for recording of LVP. The abdomen is then opened, the diaphragm cut, a medial incision made into the sternum and the ribs drawn back towards the head. A superficial suture is placed in the apex of the heart and a "lung-pressor," a curved piece of Teflon with a central hole in it, is then placed over the exposed thorax and the heart allowed to protrude through the hole. This procedure allows the heart to be clear of other organs when frozen. To prevent the surface of the heart from drying in room air, warmed saline (37 C) is dripped over the surface of the heart after it is exposed. The arrangement for rapid freezing of the hamster heart in vivo is shown in Fig. 1.

The heart is rapidly frozen by a pair of hand-triggered aluminum clamps (Bioinstrumentation Group, University of Pennsylvania) with freezing surfaces of frozen Freon 22 (-160 C).¹⁰ These clamps were previously used for rapid freezing of rat liver and rat pancreas in vivo.⁸⁻¹⁰ Freezing of the heart in vivo is achieved by gently lifting of the beating heart away from the body by the apical suture and, with the heart positioned between the opened clamps, rapid triggering of the clamps to close. The precise timepoint at which the heart is frozen is recorded as a sharp artifact on the LVP trace (Fig. 2).

Ultrathin cryosections are then cut from the surface of the frozen heart, as previously described,¹⁹ which insures that the plane of the sections is parallel to the surface of the

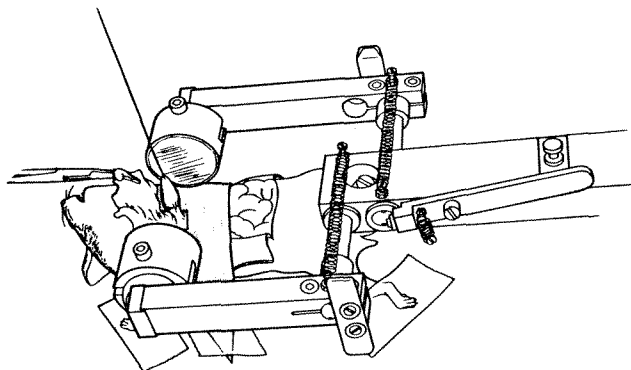


FIG. 1.--Experimental arrangement used for rapid freezing of hamster hearts in vivo. Heart is gently lifted away from the body by apical suture and lungs are kept out of path of clamps by a Teflon "lung pressor" (stippled). Al cups are filled with frozen Freon 22 (shadowed).

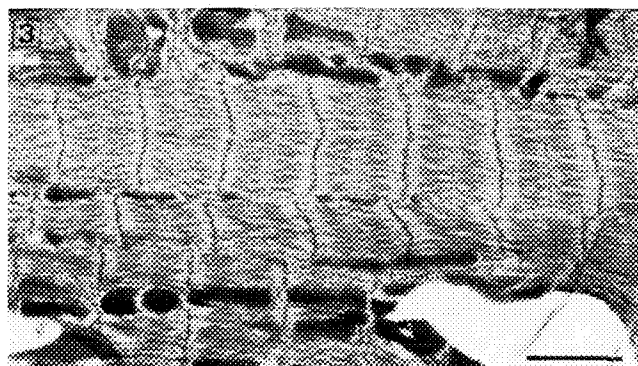


FIG. 3. Freeze-dried cryosection cut from surface of hamster heart rapidly frozen in vivo. A and I bands, as well as M-lines and Z-bands, are clearly visible. Dark, electron opaque regions: mitochondria. Scale = 2 μ m.

heart. Since the most superficial muscle fibers run parallel to the surface of the heart, the cardiac muscle cells are then longitudinally oriented in the cryosections. An example of a freeze-dried cryosection cut from the surface of a hamster heart rapidly frozen in vivo is shown in Fig. 3. Energy-dispersive x-ray spectra are obtained from subcellular compartments (A-band, mitochondria) as well as from the whole cell in cryosections from the rapidly frozen hearts.

Results and Conclusions

In view of evidence in the literature that cardiac muscle cells in hearts of the cardiomyopathic hamster may be overloaded with Ca^{2+} ,²⁰⁻²² subcellular Ca^{2+} composition in normal and cardiomyopathic hamster hearts, rapidly frozen in vivo in diastole, was compared (Table 1).

The mitochondrial Ca^{2+} content measured in normal hamster hearts ("control;" Table 1) was found to be very low and within the range of values previously measured by EPMA in other tissues both in vivo and in vitro.^{2,3,8,9} Thus, in the beating heart in vivo, where mitochondria constitute 35-40% of the cell volume, these EPMA

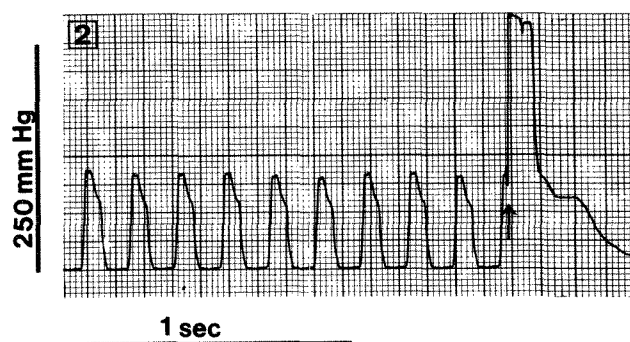


FIG. 2.--Left ventricular pressure trace from contracting hamster heart in vivo, indicating precise timepoint (upward arrow) at which beating heart is rapidly frozen by clamps.

TABLE 1.-- Cellular and subcellular Ca^{2+} composition of normal and myopathic hamster hearts rapidly frozen in vivo.

(mmol Ca^{2+} /kg dry wt \pm SEM)				
AGE	STRAIN	CELL	MITOCHONDRIA	A-BAND
50 days	CONTROL	3.4 \pm 0.7	0.9 \pm 0.2	2.6 \pm 0.4
50 days	MYOPATHIC	2.9 \pm 0.5	0.7 \pm 0.2	3.0 \pm 0.4
97 days	CONTROL	2.5 \pm 0.7	1.2 \pm 0.4	3.7 \pm 0.8
97 days	MYOPATHIC	3.3 \pm 0.5	0.9 \pm 0.3	3.6 \pm 0.4

No statistically significant differences were found in Ca^{2+} concentration within subcellular regions, amongst the four groups

results indicate that mitochondria do *not* appear to act as significant Ca^{2+} storage sites. The Ca^{2+} concentrations measured in the A-band and whole cell are somewhat higher than previously measured in cryosections of rapidly frozen papillary muscle preparation.^{15,18} This is likely to be due to the fact that the in vivo heart rate (4-6 Hz in the hamster¹⁹) is significantly higher than the rate of electrical stimulation of isolated papillary muscles (generally less than 0.5 Hz). Thus, in the hearts frozen in vivo, less time is available between beats for removal of Ca^{2+} from the cytoplasm (e.g., from Ca^{2+} binding sites on troponin C), by uptake of Ca^{2+} into the sarcoplasmic reticulum and/or by efflux from the cell.

In regards to subcellular Ca^{2+} content in cardiomyopathic hamster hearts, these studies reveal that, contrary to expectations based on previous measurements of total Ca^{2+} content of homogenates of whole hearts,^{21,23} in general, cardiac muscle cells of myopathic hamster hearts do *not* appear to be Ca^{2+} overloaded. Nevertheless, highly localized elevations of cellular and subcellular Ca^{2+} were found in damaged or dying cardiac myocytes in the vicinity of necrotic foci.¹⁹ These measurements therefore demonstrate that there is a marked heterogeneity in cellular Ca^{2+} content

throughout the hearts of cardiomyopathic hamsters and refute the hypothesis of a generalized and widespread Ca^{2+} overload, at least under baseline conditions (absence of inotropic stimulation).

The EPMA measurements of subcellular Ca^{2+} content in normal and myopathic hamster hearts reported here, and in detail elsewhere¹⁹ testify to the feasibility of measuring subcellular elemental content by EPMA in freeze-dried cryosections from the intact beating heart, rapidly frozen in vivo. For some investigations, e.g., the effects of altered coronary blood flow on cardiac performance and on elemental composition, or the actions of circulating hormones on cardiac metabolism, the option of "in vivo EPMA" should prove to be a useful and valid experimental approach.

References

1. A. P. Somlyo, *Cell Calcium* 6: 197, 1985.
2. A. LeFurgey, M. Bond, and P. Ingram, *Ultramicroscopy* 24: 185, 1988.
3. M. Bond, H. Shuman, A. P. Somlyo, and A. V. Somlyo, *J. Physiol.* 357: 185, 1984.
4. A. V. Somlyo, H. Gonzalez-Serratos, H. Shuman, G. McClellan, and A. P. Somlyo, *J. Cell Bio.* 90: 577-594, 1981.
5. E. Murphy, D. M. Wheeler, A. LeFurgey, R. Jacob, L. a. Lobaugh, and M. Lieberman, *Am. J. Physiol.* 250: C442, 1986.
6. L. M. Buja, K. P. Burton, and H. K. Hagler, *Circ.* 68: 872-882, 1983.
7. H. Y. Elder, C. C. Gray, A. G. Jardine, J. N. Chapman, and W. H. Biddlecombe, *J. Microscopy* 126: 45-61, 1982.
8. A. P. Somlyo, M. Bond, and A. V. Somlyo, *Nature* 314: 622-625, 1985.
9. M. Bond, G. Vadasz, A. V. Somlyo, and A. P. Somlyo, *J. Biol. Chem.* 262: 15630-15636, 1987.
10. A. V. Somlyo, M. Bond, J. D. Silcox, and A. P. Somlyo, *Proc. EMSA 43rd Ann. Meet.*, 10-13, 1985.
11. A. P. Somlyo, R. Urbanics, G. Vadasz, AGB Kovach, and A. V. Somlyo, *Biochem. and Biophys. Research Commun.* 132: 1071-1078, 1985.
12. R. G. Eckenhoff and A. P. Somlyo, *Am. Physiol. Soc.* 254: C614-620, 1988.
13. F. Beck, A. Dorge, R. Rick, and K. Thureau, *Kidney International* 25: 397-403, 1984.
14. G. L. Becker, G. Fiskum, and A. L. Lehninger, *J. Biol. Chem.* 255: 9009-9012, 1980.
15. E. S. Wheeler-Clark, and J. McD. Tormey, *Circ. Res.* 60: 246-250, 1987.
16. M.-F. Wendt-Gallitelli, and H. Wolburg, *J. Elect. Microsc. Tech.* 1: 151-174, 1984.
17. D. Johnson, K. Isutsu, M. Cantino, and J. Wong, *Ultramicroscopy* 24: 221-236, 1988.
18. A. O. Jorgensen, R. Broderick, A. P. Somlyo, and A. V. Somlyo, *Circ. Research* 63: 1060-1069, 1988.
19. M. Bond, A.-R. Jaraki, C. H. Disch, and B. Healy, *Circ. Research* 64: 1001-1012, 1989.
20. K. Lossnitzer, J. Janke, B. Hein, M. Stauch, and A. Fleckenstein, *Rec. Adv. Card. Struct. Metab.* 6: 207-217, 1975.
21. K. Wrogieman and E. G. Nylen, *J. Molec. Cell. Card.* 10: 185-195, 1978.
22. J. A. Wagner, I. J. Reynolds, H. F. Weisman, P. Dudeck, M. L. Weisfeldt, and S. H. Snyder, *Science* 232: 515-518, 1986.
23. L. Proschek, and G. Jasmin, *Muscle Nerve* 5: 26-32, 1982.

COMPARISON OF DAMAGE PRODUCED BY PHOTON AND ELECTRON EXCITATION

D. B. Wittry, D. M. Golijanin, and S. Sun

Many investigators who are accustomed to using electron beams for exciting x rays and who have a knowledge of x-ray interactions with matter are still unaware of the large difference in the damage produced by x-ray photons and by electrons in the range of 5-100 keV when photons or electrons are used as a means of excitation for x-ray spectrochemical analysis. In this paper, we compare the energy dissipation in specimens of various atomic number produced by electrons and by x rays. The comparison is made first on the basis of the energy loss for a given path length, then on the basis of the number of inner-shell excitations produced for a given energy dissipation, and finally on the basis of the energy dissipated in a specimen when detecting elements present at a given limit of detectability. It is shown that not only are x rays less damaging than electrons, but because of the selective excitation by x-ray photons and the lower background produced in the specimen, the damage produced can be up to six orders of magnitude less than when electron excitation is used.

Energy Loss per Unit Path Length

For x-ray photons, the energy absorbed by a specimen in a path length dx is given by

$$dE_1 = E_\nu \sum_i \left(\frac{\mu}{\rho} \right)_i c_i \rho dx \quad (1)$$

where E_ν is the photon's energy, c_i is the weight fraction of element i , ρ is the density, and $(\mu/\rho)_i$ is the mass absorption coefficient of element i . The corresponding quantity for electrons is given by Bethe's retardation law:¹

$$dE_2 = \frac{7.85 \times 10^4 \rho \bar{Z} dx}{E \bar{A}} \ln \frac{1.166 E}{J} \text{ keV} \quad (2)$$

In this expression, \bar{Z} is the average atomic number, \bar{A} is average atomic weight, E is the electron energy in keV, and the average ionization energy J is given by

$$J = (9.76 \bar{Z} + 58.5 \bar{Z}^{-0.19}) 10^{-3} \text{ keV} \quad (3)$$

The specimen's density occurs in both of these expressions and hence it is convenient to

D. B. Wittry is in the Departments of Materials Science and of Electrical Engineering, and S. Sun is in the Department of Materials Science at the University of Southern California, Los Angeles, CA 90089-0241; D. M. Golijanin is in the Electronics Division, Xerox Corp., A3-26, El Segundo, CA 90245.

plot $dE/d(\rho x)$ as a measure of the energy loss per unit path length. The results are shown in Fig. 1 for elemental specimens based on mass absorption coefficients of Heinrich.²

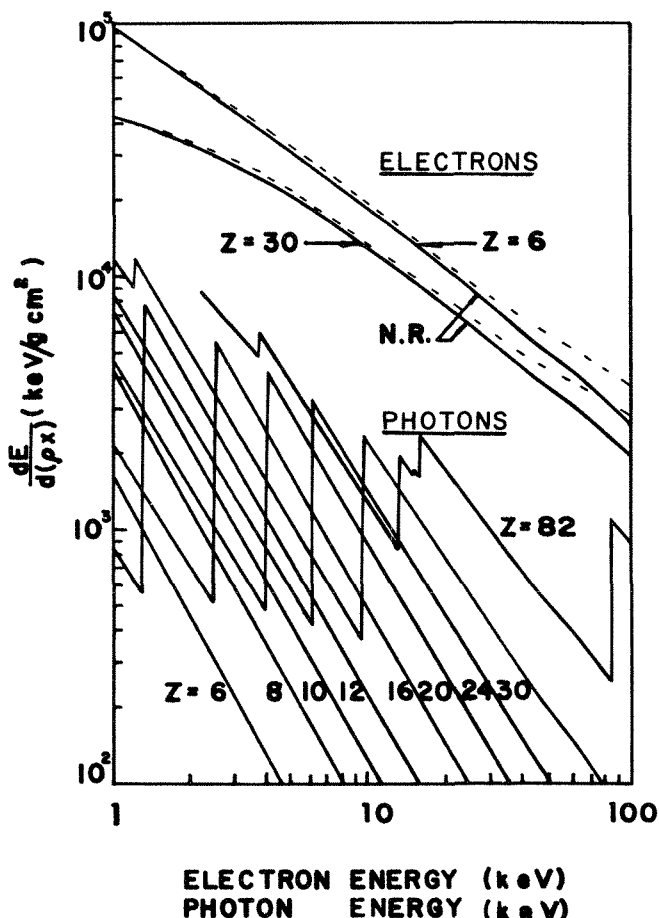


FIG. 1.--Mass stopping power of elemental specimens for electrons and photons as a function of particle energy.

Characteristic Excitations for a Given Damage

X rays are inherently more efficient for generation of inner-shell excitations than are electrons. That is true because the fraction of the x-ray photon's energy absorbed by atoms that goes into inner-shell excitation is given by

$$f = \frac{r_i - 1}{r_i} \quad (4)$$

where r_i is the absorption jump ratio corresponding to level i (e.g., r_K for K excitation). The absorption jump ratio for the K edge varies from about 14 for low atomic number to a little over 4 for high atomic number.²

Thus, the fraction of energy absorbed that produces K ionization ranges from 93% to 75%. The number of K ionizations of element A per unit path length for x-ray excitation is given by

$$dn_1 = \left(\frac{\mu}{\rho}\right)_A \left(\frac{r_K - 1}{r_K}\right) c_A \rho dx \quad (5)$$

Then, for x-ray excitation, the ratio of the number of ionizations to the energy dissipated is given by

$$\frac{dn_1}{dE_1} = c_A \left(\frac{\mu}{\rho}\right)_A \left(\frac{r_K - 1}{r_K}\right) [E_\nu \sum_i \left(\frac{\mu}{\rho}\right)_i c_i]^{-1} \quad (6)$$

The corresponding ratio for electron excitation may be obtained from the following expression for the number of ionizations in a layer of thickness dx :

$$dn_2 = c_A (\rho N/A) Q_K(E_K, E) dx \quad (7)$$

where $Q_K(E_K, E)$ is the cross section for K ionization for which the Bethe cross section³ may be used:

$$Q_K = \frac{7.058 \times 10^4}{N E_K E} \ln\left(\frac{0.65 E}{E_K}\right) \quad (8)$$

where N is Avogadro's number, E_K is the critical excitation energy in keV, and E is the electron's energy in keV. By using Eq. (2) for the energy dissipation of an electron beam, we obtain the following ratio of the number of ionizations to the energy dissipated in the specimen for electron excitation:

$$\frac{dn_2}{dE_2} = \frac{0.9 c_A \ln(0.65 E/E_K)}{\bar{Z} E_K \ln(1.166 E/J)} \quad (9)$$

The ratio of Eq. (6) to Eq. (9) gives the relative efficiency of photons compared with electrons for exciting K levels in a specimen.

Because of the importance of nondestructive analytical techniques for biological materials, we illustrate this ratio for a specific case, namely Ti $K\alpha$ radiation exciting Ca K levels. Without considering the details of the specimen composition, we assume that a nonhydrated biological specimen would consist almost entirely of water; a dehydrated specimen would have a composition that would more closely resemble pure carbon. These limiting cases are shown in Fig. 2, which compares the efficiency of Ti $K\alpha$ photons with the efficiency of electrons for exciting Ca K levels. In addition, we have also shown the case for calcium phosphate which in bone consists of $\text{Ca}_3(\text{PO}_4)_2$ and in teeth is in the form of apatite, $\text{Ca}_5(\text{PO}_4)_3(\text{OH}, \text{Cl}, \text{F})$. The mass absorption coefficients used in Fig. 2 were as follows:

- (μ/ρ) for calcium = 772.2 cm^2/gm
- (μ/ρ) for water = 58.2 cm^2/gm
- (μ/ρ) for carbon = 23.8 cm^2/gm
- (μ/ρ) for phosphorus = 370.0 cm^2/gm

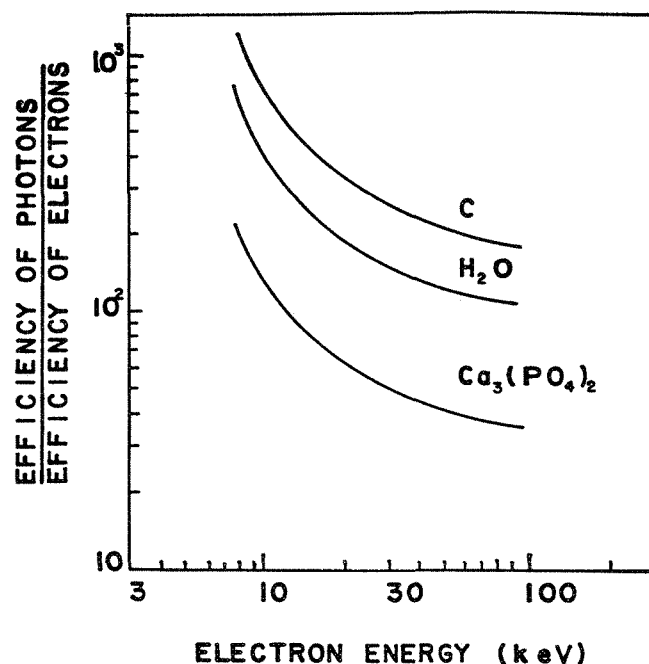


FIG. 2.--Relative efficiency for excitation of calcium K levels by titanium $K\alpha$ radiation and electrons of various energy.

Damage Produced for Comparable Detection Limits

In a previous paper⁴ we compared the detection limits for x-ray analysis based on electrons and photons. For a measurement time of 100 s, it was anticipated that the detection limit based on wavelength-dispersive spectrometry would be as low as 2.67×10^{-7} parts by weight. This estimate may be compared with a typical value for electron-probe microanalysis of 10^{-4} . The factor of 370 lower detection limit is almost entirely due to the fact that the photon excitation produces less background than the electron excitation (e.g., the signal/background ratio for a pure specimen is about 10^5 for photon excitation vs 10^3 for electron excitation). Since the detection limits are inversely proportional to the square root of the background, the damage produced for comparable detection limits would be reduced for photon excitation by an additional factor of approximately 10^4 .

References

1. J. I. Goldstein et al., *Scanning Electron Microscopy and X-ray Microanalysis*, 1981, 58; for the relativistic case, refer to D. B. Brown, D. B. Wittry and D. F. Kyser, "Prediction of x-ray production and electron scattering in electron probe analysis using a transport equation," *J. Appl. Phys.* 40: 1627-1636, 1969.
2. K. F. J. Heinrich, "X-ray absorption uncertainty," in T. D. McKinley, K. F. J. Heinrich, and D. B. Wittry, Eds., *The Electron Microprobe*, New York: Wiley, 1966, 296-377.
3. Ref. 1, p. 104.
4. D. B. Wittry and D. M. Golijanin, "Detection limits in microprobe x-ray fluorescence analysis," *Microbeam Analysis--1988*, 394.

AN ELECTRON SPECTROSCOPIC STUDY OF ICE

J. R. Dunlap, Suichu Luo, R. D. Bunn, and D. C. Joy

It is now standard practice to perform microanalysis on biological specimens in their frozen hydrated form. The technique of cryofixation preserves structure and the distribution of diffusible elements within the materials, while minimizing the unavoidable background of extraneous elements introduced by chemical fixation. The resultant sample is then to a first approximation a dilute solution of various elements and compounds in ice and consequently the properties of the ice become important to the interpretation of any spectra and images obtained. In this paper we report on some preliminary observations of, and calculations on, the inelastic mean free path and plasmon loss energy for vitreous ice.

Methods and Materials

Samples of vitreous ice were obtained from the Controlled Environment Vitrification System (CEVS) described by Bellare et al.¹ A 5ml drop of water was pipetted onto a holey carbon film, then thinned and flash frozen in liquid ethane. This technique produces a thin layer of vitrified ice spanning the holes in the film. Samples were transferred to an Hitachi H 800 TEM/STEM using a Gatan cryo-transfer holder, and observed at 200 keV in the scanning transmission electron microscopy (STEM) mode while being maintained at a temperature of about 100 K. Annular dark-field (ADF) and energy-filled (EF) images were collected, through a carefully linearized video chain,² by an ORTEC EDSII digital imaging unit. The ADF and EF images were acquired simultaneously as 256 × 256 pixel × 16 bit arrays. Stored images were transferred to (and subsequently analyzed on) a VAX based Perceptics 9200 image analysis system. Spectra were collected through a GATAN 607 electron energy loss spectrometer system also interfaced to the ORTEC EDSII multichannel analyzer.

Results and Discussion

The thicknesses of the ice film were determined from images of the type shown in Fig. 1. From the known mass-thickness variation of the polystyrene spheres with radial position, a calibration curve of absolute fractional dark-field signal intensity (i.e., dark-field signal normalized by the incident beam current) vs mass thickness was constructed (Fig. 2). The thickness of the ice film at any position within the field of a stored image could then be read off directly from the digitized intensity

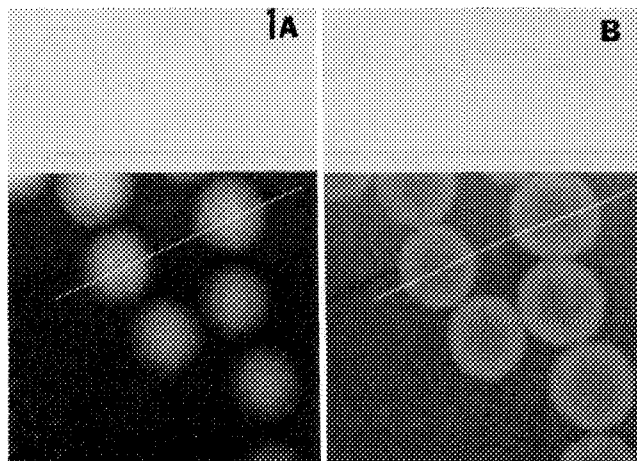


FIG. 1.--Vitrified sample of 264nm polystyrene spheres in water. Line trace shows relative intensity across two spheres. (a) ADF-STEM, (b) EF-STEM image. Note intensity inversion with increasing thickness.

and the calibration data. Films were generally found to range in thickness up to 350 nm depending on the position analyzed. As noted by Carlemalm et al.,³ even at relatively high mass thicknesses ice films have a low inherent contrast and therefore form a good matrix for imaging purposes.

Electron energy loss spectra were then recorded in standard serial acquisition mode from regions of thickness determined as described above. A typical example (Fig. 3) shows a well-resolved zero-loss peak and the somewhat broad "plasmon" peak. The averaged value of the plasmon energy loss peak E_p is 21 eV, with a FWHM of about 22 eV (at an instrumental resolution of 8 eV). The experimentally determined value of E_p is in good agreement with a theoretical estimate based on the model of Ashley,⁴ assuming that vitreous ice and water have essentially the same physical parameters. The fact that the E_p value for ice falls below the 24eV value measured from most biological tissue means that frozen hydrated tissue will display a composite plasmon peak that will be broad and possibly complex in shape. However, the energy separation also means that the energy-filtered image can be used to enhance the contrast of tissue against the ice background.

Values of the inelastic mean free path λ were obtained by simultaneous measurement of the thickness t of the ice from the dark-field image and determination of the ratio t/λ from the relation

$$t/\lambda = \ln(I_{\text{tot}}/I_{\text{zeroloss}}) \quad (1)$$

The authors are with the Electron Microscopy Program at The University of Tennessee, Knoxville, TN 37996-0810.

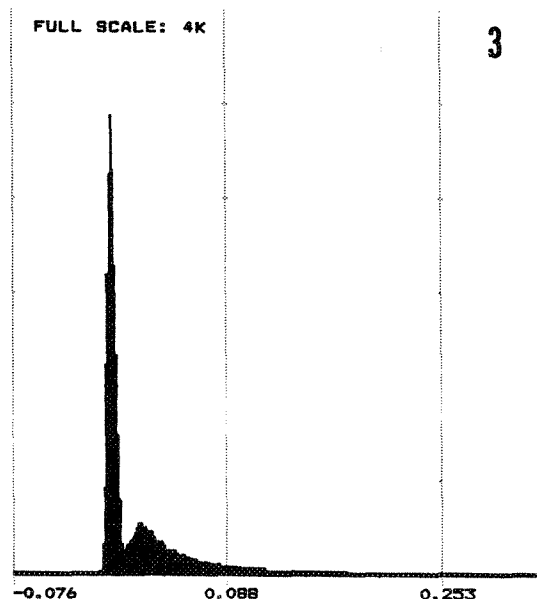
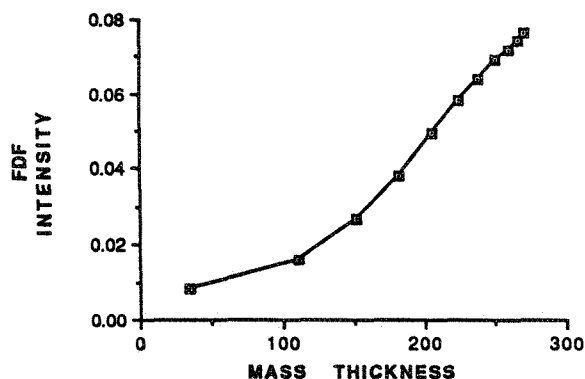


FIG. 2.--Normalized ADF image intensity (FDF) vs mass thickness of polystyrene sphere like those shown in Fig. 1.

FIG. 3.--Electron energy loss spectrum collected from vitrified ice with estimated thickness of 100 nm.

where I_{tot} is the total intensity in the energy loss spectrum, integrated from the onset of the zero loss peak to the end of the scanned spectrum; and I_{zeroloss} is the corresponding zero-loss intensity integrated over the full width (instrumental resolution) of the peak. Initial preliminary results show that for vitreous ice λ is ca 250 nm at 200 keV, although exact measurement is difficult because of rapid beam induced damage. The figure obtained for vitreous ice is in good agreement with theoretical estimates based on optical data and Hartree-Fock atomic cross sections, which gave λ_{ice} as 150 nm at 100 keV.⁵

The high sensitivity of the ice to beam interactions is possibly due to the attack of the film by ionized hydroxyl groups generated by the incident electrons. Calculations based on the standard theory of Talmon⁶ show that, for the beam conditions used here ($3.5 \times 10^3 \text{ e/nm}^2$), the local heating would only be a few degrees Kelvin; given the operating vacuum of the microscope, this heating would be insufficient to raise the vapor pressure to a level at which thermal mass loss is a significant factor. This same mechanism might also lead to enhanced mass loss from tissue embedded in the ice. From the experimentally determined value of λ , subsequent thickness measurements of the ice were made by application of Eq. (1) to spectra collected from various areas of the sample.

Conclusions

Preliminary experiments show that for vitreous ice the dominant excitation occurs at 21 eV. This peak is similar in shape to that observed for amorphous carbon, but is broader (approximately 22 eV at FWHM) and occurs at a

lower energy. At 200 keV the measured total inelastic mean free path λ for this excitation is about 250 nm, which is in good agreement with previous theoretical estimates. Work is now in progress to determine the radiation sensitivity and other significant parameters of ice so that its properties as an embedding medium for biological analytical electron microscopy can be quantified.

References

1. J. R. Bellare, H. T. Davis, L. E. Scriven, and Y. Talmon, "The controlled environment vitrification system (CEVS): An improved sample preparation technique," *J.E.M. Tech.* 10: 87, 1988.
2. R. D. Bunn, J. R. Dunlap, and D. C. Joy, "Toward improved Z-contrast imaging," *Proc. 46th Ann. Meet. EMSA*, 1988, 650.
3. E. Carlemalm, C. Colliex, and E. Kellenberger, "Contrast formation in electron microscopy of biological material," *Adv. Elect. and Elect. Phy.* 63: 269, 1985.
4. J. C. Ashley, "Stopping power of liquid water for low-energy electrons," *Rad. Res.* 89: 25, 1982.
5. R. F. Egerton, "Some problems in electron energy loss spectroscopy, elemental mapping and Z-contrast imaging," *Inst. Phys. Conf. Ser.* 68: 97, 1983.
6. Y. Talmon, "Electron beam radiation damage to organic and biological cryospecimens," in R. A. Steinbercht and K. Zierold, Eds., *Cryotechniques in Biological Electron Microscopy*, Berlin: Springer-Verlag, 1987, 64.

ELECTRON MICROSCOPY STUDY OF MICROBIOLOGICALLY INFLUENCED CORROSION

Xiao Zhang, C. Joy, and R. A. Buchanan

In recent years, microbially influenced corrosion (MIC) has been recognized as a serious worldwide problem in many industries, particularly the power-generating industry, the petrochemical industry, gas transmission lines, and naval systems. MIC may be defined as the degradation of metallic structures resulting from the activity of a variety of microbes that either produce aggressive metabolites to render the environment corrosive, or are able to participate directly in the electrochemical reactions occurring on the metal surface.¹ The study of MIC is an interdisciplinary subject that requires a knowledge of microbiology in addition to that of corrosion science. Generally, MIC is associated with biofouling, which is caused by the activity of microbes that produce deposits of gelatinous slime or biogenically induced corrosion products on metal surfaces. A wide range of genera and species of microbe are involved in MIC. They may be classified into three groups: (1) aerobic and anaerobic bacteria, (2) fungi, and (3) algae and diatoms. Materials involved in MIC include carbon steel, some stainless steels, copper and copper alloys, nickel and some nickel alloys, cast iron, and aluminum.

The variety of microbes and degraded materials encountered in MIC results in the complexity of mechanisms of MIC. So far, most MIC studies have focused on the effects of sulfate-reducing bacteria (SRB) and marine bacteria which are present as mixed cultures in most cases. Although several MIC-associated mechanisms, such as cathodic depolarization, have been proposed by which MIC could function with metals, the understanding of MIC is far from complete. The fundamental aspects of these processes require further investigation. For example, under what surface physical and chemical conditions can MIC occur? What is the mechanism of microbe attachment to a metal surface? Which types of microbes are involved? What is the relation between the metabolic activity of microbes and the dissolution of metal ions in aqueous solution? And how can MIC be identified, monitored, and controlled? Electron microscopy (EM) and microanalysis techniques are suitable for the characteristic

The authors are with EM facility, University of Tennessee, Knoxville, and with the Department of Materials Science and Engineering, University of Tennessee, Knoxville, TN 37996. They wish to acknowledge the isolation of A6F bacterium by A. Vass of the Institute for Applied Microbiology of UTK, the surface fixation effort of R. Williams, the part of SEM and EDS work of B. L. McGill, and the helpful discussions with J. C. Danko.

evaluation of the surface and/or interfacial condition of MIC, such as bacterial attachment, microstructure and composition of the biofilm and metal surface, and the relationship of surface defects and bacterial attack.

SRB do not appear to be the most prevalent biological contributors in nuclear power plant systems, unlike MIC in many other industries.² Stainless steel (SS) is widely used as a structural material in the system. SS is thought to be corrosion resistant under oxidizing conditions (if no significant amounts of halide exist), but not usually resistant to reducing environments. Areas depleted of oxidants such as crevices or areas lying under bacteri-produced slime deposits, are therefore quite susceptible to localized corrosion. Pitting of SS welds induced by bacteria is most frequently observed in the weld metal.² In this paper, a laboratory-based EM study of MIC by a single bacterial strain (other than SRB) on an SS weld metal is presented. Previous electrochemical studies have shown the aggressiveness of the bacteria used in this study toward E308 SS weld metal, and have also suggested the mechanism of enhanced anodic dissolution of the weld metal by bacterial action.^{3,4}

Experimental

A single bacterial strain, designated as A6F and extracted from a known MIC failure site in a nuclear power industrial fresh-water system, was used in the present studies. The A6F bacterium was characterized as a gram-negative, facultatively anaerobic, acetic acid producing, rod-shape bacterium. A synthetic fermenter-enriched medium containing dextrose and mineral salts was used as the nutrition source. An as-deposited E308 SS weld metal specimen with a 600 grit polishing surface was immersed into the medium solution for 72 h. A6F bacteria grew in a batch condition. After exposure, the surface of E308 weld metal was sequentially fixed by 4% glutaraldehyde buffer solution, rinsed with phosphate buffer solution, dehydrated gradually by 25%, 50%, 75%, and 100% acetone, and finally critical-point dried. The specimen surface was then coated with carbon. Surface analyses were carried out by optical microscopy, scanning electron microscopy (SEM), and energy-dispersive x-ray spectroscopy (EDS).

Results

When a metal specimen is immersed in a bacterial solution, the corrosion process of metal and adhesion of bacteria to the metal surface take place simultaneously. These two processes initially start independently, and after a

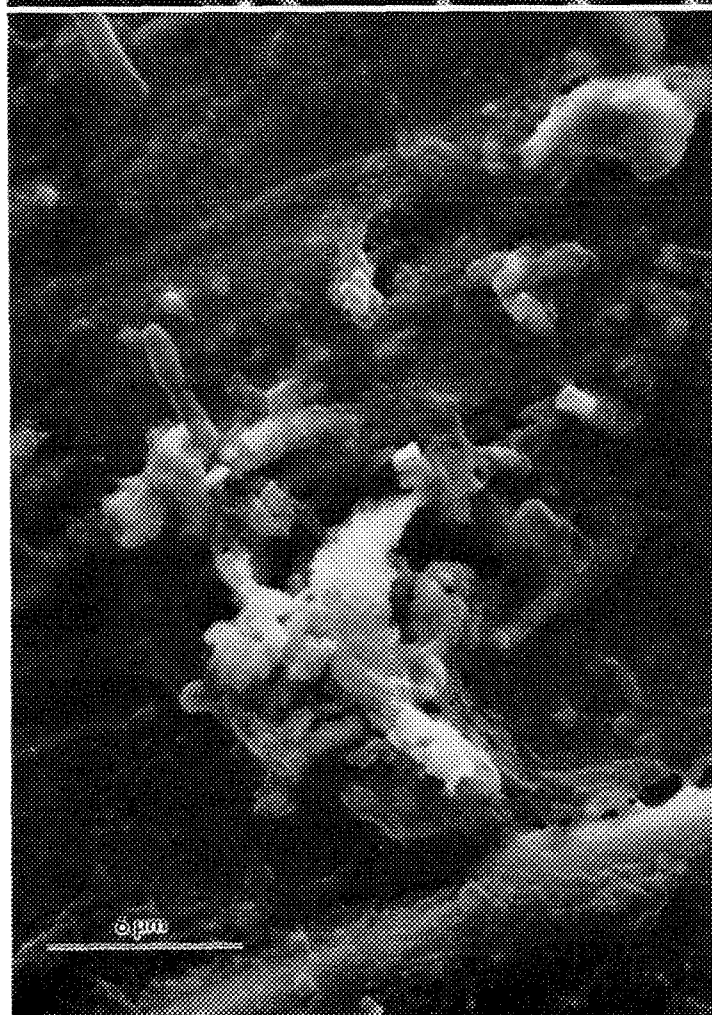
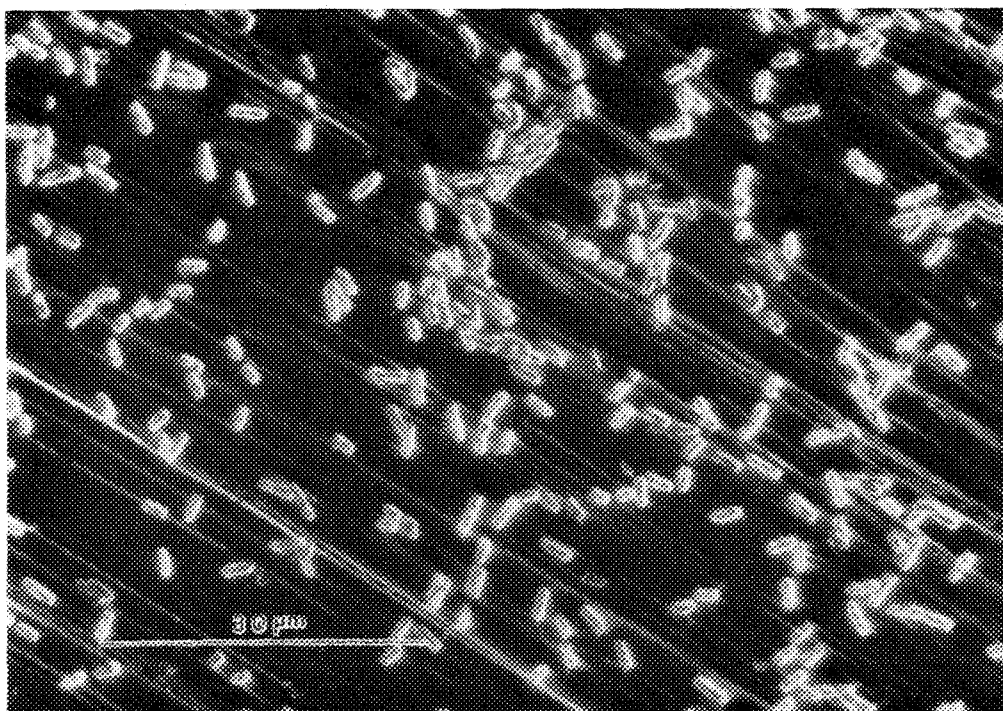


FIG. 1.--Polarized dark-field light micrograph of bacterial cells on surface of as-deposited E308 weld metal after 72h exposure.

FIG. 2.--Microniche deposits on E308 weld metal surface, showing pit formed underneath. Note also bacterial cells inside microniche, covered by thin extracellular film.

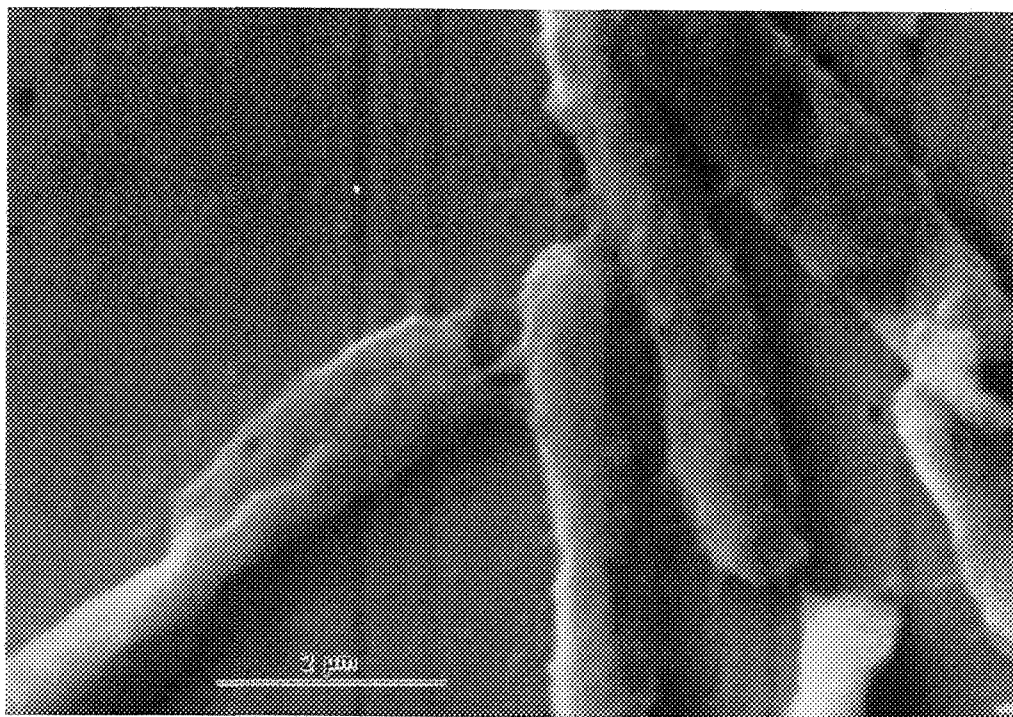


FIG. 3.--Bacterial cells bonded by microbial synthesized polymer material adhere to E308 weld metal surface.

while they interfere with each other. Bacteria very quickly adhere to the metal surface due to the enriched nutritional environment. As an example, as seen in the polarized dark-field image of a light microscope, the surface of E308 weld metal revealed a large population of rod-shape A6F bacteria after 76 h exposure (Fig. 1). The bacteria are distributed nonuniformly either in single cells or in small groups, or are "glued together" as members of a colony or microniche (Fig. 2). Either nonuniform corrosion (due to the heterogeneous surface composition or surface defects) or a different pH and oxygen reaction rate over anode and cathode could induce nonuniform bacterial adhesion, which later promotes the growth of bacterial microniches. Electrostatic interaction at the metal/bacterial interface also facilitates nonuniform bacterial adhesion.⁵ The microniches encourage the formation of the nonuniform deposits characteristic of MIC in many cases.⁶

It was found that bacterial cells were bonded by a gel-like network of extracellular material (Fig. 3) which was secreted from metabolic activity. With the development of a critical mass of bacterial cells, extracellular polymeric substances, and corrosion products, a microniche was formed (Fig. 2). A microbe-synthesized polymer film appears to mediate irreversible attachment of the bacterial cells and microniches (Figs. 2 and 3) and is favorable for the overcoming of the energy barrier of electrostatic interaction between bacterial cells and metal surface.^{5,7}

A microbial microniche would produce a local occlusive geometry (Fig. 2), which could induce

the formation of differential oxygen concentration cells and local acidification resulting from the bacterial metabolism. It is estimated that the pH under the deposit could be as low as zero.⁵ The area under the deposit may become anodic relative to the surrounding area. Chloride ions would migrate into the occlusive area due to the requirement of charge balance. The local acidification and chloride ion concentration could cause the breakdown of passive films of the weld metal surface, and thus induce localized corrosion.

Figure 4 shows a pair of SEM micrographs based on different image models. Figure 4(a) is a secondary-electron image showing a pit formed under a thick film. The metal substrate is revealed around the pit. Figure 4(b) is the backscattered electron image showing that the film around the pit is of low atomic number, with the metal substrate brighter in contrast. It is also evident that nodules in the pit are composed of low-atomic-number matter. Based on the above information, it is thought that the film is composed of organic metabolic products produced by the bacteria. The nodules in the pit are probably part of the microniche which has been broken during the fixation, since the microniche originally contained some water.

In Figure 5, another pit was found with a skeleton-like dendrite microstructure under a tubercle. Close examination of the dendrite microstructure revealed a transparent extracellular film covering the dendrite (Fig. 6). Several small nodules were associated with the film. The dendrite was identified as δ -ferrite based on EDS results (Fig. 7a). Since E308 SS weld metal has ferrite-austenite duplex phases,

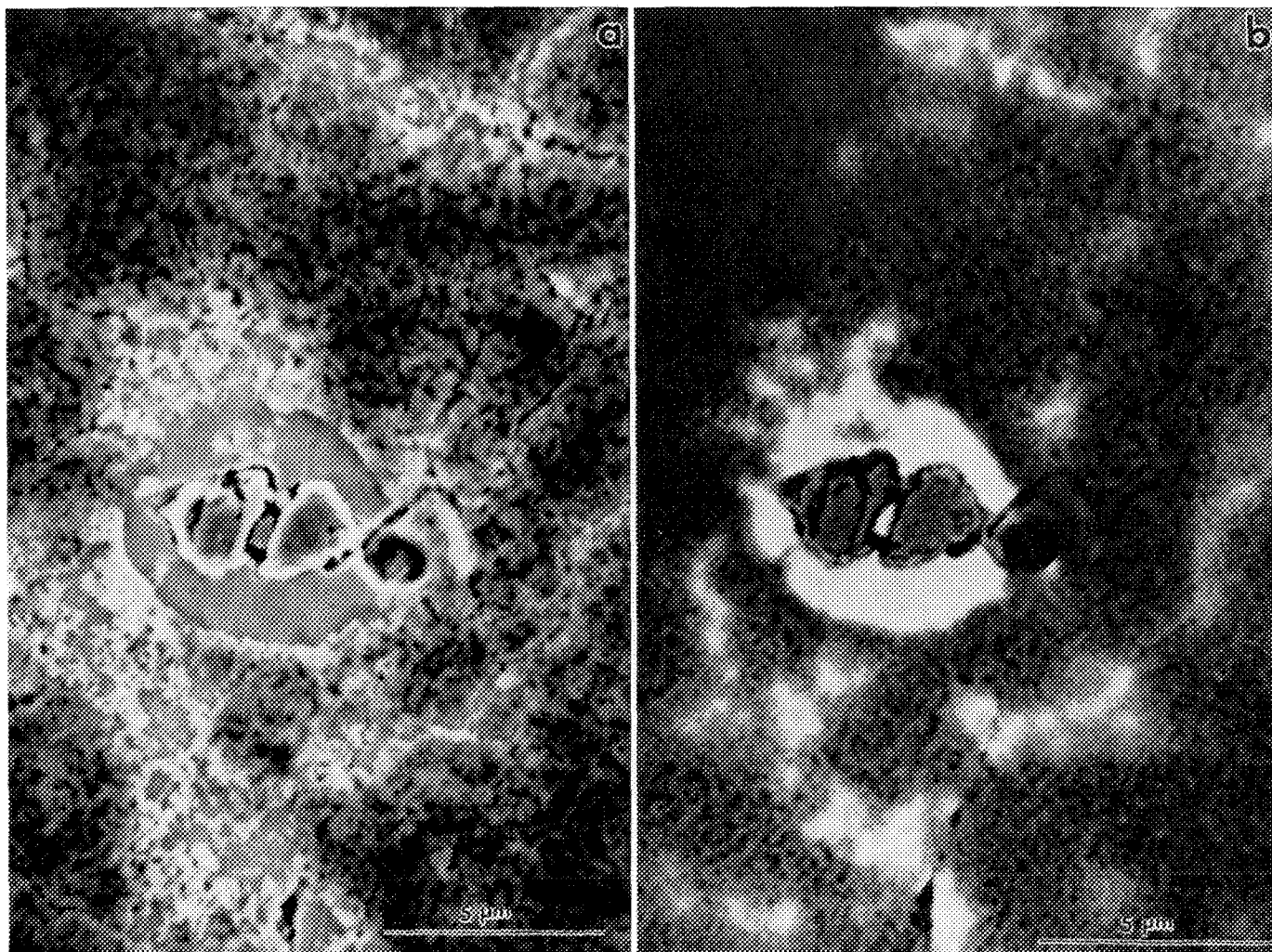


FIG. 4.--SEM image models of pit and associated film: (a) secondary-electron image, (b) back-scattered electron image.

the A6F bacteria result in a preferential attack on the austenite phase of E308 weld metal. EDS analysis of the nodules shown in Fig. 7(b) revealed that phosphorus, chromium, sulfur, and chlorine are the dominant elements inside the nodule. Although the chlorine might come in part from the fixing process, the existence of high chlorine (relative to the content of bulk solution of about 10 ppm) confirmed the above postulated mechanism of localized corrosion induced by A6F bacteria. The high phosphorus may result from the penetration of phosphate buffer solution during the fixation process. Phosphorus, sulfur, and calcium are well known as major required nutrients for bacterial growth.⁸ The high chromium content may be due to the dissolution of austenite. The conclusion is that these nodules are composed of bacterial cells, metabolic products and corrosion products. The absence of iron and nickel, expected in the EDS results, is not quite understood at this time. They may be bonded with bacterial cells locally or they may be resisted by the extracellular film as toxicants. Further work is needed with regard to this ques-

tion. The small white spots suspended in the film were identified as Mn-based inclusions which were originally present in δ -ferrite/austenite phase boundaries.⁹

Conclusions

Electron microscopy studies of MIC of as-deposited E308 SS weld metal induced by A6F bacteria revealed several important characteristics which enabled us to postulate the following mechanism of MIC in this experimental condition.

The microniche induced by the metabolism of the A6F bacteria on the E308 weld metal surface resulted in the formation of differential oxygen concentration cells, which in turn induce the local acidification and chloride ion concentration that directly caused the breakdown of the passive film and the pit formation.

References

1. W. P. Iverson, *Adv. Appl. Microbiology* 32: 1, 1987.
2. G. J. Licina, *Corrosion '88*, NACE, 1988, paper 268.

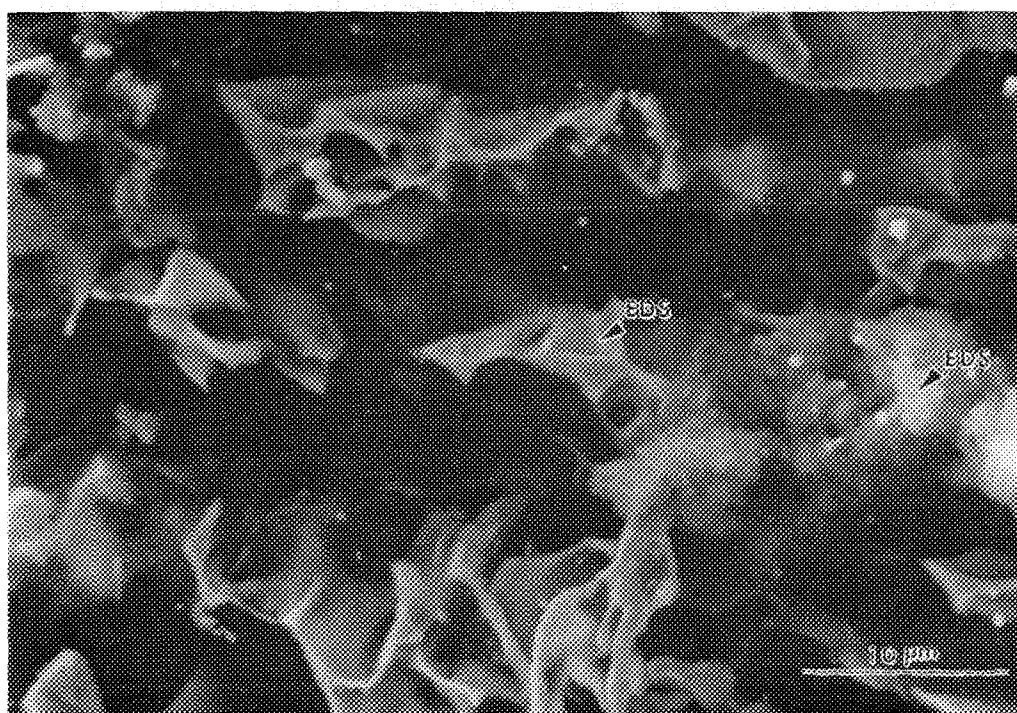
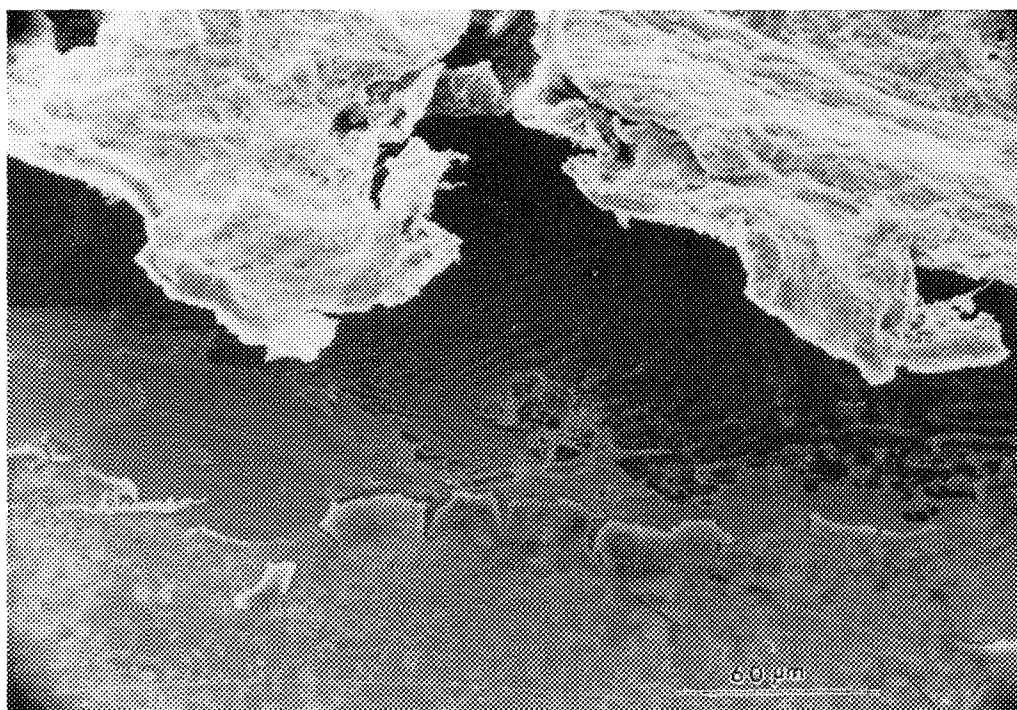


FIG. 5.--Pit revealed under tubercle, showing dendrite phase which was confirmed as δ -ferrite by EDS (Fig. 7a).

FIG. 6.--Dendrite phase covered by transparent extracellular film. Several nodules composed of excreted metabolic products, bacterial cells, and dissolved metal ions are suspended inside film.

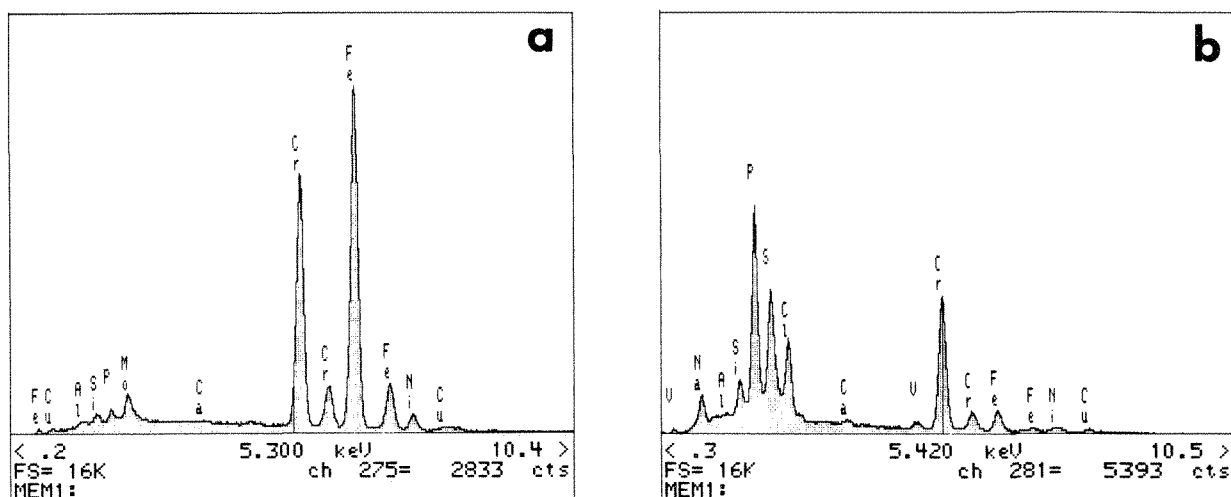


FIG. 7.--EDS results of Fig. 6: (a) dendrite phase, and (b) nodules suspended inside the extracellular film.

3. X. Zhang, R. A. Buchanan, E. E. Stansbury, and N. J. E. Dowling, *Corrosion '89*, NACE, 1989, paper no. 512.

4. X. Zhang, R. A. Buchanan, E. E. Stansbury, and J. Danko, "Microbially influenced corrosion of stainless steel weld metal induced by a single bacterium" (in preparation).

5. X. Zhang, R. A. Buchanan, and E. E. Stansbury, "Electrostatic model of bacterial adhesion to metal surface" (in preparation).

6. R. E. Tatnall, *Material Performance* 8: 56, 1988.

7. K. C. Marshall, in D. C. Savage and M. Fletcher, Eds., *Bacterial Adhesion: Mechanisms and Physiological Significance*, New York: Plenum Press, 1984, 152.

8. G. Gottschalk, *Bacterial Metabolism*, New York: Springer-Verlag, 1979, 1.

9. K. Easterling, *Introduction to the Physical Metallurgy of Welding*, London: Butterworths, 1983, 85.

COMPARATIVE ULTRASTRUCTURE AND X-RAY MICROANALYSIS OF *SALMONELLA* TYPHIMURIUM BY CTEM, CRYOFIXATION, AND SCANNING ELECTRON MICROSCOPY

D. A. Armstrong and D. C. Joy

There has been numerous contributions of immunocytochemistry to cell biology. Many of these contributions have focused on enzyme cytochemistry for a fuller understanding of cell structure and function. Immunocytochemistry is also a potentially powerful tool for examining metal accumulation in a variety of cell systems.¹ The use of immunocytochemical labeling is one of the initial steps we employ to gain an understanding of copper accumulation in our cell system, a spontaneously generated mutant cell line of *Salmonella typhimurium*. The immunocytochemistry work is complemented by energy-dispersive spectroscopy (EDS) and electron energy loss spectroscopy (EELS) studies. Quantitative analysis of elemental concentrations is based on comparative studies with resin-based standards currently being developed by this laboratory.² Several focal points of these studies include determination of the metal being accumulated and of the concentration of metal per cell basis, and identification of the valence state of the metal being accumulated. This may also be a good model system to examine the phenomenon of elemental translocation. First, conventionally fixed, resin-embedded cells; second, cryofixed whole cells; third, mildly fixed cells, typical of immunocytochemical studies; and ultimately frozen hydrated thin sections, will be compared.

Experimental

Our mutant cell line has been shown to accumulate copper.³ We are interested in finding out why, in characterizing the copper accumulation, and in seeing whether other metals likewise accumulate in this bacterium. If the answer is yes, we can apply this information in a beneficial manner to situations where effects associated with metal accumulation in bacteria are of concern, for example in microbially induced corrosion in metal. When our mutant cell line is grown in the presence of copper-supplemented growth medium, there is production of at least one copper binding factor that sequesters the metal and may play a detoxification role. Isolation of this binder and subsequent development of a monoclonal antibody targeted against the binder is one of the first steps toward quantitative biological analysis of this cell system. Concurrently, it

is important to evaluate elemental distributions in conventional transmission electron microscopy (CTEM), preparations for possible insights into copper ion translocation, and translocation of other more freely diffusible elements.

The bacterial cells were grown in the presence of 0.01 M copper supplemented growth medium and their growth was monitored. Cells were harvested at an optical density of 0.20 units/ml of culture at 420 nm, and processed for TEM and SEM as described previously.^{4,5} Whole cells were cryofixed in a controlled environment vitrification system (CEVS).⁶ This system allows rapid cooling to a vitreous solid state of hydrated biological samples and colloidal dispersions by plunging of the sample into a reservoir of liquid ethane or propane at a high speed. Figure 1 briefly outlines the sequence of steps in the three preparation methods.

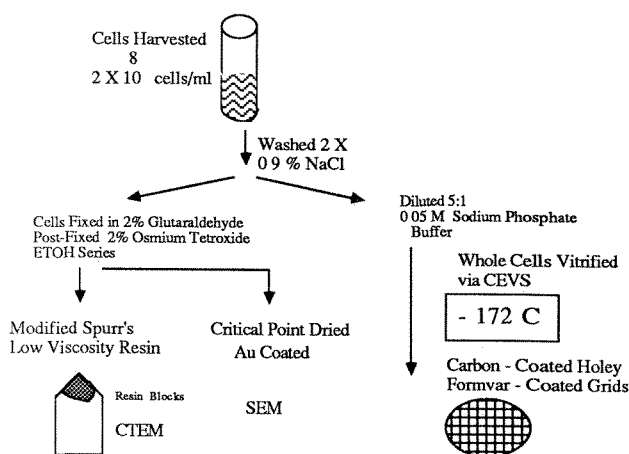


FIG. 1.--Outline of sample preparation methods.

Analysis of frozen hydrated thin sections is the preferred method for quantitatively examining elemental distributions in biological systems. Toward this goal, our first step is to determine the freezing capabilities of our freezing apparatus by freeze-substitution methods. Samples for freeze substitution were prepared as previously described.⁷ Briefly, a pellet of cells is applied to filter paper, which is in turn glued to foam fitted onto a freezing probe. The probe is released and allowed to drop onto a copper block held at liquid-nitrogen temperature. Osmium tetroxide vapor fixing and freeze-substitution of our cells prepared using the "Gentleman Jim" instrument (Ted Pella, Inc., Redding, Calif.) show freezing depths of approximately 20 μ m without significant ice crystal damage (unpublished data).

D. A. Armstrong is with the program in Cellular, Molecular and Developmental Biology, and D. C. Joy is with the EM Facility, Walters Life Science Building, University of Tennessee, Knoxville, TN 37996.

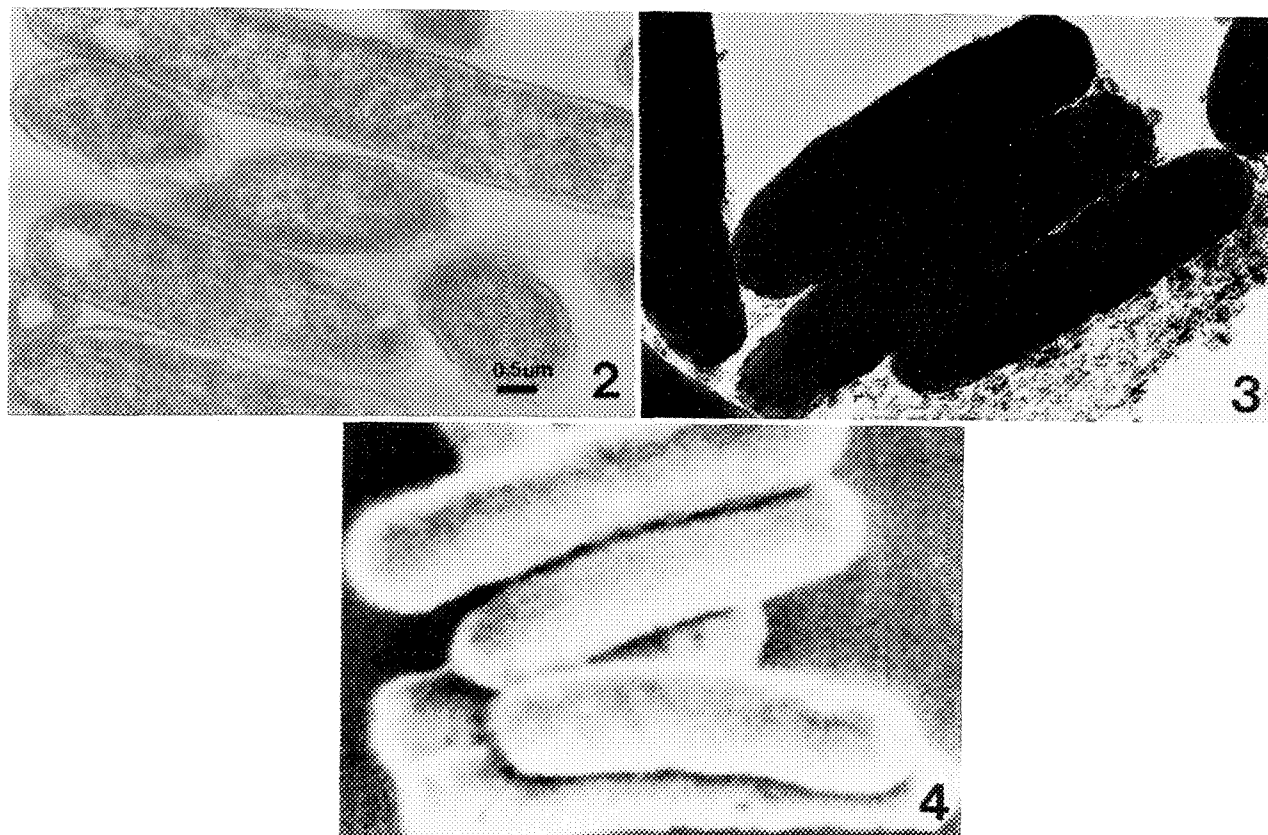


FIG. 2.--Conventionally prepared *Salmonella typhimurium* cell mutants.
 FIG. 3.--Cryofixed whole cells, *S. typhimurium*.
 FIG. 4.--SEM image, *S. Typhimurium*.

A Hitachi H-800 STEM equipped with a Kevex UTW Quantum x-ray detector, and a Hitachi S-800 high-resolution SEM were used in these studies. Energy-dispersive spectroscopy was done on both the TEM preparation and the CEVS-prepared cells. For EDS analysis, special attention has been paid to reducing the systems background of copper x-ray emissions, mainly by the use of a modified and colloidal graphite-coated specimen holder,⁸ and by mounting all specimens on silver grids.

Results

Comparative ultrastructures are shown in Figs. 2 (CTEM), 3 (CEVS), and 4 (SEM). Resin-embedded cells show the typical subcellular morphology associated with enteric bacteria (i.e., ribosomes, cell wall, nucleoid), indicating a generally healthy population of cells. We note that in cells post-stained with uranyl acetate and lead citrate present there are irregularly occurring electron dense particles within the bacterial cell body. These electron dense particles range from approximately 5 to 50 nm in diameter. EDS of these particles does not yield any information regarding localization of copper accumulation. The particles cannot be visualized in nonpost-stained cells, which may indicate that these particles have an affinity for heavy metal ions in the stains. One possibility could be that the metal ions of

the stains are replacing other ions that have been displaced by one of the steps in fixing and embedding process. At this point we cannot suggest that these particles play any role in the metal accumulation phenomenon. Protein analysis of fractionated cells by polyacrylamide gel electrophoresis should yield information regarding cell translation products and indicate any translation enhancement due solely to the spontaneously generated mutation and/or growth of the cells in copper supplemented medium. A representative x-ray spectrum from nonpost-stained CTEM prepared cells is shown in Fig. 5. The trace accumulation of copper in the cells prepared for CTEM has not been localized subcellularly.

Cryofixed cells, whether prepared via CEVS or frozen thin sections, should preserve the subcellular elemental distribution. Morphologically, cells prepared via CEVS were essentially identical: oblong, 3-4 μm long, and 1-1.5 μm in diameter. This surface morphology was also confirmed by SEM (Fig. 4). A representative x-ray spectrum from whole cells prepared by CEVS dryofixation is shown in Fig. 6. The atomic absorption spectroscopy data from samples prior to preparation indicate a copper concentration in the 5-10 micromolar range for bulk whole cells. There are several possibilities that we cannot rule out regarding the lack of copper x-ray emissions. Perhaps copper and other ions could be lost from the cells during

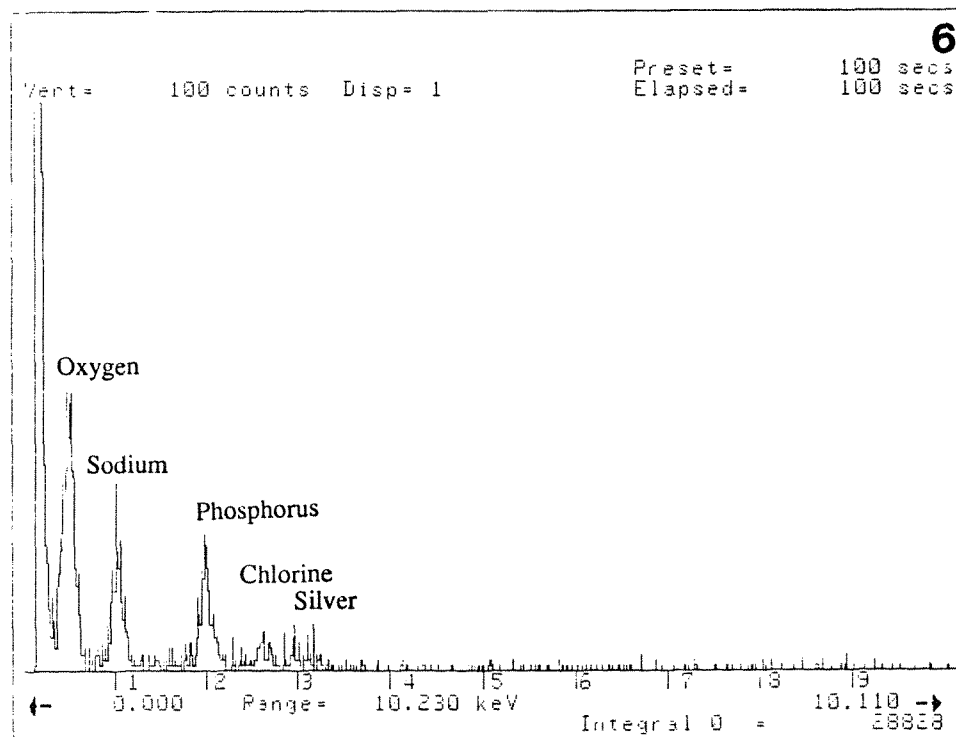
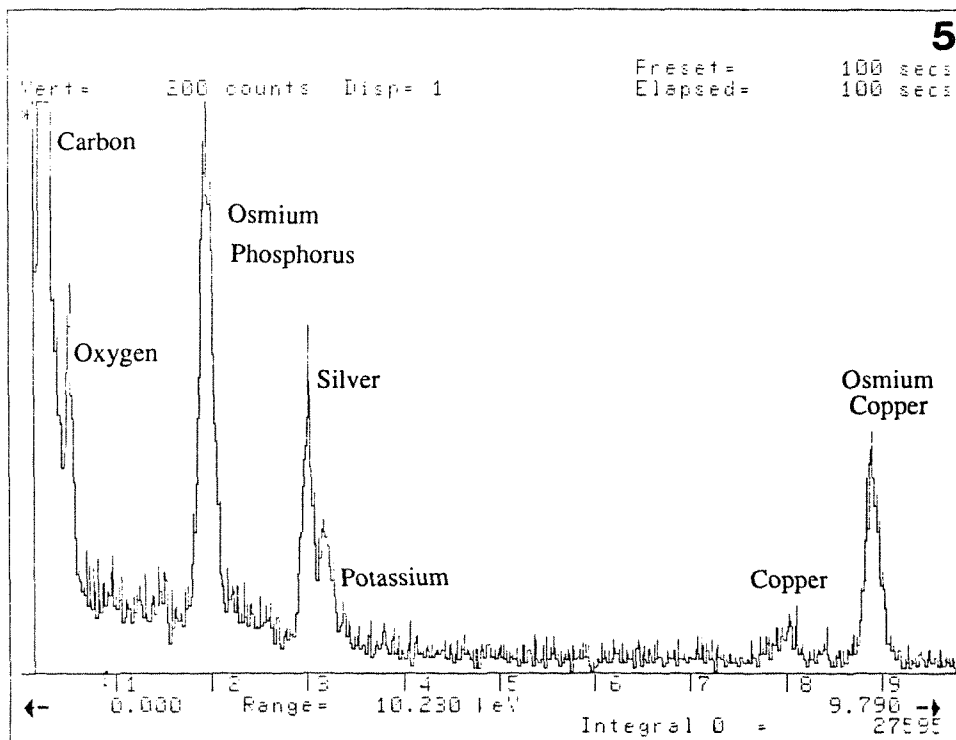


FIG. 5.--X-ray spectrum from CTEM-prepared cells, nonpost-stained.
FIG. 6.--X-ray spectrum from CEVS-prepared cells.

dilution with sodium phosphate buffer. However, the osmolarities of the saline (300 mOsm) and the buffer (300 mOsm) are comparable to the osmolarity of the growth medium (395 mOsm), so that large ion efflux due solely to the difference in osmolarities seems unlikely. Another possibility is that a subpopulation of cells exists within the overall culture that accumulate and account for a large majority of the copper in bulk whole cells, thus giving an average copper concentration per cell which is in fact not representative of each individual cell. Copper levels in the remaining cells may be below minimum detectability limits. The immunocytochemistry and hydrated frozen sections should provide more information on this subpopulation theory.

CETM-prepared cells provide no insight to this question, as a uniform copper emission is seen within each cell and in the resin directly surrounding the cells. This outcome may be due to elemental translocation as the resin infiltrates the pellet of cells; this is evidently not a satisfactory preparation technique for examining native elemental distribution.

Conclusions

We present ultrastructural and EDS data from initial studies of our model for quantitative examination of metal accumulation in a biological system. Bulk whole-cell studies with atomic absorption spectroscopy show a copper accumulation in the micromolar range. EDS studies on conventionally fixed and embedded cells that have been thin sectioned indicate trace amounts of copper present but subcellular localization was not possible. EDS studies with cells prepared by CEVS tell us that in the individual cells analyzed to date, the copper was somehow lost in the dilution step or that the copper present is below minimum detectability limits. However, this result does not rule out the possibility that in these initial studies, if a subpopulation exists within the overall culture, they may have been randomly excluded from EDS analysis.

On the one hand, these studies represent a

worst-case scenario for metal ion translocation and in vivo conservation of macromolecules in their native state; on the other, a physical fixation that freezes subcellular contents in their native structure and native distribution.

We are encouraged by the presence of copper even in the CETM-prepared cells and anticipate a localization of copper by immunocytochemical studies and quantitative elemental analysis of frozen hydrated thin sections in the near future.

References

1. A. J. Morgan, "Quantitative electron probe x-ray microanalysis of heavy metal accumulation in subcellular structures," Schloss Ringberg (Max Planck Institute), 1988.
2. D. C. Joy, C. S. Joy, and D. A. Armstrong, "Resin-based standards for biological EDS and ELS microanalysis," *ibid.*
3. D. A. Armstrong, *Resistance to Copper Toxicity in a Spontaneously Generated Mutant of Salmonella typhimurium*, Master's Thesis, University of Tennessee, Knoxville, 1987.
4. A. M. Glauret, "Fixation, dehydration, and embedding of biological specimens," in *Practical Methods in Electron Microscopy*, Amsterdam: Elsevier/North Holland, vol. 3, Pt. 1.
5. D. E. Newbury, D. C. Joy, P. Echlin, C. E. Fiori and J. I. Goldstein, *Advanced Scanning Electron Microscopy and X-Ray Microanalysis*, New York: Plenum Press, 1986, 325.
6. J. R. Bellare, H. T. Davis, L. E. Scriven, and Y. Talmon, "Controlled environment vitrification system: An improved sample preparation technique," *J. Electron Microsc. Technique* 10: 87, 1988.
7. T. E. Phillips and A. F. Boyne, "Liquid-nitrogen-based quick freezing: Experiences with bounce-free delivery of cholinergic nerve terminals to a metal surface," *J. Electron Microsc. Technique* 1: 9, 1984.
8. R. R. Warner, M. C. Myers, and D. A. Taylor, "Inaccuracies with the Hall technique due to continuum variation in the analytical microscope," *J. Microscopy*, 138: 43, 1985.

EDX AND EELS MEASUREMENTS OF Ca-DOPED THIN SECTIONS

Roland Wurster and Stefan Lehner

Elemental standards are required for the testing of the sensitivity of microanalytical systems that are applied to biological specimens. Ion exchange material consisting of polymeric networks with fixed ionic groups and exchangeable counterions provide a versatile means for the design of standard sets.¹ Ca-containing thin sections were investigated with an electron probe and the newly available EELS/ESI electron microscope (CEM 902, Zeiss, Oberkochen, FRG) in order to verify the usefulness of the standards in terms of the most important criteria,² and to provide a means for quantitation of qualitative results.³

Experimental

The strongly acid exchange membrane SC-1 (Stantech Inc., Palo Alto, Calif.) is a type of a polystyrene-divinyl-benzene sulfonate and has a wide range of selectivity for various cations. It has been shown previously that this membrane can be single or double loaded with elements at different concentration levels up to a maximum value of about 1000 mmol/kg.⁴ After embedding in Spurr's resin, the membranes were thin-sectioned and deposited on filmed grids for electron-probe and electron microscope measurements. Most of the results was obtained with the electron probe JXA 50 A (JEOL, Tokyo), using a horizontal Si(Li) spectrometer at the most efficient (near to specimen) position that is achieved by operating the scanning microscope a few millimeters below the nominal working distance of 13 mm with a modified sample holder. To reduce production of extraneous x rays, the sample holder is made of spectrochemically clean carbon stubs. Since the objective aperture is a major source for spurious x-ray contributions to the EDX spectra, two aperture diameters (600 μm , 200 μm) were selected for comparison purposes.

An on-line operated image processing and analysis system (SEM-IPS, Kontron, Munich) performs several important functions. Nominal magnification can be easily corrected for the effect of nonstandard working distance. Evaluation of gray-level line-scans at sharp edges provides a quick determination of the primary beam diameter. Based on digital pictures, spectral data can be collected automatically.

Imaging of the specimen at highest resolution and contrast is done with a transmitted electron detection device that permits bright- and dark-field operation.

Preliminary results were obtained with the

commercially available Zeiss CEM 902 electron microscope⁵ with a column-integrated imaging electron spectrometer.⁶

Results

All measurements with the SEM/EDX-system were performed at a beam voltage of 25 kV. The electron source is a conventional tungsten hairpin cathode. With a beam current of $i_{\text{p}} = 1.2 \times 10^{-10}$ A, as later used in acquiring x-ray spectra, digitized pictures (512 \times 512 pixels) of laser-induced holes in a metallic film were recorded in dark-field mode at high magnification (20 000 \times). Evaluation of several gray-level linescans perpendicular to the rim of a perforation yields the actual beam diameter, which is the distance for a 10% to 90% rise in gray level. For the two objective apertures (200 μm , 600 μm), beam diameters of about 12 nm and 20-25 nm, respectively, are obtained. Beam broadening⁷ in the thin sections (40-50 nm thick) of the embedded ion exchange membrane only produces a small relative change of the spatial resolution, the analytical volume, and the electron dose. Homogeneity of the Ca-loaded ion exchange membrane was tested both on a millimeter scale by analysis of bulky parts of the membrane and on a microscopic scale within the thin sections. Considering the net counts of Ca K α , the variance is typically less than 10%, whereas Ca K α to S K α intensity ratios show a variance less than 4%. Continuous electron bombardment at the given conditions during 30 min has no significant effect on the Ca K α count rate, but growing contamination becomes apparent by a decreasing video signal. However, the electron dose of some 10^6 e/ \AA^2 as calculated from the beam current, beam diameter, and the acquisition time is of an order that can cause serious beam damage and mass losses to organic matter. Figure 1 shows x-ray spectra as obtained with aperture diameters of 200 and 600 μm , respectively, but otherwise unchanged excitation conditions and analyzed area. Extraneous background and characteristic line contributions (supporting grid) to the first spectrum are obviously higher, but can be compensated for by subtraction of corresponding spectra that are acquired with the primary beam going through holes or artificial perforations.⁸ X rays that are produced at the scintillator of the transmitted electron detection device (40 cm below the sample holder) cannot be seen by the EDX detector. The processed spectra are nearly identical to each other and thus show the usefulness of this simple correction procedure. Assuming linearity between x-ray intensity and Ca concentration, one can estimate from counting statistics

The authors are at the Institut für Physik, Universität Hohenheim, Barbenstrasse 30, D-7000 Stuttgart 70, Fed. Rep. of Germany.

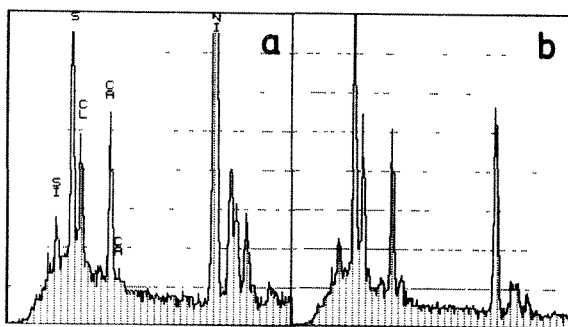


FIG. 1.--X-ray spectra of thin section of Ca-loaded ion exchange membrane with objective aperture diameter of (a) 200 μm , (b) 600 μm .

a minimal detectable mass fraction of about 0.2 wt%. At the best spatial resolution obtained with the given beam voltage, beam current, and 200 μm objective aperture, the minimal detectable mass would be 10^{-20} g Ca. The peak-to-background value is about 12. This value can compete with or even exceed corresponding values in the literature.

Reasonable application of EELS and ESI capabilities of the CEM 902 (beam voltage 80 kV) is possible only when ultrathin sections less than 40 nm thick are used. Electron spectroscopic imaging of the thin sections with zero loss electrons produces increased contrast showing granular membrane structure with dimensions of about 50 nm. Although the section thickness of 40 nm is at the upper limit of a meaningful thickness scale, the EELS spectrum (Fig. 2) shows a well-resolved Ca $L^{2,3}$ edge and thus the good performance of the electron spectrometer.

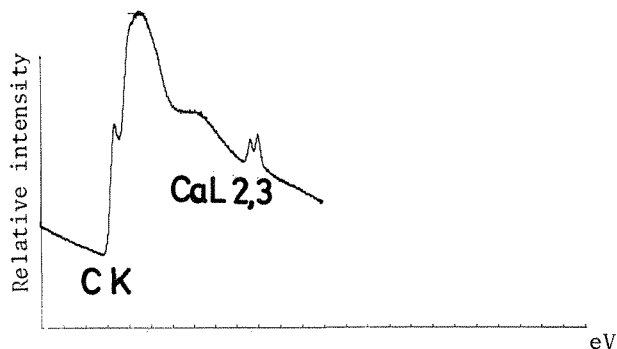


FIG. 2.--EELS spectrum of 40 nm thin section of Ca standard showing well-resolved Ca $L^{2,3}$ edge and C K edge. (Courtesy of W. Probst, Zeiss, Oberkochen.)

Conclusion

The ion exchange membrane is a suitable matrix material for electron probe microanalysis. Homogeneity of the elemental loadings is well down to a 10 nm scale and thus sufficient for electron-probe x-ray microanalysis. Homogeneity at the spatial scale below 10 nm still has to be proven by electron-spectroscopic imaging of sufficiently thin sections.

References

1. W. C. de Bruijn, "Ideal standards for quantitative x ray microanalysis of biological specimens," *SEM/1981 II*, 357.
2. G. M. Roomans, "Standards for x ray microanalysis of biological specimens," *SEM/1979 II*, 649.
3. W. Probst and H. Seiler, "Microanalytical methods and identification of calcium in vertebrate nervous tissue," *J. Electron Microscopy* 35/I (Suppl.): 579, 1986.
4. S. Lehner et al., "Investigation of thin sections of doped cation exchange membrane by EDX, AES, EELS, and LAMMA," *Conf. on Progress of Electron Probe Microanalysis in Biology and Medicine*, Schloss Ringberg, 1988.
5. R. Bauer et al., "High resolution imaging of thick biological specimen with an imaging electron energy loss spectrometer," *Optik* 77: 171, 1987.
6. F. D. Ottensmeyer, "Electron spectroscopic imaging: Parallel energy filtering and microanalysis in the fixed-beam electron microscope," *J. Ultrastruct. Res.* 88: 121, 1984.
7. J. I. Goldstein et al., "Quantitative x-ray analysis in the electron microscope," *SEM/1977 I*, 315.
8. N. J. Zaluzec, "Quantitative x-ray microanalysis: Instrumental considerations and applications to materials science," in J. J. Hren et al., Eds., *Introduction to Analytical Electron Microscopy*, New York: Plenum Press, 1979, 122.

EFFECTIVE USE OF A TN5500 X-RAY ANALYZER TOGETHER WITH A PERSONAL COMPUTER FOR MICROANALYSIS OF BIOLOGICAL SAMPLES

M. C. Foster

Investigations with x-ray microanalysis can be facilitated by customized software that uses the best features of commercially available x-ray analyzers and personal computers. Commercial x-ray analyzers are generally user-friendly and convenient for collecting and fitting spectra. Personal computers are well suited to doing sophisticated data analysis or making presentation-quality graphs. Software that utilizes and enhances these features not only saves labor, it also encourages the investigator to use new ways of looking at data. Data-handling routines have been written for the Tracor Northern TN5500 x-ray analyzer that can be used to write summary files for each spectrum; to read, sort, tabulate, and do calculations on data in summary files; and to transmit data and spectra to personal computers. Use of this software is illustrated by analysis of cryosections from rat pancreatic islets, in which x-ray microanalysis disclosed what other techniques could not--the existence of "rebel" or nonconformist secretory granules within a single cell. The software, written in FLEXTRAN (the language for TN5500 x-ray analyzers) can be readily adapted for other users.

Data-handling Tasks

1. *Write summary files for each spectrum.* Summary files contain fitted peak counts, uncertainty in counts, and concentrations for every element, as well as file number, file text label, acquisition time, gross continuum, film correction, net continuum, and χ^2 . Routines to make the summary files are called up from the Tracor Northern BIOQ program, which calculates counts in spectral peaks by a multiple least-squares fitting algorithm and concentrations in thin sections by the peak-to-continuum (Hall) method. In addition to saving summary files, the custom software facilitates batch processing of spectra and use of averaged film spectra for the film correction.

2. *Read, sort, tabulate, and analyze summary files.* For each element of interest, peak counts, uncertainties in peak counts, and concentrations are tabulated. Each spectrum is identified by a file number and text label.

The author is at the Biomedical Engineering and Instrumentation Branch, DRS, National Institutes of Health, Bethesda, MD 20892, and thanks R. D. Leapman and W. A. Hagins for stimulating collaborations, Grant Baughman and Jon McCarthy for help with Tracor Northern programs, and S. B. Andrews, C. R. Swyt, and C. E. Fiori for useful discussions.

Other quantities associated with the spectrum, such as acquisition time, film correction, net continuum, and χ^2 , are listed. Optional calculations can be made before tabulation. Following the tabulation, averages and standard deviations are calculated for the quantities listed for each element. In addition to unweighted averages, averages weighted with the inverse of the square of the statistical uncertainty are also calculated. The ability to sort on the text label is a very useful feature. Different organelle or cell types may be tabulated and averaged separately. For example, summaries for all mitochondria may be printed by selecting spectra with the combination of letters MIT in the spectrum label. Selection criteria may be one of several letter combinations.

3. *Transmit summary files to personal computer.* ASCII characters are transmitted, with tabs separating values in a summary file and carriage returns between each file, so that data can be read directly into a spreadsheet. Files may be selected for transmission according to text labels, as well as file numbers. A Tracor Northern routine, in conjunction with a Digital Equipment four-channel serial board (DLV-11J), directs data from the printer port to a cable connecting the analyzer and a personal computer.

4. *Transmit spectra to personal computer.* ASCII characters are transmitted, with counts separated by carriage returns, so that spectra can be read directly into a column of a spreadsheet for plotting. A header containing file number, label, and other available information may be transmitted for each spectrum. Spectra can be sent singly or in batch mode. Data are directed, as above, from the printer port to a cable link. A simple example of code is given in the Appendix.

Use of Data-handling Software for Microanalysis of Biological Samples

Data-handling programs facilitated both short-term and long-term analyses (Fig. 1). On the TN5500, spectra were processed daily in batch mode. Summary files were selected for organelle and cell type, and quantities were tabulated and averaged (Fig. 2). Periodically during an experiment, summary files and spectra were sent from the TN5500 to a Macintosh Plus for further processing and plotting. Spectral files were then read directly into a graphics program, and summary files into a database program. In the database program Microsoft EXCEL, additional calculations and

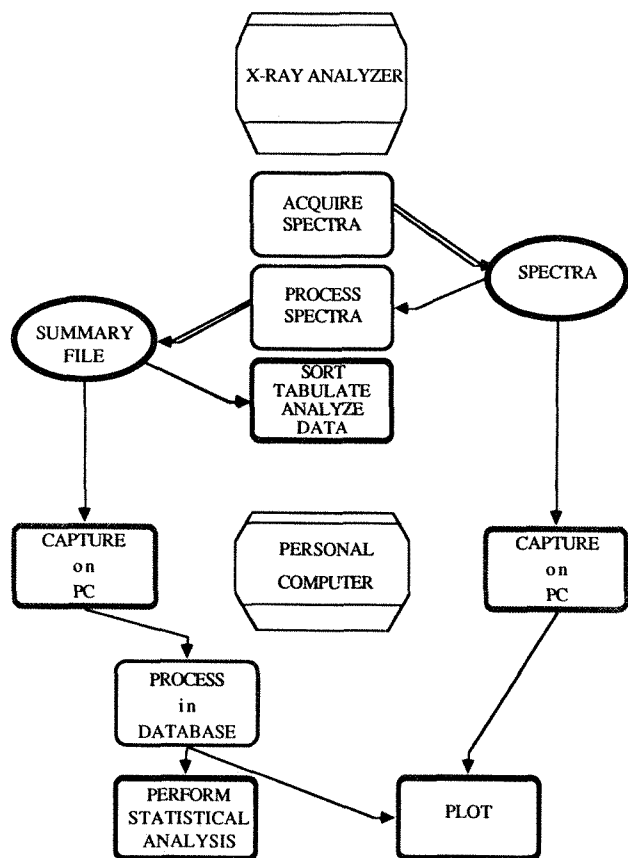


FIG. 1.--Data-flow for x-ray microanalysis of biological samples. Custom data-handling routines for TN5500 x-ray analyzer are used to make summary files; to sort, tabulate and analyze data from summary files; and to transmit summary files and spectra to personal computer.

selections were made, which were transferred with the Macintosh clipboard to other applications for statistical analysis and for making presentation-quality graphs.

The data-handling software was especially useful in analyzing cryosections from rat pancreatic islets because of the numerous comparisons and correlations that needed to be made. Cryosections contained two major cell types. Each cell type had secretory granules with distinctive composition (Fig. 3), but with a few granules that appeared to be granules of the other cell-type (Fig. 4). Analyses were required to separate the two cell types, to analyze the composition of secretory granules and other organelles in each cell-type, and to examine the composition of the outlier granules. A preliminary report of this work has appeared.¹

Discussion

Data-handling routines have also been written for the TN2000 to facilitate x-ray microanalysis of bulk samples.² Routines to write summary files are called from the routine ZAFPB,³ which calculates concentrations in bulk samples by the peak-to-local-background method. Routines to read and tabulate summary files have a number of optional calculations. For

example, linear fits may be made to values from a series of spectra. This option has been used in two ways: (a) to examine stability of samples in the electron beam, and (b) to measure elemental concentration gradients in cells. Quantities that may be tabulated include ratios of peaks or concentrations of elements, the membrane potential under the assumption that Cl is passively distributed, electromotive driving forces, and the equilibrium free calcium concentration calculated for sodium/calcium exchange.

Useful Features of this Custom Software

(a) Results are tabulated by computer and not by hand.

(b) Each spectrum is identified by a text label and file number.

(c) Selections may be made on text labels in order to analyze separately results on different organelles or different cells.

(d) Additional calculations may be performed on data saved in summary files.

(e) Averages and standard deviations are calculated for concentrations or for other values listed for each element of interest.

(f) Corrections for contributions of support film to spectra of thin sections may be made from averages of a number of film spectra.

Custom software has been written that facilitates x-ray microanalysis of biological samples, with use and enhancement of the strong points of a commercial x-ray analyzer, the TN5500, and a personal computer. The data-handling routines help monitor results in the short term by providing a means to select and tabulate data according to organelle or cell type. They help in the long term by providing a means to transmit data and spectra to personal computers where many options exist for visualizing, correlating, and analyzing data. Versions of these routines are in use in three laboratories at NIH and in several laboratories in other parts of the country. Diskettes and listings are available upon request.

References

1. M. C. Foster, R. D. Leapman, M. X. Li, R. L. Ornberg, and Illani Atwater, "Composition of secretory granules by electron probe microanalysis of cryosectioned rat pancreatic islets," *Biophys. J.* 55: 431a, 1989.
2. M. C. Foster and W. A. Hagins, "Energy-dispersive x-ray microanalysis by the peak-to-background method: Empirical corrections for detector-degraded counts," *Microbeam Analysis--1982*, 131-137.
3. Jon McCarthy, personal communication.

FIG. 2.--Example of output from routine written to select, tabulate, and analyze data in summary files on the TN5500. Selection for "GRA" in text label.

**PEAK COUNTS
UNCERTAINTY IN COUNTS
CONCENTRATIONS**

**TEXT LABEL
FOR SELECTION**

**FILE NUMBERS
TEXT LABELS**

AVERAGES

*
G LIST AND AVERAGE SPECTRUM SUMMARIES
PRINT CONCENTRATIONS (Y/N) ?Y
OTHER CALCULATION (Y/N) ?N

TYPE LABEL
PANCREATIC ISLET CELL2 GRANULES

READ BEGINNING SUMMARY NO ?1196 END FILE NO ?1287
DRIVE NO ?6
SPECIFY FILE LABEL?Y
NO. OF ALTERNATIVE LABELS?1
DO YOU WANT TO TYPE IN LABELS? ?Y

LABEL GRA

	TIME	FLMCDR	NETCNT	NA	MG	P	S	CL	K	CA	SI	ZN	C	U
1197 GRA1 CELL2 380KR	100	133	261	16	25	981	325	88	858	-8	23	4	18	
UNC COUNTS				18	21	39	38	23	63	22	25	14	18	
CONC MM/KG DRY				67.58	33.15	638.68	195.86	45.88	438.89	-8.43	16.18	1.61	8.00	
1198 GRA2 CELL2 380KR 5.6 ISL16C 27	100	133	316	12	43	958	467	57	655	181	4	28	14	
UNC COUNTS				19	22	39	33	24	62	24	26	17	17	
CONC MM/KG DRY				41.47	46.78	584.44	238.53	26.27	289.45	36.57	2.31	6.59	8.00	
1199 GRA3 CELL2 380KR 5.6 ISL16C 27	100	133	369	3	31	993	533	73	885	8	6	-3	-7	
UNC COUNTS				28	23	48	34	24	64	22	27	17	18	
CONC MM/KG DRY				8.84	28.78	445.72	224.29	28.68	282.29	2.47	2.95	-1.11	8.00	
1200 GRA4 CELL2 380KR 5.6 ISL16C 27	100	133	388	96	-9	588	963	133	289	275	1	67	35	
UNC COUNTS				21	22	36	48	26	55	26	25	28	18	
CONC MM/KG DRY				342.13	-11.19	314.98	498.29	63.28	122.62	182.68	8.68	22.75	8.00	
1201 GRA5 CELL2 380KR 5.6 ISL16C 27	100	133	392	31	34	1143	413	142	868	58	4	22	34	
UNC COUNTS				21	24	43	34	25	69	23	28	18	20	
CONC MM/KG DRY				86.19	29.71	484.23	164.83	52.64	284.64	16.98	1.86	5.83	8.00	
1202 GRA6 CELL2 380KR 5.6 ISL16C 27	100	133	329	37	48	1082	344	57	796	28	79	13	40	
UNC COUNTS				19	22	39	38	24	64	23	27	16	19	
CONC MM/KG DRY				122.78	41.72	586.67	172.56	25.22	314.46	6.96	43.78	4.11	8.00	
1204 GRA7 CELL2 380KR 5.6 ISL16C 27	100	133	298	13	53	745	367	44	583	33	-18	5	7	
UNC COUNTS				18	21	36	38	21	59	28	25	15	17	
CONC MM/KG DRY				48.58	62.25	424.19	195.91	21.93	223.75	12.92	-6.84	1.78	8.00	
1205 GRA8 CELL2 380KR 5.6 ISL16C 27	100	133	218	-17	48	889	388	41	578	21	81	-11	28	
UNC COUNTS				17	28	35	27	21	53	19	23	15	14	
CONC MM/KG DRY				-94.85	65.78	644.22	223.97	28.57	359.59	11.58	78.55	-5.96	8.00	
1206 GRA9 CELL2 380KR 5.6 ISL16C 27	100	133	256	183	1	545	554	218	331	75	35	27	7	
UNC COUNTS				28	28	33	33	25	53	21	25	17	18	
CONC MM/KG DRY				448.87	1.35	354.83	338.14	124.19	168.36	33.57	24.93	18.99	8.00	
1207 GRA10 CELL2 380KR 5.6 ISL16C 2	100	133	252	88	17	494	784	126	487	114	34	59	19	
UNC COUNTS				19	21	33	37	26	53	22	24	20	18	
CONC MM/KG DRY				349.69	23.36	329.84	489.56	73.44	211.79	52.21	24.77	24.57	8.00	

FOR AVERAGE, TYPE 0, FOR NEW TAPE, TYPE 1 ?0

	TIME	FLMCDR	NETCNT	NA	MG	P	S	CL	K	CA	SI	ZN	C	U
18 AVE PANCREATIC ISLET CELL2 GRANULES														
WEIGHTED AVE			COUNTS	35	27	793	469	92	576	62	27	15	18	
STATISTICAL UNCERTAINTY				6	7	12	18	7	19	7	8	5	6	
AVERAGE (NOT WEIGHTED)	100	133	298	37	27	825	587	97	688	78	25	28	19	
STD ERROR OF ESTIMATE	8	8	18	13	6	71	68	18	69	26	18	8	5	
AVERAGE (NOT WEIGHTED) CONCENTRATION														
				141.32	32.14	463.89	272.51	48.91	266.78	27.33	18.18	7.11	8.00	
STD ERROR OF ESTIMATE				35.11	7.64	36.26	39.27	18.87	28.62	9.88	7.58	3.11	8.00	

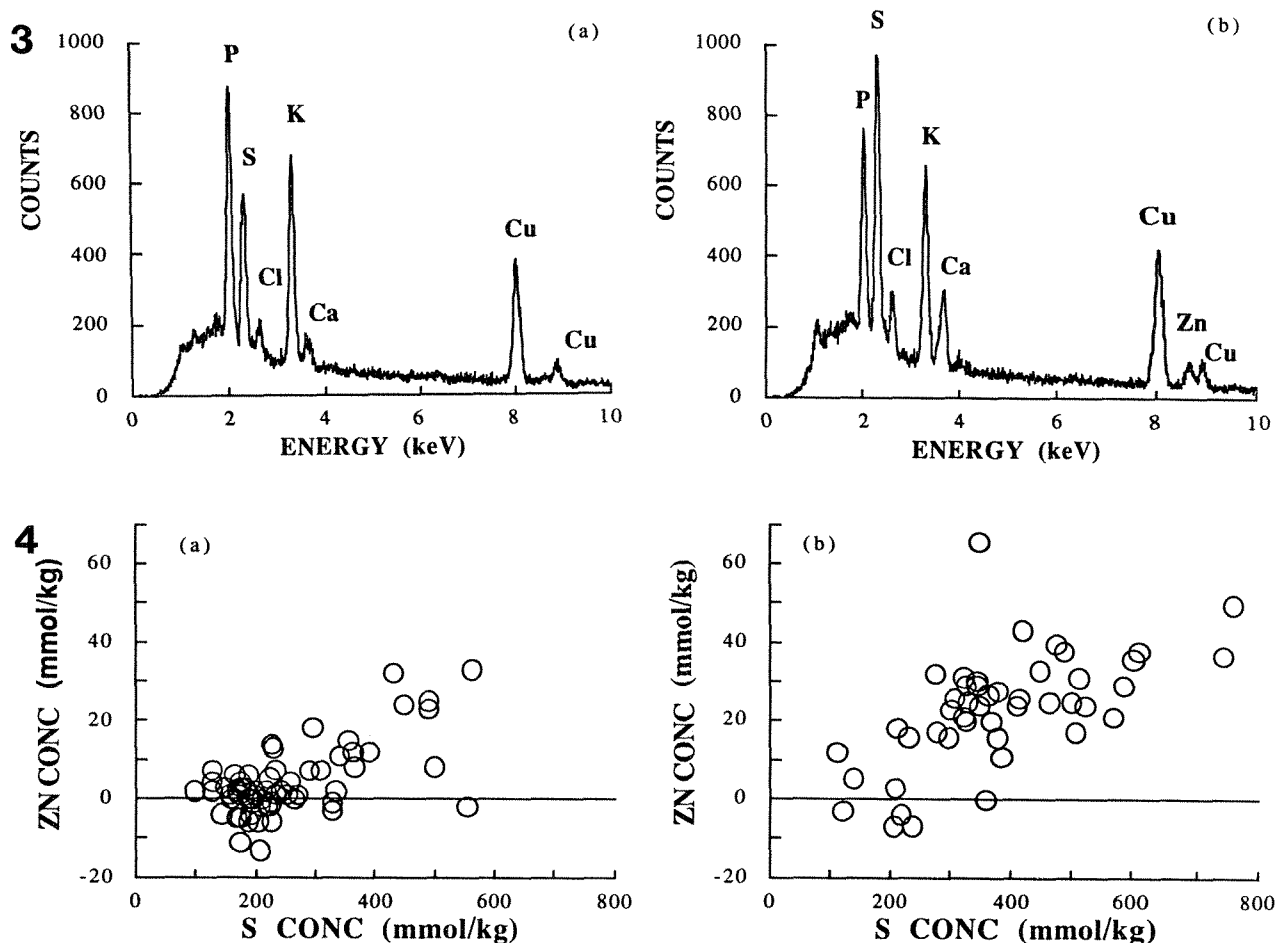


FIG. 3.--X-ray spectra of granules from (a) non-beta, (b) beta cell from cryosection of rat pancreatic islet, illustrating high concentrations of sulfur and zinc associated with insulin-containing granules of beta cell. Each spectrum is sum of spectra from 10 granules in single cell. (10×100 s; 100keV, 1nA electron beam; approx. -60°C sample temperature.) Custom data-handling routine was used to transfer spectra from TN5500 x-ray analyzer to Macintosh Plus. A LaserWriter was used for printing.

FIG. 4.--Zinc vs sulfur for granules in (a) non-beta, (b) beta cells of cryosections from rat pancreatic islets, illustrating differences in composition of granules in non-beta and beta cells and existence of some beta-type granules in non-beta cells. Graphs, printed on a LaserWriter, were plotted from data in summary files which were transferred from TN5500 analyzer to Macintosh Plus with the help of custom data-handling routines.

Appendix

The following code, written in FLEXTRAN, may be used to transmit a spectrum from the memory of a TN5500 x-ray analyzer to a personal computer.

```
1,6 %USE +DV n TO DIRECT PRINT TO PORT n
1,8 %SEND 1 COL AND N1 + 1 ROWS
1,10 S M=12;%1ST HALF OF MEMORY
1,20 S N1=1023;%NO. OF CHANNELS - 1
1,30 A E1(N1)

2,20 S AR='015';ASCII CARRIAGE RETURN

5,10 $LI 0,10,16
5,20 F I=0,N1;S E1(I)=$DA(M,I)
5,30 P <H1>AR;F I=0,N1;P <F9>E1(I),<H1>AR
```

INTERFERENCE-ENHANCED RAMAN SCATTERING FROM THIN FILMS AND INTERFACES

R. J. Nemanich

Recent improvements in experimental apparatus has permitted the application of Raman spectroscopy to microprobing configurations. A lateral resolution of less than $1\text{ }\mu\text{m}$ can be achieved. In contrast there are few schemes for improving the depth characterization methods of Raman scattering. For transparent materials the depth resolution is determined by the optics and scattering geometry; for opaque materials the light probes a depth equal to the optical absorption length. Two major problems associated with surface and interface characterization are to increase the sensitivity of the Raman signal from highly absorbing films and to increase surface or interface sensitivity. In this paper the properties of interference-enhanced Raman scattering (IERS) are described and related in particular to these issues.¹

Raman spectroscopy has proved to be an important characterization method for semiconductors and insulators.² The method is used to display the vibrational modes of the material, and the vibrational modes can be related to the atomic bonding configurations of the material. In general, the results are analyzed by one of two methods: (1) detection of particular structures by comparison with previous measurements, and (2) analysis using a model of the vibrational modes or the Raman scattering process for the materials being examined. The first method is often termed a "fingerprint" scheme and has proved particularly useful for characterization of process-induced changes. The second method involves the use of a model to analyze the symmetry, peak position, or peak width of the Raman scattering results. Many of the early studies of Raman scattering from crystals involved relating the symmetry of the vibrations to the symmetry of the lattice. In current studies of thin-film processes, sharp features are used to indicate crystalline

structures, whereas very broad weak features indicate amorphous structures. One aspect that has proved particularly important in precision engineering is the determination of stress near a processed surface, and analysis of the shift of the LO phonon frequency can often be related to the stress in the sample.³

It has been recently shown that multilayered thin-film structures can lead to the enhancement of the light intensity in particular regions in the structure.¹ The interference-enhanced Raman scattering configuration employs multilayered thin-film samples to use optical interference properties to enhance the Raman signal and to increase surface sensitivity. In this paper, the general aspects of the IERS configuration are described. Application of the method to highly absorbing thin films and interface properties are then reviewed.

Characteristics of Interference-enhanced Raman Scattering

The general aspects of the thin-film structure used to obtain IERS was developed for media used in digital optical recording.⁴ In the original structures, the goal was to increase the light intensity in the surface layer of the structure so that it could be used to change the properties of the material. Ablation of the film was often employed, but other methods of modifying the optical properties were also studied. It was recognized that the same configuration could be used to achieve an enhancement of the Raman scattering signal from very thin films.

The basic property of the IERS technique is determined by the fact that light reflected from a metallic or semiconducting surface interferes with the incident light to form a standing wave (Fig. 1). In normal Raman back-scattering from metallic or semiconducting surfaces, the Raman signal is determined by the intensity of light penetrating into the film. An examination of the light intensity shown in Fig. 1 shows that the intensity is maximum at $\lambda/4$ (λ is the incident wavelength) in front of the surface and is many times more intense than the light inside the metal or semiconductor.

Thus, to enhance the signal the sample

The author is at the Departments of Physics and of Materials Science and Engineering, North Carolina State University, Raleigh, NC 27695-8202. He acknowledges with appreciation the close collaboration with Neville Connell and Chuang Chuang Tsai at Xerox PARC that led to the development and application of the IERS technique.

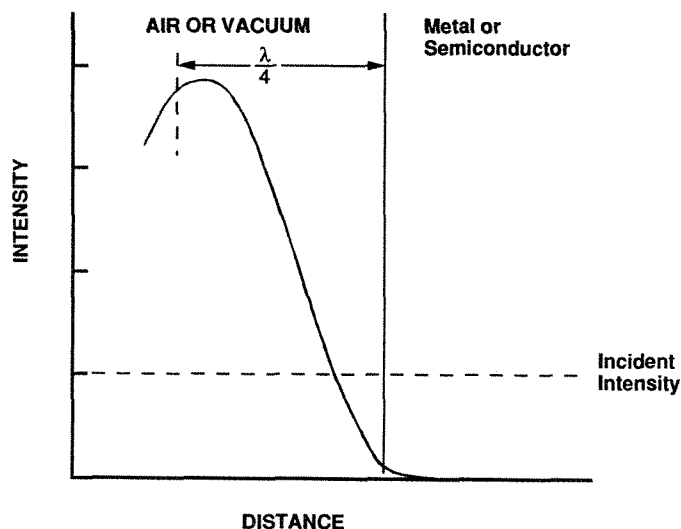


FIG. 1.--Light intensity near the surface of a metal or semiconductor. Figure is modeled for monochromatic visible light incident from left. Dashed line represents intensity of incident light; solid line represents intensity of light due to interference of incident and reflected beams. First peak in intensity occurs at $\sim \lambda/4$ in front of the surface, and intensity is ~ 4 times incident intensity for good metal.

should be placed at the peak of the intensity, which one can accomplish by constructing a multilayered sample using a transparent spacer layer and then depositing a thin layer of the material to be studied. We have developed a computer program that calculates the light intensity inside a multilayered sample. An example of the light intensity inside a tri-layer sample is shown in Fig. 2. We have used 514.5nm incident light and the optical properties of Te, SiO₂ and aluminum for the upper layer, the dielectric layer, and the lower reflecting layer, respectively. The film thicknesses were 50 Å for the Te and 750 Å for the SiO₂. In this case the intensity is now maximum at the thin-film surface, and the reflectivity of the multilayer structure is less than 5%. Thus Raman scattering can be efficiently excited in the thin film (or Te) region. The same interference conditions that result in the enhancement of the incident light also come to play in the Raman scattered light, as one can see by considering the Raman scattering to be an oscillating dipole source. The basic structure is then a dipole a distance of $\sim \lambda/4$ in front of a metal, which then exhibits an image dipole $\sim \lambda/4$ behind the metal surface. The light emission from the dipoles exhibits a phase difference of 2π normal to the film and π parallel to the film. Thus the light intensity is interference-enhanced in the normal direction, which contributes an enhancement of the signal of the same magnitude as the incident light enhancement.

The enhancement of the Raman signal obtained with the IERS configuration for transparent thin films is 16. This figure is obtained from a factor of 4 enhancement on coupling the light into the sample and a similar factor for coup-

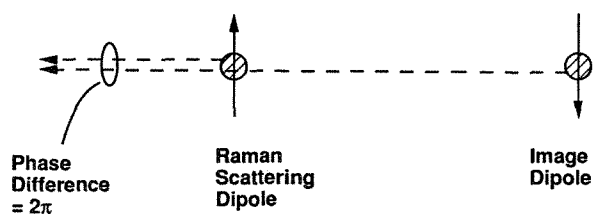
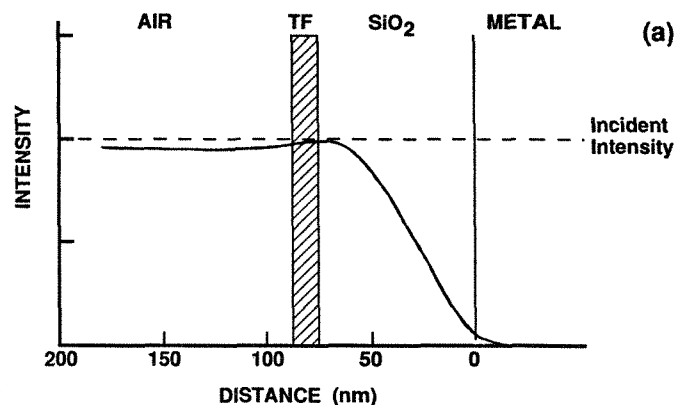


FIG. 2.--(a) Light intensity in multilayer sample used to achieve IERS, (b) oscillating dipole corresponding to Raman scattering from upper layer, and image dipole. Layer thicknesses for this example correspond to 50 Å of metal or semiconducting thin-film (TF) layer; 750 Å spacer layer of SiO₂; and thick lower layer of aluminum. Light intensity is maximum in upper layer; Raman scattering from this layer is also enhanced for normal emission since the two dipoles have phase difference of 2π .

ling the Raman scattered light out of the sample. The enhancement of the Raman signal for opaque samples can be much higher, ranging up to 1000, depending on the optical constants of the material.¹ In this case it is more relevant to calculate the ratio of the intensity of Raman scattering from a thick sample to that of a thin layer in the IERS configuration. It has been shown that the gain, G , is given by

$$G = I_{TL}/I_{SI} = 8\alpha t/(1 - R)^2 \quad (1)$$

where I_{TL} AND I_{SI} represent the Raman intensity from a trilayer and semi-infinite sample, respectively, α and R are the absorption constant and reflectivity of the material, and t is the thickness of the film.¹

The effect was first demonstrated from Te (Fig. 3). The Raman spectra were obtained with ~ 50 mW of 514.5nm light from an Ar ion laser, which was focused to a line of $\sim 100 \mu\text{m} \times 3 \text{ mm}$ on the surface. The Raman scattered light was collected at the normal and dispersed with a triple grating monochromator. A single channel photomultiplier was used to detect the signal. The signal from the thin film in the IERS configuration is more than 20 times stronger than that from an optically thick film. From the optical properties of Te and

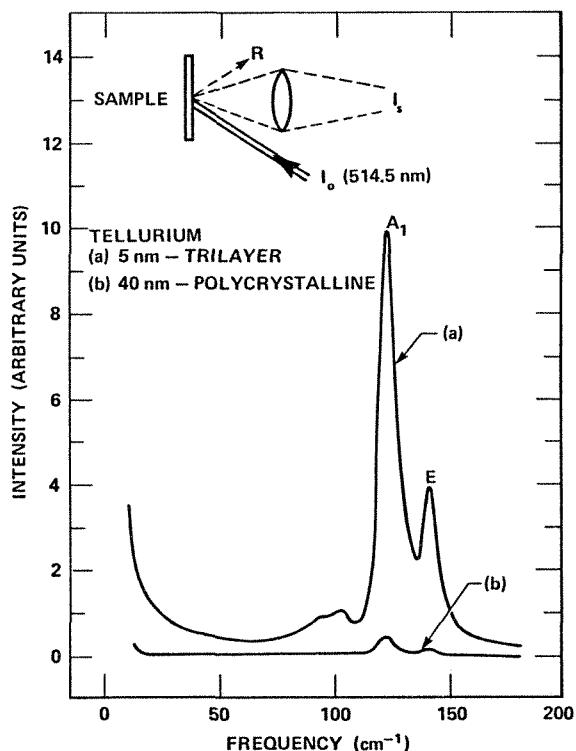


FIG. 3.--Raman spectra of 50 Å Te film obtained in IERS c-nfiguration compared with that from an optically thick film in standard backscatter configuration.¹ Experimental configuration was the same for both samples, but IERS configuration yielded enhancement of 20.

Eq. (1), an enhancement of 22 would be predicted. Thus the interference model describes the results adequately.

IERS from Thin Films

In this section the Raman spectra of two unique thin-film experiments are described to display some of the advantages of interference-enhanced Raman scattering. In the first case, use of IERS to focus selectively on a thin region is exploited, in the second case, the Raman spectrum is obtained from a pure metal which exhibits a very weak signal.

Thin films of Si can be deposited by plasma decomposition of silane onto a substrate held at temperatures ranging from room temperature up to 400 C. These samples are usually termed hydrogenated amorphous Si and contain ~35 at.% H for RT deposition down to less than 2 at.% H at 400 C deposition. Electrical experiments showed that films produced at substrate temperatures near 250 C exhibited the lowest level of defects in the bandgap. Annealing experiments of films showed that H evolved at temperatures above the deposition temperature. The annealing experiments were carried out by ramping of the temperature of the films up to 700 C. Due to sensitivity limitations, the annealing experiments were carried out on films thicker than 1 μm. These films showed a peak in the H evolution at ~600 C. The question was whether

the H evolution was limited by diffusion. Thus a series of Raman measurements using the IERS configuration were carried out for 100 Å films of a-Si:H.⁵ The results are shown in Fig. 4. The series of modes below 600 cm⁻¹ represent the vibrations of the Si atoms in the amorphous Si network. The broad features indicate that the structure is indeed amorphous. The feature at 2000 cm⁻¹ is due to vibrations of H bonded to Si. Thus, the intensity of this feature can be related to the H concentration. The features were monitored after various annealing steps. Here it was found that H was completely evolved from the thin film by annealing at 450 C. This finding indicated that the H diffused from site to site in the a-Si network until the atoms could leave the film from near the surface. In addition, because of the exceedingly high signal to noise obtained from these samples, it was possible to identify weak features in the spectrum Si network vibrations that were related to different bonding configurations after the H was evolved from the sample. These measurements would have been impossible to obtain from thicker films. The H depletion only occurred in the first few 100 Å, but Raman scattering from thick films would measure ~2000 Å, and the effect would be hidden by the unaffected regions. In addition the signal enhancement of the IERS configuration allowed observation of weak features that would not have been observed with the signal-to-noise ratio obtainable in standard backscattering configurations.⁵

The use of IERS for measuring the Raman spectra from samples with weak signals was demonstrated by measurements from Ti thin films.⁶ Because of the metallic character of Ti, it was not previously possible to obtain the Raman spectrum from bulk Ti samples. A trilayer configuration with a Ti sample layer was constructed; the measured results are shown in Fig. 5. The results showed a relatively sharp weak feature centered at 138 cm⁻¹. This feature was assigned to the optic vibration of metallic Ti.

IERS from Interfaces

More complicated structures could also be constructed that employ IERS techniques. The configuration was modified to examine the reactions at the interface of metals and a-Si:H.⁷⁻¹¹ The motivation of these studies was to characterize the Schottky barrier on a-Si:H. A multilayered configuration similar to that for the a-Si:H measurement described earlier was employed. In this case, the spacer layer of SiO₂ was only 400 Å thick and the a-Si:H layer was still 100 Å. The Raman measurements of the trilayer structure again showed a significant enhancement of the signal, but the real utility of the configuration was achieved when a thin layer of metal was deposited on top of the a-Si:H. The light intensity for Pd/a-Si:H in the IERS configuration is shown in Fig. 6.⁸ An important aspect

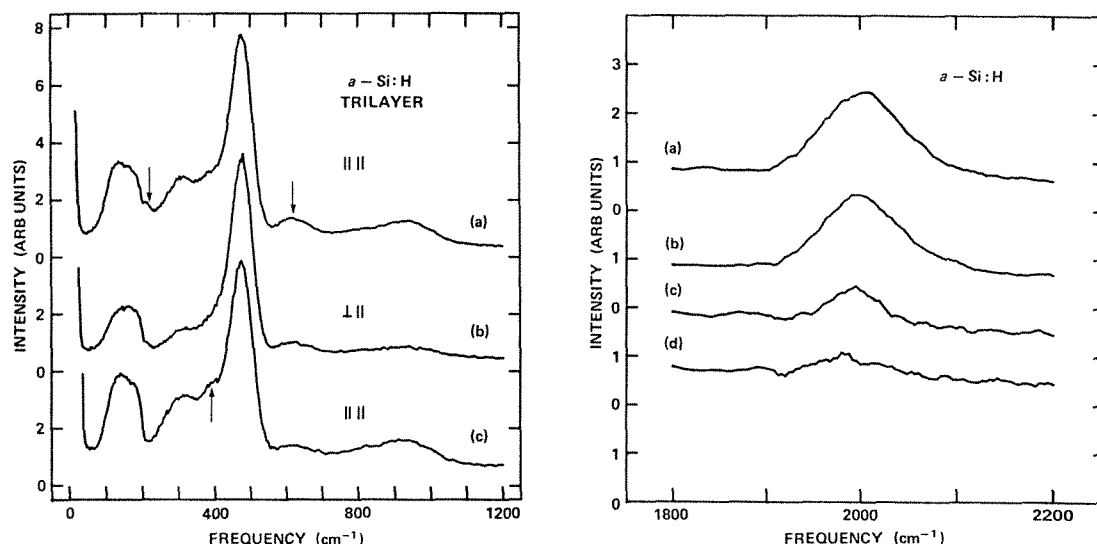


FIG. 4.--Raman spectra of a-Si:H in IERS configuration.⁵ Curves on left show Si network vibrations, curves on right show Si-H vibrations. Relative intensity of Si-H vibrations is increased by factor of 10. Si-H spectra are from (a) as-deposited sample, (b) annealing at 300 C for 10 min, (c) 450 C for 10 min, (d) 450 C for 40 min. For Si network vibrations, spectra (a) and (b) were obtained from as-deposited film and different polarization geometries; curve (c) was obtained after annealing at 450 C for total of 40 min. Arrows indicate features that increase or decrease during annealing process.

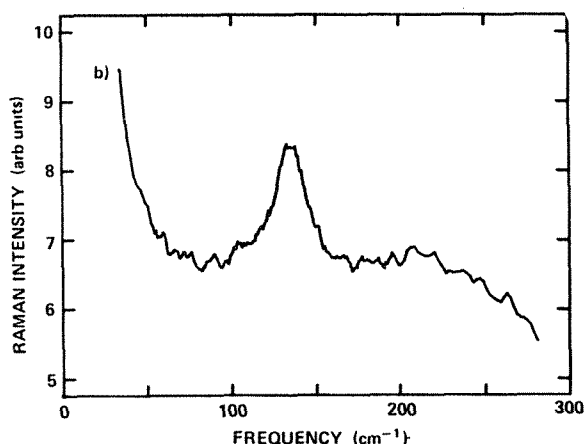


FIG. 5.--Raman spectrum of 50Å Ti film obtained in IERS configuration.⁶ Sharp feature at $\sim 138\text{cm}^{-1}$ is due to optic vibration of Ti crystal.

shown in this figure is that the light intensity drops off very rapidly inside the trilayer sample. This effect is amplified because the same conditions apply for the exiting Raman scattered light. Thus the IERS technique is interface selective.

The Raman spectra of 50 Å of Pd deposited on a-Si:H obtained in the IERS configuration is compared to that obtained from a similar 50 Å layer of Pd on a thick a-Si:H film in Fig. 7. The Raman spectra obtained in the IERS configuration show a series of sharp lines which have been identified by comparison (or "fingerprint") as Pd₂Si. Thus the results show that the Pd₂Si compound forms spontaneously at am-

bient temperature at the interface of Pd and Si. The interface selectivity is apparent in comparison with the Pd deposited on the thick a-Si:H. The first observation is that the overall signal is much stronger for the IERS configuration. The second observation is that the interface signal dominates the IERS spectra, but the interface features are difficult to observe in the standard configuration due to the strong substrate signal in the same frequency region.

Concluding Remarks

This paper describes the use of optical interference to enhance the Raman scattering from very thin film structures. By using multilayered thin film structures, the IERS configuration can be used to obtain high-quality spectra from very thin samples. The IERS technique can achieve a signal enhancement of a factor of 16 for transparent films, but the real advantage of the technique is for opaque films in which enhancements of up to 1000 are obtainable. The technique has three major characteristics: (1) the signal from the thin film is actually stronger than that from a bulk or thick film sample; (2) by proper choice of structure, the signal at an interface or surface can be selectively measured; (3) the technique is applicable to all materials.

In this report the IERS measurement has been reviewed. The effect has been modeled, and the theoretical sensitivity has been verified by IERS measurements of Te. The signal enhancement capabilities have been shown for Ti, a-Si:H, and Pd/a-Si:H structures. The largest enhancement obtained was that of IERS measurements of a 50 Å film of metallic Ti

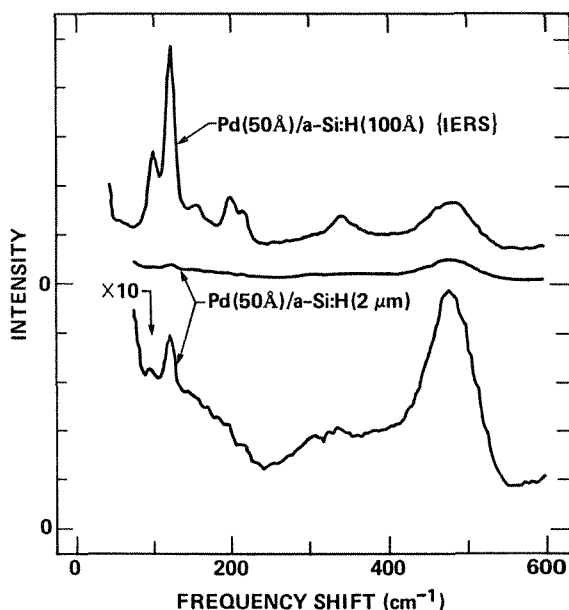
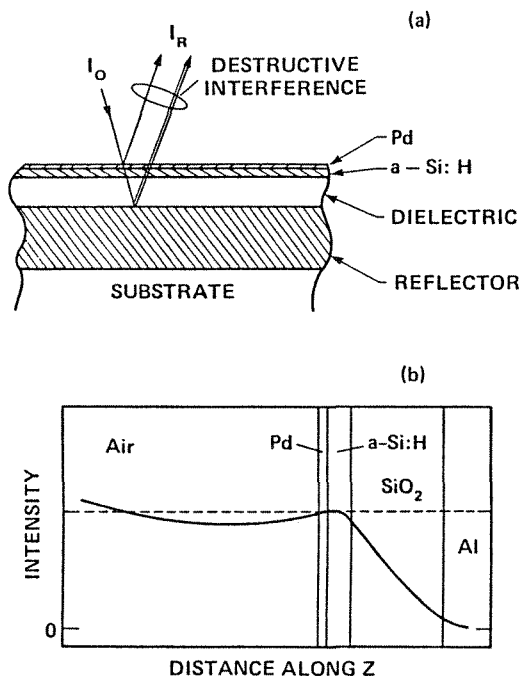


FIG. 6.--(a) Thin-film configuration for IERS from metal/a-Si interfaces, (b) light intensity in multilayer structure.⁸ Light intensity is maximum at interface and is equal to incident intensity.

FIG. 7.--Raman spectra of 50 Å of Pd on a-Si:H in IERS configuration and on thick a-Si:H film in standard backscatter configuration.⁸ Lower spectrum is blown up by a factor of 10 to show that same features are detected. Strong sharp lines from 80 to 230 cm^{-1} are due to Pd_2Si , which has formed at interface.

which exhibits a very weak Raman signal. The surface and interface selectivity of the technique was shown with the measurements of H evolution from a-Si:H, and interface reactions of Pd and a-Si:H.

Future applications will almost certainly require complex heteroepitaxial crystalline structures. The surface of these structures can then be measured with all the advantages of the IERS technique.

References

1. G. A. N. Connell, R. J. Nemanich, and C. C. Tsai, "Interference enhanced Raman scattering from very thin absorbing films," *Appl. Phys. Lett.* 36: 31, 1980.
2. R. J. Nemanich, "Raman spectroscopy for thin film analysis," *Mat. Res. Soc. Symp. Proc.* 69: 23, 1986.
3. R. G. Sparks and M. A. Paesler, "Micro-Raman analysis of stress in mechined silicon and germanium," *Proc. Eng.* 10: 191, 1988.
4. A. E. Bell and R. A. Bartolini, "High-performance Te trilayer for optical recording," *Appl. Phys. Lett.* 34: 275, 1979.
5. C. C. Tsai and R. J. Nemanich, "Structural studies of amorphous semiconducting thin films using interference enhanced Raman scattering," *J. Non-Cryst. Solids* 35-36: 1203, 1980.
6. R. J. Nemanich, C. C. Tsai, and G. A. N. Connell, "Interference enhanced Raman scattering of very thin titanium and titanium oxide films," *Phys. Rev. Lett.* 44: 273, 1980.
7. R. J. Nemanich, C. C. Tsai, and T. W. Sigmon, "Structure and growth of the interface of Pd on a-Si:H," *Phys. Rev.* B23: 6828, 1981.
8. R. J. Nemanich, C. C. Tsai, M. J. Thompson, and T. W. Sigmon, "Interface enhanced Raman scattering study of the interfacial reaction of Pd on a-Si:H," *J. Vac. Sci. Technol.* 19: 685, 1981.
9. C. C. Tsai, R. J. Nemanich, and M. J. Thompson, "Interfacial reactions between Au and hydrogenated amorphous Si," *J. Vac. Sci. Technol.* 21: 632, 1982.
10. R. J. Nemanich, M. J. Thompson, W. B. Jackson, C. C. Tsai, and B. L. Stafford, "Initial reactions at the interface of Pt and amorphous silicon," *J. Vac. Sci. Technol.* B1: 519, 1983.
11. R. J. Nemanich, R. T. Fulks, B. L. Stafford, and H. A. Vander Plas, "Initial reactions and silicide formation of titanium on silicon studied by Raman spectroscopy," *J. Vac. Sci. Technol.* A3: 938, 1985.

HADAMARD TRANSFORM RAMAN MICROSCOPY

M. D. Morris and P. J. Treado

Hadamard transform imaging is a multiplexing technique that provides spatially and spectrally resolved images from unfocused laser beams. Hadamard imaging is advantageous for use with laser sources whose peak or average intensity would otherwise damage samples. We describe the design principles and performance of a second-generation single-channel detector Hadamard Raman microprobe capable of diffraction-limited resolution.

Principles of Hadamard Transform Imaging

Hadamard transform theory and application to spectroscopy and imaging have been reviewed.¹⁻³ The exciting laser beam, or the signal from the illuminated sample, is encoded with a series of n masks. Each mask is composed of a pseudorandom array of open and closed apertures, which are represented mathematically by 1's and 0's. With each mask in place, the encoded beam is presented to a detector, which sums the intensities from all open elements. The image is recovered by inverse Hadamard transformation of the vector of observed signals.

The masks are fabricated as opaque and transparent regions on a suitable substrate. Cyclic Hadamard sequences are employed, so that a single long mask can be translated to generate the successive sequences. Alternatively, the mask sequences can be generated by impressing the proper bit patterns on a spatial light modulator.^{4,5} In this case there is no need for mechanical translation.

The MTF of a Hadamard mask system is ideally given by the MTF for convolution with and diffraction by a single aperture.⁶⁻⁸ If the mask is translated continuously, there is a blur term as well.

If the encoding mask is viewing a magnified image, the mask aperture can be coarse. For work in the ultraviolet or visible, 20-100 μm square apertures will usually be sufficient. In this case, the diffraction term is negligible. Equation (1) gives the convolution for a one-dimensional system.

$$\text{MTF}_a = 1 - f_x d/M \quad (1)$$

where f_x is spatial frequency, d is the width of the unit aperture and M is the total magnification of the image before encoding. To the extent that the contrast remains close to 1, Hadamard multiplexing has a negligible effect on the recovered image.

The authors are at the Department of Chemistry, University of Michigan, Ann Arbor, MI 48109-1055.

As with other multiplexing techniques, A/D converter dynamic range r is distributed between number of pixels encoded n and signal dynamic range s according to Eq. (2).

$$r = sn^{1/2} \quad (2)$$

In practice, with a single-channel detector and a 12-14 bit A/D converter, about 10^3 pixels can be encoded if 256 gray levels are required. With a linear-array detector, this spatial resolution is obtainable at each frequency (wavelength) viewed by the array. With a two-dimensional array detector, spatial multiplexing of one-dimension allows acquisition of complete spatially resolved spectra at the customary 256 K pixel level. Such a instrument could allow use of the same array detector for micro-imaging, microprobe spectra, or conventional large-sample spectra.

A Second-generation Raman Microprobe

Figure 1 shows the schematic diagram of a second-generation Hadamard transform Raman microprobe. The device is constructed from modular microscope components and employs the conventional epi-illumination configuration. An auxiliary lens (not shown) is used to provide controlled defocusing of the incident laser. To allow maximum flexibility in choice of illumination wavelength a beam splitter is used, rather than a dichroic mirror. The Raman spectrometer is conventional and has been previously described.⁹ For these experiments, Ar^+ 514.5 nm radiation was employed.

The magnified image is collimated before encoding, to facilitate convenient placement of the encoding masks in the optical train. The encoded image is spectrally dispersed through a triple monochromator. A photomultiplier is the detector. The Hadamard-encoded image is generated by translation of the mask, with recording of the total Raman intensity at the observation wavelength at each mask position. The image is recovered by inverse Hadamard transformation.

For the experiments described here, a 18 \times objective, 20 \times eyepiece and 80mm collimating lens are employed. The total magnification after collimation is 114. The collimating mask is fabricated photographically, with 100 μm square unit apertures, so that each aperture encodes an unmagnified square region of the image with 0.88 μm sides.

Results

Figure 2 shows a typical Raman image of N,N-dimethyl-p-nitroaniline, obtained at 1310 cm^{-1} , the nitro symmetric stretching mode.

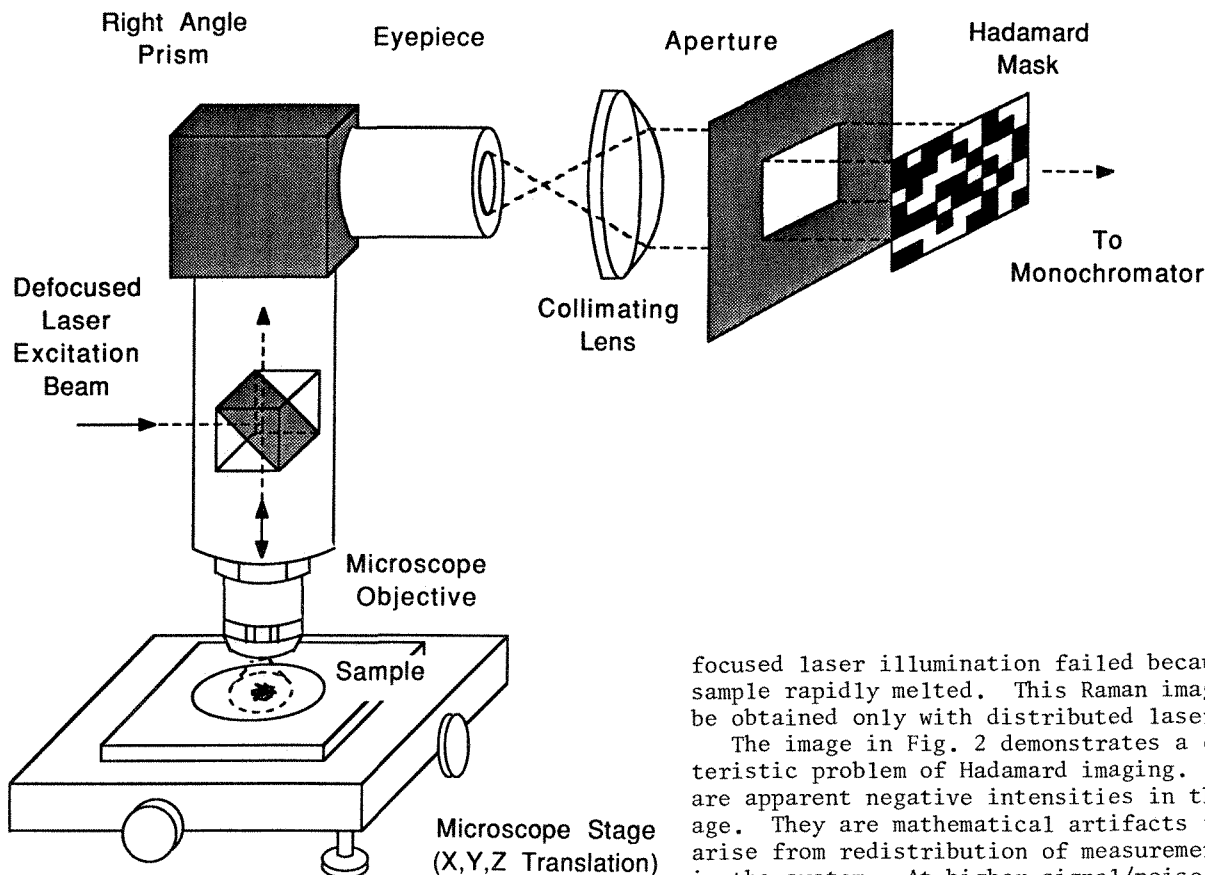


FIG. 1.--Diagram of Hadamard Raman microprobe.

The diffraction-limited (Rayleigh criterion) resolution for the microscope objective is about $0.96\ \mu\text{m}$ at $550\ \text{nm}$. The Raman image preserves the shape of the crystal. The observed dimensions agree with those obtained by reticule measurements.

From the (Nyquist) sampling theorem for the Hadamard transform, it is only necessary to sample with an aperture whose dimension is the inverse of the highest spatial frequency desired. In this case, sampling the magnified image with a $100\ \mu\text{m}$ square aperture encodes the highest resolvable spatial frequency with approximately 10% contrast. Thus, the multiplexing system does not appreciably degrade the resolution of the microscope itself.

The choice of coupling optics for our system is a compromise between the requirements of the microprobe and the requirement for rapid changeover to other Raman experiments which at present share the same monochromator entrance port. Multiplexing of a collimated beam has been achieved at the expense of a substantial reduction of total magnification. A *de novo* design can, of course, avoid this problem.

Available stepping motor and mask fabrication technology will allow easy construction and operation of masks with $20\ \mu\text{m}$ unit apertures. Upgrading the performance of our instrument with finer masks is quite feasible.

The nitroaniline crystal is yellow and partially absorbs green laser light. The sample is illuminated under pre-resonant Raman conditions. Attempts to obtain Raman images with

focused laser illumination failed because the sample rapidly melted. This Raman image could be obtained only with distributed laser power.

The image in Fig. 2 demonstrates a characteristic problem of Hadamard imaging. There are apparent negative intensities in the image. They are mathematical artifacts that arise from redistribution of measurement noise in the system. At higher signal/noise ratio, negative intensities are not observed.

Conclusion

Hadamard multiplexed imaging is an effective technique for observing spatially/spectrally resolved Raman images. With a single-channel detector, images are obtainable, but only with 256-4096 pixels encoded. However, if the photomultiplier is replaced by a two-dimensional array detector, a complete spatial/spectral image with 512×512 pixels can be obtained with our current technology.

References

1. M. O. Harwit and N. J. A. Sloane, *Hadamard Transform Optics*, New York: Academic Press, 1979.
2. R. M. Hammaker, J. A. Graham, D. C. Tilotta, and W. G. Fateley, in J. W. Durig, Ed., *Vibrational Spectrum and Structure*, Vol. 15, Amsterdam: Elsevier, 1986, 401.
3. P. J. Treado and M. D. Morris, *Anal. Chem.* (in press).
4. D. C. Tilotta, R. M. Hammaker, and W. G. Fateley, *Appl. Spectrosc.* 41: 727, 1987.
5. D. C. Tilotta, R. D. Freedman, and W. G. Fateley, *Appl. Spectrosc.* 41: 1280, 1987.
6. F. K. Fotiou and M. D. Morris, *Anal. Chem.* 59: 1446, 1987.
7. P. J. Treado and M. D. Morris, *Appl. Spectrosc.* 42: 1487, 1988.
8. P. J. Treado and M. D. Morris, *Proc. Int. Laser Sci. Conf. IV* (in press).
9. P. J. Treado and M. D. Morris, *Appl. Spectrosc.* (in press).

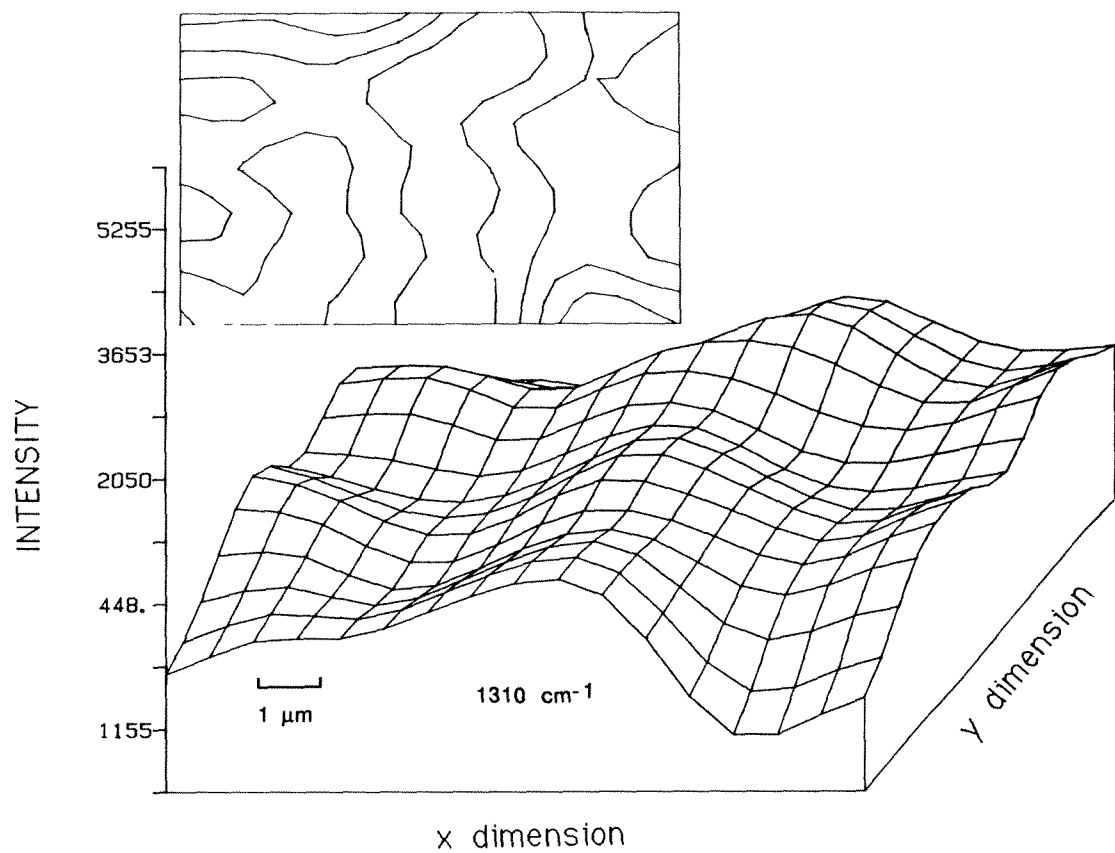


FIG. 2.--Hadamard Raman image of N,N-dimethyl-p-nitroaniline crystal represented as an axonometric plot and contour plot (insert), 1310 cm⁻¹ band. 50 mW, 514.5 nm excitation. Total magnification, 114×.

DEVELOPMENT OF A HIGH AXIAL RESOLUTION MICRO-RAMAN TECHNIQUE FOR STUDYING THE EFFECTS OF MACHINE PARAMETERS IN MACHINED SEMICONDUCTORS

R. G. Sparks, W. S. Enlow, and M. A. Paesler

Micro-Raman spectroscopy has been used to measure residual stresses in machined surfaces with lateral resolution near the diffraction limit.¹ We extend this technique to incorporate axial resolution (i.e., depth into the sample) by measuring residual stresses in single point diamond turned semiconductors with a lateral resolution of $\sim 1.0 \mu\text{m}$ and an axial resolution of $0.01 \mu\text{m}$. Residual stresses are sampled across ductile feed cuts in $\langle 100 \rangle$ silicon and germanium which were single point diamond turned using a variety of feed rates, rake angles and clearance angles. The use of both 514.5nm and 488.0nm excitation wavelengths, by virtue of their differing characteristic penetration depths in the materials, allows determinations of stress profiles as a function of depth into the sample. Greater and greater depths in the material may be probed by using successively longer wavelengths of light, thus leading to a superposition of a continuum of Raman peaks and resulting in an asymmetrical broadening of the spectral features. Depth profiles of residual stress are obtained using computer deconvolution of the resulting asymmetrically broadened Raman spectra.

Experimental

The excitation source consists of an argon ion laser with strong outputs at 514.5 and 488.0 nm. The light from the laser is plane polarized in a direction normal to the plane formed by the optical table on which the laser is mounted. The plane-polarized monochromatic beam is then steered by plane mirrors through an achromatic half-wave plate (Fresnel rhomb). The effect of the half-wave plate is to rotate the polarization state of the excitation beam by a known angle with respect to the original polarization state. Since the Fresnel rhomb introduces some ellipticity in the emerging beam, a Glan-Thompson prism polarizer mounted to a calibrated rotation stage is used to provide a pure linear polarization state at a known angle. The light is then steered into the apparatus (SPEX Micramate), where light of a known polarization state is focused by a $40\times$ microscope objective onto the sample with a particular orientation to the sample's crystal direction. The microscope objective collects the scattered light, but since the excitation beam is incident normally onto the sample, the specularly reflected beam is collected as well. The scattered and reflected light is then fo-

cused by the coupling optics on the entrance slit of a double Czerny-Turner 0.85m holographic grating spectrometer (SPEX 1402), where the collected light is dispersed. In order to increase stray light rejection, the dispersed light is then passed into a third monochromator stage (SPEX 1442U), which functions as an additional spectral filter. The rejection of stray light provided by the third monochromator stage for micro-Raman spectroscopy (where the specularly reflected beam cannot be geometrically rejected) becomes critical, especially for materials with Raman spectral features close to the exciting laser line. The resulting Raman spectra typically exhibit asymmetrically broadened peaks which result from the superposition of a continuum of stress states as the sample depth is increased. Deconvolution of the resulting asymmetrically broadened Raman spectra yield depth profiles of the residual stresses in the single point diamond machined samples.²

Results

Machine parameters such as feed rate (50 and 100 in./rev) and spindle speed (1000 and 2500 rpm) showed little differences in their spectra, and the resulting surface stresses were always compressive (10° rake angle, 6° clearance angle). The depth at which the transition from compressive to tensile stress was evident was approximately constant for all feed rates and spindle speeds used and occurred at a depth of $0.65 \pm 0.01 \mu\text{m}$. Our results indicate that the effects of these particular feed rates and spindle speeds on the residual stress field are not significant. Further investigation with a wider range of feed rates and spindle speeds is therefore indicated for a fuller understanding of the effects of these parameters. However, quite marked differences are evident in the case of rake angles. Germanium samples turned at 0° and -30° rake angles (100 $\mu\text{in./rev}$ feed rate, 1000 rpm spindle speed, 240-500 μm -depth of cut, 6° clearance angle) show clear evidence of superposition broadening with significant variations in the spectra obtained using 514.5nm and 488.0nm probes (Fig. 1). Depth profiles generated from these spectra (Fig. 2) indicate that a plastically deformed zone exhibiting a relatively constant compressive stress then increases dramatically as the depth increases, abruptly changes sign, and rapidly reaches a maximum tensile value. The existence of the rapid change from compressive to tensile stress is indicative of a transition from plastic to elastic deformation.³ This transition has been associated with a

The authors are at the NCSU Department of Physics and Precision Engineering Center, Raleigh, NC 27695. Work supported by ONR contract N00014-86-k-0681 and the P.E.C. industrial affiliates.

defect layer occurring at this depth.⁴ The residual tensile stress smoothly relaxes to zero as the depth increases.

Conclusions

Micro-Raman spectroscopy coupled with the use of computer deconvolution of the resulting spectra has yielded a wealth of information concerning the effects of machine parameters on the residual stress field in single-point diamond turned silicon and germanium. Our investigations show that for the feed rates and spindle speeds studied, no significant variations in the residual stress field are noted. All feed rates and spindle speeds examined in our study resulted in a compressive surface stress which showed a rapid increase to a maximum values of 3-7 kbar at depth of 0.05-0.07 μm . However, significant variations in the stress field were noted for the various rake

angles studied. These variations seem to indicate both changes in the magnitude of the surface stress and significant variations in the region of plastic/elastic transition in such samples.

References

1. R. G. Sparks and M. A. Paesler, "Micro-Raman analysis of stress in machined silicon and germanium," *Prec. Eng.* 10: 4, 1988.
2. W. S. Enloe, R. G. Sparks, and M. A. Paesler, *NCSU Precision Engineering Center Mid-year Report*, 1988, VI.
3. K. L. Johnson, "The correlation of indentation experiments," *J. Mech. Phys. Solids* 18: 1970.
4. Stefan Johansson and Jan-Ake Schweitz, "Contact damage in single-crystalline silicon investigated by cross-sectional transmission electron microscopy," *J. Am. Ceram. Soc.* 71: 8, 1988.

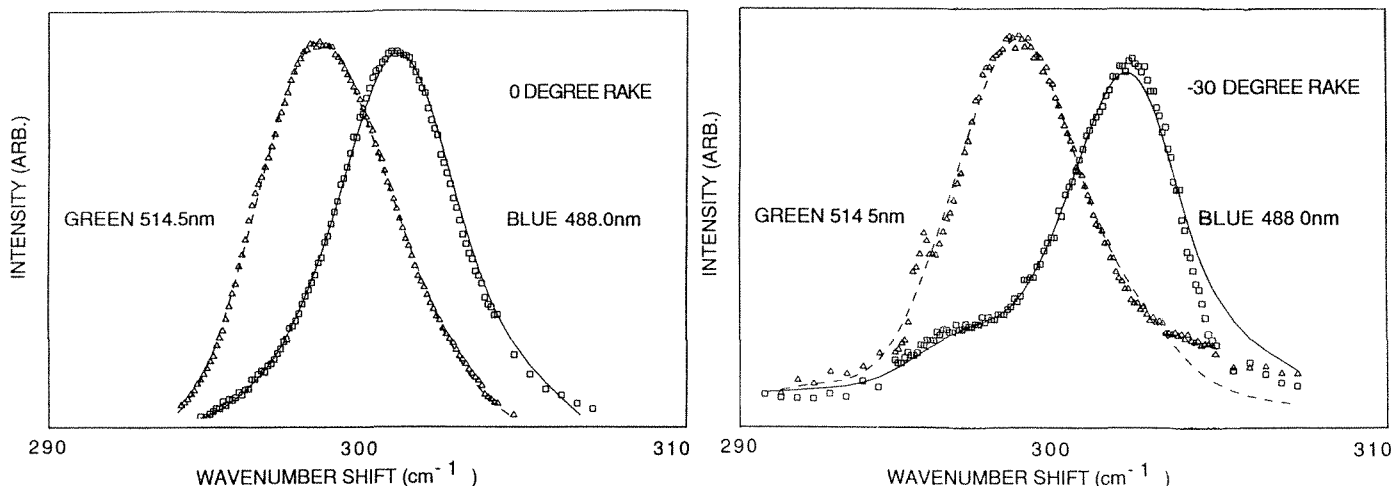


FIG. 1.--Raman spectra for 0° and -30° rake angles. Raman spectra were taken at both 488.0 (blue) and 514.5 nm (green) probe wavelengths. Note the asymmetrical broadening and shifts of resulting peaks.

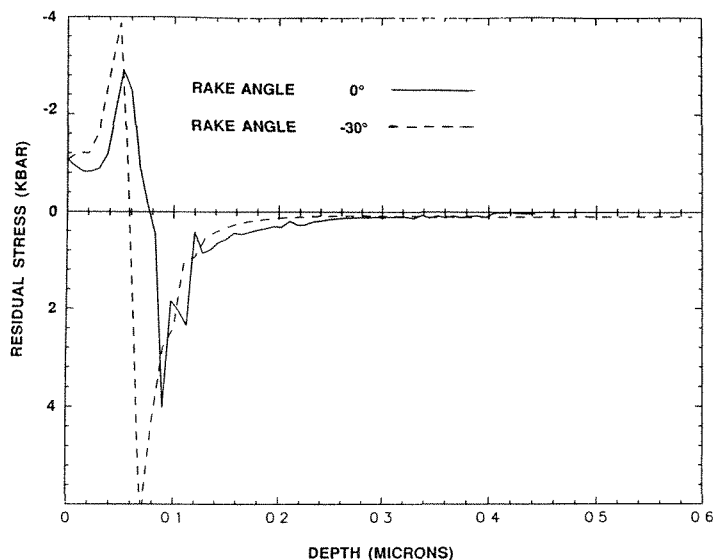


FIG. 2.--Depth profiles generated from micro-Raman spectra for both 0° and -30° rake angles. Magnitude of the residual stress is greater for -30° rake angle but penetrates to shallower depth into sample.

POLARIZED SPECULAR REFLECTANCE UV-VISIBLE SPECTROSCOPY OF CHARGE-TRANSFER TRANSITIONS IN BIOINORGANIC AND ONE-DIMENSIONAL SYSTEMS

R. L. Musselman

Polarized specular (mirror-like) reflectance spectroscopy is valuable not only in the infrared for observation of metallic properties, but in the visible and ultraviolet as well for the determination of the polarizations of charge transfer transitions in a wide range of materials. In this paper we review our recent work in UV-visible specular reflectance spectroscopy on both binuclear metalloprotein models and one-dimensional conductors.

Charge-transfer (CT) transitions are an essential element in understanding the electronic structure of transition metal complexes. Most CT transitions are electric-dipole allowed in one or two directions and thus a knowledge of the polarization of a transition can be of great help in assigning transitions. However, holding complexes in a known orientation and getting light through the highly absorbing sample usually proves to be difficult experimentally and thus most charge-transfer spectra are obtained from solution. However, single crystals with smooth faces may successfully be observed with specular reflectance spectroscopy. Specular reflectance is a phenomenon that closely follows absorbance and is thus greatest at highest absorbances. It is therefore most effective for the study of intense electronic electric dipole-allowed transitions in any molecule that can be crystallized. The present lower limit of detection for specular reflectance is $\epsilon \approx 500 \text{ M}^{-1}\text{cm}^{-1}$, and there is no upper limit, making specular reflectance a complementary technique to polarized absorbance spectroscopy for which a practical upper limit of detection is $\epsilon \approx 1000 \text{ M}^{-1}\text{cm}^{-1}$. Polarized single crystal specular reflectance spectroscopy has begun to be recognized as a powerful tool for determining the polarizations of charge transfer transitions in both inorganic and organic molecules. It can also observe solid-state perturbations present in crystals, especially when planar complexes are arranged closely as in one-dimensional conductors and their precursors.

The use of polarized specular reflectance

The author is at the Department of Chemistry, Franklin and Marshall College, Box 3003, Lancaster, PA 17604-3003. He thanks the many individuals in his laboratory who have contributed to this work, including Stephanie Bell, Heather Bunting, Michael Heagy, Elizabeth John, Dean Rende, Glenn Shaffer, and Dr. William Heuer. The support of the donors of the Petroleum Research Fund of the American Chemical Society and of the National Institutes of Health (Grant 1 R15 GM37481-01) is gratefully acknowledged.

for electronic spectroscopy on molecules was reported in 1960 by Anex and Simpson¹ on molecular crystals, such as naphthalene and anthracene, with high reflectances in the visible and ultraviolet regions. Later work by Anex and coworkers included specular reflectance of Magnus's Green Salt^{2,3} and bis(dimethylglyoximate)nickel and related complexes.⁴ Anex summarized the principles and early applications of polarized reflection spectroscopy in a review in 1966.⁵ Subsequent use of polarized specular reflectance on molecular species has been limited with a few examples in the U.S.,⁶ USSR,⁷ France,⁸ and Japan.⁹ Recently our laboratory has been quite active in the determination of CT transition polarizations in discrete molecules.¹⁰⁻¹²

Specular Reflectance Theory

Specular reflectance is a fundamental optical property of materials and its theory has been well developed.¹³ Since this paper emphasizes molecular and interband transitions, we shall briefly outline reflectance theory to identify only the relationships between extinction coefficient k and the reflectivity R . Metallic parameters may also be readily obtained. In transparent regions where $k = 0$, the reflectivity R is given by $R = r^2 = (n - 1)^2 / (n + 1)^2$, where r is the amplitude of the reflected light. The index of refraction n may be obtained from the Cauchy equation $n = A + (B/\lambda^2) + (C/\lambda^4)$. This dependence of n on λ is called "normal dispersion" and is most familiar in transparent materials on the low-energy side of significant absorptions as in quartz in the visible and near ultraviolet regions.

In regions of absorption, reflection becomes complex:

$$\rho = re^{i\theta} = \frac{(n - 1)e^{i\theta}}{n + 1} = \frac{n - ik - 1}{n - ik + 1}$$

where ρ is the phase change upon reflection. Here, n undergoes dramatic changes known as "anomalous dispersion," such as in quartz in the far ultraviolet. Both n and k are thus functions of θ and r , and θ may be determined through a Kramers-Kronig transformation⁵ in which

$$\theta(\omega_i) = \frac{2\omega_i}{\pi} \int_0^\infty \frac{\ln r}{\omega_1^2 - \omega^2} d\omega$$

Some manipulation is necessary to account for $\omega = \omega$ and the experimentally inaccessible regions of the infinite range of frequencies indicated. The relationships between R and k are shown in Fig. 1 for a typical spectrum.

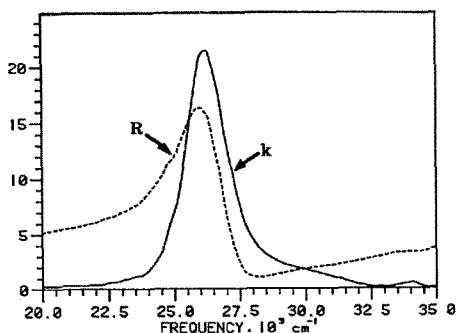


FIG. 1.--Relationship between R and k.

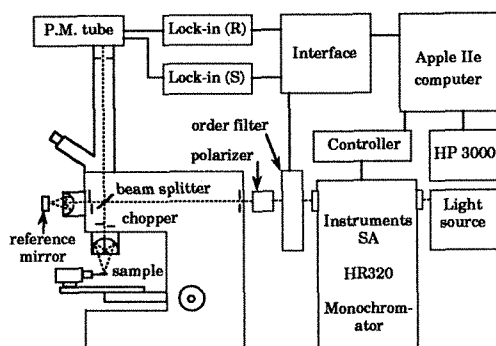


FIG. 2.--Diagram of polarized specular reflectance microspectrophotometer.

Instrumentation

The polarized specular reflectance microspectrophotometer in our laboratory is derived from a design by Anex⁵ with several recent enhancements (Fig. 2). The optics are based on a reflecting microscope with two internal light choppers, beam splitter, and reference mirror for double-beam operation. The reference mirror is calibrated to an NBS standard mirror. The light sources used are a xenon arc lamp and a tungsten halogen lamp housed in an F4.5 reflecting universal lamp housing for UV and visible regions. An Instruments SA 32cm Czerny-Turner monochromator is computer-controlled in increments as small as 1 Å with a typical resolution of 0.2 Å in the UV and visible. A Glan-Thompson prism polarizer, collimating mirrors, and order filters complete the optical path. Detection is by a photomultiplier tube and lock-in amplifiers. An Apple IIe computer controls the instrument through monochromator advances, data collection, sensitivity selection, and order filter charges. Data are statistically evaluated during collection and are sent to a Hewlett-Packard 3000 computer for Kramers-Dronig analysis. Temperature control is achieved with an Air Products liquid nitrogen cryotip refrigerator, which allows continued temperature control from room temperature down to 80 K. Isolation from atmosphere is via a vacuum shroud with a fused silica window. Regions as small as 30 μm in diameter may be chosen for observation, which allows selection of good regions from pitted surfaces of large (~1mm) crystals and observation of very small crystals with flat surfaces.

Binuclear Metalloprotein Models

Iron and copper ions form active sites in a large number of proteins responsible for fundamental electron transfer and oxygen interaction.^{15,16} Spectroscopic study of these active sites is usually hampered by the strong UV absorptions of the protein. We are studying the active sites of both binuclear iron and copper proteins involved in oxygen transport and reaction using inorganic models that contain ligands similar in appearance and neighboring geometry to the central metals as in the protein but without contributing interfering absorbances.

Iron Models. Iron is well known as the active site in the non-heme proteins hemerythrins, ribonucleotide reductase, acid phosphatases, and methane monooxygenase.^{15,16} Our principal focus in iron proteins has been hemerythrins, oxygen transporting proteins that exist in invertebrates such as earthworms and lamp shells, and have as many as eight binuclear iron sites. Hemerythrin exists naturally in two principal forms shown in Fig. 3: (a) oxyhemerythrin with each active site having two six-coordinate ferric ions bridged by an oxo and two carboxylate groups with a hydroperoxide bound to one of the irons and likely hydrogen-bonded to the oxo-bridge¹⁷; and (b) deoxyhemerythrin, where the dioxygen has been removed, leaving a pair of triply bridged ferrous ions, one being only five-coordinate, and a protonated oxo bridge.¹⁸ Loss of hydroperoxide from oxyhemerythrin without reduction of irons gives an "aquo-met" hemerythrin or simply "methemerythrin" (metHr), again with one five-coordinate iron.¹⁹ The uncoordinated site in metHr can be occupied by one of several anions, including N₃⁻, OCN⁻, SCN⁻, SeCN⁻, and halide ions. The oxy- and met-hemerythrins have intense UV transitions that have been assigned as oxo-Fe(III) charge-transfer transitions.²⁰ Our interest is in the interpretation of the UV transitions in relation to the nature of the bridging groups and the bonding angles at the active site.

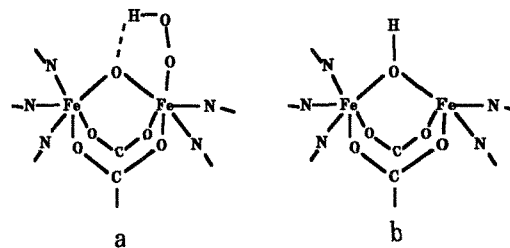


FIG. 3.--Natural forms of hemerythrin: a = oxy-hemerythrin, b = deoxyhemerythrin.

The principal efforts on oxo-bridged iron models have been directed toward the iron III form, methemerythrin. The structures of the active sites in metHr and azidomethemerythrin (metN₃Hr) (where the sixth position on the available iron is an azide group) have been

determined to 2.0\AA resolution.¹⁹ There is an opening of the Fe-O-Fe bond angle upon addition of the azide group, from 127° to 135° , and a similar effect might be expected upon addition of a peroxo group at the same site. We are interested in models that allow a study of the spectroscopy of the active site. Two immediate questions arise: (1) which bridging groups contribute to the spectroscopic characteristics in the UV; and (2) what electronic structure role does the Fe-O-Fe bond angle play? The possibility of simultaneous pair excitation (SPE) of ligand field transitions²¹ has been considered and we conclude that the UV spectroscopic features are primarily due to oxo-Fe(III) CT transitions.^{12,20} The question about the spectroscopic contribution from bridges has been approached by choosing a model that contains only one bridge such as HEDTAFe-O-FeHEDTA, but in this case the Fe-O-Fe bond angle, $\sim 165^\circ$,²² is much greater than in hemerythrin. Thus, the question of the effect of bond angle must also be considered. We have developed a model¹² to account for the effect of Fe-O-Fe bond angles from 90° to 180° , which will now be summarized.

The Fe-O-Fe group may be viewed as two Fe-O groups each affected by the additional iron mainly through its effect on the oxygen orbital alignment. Figure 4(a) depicts the resultant energy levels for a linear arrangement. Only one $a_1\text{oxo} \rightarrow \text{Fe(III)}$ transition is allowed: $a_1(\text{O}) \rightarrow a_1(\text{FeIII})$, in the Fe-Fe(z) direction. Several transitions are allowed from $e(\text{O})$, but the $p_{x,y} \rightarrow d_{xz,yz}$ (allowed z) is most intense due to greatest overlap between the involved orbitals.

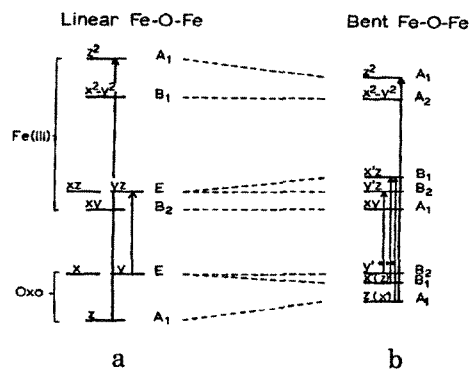


FIG. 4.--Fe and O energy levels resulting from two geometries of the Fe-O-Fe bond angle. (From Ref. 12.)

As the Fe-O-Fe angle becomes bent, the orientation of the oxygen p orbitals changes. The change in point group to C_{2v} allows the linear degenerate orbitals to split. The $e \rightarrow e$ transition becomes two and a forbidden $a \rightarrow e$ transition becomes allowed as $a_1 \rightarrow b_1$. The high-energy transition remains as $a_1 \rightarrow a_1$ in C_{2v} . All transitions except $a_1 \rightarrow b_1$ are symmetry-allowed in the $z(\sim \text{Fe-Fe})$ direction, and the $a_1 \rightarrow b_1$ is also believed to be allowed $\sim \text{Fe-Fe}$ due to mixing of p orbitals.

We prepared $\text{H}_2\text{en}(\text{HEDTA Fe})_2\text{O}$ and have ob-

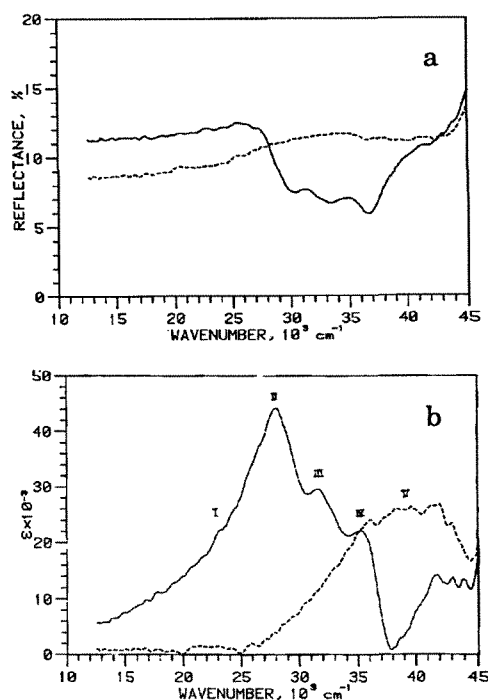


FIG. 5.--Polarized spectra from $\text{H}_2\text{en}(\text{HEDTAFe})_2\text{O}$: a = specular reflectance, b = transformed into absorbance; solid line, electric vector parallel to Fe-Fe; dashed line, perpendicular to Fe-Fe.

tained polarized specular reflectance spectra and their transformed absorbance spectra (Fig. 5).¹² The three transitions II, III, and IV are consistent with the predicted low-energy transitions from Fig. 4(b) and have been assigned as oxo $p_{y'}(b_2) \rightarrow \text{Fe } d_{y'z}(b_2)$, oxo $p_{x'}(z)(\sim b_1) \rightarrow \text{Fe } d_{x'z}(\sim b_1)$, and oxo $p_{z'}(x')(\sim a_1) \rightarrow \text{Fe } d_{x'z}(\sim b_1)$. Transition V is attributed to an iron to carboxylate oxygen transition, polarized normal to the Fe-Fe direction. It is interesting to note that modest features in reflectance become significant peaks in absorption. In fact, the relative intensities agree well with the predictions for peaks II, III, and IV of decreasing intensities for the peaks as energy increases.

Models of Copper-containing Proteins and Enzymes. Copper has a variety of functions when incorporated into proteins and enzymes, including dioxygen binding and transport as in hemocyanins, incorporation of oxygen atoms into organic molecules as with the monooxygenase tyrosinase, and the reduction of oxygen into water as with the copper oxidase laccase. These functions are performed at binuclear or multinuclear copper sites which are currently being studied to understand the electronic structure related to reversible dioxygen binding and activation for hydroxylation. Our interest in these systems has been the determination of the polarizations of charge-transfer transitions related to copper-dioxygen bonding through the study of inorganic models of the binuclear copper site.

Hemocyanins are found both in arthropods

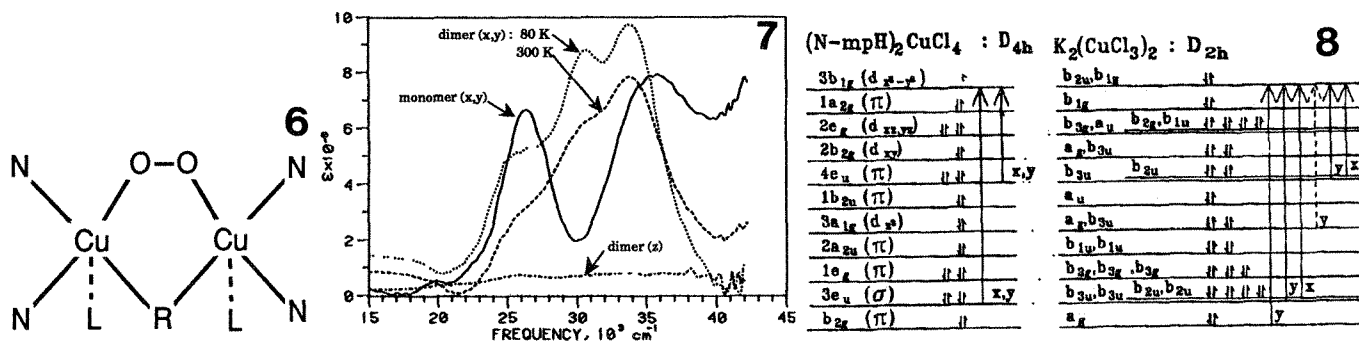


FIG. 6.--Structure of active site in oxyhemocyanin.

FIG. 7.--Polarized absorbance spectra from CuCl_4 monomer and K_2CuCl_6 dimer.

FIG. 8.--Transitions for D_{4h} and D_{2h} copper chlorides.

and in molluscs; the spectral responses upon uptake of oxygen are similar in both types. Crystal structures of deoxyhemocyanin (Hc) and oxyhemocyanin (oxyHc) have been determined with resolutions of 3.2 and 5 Å, respectively.^{23a,b} Although the resolution in oxyHc is too low to determine the orientation of oxygens, a possible arrangement is shown in Fig. 6 along with the protein coordination sites. Before this x-ray study on oxyhemocyanin was available, spectroscopic methods were used to determine several characteristics of the active site, which continue to be critical for both additional structural information and for insights into the electronic structure of the binuclear copper site.

As with hemerythrin, it has proved to be beneficial to study models that resemble the oxyHc active site and whose structures are precisely known. We have begun with models that may be used to determine the general spectral consequences of dimer formation in binuclear copper complexes.

Copper chloride is a simple system that is known in both monomeric and dimeric forms. We contributed to the definitive assignment of CuCl_4 transitions¹⁰ and have begun a study of the dimeric $\text{K}_2\text{Cu}_2\text{Cl}_6$. The monomer $(\text{N-mph})_2\text{CuCl}_4$ showed two prominent transitions in the UV (Fig. 7) both polarized x,y in agreement with predictions for a D_{4h} system (Fig. 8). (Transitions polarized z are also allowed from group theory, but have no intensity due to a lack of overlap of orbitals involved.) The dimer $\text{K}_2\text{Cu}_2\text{Cl}_6$ is being studied to find the effects of bridging on the CT transitions. We have determined the morphology in relation to the atomic positions (Fig. 9) and have obtained polarized spectra on the (010) face, yielding an x,y and a z polarization (Fig. 7). As predicted for D_{2h} from simple correlation with D_{4h} , degeneracies should be split and new transitions become allowed. The combined x,y polarized spectra show at least one prominent additional peak, which may be tentatively assigned as due to the new D_{2h} symmetry.

One-dimensional Conductors: Metallorporphyrins and Analogs

One-dimensional conductors and their precursors have been of interest for many years²⁴ and have been actively studied by us for the past two decades,^{6C,25-31} including

both inorganic complexes such as stacked planes of $\text{Pt}(\text{CN})_4^{2-}$ ²⁵ in which conductivity is through the metal atom chain, and organic compounds such as $(\text{TMTSF})_2\text{ClO}_4$ ³⁰ in which conductivity is through the π system. As an extension of this work we have recently become interested in partially oxidized metallo-phthalocyanines $[\text{M}(\text{pc})']$ s and other metallo-porphyrins which have been found to exhibit metal spine conductivity in some members and π ring conductivity in others.³²⁻³⁶ Our work²⁵⁻²⁹ and that of others^{24e} on the simpler systems such $\text{M}(\text{CN})_4^{2-}$, and the work of others on $\text{M}(\text{dmg})_2$ ⁴, where dmg = dimethylglyoximate ion (Fig. 10a) showed prominent red shifts upon crystallization and closer stacking for transitions related to one-dimensional conductivity. This result led to many theoretical interpretations, none of which appeared sufficient in itself to explain these spectral observations. Very recent calculations³⁷ appear to be more successful and compare favorably with the existing spectroscopic data on $\text{M}(\text{CN})_4^{2-}$ and $\text{M}(\text{dmg})_2$ -type systems.

Tetracyano and Glyoximate Complexes. One of the most thoroughly studied systems is that of $\text{Ni}(\text{CN})_4^{2-}$, $\text{Pd}(\text{CN})_4^{2-}$, and $\text{Pt}(\text{CN})_4^{2-}$, where in each case of a salt containing closely stacked planes, a prominent transition appears to the red of the solution absorption region. This leads to highly colored salts in most of the $\text{Pt}(\text{CN})_4^{2-}$'s. Partial oxidation of $\text{Pt}(\text{CN})_4^{2-}$ leads to metal spine conductors (KCP's) where the d_{z^2} band is generally thought to be the conducting band.³⁰ The d_{z^2} orbital and the out-of-plane transition originating from it have thus received close attention. The behavior of the out-of-plane transition in a series of $\text{Pd}(\text{CN})_4^{2-}$ salts is shown in Fig. 11, where the prominent peak is red-shifted from the solution region as the interplanar spacing diminishes.²⁸ Both band theory^{39a} and excitation theory^{39b} have been invoked to explain the red shift, but SCF-X α -SW calculations by Interrante and Messmer⁴⁰ on $\text{Pt}(\text{CN})_4^{2-}$ and its dimer appear to be more successful in describing the red shift. For a dimer with 2.9 Å spacing, a shift of 14 030 cm^{-1} is predicted. The red shift for the wider spaced $\text{Ba}[\text{Pt}(\text{CN})_4] \cdot 4\text{H}_2\text{O}$ is 12 400 cm^{-1} , which is in qualitative agreement with the X α calculations.

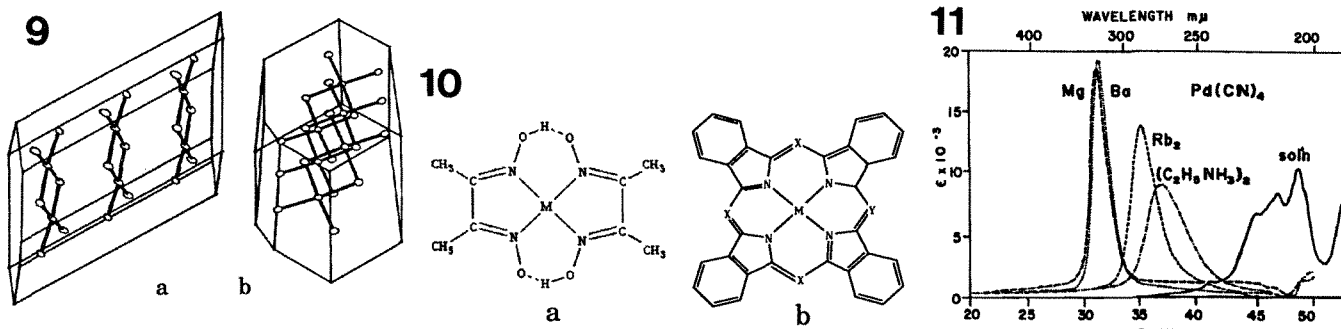


FIG. 9.--Morphology of $K_2Cu_2Cl_6$, viewed (a) normal to the (010) face, (b) (102) face. (Atomic positions from Ref. 23c.)

FIG. 10.--Structures of (a) $M(dmgl)_2$, (b) pc type complexes, where for pc, $X = Y = N$; tbp, $X = Y = C$; tatbp, $X = N$, $Y = C$.

FIG. 11.--Out-of-plane spectra of several $Pd(CN)_4^{2-}$ salts, showing red shift as interplanar spacing decreases. (From Ref. 28.)

Metallophthalocyanines. Phthalocyanines have been known since iron phthalocyanine was inadvertently formed in 1928,⁴¹ and have been used as textile dyes for many years. The observation that partial oxidation of metallophthalocyanines gives rise to conductive derivatives⁴² has renewed interest in these and similar macrocyclic compounds. Metallophthalocyanines (Fig. 10c) have a structure similar to that of the dmgl's, but are more closely related to the metalloporphyrins. Several reviews of the structure, spectra, and conductive properties of metallophthalocyanines are available.^{32,36,43} The crystalline structure of unoxidized $M(pc)$ consists of planes stacked in a herringbone fashion $\sim 20-40^\circ$ off the plane normal, with an interplanar distance of about 3.4 \AA .⁴⁴ The conductivity is low ($\sim 10^{-7} - 10^{-14} \Omega^{-1} \text{ cm}^{-1}$) and the unpolarized spectra are dominated by $\pi \rightarrow \pi^*$ transitions in the visible and UV.^{43,45,47}

Partial oxidation of phthalocyanines results in a straightening of the stacking architecture, a slight closing of the interplanar spacings to $\sim 3.2 \text{ \AA}$, and a very large increase in conductivity. Temperature-dependent conductivity, magnetic susceptibility, thermoelectric power, and EPR data on $Ni(pc)I$ ^{33,35} and $Co(pc)I$ ³⁴ show the former to be a metallic conductor with partial oxidation occurring on the pc (ring conductivity), to give a 5/6 filled macrocycle-based valence band. A schematic diagram of energy levels is given in Fig. 12. In contrast, the $Co(pc)I$ has semiconductor character, with partial oxidation occurring on the metal (metal spine conductivity). In this compound the d_{z^2} band, initially 1/2 full, is proposed as the site of one-electron oxidation for every third Co, thus reducing the band filling to 1/3. The charge compensation in both cases is by I_3^- ions, whose periodicity apparently causes gaps in the bands at 1/3 and 2/3 filling which, in the case of $Co(pc)I$, results in its observed semiconductivity.³⁴ Because the highest energy occupied orbital is the one that becomes oxidized, it appears that in $Ni(pc)I$ the d_{z^2} band is below the HOMO (valence) macrocycle-based

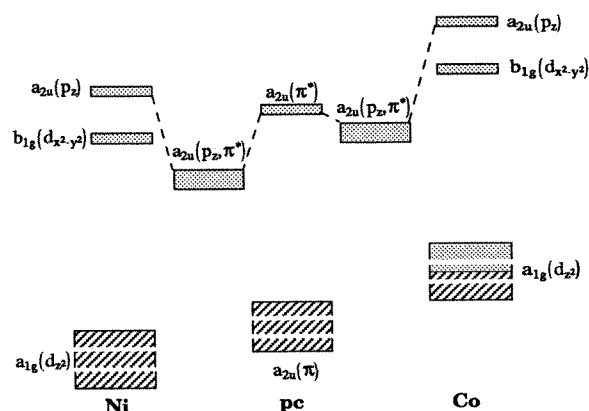


FIG. 12.--Energy level diagram of selected orbitals and bands in Ni, Co, and pc, showing unoxidized filling and band gaps for $M(pc)I$ crystals.

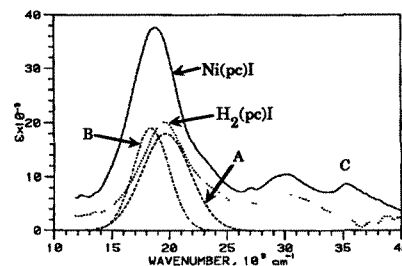


FIG. 13.--Out-of-plane spectra of $Ni(pc)I$ and $H_2(pc)I$. Peaks A and B are extracted from $Ni(pc)I$ curve. A is from I_3^- and B is d_{z^2} to p_z transition.

$a_{2u}(\pi)$ band and in $Co(pc)I$ it is above this $a_{2u}(\pi)$ band.³⁴

We have recently obtained visible and UV polarized specular reflectance spectra of $Co(pc)I$, $Ni(pc)I$, $Cu(pc)I$, and $H_2(pc)I$.⁴⁸ Portions of the Ni and H_2 spectra are shown in Fig. 13. Previous studies reporting near IR and visible reflectance spectra of $Ni(pc)I$ and $Co(pc)I$ attributed a broad reflectance ($\sim 17\,000 - 20\,000 \text{ cm}^{-1}$) to a single broadened I_3^- transi-

tion.^{33,34} Through a Kramers-Kronig transformation of the reflectance of Ni(pc)I and Co(pc)I, we found evidence of two peaks in this region: peak A which corresponds to a 20 000 cm^{-1} $\sigma_{\text{G}} \rightarrow \sigma_{\text{U}}^* \text{I}_3^-$ transition in other compounds with similar relative I_3^- arrangements, and a separate transition B, at 16 000 cm^{-1} in Co(pc)I and 17 500 cm^{-1} in Ni(pc)I, which we assigned as $a_{1g}(\text{d}_{z^2}) \rightarrow a_{2u}(\pi^*, \text{p}_z)$ in the metal.⁴⁸ Cu(pc)I shows the $\text{d}_{z^2} \rightarrow \text{p}_z$ to be at $\sim 18\,500\text{ cm}^{-1}$, and $\text{H}_2(\text{pc})\text{I}$ shows only a 20 000 cm^{-1} peak, as is expected. This is the first time a $\text{d}_{z^2} \rightarrow \text{p}_z$ transition has been identified in a metallo-phthalocyanine.

Another new observation in the M(pc)I's relates to the relative energy levels of metal d and ligand orbitals. In the ultraviolet spectra of Ni(pc)I and Co(pc)I we have found a z-polarized transition, C, in Co(pc)I at 40 000 cm^{-1} and its counterpart in Ni(pc)I at 35 000 cm^{-1} (Fig. 13). We have assigned them as $b_{2u}(\pi) \rightarrow b_{1g}(\text{d}_{x^2-y^2})$ which is in agreement with Gouterman's calculation of the Co b_{1g} being $\sim 5000\text{ cm}^{-1}$ higher than the Ni b_{1g} .⁴⁹

Specular reflectance spectroscopy is thus capable of providing valuable polarization information on symmetry-allowed single-molecule electronic transitions and intraband transitions in conductors, and can observe transitions hidden under more prominent transitions of different polarizations.

References

1. B. G. Anex and W. T. Simpson, *Rev. Mod. Phys.* 32: 466, 1960.
2. B. G. Anex, M. E. Ross, and M. W. Hedgcock, *J. Chem. Phys.* 46: 1090, 1967.
3. B. G. Anex, S. I. Foster, and A. F. Fucaloro, *Chem. Phys. Letters* 18: 126, 1973.
4. B. G. Anex and F. K. Krist, *J. Am. Chem. Soc.* 89: 6114, 1967.
5. B. G. Anex, *Molecular Crystals* 1: 1, 1966.
6. For example (a) P. R. Callis and W. T. Simpson, *J. Am. Chem. Soc.* 92: 3593, 1970; (b) C. J. Eckhardt, H. Muller, and J. Tylicki, *J. Chem. Phys.* 65: 4311, 1976; (c) R. L. Musselman, L. C. Stecher, and S. F. Watkins, *Inorg. Chem.* 19: 3400, 1980.
7. A. Audzjonis and A. Karpus, *Liet. Fiz. Rinkiny* 10: 917, 1970.
8. (a) A. Macadre and C. Moncuit, *C.R. Acad. Sc. Paris* 261: 2339, 1965; (b) J. G. Gross, S. Lewonczuk, M. A. Khan, and J. Ringeissen, *Solid State Commun.* 30: 181, 1979; (c) B. Khelifa, A. Delahaigue, and P. Jouve, *J. Phys. Chem. Solids* 36: 457, 1975.
9. N. Ohno, M. Fujita, Y. Nakai, and K. Nakamura, *Solid State Commun.* 28: 137, 1978.
10. S. R. Desjardins, K. W. Penfield, S. L. Cohen, R. L. Musselman, and E. I. Solomon, *J. Am. Chem. Soc.* 105: 4590, 1983.
11. S. R. Desjardins, D. E. Wilcox, R. L. Musselman, and E. I. Solomon, *Inorg. Chem.* 26: 288, 1987.
12. R. C. Reem, J. M. McCormick, D. E. Richardson, P. J. Stephens, R. L. Musselman, and E. I. Solomon, *J. Am. Chem. Soc.* (in press).
13. J. M. Ziman, *Principles of the Theory of Solids*, New York: Cambridge University Press, 1972.
14. R. Kronig, *J. Opt. Soc. Am.* 12: 547, 1926.
15. (a) E. I. Solomon, J. E. Pate, T. D. Westmoreland, L.-S. Kau, M. D. Allendorf, and D. J. Spira-Solomon, in *Organic and Inorganic Low Dimensional Crystalline Materials*, NATO ASI, Series B (vol. 168), New York: Plenum Press, 1988, 243-269; (b) E. I. Solomon, in K. D. Karlin and J. Zubieta, Eds., *Copper Coordination Chemistry: Biochemical and Inorganic Perspectives*, Giulderland, N.Y.: Adenine, 1983, 1-22; (c) T. G. Spiro, G. L. Wolery, J. M. Brown, L. Powers, M. E. Winkler, and E. I. Solomon, *ibid.*, 23-42.
16. S. J. Lippard, *Angew. Chem. Int. Ed. Engl.* 27: 344, 1988.
17. (a) A. K. Shiemk, T. M. Loehr, and J. Sanders-Loehr, *J. Am. Chem. Soc.* 108: 2437, 1986; (b) A. K. Schiemke, T. M. Loehr, and J. Sanders-Loehr, *J. Am. Chem. Soc.* 106: 4951, 1984.
18. R. C. Reem and E. I. Solomon, *J. Am. Chem. Soc.* 109: 1216, 1987.
19. R. E. Stenkamp, L. C. Sieker, and L. H. Jensen, *J. Am. Chem. Soc.* 106: 618, 1984.
20. (a) E. I. Solomon and D. E. Wilcox, in R. D. Willett et al., Eds., *Magneto-Structural Correlations in Exchange Coupled Systems*, Amsterdam: Reidel, 1985, 463; (b) A. K. Shiemke, T. M. Loehr, and J. Sanders-Loehr, *J. Am. Chem. Soc.* 106: 4951, 1984.
21. H. J. Schugar, G. R. Rossman, C. G. Barraclough, and H. B. Gray, *J. Am. Chem. Soc.* 94: 2683, 1972.
22. S. J. Lippard, H. Schugar, and C. Walling, *Inorg. Chem.* 6: 1825, 1967.
23. (a) K. A. Magnus and W. I. Love, *Life Chemistry Reports* 1983, 61; (b) W. P. J. Gayhmer, A. Volbeder, and W. G. J. Hol., *J. Mol. Biol.* 187: 255, 1985; (c) R. D. Willett, C. Dwigens Jr., R. F. Krub, and R. E. Rundle, *J. Chem. Phys.* 38: 2429, 1963.
24. (a) J. S. Miller and A. J. Epstein, Eds., *Synthesis and Properties of Low-dimensional Materials*, Annals of N.Y. Academy of Sciences, 1978, 313; (b) J. T. Devresse, R. Evrard, and V. E. van Doren, Eds., *Highly Conducting One-dimensional Solids*, New York: Plenum, 1979; (c) J. S. Miller, Ed., *Extended Linear Chain Compounds*, New York: Plenum, 1981, vols. I and II; 1983, vol. III; (d) R. B. King, Ed., *Inorganic Compounds with Unusual Properties*, I and II, Washington, D.C.: ACS Adv. Chem. Series 150 & 173, 1976 & 1979; (e) M. L. Moreau-Colin, *Structure and Bonding (Berlin)* 10: 167, 1972; (f) I. V. Interrante, Ed., *Extended Interactions between Metal Ions in Transition Metal Complexes*, Washington, D.C.: ACS Symposium Series 5, 1974.
25. R. L. Musselman and J. M. Williams, *J. Chem. Soc. Chem. Commun.* 1977, 186.
26. B. G. Anex and R. L. Musselman, *J. Phys. Chem.* 84: 883, 1980.
27. R. L. Musselman, J. B. Cornelius, and

- R. M. Trapp, *Inorg. Chem.* 20: 1931, 1981.
28. R. L. Musselman and B. G. Anex, *J. Phys. Chem.* 91: 4460, 1987.
29. G. C. Arndt, E. D. Danielson, A. D. Fanta, and R. L. Musselman, *Inorg. Chem.* 27: 1400, 1988.
30. R. L. Musselman, B. M. Wolfe, N. E. Brener, R. J. Gale, R. G. Goodrich, and S. F. Watkins, *Solid State Commun.* 63: 595, 1987.
31. R. L. Musselman, A. F. Rees, and S. W. Peterson (in preparation).
32. P. Sayer, M. Gouterman, and C. R. Connell, *Acc. Chem. Res.* 15: 73, 1982.
33. J. Martinsen, S. M. Palmer, J. Tanaka, R. C. Greene, and B. M. Hoffman, *Phys. Rev. B* 30: 6269, 1984.
34. J. Martinsen, J. L. Stanton, R. L. Greene, J. Tanaka, B. M. Hoffman, and J. A. Ibers, *J. Am. Chem. Soc.* 107: 6915, 1985.
35. C. J. Schramm, R. P. Scaringe, D. R. Stojakovic, B. M. Hoffman, J. A. Ibers, and T. J. Marks, *J. Am. Chem. Soc.* 102: 6702, 1980.
36. B. M. Hoffman and J. A. Ibers, *Acc. Chem. Res.* 16: 15, 1983.
37. T. Ziegler, J. K. Nagle, J. G. Enijders, E. J. Baerends, and W. Ravenek (personal communication).
38. (a) J. M. Williams in W. E. Hatfield, Ed., *Molecular Metals*, New York: Plenum, 1978, 337-368; (b) K. Krogmann, *Angew. Chem. Int. Ed.* 8: 35, 1969.
39. (a) M.-H. Whangbo and R. J. Hoffman, *J. Am. Chem. Soc.* 100: 6093, 1978; (b) P. Day, *J. Am. Chem. Soc.* 97: 1588, 1975.
40. L. V. Interrante and R. P. Messmer, in Ref. 24f, p. 382.
41. R. P. Linstead, *J. Chem. Soc.*, 1934, 1016.
42. J. L. Petersen, C. S. Schramm, D. R. Stojakovic, B. M. Hoffman, and T. J. Marks, *J. Am. Chem. Soc.* 99: 286, 1977.
43. A. B. P. Lever, *Adv. Inorg. Chem. Radiochem.* 7: 28, 1965.
44. R. Mason, G. A. Williams, and P. E. Fielding, *J. Chem. Soc. Dalton* 1979, 676.
45. A. B. P. Lever, S. R. Pickens, P. C. Minor, S. Licoccia, B. S. Ramaswamy, and K. Magnell, *J. Chem. Soc.* 6800: 103, 1981.
46. B. W. Dale, *Trans. Faraday Soc.* 65: 231, 1969.
47. M. Whalley, *J. Chem. Soc.* 1961, 866.
48. (a) M. D. Heagy, D. E. Rende, G. W. Shaffer, B. M. Wolfe, K. Liou, B. M. Hoffman, and R. L. Musselman, *Inorgan. Chem.* 28: 283, 1989; (b) W. B. Heuer, D. E. Rende, M. D. Heagy, K. Liou, B. M. Hoffman, and R. L. Musselman, *Chem. Mater.* (submitted).
49. A. M. Schaffer, M. Gouterman, and E. R. Davidson, *Theoret. Chim. Acta* 30: 9, 1973.

INVESTIGATION OF THE MINERAL PHASES ON THE SURFACES OF DENTAL IMPLANTS BY THE RAMAN MICROPROBE MOLE

Fran Adar and Michael Weinlaender

Raman microprobe spectra of several dental implants consisting of titanium plasma-sprayed with hydroxyapatite (HA) were recorded. Since the chemical and crystallographic composition of the coating influences the long-term mechanical effectiveness of the implant, the identification of the phase(s) with the Raman microprobe is useful in qualifying the devices. The coatings were confirmed to be crystalline HA, with a second phase, probably amorphous HA, which is known to have significant effects on the in situ chemical and mechanical performance of the implants.

Background

The ultimate goal of implantation of prostheses in the skeleton is to produce full integration of the nonliving implant with the living bone. The physical and chemical properties of the implant and their interactions with the living bone are the key points in achieving mechanical integration.

The oral and craniofacial rehabilitation of partially or fully edentulous patients with implant-supported prostheses has progressed with the work of Branemark's group in Sweden.¹ This group, and a group of German researchers directed by Kirsch and Koch (IMZ), introduced titanium as the raw material for the production of endosseous implants.² The biologically active surface of both types of implants is a dense protective oxide layer between 15 and 50 Å thick. This oxide layer (TiO₂) is formed seconds after machining or plasma-flame spraying and is resistant to chemical attack. Further, the high dielectric constant of all the oxides results in strong van der Waal's bonds at the surface. Both the Branemark and IMZ types of implants have a high success rate and are suitable for a large number of implant placements.

However, there are occasions where the pre-existing bone is inadequate either in quality or quantity, which leads to difficulties in implantation, especially in posterior mandible and maxilla. Titanium and many other biomaterials have been studied for use as implants. A choice of material for successful implantation must meet many stringent requirements. It should have certain mechanical (physical) and biological (chemical) properties and also be suitable for fabrication into functional devices. Interest in the Ca phosphate ceramics for medical and dental applications derives from the absence of toxic components in

their composition and their resemblance to the inorganic phase of the human skeleton.

Among the more recent bioceramics used for implantation materials are hydroxyapatite, Ca₁₀(PO₄)₆(OH)₂, (HA); and tricalcium phosphate, Ca₃(PO₄)₂ (TCP)--because of their excellent compatibility with living hard tissue. They can be fabricated with properties simulating hard tissues. Dense sintered ceramics can have compressive strength up to 5000 kg/cm²; macroporosities, with values between almost 0 to more than 50%, exhibit values close to those of bone. The more porous structures allow for bony ingrowth and are therefore essential for mechanical stabilization of the implant.

One of the most unique and potentially valuable features of the Ca phosphate implants, both dense and porous, is their apparent ability to become directly bonded to bone. At the interface of the implants, bone is usually found to be deposited directly to the surface without an intervening fibrous capsule. Because Ca phosphate ceramics are composed of the same ions as natural bone mineral, these ceramics are capable of participating in solid-solution equilibrium interactions at their surfaces. The required ions needed to establish these equilibria may be derived from the implant, the surrounding bone, or both. It is to be expected that the composition of any solids deposited on the surface of these implants would be largely determined by the surrounding physiological media, i.e., biological apatite.

Studies of biodegradability of Ca phosphate ceramics, both dense and porous, remain controversial. Materials with Ca/P molar ratios between 1.50 and 1.67 are actively studied; TCP and HA occur with these ratios, respectively. Posner et al. review the chemical behavior of calcium phosphates of various compositions (chemical and crystallographic) and history of formation.³ Factors presumed to govern the biodegradation of the Ca phosphates that are most often mentioned in the literature include the molar Ca/P ratio, the crystallographic structure (including the amorphous phases), and the degree of porosity. It has been assumed that dense HA materials exhibit slow resorption, whereas porous TCP are resorbed more rapidly than HA materials with similar porosity. Two types of porosity of ceramics have been discussed. Microporosity refers to the spaces remaining between the particles following sintering; these spaces are of the order of microns in size. Macroporosity describes pores larger than 100 μm, and as such allow for bone ingrowth.

The principal limitation in the use of the

Fran Adar is with Instruments S.A., Edison, NJ 08820; Michael Weinlaender is Maxillofacial Surgical Implant Fellow, UCLA Medical Center, Los Angeles, CA 90024.

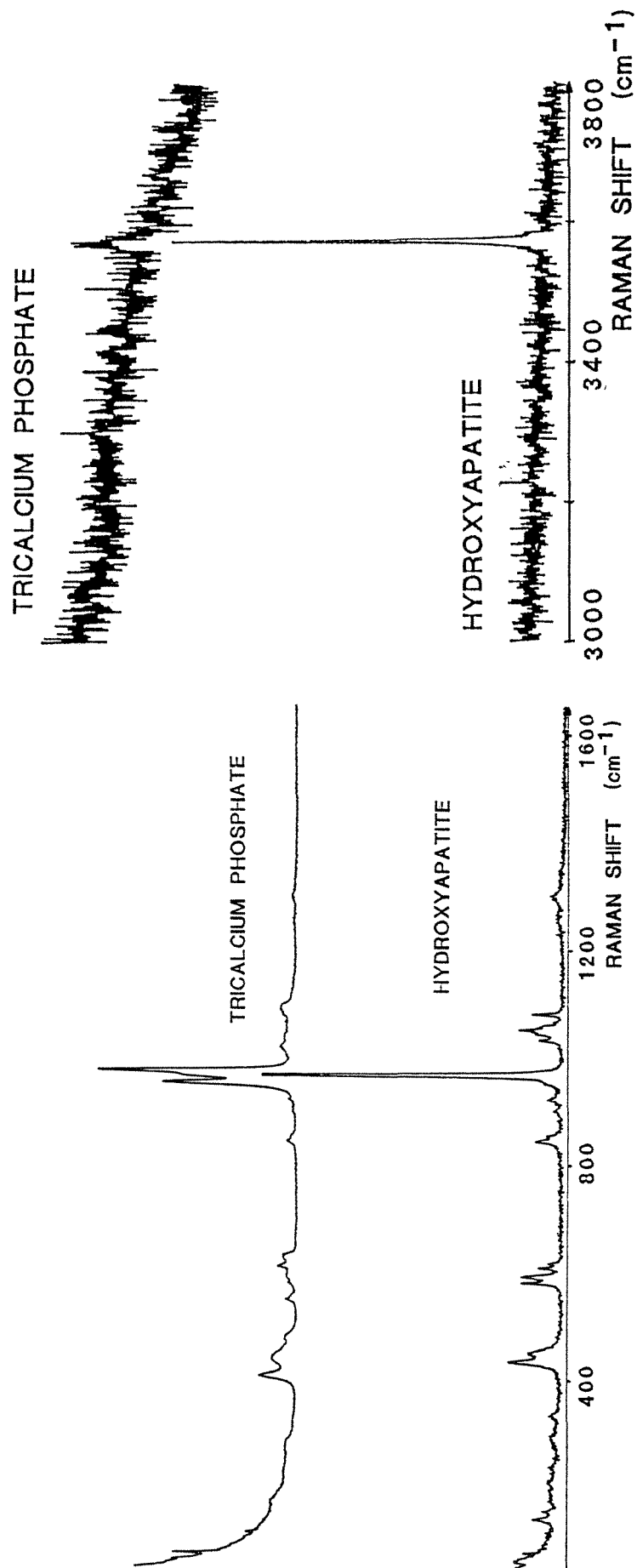


FIG. 1.--(a) Raman microprobe reference spectra of tricalcium phosphate and hydroxyapatite between 50 and 1650 cm^{-1} . Spectra were acquired with laser radiation at 514.532 nm, ca 5 mW at sample, 300 μm slits, 100 \times objective, scanning 1 $\text{cm}^{-1}/\text{sec}$ /data point. (b) Raman microprobe reference spectra acquired between 3000 and 3800 cm^{-1} . Same conditions in (a).

Ca phosphate ceramics for implantation is derived from their mechanical brittleness. Ceramics are characteristically stronger in compression than in tension. Brittleness makes them mechanically inferior to both bone and metal. They are useful only in applications where the forces are compressive.

The idea of combining the superior mechanical properties of a metallic base (Ti) with a Ca phosphate ceramic possessing superior biological and osteophilic properties was introduced by the production of hydroxyapatite-coated Ti implants. The coating is applied by the plasma flame spray technique.⁴ In this process, pulverized HA particles 50-100 μm in size are injected into an Ar gas stream and carried into a plasma flame whose temperature is between 15 000 and 20 000 C. The particles are partially melted in the plasma and then deposited on a titanium surface to thicknesses of about 50 μm .

These implants are expected to produce a faster rate of incorporation due to simultaneous deposition of bone on the prepared bone site and the implant surface. However, problems are to be expected. The thermal expansion characteristics of the coating and the metal are different. At high temperatures, Ti ions can possibly migrate into the ceramic and alter the properties of the bioactive surface. It is also possible that the crystallographic properties of the HA, altered during the plasma spray, may affect the bioactivity. The present study was initiated to examine the crystallographic properties of the plasma-sprayed coatings of four commercial dental implants. Raman microprobe analysis requires absolutely no sample preparation. It produces information concerning the crystallographic phase, including the presence of amorphous material.

Experimental

Samples of the following dental implants were examined: Integral from Calcitek, Lamellar HA Coated Endosteal Implant from Interpore IMZ, and Steri-OSS from Denar Corp. Reference samples of TCP (Synthograft from Johnson & Johnson) and HA (Calcitite from Calcitek) were also examined.

Spectra were acquired on the U1000 Raman microprobe which is described elsewhere.⁵

Results

Complete spectra of the two reference materials are shown in Fig. 1. Part A shows spectra in the fingerprint region; Part B, in the OH stretching region. The spectrum of HA reproduces that reported in the literature⁶ where the spectrum was interpreted in terms of the C_{6h}^2 space group instead of the C_{6h}^6 space group. Apparently the lowering of symmetry produced by the position of the OH⁻ groups in the unit cell does not affect the coupling of the phosphate vibrations. The symmetric stretch ν_1 , appears as a single line at 964 cm^{-1} . Other bands were split by effects of packing of the ions in the crystal. The bands

between 425 and 450 cm^{-1} have been assigned to components of ν_2 . Those between 575 and 615 cm^{-1} were assigned to ν_4 and those between 1025 and 1085 cm^{-1} to ν_3 .

The low intensity in the OH⁻ stretching region of TCP is consistent with its composition; the residual intensity at 3574 cm^{-1} probably indicates HA contamination in TCP.

Initially it was thought that variations in the performance of the implants might be due to deposition of small amounts of TCP in place of some of the HA. Therefore, the reference spectra were examined to determine the best region of the spectrum to use for determination of phase. It was apparent that the PO_4^{3-} symmetric stretching region near 965 cm^{-1} presents the most sensitive region for diagnostics of phase. Raman microprobe spectra of the implants in this region were recorded.

The spectrum of the Integral implant is overlaid with that of the reference materials in Fig. 2. All the implants gave characteristically the same spectrum. The strong phosphate band of HA dominates the spectrum of the implant. However, there is another band at lower frequency, somewhat broader than bands of the reference materials. This band does in fact overlap with a band of TCP, but is not being assigned to TCP for the following reason. The TCP spectrum shows another band, of even greater intensity, on the high-frequency side of the HA band that was absent in all implant spectra. Since there is always the possibility that relative intensities of Raman bands can be distorted when single crystals are probed, several spectra of particles of TCP were examined and showed the same pattern as that in Fig. 2. Therefore, the extra low frequency band would have had to be accompanied by a higher-frequency band if its origin were TCP.

An alternate explanation for the extra band is that it comes from amorphous material co-deposited during plasma spraying. The assignment of this band to the amorphous phase comes by inference, since no sample of amorphous HA was available for examination. It is known that the Raman spectra of amorphous phases are analogous to spectra of the crystalline phases of the same material; the principal differences are that the bands tend to be broadened and shifted to lower frequency. These effects arise from the reduction in size of ordered regions of the materials and a breakdown of the selection rules due to lack of symmetry. The resulting coarseness of the mesh in the Brillouin zone leads to scattering wavevectors significantly different from zero producing a spectrum of bands weighted by the phonon density of states.⁷

This explanation is in fact consistent with the plasma spray process which is known to melt the particles partially.⁴ It is also an explanation that will be useful in rationalizing the degree of success of the implantation since the rate of resorption of HA will be different for crystalline vs amorphous materials.³

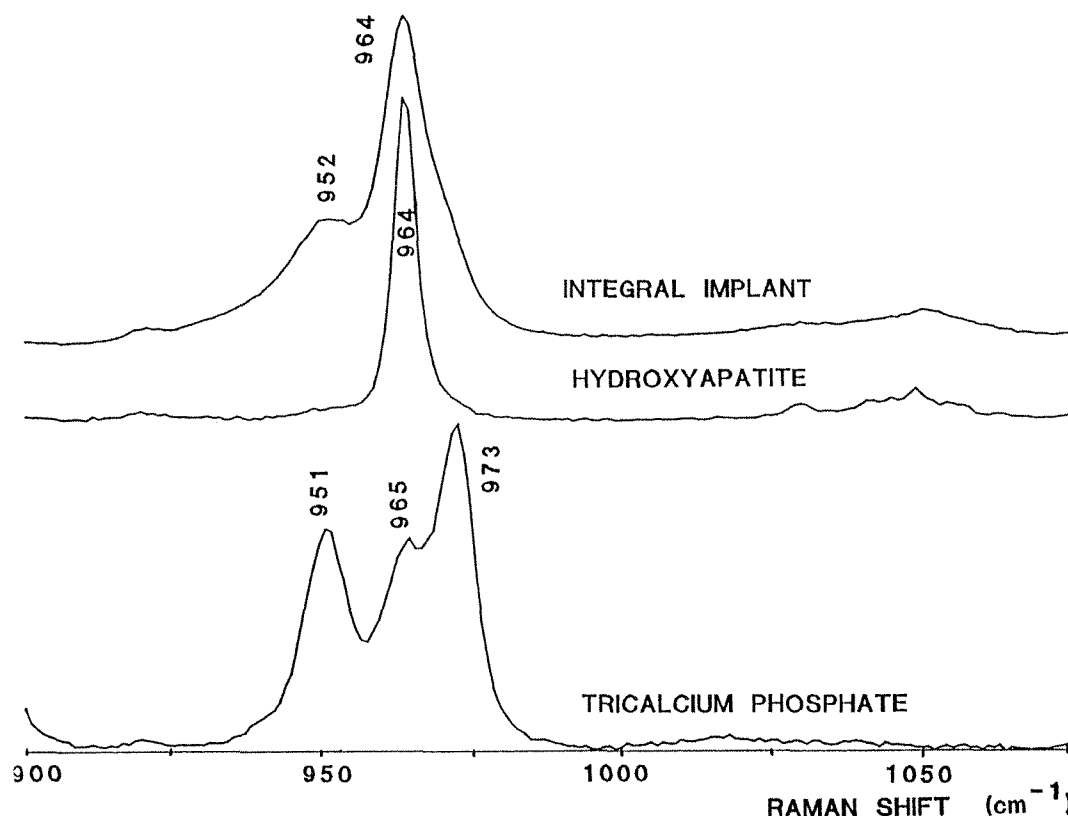


FIG. 2.--Raman microprobe spectra between 900 and 1075 cm^{-1} of reference materials and Integral implant from Calcitek.

Conclusion

Raman microprobe spectra of dental implants confirm that the deposition of CA phosphate during plasma spraying produces crystalline HA. Co-deposited with crystalline HA is a second phase, probably amorphous HA. The ratio of crystalline to amorphous HA, which affects the performance of the implants, can be monitored by the Raman microprobe.

References

1. P. I. Brannemark, G. Zarb, and T. Albrektsson, Eds., *Tissue-Integrated Protheses: Osseo Integration in Clinical Dentistry*, Chicago: Qunitessence, 1980.
2. A. Kirsch, "The two phase implantation method using IMC (Intramobile Cylinder Implant)," *J. Oral Implantol.* 11: 197-210, 1983.
3. A. S. Posner, N. C. Blumentahl and F. Betts, "Formation and structure of chemically precipitated hydroxyapatites," *Proc. 2nd Intern. Cong. Phosph. Comp.*, Paris: IMPHOS, 1980.
4. H. Herman, "Plasma spray deposition processes," *MRS Bull.*, December 1988, 60-67.
5. Fran Adar, "Developments of the Raman microprobe: Instrumentation and applications," *Microchem. J.* 38: 50-79, 1988.
6. K. C. Blakeslee and R. A. Condrate Sr., "Vibrational spectra of hydrothermally prepared hydroxyapatites," *J. Am. Ceram. Soc.* 54: 559-564, 1971.
7. W. Hayes and R. Loudon, *Scattering of Light by Crystals*, New York: Wiley, 1978, 139.

APPLICATIONS OF INFRARED MICROIMAGING TO COATINGS

R. T. Carl

During the past five years, infrared (IR) microspectroscopy has progressed from an exotic and difficult technique to a routine method of analysis. This advance is due to the merger of highly sensitive Fourier transform IR spectrometers with precision IR and optical microscopes. IR microspectroscopy is now widely used in failure analysis, forensic chemistry, and polymer science. Typically, an experiment would involve obtaining a single IR spectrum of a trace contaminate or investigation of a single polymer defect.

Recently there has been an interest in using the IR microscope as an imaging probe.¹⁻⁴ Imaging techniques are used in technologies such as electron microprobes,⁵ laser electron microscopy,⁶ surface-enhanced Raman spectroscopy,⁷ and nuclear magnetic resonance.⁸ IR imaging begins by coupling an IR microscope to a computer-controlled, two-dimensional motorized stage. A series of infrared spectra can be obtained at specific X and Y positions of the sample. This four-dimensional data array (X vs Y vs frequency vs intensity) can be compressed to three dimensions by choice of a specific frequency over the spatial range of the sample. A series of images based on different functional groups can be obtained by variation of the frequency to be displayed. These Functional Group Images (FGI)^{1,4} provide a means of nondestructive evaluation of the chemical composition of a sample on a microscopic scale. Nondestructive testing is of particular importance in the coating industry, since removal of the coating changes the physical and/or chemical composition of the sample. With the use of IR microimaging, the sample can be investigated without removal from its physical environs.

Experimental

All data were collected on a Nicolet System 740 spectrometer interfaced to an IR-PLAN microscope equipped with a proprietary Nicolet high-sensitivity, narrow-band 0.25mm MCT detector. A Spectra-Tech 6 × 6in. X-Y motorized stage was mounted on the microscope along with a 15X Cassegrainian objective (0.58 numerical aperture). All collection, stage-movement, and data-reduction routines were controlled by the Nicolet data station. All spectra were collected at 8 cm⁻¹ resolution in 128 co-added scans for a measurement time of 22 s. Redundant Aperturing was used in every case to collect spectra of high spatial purity and photo-

metric accuracy.⁹ Coated steels and paper samples were obtained from industrial sources.

Results

The first sample investigated was a section of high-grade steel coated with an organic material. This proprietary material was applied as a rust preventative and corrosion inhibitor. Minimizing the thickness of the coating to the point where the material would still retain its anticorrosive properties could reduce costs in the production of this material. A tedious, destructive, wet gravimetric method could be used to determine the coating thickness. Unfortunately, this procedure would only yield an average thickness and large variations in the thickness could still lead to ineffectual protection. Therefore, the purpose of performing an IR imaging experiment on this sample was to determine the variation of the coating thickness in order to tailor the production process for consistency.

As a first step in setting up the IR imaging experiment, the bulk sample (75 × 100 mm) was mounted on the X-Y stage. Since the sample was originally intended to study the effects of weathering, only half the steel surface was coated and the other half remained uncoated. For this study, both the aperture size and stage step size was set to 400 μm. The area to be investigated was approximately 0.8 × 0.8 mm. Thus, the spectrometer was set up to collect a 20 × 20 spectral matrix. The infrared microscope was set up to collect data in the reflectance mode, since steel is a highly reflecting substrate. A new background on the uncoated portion of the steel was collected after each row (X varied, Y fixed) of sample spectra had been collected. This procedure was intended to minimize any effect of purge changes over the several hours of data collection.

After all the spectra were collected and processed, an individual spectrum was examined to determine the absorption frequency for analysis. A band in the C-H stretching region was selected as diagnostic of the coating thickness.

The data reduction can be performed either by use of the peak height of a band or its integrated absorbance. In addition, a pair of bands could be selected and the ratio of either peak heights or integrated absorbances of these bands could be displayed. This type of data reduction is important in investigation of polymer blends where the sample thickness also varies. In this case, the peak height of the single frequency was selected to be used in the data compression. A contour

The author is at Nicolet Spectroscopy Research Center, 5225 Verona Rd., Madison, WI 53711.

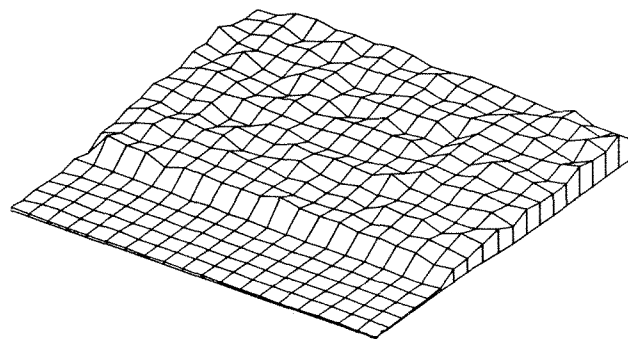
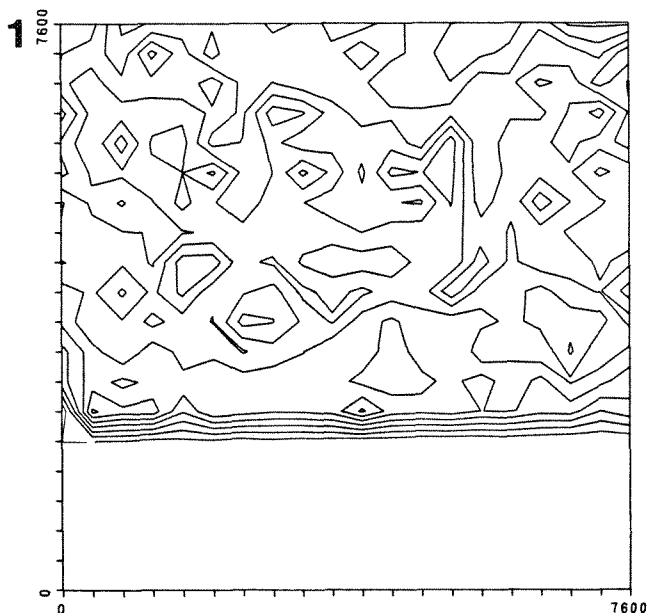


FIG. 1.--Contour display of coating on steel surface, Step size: $400 \times 400 \mu\text{m}$, peak height.

FIG. 2.--Axonometric display of coating on steel surface. Step size: $400 \times 400 \mu\text{m}$, peak height.

plot of the result is shown in Fig. 1. This plot represents 400 spectra taken over a sample area of $0.8 \times 0.8 \text{ mm}$. The bottom portion of the plot shows no IR activity for the frequency selected since this is the uncoated portion of the steel surface. At approximately $2000 \mu\text{m}$ in the Y direction, the contour lines begin and are closely spaced. This indicates an area of rapidly increasing intensity which should correspond to the edge of the coating. The contour lines soon become more widely spaced, which shows the coating is being sampled. An axonometric projection of the contour plot is shown in Fig. 2. As can be seen, there is variation throughout this coated area. The smallest peak height is 0.04 A ; the largest, 0.09 A , a variation of over 100%. This variation is in excess of manufacturing specifications for this product.

In order to investigate the variation on a smaller scale, the aperture and step size were set to $100 \mu\text{m}$. A 20×20 matrix was collected and the data compression performed at the same C-H stretching frequency. The contour and axonometric projection are shown in Figs. 3 and 4. Since the area sampled was only $0.2 \times 0.2 \text{ mm}$, the variation in thickness is less than in the previous case. However, the edge of the coating is being explored in much more detail. As can be seen in the figures, there is a gradual slope from the uncoated portion of the steel to the maximum coated level. This slope can be used as an indication of the speed of the curing process. A rapidly cured product would have a very steep slope since the curing would be completed before the product had a chance to cold flow. A slowly cured product would likewise have a gentle slope, since a large amount of flow would occur before the product completely cured.

The second product examined was a latex-coated paper sample. This product had failed one of the quality control inspection tests after it was manufactured. This particular test consists of applying ink to the coated side of the paper and monitoring for evenness

of the ink surface. When the ink appears blotchy or mottled, it is an indication of product failure. Did the mottled appearance come from the bulk paper or the latex coating? Previous studies using ultraviolet (UV) imaging have indicated that variations in the latex coating gives rise to the mottled appearance.¹⁰ Additional surface studies of latex-coated papers have used techniques such as electron spectroscopy for chemical analysis (ESCA)¹¹ and electron probe x-ray microanalysis.¹² In this case, IR imaging was used to determine whether there are differences in the latex uniformity that could possibly cause mottling during the ink test.

A sample was removed from the paper sheet that had failed the ink test. Initial studies on the microscope in transmission mode indicated that portions of the IR spectrum would be totally absorbed due to the thickness of the paper. However, a band at 1509 cm^{-1} could be identified as being due to the latex coating by comparison with a pure spectrum of the latex. The area to be mapped was $4 \times 4 \text{ mm}$ with a step size of $200 \mu\text{m}$. The dual apertures on the microscope were also set to $200 \mu\text{m}$. A 20×20 spectral matrix was collected over 4 h. The data reduction was performed by analyzing the peak area of the 1509 cm^{-1} band. A plot of the contour map is shown in Fig. 5 and indicates variations in the thickness of the latex coating. The axonometric plot is shown in Fig. 6. These results indicate that this latex variation may be causing the mottling in the ink test. Additional work on a sample that passed the quality control test is still needed to confirm this postulate.

In conclusion, the coupling of an IR microscope with a motorized X-Y stage allows the technique of IR imaging to be employed. Ease of use is facilitated by having flexible software available on the spectrometer data station which can execute rapid data reduction and displays. The application of IR imaging in both reflectance and transmission can yield valuable information about the thickness and variation of coatings.

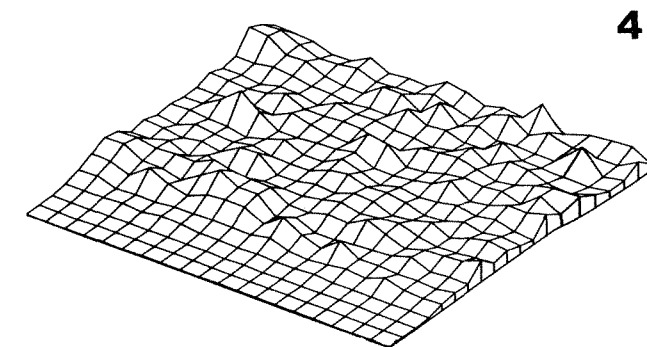
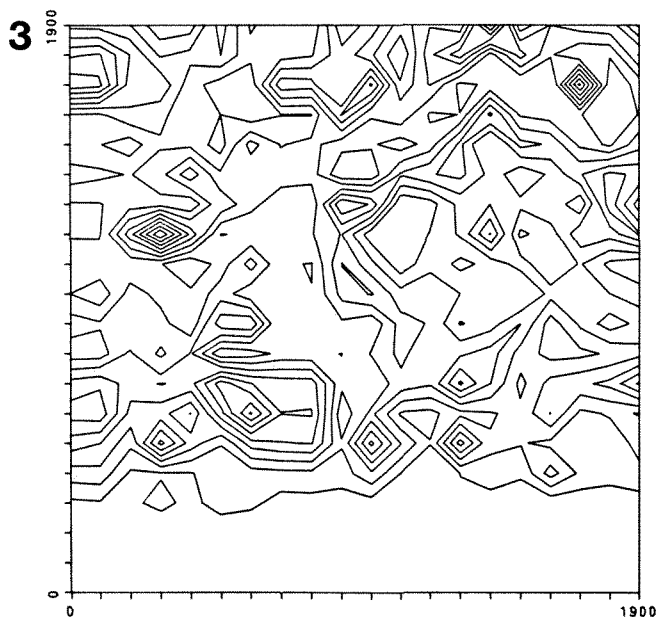


FIG. 3.--Contour display of coating on steel surface. Step size: $100 \times 100 \mu\text{m}$, peak height.

FIG. 4.--Axonometric display of coating on steel surface. Step size: $100 \times 100 \mu\text{m}$, peak height.

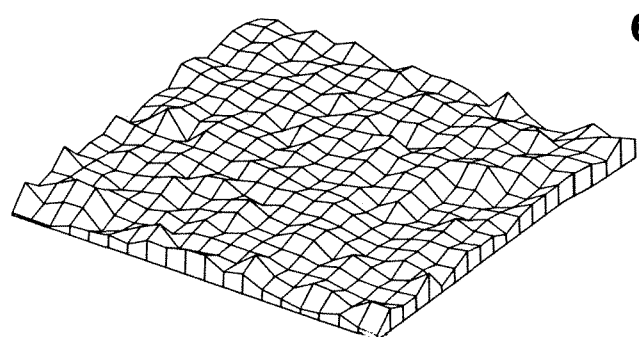
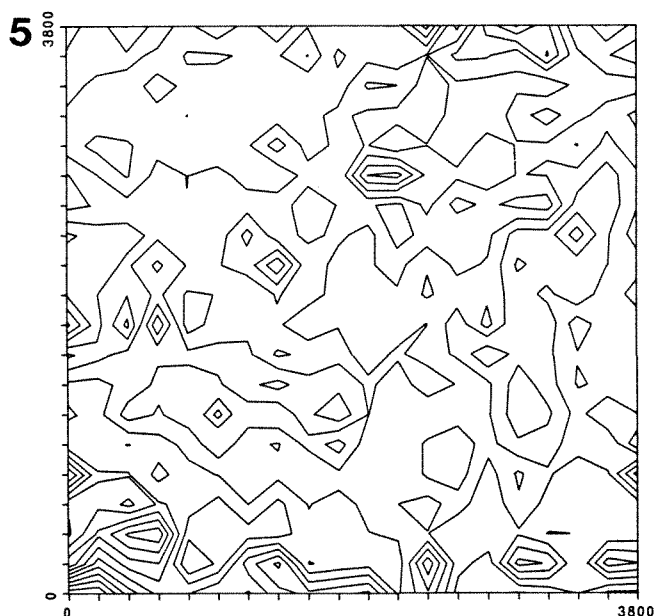


FIG. 5.--Contour display of latex coating on paper. Step size: $200 \times 200 \mu\text{m}$, peak area.

FIG. 6.--Axonometric display of latex coating on paper. Step size: $200 \times 200 \mu\text{m}$, peak area.

References

1. M. A. Harthcock and S. Atkin, *Appl. Spectrosc.* 42: 449, 1988.
2. M. A. Harthcock, S. C. Atkin, and B. L. Davis, "Infrared microspectroscopy functional group imaging as a probe into the compositional heterogeneity of polymer blends," *Microbeam Analysis--1988*, 203.
3. M. A. Harthcock and S. C. Atkin, "Infrared microspectroscopy: Development and applications of imaging capabilities," in R. G. Messerschmidt and M. A. Harthcock, Eds., *Infrared Microspectroscopy: Theory and Applications*, New York: Marcel Dekker, 1988, 21.
4. M. A. Harthcock and S. C. Atkin, "Compositional mapping with the use of functional group images obtained by infrared microprobe spectroscopy," *Microbeam Analysis--1987*, 173.
5. R. B. Marinenko, R. L. Myklebust, D. S. Bright, and D. E. Newbury, *Microbeam Analysis--1985*, 159.
6. T. J. Manuccia, Paper #630, Federation of Analytical Chemistry and Spectroscopy Societies Meeting XIII, 1986.
7. R. P. Van Duyne, K. L. Haller, and R. I. Altkorn, *Chem. Phys. Lett.* 126: 190, 1986.
8. S. L. Smith, in S. A. Borman, Ed., *Instrumentation in Analytical Chemistry*, Washington, D.C.: American Chemical Society, 1986, 303.
9. R. G. Messerschmidt, "Minimizing optical non-linearities in infrared microspectroscopy," Ref. 3, p. 1.
10. H. Fujiwara and J. E. Kline, *Tappi J.* 97, 1987.
11. H. Tomimasu, S. Ogawa, Y. Sakai, T. Yamasake, and T. Ogura, in *Coating Conference Proceedings*, Atlanta: Tappi Press, 1986, 35.
12. T. Hamada and M. Khone, *Japan Tappi*, 39: 43, 1985.

A MICROEXTRACTION TECHNIQUE FOR THE DIRECT ISOLATION OF LIQUID DROPLETS CONTAINED WITHIN A MATRIX

L. S. Darmon and D. L. Pierce

The analysis of particles directly isolated from a matrix has specific advantages. Spatial resolution is increased without a decrease in the beam dimension, which optimizes throughput and minimizes diffraction effects. Direct isolation also circumvents the need to infer that the material of interest is contained in a bulk extract. This feature increases the confidence that the analytical information obtained pertains to the originally observed specimen. As a general rule, solid particles are easier to manipulate and to isolate from a matrix than liquid droplets of the same dimensions due to their rigidity. Some 40 μ m droplets have been large enough to be manipulated physically for analysis. However, the droplet size of many problems encountered is approximately 10 μ m, with an occasional 25 μ m droplet. These 25 μ m droplets can be successfully isolated by extraction by a 10 μ l syringe and organic solvent. In addition, this technique can also be used to transfer films of low viscosity liquids from the surface of a coating to the appropriate substrate for chemical analysis. Once isolated, microscopy techniques for the preparation of samples at the nanogram level are documented in the literature;^{1,2} microspectroscopy thus becomes a valuable tool in contamination analysis. Two instances in which this technique was used to isolate material from a gelatin matrix are described. The isolation and the microinfrared analysis was accomplished in under 2 h. This technique enables the direct isolation and analysis of material under the restrictive time lines necessitated by industrial problem solving.

Procedure

The sample is viewed under a stereomicroscope in order to identify the area of interest. The surface of the coating is punctured with a sharp probe to expose the bubble and a drop of solvent is applied through a 10 μ l syringe. The surface mixture is next withdrawn into a second syringe to prevent cross contamination. This mixture is transferred to an infrared substrate or a watch glass. The procedure is repeated until a sufficient quantity of material is collected for analysis.

Discussion

In the first example, samples received for analysis contained bubbles of a nonwater-soluble material included in a gelatin matrix.

Some of these bubbles had broken the surface of the gelatin layer and smeared across the surface of the coating. These areas were extracted by use of approximately 20 μ l of 2,2,4-trimethylpentane. The extracts were transferred to a watch glass and the extraction solvent was allowed to evaporate. The infrared spectrum obtained identified the major component of the residual to be an aromatic phosphate ester. This was a known component of the solution being coated. An adjacent area, free of the liquid, was chosen as a blank and surface extracts showed negligible residue indicating that the material isolated was indicative of the manufacturing problem and not an artifact of the isolation procedure. Based on this information, the solution preparation procedure was restructured and the coating problem was eliminated.

In the second example, samples of a coated product contained liquid bubbles in the range of 10-25 μ m in diameter. Several bubbles were exposed by a sharp probe and the material was collected by the microextraction procedure. This material was identified by infrared spectroscopy and gas chromatography-mass spectrometry as di(2-ethylhexyl)phthalate. Tubing containing this plasticizer was removed from the solution delivery system and the coatings resumed without further incident.

Conclusion

Microextractions have enabled the direct isolation and chemical identification of approximately 25 μ m-diameter bubbles from a gelatin matrix. Since the material was directly isolated, confusion was avoided in the interpretation of the data. Direct isolation techniques also increase spatial resolution without decreasing beam dimensions. This microextraction technique, although applied here to the isolation of material in a gelatin matrix, has general applicability to other polymeric systems.

References

1. R. Cournoyer, J. C. Shearer, and D. H. Anderson, *Anal. Chem.* 49: 2275, 1977.
2. H. J. Humecki, *ASTM Spec. Tech. Publ.* 949: 39, 1987.

The authors are with the Chemicals Quality Services Division, Eastman Kodak Co., Rochester, NY 14652-3702.

INFRARED SPECTRAL MAPPING OF POLYMERS BY FT-IR MICROSCOPY

J. A. Reffner

Infrared microspectrometry (FT-IR microscopy) provides a direct method for analysis and mapping of molecular species in materials. Applications of FT-IR microscopy to the mapping of molecular species in polymers is reported to demonstrate the utility of this technology. Microscopists have contributed greatly to our understanding of polymer science, and FT-IR microscopy promises to expand these contributions. Polymer microscopy has been limited to observing morphology, measuring optical properties, and (in crystalline polymers) recording electron or x-ray diffraction patterns. Identifications are made by comparing observations with recorded values or by selective staining techniques.^{1,2} Refractive index, birefringence, and thermal properties are the classic light-microscopy measurements, but none of these quantities are direct observations of the molecular structure. FT-IR microscopy records the molecular structure.^{3,4}

FT-IR microscopy is a microbeam analytical technique. Microbeam analysis has three primary objectives: to identify small samples chemically, to generate quantitative analyses of small sampling areas, and to image the sample in order to relate the chemical and morphological structure. Because of the advances in IR spectroscopy, IR microspectroscopy has become a practical reality. Fourier transform IR spectrometry has greatly improved spectral quality and spectrometer throughput and dramatically increased signal-to-noise response. Improved spectral quality also enhances our ability to interpret the complex IR spectra of polymeric materials.⁵ FT-IR microscopy is the combination of light microscopy with IR spectroscopy. It is by combining imaging, spectroscopy, and quantitative photometry that mapping a polymer's molecular structure with its morphology has been achieved.

FT-IR microscopy differs from traditional electron-beam microanalysis in its spatial resolution, in the experimental conditions, and in the nature of the spectrographic information obtained. IR radiation has a longer wavelength than visible light. Resolution is limited by diffraction and optics so that the practical IR probe size approaches the wavelength. In the mid-IR this factor limits the sampling area to $10 \times 10 \mu\text{m}$. If resolution is its weakness, the molecular spectral information is FT-IR microscopy's real strength. The experimental conditions for FT-IR microscopy are also an advantage, since the samples are examined in air; no vacuum is required.

Three mapping applications of FT-IR micros-

copy to polymer science are presented: (1) the qualitative analysis of a multilayered laminate, (2) the IR dichroic analysis of a single acrylic fiber, and (3) the measurement of the oxidative degradation of polypropylene exposed to environmental weathering. These examples were chosen to show some of the advantages gained by this combination of technologies.

Experimental

All infrared spectra reported in this work were obtained with a Nicolet 20 SXB FT-IR TM spectrometer equipped with an IR-plan FT-IR microscope. Spectra were recorded at 4cm^{-1} resolution by means of a 0.25mm MCT detector operating at 77 K. Polarized IR measurements were made with a wire grid polarizer. The wire grid polarizer has 1200 aluminum wires per millimeter on zinc selenide, providing a range of 5000 to 500cm^{-1} .

Polymers used in this work were all commercial materials. The polymer laminate is a proprietary food container. The acrylic fiber was Fiber No. A0159, from Reference Collection of Synthetic Fibers, Collaborative Testing Services, Inc., Herndon, Va. The polypropylene studied was a charcoal lighter fluid container cap exposed to the environment on the author's patio for two years. Thin cross sections of polymeric samples were prepared by conventional microtome sectioning techniques, with an American Optical Co. rotary microtome with a steel knife.

Results

Analysis of a Plastic Laminate. Laminating plastic films to form composite structures with improved properties is an expanding technology. These composite structures offer a new level of complexity, challenging the polymer analyst. It is often difficult to separate the laminate into its basic constituents by conventional methods. FT-IR microscopy provides the best solution for the direct analysis of these materials. The preparation of a laminated structure for IR microscopical analysis requires that a 5-20 μm -thick cross section be prepared. Layers of the laminate can then be analyzed by IR spectroscopy by use of the microscope and remote image plane masks to isolate each layer. Individual layers as thin as 15 μm can be isolated and analyzed.

The laminate shown in Fig. 1 contains five discrete layers. The microtome sectioning of this plastic laminate, the mounting of sections for analysis, and the collection of the IR spectra required less than 1 h to complete. The micrograph in the figure represents what is seen when one views the laminate's cross sec-

The author is with SPECTRA-TECH Inc., Stamford, CT 06906.

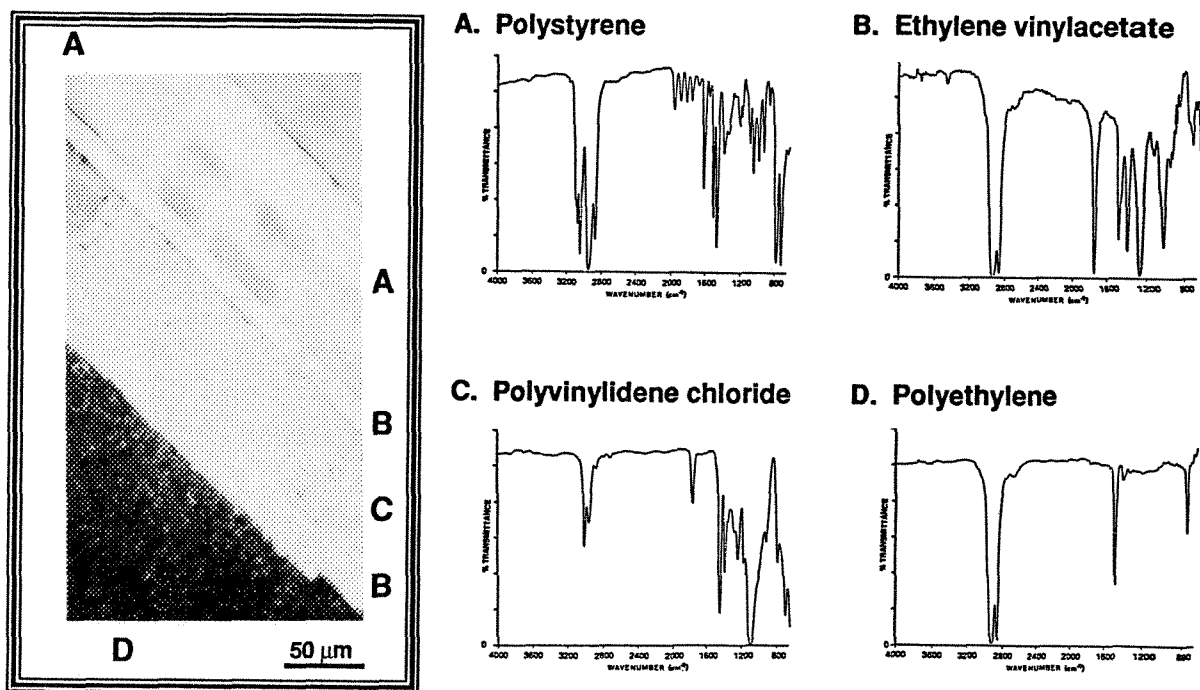


FIG. 1.--IR microanalysis of plastic laminate.

tion through the microscope. After masking with the dual remote image plane masks provided in the IR-PLAN microscope, the IR absorption spectrum of each layer was recorded. The thickness and identification of each layer of this laminate is listed in Table 1. The adhesive layers 2 and 4 are both less than 20 μ m thick and their spectra were obtained without interference from neighboring layers. Although laminates are complex materials, FT-IR microscopy allows their composition to be determined while retaining the details of their geometry and order within the composite.

TABLE 1.--FT-IR microscopical analysis of laminate.

Layer number	Thickness (μ m)	Composition
1	81.4 \pm 2.0	Polystyrene
2	12.9 \pm 1.5	Ethylene vinylacetate
3	55.7 \pm 2.0	Polyvinylidene chloride
4	17.1 \pm 1.5	Ethylene vinylacetate
5	>300	Polyethylene

Linear Dichroism of a Single Acrylic Fiber. The orientation of molecules in a processed polymeric material is an important factor in establishing the properties of the product. IR spectra can be used to measure molecular orientation when polarized IR radiation is used. Polarization of the IR radiation gives it an

orientation that can be used to probe a polymer's molecular orientation. The importance of molecular orientation in polymer science is well established.^{6,7} While polarized infrared studies of films have been possible with bulk samples, the analyses of single fibers require FT-IR microscope.⁸ The IR linear dichroic analysis of a single acrylic fiber illustrates the utility of the IR microscope for these studies.

In synthetic fibers the molecular chains are oriented by the extruding and drawing processes. In acrylic fibers the carbon chains become aligned with the fiber axis, causing the nitrile groups to become oriented perpendicular to the fiber axis. Because the nitrile groups are highly polarizable, the optical birefringence of acrylic fibers is small and often negative (i.e., the perpendicular index of refraction is higher than index of refraction measured parallel to the fiber axis). Linear dichroic IR spectra specifically measure the orientation of the nitrile groups in a single acrylic fiber.

The measurement of the orientation of nitrile groups in a single acrylic fiber involves three steps: (1) sample preparation, (2) recording spectra with the FT-IR microscope, and (3) analysis of the dichroic spectral data.

Single CRESLAN acrylic fibers (AO159) were removed from a 6in.-long section of a continuous filament tow and mounted over a 13mm circular opening in a microsample slide. Great care was used not to stretch or deform the fiber during its mounting. Pressure-sensitive tape was used to secure the fiber section on the slide. When examined microscopically, the fibers were straight longitudinal sections 21 μ m in diameter.

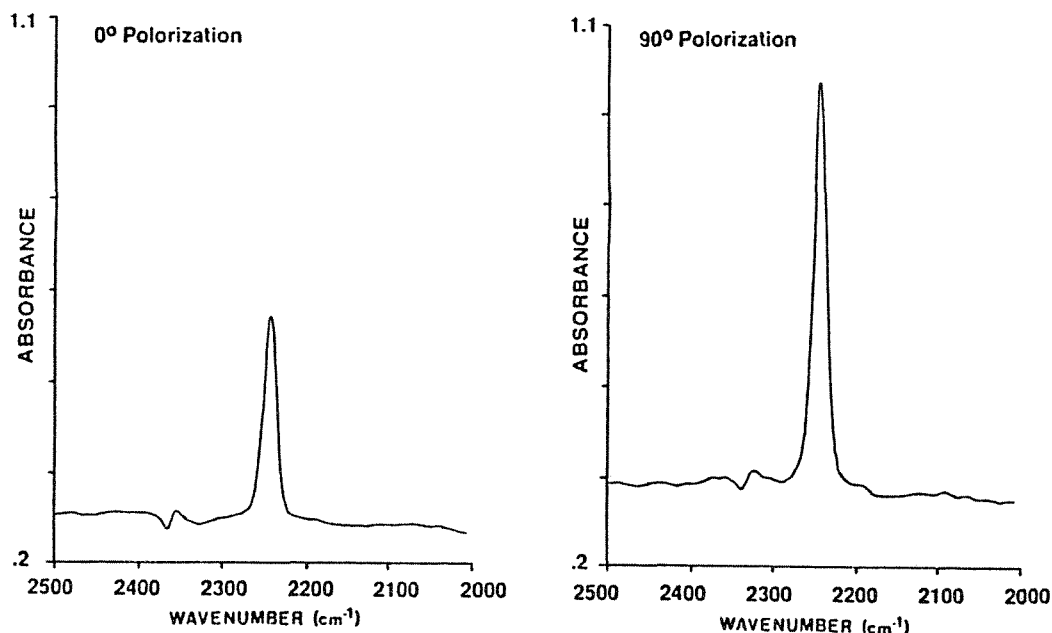


FIG. 2.--Linear dichroic spectra of nitrile groups in single acrylic fiber.

The linear dichroic IR transmission spectra were recorded on a small portion ($15 \times 200 \mu\text{m}$) of a single fiber with the use of dual remote image plane masks to define the measuring field. The polarizer was aligned both parallel to the fiber axis and perpendicular to it. Two spectra were necessary at each orientation of the polarizer: sample and background. Sample and background single-beam spectra were ratioed to obtain transmittance or absorbance values. Figure 2 shows the linear dichroic spectra of the nitrile group in a single acrylic fiber. In a uniaxially oriented fiber composed of low symmetry molecules, Fraser's analysis of dichroic spectra can be applied.⁹ In this analysis it is assumed that a nonoverlapping, purely polarized transition can be found. This is the case for the nitrile absorption band in the acrylic fiber. The dichroic ratio A is defined as the absorbance ratio of the bands measured parallel (0°) and the perpendicular (90°) to the fiber axis. Fraser assumed a model based on a two-component mixture. One fractional component (f) in this mixture has perfect uniaxial orientation; the second fraction ($1 - f$) has completely random orientation. If the angle between the transition moment of the vibration involved and the stretched polymer axis is α , then Fraser's formula is given by

$$R = \frac{A(0)}{A(90)} = \frac{f \cos^2 \alpha + (1 - f)/3}{\frac{1}{2}(f \sin^2 \alpha) + (1 - f)/3}$$

This expression can be reduced for the acrylic fiber because $\alpha = 90^\circ$ for the nitrile groups relative to the chain axis. For the acrylic fiber, the fraction of nitrile groups oriented 90° to the polymer chain is

$$f = \frac{1 - R}{1 - 0.5R}$$

The dichroic ratio $R = 0.50$ was determined from the linear dichroic spectra data shown in Fig. 2. For an $R = 0.50$, 40% of the nitrile groups are oriented 90° to the stretch direction of the fiber. The FT-IR microscope makes it practical to measure routinely the linear dichroic spectra of single fibers.

Oxidative Degradation of Polypropylene. In general use, most commercial polymers are exposed to the environment and to oxidative degradation. The polymer's resistance to this degradation is an important performance property. Much research has been done to develop antioxidants to retard this process and many tests are used to measure this degradation. IR spectroscopy has been used extensively to record the chemical changes that occur on the surface of a weathered polymer. The FT-IR microscope provides a new dimension to the study of the degradation process. By examination of cross sections of a weathered polymer, the FT-IR microscope can record an in-depth profile of the degradation process. A study of polypropylene illustrates this method.

A polypropylene container cap used in this study had been exposed outdoors for two years. There were visible signs of exposure, fading of the dye and surface cracking. A micrograph of a cross section of the polypropylene cap is shown in Fig. 3. Sections $30 \mu\text{m}$ thick were cut normal to the exposed surface. The IR sampling field was $20 \times 20 \mu\text{m}$, with the narrow dimension parallel to the exposed surface. Although smaller sampling areas could have been selected, this area provided the most reproducible results near the crazed surface. After comparing the spectra of the exposed surface with that from an unexposed interior portion, it was decided to use the ratio of the 1712cm^{-1} absorption to that of the 1163cm^{-1} band as a measure of the polymer's oxidative

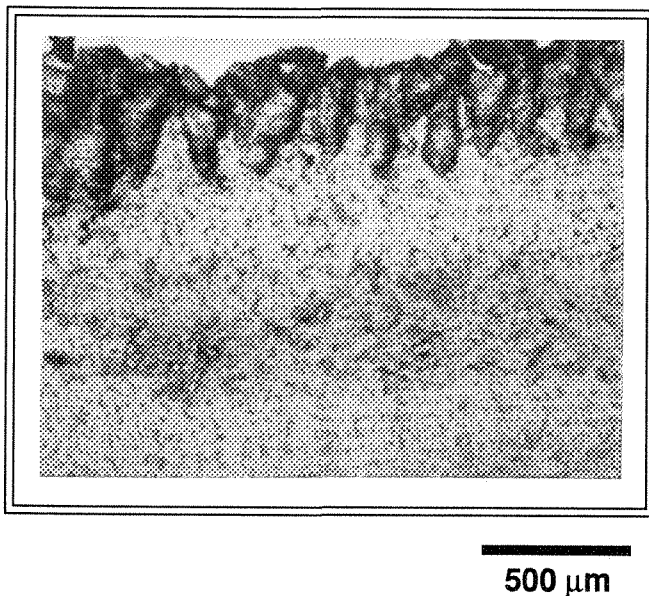


FIG. 3.--Micrograph of cross section of weathered polypropylene

degradation. A carbonyl absorption (1712 cm^{-1}) was found in the IR spectrum near the degraded surface, but this peak was not present in the unexposed polymer. Figure 4 is a plot of absorbance ratio as a function of distance from the exposed surface. The degradation of the polypropylene extends deep within this sample and is not limited to the polymer at the exposed surface. The oxidation follows an exponential decrease from the outer surface, which is expected either for a diffusion controlled process or photodegradation. This sample was used only to demonstrate the FT-IR microscopy technique. Since the formulation of this polypropylene container cap is unknown, no conclusions should be drawn from these data.

Discussion

The three examples of polymer IR microbeam analysis illustrate that combining the techniques of FT-IR spectroscopy and light microscopy presents an advance in technology for the polymer materials scientist. In material science the relationship between structure and properties is paramount. The ability to correlate molecular structure with microstructure is of major importance in the study of polymers. With the FT-IR microscope, simultaneous examination of these two structures is possible and is a practical reality.

References

1. D. E. Hemsley, *The Light Microscopy of Polymers*, London: Oxford University Press, 1984.
2. L. C. Sawyer and D. T. Grubb, *Polymer Microscopy*, London: Chapman and Hall, 1987.
3. N. H. Hartshorne and A. Stuart, *Crystals and the Polarizing Microscope*, London: Edward Arnold, 1970.
4. T. G. Rochow and E. G. Rochow, *Resinography*, New York: Plenum, 1976.

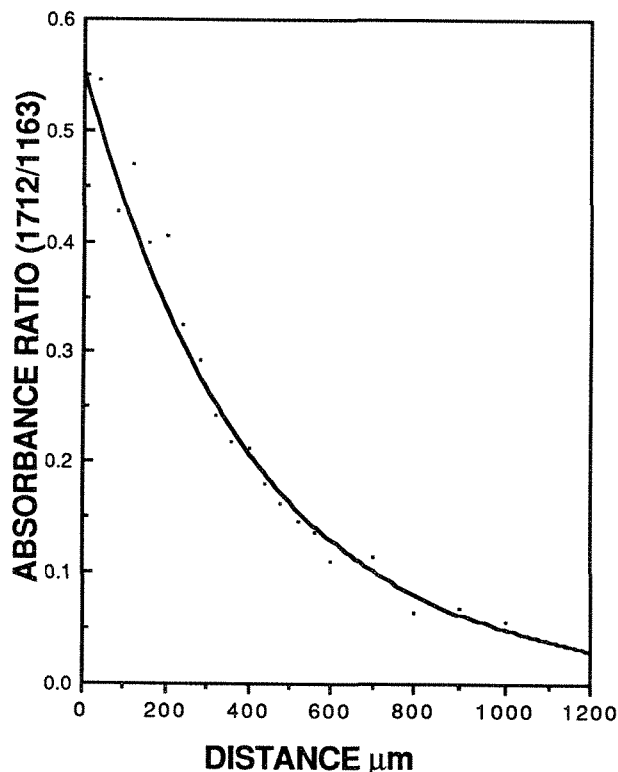


FIG. 4.--Plot of 1712/1163 absorbance ratio as a function of distance from exposed surface of weathered polypropylene.

5. J. L. Koenig, *Anal. Chem.* 95: 1141A, 1987.
6. I. M. Ward, *Structure and Properties of Orientated Polymers*, New York: Wiley, 1975.
7. A. E. Zachariades and R. S. Porter, *The Strength and Stiffness of Polymers*, New York: Marcel Dekker, 1983.
8. F. M. Mirabella, *J. Poly. Sci.* B25: 591, 1987.
9. R. D. B. Fraser, *J. Chem. Phys.* 21: 1511, 1953.

RAMAN CHARACTERIZATION OF STRAIN IN GaAs EPITAXIAL FILMS GROWN ON SAPPHIRE AND SILICON-ON-SAPPHIRE SUBSTRATES

T. P. Humphreys, J. B. Posthill, K. Das, C. A. Sukow,
N. R. Parikh, and R. J. Nemanich

The growth of heteroepitaxial GaAs films on semiconducting,¹ insulating,² and semiconductor-on-insulator³ substrates has been reported for the potential application of monolithic integration of electronic and optoelectronic devices. However, it has been demonstrated that the realization of high-quality GaAs device layers is inhibited by the presence of a high density of microstructural defects and a large residual tensile strain.¹ Indeed, it has been reported that the performance of GaAs lasers fabricated on Si substrates degrades very rapidly as a result of thermally-induced strain.⁴ Moreover, wafer bowing and the formation of microcracks in the GaAs epilayer have also been reported. Consequently, it is believed that a fundamental requirement for achieving high performance and reliable optoelectronic devices in heteroepitaxial GaAs is the growth of strain-free epitaxial layers. It is envisaged that by selection of a sapphire-based material system in which there is a close match with the thermal expansion coefficient of GaAs, high-quality strain-free epitaxial GaAs layers can be achieved.⁵

In the present study, the technique of Raman spectroscopy has been systematically employed to characterize the strain in GaAs epitaxial films that have been grown on (0001) and (10 $\bar{1}2$) sapphire (α -Al₂O₃) substrates. For integration with Si circuitry, heteroepitaxial GaAs has also been grown on commercially available chemical vapor deposited (CVD) silicon-on-sapphire (SOS) and SOS that has been upgraded by the double solid-phase epitaxy (DSPE) process.⁶ We report that the GaAs films deposited directly on sapphire exhibit no measurable strain, and the GaAs layers grown on SOS substrates display a residual tensile strain. The magnitude of the strain in the GaAs-on-SOS is substantially less than that observed in GaAs films deposited directly on Si(100) substrates.

T. P. Humphreys is at Bell-Northern Research Ltd., Ottawa, Ont., Canada K1Y 4H7; J. B. Posthill is at the Research Triangle Institute, Research Triangle Park, NC 27709-2194; K. Das is with the Department of Materials Science and Engineering, North Carolina State University, Raleigh, NC 27695-7907; N. R. Parikh is at the Department of Physics and Astronomy, University of North Carolina, Chapel Hill, NC 27599-3255; and C. A. Sukow and R. J. Nemanich are with the NCSU Department of Physics, Raleigh, NC 27695-8202. The authors are grateful to Dr. E. D. Richmond (Naval Research Laboratory) and to W. Dubbelday and Dr. R. E. Reedy (Naval Ocean Systems Center) for kindly providing the SOS substrate materials.

Experimental

The GaAs epitaxial layers were grown by molecular beam epitaxy (MBE), as described elsewhere.⁵ The Raman measurements were performed in a backscattering configuration with a 514.5nm Ar ion laser. The Raman spectra were obtained with 150 mW of laser power, and all measurements were made at room temperature. The position of the Raman peaks was measured with an accuracy of ± 0.2 cm⁻¹ and the line widths with a spectral resolution better than 0.2 cm⁻¹.

Results

Shown in Fig. 1 are the first-order Stokes-Raman spectra from the GaAs/ α -Al₂O₃ heterostructures. Both the longitudinal optical (LO) and transverse optical (TO) phonon modes were observed in the GaAs layers and are shown with a spectrum from homoepitaxial GaAs (100). The relatively large intensity of the TO phonon mode is consistent with (111) GaAs epitaxial growth.⁵ The corresponding Raman spectra from (100) GaAs epitaxial films grown on SOS are shown in Fig. 2. Although the TO mode is forbidden for scattering from a (100) GaAs surface, the observation and relative intensity of the TO mode is believed to be indicative of disorder-induced scattering. However, it is not clear at this time whether the magnitude of the TO peak is due solely to orientational disorder in the near-surface region (i.e., the presence of microtwins and dislocations), or whether the surface roughness can affect the Raman selection rules. The peak position of the LO mode can be related to the residual strain in the film. Indeed, the LO peak frequencies shown in Fig. 2 are less than the natural LO frequency of GaAs, which is indicative of tensile strain in the GaAs layers. The elastic strain in the films can be determined from the LO peak frequency shift from the expression $\Delta\omega/\omega_0 = -1.5S$, where $\Delta\omega$ is the shift in the LO peak from its natural frequency ω_0 , and S is the strain.⁷ It can be seen from the data presented in Table 1 that the GaAs/ α -Al₂O₃ heterostructures exhibit no measurable strain, whereas the GaAs/SOS composite structure has a residual tensile strain. Of interest is that the magnitude of the strain in the GaAs films grown on SOS substrates upgraded by the DSPE process is considerably less than that observed in the GaAs layers deposited on CVD SOS substrates.

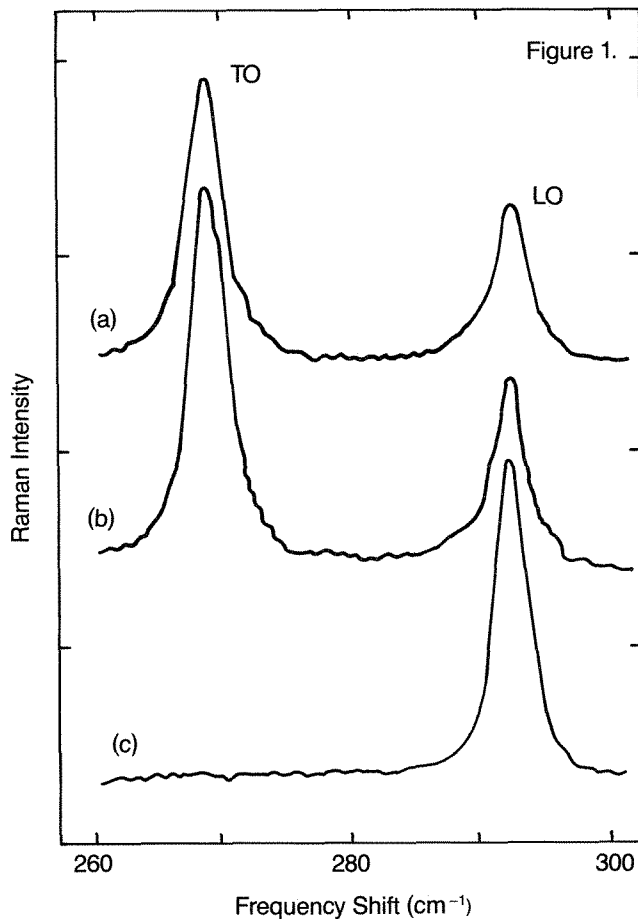


FIG. 1.--Raman scattering spectra comparing (a) GaAs/(0001) α -Al₂O₃, (b) GaAs/(10 $\bar{1}$ 2) α -Al₂O₃, (c) homoepitaxial GaAs (100).

TABLE 1.--Summary of Raman scattering results from GaAs heteroepitaxial films.

Substrate	LO Phonon Peak Frequency (cm ⁻¹)	LO Phonon Peak Shift (cm ⁻¹)	LO Phonon FWHM (cm ⁻¹)	Elastic Strain [Tensile] x10 ⁻³
CVD-SOS	291.4	-0.5	3.2	1.1
DSPE-SOS	291.7	-0.2	3.3	0.5
(10 $\bar{1}$ 2) α -Al ₂ O ₃	291.9	0.0	3.0	0.0
(0001) α -Al ₂ O ₃	291.9	0.0	2.7	0.0
Si(100)	291.0	-0.9	3.3	2.1

Conclusions

The Raman measurements presented in this paper demonstrate that the heteroepitaxial GaAs films grown directly on sapphire substrates are strain free. In comparison, the GaAs/SOS heterostructures exhibit a residual tensile strain. However, the magnitude of the strain is substantially less than that observed in GaAs films grown directly on Si(100) substrates. Clearly, the use of sapphire-based substrates, which have a more closely matched coefficient of thermal expansion with

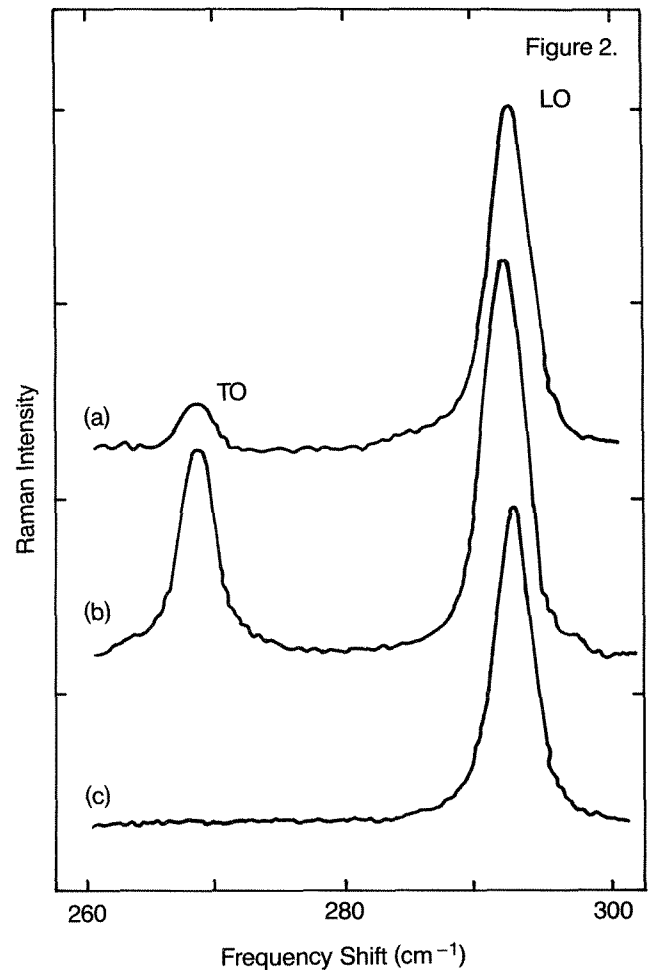


FIG. 2.--Raman spectra from GaAs grown on: (a) DSPE-SOS, (b) CVD-SOS, (c) GaAs (100) substrates.

GaAs than does Si, results in an elastic strain decrease in the grown GaAs films.

References

1. T. P. Humphreys, K. Das, J. B. Posthill, J. C. L. Tarn, B. L. Jaing, J. J. Wortman, and N. R. Parikh, *Jpn. J. Appl. Phys.* 27: 1458, 1988.
2. H. Manasevit, *Appl. Phys. Lett.* 12: 156, 1968.
3. K. Das, T. P. Humphreys, J. B. Posthill, J. C. L. Tarn, J. J. Wortman, and N. R. Parikh, *J. Appl. Phys.* 64: 3934, 1988.
4. J. P. van der Ziel, R. D. Dupuis, R. A. Logan, and C. J. Pinzone, *Appl. Phys. Lett.* 51: 89, 1987.
5. T. P. Humphreys, N. R. Parikh, K. Das, J. B. Posthill, R. J. Nemanich, M. K. Summer-ville, C. A. Sukow, and C. J. Miner, *Mater. Res. Soc. Symp. Proc.* (in press).
6. R. E. Reedy and G. A. Garcia, *Mater. Res. Soc. Symp. Proc.* 107: 365, 1988.
7. H. Shen and F. H. Pollak, *Appl. Phys. Lett.* 45: 692, 1984.

RAMAN MICROPROBE OBSERVATIONS OF CARBON AND OXYGEN STABLE ISOTOPES IN GEOLOGIC MATERIALS

R. C. Burruss, Tom Ging, and Dennis Carlson

Variations in the ratios of the stable isotopes of carbon and oxygen in geologic materials provide important information on the origin and history of terrestrial materials.¹ Stable isotope ratios are routinely measured by gas-source ratio-mass spectrometry (RMS) after conversion of the carbon and oxygen of the sample to CO₂ gas. Sample preparation and conversion to gas is time consuming and routine measurements require hundreds of micromoles of CO₂. Some of the first papers describing the application of the laser Raman microprobe (LRM) to geologic materials mentioned the possibility of observing the Raman bands of stable isotopes, in particular the ¹³C band in liquid CO₂ fluid inclusions.^{2,3} If stable isotope ratios can be measured by LRM with an accuracy and precision that is geologically useful, i.e., ±1 ppt, then not only is sample preparation simplified, but more important, isotopic measurements on zoned minerals are possible with micrometer spatial resolution, fluids in individual fluid inclusions can be studied, and the minimum sample size approaches the focal volume of a high-magnification, high-aperture microscope objective, i.e., about 10⁻¹² cm³.

The first LRM observation of ¹³C/¹²C ratios in liquid CO₂ fluid inclusions stated precisions ranging from ±10 to ±37 ppt,^{2,3} significantly lower than the routine precision of RMS of less than ±1 ppt. The difficulty of applying LRM to stable isotope measurements is best illustrated by considering that the natural abundance of ¹³C is 1.11% and ¹⁸O is 0.204%. Variations in the ratio of the rare to abundant isotope in an unknown R_{unk} are measured in ppt relative to the ratio in a standard R_{std} calculated as follows:

$$[(R_{\text{unk}} - R_{\text{std}})/R_{\text{std}}] \times 1000 = \delta \text{ (ppt)}$$

Therefore, variations in the δ value of 1 ppt in ¹³C or ¹⁸O are in fact variations in the absolute abundance of 1 part in 10⁵ and 2 parts in 10⁶ in ¹³C/¹²C and ¹⁸O/¹⁶O, respectively. Achieving this level of precision in Raman spectroscopy is difficult. Most discussions of quantitative Raman spectroscopy state that detection limits are of the order of 1:100 to 1:1000, with precisions of about 1% relative.^{4,5}

The recent evolution of LRM technology

R. C. Burruss and T. Ging are with the U.S. Geological Survey, Denver, CO 80225. D. Carlson is with EG&G, Princeton Applied Research, Evergreen, CO 80439. The authors gratefully acknowledge the loan of an OMA III system by EG&G.

toward high-efficiency coupling of microscope to monochromator and the improved signal-to-noise (S/N) ratio possible with multichannel detectors suggest that it may be feasible to measure geologically meaningful (± 1ppt) stable isotope ratios via LRM. To investigate this possibility we made measurements on three types of samples: (1) one synthetic CO₂-rich fluid inclusion in Brazilian quartz,⁶ (2) one natural CO₂-rich fluid inclusion in quartz from a gold-bearing vein system in S. E. Alaska,⁷ and (3) five samples of RMS analyzed calcite from different localities. The inclusion samples were used to evaluate the possibility of simultaneous observation of both ¹³C and ¹⁸O. The strongly scattering ν_1 mode of CO₃²⁻ in calcite was used to test whether the LRM measurement can be "calibrated" with RMS measurements.

Instrumentation

All measurements were made with an Instruments SA Ramanor U-1000, 1 m double monochromator system equipped with 1800-groove/mm holographic gratings and an Olympus microscope with an Olympus MSPLAN 50× (0.8 NA) objective lens. Scattered radiation was detected with either a single-channel, photon-counting system (RCA 31034A PMT at -20 C, Pacific Instruments amplifier-discriminator, ISA Spectralink, and IBM-AT computer running ISA PRISM software), or a cooled, 700-channel intensified diode-array detector (Princeton Applied Research Corp., Model 1455 detector at -35 C and OMA III computer system). For single-channel measurements all slits were set at 200 μm to give spectral resolution of 1.8 cm⁻¹. During multichannel measurements the entrance slit remained at 200 μm and the intermediate slits were opened to 25 mm. Spectra were measured relative to the 514.532nm line of a Spectra-Physics Model 2025-5 argon ion laser regulated in the power mode. Two Pellin-Broca prisms and a spatial filter removed plasma lines. The laser power at the entrance to the microscope was 100 mW.

Data were collected with long integration times to yield high S/N. For single-channel measurements the step size was 0.2 cm⁻¹, integration time was 30 s/pt, and the spectrum was scanned 30 times and averaged. The OMA III data system was equipped with a 14-bit A/D converter, so that exposure times were set to yield about 15 500 counts on the abundant isotope peak and 1000 exposures were summed. Peak ratios were calculated as the ratio of peak heights after subtracting background. (NOTE: Manufacturer's names are for information only and do not constitute endorsement by the U.S. Geological Survey.)

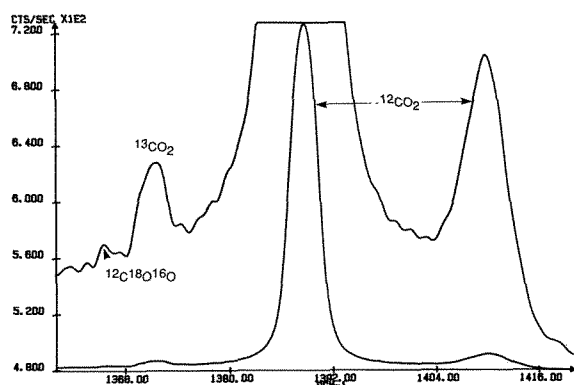


FIG. 1.--Full-scale and expanded and smoothed plot of $2\nu_2$ of Fermi diad of CO_2 in liquid CO_2 fluid inclusion (20 μm largest dimension) in quartz from an Au-bearing vein. Single-channel data.

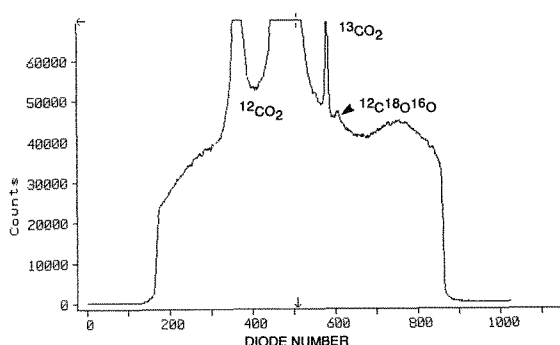


FIG. 2.--Spectrum of same features as in Fig. 1 for different fluid inclusion. OMA III array detector data. X-axis is in diode number with dispersion of about $0.2 \text{ cm}^{-1}/\text{diode}$. Increasing wavenumber to the left (opposite of Fig. 1). Data collection time 1 h 40 min. compared to 15 h for Fig. 1.

TABLE 1.--Comparison of single-channel analyses of $^{13}\text{C}/^{18}\text{C}$ in one CO_2 -rich fluid inclusion. Single standard deviation σ (in ppt) is much larger than predicted from counting statistics.

run #	Total Counts ^{13}C	Total Counts ^{12}C	$^{13}\text{C}/^{12}\text{C}$
syn1_2	31929.6	2386952.4	0.013377
syn1_3	20938.5	1539565.2	0.013600
syn1_4	19864.2	1493828.7	0.013298
syn1_6	16771.2	1185255.9	0.014150
		mean	0.013606
		σ	0.000333
		σ , ppt	24.47

Results and Discussion

A typical spectrum of the $2\nu_2$ peak of CO_2 in a CO_2 liquid inclusion (room temperature) is shown in Fig. 1. The $^{13}\text{CO}_2$ peak is resolved from the $^{12}\text{CO}_2$ peak and a weak signal appears at 1365 cm^{-1} , the reported position of the $^{12}\text{C}^{18}\text{O}^{16}\text{O}$ peak.⁸ The spectrum in Fig. 2, from

different inclusion, shows the improved S/N possible with a multichannel detector and clearly shows the presence of the $^{12}\text{C}^{18}\text{O}^{16}\text{O}$ peak.

The precision of LRM measurements of $^{13}\text{C}/^{12}\text{C}$ in a single CO_2 fluid inclusion was evaluated from four sets of observations, with each set requiring about 15 h to accumulate $1-2 \times 10^6$ counts on the $^{12}\text{CO}_2$ peak. The results are summarized in Table 1. A single standard deviation of the mean, recalculated in ppt, is 24 ppt, within the range of previously published values. However, this value is considerably larger than the 9ppt variation predicted from counting statistics alone. This finding suggests that other sources of noise are affecting the results. One obvious source of noise is amplitude fluctuations in the laser. In the power-regulation mode, fluctuations in amplitude should be no more than 0.1% rms, even that will cause variations in the peak ratio of about 10 ppt. These variations are too large for geologically useful measurements.

Noise from laser fluctuations can be limited by use of a multichannel detector. The isotope bands occur within the 140 cm^{-1} range of a 700-channel detector, which eliminates the need to step the monochromator and allows all the isotope bands to be recorded simultaneously. Any variations in laser intensity are eliminated by integration over the exposure time of the detector.

We made several sets of measurements with a multichannel detector on five samples of calcite that have different isotopic compositions previously determined by RMS. Calcite was chosen for several reasons. First, the ν_1 mode of CO_3^{2-} causes intense Raman scatter, decreasing the time necessary to collect large data sets; second, isotopic ratios measured by RMS are readily available; and third, many natural calcites are chemically and isotopically zoned. Therefore, if we can demonstrate accurate measurements of stable isotope ratios in calcite by LRM, we shall have an ideal case for testing the feasibility of spatially resolved isotope measurements. One important consequence of measuring the symmetric stretching ν_1 mode of CO_3^{2-} is that the only isotopic band allowed by the symmetry of the CO_3^{2-} ion in the calcite lattice is due to substitution of ^{18}O . Symmetric stretching of the C-O bonds does not involve displacement of the carbon atom at the center of mass of the ion; therefore isotopic substitution of the C atom does not cause a shift in energy of the ν_1 mode.⁹

The data are summarized in Table 2 and displayed in Fig. 3. Two results are obvious. First, three of the five samples have standard deviations similar to that predicted by counting statistics; the other two samples showed much larger variations. Second, although there appears to be a rough correlation between the measurements by LRM and RMS, the scatter in the points shows that significant factors are affecting the LRM measurements, which must be understood before we can "calibrate" the LRM measurements by RMS. One

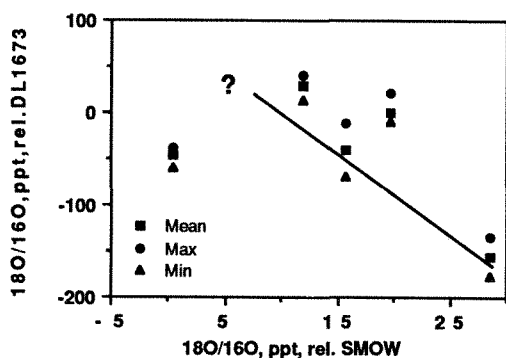


FIG. 3.-- $^{18}\text{O}/^{16}\text{O}$ ratio in ppt (relative to sample DL 1673) in five samples of calcite based on LRM measurements vs ratio measured by gas source, RMS, relative to MSOW (Standard Mean Ocean Water). Line is to guide the eye and suggests correlation between various types of measurements. An important source of variation may be fluorescence. (See also Fig. 4.)

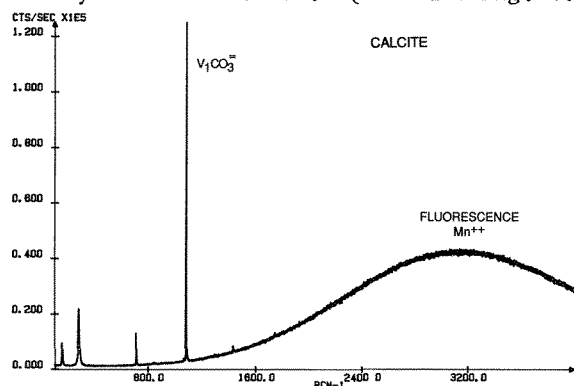


FIG. 4.--Raman and fluorescence spectrum of calcite sample DL 1674. Broad emission band at about 3200 cm^{-1} (615 nm) is due to Mn^{2+} in calcite lattice.

TABLE 2.--Comparison of RMS measured $^{18}\text{O}/^{16}\text{O}$ relative to SMOW (Standard Mean Ocean Water) with peak height ratio measured by Raman microprobe for five samples of calcite. In three samples the observed σ is comparable to theoretical σ from counting statistics.

Sample	$^{18}\text{O}/^{16}\text{O}$ RMS, ppt, rel. SMOW	Raman, $^{18}\text{O}/^{16}\text{O}$	σ , ppt	Theor σ , ppt	Raman, ppt, rel DL1673
DL 1673	19.6	0.00457088	7	<7	0
FR3-20-1	15.7	0.00438528	20	<7	-41
Harding Peg	11.9	0.00470547	9	<7	29
NBS-19	28.5	0.00385686	18	<7	-156
PACM-6-5	0.4	0.00435808	7	<7	-47

factor is obvious in the Raman spectrum of sample DL1673 shown in Fig. 4. The broad fluorescence emission at about 3200 cm^{-1} (615 nm) is due to trace amounts of Mn^{2+} in the calcite lattice.^{10,11} This emission contributes a significant background to the Raman isotope bands at 1060 to 1087 cm^{-1} . The intensity of the fluorescence background varies from sample to sample and it is not clear whether this variation is due to different amounts of Mn^{2+} or whether other trace metals or organic components are

activating the fluorescence.¹¹ In any case, spectroscopic techniques such as time-resolved Raman spectroscopy that can separate Raman bands from fluorescence emission will be necessary before LRM methods can be routinely applied to stable isotope measurements in geologic samples.

Conclusions

Measurement of meaningful stable isotope ratios in geologic materials by LRM is difficult but feasible. The basic limitations are counting statistics and background fluorescence. Multichannel detectors can solve some problems due to laser noise and improve counting statistics. However, eliminating background fluorescence is a more difficult problem that will require time-resolved Raman spectroscopic techniques.

References

1. K. T. Kyser, Ed., *Stable Isotope Geochemistry of Low Temperature Fluids*, Short Course Handbook 13, Toronto: The Mineralogical Association of Canada, 1987.
2. G. J. Rosasco et al., "Laser-excited Raman spectroscopy for nondestructive partial analysis of individual phases in fluid inclusions in minerals," *Science* 190: 557-560, 1975.
3. P. Dhamelincourt et al., "Analyse d'inclusions fluides à microsonde MOLE à effet Raman," *Bull. Min.* 102: 600-610.
4. T. Hirschfeld, "Microspectroscopy," *Microbeam Analysis--1982*, 247.
5. J. D. Pasteris et al., "Practical aspects of quantitative laser Raman microprobe spectroscopy for the study of fluid inclusions," *Geochim. Cosmochim. Acta* 52: 979-988, 1988.
6. S. M. Sterner and R. J. Bodnar, "Synthetic fluid inclusions in natural quartz: I. Compositional types synthesized and applications to experimental geochemistry," *Geochim. Cosmochim. Acta* 48: 2659-2688, 1984.
7. R. J. Goldfarb et al., "The Juneau gold belt: A mother-lode type system in southeastern Alaska," *GSA Cordilleran Section* (Abs. with Prog.) 19: 382, 1988.
8. H. Finsterholzl, "Raman spectra of carbon dioxide and its isotopic variants in the Fermi resonance region: Part III. Analysis of rovibrational intensities for $^{12}\text{C}^{16}\text{O}_2$, $^{13}\text{C}^{16}\text{O}_2$, $^{12}\text{C}^{18}\text{O}_2$ and $^{12}\text{C}^{16}\text{O}^{18}\text{O}$," *Ber. Bunsenges. Phys. Chem.* 86: 797-805, 1982.
9. R. K. Sato and P. F. McMillan, "An infrared and Raman study of the isotopic species of α -quartz," *J. Phys. Chem.* 91: 3494-3498, 1987.
10. W. L. Medlin, "The nature of traps and emission centers in thermoluminescent rock materials," in D. J. M-Dougall, Ed., *Thermoluminescence of Geological Materials*, New York: Academic Press, 1968, 193.
11. V. A. Pedone et al., "Identification of inorganic and organic activators of photoluminescence in calcite by high resolution, laser microprobe spectroscopy," *AAPG Bull.* (in press).

INTERNAL AND SURFACE MEASUREMENTS WITH THE CONFOCAL SCANNING LASER MICROSCOPE

John C. Russ

The confocal scanning laser microscope (CLSM) is useful for viewing rough and irregular surfaces as well as imaging very shallow planes of focus within transparent or translucent matrices to perform optical sectioning of three-dimensional structure. In the latter application, the light passes through the sample (usually twice in a true confocal instrument). It is also possible to use the incident light to excite selectively fluorescent dyes used to stain structures, and recover the emitted light from shallow planes of focus. All these techniques take advantage of the very shallow depth of field of the confocal imaging technique. A point source of light is focused on (or in) the specimen, and the returned light (perhaps after passing through the specimen and being reflected back) would ideally return to the point of origin. In some instruments such as the acoustic microscope, which is also confocal, that is exactly what happens (the transducer that produces the signal is also the detector). In the light microscope, a beam splitter is used to divert the returned light to a separate detector, but from an optical point of view it still lies at a point confocal with the source.

In this configuration light scattered from another point in the sample displaced either laterally or in depth from the focus point is not returned to the detector, and contributes very little brightness to the image, which makes for extremely high contrast and shallow depth of field. With objective lenses of suitably high numerical aperture, the depth of field can be less than $0.25\ \mu\text{m}$. Even more important, the background brightness due to scattered light from other parts of the sample is absent, which allows imaging without loss of contrast or resolution to the scattering and permits imaging within matrices that are translucent, provided that the light source is monochromatic (e.g., a laser), so that variation in the refractive index of the sample with wavelength does not cause blurring or color fringing.

As in all scanned image microscopy, the signal is returned from only one point at a time, and raster scanning is used to build up an entire image. In many systems, the tradeoff between the use of white light and laser light to achieve sharp optical sectioning is accompanied by a slower image acquisition speed so that real-time processes cannot be monitored. In the particular instrument we are using (Laser-tec 1LM11) this restriction has been bypassed: video rate imaging with monochrome 682nm (red)

light is provided, and we have been able to videotape real-time dynamic processes. The images can also be captured in real time by an image analysis system (Dapple Prism) which can process and measure them.

One mode of operation is to focus on internal structure in matrices that are transparent. Figure 1 shows a single frame from a videotape of such an image, in which a paramecium swimming in a drop of pond water is captured as it passes through the focal plane. Only one plane of information through the paramecium is revealed, as well as individual cilia along its periphery.

In a less transparent matrix, images can also be obtained and measured. Pores in highly dense alumina are difficult to characterize because they are small ($<1\ \mu\text{m}$) and generally located at grain junctions such as quadruple points, due to the sintering process. They are important in determining the transparency of the material due to the scattering of light, and also influence mechanical properties. The conventional metallographic light microscope does not show the pores well because of the low probability of intersecting them with a plane of polish. Transmission light imaging is not used because resolution degrades quickly with thickness, and transmission electron microscopy cannot image sections thick enough to contain entire pores.

With the CSLM we were able to image pores at depths in excess of $100\ \mu\text{m}$ in translucent alumina, with an effective depth of field of much less than the nominal $0.2\ \mu\text{m}$ resolution of the optics, because of the high contrast which they produce. Figure 2 shows the same area in depth and collecting a series of images, the complete pore distribution was quantitatively determined. The X,Y location of each pore in the images, and the Z coordinate from the stage drive, were written into a disk file for analysis to determine the pore density N_V without bias or assumptions about pore or grain shape.² Figure 3 is the histogram of the nearest neighbor distance between pores, showing a strong tendency for clustering at small spacings due to the sintering and densification process.

Surface relief can also be measured, since only the in-focus points of an irregular surface are seen at any single focusing distance (z-coordinate). This amounts to an iso-elevation contour of the surface. Recording of several such contours permits direct measurement of surface relief. By scanning the z-coordinate (the focusing knob on the microscope stage) and recording the value at which the maximum (in-focus) signal is detected from each point along a line, a direct measurement

The author is at the Materials Science and Engineering Department, North Carolina State University, Raleigh, NC 27695.



FIG. 1.--Transmission CSLM image (one frame from videotape) showing in real time swimming paramecium passing through plane of focus, revealing internal structure and external cilia.

of surface elevation profile is obtained (Fig. 4). This profile consists of 1000 individual points measured along a scan line across the sample. The vertical resolution is easily able to show steps in metallization and other structures in integrated circuits of $0.1\ \mu\text{m}$ or less, as well as providing lateral resolution of about $0.25\ \mu\text{m}$. This technique for noncontacting profilometry has found application in IC metrology and is also useful for a variety of other similar problems in materials science, such as measuring the depth of pits produced during erosion or machining operations which are often too small and too deep for contacting profilometers.

By use of the microscope's RS-232 serial connection for control and data readout, extension of this method to produce contour maps of entire surfaces is a straightforward application of computer storage and graphics techniques. Depth imaging of surfaces can also be performed with the same computer image presentation as used for serial section reconstruction.³ Figure 5 shows a reconstructed contour presentation from sequential images that were collected and processed to locate edges. The specimen is a loose conglomerate of particles.

Using the same principle, namely that the brightest signal of light reflected from the specimen at each location corresponds to the in-focus point, one can also directly accumulate an image with sharp focus over a depth of field limited only by the working distance of the objective lens. For surfaces that are not man-made, the variation in orientation is more gradual and random. Figure 6 shows an example, the bottom of a leaf containing stomata. For comparison another area of the same leaf is shown as it appears in the scanning electron microscope (SEM). Of course, the CSLM does not require any preparation of the sample such as a conductive coating, or exposure to vacuum. The video-rate imaging also permits study of the surface during real-time experiments, such as observation of the reaction of the leaf surface to exposure to saline solution.

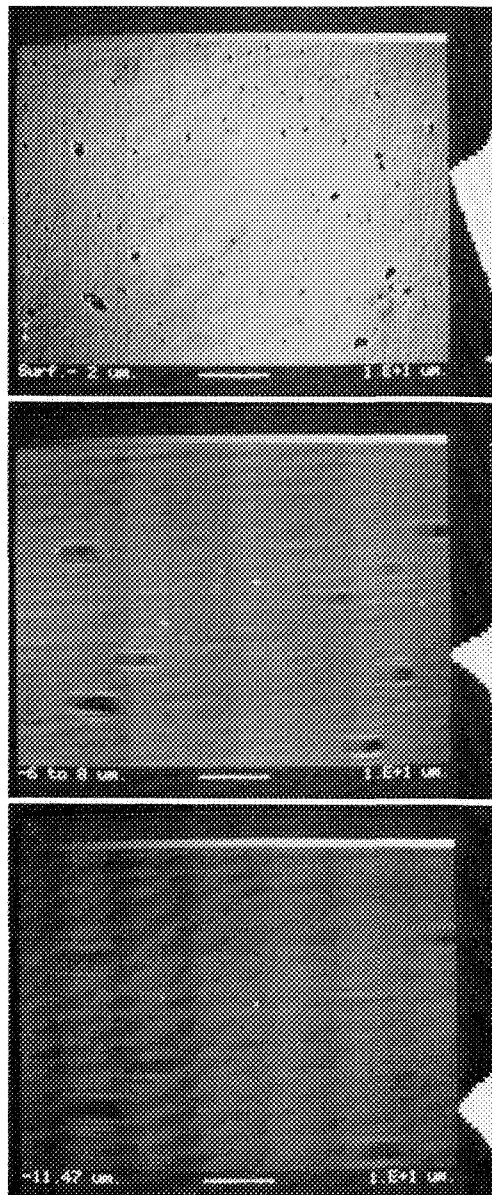


FIG. 2.--Reflection CSLM images of same area of alumina sample, at focus depths near surface, at 6 to 8, and more than $11\ \mu\text{m}$ below surface. Bright spots are areoles. Material is highly translucent alumina processed to high density ($D \approx 0.9995$) with a very fine ($\sim 1.5\ \mu\text{m}$) and uniform grain diameter.

The shading contrast in the CSLM image is different from that in the SEM. The effective light source is in the same position as the viewer's eye, rather than being a variable diffuse light source as in the SEM image. Hence, these images are readily measured by the principles of shape-from-shading⁴ and texture-from-shading.⁵ One consequence of this is the ability to measure local surface roughness. We have previously shown⁶ that the measurement of image texture (defined in terms of the variation of pixel brightness as a function of distance) can be applied to SEM images, and

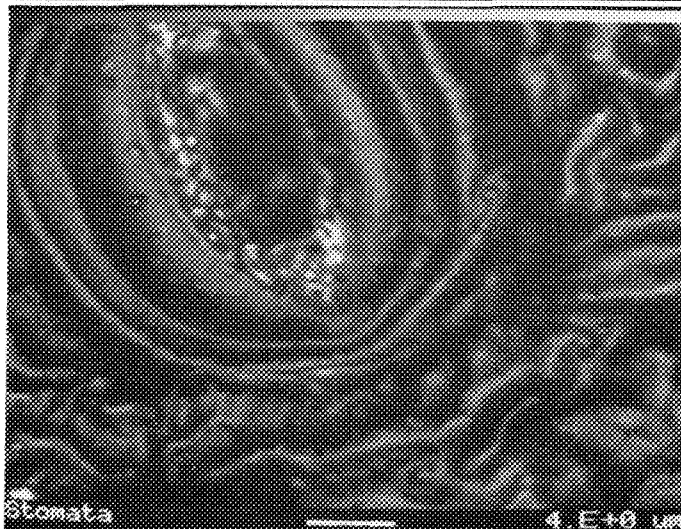
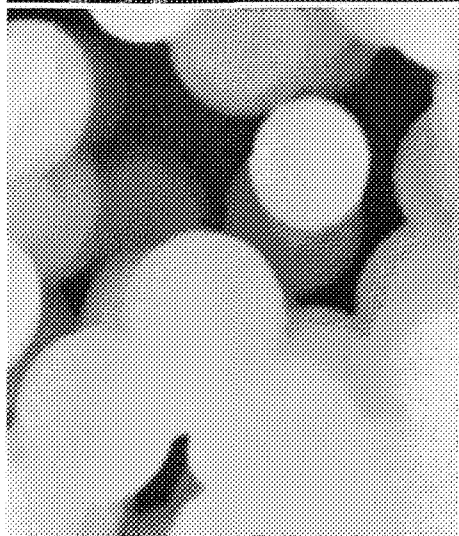
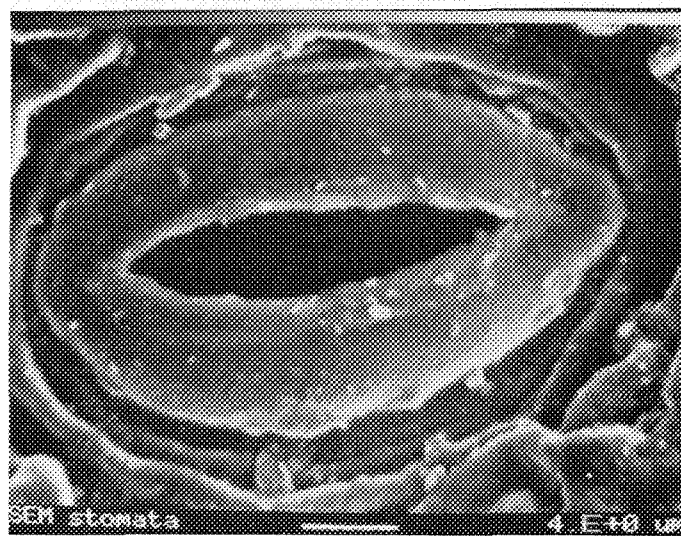
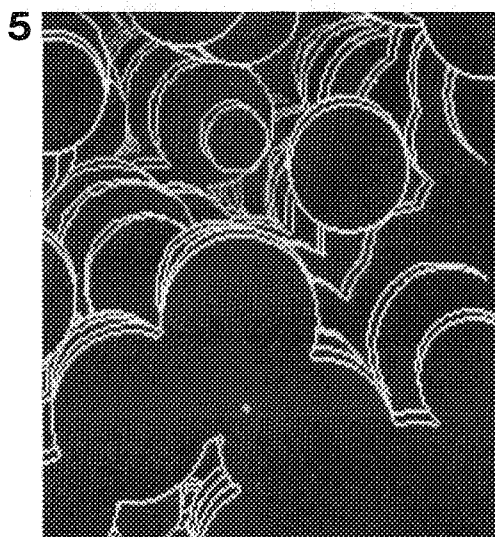
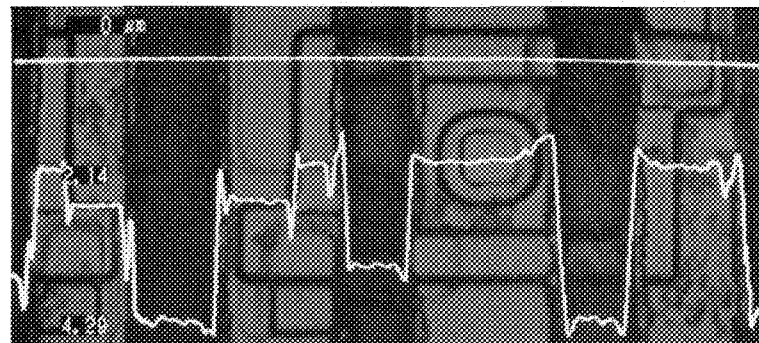
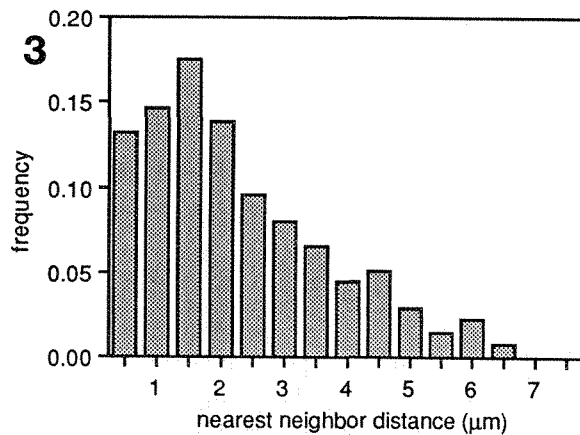
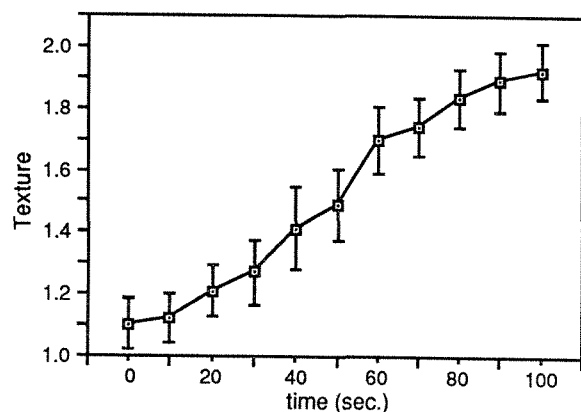


FIG. 3.--Frequency plot for 3-D distance to nearest neighbor for pores in Fig. 2.
 FIG. 4.--Reflection CSLM image of surface of a microelectronic device, with superimposed elevation profile along position indicated by solid line.
 FIG. 5.--Computer-generated view of contours from CSLM images of particles in conglomerate.
 FIG. 6.--SEM (top) and reflection CSLM (bottom) images of bottom surface of leaf, showing stomata.



10. P. Corcuff et al., "Skin relief and aging," *J. Soc. Cosmet. Chem.* 34: 177, 1983.

FIG. 7. Measured image texture (with 2σ variation from 20 region measurements) as a function of time.

Pentland has shown⁷ that it works for macroscopic surfaces under various lighting conditions. Such studies with the SEM and visible light have been used to measure wear of surface,⁸ roughness of metal fractures,⁹ and wrinkling of human skin with aging.¹⁰ As an example of this technique with the CSLM, we collected images of the surface of plant tissue over a period of several minutes while it was exposed to a saline solution. The increase in surface roughness (Fig. 7) is a quantitative measure of surface wrinkling.

From these examples, it is evident that the various imaging modes in the CSLM can be used to show and to measure internal structure and surface relief in a variety of ways. The images are familiar to the eye and permit easy visual interpretation. Coupling of the microscope to an image analysis system allows measurements which can be used for surface and internal metrology and stereology.

References

1. J. C. Russ et al., "Direct 3-D pore measurement in alumina, *Journal Microscopy* (submitted).
2. J. C. Russ, *Practical Stereology*, New York: Plenum Press, 1986.
3. J. C. Russ, *Computer Assisted Microscopy*, Raleigh, N.C.: NCSU Extension Service, 1988.
4. K. Ikeuchi and B. K. P. Horn, "Numerical shape from shading and occluding boundaries," *Artificial Intelligence* 15: 141-184, 1981.
5. A. P. Pentland, Ed., *From Pixels to Predicates*, Norwood, N.J.: Ablex Publ., 1986.
6. J. C. Russ and J. C. Russ, "Feature-specific measurement of surface roughness in SEM images," *Particle Characterization*, 1987.
7. A. P. Pentland, "Fractal-based description of natural scenes," *IEEE Trans. PAMI*-6: 661, 1983.
8. J. C. Russ et al., "SEM low magnification stereoscopic technique for mapping surface contours," *J. Microscopy* 144: 329, 1986.
9. V. B. Haywood et al., "Quantitative analyses of the surface roughness of etched dental alloy: Relationship to bond strength," *J. Dent. Res.* (in press).

New or Emerging Microprobes

ULTRATRACE ELEMENT MICROCHARACTERIZATION OF SURFACES AND SOLIDS WITH SIRIS

H. F. Arlinghaus, Norbert Thonnard, and H. W. Schmitt

Sputter-initiated resonance ionization spectroscopy (SIRIS) is a new and unique technique for the microcharacterization of surfaces and solids.¹ SIRIS combines the resolution and surface analysis capabilities of sputtering with the highly efficient, element specific and general resonance ionization spectroscopy (RIS) technique. RIS, which is practical for most elements of the periodic table, is used to ionize the abundant neutral atoms released by the sputtering process, thereby increasing quantitation and sensitivity. Through precise tuning of wavelength, only atoms of a selected element are excited, ionized, and counted in a magnetic sector or time-of-flight mass (TOF) analyzer, thereby eliminating isobaric and other interferences. Recent measurements indicated a total detection efficiency of 20%, resulting in sub-ppb detection limits with RIS. This high efficiency reduces the required sample size and lowers detection limits by orders of magnitude with respect to other techniques. For ion-induced imaging, spatial resolution of 5 μm is possible in the present configuration. The SIRIS technique is being evaluated for application in research fields as varied as semiconductors and optical materials, biomedical and environmental sciences, and geochemistry and cosmochemistry.

Experimental

Resonance ionization spectroscopy is a new laser-based technique for ultratrace element analysis. The concept of RIS was introduced by G. S. Hurst and co-workers^{2,3} at Oak Ridge National Laboratory. They used RIS to detect a single cesium atom in a background of 10^{19} argon atoms and 10^{18} CH_4 molecules.⁴ Subsequently the RIS concept was generalized and shown to be potentially feasible with present-day laser techniques for all elements of the periodic table except He and Ne.⁵

In RIS, tunable lasers are used sequentially to excite and then ionize neutral atoms of the element selected for analysis. The spectrum of particular excited states for RIS analysis permits great selectivity (i.e., lack of interferences). In Fig. 1, in scheme (a) a single laser beam is tuned to the wavelength that excites the atom to a resonance labeled First Excited State; another photon of the same wavelength further excites the atom to ionization. In scheme (b) three colors are used: the second color excites the atom from the first to a Second Excited State, and the third color excites the atom to ionization. Scheme (c) again uses

a single wavelength, but excitation to the Two-photon Allowed State requires the incidence of two photons, then ionization by a third photon of the same wavelength, thereby also allowing ionization of elements having high ionization potentials. To demonstrate this ultrahigh-element specificity of the RIS process, we irradiated a silicon sample containing 58 ppm Ga with an atomizing laser (instead of ion sputtering) and detected the resonantly ionized Ga atoms in a TOF mass spectrometer without secondary-ion suppression. Figure 2 shows the TOF spectrum for both the RIS laser tuned to gallium (upper plot) and detuned by 0.07 nm (lower plot). Most of the signal in the lower plot is due to the laser atomization process, but, assuming that all of the signal in the mass 28 channel was due to nonresonant photoionization, the upper limit to the nonresonant ionization signal is $<2 \times 10^{-9}$ as compared to the resonant signal. Since the isotope shifts of most elements are small in comparison with the bandwidth of the RIS lasers used in these measurements, all isotopes of a chosen element are ionized with essentially equal sensitivity and then separated with the mass spectrometer. The requirements for the mass spectrometer are reduced to resolving neighboring isotopes, because the high specificity virtually eliminates interferences from molecular ions, isobars, or scattered ions from the major constituents of the sample.

In addition to the high selectivity of RIS, the process is extremely sensitive. The intensity of modern pulsed dye lasers is sufficient to saturate both the bound-bound transitions and the ionization step, thereby assuring unit probability of ionizing all atoms of the selected element that are in the ionizing laser beam. Figure 3 shows the correlation of the indium concentration in silicon samples with the indium SIRIS signal. These measurements were obtained with a 0.7 μA sputtering ion beam current (500ns pulse width) for 5000 laser shots (less than 3 min). The 2σ detection limit (5 counts) is at 300 ppt and the background at 60 ppt. It was found that the background is caused by neutral particles in the primary ion beam, which cannot be deflected; they hit the target while the RIS laser is on and produce secondary ions that cannot be suppressed. (Suppression of secondary ions produced by the sputtering process is achieved by a combination of relative timing between ion sputtering and RIS, timed extraction voltage switching, and electrostatic energy analysis.)

Since the sputtering yield and the number of primary ions per pulse is known, and assuming an ionization efficiency of 100% in the overlap of the sputtered atom cloud and RIS laser beams,

The authors are at Atom Sciences, Inc., 114 Ridgeway Center, Oak Ridge, TN 37830.

Resonance Ionization of Neutral Atoms

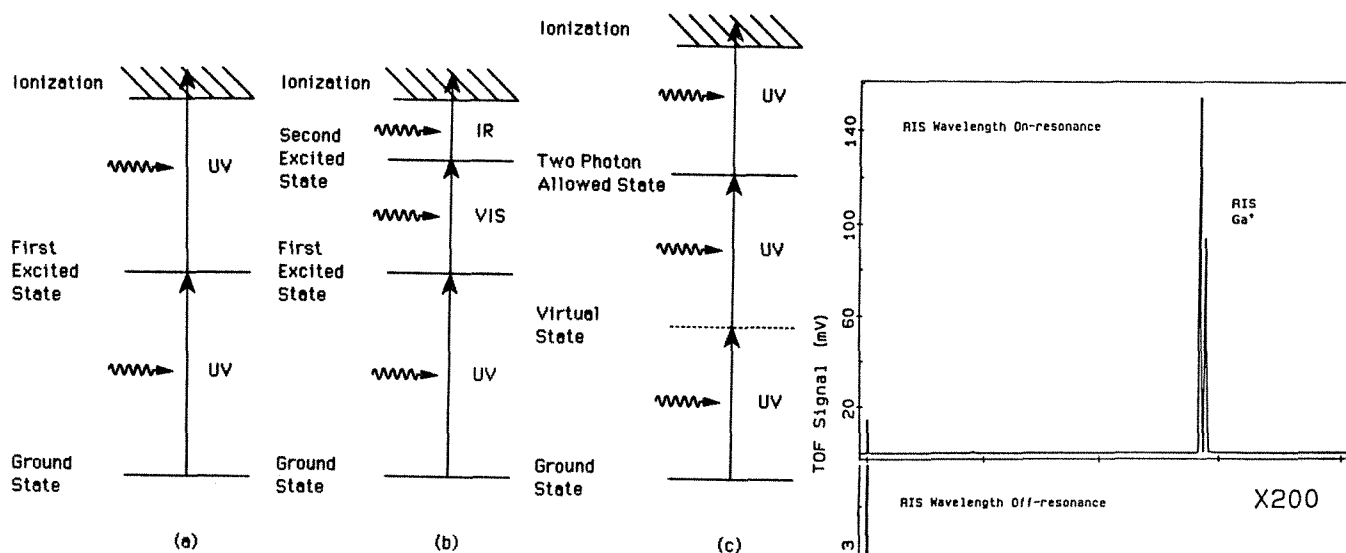


FIG. 1.--Illustration of possible resonance ionization schemes.

FIG. 2.--Demonstration of the mass selectivity of the RIS process. Upper plot: TOF spectrum with the RIS laser tuned to gallium. Lower plot: Same as above, with RIS laser detuned by 0.07 nm without secondary ion suppression.⁶

the total detection efficiency can be calculated, which agrees with the measured 20% value. For short ion pulses (<50 ns) and a large laser volume, total detection efficiency up to 50% can be obtained. Raising the analysis time to 30 min and sputtering ion beam current to 5 μ A (possible with the present Perkin Elmer microbeam ion gun) lowers the detection limit into the low parts per trillion range. Still lower detection limits could be achieved with laser atomization RIS (LARIS). By use of a separate laser pulse instead of an ion pulse for the atomization process, up to 10^{10} particles per 10ns pulse could be released from the sample (the practical limit for SIRIS is 10^7 per 500ns ion pulse), thereby achieving a much lower detection limit in the same analysis time. The advantages of LARIS as compared to SIRIS are expected to be higher sensitivity and no charging effects on insulators; advantages of SIRIS are better quantitation, spatial resolution, and depth resolution.

The third salient property of the RIS process is its generality. Using presently available lasers, one can ionize over 80% of the elements in the periodic table by schemes (a) and (b), which yield extremely high selectivity and sensitivity at the few-atom level. The remaining elements (except for helium and neon) can be ionized by scheme (c) at a factor of up to 100 less sensitivity, but still considerably more sensitive than with competing techniques. A schematic of the SIRIS and/or LARIS instrument is shown in Fig. 4. The present system consists of a Perkin Elmer microbeam ion gun, a RIS laser system, and electron imaging system, a computer-controlled (x,y,z, θ) sample holder

which can hold in the present configuration up to ten $3/4 \times 3/4$ in. targets, a sample interlock system, and a detection system. A second Nd:YAG laser system with its associate optics is available for LARIS analyses. Typical primary ion beam pulses are in the 50-2000ns range, which permits efficient sample utilization. The atomization laser beam can be focused with an x-y adjustable fused silica lens onto the sample. Spatial microcharacterization is obtained in two ways: (a) for small areas by scanning the ion beam, (b) for larger areas by changing the coordinate of the target position for a fixed ion or laser position. By blocking the RIS laser beams, one can also use the system in the Secondary Ions Mass Spectrometry (SIMS) mode, a well-established analytical technique.

RIS analysis requires free atoms in the gas phase. As depicted in Fig. 4, the RIS lasers selectively ionize atoms in the gas cloud of the chosen element that are subsequently extracted and directed through an electrostatic energy analyzer and magnetic sector mass spectrometer or TOF mass spectrometer onto an ion detector system, to be measured in the charge digitization or single-ion counting mode. By suitable choice of timing and electrostatic-field pulsing techniques, secondary ions produced by the impact of the atomizing ion beam or laser can be suppressed, which reduces residual background effects and increases quantitation because positive atomic and molecular ions cannot leave the surface. Further improvement in quantitation can be achieved by control of the molecule or cluster-fragmentation process by control of the power density

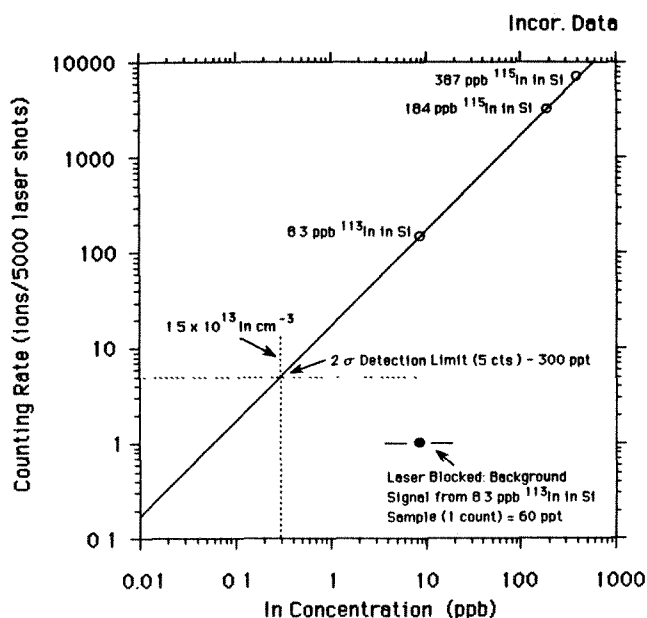


FIG. 3.--Correlation of indium in silicon concentration with indium RIS signal.

of the RIS laser.^{7,8}

The efficiency of ionizing the selected element from the sputtered cloud, and then counting the ions in a detector, depends on the temporal and spatial overlap of the sputtered particles, and the efficiency and passband of the electrostatic energy analyzer and mass spectrometer. One can determine the velocity distribution (and hence kinetic-energy distribution) of particles ejected from a surface from time-of-flight measurements by varying the delay time between the firing of the atomizing ion beam or laser pulse and the time of ionizing the particles with the RIS lasers when using short (less than microsecond) ion or laser pulses. The yield can be optimized by adjustment of the delay between atomization and ionization.

Semiconductor and Electro-optics Application

The semiconductor and electro-optics industries are continually searching for solutions to the many analytical problems limiting progress in functional ability. The analysis of semiconductor and electro-optics materials by SIRIS has been shown in the past to be very useful to measure accurate element contaminants in bulk materials and/or devices; element compositions, including impurities and dopants as a function of depth and lateral position; studies of impurity and dopant concentration at interfaces; and investigations of thermal diffusion into substrates as a function of annealing temperature.⁹⁻¹² Figure 5 shows as an example the neutral silicon and indium atom signals in a depth profile through a Au-SiO₂-InP sample. The sample was scanned over a 1 × 2 mm² area with a DC ion beam to make the crater, and the data were taken with a 50 μm pulsed ion beam spot at the center. The signal has not been normalized, which shows the essentially identical response

to Si and In by the RIS process. The large In and Si signal is due to redeposition of In and Si from previous depth-profile measurements on the same sample. The In peak on the SiO₂ surface shows the segregation process from the In through the SiO₂ surface. The exponential decrease of the Si signal in InP indicates the thermal diffusion of Si into InP substrate. The slope of this decay is a function of the annealing temperature. More detailed studies of the diffusion process have been done for titanium diffusion into lithium niobate (Fig. 6). An absolute concentration calibration is normally achieved by a comparison of the SIRIS signal obtained from the analyzed sample with the signal obtained from a calibrated standard (i.e., NBS standard). The depth scale is calibrated by measurement of the depth of the rastered craters with a Dektak profilometer. In an ongoing research program, impurities and concentration of dopants are studied in new semiconductors as a function of depth and lateral position with sensitivity in the sub-ppb range and lateral resolution down to 10 μm.

An important area of SIRIS applications in the semiconductor and electro-optics research and development community is the measurement of impurity concentrations at the ppt range with high accuracy in the new materials used to make single-crystal substrates, the substrates before processing, and the completed devices. Analysis of amorphous semiconductors is especially important, as many of the present analytical techniques sensitive to these levels depend on the crystalline nature of the substrate. The absolute calibration in the ppt range is difficult for some elements because of the unavailability of standards at the lowest levels.

The SIRIS technique has several advantages when compared to other surface analysis techniques, such as SIMS and AES (Auger electron spectroscopy). Since the majority of sputtered particles are ground-state neutrals, their effective ionization with RIS dramatically reduces the matrix dependence of the detected signal, in contrast to sputtered ions. The variation in SIRIS signal of a chosen element is small in different matrices (less than a factor of 4; Table 1) when compared to the SIMS signal variations (up to several orders of magnitude).⁹ This feature leads to significant improvement in quantitation. Because of the ultrahigh sensitivity of the SIRIS technique, a much higher dynamic range can be obtained, in (for example) depth profiles, as compared to both SIMS and AES. The high selectivity in the ionization process essentially eliminates isobaric and molecular interferences, thereby enabling analyses that would only be possible for some cases with SIMS at very high mass resolution (and consequently further reduced sensitivity).

Biomedical Applications

A significant portion of the RIS potential resides in its application to specific problems

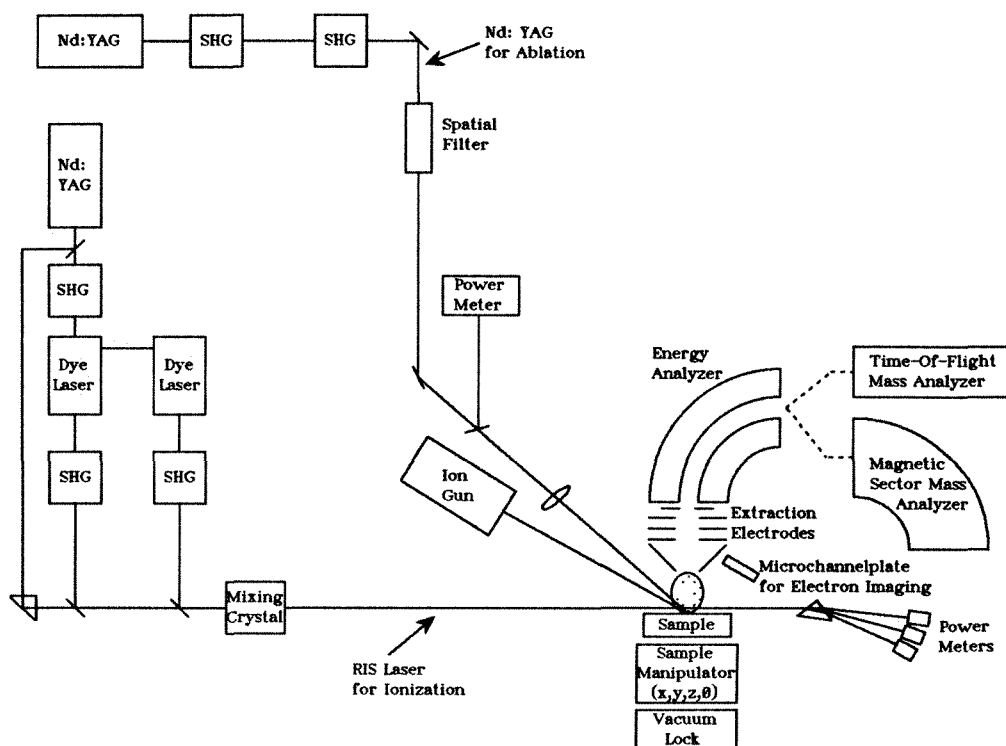


FIG. 4.--Schematic diagram of SIRIS and LARIS experimental arrangement.

and analyses in medicine and biology. There are 15 trace elements known to be essential in human physiology¹³ (Table 2), whose deficiency has been related to numerous conditions or disorders, or whose presence is necessary to sustain metabolic functions. To achieve the required detection limits, traditional methods require milliliter or larger sample volume. RIS can measure all these elements in samples of tens of microliters or less, and with considerably higher accuracy. Some of these elements are difficult or nearly impossible to assay with other techniques available at present, regardless of sample size. For biological tissues or fluids, the sample is chemically ashed and deposited on a pure substrate, such as 99.9999% pure gold foil. Quantitation is by the isotopes dilution method. Due to the small sample size and very low analyte concentration (ppb level), frequently much less than a single monolayer of material is available on the substrate. Therefore, only the high efficiency of SIRIS makes these analyses possible.

One example of the many potential biomedical applications of RIS is the investigation of the role of trace and ultratrace elements in microliter serum samples obtained from premature infants. Two important trace elements are copper and molybdenum. In these studies, copper was determined in serum samples as small as 30 μ l at 180 ppb concentrations, with replicate precisions of 5-10%. Typical isotope ratio accu-

racies of 1-2%, with attendant errors of the mean of 0.25%, can also be achieved. Picogram-level sensitivity has been demonstrated for Mo in serum.¹³ Preliminary data for Mo in samples of <100 μ l bovine serum reference material (RM 8419) yielded a concentration of 19 ppb,¹³ in good agreement with the suggested value of 16 ppb.¹⁴ More recently chromium, another biologically important element, was measured at the 70 femtogram level from a biological sample of a few milligrams.¹⁵

It is not only important to know the concentration of a particular element, but also the spatial distribution. In a current research program, SIRIS is adapted to provide structural imaging and quantitative element concentration imaging of biological tissue sections. Iron and aluminum concentrations are imaged in tissue sections from brains of Alzheimer's disease victims and correlated with surface structure visible in secondary-electron images from the identical location, and optical microscopy of adjacent stained sections (Fig. 7). In the future, RIS imaging of trace elements will help researchers answer fundamental questions such as the association of iron and aluminum concentration in certain parts of the brain with Alzheimer's disease.

Geological Measurements

The same characteristics that allow the SIRIS technique to solve new problems in the

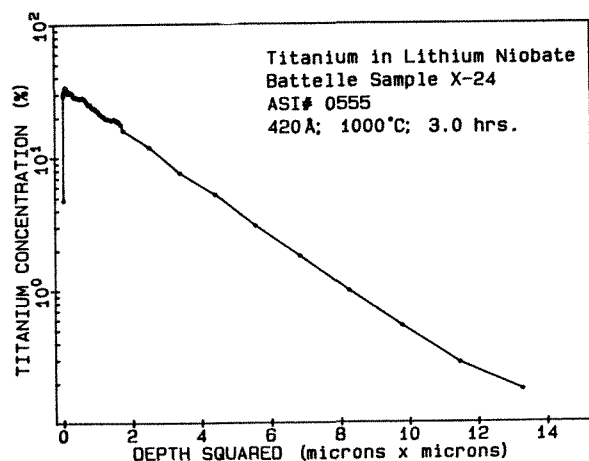
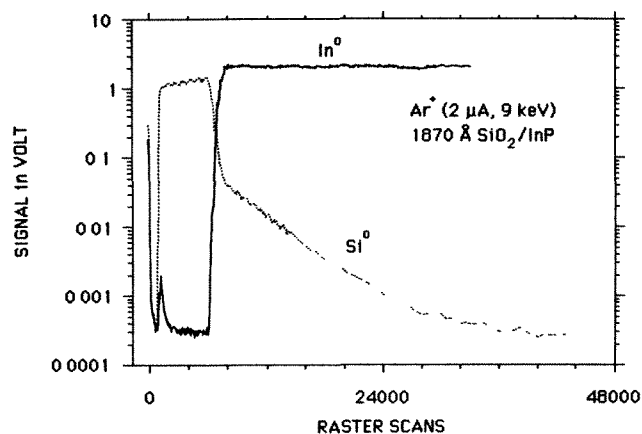


FIG. 5.--Depth profile of In and Si in Au-SiO₂-InP.

FIG. 6.--Depth profile of Ti in LiNbO₃.⁹

TABLE 1.--Relative SIRIS response for silicon and boron in various matrices.

Matrix	Element	Relative SIRIS Response
Si	Si	1.00
Al	Si	0.96
PdSi ₂	²⁸ Si	0.96
PdSi ₂	³⁰ Si	0.96
TiSi ₂	Si	3.60
GaAs	Si	3.65
Si	B	1.00
GaAs	B	0.77
BPSG	B	0.23

semiconductor and biomedical fields are also of importance in the geosciences. Important information on the age, thermal history, evolution, and environment of terrestrial and extra-terrestrial rocks and minerals can be inferred from isotopic ratio measurements of key elements. Frequently, the accuracy of these measurements is compromised by molecular or isobaric interferences. Other important measurements would be to study the trace element con-



FIG. 7.--Secondary electron image generated by rastering micro-ion beam over thin brain tissue section, resulting in resolution of ~10 μm (1 division = 100 μm).

centration as a function of position on minerals and at grain boundaries, where the transition from one type of crystal to another occurs. The element specificity and reduced matrix effect of SIRIS will significantly enhance these measurements. A third advantage is the generality of the RIS process. Most elements in the periodic table are accessible with equal sensitivity, thereby allowing analysis for elements that were not possible before, i.e., Re and Os.¹⁶

To demonstrate the utility of SIRIS in the geosciences we have started spatially resolved microanalyses of Ca and Ti isotope ratios in hibonite, a mineral that is found both in terrestrial and meteoritic samples. In these measurements calcium, which is much more abundant than titanium and is easier to ionize than titanium with conventional techniques, can cause interferences at ⁴⁶Ti and ⁴⁸Ti. Also, in cases where the Ti concentration is approximately equal to the Ca concentration, difficulties are encountered in the ⁴⁶Ca and ⁴⁸Ca measurements. The element specificity of the RIS process should essentially eliminate these problems.

Conclusions

Resonance ionization spectroscopy has been shown to be a very sensitive and uniquely selective process that eliminates isobaric and other interferences. Its ultimate sensitivity reduces the sample size required for analysis by orders of magnitude with respect to other techniques. In combination with microbeam analysis, SIRIS is a powerful tool for studying the concentration and distribution of dopants and impurities in semiconductor materials, as well as the trace element distribution in biomedical tissues. Continuing development of its applications will help researchers in the future to solve a variety of problems in fields as diverse as semiconductor and optical materials, biomedical and environmental sciences, and

TABLE 2.--Trace elements essential in human physiology.

Essential Element	Associated Metabolic Disorders/Functions
Zn	Sickle cell disease, liver disease, gastrointestinal disorders, impaired wound healing, genetic disorders (acrodermatitis enteropathica)
Cu	Wilson's disease, Menkes disease, anemia
Cr	Diabetes mellitus, cardiovascular disease, impaired glucose tolerance, elevated serum cholesterol
Se	Keshan disease (Se-responsive cardiomyopathy), atherosclerosis, muscular dystrophy, cystic fibrosis
Mn	Skeletal abnormalities, ultrastructural abnormalities, blood cholesterol level
Mo	Enzymatic reactions, severe bifrontal headache, night blindness, nausea, lethargy, disorientation, coma
Co	Part of vitamin B-12, interacts with iron
I	Hyperthyroidism, cretinism

Essentiality demonstrated for animals only ---

Ni	Depressed hematocrit, ultra-structural liver abnormality
As	Depressed birth weight, impaired fertility, elevated hematocrits
Si	Aberrant connective tissue and bone metabolism, atherosclerosis, hypertension, aging process
V	Cardiovascular disease, renal disease, kwashiorkor
Cd, Pb, Sn	Growth factor unknown

geochemistry and cosmochemistry.

References

1. U. S. Patent 4,442,354, issued 10 April 1984.
2. G. S. Hurst, M. G. Payne, M. H. Nayfeh, J. P. Judish, and E. B. Wagner, "Saturated two-photon resonance ionization of He(2₁S)," *Physics Rev. Letters* 35: 82, 1975.
3. M. G. Payne, G. S. Hurst, M. H. Nayfeh, J. P. Judish, C. H. Chen, E. B. Wagner, and J. P. Young, "Kinetics of He(2₁S) using resonance ionization spectroscopy," *Physics Rev. Letters* 35: 1154, 1975.
4. G. S. Hurst, M. H. Nayfeh, and J. P. Young, "A demonstration of one-atom detection," *Applied Phys. Letters* 30: 229, 1977.
5. G. S. Hurst, M. G. Payne, S. D. Kramer, and J. P. Young, "Resonance ionization spectroscopy and one-atom detection," *Rev. Modern Phys.* 51: 767, 1979.
6. D. W. Beekman and N. Thonnard, *Laser Ablation as an Atomization Source for Ultratrace Element Analysis Using Resonance Ionization Time-of-flight Mass Spectrometry*, Inst. Phys. Conf. Ser. No. 94, 1988, 163.
7. U. Boesl, J. Grotemeyer, K. Walter, and E. W. Schlag, *Resonance Ionization and Time-of-flight Mass Spectrometry: High Resolution, In-volatile Molecules*, Inst. Phys. Conf. Ser. No. 84, 1986, 223.
8. H. F. Arlinghaus, W. F. Calaway, C. E. Young, M. J. Pellin, D. M. Gruen, and L. L. Chase, "Analysis of ion-bombarded and laser irradiated ZnS and Zn surfaces via high-resolution multiphoton laser-induced fluorescence spectroscopy," *J. Vac. Sci. Technol.* (in press).
9. J. E. Parks, M. T. Spaar, and P. J. Cressman, "Analysis of high purity solids by resonance ionization spectroscopy," *J. Crystal Growth* 89: 4, 1988.
10. J. E. Parks, M. T. Spaar, D. W. Beekman, L. J. Moore, and P. J. Cressman, *Applications of Sputter-initiated Resonance Ionization Spectroscopy: Recent Results*, Inst. Phys. Conf. Ser. No. 94, 1988, 197.
11. J. E. Parks, D. W. Beekman, H. W. Schmitt, and M. T. Spaar, *Ultrasensitive Element Analysis of Materials Using Sputter Initiated Resonance Ionization Spectroscopy*, Mat. Res. Soc. Symp. Proc. 48, 1985, 309.
12. J. E. Parks, H. W. Schmitt, G. S. Hurst, and W. M. Fiarbank Jr., *Sputter Initiated RIS (SIRIS) for Analysis of Semiconductor Impurities*, Inst. Phys. Conf. Ser. No. 71, 1984, 167.
13. L. J. Moore, J. E. Parks, E. H. Taylor, D. W. Beekman, and M. T. Spaar, *Medical and Biological Applications of Resonance Ionization Spectroscopy*, Inst. Phys. Conf. Ser. No. 84, 1986, 239.
14. C. Veillon, S. A. Lewis, K. Y. Patterson, W. R. Wolf, J. M. Harnley, J. Versieck, L. Vanballenberghe, R. Cornelis, and R. C. O'Haver, "Characterization of a bovine reference serum reference material for major, minor and trace elements," *Anal. Chem.* 57: 2106, 1985.
15. L. J. Moore (private communication).
16. R. J. Walker, S. B. Shirey, and O. Stecher, "Comparative Re-Os, Sm-Nd and Rb-Sr isotope and trace element systematics for archaen komatiite flows from Munro Township, Abitibi Belt, Ontario," *Earth and Planetary Sci. Letters* 87: 1, 1988.

FURTHER DEVELOPMENTS IN INSTRUMENTATION FOR MICROPROBE X-RAY FLUORESCENCE ANALYSIS

D. M. Golijanin, D. B. Wittry, and S. Sun

Microprobe x-ray fluorescence analysis (MXRF) is a new technique for materials characterization that is highly sensitive for trace elements; provides accurate quantitative elemental analysis in a small volume; and since it is essentially nondestructive, can be applied to a variety of volatile, insulating, and radiation-sensitive materials.

There are at present three sources of monochromatic x-ray excitation suitable for use as an x-ray microprobe: (1) high-power x-ray tubes with collimators, (2) synchrotron radiation with focusing by mirrors, and (3) micro-focus x-ray tubes with focusing by doubly curved diffractors.

In the first method, the monochromatic radiation is partially achieved by filtering, which improves S/B ratio at the expense of reduced total intensity, but does not remove background sufficiently. A small x-ray probe is obtained by collimation of the beam, which further reduces the available intensity in the probe. In an x-ray tube, x rays are emitted into a 2π -steradian hemisphere, whereas a collimator accepts only a minuscule fraction of that solid angle, even if a close-coupling design is employed.

The second method of focusing the continuum ("bending") radiation from a storage ring by an ellipsoidal mirror could be a good candidate for an x-ray microprobe. An appropriate monochromator must be used, since the synchrotron radiation is polychromatic. The x-ray optical elements as well as the final collimator or the pinhole significantly decrease the intensity in the x-ray probe. That is why the most attractive feature of the synchrotron-based XRF--the high intensity--is lost. Other disadvantageous factors include very stringent tolerances in machining the x-ray mirrors (slope error less than $5 \mu\text{rad}$), instabilities due to the heating of x-ray optical elements, decay of the beam in the ring with time, and the inconvenience of having to conduct an experiment at a remote site and on a tight schedule.¹

Microprobe x-ray fluorescence analysis (MXRF) based on a laboratory excitation system uses a doubly curved crystal that also acts as a monochromator and a focusing x-ray optics element. One obtains the diffractor by cutting a thin cylindrically curved lamella from a block of

single crystal and by bending it plastically over a convex mold. The radius of the curved crystal planes in the horizontal plane ($2R_1$) is twice the radius of the bent crystal lamella (R_1). The Johansson geometry is achieved not only in the horizontal plane but also in all radial planes, as can be seen when the Johansson configuration is rotated about a line passing through the source and the image. This dispersion arrangement provides exact three-dimensional focusing of a point source to a point image for a selected x-ray line. The necessary requirements for point-to-point x-ray focusing are that the source, the crystal, and the image all lie on the focal circle of radius R_1 (Rowland condition) and that the crystal surface conforms to the focal circle (Bragg condition). Both requirements are met in the Johansson geometry.

The exact point-to-point focusing is achieved for one x-ray wavelength only. To excite almost all the elements in the periodic table, three or four characteristic wavelengths and diffractors have to be used.² For several crystals with different d-spacing to focus different wavelengths from a fixed source position to a fixed image location, the "parfocal" condition must be satisfied.³

The clear advantage of doubly (toroidally) bent crystals over singly (cylindrically) curved crystals is not only a smaller x-ray image (point focus vs line focus), but also a much higher x-ray photon intensity in the spot, due to the use of a larger portion of the crystal's surface than is possible with singly curved crystals of either the Johann or the Johansson geometry. The latter advantage can also provide higher collection efficiency and peak-to-background ratio when doubly curved crystals are used in x-ray spectrometers or monochromators as discussed in the last section of this paper.

Plastic Deformation of a Crystal by Slip

The plastic deformation of a crystal occurs by slip along certain planes (the slip plane) in a preferred crystallographic direction (the slip direction). The crystallographic *slip system* is specified by the slip direction and the slip plane. The available slip systems should be carefully examined so that the crystal can be oriented, if possible, in such a way as to achieve the most uniform deformation possible.

The analysis of the case of single slip has been described by many authors, e.g., Johari and Thomas.⁴ Their analysis indicates that the (135) pole is the most favorable stress direction for single slip in a face centered cubic structure which has the (111) $\langle 110 \rangle$ slip

D. M. Golijanin is in the Electronics Division, Xerox Corp., A3-26, El Segundo, CA 90245; D. B. Wittry is in the Departments of Materials Science and of Electrical Engineering, and S. Sun is in the Department of Materials Science, University of Southern California, Los Angeles, CA 90089-0241. The collaborative research with J. Tormey was supported by NIH grant HL31249.

system. However, single slip is not sufficient to form a doubly curved crystal, and it is more difficult to determine the optimum orientation of the crystal for deformation with the least distortion. For obtaining toroidally curved crystal planes, crystals should be oriented if possible so that the slip occurs most readily in a direction corresponding to the direction of least stress. An alternative criterion would be to use an orientation such that the crystal is symmetric about the direction parallel to the plane of the focal circle. In our most recent experiments, we have used the latter criterion.

Ge Crystal Diffractor

Our first choice of a crystal diffractor material was single-crystal germanium, which has a large atomic scattering factor at large $(\sin \theta)/\lambda$. The Bragg angle for a Cu $K\alpha$ (333) reflection is almost 45° (44.91°). This angle is found to be very convenient because a general case of toroidal bending could be well approximated⁵ by bending over a spherical mold that can be more easily machined. Germanium has diamond cubic structure and deforms like other face-centered cubic crystals with a slip system consisting of $\{111\}$ slip planes and $\langle 110 \rangle$ slip directions. A thin germanium lamella was cut parallel to $\{111\}$ planes and it was hoped that a slip which occurs on these planes would yield a satisfactory plastic deformation at an elevated temperature. Since a starting block of germanium was intended for use in the electronic industry, it was hoped that its high purity and crystallographic perfection would make this crystal particularly suitable for fabricating a high-efficiency diffractor.

The mechanical properties of germanium single crystal are such that it could be easily cut, ground, polished, and obtained in the form of thin lamellae. The ratio of crystal thickness to the radii of curvature of the bent crystals is empirically found typically not to exceed 10^{-3} . Our successfully bent lamellae had a ratio of $2.5-3 \times 10^{-3}$.

The experimental results with germanium have shown⁵ that the focus consisted of highly intense central spot about $100 \mu\text{m}$ in diameter and a halo extending over a larger area. The x-ray photon intensity in the focal spot was measured and found to be about two orders of magnitude less than expected from calculations.^{1,6} Part of the discrepancy was due to changes in the x-ray source intensity due to pitting or contamination of the target in the x-ray source. The remaining discrepancy was attributed to a number of factors, some of which could be corrected by more precise crystal and mold preparation; but the most important factor, namely the imperfect bending of the crystal, requires further consideration.

In germanium, the dislocations created by deformation during bending lined up in arrays that formed various structures. Optical microscopy on etched $\{111\}$ surfaces of the bent crystal's faces showed arrays of dislocation etch pits near the edges of the crystal which

were aligned exactly with the traces of the $\{111\}$ slip planes and not along the plane normals as would be the case for normal polygonization.⁷

Polygonization has unfortunately been confounded in some of the literature on fabrication of curved crystal diffractors with the growth of coarse grains due to annealing after deformation. We believe this is an incorrect use of the term polygonization. True polygonization results from the climb of dislocations into walls normal to the slip plane to form a low-energy array or substructure. This array of dislocations is essential to allow for curvature in a bent crystal. It results in an increase in the width of the rocking curve of the crystal but is not a serious limitation for the fabrication of singly or doubly curved crystal diffractors if the subgrains or blocks are sufficiently small. The block size was reported by Vogel⁷ to be about 10^{-3} cm in germanium crystals bent to a radius of 5 cm at 800 C.

The absence of a polygonized structure in bent crystals of silicon has been attributed by Vogel⁸ to the formation of immobile Lomer-Cottrell barriers. Lomer-Cottrell barriers are formed due to slip on two intersecting slip systems (e.g., $\{111\} \langle 10\bar{1} \rangle$ and $\{11\bar{1}\} \langle \bar{1}01 \rangle$) when the partials form a new dislocation (e.g., $[110]$) whose Burgers vector does not lie in a plane of easy glide and is therefore sessile. In the present case, the possibility of easy motion of some of the dislocations and resulting slip bands, combined with the more difficult motion of the sessile dislocations, is thought to be the principal cause of undesirable distortion of the crystal planes in the doubly curved crystals of germanium we have studied.

LiF Crystal Diffractor

As noted, three or four crystals diffracting the appropriate x-ray wavelengths should be sufficient to excite almost all the chemical elements. For studying biological elements, for example, it is important to excite efficiently elements of biological importance: Na, Mg, Al, Si, P, S, Cl, K, and Ca. This goal is most readily reached by use of the appropriate characteristic x-ray radiation to form an x-ray microprobe. The efficiency of exciting an element in a thin specimen is directly proportional to the mass absorption coefficient of the element for the exciting radiation. All elements Na through Ca in the periodic table are excited by Ti $K\alpha$ radiation and this is the most generally useful radiation for a wide variety of biological specimens (for example, Ca is excited 4.9 times more efficiently by Ti $K\alpha$ radiation than it is by Cu $K\alpha$ radiation).

It is very easy to change the target in our x-ray source. Focusing of Ti $K\alpha$ radiation requires in addition either a different diffractor geometry, a different diffractor material, or both. Ge or Si crystals would provide a geometry that can be fabricated as readily for

Ti $K\alpha$ radiation as for Cu $K\alpha$ radiation if the (111) reflection is used instead of the (333) reflection, since the Bragg angle would still be close to 45° and the same slip planes would be involved. However, other crystals could be used, for example LiF, which has a Bragg angle of almost 43° for the (200) reflection of Ti $K\alpha$ radiation. It is well known that LiF can be easily bent plastically and that it has a high reflection efficiency. However, it is a mosaic crystal and may not produce as accurate a focus due to the greater width of the rocking curve. But it may be possible that a mosaic crystal could be more readily deformed to a double curvature than a highly perfect crystal such as Ge, for the reasons discussed in the foregoing section. If the width of the rocking curve after bending is not greater than 1.3×10^{-3} radian, the crystal would still be usable to form x-ray microprobes of high intensity and focal spot diameters of the order of $100 \mu\text{m}$. In addition, the possibility of obtaining a doubly curved crystal with minimum deviation from the desired geometry should be enhanced by the fact that LiF has two slip systems; at low temperature only the $\{110\} \langle 110 \rangle$ is activated, whereas at higher temperature the $\{100\} \langle 110 \rangle$ system is also activated.⁹

Since the Bragg angle for (200) reflection of Ti $K\alpha$ from LiF is not exactly 45° , the crystal's surface has to be bent toroidally. The convex mold over which thin crystal lamellae were bent had to be machined to a toroidal surface with radii of curvature $R_1 = 51.8 \text{ mm}$ and $R_2 = 48.6 \text{ mm}$. Single-point machining and randomized polishing with a cylindrical hollow tool used in making of the spherical molds (Ge and (333) Cu $K\alpha$ reflection) could not be used for toroidal molds. The milling-drilling machine located in our laboratory was modified by the addition of a motorized rotary table and a motorized spin-indexing fixture which holds the work piece; they provided for rotation about two perpendicular axes which could be set with the necessary distance between them. The work piece is advanced toward a motorized grinding wheel assembly, which is mounted on the quill of the milling-drilling machine, by use of the translation motion of the x-y table. With the use of coarse wheels for grinding, finer wheels for polishing, and a Teflon disk with graded series of diamond pastes for a final mirror finish, an almost scratch-free toroidal surface was obtained. The fixture for grinding and polishing the molds is shown in Fig. 1, with a Teflon wheel in place for the final polishing operation.

Cutting and polishing of the LiF crystal lamellae also proved to be different from Ge: thin lamellae of LiF turned out to be more brittle than Ge for the same thickness. But the thicker lamellae of LiF (e.g., $250 \mu\text{m}$) did not bend as readily at the temperatures used ($\sim 500^\circ\text{C}$) as the thinner Ge lamellae did at 700°C . In addition, we were attempting to fabricate larger crystals than we had previously done with Ge, which caused further problems with crystal breakage and with distortion of

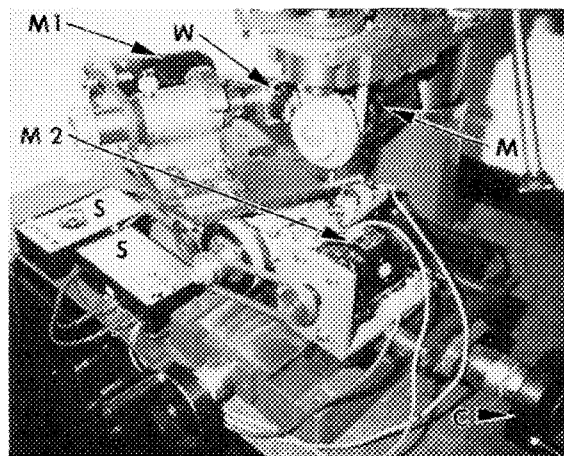


FIG. 1.--Modified milling-drilling machine for making toroids, showing work piece W, motor M that drives grinding wheel or polishing disk, motor M1 that drives work piece holder, motor M2 that drives rotary table, control C that sets depth of cut during grinding, and switch boxes S for controlling the three motors.

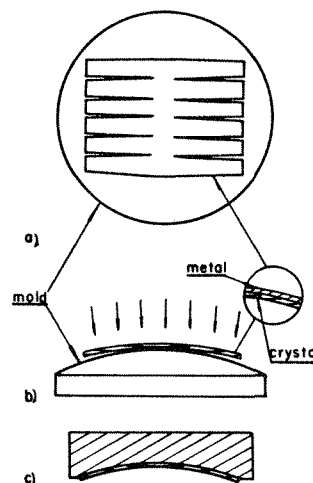


FIG. 2.--Fabrication of doubly-curved crystal diffractors, showing (a) crystal and metal backing plate after patterning, (b) crystal and backing plate in position on the mold for bending, and (c) completed diffractor assembly.

the crystal planes from the desired geometry. Our attempt to resolve these problems has resulted in the following procedure (Fig 2).

Before the crystal is ground to its final thickness, a metallic backing is attached to the convex side of the crystal with a high-melting-point cement. Next, the crystal is polished to the final thickness and the crystal and backing are patterned by etching so that slots of suitable shape are formed in the direction parallel to the focal circle (Fig. 2a). The crystal and ductile metal backing are then formed over the convex mold at elevated temperature by application of a uniform pressure (Fig. 2b). Finally, the metal backing is

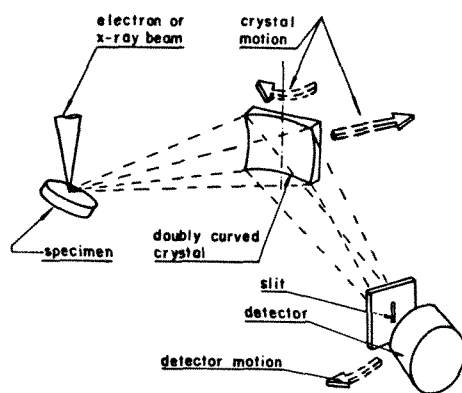


FIG. 3.--Miniature scanning x-ray monochromator with doubly curved crystal.

cemented to a rigid holder to form the completed diffractor assembly (Fig. 2c).

Fixed and Scanning Monochromators

The technology of toroidally curved crystals that has been developed for the fabrication of diffractors for MXRF has applications to improved x-ray monochromators for the measurement of characteristic x-ray line intensities. Two possibilities are currently being investigated; both take advantage of the high collection efficiency of doubly curved crystals. The first possibility is the use of a doubly curved crystal of a particular geometry in a scanning monochromator; the second, the use of toroidally curved crystals for a fixed monochromator to detect a particular characteristic x-ray line.

It has been shown by Wittry¹⁰ that a crystal with spherically curved crystal planes and a toroidally curved surface can provide higher x-ray collection efficiency than a singly curved crystal over a wide range of Bragg angles. The use of small radii of curvature for the crystal provides even greater collection efficiency when crystals of reasonable size are used. Such a miniature x-ray spectrometer, shown in Fig. 3, has applications in a variety of electron-beam instruments such as scanning electron microscopes, scanning Auger microprobes, and transmission electron microscopes, as well as in the detection of characteristic x rays in MXRF. Development of crystals suitable for use in such scanning x-ray monochromators is currently in progress at USC, partly in conjunction with a project at Lehigh University that is concerned with the development of a miniature scanning monochromator for use with a field emission scanning transmission electron microscope.¹¹

The use of toroidally curved crystals in a fixed x-ray monochromator has applications to specific problems that require very low detection limits and high spatial resolution. An example is the detection of calcium in biological specimens, which has been typically done in TEM instruments with an energy-dispersive x-ray spectrometer. In this case, the detection limits are adversely affected by the presence of

high concentrations of potassium, since the $K\alpha$ line of potassium differs in energy from the $K\alpha$ line of calcium by only 101 eV. A crystal is being developed at USC for use in a fixed monochromator for detection of Ca $K\alpha$ radiation. This work is being done in collaboration with John McD. Tormey of the University of California at Los Angeles and is based on the use of a JEOL 100CX. This instrument has the appropriate geometry for incorporation of the Ca monochromator without any substantial modifications.

The calcium monochromator configuration is shown in Fig. 4. It is based on the use of a LiF crystal employing the (111) reflection for which the Bragg angle is 46.37° . The crystal accepts x rays in the direction opposite to that of the incident electron beam, which has the advantage that the x-ray continuum from thin specimens is minimized. The radius of the focal circle is 72.7 mm, and the x-ray detector is located outside the instrument and receives the diffracted x-rays via an existing port at the front of the electron microscope. It is planned to use either a flow-proportional counter or a Peltier-cooled silicon detector. The solid angle subtended by the crystal at the specimen is 0.072 sterad, which is comparable to the solid angle that has been used for EDS systems. However, this angle could be somewhat increased if the anticontamination trap were redesigned.

Even with no increase in solid angle and allowing for less than 100% efficiency of the crystal, a significant improvement in the statistics for the analysis is possible. For example, if the crystal efficiency were 33%, and the reduction in background due to improved resolution is approximately a factor of 20, the detection limits would be lower than measurements by EDS by a factor of about 1.5. But the improvement in practice can be much greater than that for three reasons: (1) the x-ray continuum from a thin specimen has its minimum value in the direction opposite to the incident electron beam, (2) stray background due to scattering from the walls of the instrument is lower than for EDS because the crystal monochromator accepts radiation only from a small region that lies on the focal circle, and (3) the contribution to the back-

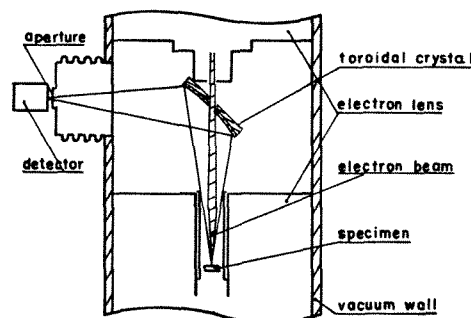


FIG. 4.--X-ray monochromator for detecting calcium $K\alpha$ radiation in JEOL 100CX transmission electron microscope.

ground from the potassium K β peak can be completely eliminated. Thus, the use of a crystal monochromator for the study of calcium in biological specimens would provide shorter measurement times for the same detection limits, or lower detection limits or smaller analysis volumes with the same measurement time.

References

1. D. B. Wittry and D. M. Golijanin, "X-ray microprobes: A comparison of laboratory and synchrotron sources," *Proc. 11th ICXOM*, 1986, 51-55.
2. M. Kotera and D. B. Wittry, "X-ray fluorescence analysis with monochromatic x rays," *J. de Physique* 45: C2-281-284, 1984.
3. D. B. Wittry, U.S. Patent No. 4 599 741, 8 July 1986.
4. O. Johari and G. Thomas, *The Stereographic Projection and Its Applications*, New York: Interscience, 1969.
5. D. B. Wittry and D. M. Golijanin, "Large aperture point-focusing diffractor for x rays," *Appl. Phys. Lett.* 52: 1381-1382, 1988.
6. L. M. Golijanin, Thesis, University of Southern California, Los Angeles, Calif.
7. F. L. Vogel Jr., "Dislocations in polygonized germanium," *Acta Met.* 3: 95-96, 1955.
8. F. L. Vogel Jr., "On the orientation effect in the polygonization of bent silicon crystals," *Acta Met.* 6: 532-534, 1958.
9. J. J. Gilman, "Plastic anisotropy of LiF and other rocksalt-type crystals," *Acta Met.* 7: 608-613, 1959.
10. D. B. Wittry, U.S. patent 4 807 286, 21 February 1989.
11. J. I. Goldstein, C. E. Lyman, and D. B. Williams, "The wavelength dispersive x-ray spectrometer and its proposed use in the analytical electron microscope," *Ultramicroscopy* (in press).

X-RAY MICROSCOPY WITH THE USE OF SYNCHROTRON RADIATION

K. W. Jones, B. M. Gordon, A. L. Hanson, J. G. Pounds, M. L. Rivers,
George Schidlovsky, J. V. Smith, Per Spanne, and S. R. Sutton

Present accomplishments in high-energy x-ray microscopy have been reviewed recently.¹ It was pointed out that the x-ray microscope (XRM) is capable of making determinations of trace elements approaching femtogram sensitivity with lateral resolution of 10 μm or less. Hence, the XRM in its present state of development is becoming an analytical tool that can be used effectively in many ways. On the other hand, there are still many ways in which the XRM can be improved and extended in its areas of applicability. In particular, a combination of approaches that make it feasible to do chemical speciation of trace elements on a micrometer scale with the XRM will result in a chemical-speciation x-ray microscope (CSXRM) that will greatly extend analytical capabilities in the chemical sciences.

The system for x-ray microscopy now being developed at the X-26 beam line of the Brookhaven National Synchrotron Light Source (NSLS) is described here. Examples of the use of x-ray microscopy for trace element geochemistry, biology and medicine, and materials investigations are given to emphasize the scientific applications of the technique. Future directions for the improvement and further development of the X-26 microscope and of x-ray microscopy in general are discussed.

Description of the NSLS X26 XRM

The X26 XRM is representative of the first-generation instruments developed at several laboratories. It is based on the use of the continuous x-ray spectrum produced by the 2.5 GeV electron-storage ring of the National Synchrotron Light Source (NSLS). The XRM is used on two different beam lines at locations which are 20 m and 9 m from the x-ray source. Spatial resolution is obtained either by direct collimation of the beam alone or with focusing after the collimator. Beam sizes in either mode of operation have been as small as 5 μm .

The x-ray flux at energies above 5 keV is about 3×10^7 photons/(μm^2 s) at a storage-ring current of 100 mA at the 20m location and a factor of 5 higher at the 9m station. The flux at the two locations is increased by the use of focusing mirrors that produce an image

of the x-ray source at the XRM. Use of mirrors increases the flux by about 100-500, depending on the beam line. The focused image size at unity magnification is about $250 \times 750 \mu\text{m}$ in the horizontal and vertical directions, respectively, at the 2σ width.

The flux per unit energy interval is a maximum at low energies and begins to drop very sharply at energies above 15 keV. Despite the decrease with energy, there is sufficient flux to make measurements on elements as heavy as lead. Naturally, the trace element sensitivity for a given spatial resolution is less at the higher energies.

The most sensitive region for trace-element determinations by energy-dispersive detection of the K-shell photons is from about iron to molybdenum. Absolute minimum detection limits of a few femtograms have been achieved.⁴

Scientific Uses of the XRM

The XRM in its present state of development represents a substantial improvement in several ways over the now traditional methods of electron microscopy with energy- or wavelength-dispersive fluorescent x-ray detection and over the ion microprobe. That is not to say that the older methods are obsolete, but that improved approaches are possible for several types of determinations that make it feasible to characterize or investigate substances of interest more completely.

XRM is being introduced into general scientific applications because of the close interaction among scientists in various disciplines cooperating on a project of common interest. For best results the developers of the XRM need broad scientific skills that will enable them to pick out scientific areas that can benefit from the XRM and then to play a leadership role in the implementation of specific experiments.

This has been the model used for the work on the BNL XRM. Specific examples taken from work in progress at the XRM are displayed here to illustrate this point.

Trace-element Geochemistry Experiments

In trace-element geochemistry work measurement of concentrations of the rare earth elements (REE) is difficult when detection of their L x rays is used because of interferences with the K x rays emitted by lighter elements. The problem is simplified when it is possible to use K x rays. The interpretation of the REE concentrations is an important approach to the understanding of the formation and evolution of the Earth's crust. The use of the XRM can, in principle, be of importance

The authors are at the Brookhaven National Laboratory, Upton, NY 11973, except M. L. Rivers, J. V. Smith, and S. R. Sutton (Geophysical Sciences, University of Chicago, Chicago, IL 60637) and Per Spanne (Radiation Physics, Linköping University, Linköping, Sweden). The research was supported by DOE contract DE-AC02-76CH00016, NIH Grant P41RR01838, NSF Grant EAR-8618346, and NASA Grant NAG 9-106.

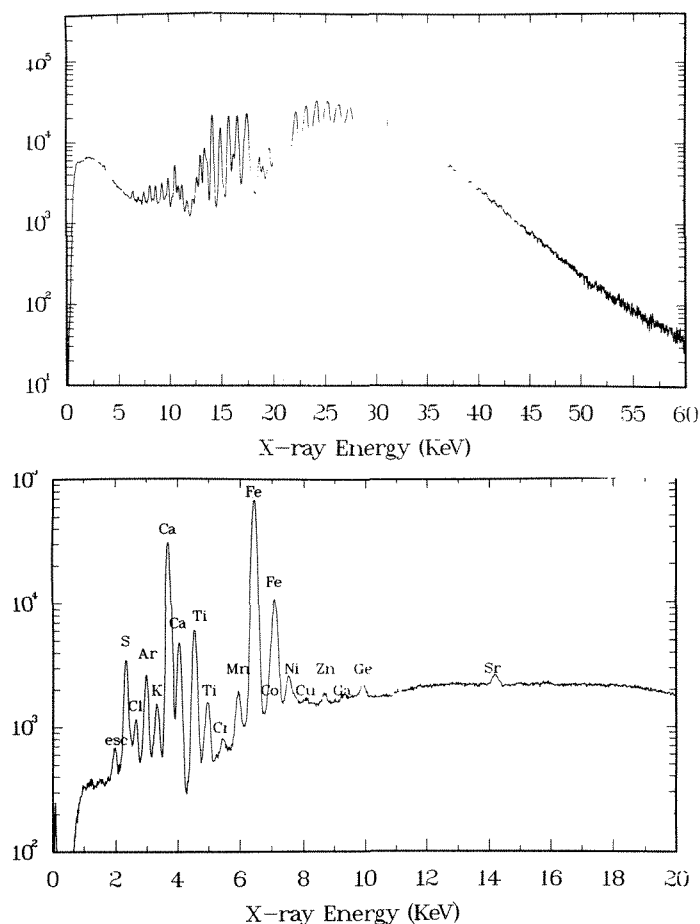


FIG. 1.--Spectrum for NIST Standard Reference Material No. 612, which contains REE at 50ppm level.

FIG. 2.--Spectrum obtained from polished section of coal taken from Lee Ranch Mine in San Juan Basin region of New Mexico.

in this area of research since the extent of the synchrotron white light spectrum makes it feasible to observe K x rays from all rare earths.

As an example of performance, a spectrum obtained from the National Institutes of Science and Technology (NIST) Standard Reference Material No. 612 which contains REE at the 50ppm level is shown in Fig. 1. The spatial resolution was $55 \times 55 \mu\text{m}$. The total photon flux incident on the sample was 2×10^5 photons/ $(\mu\text{m}^2 \text{ s})$ above 30 keV energy at a storage-ring current of 68 mA. Approximate minimum detection limits of 50 ppm could be obtained under these conditions. This performance is useful for many experiments; for example, Chen, Chao, Minkin, and Back have obtained preliminary results from examination of Chinese ores containing REE from the Bayan Obo deposits.² A general examination of the use of synchrotron radiation for REE work has also been reported.³

Other recent experiments have utilized the XRM for study of trace-element distributions in coal.^{4,5} Trace elements in coal are used as markers that can indicate how the coal was formed and to understand the processes by which sedimentary basins are formed. A spectrum obtained from a coal taken in the San Juan basin in New Mexico is shown in Fig. 2.

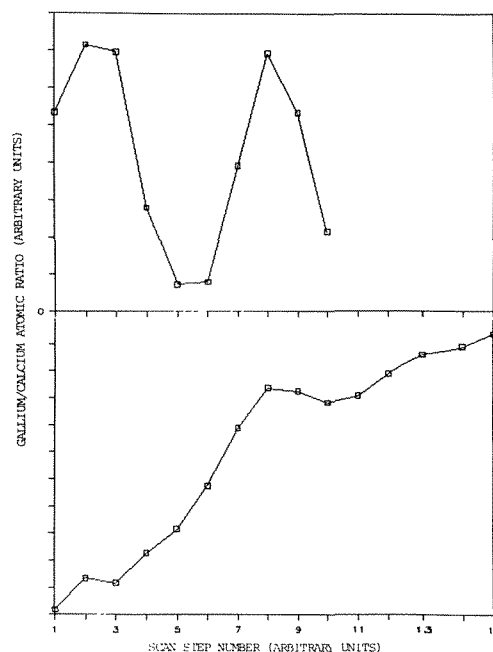


FIG. 3.--Scan across shaft of thin section of bone from tibias of two rats showing change in the Ga concentration relative to that of Ca for two different treatments with $\text{Ga}(\text{NO}_3)_3$: endosteum (left) and periosteum (right).

Samples taken at various depths in the seam were analyzed and the variation of the trace elements with depth was deduced. The results will be interpreted in terms of several models for fluid flow through the sedimentary basin in which the coal lies.

Biomedical Experiments

Mapping of trace element concentrations in bone is well suited to the XRM. The relatively high-Z matrix makes work with the SEM impossible for low-concentration measurements. However, the XRM is easily able to cope with values at the ppm level with good sensitivity. Two specific applications are mentioned here: the study of metals used in cancer therapy and the study of toxic elements, notably lead.

The therapeutic agent $\text{Ga}(\text{NO}_3)_3$ is being used to stop bone resorption in hypercalcemia brought on by several types of bone cancer. The mechanisms by which it acts are not known. Determination of the distribution and concentration in bone is necessary to improve the treatment protocols and to find optimum treatment modes. An initial investigation of the distribution of Gallium in the rat tibia following administration of $\text{Ga}(\text{NO}_3)_3$ was carried out at the XRM.⁶ This work showed that the gallium concentrated in regions of the bone that were metabolically active and that the concentrations in the bone depend on the amounts of gallium administered. Later work is investigating the effects of hormone therapy administered in conjunction with the gallium nitrate. A scan across the diaphysis of rat tibia from periosteum to endosteum showing the concentration of gallium relative to that of calcium is displayed in Fig. 3. The form of the distribution is affected by the protocol used for the treatment. Systematic inves-

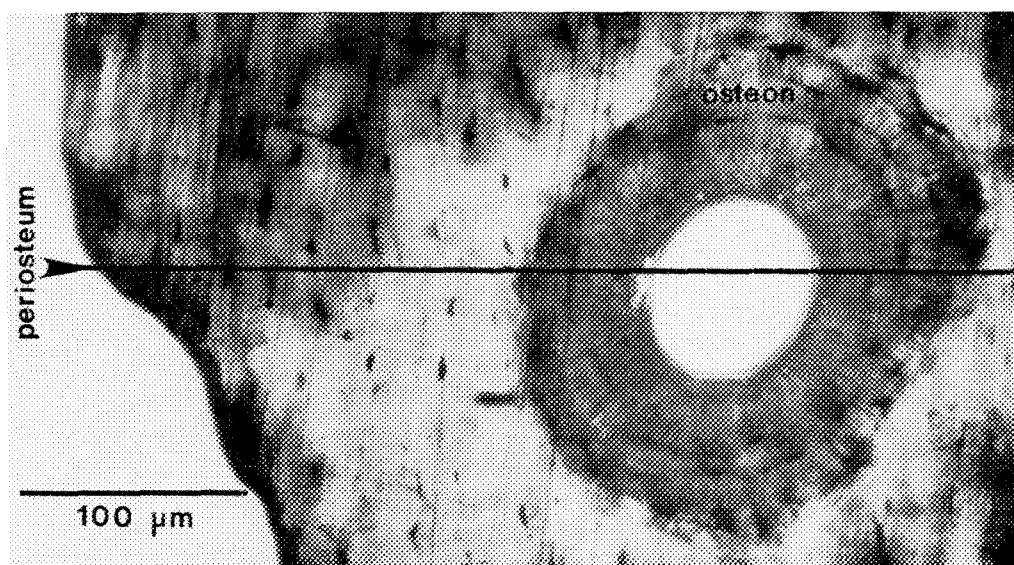


FIG. 4.--Thin section of bone taken from human tibia: circular structure is an osteon and associated Haversian Canal. Left edge of section is periosteum. Total distance across specimen is approximately 500 μm .

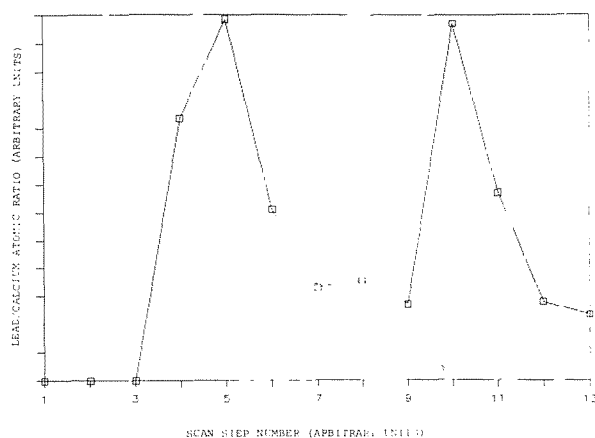


FIG. 5.--Scan across specimen of Fig. 4 showing increase of Pb relative to Ca at periosteum and at edges of osteon for thin sections of rat tibia from vitamin D-deficient rats treated with $\text{Ga}(\text{NO}_3)_3$.

tigation of the gallium concentration will give a better understanding of the pharmacokinetics of the treatment.

Measurements in bone of the toxic element lead are of great importance for improved understanding of the mechanisms by which the lead can affect the nervous and other body systems. The biological lifetime of lead in bone is of the order of decades, so that it can also be an excellent long-term indicator of time-integrated lead exposure. The latter point has stimulated interest in the in vivo determination of the lead in bone by K or L x-ray fluorescence methods.

Accurate mapping of the lead distribution in the bone is required not only for the understanding of the basic biological mechanisms,

but also for the interpretation of the results of in vivo measurements. For this reason, a program to measure the lead in thin sections of human tibia has been undertaken. The structure of a thin section of bone near the periosteum is shown in Fig. 4. The particular feature of interest in this case is the circular osteon and Haversian canal. The XRM was used to measure the lead levels from the periosteum to the Haversian canal with a spatial resolution of better than 60 μm . The concentration of lead relative to calcium is shown in Fig. 5 for a scan from periosteum through the osteon. The values obtained depend strongly on the region of bone measured and the concentration changes across the osteon. Systematic work to look at different stages of the osteon lifetime and different levels of lead exposure is necessary and is being undertaken.

An example of a possible application of the high-energy x rays is the in vivo determination of lead in the human tibia. A typical instrument developed at Brookhaven⁷ and used for clinical measurements⁸ uses a radioactive source, ^{109}Cd , to produce lead K x rays. The flux at the tibia from a 100mCi Cd source placed 4 cm from the bone and emitting into an angular range of $\pm 10^\circ$, corresponding to a solid angle of 0.096 sr, is 6×10^5 photons/(cm^2 s). In contrast, the flux in a 1keV band of synchrotron radiation at 88keV Cd photon energy is 6×10^7 photons/(cm^2 s) for a wiggler source at a ring current of 100 mA. The synchrotron XRM can therefore have useful and novel applications for clinical research employing both the high-energy and low-energy ends of the synchrotron spectrum to produce K- and L-shell vacancies in lead, respectively.

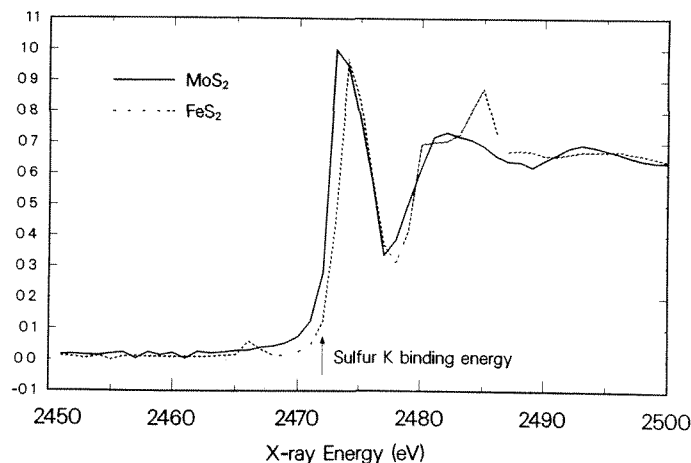


FIG. 6.--Typical EXAFS spectrum for MoS₂ and FeS₂ showing effects of chemical structures.

Experiments in the Chemical Sciences

There are many applications for microanalysis in the energy-related chemical sciences. Chemical methods used to treat coal or oil prior to combustion rely on use of catalysts to improve combustion properties and to remove environmentally damaging components such as sulfur. Some initial measurements have begun on these topics employing the multielemental detection capability of the XRM. However, the use of chemical speciation and structure measurements by means of the x-ray absorption near edge spectroscopy (XANES) or extended x-ray absorption fine structure (EXAFS) methods using the XRM will be of equal or even greater importance for microchemical work.

Examples of conventional EXAFS spectra are given in Fig. 6, which shows the results obtained on the NSLS X19 EXAFS beam line for MoS₂ and FeS₂ taken by a point-by-point scan through the energy region at the sulfur K absorption edge. The time for a single scan was around 15 min with a 4 × 15mm beam.

It can be seen that major changes will be necessary to the apparatus to make it feasible to operate with spatial resolutions on the order of 10-20 μm. One approach that is useful has been put into operation by Fontaine et al.⁹ at the Laboratoire d'Utilisation du Rayonnement Electromagnetique (LURE). They used an optical arrangement which gave a focused x-ray beam at the sample, but with an angular dispersion dependent on the energy of the x ray. A position-sensitive detector then made it possible to collect a complete spectrum in a matter of milliseconds. They were successful in studying a time-resolved chemical reaction. The focused beam makes it possible to study areas of 400 μm in diameter.

At the NSLS on X26, use of a 4-crystal silicon monochromator and detection of fluorescent x rays will give resolutions for XANES at a spatial resolution of better than 50 μm and

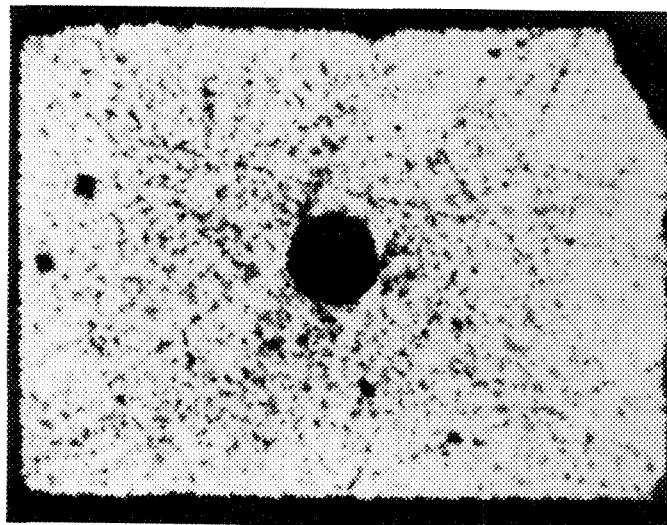


FIG. 7.--Microtomogram of ceramic with void. Pixel size was 10 × 10 μm; tomogram is 311 × 311 pixels.

detection limits of 10 ppm.

Future work that makes it possible to do EXAFS and XANES at the micrometer resolution level on the millisecond scale will be of great importance. The sensitivity of the device should be such that it can detect elements at the trace level, which implies that it will be necessary for it to operate with high-efficiency detection of the fluorescent x rays.

Experiments in Materials Sciences

A pilot study is now going on to measure the location of small voids in ceramic materials by computed microtomography (CMT).¹⁰ A very simple apparatus is used.¹¹ A pencil beam is defined by appropriate collimation and the sample is then translated through the beam for a set of different angular positions. The number of transmitted photons is measured with a CsI(Tl) photon detector operated in current mode.

In the first work that was done the collimator produced a beam that was 15 μm wide in the horizontal dimension and 20 μm tall in the vertical dimension. The first images were of test samples of silicon carbide with a small hole drilled in them at various places in different samples. It was possible to find voids down to about 10-20 μm in diameter in samples that were about 2-3 mm thick. An image reconstructed from the scans is shown in Fig. 7. The 250μm-diameter artificial void can be seen at the center of the picture, as can several smaller natural voids close to the edges of the scan. This demonstration shows that CMT

can be used for nondestructive analysis of ceramics.

Future Directions in X-ray Microscopy

In the brief examples of experiments in various scientific fields given above we note that the XRM in its present form can already be used for many new types of experiments that are not otherwise feasible. It is pleasing to be able to say that there are still many ways in which the XRM can be improved in the future.

Some of the work that needs to be done is quite obvious. We must certainly optimize the use of all the photons in the beam by using detection systems of maximum efficiency. Improved energy-dispersive systems that can handle higher counting rates will be helpful. Wavelength-dispersive spectrometers with position-sensitive detectors will help to give better detection limits. Further application of the CMT method and use of coded apertures may help to increase the data-taking efficiency and help to relieve the demands on x-ray optics and collimators imposed by the need to improve spatial resolutions.

For the most part these are developments that are aimed at improving the techniques for trace-element determinations. A change that seems to be taking place in the field now is the recognition that XRM must not be defined in a narrow sense of trace-element detection or even of measurement of density differences as in CMT in the transmission mode. Rather it should be recognized that the XRM will evolve in a way similar to the SEM or to the use of various techniques for surface analysis that co-exist in a single experimental station. Thus, in a similar way, the XRM of the future will be able to image a material or chemical substance in a variety of independent modes that combine transmission and fluorescence measurements with simultaneous ability to look at the chemical and other parameters of the material through EXAFS, XANES, Auger electron spectroscopy (AE), X-ray photoelectron spectroscopy (XPS), X-ray diffraction (XRD), and electron microscopy that is an obvious direction, since all these techniques are now used at synchrotrons, but generally independently on different beam lines. A judicious combination of these methods in a single XRM instrument is a logical next step that should go on in parallel with the other developments of the fluorescence approach.

These thoughts naturally suggest that the addition of other complementary analytical methods could also be considered. The use of low- and high-energy ion beams for surface analysis and isotopic determinations would be logical. Present-day ion-beam equipment is reasonably small and does not preclude installation on a typical synchrotron beam line.

New synchrotron radiation sources that are now under construction will have a major impact on the XRM when they start operation about 5-7 years from now. An example of such a new facility is the 7GeV machine now under construc-

tion at Argonne National Laboratory and the similar machine being built at the European Synchrotron Radiation Facility at Grenoble. The use of an undulator-type insertion device will do the same at high energies.

References

1. K. W. Jones and B. M. Gordon, "Trace element determinations using Synchrotron-Induced X-Ray Emission (SRIXE)," *Anal. Chem.* 61: 341A, 1989.
2. J. R. Chen, private communication.
3. M. L. Rivers and S. R. Sutton, "Synchrotron x-ray fluorescence analysis of rare-earth elements," abstract for 1989 Spring Meeting of the American Geophysical Union, Baltimore, Md., 7-12 May 1989.
4. C. J. Suen, S. R. Sutton, M. L. Rivers, K. W. Jones, C.-L. Chou, and F. J. Kuellmer, "Trace element geochemistry of coal from the Illinois and San Juan Basins using the synchrotron x-ray fluorescence microprobe," *ibid.*
5. K. W. Jones, S. R. Sutton, M. L. Rivers, E. J. Daniels, and S. Altaner, "Trace element compositions of cleat clays from anthracite coal, Eastern Pennsylvania, USA," *ibid.*
6. R. S. Bockman, M. Repo, D. Warrell, J. G. Pounds, W. M. Kwiatek, G. J. Long, G. Schidlovsky, and K. W. Jones, "X-ray microscopy studies on pharmacodynamics of therapeutic gallium in rat bones," in D. Sayre, M. Howells, J. Kirz, H. Rarback, Eds., *X-Ray Microscopy II*, New York: Springer-Verlag, 1988, 391.
7. K. W. Jones, G. Schidlovsky, F. H. Williams Jr., R. P. Wedeen, and V. Batuman, "In vivo determination of tibial lead by K x-ray fluorescence with a ^{109}Cd source," in K. J. Ellis, S. Yasumura, and W. D. Morgan, Eds., *In Vivo Body Composition Studies*, London: Institute of Physics Sciences in Medicine, 1987, 363.
8. R. P. Wedeen, V. Batuman, F. Quinless, F. H. Williams Jr., J. Bogden, G. Schidlovsky, and K. W. Jones, "Lead nephropathy: In vivo x-ray fluorescence (XRF) for assessing body lead stores," in K. J. Ellis, S. Yasumura, W. D. Morgan, Eds., *loc. cit.* 357.
9. A. Fontaine, E. Dartyge, J. P. Itie, A. Jucha, A. Polian, H. Tolentino, and G. Tourillon, "Time-resolved x-ray absorption spectroscopy using an energy dispersive optics: Strengths and limitations" (to be published).
10. A. S. Krieger, "Future directions in synchrotron-based computer microtomography," presented at Tenth Conf. on the Application of Accelerators in Research and Industry, Denton, Tex., 1988, *Bull. Am. Phys. Soc.* 33: 1698, 1988.
11. P. Spanne and M. L. Rivers, "Computerized microtomography using synchrotron x rays," *Nucl. Instrum. and Methods B24/25*: 1063, 1987.

MATERIALS ANALYSIS WITH NUCLEAR MICROPROBES: SUPERCONDUCTORS AND BURIED CONDUCTORS

J. C. Barbour and B. L. Doyle

Nuclear microprobe analysis (NMA) is a unique form of microbeam analysis in that it combines high lateral resolution with the high depth resolution techniques of conventional ion beam analysis (IBA) for nondestructive determination of sample composition in three dimensions. By use of depth-sensitive IBA techniques such as Rutherford backscattering spectrometry (RBS), enhanced backscattering spectrometry (EBS), or elastic recoil detection (ERD), NMA finds its greatest utility in analyses requiring the following information: (1) 1-100ppm sensitivity, (2) nondestructive three-dimensional depth profiling, and (3) quantitative light element analysis (e.g., the first two rows of the periodic table). This paper demonstrates the continuing evolution of NMA capabilities through two examples. First, the unique capabilities afforded NMA are shown in a simple yet accurate method to measure both oxygen and metal atom concentrations in Y-Ba-Cu-O alloys with micro-area ion-beam analysis. Second, a NMA of buried tungsten lines in a silicon wafer demonstrates the complementary nature of information determined by NMA and scanning electron microscopy (SEM).

Sandia Nuclear Microprobe

The Sandia nuclear microprobe^{1,2} is one of five beam lines attached to an EN tandem Van de Graaff accelerator. This accelerator is used to obtain high-energy ion beams which are focused onto object slits set at $25 \times 3 \mu\text{m}$ (horizontal \times vertical). The beam is then defined by an aperture slit ($1 \times 1 \text{ mm}$), which is upstream from a small magnetic hexapole lens. A magnetic quadrupole doublet lens, which can steer the beam electrostatically as well as focus it magnetically, is positioned immediately after the hexapole lens. This quadrupole doublet lens is used for final focusing of the beam onto the target. The target chamber is kept at high vacuum ($<10^{-6}$ Torr) and contains a secondary-electron detector used for imaging the sample surface, an annular particle detector used for RBS and EBS, and a Si(Li) detector used for particle-induced x-ray emission (PIXE, when proton beams are used; or HIXE, for He beams). The distance between the doublet lens and the target can be as small as 5 cm, which results in a horizontal demagnification of 1/25

and a vertical demagnification of 1/3. These optics should define a $1\mu\text{m}$ -diameter spot on target; typically a $1\text{--}2\mu\text{m}$ -diameter spot is obtained. The operational portion of the nuclear microprobe, from the object slits to the target chamber, is 1.5 m long.

The focusing procedure for the nuclear microprobe has been described in detail previously³ and therefore only a brief description is given here. The object and aperture slits are opened to allow a broad beam to illuminate the hexapole and quadrupole lenses, and the beam is imaged on a fluorescing glass slide in the target chamber. The initial image ($100\text{--}300 \mu\text{m}$ on a side) is an 8-pointed star defined by the eight polepieces of the doublet lens. Aberrations in the lens system are removed by adjustment of the quadrupole lens to form a symmetric star pattern such that the principal focal planes of two singlets are exactly 90° apart. The aperture slits are inserted to define a smaller spot from just the center portion of the beam and the quadrupole is used to focus the beam to a spot $\sim 50 \mu\text{m}$ on a side. At this point, aberrations from the quadrupole lens, which may cause the spot to appear as a trapezoid, are removed by adjustment of the hexapole lens to obtain a rectangular spot. The quadrupole lens can then be readjusted for optimum focus. The object slits are partially closed until the image (at optimum focus) becomes a dim circular spot. (An iterative adjustment of the quadrupole and hexapole lenses are usually required during this step.) A computer-controlled scanning system is used to raster the beam over a 400 mesh ($25\mu\text{m}$ -wide holes) Cu TEM grid and the secondary electron image of this grid is observed on an oscilloscope. The final focus is obtained by adjustment of the quadrupole and the object slits to optimize the clarity of the secondary-electron image.

Computer-assisted data collection and reduction are essential for NMA in order to process the vast amount of information gathered, and because of the complexity of some of the techniques. A typical data-acquisition system collects data in the following forms: yield (counts from an SCA) vs X and Y position, useful for imaging secondary electrons and for producing single-element maps with RBS, NRA, or PIXE; yield vs event energy (E) and position, useful for line scans; and yield vs E, X, and Y, useful for mapping multiple elements with PIXE and NRA, or for three-dimensional profiling with RBS, ERD, or EBS.

The authors are at the Sandia National Laboratories, Albuquerque, NM 87185. The work was supported by the U.S. Department of Energy under Contract DE-AC04-76DP00789. The authors thank J. A. Knapp, N. D. Wing, T. L. Aselage, and R. S. Blewer for their assistance in this work.

Y-Ba-Cu-O ALLOY, MIXED PHASES, 123 AND 211

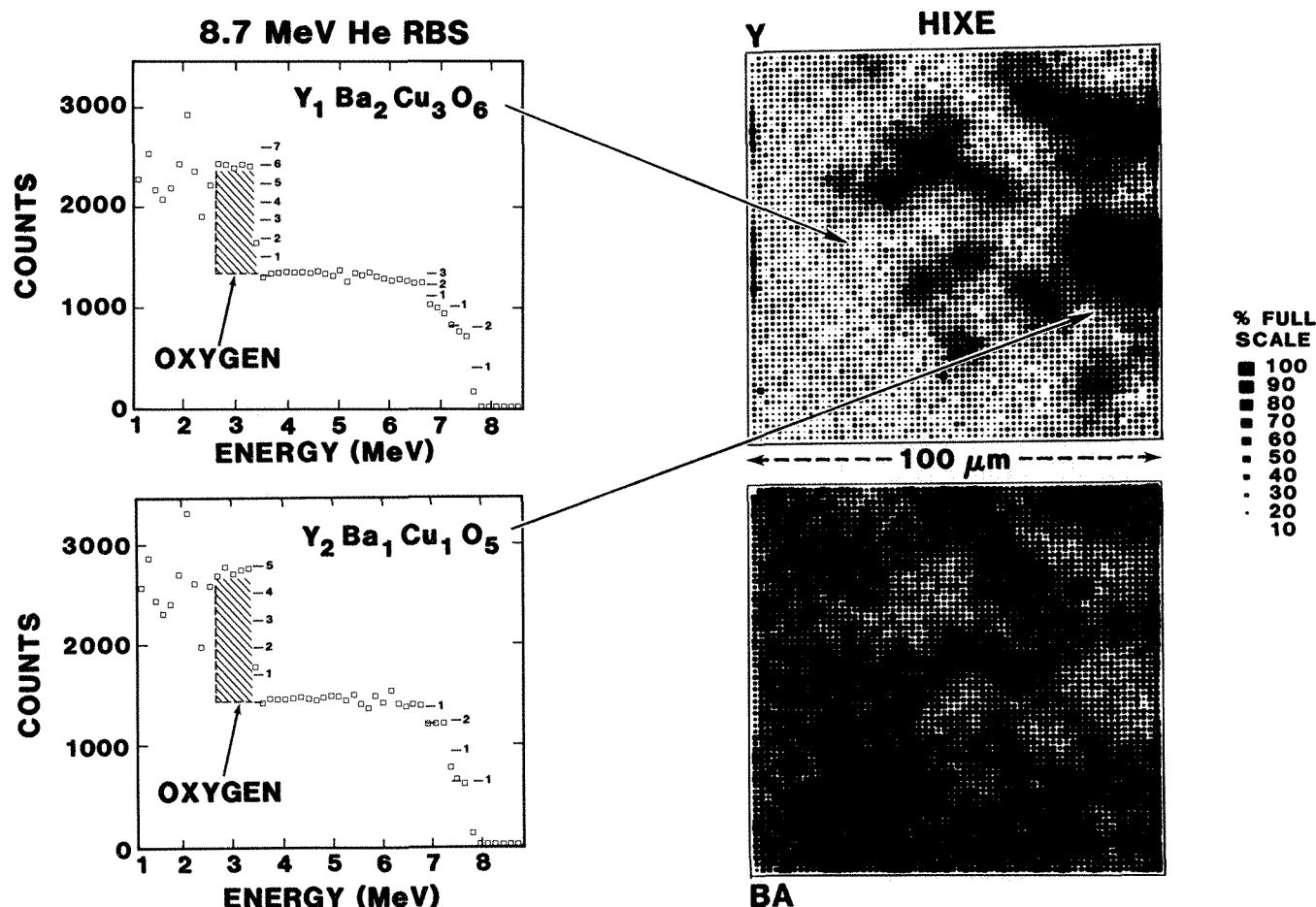


FIG. 1.--Both RBS and HIXE were used to obtain elemental maps of Y-Ba-Cu-O alloy. Gray scale for HIXE maps is such that dark region represents high intensity of x rays. RBS spectra were collected with 2 μ m-diameter beam from two regions (dark and light) indicated by arrows in the Y-HIXE map.

Superconductors

The dependence of superconductivity on the oxygen content in high-temperature superconducting (HTSC) alloys has stimulated new studies to measure oxygen concentrations from grain to grain in polycrystalline materials. The orthorhombic YBa₂Cu₃O_{7- δ} phase (1237 composition) has been identified⁴ as the superconducting phase with properties that are sensitive to the oxygen content; and weight-loss measurements⁵ have been used to determine the level of oxygen in homogeneous bulk samples (demonstrating a loss of superconductivity for $\delta > 0.5$). Further, SEM analyses in conjunction with energy-dispersive x-ray spectroscopy have been used to measure metal atom concentrations with high lateral resolution,⁶ but these SEM-based techniques do not yield information on oxygen. Therefore, we have used EBS, HIXE, and RBS in the nuclear microprobe to measure the uniformity of the oxygen and metal atom concentrations of a bulk Y-Ba-Cu-O alloy.

Laterally, nonuniform bulk samples were prepared by cooling a melt containing Y₂O₃, BaO,

and CuO. The melt was cooled in an oxygen ambient and analyzed, as-cooled, without an annealing treatment to form a homogeneous superconductor. A mixture of phases was observed at a magnification of 100 \times in an optical microscope. The sample was determined to be nonsuperconducting, but the presence of several phases suggested that small grains of 1237 material may be isolated within a matrix of non-superconducting alloy. A portion of the sample near the edge of the melt was analyzed by NMA to determine whether regions of material with the proper 1237 composition were present. A 2 μ m-diameter He beam, at an energy of 8.7 MeV (scattering angle of 167 $^\circ$), was used to analyze several areas of the sample; and in each area, the beam was rastered over a region 100 \times 100 μ m. Figure 1 is representative of the back-scattering and HIXE results from this sample. The HIXE maps (at right) show that the Y-rich regions (dark in the upper map) correspond to Ba-poor regions (light in the lower map). In comparison, the Cu x-ray signal and secondary-electron image showed little contrast over the same area. These HIXE maps also show that

the Y-rich grains range in size from 10 to 30 μm in diameter and are embedded in a Ba-rich matrix. Based on these elemental maps, the beam was positioned at a point and RBS spectra (shown at left) were collected in each region in order to determine the composition of the matrix and the embedded grains quantitatively.

Ion backscattering analysis has been described by Chu et al.⁷ for the case in which the ion-scattering cross section σ obeys the Rutherford cross-section formula σ_R to within a few percent. At 8.7 MeV, α scattering from Ba is Rutherford, but the oxygen scattering cross section is non-Rutherford. The yield for Rutherford scattering is greater for high-Z elements (e.g., Ba) than for low-Z elements (e.g., O), and the amount of backscattering decreases as the incident ion energy increases. Therefore, low energy (≤ 3.5 MeV α) RBS of superconductors is more accurate for measuring the heavy element concentrations than for measuring the oxygen content because the small O single (low σ_R for oxygen) sits on the large metal atom background. However, high-energy ion beams take advantage of the fact that the scattering cross sections for the heavy elements decrease as σ decreases, thereby yielding a lower background and better counting statistics for oxygen (greater accuracy). Reference 8 examined the use of EBS with a broad beam of 8.7 MeV He and determined that $\sigma(\text{oxygen})$ is 22 times greater than σ_R ; and therefore the oxygen content in a thin-film HTSC could be determined to within 2-3%.

The EBS technique given above was used in the present experiment to measure the oxygen content of the bulk sample with the 2 μm lateral resolution afforded NMA. The oxygen cross section was found to be enhanced over σ_R (oxygen) by a factor of 27 for the scattering geometry in this experiment. The following table summarizes the capabilities of EBS with 8.7 MeV α in the nuclear microprobe.

θ	167°	Depth resolution	50 nm
σ/σ_R (oxygen)	27	Lateral resolution	2 μm
Analysis range	1.7 μm	Sensitivity	$10^{21}/\text{cm}^3$

where θ is the backscattering angle and $\sigma/\sigma_R(\text{oxygen})$ is the cross-section ratio relative to Rutherford scattering. The analysis range is limited to a few microns because $\sigma(\text{oxygen})$ oscillates strongly with energy below 8.3 MeV, as reflected in the RBS spectra below 2.5 MeV. The shaded portions of the oxygen signals in Fig. 1 correspond to a depth of $\sim 1.7 \mu\text{m}$ in $\text{YBa}_2\text{Cu}_3\text{O}_7$. The depth resolution is determined from the energy resolution of the particle detector and the stopping power of α particle in an Y-Ba-Cu-O alloy. The accuracy of EBS given above is also applicable for NMA and yields a detectable variation in δ of $\Delta\delta = 0.3$ (where $7-\delta$ is the subscript for the 1237 composition).

Surface scattering energies E for the constituent atoms in the RBS spectra of Fig. 1 are 7.754, 7.282, 6.782, and 3.170 MeV. The signals from the Y, Cu, and O atoms appear at lower energies in the RBS spectra than the Ba signal, and overlap the Ba signal because the

sample is a bulk alloy. However, the Y and Ba signals are sufficiently separated so that the oxygen yield can be measured relative to the Ba yield alone. The equations from conventional backscattering spectrometry⁷ can then be applied to determine the oxygen content from $\sigma/\sigma_R = 27$, for oxygen. The concentration scales plotted next to the yield for each element are given in atoms per formula unit.

Results of NMA showed that the matrix and grains were uniform in composition in all three dimensions. The Ba-rich matrix had a composition of $\text{YBa}_2\text{Cu}_3\text{O}_6$, which is the composition for the nonsuperconducting tetragonal phase; and the Y-rich grains had a composition of Y_2BaCuO_5 , which is the composition for a semiconducting phase. Therefore, these results confirmed the absence of a superconducting phase in the as-cooled sample and showed that a post-melt oxygen anneal is necessary for superconductor formation. An NMA measurement of the matrix oxygen content proved critical to this evaluation.

Buried Tungsten Conductive Layers

Buried conductors in single-crystal Si wafers are of interest for metallization of three-dimensional device structures. Multi-level metallization may increase both device speed and radiation hardness. This work investigates a process in which a W layer was buried beneath an Si island through the use of low-pressure chemical vapor deposition (LPCVD).⁹ The W is selectively deposited in a porous Si layer beneath the island; the single-crystal island is left in an undamaged state, which is compatible with further processing to form microcircuits. The object of this work is to characterize a patterned Si wafer exposed to the tungsten LPCVD treatment, and in particular to characterize the extent of W deposition and reaction around the Si island. The samples were patterned in long strips of Si islands $\sim 50 \mu\text{m}$ wide and 9 μm apart. Nuclear microprobe analysis and scanning electron microscopy were used to determine the extent of the W deposition reaction and the crystalline quality of the Si islands.

Scanning electron microscopy, in conjunction with electron channeling, showed that the Si remaining in the island region was single crystalline with approximately the same orientation as the substrate Si. The W reaction begins between the islands, where the overlay was removed down to the buried porous Si layer, and proceeds from the edge toward the center of the islands. The extent of the W deposition was easily seen when the sample in the SEM was tilted to 70° in order to obtain a cross-sectional view. Figure 2 shows a back-scattered electron image of the sample in cross section. The buried W was deposited under the island leaving a small gap of porous Si centered below the island.

NMA (with both RBS and HIXE) was done to determine the extent of a silicide-forming

**8.7 MeV He⁺⁺
BACKSCATTERING**

3 μm PROBE

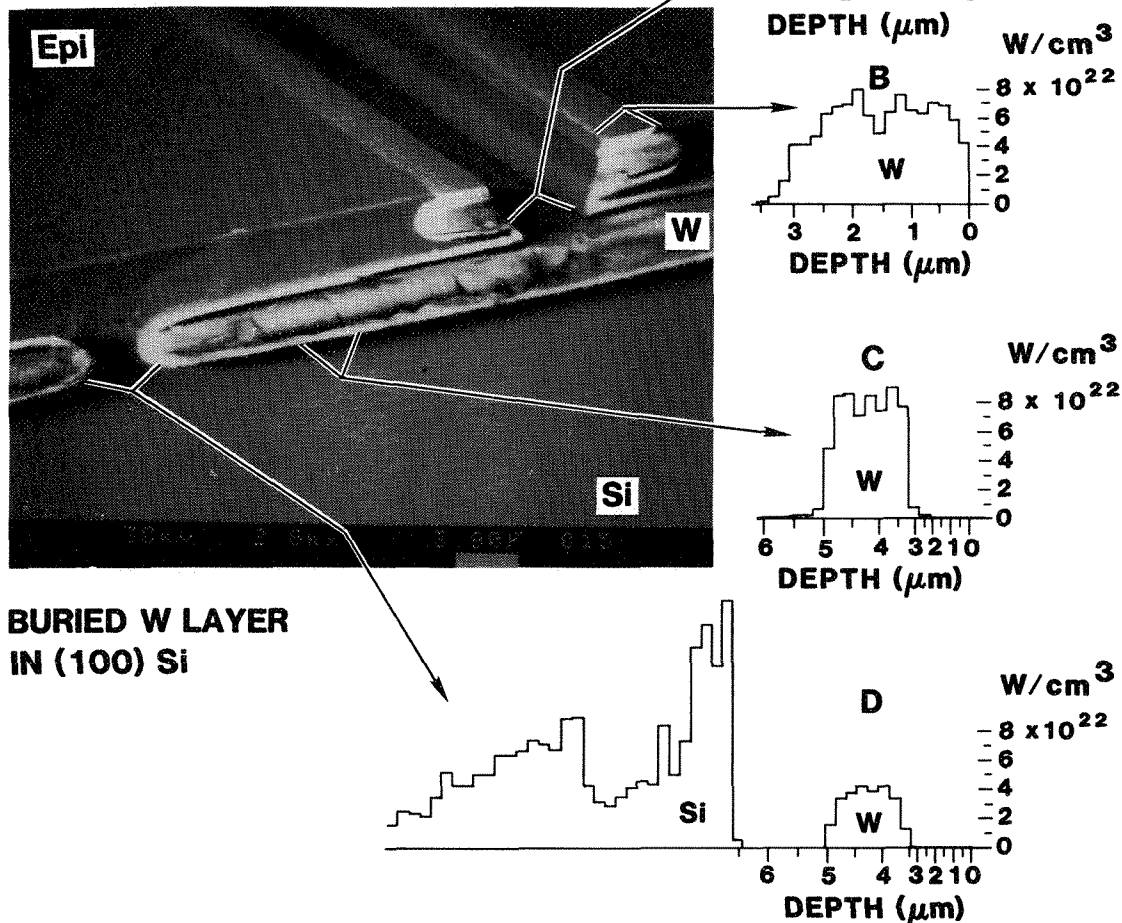


FIG. 2.--Backscattered electron image of edge of silicon wafer treated to form buried W layers beneath epitaxial (epi) Si islands. Sample was tilted 70° to obtain SEM image. Four depth scales shown at right were measured from RBS spectra collected in linescan across Si islands. Concentration of W is in atoms/ cm^3 . Zero for depth scale in A begins at W surface, which is $3 \mu\text{m}$ deeper than surface of Si island. Si profiles are shown only as reference for relative position of W and Si signals in RBS spectra. Oscillatory Si concentration as a function of depth results from non-Rutherford Si cross section, which was not deconvoluted from these profiles.

reaction between the Si in the islands and the deposited W. The RBS data were collected by scanning an 8.7 MeV He beam ($3 \mu\text{m}$ in diameter) in a line $100 \mu\text{m}$ long across the Si islands. The yield of backscattered ions vs energy was collected at each point along the scan and several spectra from each point were summed to improve statistics. The concentration vs depth, determined from the RBS spectra for four regions of the sample, is plotted in Fig. 2. These results indicate that the W reacts with the sides of the Si islands and forms a silicide. This silicide region is uniform and approximately $3 \mu\text{m}$ -thick on both sides of the is-

land. Further, the discontinuity in the buried W layer was found to be a $3 \mu\text{m}$ -wide region of unreacted porous Si beneath the center of the Si island. A study of the W deposition and silicide formation kinetics is planned by repetition of the NMA measurements for various times during the LPCVD process.

A comparison of the resolution limits for NMA- and SEM-based composition analysis shows that the nuclear microprobe yields both unique and complementary quantitative composition information. Current nuclear microprobes have a lateral resolution poorer by a factor of 10 than the lateral resolution in an SEM; but

SEM analyses have very limited depth resolution, whereas NMA has a depth resolution down to 10 nm for 2MeV ion scattering. The lack of depth resolution in the SEM is a particular problem in the analysis of layered samples in which the x-ray peaks of elements from different layers overlap (e.g., thin-film superconductors on SrTiO₃ substrates). The NMA yields a three-dimensional analysis of the composition in which the effects of the substrate can be easily separated from that of the thin film. Further, the nuclear microprobe is compatible with several techniques such as RBS, EBS, and ERD, which not only give compositional information on heavy elements (from the third row of the periodic table and above) but also give quantitative analyses on elements in the first two rows of the periodic table.

References

1. B. L. Doyle et al., *Microbeam Analysis--1981*, 79-81.
2. B. L. Doyle, *Microbeam Analysis--1986*, 15-21.
3. B. L. Doyle, *12th International Symposium on Applications of Ion-Beams in Materials Science*, Tokyo: Hosei University Press, 153, 1988.
4. R. Beyers, G. Lim, E. M. Engler, V. Y. Lee, M. L. Ramirez, R. J. Savoy, R. D. Jacowitz, T. M. Shaw, S. La Placa, R. Boehme, C. C. Tsuei, Sung I. Park, M. W. Shafer, and W. J. Gallagher, *Appl. Phys. Lett.* 51: 614, 1987.
5. H. U. Krebs and R. Wordenweber, *J. Appl. Phys.* 63: 1642, 1988.
6. J. A. Knapp, private communication.
7. W.-K. Chu, J. W. Mayer, and M.-A. Nicolet, *Backscattering Spectrometry*, New York: Academic Press, 1978, 21-218.
8. J. C. Barbour, B. L. Doyle, and S. M. Myers, *Phys. Rev. B* 38: 7005, 1988.
9. R. S. Blewer, S. S. Tsao, and G. M. Gutierrez, *Mat. Res. Soc. Symp. Proc.* 107: 287, 1988.

NOVEL APPLICATIONS OF THE FIELD ION MICROSCOPE AND ATOM PROBE

G. L. Kellogg

Introduced in 1951 and 1966 respectively, the field ion microscope¹ and atom-probe² mass spectrometer can hardly be considered new or emerging microprobes. Over the years, the ability to use these instruments to examine the structure and composition of various materials at the atomic level has been well established.³⁻¹² However, recent advances in more conventional microanalytical techniques, particularly progress toward a higher degree of spatial resolution, has created renewed interest in all techniques capable of analysis on a very fine scale. Also, there has been an increased emphasis over the past several years in the application of the field ion microscope and atom probe to problems of greater general interest in surface and materials science. It is therefore not totally inappropriate to discuss the field ion microscope and atom probe within the context of "emerging" microprobes. The intent of this paper is to familiarize the reader with the techniques of field ion microscopy and atom-probe mass spectroscopy and describe several recent applications that demonstrate some of their unique attributes.

Field Ion Microscopy

Conceptually, the field ion microscope is a very simple instrument. Shown schematically in Fig. 1, the microscope consists of a cryogenically cooled sample "tip" placed opposite a fluorescent screen in an ultrahigh-vacuum chamber. In addition, modern-day field ion microscopes almost always include a channel plate next to the fluorescent screen for image intensification (not shown in the figure). An image of the surface atoms at the apex of the tip is produced by the application of a high positive voltage (typically 5-20 kV) to the tip in the presence of an imaging gas such as He, Ne, or Ar. The extremely high electric field (of the order of tens of volts per nanometer) caused by the applied voltage ionizes the imaging gas atoms in a region directly above the protruding surface atoms. The positive ions formed in this process are accelerated away from the positively charged tip and travel to the screen, where they form image spots. Because the ions are created preferentially above the protruding surface atoms, the pattern of spots that appears on the fluorescent screen is a direct image of those atoms. The magnification of the field ion microscope, given roughly by the ratio of the tip-to-screen distance to

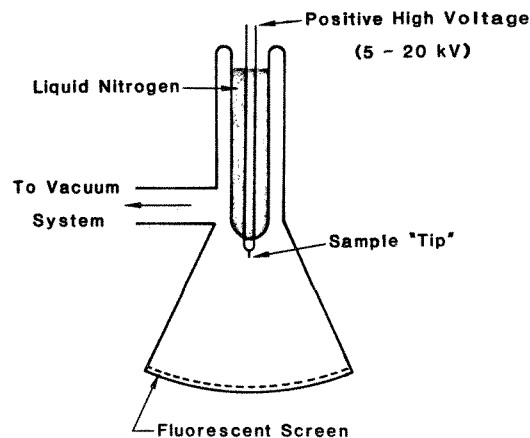


FIG. 1.--Schematic drawing of field ion microscope.

the tip radius, is of the order of several million. The resolution of the field ion microscope is a function of tip temperature and is sufficient to resolve individual atoms when the tip is at cryogenic temperatures.

Fig. 2 shows an example of a field-ion-microscope image taken from a rhodium sample. The dark, circular regions seen in the image correspond to the flat low-index planes of the surface. These regions are dark because the atoms within the plane do not protrude sufficiently to cause a local enhancement of the electric field. The rings of spots surrounding the dark regions correspond to the atoms at the edges of individual atomic layers. The smallest diameter ring corresponds to the edge of the topmost atomic layer and successively larger rings correspond to the edges of successively deeper atomic layers.

If the applied voltage to the tip is increased beyond that which produces a stable field-ion-microscope image, the electric field at the surface becomes high enough to ionize and remove the surface atoms themselves. This process is known as either field evaporation or field desorption.³⁻⁷ In the region of low-index planes, field evaporation removes the substrate atoms from the edge of the plane inward, one layer at a time. The field evaporation process is very useful as the final step of sample preparation before field-ion imaging because it produces a surface that is free of contaminants and is smooth on an atomic scale. Field evaporation is also routinely used to probe into the near-surface region of the tip to find structural defects that may not extend to the initial surface.

The author is at Sandia National Laboratories, Box 5800, Albuquerque, NM 87185. This work was supported by the U.S. Department of Energy under contract DE-AC04-76DP00789.

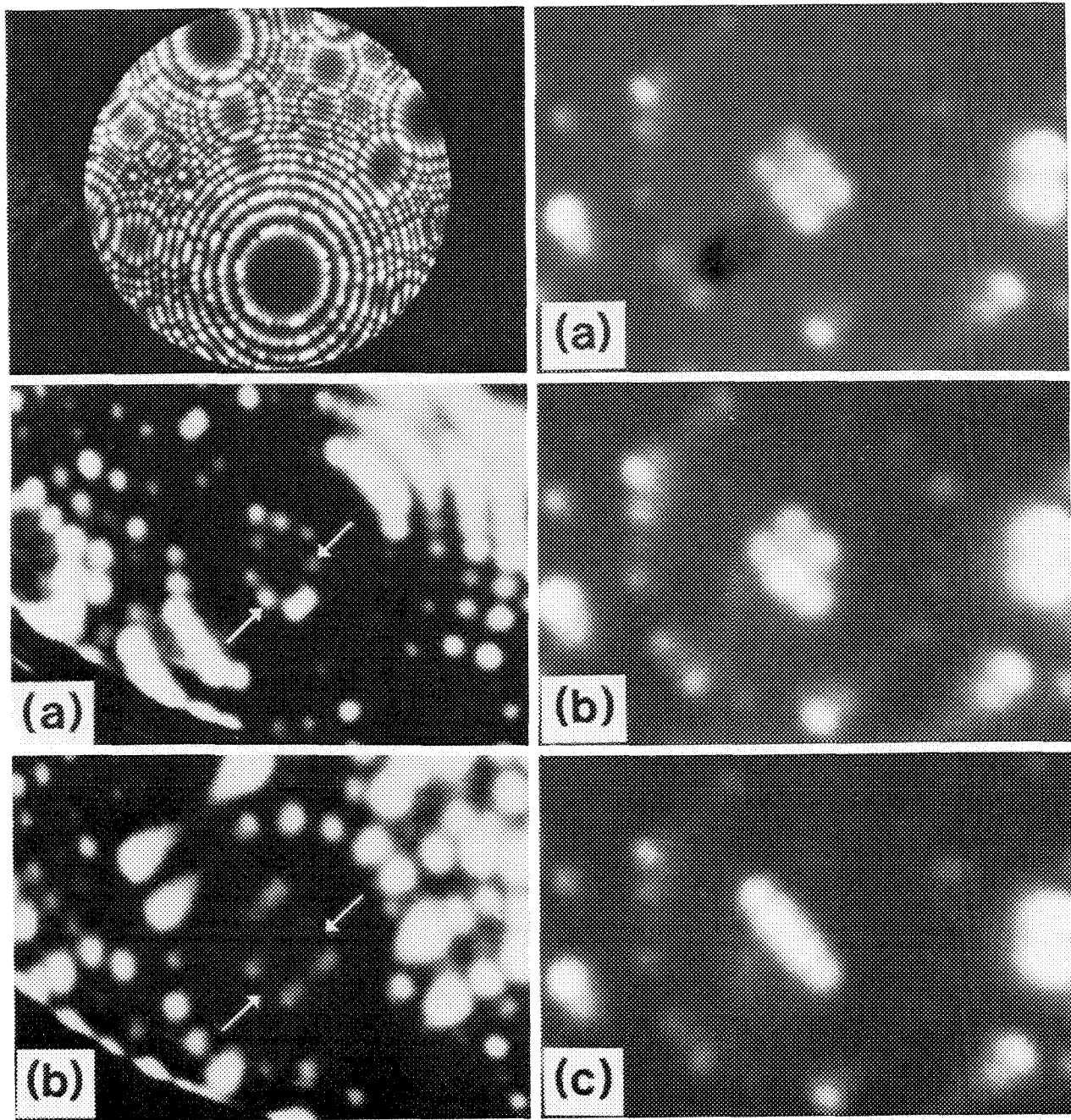


FIG. 2.--Helium field ion microscope image from Rh at 6.6 kV.

FIG. 3.--Field ion micrographs showing reconstruction of Pt(110): (a) unreconstructed surface, (b) reconstructed to missing-row structure (from Ref. 19).

FIG. 4.--Field ion micrographs showing the stability of Ir adatom clusters on Ir(100): (2) stable island of six atoms, (b) metastable island of five atoms produced by field evaporation of corner atom, (c) stable chain of five atoms produced by heating five-atom island (from Ref. 29).

As described later, the field ion microscope can be used in combination with the atom-probe mass spectrometer to gain information on the chemical composition as well as the atomic structure of the surface and near-surface region of a solid sample. However, even by itself, the field ion microscope continues to make contributions in various scientific disciplines. For example, one of its unique applications has been the investigation of the diffusion and interaction of individual surface

atoms. Pioneered by Ehrlich and co-workers¹³ these studies have provided quantitative diffusion parameters and interaction potentials for a variety of adsorbate-substrate systems.¹⁴⁻¹⁷ The field ion microscope has also made many significant contributions in metallurgy and materials science. For more information on these applications, the interested reader is referred to several review articles.⁸⁻¹¹

In this report two examples of applications

to surface science are described. The first involves the reconstruction of clean metal surfaces. It has been well established by low energy electron diffraction (LEED), ion scattering, and other techniques that the atomic structure of a single-crystal surface may differ from a simple termination of the bulk structure.¹⁸ Yet the detailed arrangement of surface atoms is often difficult to discern from these techniques. An example is the (110) surfaces of Pt, Ir, and Au. The (110) surface of these fcc materials consists of close-packed rows of atoms aligned along the [110] direction. Investigations by LEED have shown very clearly that the atoms in the topmost (110) layer of Pt, Ir, and Au are rearranged with respect to the bulk and have a (1x2) periodicity.¹⁸ This periodicity means that atoms along the rows have the same atomic spacing as atoms in the bulk, but the spacing between rows is twice that of the bulk. In the particular case of Pt, although all investigators agree on the (1x2) periodicity, there has been considerable controversy over the exact atomic arrangement giving rise to this periodicity.¹⁸

As indicated in Fig. 3, investigations with the field ion microscope have shown unambiguously that the (1x2) periodicity of the reconstructed Pt(110) surface is due to alternate missing rows of atoms.¹⁹ Figure 3(a) shows an image of a field-evaporated Pt surface in the vicinity of the (110) plane. The arrows indicate the direction of one of the close-packed rows of atoms in the topmost (110) layer. From the edge atoms of the underlying layer it is possible to determine that the rows of atoms in this field-evaporated surface lie in adjacent channels of the next layer down; i.e., the surface is not reconstructed. The ability to produce atomically perfect, unreconstructed surfaces by low-temperature field evaporation is a particularly useful feature of the field ion microscope for the investigation of surface reconstructions at the atomic level. Figure 3(b) shows an image of the same surface after it had been heated to 350 K for 1 min. During the heating interval the applied voltage was turned off to avoid any influence of the electric field on the reconstruction process. Careful analysis of this image along with slow field evaporation of the topmost layer indicate that the rows of atoms in Fig. 3(b) are in every other channel of the underlying surface. The arrows point to an empty channel that was occupied by a row of atoms prior to the reconstruction. The arrangement of atoms in Fig. 3(b) corresponds to the so-called "missing-row" structure, which is now the accepted structure for Pt(110)(1x2). In similar experiments it was shown that the missing-row structure could be produced for as few as five atoms in the topmost layer, which shows that the reconstruction is driven by short-ranged atomic interactions.¹⁹ These types of investigations have now been extended to other reconstructed surfaces of Pt and Ir.²⁰⁻²² It has also been demonstrated that the field ion microscope can be used to investigate reconstructions of some

of the higher index planes of Si²³ as well as adsorbate-induced reconstruction on Ni.²⁴

The second application of the field ion microscope discussed in this paper involves the nucleation of clusters on atomically perfect metal surfaces. Despite the fact that classical theories²⁵ of crystal growth either predict or assume that the growth of new atomic layers begins with a two-dimensional cluster nucleus, past observations with the field ion microscope have identified metal-metal overlayer systems in which the initial nucleus is a linear chain.²⁶⁻²⁸ These chain nuclei are typically stable for clusters up to a critical number of atoms, beyond which two-dimensional islands are stable. On a W(110) substrate the critical number for Ni atoms is four, for Pd it is eight, for Ir it is approximately twelve, and for Pt stable chains of up to 24 atoms have been observed. It had been assumed that the asymmetry of the W(110) surface structure or the difference in the size of the adsorbate atoms compared to the substrate atoms influenced the formation of the stable chain structures.

In more recent work it has been shown that chain nuclei can also occur in homogeneous nucleation on symmetric substrates.^{29,30} For example, field ion microscope images of Ir atoms on an Ir(100) surface have shown directly that chain configurations are stable for five or fewer atoms and two-dimensional island configurations are stable for six or more atoms.²⁹ Photographs that illustrate this interesting phenomenon are shown in Fig. 4. Figure 4(a) shows the topmost layer of atoms on an Ir(100) surface after it had been field evaporated such that just six atoms remain. The six Ir atoms are arranged in a rectangular configuration that reflects the symmetry of the fcc(100) surface. The rectangular configuration is stable upon heating up to temperature of 460 K. Above this temperature the island dissociates and the atoms migrate off the topmost plane. Figure 4(b) shows the same cluster with one of the corner atoms removed by field evaporation. When this atomic cluster is heated to 450 K, the five atoms transform irreversibly to the linear chain shown in Fig. 4(c). This chain configuration is stable and does not transform back to the island with additional heating. However, if a sixth atom is added to the surface (from an external deposition source) and allowed to migrate to the end of the chain, the six-atom chain readily transforms back to a two-dimensional configuration.²⁹ These experiments clearly demonstrate the stability of five-atom chains and six-atom islands. Additional experiments demonstrate the stability of three- and four-atom chains and islands larger than six atoms. The stability of these atomic clusters is now being used to determine the relative strengths of adatom-adatom bonds on single-crystal surfaces. Models based on a two-dimensional lattice gas indicate that interactions extending to second-nearest neighbors are required for the chain nuclei to

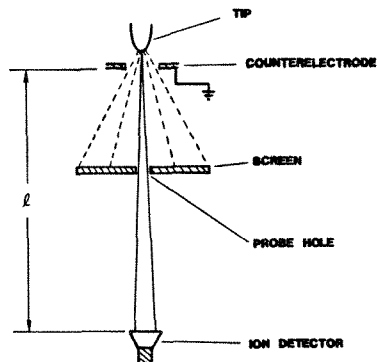


FIG. 5.--Schematic drawing of probe-hole atom-probe field ion microscope.

occur, which suggests the presence of relatively long-ranged interactions in cluster nucleation on this surface.³¹

In similar investigations it has been shown that Pt adatom clusters on the Pt(100) surface actually oscillate between stable chain and island structures as the number of atoms is increased from two to six: i.e., chain configurations are stable for three and five atoms, whereas island configurations are stable for four, six, and more atoms.³⁰ The stability of these structures is predicted by calculations based on the Embedded Atom Method if lattice relaxations are included in the model. The calculations point to the strong repulsive interaction between atoms at the next-nearest separation and the surprisingly large four-body attractive interaction as the interactions that are responsible for driving these unusual oscillations.

Atom-probe Mass Spectroscopy

The field ion microscope is primarily a probe of atomic structure. Chemical identification of species on the surface of a field ion tip became possible with the introduction of the atom-probe field ion microscope² or atom-probe, for short. This instrument combines a conventional field ion microscope with a sensitive time-of-flight mass spectrometer. In the most commonly used design (Fig. 5), a small hole is placed in the viewing screen of a field ion microscope, and a detector sensitive to the impact of individual ions is placed at the end of a drift tube positioned behind the probe hole. The tip is externally adjusted to align an atom or group of atoms of interest with the probe hole. Surface atoms are removed (field evaporated) as positive ions by the application of a short-duration (10-100ns), high-voltage (0.5-3kV) pulse superimposed on the dc imaging voltage. The ions of interest travel through the probe hole to the detector. From the measured flight time of the ions and the known

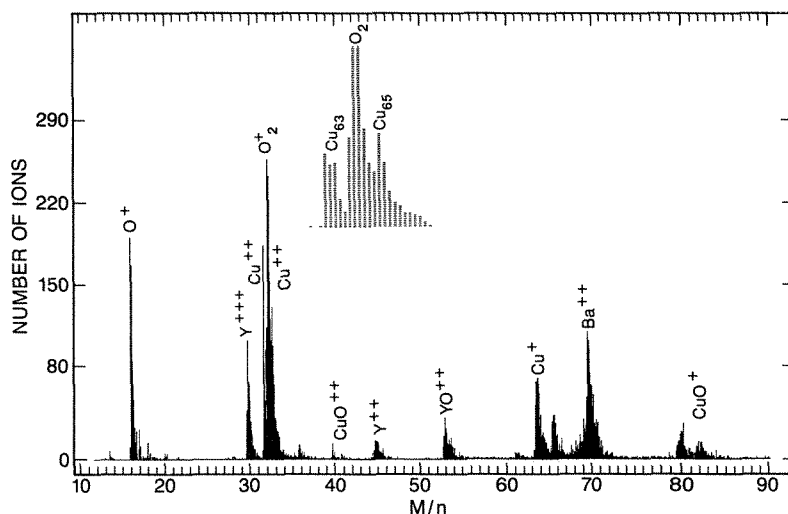


FIG. 6.--Histogram of field evaporated ions from sample of $\text{YBa}_2\text{Cu}_3\text{O}_{7-x}$ (from Ref. 32).

length of the drift tube it is a simple calculation to determine the mass-to-charge ratio of the field evaporated ions. If the tip is pulsed repetitively with the probe-hole over a given area of the surface, the chemical composition of a small volume of the sample can be determined. It is common to plot out the compositions as histograms of field-evaporated species. An example of such a histogram from a sample of $\text{YBa}_2\text{Cu}_3\text{O}_{7-x}$ is shown in Fig. 6 (from Ref. 32). Because chemical analysis in the atom probe can be made specific to a given region (e.g., near an extended defect), the probe-hole type of atom probe is well suited for the investigations of metallurgical problems such as impurity segregation to grain boundaries and other defects.⁸⁻¹¹ A significant increase in mass resolution can be achieved with the use of an energy-focusing lens in place of the straight drift tube.³⁵ The isotopes of all commonly studied materials can be resolved with the energy-focused atom probe.

One disadvantage of the probe-hole atom probe is that the majority of species which are field evaporated from the surface do not pass through the probe-hole and are not detected. Studies of surface adsorption and reaction processes may therefore require many cycles of dosing and desorption to obtain statistically significant surface compositions. This problem can be addressed with a different type of atom probe known as the imaging atom probe.³⁴ A schematic diagram of the imaging atom probe is shown in Fig. 7. In this instrument the viewing screen of the field ion microscope is an imaging detector sensitive to the impact of single ions. Each ion that strikes the front surface of the detector produces a current pulse which is amplified and displayed on the sweep of a fast-waveform digitizer. The detector also displays an image spot at the position of ion impact. Surface species field desorbed from anywhere on the imaged portion

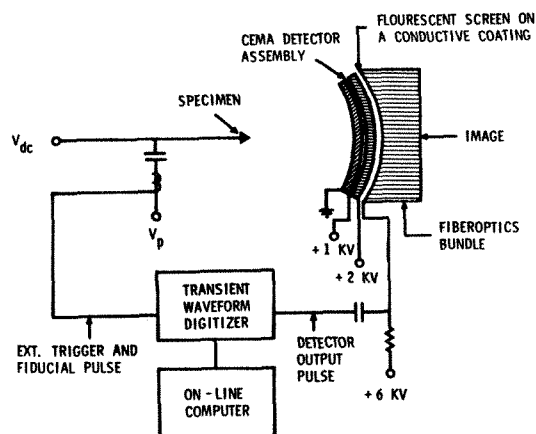


FIG. 7.--Schematic drawing of imaging atom probe.

of the surface are detected and identified by their flight times. Although the increased signal makes the imaging atom probe better suited to the study of surface adsorption processes, its shorter flight path results in significantly poorer mass resolution. An additional feature of the imaging atom probe is the ability to obtain elemental maps of selected surface species.³⁴ These maps are obtained by switching on of the detector during the arrival time of a given species. The transient image of spots appearing on the detector, which corresponds to the selected species only, can be photographically recorded. The "time-gated" image can then be superimposed on a field-ion image taken with the same detector at reduced gain to determine where on the surface the selected species originated.

Another type of atom probe, known as the pulsed-laser atom probe,^{35,36} has greatly facilitated atom-probe investigations of semiconductors and insulators. In the pulsed-laser atom-probe a short-duration (0.1-10ns) laser pulse is applied to a tip which is simultaneously subjected to a dc applied voltage. The combination of the thermal stimulation produced by the laser pulse and the high electric field provided by the applied voltage initiates field desorption. Time-of-flight mass analysis is carried out the same way as in either the probe-hole or imaging atom probe. The use of laser pulses permits analysis of high-resistivity materials that do not transmit the high-voltage electrical pulses. Elimination of the high-voltage pulses also leads to a significant improvement in mass resolution. In addition, it has also been shown that the pulsed-laser atom probe is useful for the investigation of a variety of surface reaction and desorption phenomena. A recent review of the pulsed-laser atom probe can be found in the literature.³⁷

The atom-probe field ion microscope has been applied to a variety of problems in a wide range of scientific disciplines. Discussions of these applications can be found in a number of review

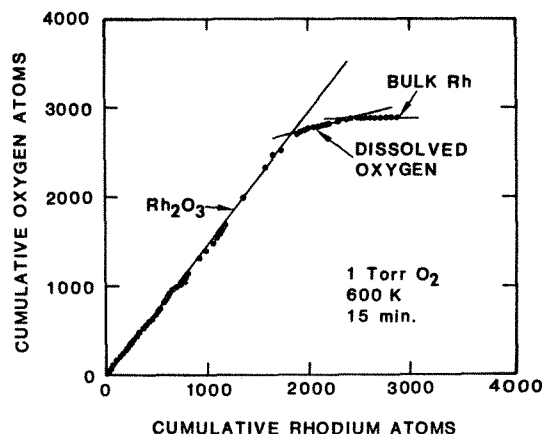


FIG. 8.--Cumulative plot of field desorbed oxygen atoms vs field-desorbed rhodium atoms. Slope of plot identified chemical form of oxide (from Ref. 38).

articles.⁶⁻¹² Here, an example of how the atom probe has been applied to the study of surface oxide formation is provided to illustrate the quantitative nature of the chemical analysis that can be performed. The formation of thin metal oxides is of considerable interest in research areas such as corrosion, catalysis, and adhesion. Metal oxides have also become important in microelectronics, where a need for very thin insulating materials has developed. Crucial to the characterization of thin metal oxides is the ability to determine the composition of the film from the surface through the metal-oxide interface. In the example presented here it is shown that this type of characterization is possible with the atom probe.

The metal substrate used in this study was rhodium.³⁸ The choice of rhodium was motivated by its well-known catalytic properties and the influence of surface oxides on the catalytic activity.³⁹ The experimental apparatus consisted of two UHV chambers: a reaction chamber, in which the rhodium tips were oxidized; and an analysis chamber, in which field ion microscopy and imaging atom-probe mass spectroscopy were carried out. A rhodium tip was first introduced into the analysis chamber and its surface was cleaned by neon ion bombardment and dc field evaporation. The atomic structure of the surface was examined by field ion microscopy. The sample tip was then transferred under ultrahigh vacuum to the reaction chamber where it was oxidized in 1 Torr O₂ at 600 K for 15 min. The oxygen was removed from the reaction chamber and the tip was returned to the analysis chamber without exposure to air.

The composition of the oxide was examined in the analysis chamber. The oxide layer was removed by pulsed-voltage field evaporation and the desorbed species were mass analyzed. The primary species detected in the mass scans

were atomic and molecular oxygen, water, and various charge states of rhodium and rhodium oxide. Oxide film was removed at a rate of about one layer per pulse with a total of 50-70 pulses used to remove the entire film. For these studies only a small region of the surface was probed for a better examination of the metal-oxide interface. This examination was accomplished by positioning of a disk with a small aperture in front of the tip during analysis. The chemical composition of the oxide was obtained from a plot of the cumulative number of oxygen atoms detected vs the cumulative number of rhodium atoms.

An example of such a cumulative plot is shown in Fig. 8. It is obvious from the graph that there are three distinct slopes in the plot. The initial slope is $3/2$, which shows that the outer oxide is stoichiometric Rh_2O_3 . This is the stable form of rhodium below 1023 K and has the corundum structure.⁴⁰ The thickness of the oxide film is estimated to be of the order of 50-60 layers. The next region has a slope that varies from 0.3 to 0.5. This slope does not correspond to any expected suboxide and varies somewhat from experiment to experiment. Most likely the region contains a mixture of suboxides and dissolved oxygen and is thus labeled "dissolved oxygen." The thickness of the transition region is 5-15 Rh layers. The third region of the plot has slope 0 and corresponds to bulk Rh.

The results of the above investigation showed quite explicitly that thin oxide films grown on Rh at elevated temperatures consist of a single phase of Rh_2O_3 . Moreover, it was discovered that the transition region from this oxide to the metal substrate is very narrow, extending only a few atomic layers. This type of experiment clearly demonstrates that detailed information on the composition of thin oxide films can be obtained in controlled studies with the atom probe. In additional studies it was shown that the growth law, the activation energy for oxygen uptake, and the conditions under which the Rh oxide layer could be removed by CO reduction can also be obtained in studies with the imaging atom probe.⁴¹ Similar experimental methods have been used to investigate oxide growth on other metal surfaces with atom-probe techniques.^{9,43-45}

Summary

The unique attributes of the field ion microscope and atom-probe mass spectrometer permit structural and chemical analysis at the atomic level. In this paper a brief overview of the operating principles for the two instruments was given. In addition, three specific examples, which illustrate the type of analysis possible with the techniques, were discussed. These examples were chosen primarily based on the author's recent research interests. Many other applications, which emphasize other novel aspects of the field ion microscope and atom probe, are reviewed in the literature.³⁻¹²

References

1. E. W. Müller, *Z. Physik* 131: 136, 1951.
2. E. W. Müller, J. A. Panitz, and S. B. McLane Jr., *Rev. Sci. Instrum.* 39: 83, 1968.
3. J. J. Hren and S. Ranganathan, Eds., *Field Ion Microscopy*, New York: Plenum, 1968.
4. E. W. Müller and T. T. Tsong, *Field Ion Microscopy, Principles and Applications*, New York: Elsevier, 1969.
5. K. M. Bowkett and D. A. Smith, *Field Ion Microscopy*, Amsterdam-London: North Holland, 1970.
6. E. W. Müller and T. T. Tsong, "Field ion microscopy, field ionization, and field evaporation," in S. Davison, Ed., *Progress in Surface Science*, New York: Pergamon, 1973, vol. 1, part 4.
7. J. A. Panitz, *J. Phys.* E15: 1281, 1982.
8. S. S. Brenner, *Surface Sci.* 70: 427, 1978.
9. B. Ralph, S. A. Hill, M. J. Southon, M. P. Thomas, and A. R. Waugh, *Ultramicroscopy* 8: 361, 1982.
10. G. D. W. Smith, "Field ion microscopy and atom-probe microanalysis," in R. E. Whan, Ed., *Metals Handbook*, Metals Park, Ohio: Am. Soc. for Metals, 1986, 583.
11. M. K. Miller, *Materials Rev.* 32: 221, 1987.
12. T. T. Tsong, *Surface Sci. Reports* 8: 127, 1988.
13. G. Ehrlich and F. G. Hudda, *J. Chem. Phys.* 44: 1039, 1966.
14. G. L. Kellogg, T. T. Tsong, and P. L. Cowan, *Surface Sci.* 70: 485, 1978.
15. T. T. Tsong and P. L. Cowan, *CRC Crit. Rev. Solid State Mater. Sci.* 7: 289, 1978.
16. G. Ehrlich and K. Stolt, *Ann. Rev. Phys. Chem.* 31: 603, 1980.
17. D. W. Bassett, "Observing surface diffusion at the atomic level," in V. T. Binh, Ed., *Surface Mobilities on Solid Materials*, New York: 1983, 63.
18. P. J. Estrup, "Reconstruction of metal surfaces," in R. Vanselow and R. Howe, Eds., *Chemistry and Physics of Solid Surfaces*, Berlin: Springer-Verlag, 1984, vol. 5, 205.
19. G. L. Kellogg, *Phys. Rev. Lett.* 55: 2168, 1985.
20. J. Witt and K. Müller, *Phys. Rev. Lett.* 57: 1153, 1986.
21. Q. Gao and T. T. Tsong, *Phys. Rev.* B36: 2547, 1987.
22. G. L. Kellogg, *J. Vac. Sci. Technol.* A5: 747, 1987.
23. H. Liu, T. T. Tsong, and Y. Liou, *Phys. Rev. Lett.* 58: 1535, 1987.
24. G. L. Kellogg, *Phys. Rev.* B37: 4288, 1988.
25. J. P. Hirth and G. M. Pound, "Condensation and evaporation, nucleation and growth kinetics," in *Progress in Materials Science*, New York: Pergamon, 1963, vol. 2.
26. D. W. Bassett, *Thin Solid Films* 48: 237, 1978.
27. H. W. Fink and G. Ehrlich, *Surface Sci.* 110: L611, 1981.

28. P. R. Schwoebel and G. L. Kellogg, *Phys. Rev.* B38: 5326, 1988.
29. P. R. Schwoebel and G. L. Kellogg, *Phys. Rev. Lett.* 61: 578, 1988.
30. P. R. Schwoebel, S. M. Foiles, C. L. Bisson, and G. L. Kellogg, *Phys. Rev. Lett.* (submitted).
31. P. R. Schwoebel, P. J. Feibelman, and R. L. Schwoebel, *Surface Sci* (submitted).
32. S. S. Brenner and G. L. Kellogg, *Proc. MRS Symp. High- T_c Superconductors*, Boston, 1987.
33. E. W. Müller and S. V. Krishnaswami, *Rev. Sci. Instrum.* 45: 1053, 1974.
34. J. A. Panitz, *Rev. Sci. Instrum.* 44: 1043, 1973.
35. G. L. Kellogg and T. T. Tsong, *J. Appl. Phys.* 51: 1184, 1980.
36. W. Drachsel, S. Nishigaki, and J. H. Block, *Int. J. Mass Spectrom. Ion Phys.* 32: 333, 1980.
37. G. L. Kellogg, *J. Phys. E: Sci. Instrum.* 20: 125, 1987.
38. G. L. Kellogg, *Appl. Phys. Lett.* 51: 100, 1987.
39. G. L. Kellogg, *J. Catal.* 92: 167, 1985.
40. J. M. D. Coey, *Acta Crystallogr. Sec. B* 26: 1876, 1970.
41. G. L. Kellogg, *Surface Sci.* 171: 359, 1986.
42. Y. S. Ng, S. B. McLane Jr., and T. T. Tsong, *J. Appl. Phys.* 49: 2517, 1978.
43. G. K. L. Cranstoun, D. R. Pyke, and G. D. W. Smith, *Appl. Surface Sci.* 2: 375, 1979.
44. K. Hono, T. Sakurai, and H. W. Pickering, *J. de Physique* (Paris), Colloque C6, 48: 505, 1987.
45. Z. G. Liu, Y. Chen, and X. Z. Wen, *Surface Sci.* 208: L15, 1989.

QUANTITATIVE EPMA OF OXYGEN

G. F. Bastin and H. J. M. Heijligers

It has been demonstrated on several occasions¹⁻⁴ that quantitative analysis of ultraviolet elements like B and C is possible with surprisingly high accuracy, provided that the effects of peak shifts and certainly those of peak shape alterations are taken into account. The latter effects require in principle that the intensity measurements are carried out in an integral fashion, which is of course a very time-consuming process for a wavelength-dispersive spectrometer. We have shown before that the measuring efforts can be considerably reduced by the introduction of the Area-Peak Factor (APF) concept. This approach requires the one-time accurate determination of the ratio between the (true) area (or integral) k-ratio and the peak k-ratio for a specific compound relative to the selected standard. Once such an APF is available, subsequent measurements can quickly be carried out on the peak again and the peak intensity ratio can be easily converted into the correct integral k-ratio by multiplication by the APF.

The acquisition of accurate integral k-ratios is one thing; their conversion into correct concentrations is another. This procedure depends not only strongly on the quality of the particular matrix correction program used but equally strongly on the quality of the mass absorption coefficients (mac's) the program has to work with. Therefore, our research efforts in the past in the field of ultraviolet element analysis have been aimed at setting up large databases of light-element k-ratios on which various current correction programs could be tested in conjunction with various sets of mac's. In the light of the recent developments in matrix correction programs,⁵⁻⁷ as a result of which the performances of these programs approach each other more and more closely, the former aspect has perhaps lost some of its original weight. Nevertheless it is still of the greatest importance to have such databases available in order to test the correctness and consistency of the various sets of mac's published in literature. Another sometimes overlooked problem can be the occurrence of systematic anomalies in x-ray emission⁸; these cases too can only be discovered by large series of measurements.

In the present paper we give some preliminary results of our work on oxygen, performed on more than 30 oxides at accelerating voltages between 4 and 40 kV. To avoid the problems associated with a lack of electrical conductivity

and the inherent use of conductive coatings only oxides exhibiting sufficient conductivity were selected; hence, no coatings had to be applied at all. A database of more than 300 measurements was collected and our own program PROZA⁷ proved highly successful: an average value of $k_{\text{calc}}/k_{\text{meas}}$ of 0.999 and a relative root-mean-square error of less than 2.5%

Experimental

The microprobe used was an automated JEOL 733 Superprobe equipped with four wavelength-dispersive spectrometers and an EDX-system (TRACOR Northern TN-2000). The automation system was also supplied by TRACOR Northern (TN-1310). One spectrometer contained a conventional lead-stearate crystal ($2d \approx 100 \text{ \AA}$) with which the elements B through O can be measured; another spectrometer contained two synthetic multilayer crystals both supplied by Ovonic Synthetic Materials Co. (USA). One of the latter crystals (W-Si multilayer, $2d = 59.8 \text{ \AA}$) has been used in the past few years with great success in our laboratory for accurate analysis of N and O, giving strongly improved peak count rates and usually strong suppression of higher-order reflections. The other multilayer (Mo/B4C, $2d = 144.8 \text{ \AA}$) shows a very much improved performance for B and Be.

The oxygen measurements were carried out relative to a natural hematite (Fe_2O_3) standard which was found to exhibit sufficient electrical conductivity over the full range (4-40 kV) of accelerating voltages. The test on electrical conductivity of the oxide specimens was carried out by measurement of the value of the short-wavelength cutoff in the EDX spectrum over the full range in accelerating voltages.

Integral O K α spectra, necessary for the determination of the APFs, were recorded using the stearate (STE) as well as the W-Si multilayer (LDE) crystal simultaneously at an accelerating voltage of 10 kV and a beam current of 50 nA. The spectrometers were instructed to scan the wavelength range of the O K α peak in small steps, acquiring 10 s counts after each step, after which the number of counts were stored in successive channels of the multichannel analyzer of the EDX system. After completion of the spectra they were stored on floppy disk, to be processed later on. A particular problem was the determination of the background of the O K α peak on the left-hand (short-wavelength) side for the STE crystal. Due to the proximity of a mechanical limit of the spectrometer it proved to be virtually impossible to start sufficiently far away from the maximum in the peak. Therefore, the

The authors are at the Laboratory for Physical Chemistry - Centre for Technical Ceramics, University of Technology, P.O. Box 513, NL-5600 MB Eindhoven, The Netherlands.

measurements on the STE crystal have not been included in the final database.

Once the APFs were determined, large series of peak k-ratios for oxygen were measured and were subsequently converted into integral k-ratios by multiplication with the appropriate APFs

Results

It was soon discovered that the effects of peak shape alterations, expressed in the deviations of APFs from unity, which can be very large indeed for B K α and C K α ,^{1,8} were much less serious for O K α , at least when the LDE crystal was used. The APF values for the STE crystal were usually slightly more extreme as a result of the better spectral resolution of this crystal as compared to that of LDE. However, due to the problems with the background determination mentioned before, the results of the STE crystal must be considered less reliable. Table 1 shows a small selection of APFs for O K α radiation measured with LDE relative to Fe₂O₃. It is evident that the effects of peak shape alterations are small indeed and in many cases we investigated so far they could almost safely be ignored altogether. An exception here is B₂O, in which the O K α peak is the broadest observed until now. To some extent the magnitude of the APFs depends of course on the selection of the standard; apparently the O K α peak emitted from Fe₂O₃ has an "average" width resulting in APFs for the other oxides of either 1-2.5% above or below unity.

The superior performance of the LDE crystal is clearly visible in Fig. 1. The peak count rates are 2.5-3 times higher and the suppression of the second-order Zn L α line is evident. On top of that the background determination is much easier with the LDE crystal because the smaller 2d spacing of 59.8 Å produces a shift in the O K α peak position toward the middle of the mechanical range of the spectrometer. On the other hand, the better spectral resolution of the STE crystal becomes immediately apparent in the asymmetry of the O K α peak, which reveals signs of an additional component on the short-wavelength side of the peak that cannot be discerned by the LDE crystal. Strange as it may seem, the latter effect must be considered as an advantage in ultralight element analysis because it leads to APFs closer to unity.

TABLE 1.--Area-peak factors for O K α radiation in some oxides relative to an Fe₂O₃ standard; LDE crystal.

Oxide	APF
B ₂ O	1.063
TiO ₂	0.980
Cr ₂ O ₃	0.993
NiO	1.015
Nb ₂ O ₅	0.984
RuO ₂	1.011
SnO ₂	0.974

Once the APFs were established large series of peak intensity ratio measurements were carried out (with LDE exclusively) between 4 and 40 kV and the results were converted into integral k-ratios by multiplication by the APFs. Figure 2 shows two typical examples of such measurements for RuO₂ and SnO₂, which both constitute cases of very heavy absorption for O K α x rays. For RuO₂ excellent agreement is obtained between the calculations (solid curve) of our latest correction program (PROZA⁷) and the actual measurements. In this case Henke et al.'s⁹ mac of 19 700 for O K α in Ru was used, apparently with success over the full range of voltages. For SnO₂, on the other hand, the use of Henke et al.'s value of 23 100 for O K α in Sn led to an extreme discrepancy between calculations (open squares in Fig. 2) and measurements. Since the elements Ru and Sn are rather close in the periodic system, it is impossible that any correction program could produce such a discrepancy; hence, it is more likely that something is wrong with physical numbers such as the mac's. A series of calculations in which the mac was decreased from 23 100, which produced an average value of 0.675 for k_{calc}/k_{meas} and a relative rms value of 7.01% for this set of 11 measurements, down to 15 050 showed that this latter value led at the same time to a much better k'/k ratio of 0.997 as well as an improved rms figure of 3.25% (see also Fig. 2).

Apparently the equations used in the literature for the calculations of mac's have in this case been extrapolated over the M5 absorption edge of Sn. By the way, this is a nice example of the benefits of having large data sets available because such adjustments can never reliably be made through one solitary measurement. Similar tests with all other oxides showed that in general Henke's⁹ latest mac's for O K α x rays were quite satisfactory with a few exceptions. Apart from Sn, mentioned before, major adjustments were found necessary for elements such as Zr, Nb, and Mo. Our optimized mac's are between Henke's latest values (1982) and his previous¹⁰ ones and in fact much closer to the older ones. Quite similar observations were made for B K α and C K α x rays in these metals.^{3,4,8} Apparently the proximity of the M5 edge leads to great difficulties in establishing the correct mac's. It is obvious, though, that the use of a good matrix correction program, like several that are available nowadays, when applied to a well-measured set of consistent k-ratios, provides an elegant procedure for establishing consistent sets of mac's.

As stated in the introduction an average value for k'/k of 0.999 and a relative rms figure of less than 2.5% was finally obtained on the complete database containing more than 300 measurements. Considering the fact that the measurements were carried out over a very wide range in accelerating voltages ranging from as low as 4 kV up to as high as 40 kV, these results can be called remarkable. In fact they are quite comparable to the numbers quoted for

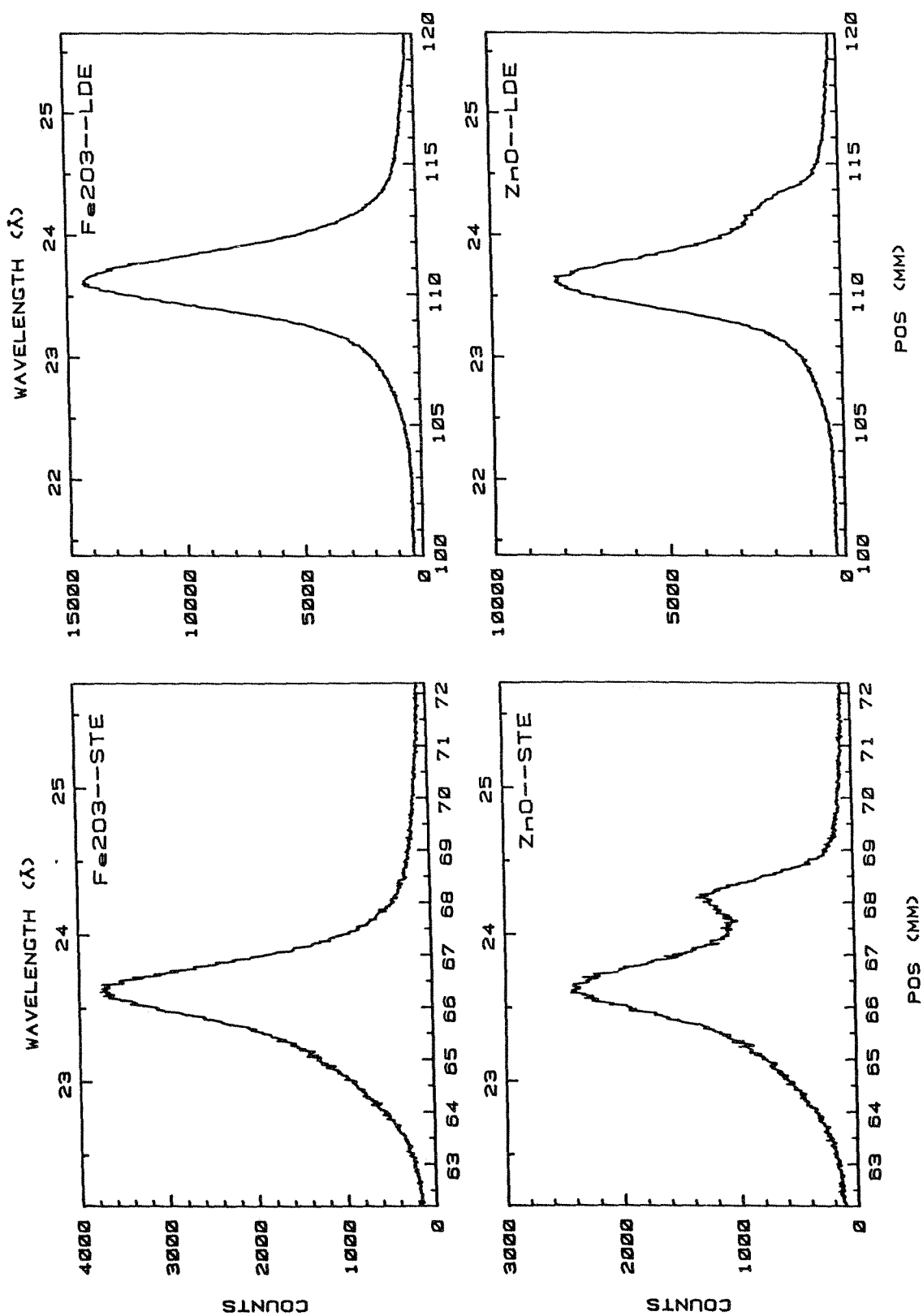


FIG. 1.--0 K α spectra from Fe $_2$ O $_3$ and ZnO measured with STE crystal (left) as compared to the LDE crystal (right): 10 kV, 50 nA beam current.

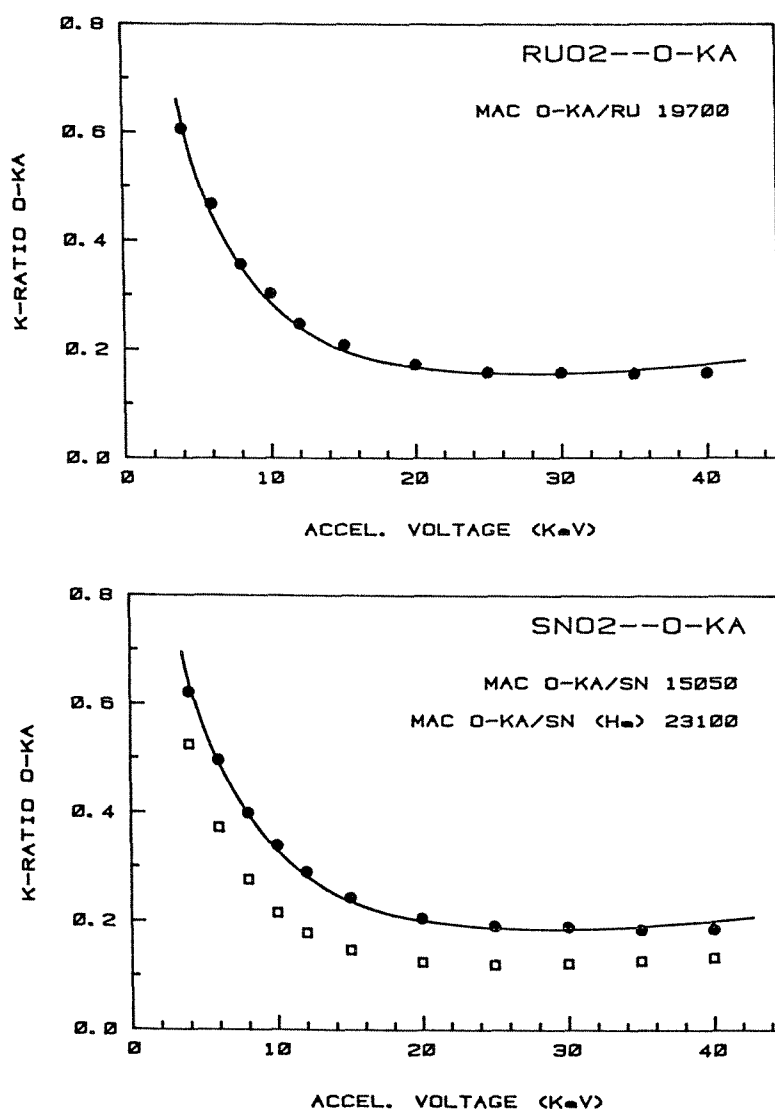


FIG. 2.--Integral k-ratios for O K α x rays relative to Fe₂O₃ standard as function of accelerating voltage (LDE crystal). Top: RuO₂; bottom: SnO₂. Solid dots represent experimental results, solid curves correspond to calculations of our latest correction program PROZA.⁷ Open squares represent calculations with a mac for O K α in Sn of 23 100 (Henke et al.⁹).

a database⁸ consisting of measurements on medium-to high Z element radiations. That proves again that surprisingly high accuracy can be obtained for ultralight element analysis provided that the measurements are carried out with sufficient care and that matrix correction is done with a good correction program in conjunction with the proper mac's. At the moment the x-ray lines of the metal components in the oxides are being measured and in the near future more details of the present work will be supplied in a number of publications.

References

1. G. F. Bastin and H. J. M. Heijligers, "Quantitative electron-probe microanalysis of carbon in binary carbides," *Microbeam Analysis--1984*, 291.
2. G. F. Bastin and H. J. M. Heijligers, "Quantitative electron-probe microanalysis of very light elements," *Microbeam Analysis--1985*, 1.
3. G. F. Bastin and H. J. M. Heijligers, "Quantitative electron probe microanalysis of carbon in binary carbides," *X-ray Spect.* 135, 1986.
4. G. F. Bastin and H. J. M. Heijligers, "Quantitative electron-probe microanalysis of boron in some binary borides," *Microbeam Analysis--1986*, 285.
5. J. L. Pouchou and F. Pichoir, "A new model for quantitative x-ray microanalysis," *Réch. Aéropat.* 3: 13, 1984.
6. V. D. Scott and G. Love, "An EPMA correction method based upon a quadrilateral $\phi(\rho z)$ profile," *NBS Workshop*, Gaithersburg, Md., 1988 (in press)
7. G. F. Bastin and H. J. M. Heijligers, "Quantitative electron probe microanalysis of ultra-light elements (boron-oxygen)," *ibid.*
8. G. F. Bastin and H. J. M. Heijligers, "Quantitative electron probe microanalysis of ultra-light elements," *J. Microsc. Spectr. Electron.* 215, 1986.
9. B. L. Henke et al., "Low-energy x-ray interaction coefficients: Photo absorption, scattering and reflection," *Atomic Data and Nuclear Data Tables* 27, 1982, 1-144.
10. B. L. Henke and E. S. Ebsu, "Low energy x-ray and electron absorption within solids," *Adv. in X-ray Anal.* 17: 150, 1974.

ANALYSES OF LAYERED SPECIMENS IN THE ELECTRONPROBE MICROANALYZER

Rod Packwood, Vera Moore, and Sandra Thomas

Our laboratory handles a fair amount of service work and several times we have been asked to use the microprobe to verify that a thin layered material was indeed what the client believed it to be. We were pleased to try. The notion of having "known" material to work with was novel; most specimens suffer from large uncertainties associated with some aspect of their composition or distribution; and so on each occasion it seemed to be a good opportunity to combine pure and applied research. The idea was to compare the microprobe data with the predictions of the PM equations for x-ray intensity as a function of accelerating potential and layer thickness.¹ However, it was not to be that easy, because each time the situation turned around and we ended up using the predictions of the PM equations to make new forecasts for both thickness and composition that were to be substantiated on other grounds. The clients were pleased but we were no further ahead with the attempt to test the theory. Work on data in the published literature suggested that the method was on a solid footing, but it would be better if we could work with well-documented material. Despairing of obtaining, fortuitously, specimens with the appropriate credentials, we decided to manufacture our own test material. Budget constraints dictated that the apparatus be made in house and employ such facilities as were already available. Fortunately there was a Sloan 200 digital film-thickness monitor, purchased some time previously, that could be mounted on the Edwards Hi-Vac evaporator unit; of necessity thermal evaporation was the deposition route. The remainder of the apparatus was in the nature of *objets trouvés* that required some degree of modification to be made suitable for our purposes.

Manufacture of Plaid Deposit Arrays

As shown in Fig. 1, a rotary vacuum feed-through turns a small capstan 1, fixed to a metal support on which slides an oblong metal shuttle 2, which carries the specimen 3, attached to its underside but not in contact with the metal support. Thin metal shim-stock was used for the slits; centered below them at x is the tungsten basket for the evaporant, which is some 11 cm distant. Close to and at the same

Rod Packwood and Vera Moore are at the Canada Centre for Mineral and Energy Technology, 568 Booth St., Ottawa, Canada K1A 0G1; at the time of this work Sandra Thomas was a co-op student at the University of Waterloo, Ontario. The authors thank Hasan Mahmood for assistance with the later part of this study.

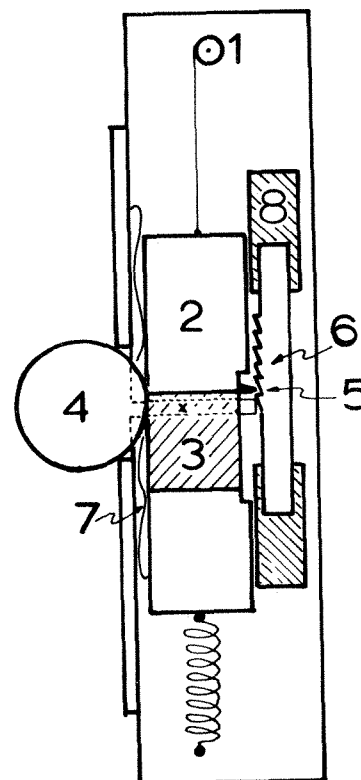


FIG. 1.--Schematic of substrate holder and translation mechanism.

height as the specimen is the thickness monitor sensor 4, with its face tilted through about 5° in order to receive evaporant at 90° to the surface. The separation between the sensor and x is about 2 cm. As the shuttle moves down the slide, a steel point 5 traces along the precision sawtooth template 6, as a means of locating each new deposit. The shuttle is restrained by a long spring that takes up backlash, and a second flat spring 7 keeps the pointer firmly against the template or the glide blocks 8, as the case may be. The slit width is chosen to be roughly 3/4 of the sawtooth waveform on the template, i.e., 1.5 vs 2.0 mm, respectively. Various thickness layers of Al, Cu, Ag, and Ni were deposited on Si, Cu, Sn, and Pb substrates. The deposits were chosen so as to give reasonably well spaced thicknesses ranging from 75 to 1500 Å per single deposit. After a sequence of bands has been laid down, the substrate is detached and remounted at right angles to the first orientation, and a new sequence of deposits is made with thicknesses in between those of the first set. The result is a series of bands, each of which is overlaid by all the deposits

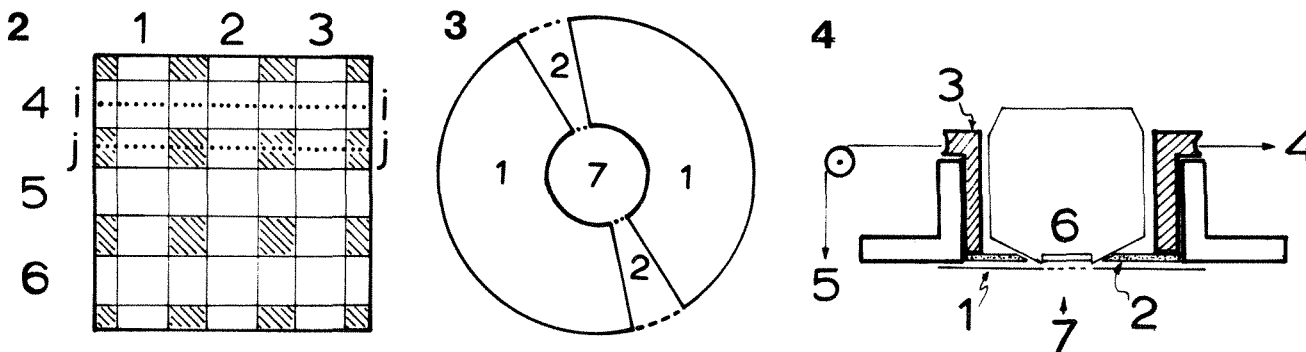


FIG. 2.--3 × 3 plaid deposit array.

FIG. 3.--Schematic of segment mask for ρ - θ deposit arrays.

FIG. 4.--Schematic of side view of ρ - θ substrate holder and rotation mechanism.

of the different known thicknesses. A simple variation on the slit geometry would also have given an accumulation of deposits 1, 1 + 2, 1 + 2 + 3, etc., a considerable advantage when one is trying to manufacture thick layers for tests at higher accelerating potentials. The specimens analyzed in our Camebax Micro by step scans of 20s count every 20 mm for both deposit and substrate x rays along paths such as i-j and j-j. Comparisons of the first, last, and intermediate values for band 2 give a direct indication of the deposit's uniformity; it was found to be better than 95%. Data reduction was performed in two stages: averaging the signals from the individual regions, ignoring the obvious shadow/edge values, was done manually; the combination pairwise, background subtraction and all subsequent manipulation was done in EXCEL on a Macintosh SE.

The aluminum evaporations were difficult because the reaction between W and Al was much more vigorous than anticipated, so that part of the experiment awaits an alternative mode of deposition. On the other hand, Cu and Ag were trouble free; the filaments lasted 20 or more evaporations. The Si and Cu substrates were simple to prepare but Ag and Pb needed some thought because their extreme softness rules out conventional metallographic procedures. We settled for cutting fresh slices of them from small ingots, squashing the clean surface flat between polished anvils in a specimen mounting press (approx. 10 000 psi), and trimming to size with a sharp blade. The prepared Ag and Pb specimens were then glued to stiff copper support coupons in order to facilitate handling.

Manufacture of Annular Deposit Arrays

The relatively limited depth of field in the Cameca microscope meant that the plaid deposits were rather tricky to use for tilted sample measurements. We decided that this restriction could best be overcome if instead of x-y geometry for the array of deposits we used r- θ as in a darts board configuration, which allowed us to focus the microprobe at a given r value and bring the various deposits under the beam by simply rotating the specimen. This last is a manual operation on our machine and could be a drawback if a very large number of

readings are contemplated, but it also permits the thickness monitor sensor to be in close proximity to the substrate if a hole is made in the center of the latter. By this means the average separation was reduced to about 1 cm.

A second method for making the measurements was to bring the tilt axis and the 90° of the annular array into coincidence and use the stepping motor to run the traverse along that direction. For large angles of tilt, rotation of the standard specimen holder brings it into contact with the polepiece coverplate and the specimen must then be partially rotated in the holder if all locations on the specimen are to be reached.

We made the annular ring areas by masking off the substrate with a set of circular apertures. The radial segments were made with the mask 1, shown schematically in Figs. 3 and 4. It was fixed beneath the substrate 2, on its holder 3, which could itself be rotated through a known angle via a thin wire on a pulley 4 and the rotary vacuum feedthrough mentioned previously. Tension on the pulley was maintained by a 50g weight 5, hanging down from the other end of the wire. The thickness monitor sensor 6 remained stationary and at the same height as the substrate above the tungsten filament 7. Small differences in distance could be allowed for on the basis of an inverse-square-law variation with distance. For $\phi(\rho z)$ work two different tracer layers could be put on the opposite halves of the substrate and then covered at the same time by the various deposits of substrate metal.

Theory

The PM equations have been published previously;^{2,3} only the general equation will be quoted here. The observed intensity to be expected from a layer buried between δ and δ' mass thicknesses of absorption factor χ inside a medium of absorption χ' is given by

$$I_{\text{obs}} = C_A (\sqrt{\pi}/2\alpha) \cdot \{ \gamma_0 \cdot \exp(\chi/2\alpha)^2 \cdot (\text{erf}[\alpha\delta + (\chi/2\alpha)] - \text{erf}[\alpha\delta' + (\chi/2\alpha)]) - (\gamma_0 - \phi_0) \cdot \exp[(\chi + \beta)/2\alpha]^2 (\text{erf}[\alpha\delta + (\chi + \beta)/2\alpha] - \text{erf}[\alpha\delta' + (\chi + \beta)/2\alpha]) \} \cdot \exp[-\delta'(\chi' - \chi)]$$

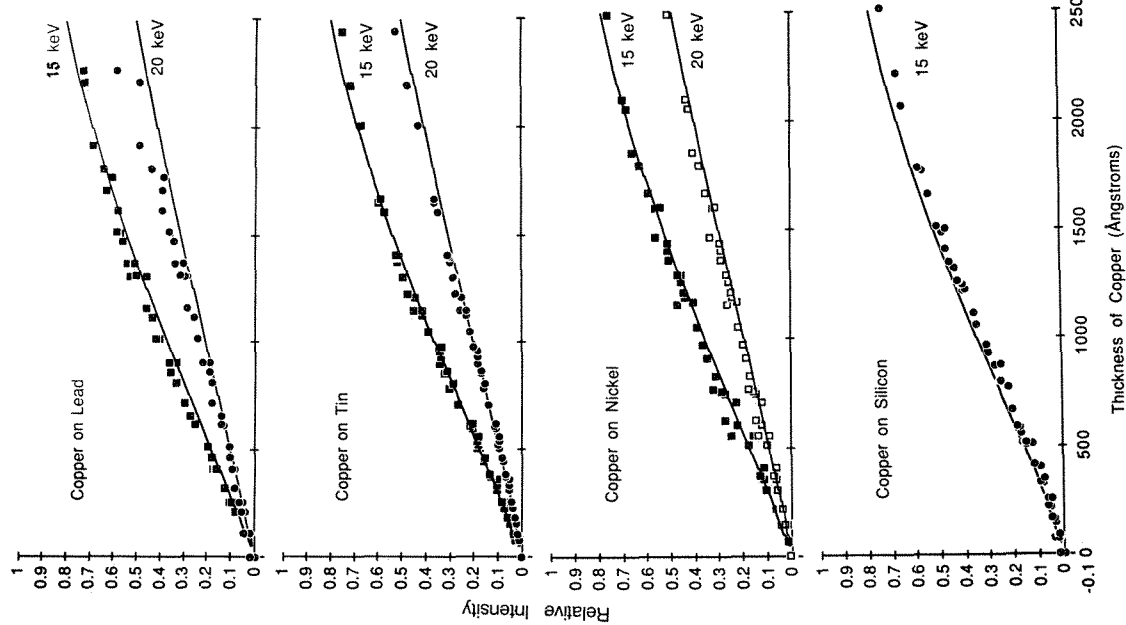


FIG. 5.--Observed and predicted relative intensities for Cu $K\alpha$ from Cu deposited on Si, Ni, Sn, and Pb.

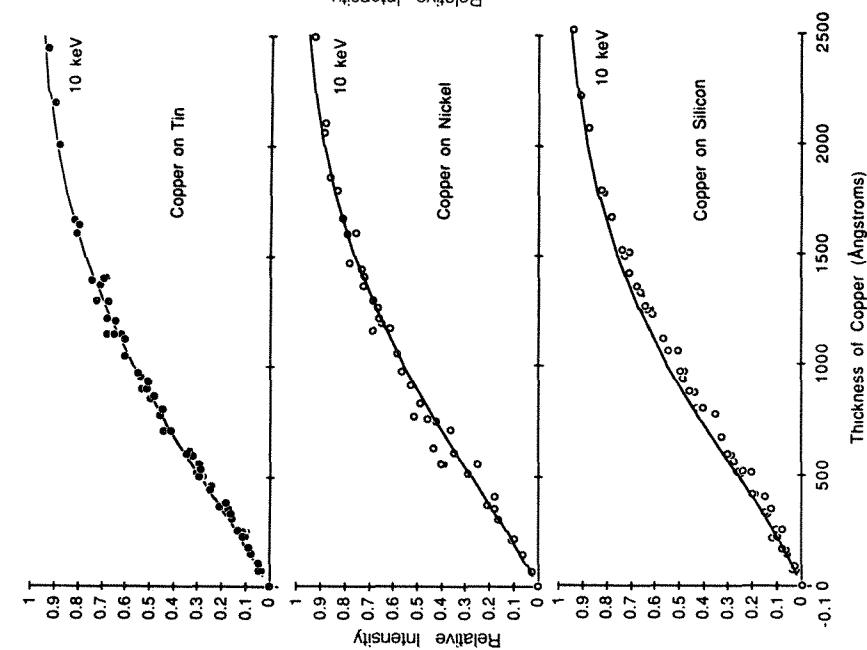


FIG. 6.--Observed and predicted relative intensities for Cu $L\alpha$ from Cu deposited on Si, Ni, and Sn.

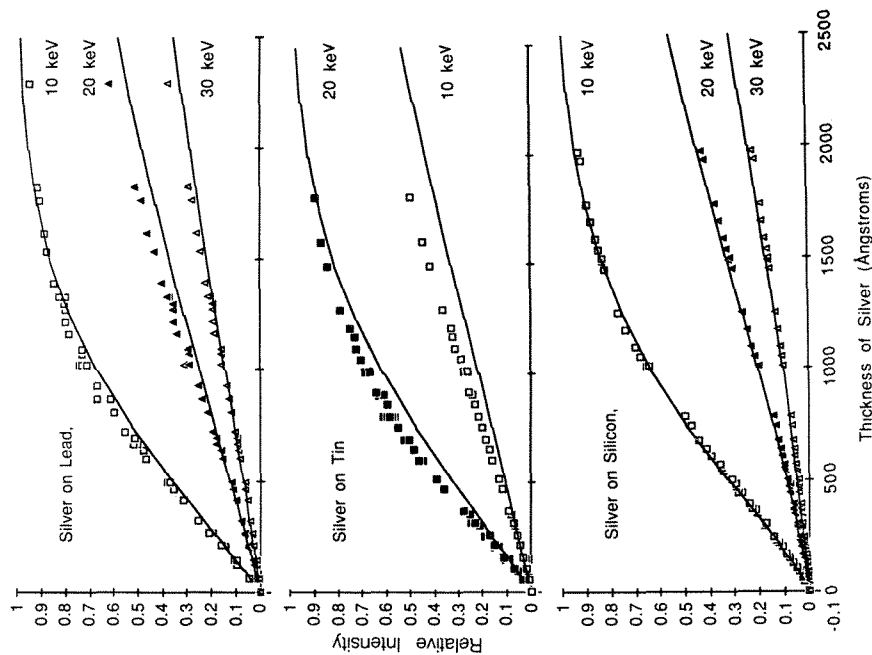


FIG. 7.--Observed and predicted relative intensities for Ag $L\alpha$ from Ag deposited on Si, Sn, and Pb.

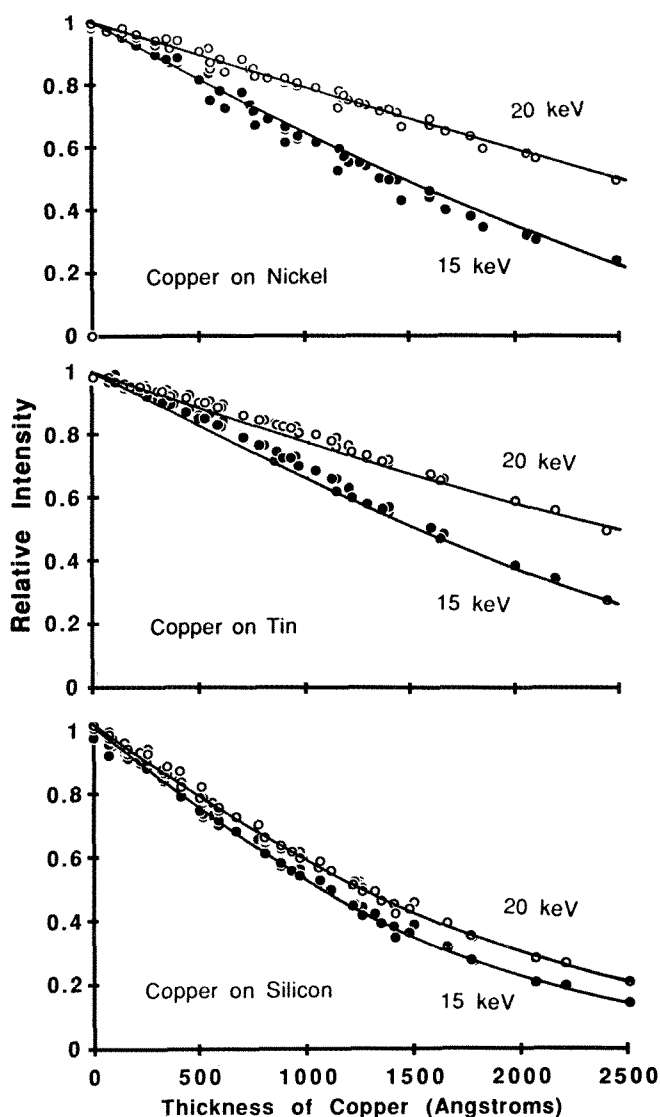


FIG. 8.--Observed and predicted relative intensities of Si $K\alpha$, Sn $L\alpha$, and Ni $K\alpha$ from substrates covered in Cu.

where the other variables have their usual meanings. The assumption has been made that the overall $\phi(\rho z)$ can be represented by some combination of the curves for the two component materials. Exactly how the average values of the various parameters should be calculated is one of the questions to be answered. The method of weighting surface and substrate contributions by error functions in 2α has already been suggested and is further tested here.

Results

Results obtained with Cu $K\alpha$ and Cu $L\alpha$ from Cu deposits are shown in Figs. 5 and 6. They were achieved by application of a 2α error function weighting for deposit and substrate contributions to the ϕ_0 and β parameters for the combined $\phi(\rho z)$ curve; α was weighted with a 1α error function; and γ_0 , α , β , and ϕ_0 are as reported elsewhere. For Ag $L\alpha$ the results were not quite as good when the normal α value was used (Fig. 7), Ag on Sn. However, if the

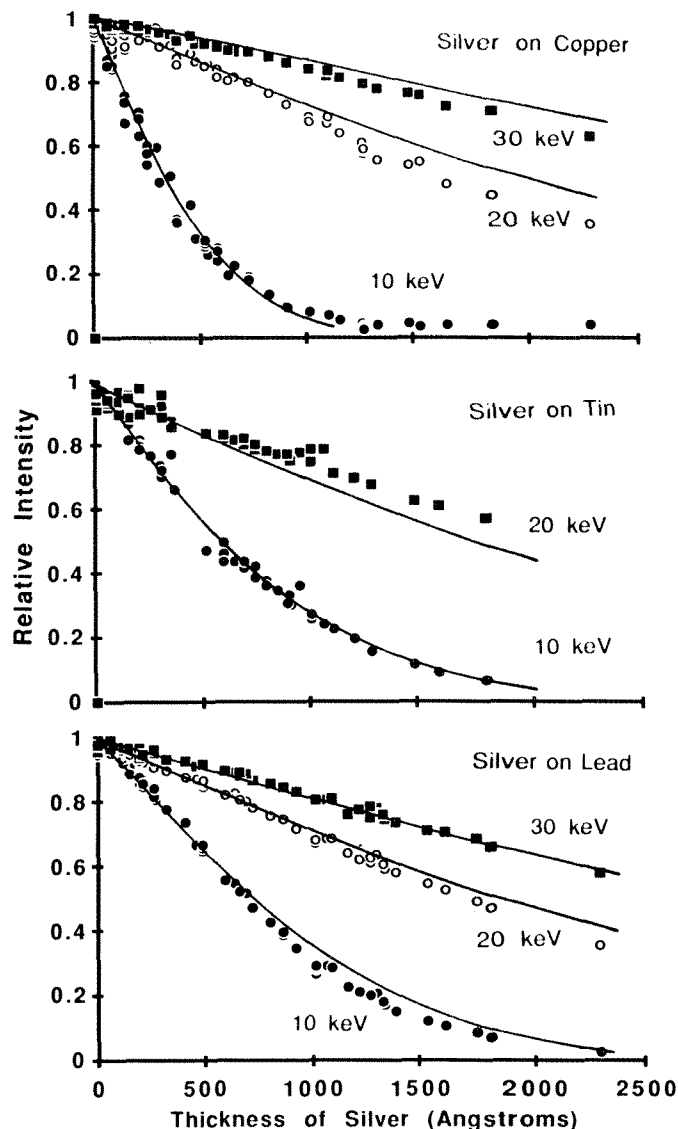


FIG. 9.--Observed and predicted relative intensities of Pb $M\alpha$, Sn $L\alpha$, and Cu $K\alpha$ from substrates covered in Ag.

constant in α is increased from 4.5×10^5 to 5.0×10^5 , there is some improvement, i.e., Ag on Si and Pb. Whether this is a real shift in the α value or just a result of some experimental error or oversight is not clear at this time.

For the substrate data we have Si $K\alpha$, Sn $L\alpha$, and Ni $K\alpha$ data from underneath Cu deposits (Fig. 8) and Pb $M\alpha$, Sn $L\alpha$, and Cu $K\alpha$ from underneath Ag deposits (Fig. 9). On the whole the agreement between the observations and the predictions is quite reasonable.

The $\phi(\rho z)$ measurements comparing horizontal and tilted specimens were described previously.⁴

References

1. R. H. Packwood and K. S. Milliken, "A general equation for predicting x-ray intensities from stratified samples in the electron microprobe," CANMET Report PMRL 85-25 (TR), May 1985.

2. Rod Packwood, "A general equation for predicting x-ray intensities from stratified samples in the electron microprobe," *Microbeam Analysis--1986*, 268.

3. R. Packwood et al., "The electroprobe microanalysis of compositionally stratified materials," *Proc. 11th ICXOM*, 1987, 274.

4. Rod Packwood et al., " $\phi(\rho z)$ for tilted specimens in the electroprobe and SEM," *Microbeam Analysis--1988*, 258.

MASS CONCENTRATION VERSUS ATOMIC CONCENTRATION IN ELECTRON PROBE MICROANALYSIS/ANALYTICAL ELECTRON MICROSCOPY: WHICH IS THE PROPER CHOICE?

D. E. Newbury and E. B. Steel

One aspect of quantitative electron probe microanalysis (EPMA) that has always appeared curious is the manner in which many electron-specimen interaction parameters scale as a function of the mass (weight) concentration C_W of the elemental constituents rather than as the apparently more obvious atomic concentrations C_A . To review the situation briefly, the following cases stand out prominently.

1. Castaing's first approximation¹ provides the basis for quantitative x-ray microanalysis.

$$k = I_{\text{spc}}/I_{\text{std}} \propto C_{\text{spc}}/C_{\text{std}} \quad (1)$$

where I is the measured characteristic x-ray intensity, and C is the mass concentration. For pure element standards with $C_{\text{std}} = 1$, $k \propto C_{\text{spc}}$.

2. X-ray bremsstrahlung. When multi-element specimens are examined, the intensity of the x-ray bremsstrahlung I_B at a given energy E is given by²

$$I_{E,\text{spc}}^B = \sum_i C_i I_{E,Z}^B \quad (2)$$

where $I_{E,Z}^B$ represents the bremsstrahlung produced by a pure element target with atomic number Z , C is the mass fraction, and the summation is taken over all the elements in the specimen.

3. Backscattered electron coefficient. Heinrich³ has demonstrated that the backscattered electron coefficient η of a mixture scales so perfectly with the mass fraction of the elemental constituents that it can be used as a basis for a technique of quantitative analysis:

$$\eta_{\text{spc}} = \sum_i C_i \eta_Z \quad (3)$$

The following discussion considers the first of these cases, Castaing's first approximation for characteristic x rays.

Thin-specimen Case

The starting point for the development of the mathematical description of x-ray generation in a bulk solid is consideration of the generation of x rays in a layer of infinitesimal thickness.^{4,5} This is actually the specimen configuration that is approximated experimentally in analytical electron microscopy (AEM).⁶ A typical specimen thickness in AEM is 50-100

nm, which is of the order of 5% of the range of 20keV electrons in a bulk solid of the same composition. In addition, the effects of elastic scattering in the AEM thin-foil case are further reduced, compared to the situation in EPMA, by operation at a beam energy of 100 keV or more. In the absence of significant elastic scattering, the production of characteristic x rays dn in a pure element thin foil of thickness dx is given by the expression⁶

$$dn = Q\omega N_A \rho \, dx/A \quad (4)$$

where Q is the ionization cross section [ionizations/e²(atom/cm²)], ω is the fluorescence yield (x rays/ionization), N_A is Avogadro's number (atoms/mole), a is the ratio of the measured x-ray line to the total x-ray emission from the shell of interest, ρ is the density (g/cm³), dx is the target thickness (cm), and A is the atomic weight (g/mole). The cross section includes the term "atoms per unit area" and the other quantities ($N_A \rho \, dx/A$) in Eq. (4) collectively calculate the atom area density.

When a mixture of atoms is considered, Eq. (4) must be multiplied by an appropriate concentration (either atomic or mass) to correct for the dilution of species i by the presence of additional species j . Since the dimensional argument for the production of x rays given in Eq. (4) involves consideration on a per atom basis, it seems reasonable to assume that the concentration should be in terms of atomic fraction. In fact, in the development of a theoretical approach for AEM quantitation as an extension of solid-specimen quantitation theory, the mass concentration has been utilized for quantitative calculation of concentration ratios.⁶

Because of the difficulty in making sequential measurements of unknowns and standards in the form of thin foils, AEM quantitation has developed along the line of determining relative elemental concentration ratios. Equation (4) provides the basis for calculating the concentration ratio from the ratio of x rays measured with a spectrometer from two elements, A and B. Following the development of Goldstein et al.,⁶

$$\frac{C_A}{C_B} = \frac{n_A}{n_B} \frac{Q_B}{Q_A} \frac{\omega_B}{\omega_A} \frac{a_B}{a_A} \frac{A_A}{A_B} \frac{\epsilon_B}{\epsilon_A} f_{AB} \quad (5)$$

The term ϵ is the efficiency of the x-ray spectrometer for the x-ray line measured and f is the correction factor for the absorption of the radiation in the specimen.⁶ By measuring n for two elements in a thin-film reference and calculating the other needed terms in Eq. (5) (Q , ω , ϵ , f), one can predict the ratio of

The authors are with the Center for Analytical Chemistry, National Institute of Standards and Technology (formerly the National Bureau of Standards), Gaithersburg, MD 20899.

elemental concentrations and compare it with the known values.

Experimental Process

NIST Standard Reference Material (SRM) 2063 is the first SRM specifically devised for use in AEM.⁷ The concentrations of Mg, Si, Ca, and Fe are certified by independent chemical measurements. The thickness (measured and reported but not certified) of the film is 105 nm. SRM 2063 contains elements with widely separated atomic weights, which results in distinct differences in mass concentration and atomic concentration ratios and makes it an ideal specimen to carry out the test given by Eq. (5). Ultra-thin window energy-dispersive x-ray spectra of SRM 2063 were obtained in an AEM operating with a beam energy of 100 keV. Peak intensities were obtained for Mg and Si $K\alpha, \beta$, and Fe $K\alpha$ and Fe $K\beta$ by integration over the entire peak width and correcting for background.

The necessary factors in Eq. (5) were calculated as follows: ω was taken from the work of Bambynek et al.⁸ The detector efficiency ϵ was calculated for a UTW configuration from a modification of the efficiency expression described by Fiori et al.⁹ In addition to the gold electrode (20 nm) and the silicon dead layer (200 nm), absorption was calculated for the thin window (100 nm) and the omnipresent ice layer (1 μm). The absorption factor was calculated from the expression of Goldstein et al.⁶ The sum of $K\alpha$ and $K\beta$ was used, so that $a = 1$. Because of the considerable debate that has occurred over the best expression to use for the cross section, both a nonrelativistic (Bethe) and a relativistic (Williams) equation were used (Goldstein et al.⁶). Both cross sections were calculated with the constants described by Powell. When taken as a ratio, $Q_{\text{Fe}}/Q_{\text{Si}}$ at 100 keV is actually insensitive to the choice of cross section, whether relativistic or non-relativistic.

Table 1 reports the measured count ratio (with the associated measurement statistics based on the number of counts above background and the relative standard deviation observed for five measurements) and the calculation of $C_{\text{Si}}/C_{\text{Fe}}$ and $C_{\text{Mg}}/C_{\text{Fe}}$ from the two different expressions for Q . These calculated concentration ratios are compared in Table 1 with the mass concentration ratio and the atom concentration ratio as calculated from the certified concentrations in SRM 2063. It is clear that the certified mass concentration ratio is in good agreement with the concentration ratio predicted from Eq. (5). The assumption of mass concentration rather than atom concentration for AEM quantitation is thus confirmed as reasonable.

Discussion

The AEM thin-film experiment confirms the choice of mass concentration ratios for *inter-element* measurements in the thin-foil case. It seems reasonable to assume that this finding would be confirmed for *intraelement* measurements,

TABLE 1.--Comparison of predicted and certified concentrations (SRM 2063; 100 keV AEM; UTW EDS).

Elemental Ratio	Measured X-ray Intensity Ratio	Conc ratio predicted with non-relativistic cross section	Conc. ratio predicted with relativistic cross section	Atom Conc Ratio (SRM)	Mass Conc. Ratio (SRM)
Mg/Fe	0.700 (single determination 1s=3.7%) (RSD for five measurements = 6.8%)	0.650	0.658	1.49	0.647
Si/Fe	2.47 (single determination 1s=1.8%) (RSD for five measurements = 2.8%)	1.79	1.81	3.82	1.92

i.e., intensity-ratio measurements involving a single element in separate unknown and standard foils. Once this point has been established for the infinitesimal-foil case, it is clear that x-ray generation for a thick bulk specimen can be approximated as a sequence of infinitesimal layers, with appropriate adjustments for the loss of electrons due to back-scattering and the decrease in energy due to inelastic scattering as the beam penetrates into the specimen. The mass concentration dependence for characteristic x rays found in the case of the thin foil should also be correct for bulk targets as stated in Castaing's first approximation.

Although we have demonstrated empirically that mass concentration is the appropriate choice for scaling characteristic x-ray intensities in alloy thin foils, is there a theoretical basis for this choice? Since the choice of mass concentration holds for the simplest case, that of the foil, such a basis must come directly from the formulation for x-ray generation given by Eq. (4). Cross sections are usually thought of as having dimensions of area (cm^2), but when the "dimensionless" terms are included, a more rigorous description of the cross-section dimensions is events/incident particle/(atom/ cm^2). In fact, the complete definition of the dimensions of the cross section is $(\text{events}/\text{cm}^2)/[(\text{incident particle}/\text{cm}^2)(\text{atom}/\text{cm}^3)]$.¹¹ This full description consists of terms that describe the exciting beam (incident particle/ cm^2), the target (atom/ cm^3), and the product of the interaction with the target (events/ cm^3). Obviously the terms containing the dimensional unit cm^3 in the numerator and denominator of the expression cancel, giving the dimensionality with the term "atoms/ cm^2 ."

The origin of the use of mass concentration for scaling mixtures arises in this particular form of the dimensionality of the cross section. In Eq. (5), if the term involving the ratio of atomic numbers is removed, the predicted concentration ratio actually agrees with the atom concentration ratio. When an atom concentration ratio is divided by the ratio of atomic weights, it is converted into a mass concentration ratio. Having the "per atom" term in the ionization cross section requires the use of the ratio of Avogadro's number to the atomic weight as a multiplicative factor in Eq. (4).

If the cross section for ionization had been defined, however illogically, on a basis that did not include a "per atom" term (for example, if mass thickness had been used), the atomic weight would not appear in the sequence of multiplicative terms. The scaling of mixtures would then take place on the basis of atomic concentrations. Thus, somewhat contrary to expectations, the use of a "per atom" term in the cross section results in mass concentration scaling, whereas the use of a "per mass" term would result in an atom concentration scaling! Mass concentration scaling of characteristic x-ray measurements in quantitative electron probe analysis is therefore a direct consequence of the way in which the dimensionality of the basic cross section for inner shell ionization is defined.

References

1. R. Castaing, Ph.D. Thesis, University of Paris, 1951.
2. G. Moreau and D. Calais, *J. Phys.* 25 (Suppl. 6): 83, 1964.
3. K. F. J. Heinrich, in R. Castaing, P. Deschamps, and J. Philibert, Eds., *X-ray Optics and Microanalysis*, Paris: Hermann, 1966.
4. J. I. Goldstein, D. E. Newbury, P. Echlin, D. C. Joy, C. Fiori, and E. Lifshin, *Scanning Electron Microscopy and X-ray Microanalysis*, New York: Plenum, 1981, 306.
5. K. F. J. Heinrich, *Electron Beam X-ray Microanalysis*, New York: Van Nostrand, 1981, 59.
6. J. I. Goldstein, D. B. Williams, and G. Cliff, "Quantitative x-ray analysis," in D. C. Joy, A. D. Romig, and J. I. Goldstein, Eds., *Principles of Analytical Electron Microscopy*, New York: Plenum, 1986, 155.
7. E. B. Steel, National Institute of Standards and Technology Standard Reference Material 2063, *Microanalysis Thin Film Mg-Si-Ca-Fe*, available from the Office of Standard Reference Materials, NIST, Gaithersburg, MD 20899.
8. W. Bambynek, B. Craseman, R. W. Fink, H. V. Freund, H. Mark, C. D. Swift, R. E. Price, and R. P. Venugopalu, *Rev. Mod. Phys.* 44: 216, 1972.
9. C. E. Fiori, R. L. Myklebust, K. F. J. Heinrich, and H. Yakowitz, *Anal. Chem.* 48: 172, 1976.
10. C. Powell, *Rev. Mod. Phys.* 48: 33, 1976.
11. *Van Nostrand's Scientific Encyclopedia*, 3rd ed., New York: Van Nostrand, 1981, 327.

THE APPLICATION OF A NUMERICAL PROCEDURE IN THE CALCULATION OF THE ATOMIC-NUMBER CORRECTION IN ELECTRON PROBE MICROANALYSIS

R. L. Myklebust and C. E. Fiori

The conventional procedure to convert relative x-ray intensities into concentration values is to consider separately the effects of x-ray generation, absorption, and fluorescence (ZAF). Electron beam x-ray microanalysis is a mature field spanning 38 years since Castaing's thesis. The data on which the conventional quantitative theory is based were taken many years ago, and the mathematical form of the equations was developed during this period of slide rules and mechanical calculators. It could only be expected that the required simplifications concealed the underlying physical principles.

During the last several years, small laboratory computers have become sufficiently powerful to permit the evaluation of a more physically explicit formulation of these equations in a reasonable time. We feel that the conventional formulation, but with all the currently available physics and recent parameterizations explicitly included, results in a very robust and accurate algorithm to convert x-ray intensity ratios to elemental concentrations. Since our field is still evolving, a flexible formulation of the quantitative algorithm allows easy modification to include new knowledge as it becomes available.

This communication discusses the use of an appropriate numerical procedure to compute the various quantities required in the x-ray generation term (atomic-number correction) of a conventional ZAF procedure.

The conventional ZAF procedure divides the atomic number correction into two components: the x-ray loss due to backscattered electrons and the electron stopping power. There have been several formulations for the x-ray loss due to backscattered electron $(1 - R)$ that have appeared in the literature in the past few years.¹⁻⁶ Myklebust and Newbury⁷ have recently compared all the currently used expressions for R and have proposed an equation that requires the full integration of the expression due to Webster et al.,⁸

$$R = 1 - \int_{w_k}^1 \frac{d\eta}{dw} \int_{E_k}^{wE_0} \frac{Q}{S} dE dw \int_{E_k}^{E_0} \frac{Q}{S} dE \quad (1)$$

where w is the reciprocal of the overvoltage $U = E/E_0$, the beam voltage is E_0 , and the x-ray excitation potential is E_k . The formulation of

the energy distribution of backscattered electrons, d/dw , employed was that of Czyzewski and Szymanski:⁹

$$\frac{d\eta}{dw} = \text{tspn} \frac{w^{(t-1)}}{(1 - w^t)^{(1+p)} \{1 - s + [s/(1 - w^t)^p]\}^2}$$

where $t = 1.6$, $p = (0.8 + 2) \ln(1/\eta)$,

$$s = 0.1054 \{2^p - 1 + [1/(2.25 \cos \alpha)]^p\} \quad (2)$$

η is the electron backscatter coefficient, and α is the electron beam incidence angle. This equation was parameterized by Czyzewski and Szymanski from the data of Darlington.¹⁰ Myklebust and Newbury⁷ compared the energy distributions computed with this expression to Bishop's data¹¹ and to their own Monte Carlo calculations and found the predictions of Eq. (2) to be in good agreement with all three data sets.

For the characteristic K-shell cross section, we have selected a cross section proposed by Fabre de la Ripelle¹² and recommended by Powell,¹³ which is a modification of the Bethe cross section for the K-shell that is satisfactory near the threshold for ionization:

$$Q = C \{ \ln U / [U + 1.32] E_k^2 \} \quad (3)$$

where U is the overvoltage and C contains all of the constant terms. This function is mathematically well behaved in the closed interval between E_k and E_0 , which is a requirement in the numerical procedures described below. We are currently evaluating similarly appropriate expressions for the L and M shells.

The stopping power S is traditionally derived from the well known Bethe law for the slowing down of electrons in matter:¹⁴

$$S = c \frac{Z}{A} \frac{1}{E} \ln (1.166E/J) \quad (4)$$

where J is the mean excitation energy of an atom. A generally accepted expression for J is due to Sternheimer,¹⁵

$$J = Z(9.76 + 58.8Z^{-1.19}) \quad (5)$$

This form of the stopping power is mathematically poorly defined for low electron energies and introduces an asymptote in the volume to be integrated. To avoid this problem, we have employed a recently proposed empirical expression by Pouchou and Pichoir,⁴ which is equivalent to the Bethe expression between 30 and 50 keV and is well behaved at low energies:

R. L. Myklebust is with the Center for Analytical Chemistry, National Institute for Standards and Technology, Gaithersburg, MD 20899; C. E. Fiori is with the National Institutes of Health, Bethesda, MD 20892.

$$S = \frac{dE}{d\rho s} = - \frac{M}{J} \frac{1}{f(V)} \quad (6)$$

where $M = \sum_i C_i Z_i / A_i$

$$J_i = 0.001 Z_i [10.04 + 8.25 \exp(-Z_i/11.22)]$$

$$f(V) = \sum_{k=1}^3 D_k V^{P_k} \quad V = E/J$$

and with $D_1 = 6.6 \times 10^{-6}$

$$D_2 = 1.12 \times 10^{-7} (1.35 - 0.45J^2)$$

$$D_3 = 2.2 \times 10^{-6}/J$$

$$P_1 = 0.78$$

$$P_2 = 0.01$$

$$P_3 = -(0.5 - 0.25J)$$

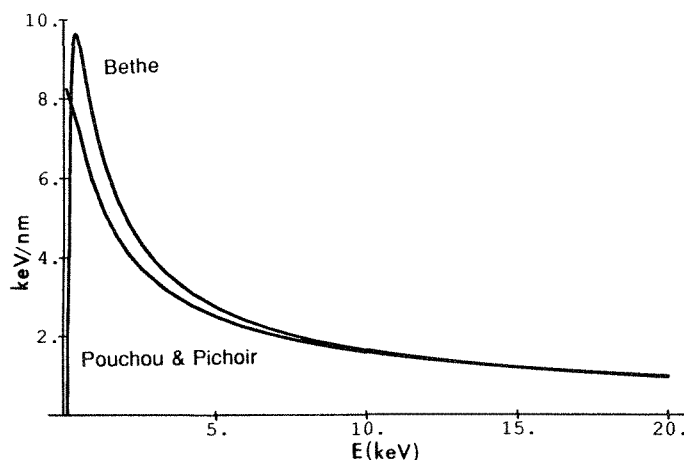


FIG. 1.--Slowing down of electrons in silicon as predicted by Bethe law (Eq. 4) and by the expression of Pouchou and Pichoir (Eq. 6). At low energies the Bethe law drops quickly to negative infinity.

Figure 1 is a comparison of this function with that of the Bethe law, where S is plotted vs electron energy for silicon. It is obvious that the Bethe law is not satisfactory, because as the quantity $1.166E/J$ becomes less than one, S decreases rapidly to a very large negative value and produces an asymptote.

In Fig. 2, the volume below the surface $(dn/dw) (Q/S)$ from $w = w_K$ to 1 and $E = E_K$ to wE_0 represents the number of x rays lost due to backscattered electrons. The plots in Fig. 2 are the full surfaces from $w = w_K$ to 1 and $E = E_K$ to E_0 . What we integrate is the volume under the surface and to the rear of the diagonal plane shown in the figure. Except when $w = 1$, the surface is continuous and slowly varying. This class of function is well suited to a Romberg form of numerical integration.¹⁶ The Romberg algorithm is quite powerful for sufficiently smooth analytic integrands, which are integrated over intervals that contain no singularities, and with endpoints that are also nonsingular. If these conditions are met, the Romberg algorithm is considerably faster than alternative numerical

procedures. We note that in the denominator of Eq. (2), a singularity occurs as w approaches 1. To permit the use of the closed form version of the Romberg algorithm, we set the upper integration limit of w to 0.9999 instead of 1. This minor modification produces an inconsequential error. One of the parameters used in the Romberg integration is a quantity known as the extrapolation error estimate. This quantity imposes a trade-off between accuracy and speed. We have determined that in the FORTRAN program we are using,¹⁶ this value should be 0.00005.

Discussion

Integration of the denominator in Eq. (1) produces a quantity proportional to the total x-ray generation from a particular absorption edge of energy E_K for electrons of energy E_0 in a target of atomic number Z . The double integration in the numerator of Eq. (1) yields a quantity proportional to the number of x rays lost due to backscattered electrons from the target. Therefore, the ratio in brackets in Eq. (1) represents the fraction of the total x-ray generation that is lost due to the backscattering of electrons from the specimen and R is the fraction of x rays that are generated.

The integration of Q/S has been performed explicitly, in closed form, by Philibert and Tixier¹⁷ by use of the logarithmic integral. This form was employed by Henoc et al. in the quantitative analysis program COR.¹⁸ This technique puts severe restrictions on the form of both Q and S to satisfy the conditions for the logarithmic integral and makes it difficult to change the expression for either Q or S . Numerical procedures are more flexible and allow expressions of any form to be integrated. This type of computation was not practical until recently when fast, small, and inexpensive computers have become readily available.

The method described in this paper produces R values that are very similar to values obtained by several recently published methods. The R values computed by the integration method are plotted in Fig. 3 together with the values calculated with four different expressions. That does not mean that these values are accurate, since the results depend heavily on the expressions used for the x-ray generation cross section and the slowing down of the electrons. This method described in this paper is designed so that when more accurate expressions become available, they can easily be introduced into quantitative analysis procedures.

References

1. P. Duncumb and S. J. B. Reed, *The Calculation of Stopping Power and Backscatter Effects in Electron Probe Microanalysis*, NBS Spec. Pub. 298, 1968, 133.
2. R. L. Myklebust, "An evaluation of x-ray loss due to electron backscatter," *J. de Physique* 45: C2, 1984.
3. G. Love and V. D. Scott, "Evaluation of a new correction procedure for quantitative

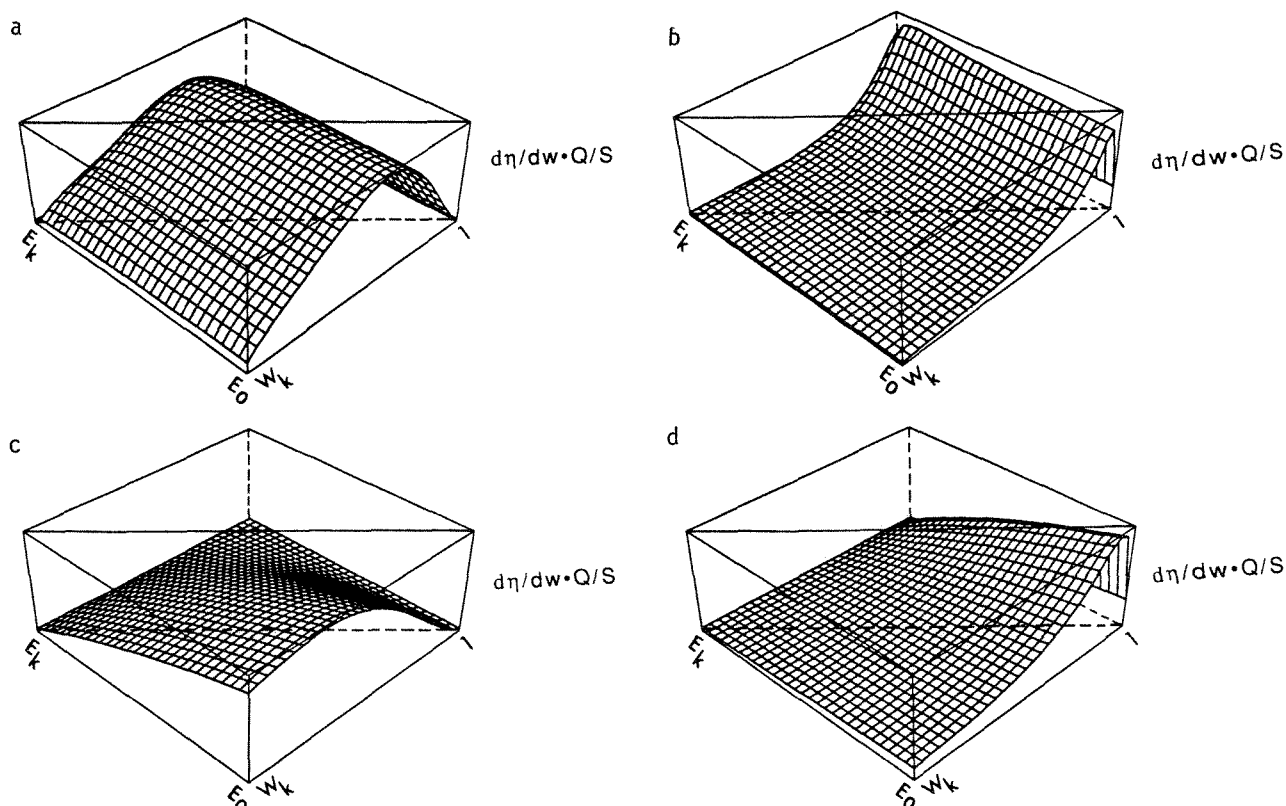


FIG. 2.--Four three-dimensional plots of surface $(d\eta/dw) \cdot (Q/S)$. Vertical scale for each plot is number of x rays lost due to backscattered electrons. All plots were done for electron-beam energy of 20 keV. (a) Carbon K x rays from matrix of pure carbon, (b) carbon K x rays from a matrix of pure gold, (c) copper K x rays from matrix of pure carbon, (d) copper K x rays from matrix of pure gold.

R Values for K-Lines at 20keV

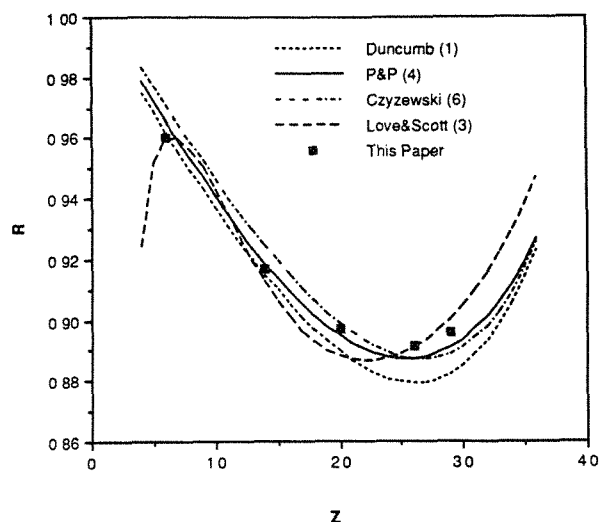


FIG. 3.--Comparison of R values for K x rays of range of elements from each pure element. Results from four published methods are shown together with values obtained for several elements by the method described in this paper.

electron probe microanalysis," *J. Phys.* D11: 1369, 1978.

4. J.-L. Pouchou and F. Pichoir, "Basic expressions for PAP computation for quantitative EPMA," *Proc. 11th IXCXOM*, 1986, 249.

5. H.-J. August, R. Razka, and J. Wernisch, "Calculation and comparison of the backscattering factor R for characteristic x-ray emission," *Scanning* 10: 107, 1988.

6. Z. Czyzewski, "Backscattering factor of the ZAF-correction procedure in quantitative electron-probe microanalysis," *Phys. Stat. Sol.* A92: 563, 1985.

7. R. L. Myklebust and D. E. Newbury, *The R Factor: The X-Ray Loss Due to Electron Backscatter*, NIST Special Publication (in press).

8. D. L. Webster, H. Clark, and W. W. Hansen, "Effects of cathode-ray diffusion on intensities in x-ray spectra," *Phys. Rev.* 37: 115, 1931.

9. Z. Czyzewski and H. Szymanski, *Proc. 10th ICEM* 1: 1982, 261.

10. E. Darlington, "Backscattering of 10-100 keV electrons from thick targets," *J. Phys.* D8: 85, 1975.

11. H. E. Bishop, "Some electron backscattering measurements for solid targets," *Proc. 4th IXCXOM*, 1966, 153.

12. M. Fabre de la Ripelle, "Etude sur les coefficients spécifiques d'ionisation," *J. Phys. (Paris)* 10: 319, 1949.

13. C. J. Powell, *Evaluation of Formulas for Inner-shell Ionization Cross Sections*, NBS Special Publ. 460, 1975, 97.

14. H. A. Bethe, "Theory of the transmission of corpuscular radiation through matter," *Ann. Phys.* 5: 325, 1930.

15. R. M. Sternheimer in K. F. J. Heinrich, Ed., *Electron Beam X-ray Microanalysis*, New York: Van Nostrand Reinhold, 1981, 231.

16. W. H. Press, B. P. Flannery, S. A. Teukolsky, and W. T. Vetterling, *Numerical Recipes*, Cambridge: Cambridge University Press, 1986, 114.

17. J. Philibert and R. Tixier, *Some Problems with Quantitative Electron Probe Microanalysis*, NBS Spec. Pub. 298, 1968, 13.

18. J. Henoc, K. F. J. Heinrich, and R. L. Myklebust, *A Rigorous Correction Procedure for Quantitative Electron Probe Microanalysis (COR 2)*, NBS Tech. Note 679, 1973.

AN EVALUATION OF X-RAY ABSORPTION EXPRESSIONS FOR PURE AND MULTIELEMENT TARGETS

J. A. Small and R. L. Myklebust

Definitions of Terms

I^* = emitted x-ray intensity
 I_0 = generated x-ray intensity
 E_0 = acceleration potential of electron beam
 E_c = critical excitation potential of the x-ray line of interest
 μ/ρ = mass absorption coefficient
 ψ = x-ray emergence angle
 $\chi = (\mu/\rho) \csc \psi$
 Z = atomic number of the sample
 A = atomic weight of the sample
 I_ψ = the x-ray intensity for a given emergence angle ψ
 I_{\max} = the x-ray intensity at the maximum emergence angle measured for a given sample

In routine electron-probe analysis involving samples that are electron opaque, polished, and conductive, the mechanisms describing the interaction of the beam electrons with the target atoms and the subsequent x-ray generation, absorption, and detection are well known. Various correction procedures are currently available for routine quantitative analysis that offer accuracy, on the order of 2% relative.¹ There are several important classes of samples and analytical conditions for which accurate quantitative analysis is not possible because the various mechanisms of electron-beam specimen interactions and x-ray generation and absorption are not sufficiently well known. An important example is analysis under high-absorption situations, which is the case in light-element analysis.

We have previously described the design of an electron optical bench for the study of x-ray microanalytical parameters.² The initial experiment proposed for the instrument was the study of the x-ray absorption term $f(\chi)$:

$$f(\chi) = \frac{I^*}{I_0} \quad (1)$$

For this study we measured the emitted x-ray intensities from electron-opaque targets at several different x-ray emergence angles. Since it is possible to measure only the emitted x-ray intensities from a given target and not the generated intensities, it is necessary to apply a correction factor to the experimental data to obtain the correct $f(\chi)$ values. In our earlier work we followed Green, who used a graphical method to obtain the correct $f(\chi)$ values from the emitted intensity ratios

by extrapolating χ to zero.³ In this work, as shown in Eq. (2), we use a numerical method for this correction multiplying the experimental ratios by an $f(\chi)$ term calculated from the quadratic model at the largest emergence angle measured for the sample.

$$f(\chi)_\psi = \frac{I_\psi}{I_{\max}} f(\chi)_{\max}^{\text{quad}} = \frac{I_\psi}{I_{\max}} \times \frac{I_{\max}}{I_0} = \frac{I_\psi}{I_0} \quad (2)$$

In general, we feel that correcting the data with an existing model is preferable to the fitting of the experimental points since the value of the ratio at $\chi = 0$ from the extrapolation is highly dependent on the minimum angle included in the data set.

The selection of the quadratic model, defined in Table 1, is somewhat arbitrary. Any of the various absorption models would be suitable since they all accurately predict experimental results for high x-ray emergence angles. This method of correction was not available to Green at the time of his investigation.

For this experiment, two different sample compositions were studied, elemental Si and FeS₂. Experimental measurements were taken on the Si target at beam energies of 20 and 30 keV, and on the FeS₂ target at 20 keV. At least two measurements were taken at each x-ray emergence angle. The uncertainties in $f(\chi)$ are expressed as vertical bars and are the combined uncertainties resulting from the propagation of Poisson counting statistics for both the numerator and the denominator. The measurement uncertainty of ψ , estimated at 0.1°, is indicated on the plots as horizontal error bars for each angle. The experimental data and the literature models plotted as $1/f(\chi)$ vs χ are shown in Fig. 1. The curves for the various literature models displayed in Fig. 1 are not fits to the experimental data but represent independent calculations of $f(\chi)$ for a given target and a given set of experimental parameters. The formulations of the four absorption models studies are listed in Table 1.

To evaluate the performance of each model, we constructed residual plots that display the % deviations among the several models and the experimental data defined according to

$$\% \text{ res} = 100 \{ [f(\chi)_{\text{model}} - f(\chi)_{\text{exp}}] / f(\chi)_{\text{exp}} \} \quad (7)$$

The evaluation of the performance of a given model was based on two criteria: the magnitude of the residuals and the structure observed in the plot of the residuals vs the x-ray emergence angle. The better the perfor-

The authors are at the Center for Analytical Chemistry, National Institute of Standards and Technology, Gaithersburg, MD 20899.

TABLE 1.--Summary of literature models for $f(\chi)$.

Quadratic---- Heinrich⁴

$$f(\chi) = \left(1 + 1.2 \times 10^{-6} \gamma \chi\right)^{-2} \quad (3)$$

where $\gamma = (E_0^{1.65} - E_c^{1.65})$ and $\chi = (\mu/\rho) \csc \psi$

Duplex----- Heinrich⁵

$$f(\chi) = \frac{\left(1 + 1.65 \times 10^{-6} \gamma \chi\right)^2}{\left[1 + \alpha \left(1.65 \times 10^{-6} \gamma \chi\right)\right]} \quad (4)$$

where $\alpha = 0.18 + 2/\gamma + (8 \times 10^{-9}) E_c + 0.005 \sqrt{z}$

Philibert⁶

$$1/f(\chi) = \left(1 + \frac{\chi}{\sigma}\right) \left(1 + \frac{h}{1+h} \frac{\chi}{\sigma}\right) \quad (5)$$

where $h = 1.2A/Z^2$

Pouchou⁷

$$f(\chi) = [F_1(\chi) + F_2(\chi)]/F \quad (6)$$

where F_1 , F_2 , and F are complicated integral expressions for which the reader is referred to reference 7 for details.

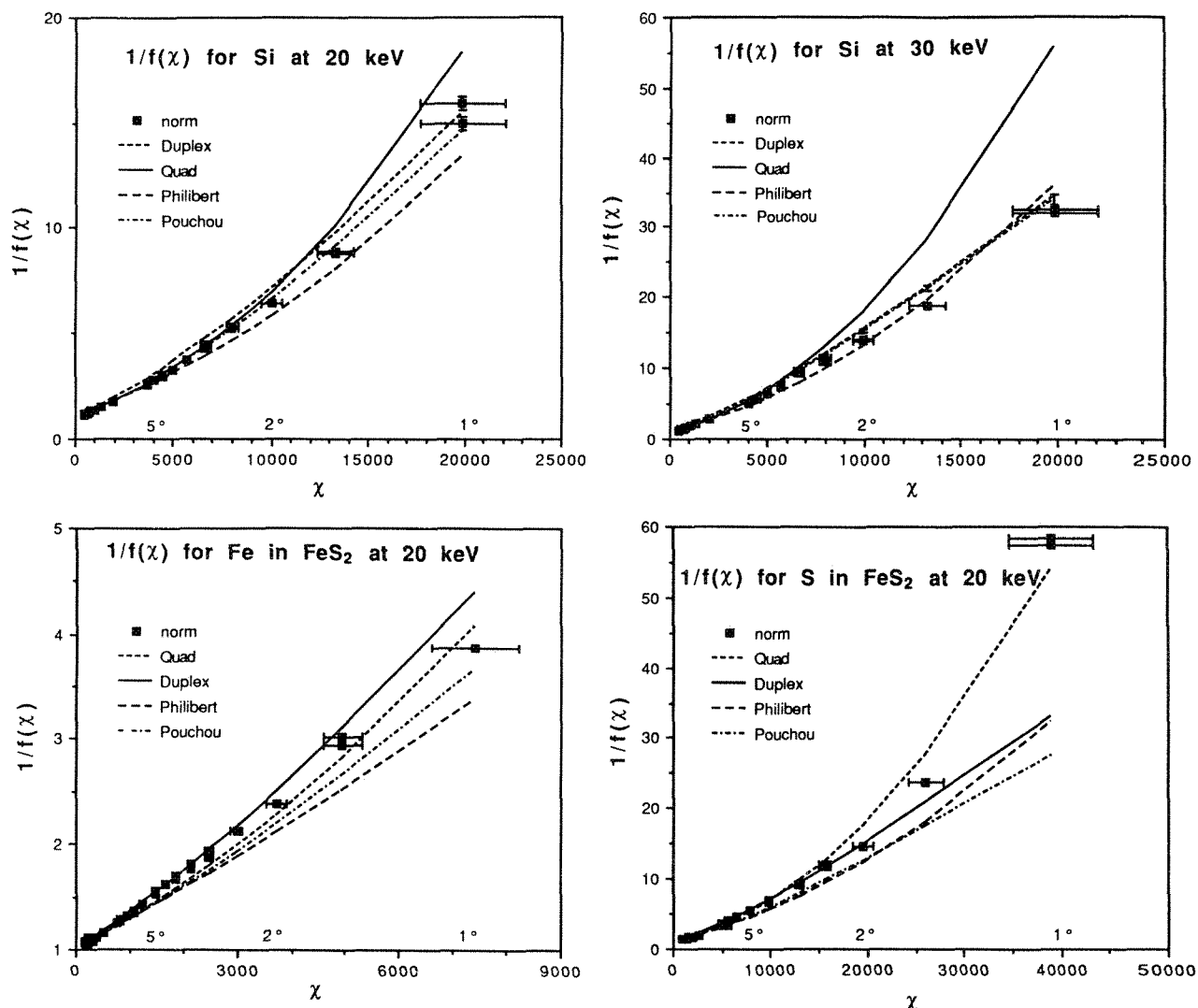


FIG. 1.--Plots of the experimental data and literature models for $f(\chi)$.

mance of a given model, the smaller the residuals and the less structure in the plots, with the values distributed randomly around zero.^{8,9} For the purpose of this discussion, lack of structure is the absence of any discernible pattern in the residuals.

Results

The magnitude of the residuals from the different models are shown in Fig. 2. These plots show the ranges of the residuals from the models for three distinct regions of χ : high absorption, $\chi > 10\,000$; medium absorption $1000 < \chi < 10\,000$; and low absorption, $\chi < 1000$. There is no high-absorption region for Fe because the Fe K α x ray at 6.4 keV has a low mass absorption coefficient in FeS₂ and it was not possible to measure accurately angles low enough to provide χ values in excess of 10 000.

An example of the information provided in these plots can be seen in the residuals for the low-absorption region. In this region, which corresponds to measurements taken at high emergence angles, the residuals have the

smallest ranges and are the closest to zero. In general, for the targets studied, the low-absorption regions for all models are within the expected experimental uncertainties.

The structure of the residuals for the different models is shown in Figs. 3 through 6. These figures are residual plots vs x-ray emission angle for the various targets. In all cases, the duplicate runs at each emission angle were averaged and displayed as a single bar. An example of what is meant by structure can be seen in the Philibert and Pouchou residual plots for Si at 20 keV (Fig. 3). The residual plot for the Pouchou model has minimal structure, remaining relatively flat for all emergence angles. In contrast, the residual plot for the Philibert model has considerable structure with increasing negative residuals over almost the entire range of angles.

Conclusions

Based on the results of this initial study we were able to draw the following general conclusions regarding the performance of the several absorption models.

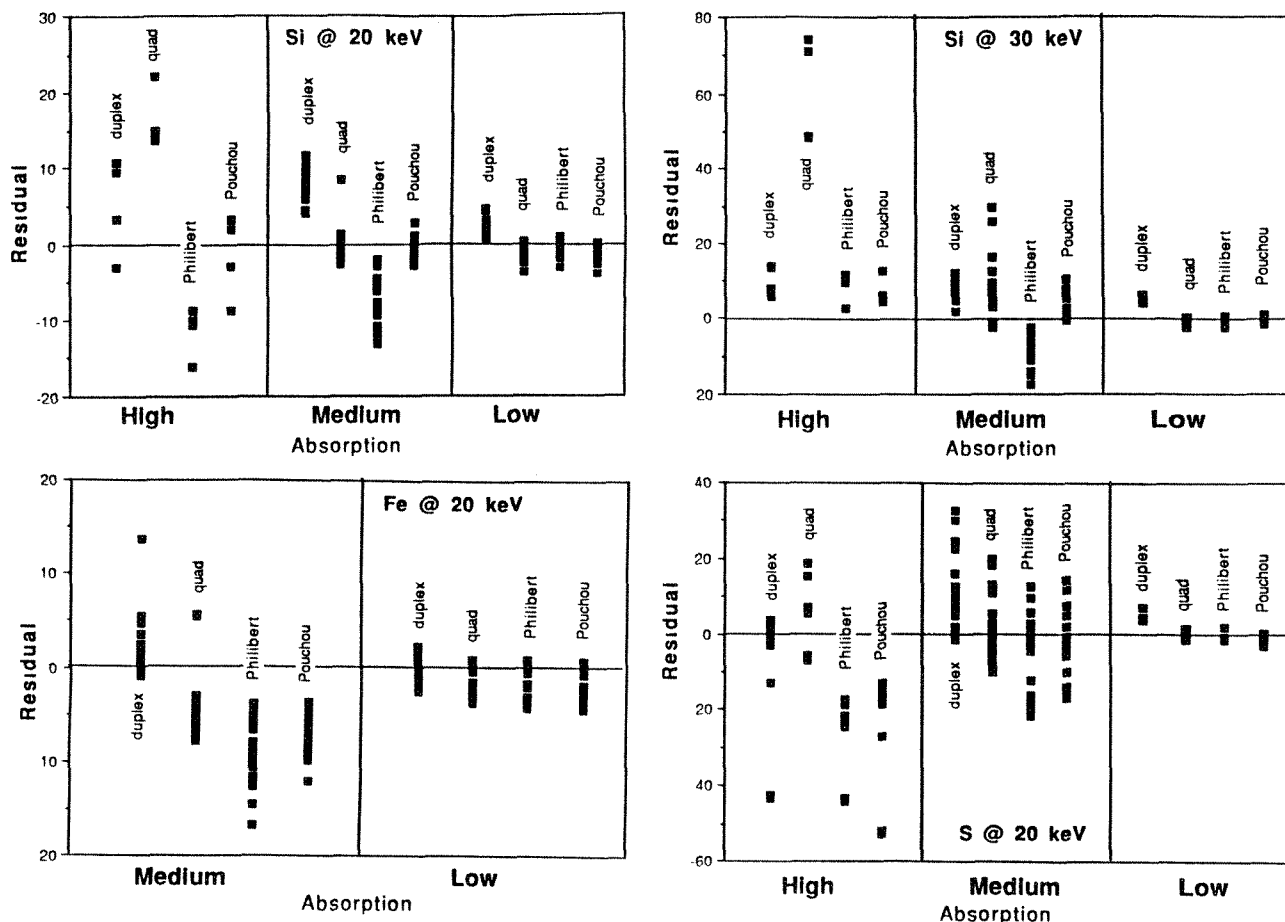


FIG. 2.--Plots of residual ranges from the various models.

a. The performance of a given model depends on the target composition as well as χ . The following is a list of which models performed best on a given target.

1. Si 20 and 30 keV (Pouchou)
2. Fe in FeS_2 (duplex)
3. S in FeS_2 (quadratic)

b. Of the four models studied no single model outperformed the others for all targets and conditions.

c. For the targets and conditions studied in this experiment, all the models have some structure in their residual plots. As a result it should be possible, with an expansion of the experimental database, to improve the formulation of the absorption term used in microanalysis.

References

1. J. I. Goldstein, D. E. Newbury, P. Echlin, D. C. Joy, C. Fiori, and E. Lifshin, *Scanning Electron Microscopy and X-Ray Microanalysis*, New York: Plenum Press, 1981, 330.
2. J. A. Small, D. E. Newbury, R. L. Myklebust, C. E. Fiori, A. A. Bell, and K. F. J. Heinrich, "An electron/x-ray optical bench for the measurement of fundamental parameters for electron probe microanalysis," *Microbeam Analysis--1988*, 263.

3. M. Green, "The target absorption correction in x-ray microanalysis," in H. H. Pattee, V. E. Cosslett, and A. Engstrom, Eds., *X-Ray Optics and X-Ray Microanalysis*, New York: Academic Press, 1973, 361-377.

4. K. F. J. Heinrich, *Electron Beam Microanalysis*, New York: Van Nostrand Reinhold, 1981, 291-292.

5. K. F. J. Heinrich, personal communication.

6. J. Philibert, in H. H. Pattee, V. E. Cosslett, and A. Engstrom, Eds., *X-Ray Optics and X-Ray Microanalysis*, New York: Academic Press, 1973, 379.

7. J. Pouchou and F. Pichoir, "Quantitative analysis of homogeneous or stratified microvolumes applying the model PAP," to be published in the proceedings of the NIST workshop on quantitative electron probe analysis held at Gaithersburg, Md., August 1988.

8. F. J. Anscombe, J. W. Tukey, "The examination and analysis of residuals," *Technometrics* 5: 141-160, 1963.

9. J. J. Filliben, "Testing basic assumptions in the measurement process," in J. R. De Voe, Ed., *Validation of the Measurement Process*, ACS Symposium Series, No. 63, 1977, 30-113.

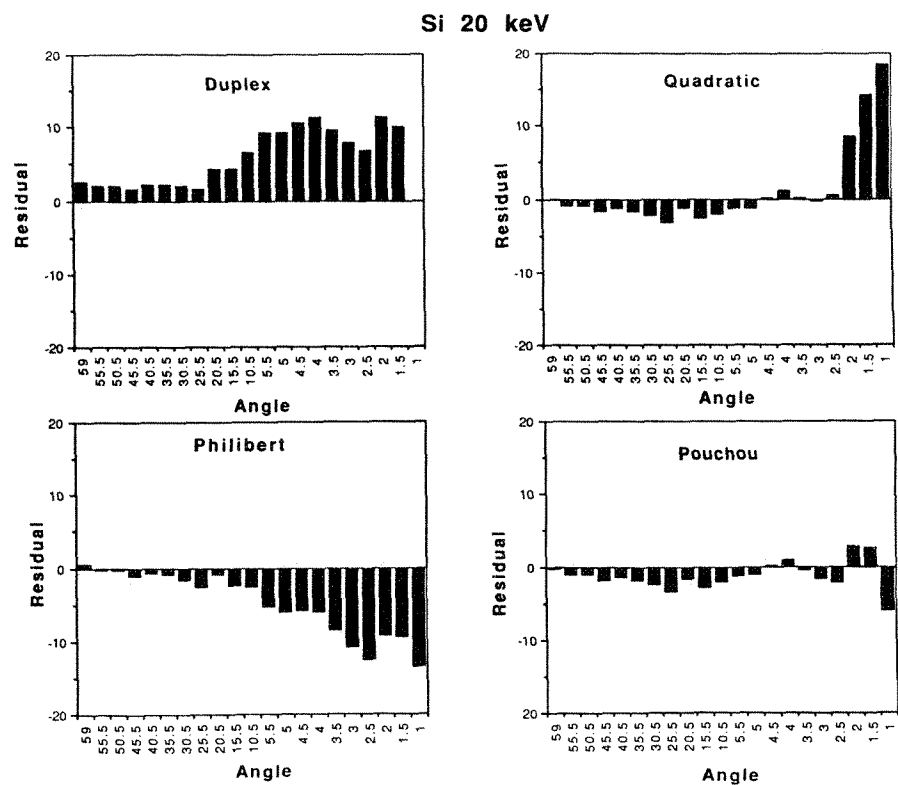


FIG. 3.--Residual plots vs χ for Si at 20 keV.

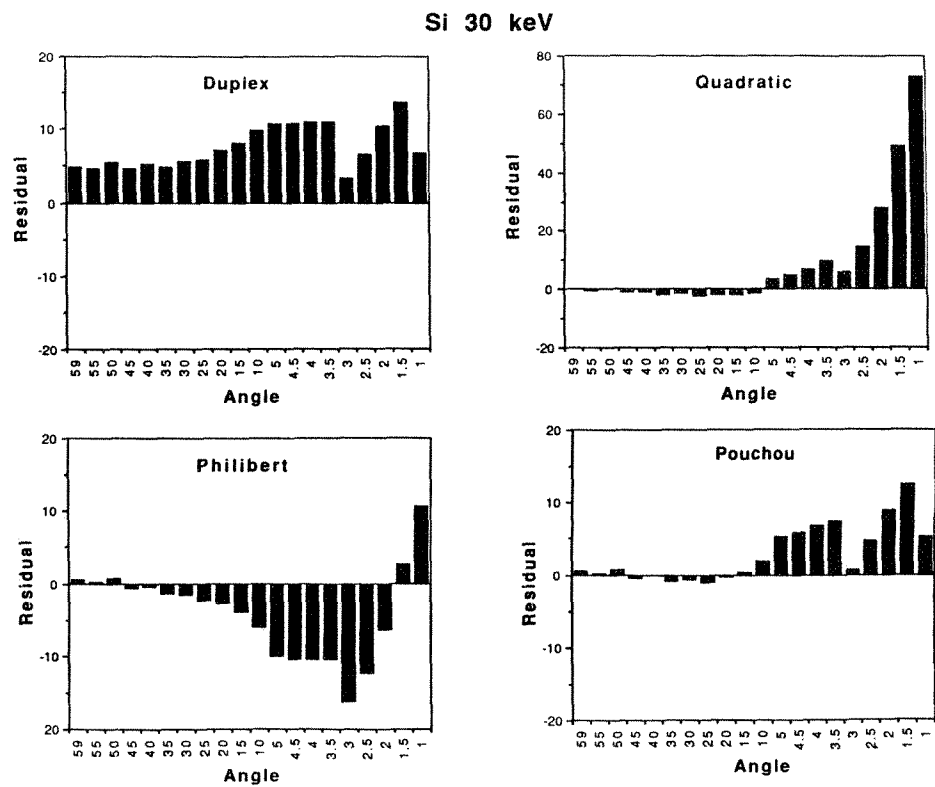


FIG. 4.--Residual plots vs χ for Si at 30 keV.

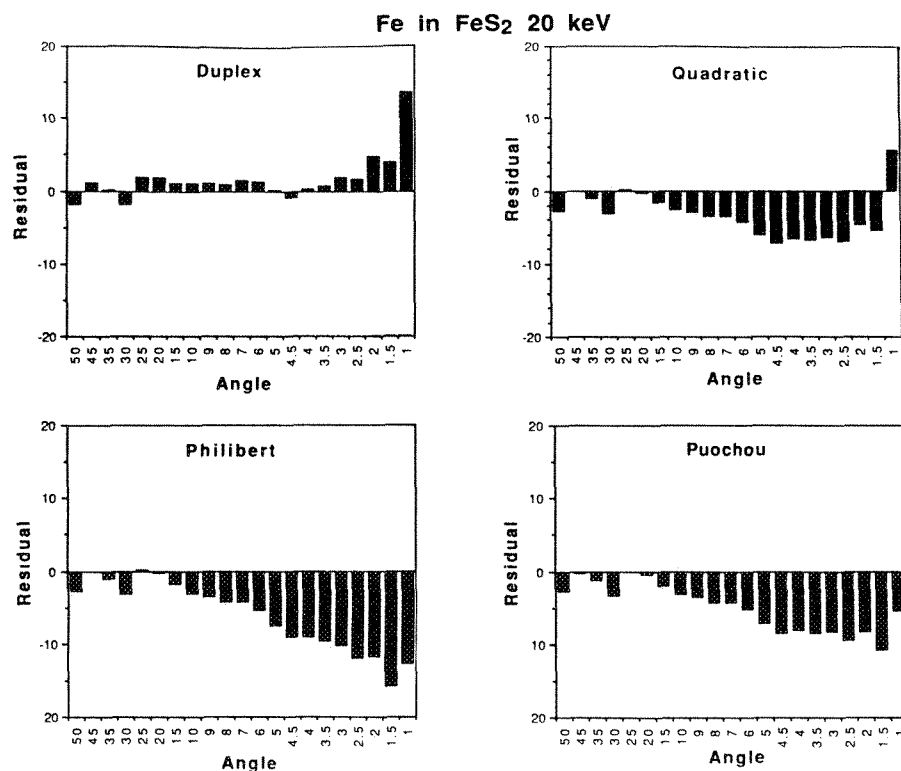


FIG. 5.--Residual plots vs χ for Fe in FeS₂ at 20 keV.

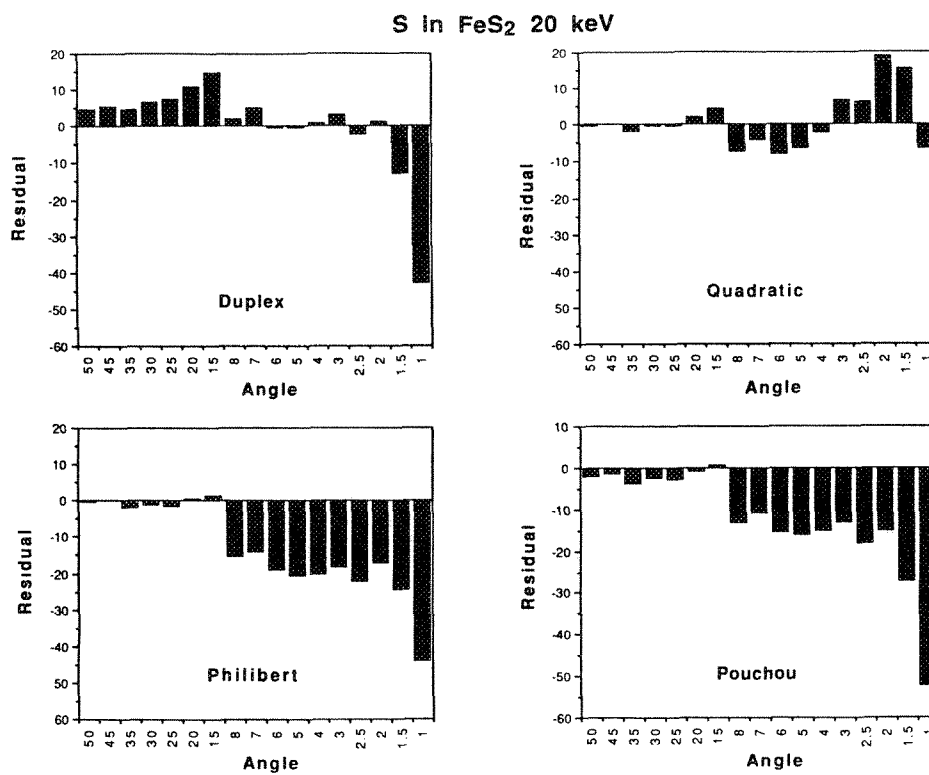


FIG. 6.--Residual plots vs χ for S in FeS₂ at 20 keV.

ESCAPE AREA OF SINGLY AND PLURALLY BACKSCATTERED ELECTRONS IN THE SCANNING ELECTRON MICROSCOPE

O. C. Wells

The (totally different) escape areas of the diffused backscattered electrons (BSE) and of the (collectively) singly or plurally scattered BSE in the scanning electron microscope (SEM) can be calculated from the observed energy spectrum of BSE from a solid target with normal incidence. The first step is to obtain the spatial distribution of the total BSE emission. One does it by assuming that all BSE with the same energy have penetrated for the same distance in the target, and that they then emerge uniformly within a circle of radius equal to that distance. The logarithm of the total emission density as derived in this way is plotted against the radius squared. The straight part of this curve as extrapolated to the axis gives the diffused BSE distribution. A sharply rising excess near to the axis gives (collectively) the singly and plurally scattered BSE.

The high-magnification secondary-electron (SE) image of a solid sample in the scanning electron microscope (SEM) is affected by SE excited by backscattered electrons (BSE). The spatial distribution of the BSE is therefore important and is discussed here. BSE can be divided into single scattered, plurally scattered, or diffused BSE based on the number of elastic scattering events, where the word "diffused" implies that the motion is equally likely in all directions.¹ It is to be expected that the diffused BSE will excite SE with a Gaussian distribution over an area with a radius comparable to the electron penetration depth, whereas singly and plurally scattered BSE will excite SE closer to the entry point of the electron beam.

The expression "high resolution" as applied here to the SE or BSE image means that the escape area for some specified type of SE or BSE is considerably smaller than the escape area for the diffused BSE. Recently, Peters (1989) has suggested that singly and plurally scattered BSE might emerge sufficiently close to the incident beam so as to modify significantly the high-resolution SE image in the case when a low-density specimen is covered with a thin high-density metal film. We must therefore ask how much these BSE might affect the high-resolution SE image in other situations, also.

Initially it was believed (in effect) that only SE excited by the incoming beam and by the diffused BSE were important for the formation of the SE image. Thus, von Ardenne (1940), with reference to his diagram shown in Fig. 1, wrote (free translation):

The author is at the IBM Thomas J. Watson Research Center, Box 218, Yorktown Heights, NY 10598.

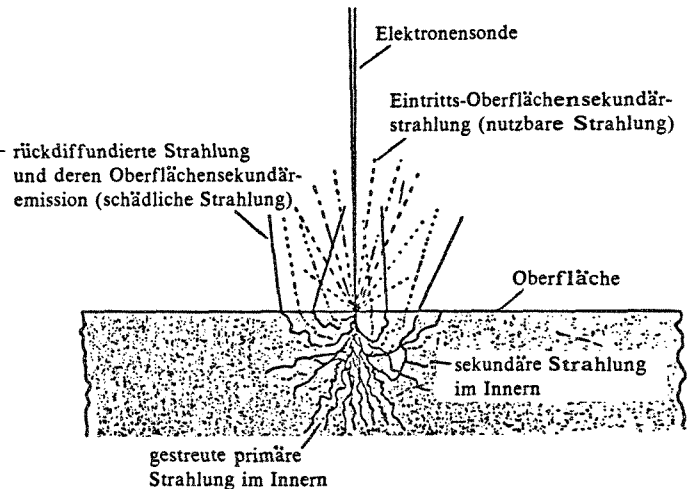


FIG. 1.--Electron penetration into solid target in SEM showing primary-excited and BSE-excited Se (relettered from von Ardenne 1940).

"... the diameter of the specimen surface traversed by the BSE current ["reverse-diffusing-radiation"] is larger than the diameter of the incoming electron beam ["diameter of the exposed part of the object zone"]. One may therefore assume that the BSE current does not vary with the position of the probe, so that only changes in the SE-I signal ["entrance-surface-secondary-radiation"] are observable. The BSE current is therefore harmful because it reduces the image contrast. . . . The image contrast would have been reinforced again by compensating measures taken at the output of the secondary emission amplifier."

Independently of the above, Everhart et al. (1959) wrote:

"Another factor . . . is the production of secondary electrons by reflected electrons. . . . their number is unlikely to bear much relation to the condition of the surface at the point of entry of the primary beam. It seems probable therefore that these secondaries . . . will contribute to the background noise rather than to signal in a high-resolution micrograph. At lower resolution, when the escape area of these electrons does not exceed the dimensions of a picture element, they will contribute usefully to the signal."

Pease and Nixon (1965) wrote:

"At high magnifications . . . only the primary excited secondaries contribute usefully to the signal. The backscattered electrons and the backscattered excited secondaries emerge from outside the picture element and in general appear as spurious signal."

The same idea is described in later papers also. As a part of the above discussion, the spatial distribution of the primary-excited SE was calculated on the assumption that the incoming electrons penetrate along a straight line, with a constant probability of SE excitation, to below the escape depth for the SE (Wells 1957).

At the present time, SE that are excited by primary electrons at the point of incidence are referred to as SE-I, whereas SE-II are excited by the BSE at the surface of the specimen and SE-III from the surrounding objects in the specimen chamber (Peters 1982). Ideally, the SE-II should be subdivided into those that arise from singly scattered, plurally scattered, or diffused BSE. The situation can become quite complicated, for example, if an incoming electron is scattered out of the specimen again before passing below the escape depth of SE, or if the incident energy is such that the penetration depth is small in comparison with the beam diameter. Here, it is assumed that the incident electrons penetrate to a depth that is considerably greater than either the beam diameter or the SE escape depth.

Singly and plurally scattered BSE in the forward scattering direction from a tilted solid sample have been used for many years in the SEM to give either the reflected electron image (with no energy filter) or the low-loss electron image (with an energy-filtering detector) (McMullan 1953, Wells 1971). Ong (1970) formed high-resolution BSE images from low-density biological samples by coating them with heavy metal. In all these cases, BSE are scattered by only one (or at most only a few) wide-angle scattering events.

Cosslett and Thomas (1965) measured BSE from thin films of copper and gold and concluded that 50% arose from single scattering. Murata (1974) published Monte Carlo calculations of the BSE escape area from a solid target at right angles to the beam, and found a strong central peak. He calculated that about half of the total BSE was from singly and plurally scattered electrons. The question is whether the escape of singly and plurally scattered BSE will be sufficiently localized for these electrons to contribute usefully to the high-resolution component of the SE image. If that is the case, then the central peak that was described by Murata can be expected to have a significant effect in high-resolution SE imaging in general.

Escape Area of BSE: Theory

Murata calculated the escape area for BSE by the Monte Carlo method, in which electron trajectories are simulated by use of random numbers and electron scattering data. Here, we try a different approach that can be applied in the case of normal electron incidence; we estimate the escape area from published BSE energy distribution curves without making any detailed assumptions about the individual scattering events in the target. To do so we must make two main assumptions (either of which can be changed

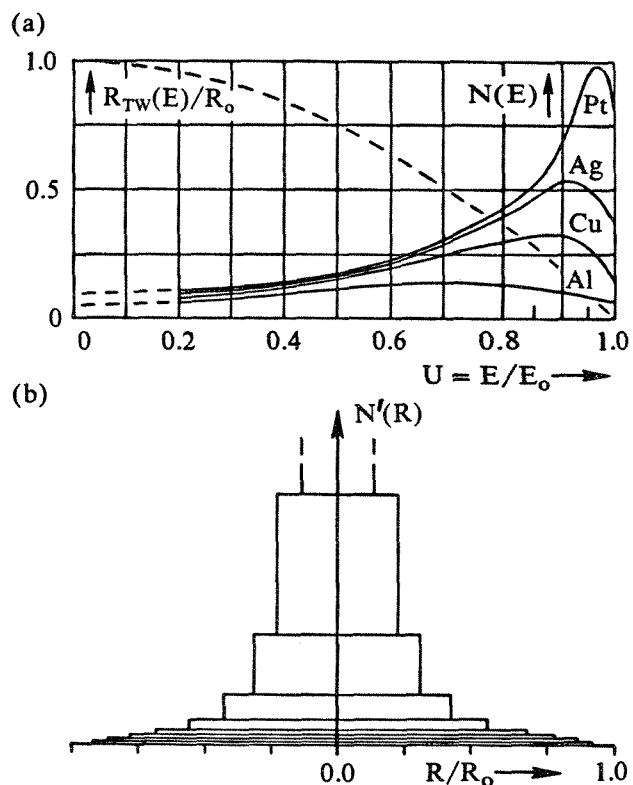


FIG. 2.--(a) Solid lines: energy spectrum of BSE from Pt, Ag, Cu, and Al with normal electron incidence for $20 \text{ keV} < E_0 < 40 \text{ keV}$ with arbitrary vertical scale (from Kulenkampff and Spyra 1954). Dashed line: Normalized range from Eq. (8). (b) Spatial distribution of BSE from Pt as calculated from (a) by present model.

later should the need arise). The first is the continuous slowing-down approximation, in which any BSE with energy E has penetrated for the same distance $R_{TW}(E)$ through the target as given by the Thomson-Whiddington law. It is clear that these BSE must emerge in some manner within a circle of radius R equal to $R_{TW}(E)$. It is assumed here that the emission of BSE of energy E is uniform within this circle.

Four quantities characterize the escape of BSE from a solid target (Fig. 2):

First is $N(E)dE$, which is the probability of a BSE in the energy range from E to $E + dE$ at any point on the surface for a single primary electron, where $N(E)$ has the dimensions probability per eV. Thus the solid lines in Fig. 2(a) show the energy distribution of BSE from Pt, Ag, Cu, and Al with normal electron incidence as measured by Kulenkampff and Spyra (1954). In what follows, it is helpful to think in terms of vertical strips of height $N(E)$ and width dE under these curves, each of which corresponds to a circular emission area of radius $R_{TW}(E)$ on the surface of the specimen.

The next important quantity is the probability density function $N'(E,R)dE$ per cm^2 of a BSE in the energy range from E to $E + dE$ at distance R from the incident electron beam

(again, for a single primary electron). Thus, if the BSE of energy E emerge uniformly within circle of radius $R_{TW}(E)$, we obtain the total probability density $N'_{total}(R)$ per cm^2 by adding together the contributions of the disks shown in Fig. 2(b), each of which corresponds to one of the vertical strips in Fig. 2(a).

The probability that a single primary electron will give rise to a BSE within a distance R of the probe in two ways. First is $\eta(R)$, which one obtains by integrating the density function $N'_{total}(R)$ times the radius from the origin out to radius R . Thus, if a pixel in the image corresponds to a circle of radius R_{pixel} on the surface of the specimen, then $\eta(R_{pixel})$ is the probability that a BSE will be emitted within the pixel on the specimen surface.

Finally, it is possible to argue that the signal-to-noise ratio of the recorded image should be calculated from a slightly smaller number $\eta_{SNR}(R)$, which one obtains by summing the contributions of disks having a radius smaller than R_{pixel} while ignoring the central regions of the larger disks as being part of the background.

These four quantities will now be considered in more detail. The BSE coefficient η is expressed in terms of $N(E)$ as follows:

$$\int_0^{E_0} N(E) dE = \eta \quad (1)$$

The normalized energy distribution $N_n(U)$ is defined by

$$N_n(U) = E_0 N(E) \quad (2)$$

where E_0 is the incident energy, and

$$E/E_0 = U \quad (3)$$

from which

$$\int_0^1 N(U) dU = \eta \quad (4)$$

The related functions $\eta(R)$ and $\eta_{SNR}(R)$ are given in Eqs. (13) and (14) below.

According to the Thomson-Whiddington law, the thickness $R_{TW}(E)$ of a self-supported film having a most probable exit energy E for the transmitted electrons is given by

$$R_{TW}(E) = k (E_0^2 - E^2) \quad (5)$$

where k is a constant (Whiddington 1912 and 1914; Terrill, 1923). The electron range R_0 is given by putting $E = 0$:

$$R_0 = R_{TW}(0) = k E_0^2 \quad (6)$$

The normalized penetration depth $R_n(U)$ is given by

$$R_n(U) = R_{TW}(E)/R_0 \quad (7)$$

$$= 1 - U^2 \quad (8)$$

from Eqs. (3), (5), and (6). The dashed line

in Fig. 2(a) shows $R_n(U)$ as a function of U .

The probability $N'(E,R)dE$ per cm^2 of a BSE in the energy range from E to $E + dE$ at distance R from the incident electron beam is derived from the appropriate vertical strip under the BSE spectrum curve in Fig. 2(a). Thus, if the BSE in the energy range from E to $E + dE$ emerge uniformly within the circle given by $0 < R < R_{TW}(E)$, then

$$N'(E,R) dE = \frac{N(E) dE}{\pi R_{TW}^2(E)} \text{ if } R < R_{TW}(E) \quad (9)$$

and is zero if $R > R_{TW}(E)$. The total probability density of BSE $N'_{total}(R)$ per cm^2 per incident electron at radius R is obtained by integration of $N'(E,R)$ on E for the circular contributions that extend to or beyond R :

$$N'_{total}(R) = \int_0^{E(R)} N'(E,R) dE \quad (10)$$

where $E(R)$ is the energy of BSE corresponding to a penetration distance equal to R . It follows that

$$N'_{total}(R) = \frac{1}{\pi R_0^2} \int_0^{E(R)} \frac{N(E)}{[1 - (E^2/E_0^2)]^2} dE \quad (11)$$

$$= \frac{1}{\pi R_0^2} \int_0^{U(R)} \frac{N(U)}{(1 - U^2)^2} dU \quad (12)$$

from Eqs. (8) and (9), where $U(R)$ is the value of U corresponding to radius R .

The functions of $\eta(R)$ and η_{SNR} are given by

$$\eta(R) = \int_0^R N'_{total}(R) dR \quad (13)$$

and

$$\eta_{SNR}(R) = \int_{E(R)}^{E_0} N(E) dE \quad (14)$$

Escape Area of BSE: Numerical Calculations

The above theory was applied to the numerical data for Pt and Al in Fig. 2(a) as follows. We plotted curves for $\eta_{SNR}(R)$ as given by Eq. (14) by estimating the areas under the BSE energy distribution curve and then normalizing so that $\eta_{SNR}(R_0) = 1$. Plots for Pt and Al are shown in Fig. 3. The curve for Pt shows a higher concentration of emitted BSE closer to the beam, as is to be expected from the greater proportion of faster BSE for Pt as shown in Fig. 2(a).

The BSE spatial density distribution function shown in Fig. 2(b) was derived from the curve for Pt in Fig. 2(a) as follows. First, the U axis in Fig. 2(a) was divided into five

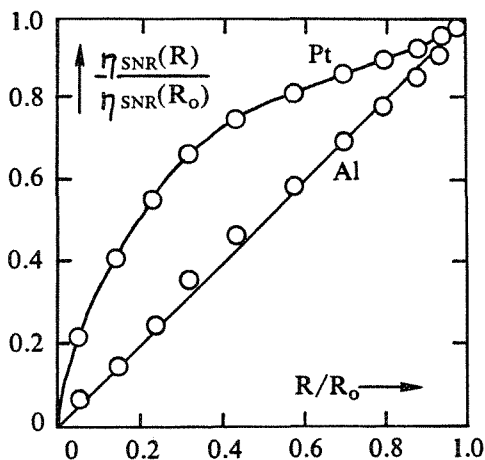


FIG. 3.--Plots of $\eta_{\text{SNR}}(R)/\eta_{\text{SNR}}(R_0)$ for Pt and Al.

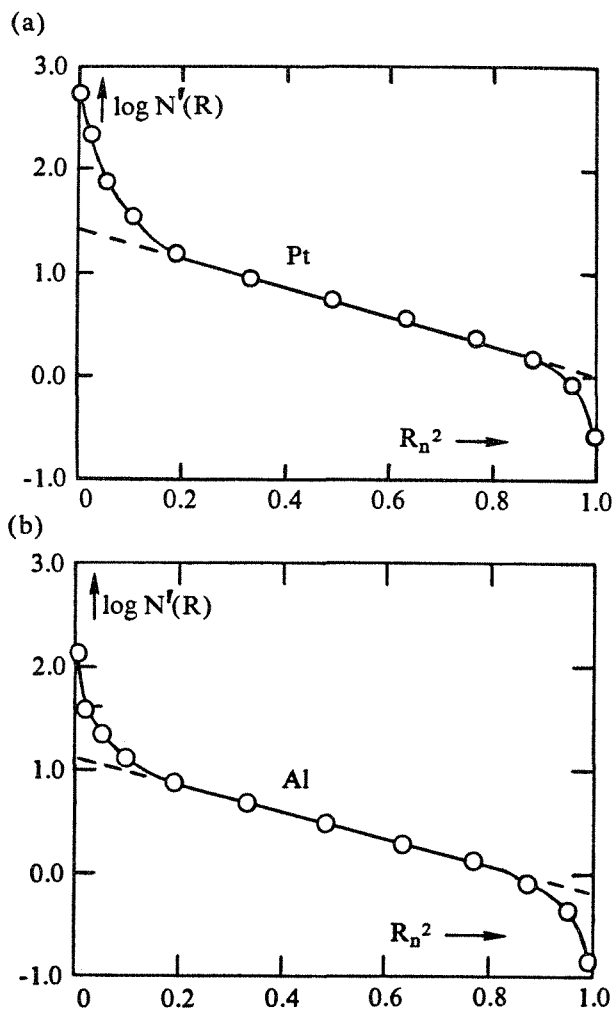


FIG. 4.--Plots of $\log N'_{\text{total}}(R)$ vs R_n^2 ; circles show midpoints of vertical steps in Fig. 2(b) with arbitrary vertical scale. (a) Curve for Pt. (b) Curve for Al. Both curves have straight portion corresponding to Gaussian distribution of diffused BSE, with peak at $R = 0$ corresponding to singly and plurally scattered BSE.

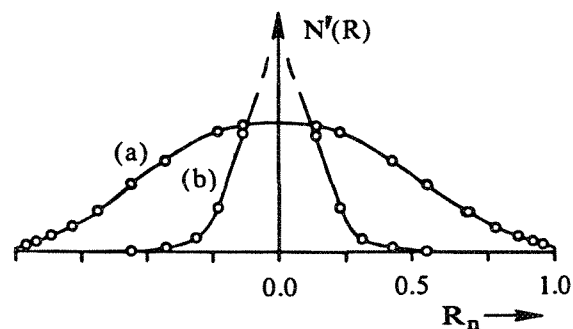


FIG. 5.--Data from Fig. 4 replotted with linear axes: (a) Extrapolated straight line in Fig. 4 shows escape density for diffused BSE. (b) Residual emission (plotted with vertical scale reduced by factor of 20) shows collectively contribution of singly and plurally scattered BSE.

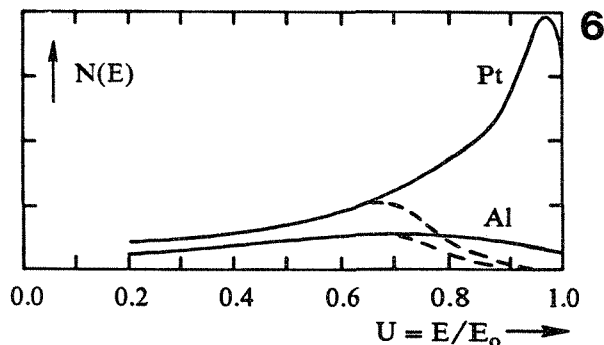


FIG. 6.--Data from Fig. 4 referred back to BSE energy distribution curves for Pt and Al. Dashed lines show approximate delineation between diffused BSE (below dashed line), and collectively singly and plurally scattered BSE (above).

strips of width $U = 0.1$ in the range $0.3 < U < 0.8$ and into four strips of width $U = 0.05$ for $0.8 < U < 1.0$. Then, starting from $U = 0$, each strip was transformed into a disk of radius equal to the height of the dashed curve in Fig. 2(a) and of thickness given by Eq. (9). These disks are stacked in Fig. 2(b) to show the spatial distribution of BSE density. The surprising result is how rapidly the disks increase in thickness as the axis is approached. Thus, the remaining three disks that are above the diagram at the center of Fig. 2(b) (i.e., for $U > 0.85$) reach a total height more than seven times the height shown.

The data for Pt are shown on a plot of $\log N'_{\text{total}}(R)$ against R_n^2 in Fig. 4(a), where the circles correspond to the midpoints of the vertical steps in Fig. 2(b). The corresponding curve for Al is shown in Fig. 4(b). Over the range $0.2 < R_n^2 < 0.95$ the points lie on a straight line, which gives the Gaussian distribution expected for the diffused BSE. For points close to the beam there is a sharp increase in emission, corresponding to the singly and plurally scattered BSE.

Figure 5(a) shows the data points on the extrapolated straight line in Fig. 4(a) with linear scales to show the spatial distribution of

the emission density of the diffused BSE. Figure 5(b) shows the excess emission density of BSE close to the beam with the vertical scale factor smaller by a factor of 20 in comparison with Fig. 5(a). We see a component of BSE emission density that is sharply peaked on the axis, as is to be expected from singly and plurally scattered BSE.

By reversing the steps of the calculation, the probability density of the diffused BSE was referred back to the energy-distribution curve for BSE. In Fig. 6, the diffused BSE are below the dashed line and consist mainly of the faster BSE. By measuring the areas under the curves, we find that the fraction of η that corresponds to singly and diffused BSE is $\sim 80\%$ of the total for Pt, whereas for Al the fraction is $\sim 20\%$. (There were some rounding errors in the reverse calculation, so these results are preliminary.) These curves show that the singly and multiply scattered BSE have higher energy than the diffused BSE, and Fig. 4 shows that they emerge more closely to the incident beam.

Discussion

These calculations confirm that for both Pt and Al, approximately half of the singly and multiply scattered BSE emerge within a distance of about $0.2R_0$ of the incident beam, and that the emission density increases rapidly within circles that are still smaller. It is therefore quite in order to suppose that they contribute usefully to the recorded image at magnifications for which the diffused BSE give an effectively uniform background. The low-loss part of the singly scattered signal (i.e., BSE that have lost less than 100 or 200 eV in being scattered from a solid target) can be expected to contribute usefully up to the highest magnifications, and the fraction of unfiltered BSE that contribute usefully to the signal diminishes as the magnification is increased.

This method for calculating the BSE escape area is more limited than the Monte Carlo approach because it cannot be applied with an oblique angle of incidence or with special specimen geometries. However, it did seem to be worth while to determine what conclusions could be drawn from the published BSE energy-distribution curves, and whether the way in which the shape of these curves changes with increasing atomic number can be related to the expected increase in singly and plurally scattered BSE.

Certainly, it is encouraging to see the way in which the plots of $\log N'(R)$ against R^2 shown in Fig. 4 consists so clearly of a straight line that shows the contribution made by the diffused BSE, with a peak centered on the beam that corresponds to the singly and plurally scattered signal. By referring the data back to the energy distribution curve, we can make an estimate of the division of the BSE between the diffusion model as described by Archard (1961) and the wide-angle scattering model of Everhart (1960).

As compared with Monte Carlo method, this model is based more closely on experimental

data and does not involve any detailed assumptions about energy loss or scattering events. The results obtained by this preliminary investigation of the model are sufficiently encouraging for the next step to be taken: write a computer program to process more of the available energy spectra for BSE and try various ways of distributing the BSE with energies between E and $E + dE$ over the circle of radius $R_{TW}(E)$. Allowance must be made for energy straggling. Detailed comparisons must be made with results obtained by the Monte Carlo method. Also, further investigations are needed of the allocation of the areas under the energy distribution curves for BSE between the diffused and more locally scattered electrons.

This model shows a singularity in $N'(R)$ at the origin if $N(E_0)$ is nonzero. This singularity disappears when $R_{TW}(E)$ is given a minimum value equal to the mean free path between inelastic scattering events.

Bibliography

- G. D. Archard (1961), "Back scattering of electrons," *J. Appl. Phys.* 32: 1505-1509.
- M. von Ardenne (1940), *Elektronen-Übermikroskopie*, Berlin: Springer, (1940); Ann Arbor: Edwards (1943). [For a summary, see McMullan (1988), cited below.]
- V. E. Cosslett and R. N. Thomas (1965), "Multiple scattering of 5-30 keV electrons in evaporated metal films: III. Backscattering and absorption," *Brit. J. Appl. Phys.* 16: 779-796.
- T. E. Everhart, O. C. Wells, and C. W. Oatley (1959), "Factors affecting contrast and resolution in the scanning electron microscope," *J. Electronics Control* 7: 97-111.
- T. E. Everhart (1960), "Simple theory concerning the reflection of electrons from solids," *J. Appl. Phys.* 31: 1483-1490.
- H. Kulenkampff and W. Spyra (1954), "Energy distribution of backscattered electrons" (in German), *Z. Phys.* 137: 416-425.
- D. McMullan (1953), "An improved scanning electron microscope for opaque specimens," *Proc. IEE* 100(Pt. II): 245-259.
- K. Murata (1974), "Spatial distribution of backscattered electrons in the scanning electron microscope and electron microprobe," *J. Appl. Phys.* 45: 4110-4117.
- P. S. Ong (1970), "Contrast and resolution in scanning electron microscopy using backscattered electrons," *Proc. 28th Ann. Meeting EMSA*, pp. 392-393.
- R. F. W. Pease and W. C. Nixon (1965), "High resolution scanning electron microscopy," *J. Sci. Instrum.* 42: 31-35.
- K.-R. Peters (1982), "Conditions required for high quality high magnification images secondary electrons in scanning electron microscopy," *SEM/1982*, 1359-1372.
- K.-R. Peters (1989) (unpublished work and private discussions).
- O. C. Wells (1957), *The Construction of a Scanning Electron Microscope and Its Application*

- to the Study of Fibres*, Ph.D. Dissertation,
Cambridge University, England.
- O. C. Wells (1971), "Low-loss image for scanning electron microscope," *Appl. Phys. Lett.* 19: 232-235.
- R. Whiddington (1912), "The transmission of cathode rays through matter," *Proc. Roy. Soc.* A89: 554-560.
- H. M. Terrill (1923), "Loss of velocity of cathode rays through matter," *Phys. Rev.* 22: 101-108.

FILTERED LEAST-SQUARES FITTING OF EDS SPECTRA WITH DERIVATIVE REFERENCES: PROBLEMS AND LIMITATIONS IMPOSED BY COUNTING STATISTICS

T. E. Bostrom and C. E. Nockolds

Systematic errors in fitted intensities are introduced when the filtered least-squares (FLS) method of spectrum deconvolution^{1,2} is used with spectra in which the centroid positions and/or the resolution differ from those of the reference spectra. These fit errors can be particularly serious when overlaps are involved.^{1,3} There are several, mostly unavoidable sources from which miscalibrations can occur: the use of reference peaks obtained at different count rates; long- or short-term amplifier instability; and changes due to exposing the detector to sudden massive count rates such as occurs when a grid bar in a TEM is hit, following which the electronics may take some time to restabilize.

A moderate miscalibration can be generally corrected for by incorporating the first and second derivatives of the reference profiles in the fit.^{3,4} In our experience this procedure works well with peaks with good counting statistics; the corrected intensities remain approximately within the statistical error.⁵ In addition, a good estimate of peak shift can be obtained from the derivative fit, as previously shown.⁴ However, a large statistical variation in the results is observed when derivatives are applied to peaks that are relatively noisy, such as peaks for minor elements with low weight fractions, or spectra from beam-sensitive biological materials. Derivatives can be omitted from very small peaks, since the systematic error is within counting statistics, but for moderate peaks the systematic error can be significant. An overlap of a small peak by a large one presents a particular problem when miscalibration is present. Applying derivatives to both peaks decreases the precision of the fit, and produces a large statistical error for the small peak. Kitazawa et al.³ used derivatives only with the large peak to resolve the K/Ca overlap, but in general this procedure would leave a systematic error in the overlapped peak if it were of moderate size.

In this paper we have examined the limitations due to counting statistics on the use of derivatives with relatively small peaks, of peak heights ≤ 1000 counts and intensities ≤ 12000 (at 10 eV/channel). We also suggest an improved procedure for dealing with miscalibration in spectra containing both large and small peaks to be fitted. In this approach, the mean peak shift and resolution determinations from an initial derivative fit of the largest peaks

are used to fix these parameters for the smaller peaks during a subsequent fit of the spectrum.

Methods

Theory. From McMillan et al.,⁴ if $S'(E, \epsilon, \tau)$ represents a Gaussian $S(E)$ of original width parameter σ , after a centroid shift of ϵ and new width $\sigma + \tau$, then

$$S'(E, \epsilon, \tau) = S(E) - \epsilon \frac{\delta S}{\delta E} + (\tau\sigma + \frac{1}{2}\epsilon^2) \frac{\delta^2 S}{\delta E^2}$$

If $S(E)$ is the reference peak and k_0 is the intensity factor between the unknown and the reference, then the equation actually solved is

$$S'(E, \epsilon, \tau) = k_0 S + k_1 \frac{\delta S}{\delta E} + k_2 \frac{\delta^2 S}{\delta E^2}$$

where $k_1 = -k_0\epsilon$, and $k_2 = k_0(\tau\sigma + \frac{1}{2}\epsilon^2)$. We can then solve for ϵ and τ , and calculate the shift and resolution change in eV after appropriate scaling.

Test Spectra and Calculations. Calculations were mostly carried out on generated spectra to which a Gaussian noise function was applied. This function had been previously shown to simulate accurately the physical noise in real spectra. The generated spectra had the advantage that the centroid shifts, resolution changes, and intensities were known exactly. Routines were programmed in Micro-soft QuickBasic on an IBM PC/AT compatible microcomputer to carry out a full weighted filtered least-squares fit with derivatives, in which a $6 + 13 + 6$ channel digital filter (at 10 eV/channel) was used. Reference peaks were generated at a FWHM (full-width-at-half-maximum) of 120 eV. A level background of height 100 counts was included. All peak intensities are expressed in terms of the intensity within 1.2 FWHM of the centroid. Results in the tables are given as mean \pm S.D.

For some tests, real spectra were collected with an EDAX detector on a Philips 505 SEM, and calculated by use of a program (PVEDXT) written to carry out FLS fitting with derivatives on an EDAX PV9900 MCA system.

Results

Statistical Variation. To test the precision of the derivative fit as a function of peak size and noise, unmodified generated peaks ranging in height from 0 to 1000 counts, with noise, were fitted, and the errors from 30 replicate fits at each peak size are shown in

The authors are with the Electron Microscope Unit, University of Sydney, Sydney, NSW 2006, Australia.

TABLE 1.--Statistical variation in fitted intensities, estimated peak shifts, and resolution changes as function of peak size. Peaks at 120 eV FWHM on background of height 100, with statistical noise. No centroid shift or resolution change ($n = 30$).

Peak height	True net intensity	No derivatives		With derivatives	
		Intensity	Intensity	Calc shift (eV)	Calc resolution change (eV)
0	0 (± 55) ^a	9 ± 53	8 ± 93	n a ^b	n a ^b
100	1098 (± 64)	1096 ± 85	1094 ± 101	-0.69 ± 2.98	-1.03 ± 9.12
200	2196 (± 72)	2203 ± 62	2186 ± 95	-0.08 ± 1.92	-1.05 ± 4.65
500	5490 (± 92)	5487 ± 86	5494 ± 145	0.08 ± 0.72	0.07 ± 2.46
1000	10980 (± 118)	11005 ± 127	11005 ± 139	-0.04 ± 0.61	-0.03 ± 1.71

^a Expected statistical error $\sqrt{(1+2B)}$, where I is the net intensity and B is the integral background count

^b Not valid measurements for an unconstrained fit and zero peak

Table 1. The statistical variation was always greater when derivatives were used, but the difference was less pronounced with the largest peak size. Similar calculations on real spectra from a carbon specimen containing small amounts of S and Ca typically gave a standard deviation with derivatives of about twice that obtained when derivatives were omitted. The centroid shift may be estimated to within about 1 eV from a peak of about 5000 counts net intensity, but the resolution change is less well determined and can only be calculated to within about 3 eV from a peak of this size. Table 1 indicates that for peak intensities much below 5000 counts, the statistical variation in the estimated centroid shifts and resolution changes is too great for derivatives to be useful.

Measurements of Resolution Change. McMillan et al.⁴ demonstrated that peak shifts could be accurately measured from derivative fits, a result we have also observed. We have tested whether resolution changes could be similarly determined. Gaussian peaks of height 1000 (with or without noise) were generated at different FWHM, and fitted with a reference peak at 120 eV FWHM. The calculated resolution changes are given in Table 2 and show a reasonable correspondence with the true values, but the results with non-noisy peaks indicate a small systematic error in this measurement. Table 2 also shows the percentage error in the measured intensities with changes in resolution, in agreement with the results of McMillan et al.⁴

Methods of Using Derivatives. We have tested our proposed method of applying derivatives to spectra with large and small peaks, in which the estimated peak shift and resolution from the large peaks (intensity >5000 counts) is used to fix the shift and resolution parameters

TABLE 2.--Measured resolution changes from derivative fit, and effect of resolution changes on fitted intensity. Generated Gaussian peaks of height 1000 at various values of FWHM, with or without added noise, fitted with reference peak of 120 eV FWHM. No centroid shift ($n = 20$ except for zero case, where $n = 30$).

	APPLIED RESOLUTION CHANGE (eV)				
	-10	-5	0	+5	+10
A Measured resolution change (eV):					
No noise	-12.06	-5.75	0	5.26	10.07
With noise	-12.06 ± 1.44	-5.30 ± 1.50	-0.03 ± 1.71	5.51 ± 1.54	9.93 ± 0.86
B Intensity error (fitted - true) in %:					
(1) Without derivatives					
No noise	+5.4	+2.7	0	-8.1	-11.1
With noise	+5.1	+2.7	+0.2	-8.3	-11.2
(2) With derivatives					
No noise	-4.8	-2.3	0	-3.5	-2.1
With noise	-5.1	-2.0	+0.2	-3.4	-2.4

TABLE 3.--Fitted intensities from peak overlap determined by various methods of applying derivatives. Gaussian peak of height 1000 (intensity 12134) overlapping peak of height 50 (intensity 607), 100 eV apart. Centroid shift is 10 eV, resolution change +10 eV. ($n = 20$.)

FITTING PROCEDURE	Derivatives not used		Derivatives with both peaks		Derivatives on large peak only		Derivatives on large peak, parameters for small fixed	
	1	2	1	2	1	2	1	2
A Without noise								
Intensity	10981	2070	11100	1412	11595	882	11858	804
Accuracy ^a (%)	-9.5	+241	-8.5	+133	-4.4	+45	-2.3	+33
B With noise								
Intensity \pm S.D.	11022 ± 112	2058 ± 71	11046 ± 740	1477 ± 785	11622 ± 137	864 ± 122	11805 ± 216	812 ± 135
Accuracy (%)	-9.2	+239	-9.0	+143	-4.2	+42	-2.7	+34

^a (fitted - true)/true intensity, in %.

for the smaller peaks in a subsequent fit. This method has been compared to using derivatives on large peaks only, and to using derivatives on all peaks, as well as to a fit without derivatives. The test spectrum consisted of a simulated overlap of a peak of height 50 by a peak of height 1000, 100 eV apart, in which the effect of a 10eV zero shift was compounded by a broadening of the resolution by 10 eV. Table 3 shows the fitted intensities for the large and small peak, obtained by application of the four methods to a noise-free spectrum (A), and to 20 replicates of normally noisy spectra (B). The most accurate results are obtained by the two methods in which derivatives are applied to the large peak only, but

the suggested procedure of fixing the shift and resolution parameters of the overlapped peak to the values derived from the large peak yields the smallest differences from the true values. The residual differences can be explained by the systematic error in the resolution change calculated from the derivative fit of the large peak.

Discussion and Conclusions

The greater number of parameters in a derivative fit means that with noisy peaks, combinations of solutions may be obtained that satisfy the equations but are far from the "true" values. This observation explains the greater statistical variation in the results when derivatives are used, and places an approximate limit on the peak size below which derivative fits are not reliable--from our tests, about 5000 counts intensity, or 500 counts peak height. Below this limit, errors in individually measured intensities can be quite large, and are associated with erroneous values for the shift and resolution change.

The suggested procedure of fixing the shift and resolution values of the small peaks in a miscalibrated spectrum to those estimated from large peaks seems to offer the best solution to the problem of fitting small peaks, but in the general case it does require that a preliminary fit be made to identify suitably large peaks and to calculate the appropriate parameters. Clearly, if no large peaks are identified, derivatives are not used. The alternate method of applying derivatives to the large peaks and fitting the intensities only of the small peaks is equivalent to setting their shift and resolution changes to zero. Although the shift and resolution parameters may not be entirely accurately determined from a single large peak, the presence of two or more such peaks allows mean values to be used, which are more reliable.

We conclude that statistical noise generally limits the usefulness of the derivative fit to peaks of about 5000 counts intensity or greater. For these peaks reasonably accurate estimates of the shift and resolution can be derived. Smaller peaks may then be most accurately calculated by applying these estimates to such peaks in a subsequent fit.

References

1. P. J. Statham, "Deconvolution and background subtraction by least-squares fitting with prefiltering of spectra," *Anal. Chem.* 49: 2149-2154, 1977.
2. F. H. Schamber, "Curve fitting techniques and their application to the analysis of energy dispersive spectra," in *NBS Special Publication 604*, National Bureau of Standards, Washington, D.C., 1981, 193-231.
3. T. Kitazawa, H. Shuman, and A. P. Somlyo, "Quantitative electron probe analysis: Problems and solutions," *Ultramicroscopy* 11: 251-262, 1983.
4. D. J. McMillan, G. D. Baughman, and F. H. Schamber, "Experience with multiple-least-squares fitting with derivative references," *Microbeam Analysis--1985*, 137-140.
5. T. E. Bostrom, "Filtered least-squares fitting of biological EDS spectra using derivative references," *Proc. 10th Aust. Conf. on Electron Microscopy*, Adelaide, South Australia, 1988 (abstract).

THE USE OF THEORETICALLY GENERATED SPECTRA TO ESTIMATE DETECTABILITY LIMITS AND CONCENTRATION VARIANCE IN ENERGY-DISPERSIVE X-RAY MICROANALYSIS

C. E. Fiori and C. R. Swyt

The microprobe assay of a specimen must provide both a mean and the variance about this mean for each analyte. Since we are concerned here with microanalysis, the mean refers to the estimate of the weight or atom concentration at a single analytical point, or some local grouping of points, from a homogeneous region of the specimen. The *variance* about this mean then represents the uncertainty due to counting statistics plus those aspects of the data reduction procedure which will contribute uncertainty, such as peak unraveling and continuum suppression. The *accuracy* of the estimate is a measure of the closeness of our estimate to the true value of the concentration. The task of predicting the variance about this estimated concentration can range from easy to quite difficult. As the specimen is further examined at many points, any variance greater than that determined above will represent true compositional variation.

Discussion

As with all measuring devices, the energy-dispersive x-ray analysis system has for a given set of conditions a sensitivity which translates into a minimum concentration of analyte that can be reported with a certain level of confidence. This quantity is often referred to as the minimum detectable limit (MDL) and its estimation can also range from easy to quite difficult. We affect the MDL by choices of experimental conditions such as the operating potential, the analytical x-ray lines used for analysis, choice of data-reduction algorithm, etc.

This paper considers a computer procedure to estimate accurately the MDL for a trace analysis and to estimate accurately the variance about each concentration in an analysis which encompasses a range of concentrations from minor to major element. The procedure we propose will work when either of the above situations does not lend itself to treatment by conventional statistical methods, a frequently occurring situation. We begin by describing the analytical conditions under which standard statistical methods are difficult to apply for the determination of MDL and concentration variance.

Statement of the Problem

A spectrum observed with an energy-dispersive spectrometer (EDS) consists of x rays

arising from both the characteristic and the continuum process. The x-ray peaks arising from the characteristic process contain the analytical information we seek. Often the peaks we wish to determine overlap with the peaks from other elemental constituents of the specimen. Furthermore, the peaks are always superposed onto a smoothly varying spectrum of x rays arising from the continuum process; and both the characteristic and continuum signals are modulated by the effects of counting statistics.

The MDL and variance about a measured concentration depend on the magnitude of the peak and background intensities, the degree of peak overlap, and the algorithms used to extract the required peak intensity and background intensity values below the peak. In general there is no straightforward way of estimating the quantities required for standard statistical treatment. Therefore, many analysts, when faced with the problem of providing good error estimates, resort to the time-consuming but extremely reliable technique of direct measurement. In this method the specimen is sampled n times at a number of representative locations. For each of the n replicate measurements at each location one goes through all the spectral processing and data reduction steps required to arrive at an elemental concentration. From the n results at each location the analyst can then predict by conventional statistical methods the expected variance for each of the elemental concentrations at the various presumably representative locations. Knowing the expected variances the analyst can then proceed on with a strategy of single measurements at each analytical point in the specimen. For specimens with many phases or a wide range of compositions this procedure can be quite daunting.

There is an ever-growing body of knowledge concerning the physics of electron-specimen interaction and of the energy-dispersive x-ray spectrometer used to detect the resulting x rays. We contend that the requisite knowledge is now at hand to generate from first principles an x-ray spectrum that is more than sufficiently close in all of the germane physical and statistical properties to represent an actual spectrum from a real specimen. From a generated spectrum one can then deduce accurate estimates of variance about mean compositional values. One may also accurately estimate the MDL of any analyzable stable element in any stable matrix without the need to produce a set of calibration standards. Furthermore, one may adjust the experimental parameters to determine the optimum set that will produce the

The authors are at the Biomedical Engineering and Instrumentation Branch, National Institutes of Health, Bethesda, MD 20892.

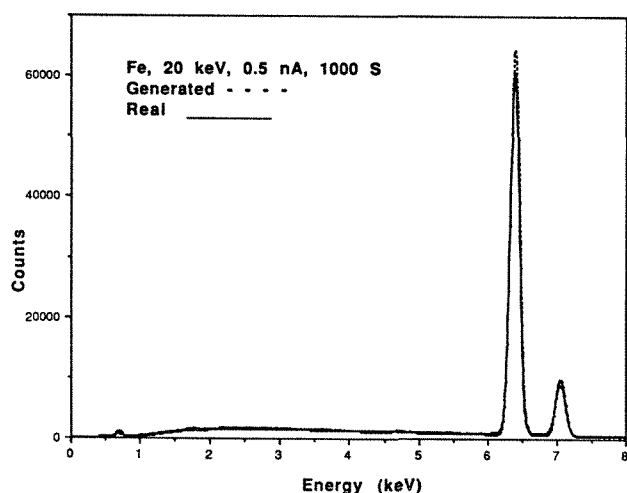


FIG. 1.--Real spectrum (solid line) from pure iron specimen in Cameca electron probe with 20kV, 0.5nA beam. Acquisition time was 1000 s; the 9mm² detector was 52 mm from specimen; take-off angle was 40°. Dashed line is spectrum generated from first principles for same conditions.

lowest MDL. One can do that relatively rapidly before even presenting a specimen to the electron beam.

Computational Aspects

It is not possible to cover even cursorily all the physical, statistical, and mathematical ingredients of the proposed procedure in the limited space remaining. However, we can catalog the critical components and provide the computer source code (Pascal) to anyone who requests it from one of the authors. The program was written for an Apple Macintosh II computer and makes extensive use of the graphic environment of this computer. However, with some effort, it should be possible to extract the relevant sections of code and transfer this information to another computational environment. The computer code discussed here is a component of a series of programs being developed at the National Institutes of Health which allow the Macintosh II computer, with the addition of several plug-in boards, directly to acquire, process, and display spectra and images from all the scanning electron column instruments in our laboratory.

The program has a series of dialogs that allow the user to specify all the relevant characteristics of the electron column and x-ray detector system. Quantities such as excitation potential, beam current, acquisition time, specimen-to-detector distance, detector size, specimen composition, etc., are all required. The entered values are retained as default values until changed. We have collected the most widely applicable and generally accepted mathematical representations of the physics and physical data available in the literature. From these data we can predict from first prin-

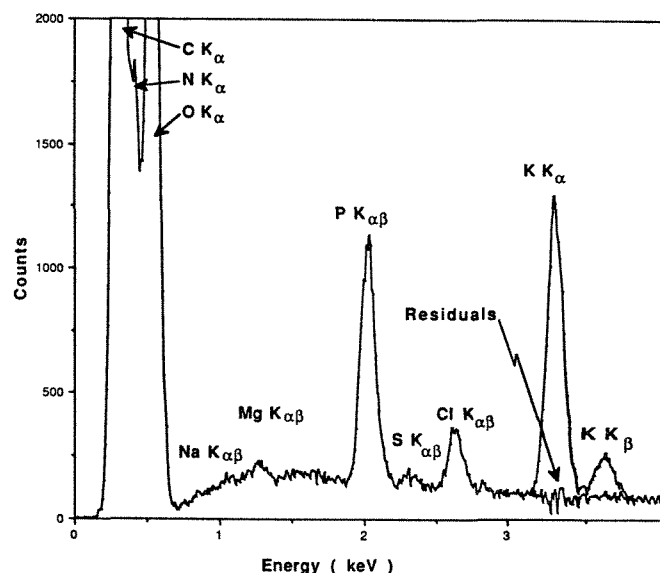


FIG. 2.--Theoretically generated specimen from typical biological matrix.

ciples the detected characteristic and continuum distributions from either thin or bulk film specimens. We can then repeatedly add true Poisson counting statistics to the same spectrum to determine the required variance about a concentration mean and the MDL.

In Fig. 1 is plotted a spectrum from bulk iron acquired in a Cameca electron probe operation at 20 kV and 0.5 nA. The acquisition time was 1000 s and the 9mm² detector was 52 mm from the specimen. Also plotted is a spectrum generated from first principles by the program using the same experimental parameters. No arbitrary scaling was used for either the continuum or characteristic distributions. The purpose in showing this plot is simply to illustrate that the program can generate a sufficiently close approximation to a real spectrum to enable accurate statistical information to be extracted. A similarly good match is possible for the L family of lines; the M family, not surprisingly, is less than satisfactory and requires arbitrary scaling of the characteristic cross section.

The well-known K-Ca overlap problem typical in biological x-ray microanalysis provides a good example of a case in which conventional statistical procedures cannot provide accurate estimates of the variances because one cannot extract independent estimates of the peak and background under the peak. When the peak-to-background ratio is small, as it is for the Ca peaks in our chosen example, the uncertainty in the peak estimation is strongly influenced by the continuum statistics and the effect of the overlapping K K β peak. The technique of spectrum generation proposed in this paper permits a rapid simulation of n spectra each of which has the statistical properties of actual spectra acquired for typical experimental times. Each spectrum can be analyzed by any of the procedures normally used to extract peak areas. The variance about the mean can then be calculated directly.

To demonstrate this procedure we generated

25 spectra, identical except for the counting statistics, representing a typical biological matrix which contains 0.02 weight fraction K and 0.00022 weight fraction Ca. An example is presented in Fig. 2. The spectrum was generated with parameters for our Vacuum Generators HB 501 dedicated STEM operating with a 100kV, 0.5nA beam for 1000 s of acquisition time. A UTW Si(Li) detector with 0.18 steradian solid angle was the x-ray detector.

We analyzed the spectra using the sequential simplex algorithm.¹ The mean value and standard deviation obtained for K were 10462 ± 143 and for Ca, 80 ± 71 . Clearly, to extract this weight fraction of Ca with 97% certainty will require a considerably longer acquisition time per spectrum and/or more spectra.

An MDL can be similarly calculated from the mean and variance obtained by analyzing n generated spectra from a specimen with zero concentration of the element in question.

Conclusion

We have attempted to demonstrate the power of using theoretically generated spectra to provide accurate estimates of detectability limits and concentration variance. Since the program provides reasonably correct spectra for given experimental conditions, it has great utility in establishing that the microscope is not producing artifacts which can reduce analytical capability. In addition, the program can be used to predict the best operating conditions to perform a given analysis.

References

1. C. E. Fiori, C. R. Swyt, and K. E. Gorlen, "Application of the top-hat digital filter to a nonlinear spectral unraveling procedure in energy-dispersive x-ray microanalysis," *Microbeam Analysis--1981*, 320.

ON THE PEAK-TO-BACKGROUND RATIO IN MICROPROBE ANALYSIS OF POROUS MATERIALS

S. A. Abo-Namous

The electron microprobe analyzer (EPMA) is a powerful tool for quantitative point analysis of polished surfaces. In quantitative analysis, the net intensity of the characteristic x ray of the unknown $(P-B)_u$ is compared with that of a standard $(P-B)_s$ of a known elemental composition. The ratio between $(P-B)_u$ and $(P-B)_s$ for pure-element standards is known as K ratio. These K ratios are corrected by a conventional ZAF method for matrix effects; atomic number Z, matrix absorption A, and fluorescence F.

The problems of electron backscattering and differential absorption, associated with rough and porous surfaces, has made the above method inapplicable for quantitative analysis of such surfaces. Rough surfaces cause particle effects. In particle analysis, incident electrons do not strike the surface at the same angle at all points. Also, x-ray take-off angle and the absorption path length vary with the position of the generated x ray. The problems associated with the analysis of such materials have been reported in literature.^{1,2}

In this paper, a slight modification is introduced to the above correction method so that it can work for porous materials analysis. It has been suggested that, to a first approximation, the continuum radiation and characteristic x ray are equally influenced by particle effects, where the depth distribution of the continuum and characteristic x rays is approximately the same.^{3,4} According to this suggestion, any influence from surface structure on the characteristic peak intensity will have approximately the same influence on the local background level. Hence, the ratio of the net intensities of the characteristic peak P-B to background under the peak B for particle and for bulk, and for bulk material of the same composition, may be equal. This suggestion was applied in this study to porous materials (such as gamma-alumina extrudates) that can be dealt with as an aggregation of small particles.

Experimental

Pure gamma-alumina extrudates 2 mm in diameter were used in the analysis. The extrudates were used as pellets, since analysis is usually carried out to find the elemental distribution throughout the cross section of the spent catalyst. The pore fraction of these extrudates ranged from about 0.5 to about 0.8 as measured by a mercury porosimeter. The extrudate pellets were mounted on a plastic resin in a Meta-

The author is with the Central Analytical Laboratory, Kuwait Institute for Scientific Research, P.O. Box 24885, Safat 13109, Kuwait.

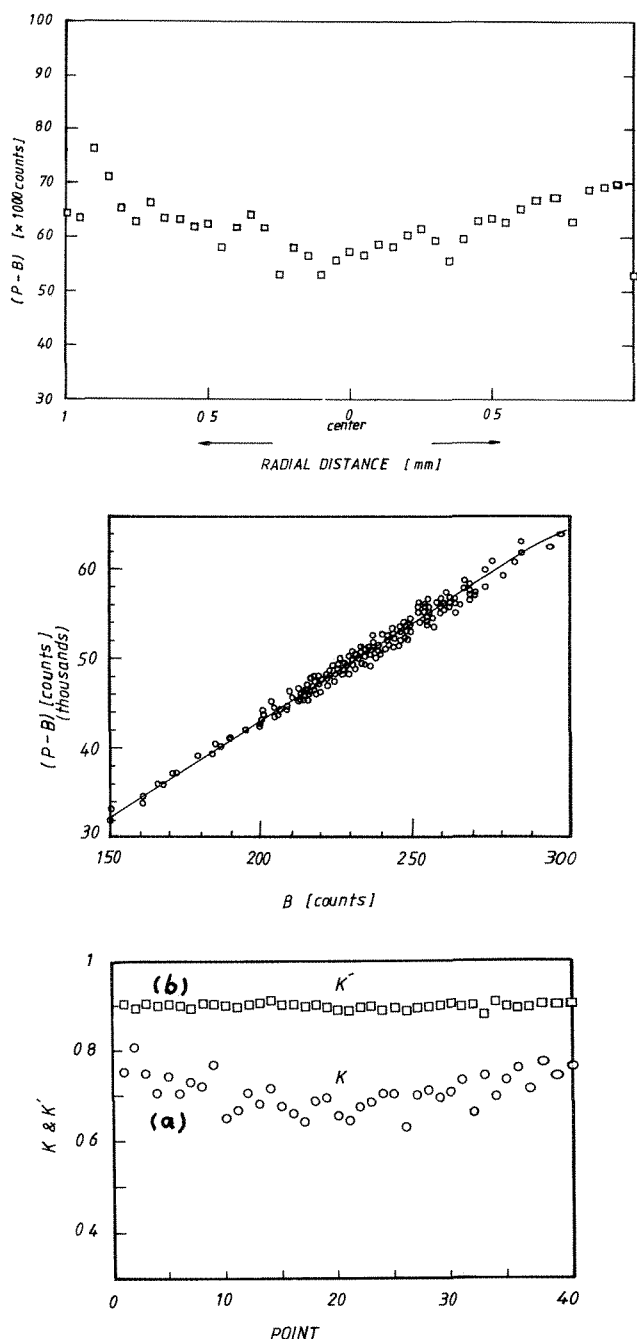


FIG. 1.--Net x-ray intensity of Al $K\alpha$ line as function of position on pellet cross section. Space between two points is 50 μ m.
 FIG. 2.--Local background signal as function of net peak intensity of Al $K\alpha$ line.
 FIG. 3.--K-ratio calculated (a) from ratio of net peak-intensities of extrudate and standard, (b) from ratio of peak-to-background ratios for extrudate and standard. Point 0 is at one edge; point 40, at the other.

surf mounting press machine and then polished by sequential grades of SiC papers; ending with a 600-mesh (particle size ca 20 μm). For standard calibration "compact" alpha-alumina was used as aluminum standard. To expose both the samples and the standard to the same preparation conditions, they were mounted on the same holder, simultaneously polished and then coated with a thin layer of carbon to provide a conductive surface. For a uniform layer of carbon a Balzers high-vacuum coating system was used. Silver paste was applied closely around the pellets to insure good electrical conduction.

Wave-length-dispersive spectrometers (WDS) attached to a Cameca EPMA were used for the analysis. The accelerating voltage of electrons was 15 keV. The intensity of the Al $K\alpha$ characteristic x-ray line and the corresponding background were measured point by point along the diameter of the pellet. A typical diameter of the electron beam was slightly less than 20 μm as limited by the Roland circle. The oxygen content was calculated by a stoichiometry correction.

Results and Discussion

It has been found that the alumina extrudates have a range of pore volume, and accordingly a range of particle size. The pore volume varied systematically across the extrudate.⁵ The microprobe point analysis was carried out over the cross section of the extrudate. This analysis gave a relation between the measured peak intensity of the Al $K\alpha$ line and the pore volume, as represented in Fig. 1 by the position of the point with respect to the edge of the extrudate. In Fig. 1, the higher peak intensity represents smaller pore size near the edges, whereas lower peak intensity is a manifestation of large pore volume.

On the other hand, in considering a large number of extrudates to give a range of pore volume, it was found that the net peak intensity of Al $K\alpha$ is linearly proportional to the corresponding local background under the peak (Fig. 2) when the measurements were made under the same beam conditions. The variation in peak intensity is due to variation of porosity throughout the extrudate, which shows that the peak-to-local background ratio is independent of the pore volume within the range considered. The dependence of local background on the peak intensity agrees with the results of particle analysis of others.^{6,7} It is worth mentioning that the peak-to-background ratio is particularly accurate in the case of a well-defined background, whereas in the case of overlapping peaks the determination of true local background can be difficult and may lead to errors in the peak-to-background ratio.

The net peak intensity across the extrudate was measured and found to vary with the position of measurement. This variation in the intensity reflected on the corrected weight percentage using ZAF method. A typical variation is shown in Fig. 3 (curve a). On the

other hand, when the net peak-to-background ratio was considered, it was almost independent of the measurement site. This ratio is compared with that of a known standard, to give the new K ratio. With the latter ratio, the ZAF correction method gave corrected weight percentages of alumina close to 100% across the pellet, as can be seen from curve b of Fig. 3.

Scanning electron microscopy (SEM) at high magnification revealed that the grain size in the extrudates considered is below a few microns, except for rare cases where agglomerates of grains were present. The width of these agglomerates was less than 20 μm , which means that an electron beam with a 20 μm diameter will "see" the average structure of several or many grains. Furthermore, the top surface of the grains partly has a flat shape. Accordingly, a considerable fraction of the incident beam strikes the surface at angles close to normal, so that the electron backscattering yield is close to that of the bulk material.

In the conventional ZAF correction method, the K ratio is calculated from

$$K = (P-B)_U / (P-B)_S \quad (1)$$

When this ratio is incorporated into the ZAF correction, it does not account for the differences in electron backscattering and x-ray absorption between bulk and particles. Even if the backscattering yield were the same, the absorption of x rays generated deep below the surface of porous material is different from that for the bulk material. Therefore, the corrected weight percentage of alumina deviates from 100%, where the deviation depends on the porosity of the area analyzed (Fig. 3, curve a).

On the other hand, if we use

$$K' = P_U / P_S \quad (2)$$

instead of the conventional K ratio in the ZAF correction, it seems to take care of the particle effect, since the background is always proportional to the peak intensity (Fig. 2). The P_U and P_S values in Eq. (1) are the net peak-to-local background ratios of the unknown and the standard, respectively. As a result, the ZAF-corrected weight percentage of alumina is independent of the porosity of the area analyzed, and its value is close to 100% (Fig. 3, curve b). It is assumed that particle effects are almost the same for the background radiation and characteristic x ray. Therefore, absorption pathlengths for the characteristic x ray and the corresponding background radiation are expected to be similar. Accordingly, the height of the background is proportional to the intensity of the characteristic peak.

The peak-to-local background ratio seems to be convenient for materials with a single compound, since the standard would always have the same chemical composition as the unknown. In applying this method to multicomponent materials, the standard materials should be

carefully selected so that the standard has a composition similar to that of the unknown. Preliminary work on Mo-Ni/alumina catalyst showed that the peak-to-background ratio ratio method can give total weight percentage of almost 100%, although the conventional K ratio (Eq. 1) resulted in a deviation from the 100% value. However, this topic needs further detailed investigation. The method would be of great value for quantitative analysis of materials where fine polish is avoided or difficult, e.g., corrosion products and rocks.

Conclusions

Although the net intensity of the characteristic x-ray line depends on the porosity of the materials at the point of measurement, the net peak-to-background ratio is almost independent of the porosity. The above results demonstrate that the peak-to-local background ratio is more suitable for elemental concentration analysis of porous materials. The procedure is simple and requires only a slight modification of a conventional ZAF correction method.

References

1. T. Araya and K. Mukaida, "Influence of pore structure on x-ray intensity in EPMA quan-

titative analysis of porous matter," *J. Soc. Mater. Sci. Japan* 28: 798, 1979.

2. S. A. Abo-Namous, *Problems Associated with Quantitative Electron Microprobe Analysis of Porous Alumina and Suggested Methods to Solve Them*, KISR Annual Research Reports, 1987.

3. J. A. Small, K. F. J. Heinrich, C. E. Fiori, R. L. Myklebust, D. E. Newbury, and M. F. Dilmore, "The production and characterization of glass fibers and spheres for microanalysis," *SEM/1978* I, 445.

4. P. J. Statham and J. B. Pawley, "A new method for particle x-ray microanalysis based on peak to background measurements," *SEM/1978* I, 469.

5. S. A. Abo-Namous, unpublished data.

6. J. A. Small, K. F. J. Heinrich, D. F. Newbury and R. L. Myklebust, "Progress in the development of the peak-to-background method for the quantitative analysis of single particles with the electron probe," *SEM 1979* II, 807.

7. A. Boekestein, F. Thiel, A. L. H. Stols, E. Bouw, and A. M. Stadhouders, "A new method for particle x-ray microanalysis based on peak to background measurements," *J. Microscopy* 34: 327, 1984.

A BINARY ALLOY DATA SET FOR COMPARISON OF QUANTITATIVE ELECTRON-PROBE CORRECTION PROCEDURES

K. F. J. Heinrich

An extensive set of relative intensities obtained by electron-probe microanalysis on binary specimens is being assembled. It contains data taken from various collections as well as information not previously used in such tabulations. When the assembly is completed, the number of entries will be more than 1400.

The use of experimental results on specimens is the ultimate test of accuracy of electron-probe quantitation procedures. To be free of bias, the test should be ideally performed on data not used in the development of the procedure. However, given the paucity of such data, and the labor involved in preparing the specimens and measuring relative x-ray intensities, this requirement is never met in practice. The alternative is to have as comprehensive a collection as possible.

In parallel with the assembly of the table, menu programs are being written that permit comparison of any combination of correction procedures with statistical evaluation.

The usual process of submitting the entire available data set to a complete analytical procedure has serious disadvantages. If a discrepancy occurs between observed and calculated relative intensities, it is not obvious which part of the correction procedure is responsible for the error. Conversely, the effects of a given correction, for example for absorption or fluorescence, are in such a process diluted by the random errors obtained on a large number of binaries in which this effect is not significant. We therefore propose the use of subsets for the separate testing of the corrections for stopping power, backscatter, absorption, and fluorescence (both characteristic and continuous). Unfortunately not all procedures at present in use permit the separation of stopping power and backscatter effects, but separation of the rest will be possible.

Subsequently, we plan to extend this work to specimens having more than two components (e.g., glass standard reference materials), in which certain effects will be particularly significant.

Specimens in which low electrical conductivity may require coating or otherwise affect the measurement were not included in the set. A set of measurements performed with instruments having a low take-off angle ($<30^\circ$) is included so that the effect of this angle on overall accuracy can be determined.

The author's address is 804 Blossom Drive,
Rockville, MD 20850.

MICROPROBE ANALYSIS OF THIN $\text{YBa}_2\text{Cu}_3\text{O}_{6+x}$ SUPERCONDUCTING FILMS

Eric Lifshin, L. A. Peluso, Antonio Mogro-Campero, and L. G. Turner

Relatively few studies have been reported of electron microprobe analysis of multielement thin films deposited on bulk substrates. Because the electron beam can penetrate through such films, the measured x-ray intensities from each element depend not only on the film composition but also on the film thickness and the substrate composition. Conventional ZAF analysis is unsuitable for thin films, and the principal analytical correction methods used have been based on Monte Carlo calculations^{1,2} and modified $\phi(\rho z)$ curves,^{3,4} neither of which is routinely used. The amount of published experimental data relating x-ray emission to film thickness and operating voltage is scarce, and much of it refers only to pure elemental films. Nor has there been much discussion of the practical experimental problems encountered in measuring thin films. The current study is directed at providing additional information in these areas.

X-ray measurements were made on a series of superconducting films of YBCO ($\text{YBa}_2\text{Cu}_3\text{O}_{6+x}$) of different thicknesses deposited on SrTiO_3 . Such films are being evaluated at present for use in a variety of microelectronic devices. From the point of view of microanalysis, YBCO was chosen because it is electrically conducting, and it has been previously established to have a very well-defined cation stoichiometry.⁵ Furthermore, only minor variations in the oxygen concentration are permitted if it is to perform as a high-temperature superconductor (x is typically in the range of about 0.7 to 0.9).

Experimental

Films of YBCO were deposited on polished SrTiO_3 (100) substrates. They were prepared by coevaporation of Y, BaF_2 , and Cu followed by furnace annealing. The deposition was at ambient temperature and the samples were then annealed at 850 C for 3.5 h in oxygen and water vapor. During furnace cooling the samples were held at 550 C for approximately 0.5 h. The series of samples prepared included films of thicknesses of 0.25, 0.50, 0.75, 1.00, 2.00, and 3.00 μm . These thicknesses were selected because over the range of electron-beam voltages used, thicker films were expected to behave as bulk materials whereas the thinner films were not expected to contain the region

of direct electron x-ray excitation. Superconducting transition temperatures were determined by four-point resistivity measurements for all of the samples in this study. Thicknesses were determined both by direct measurement of sectioned samples in a scanning electron microscope (SEM) and by Rutherford backscattering (RBS) at the microbeam facility at the State University of New York at Albany.

Electron microprobe analysis was done with a Cameca MBX equipped with a Tracor Northern automation package run under the TASK program. The analyzing crystals used were TAP for Y $L\alpha$, PET for Ba $L\alpha$, and LiF for Cu $K\alpha$. The standards used were Y_2O_3 , NBS glass standard K458 for Ba, and pure Cu metal. In addition, measurements were made at the same time on a bulk YBCO standard described in detail previously. Measurement of this standard served to indicate when the region of direct electron x-ray excitation was fully contained in the YBCO films.⁵ It also provided a cross check on the overall experimental procedure. The beam currents used were about 7 nA and measurements were made at 12, 16, and 20 kV. Counting times of 100 s were used, so that the total number of counts measured at each data point varied between 10^4 and 8×10^4 depending on the film thickness examined and beam voltage used. Typically four points were measured on each film at each voltage and the resulting data were averaged.

Results

Figures 1 and 2 are SEM micrographs taken of the 1 and 3 μm films, respectively. They both show a most unusual fibrous microstructure of the outer surface, which indicates that it is far from planar. Transmission electron microscopy (TEM) has shown that these fibers correspond to various regions of YBCO in which the "c" axis of each region is oriented in one of three orthogonal directions. This effect does not occur over the total thickness of the film, but only in an outer layer that grows on top of normal epitaxially grown material which has its c axis perpendicular to the plane of the substrate. In addition, films of 1 μm and thinner showed the presence of a second phase, believed to be BaCuO_2 based on energy-dispersive x-ray and TEM measurements.⁶ The presence of this phase was noted during microprobe analysis and it was avoided. Analysis was done on the principal phase, which was assumed to be YBCO. This assumption is consistent with the fact that the transition temperatures measured on all the samples were between 89 and 90 K. A more serious experimental concern is the surface roughness, which is believed to have developed when the samples were converted from the as-deposited amorphous films

The authors are with GE Corporate R&D, Schenectady, NY 12301. They wish to thank H. Bakru of SUNY Albany for the RBS measurements, N. Lewis and E. L. Hall for the TEM work and helpful discussions, D. E. Newbury of NIST for running Monte Carlo calculations, and R. B. Bolon for his helpful discussions.

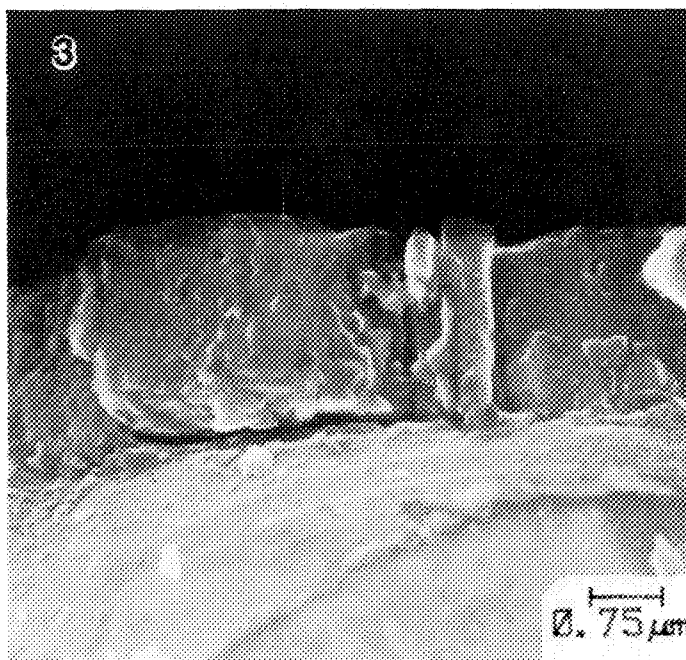
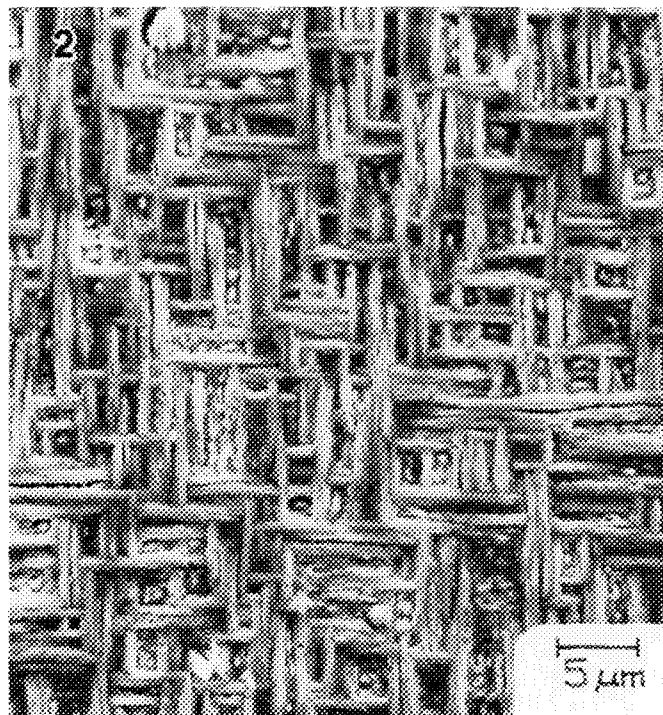
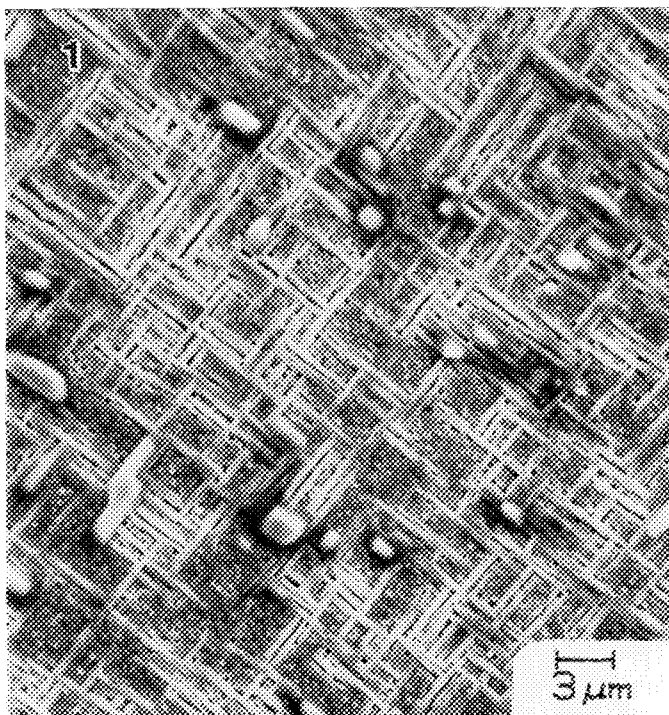


FIG. 1.--SEM micrograph of surface of 1 μ m YBCO film deposited on SrTiO₃.

FIG. 2.--SEM micrograph of surface of 3 μ m YBCO film deposited on SrTiO₃.

FIG. 3.--SEM micrograph of cross section of 2 μ m YBCO film deposited on SrTiO₃.

to YBCO during the annealing step.

Both the RBS and SEM examination of cross sections suggest that that average film thicknesses given are probably accurate to within 10%; however, more detailed TEM measurements are currently under way to fully validate these results. Figure 3 is an SEM micrograph of a cross section of the 2 μ m film. The surface appears to be somewhat irregular, but there is no indication of second phases within the film, although some porosity was detected during the examination of a different region of the sample. Point-to-point variations in thickness are

somewhat more difficult to establish because of the difficulty in getting good cross-sectional images of samples. However, TEM observations of similar samples have suggested that at the 0.1 μ m scale regions of the specimen might be found where the thickness variation is greater than 20% of the average. Since the probe size is estimated to be about 0.5 μ m, these irregularities are somewhat averaged out. As an example, 12kV data taken from ten data points on the 1.0 μ m films gave 2 σ variations of 11.6% for Y L α , 3.2% for Cu K α , and 3.5% for Ba L α . Although these numbers are larger than the 1-2% 2 σ variation based on expected counting statistics for a film of uniform thickness, it is clear that some averaging of the data has taken place in the sampling volume. The large variation in the Y data is consistent with the fact that Y L α x rays undergo the largest amount of absorption and would be most affected by an irregular surface.

Figure 4 summarizes the results obtained for relative intensity ratios (K) vs film thickness for each of the elements. Error bars are not shown to avoid cluttering the figure, but the 2 σ variations are expected to be comparable to the numbers given above. The qualitative trends in each curve are roughly consistent with expectations. In each case the K ratios increase with thickness up to film thicknesses of 1-2 μ m. The K ratios also decrease with increasing voltage for a given film thickness, indicative of the greater penetration of the beam through the films. The fact that some of

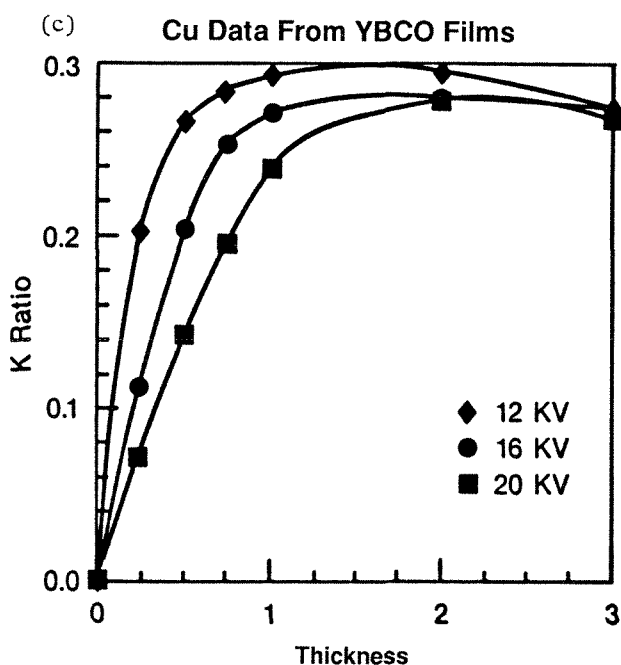
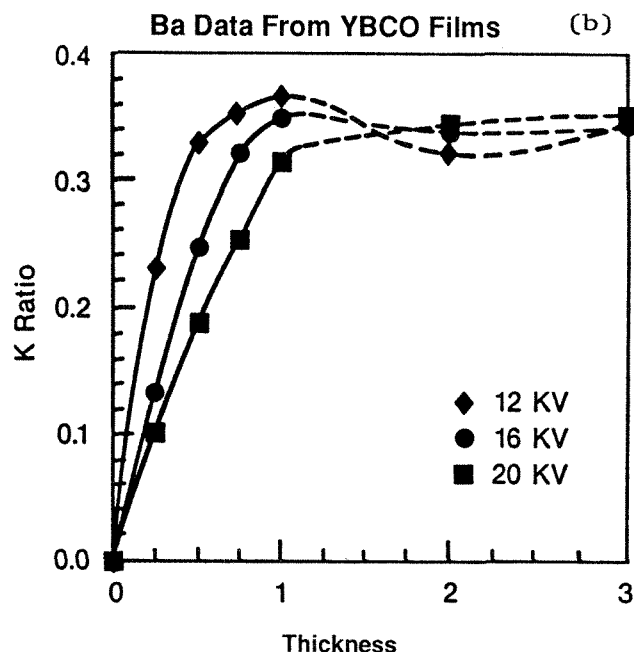
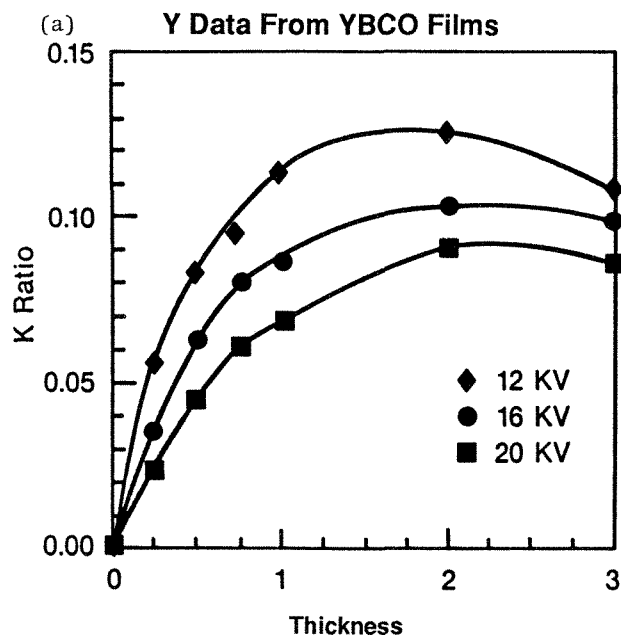


FIG. 4.--K ratios relative to pure elemental standards vs film thickness for YBCO films deposited on SrTiO_3 : (a) Y $L\alpha$, (b) Ba $L\alpha$, (c) Cu $K\alpha$.

TABLE 1.--Measured $3\mu\text{m}$ YBCO thick-film and bulk K ratios compared with ZAF theory.

	Y		
	12 KV	16 KV	20 KV
3.0 micron	0.106	0.0975	0.0855
bulk	0.105	0.0945	0.0861
ZAF	0.104	0.0941	0.0864
Cu			
	12 KV	16 KV	20 KV
3.0 micron	0.274	0.273	0.267
bulk	0.299	0.290	0.282
ZAF	0.298	0.290	0.282
Ba			
	12 KV	16 KV	20 KV
3.0 micron	0.344	0.342	0.352
bulk	0.366	0.374	0.380
ZAF	0.356	0.369	0.378

the data appear to go through a maximum and then decrease slightly to the values measured for $3\mu\text{m}$ is somewhat surprising, but may be related to the effect of a changing topography with film thickness. Table 1 contains a comparison of the $3\mu\text{m}$ results with both bulk measurements and K values predicted by conventional ZAF procedures. The good agreement between the bulk K values and theory is consistent with results reported previously and helps confirm proper operation of the instrument. The fact that the $3\mu\text{m}$ readings for Cu and Ba are slightly lower than the bulk at all voltages may be attributable to the decreased indirectly excited characteristic signal generated by the continuum for the thin-

film samples. Because the x-ray continuum is capable of generating x rays from points many micrometers from the point of electron-beam impact, one would expect that more x rays would be generated in a bulk sample than from a thin film even if the electron interaction volume were reasonably well contained within both samples. This effect has been observed elsewhere, but is difficult to estimate.¹

Conclusions and Comments

A data set of K ratios vs film thickness has been developed for the metallic elements in YBCO. The results suggest that almost all the x rays are produced within the first 1-2 μm for each of the elements measured over the range from 12 to 20 kv. Variations in surface roughness appeared to be the largest factor influ-

encing the accuracy of point-to-point results ($\pm 10\%$). Nevertheless, given the lack of models and the lack of data in this area, the current findings may prove useful in validating thin-film microanalysis models. Preliminary results using the Caltech CITZAF particle/thin-film analysis program⁷ applied to these same materials suggest that the discrepancies between theory and experiment are much larger than $\pm 10\%$. We shall report on these findings and their significance in the near future. The data presented may also prove useful in estimating film thicknesses for YBCO microelectronic devices.

References

1. R. B. Bolon and E. Lifshin, *SEM/1973*, 281.
2. D. F. Kyser and K. Murata, *IBM J. Res. and Develop.* 18: 352, 1974.
3. J. L. Pouchou and F. Pichoir, *Rech. Aerosp.* n1984-85, p. 47.
4. H. Yakowitz and D. E. Newbury, *SEM/1976*, 151.
5. E. Lifshin, L. A. Peluso, and R. H. Arendt, *Microbeam Analysis--1988*, 519.
6. A. Mogro-Campero, L. G. Turner, and E. L. Hall, *J. Appl. Phys* (in press).
7. J. T. Armstrong, Division of Geological and Planetary Institute of Technology, Pasadena, CA 91125.
8. D. E. Newbury, private communication.

A CASE STUDY OF TEMPERATURE-RELATED PEAK SHIFT IN WDS MICROPROBE ANALYSIS

S. Vincent Yang, Jerry Wagstaff, and Gordon McKay

Minor changes in room temperature can cause significant peak drift during quantitative electron microprobe analysis. Some quantitative data acquired by a CAMECA MBX electron microprobe are reported in this study. A spectrometer verification (insuring that one element is aligned with an absolute reference position on each spectrometer) before each analysis helped correct the peak-drift problem.

Experimental

A CAMECA MBX electron microprobe at NASA/Johnson Space Center was programmed to perform 200 analyses of a Kaersutite standard with three wavelength-dispersive x-ray spectrometers. All data discussed in this report were acquired with the CAMECA MBX fully automated scanning electron microprobe at NASA/JSC. The original analytical software was modified to verify all spectrometers before each analysis as well, as to record the amount of peak drift. Initially, a microprocessor get-element function (moving the spectrometer to a theoretical elemental peak position) was used to move the spectrometers to their peak verification positions; Fe K α for the LIF crystal, Ca K α for the PET crystal, and Si K α for the TAP crystal. Next, a microprocessor peak function was used to locate the true peak position for each spectrometer. These new peak positions were subtracted from the previous peak positions and the data were written to a file. Finally, a microprocessor set-motor-position function was used to correct the spectrometer motor positions for the subsequent analysis. In case the peak intensity was insufficient for a valid peak determination on any one of the spectrometers, a discriminatory algorithm would prevent resetting of that spectrometer motor position. The resulting variations in peak positions of the overnight analyses can be seen in Fig. 1.

Conclusions

1. Estimations based on peak shapes suggest that, if there was no spectrometer verification before analyses and if the peak position changed by 20 steps, Ca K α peak intensities could decrease by up to 16%, Fe K α peak intensities by 8% to 10%, and Si K α peak intensities by as much as 26%.

2. Figure 2 illustrates that spectrometer

verification helped correct the peak-drift problem caused by a variation of the laboratory temperature.

3. Figure 3 reveals that spectrometer verification and spectrometer motor position resetting also helped to correct the peak drift for additional elements on individual spectrometers without verifying these elemental peak positions.

4. Verification of high-precision wavelength-dispersive x-ray spectrometers before individual analyses can help correct for peak-drift due to changes in instrument temperature caused by environmental factors other than changes in room temperature.

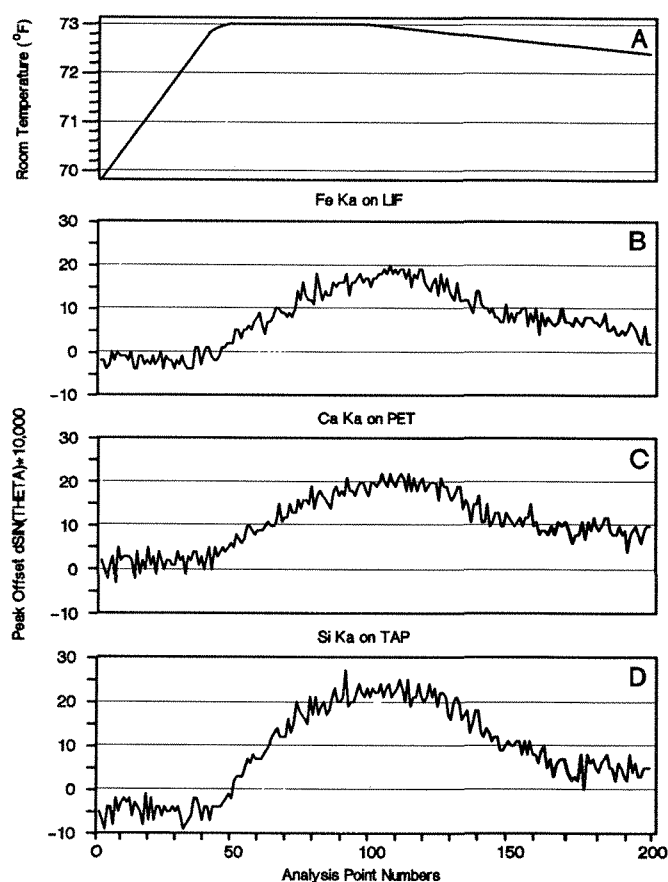


FIG. 1.--Graph A displays variation in laboratory temperature during programmed analytical session. Graphs B through D exhibit changes in peak positions resulting from this temperature fluctuation. Note lag time between change in laboratory temperature and subsequent change in peak positions.

S. Vincent Yang and Jerry Wagstaff are with Lockheed Engineering & Science Co., 2400 NASA Road 1, C23, Houston, TX 77058-3711; Gordon McKay is at the NASA Johnson Space Center, Houston, TX 77508.

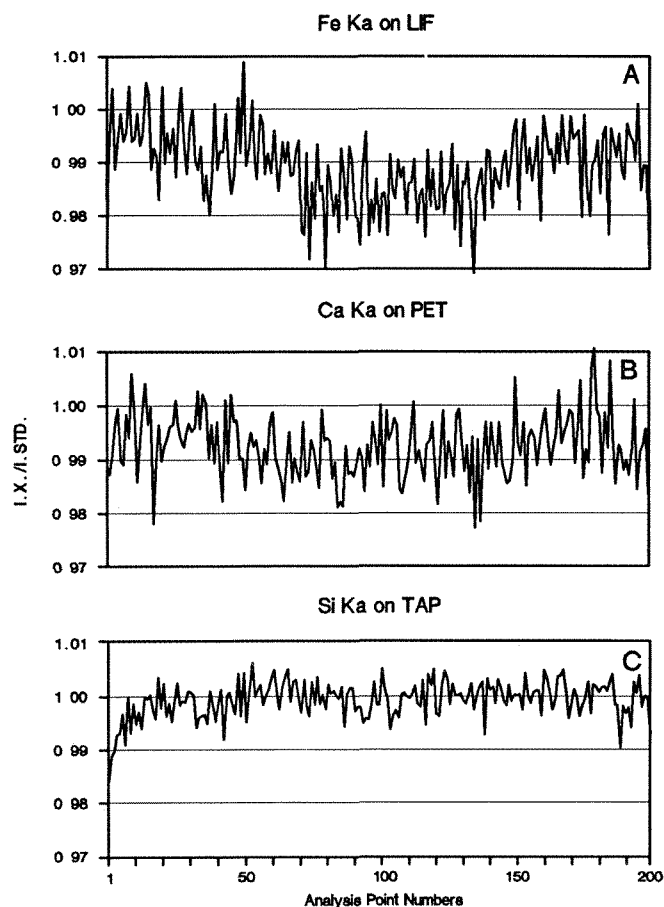


FIG. 2.--Graphs A through C indicate that spectrometer verification prior to each analysis kept peak intensities generally within 1% of original intensities even with significant changes in peak positions during analytical session.

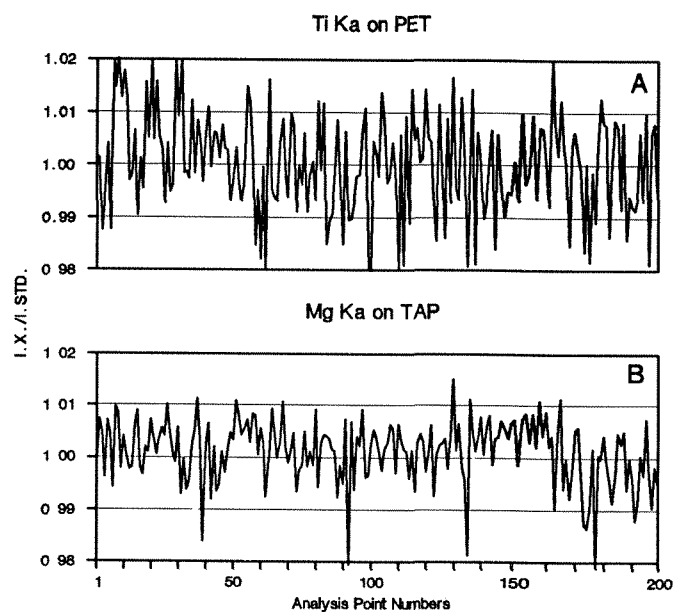


FIG. 3.--Graphs A and B illustrate that spectrometer verification prior to each analysis also kept peak intensities for additional elements on verified spectrometer generally within 1%.

QUANTITATIVE COMPOSITIONAL MAPPING IN A SCANNING ELECTRON MICROSCOPE WITH AN ENERGY-DISPERSIVE SPECTROMETER

R. W. Anderhalt and A. O. Sandborg

Compositional mapping has been demonstrated recently¹⁻³ with the electron microprobe. In the electron microprobe, the scanning electron beam produces x rays which are detected with a wavelength-dispersive detection system (WDS). The x-ray intensities are converted to concentrations at each analysis location, usually by the ZAF method. In this work, the scanning electron microscope is used with an energy-dispersive spectrometer.

One very important requirement for success with the electron microprobe is beam current stability. The counting or dwell time at each analysis location is relatively long because each element is usually measured sequentially. If an energy-dispersive detection system (EDS) is used, the dwell time may be reduced because the elements are determined from one spectrum at each location. The beam-current stability requirement may also be relaxed, since EDS can utilize a standardless technique. The standardless method uses calculated relative pure element intensities instead of measured absolute pure element intensities, and relies on normalization in order to obtain absolute concentrations. Because beam current stability is not as important if the EDS method is used, an SEM can be used to scan the sample to produce the x-ray map.

Each of the two x-ray detection methods has significant problems to be solved in order to produce meaningful concentration maps. The WDS method must correct for the defocusing effect of the spectrometer when maps are made at low magnification.⁴ Several methods have been developed to solve this problem.⁵⁻⁷ The EDS method must overcome the problems caused by the inherently poorer resolution of the EDS detector. Background and peak overlap corrections must be applied to obtain net elemental intensities from the EDS spectrum. It is impractical to store a full spectrum at each analysis location of the map, so the corrections must be made "on the fly." Normally it requires tens of seconds to obtain net elemental intensities and to convert them to concentrations with a ZAF technique. In this work these times have been reduced to fractions of a second by the use of optimized programming of the various correction procedures.

R. W. Anderhalt is at Philips Electronic Instruments, Inc., 85 McKee Drive, Mahwah, NJ 07430; A. O. Sandborg is at Philips Electronic Instruments, Inc., 150 West Center Court, Schaumburg, IL 60195. They acknowledge the effort of H. M. J. M. van Ass, the author of the HAX software.

Experimental

The system used in this work is called the PHAX-SCAN system.⁸ It consists of an SEM with an EDS detector mounted to the electron column, and the EDS electronics connected to the SEM. The nature of this connection permits digital beam control of the microscope, as well as control and monitoring of general microscope functions. The SEM's monitors are used to produce the output of compositional images as well as other information relating to the mapping data. The SEM's monitors are under control of the EDS computer during the production of the outputs. The software to acquire the x-ray maps and reduce the data is part of the HAX software.⁹ It was written for a specific set of hardware in order to optimize the analysis speed.

The material analyzed was an aluminum alloy of high silicon content: BCS 182/2, a nominal 11% Si alloy. The operating conditions are given in Table 1. The total time of analysis was 140 min. The size of the digital scanning matrix is 128 × 100, so the dwell time at each pixel is 0.66 s. After the x-ray spectrum is accumulated at each pixel, background is subtracted, peak overlap corrections are applied, and ZAF factors are calculated and applied. These processing steps are accomplished in 100 ms due to the optimization of the HAX program. Background is subtracted by fitting of a modified Kramers law equation in segments across the spectrum. The segments were chosen automatically, but could be specified if desired. The peak overlap corrections were derived by a least-squares fitting of shell multiplets to the spectrum. The ZAF corrections applied were calculated with the models from the NBS FRAME method. All calculations that can be made in advance of data accumulation are done once the necessary experimental parameters are known.

Results

Figure 1 is a backscattered electron micrograph of the area of the sample which was scanned. Figure 2 shows some of the elemental maps obtained from the mapping procedure. The gray levels shown are related to concentration, not intensity. Black in these images represents 0 wt%; white, the highest concentration for that element in the image. The images are presented in up to 8 gray levels. In addition to the concentration images, other types of information are available. Table 2 is an affinity matrix that has been calculated for this set of images. The numbers in the matrix represent the relative amount of correlation

TABLE 1.--Operating conditions during the mapping of 182/2.

Accelerating voltage	20 kV
Sample tilt angle	0°
Detectro takeoff angle	35°
Working distance	10 mm
Spot size	200 nm
Average count rate	3800 cps
Magnification	5000×
Pixel dwell time	0.66 s
Detector resolution	146 ev @ 5.9 keV

TABLE 2.-- Elemental affinity matrix from the compositional map: the relative correlation of concentrations.

	Al	Si	Ti	Mn	Fe	Ni
Al	100	-76	03	-15	-20	-01
Si	-76	100	-05	-01	0	-07
Ti	03	-05	100	-09	-11	-01
Mn	-15	-01	-09	100	31	04
Fe	-20	0	-11	31	100	09
Ni	-01	-07	-01	04	09	100

TABLE 3.--Selected averages: concentrations of selected regions of the compositional map.

(a) Average analysis of the entire map: subpopulation selected from wt% Al distribution.

Window setting, from 50.8 to 100%
 Window area fraction, 100.0%
 Average density, 2.62 g/cm³
 Average tot. peak rate, 1484 cps
 Average gray level, 1764
 Average chemical composition:

Element	Al	Si	Ti	Mn	Fe	Ni
wt%	82.30	14.90	0.30	0.60	1.30	0.70

(b) Average analysis of the high-Si region: subpopulation selected from wt% Si distribution.

Window setting, from 19.2 to 47.2%
 Window area fraction, 26.95%
 Average density, 2.43 g/cm³
 Average tot. peak rate, 1475 cps
 Average gray level, 1684
 Average chemical composition:

Element	Al	Si	Ti	Mn	Fe	Ni
wt%	72.10	25.70	0.30	0.50	0.90	0.60

(c) Average analysis of the high-Fe region: subpopulation selected from wt% Fe distribution.

Window setting, from 2.8 to 15.6%
 Window area fraction, 12.44%
 Average density, 2.78 g/cm³
 Average tot. peak rate, 1369 cps
 Average gray level, 2204
 Average chemical composition:

Element	Al	Si	Ti	Mn	Fe	Ni
wt%	77.9	12.70	0.30	1.80	6.10	1.0

between elements. A positive number indicates a positive correlation; a negative number, a negative correlation. From this matrix can be seen indications that Al and Si are negatively related; that is, as the Si concentration increases, the Al concentration decreases. Mn and Fe occur together in the sample, and Ni occurs with Fe, but not in all locations. Ti is evenly distributed in the sample. Since all the concentrations are known, the density at any pixel can also be calculated and displayed. Figure 3 is the map of density in the sample, ranging from 2.04 to 3.23 g/cm³. Histograms of the elemental intensities, concentrations, density, gray scale of the electron image, and total peak counting rate can also be produced and displayed. Figure 4 is the Si concentration histogram. From these histograms, regions of interest can be selected, and the average concentrations from the pixels in this region can be calculated. Table 3 shows selected averages for various regions. The regions of interest selected can also be used to produce binary maps, where pixels in the region are white and all others are black. Figure 5 presents binary maps of Si and Fe above a threshold of concentration.

Figure 6 is the output of a linescan across the sample for Si and Al showing the complementary nature of these elements in this sample. The linescan was produced in much the same manner as the map, and the same quantitative procedure was used. It is presented here to complement the map data.

Discussion

In a small region of the aluminum alloy studied here, BCS 182/2, variations in concentration have been revealed. Regions of very high Si are obvious, as are other crystallites with Mn, Fe, and Ni. At first glance the concentration maps may not seem more revealing than x-ray intensity maps, but much more information can be obtained. A density map (Fig. 3) shows the overall variation in chemical concentration. Thresholds can be set to show those areas in which a certain concentration is exceeded. If only intensities were available, one would be uncertain as to the concentration level that were being exceeded. Although at any one pixel, the statistical accuracy of analysis is poor because of the short dwell time, averages are easily produced over selected regions. These averages can be selected over gray-level features, density features, or from any elemental histogram. They are statistically valid if the selected region encompasses tens of pixels or more.

The ability to acquire images of elemental composition has been demonstrated. Because of the high-speed reduction of data, the accumulation of the data does not take longer than it would take to accumulate an x-ray intensity map of good quality. The composition maps contain much more than that inferred from a normal x-ray intensity map.

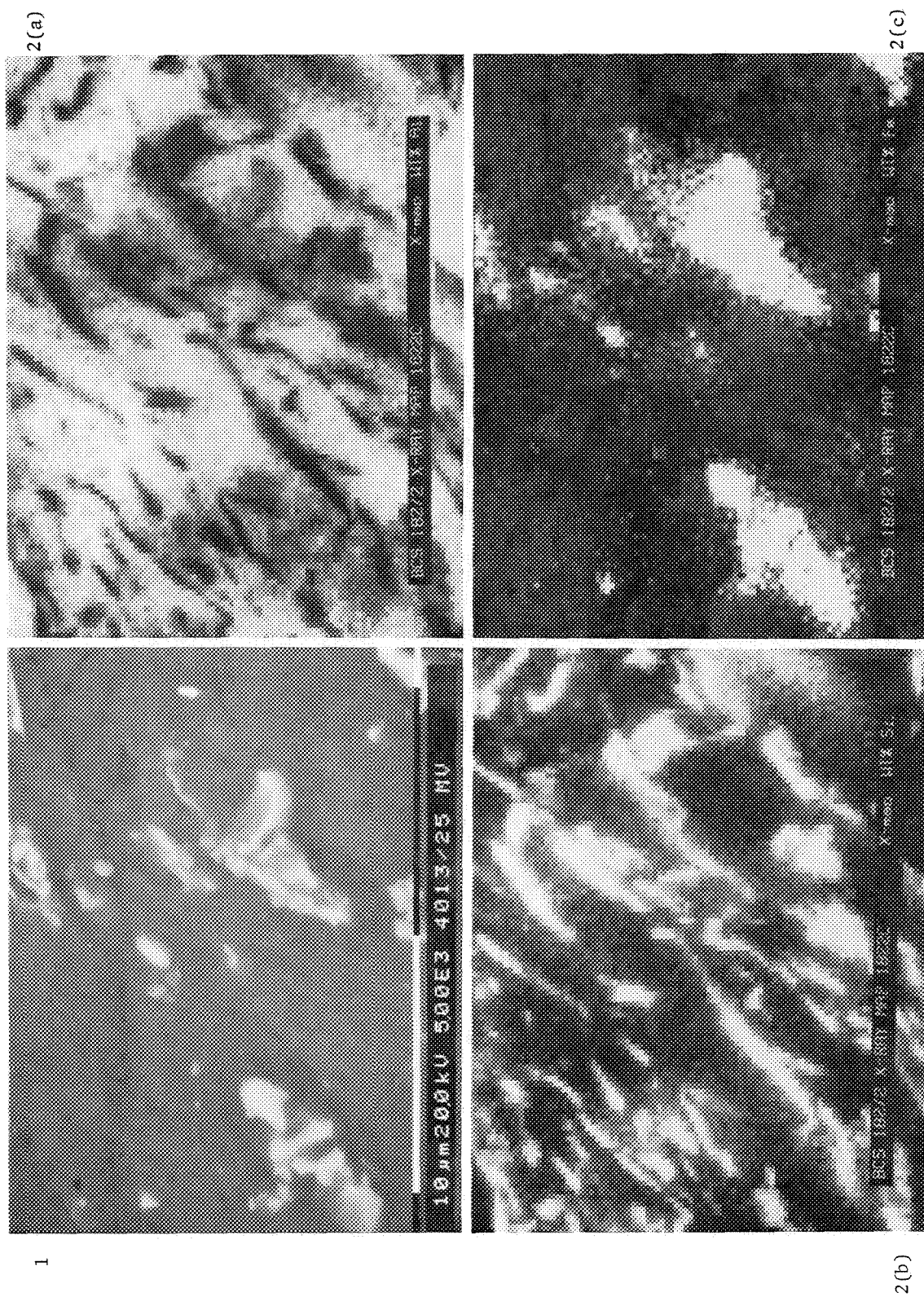
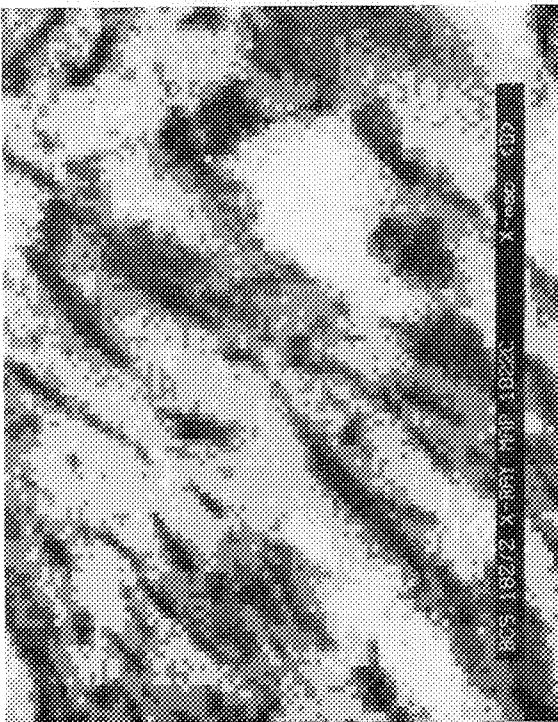
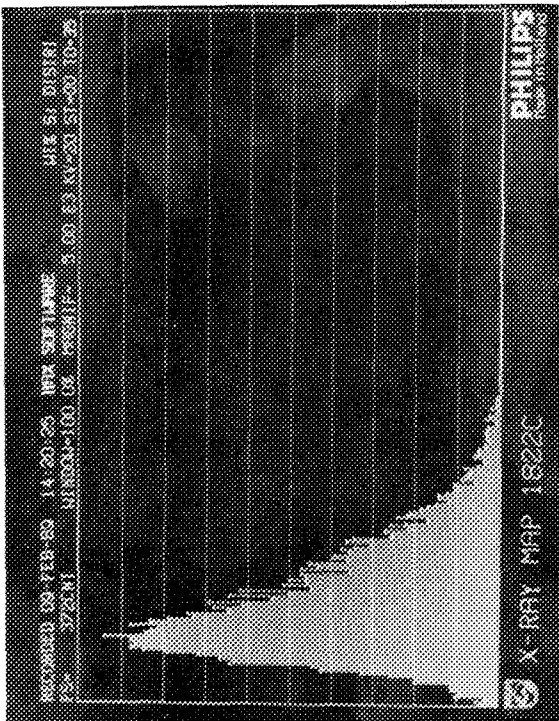


FIG. 1.--Backscattered electron micrograph of Al alloy 182/2.
 FIG. 2.-- Compositional x-ray maps of same area of 182/2 as shown in Fig. 1. (a) Al, 50.8% = black, 100% = white; (b) Si, 0% = black, 47.2% = white; (c) Fe, 0% = black, 15.6% = white.

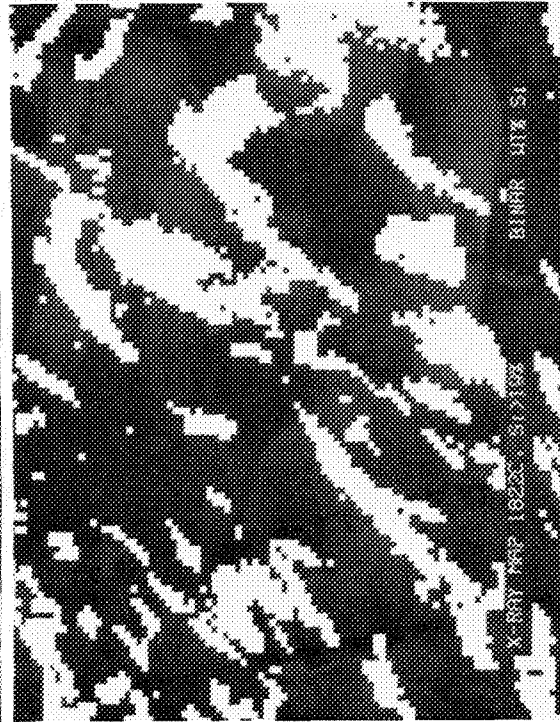
3



4



5 (a)



5 (b)

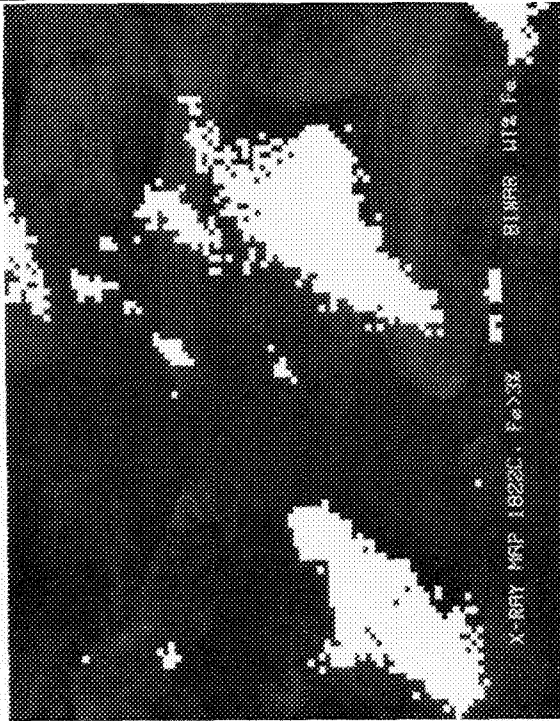


FIG. 3.--Density map of Al alloy 182/2, same area as Fig. 1.
FIG. 4.--Histogram of Si concentration from Fig. 2(b).
FIG. 5.--Binary images of elemental concentrations. (a) Si greater than 19%; (b) Fe greater than 3%.

References

1. R. L. Myklebust, R. B. Mareninko, D. E. Newbury, and D. S. Bright, "Quantitative calculations for compositional mapping techniques in electron probe microanalysis," *Microbeam Analysis--1985*, 101.
2. D. E. Newbury, "Compositional mapping of thick specimens," *Microbeam Analysis--1985*, 204.
3. C. E. Fiori, R. D. Leapman, and K. E. Gorlen, "Computer-aided compositional mapping in scanning electron column devices," *Microbeam Analysis--1985*, 219.
4. R. B. Marinenko, R. L. Myklebust, D. S. Bright, and D. E. Newbury, "Wavelength-dispersive techniques for compositional mapping in electron-probe microanalysis," *Microbeam Analysis--1985*, 159.
5. C. R. Swyt and C. E. Fiori, "Large-field x-ray compositional mapping with dynamically focused wavelength-dispersive spectrometers," *Microbeam Analysis--1986*, 482.
6. K. A. Thompson and L. R. Walker, "Quantitative and low-magnification mapping by the electron microprobe," *Microbeam Analysis--1986*, 491.
7. R. L. Myklebust, D. E. Newbury, R. B. Marinenko, and D. S. Bright, "Defocus modeling for compositional mapping with wavelength-dispersive x-ray spectrometry," *Microbeam Analysis--1986*, 495.
8. Philips 5X5 SEM, EDAX 9900 EDS system and HAX software.
9. H. M. J. M. van Ass of Eindhoven, The Netherlands, is the author of the HAX software.

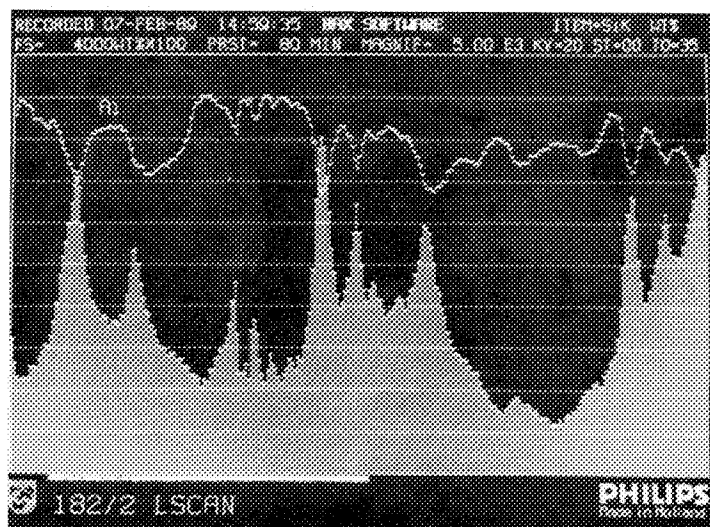


FIG. 6.--Concentration line scan across sample of Fig. 1; Si and Al concentrations are displayed.

PREPARATION AND PRELIMINARY ANALYSIS OF K-411 GLASS MICROSPHERES

R. B. Marinenko, J. A. Small, D. H. Blackburn, D. R. Retorick, and N. J. Shire

During the past several years, preliminary work has been done on the development of a glass microsphere standard in the 1-20 μ m size range. The purpose of this standard is to provide the analyst involved in the microanalysis of particles with a standard of known shape and elemental composition. The work described in this paper is the initial phase of a thorough characterization of these glass microspheres for certification as a National Institute of Standards and Technology (NIST) Standard Reference Material (SRM).

Experiment

Previous work on this standard has been concerned with the development of techniques for manufacturing the microspheres^{1,2} and with the analysis of the microspheres to determine the composition and interspecimen homogeneity of the microspheres. National Bureau of Standards (NBS) Glass K-411 was chosen for these studies for the following reasons.

1. It is available in bulk form as NBS SRM 470,* Mineral Glasses for Microanalysis.³ As such, the glass was shown to be homogeneous on the μ m scale, and the elemental concentrations are accurately known.

2. The glass is available in thin film form as SRM 2063, a 101nm film designed for use in analytical electron microscopy.

3. The glass contains no volatile or highly mobile elements that could easily escape from or migrate in the matrix during preparation or electron beam analysis of the glass microspheres.

4. The glass is similar in composition to many types of particles found in the environment.

A bulk, 300 g sample of the glass was prepared by standardized procedures^{1,2} of accurately weighing the oxides, placing the oxides in a platinum crucible, heating, melting, and stirring until the glass was homogeneous. The bulk glass was ground in a carbide mortar and pestle until shards of the desired particle size were obtained. The shards were injected into the base of a tube furnace, where they were heated to just below the melting temperature of the glass and formed into spheres as

they traveled in the upward draft of the furnace.

One problem, which was recently solved, was that of keeping the particles separated during the sphere-forming process to prevent them from fusing together. Separation was achieved by mixing large quartz particles (greater than 10 μ m) with the glass shards before melting. The quartz reaches the heating zone but is not melted. Because of their large size, the quartz particles are not carried by the plume to the collection device, but they serve to keep the K-411 shards separated in the early stages of the melting process.

The microspheres are collected on a filter located at the top of the tube furnace. All sizes of spheres are at present collected together. In the future, some methods may be used to separate them according to size at the collection point.

Quantitative Analysis

The microspheres are analyzed quantitatively by electron probe microanalysis (EPMA) to determine whether the elemental concentrations in the glass microspheres were the same as those in the bulk material. In a preparation procedure such as the one used to make the microspheres, there is always the possibility of losing some of the components during the heating process.

Since successful quantitative matrix correction procedures are based on flat, polished, bulk specimens, quantitative analysis of microspheres is less accurate than bulk analysis. The size and shape of the sphere introduces unique problems.⁴ First, since the microsphere is smaller than the excitation volume of the electron beam, fewer x rays are generated than would be generated in a bulk specimen. Second, because of the curvature of the sphere surface, the absorption path length of the emitted x rays is shorter than for a bulk specimen. Third, because of the limited volume of the microsphere, secondary fluorescence by the continuum and characteristic x rays is less than for the bulk material since the majority of these x rays exit the specimen volume before interaction.

To reduce these problems, the microspheres were mounted in epoxy, ground, polished, and carbon-coated such that the cross sections of the microspheres were exposed for analysis. As far as the absorption of x rays was concerned, the microspheres exceeding 2-3 μ m would in this way be most similar to the bulk material when analyzed by the electron microprobe.

Two different instruments were used to analyze the microspheres, the Cameca electron mi-

The authors are at the Center for Analytical Chemistry, National Institute of Standards and Technology (formerly the National Bureau of Standards), Gaithersburg, MD 20899.

*Standards labeled NBS Standard Reference Materials (SRMs) will remain NBS standards until the present supply is depleted, at which time they will be reissued under the new NIST name.

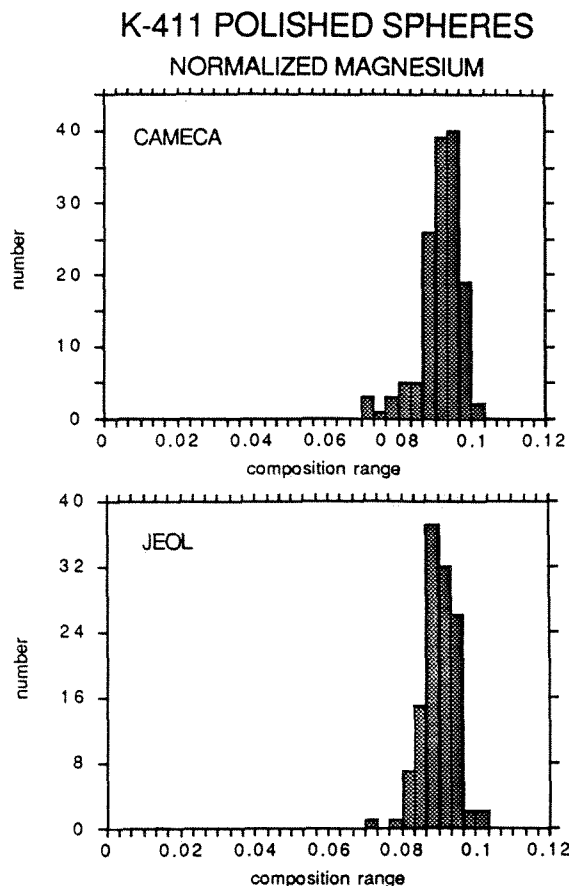


FIG. 1.--Histogram plots for normalized magnesium results obtained from two instruments used in the analysis of K-411 microspheres.

croprobe and the JEOL 840 scanning electron microscope (SEM).^{*} Energy-dispersive (EDS) analysis was used with both instruments, and the data reduction procedure FRAMEC was used for the quantitative calculations. The elements magnesium, silicon, calcium, and iron were measured directly against the bulk K-411 glass standard. The oxygen concentration was calculated from assumed stoichiometry. For this preliminary work, microspheres of all sizes were analyzed; 143 were analyzed with the Cameca and 123 were analyzed with the JEOL. The primary purpose was to make a comparison with the bulk glass and compare the results from the two different instruments. In an effort to compensate for the reduced mass of the microspheres compared to the bulk glass, the results were normalized by making the sum of all five elements present equal to 100%. The normalized results from the two instruments overlap in the histogram plots, showing consistency between the two instruments. An example of these histogram plots is in Fig. 1, where the results for magnesium from the two instruments are compared.

^{*}Certain commercial equipment, instruments, or materials are identified in this paper to specify adequately the experimental procedure. Such identification does not imply recommendation or endorsement by NIST, nor does it imply that the materials or equipment identified are necessarily the best available for the purpose.

The average of the normalized values for each element is compared to the certified value in Table 1. The differences between the averages of the normalized values and the certified bulk SRM values are less than ± 5 wt% for all elements except calcium analyzed by the JEOL where the difference is -9 wt%. In the results from both instruments, the elemental concentrations of magnesium and silicon are greater than the certified values; the calcium and iron values are both less than the certified values. This discrepancy may be the result of particle effects that have not been corrected in the sample preparation or concentration normalization.

Conclusion

These initial results show that the integrity of the composition of the bulk glass has been maintained in the microspheres within the error limits of $\pm 10\%$. Additional work is being done to verify whether the observed differences are real, i.e., whether they consistently occur in the direction indicated here, and whether they apply consistently to the same elements. Also, analyses on larger spheres (diameters greater than 3-4 μm) will in future work be separated from those on smaller microspheres to determine whether elemental segregation depends on size. Another requirement of this certification process will be to collect several grams of the microspheres for quantitative wet chemical analysis of each element, as is normally done for certification of the bulk glasses.

References

1. J. A. Small, K. F. J. Heinrich, C. E. Fiori, R. L. Myklebust, D. E. Newbury, and M. E. Dilmore, "The production and characterization of glass fibres and spheres for microanalysis," *SEM/1978 I*, 445-454.
2. J. A. Small, J. J. Ritter, P. J. Sheridan, and T. R. Pereles, "Methods for the production of particle standards," *J. Trace and Microprobe Techniques 4*: 163-183, 1986.
3. R. B. Marinenko, *Preparation and Characterization of K-411 and K-412 Mineral Glasses for Microanalysis*; SRM 270, Nat. Bur. Stand. Spec. Publ. 260-74, 1982.
4. J. A. Small, "Quantitative particle analysis in electron beam instruments," *SEM/1981 I*, 447-461.
5. R. L. Myklebust and B. B. Thorn, *A FORTRAN Version of the Quantitative Energy-dispersive Electron Beam X-ray Analysis Program FRAMEC*, Nat. Bur. Stand. Tech. Note 1200, 1984.

TABLE 1.--Quantitative electron microprobe analysis of K-411 spheres concentrations in weight percent.* (Oxygen calculated from stoichiometry.)

	<u>Mg</u>	<u>Si</u>	Element <u>Ca</u>	<u>Fe</u>	<u>O</u>
<u>Probe</u>					
Cameca	9.2±1.2(13.0)	26.1±0.8(3.0)	10.8±1.0(9.3)	10.7±1.2(11.2)	43.2±0.6(1.4)
JEOL	9.0±0.8(8.9)	26.0±0.8(3.0)	10.1±0.8(7.9)	10.7±1.0(9.3)	44.2±0.4(0.90)
<u>SRM 470</u>					
<u>Certified</u>					
<u>Values</u>	8.85±0.12(1.4)	25.38±0.09(0.35)	11.06±0.14(1.3)	11.21±0.16(1.4)	42.36±0.24(0.57)
(bulk)					

* Error is two standard deviations for 143 experiments on the Cameca and 122 experiments on the JEOL. The coefficient of variation is in parentheses. Errors for the certified values for each element are estimates taken from the 2-sigma values assigned to the oxides in the SRM certificate.

DESIGN OF A PROTOCOL FOR AN ELECTRON PROBE MICROANALYZER k-VALUE ROUND ROBIN

D. E. Newbury and R. B. Marinenko

The fundamental experimental measurement of quantitative electron probe microanalysis is the k-value, which is defined as the ratio of the measured x-ray intensity of the sample (unknown) to a reference (standard), or $k = I_{\text{sam}}/I_{\text{ref}}$. For several reasons, the need has arisen to conduct an electron probe microanalysis round robin for the measurement of k-values.

First, the correction procedures for quantitative electron probe microanalysis have undergone re-examination and improvement in recent years, as evidenced by the extensive discussions presented in *Microbeam Analysis--1988* and at the subsequent Workshop on Quantitative Electron Probe Microanalysis held at the National Institute of Standards and Technology (NIST).^{1,2} Testing of new correction procedures and of modifications to existing procedures is at present carried out with the use of nonstandardized compilations of k-values, which makes comparison of results among the various models and variations difficult. Thus, it would be useful to establish a reference database of k-values that are universally acceptable and against which all models could be tested.

Second, the error distributions presented by the various promulgators of correction models are narrowing to the point that 1 - σ of the distribution corresponds to an error of less than 2% relative. If uncertainty in the composition of the standards is not to be a limiting factor in these error distributions, the standard compositions clearly have to be known to better than 1%. Some of the k-values in the various compilations were measured on standards whose compositions are not known with sufficient accuracy by independent analytical means to satisfy this criterion.

Third, the basic instrumental procedures for measuring k-values must also be examined closely to insure that accurate measurements are obtained. This is potentially the most important limiting aspect that will determine the reliability of a k-value database. Most existing k-value compilations consist of measurements made on a variety of instruments, but the individual k-values are often only measured on a single instrument and not corroborated by other measurements. It is not possible to determine whether any systematic errors have occurred in the measurement process. The measurement problems encountered obtaining high accuracy k-value measurements by means of energy-dispersive x-ray spectrometry (EDS) in electron-beam instruments

have been extensively described.^{3,4} Often it is assumed k-value measurements by wavelength-dispersive x-ray spectrometry (WDS) are less prone to measurement errors. However, recent results suggest that this might not be the case. Armstrong⁵ has reported problems associated with two critical aspects of k-value measurement in a current state-of-the-art microprobe. In one situation, the take-off angle was inconsistent between two nominally identical wavelength-dispersive spectrometers on the same microprobe due to faults in the fabrication and mounting of the diffraction crystals. This particular problem led to errors of the order of 5% relative in the measured k-value (Cu L α in 80 Au-20 Cu alloy). A second problem involved the pulse-processing circuitry and was manifested as a variable deadtime with x-ray energy. Errors of 0.8 μ s in a nominal deadtime of 1 μ s were observed, which could lead to relative errors significantly in excess of 1% in a k-value measured at high deadtime.

The design of a useful k-value round robin must therefore consider the issues of sample and measurement integrity. The initial stages of this round robin will use NIST Standard Reference Materials (SRMs) for microanalysis as unknowns, where the questions of sample composition and microhomogeneity have been addressed in detail during the certification process. Specimen preparation (mounting, polishing, and carbon coating) will be carried out at NIST to insure uniformity. Pure element and compound standards will be mounted with the SRMs to insure that all are subjected to identical measurement conditions. Sample issues are not considered further in this paper, the balance of which covers the second point, that of the protocol for measurement.

Design of a Protocol

A major goal of the k-value round robin will be to obtain measurements that can be compared among several laboratories executing nominally identical measurement procedures to assess the interlaboratory variability. If the valuable time expended by the participants in a round robin is to yield the maximum amount of information, the protocol for making measurements and reporting data is critical. This is particularly true if, as in the present case, the data so obtained are to form the basis for a community reference database. If questions arise in the future concerning the measurements taken in the round robin, the protocol should be designed to collect enough ancillary information to answer those questions. This paper therefore presents the first design for the measurement protocol in order to provide the microanalysis community with an opportunity to

The authors are with the Center for Analytical Chemistry, National Institute of Standards and Technology (formerly the National Bureau of Standards), Gaithersburg, MD 20899.

offer constructive criticism in the hope of improving the final product.

Protocol for k-value Determination by WDS

The following protocol for k-value determination by WDS provides the general model for the round robin. Table 1 lists the information requested from each participant. The sequence of measurements to be performed is:

Reference (standard): 3 measurements at different locations

Unknown: 10 measurements at different locations

Reference (standard): 3 measurements at different locations

The measurement sequence of reference/unknown/reference is followed to reveal any systematic measurement errors due to drift. The target is translated between measurements to reduce problems that might arise due to contamination, as well as to avoid any undue influence from inhomogeneities or surface defects introduced during preparation. Each analyst's calculation of k-values and the complete data output necessary for the k-value determination will be reported. The k-value measurement will be made over a series of specified specimen beam energies, e.g., 10, 15, 20 keV, to develop a database that will be useful for a variety of tests. By requiring measurement of the Duane-Hunt continuum limit, we can obtain a check for the accuracy of the setting of the beam energy. To insure adequate statistical precision in the k-value ratio, participants will be requested to accumulate at least 200 000 counts for both the standard and the unknown, which should result in a precision of better than 0.5% in the k-value.

TABLE 1.--WDS round robin protocol.

A. General

Instrument spectrometer configuration (schematic diagram requested showing spectrometer locations)

B. Electron beam conditions

1. Beam energy (confirmed by Duane-Hunt limit)
2. Beam current (measured in a Faraday cup)
3. Beam incidence angle to specimen surface

C. Wavelength-dispersive spectrometer characteristics

1. Take-off angle
2. Azimuthal angle (relative to specimen tilt axis)
3. Diffraction crystal
4. Pulse height distribution, threshold, and window
5. Specify deadtime, how determined, and deadtime correction method applied.

D. Measurement procedure

1. Peak position (in $\sin \theta$ units, mm, or other spectrometer calibration).
2. Specify background correction method(s):
 - a. If by detuning, specify spectrometer positions for background measurements (exact defocusing conditions).

- (1) Provide background counts and count in-

terval at each position.

(2) Give calculated background counts at peak position.

(3) Give background-corrected peak counts.
b. If by use of another pure element, specify element, counts at the peak position on that element, and your calculation of the background appropriate to the measurement.

3. Measurements on standard.

Raw peak count

Deadtime-corrected peak count

Background-corrected peak count, $i(\text{standard})$, and $i(\text{unknown})$

4. The average background and deadtime corrected standard intensity is calculated.

The k-value for each measurement on the specimen is calculated as: $k = i(\text{unknown})/i(\text{standard, average})$

WDS Report Table (repeat table for each line measured)

Crystal

Peak height distribution:

Peak =

Threshold =

Window =

Pulse counting circuitry deadtime =

Spectrometer peak position =

Spectrometer background position(s) =

Background calculated at peak position =

Standard

	Raw	Deadtime-corrected count rate	Background corrected count rate
# counts			

Unknown

	Raw	Deadtime-corrected count rate	Background-corrected count rate	k
# counts				

Protocol for k-value Determination by EDS

For the determination of k-values by EDS, the WDS protocol is modified as shown in Table 2. Detailed information is requested on the energy-dispersive spectrometer operating characteristics. In addition to the participants' calculation of k-values using their local data reduction scheme, archival information is requested in the form of spectra measured on pure carbon, which is useful for fitting detector parameters, as well as all spectra from standards and unknowns. Permanent recording of the actual EDS spectra is important. Since several different spectral processing techniques are in use in the wide variety of commercial and individually developed software systems, details on the calculation procedures are requested. In this case, the participants' measurement of the k-value will be critical, since it may not be possible to reconstruct, at a later date, the exact mathematical procedures that were applied to the spectra. The archived spectra will provide a permanent record, which can be subjected to uniform spectral processing techniques by a single method.

Laboratory testing of the protocols has been

initiated to determine whether all necessary aspects of the data measurement have been adequately addressed.

TABLE 2.--EDS round robin protocol.

C. Energy-dispersive spectrometer characteristics

1. Take-off angle
2. Azimuthal angle (relative to specimen tilt axis)
3. Detector size (mm^2)
4. Distance from beam impact point (mm)
5. Window material: Thickness (μm)
Dead layer thickness (μm):
First surface electrode material Thickness (μm)
Ice layer thickness estimate (μm):
6. Spectrometer set-up information
 - a. Energy per channel, eV/channel:
 - b. Number of channels:
 - c. Pulse processing (shaping) time (μs):
 - d. Energy resolution FWHM (eV) for Mn K α under measurement conditions used for k-values:
 - e. Total livetime for spectrum accumulation:
7. Calibration error on
 - a. SiK (1.740 keV) actual:
 - b. Mn K α (5.890 keV) actual:
 - c. Cu K α (8.040 keV) actual:
8. Measure a 1000s EDS spectrum on carbon; provide disk and hard copy.
9. Provide the spectra measured on each standard and unknown in disk copy, with one representative hard copy.
10. Specify disk format.

D. Measurement procedures

1. Provide description of background correction and peak.
2. Provide description overlap correction methods used.

References

1. Various authors, *Microbeam Analysis--1988*, 239-319.
2. Workshop on Quantitative Electron Probe Microanalysis, August 1988, National Institute of Standards and Technology (in press).
3. C. E. Fiori and D. E. Newbury, *SEM/1978* I, 401.
4. J. I. Goldstein, D. E. Newbury, P. Echlin, D. C. Joy, C. E. Fiori, and E. Lifshin, *Scanning Electron Microscopy and X-ray Microanalysis*, New York: Plenum, 1981, 205.
5. J. Armstrong, Ref. 2.

LAMMS: Fundamentals & Ion Formation Processes

ARE LASER-ABLATED MONOLAYERS ACCURATELY CHARACTERIZED BY THEIR ION EMISSION?

R. W. Dreyfus

Laser microprobe mass analysis (LAMMA) is an enticing analytical tool. Some of its advantages are: submonolayer sensitivity; easy sample preparation and interpretation of results, applicable to most materials; and reasonable vacuum requirements. In considering the best applications of LAMMA, one has to ask how the ions sampled by a mass spectrometer are related to a given solid surface. This question can be divided into three steps: efficiency of converting a solid surface into a vapor, ionization of the species in the vapor, and survival of the ions for the time needed to pass through a mass spectrometer. Even in experiments in which one utilizes a second laser or electron beam to ionize the neutral species in the original vapor, one still has to deal with the first and last steps. One can sum up all the steps by asking what is the relationship of the detected ion signal on the following etch-laser parameters: wavelength λ , pulse length τ , and power density P . The goal, of course, is to estimate how quantitative is LAMMA when applied to monolayer analysis. Examples are drawn from graphite, copper, and sapphire UV-photoablation to demonstrate that if only one monolayer is ablated the ion yield is not a good reflection of the surface composition. This poor correlation is primarily due to the ion-forming step operating too close to its threshold power.

Experimental Technique

Our primary experimental method is to use laser-induced fluorescence (LIF) as a probe of the solid \rightarrow vapor (atom, diatomic or ion) transition. This probing is done in the etch plume some millimeters or centimeters above the ablated surface, as has been described in detail elsewhere.^{1,2} LIF has the advantage that density information is obtained about specific (neutral or charged) species in specific energy states. The disadvantage is that sometimes one cannot see the forest for the trees; i.e., LIF is not a particularly good survey tool, it is only exceptional in its ability to follow a specific species. It is our belief that following a specific species often gives significant insight into formation and transport processes related to atoms or ions. Also, LIF of neutrals provides milestones along the pathway to ion formation. In contrast to the above, large pieces of surface can be removed by exfoliation (where "sheets" of material explode or fracture off the surfaces), or hydrodynamic

splashing (the spray from the crests of waves on a molten surface).³ Both these etching mechanisms do not provide atom or molecular species suitable for LIF probing or LAMMA directly and hence will not enter into the present cases of removing monolayers of a surface. We shall simply acknowledge that these mechanisms exist but limit our discussion to cases that are amenable to detailed LIF probing, including the formation of ions. These cases are carbonaceous materials (graphite, frozen benzene monolayers, and polymers) and metals (primarily copper and aluminum). The sensitivity of LIF is such that one can commonly follow the removal of $\sim 10^{-3}$ monolayers of atoms or ~ 0.1 monolayers of diatomics.

The primary question, of course, is the production of ions from a surface. As we shall see, the LIF technique can not only detect specific neutral species, but direct comparison to ion densities is possible by a simple adjustment of the LIF excitation-laser wavelength.

Experimental Results

Graphite. The laser vaporization of graphite represents an outstandingly simple yet interesting example of sublimation. Despite the relatively high temperatures required to generate vapor pressures of ~ 1 at., laser fluences of >1 J/cm² produce intense plumes of C₂, C₃ radicals and presumably C atoms.² The lack of complications in this sublimation are deduced from the facts that the surface morphology,⁴ the vaporization rate, and the internal (rotational and vibrational) energies of the C₂ diatomics all agree with the same peak temperature; i.e., 3750 ± 300 K. What is of greater importance for present purposes is that ion or free-electron effects are usually negligible, as detailed below.

With graphite sublimation, no intensely luminous plasma plume is observed. In the past, interferometer measurements of the free electrons have shown that such a flash correlates with a high density of free electrons in the plume.⁵ Also, no LIF signals from either C₂⁻ or C₂⁺ ions were observed. On the other hand, the much higher sensitivity of mass spectrometers have allowed for the observation of C_n⁺, although these signals are commonly deduced to arise as a coalescence product within plumes.⁶ It has also been suggested that cratering of the surface also enhances the coalescence to larger particles or ions.⁶

The reasons for not observing a free-electron plasma or ions following graphite ablation seem to arise from several factors. First, graphite ablates easily above 10^8 W/cm²; this

The author is at the IBM Research Division, T. J. Watson Research Center, Yorktown Heights, NY 10598.

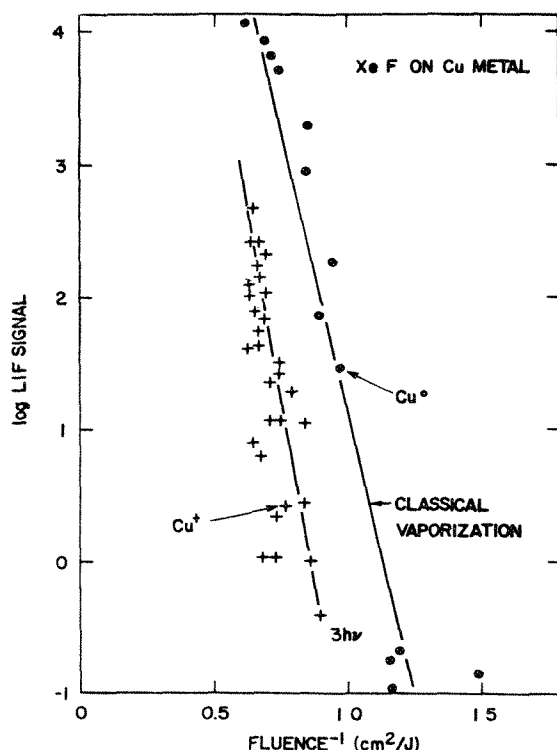


FIG. 1.--Relative Cu ground state atom and Cu^+ metastable ion LIF signals due to ablating copper with a (351nm, XeF) excimer laser vs the reciprocal laser fluence. The reason for plotting the abscissa as reciprocal fluence is so that thermal vaporization gives a straight line with the slope determined by the heat of vaporization. Note that the slope of the ion signal is distinctly higher than the slope of the atom signal and thus is in agreement with a multiphoton process for ionizing the Cu atoms.

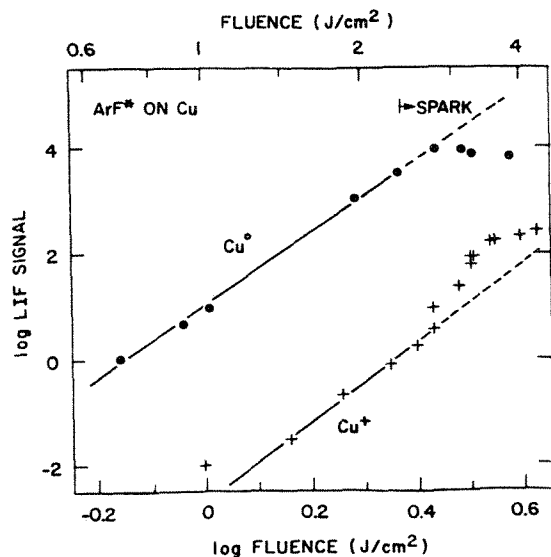


FIG. 2.--Similar to Fig. except etch laser is now at 193 nm. Note the difference in slopes between ion and atom signal is no longer large. The avalanching of ionization due to free electrons colliding with atoms is noted to accelerate

the ionization above $3\text{J}/\text{cm}^2$. Atom signal then ceases to increase, presumably due to most of the copper vapor now appearing in one of the ionic states.

range rarely produces intense ionization, which has a sharp onset in the $2\text{--}4 \times 10^8 \text{ W}/\text{cm}^2$ region. Second, C_2^- is extremely stable (ionization energy of 3.54 eV) and hence probably acts as an electron sink, perhaps through a $\text{C}_3 + e^- \rightarrow \text{C}_2^- + \text{C}$ reaction. Third, both C_2 and C should require two photons (even for 193nm etching) to ionize, so that a reduced density of free electrons is generated.

The above observations depend on the crystalline form of the carbon; it has been noted⁵ that diamond gives an intensely luminous plume. These differences appear due to the fact that diamond requires $\sim 10^9 \text{ W}/\text{cm}^2$ for ablation, presumably because its exceptionally high thermal conductivity hinders vaporization. This comparison of graphite to diamond brings out the fact that the ion yield depends not only on the surface composition, but also its crystalline form. With sufficient laser power ions are doubtless produced from graphite surfaces, but this power domain does not appear to overlap the region where only ~ 1 monolayer of surface is removed per etch pulse.

Copper. Metallic copper samples make for an interesting comparison with the above results with graphite. At just above threshold fluences ($\geq 0.6 \text{ J}/\text{cm}^2$ or $\geq 6 \times 10^7 \text{ W}/\text{cm}^2$) the two systems are similar. The atoms and diatomics in the plume arise from thermal vaporization in both cases. As the fluence increases into the $1.5 \text{ J}/\text{cm}^2$ region, multiphoton ionization sets in and an LIF signal from Cu^+ metastables approaches the magnitude of the Cu^0 signal. Ground state Cu^+ is not easily observed by LIF, but Langmuir-probe measurements suggest that both the ground state and metastable state densities behave similarly.⁸ The generation of the ions apparently goes through the following steps (Figs. 1 and 2) as the etch laser power increases: first, multiphoton ionization generates the initial electron ion pairs (neglecting thermionic emission, which may have freed up to 10^9 electrons/ cm^2); second, inverse bremsstrahlung then couples the etch laser light directly into the electron cloud; and third, the electron cloud eventually becomes sufficiently energetic to produce both secondary ionization and dissociation of Cu_2 diatomics simultaneously. In competition with the above, three-body recombination may eliminate some of the cooler free electrons.

Discussion

One may ask, when one has the three variables (λ , τ , and P) for the etch laser, which quantity promotes the ion formation necessary for LAMMA analysis? As shown above and generally obvious is that large P ($> 4 \times 10^8 \text{ W}/\text{cm}^2$) rapidly accelerates ion formation.¹⁰ Long pulse length τ enhances etching but only slowly

($\tau^{1/2}$ dependence¹⁰). The increase of ionization with wavelength is somewhat more complicated. First, inverse bremsstrahlung can go up as fast as λ^2 . (That occurs primarily for UV wavelengths, where the plume rarely achieves the electron density of $\geq 10^{20}$ cm⁻³ required for the formation of an optically opaque plasma.) On the other hand, with near threshold P, multiphoton ionization is promoted by short wavelength (small λ). One thus concludes that the λ dependence is the result of two conflicting dependences and hence not obvious. This situation is also material dependent as plume atoms in one particular state may or may not provide a large cross section for multiphoton- or fast-electron-induced ionization.

Conclusion

One can now see two general features of monolayer LAMMA results. First, the ion yield can depend more sensitively on the etch laser (τ , λ , and P) or the sample's physical state than is desirable for quantitative analysis. Second, going to high etch fluences results in coupling the laser energy into the free electron cloud, which is probably desirable as one then has predictable energy coupling into the plume and from the plume to the surface,¹⁰ and to the atoms (within the plume) so as to facilitate a high degree of ionization. However, what limits this latter approach is that when low etch fluences are utilized to remove only ~1 monolayer of surface, the resultant ion densities may only be a crude indication of the surface composition. In some cases a reconciliation of the above fluence difference may lie in bringing in the etch laser at grazing incidence, thereby increasing the plume fluence while leaving the etch fluence low.

References

1. R. W. Dreyfus, J. M. Jasinski, G. S. Selwyn, and R. E. Walkup, "Laser spectroscopy in materials processing research," *Laser Focus* 22: 62, 1986.
2. R. W. Dreyfus, Roger Kelly, R. E. Walkup, and R. Srinivasan, "Studies of excimer laser etching mechanism using laser induced fluorescence measurements," *Proc. Soc. Photo. Optical Instr. Eng.* 710: 46, 1987.
3. Roger Kelly, J. J. Cuomo, P. A. Leary, J. Rothenberg, B. E. Braren, and C. F. Aliotta, "Laser sputtering, Part I: On the existence of rapid sputtering at 193 nm," *Nucl. Instr. and Meth.* B9: 329, 1985.
4. Scanning electron micrographs of the graphite surface after etching indicate negligible melting. The melting temperature of graphite is about 4500 K (A. Cezairliyan and A. P. Miller, "Preliminary determination of the triple-point temperature of graphite from measurements by a pulse heating technique," *Bull. Am. Phys. Soc.* 32: 608, 1987), hence the peak surface temperatures are below this value.
5. R. E. Walkup, J. M. Jasinski, and R. W. Dreyfus, "Studies of excimer laser ablation of solids using a Michelson interferometer," *Appl.*

Phys. Letters 48: 1690, 1986.

6. A. O'Keefe, M. M. Ross, and A. P. Baronavski, "Production of large carbon cluster ions by laser vaporization," *Chem. Phys. Lett.* 130: 17, 1986.

7. D. Feldmann, "Photoablösung von Elektronen bei einigen stabilen negativen Ionen," *Zeit Natur.* 25a: 621, 1970.

8. R. W. Dreyfus and R. J. von Gutfeld, "Laser-induced fluorescence and Langmuir probe studies of copper photoablation," *Conf. on Lasers and Elec. Opt.*, Baltimore, 1989.

9. T. W. Johnston and J. M. Dawson, "Correct values for high frequency power absorption by inverse bremsstrahlung in plasmas," *Phys. Fluids* 16: 722, 1973.

10. C. R. Phipps, T. P. Turner, R. F. Harrison, G. W. York, W. Z. Osborne, G. K. Anderson, X. F. Corlis, L. C. Haynes, H. S. Steele, and K. C. Spicochi, "Impulse coupling of targets in vacuum by KrF, HF, and CO₂ single pulse lasers," *J. Appl. Phys.* 64: 1083, 1988.

ELECTRON-OPTICAL EXAMINATION OF LAMMS CRATERS IN TRANSVERSE SECTION

L. J. Matthews, C. S. Baxter and J. A. Leake

To improve quantification of LAMMS analyses it is necessary to understand the relationship between the composition of the specimen and the composition of the material evaporated by the laser pulse. Careful monitoring of the laser power and focus, and of the total number of ions produced, enables results from closely similar samples to be compared, but the problem of relative sensitivities varying from matrix to matrix still remains. Furthermore, complications may arise when multiple shots are taken in one location, since changes in the stoichiometry or microstructure just beneath the surface of a crater would be expected to affect the analysis obtained from a subsequent shot in the same place. Multiple shots are frequently used in reflection-mode LAMMS either to reduce the effects of surface contamination or as a crude depth-profiling technique, and in some cases the effect of crater depth on laser focus alone is sufficient to alter the results.

Recent analyses of a copper-boron melt-spun alloy on the LIMA-2A in our laboratory showed an unusually high degree of scatter in the ion ratios of copper and boron.¹ It was not clear whether this result was due to variations in sample composition (for example, undissolved boron particles or grain boundaries with a higher proportion of boron), or the effect of taking multiple shots in each position and thus "laser-processing" the surface to be analyzed. Since the original microstructure of this sample was thermodynamically unstable, a change in microstructure on heating the surface was a strong possibility. Work on large-scale laser-surface treatment of inorganic materials^{2,3} indicates possible changes that may occur on very rapid solidification from the melt. These include significant changes in microstructure (for example, where the material can be quenched to form a homogeneous glassy phase), segregation to the surface of dissolved impurities, or mixing and solute-trapping to give a higher concentration of solute than would occur at equilibrium. The velocity of the resolidification front plays a crucial part in determining which of the above effects will occur. This velocity is in turn influenced by the total energy absorbed by the sample, the

depth over which significant heating occurs prior to resolidification, and the diffusion rates and thermal conductivities of the elements concerned.

Even in samples known to be of uniform composition, relative ion yields vary on multiple-shot analysis. Work on gallium arsenide⁴ indicated statistically significant differences between the average Ga/As ratios obtained from fifth-shot and twentieth-shot data at any one laser power.

The effect of the highly localized and non-uniform laser spot used in LIMA analysis is difficult to calculate from first principles. An examination of the LIMA craters has therefore been started in order to study their shape and to assess the actual degree of resolidification and accompanying microstructural or stoichiometric changes induced in selected materials. Casual observation of the craters indicates that the apparent depth and width vary with sample type as well as with laser power and focus, while scanning electron microscope (SEM) photographs of the cratered surface reveal a central depression surrounded by a "splash" zone which apparently contains material resolidified from the melt. The craters are now being studied in cross section, and preliminary results on a semiconductor sample are presented to show the potential of this approach.

Experimental

Samples of a semiconductor were chosen for initial work because they were easily obtained with smooth, flat surfaces and because the craters produced in this material had previously been noted to be large. The sample consisted of a layer of Ga-In-Al-As (composition 15.3at.% Ga, 26.0at.% In, 8.5at.% Al, 50.2at.% As, nominal thickness 4 μm) deposited on an indium phosphide substrate approximately 0.4 mm thick.

A strip of this sample of approximately $4 \times 1.5 \times 0.4 \text{ mm}^3$ was mounted in the LIMA with the longest straight edge parallel to the horizontal traverse direction. The eventual aim was to prepare transmission electron microscope (TEM) samples in cross section, which imposed limits on the width and depth of sample that could be used. In order to maximize the chances of any transverse section containing a visible crater, a row of single-shot craters spaced at 5 μm intervals was made. A second row of craters produced by taking ten shots at 5 μm intervals was made, parallel to the single-shot row and at a vertical distance of 25 μm from it; it was intended that this row should act as a marker. A Q-switch delay setting of 5.5 was used throughout, which corresponds to about

The authors are at the Department of Materials Science and Metallurgy, University Cambridge, Pembroke Street, Cambridge, England CB2 3QZ. The authors are grateful to the Science and Engineering Research Council for a research maintenance grant (LJM), and to Prof. D. Hull for provision of laboratory facilities. Thanks are offered to E. R. Wallach, K. W. Hutt, J. Housden, and W. F. Gale for practical help and advice.

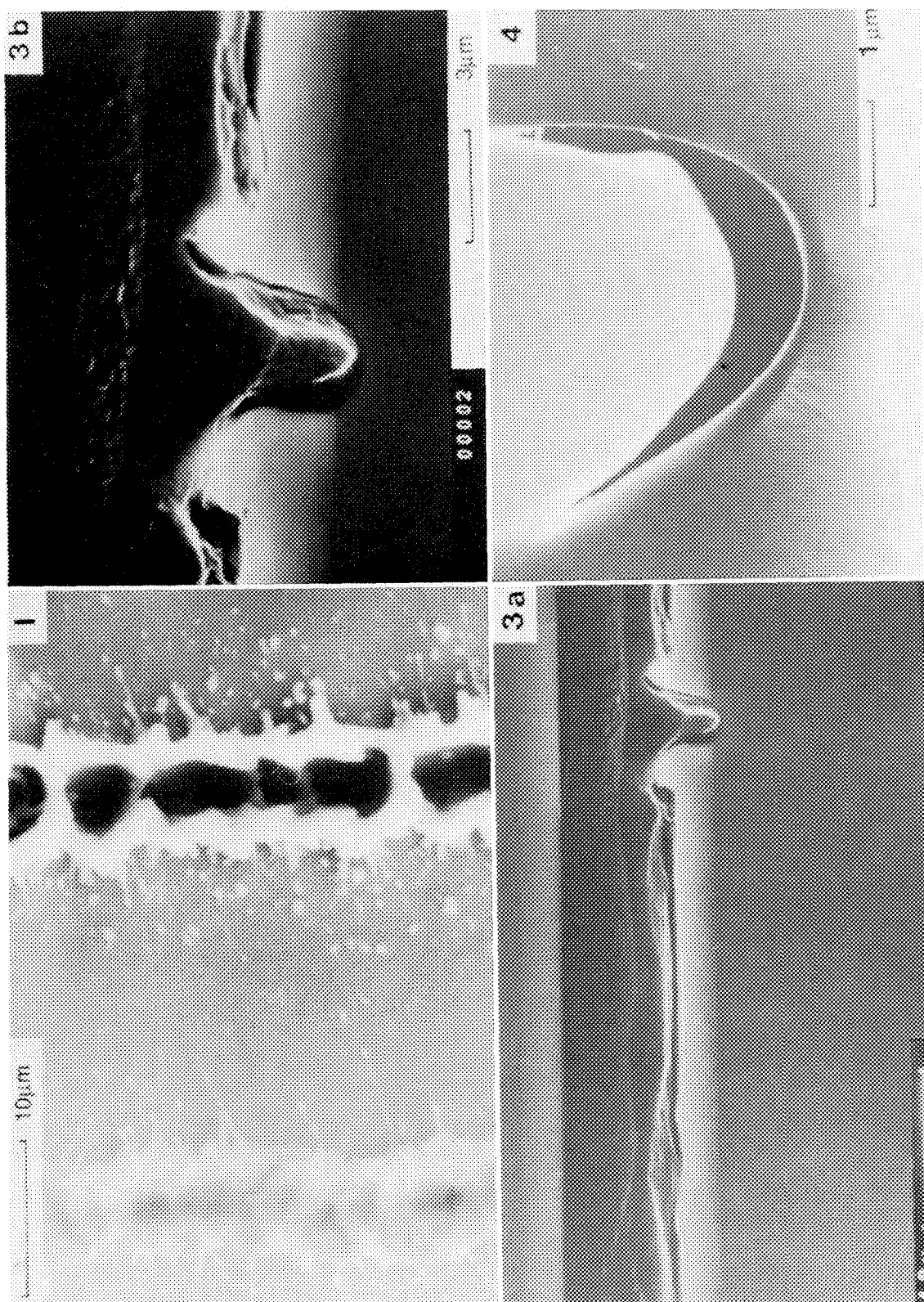
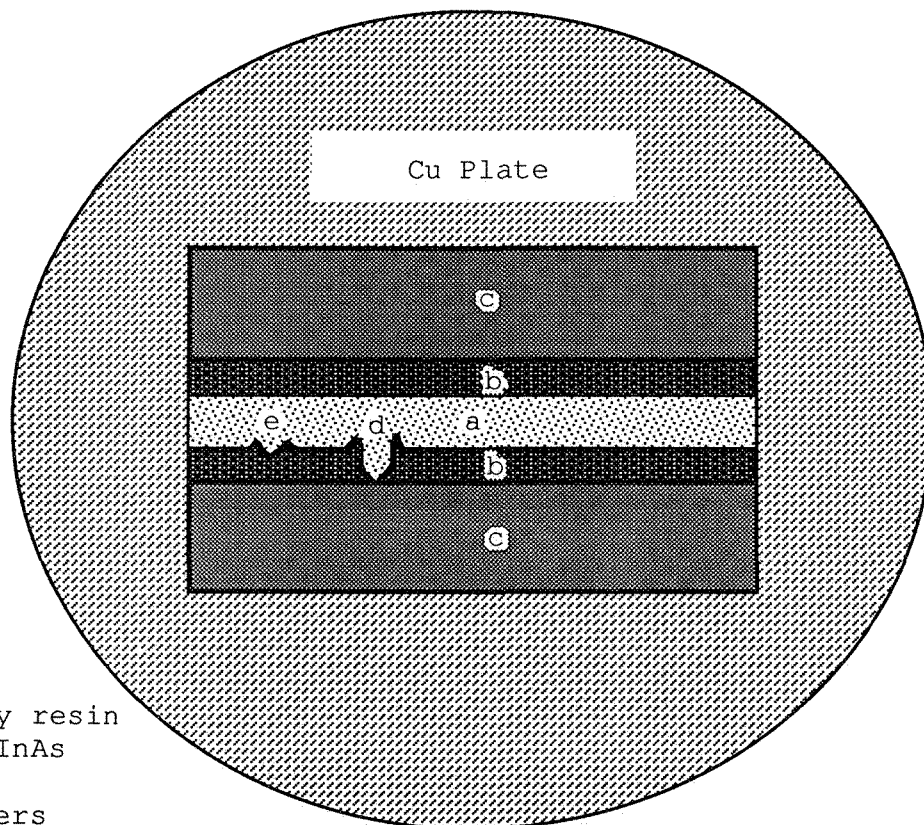


FIG. 1.--SEM micrograph showing part of ten-shot and single-shot crater arrays as seen from surface.
 FIG. 3.--(a) SEM micrograph of single-shot and ten-shot laser craters in cross section. Scale same as Fig. 1. Part of second, uncratered top piece of semiconductor can be seen at top of micrograph, and layer of epoxy resin (about 7 μm thick) lies beneath this and cratered surface. Lighter layer on each piece of semiconductor is GaAlInAs, darker substrate is InP. (b) As in (a), with ten-shot crater enlarged to show steep sides and high rim. Crater has penetrated to InP substrate. Taken from 400 reflection with microscope in two-beam condition. From top to bottom, micrograph shows epoxy resin (which does not reach bottom of crater in this case), gap, dark region just around floor and walls of crater, and unaffected InP which is contributing to 400 reflection.



- a - epoxy resin
- b - GaAlInAs
- c - InP
- d,e - craters

FIG. 2.--Schematic cross section through copper-plated semiconductor "sandwich" (not to scale).

3 μ J per pulse at the sample surface and is the maximum power setting on our instrument. The LIMA signal was monitored and representative spectra recorded for later analysis. Figure 1 shows part of the single-shot row and the ten-shot marker "trench" produced.

The cratered surface was protected by glueing a second, flat section of the same semiconductor sample over it, using as thin a layer as possible of slow-setting epoxy resin. As the material is very brittle, the entire "sandwich" was then electroplated with copper for two days to build up a thick (~ 1 mm) protective coating. A fine slitting wheel was used to cut transverse sections, perpendicular to the rows of craters, from the plated block. Figure 2 shows the arrangement schematically.

The resultant slices, each ~ 0.2 mm thick, were ground briefly on 1200-grit silicon carbide paper and polished to a 1 μ m finish. In some cases, examination under the optical microscope was sufficient to locate a ten-shot crater at this stage. Argon ion beam milling was used to remove the remaining unevenness, leaving the craters (and some cleavage cracks in the sample) as the only features noticeable along the interface between resin and semiconductor. Both the epoxy resin and the semiconductor thin back rapidly under argon ion milling; the micrograph shown in Fig. 3 was taken after 1 h with the ion guns set at 6 kV and 0.6 mA, but 15 min proved to be enough to produce a "clean" interface.

To prepare the specimens for TEM work, a thin region close to the crater arrays was re-

quired. One slice was therefore set in low-melting-point mounting wax with the uncratered end raised by ~ 100 μ m (by resting it on a folded piece of aluminum foil) and ground back carefully until the thin portion of the wedge thus produced was within a few hundred micrometers of the craters. The surface was polished again to a 1 μ m finish and the wedge-shaped sample removed, washed in acetone and mounted on a single-slot TEM grid. Final thinning was carried out by ion beam milling, with frequent inspection of the sample optically and by SEM, until the thin region was less than 2 μ m from the bottom of the ten-shot crater and at least part of the cratered region was likely to be electron-transparent. The preparation method used here is based on a technique described in the TEM literature,⁵ which has been used for the preparation of TEM foils "edge-on."

Results

Figure 3 shows a typical cross-sectional SEM micrograph of both the single-shot and multiple-shot craters, at the same magnification as Fig. 1. The single-shot crater would be difficult to detect in the absence of the ten-shot marker row, but here its position can readily be identified. The section through the one-shot crater seen here is less than 0.2 μ m deep, whereas the ten-shot crater is more than 2 μ m deep at its lowest point. As the multiple-shot "trench" was being produced, it was obvious from the appearance of a ^{31}P signal and

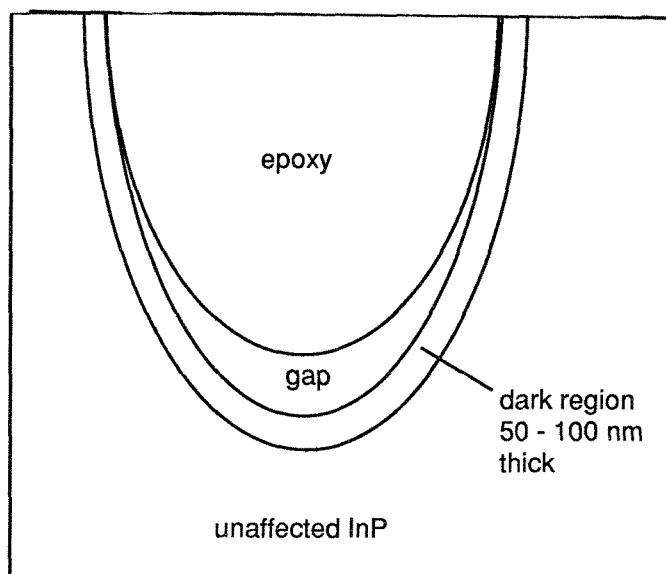


FIG. 5.--Schematic diagram indicating regions of interest in dark-field micrograph.

the increased In signal in the LIMA spectrum that penetration through the GaAlInAs layer into the InP substrate was occurring. Ten shots were generally sufficient to penetrate through the top layer and in some cases as few as seven shots were required. An example can be clearly seen in Fig. 3(b), where the 10-shot crater extends into the darker InP substrate.

There is a striking difference in shape between single- and multiple-shot craters in this material, with the ten-shot craters having a near-constant width of 2-3 μm and a high "splashed" rim, whereas sections through single-shot craters show either a shallow and featureless depression between slightly raised edges or (occasionally) a central dip of width $<0.5 \mu\text{m}$ in the middle of this smooth hollow. However, the overall width of the hole plus "splash" zone is similar for the single-shot and multiple-shot craters, about 10 μm from rim to rim. The next crater, 5 μm away, is therefore likely to have intersected at least part of the "splashed" lip, and it is obvious from Fig. 1 that the craters do overlap. Actual observation of the LIMA signal during production of the 10-shot trench showed that, following a final shot at position x which penetrated to the InP substrate, the first shot in the next position ($x + 5 \mu\text{m}$) frequently picked up small amounts of phosphorus, but that this element did not reappear until about the seventh subsequent shot. This result indicates that material from the bottom of the crater had been re-deposited on the top of the crater lip.

Any micrograph of the craters can show only one of the possible sections through the crater arrays, and the profiles seen depend on just which line is taken. The gradual removal of material by ion-beam thinning, coupled with SEM inspection, allows measurements of profiles to be made from several parallel cross sections, which gives a more representative idea

of the crater depths. However, an order-of-magnitude estimate of the amount of material removed in ten shots was obtained by treating the crater shown in Fig. 3 as if it were isolated rather than part of a continuous trench, and considering it to have axial symmetry. Approximate calculations suggest that 30 μm^3 is missing, or $\sim 3 \mu\text{m}^3$ per shot, representing about 3×10^{10} atoms. The total number of ions produced from this sample in a single shot, measured with a current probe, was typically 2×10^9 ions; an ionization efficiency of a few percent is therefore indicated for this material at high laser power. The measurement of ion yield was made at the sample stage and does not refer to the number of ions detected at the electron multiplier, which would be several orders of magnitude smaller.⁶

Preliminary TEM observations were taken when the sample had thinned back to within 2 μm of the ten-shot crater. The dark-field micrograph shown in Fig. 4 was taken with the microscope set up in the two-beam condition for strong reflection from 400; for an annotated diagram explaining the main features visible, see Fig. 5. There is an abrupt change in contrast between the unaffected InP substrate, which gives a strong contribution to the 400 reflection, and the region directly below the floor of the crater. From this and other dark-field images it appears that this region is not diffracting. The same region also appears darker than the unaffected InP in bright-field images; taken together, these observations suggest that the region may be amorphous. Further thinning will be required before the nature of the region can be verified and before its extent around the sides of the crater can be seen. It is also planned to examine the affected zone beneath the single-shot crater in this sample to obtain an idea of the damage produced in a more typical LIMA analysis.

Conclusions

The feasibility of studying LIMA in cross section has been demonstrated, and details of the preparation method have been given for a semiconductor sample. Typical crater profiles obtained by SEM, together with measurements of the total ion yield per shot, suggest an ionization efficiency (ions created per atom removed) of a few percent. When further information on typical crater depths is available, it should be interesting to compare the ionization efficiencies for various materials with the results of LAMMS workers using post-ablation ionization to improve ion yields.⁷ Further information on the resolidification processes and depth of damage in the laser-affected region can be provided by TEM. Initial results suggest that the affected zone extends for 50-100 nm below the floor of the ten-shot crater examined, and that it may be amorphous. Although much work remains to be done before the effects of the laser pulse can be stated with any certainty, the preliminary results are encouraging and show that useful informa-

tion should be obtainable from microstructural investigation of the laser craters.

References

1. P. S. Hill, L. J. Matthews, J. A. Leake, and R. Cochrane, "Solidification of melt-spun copper-boron: Investigation by LAMMS and EDX analysis," presented at UK Informal Conference on Rapid Solidification and Metastable Phases, Selwyn College, Cambridge, April 1988.
2. M. J. Aziz, "Model for solute redistribution during rapid solidification," *J. Appl. Phys.* 53: 1158-1168, 1982.
3. M. von Allmen, "Laser quenching," in "Glassy Metals," *Topics in Applied Physics* 53, H. Beck and H. J. Güntherodt, Eds., Springer-Verlag, 1983.
4. A. W. Harris, *Laser Microprobe Mass Spectrometry: Quantitative Inorganic Analysis*, Ph.D. thesis, University of Cambridge, England.
5. S. B. Newcomb, C. S. Baxter, and E. G. Bithell, *EUREM 88* (York, England), Inst. Phys. Conf. Ser. 93 (vol. 1): p.43, 1988.
6. K. W. Hull and E. R. Wallach, "Anomalous ion transmission in a laser microprobe (LAMMS): Investigation by high-frequency monitoring of the current through the sample/target," *Int. J. Mass Spec. Ion P.* (submitted).
7. Bruno Schueler and R. W. Odom, "Nonresonant multiphoton ionization of the neutrals ablated in laser microprobe mass spectrometry analysis of GaAs and $\text{Hg}_{0.18}\text{Cd}_{0.22}\text{Te}$," *J Appl. Phys.* 61: 4652-4661, 1987.

EVOLUTION OF ION ENERGY DISTRIBUTIONS WITH INCREASING ION YIELDS IN A LASER MICROPROBE MASS SPECTROMETER (LAMMS)

Jonathan Housden, K. W. Hutt, and E. R. Wallach

In a recent publication,¹ it was shown that ion transmission in a laser microprobe mass spectrometer (LAMMS) was dependent on the total number of ions produced N_p , and not necessarily on the number detected at the multiplier N_d . Typically, as N_p was increased from 10^8 to 10^{10} , the transmission efficiency N_d/N_p would fall from 10^{-4} to 10^{-6} . The motivation for the work presented in this paper was to insure that ion losses through the energy-correcting reflectron in the time-of-flight (TOF) tube were not significant. In the Cambridge Mass Spectrometry LIMA 2A,² any ion which has an energy of more than 100 eV above the applied extraction potential is transmitted through the reflectron and consequently is not reflected back to the ion detector. (Any ion with energy lower by, say, 100 eV than the applied extraction potential can be selectively filtered out by an appropriate potential applied to a grid in front of the ion detector.) This paper summarizes results concerning energy distributions at the reflectron position as a function of the total number of ions produced.

The reflectron is normally located at the end of the TOF tube, i.e., in the middle of the flight path. It was replaced by an electron multiplier (EMI 119), which thus removes both ion energy focusing and ion energy filtering (Fig. 1). In this way, a measure of the original ion energies and distributions was obtained. Correlations between the numbers of ions collected in this mode and ions produced from the specimen were made by measuring the total charge flowing through the specimen stage following each laser pulse.¹

Two of the main factors that together adversely affect mass peak widths in TOF mass spectrometry have long been recognized and clearly described.³ First, ions of identical mass, charge, and energy entering a drift region may be separated in space along the TOF axis and therefore arrive separately (spatial spread). Second, ions entering the drift region simultaneously, but with a range of kinetic energies and associated range of velocities along the flight axis, result in a range or spread of flight times. (The reflectron in the LIMA 2A is designed to compensate for the energy spread of the ions which arrive subsequently at the electron multiplier.) A third factor en-

visaged to contribute to a spread of flight times may occur in the drift region by repulsion of like charges. This effect is reduced, perpendicular to the flight axis, in the LIMA 2A by a flight wire along the drift axis biased at -17 V relative to ion polarity and ground.

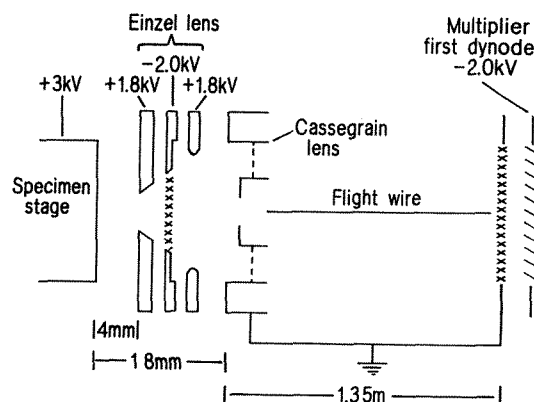


FIG. 1.--Schematic experimental layout of modified LIMA 2A biased to detect positive ions. Reflectron was replaced by electron multiplier ion detector thereby removing ion energy focusing and ion energy filtering.

Results

Reasonably good mass resolution for silicon at low N_p ($\sim 10^6$) and N_d ($\sim 10^2$) can be seen for peak a in Fig. 2. Such data enabled flight-time-to-mass calibration. For additional samples (aluminum, silver, and gold), good agreement between theoretical and measured ion flight times t was obtained for any particular mass m by use of the equations below (after allowing for the times spent in the extraction region and in the detector):

$$eV_0 = \frac{1}{2} mv^2$$

where

$$t = \frac{\ell^2}{2eV_0} m^{1/2}$$

where V_0 is the extraction voltage and ℓ is the flight path length in the spectrometer. Calculation of theoretical ion flight times assumes that the ions have acquired the full 3 keV available from the extraction field. Therefore this agreement confirms that for $N_p < 10^6$, ion formation represents a good approximation to the ideal TOF ion source, i.e., an instantaneous point ion source (no temporal or spatial broadening). Accordingly for the

The authors are at the Department of Materials Science and Metallurgy, University of Cambridge, Pembroke Street, Cambridge, England CB2 3QZ. The authors are grateful for financial support from AWE, Aldermaston (J.H.) and the Alvey Directorate and Science and Engineering Research Council (K.W.H.).

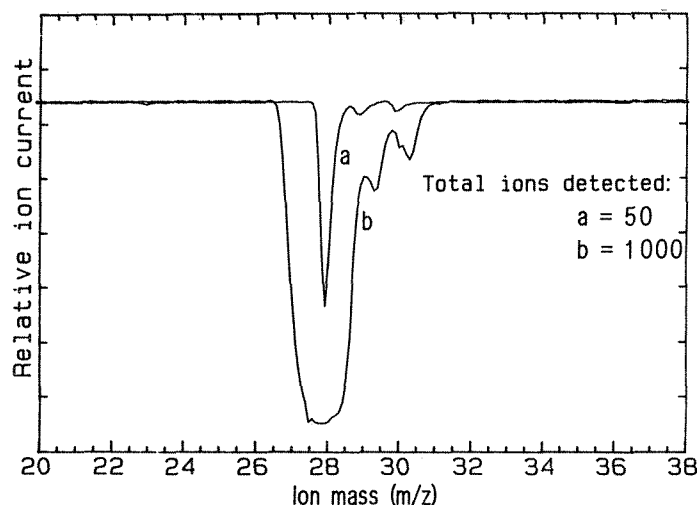


FIG. 2.--Overlaid spectra of silicon showing (a) reasonably good mass resolution achieved for silicon at very low ion production and detection levels, (b) degradation of mass resolution with increasing ion production and detection levels. Vertical scale (per division) $a/b = 1/3$. (Spectra are inverted compared with those normally published due to use of inverting amplifier in present investigation.)

geometry adopted in these experiments and for $N_p < 10^6$, a spread in flight times about the ideal for a given mass provides a reasonable measure of the spread of ion energies for that mass.

For high ion production levels ($N_p > 10^8$, $N_d \sim 10^3$), it was found that mass resolution, peak width and peak shape all degrade progressively with increased ion production (Fig. 3). (This result confirms that the reflectron and ion energy filters perform well in the conventional mode of operation.) A repeatable five-step sequence of mass-peak shape evolution was observed (see, for example, Fig. 3) with increasing N_p and N_d :

- (1) symmetrical peak for low ion yield with reasonable mass resolution (Fig. 3a)
- (2) peak "bends" to right and broadens (Fig. 3b)
- (3) "shoulder" appears on left and peak broadens (Fig. 3b)
- (4) peak "splits" and broadens further (Fig. 3c)
- (5) "tail" appears to the right--very poor mass resolution (Fig. 3c)

Also, by overlaying mass peaks (Figs. 4 and 5), it was observed, first, that the main peak moves to longer flight times with increasing N_p ; and second, that the peak width increases asymmetrically about the ideal mass such that the time from detection of the first ion to the time for the ideal is less than that for the ideal mass to the time for arrival of the last ion.

From stage current measurements,¹ the time T_E taken for most ions to pass the einzel lens was shown to increase with increasing total ion

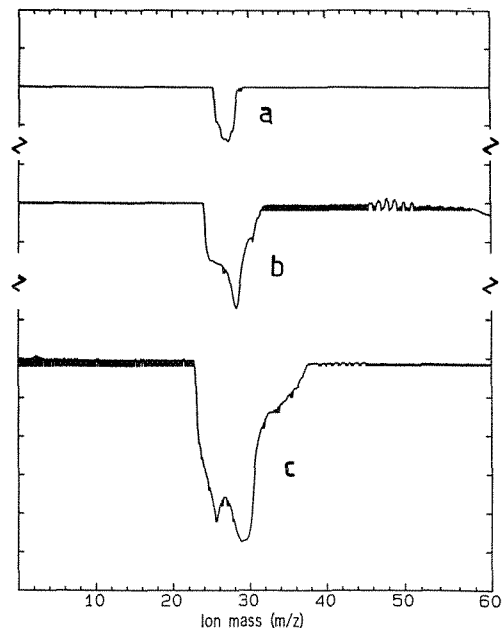


FIG. 3.--Sequence of mass-peak shape evolution with increasing ion production (for aluminum). Five steps can be seen as described in text.

production (see, for example, Fig. 6). However T_E , which sets a maximum for the temporal spread of ions entering the TOF tube, is significantly shorter than the time over which individual mass peaks arrive at the detector. For example, for the gold mass peak in Fig. 7, T_E has a value of $< 1 \mu s$ and the spread of arrival times at the detector is about $7 \mu s$. Therefore, for a given mass, the spread in arrival times at the detector seems to originate mainly from a spread of ion energies.

If it is assumed that the spread in flight times is due only to an initial spread in ion energies (and hence velocities), then the spread in ion kinetic energies can be calculated from the ion arrival times. Results are shown below for the gold peak of Fig. 7:

First arrival	Au-fast	$= 3.54 \times 10^3 \text{ eV}$
Ideal mass	Au-ideal	$= 3.00 \times 10^3 \text{ eV}$
Most common	Au-mode	$= 2.66 \times 10^3 \text{ eV}$
Last arrival	Au-slow	$= 2.12 \times 10^3 \text{ eV}$

Comparison of these results with the numbers of ions at various positions in the mass peak from which they were calculated (Fig. 7), makes it apparent that a few ions have energy 18% higher than the ideal, most have energy 11% lower, and some as much as 29% lower than the ideal.

Ion-ion repulsion in the drift region within the TOF mass spectrometer could, in principle, cause ion energy transfer such that some ions have energies higher than the ideal. However, this mechanism is likely to cause symmetrical distortion of mass peaks about the ideal mass, which is not observed. Therefore it is believed that the fall in average ion energy (and the associated delay and distortion of mass peaks) originates from processes occurring

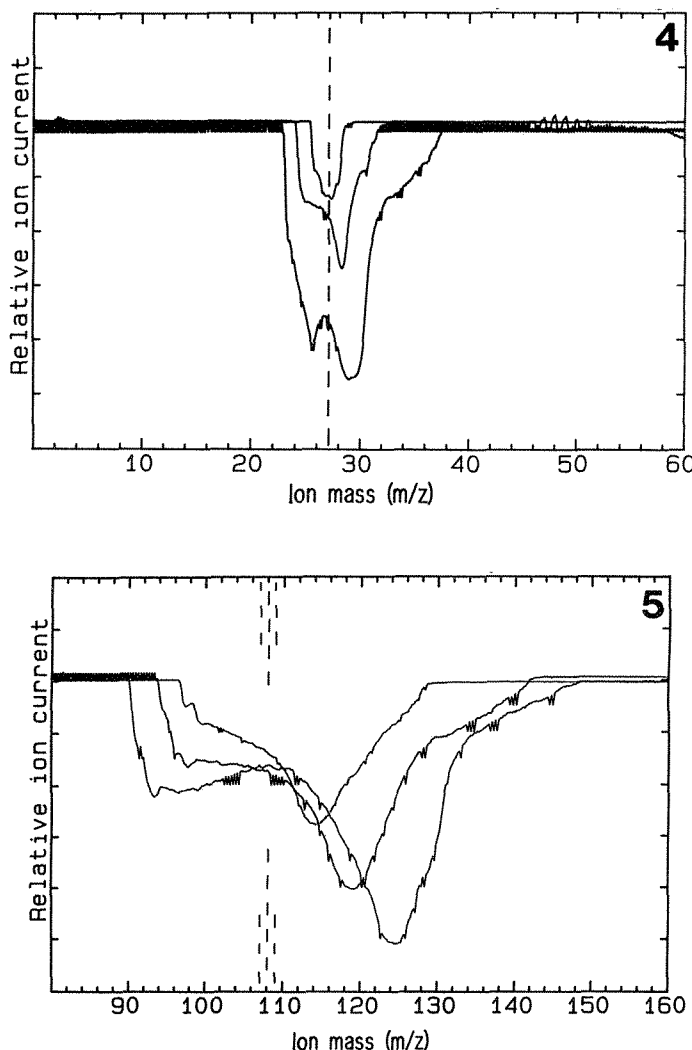


FIG. 4.--Three overlaid high ion production spectra of aluminum. Main mass peak moves to right with increasing ion production and peak width increases asymmetrically about ideal. FIG. 5.--As Fig. 4 but for silver. Isotope peaks at m/e of 107 and 109 Daltons are thoroughly merged at these high production levels. Small spikes are fast noise originating in postmultiplier pre-amplifier.

mainly in the extraction region.

One possible explanation for the fall in average ion energy could be that, when N_p is high ($\sim 10^8$), ions do not experience uniform acceleration from the extraction field until they are at a significant distance above the sample surface. Taking the Au-mode energy of 2.66×10^3 eV in the example above, this would correspond to a distance equivalent to 340 V into the extraction field, i.e., 1.1 mm above the sample surface. [This figure for the Au-mode is calculated as follows. Assume that the electrostatic extraction field is linear and also is not affected by the presence of the ions. The loss of energy of the Au-mode

ions is given by $3.00 - 2.66 = 340$ eV. The first lens plate is 4 mm from the specimen with 1200 V between the two (Fig. 1). Thus the distance equals $4 \times (340/1200) = 1.1$ mm.] Similarly, the last ion detected (Au-slow) would have been accelerated from about 3.4 mm above the surface.

The most obvious mechanism for this disruption from the ideal condition of uniform acceleration is ion-neutral collisions. (If it is assumed that an ion loses all its energy in such a collision, then ion-neutral collisions are significant, e.g., up to a distance of 3.4 mm above the surface of the Au peak in Fig. 7.) This mechanism would also explain the increased stage current duration with increased ion production and probable increased neutral production. Clearly collisions causing loss or transfer of kinetic energy from ions to neutrals would also delay ion extraction. It may be that at low ion production levels, the plasma densities are sufficiently low so that most ions accelerate through the extraction region relatively unobstructed, which would explain the good mass resolution with 3 keV average energy observed for low ion yield spectra, and also in TOF-SIMS with the same spectrometer.⁴

The results described in this paper are in broad agreement with earlier work on a transmission-mode LAMMA 500 in which ion energies were estimated by a different method.⁵ In both cases, the average ion energy was found to be less than the ideal applied potential value and to decrease with increased laser energy.

The five-step sequence of mass peak shape evolution described above bears strong resemblance to elements of theoretical peak shapes calculated for the LAMMA 500 instrument,⁶ which also uses an einzel lens. Vertes et al.⁶ calculated theoretical peak shapes assuming different initial energy spreads and angles of divergence, symmetrical peaks were predicted, whereas very asymmetric peaks with a shoulder on the left side were predicted for high energy spread and high angle divergence. This result is in agreement with the present observations. In contrast to their theoretical results, the present experimental results show a shift to longer rather than shorter flight times as asymmetry increases. Comparisons should be made only tentatively at this time because of possible differences in behavior of reflection and transmission geometry LAMMS. Furthermore, the calculated peak shapes⁶ are based on a geometry that includes the reflectron.

However, the energy spread and angle of divergence parameters may well correlate with the parameter of ions produced N_p used here. It may be that low ion production (produced by low laser irradiancies) results in narrow energy spreads and low angles of divergence. Conversely, high plasma densities, increased collisions, and space charge effects may well lead to broad energy spreads and high angles of divergence at high N_p . Continuing work will

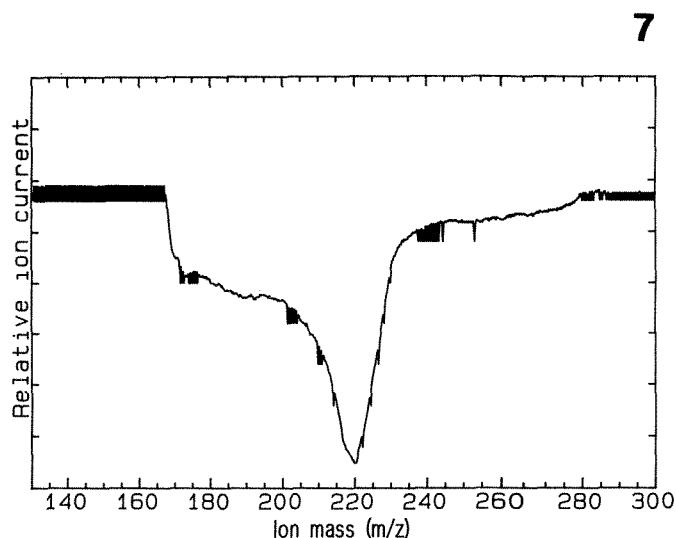
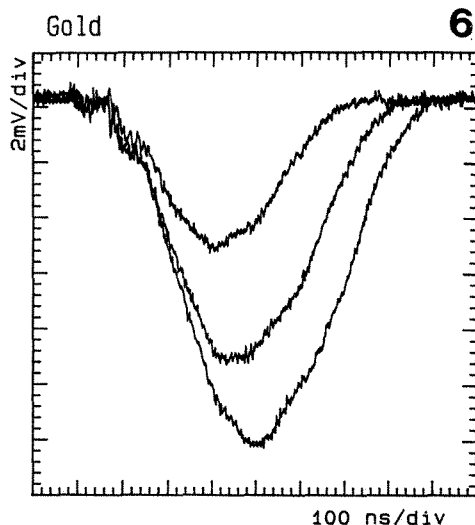


FIG. 6.--Three overlaid stage current profiles obtained with gold sample. As total ion production (i.e., area under curve) increases, current duration increases and current peak moves to right. Oscilloscope was triggered from Q-switch synchronized pulse.

FIG. 7.--Spectrum of gold for high ion production (350 000 ions detected) occurring over very wide apparent mass range of 167 to 279 Daltons, equivalent to arrival times of 24-30.9 μ s.

include calculations of theoretical peak shapes for the LIMA 2A geometry and modeling of space charge and collisional/density effects.

Conclusions

1. Average ion flight times increase with increased ion production N_p , which implies a fall in average ion energy.
2. At low N_p , the spread in flight times about the ideal is narrow.
3. A five-step mass-peak shape evolution sequence has been observed with increased ion production.
4. At high N_p , stage current durations provided a measure of the maximum spread in time of the ions on entering the TOF tube. This temporal spread represents only about 10% of the total spread in ion arrival time for any single mass peak. Therefore this spread results primarily from ion energy spreads and the observed five-step sequence reflects evolution in ion energy distribution with increasing ion production.
5. Ion energies are distributed asymmetrically about the ideal energy for all but very low N_p . This finding indicates that mass peak distortion originates from processes operating in the extraction region and not in the drift region.

Future work should include modeling of the effects of ion-neutral collisions with increasing plasma density in order to find a mechanism for ion extraction delay and ion energy loss.

References

1. K. W. Hutt, J. Housden, and E. R. Wallach, "Anomalous ion transmission in a Laser Microprobe (LAMMS): Investigation by high frequency monitoring of the current through the sample/target," *Int. J. Mass Spectrom. Ion Proc.* (in press).
2. M. J. Southon, M. C. Witt, A. Harris, and E. R. Wallach, "Laser-microprobe mass-analysis of surface layers and bulk solids," *Vacuum* 34: 903, 1984.
3. W. C. Wiley and I. H. McLaren, "Time-of-flight mass spectrometer with improved resolution," *Rev. Sci. Instr.* 26: 115, 1955.
4. T. Dingle and S. J. Mullock, Cambridge Mass Spectrometry (private communication).
5. T. Mauney, Thesis, Colorado State University, 1984.
6. A. Vertes, P. Juhasz, and L. Matus, "Peak shape determination in laser microprobe mass analysis," *Int. J. Mass Spectrom. Ion Proc.* 73: 109, 1986.

TARGET HEATING, PLASMA FORMATION, AND EXPANSION PROCESSES DURING LASER IONIZATION

Akos Vertes, Peter Juhasz, Laszlo Balazs, and Renaat Gijbels

Continuing experience with laser ionization and especially with laser microprobing in mass spectrometry of solids indicates extreme sensitivity of the resulting mass spectra toward many properties of both the target and the laser beam.¹ Our previous efforts in order to rationalize the details of laser-target interaction²⁻⁵ led to the distinction of at least three different regimes of laser ionization. Each regime can be characterized by the deposited energy density in a single laser pulse: $(1 - R)\phi\alpha\tau$, where ϕ and τ are the irradiance and pulse length of the laser shot and α and R are the absorption and reflection coefficients of the material respectively.

Assuming moderately reflecting opaque targets and Q-switched lasers we can translate the distinctions into laser intensities.

a. *Low irradiance* ($\sim 10^5$ - 10^6 W/cm²). Physical processes are dominated by surface heating and ionization of target particles. Mass transfer is negligible across the solid/vacuum interface. The mass spectrum contains a significant amount of molecular ions. This regime is favored in molecular-weight determination of organic molecules.

b. *Medium irradiance* ($\sim 10^7$ - 10^8 W/cm²). Evaporation of the sample becomes non-negligible. Laser energy is absorbed both by the ionized vapor in front of the target and by the target itself. In this case complicated fragmentation and recombination processes and/or ion molecule reactions take place in the expanding plume. The mass spectra may provide structural information for organic samples.

c. *High irradiance* ($\sim 10^9$ - 10^{11} W/cm²). The deposition of laser energy is governed by the strong absorption of the expanding plasma cloud created in the early phase of the laser pulse. Elemental lines are abundant in the mass spectra providing fair possibilities for trace analysis of inorganic solids.

In the following sections simple phenomenological models are presented and analyzed for the three cases. Temporal and radial distributions of surface temperature are calculated for poor and good heat conductors. Low thermal conductivity yields a "hot spot" in the center of the beam and leads to slow decay of the excitation after the laser pulse. Elevated thermal conductivity leads to opposite effects: lower maximum temperature, larger lateral spread of the temperature rise, and faster decay following the pulse.

For medium and high irradiance, temperature

profiles perpendicular to the surface are calculated. Medium-intensity pulses lead to mass transport across the sample surface and to a temperature maximum in the expanding plume. If the laser intensity is increased to the high-irradiance domain, the heating process exhibits two mechanisms. At the beginning of the laser pulse light is mainly absorbed by the solid. The temperature profiles are similar to the medium-irradiance case. As the density of the ionized plume increases in front of the sample, plasma absorption gains importance and reaches a point where it dominates all other forms of energy deposition. This leads to a sudden temperature rise accompanied by intense ionization.

Theoretical

1. *Low Irradiance*. As an approximation the complicated process of laser-target interaction is modeled as heating of a semi-infinite solid by a penetrating source:

$$\frac{\partial}{\partial t}[\rho e] = \nabla[\kappa \nabla(\rho e)] + (1 - R)\alpha\phi \quad (1)$$

where κ is the thermal diffusivity of the material (usually a nonlinear function of the temperature) and ρe denotes the energy density of the material. The TEM₀₀ mode of the laser has a Gaussian radial distribution with beam radius w . The time dependence is replaced by a rectangular impulse composed of $u(t)$ step functions:

$$\phi(r, z, t) = \phi_0 e^{-r^2/w^2} e^{-\alpha z} [u(t) - u(t - \tau)] \quad (2)$$

For the sake of simplicity we assume constant thermal diffusivity here. If neither phase transformation nor mass transfer becomes significant and heat loss is negligible through the interface, this model can be solved to yield the surface temperature distribution⁶ $T(r, z = 0, t)$:

$$T(r, z = 0, t) = \frac{(1 - R)\phi_0\alpha}{\rho c_p} \int_0^{t^*} \frac{w^2 e^{-r^2/[w^2 + 4\kappa(t-t')]} }{w^2 + 4\kappa(t - t')} \cdot e^{\alpha^2 \kappa (t-t')} \operatorname{erfc}(\alpha \sqrt{\kappa(t - t')}) dt' \quad (3)$$

where $t^* = \begin{cases} t, & \text{if } t \leq \tau \\ \tau, & \text{if } t > \tau \end{cases}$

and c_p denotes the specific heat of the material. Numerical evaluation of this formula

The authors are at the Department of Chemistry, University of Antwerp, Universiteitsplein 1, B-2610 Wilrijk, Belgium.

yields the temperature distribution on the surface during and after the laser pulse.

2. *Medium and High Irradiance.* If mass transfer across the surface is considerable we have to include all three conservation laws in the description. The one-dimensional form of mass, momentum, and energy conservation has the following form³;

$$\frac{\partial}{\partial t}[\rho] = - \frac{\partial}{\partial z}[\rho v] \quad (4)$$

$$\frac{\partial}{\partial t}[\rho v] = - \frac{\partial}{\partial z}[p + \rho v^2] \quad (5)$$

$$\frac{\partial}{\partial t}[\rho(e + v^2/2)] = - \frac{\partial}{\partial z}\left[\rho v\left(e + \frac{p}{\rho} + \frac{v^2}{2}\right)\right] + (1 - R)\alpha\Phi \quad (6)$$

where v denotes the hydrodynamic velocity and p stands for the pressure. Since thermal conduction transports a negligible fraction of the energy, especially at high intensities, we omitted the corresponding term in Eq. (6) (cf. Eq. 1). The equations of conservation have to be complemented by the equation of state relating pressure to density and energy. From the ideal gas law, we have the well-known form

$$p = (1 + \eta)\rho kT/m \quad (7)$$

where η is the degree of ionization $\eta = n_i/n_{\text{total}}$, expressed by the number density ratio of ions and all particles; m denotes the mass of the particles. The internal energy density is related to the state variables:

$$\rho e = \frac{\rho}{m}\left[\frac{3}{2}(1 + \eta)kT + \eta I_p\right] \quad (8)$$

where I_p is the ionization potential.

To determine the degree of ionization, the Saha-Eggert equation was used with the customary simplifications:

$$\frac{\eta^2}{1 - \eta^2} = \frac{m}{\rho} \left(\frac{2\pi k T m_e}{h^2} \right)^{3/2} e^{-I_p/(kT)} \quad (9)$$

where m_e denotes the mass of the electron.

The linear light absorption coefficient $\alpha(z, t)$ consists of two terms. The first accounts for the normal absorption α_0 of the solid without ionization; the second takes into account the absorption α_{p1} of the plasma cloud

$$\alpha(z, t) = \alpha_0(z, t) + \alpha_{p1}(z, t) \quad (10)$$

Finite-difference solution of this one-component, one-dimensional (1C-1D) model requires special techniques due to the abrupt changes caused by the laser pulse. Further details of the model and the solution techniques were described earlier.³

Results

At low irradiance radial distributions of surface temperature were calculated at various

instances. The results for a nonreflecting strong absorber ($R = 0$; $\alpha = 2.7 \times 10^5 \text{ cm}^{-1}$) are depicted in Fig. 1. The density and specific heat of the solid were $\rho = 8 \text{ g/cm}^3$ and $c_p = 0.385 \text{ J/gK}$, respectively. To emphasize the importance of a widely neglected factor in laser ionization studies, the behavior of a poor and a good heat conductor is demonstrated. In Fig. 1(a) we used $\kappa = 0.0195 \text{ cm}^2/\text{s}$ for low thermal conductivity; in Fig. 1(b) we set $\kappa = 0.195 \text{ cm}^2/\text{s}$ to represent a good heat conductor.

Dramatic differences can be observed in the surface temperature distributions for the two cases. The most significant are that the poor conductor is heated to much higher temperatures and retains elevated values for a longer time.

The temperature distribution perpendicular to the surface at the end of a moderate-intensity ruby laser pulse is shown in Fig. 2 on the basis of our 1C-1D model. The nonreflecting opaque sample ($R = 0$; $\alpha_0 = 10^3 \text{ cm}^{-1}$) had $n_{\text{total}} = 10^{22} \text{ cm}^{-3}$ number density and consisted of $m = 4 \times 10^{-25} \text{ g}$ particles. For the ionization potential I_p , a value of 12 eV was used. Although the solid had an absorption coefficient 270 times lower than the target of the low-intensity calculation, and although the irradiance was only less than an order of magnitude higher, we could observe stronger heating, especially in the plasma cloud in front of the sample.

The same target was exposed to a 100 times larger irradiance laser pulse in the next calculation. Temperature profiles at consecutive time stages are displayed in Fig. 3. Strong heating can be observed during the first quarter of the laser pulse (Figs. 3a and b), leading to almost complete ionization in the expanding plume. In the second half of the laser pulse the plasma absorption substantially outweighs the normal absorption. As a result a sudden change in the character of the temperature profiles can be observed. The plasma heats up inducing further ionization and that in turn increases the absorption. This positive feedback produces an extreme temperature rise and fast expansion of the plasma. Details of these processes are described in other papers.^{3,5}

Conclusions

The large body of experimental observation on laser ionization of solids can be divided into categories according to the amount of deposited energy and the quantity of ablated material.

For low energy deposition and negligible mass transfer across the sample/vacuum interface, lateral distributions of surface temperature can be calculated. These results open the way to checking previous qualitative models based on the cross-sectional structure of the illuminated spot in laser ionization experiments.⁷ On the basis of surface temperatures it also becomes possible to judge to what extent the temperature rise is responsible

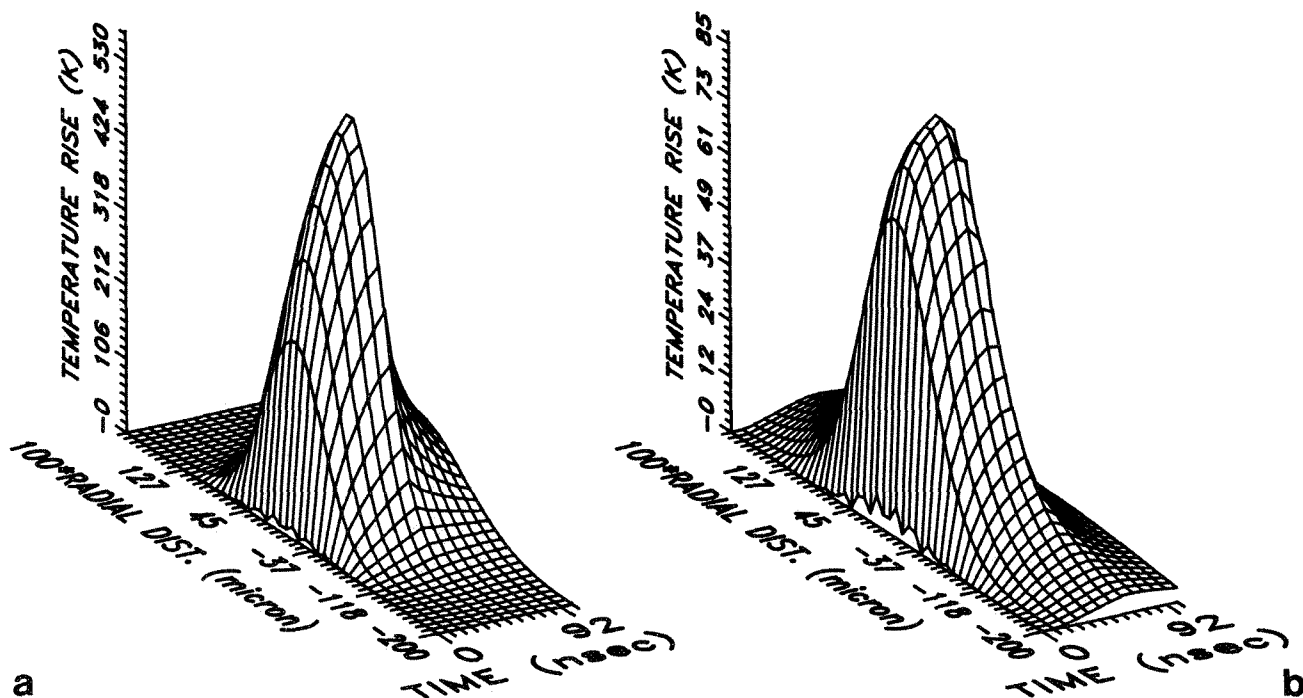


FIG. 1.--Surface temperature rise of strongly absorbing target due to low-power-density laser pulse ($\Phi_0 = 1.6 \times 10^6$ W/cm²; $\tau = 50$ ns); beam radius is $w = 0.5$ μ m. (a) Poor heat conductor, (b) good heat conductor.

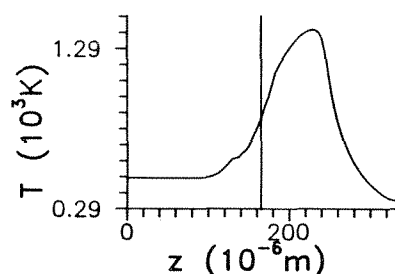


Fig. 2.--Heating opaque sample by moderate-intensity ruby laser pulse ($\Phi_0 = 10^7$ W/cm²; $\tau = 50$ ns). Vertical line shows original position of solid (left)/vacuum (right) interface; light is arriving from vacuum side.

for ion formation. Other mechanisms such as multiphoton ionization or Coulomb repulsion can be compared to thermally induced processes.

Material transport across the sample surface is an important factor at medium and high energy deposition. In the medium range the emphasis from solid-phase light absorption shifts toward absorption by the plume. Temperature, density, velocity, and ionization degree profiles can be calculated perpendicular to the surface.³ With irradiance increasing above a certain threshold (plasma ignition threshold⁴) the ionized plume absorbs heavily (shielding the surface from radiation) and reaches extremely high temperatures.

References

1. L. Van Vaeck, J. Bennett, W. Lauwers, A. Vertes, and R. Gijbels, "Laser microprobe mass spectrometry: Possibilities and limitations," *Microbeam Analysis--1988*, 351.
2. A. Vertes, P. Juhasz, P. Jani, and A. Czitrovszky, "Kinetic energy distribution of

ions generated by laser ionization sources," *Int. J. Mass Spectr. Ion Proc.* 83: 45, 1988.

3. A. Vertes, P. Juhasz, M. De Wolf, and R. Gijbels, "The role of energy deposition processes in the understanding of laser microprobe analysis mechanisms," *Scanning Microscopy*, 2: 1853, 1988.

4. A. Vertes, M. De Wolf, P. Juhasz, and R. Gijbels, "Threshold conditions of plasma ignition in laser ionization mass spectrometry of solids," *Anal. Chem.* (in press).

5. A. Vertes, P. Juhasz, M. De Wolf, and R. Gijbels, "Hydrodynamic modeling of laser ionization processes," *Int. J. Mass Spectr. Ion Proc.* (in press).

6. B. J. Bartholomeusz, "Thermal response of a laser-irradiated metal slab," *J. Appl. Phys.* 64: 3815, 1988.

7. D. M. Hercules, R. J. Day, K. Balasankum, T. A. Dang, and C. P. Li, "Laser microprobe mass spectrometry: 2. Applications to structural analysis," *Anal. Chem.* 54: 280A, 1982.

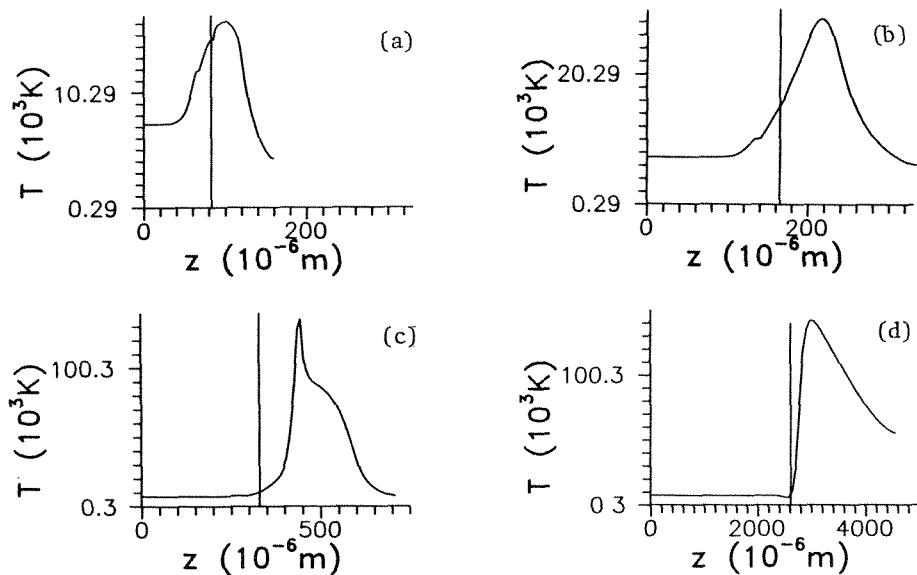


FIG. 3.--Time development of temperature profile during high-intensity ruby laser pulse ($\phi_0 = 10^9 \text{ W/cm}^2$; $\tau = 50 \text{ ns}$) hitting same target as in Fig. 2. (a) after 7 ns, (b) 12 ns, (c) 21 ns, (d) 50 ns.

ION FORMATION BY DESORPTION FOR LASER-MICRO-MASS-SPECTROMETRY

Franz Hillenkamp

During the past 15 years, since the first reports appeared in the literature, laser-micro-mass-spectrometry has been used for many diverse purposes and has found a large variety of applications. Although the combination of a well-focused laser beam and a (most often time-of-flight) mass spectrometer has been used in all these cases, it should not come as a surprise that depending on the specific analytical information sought, quite different ion formation processes may have been involved. The main laser parameters influencing the induced processes are wavelength, pulse width, and irradiance on the sample. Wavelengths in the ultraviolet region of the spectrum and pulse widths in the range below about 100 ns have been used most commonly, but some work has also been done with wavelengths as long as 10.6 μm and pulse widths up to about 1 ms. The irradiances vary from about 10^6 to 10^9 W/cm^2 .

Besides the high spatial resolution in the submicrometer range, laser ionization has generally proved to be a very sensitive technique. However, depending on the specific analytical goal at hand (i.e., search for atomic or molecular constituents), highest sensitivity for only one atomic species or as uniform as possible a sensitivity for a larger variety of them, relative or even absolute quantification, etc.), the laser parameters and the ensuing ion formation processes may vary considerably. This paper deals only with desorption as distinguished from ablation and plasma formation. It is also mainly restricted to the process of desorption of ions, as against the desorption of neutrals to be ionized separately by a second laser beam.

The Process of Ion Desorption

Unfortunately the term "desorption," though commonly used, is not very helpful in understanding the underlying processes; nor is "soft ionization," the other frequently used phrase. Generally desorption is used in all cases--such as organic secondary ion mass spectrometry (SIMS), fast atomic bombardment (FAB), plasma desorption (PD), or field desorption (FD)--in which ions of nonvolatile, thermally unstable molecules are generated and are stable enough to be detected in the mass spectrometer. Even though such desorption spectra may also

contain signals of atomic ions, particularly of alkalines, the desorption mode is usually not desirable for the analysis of atomic constituents. Since the appearance of parent molecular ions and/or the degree of their fragmentation is the main and often the only accessible or reported information by which the spectrum is characterized as a "desorption spectrum," the term may and in all likelihood does encompass quite a variety of different physical and chemical mechanisms. For example, it has been shown that at a wavelength of 193 nm spectra of organic compounds change qualitatively with increasing irradiance most probably because a sequence of different physico-chemical processes are induced or dominate.¹

Even for the "soft" laser desorption of organic molecules with a wavelength resonantly absorbed by them, the necessary irradiance is quite high. For the amino acid tryptophane, for example, desorbed resonantly with a wavelength of 266 nm, the threshold irradiance for the detection of molecular ions is typically 2×10^7 W/cm^2 , corresponding to an energy deposited per single molecule at the surface of about 20 eV (4-5 photons per molecule) even if only linear absorption is assumed.² If all the excess energy above that needed for removal of the molecule from the surface or out of the bulk, and its ionization, remain in the molecule, it would surely dissociate into several small fragments. In reality the metastable decay has been shown to be quite limited for the vast majority of laser desorbed ions.³ Initial energies of such ions usually spread over a range of several to several tens of electron volts. As discussed below, these initial energy distributions most probably do not reflect a direct energy transfer during the desorption/ionization process because they are usually associated with an overall energy deficit relative to the total acceleration potential used in the mass spectrometer.

Depth Resolution of Laser Desorption

At first sight, one might assume that by definition of the term desorption is strictly a surface process, removing physically or chemically adsorbed molecules. This may indeed be the case in static SIMS of monolayers or submonolayers of organics on well-prepared substrate surfaces; for laser desorption this seems to be hardly ever the case, independent of whether one uses the "LAMMA 500" transmission geometry or the "LAMMA 1000" bulk surface analysis arrangement. Figure 1 can serve as a demonstration of the involvement of the bulk material even at threshold irradiance. All four figures show spectra of tryptophane,

The author is at the Institut für Medizinische Physik, Universität Münster Hufferstr. 68, D-4400 Münster, Federal Republic of Germany. This work was supported by the Deutsche Forschungsgemeinschaft and the Bundesministerium für Forschung und Technologie.

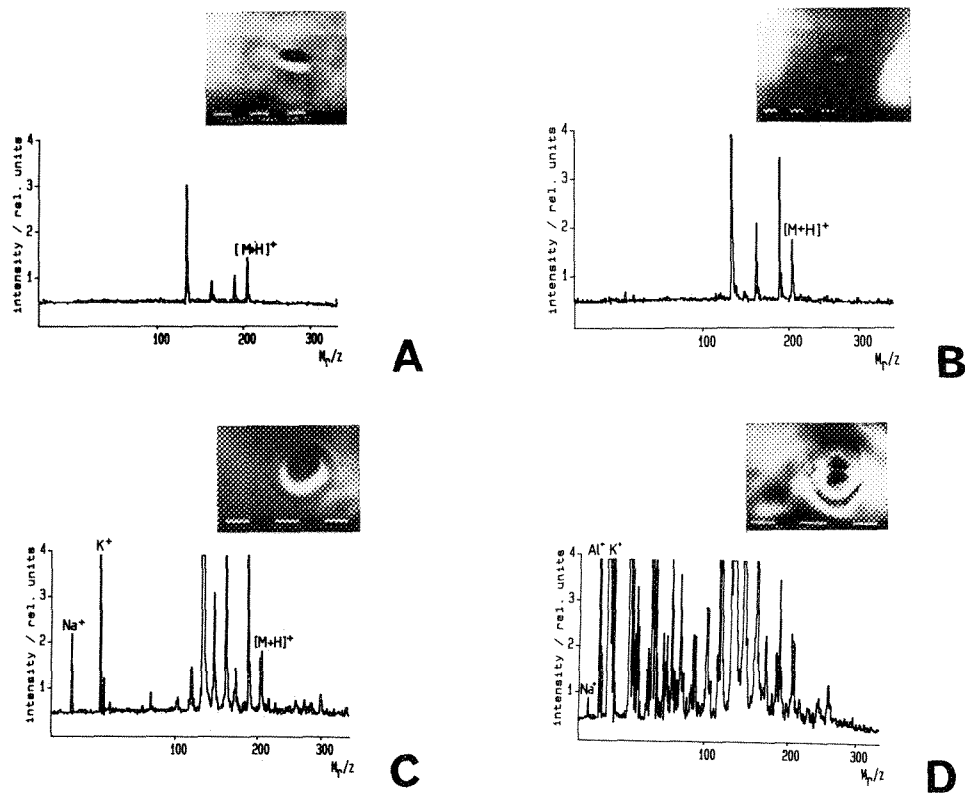


FIG. 1.--Laser desorption mass spectra of tryptophane ($\lambda = 266$ nm, $\tau = 15$ ns) with corresponding scanning electron micrographs (white bar = $1\ \mu\text{m}$). Irradiances: A: $I_0 = I = 2 \times 10^7$ W/cm² (threshold); B: $I = 2I_0$; C: $I = 6I_0$; D: $I = 20I_0$.

prepared by drying a drop of about $1\ \mu\text{l}$ of a 10^{-5} mol/l⁻¹ aqueous solution onto an aluminum substrate, thus forming a layer of solid tryptophane about $1\ \mu\text{m}$ thick. The insets are the corresponding SEM micrographs of the irradiated spots. At threshold irradiance (Fig. 1a) and a factor of two above threshold (Fig. 1b), only sample specific ions appear in the spectrum and a slight indentation can be seen in the SEM pictures at the irradiated spot. At six times threshold irradiance (Fig. 1c) most of the ions can still be related to the parent molecule, but fragmentation has increased considerably. Also, signals of sodium and potassium appear in the spectrum. The latter signals most probably indicate that the substrate surface had at least momentarily been exposed during the laser irradiation, even though no Al signal is recorded yet; this assumption is also supported by the corresponding SEM picture. At about 20 times threshold irradiance (Fig. 1d) the spectrum contains mostly signals of unspecific organic ions resulting from strong rearrangement reactions besides pure fragmentation of the tryptophane molecule. Now the substrate is clearly involved, as documented by the Al^3+ signal in the spectrum and the crater in the SEM picture. The lateral resolution is about $1\ \mu\text{m}$ in these analyses up to about 6 times threshold irradiance, even though the nominal lateral resolution of the LAMMA 1000 instrument used for these experiments is only about $3\ \mu\text{m}$.

The depth resolution of laser desorption deserves some attention in this context. Even

though it is clearly not a pure surface process as demonstrated above, the depth resolution can be quite high. A resolution of only a few nanometers has been demonstrated repeatedly for sandwich structures of various metals or their oxides. (For details see Bahr's paper in this volume.) In these cases a sufficiently different threshold irradiance for the successive layers seems to be a prerequisite for such a high depth resolution. A similar resolution has also been demonstrated for the system of tryptophane, evaporated in controlled layers onto etched silver substrates.⁴ For a nominally 10nm-thick layer, Ag^+ ions appeared typically only in the second to third spectrum obtained from the same spot on the sample; for thicker layers correspondingly more shots were required. It was suggested that nonlinear absorption causes this shielding of the substrate surface, because over 95% of the incident energy should otherwise have been transmitted to the substrate surface by the 10nm layer. The SEM pictures shown here may actually be somewhat misleading in estimating the depth resolution. At least near threshold, most of the alteration seen may only reflect mechanical movement of the sample due to elastic deformation during the laser exposure and is therefore not directly related to the depth from which ions are generated. None of these observations is fully understood; further investigation is needed.

It has been noted by many investigators that the spectra of organics obtained by various desorption techniques exhibit strong similarities, in particular the preference for even electron ions. This may have been another reason for using the term "desorption" in all these cases. On the other hand, there is growing evidence that these similarities mostly reflect selection rules for ion stability in the chemistry going on during or after the actual formation of the primary ions and therefore, do not reflect equal or even similar physical processes of ion formation and desorption. A series of investigations on tryptophane and other indol derivatives in the authors group^{5,6} have shown that one can find radical precursor ions in many cases which seem to reflect a type of photochemistry typical for a resonant photoexcitation of the system. One can certainly speculate that such precursor ions are generated in all cases, but are often too reactive or unstable to be detected even under the special conditions used in these experiments (low sample temperature, delayed ion extraction). It is this very intermediate chemistry that makes attempts to infer details of the primary desorption/ionization process from the features of the recorded spectra so very difficult and often misleading. Moreover, this chemistry takes place on a nanosecond time scale and in a phase of very high density of reactants without any solvent shielding the molecules from each other, a phase similar to a liquid above the critical point.

Recently we have demonstrated that laser desorption can generate ions of proteins as large as 230 000 Dalton (see M. Karas's paper in this volume). It is assumed that another or an additional mechanism or mechanisms are involved in the formation of such monster ions. The above-mentioned energy deficit of most laser-desorbed ions may provide a clue. The current model for this type of a desorption assumes that the laser irradiation of the sample leads to a sort of micro explosion of the solid, consisting of the matrix-dissolved proteins. The randomly charged particles or clusters generated in this explosion would then successively lose matrix molecules through evaporation until the cooled and charged protein remains as a stable entity and can be detected. This model clearly constitutes the transition from what is usually considered desorption to a sort of ablation process.

As mentioned above, laser-desorbed ions usually show a distribution of initial energies ranging from several to several tens of electron volts. In the past, this distribution has frequently been taken as an indication for the specific features of the laser desorption/ionization process. More recently we have measured the initial energy distribution of the neutrals, desorbed along with (and usually in much larger quantities than) the ions.⁷ Their initial energy of only a few milli-electron volts, corresponding to "temperatures" at or below room temperature, differs greatly from those of the ions. Inasmuch as the ion initial energy had

indicated a "temperature" much too high for the formation of stable molecular ions, assuming a thermal evaporation process, the initial energy of the neutrals corresponds to a temperature much too low for such a process. We therefore conclude that the process of desorption cannot be described as an equilibrium process.

Conclusions

Laser desorption has proved to be a very valuable tool in organic mass spectrometry, particularly of large biopolymers. Its full potential has not been exploited so far, nor are the details of the mechanisms understood in sufficient detail. In particular, it is the influence of the laser pulse width that has not yet been investigated in any detail. With continuously variable pulse-width lasers becoming available, a new era of further optimization and novel applications of laser desorption may well lie ahead of us. Laser post-ionization and laser photofragmentation may add even more versatility to this technique. As has been explained above, laser desorption (and desorption processes in general) encompasses a rather large variety of steps and processes. Though it is tempting to look for the unifying model as the final goal in understanding and knowledge, progress in practical applicability of the technique will more likely result from attempts to observe and exploit the more subtle differences and the effects of the experimentally accessible parameters.

References

1. B. Spengler, M. Karas, U. Bahr, and F. Hillenkamp, "Excimer laser desorption mass spectrometry of biomolecules at 248 and 193 nm," *J. Phys. Chem.* 91: 6502-6506, 1987.
2. M. Karas, D. Bachmann, and F. Hillenkamp, "Influence of the wavelength in high irradiance ultraviolet laser desorption mass spectrometry of organic molecules," *Anal. Chem.* 57: 2935-2939, 1985.
3. J. Rosmarinowsky, M. Karas, and F. Hillenkamp, "Metastable decay of laser-desorbed ions from aromatic organic compounds," *Int. J. Mass Spectrom. Ion Proc.* 67: 109-119, 1985.
4. F. Hillenkamp, M. Karas, D. Holtkamp, and P. Kluesener, "Energy deposition in ultraviolet laser desorption mass spectrometry of biomolecules," *Int. J. Mass Spectrom. Ion Proc.* 69: 265-276, 1986.
5. M. Karas and F. Hillenkamp, "Photochemical reaction pathways and their relevance to ultraviolet laser desorption mass spectra," *Proc. 4th Intern. Conf. Ion Formation from Organic Solids* (in press).
6. H. Ehring, *Entwicklung eines Heiz- und kühlbaren Probenhalters und Untersuchung des Temperatureinflusses in der Laser Desorptions Massenspektrometrie*, Diploma Thesis (Physics) University of Frankfurt, 1989.
7. B. Spengler, U. Bahr, and F. Hillenkamp, "Parameters of UV-laser desorbed neutral molecules as measured by multiphoton postionization," *Inst. Phys. Conf. Series* 94 (section 2), 1989, 137-140.

GENERAL LASER POST-IONIZATION

C. H. Becker, T. N. Tingle, and M. F. Hochella

Matrix effects and nonreproducibility in laser microprobe mass spectrometry and secondary ion mass spectrometry have led numerous workers to ionize the *neutral* component after desorption or sputtering (so-called post-ionization) in order to alleviate these difficulties. The specific approach developed at SRI has been to use untuned pulsed laser radiation to perform an efficient and general (nonselective) ionization, followed by time-of-flight (TOF) mass spectrometry. Initial developments with both sputtering and laser desorption have been obtained for inorganic systems by nonresonant multiphoton ionization with intense ($\sim 10^{10}$ W/cm²) ultraviolet laser radiation.¹⁻³ More recently, organic systems (bulk polymer surfaces and organic adsorbates) have been investigated by single-photon ionization at 118 nm (10.5 eV) in the vacuum ultraviolet by generation of the 9th harmonic of the Nd:YAG laser.^{4,5} Although most of our work has used spatially well-defined desorption beams, the following example of the chemical analysis of the Murchison meteorite by means of thermal desorption exemplifies the difference between selective and nonselective photoionization.

The Murchison meteorite is a carbonaceous chondrite containing about 2% C by weight. Because relatively large quantities of the meteorite are available, extensive analysis has been performed with 1-10g samples by solvent extractions followed by gas chromatography and mass spectrometry (GC-MS), and has conclusively shown a wide mixture of sulfur compounds, alkanes, polycyclic aromatic hydrocarbons, and even amino acids (see, for example, Ref. 6). Smaller, milligram-size samples have been studied recently by Zare and coworkers⁷ using pulsed CO₂ laser blow-off from a mixture made of glycerol and pulverized sample, followed by photoionization at 266 nm and TOF mass spectrometry. The 266nm results are in agreement with this study: this wavelength is selective by resonantly enhanced multiphoton ionization for the polycyclic aromatic hydrocarbon component, though not with equal sensitivity among these species.

Experimental Details

A specimen from the Murchison meteorite fall in Australia, encapsulated in fusion crust, was fractured in the laboratory and a small piece weighing a few milligrams was placed in the

analysis vacuum chamber on a Ta foil strip heater. The sample temperature was then raised in increments from room temperature to about 600 C. Photoionization was performed alternatively with 118nm and 266nm coherent beams focused about 1 mm above the sample in front of the reflecting time-of-flight mass spectrometer. The laser light passed above and parallel to the sample stage and did not interact with the solid sample. The general apparatus design and procedures are described in more detail elsewhere.¹⁻⁴ Blanks, such as fractured optical quality quartz, were examined to check for laboratory contamination, which was found to be negligible.

Results

Figure 1 displays the mass spectrum taken with 266 nm (4.66eV photons). The following assignments are readily made: m/z 128 naphthalene, 142 methyl-naphthalene, 156 C-2 naphthalene, 178 phenanthrene/anthracene, 192 methyl-phenanthrene, 202 pyrene, and 206 C-2 phenanthrene. Figure 2 shows the mass spectrum taken from a different but nearby interior fragment of the same Murchison meteorite specimen. A much more complex spectrum is readily apparent, due to the nonselective photoionization for compounds having ionization potentials ≤ 10.5 eV (which includes nearly all organic molecules). Though 10 times more laser pulses were averaged in Fig. 2 than Fig. 1, the dynamic range is more than 10 times higher in Fig. 2. No sensitivity is lost whatsoever in using single-photon ionization. Figure 1 has the advantage of being a simpler spectrum but at the significant disadvantage of omitting much chemical information.

A more detailed analysis of the meteorite sample by use of Fig. 2 and similar spectra at various temperatures is forthcoming and beyond the scope of this brief report, but some features follow. First, the polycyclic aromatic hydrocarbon mass peaks in Fig. 1 are still clearly evident in Fig. 2. A rich variety of alkane and alkene series dominate Fig. 2. For example, the strong series of m/z 42, 56, 70, 84, 98 suggest alkane branching at positions 2, 3, 4, and 5, though m/z 84 also is thiophene and 98 methyl-thiophene. Mass 106 is ethylbenzene/benzaldehyde. The family of odd-masses m/z 135, 151, 163, and 235 may be from a benzothiophene based carboxylic acid series, but more work is required before this explanation can be regarded as conclusive, including deliberate introduction into the analysis chamber of low levels of the suspected compounds for comparisons. Mass 17 is NH₃, 30 is NO, 34 is H₂S, 48 is CH₃SH, and 64 is S₂. The spectrum

Authors Becker and Tingle are at the Molecular Physics Laboratory, SRI International, Menlo Park, CA 94025; author Hochella is at the Department of Geology, Stanford University, Stanford, CA 94305.

extends to about m/z 350.

The Allende meteorite has also been examined. Its carbon content is about ten times lower than for the Murchison meteorite and fewer organic compounds evolve from the sample, but there is no difficulty in observing with 118 nm a dramatically different yet extensive hydrocarbon pattern, weighted toward high masses.⁸

Conclusion

Single-photon ionization in the vacuum ultraviolet, combined with TOF mass spectrometry, is a powerful approach to mass spectrometric analysis of organic compounds. For the complex sample examined here, the Murchison meteorite, a wide range of compounds is found to evolve over a range of temperatures. Subfemtomole sensitivities have previously been found for this ionization scheme.⁴ Multiphoton ionization at 266 nm produces selective ionization, showing only the polycyclic aromatic hydrocarbon component. The prospects are excellent for applying these ionization methods with

spatially resolved stimulated desorption by ion, electron, or laser beams. In fact ion and electron beam desorption have been used previously with the single-photon ionization approach.^{4,5}

References

1. C. H. Becker and K. T. Gillen, *Anal. Chem.* 56: 1671, 1984.
2. J. B. Pallix, C. H. Becker, and K. T. Gillen, *Appl. Surf. Sci.* 32: 1, 1988.
3. J. B. Pallix, C. H. Becker, and N. Newman, *Mat. Res. Soc. Bull.* 12: 52, 1987.
4. U. Schühle, J. B. Pallix, and C. H. Becker, *J. Am. Chem. Soc.* 110: 2323, 1988.
5. J. B. Pallix, U. Schühle, C. H. Becker, and D. L. Huestis, *Anal. Chem.* (in press).
6. M. H. Studier, R. Hayatsu, and E. Anders, *Geochim. Cosmochim. Acta* 36: 189, 1972.
7. J. H. Hahn, R. Zenobi, J. L. Bada, and R. N. Zare, *Science* 239: 1523, 1988.
8. T. N. Tingle, C. H. Becker, R. Malhotra, and M. F. Hochella (in preparation).

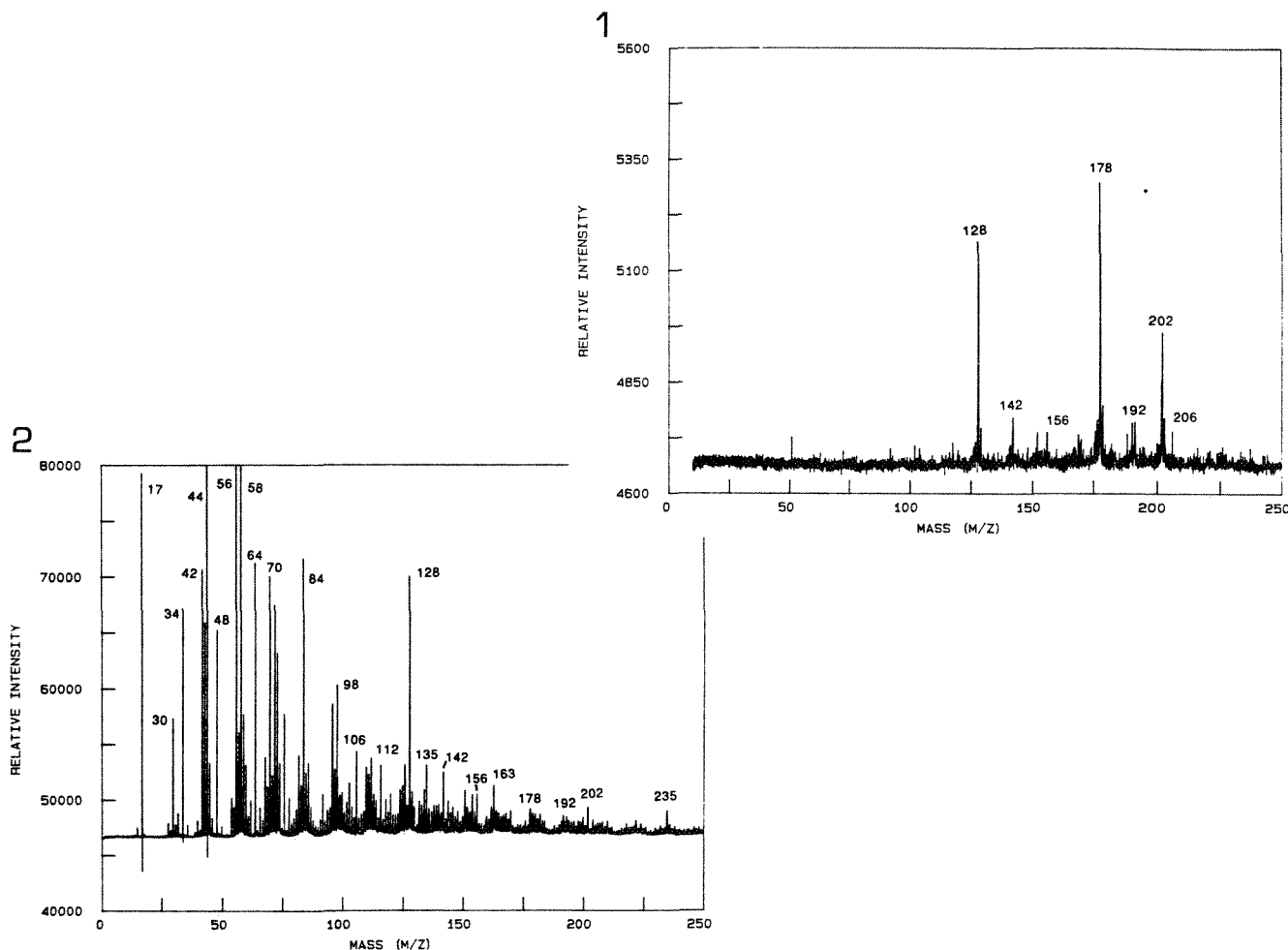


FIG. 1.--Photoionization TOF mass spectrum obtained by use of 266nm light (multiphoton ionization) from thermal desorption of interior fragment of the Murchison meteorite. Spectrum was taken at sample temperature of 240 C and represents average of 100 laser pulses.

FIG. 2.--Photoionization TOF mass spectrum obtained by use of 118nm light (single-photon ionization) from thermal desorption of interior fragment of the Murchison meteorite. Spectrum was taken at sample temperature of 270 C and represents average of 1000 laser pulses.

LAMMS: Pattern Recognition & Cluster Ions 7-B

POLYMER CHARACTERIZATION AND CLASSIFICATION BY USE OF LAMMS AND PRINCIPAL-COMPONENT ANALYSIS

R. W. Odom, Filippo Radicati di Brozolo, P. B. Harrington, and K. J. Voorhees

The objectives of this work were to determine how well the LIMS technique could produce unique, characteristic mass spectra from various organic polymer formulations and to what extent these mass spectra provide a means for identifying an unknown polymer. Principal-component/discriminant analysis techniques were applied to the mass spectral data produced from the LIMS analysis of 19 organic polymers to determine the uniqueness of the mass spectra. The results described below demonstrate that LIMS mass spectra of different polymers are often quite distinct and can be readily resolved using pattern recognition techniques.

Experimental

A number of the polymers analyzed in this study are common polymers employed in a variety of applications. For example, Nylon 6 and 12, polycarbonate, Mylar 500D, Texin polyurethane, and polystyrene are used extensively in various polymer products. The polyimide and photore-sist samples are commonly used in the micro-electronics industry. A set of DDS/TGDDM epoxy material was analyzed in an attempt to determine whether the LIMS/pattern recognition procedure could distinguish various stoichiometries within the same polymer class. The DDS/TGDDM material is a mixture of a few parts per hundred amine function of 4,4'-diaminodiphenyl sulfone (DDS) with 80-90% by weight of tetraglycidyl 4,4'-diamino diphenylmethane (TGDDM) and 10-20% of a polyglycidyl ether of bisphenol A Novolac epoxy. The various DDS/TGDDM epoxies analyzed contained different ratios of hardener (DDS) to resin (TGDDM). This epoxy system is a commonly used binder matrix for continuous carbon fiber reinforced composites.¹ The polymers were either thin films (~1 μ m thick) or bulk solids. We prepared the thin-film samples by embedding beads or powders of the samples into Spurr's epoxy resin and micro-toming thin sections, which were mounted onto Si substrates. The locations of the embedded polymers were readily apparent in the optical microscope of the laser microprobe. Thin sections of pure Spurr's were also analyzed in this evaluation. We prepared the bulk (thick) samples by cutting out a section of the sample or

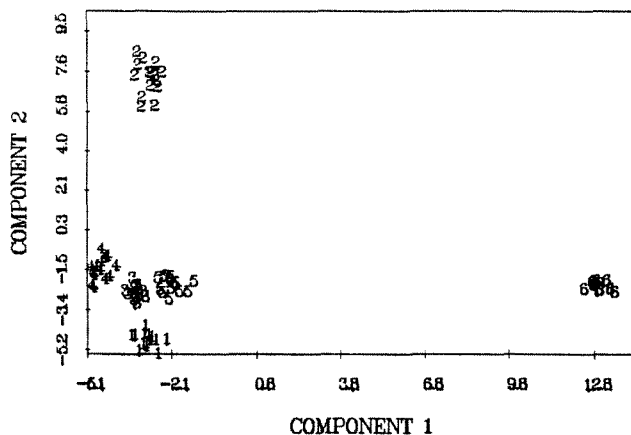
by scraping away the top 1 mm of sample surface. Both the cutting or scraping were performed with cleaned surgical knives in order to avoid contaminating the sample surfaces. The LIMS analyses were performed on a Cambridge Mass Spectrometry Model LIMA 2A reflection-mode laser microprobe, an instrument that has been described in detail elsewhere.² Fifteen positive and negative ion laser microprobe spectra were obtained at three different laser irradiances for each of the 19 polymers. The laser irradiances corresponded to the threshold for ionization and irradiance values that produced 5 and 25 times the threshold ion intensity. Mass spectra were typically acquired over a mass range from 0 to 300 atomic mass units (amu).

The pattern-recognition routines express the individual peak intensities as a percentage of the total intensity in each spectrum. The spectra are then autoscaled and an eigenvector transformation is performed on the autoscaled data. Each set of data discussed below formed a training set and the number of eigenvectors (principal components) retained in each training set was at least one-third of the total number of spectra within the set. These eigenvectors also represented at least 80% of the variance of the training set. Sample distributions are converted from a multi-dimensional space to a two-dimensional space by plotting of the eigenvectors two at a time (Karhunen-Loeve plots). Linear discriminant analysis was performed on the principal-component data.³

Cross validations of the discriminant analysis canonical variates were performed as part of the pattern-recognition procedures. Cross validation of the canonical variates provides an unbiased measure of the predictive ability of the various canonical variates for classifying the spectra into the correct category. One accomplishes the cross validation by removing spectra one at a time from the data set, building a model based on the canonical variates, and then determining how well the model predicts the category of the unknown spectrum. All calculations were performed on an IBM PS/2 Model 60 computer operating under MS-DOS 3.3. All computations were performed by the RESOLVE software package, which is a general-purpose data analysis system.⁴

The pattern recognition procedures employed in this study were based on principal-component analysis/discriminant analysis techniques which employ the basic assumption that the data can be described by a linear combination of various factors (in this case, ion masses) having different weights or loadings.⁵ The

Authors Odom and Radicati di Brozolo are with Charles Evans & Associates, 301 Chesapeake Drive, Redwood City, CA 94063. Authors Harrington and Voorhees are with the Department of Chemistry and Geochemistry, Colorado School of Mines, Golden, CO 80401. This research was supported by NSF's Small Business Innovation Research Program under Grant ISI-8760431.

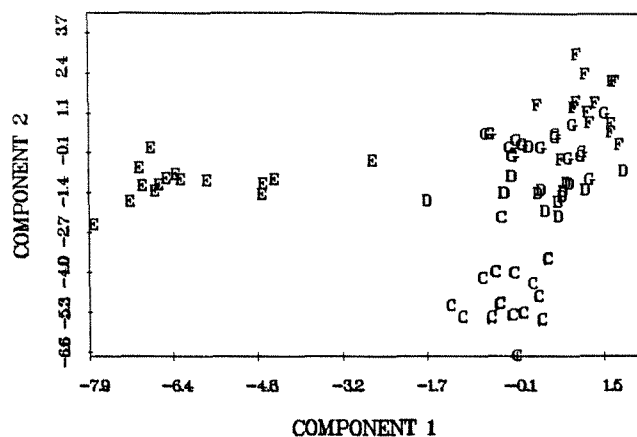


HIGH IRRADIANCE: - IONS

5 POLYIMIDES, 1 PHOTORESIST, 15 MASS SPECTRA PER POLYMER

LEGEND:

- 1 Polyimide S-11
- 2 Polyimide S-09
- 3 Polyimide S-24
- 4 Polyimide S-10
- 5 Polyimide S-19
- 6 Photoresist 1400-33



LOW IRRADIANCE: + IONS

5 DDS/TGDDM EPOXIES, 15 MASS SPECTRA PER POLYMER

LEGEND:

- C 59301 Epoxy (0.2)
- D 59304 Epoxy (0.75)
- E 59307 Epoxy (1.5)
- F Production Epoxy
- G 59306 Epoxy (1.0)

FIG. 1.--Component scores for the first two canonical variates.

FIG. 2.--Component scores for the first two canonical variates.

first step in all of the several commonly utilized factor analysis/discriminant analysis procedures is to determine the primary factors or principal components that best describe the data set.⁶ Principal components can be calculated by several techniques; the power method was employed for the analysis discussed in this paper.⁷ Each principal component is a linear combination of the mass spectra in the data set. Spectra composed of principal components are referred to as factor spectra. Each detected mass in the spectrum has a corresponding loading on a principal component. A score is the projection of a given mass spectrum onto a single principal component.

Once the principal components have been determined, discriminant-analysis techniques can be used to classify these components. The principal-component mass spectrum for each polymer set is assigned to a category and the discriminant analysis maximizes the differences of the average score of the components between each category while minimizing the variance within a category.³ The discriminant-analysis procedure generally further reduces the number of relevant components. The optimum number of components is given by $n - 1$, where n is the number of different categories. This reduced set of principal components is referred to as the canonical variates. The original data can then be employed to cross validate the canonical variates.

Results and Discussion

Figures 1 and 2 illustrate component scores for the first two canonical variates observed in the analysis of the two different polymer sets.

The percent variance in these canonical variates is ranked from highest (first component) to the lowest (last component) and the largest contribution to the total variance is generally contained in the first few components. Figure 1 shows the scores for these two components obtained in the high-irradiance negative-ion analysis of five polyimide and one photoresist samples. This data set consists of 15 mass spectra (observations) for each polymer; the component score plot indicates good separation between the various classes of polymers as well as reasonably good (tight) clustering of the spectra in each class. Thus, the discriminant-analysis technique qualitatively separates the spectra of the different polymers. A more quantitative measure of the uniqueness of these spectra is the accuracy of the cross validation analysis. Cross validation of the discriminant-analysis results accurately classified 60% of the mass spectra. These classification accuracies are considered quite good for this group of polymers.

The photoresist spectra (group 6) are readily distinguished from the various polyimides, and there is good separation of the group 1 and 2 polyimides. The analysis and classification of the spectra of polyimides and photoresists has very important applications in the microelectronics industry, in which it is often necessary to determine the composition of suspected organic residues of these types of compounds on Si or GaAs substrates.

The component scores illustrated in Fig. 2 represent an even more difficult analytical problem. The data set for this analysis was the low-irradiance positive-ion mass spectra

produced from various DDS/TGDDM epoxy compositions. These compositions differed in the gram equivalent amount of DDS hardener added to the bulk TGDDM/Novolac resin mixture. It is well known that the physical properties of the DDS/TGDDM epoxy, including its ability to bond strongly continuous carbon fibers, are very dependent on the DDS/TGDDM mixture ratios.⁸ One problem associated with using this epoxy system as a carbon fiber reinforcement matrix is that although optimum bulk DDS/TGDDM mix ratios of 0.75-0.85 can be prepared, the bulk resin/hardener blend can segregate about the micrometer-diameter carbon fibers and produce poor fiber/matrix bonding. This inadequate bonding can result in delamination of the fibers from the matrix, which can have catastrophic consequences in the use of this carbon fiber/epoxy system for such applications as aerospace components. Thus, the ability to determine the DDS/TGDDM ratios at the actual fiber/matrix interface, coupled with a knowledge of the bulk hardener/resin ratios and the macroscopic physical properties of the fiber/matrix system, could provide a method for certifying the optimum DDS/TGDDM blend ratios required for adequate bonding. The component score plot in Fig. 2 illustrates that the production epoxy formulation that represents a blend ratio having good bonding characteristics can be separated from both the C and E samples. The production epoxy has an amine gram equivalent weight ratio of DDS to TGDDM of -0.8 (the gram equivalent weight ratios are given in parentheses in the legend of this plot) whereas the C samples have low (0.2) DDS/TGDDM ratios and the E samples have high (1.5) hardener-to-resin ratios. Thus the discriminant analysis technique separates the extreme DDS/TGDDM ratios; however, it does not adequately separate the resin/hardener ratios which are quite similar. The cross-validation classification accuracy of the discriminant analysis and the expert system for this data set was 60%. Although this classification accuracy is not adequate for rigorous quality control analysis of these epoxy formulations, the technique of partial least squares regression analysis⁹ could possibly provide a much higher accuracy for the classification of the spectra from this chemically complex system.

References

1. R. J. Morgan, J. E. O'Neal, and D. B. Miller, *J. Mats. Sci.* 14: 109, 1979.
2. T. Dingle, B. W. Griffiths, J. C. Ruckman, and C. A. Evans Jr., *Microbeam Analysis--1982*, 365.
3. G. L. Ritter and H. B. Woodruff, *Anal. Chem.* 49: 2116, 1977.
4. P. B. Harrington and K. J. Voorhees, unpublished results.
5. E. R. Malinowski and D. G. Howery, *Factor Analysis*, New York: Wiley, 1980.
6. D. Child, *The Essentials of Factor Analysis*, New York: Rinehart and Wilson, 1970.
7. G. Strang, *Linear Algebra and Its Applications*, New York: Academic Press, 1980.
8. H. S. Chu and J. C. Deferis, *Polymer Comps.* 5: 124, 1984.
9. P. Geladi and B. R. Kowalski, *Anal. Chem.* 185: 1, 1986.

PATTERN RECOGNITION AS A COMPLEMENTARY TOOL FOR THE EVALUATION OF COMPLEX LAMMS DATA

Buko Lindner and Ulrich Seydel

Laser microprobe mass spectrometry (LAMMS) of complex material, organic or inorganic, yields spectra comprising, besides readily interpretable ion signals, also signals that cannot be assigned straightforward to defined structures or molecular components of the object, but that may nevertheless contain valuable information. In spectra taken from a larger number of objects from the same population of particles (e.g., dust or polymer particles, bacteria) or from the same sample layer or thin section of a fairly homogeneous material, this information is hidden in a larger number of mass peaks, giving rise to a characteristic pattern of the mass spectrum (termed mass fingerprint).

By the procedure of pattern recognition the hidden information of a collection of objects is detected through indirect measurements on the individual objects. But even though the human eye is a very good pattern recognizer when dealing with a very limited number of observables (mass peaks) per object, as the number of observables and objects increases, only computerized recognition procedures can guarantee a successful handling of the data.

The mathematical-statistical tools applied for this purpose are called multivariate techniques. They may be divided into classification and discrimination procedures. *Classification* attempts to discover—usually with no prior information—the number of groups within a given data set together with details of group membership; *discrimination* involves the assignment of newly acquired or previously uncategorized samples to one of existing classes. Classification can be subdivided into *cluster analysis* and *ordination*; the latter comprises nonmetric multidimensional scaling (MDS), principal-component analysis (PCA), and factor analysis (FA).¹ Inaccurate locutions also use the notion "cluster analysis" as a general term for all these different procedures of pattern recognition.

In general, pattern-recognition techniques have proved to be powerful tools in many fields of science such as psychology, chemometrics, meteorology, sociology, and economics. In a number of applications in mass spectrometry outside LAMMS, particularly in pyrolysis mass spectrometry (PY-MS), the capabilities of these techniques have been impressively demon-

strated.²⁻⁶ Many textbooks describing the mathematical background and algorithmic procedures in detail are available.^{1,7-9} In this presentation only a short introduction to the most common multivariate techniques, characterizing their particular merits and examples for their application to LAMMS can be given. Emphasis is placed on the classification of various bacterial populations with respect to the effects of various drug regimens. We show that multivariate techniques can supply complementary information to that readily available from the directly interpretable elementary information on signals.

Experimental

In commercially available laser microprobe mass spectrometers, LAMMA (Leyboldt-Heraeus, Köln, FRG) and LIMA (Cambridge Mass Spectrometry Ltd., Cambridge, UK), small object volumes (some cubic micrometers) are vaporized and partially ionized by a UV pulse laser beam at irradiances in the range 10^6 to 10^{11} W/cm²; the positive or negative ions produced are mass separated in a time-of-flight mass spectrometer and registered in a transient recorder, and the spectra are transferred to a computer for further data handling. The data handling may involve mass scale calibration, conversion of raw spectra to line spectra by peak integration, and normalization according to total ion intensity or to the intensity of a particular ion.

Besides elemental and molecular ions, the mass spectra also contain a certain number of fragment ion species, depending on sample composition and on experimental parameters. In particular, spectra from biological and other complex organic material comprise a large number of ion signals that cannot be assigned to specific molecular structures, functional groups, or in many cases not even the elemental species because of a superposition of elemental and molecular ions. This superposition often prevents quantitative analyses. Nevertheless, these spectra may contain, under certain conditions, valuable information characteristic for the analyzed material. However, the presence of this information is not always obvious at first glance but is hidden in the complex pattern of the mass spectrum, which thus may serve as mass fingerprint.

Figure 1 shows three spectra, each averaged over 30 single analyses, all taken from bacterial organisms but from three different genera. In this example the human eye is able to distinguish between the three different patterns ("zero-order pattern recognition"). In

The authors are at Forschungsinstitut Borstel, Division of Biophysics, D-2061 Borstel, Federal Republic of Germany. The project was financially supported by the Federal Minister for Research and Technology under Grant 03 8667, and by the German Leprosy Relief Association.

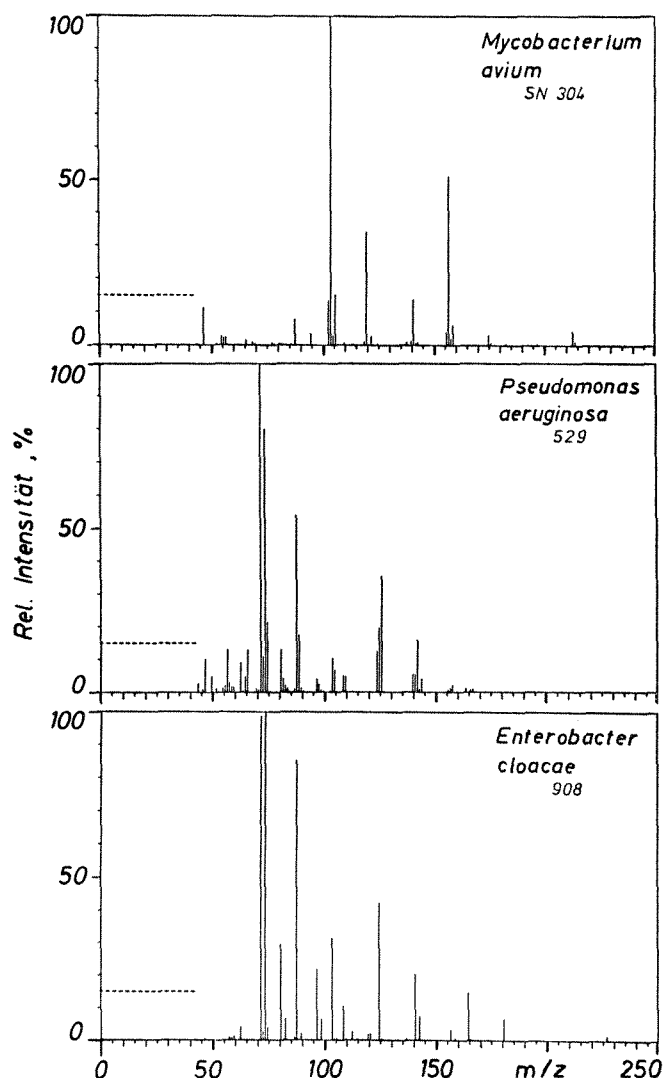


FIG. 1.--Fingerprint mass spectra from three bacterial genera (each spectrum is average over 30 single cell analyses).

the next example (Fig. 2) this direct differentiation is not possible. Here, the spectra were taken from three different species of the same genus. However, as we show later, a differentiation can be achieved by the application of more sophisticated computerized evaluation procedures.

Pattern-recognition Methods

The following is a brief survey of the main pattern-recognition techniques. Depending on the particular purpose of differentiation, one must distinguish between two principal strategies; *unsupervised* and *supervised learning*. In unsupervised learning the classes to which the objects belong are not known to the computer, which attempts to determine any natural clustering in the data set. This procedure is common to classification methods. In supervised learning the categories to which the individual objects belong are known and by means of a training set the computer evaluates a discriminant function, which makes it possible to

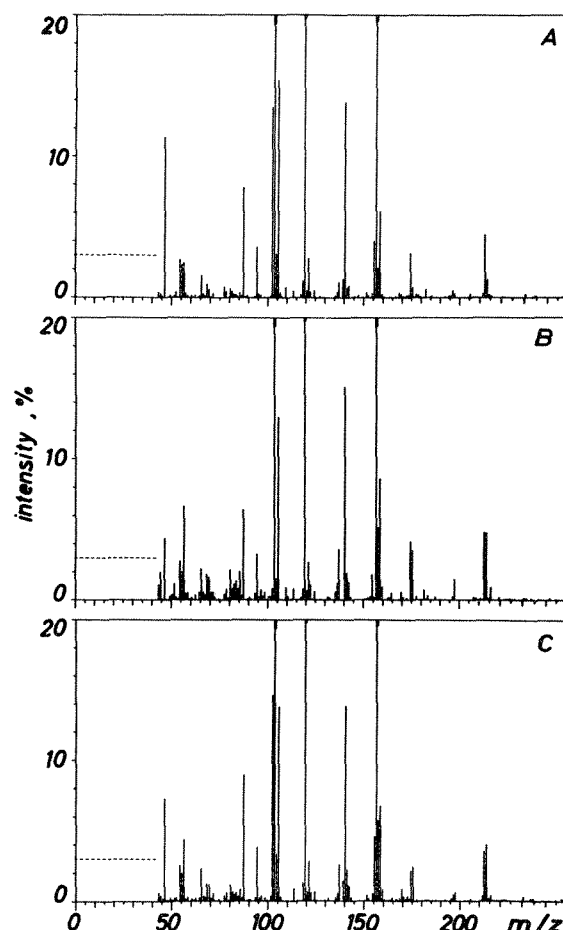


FIG. 2.--Fingerprint mass spectra from three *Mycobacterium avium* strains (each spectrum is average over 30 single cell analyses).

assign unknown objects to a particular category.

Classification. Classification covers *clustering*, which aims at ordering objects into discrete groups (hierarchical or nucleated) without the use of any further pre-information on the objects and without reduction of dimensionality of the system; and *ordination methods*, which provide for the display of inter-object similarities in a low-dimensional space. The reduction of dimensionality makes the data more readily accessible to human imagination. For this reason, it seems only logical to focus the main interest for the evaluation of laser microprobe mass spectrometric data on the ordination methods, since these experimental data normally comprise large numbers of spectra (objects), each containing large numbers of mass peaks (variables), often obtained from large numbers of different samples (groups). Such a typical set of raw data from LAMMS experiments is schematically shown in Fig. 3.

Several ordination methods are available differing in the extent and kind of information provided. Here, only the most widely used methods shall be outlined, which are *multidimensional scaling*, *principal-components*, and *factor analysis*. For the sake of complete-

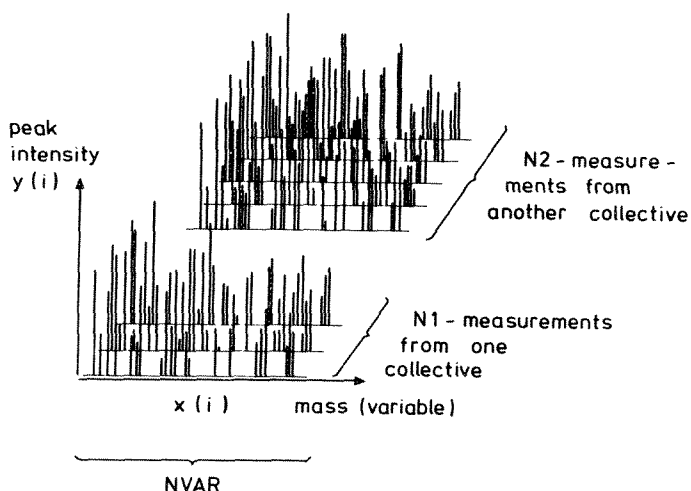


FIG. 3.--Schematic representation of typical set of LAMMS data for pattern recognition.

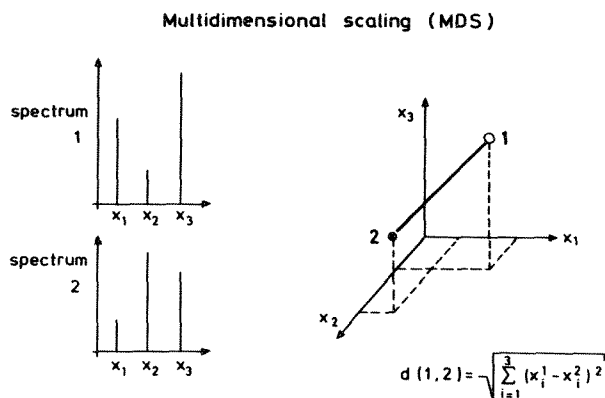


FIG. 4.--Definition of "interpoint distance" for 3-dimensional space and Euclidian geometry.

ness it should be mentioned that combinations and variations of these methods are also applied, for instance, SIMCA (soft independent modeling of class analogy), which is related to PCA and FA.¹⁰

In MDS numerical similarity or dissimilarity relationships are calculated on the basis of interpoint distances in NVAR-dimensional space, in that small distance values are representative for a high degree of similarity. This feature is demonstrated for the special case of 3-dimensional space and Euclidian geometry in Fig. 4. The two spectra, containing three mass peaks each, are represented by two points in the space put up by the three rectangular axes x_1 , x_2 , x_3 . This rather descriptive distance/similarity definition is often modified by the use of other than Euclidian geometries¹¹ and by the introduction of weighting factors.¹² Thus, for instance, different statistical significances of the contributions from the various mass peaks can be considered by these weighting factors. The similarity relationships are calculated on the basis of the outlined algorithm for each single pair of points (spectra) in the NVAR-dimensional space. Because it is practically impossible to visualize the data in the space if $NVAR > 3$, the results have to be pro-

jected as approximations of the points from NVAR space into a 2- or 3-dimensional space in a way that the interpoint distances are preserved as far as possible by a procedure termed nonlinear mapping. A special technique for this reduction of dimensionality was developed by Kruskal, which is based on a monotonal regression iteration method, and which offers a measure of the "goodness of fit" of the final space configuration output by MDS to the original NVAR-dimensional configuration.¹³ The aim of the technique is to minimize this measure.

In LAMMS it can be assumed that not all the measured data (mass peaks) are uncorrelated. Thus, for example, fragment ions will be correlated with the respective molecular ions. Therefore, a smaller set of uncorrelated variables may be introduced that describes the system completely. PCA achieves the reduction of dimensionality by finding the new set of uncorrelated variables--"principal components" (PCs)--as linear combinations of the original variables. The first PC is, among all the linear combinations, the one with the highest variance; i.e., it accounts for most of the variations in the original data. The second PC is the linear combination of variables having the maximum variance of all linear functions of the given variables that are orthogonal to the first PC, and so on:

$$PC_i = \sum_{j=1}^{NVAR} a_{ij} x_j$$

where the coefficients a_{ij} are the so-called loadings, which determine the contribution of mass x_j to the new variable PC_i . In many applications the first few PCs represent more than 90% of the system's variance. Thus, a plot of the measured data (mass spectra) in 2- or 3-dimensional space put up by two or three of these PCs reflects the similarity relationship of the original data (Fig. 5). In contrast to MDS, PCA thus allows to refer statements deduced from the low-dimensional plots to the registered mass peaks.

FA has similar aims to PCA in that it is a variable-directed technique. But whereas PCA produces an orthogonal uncorrelated transformation of the variables with no further particular assumptions required about the underlying structure of the variables, FA is based fundamentally on the hypothesis that observed correlations are mainly the result of some underlying regularities in the data. It is assumed that the observed variables are influenced by various determinants, only some of which are shared by other variables. FA can be understood as a technique by which a minimum of hypothetical variables (factors) are specified in such a way that the remaining correlations between the factors would become zero.

Principal components and factors are often distinguished as the first being defined, the latter being inferred factors. Regardless of this differentiation, the exact configuration of the factor structure is not unique: one factor solution can be transformed into another by

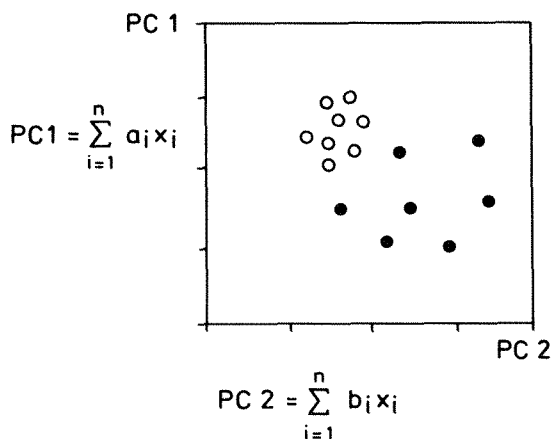


FIG. 5.--Schematic representation of two groups of objects in PC1, PC2-plane.

orthogonal or oblique rotational methods without violating the basic assumption or the mathematical properties of a given solution. It is left to the experimenter to find the configuration that allows most meaningful interpretations of his data.¹⁴

Discrimination. Discriminant analysis (DA) aims at distinguishing between two or more groups and at the assignment of newly acquired individuals to one of these groups. One accomplishes the differentiation among the various groups by finding linear combinations of the variables called "discriminant functions" (also "canonical variates"). The first discriminant function is the linear combination that of all possible combinations provides maximal separation between the groups relative to the variability within the groups; in other words, it is that artificial variable on which the variances among group means is maximal as compared to the variance within the groups. The maximum number of discriminant functions that can be derived is either one less than the number of groups or the number of discriminating variables (mass peaks), whichever is smaller. Under the assumption that the groups have homogeneous variance-covariance matrices and that the variables are normally distributed, the statistical significance of the classification of a particular individual to a particular group can be judged. The principles of DA are schematically illustrated in Fig. 6 for only two groups and two variables.

Besides the "classical" discriminant analysis there are other methods that allow an assignment of newly acquired individuals to pre-formed groups. Based on the classification with a training set--individuals of known group membership--criteria are found for quantitative statements on the enclosure or enclosure of an individual to or from a particular group. For this task rule-building expert systems are used.¹⁵

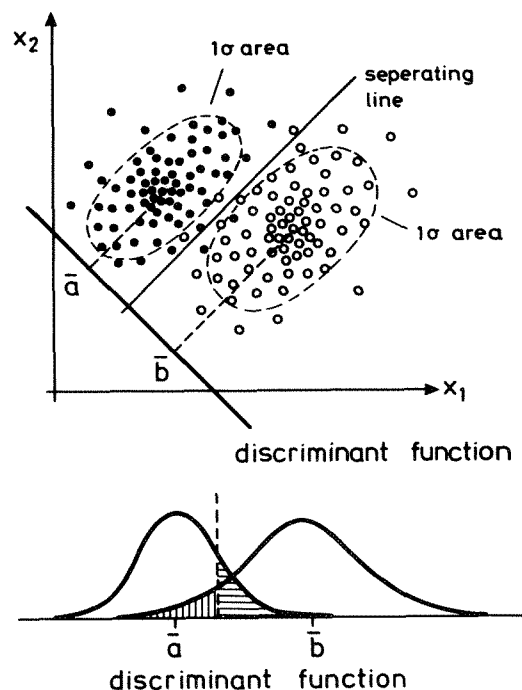


FIG. 6.--Discriminant function for two groups.

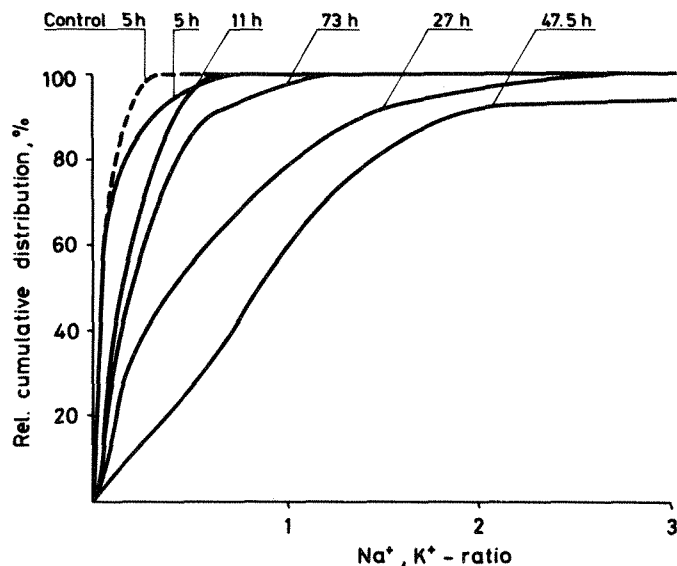
Applications

Pattern recognition techniques increasingly gain entry into LAMMS. As the applications in LAMMS are versatile--e.g., analysis of particulate matter (airborne particles),¹⁶ bacteria,¹⁷⁻²⁰ polymers,¹⁵ carbon clusters²¹--the applied statistical tools cover the whole scope outlined above. Complete software packages or subroutine libraries have been developed and most of them are commercially available (e.g., ARTHUR,²² BDMP,²³ CLUSTAN,²⁴ IMSL,²⁵ NAG,²⁶ SPSS²⁷). Furthermore, specialized systems have been developed that fit particular demands.

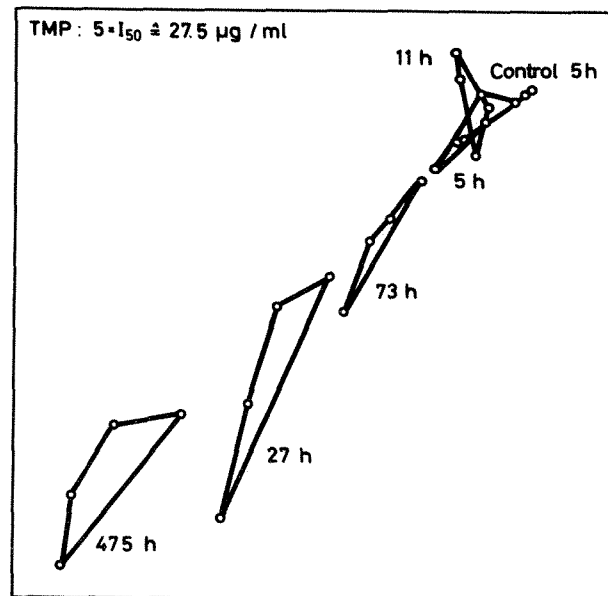
It is beyond the scope of this paper to give a complete overview of the various applications in LAMMS or to discuss the examples listed above in more detail. We prefer to concentrate on the presentation of some of our own results from the LAMMS analysis of bacterial populations. The examples are limited to the application of MDS and PCA but nevertheless reveal the capabilities of the methods.

The intention of our LAMMS work is to gain information on the physiological state of bacteria and on its changes due to the effects of drugs. This program is part of the development of a test system for therapy control in Hansen's disease, an infection caused by bacteria not cultivable in vitro.²⁸⁻³⁰ Thus, only limited numbers of organisms are available from patients' biopsies. The bacterial dimensions (appr. $0.5 \times 2 \mu\text{m}$) are such that single cells can be vaporized completely by one laser pulse. The information is deduced on the one hand directly from the cation signals of Na^+ and K^+ , measured typically from 300 single cells from one sample (which permits the calculation of distributions of the

Trimethoprim: $5 \times I_{50} \approx 27.5 \mu\text{g} / \text{ml}$

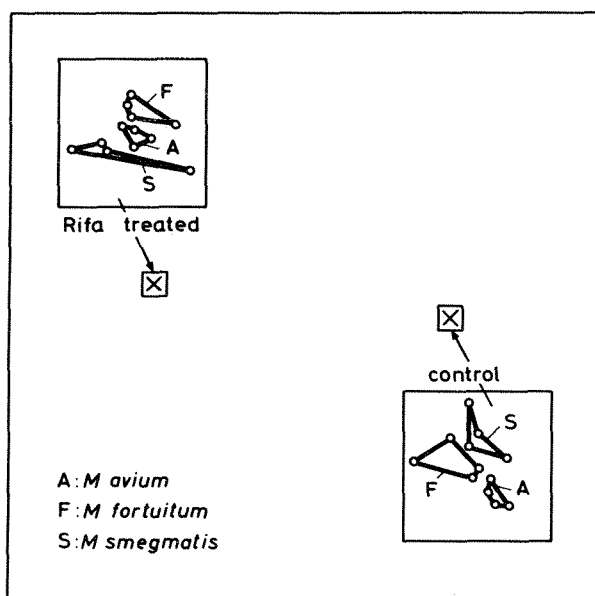


(a)

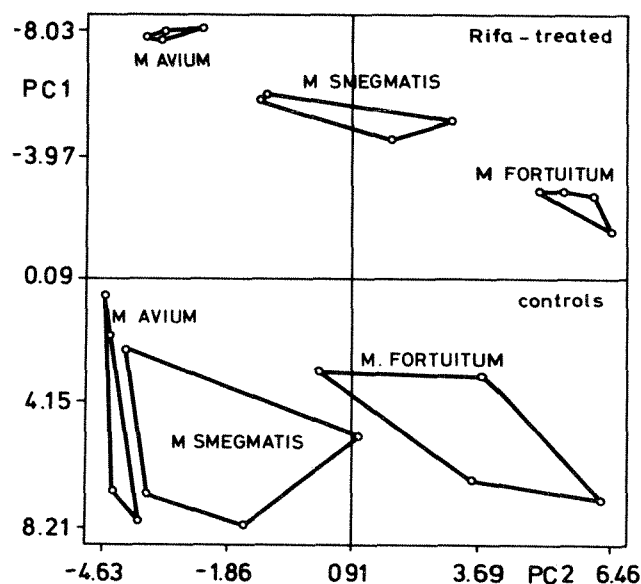


(b)

FIG. 7.--Influence of a drug (Trimethoprim) on the physiological state of mycobacteria (*M. smegmatis*): (a) relative cumulative distributions of intracellular Na^+ , K^+ -ratios at various times after administration of the drug; (b) 2-dimensional nonlinear map of the similarity relationships among the respective bacterial preparations.



(a)



(b)

FIG. 8.--Similarity relationships among three mycobacterial species (treated and untreated): (a) multidimensional scaling, (b) principal components analysis.

concentration ratios and with that of the physiological state within the bacterial population), and on the other hand indirectly from organic mass fingerprints in the mass range m/z 45 to 250.¹⁷ The evaluation of such fingerprint spectra with pattern recognition techniques is only meaningful for collectives of cells, not for individuals, because of variations in the fingerprint patterns from shot to shot due to such factors as fluctuations in la-

ser irradiance and variations in focusing conditions and in bacterial dimensions. However, this is no serious restriction as long as one is interested mainly in questions that concern the whole collective, for example in determining the effects of various drugs on the same population or a differentiation within a population according to certain well-defined morphological characteristics. In our pattern-recognition applications the evaluation is

therefore based on spectra that are the average over 30 single cell fingerprints from the same population. Details of the data processing are given elsewhere.¹⁷

Figure 7 shows the results of the measurements of the Na^+/K^+ -ratios and of the evaluation of the mass fingerprints of bacterial cultures exposed to a drug (Trimethoprim, TMP) at 5-fold the minimal inhibitory concentration for various time periods. From the relative cumulative distributions the percentage of bacteria with a Na^+/K^+ -ratio below a given value can be determined. In the example (Fig. 7a) 50% of the bacteria of the untreated control have a Na^+/K^+ -ratio below 0.05, whereas after 47.5 h of treatment the 50%-value increases to ~ 1 . This increase is indicative for the drug-induced impairment.³¹ In principle, this effect of the drug on the bacterial population is also reflected in the fingerprint evaluation. This is illustrated in Fig. 7(b) showing a 2-dimensional nonlinear map of the similarity relationships of the various cultures, where each culture is represented by four averaged spectra (as described above) that are interconnected. The increasing degree of impairment in dependence on the duration of the drug interaction and an obvious recovery of the culture after longer times (73 h), which can be explained by the multiplication of a low number of unimpaired (resistant) organisms, is expressed by the distances (similarities) between the various samples and the untreated control. The similarity relationships were determined by MDS modified according to Eshuis et al.,¹² who introduced weighting factors ("characteristicities") for the calculation of the interpoint distances. With these characteristicities the reproducibility (intersample/culture variance) and the specificity (inverse to the intrasample/culture variance) of each mass are taken into account. The graphical display of the interpoint distances were performed as described by Kruskal.¹³

In Fig. 8 a comparison of MDS and PCA is given for the evaluation of experiments on the effect of a drug (rifampicin, Rifa) on three mycobacterial species. MDS of all six cultures (three untreated and three treated) yields only two well-separated narrow assemblies of points according to the effect of Rifa; however, when properly magnified, each reveals a fine structure according to the dissimilarities among the three species in each case. This result implies that alterations in the fingerprint spectra are mainly caused by influences of the drug and are only secondarily due to species-specific influences.

The display of the spectra in the PC1, PC2-plane in Fig. 8(b) demonstrates that the drug-induced and the species-specific characteristics contribute to the separation to a comparable extent. In this example 65% of the total variance are represented by the first two PCs. PC1 differentiates between treated and untreated bacterial cultures and PC2 between the three bacterial species. The PC-loadings allow to refer to the original data (mass peaks) contributing to the separation.

Conclusions

As already proved in other fields of mass spectrometry, pattern-recognition techniques also contribute valuable information to LAMMS from the evaluation of not directly interpretable mass peak patterns. The availability of a variety of comprehensive software packages allows, in general, a convenient handling of the various pattern-recognition techniques. Particular care has to be taken on the raw data pre-processing, which may influence the clarity of the results in a non-negligible way. From our experience, a major restriction for the application of pattern-recognition techniques in LAMMS arises from the poor long-term reproducibility of the instrumental performance hampering the acquisition of data pools, which could serve as long-term training sets and standards. Not considering this feature may lead to a separation according to the receipt stamp of the samples.

The examples presented clearly demonstrate that the application of pattern-recognition techniques in LAMMS on very limited numbers of fingerprints obtained from microscopically small individual objects of a sample can provide reliable information on similarity relationships among samples. Besides the pure detection and description of classes in a sense of classification and discrimination--which give information on membership of a sample to a particular class or, as shown in the above examples, on the dynamics of alterations of a particular characteristic of a group--it is to be expected that pattern recognition will also provide support for the explanation of the underlying molecular processes responsible for the differentiation.

References

1. P. M. Mather, *Computational Methods of Multivariate Analysis in Physical Geography*, London: Wiley, 1976.
2. H. L. C. Meuzelaar, P. G. Kistemaker, W. Eshuis, and H. W. B. Engel, "Progress in automated and computerized characterization of microorganisms by pyrolysis mass spectrometry," *Proc. 2nd Intern. Symp. Rapid Methods and Automation in Microbiology*, Oxford: Learned Information Ltd., 1976, 225.
3. W. Windig and H. L. C. Meuzelaar, "Non-supervised numerical component extractions from pyrolysis mass spectra of complex mixtures," *Anal. Chem.* 56: 2297, 1984.
4. A. van der Kaaden, J. J. Boon, and J. Haverkamp, "The analytical pyrolysis of carbohydrates," *Biomed. Mass Spectrom.* 11: 486, 1984.
5. R. E. Aries, C. S. Gutteridge, W. A. Laurie, J. J. Boon, and G. B. Eijkel, "A pyrolysis mass spectrometry of pectin methylation," *Anal. Chem.* 60: 1498, 1988.
6. J. van der Greef, A. C. Tas, and M. C. Ten Noever de Brauw, "Direct chemical ionization pattern recognition: Characterization of bacteria and body fluid profiling," *Biomed. Environm. Mass Spectrom.* 16: 45, 1988.

7. W. W. Cooley and P. R. Lohnes, *Multivariate Data Analysis*, New York: Wiley, 1971.
8. L. Fahrmeier and A. Hammerle, Eds., *Multivariate statistische Verfahren*, Berlin: Walter deGruyter, 1984.
9. C. Chatfield and A. J. Collins, *Introduction to Multivariate Analysis*, London: Chapman and Hall, 1980.
10. S. Wold, "Pattern recognition by means of disjoint principal components models," *Pattern Recognition* 8: 127, 1976.
11. H. Späth, *Cluster Analysis Algorithms*, Chichester, England: Horwood, 1980.
12. W. Eshuis, P. G. Kistemaker, and H. L. C. Meuzelaar, "Some numerical aspects of reproducibility and specificity," in C. E. R. Jones and C. G. A. Cramers, Eds., *Analytical Pyrolysis*, Amsterdam: Elsevier, 1977, 151.
13. J. B. Kruskal, "Multidimensional scaling by optimizing goodness of fit to a nonmetric hypothesis," *Psychometrika* 29: 1, 1964.
14. V. Windig, J. Haverkamp, and P. G. Kistemaker, "Interpretation of sets of pyrolysis mass spectra by discriminant analysis and graphical rotation," *Anal. Chem.* 55: 81, 1983.
15. P. de B. Harrington, T. E. Street, K. J. Voorhees, F. Radicati di Brozolo, and R. W. Odom, "A rule-building expert system for classification of mass spectra," *Anal. Chem.* (in press).
16. P. Wieser and R. Wurster, "Application of laser-microprobe mass analysis to particle collections," in K. R. Spurny, Ed., *Physical and Chemical Characterization of Individual Airborne Particles*, Chichester, England: Horwood, 1986.
17. B. Lindner and U. Seydel, "Results on taxonomy and physiological state of bacteria derived from laser-induced single cell analysis," *J. Phys. Colloq. (France)* 45(C2): 565, 1984.
18. U. Seydel, B. Lindner, and A. M. Dhople, "Results from cation and mass fingerprint analysis of single cells and from ATP measurements of *M. leprae* for drug sensitivity testing: A comparison," *Int. J. Leprosy* 53: 365, 1985.
19. R. Böhm, T. Kapr, H. U. Schmitt, J. Albrecht, and P. Wieser, "Application of the laser microprobe mass analyser (LAMMA) to the differentiation of single bacterial cells," *J. Anal. Appl. Pyrol.* 8: 449, 1985.
20. J. Albrecht, E. W. Schmid, and R. Süssmuth, "Some remarks about laser-induced mass spectrometry of bacteria," *Z. Naturforsch.* 41C: 337, 1986.
21. R. A. Fletcher and L. A. Currie, "Pattern differences in laser microprobe spectra of negative ion carbon clusters," *Microbeam Analysis --1988*, 367.
22. Infometrix, Inc., Denny Building, 2200 Sixth Ave., Suite 833, Seattle, WA 98121, USA.
23. W. J. Dixon, Ed., *BMDP, Biomedical Computer Programs*, Berkeley: University of California Press, 1975.
24. D. Wishart, *CLUSTAN User Manual*, St. Andrews: Computing Laboratory, University of St. Andrews, 1987.
25. Library Reference Manual, IMSL, 2500 City-West Boulevard, Houston, TX 77042-3020.
26. FORTRAN Library, Numerical Algorithms Group Ltd., NAG Central Office, Mayfield House, 256 Banbury Road, Oxford, England.
27. N. N. Nie, C. H. Hull, J. G. Jenkins, K. Steinbrenner, and D. H. Bent, *SPSS, Statistical Package for the Social Sciences*, New York: McGraw-Hill, 1975.
28. B. Lindner and U. Seydel, "Mass spectrometric analysis of drug-induced changes in Na⁺ and K⁺ contents of single bacterial cells," *J. Gen. Microbiol.* 129: 52, 1983.
29. U. Seydel and B. Lindner, "Single bacterial cell mass analysis: A rapid test method in leprosy therapy control," *Leprosy Rev.* 57(Suppl. 3): 163, 1986.
30. U. Seydel and B. Lindner, "Monitoring of bacterial drug response by mass spectrometry of single cells," *Biomed. Environm. Mass Spectrom.* 16: 457, 1988.
31. U. Seydel, M. Haas, and B. Lindner, "In vitro effects monitored by single bacterial cell mass analysis with LAMMA," *Microbeam Analysis--1988*, 353.

MOLECULAR SPECIATION OF MICROPARTICLES: APPLICATION OF PATTERN-RECOGNITION TECHNIQUES TO LASER MICROPROBE MASS SPECTROMETRY DATA

Chul-Un Ro, I. H. Musselman, and R. W. Linton

Laser microprobe mass spectrometry (LAMMS) provides a potentially powerful tool in elucidating the major molecular species present in particles of micrometer size. For example, mass spectra for standard nickel-containing particles show characteristic cluster ion mass peaks for each compound.¹ However, the assignment of molecular species in individual nickel-containing environmental particles by LAMMS alone is complicated by inherent particle heterogeneity, both physical and chemical. This complication was illustrated in our prior microprobe studies of environmental particles produced by nickel smelters in which the chemical form of nickel is of interest because it affects particle toxicity.² Such LAMMS studies are also limited by inherent instrumental factors such as variations in laser power or focus from shot to shot, limited dynamic range, and the complexities of cluster ion formation. To exploit efficiently the molecular information present in complex LAMMS data, one must apply statistical techniques such as pattern-recognition methods. However, only a few such studies for any LAMMS application have been attempted to date.^{3,4}

In this research, LAMMS data obtained from Ni metal, NiO, NiSO₄·7H₂O, and NiS standard particles are evaluated by principal-component analysis. The cluster patterns plotted in principal-components space provide the decision rule for the assignment of nickel-containing environmental particles to specific molecular species. The successful application of these procedures relies primarily on the quality of fewer extracted features from the raw spectral data. The emphasis in this work is on evaluating statistical approaches, including spectral normalization procedures, to obtain the best subset of mass peaks to assign molecular species.

Experimental

The LAMMS data for standard and environmental particles containing various nickel compounds were obtained with a Laser Microprobe Mass Analyzer, LAMMA-500, coupled to two Bio-

mation Model 8100 transient recorders. Detailed descriptions of the experimental conditions, spectra, and sample collection/preparation are provided elsewhere.^{2,5} Two transient recorders were used to record the mass spectra simultaneously at 1 and 0.1V settings for individual standard particles. With the exception of a few atomic ions, mass spectra with lower gain exhibited no severely saturated peaks. Hence, these spectra were used to correct the saturated peaks in higher-gain spectra to increase the dynamic range.^{5,6} The software used to perform this study was the S statistical software system from AT&T Information Systems.⁷ Calculations were performed on a DEC Vaxstation II computer.

Results

After correcting for saturation, spectral normalization must be performed to help compensate for variations in the ion intensities from shot to shot due to differences in particle geometry, laser power, and laser focus. One important objective of this study was to evaluate various approaches for spectral normalization with respect to the ultimate utility of the data for pattern-recognition applications. Three options were investigated: (1) normalization of individual ion intensities to the total sum of intensities of approximately 190 mass peaks, (2) normalization to the nickel atomic ion (⁵⁸Ni⁺), and (3) normalization to the nickel dimer (¹¹⁶Ni₂⁺ was almost always observed in both the standards and the nickel-containing environmental particle samples).

The "characteristicity" values⁸ of about 190 mass peaks, which are the ratios of intergroup variance to intragroup variance, were calculated to get the most significant features for the three types of normalized spectra. The 10 mass peaks with the highest characteristicity values are listed in Table 1. They include: NiS⁺ (m/z 90, 92), NiS₂⁺ or NiSO₂⁺ (m/z 122, 124), Ni₂O⁺ (m/z 132, 134, 136), and Ni₂S⁺ or Ni₂O₂⁺ (m/z 148, 150) ions which are known to provide qualitative "fingerprints" for the standard compounds at low laser power densities.¹

The characteristicity values are dramatically increased by normalization to the nickel dimer ion (m/z 116 peak). The significance of the characteristicity was evaluated by calculations of the variance ratio or F test.⁹ With 10 data for each standard (40 total), the significance at the 99% confidence level is 4.57. With intensity normalization to the total intensity sum or to atomic nickel, only two mass peaks have significant character-

C.-U. Ro and R. W. Linton are with the Department of Chemistry, University of North Carolina, Chapel Hill, NC 27599-3290; I. H. Musselman is with the Department of Materials Science and Engineering, North Carolina State University, Raleigh, NC 27695. Support of the Environmental Protection Agency under cooperative agreement CR-812908-01-1 with Linton is gratefully acknowledged. D. S. Simons and the NIST, Gaithersburg, Md., are thanked for assistance with laser microprobe studies.

TABLE 1.--Comparison of normalization techniques for LAMMS data - mass peaks with high characteristicity for standard particles.

Normalized to Total Intensity Sum		Normalized to m/z=58 peak (Ni ⁺)		Normalized to m/z=116 peak (Ni ₂ ⁺)	
Mass No.	Characteristicity	Mass No.	Characteristicity	Mass No.	Characteristicity
90	7.20	63	2.79	150	23.27
63	5.47	90	4.63	90	20.00
150	3.04	150	2.57	148	8.53
136	3.03	135	2.55	134	8.32
132	3.03	133	2.40	92	7.81
134	2.99	132	2.32	136	7.27
135	2.66	134	2.26	132	6.19
92	2.63	136	2.25	122	4.96
133	2.60	27	2.21	63	3.88
148	2.21	148	2.11	124	3.74

isticities at the 99% confidence level. In addition, one of these two peaks is atomic copper (⁶³Cu⁺), which is a common contaminant in the spectra, as verified by consideration of ⁶³Cu/⁶⁵Cu isotope ratios. However, normalization to the nickel dimer (m/z 116 peak) results in eight characteristic mass peaks (Table 1). Such a result is not unexpected. LAMMS measurements at highest laser power density tend to generate mainly the atomic mass peaks such as atomic Ni⁺ isotopes (m/z 58, 60, 62, 63, and 64) and atomic S⁺ isotopes (m/z 32, 33, and 34).¹ Nickel ion clusters such as NiS⁺, Ni₂⁺, Ni₂O⁺, and Ni₂S⁺/Ni₂O₂⁺ are relatively more abundant at lower laser power density. Since the data were obtained at lower laser power density, the Ni cluster ions contain the primary information for molecular speciation. Other factors also limit the utility of the normalization either to total spectral intensity, or to atomic nickel ion. The former approach requires a very detailed evaluation of each mass peak for saturation. In addition, impurity elements with high atomic ion yields (e.g., Na, K, Al, Ca) can grossly affect the total spectral intensity in a fashion totally unrelated to variations in nickel speciation. The normalization to atomic nickel requires frequent saturation corrections involving the use of minor nickel isotopes. More important, the relative intensity of Ni⁺ varies with laser power density in a different way than the nickel-containing cluster ions, as we have shown previously for thin film samples.¹⁰ Since laser focus, and consequently laser power density, inevitably varies from particle to particle due to the irregular morphology and size of individual particles, normalization of cluster ion intensities to atomic nickel appears less suitable. On the other hand, the nickel dimer shows an intensity profile as a function of laser power density very similar to that of other nickel-containing cluster ions.¹⁰ Since it is the only nickel-containing cluster that appears reliably in most spectra, the nickel dimer is an obvious choice for intensity normalization.

With the eight mass peaks of highest significance in the spectra normalized to the nickel dimer, principal component analysis was applied to the 35 standard particles that had sufficiently intense nickel dimer cluster peaks. The first two principal components contain 85% of the information (variance) in the extracted data (Table 2A). The loadings of two principal

TABLE 2

A Standard Deviation of Each Principal Component

	1st	2nd	3rd	4th	5th	6th	7th	8th	total
Std Dev	1.28	0.75	0.10	0.09	0.06	0.05	0.03	0.03	2.39
% of Variance	53.6	31.4	4.2	3.8	2.5	2.1	1.3	1.3	100

B Loadings of First and Second Principal Components

m/z	90	92	122	132	134	136	148	150
First	0.10	0.04	0.00	-0.75	-0.58	-0.21	0.19	0.13
Second	-0.27	-0.13	-0.20	-0.19	-0.14	-0.05	-0.62	-0.59

components (Table 2B) indicate that the first component has the strong contributions from m/z 132 and 134 peaks (Ni₂O⁺); the second component, from m/z 148 and 150 (Ni₂S⁺, Ni₂O₂⁺). In other words, consideration of only two classes of Ni cluster ions in principal-component analysis seems sufficient to differentiate the molecular species.

In Fig. 1, standard data for the four molecular species are plotted in first and second principal-components space. The larger variances of NiSO₄·7H₂O in the first component and of NiS in the second component, compared to those of NiO and Ni metal, may be due to greater susceptibility of cluster ion formation for the former compounds to shot-to-shot variance in laser focus and power density. Of additional concern is the high water content of the sulfate standard, and possible surface oxidation of the sulfide standard.

In Fig. 2, the data for the nickel-containing environmental particles are projected onto first- and second-components space. The cluster patterns of the standards data are outlined by solid lines in Fig. 1. Two sample groups clustered to NiS and NiO species have larger variances than those of the corresponding standard data. This feature is expected to reflect greater intra- and interparticle heterogeneity in the environmental sample. On the other hand, the sample group clustered to nickel sulfate has a surprisingly smaller variance than the standard and it is located closer to the NiO group. The location shows that the Intensities of Ni₂O⁺ and Ni₂S⁺/Ni₂O₂⁺ ions in the sample group are relatively small compared to those in the standard NiSO₄·7H₂O particles, which may be explained by several factors. For example, it is known from x-ray photoelectron spectroscopy (XPS) that sulfate is surface enriched on the environmental particles which consist primarily of nickel oxides.¹¹ However, the XPS result averages over a large number of particles. Laser desorption studies also indicate the presence of surface sulfate, by use of negative ion detection.⁵ Second, the water content of the sample may differ considerably from the highly hydrated NiSO₄·7H₂O standard. The high water content of the standard probably enhances the signals observed for oxygen-containing clusters.

In addition to XPS, direct qualitative evidence for intraparticle heterogeneity has been obtained by scanning electron microscopy coupled to energy-dispersive x-ray spectroscopy (SEM/EDS) and secondary-ion mass spectrometry

(SIMS) imaging of particle cross sections.^{1,2} This evidence is consistent with the results shown in Fig. 2. Several groups of environmental particles are clustered outside the four molecular groups for the standards. These "between" clusters are shown within dotted outlines and labeled as I, II, and III in Fig. 2. The visual inspection of mass spectra of these particles clearly supports the actual presence of mixtures of nickel species, since those spectra show the "fingerprints" of more than one molecular species. However, the positions of Clusters I, II, and III in Fig. 2 do not necessarily mean that each represents a binary mixture of two molecular species from the two standard clusters directly adjacent to it. Clusters I and II probably do represent oxide/sulfate mixtures as substantiated by correlative XPS and SEM/EDS studies.^{2,11,12} Cluster III may reflect some deviation from the NiS standard because of variabilities in Ni/S stoichiometries in the environmental particles containing mainly nickel sulfides. It is known by x-ray powder diffraction² that the sample contains a significant quantity of nickel subsulfide (Ni_3S_2) in addition to NiS. Thus, it is possible that Cluster III reflects the presence of Ni_3S_2 , which is a species of particular environmental significance.^{1,2}

Of the 58 environmental particles out of 172 whose LAMMS spectra exhibit nickel-containing cluster ions, 37 are assigned as NiO, 15 as NiS, and 6 as NiSO_4 by use of the K-nearest neighbor technique (KNN) where $K = 1$.¹³ However it is apparent that some of the NiO and NiSO_4 particles contain mixtures of the two species, and that the NiS class may also include Ni_3S_2 . Results are quite similar to prior assignments achieved by correlating laser and electron microprobe data without the formal use of pattern-recognition techniques.² Sulfur-to-nickel x-ray intensity ratios obtained with SEM/EDS were combined with the qualitative identification of the presence of characteristic cluster ions. The classification results are compared in Table 3 (3A vs 3B). They are comparable except for the relative proportions of oxide and sulfate. The difference in the results reflects the use of quantitative relative intensities of cluster ions in the pattern-recognition approach. The results of pattern recognition (Table 3A) also are closer to the distribution of species obtained by wet chemical analysis, which indicate a small sulfate component and a large oxide component (Table 3C).⁵

Conclusions

This paper demonstrates the utility of pattern-recognition techniques in relating complex LAMMS cluster ion data to molecular species in individual microparticles. Results of principal-component analysis are enhanced by appropriate approaches to spectral normalization, in this instance by use of a common cluster ion. A characteristicity tests is employed to select cluster ions of highest significance in distinguishing various species. Specific results

TABLE 3

A Classification Using Pattern Recognition Method (KNN, K=1)

	No. of Particles	% of Particles
Nickel oxide	37	63.8
Nickel sulfate	6	10.3
Nickel sulfides	15	25.9
<u>Nickel metal</u>	<u>0</u>	<u>0.0</u>
Total	58	100

B Classification Using Qualitative Laser Microprobe Data^{2,5}

	No. of Particles	% of Particles
Nickel oxide	17	29.8
Nickel sulfate	9	15.8
Nickel sulfate or mixture including nickel sulfate and nickel oxide	17	29.8
Nickel sulfides	14	24.6
<u>Nickel metal</u>	<u>0</u>	<u>0.0</u>
Total	57	100

C Classification Using Wet Chemical Techniques⁵

	Weight Percent	% of Total Nickel Content
Nickel oxide	43.7	80.3
Nickel sulfate	0.8	1.5
Nickel sulfides	9.5	17.5
<u>Nickel metal</u>	<u>0.4</u>	<u>0.7</u>
Total	54.4	100

are provided for the identification of nickel compounds in environmental samples. However, a difficult problem is extensive intraparticle chemical heterogeneity. Results of cross-sectional imaging (SEM/EDS, SIMS) are used to verify the existence of intraparticle chemical variations. The LAMMS/pattern-recognition approach provides a quantitative estimate of the distribution of nickel species quite comparable to wet chemical data on bulk samples.

References

1. I. H. Musselman, R. W. Linton, and D. S. Simons, "The use of laser microprobe mass analysis for nickel speciation in individual particles of micrometer size," *Microbeam Analysis--1985*, 337-341.
2. I. H. Musselman, J. T. Rickman, and R. W. Linton, "Fingerprinting of chemical species in microparticles: Correlative laser and electron microprobe studies," *Microbeam Analysis--1987*, 361-364.
3. R. A. Fletcher and L. A. Currie, "Observations derived from the application of principal-component analysis to laser microprobe mass spectrometry," *ibid.*, 419-421.
4. U. Seydel and B. Lindner, "LAMMA as a tool in Microbiology," *ibid.*, 353-355.
5. I. H. Musselman, *Molecular and Quantitative Aspects of Laser Microprobe Mass Spectrometry for Inorganic Particle Analysis*, Ph.D. thesis, University of North Carolina at Chapel Hill, Department of Chemistry, 1988.
6. D. S. Simons, "Isotopic analysis with the laser microprobe mass analyzer," *Int. J. Mass Spectrom. Ion Proc.* 55: 15-30, 1983.
7. R. A. Becker and J. M. Chambers, *S: An Interactive Environment for Data Analysis and Graphics*, Belmont, Calif.: Wadsworth, 1984.
8. W. J. Irwin, *Analytical Pyrolysis*, New York: Marcel Dekker, 1982, 237-289.
9. M. A. Sharaf, D. L. Illman, and B. R. Kowalski, *Chemometrics*, New York: Wiley, 1986, 317-323.

10. R. W. Linton, I. H. Musselman, F. Bruynseels, and D. S. Simons, "Inorganic cluster ion formation in the laser microprobe," *Microbeam Analysis--1987*, 365-368.

11. J. T. Rickman, S. G. Maybury, and R. W. Linton, "Surface and depth profiling studies of airborne particles using XPS," *Pittsburgh Conf. Analytical Chemistry and Applied Spectroscopy* 39: Abstract #632, 1989.

12. R. W. Linton et al., "Correlative ion, laser, and electron microprobe analysis of microparticulate materials," in A. Benninghoven, A. M. Huber, and H. W. Werner, Eds., *SIMS-VI*, New York: Wiley, 1988, 569-572.

13. B. R. Kowalski and C. F. Bender, "Pattern recognition: A powerful approach to interpreting chemical data," *J. Am. Chem. Soc.* 94: 5632-5639, 1972.

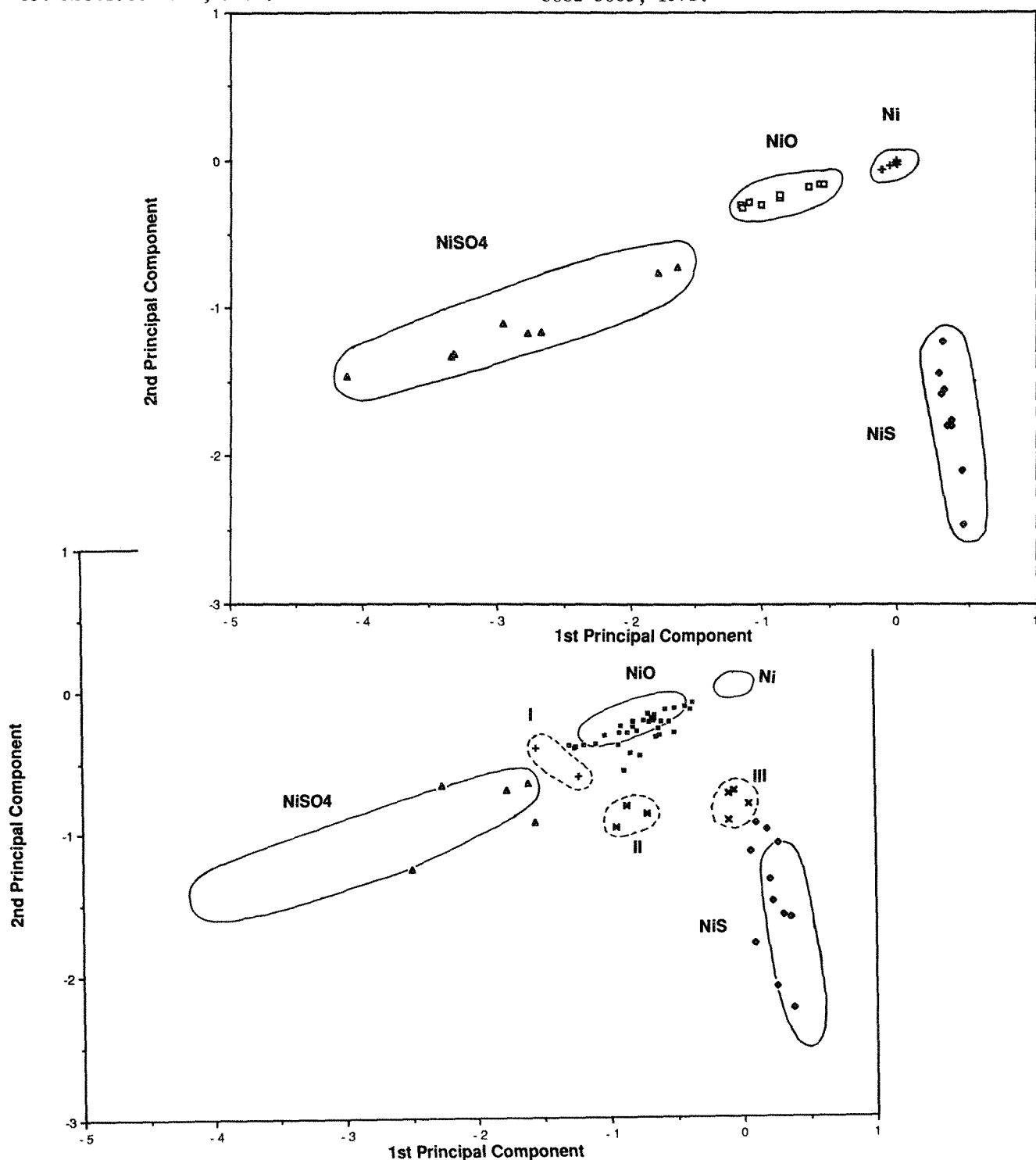


FIG. 1.--Principal component plot of standard spectra for nickel-containing compounds (8 or 9 spectra each for 4 compounds).

FIG. 2.--Principal component plot of 58 nickel-containing environmental particles (points) compared to standard data (solid outlines as also shown in Fig. 1). Clusters I, II, III (dotted outlines) apparently represent mixtures of nickel species within single environmental particles not clearly associated with clusters of individual standard compounds.

OBSERVATIONS OF CARBON CLUSTERS FROM POLYCYCLIC AROMATIC HYDROCARBONS

D. N. Lineman, S. K. Viswanadham, A. G. Sharkey, and D. M. Hercules

High-mass carbon clusters formed by laser interaction with a carbon source have been reported by several investigators^{1,2} and more recently observed in Cf^+ plasma desorption.³ High-mass carbon clusters seemingly consist only of carbon, and occur at 24amu intervals, corresponding to C_{2n} , in the range $20 < n < 300$. Efforts to resolve the structure of high-mass clusters has been an increasingly active area of research; however, little work has been done to deduce the mechanism of their formation. Recently, high-mass carbon clusters have been formed from polycyclic aromatic hydrocarbons (PAHs) in a LAMMA-1000 laser mass spectrometer.⁴ It is hoped that through the use of PAHs the mechanism by which high-mass carbon clusters are formed can be elucidated, which should lead to the resolution of their structure.

Experimental

PAHs purchased from Aldrich Chemical Co. were analyzed without further purification by use of the LAMMA-1000, described elsewhere.⁵ Samples were dissolved/suspended in volatile organic solvents (methanol, acetone, benzene)

The authors are at the Department of Chemistry, University of Pittsburgh, Pittsburgh, PA 15260.

deposited on zinc foil, and allowed to air dry before analysis. Laser power densities ranging from 10^7 to 10^8 W/cm² were achieved by defocusing at constant laser energy.

Results

Figure 1 shows the laser mass spectrum (LMS) of chrysene (mst 228). Low mass clusters of the form C_n ($1 < n < 28$) (Type I) can be seen, as well as high-mass clusters (Type III) described above. This type of clustering has been observed for all PAHs analyzed which contain at least one benzene ring. The laser power density needed to produce Type III clustering depends on the structure of the PAH. Compounds which form Type III clusters, in order of increasing laser power density required, are coronene \approx pyrene \approx chrysene $<$ anthracene \ll 9,10-dimethylanthracene \ll tetraphenylbenzene \ll acridine $<$ phenazine. By lowering the laser power density, Type III cluster formation is halted and clustering of the type $(nM - xH)^+$ (Type II) takes place; nM is a multiple of the molecular ion from 1 to 5, and xH is loss of hydrogen atoms. Hydrogen loss is compound dependent and can give structural information about the cluster formed. Figure 2 shows an example of the transition between Types II and III clustering in pyrene from lower laser power

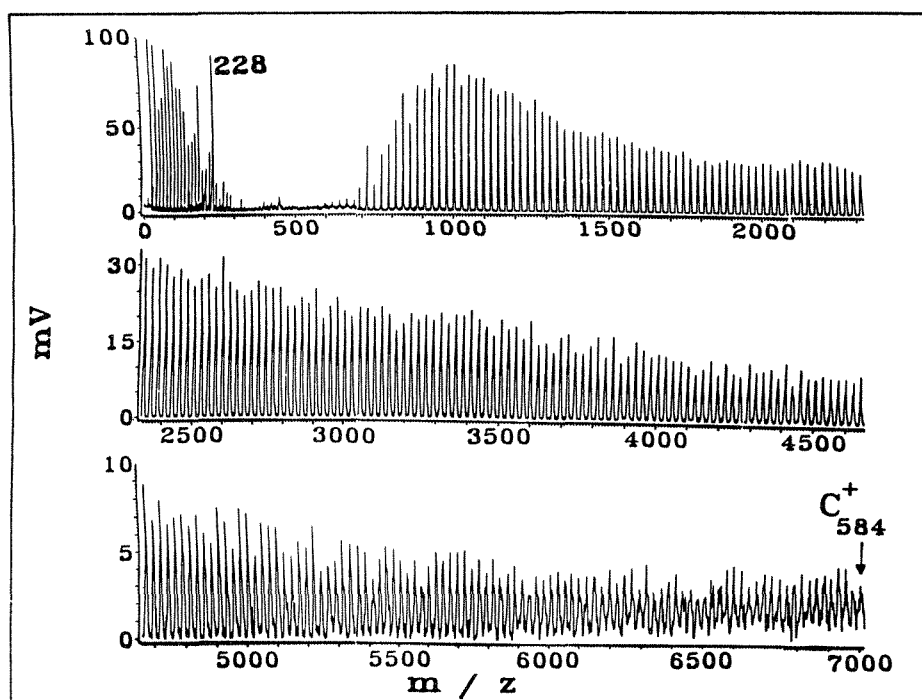


FIG. 1.--Positive-ion LMS of chrysene. Spectrum is compilation of four mass spectral regions.

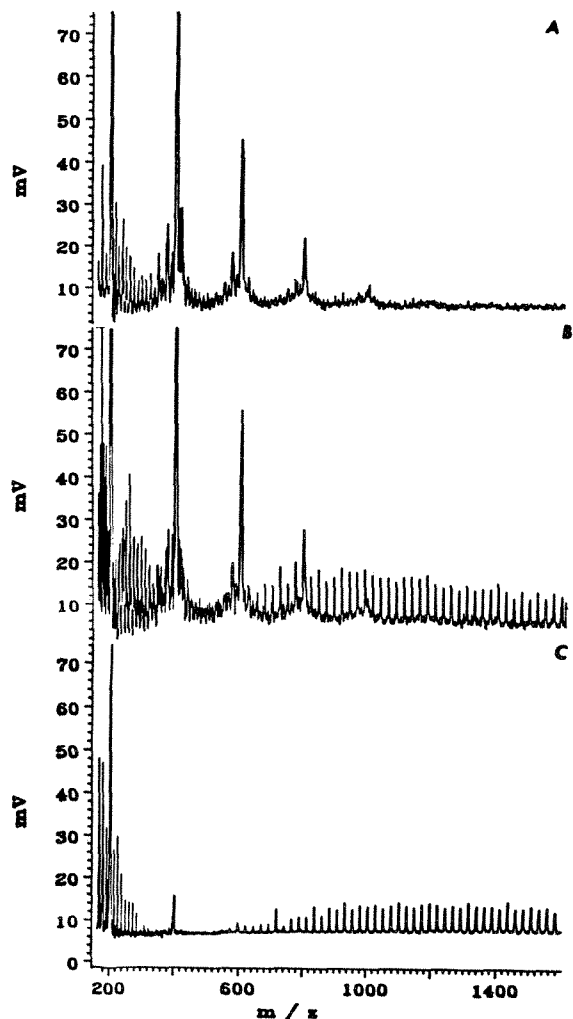


FIG. 2.--Positive-ion LMS of pyrene: (a) 325 μm defocused, (b) 275 μm defocused, (c) 250 μm defocused.

density (Fig. 2a) to high laser power density (Fig. 2c).

Discussion

To date, Type III clusters have been observed from graphite, polyamide, polyvinylidene fluoride and polyvinylidene dichloride, poly(2,5-thienylene), and PAHs. One can assume that for these structurally different compounds to form the same type of clusters, they must proceed through some common mechanism. These possibilities are:

1. Atomization and recombination of carbon atoms forming Type III clusters.
2. Transition through an acetylinic rearrangement forming Type III clusters.
3. Transition through an aromatic condensation forming Type III clusters.

If atomization of the sample to carbon atoms is a necessary stage in Type III cluster formation, then phenazine should require lower laser power density than coronene to form Type III clusters (assuming energy for atomization being

primarily that needed for bond breakage and disruption of aromaticity). However, as stated earlier, coronene clusters at a much lower laser power density than phenazine.

Laser interaction with solids can create a high-temperature plasma region. Previous studies have shown that thermal decomposition of polyvinylchloride and polystyrene results in the formation of primarily aromatic compounds. If an aromatic structure is necessary for Type III clustering, then coronene and pyrene should require low laser power density (possibly just enough for free radical formation); tetraphenylbenzene, higher power density, to break single bonds between phenyl groups; and the highest laser power density for phenazine, which would require cleavage of four C-N bonds to free aromatic rings. This type of energy ordering is observed. The appearance of Type II clusters is possibly a transitory step between simple aromatic compounds and Type III clusters. Studies will continue to determine the structure of Type II clusters and their relation to those of Type III.

References

1. E. A. Rohlfing, D. M. Cox, and A. Kalder, "Production and characterization of supersonic carbon cluster beams," *J. Chem. Phys.* 81(7): 1984.
2. W. R. Creasy and J. T. Brenna, "Large carbon cluster formation by laser ablation of polyamide and graphite," *Chem. Phys.* 126: 453, 1988.
3. A. Benninghoven, personal communication.
4. D. N. Lineman, S. K. Viswanadham, A. G. Sharkey, and D. M. Hercules, "High mass carbon clusters from polycyclic aromatic hydrocarbons observed by laser mass spectrometry," *J. Phys. Chem.* (in press).
5. D. M. Hercules, *Pure Appl. Chem.* 55: 1869, 1983.

CLUSTER ION FORMATION BY LASER-INDUCED EVAPORATION OF GROUP IV OXIDE ELEMENTS

A. Mele, D. Stranges, A. Giardini-Guidoni, and R. Teghil

The study of elemental clusters has been very active and the experiments investigating their formation have recently undergone an explosive growth due to the development of techniques such as laser evaporation and molecular beam.^{1,2} This report deals with the determination of cluster ions formed from Group IV metal oxides by use of the LAMMA technique. Laser evaporation and cluster ion formation from these compounds may be affected by their structures. The aim of the present investigation is to provide an insight in the mechanism leading to the formation of small cluster and to their stability.

Experimental

The laser irradiation of the samples and cluster ion analysis were performed in the same manner as described in a previous paper.³ A commercial LAMMA 500 instrument by Leybold-Heraeus has been employed. Solid samples were finely ground and spread onto an electron microscope grid. The frequency-quadrupled Nd-YAG laser was operated at 10^8 – 10^9 W/cm². The data were collected through a transient digitizer and processed by an "on line" computer.

Results and Discussion

The mass spectrum analysis of samples shows positive and negative cluster ions of various composition depicted by homologous series. Figure 1 describes typical mass spectra of positive ions obtained when the laser is focused on the internal side of a fused silica glass 0.3 mm thick. As can be seen from this figure, three series ($\text{Si}_n\text{O}_{2n}^+$, $\text{Si}_n\text{O}_{2n-2}^+$, and $\text{Si}_n\text{O}_{2n-1}^+$) are observed. The relative abundance of the single components of these series varies with n . All positive cluster ions with $n > 4$ have roughly comparable intensities. At $n = 2$ the relative abundance is the following: $\text{Si}_2\text{O}_4^+ > \text{Si}_2\text{O}_3^+ \gg \text{Si}_2\text{O}_2^+$. This trend parallels the intensity of $\text{Si}^+ > \text{SiO}^+ \gg \text{SiO}_2^+$. The $\text{Si}_n\text{O}_{2n}^+$ series has lower intensities in a large range of n and the trend shows intensity maxima at $n = 3$ and 7. In the mass spectra of negative cluster ions, the two series $\text{Si}_n\text{O}_{2n}^-$ and $\text{Si}_n\text{O}_{2n+1}^-$ are present, with abundance intensities of the component decreasing with n . LAMMA spectra of germanium oxide, SnO_2 , SnO , PbO , and PbO_2 show the presence of relatively small cluster ions.

A. Mele and D. Stranges are at the Dipartimento di Chimica, Università "La Sapienza," Piazzale Aldo Moro 5, I-00185 Rome, Italy; A. Giardini-Guidoni and R. Teghil are at the Istituto di Chimica, Università di Basilicata. They acknowledge the experimental contribution of M. Matricardi.

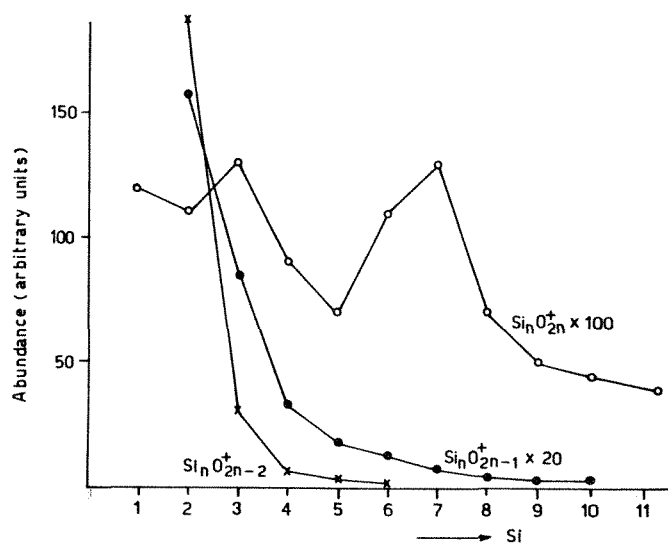
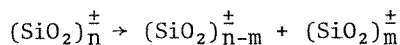


FIG. 1.--Positive ion intensity of silica specimen as a function of increasing number of silicon atom.

The sequences observed for both positive and negative ions are shown in Table 1.

The main feature that appears from the LAMMA spectra of oxides is that all positive or negative cluster ions are formed of homologous series built up of simple MeO or MeO_2 units. The silica positive series may be depicted as simple $(\text{SiO}_2)_n^+$, $\text{SiO}(\text{SiO}_2)_n$, and $\text{Si}(\text{SiO}_2)_n$ cluster ions. The negative cluster ions are composed of the $(\text{SiO}_2)_n^-$ and $\text{O}(\text{SiO}_2)_n^-$ series. The SiO_2 unit reproduces of course the stoichiometry of the solid, which may suggest a possible mechanism of ion formation. One may speculate that part of the solid silica is directly ablated by the laser-induced plasma and fragmented to produce smaller ions according to



The positive series for the other oxides result from the table and can be written as $(\text{MeO})_n$ or $\text{Me}(\text{MeO})_n$. For germanium, the negative cluster ions give rise to the same series as observed in silica; for Sn or Pb, only to MeO_n . The experimental data of the present work may be in agreement with a model depicting the process of fragmentation which is characterized by structures preserving the original pattern.⁴ The empirical model applied to an oxidized metal surface or a metal oxide for the calculation of ions formed seems to fit the experimental data. The cluster ion distributions for the positive series in silica are similar to those found in SIMS⁵ and

previous LAMMA experiments. The model proposed treats the data as a function of a so-called "fragment valence" $K = (q + 2n)/m$ for a generic ion species M_mO_n , where q is the total charge (in this case $q = 1$), and m and n are the number of metal and oxygen atoms in the clusters.

The plot of K against the mass M for the series of silica positive ions tends to $K = 4$. This value represents the most stable valence obtained at very high masses. This result would agree with the hypothesis based on the electronic structure calculations⁷ that formulate the interaction of SiO_2 molecules leading to tetrahedral conformation of Si starting from $n = 3$.

The K trend of Ge, Sn, and Pb positive series approaches a value of 2. This valence perhaps reflects the crystal structure of these metal oxides. A different coordination has in fact to be attributed to them with respect to silica.

References

1. J. C. Phillips, *Chem. Rev.* 86: 619, 1986.
2. A. W. Castleman J. and R. G. Keesee, *Am. Rev. Phys. Chem.* 37: 525, 1986.
3. M. Bertolotti, D. Consalvo, A. Mele, A. Gardini-Guidoni, and R. Teghil, *Appl. Surf. Sci.* 35: 1988.
4. C. Plog, L. Wiedmann, A. Benninghoven, *Surf. Sci.* 67: 565, 1977.
5. C. E. Richter and M. Trapp, *Int. J. Mass. Spectr. and Ion Phys.* 38: 21, 1981.
6. E. Michiels, A. Celis, and R. Gijbels, *Int. J. Mass. Spectr. and Ion Phys.* 47: 23, 1983.
7. C. Geisser and A. Shluger, *Phys. Stat. Sol* B135: 669, 1986.

TABLE 1.--Positive and negative ion sequences observed.

Me	Positive ions	Negative ions
Si	Si_nO_{2n}	Si_nO_{2n}
	Si_nO_{2n-1}	
	Si_nO_{2n-2}	Si_nO_{2n+1}
Ge	Ge_nO_n	Ge_nO_{2n}
	Ge_nO_{n-1}	Ge_nO_{2n+1}
		Ge_nO_{2n+2}
Sn	Sn_nO_n	SnO_n
	Sn_nO_{n-1}	
Pb	Pb_nO_n	PbO_n

STRUCTURAL INTERPRETATION OF SILICATE NETWORK FROM VARIOUS SILICATE ROCK-FORMING MINERALS IN LMMS ANALYSIS

Takahisa Tsugoshi, Tadashi Kikuchi, Keiichi Furuya,
 Yoichi Ino, and Yoshitaka Hayashi

It is well known that silicate rock-forming minerals have several kinds of silicate network. Fragment ions in LMMS analysis reflect the difference of the network. Thirteen kinds of silicate minerals with five kinds of network structures have been analyzed and their spectra showed characteristic patterns depending on their network structures.

Experimental

The LAMMA-1000 (Leybold-Heraeus) was used in this experiments. Thirteen kinds of rock-forming minerals with different structures (neso-, ino-, phyllo-, cyclo-, and tecto-) and compositions were chosen as samples. All mineral samples were supplied from the Bureau of Geological Science. Specimens cleaved from mother sample blocks were mounted on stubs with double adhesive tape without any pretreatment. All spectra were obtained at the lowest power density over the threshold.

Authors Tsugoshi, Kikuchi, and Furuya are at the Department of Applied Chemistry, Faculty of Science, Science University of Tokyo, 1-3 Kagurazaka, Shinjuku-ku, Tokyo, 162 Japan; authors Ino and Hayashi are with ANELVA Corp., 5-8-1 Yotsuya, Fuchu-shi, Tokyo, 183 Japan.

Results

Figure 1 shows spectra of olivine and enstatite; Table 1 shows a summary of silicate fragment ions from four types of minerals (olivine, enstatite, beryl, and albite). SiO_n ($n = 1-3$) fragment peaks originating from single SiO_4 ion were detected for olivine (neso-type silicate) and Si_mO_n ($m = 1-6$, $n = 1-12$) fragment peaks from chain structures were observed for enstatite (ino-type silicate). For albite (tecto-type silicate), fragments have $m = 1, 2$, and 4 with $n = 1, 2, 5$, and 6 , which shows that plane network silicates gave smaller fragments, whereas enstatite (ino-type silicate) and beryl (cyclo-type silicate) gave larger fragments. For enstatite, the numbers of oxygen in a fragment were richer than those of beryl (cyclo-type structure).

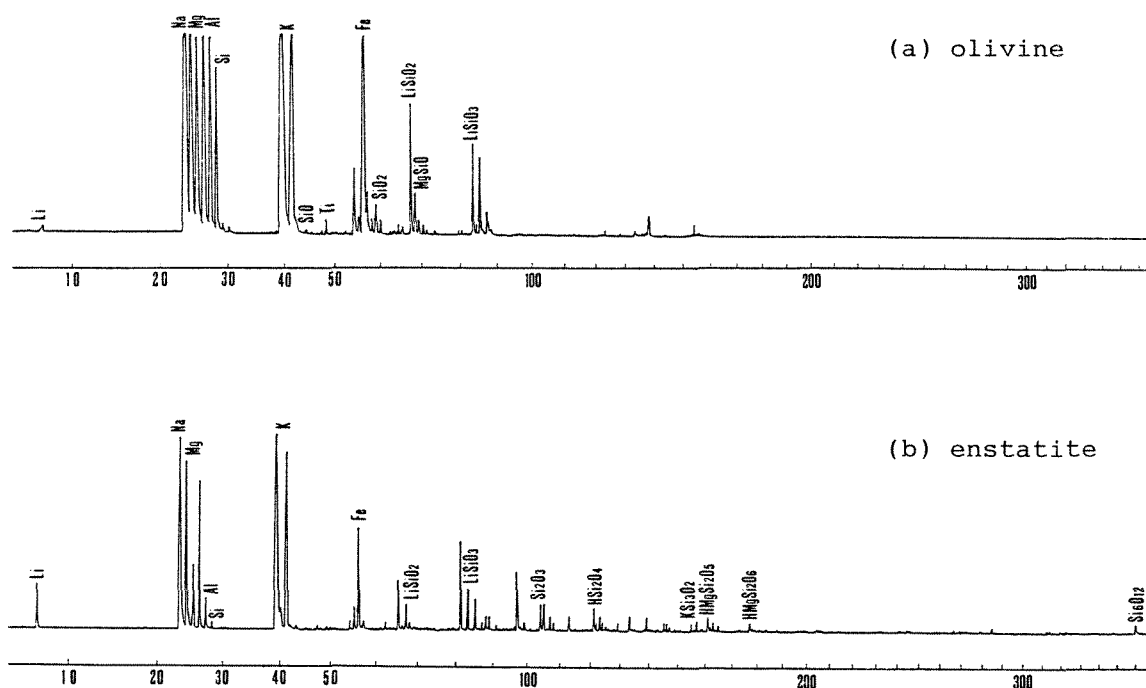


FIG. 1.--LMMS spectra of (a) olivine (nesosilicate), (b) enstatite (inosilicate).

TABLE 1.--Si-O fragment ions of silicate networks.

		Si							
		1	2	3	4	5	6	7	8
	1	○△	△						
	2	○◇△	■△	◇					
	3	○◇	◇						
	4		◇□						
	5		◇▲						
	6		◇▲	□	△				
	7		◇□		□	■			
	8				◇				
	9			◇□		□			
	10			◇					
	11				◇		□		
○	12				◇□	■	◇		
	13				◇				
	14					◇	◇		
	15					◇			
	16						◇		
	17						■	■	
	18								
	19								
	20								
	21							◇	
	22							◇	
	23								

solid marks : Al substituted

○ olivine(nesosilicate)
◇ enstatite(inosilicate)
□ beryl(cyclosilicate)
△ albite(tectosilicate)

UTILITY OF THE LASER MICROPROBE FOR SOURCE IDENTIFICATION OF CARBONACEOUS PARTICULATE MATERIAL

R. A. Fletcher and L. A. Currie

Combustion sources of carbon particulate material are of interest since they play a role in contributing to air pollution, reducing visibility, and modifying climatic conditions.¹ One of the most reliable ways of identifying carbon particle sources is through carbon-14 dating of collected aerosol.² The approach is based on the premise that fossil fuels contain no carbon-14, but modern carbon combustion sources (such as wood) do. Although this is a powerful technique, the smallest sample of collected aerosol that is useful for analysis is of the order of micrograms.³ An effort has been made to extend carbon-source detection down to the single-particle level by use of laser microprobe mass spectrometry (LAMMS).^{4,5} A summary of our efforts to characterize combustion source particles is presented.

Experiment

Two sets of carbon particles were studied: particles generated from controlled burns of "pure" materials in the laboratory, and two atmospheric particle samples collected in a national environmental study. The laboratory soots result from individual burning of heptane, kiln-dried building wood, and polyurethane. Graphite is included in the laboratory sample set. The two atmospheric samples have been characterized in terms of their carbon-14 content.¹ One sample is clearly derived from burning contemporary material, i.e., wood; the other comes from the combustion of fossil fuels. These two samples, contemporary and fossil, serve as extreme or end members for a more extensive set of collected atmospheric particles.

In all cases studied, the carbon aerosol was collected on high-purity quartz fiber filters. The filters were heat treated, before particle collection, to remove residual carbon contaminants. Quartz fibers carrying the carbon particles were transferred to a transmission

electron microscope grid that contained no film backing.⁶ Individual and small groups of particles were ablated directly from the fiber surface mounted in vacuum. The instrument used in the study was a LAMMA 500 with a 32× objective focusing 266nm radiation. Both positive and negative ion data were taken. Laser irradiances were typically of the order of 1×10^9 W/cm².

Results and Discussion

The history of the production of carbon particles is presented in Fig. 1. A carbon fuel is combusted under certain temperatures and oxygen concentrations. The carbon particles are formed by various processes and are transported to the collection site. En route they are exposed to various ambient conditions, e.g., sunlight, gas-phase chemical species, and other particles. After collection on a fiber, the particles are analyzed by LAMMS, which results in laser ablation and ionization of the chemical species in the particle. Thus, the routes for the samples measured here, from source to collection, are variable and result in atmospheric and laboratory samples that are of varying degrees of complexity. Atmospheric samples are the most inhomogeneous and complex.

For LAMMS to be useful for source identification, it must be able to distinguish carbon combustion sources on the basis of the collectible samples. Earlier results have shown that for the laboratory soots, source identification is possible by analysis of the low-*m/z* ion patterns in the laser microprobe positive ion spectra.⁴ Principal component analysis has been useful in analyzing these laboratory soots. Peaks that contain the most differentiating power were K⁺ and C₃H⁺. Figure 2 shows a plot of the first two principal components differentiating heptane soot from wood soots. However, these indicators were not useful for source identification for the two real atmospheric samples. Even the samples representing end-member extremes cannot be differentiated on the basis of low-*m/z* positive ion patterns.⁴ It was interesting to note that the fossil fuel sample (derived primarily from motor vehicle emissions) and the modern sample (from the burning of wood) both contained approximately the same amounts of lead. Thus lead--and as it turns out any other elements--could not be used as identifiers for these individual particle (non-bulk) samples.

There is new evidence for identification on the basis of certain likely chemical species in the positive-ion *m/z* region (>208) for the two atmospheric samples. Small trace peaks are present in spectra of both fossil and contempo-

The authors are at the Center for Analytical Chemistry at the National Institute of Standards and Technology, Gaithersburg, MD 20899. Certain commercial equipment, instruments, or materials are identified in this report to specify adequately the experimental procedure. Such identification does not imply recommendation or endorsement by the National Institute of Standards and Technology, nor does it imply that the materials or equipment identified are necessarily the best available for the purpose. The authors wish to acknowledge the aid of G. W. Mulholland of NIST in providing samples of the laboratory carbon soots, and EPA for the two atmospheric samples.

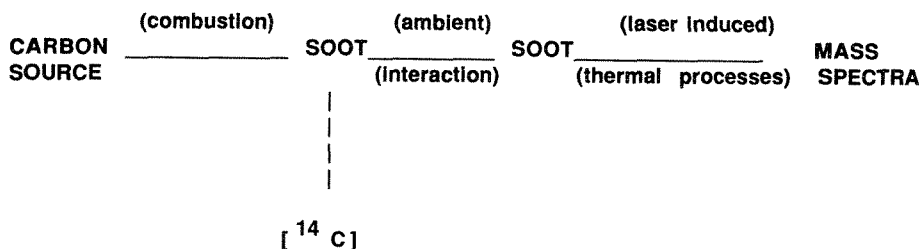


FIG. 1.--Schematic history of combustion carbon soot from source to mass analysis.

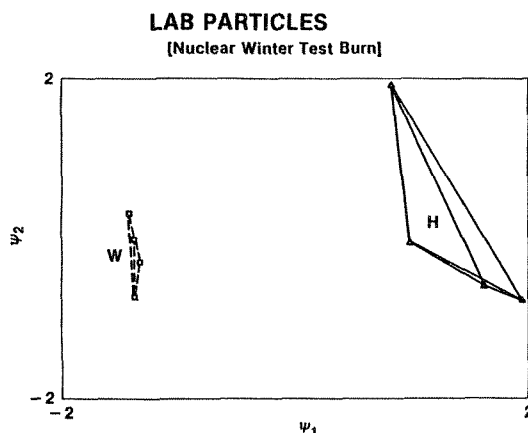


FIG. 2.--Principal component plot of laboratory wood (W) and laboratory heptane (H). Each point corresponds to single-spectrum, single-particle analysis.

rary samples that have approximate m/z values of 228, 252, 276, 278, 300, 302. Peak m/z 268 was also found in the spectra. These peaks probably correspond to polynuclear aromatic hydrocarbon (PAH) molecular ions as previously reported for similar carbon soot samples.^{7,8} The occurrence of these high- m/z peaks is more frequent for the fossil fuel sample, 34 peaks per 49 spectra compared to 8 peaks for 43 spectra in the modern sample. A potential strong candidate for source identification is m/z 276 which occurs twelve times for the fossil sample and not at all for the modern sample (Fig. 3). There are nine isomeric PAH compounds that have a molecular weight of 276. Of particular interest is benzo(ghi)perylene (BGP). It has been observed that BGP concentration increases for particle samples with increasing fossil carbon content and decreases with increasing modern carbon content determined from bulk gas chromatographic analysis.⁹ Daisey et al. present a data summary that indicates BGP concentrations are greater for auto exhaust particles collected from roadway tunnels (fossil fuel) than wood smoke from fireplace burning.¹⁰ (This reference is relevant, since wood burning in fireplaces appears to be the dominant source of modern carbon in the atmospheric sample analyzed.) The BGP concentration can only be determined by an indirect route from the Daisey et al. publication by use of their tabulated concentration values for the relatively unstable benzo(a)pyrene. Furthermore, a considerable spread in the range of the values for

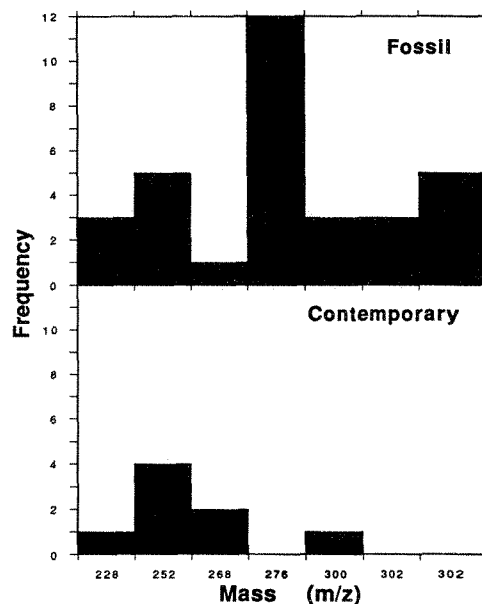


FIG. 3.--Bar graph showing frequency for high- m/z positive ion peaks. Top plot is for fossil fuel particles and bottom pertains to contemporary sample.

benzo(a)pyrene is presented in their paper for wood burning. Clearly it is of interest to determine whether BGP (or more relevant, the peak at m/z 276) provides tracer information for source identification at the single particle level.

The negative ion spectra for the laboratory and atmospheric samples have been examined. Some slight differences in low- m/z carbon cluster ratios have been observed.^{5,11}

In summary, there is new evidence that the positive-ion high- m/z peaks appear to be useful in discriminating between atmospheric samples. The laboratory soots and graphite have distinguishing low- m/z peaks that permit identification of these materials. Work is ongoing to determine the utility of negative ion carbon clusters and high mass positive ion peaks as identifiers.

References

1. L. A. Currie, G. A. Klouda, and K. J. Voorhees, *Nucl. Instr. Meth.* 233: 265, 1984.
2. L. A. Currie, G. A. Klouda, J. Schjoldager, and T. Ramdahl, *Radiocarbon* 28: 673, 1986.
3. R. M. Verkouteren, G. A. Klouda, L. A.

- Currie, D. J. Donahue, A. J. T. Jull, and
T. W. Linick, *Nucl. Instr. Meth.* 329: 41, 1987.
4. L. A. Currie, R. A. Fletcher, and G. A.
Kloda, *Nucl. Instr. Meth.* B29: 346, 1987.
5. L. A. Currie, R. A. Fletcher, and G. A.
Kloda, *Aerosol Science and Tech.* (in press).
6. Fletcher, R. A., *Anal. Chem.* 61: 914, 1989.
7. T. Mauney, Ph.D. Dissertation, Colorado
State University, 1984.
8. T. Mauney, F. Adams, and M. R. Sine, *Sci.
of the Total Environ.* 36: 215, 1984.
9. A. Sheffield, Ph.D. Dissertation, Uni-
versity of Maryland, 1988.
10. J. M. Daisey, J. L. Cheney, and P. J.
Liroy, *JAPCA* 36: 1, 1986.
11. R. A. Fletcher and L. A. Currie, *Micro-
beam Analysis--1988*, 367.

**LASER MICROPROBE FOURIER TRANSFORM ION CYCLOTRON RESONANCE MASS
SPECTROMETRY: INSTRUMENTATION AND RESULTS OF POLYMER STUDIES**

J. T. Brenna

Time-of-flight (TOF) spectrometers have in the past been the mass dispersion devices of choice for inherently pulsed ion sources such as the laser source. The chief advantage of TOF over quadrupole and magnetic sector instruments is the capability to record an entire mass spectrum from a single laser shot. Other advantages of TOF include broad mass range, excellent transmission, and simplicity of construction.

In 1974 Comisarow and Marshall¹⁻³ introduced Fourier transform ion cyclotron resonance mass spectrometry (FTICR or FTMS) as a means to effect high-resolution mass dispersion. This technique is a modification of the previous well-known technique of ion cyclotron resonance spectroscopy (ICR). In ICR, ions drifting through a static magnetic field are subjected to a frequency-swept oscillating electric field perpendicular to the static magnetic field. Under these conditions, ions gain kinetic energy only when the oscillating electric field corresponds to a particular resonance frequency given by

$$f = kB/(m/e) \quad (1)$$

where f is the ion cyclotron resonance frequency, B is the value of the static magnetic field, m/e is the mass to charge ratio of the ions, and k is a proportionality constant. The absorption of electric energy is recorded as the swept frequency passes through resonant frequencies and a spectrum is recorded. Alternatively, the electrical signal can be recorded as ions with large orbital radii strike a plate, as in the instrument known as an "omegatron."⁴

In the FTICR experiment, ions are trapped in two dimensions by a static magnetic field, and in the third dimension by a static electric field produced by a set of (trap) plates positioned perpendicular to the magnetic flux lines. For positive ions, these plates are biased with a small positive potential, around 1 V, and for negative ions they are biased with a corresponding negative potential. All other aspects of the experiment are identical for positive and negative ion modes. Ions can be trapped for macroscopic periods of time, of the order of seconds or minutes depending on their initial condition. The FTICR "cell" consists of a set of six square electrically isolated plates arranged as a cube. (Other shapes are possible.) The trap plates form the two sides of the cube perpendicular to the magnetic field. The four other plates are positioned

parallel to the magnetic flux lines. An "excite" signal is placed on one set of opposite plates. Most commonly this signal is a oscillating electric field swept through frequencies at a constant rate from DC to some high frequency, typically of the order of megahertz ("rf chirp"). As the frequency of the oscillating field comes into resonance with ions in the cell, ions pick energy coherently as ion packets, and attain stable orbits. The last set of plates are attached to a sensitive pre-amplifier circuit, and act as an antenna. The waveform induced on these "receive" plates due to the orbiting ions packets is amplified and digitized. This signal is then fast Fourier transformed (FFT) and the frequency spectrum is directly calibrated to mass. Thus, the entire m/e range of interest is obtained simultaneously.

There exist a number of distinct advantages to the Fourier transform method, among which ultrahigh mass resolution is perhaps the most celebrated. Equation (1) is also the fundamental cyclotron frequency-to-mass relation for FTICR. Since k is a constant, it can be seen directly that the cyclotron frequency depends only on the m/e for the ions and is independent of the energy. Initial kinetic energy spread results in differential orbital radii among ions within each packet, but the orbital frequency is unaffected. The FTICR experiment takes full advantage of this fact by providing simultaneous detection of each ion and thus multichannel advantage. In addition, orbiting ions are detected in more uniform electric and magnetic fields than ions that are accelerated and ejected as in the conventional ICR experiment. Figure 1 is an ultrahigh-resolution scan of the ²⁰⁶Pb peak from 266 nm laser ablation of NBS lead wire obtained with the instrument described in this paper. The full width at half maximum for this peak corresponds to a mass resolution ($m/\delta m$) greater than 4×10^5 .

Other analytical capabilities relevant to microprobe analysis include high trapping efficiency, which is analogous to transmission in conventional mass spectrometers, and the ability to perform multiple-stage MS experiments. Multiple-stage MS experiment (MSⁿ) are accomplished by repeated excite and detect events. Unwanted ions are ejected from the cell by selective excitation to orbital radii in excess of the dimensions of the cell. These ions collide with the walls of the cell and are neutralized and pumped away, leaving only ions of interest in the cell. Such a capability is currently not available for microprobe analysis by other MS techniques but would greatly increase selectivity for molecular species.

The author is with IBM Co., D/T43, 1701 North Street, Endicott, NY 13760.

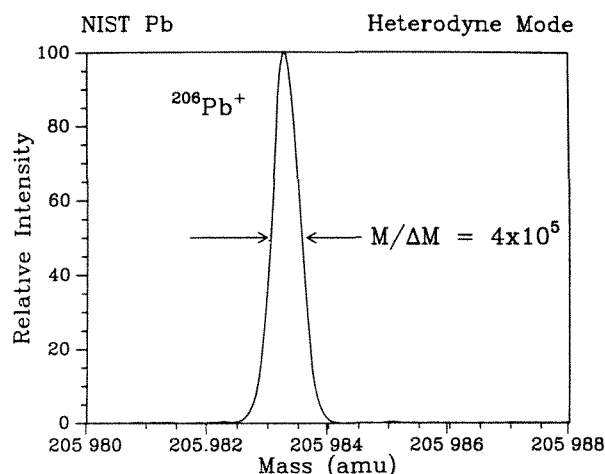


FIG. 1.--Ultra-high mass-resolution spectrum of $^{206}\text{Pb}^+$, taken by FTICR-LAMMS. This spectrum was obtained by use of heterodyne mode FTICR in which signal is mixed with waveform to shift its frequency to lower value and allow longer acquisition times. X-axis corresponds to 8 milli-amu full scale.

Apparatus

We have recently reported⁵⁻⁷ on our construction of a LAMMS interface to a commercially available FTICR instrument, the Nicolet FTMS-2000. This interface is based on a Nd:YAG laser system which is usually operated at 266 nm, but often at 532 nm and sometimes 1.06 μm . The system is set up to allow viewing of the specimen by reflected light and motion of the specimen stage to the point of laser focus.

The layout of the system is shown in Fig. 2. FTICR event sequences (make ions, excite ions, delays, etc.) must be controlled to microsecond accuracy; therefore either the laser or the FTICR must be triggered by the other. However, neither of these systems is designed to be a slave device; they are not easily triggered from an external instrument. Thus, an IBM PC-AT equipped with a commercially available interface board⁶ was interfaced to both devices. Software specially written for this system allow laser pulsing and FTICR experimental event sequences to be synchronized and controlled to 1 μs . The system allows single- or multiple-laser experiments and is compatible with any pulse firing sequence that may be generated with the FTICR control computer. During normal LAMMS operation with a single laser, the laser flashlamps pulse at their nominal 10Hz rate without firing the Q switch, which would fire the laser. This procedure allows the YAG rods to attain steady-state temperature and so optimum power reproducibility. When a laser pulse is required, the Q switch is fired one or multiple times, depending on the requirements of the experiment. Multiple laser shots allow for signal averaging, which is often necessary for weak signals when spatial resolution is not an issue.

The laser light passes through an optical attenuator and a telescope system, then passes

into the vacuum system. The telescope allows on-line focusing of the laser beam onto the specimen even though the objective lens is fixed in place within the vacuum chamber. The beam is focused by a 75mm objective lens, and onto the specimen. A vacuum-compatible fiber optic brings light onto the sample, which is then transmitted out along the same optical path that brought the laser light in. A mirror may then be inserted into place and the specimen may be viewed by reflected light through an eyepiece, or alternately directed to a recording device.

The smallest crater in polished silicon achieved by this system is of the order of 3 μm , with spot sizes of < 10 μm achieved on a routine basis.

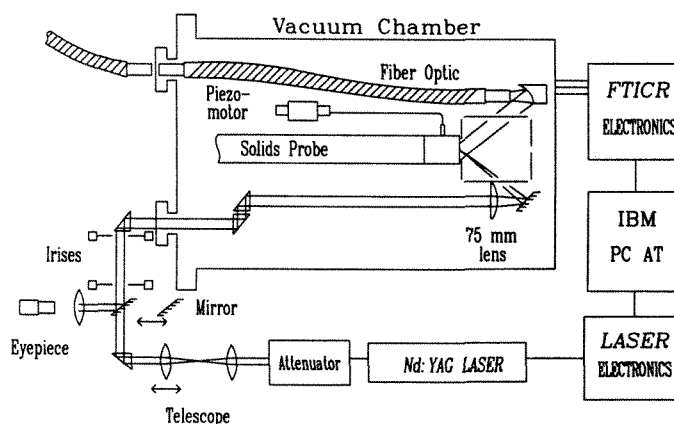


FIG. 2.--Layout of IBM-Endicott FTICR-LAMMS.

Polymer Studies

Over the years a significant amount of effort has been devoted to polymer analysis by TOF-LAMMS.^{8,9} This work has shown that ions characteristic of the original polymer are observed in LAMMS spectra. However, in most cases the ions observed are highly fragmented and/or rearranged products, with very complicated and largely unknown reaction mechanisms. During the same period, a significant amount of attention has been devoted to laser ablation of polymers with the ultimate intention of electronic-device and electronic-package fabrication and medical applications.¹⁰ Ablation experiments have yielded a significant amount of information on the product formation process and are discussed elsewhere in this volume.¹¹

With these facts in mind, we have undertaken a study of FTMS-LAMMS of a variety of common polymers in an effort to characterize product distributions with the analytical advantages of the FTICR method. Detailed accounts of some of this work have been reported elsewhere.^{9,12,13} Several trends have emerged as dominating polymer spectra ablated with 266nm light, including C clustering, stable subunit condensation, and possible attachment of small C clusters to small ions.

The first polymer examined by FTMS-LAMMS was polyimide, the structure for which is shown in Fig. 3. The positive-ion spectrum of this polymer (Fig. 4) is observed to be exclusively C cluster ions. The C clusters appear in three distinct mass distributions, characterized by (a) mass range and (b) peak distribution. We discuss these distributions in detail as they are recurrent phenomena for other polymers.

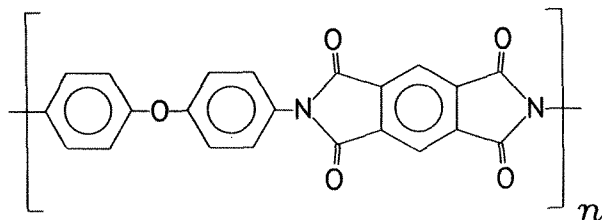


FIG. 3.--Structure of polyimide.

The *low* mass distribution is characterized by a C cluster at every C number and ranges from about C_{10} to C_{28} . Associated with these peaks are auxiliary peaks 2 amu greater than the bare C cluster. These auxiliary peaks may represent magic addition of 2 H atoms, or substitution of one of the C clusters with an N atom to yield C_{n-1} ions. The spectra obtained so far are not of sufficiently high resolution to address this question. These ions may have the structure of linear polyacetylenes with either CN groups or H's at each end. The *intermediate* mass range C cluster distribution is characterized by peaks at every mass from $m/e = 350$ to 700, with oscillatory intensities of period corresponding to 12 amu. Bare C clusters appear in the valleys, and peaks correspond to addition of 6-7 H atoms. These clusters may very well have the structure of polyaromatic hydrocarbons. The *high* mass distribution starts around mass 800 and extends past $m/e = 5000$. This distribution is characterized by peaks occurring at exclusively even C numbers, reminiscent of the "fullerene" family.^{14,15} Only C_{70}^+ is observed to be anomalously stable under these conditions.

Table 1 lists a number of other polymers that have been studied by FTMS-LAMMS and have been discussed elsewhere. Of these polymers nine exhibit in their positive ion spectra one or two of the C-cluster distributions observed for polyimide. In two cases, poly(phenylenesulfide) and the copolymer of ethylene and tetrafluoroethylene, the fullerenes are observed and show a magic number for C_{60}^+ . This molecule has been the subject of numerous investigations since it was first observed in 1984 as a product of supersonic-beam-entrained laser-ablated graphite. A significant body of evidence indicates the molecule has the shape of a truncated icosahedron, or soccerball, with C atoms occupying each of the 60 apices of this structure. (For this reason it has been given the name "buckminsterfullerene.") This is the first observation of C_{60}^+ as a particularly

TABLE 1.--Polymers studied by FTMS-LMMS.

	Repeat Unit*
Polyimide	See figure 3
Polyethylene	$-\text{CH}_2-\text{CH}_2-$
Polyethyleneglycol	$-\text{O}-\text{CH}_2-\text{CH}_2-$
Polystyrene	$-\text{CH}_2-\text{CH}(\text{Ph})-$
Polyvinylchloride	$-\text{CH}_2-\text{CH}(\text{Cl})-$
Poly(methylmethacrylate)	$-\text{CH}_2-\text{C}(\text{CH}_3)(\text{COOCH}_3)-$
Polyvinylchloride	$-\text{CH}_2-\text{CH}(\text{O}_2\text{CCH}_3)-$
Poly(phenylenesulfide)	$-\text{Ph}-\text{S}-$
Polyacrylonitrile	$-\text{CH}_2-\text{CH}(\text{CN})-$
Poly(dimethylsiloxane)	$-\text{Si}(\text{CH}_3)_2-\text{O}-$
Ethylene/Tetrafluoroethylene Copolymer (DuPont Tefzel(R))	$-\text{CH}_2-\text{CH}_2-$ & $-\text{CF}_2-\text{CF}_2-$

* Ph = Phenyl Group

stable ionic product of laser ablation of any material beside pure graphite.

In spite of the prevalence of C clusters in these polymers, all give additional ionic product distributions which may be used to distinguish them from all other polymers in either the positive- or negative-ion mode. In some cases polymers give ions that appear to be formed by direct fragmentation. It is interesting that these structural ions appear more frequently in negative-ion spectra than positive-ion spectra. Figures 5(a) and (b) are the positive- and negative-ion spectra of poly(phenylenesulfide) (PPS), respectively. Whereas the positive-ion spectrum shows exclusively the fullerene C clusters, the negative-ion spectrum shows a series of ions that fit the stoichiometry of the polymer, with rearrangement products present as a small fraction of the total ion signal. A possible mechanism for this phenomenon may be the development of an electrical potential analogous to the "plasma sheath" parallel to the surface of the polymer, which functions to draw negative ions out of the laser-induced plasma before they can undergo extensive rearrangement. This same potential may increase the residence time for positive ions in the plasma and explain the extensive rearrangement observed for these ions. Even in the absence of structural ions, each positive-ion spectrum is unique and can serve to identify the polymer. For instance, the positive-ion spectrum of PPS consists only of fullerenes, but is the only polymer we have observed to date that gives this product distribution from the first laser shot. Since the other polymers that give fullerenes also give other ions in the spectrum, this C-cluster distribution identifies the polymer.

Many polymer spectra show characteristic ions that are not simply related to the polymer's covalent structure. We have made likely elemental assignments for these ions which are consistent with the elements present in the

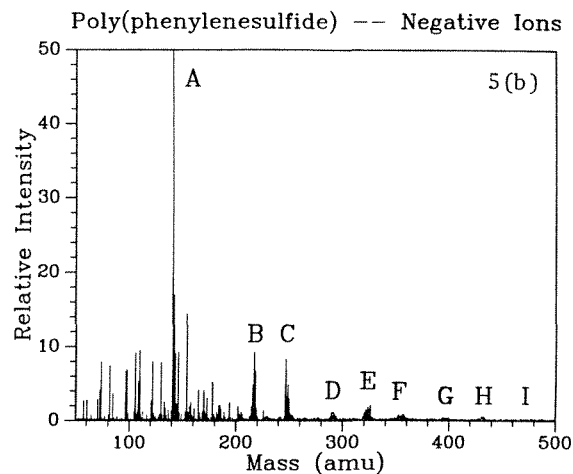
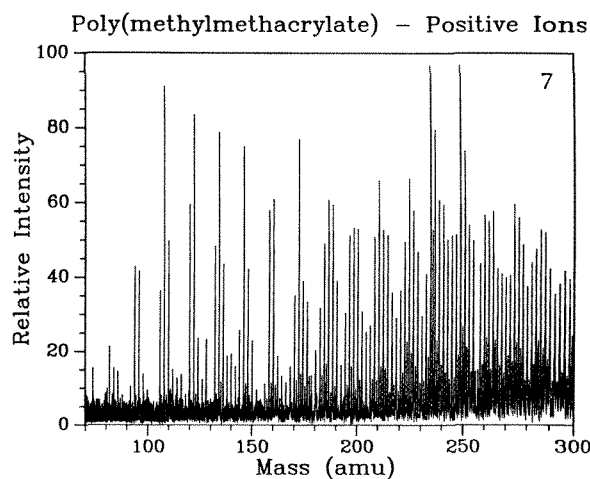
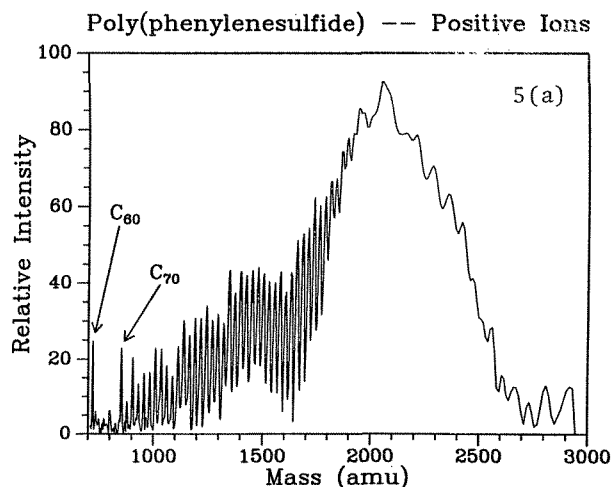
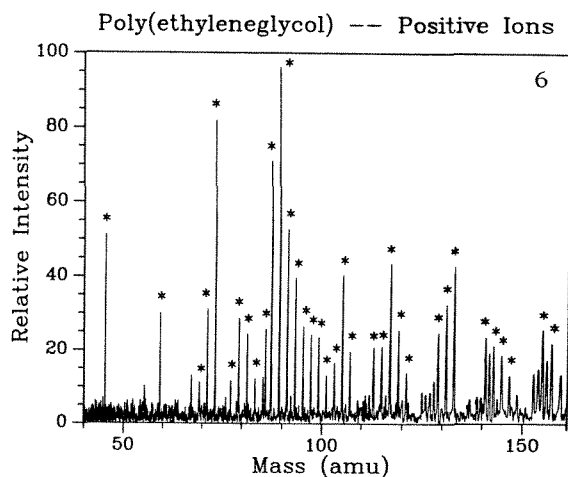
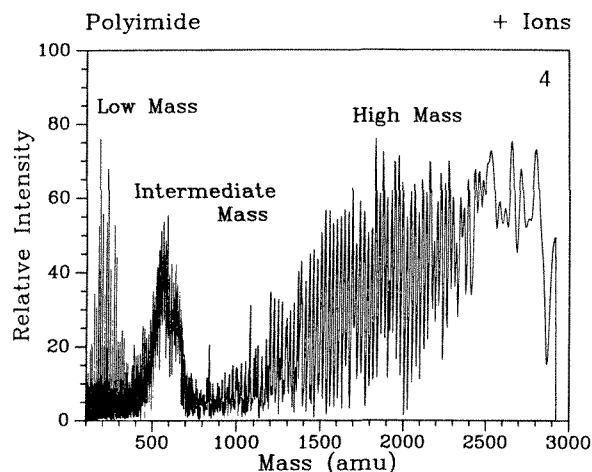


FIG. 4.--Positive-ion FTICR-LAMMS spectrum of polyimide of average molecular weight 25 000. The three distributions of C clusters are indicated on plot.

FIG. 5.--(a) Positive-ion FTICR-LAMMS spectrum of poly(phenylenesulfide) of average molecular weight 50 000. No other ions beside those in this figure are observed in positive-ion spectrum for this polymer during first few hundred laser pulses. (b) Negative ion FTICR-LAMMS spectrum of poly(phenylenesulfide). Letters refer to structural ions observed in spectrum as follows, with ordered pairs referring to numbers of phenyl and S, respectively, associated with each peak: A(1,2); B(2,2); C(2,3); D(3,2); E(3,3); F(3,4); G(4,3); H(4,4); I(4,5).

FIG. 6.--Positive-ion FTICR-LAMMS spectrum of poly(ethyleneglycol) of average molecular weight 8000. Starred peaks are all odd numbered and correspond to general formula given in text. Ions with masses greater than $m/e = 160$ are also observed in this spectrum (not shown).

FIG. 7.--Positive-ion FTICR-LAMMS spectrum of poly(methylmethacrylate). Major peaks in this spectrum are odd-numbered. Intermediate mass C cluster distribution is observed starting around mass 200 and continuing well past mass 300 (not shown).

polymer and are chemically reasonable. However, the data taken to date do not provide unequivocal evidence for these assignments. These assignments indicate two trends in polymer ablation spectra (in addition to C clustering), which will now be discussed.

The first of these trends is consistent with a relatively simple hypothesis concerning ion formation, and is illustrated by the spectrum in Fig. 6, the positive-ion spectrum of poly(ethyleneglycol) (PEG) of average molecular weight 8000. This spectrum shows a strong ion series increasing peak density with increasing mass. For PEG, these ions correspond to the general formula $H(CH_2)_mO_n$. There are more than 35 peaks in this spectrum which may be assigned this formula and only a few peaks in the series reflect the stoichiometry of the original polymer. The monomer and dimer are the only ones which show particular stability compared to the peaks around them. This hypothesis also explains the PPS spectrum obtained after about 2000 laser shots to the same spot, sufficiently many to make a hole in the polymer and expose the Al substrate. This spectrum, not presented here but published elsewhere,⁹ shows ions consistent with the formula Ph_mS_n for values of $m = 2 - 7$ and $n = 0 - 5$. The role of Al in ion formation from PPS, if any, is not known.

A second phenomena in the positive ion spectra is illustrated in Fig. 6, in which the target is polymethylmethacrylate (PMMA). The odd-numbered peaks in this spectrum are consistent with the formula $HCO_2(CH_2)_m-C_n$ for $m = 0 - 10$ and $n = 2 - 10$. Here we hypothesize a series of stable hydrocarbon ions in association with C clusters formed either by attachment one by one to the ion or attachment of the previously made cluster. This hypothesis fits ion series observed in the spectra of polystyrene and poly(vinylacetate) as well, although it must be considered the most tentative of the three mechanisms proposed here.

There are significant differences between the polymer spectra obtained by FTICR-LAMMS and TOF-LAMMS.⁹ In general, FTICR spectra show ions extending to higher mass range than the TOF spectra. This difference may be due to the detector discrimination effects. Alternatively, laser ablation in the FTICR takes place with the specimen immersed in a 3-Tesla magnetic field. This field may perhaps confine charged particles present in the laser-induced to the point where recombination to high-molecular-weight species is favored. In addition, no high-voltage extraction fields are present in the vicinity of the specimen such as are encountered in TOF. This factor would also be expected to favor growth of higher molecular weight species.

Conclusions

The other FTMS-LAMMS instruments currently in operation include a system at the IBM Laboratory in San Jose, Calif.,¹⁶ and an instrument at the University of Metz.¹⁷ The Metz instrument, based on an excimer laser operated at

249 nm, is discussed elsewhere in this volume; we shall mention salient features of the other instrument. The San Jose instrument was the first FTMS system set up to focus a laser onto the specimen with on-line specimen viewing. The laser and viewing paths are similar in design to the Endicott instrument, with laser and illumination light entry through opposite corners of the cell plates. Because this system was originally based on a CO₂ laser operated at 10.6 μ m, the minimum obtainable spot size was reported to be in the range of 30-50 μ m.¹⁶ The system has been recently modified for use with a Nd:YAG laser operated at 1.06 μ m and so is expected to attain a finer spot size.

In this paper we have discussed the design and construction of the first Nd:YAG-based LAMMS-FTICR instrument. The smallest spot size demonstrated for this system is about 3 μ m, with <10 μ m spot achievable on a routine basis. We have obtained photographs of the specimen positioned in the instrument which show detail at this resolution level. The instrument has been used to analyze a variety of common polymers, and some of the general results have been presented here. Results generated by this system have demonstrated the ability of LAMMS-FTICR to distinguish among various polymers and provide information on the laser ablation process itself.

References

1. M. B. Comisarow and A. G. Marshall, *Chem. Phys. Lett.* 25: 282-283, 1974.
2. M. B. Comisarow and A. G. Marshall, *Can. J. Chem.* 52: 1997-1999, 1974.
3. M. B. Comisarow and A. G. Marshall, *Chem. Phys. Lett.* 26: 489-490, 1975.
4. H. Sommer, H. A. Thomas, and J. A. Hipple, *Phys. Rev.* 82: 697-702, 1951.
5. J. T. Brenna, W. R. Creasy, W. McBain, and C. Soria, *Rev. Sci. Instr.* 59: 87-879, 1988.
6. W. R. Creasy and J. T. Brenna, *Comput. and Chem.*, 1989 (in press).
7. J. T. Brenna and W. R. Creasy, *Microbeam Analysis--1988*, 377-378.
8. R. J. Conzemius and J. M. Capellen, *Int. J. Mass Spec. Ion Phys.* 34: 197-271, 1980.
9. J. T. Brenna and W. R. Creasy, *Anal. Chem.*, 1989 (submitted).
10. J. T. C. Yeh, *J. Vac. Sci. Technol.* 4: 653-658, 1986.
11. R. W. Dreyfus, invited paper, this meeting.
12. W. R. Creasy and J. T. Brenna, *Chem. Phys.* 126: 453-468, 1988.
13. W. R. Creasy and J. T. Brenna, 1989, in preparation.
14. R. Curl and R. Smalley, *Science* 242: 1017-1022, 1988.
15. H. Kroto, *Science* 242: 1139-1145, 1988.
16. S. Ghaderi, *Proc. 36th ASMS Conf. Spectrom.*, Allied Topics, 1988.
17. M. Pelletier, G. Krier, J. F. Muller, D. Weil, M. Johnston, *Rapid Comm. Mass Spectrom.* 146-150.

A NEW GENERATION OF MICROPROBE: LASER IONIZATION AND FT/ICR MASS SPECTROMETRY

J. F. Muller, M. Pelletier, G. Krier, D. Weil, and J. Campana

The challenge was to combine the selectivity of laser ionization/laser desorption processes with the high mass resolving power and high mass accuracy of Fourier Transform Mass Spectrometry. This problem has its application in surface analysis studies. In 1986 it was shown that the detection limit of a given element, for laser ionization, is wavelength dependent (e.g., Cu, Cd).¹ In such an experiment the incoming photons reionized neutral atoms close to the microplasma crown, giving rise to a two photon mechanism during the single laser pulse.

Instrumentation

A two-stage laser microprobe FTMS was designed and constructed. The first prototype was assembled to evaluate the feasibility of:

- a special dual cell in which the source-side trap plate is part of the manipulator
- having a larger hole in the "conductance limit," in order to have a laser beam going through, so that the beam is oriented perpendicularly to the sample surface
- sample displacement with an x,y,z micro-manipulator, placed in front of a special dual cell, operating in a high magnetic field²

Preliminary results have shown that ion trapping and ion transfer from the source side to the analyzer side, where the pressure is lower, were efficient to provide spectra with high resolving power (e.g., separation of metal Gd^+ and oxide NdO^+ in a rare-earth doped glass; and resolution of a doublet at mass 50 in an alloy to separate ^{50}Ti from ^{50}Cr).³ From this success a second prototype was redrawn with a central laser focalization lens surrounded by inverted Cassegrain optics, which allows sample visualization with the help of a zoom telescope (15-60 \times , Fig. 1). Once the sample is in place, controlled with an endoscope, in front of the source cell (by use of a transfer rod and an external coarse manipulator), the analyzed part of the sample is positioned with the internal micromanipulator (by use of the Peltier effect on memory alloy blades). As different light paths are used with visualization and ionization optics, it is possible to control the laser spot size very easily by adjustment of the lens distance between the two lens groups of the laser beam expander. For a

given laser wavelength (e.g., excimer laser charged with KrF, 249 nm), one can adjust the minimum spot size by moving the central laser lens by means of a pulling rod. The usable laser wavelength scale is from 190 to 360 nm (excimer, Nd/YAG quadrupled, or dye laser after doubled or mixed mode). This design permits laser post-ionization in the microplasma and post-ionization of neutrals and radicals obtained with the defocused laser beam coming from the central optics.

Results

Under standard conditions, the pressure is about 10^{-8} Torr on the source side and about 10^{-9} Torr on the analyzer side, so that transferring the ions from source cell to the analyzer cell is possible by adjustment of the trap plate and conductance limit potentials as a function of the internal energy of detected ions, and by adjustment of the time during which the conductance limit is grounded for a few hundred microseconds). Low- and high-resolution spectra can be obtained with good sensitivity. In this way, in the heterodyne mode at mass 44, a resolution up to 160 000 resolved the interference between $^{88}Sr^{2+}$ and $^{44}Ca^+$ in a ceramic material (Fig. 2) with one laser shot with an excimer laser charged with KrF (249 nm), minimum spot size diameter is 4 μm at low energy (0.5 μJ). The impact localization may be obtained by use of a pilot He/Ne laser. In this case, a small amount of ions formed from the surface layers of silicon wafer are obtained (500 Å titanium/tungsten layer, 1000 Å nickel/iron layer, 500 Å tungsten/titanium layer and 1000 Å silicon dioxide layer on silicon substrate). The corresponding spectrum in direct mode (Fig. 3) shows only the elemental ions of two or three first layers: Ti^+ , W^+ , Fe^+ , and Ni^+ . With the same experimental conditions, highly resolved spectra are obtained in the heterodyne mode (Fig. 3: 65 000 FWHM res at $m/z = 184$, mixed heterodyne mode for the tungsten signal). At high energy values (e.g., 7 μJ), the outer laser diameter is about 15 μm and we detect Si^+ with the other layer's characteristic ions. Consequently, the depth of the laser spot is greater than 2 μm .

In another area of this wafer, without modifying the z position (magnetic field axis) of the surface, defocalized spectra were obtained by changing the beam expander lens distance d (Fig. 1), so that surface desorption can be achieved (intensity $1 < 10^6 W/cm^2$). With a single shot and a defocused laser beam, the second layer of the wafer is reached and the laser crater diameter is about 40 μm . With very important defocalization (laser diameter

J. F. Muller, M. Pelletier, and G. Krier are at the University of Metz (LSMCL), B.P. 794, F-57012 Metz Cédex, France; D. Weil and J. Campana are at Nicolet Corp., Madison, Wis. This work was supported by ANVAR, the Ministère de la Recherche et de l'Enseignement Supérieur, the Ministère de l'Education Nationale, and the Région de Lorraine. M.P. acknowledges the support of his thesis by ELF France.

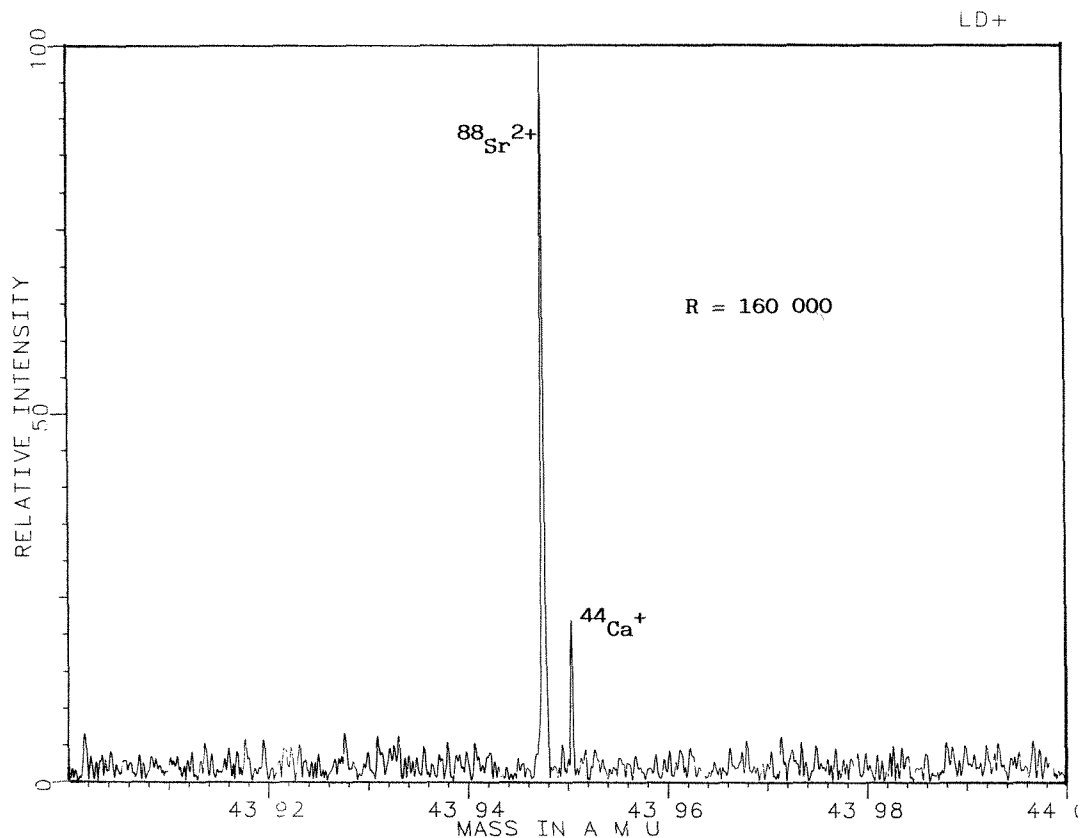


FIG. 2.--High-resolution spectra of ceramic: one excimer laser shot (249 nm).

greater than 150 μm , very small visible damage --just a little bit of crumpling), there is surface contamination, and K^+ is the major ion with TiO^+ (Fig. 4), but elements Fe^+ , Ni^+ of the second layer are also detected. W^+ in the first layer is not detected because of the physical characteristics of tungsten: high vaporization temperature and medium potential ionization (7.98 eV).

In another example, we analyze the different parts of a microcircuit: ceramic substrate, contact pin, and metallic lines (width = 25 μm). The analyzed area is reached either by the internal micromanipulator or the laser beam mirror m (Fig. 1). A gap size of a few microns between two spots is easily obtainable after the transfer rod is blocked. For the metallic lines on the ceramic substrate, a single shot at low energy gives Cr^+ and Cu^+ ions and the laser crater diameter is about 7-8 μm . At very low energy (laser defocusing), only the external surface is analyzed, so that K^+ (external pollution) and Pb^+/Sn^+ (surface contamination from the pin making process) are the major ions when not ejected (Fig. 5). Under these conditions, it was possible to obtain highly resolved spectra (mixed mode) on the lead isotope but the natural isotopic ratio was not correct (204 Pb disappears), doubtless due to an inadequate excitation of the ions (SWR = 1 kHz, not appropriate to this case) and also to the low concentration of this isotope.

In doped glass,⁵ there are 200 ppm Sr and 50 ppm Rb in the direct mode after having ejected the major ions of the glass (range 18 to 55

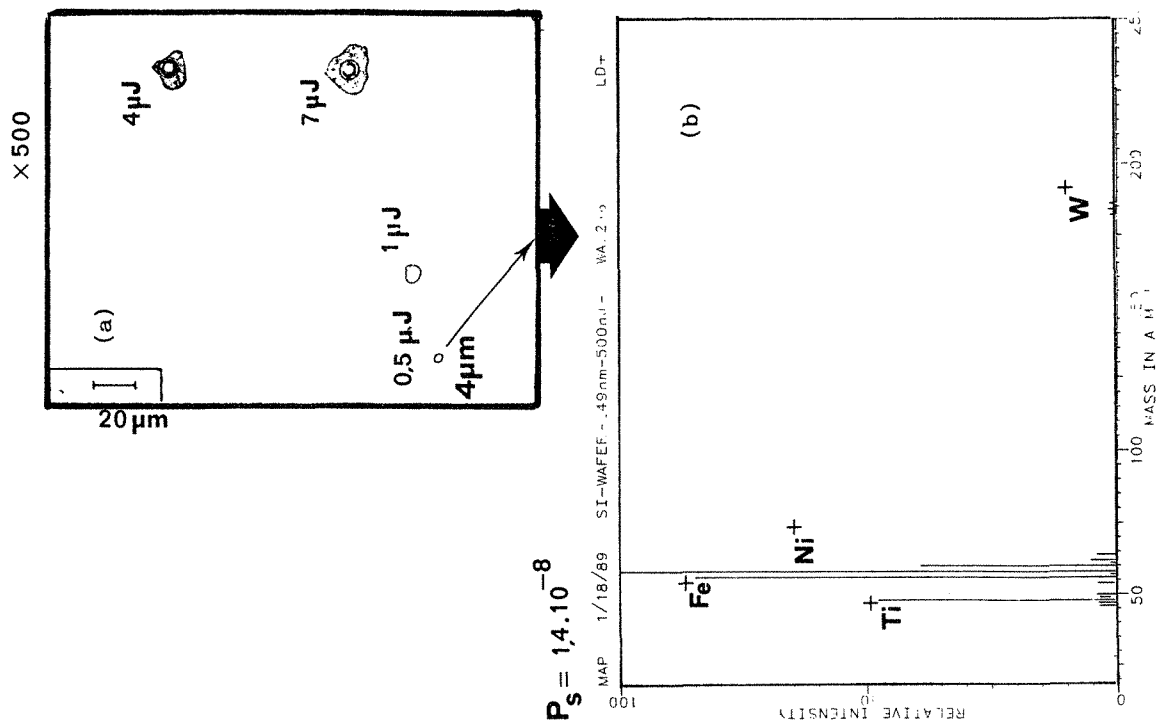
amu), the ratio of Sr/Rb corresponds to their real ratio, without correction by the ionization potential values of these elements. At high laser energy and in the direct mode with extended memory, the mass resolution power approaches 20 000 and the isotopic ratio is respected. If the same area of this glass is analyzed in the heterodyne mode, only the $^{88}\text{Sr}^+$ is detected at high resolution (Fig. 6). It is known that the minimum detection limit is of the order of 100 ions. Taking the ionization ratio of the order of 10^{-4} to 10^{-5} , which is reasonable considering that ionization yield of a glass is lower than that of a metal, we can hope that few hundred ions can be detected in the cell. For rubidium, we are close to the detection limit (1-5 ppm). It clearly appears that when elemental concentration (trace level) is lowered, it becomes more difficult to obtain very high resolution spectra in heterodyne mode with the correct isotope ratio.

Conclusion

The advantages of the Cassegrain optics laser microprobe configuration are:

- sample visualization with a magnification from 60-240 \times , which permits a laser flash or pilot laser location on the surface
- the laser beam perpendicular to the sample surface insures a homogeneous energy distribution and guarantees good and precise defocused laser beam experiments
- laser optics and visualization optics

FIG. 3.--(a) Laser shot on silicon wafer surface; (b) direct mode spectrum of low-energy laser shot (0.5 μJ); (c) mixed mode spectrum of tungsten isotopes after ejection of major ions (low laser energy: 1 μJ).



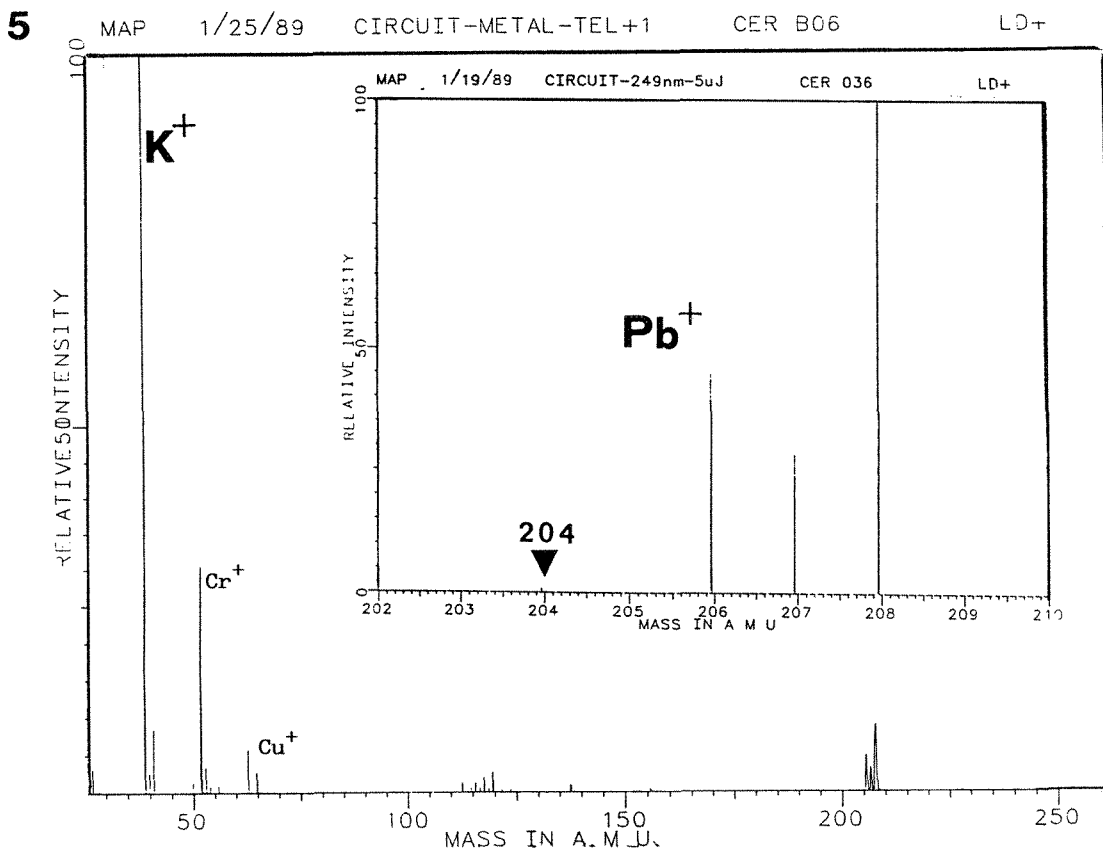
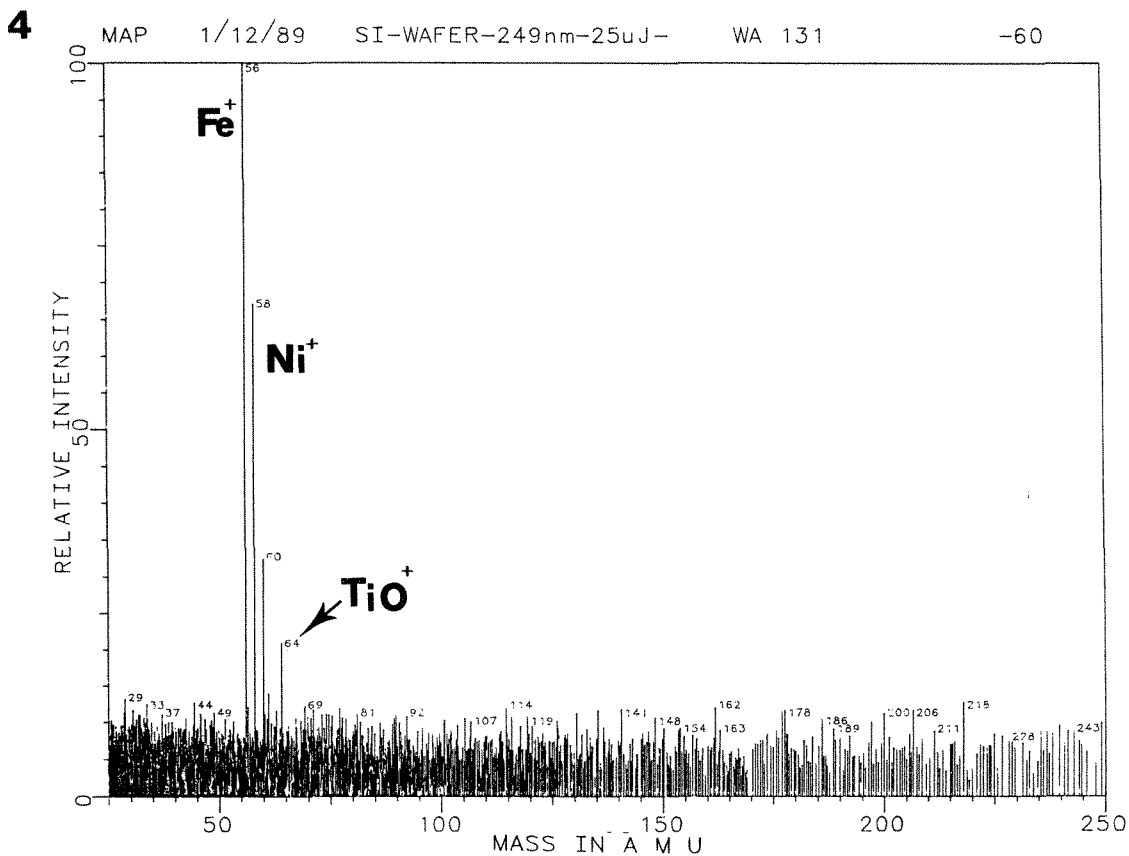


FIG. 4.--Defocalized laser beam (diameter > 150 μ m, very low laser intensity) of silicon wafer.
 FIG. 5.--Spectrum with low laser energy of metallic lines of microcircuit having surface contaminants (K, Pb/Sn).

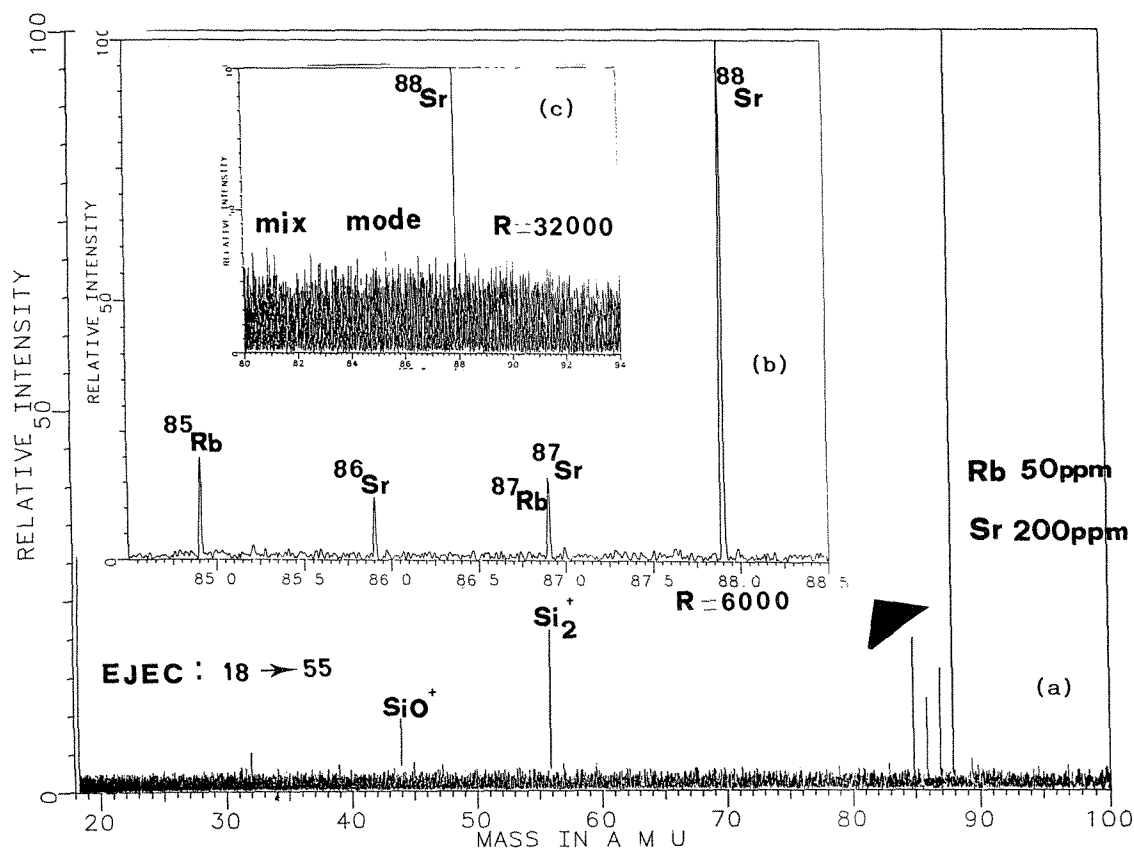


FIG. 6.--(a) Direct mode spectrum of Sr/Rb glass; (b) direct mode spectrum with reduced mass scale with 128K signal storage; (c) mixed mode spectrum of same sample under same laser conditions.

using different light paths permit post-ionization experiments

- the micromanipulator can be replaced by an electron gun which allows liquid and gas analysis introduced with a new inlet system⁶

In summary, this configuration is versatile and combines the selectivity of laser ionization with the selectivity of high mass resolving power of FTMS at reasonable sensitivity.

References

1. F. Verdun, G. Krier, and J. F. Muller, "Increased sensitivity in laser microprobe mass analysis by using resonant two photon ionization processes," *Anal. Chem.* 59: 1383, 1987.
2. J. F. Muller, F. Tollitte, G. Krier, S. Dominiak, A. Eberhardt, and M. Berveiller, French patent 86 18 244.
3. M. Pelletier, G. Krier, J. F. Muller, D. Weil, and M. Johnston, "Laser microprobe Fourier transform mass spectrometry," *Rapid Comm. Mass. Spectrom.* 2: 146, 1988.
4. J. F. Muller, F. Tollitte, G. Krier, and M. Pelletier, French patent 88 09 438.
5. By courtesy of M. Montel and M. Vidal from Clermont-Ferrand University, France.
6. M. Pelletier, F. Tollitte, and F. Muller, French patent 88 16 781.

LASER MICROPROBE MASS SPECTROMETRY FOR THE ANALYSIS OF HIGH VAPOR PRESSURE MATERIALS

Takashi Yamamoto and Akira Ishimori

Laser Microprobe Mass Spectrometry (LAMMS) generally requires the specimen to be under vacuum in the ionization chamber. So it is difficult to analyze high-vapor-pressure materials or materials containing high-vapor-pressure components, because of their abrupt evaporation under high-vacuum conditions. The aim of this work is to obtain mass spectra of specimens which are under low-vacuum conditions.^{1,2} A method in which the chamber for ion extraction under high-vacuum conditions is separated from the chamber for laser ionization of a specimen under low-vacuum conditions is investigated.

Experimental

The experimental apparatus consists of three vacuum chambers (Fig. 1). The first chamber (sample chamber) is used for holding specimens and is filled with gases. The pressure of this sample chamber is controlled in the range from 10^{-3} to 760 Torr arbitrarily. The second chamber (ion collecting chamber) containing ion collection optics is pumped by a 4in. diffusion pump. The pressure of ion collecting chamber is about 2.5×10^{-5} times the pressure of sample chamber. The third vacuum chamber containing the time-of-flight (TOF) mass spectrometer is separately pumped by a turbo molecular pump at a pressure of less than 8×10^{-6} Torr.

The 4th harmonic beam of a Q-switched Nd-YAG laser (wavelength 266 nm, pulse width 10 ns) is focused on the specimen with a spot size of about $16 \mu\text{m}$ through an aperture of $125 \mu\text{m}$ diameter (Fig. 2). The distance between the aperture and the surface of the specimen is approximately 0.2 mm.

Laser-induced ions in the sample chamber pass through the aperture toward the ion collecting chamber. The ions are accelerated and collected by the ion optics, and analyzed with the TOF mass spectrometer. The output of the ion detector is digitized at 8 bits resolution with 10 ns sampling time. The registered signal is displayed on a CRT and is transferred to a microcomputer for data processing such as averaging. The experiments described here were carried out with a power density of about $2.5 \times 10^{10} \text{ W/cm}^2$, and 10 data were averaged for each experiment.

Results

The effect of the pressure increase in the sample chamber on the mass spectrum is investi-

The authors are with Mitsubishi Electric Corp., Central Research Laboratory, Amagasaki, Hyogo, 661 Japan.

gated. Typical TOF signals of ions emitted from an aluminum plate show that the intensity of aluminum ions decreases as the ambient

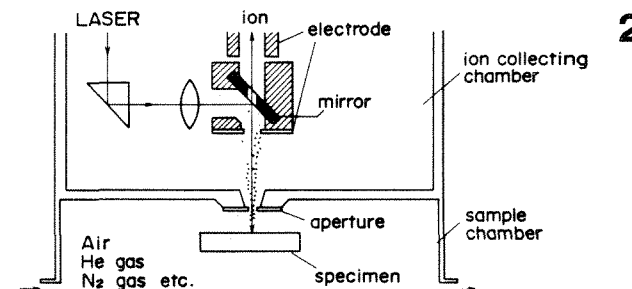
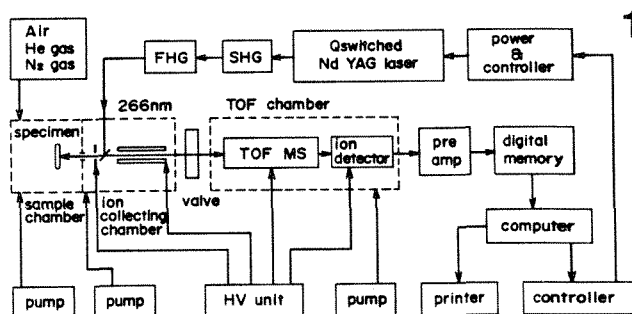


FIG. 1.--Experimental apparatus.
 FIG. 2.--Schematic diagram of laser irradiation.

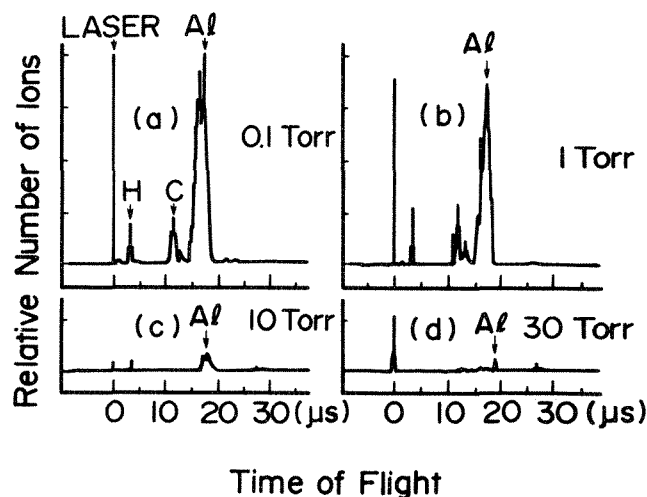


FIG. 3.--Typical TOF signals of aluminum plate at helium pressure of (a) 0.1 Torr, (b) 1 Torr, (c) 10 Torr, (d) 30 Torr.

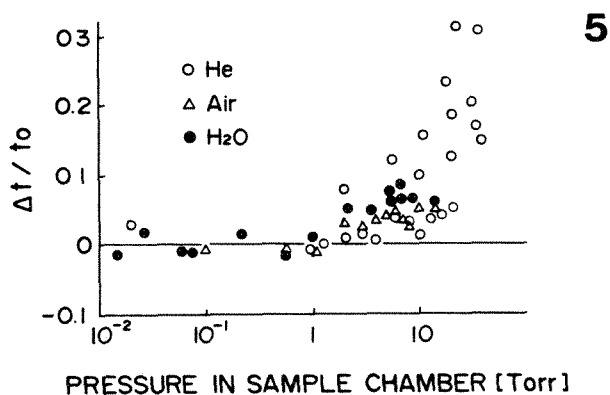
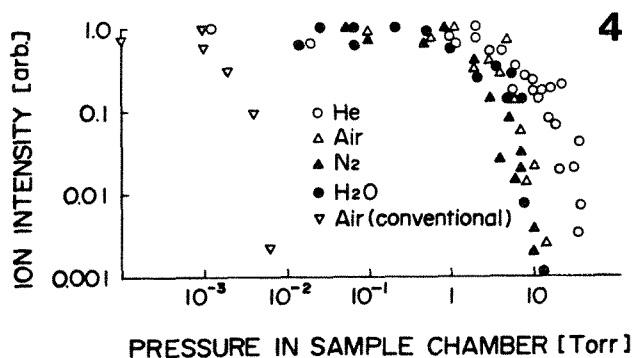


FIG. 4.--Intensity of aluminum ions vs pressure in sample chamber.

FIG. 5.--Time of flight of aluminum ions vs pressure in sample chamber. Increment of time of flight Δt is normalized with average time of flight t_0 at pressure of less than 1 Torr.

pressure of a specimen increases (Fig. 3). In addition, the time of flight of the aluminum ions increases as the ambient pressure of specimen increases.

The relation between the intensity of the aluminum ions and the pressure in the sample chamber is measured (Fig. 4). The ion intensity begins to decrease at a pressure of 2-3 Torr for He gas, N_2 gas, air, and water vapor. The ion intensity at helium pressure of 30 Torr becomes about 10^{-3} times the intensity under high-vacuum conditions. The ion intensity at a pressure of 10 Torr for N_2 gas, air, and water vapor become about 10^{-3} times the intensity under high-vacuum conditions.

Since these decreases of ion intensity are caused by the collisions of the ions with the ambient gases, these results can be explained qualitatively by the value of mean free path of each gas.³ The mean free path of He gas is 14.4×10^{-3} cm at a pressure of 1 Torr at 20 C. The mean free path of N_2 gas, air, and water vapor are 4.9×10^{-3} , 4.9×10^{-3} , and 3.2×10^{-3} cm (1 Torr, 20 C), respectively. Helium gas has the longest mean free path so that the decrease of ion intensity occurs at higher ambient pressure. Another experiment using Xe gas, whose mean free path is about 2.8×10^{-3} cm, shows that the decrease of signal intensity occurs at lower pressure.

In the case of the conventional LAMMS in

which both a specimen and an ion lens are placed in the same chamber, the increase of the ambient pressure of a specimen causes the large decrease of the mean free path in the ion optics. The signal intensity at air pressure of less than 10^{-2} Torr becomes 10^{-3} times the intensity under high-vacuum conditions.

The increase of the ambient pressure of specimens has an effect on the time of flight (Fig. 5). The increase of the time of flight of the aluminum ions appears at a pressure of a few Torr and increases as the ambient pressure of specimen increases. The pressure at which the increase of the time of flight appears agrees with the pressure at which the signal intensity begins to decrease. This degradation of signals is induced by the collision of the ions with the ambient gases along the ion path from the sample chamber to the ion-collecting chamber mainly.

Conclusion

By separating the sample chamber from the ion collecting chamber, we can analyze the specimen at a pressure of 2-3 Torr without degradation of signals. The improvement of an aperture or more powerful differential pumping would make the analysis of the aqueous solution possible with the ambient pressure of specimens maintained above the water's vapor pressure of 18 Torr at 20 C. In addition, the post-ionization in the ion collecting chamber would be expected to make this method more sensitive.^{4,5}

References

1. Reimer Holm et al., "Laser microprobe mass analysis of condensed matter under atmospheric conditions," *Analytical Chemistry* 56: 690, 1984.
2. J. J. Morelli and D. M. Hercules, "Ambient pressure laser mass spectrometry of organophosphorus pesticides on plant tissues," *Analytical Chemistry* 58: 1294, 1986.
3. E. H. Kennard, *Kinetic Theory of Gases*, McGraw-Hill Book Co., 1938, 149.
4. C. H. Becker and K. T. Gillen, "Surface analysis by nonresonant multiphoton ionization of desorbed or sputtered species," *Analytical Chemistry* 56: 1671, 1984.
5. Akira Ishimori et al., "Laser probing under atmospheric conditions for laser ionization mass spectrometry," *Microbeam Analysis--1986*, 473.

ANALYSIS BY LASER MICROPROBE AND RELATED TECHNIQUES

S. P. Thompson, Trevor Dingle, and B. W. Griffiths

Materials microanalysis generally involves irradiating a sample with a fine probe of primary particles or photons. In this, the microprobe approach, the primary beam interacts locally with the sample material producing secondary particles that are in some way characteristic of the analyzed region. Analytical techniques have been developed that exploit the range and variety of the secondary emitted particles. In this paper the discussion is confined to the case where these particles are either secondary ions, or sputtered neutrals that have been subsequently ionized by a photon-induced stepwise excitation process. Consequently, the paper deals with analytical techniques fundamentally destructive of some part of the sample, which is either ablated or sputtered. Developments in this area have been fueled by the recent availability of a variety of types of high-power lasers and inexpensive fast-pulse counting electronics.

A second approach to microanalysis involves the collection of charged secondary particles from a small region of the sample by means of an ion optical microscope. As we shall show later, the secondary-ion collection systems of multipurpose laser-ion microanalysis instruments are ion-optically suitable for microscopy but, at present, this interesting development has not been exploited.

Five types of instrument configuration are discussed. Four depend on whether the primary radiation is composed of focused beams of photons or ions/atoms that ablate either secondary ions or atoms/molecules that are subsequently ionized. The fifth configuration considers an ancillary process in which the analyte is delivered by a pulsed jet of gas or vapor and is subsequently ionized and analyzed. In every case the analysis is carried out by a time-of-flight (TOF) technique; this is a unique aspect of this type of instrument.

The discussion investigates various figures of merit which are defined below.

1. *Absolute sensitivity or detection limit.* This is the lowest detectable concentration of a particular element. This parameter is determined by the physical properties of the interaction between the material and the incident radiation, and the transmission of the mass analyzer including the detector.

2. *Relative sensitivity.* This refers to the changes in sensitivity as a function of mass across the periodic table.

3. *Useful yield.* This is an instrument-

dependent parameter equal to the ratio of the number of secondary ions per incident primary ion multiplied by the instrument transmission. It differs from (1) above in that it is independent of the intensity of the primary radiation.

4. *Abundance sensitivity.* This is defined as the relative concentration of an element (species) of mass $M \pm 1$ that can be detected in the presence of another element of mass M . A practical example of the importance of this parameter occurs when one wishes to detect a low concentration of Al^+ in the presence of a silicon substrate.

5. *Resolution (spatial).* This concerns the determination of one feature of the material from another both laterally and as a function of depth.

6. *Resolution (mass)* $R_m = m/\Delta m$. This is the ability of an instrument to detect a particular mass unambiguously. It is defined as the nominal mass of the peak, divided by the width of the mass peak at half maximum.

7. *Dynamic range.* This is the ability of an instrument to detect a dilute element over a range of concentration.

Laser Ionization Mass Spectrometry (LAMMS)

This technique is suitable for nonvolatile organic and inorganic samples which, in a typical apparatus, may be introduced and positioned opposite the secondary ion extraction electrode (Fig. 1). Sample viewing and irradiation may be accomplished by a light optical system concentric with the extraction electrode.¹ The ion-extraction lens utilizes the

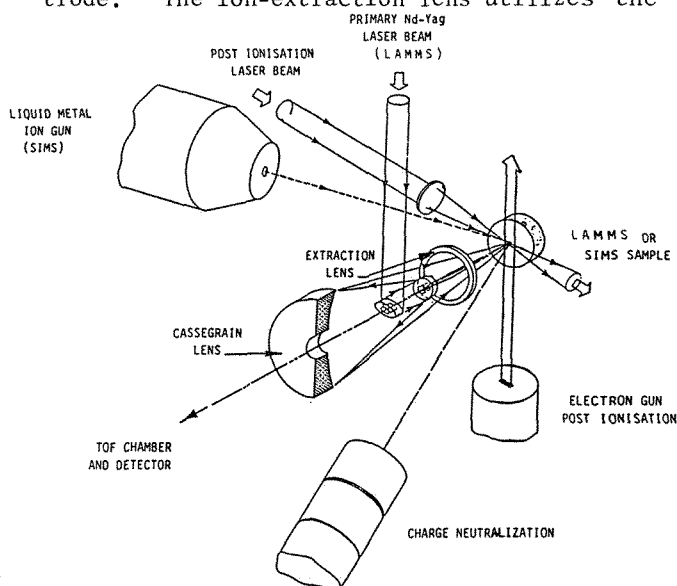


FIG. 1.--Schematic diagram of combined LAMMS and TOF SIMS instrument.

The authors are at Cambridge Mass Spectrometry Ltd, East Bridge House, Saxon Way, Bar Hill, Cambridge, England CB3 8SH.

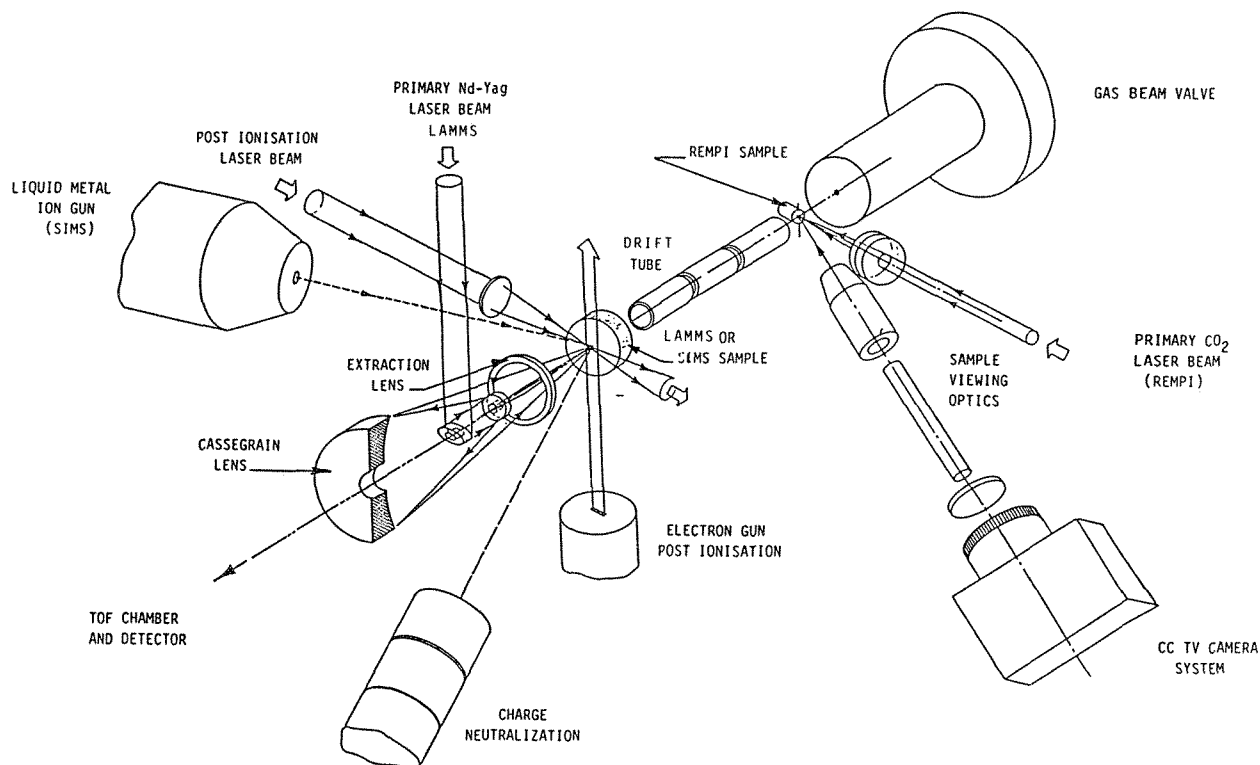


FIG. 2.--Schematic diagram of a combined LAMMS, TOF SIMS, and MPRI INSTRUMENT.

solid angle about the extraction axis; the Cassegrain light lens, which has a much lower spherical aberration coefficient, takes advantage of the solid annulus not required by the extraction beam. Laser irradiation is achieved with a Nd-YAG laser which is frequency quadrupled to a wavelength of 266 nm. The pulse duration of the laser is 5 ns.

Although the analyzed volume in a LAMMS experiment is similar to that in EPMA, LAMMS offers analytical sensitivities approaching 1 ppm. Further advantages are the ability to discriminate isotopes, to mass-analyze all elements with adequate mass resolution, and parallel detection; thus, a complete spectrum may be acquired for every shot, which makes the technique ideal for applications requiring rapid inspection. The accuracy of quantitation is generally poor, except where considerable care is taken to calibrate the instrument with standard samples.² If the calibration is to be successful, it is important to match refractive indices, to use identical laser power and focusing conditions, to site samples in the correct position with respect to the extraction optics, and to set the TOF analyzer to accept the same energy passband.

A typical application of LAMMS concerns the viewing and analysis of submicron polystyrene particles on a semiconductor wafer. The single-shot positive-ion spectrum in Fig. 3 shows ion species at $m/z = 77$ and 91 , assignable to the cyclic ions C_6H_5 and C_7H_7 (tropylium), respectively. Other recognizable peaks, due to the molecular structure of polystyrene, are at $M/z = 103$ ($M - H$) and, to a lesser extent,

$M/L = 105$ ($M + H$). The unassigned peaks can be attributed to the "backbone" of the polystyrene polymer.

Time-of-Flight SIMS

Mass analysis of the ionized plume in a LAMMS instrument is naturally achieved by a time-of-flight technique. Consequently, it is a logical step to extend the performance of the instrument by fitting a suitable pulsed ion gun and charge-neutralizing system. If the ion gun has a fine focusing capability, the result is an imaging static SIMS instrument of unrivaled performance (Fig. 1). Here, one is exploiting the sensitivity of the SIMS technique, not for absolute sensitivity, but to derive valuable chemical information from a few surface monolayers with minimal beam damage.

A recent development that extends the sensitivity of the TOF SIMS technique at the expense of spatial resolution involves the fitting of a broad-beam pulsed neutral source. Using fast neutral particles simplifies charge neutralization and minimizes radiation damage of the sample surface.

An interesting area for future development concerns the suitability of the TOF analyzer as a stigmatic imaging analyzer, capable of transmitting a time-dependent image through the analyzer to be detected on a multichannel plate array, and CCD array. At present no fundamental reason can be found to preclude that, and the advantages to be had in reduced analysis time are considerable.

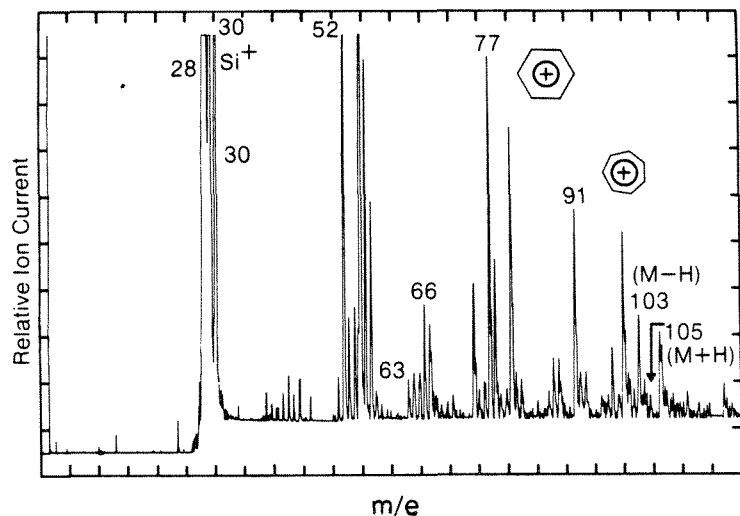


FIG. 3.--Laser microprobe mass spectrum of sub-micron polystyrene sphere on silicon substrate.

Multiphoton Ionization (MPI)

Nonresonant MPI has been applied to time-of-flight instruments fitted with either an ion beam source,³ or a laser probe,⁴ to facilitate the ionization of sputtered or ablated neutral atoms and molecules. A principal aim is to decouple the sputtering and the ionizing processes so that each process may be correctly calibrated and thus yield quantitative information regarding the surface or bulk composition of the target accordingly. Similarly, the separation of material release and ionization, in principle allows organic molecules to be desorbed intact and subsequent fragmentation to be controlled. The guiding philosophy in nonresonant MPI is to ionize neutrals while avoiding selective resonances, so that unknown samples may be analyzed. In contrast resonant MPI, while offering significant advantages in absolute sensitivity, is difficult to operate in a mode that allows an elemental survey. However, the fact remains that unless price is the determining factor, a resonant laser system could in future be used for nonresonant MPI.

Becker et al. typically use a focused excimer laser beam (193 or 248 nm) parallel to and about 1 mm away from the sample surface.³ Peak laser intensity is $\sim 10^{10}$ W/cm² to drive the ionization process to saturation, which is essential if it is desired to achieve uniformity of ionization for different chemical species and consequently similar relative sensitivities across the periodic table.

Figure 2 illustrates how such an instrument configuration could be combined with LAMMS and TOF SIMS. Laser ablation of the sample is achieved by use of a CO₂ laser, and the ablated plume can be made to interact with a supercooled inert gas jet which is delivered from a pulsed gas valve. The ablated plume is carried along the drift tube with the gas jet and is delivered to the ionization station suitably cooled. This cooling improves the selectivity and sensitivity of the resonant MPI process by freezing out the vibrational and rotational spectra, and increasing the population in the

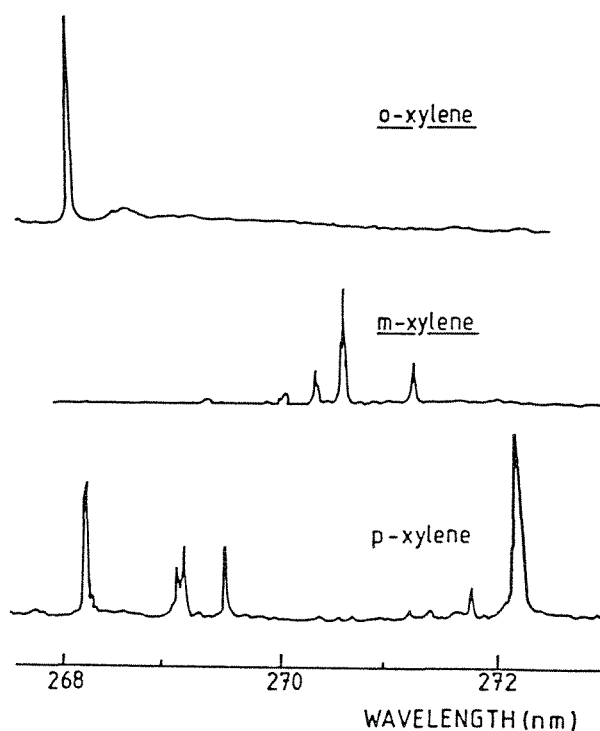


FIG. 4.--Xylene isomers discriminated by resonant multiphoton ionization. (The authors are grateful to Prof. Donovan's group at Edinburgh University for permission to use these data.)

ground state, which is particularly important since it makes the identification of isomers possible.

Figure 4 shows an example of isomer discrimination where conventional mass spectrometric methods fail completely. Xylene isomers delivered to the postionization zone by a supercooled Ar carrier gas are individually identified from their excitation spectra. The absolute detection limit for xylene isomers was 10^{10} xylene molecules per cm³.

Although in this case the ionization was performed by resonant MPI, in general either mode could be used as appropriate. The supersonic gas cooling offers no particular advantage when nonresonant MPI is chosen; however, such a device offers an alternative delivery system for organic solutes.

Conclusion

The points discussed above have been summarized in Table 1; clearly the figures may have to be revised in the light of future developments. An instrument incorporating all the techniques summarized would be versatile in that the analyst could optimize any one of a number of parameters for the particular sample being studied.

Further developments of MPI will inevitably need to incorporate some of the current practices found on high-performance dynamic SIMS instrumentation for control of the ion beam and optimization of the sputtering process,

TABLE 1.--Summary.

	Absolute sensitivity	Relative sensitivity	Useful yield	Abundance sensitivity	Spatial resolution	Mass resolution
LIMS	Few ppm to 100 ppm	Range 1-10 ²		1:10 ⁴	1 μ m in x,y 0.1 μ m in z	500
SIMS	10 ppm \rightarrow 10% ^a < 1 ppm \rightarrow 1% ^b	Range 1-10 ⁵ Range 1-10 ⁵	10 ⁻² -10 ⁻⁷ 10 ⁻² -10 ⁻⁷	1:10 ⁵	2000 Å 1 mm	2000 2000
Nonresonant MPI	1 ppm	1:3		1:10 ⁵	< 1 μ m	2000
Resonant MPI	1 ppb	1:5		1:10 ¹⁰ or better ^c	< 1 μ m	∞ ^d

^aHigh-spatial-resolution mode; exact figure depends on element.

^bBroad-beam mode; exact figure depends on element.

^cAbundance sensitivity has not its usual meaning here; what is intended is to show that the combination of two independent spectrometric techniques yields astonishing values for abundance sensitivity.

^dIn the sense that ionized molecules of identical mass can be discriminated.

for example to reject atoms from the wall of the crater. However, the use of Ar⁺ primary ions will relieve a number of instrumental artifacts that result from reactive primary ion beams.

References

1. T. Dingle et al., *Microbeam Analysis*--1984, 23-26.
2. M. J. Southon et al., *Microbeam Analysis*--1985, 310-314.
3. C. H. Becker and K. T. Gillen, *Proc. SIMS V*, Springer Verlag, 1985, 85-89.
4. Odom et al., private conversation.

LASER POSTIONIZATION TIME-OF-FLIGHT MASS SPECTROMETRY WITH A LASER-ABLATION CARRIER-GAS TRANSPORT SOURCE

Mark Nicholas, J. G. Pruett, G. J. Havrilla, and S. R. Bryan

In previously reported quantitative elemental analysis by laser ablation/laser postionization, the signal one gets at any one time depends on the time delay between ablation and ionization that one selects.¹ To account completely for this effect, one must integrate over all ablation/ionization delays. This procedure complicates laser ablation/laser postionization analysis. We have tried to eliminate this concern by homogenizing the ablated material with a pulse of rare gas before admitting the material to the ionization region of the mass spectrometer.

We have investigated the use of rare-gas-moderated ablation for elemental analysis of glasses, refractory ceramics, and tool steels. Gas-moderated ablation consists of the vaporization of a target in a gas-filled ablation cell followed by supersonic expansion of the resulting mixture toward a mass spectrometer. We used nonresonant photoionization by a focused excimer in hopes of obtaining near-uniform ionization of the effluent from the sample cell.

Experimental

A source originally designed to synthesize naked inorganic clusters was modified to provide primarily atomic species for compositional analysis. The source consists of a dead volume of 0.24 cm³ between a pulsed gas valve and a 4mm-diameter port to a vacuum system. The sample is placed in the dead volume and irradiated through a window by the focused fundamental, doubled, or tripled output of a Nd:YAG laser, which effects the ablation. The ablation laser runs at 10 Hz and is continuously moved over the sample by use of a rotating Dove prism.

The pulsed valve delivers a 100 μ s burst of helium to the sample surface. The ablation laser is timed to irradiate the sample some time within 1 ms after the helium valve begins to open. The resulting vaporization products and helium then flow into a chamber pumped by a 10in. diffusion pump (2300 l/s) over a period of about 500 μ s. The flow is aimed toward a 0.5mm-diameter skimmer, the opening of which is located 10.0 cm from the source exit. This is the entrance into the ionization region of a time-of-flight mass spectrometer. The ionization point is 16.4 cm from the source exit. The mass spectrometer is pumped by a turbomolecular pump (150 l/sec). An ArF excimer laser

operating at 193 nm with a 100mJ, 20ns pulse is triggered at variable delay times after the ablation laser to allow for travel time between the source and the ionization region. The excimer laser is focused with a 76mm focal length lens delivering 90% of the energy to a rectangular 0.15 \times 0.7mm spot. This lens is mounted on an XYZ translatable lens mount and can be moved to optimize overlap between the molecular beam and the laser beam waist.

A time-of-flight mass spectrum is obtained by timing of the arrival of ions at a microchannel plate detector following the ionizing laser pulse. Spectra are accumulated on a digital oscilloscope with 10ns resolution, averaged, and transferred to a computer for mass analysis and display.

Peaks are then integrated and area ratios calculated and compared with known atomic ratios.

Results

A target of sintered SiC was analyzed to determine whether ablation, delivery, and ionization would maintain the stoichiometry of the material. The ablation laser beam consisted of both 532nm and 1064nm light. At high photoionization laser intensities, C⁺ and Si⁺ account for 84% of the material (Fig. 1), with the remaining 16% of the C and Si atoms contained in molecular species. (The contribution to the Si/C area ratio from C and Si present in these molecular species was included in the Si/C area ratio calculation.)

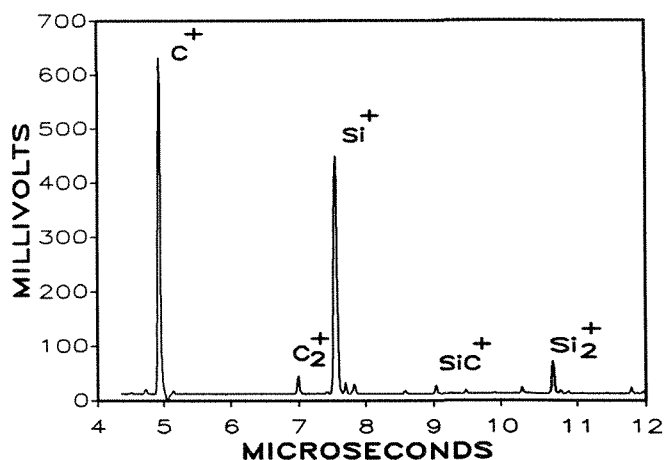


FIG. 1.--Mass spectrum produced by Nd:YAG laser ablation of SiC in helium pulse followed 180 μ s later by photoionization in focused ArF excimer beam.

The authors are with BP Research, Warrensville Research Center, 4440 Warrensville Center Road, Cleveland, OH 44128-2837.

The Si/C area ratio is rather constant over several hundred microseconds (Table 1), as was hoped, and its value at the time (180 μ s) of peak signal intensity is within 10% of the actual atomic ratio. These same observations were made when the experiment was repeated with a 355nm ablation beam.

TABLE 1.--Tabulation of the Si/C area ratio and signal intensity, as represented by $^{12}\text{C}^+$ intensity, versus ablation/ionization delay.

ABLATION TO IONIZATION DELAY (μ sec)	Si/C AREA RATIO	$^{12}\text{C}^+$ INTENSITY (arbitrary units)
110	0.82	5.1
130	1.30	6.0
150	1.46	13.1
180	1.04	28.8
350	1.24	9.1
400	1.16	2.1

In addition, other materials such as tool steel standards, glass standards, and ZnSe have been analyzed with varying degrees of success in obtaining uniform sensitivity. We suspect that some of these nonuniformities are due to the failure to saturate both the photofragmentation of molecular species and the photoionization of atomic species.

Conclusions

These preliminary results demonstrate the feasibility of using gas-moderated laser ablation/laser postionization for quantitative determination of nonconducting samples that would be difficult by ion-beam-based methods. Complexities of ablation, photofragmentation, and photoionization need to be sorted out to improve the technique.

References

1. B. Schueler and R. W. Odom, *J. Appl. Phys.* 61: 4652, 1987.

LAMMS: Applications in Materials Science

INDUSTRIAL APPLICATIONS OF LAMMA

Reimer Holm and Dieter Holtkamp

In this paper results from LAMMA experiments on a variety of technical products are presented. The examples cover the following LAMMA applications:

- LAMMA as a versatile microprobe both for inorganic and for organic samples
- LAMMA as a sensitive mass spectrometric method with "soft ionization"
- LAMMA as a technique for surface analysis

Emphasis is put on the organic microprobe capability of the LAMMA instrument, especially with respect to bulk samples.

Experimental

A LAMMA 1000 was used for all experiments. Instrumental details are omitted because another paper in this volume presents an overview of experimental techniques for laser microprobe mass spectrometry.¹ The standard sample holder² can be replaced by a heating/cooling stage and sample transfer lock for analysis of high-vapor-pressure compounds and frozen samples. Furthermore, a transmission illumination system (optionally with polarized light) for microscopic observation and subsequent analysis of thin sections can be incorporated. The laser power density and laser focus were adjusted according to the sample and kind of information required (elemental or molecular). All spectra were obtained from single laser shots.

Results

1. *LAMMA as an Inorganic Microprobe.* If an elemental analysis of bulk samples is required, the LAMMA 1000 has to compete with, for example, x-ray microanalysis and Auger electron spectroscopy (micro-AES). Although quantification is easier with the latter methods, LAMMA is generally more sensitive for all elements (including Li and B, which are not detected by x-ray microanalysis). Furthermore, the color contrast in the light microscope can be used to differentiate between particles with similar shapes, as demonstrated in Fig. 1, which shows LAMMA spectra from four different-colored types of particles in an enamel powder.³ Although the energy-dispersive x-ray spectra of the various particle types were also clearly different, the LAMMA analysis was faster, because it was impossible to distinguish between the different types of practically identical looking particles in the SEM image.

Figure 2 shows islands on the surface of a

The authors are with Bayer AG, Central Research and Development, 5090 Leverkusen, Federal Republic of Germany.

stainless steel annealed under unfavorable conditions.³ The size of these particles was such that good light scattering was obtained, resulting in some loss of gloss. The Auger spectra of the islands showed accumulations of Cr, Mn, and Si (as oxides) with a thickness of $\sim 0.1 \mu\text{m}$ (calculated from the sputter depth profile), whereas the thickness of the oxide layer in the "normal" regions was 10 nm at most. Although individual islands were not resolved in the light microscope, it was easy to find locations where the LAMMA spectra fit the Auger sputter profiles, because work with the LAMMA can be conducted at a very high speed. LAMMA provided the additional information that B and N had accumulated at all parts of the surface. If a particular particle was bombarded a second time, the intensities of Si and Mn were drastically reduced, which showed that in this experiment the information depth was of the order of the particle thickness.

2. *LAMMA as an Organic Microprobe.* Depending on the experimental conditions used in the synthesis of a certain organic compound, particles of up to three different kinds were found in different proportions (Fig. 3). As the particles were insoluble and thermally unstable, chromatographic methods could not be used to distinguish among the individual components; the particle types were therefore characterized by LAMMA. Figure 3 shows the negative mass spectra of the three types of particles. Types A and C were evidently different crystal modifications of the same organic compound, since the corresponding spectra contained the same characteristic lines. Type B was identified as the product of a side reaction, because the fragmentation pattern presented in Fig. 3 is identical with the fragmentation pattern of the byproduct (not shown), except for the signal at $m/z = 110$ atomic mass units (amu). Several ions characteristic of A were sometimes found in the positive spectra of type B. This result, together with the detection of 110^- , indicates that type B contained some portions of compound A.

Figure 4 shows a light micrograph of a rubber compound in which an ingredient was poorly dispersed and had therefore formed agglomerates. Energy-dispersive x-ray microanalysis of the particles provided merely a sulfur signal; i.e., the agglomerates were either free sulfur or another sulfur-containing ingredient (e.g., an accelerator). LAMMA made a clear identification possible, as may be seen by comparing the negative particle spectrum (below) with that of the accelerator dibenzo-

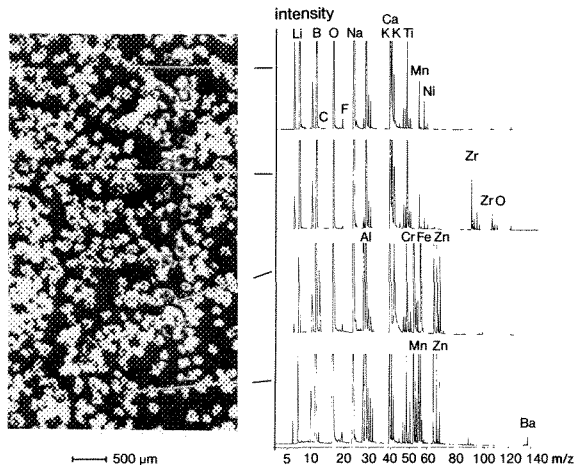
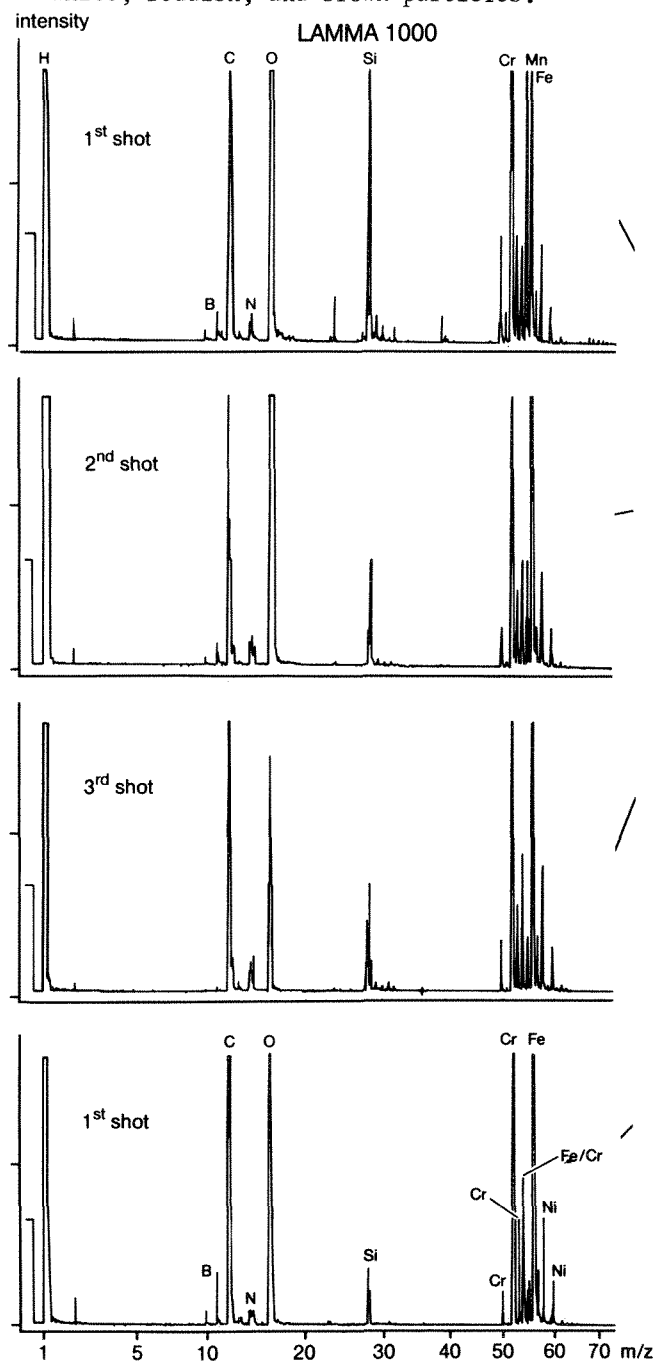


FIG. 1.--LAMMA spectra of an enamel powder. Spectra belong (from top to bottom) to clear, white, reddish, and brown particles.



thiazyl disulphide (above): in both spectra the same characteristic fragments occur, in addition to the deprotonated molecular ion at 331 amu. A similar agreement was observed in the positive LAMMA spectra.

The following example demonstrates that the use of transmission illumination with polarized light greatly extends the applications of the LAMMA 1000. Figure 5 shows a light micrograph of a thin section in the vicinity of a defect in a surface coating. The defect was caused by a structure about 10 μm in diameter which was not quite at the surface and therefore not detectable with the conventional instrument configuration. The LAMMA analysis of the thin section enabled the defect to be identified as a polyester fiber, as the positive spectrum showed the same lines as a compact polyethylene terephthalate (PETP) sample (Fig. 5); a similar agreement was obtained for

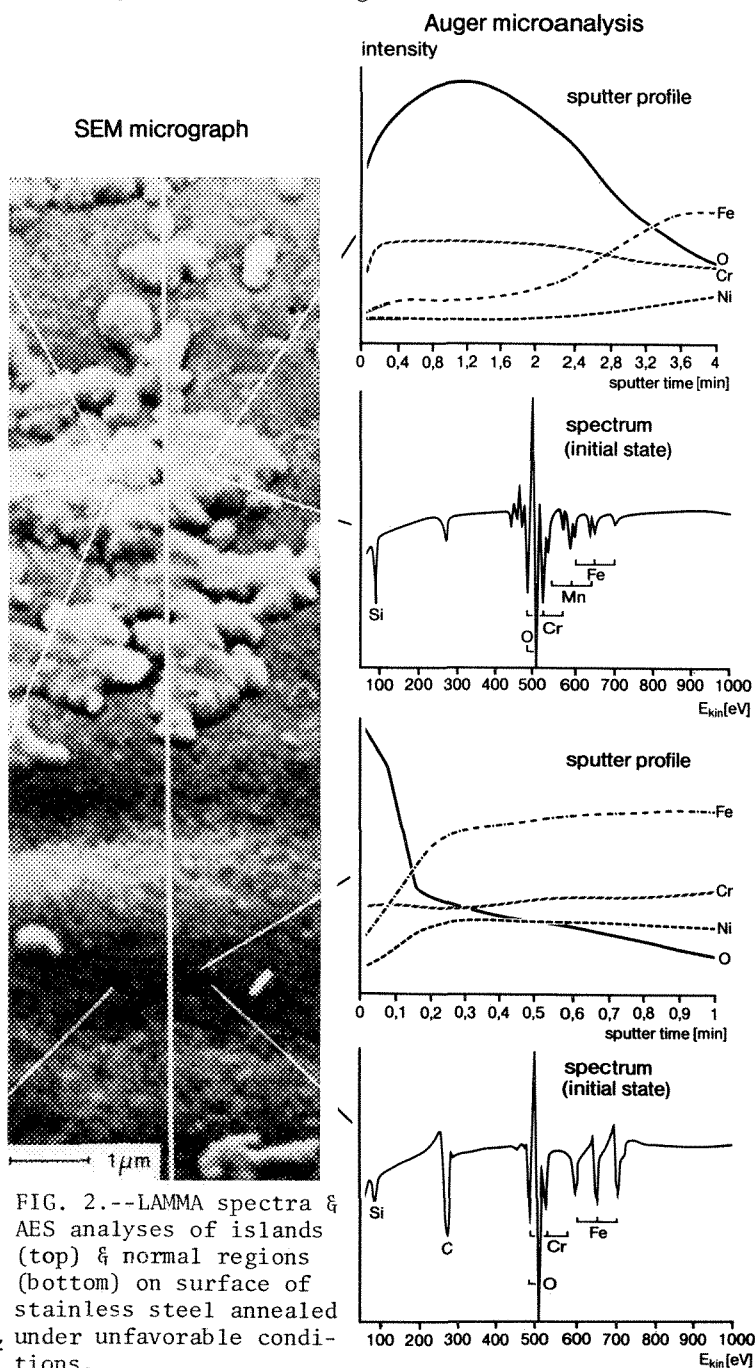


FIG. 2.--LAMMA spectra & AES analyses of islands (top) & normal regions (bottom) on surface of stainless steel annealed under unfavorable conditions.

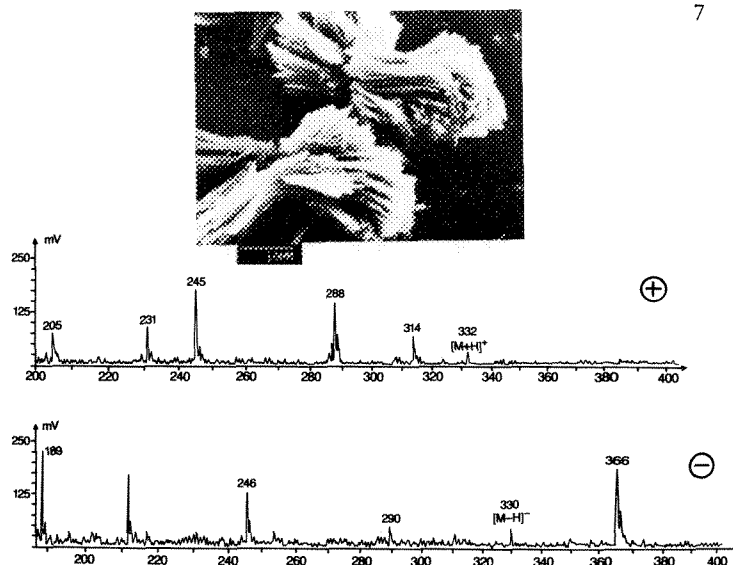
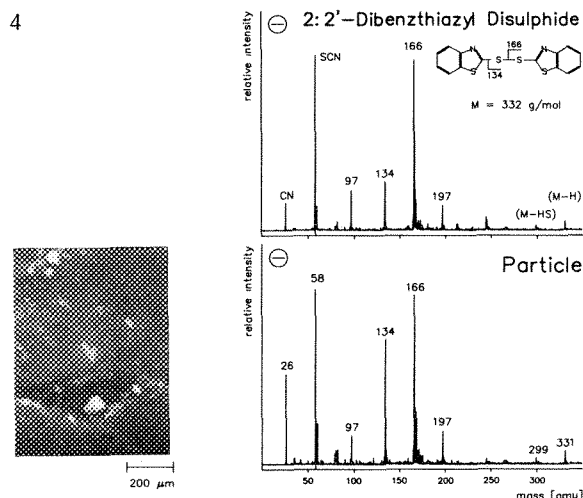
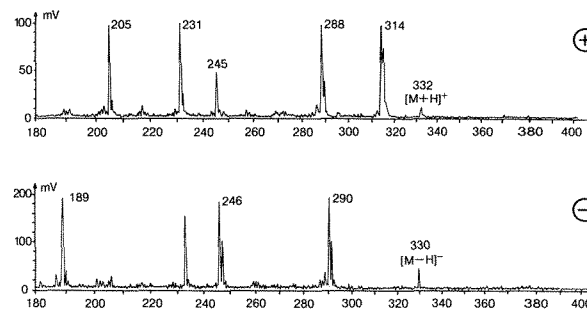
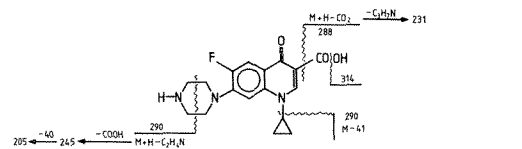
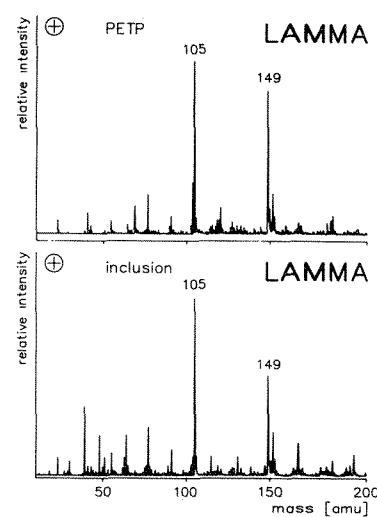
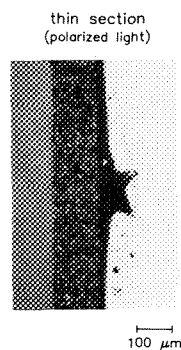
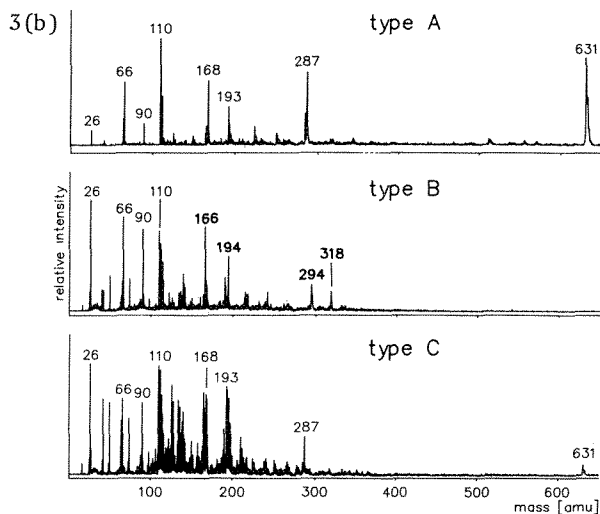
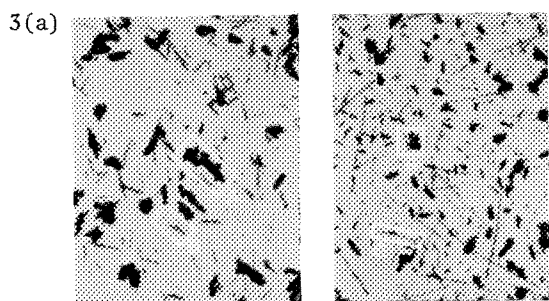


FIG. 3.--Bright-field micrograph of crystallites obtained during synthesis of certain organic compound and negative LAMMA spectra of various particle types which differed both in shape and color.

FIG. 4.--LAMMA analysis of agglomerates in rubber sample (bottom) and comparison with reference compound (top).

FIG. 5.--Bright-field micrograph of an inclusion in paint coating (polarized light). Positive LAMMA spectra of inclusion (bottom) and comparison with polyethylene terephthalate (top).

FIG. 6.--LAMMA reference spectra of ciprofloxacin (powder).

FIG. 7.--LAMMA spectra of crystals from human urine sample after ciprofloxacin administration.

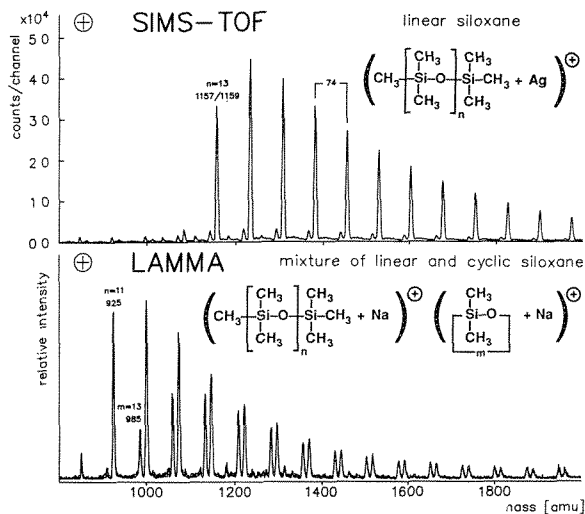


FIG. 8.--Detection of siloxane oligomers with SIMS-TOF and LAMMA. Samples were dissolved in toluene and dried onto etched Ag surface (SIMS-TOF) or Al substrate that had previously been covered with fine NaCl crystals (LAMMA).

the negative LAMMA spectra.

LAMMA is a very powerful method if discrete organic particles, e.g., filtration residues from solutions, have to be analyzed. In a pharmacokinetic study on the antibiotic ciprofloxacin the influence of urinary pH on crystalluria was examined.⁴ If an unusually high dose of the pharmaceutical was given in combination with a diet leading to alkaline urine, crystallites were observed in the urine of some volunteers. It could be possible that the pharmaceutical had been precipitated because of its low solubility product. However, the particles could also be crystals of certain metabolites which may possibly be toxic. As x-ray microanalysis and UV microspectral photometry failed to differentiate between ciprofloxacin and its derivatives, the LAMMA spectra of the crystals were compared with those of various reference compounds. Figures 6 and 7 demonstrate that both the positive and the negative spectra of the crystals were very similar to those of ciprofloxacin. It could be therefore concluded that the crystals consisted mainly of ciprofloxacin (probably as an Mg salt, which could explain both the signal $(M+Cl)^-$ at 366 amu and the ion Mg^+ in the positive spectrum), and that no other organic compound contributed to the signal, except for a certain amount of the metabolite sulfociprofloxacin, which gave nearly the same fragmentation pattern.

3. *LAMMA as a Sensitive Mass Spectrometer with "Soft Ionization."* In problems requiring mass-spectrometric investigations of thermally unstable organic compounds, LAMMA can give results similar to those of FAB or SIMS-TOF. Figure 8 compares LAMMA with SIMS-TOF in the case of siloxane oligomers. (The SIMS-TOF spectrum was recorded at the University of Munster.) In both spectra the linear siloxane oligomers appear as cationized molecular ions;

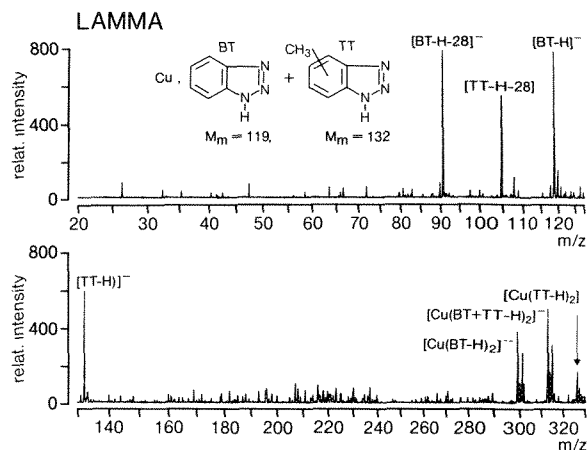


FIG. 9.--Negative LAMMA spectra of Cu after 1 min immersion in drinking water containing 5 mg/l benzotriazole (BT) and 5 mg/l tolyl-triazole (TT).

however, the intensity distributions are different. The LAMMA spectrum shows in addition a series shifted 14 amu, which is attributable to cationized cyclic oligomers. They were admixed to the linear siloxanes in the ratio 1:1 (by weight), which shows that the ionization probabilities are approximately equal for the two species. As a corresponding series also appears in the SIMS-TOF spectrum, it may be concluded that these ions are not fragments but likewise cyclic oligomers (contained in the sample); this conclusion was recently confirmed by high-resolution SIMS-TOF experiments.⁵ This example shows that LAMMA (and also SIMS-TOF) supply more information than that obtainable by gas chromatography, gel permeation chromatography, and high pressure liquid chromatography (e.g., identification of terminal groups in oligomers). However, the samples must be prepared from a suitable solution because for compact polymers only fragments in the mass range up to about 500 amu are found.

4. *LAMMA as a Technique for Surface Analysis.* Although the information depth of LAMMA is about 10-100 nm and thus considerably greater than for AES, ESCA, and SIMS, it is nevertheless possible to detect a few molecular layers of an organic adsorbate--provided that the ionization probability is sufficiently high. This feature can be seen in Fig. 9:⁶ a copper sample was immersed for 1 min in water containing the corrosion inhibitors benzotriazole and tolyltriazole in the ratio 1:1. Whereas intense protonated molecular ions were detected in the case of the pure substances (spectra not shown), these ions were not found on the copper surface. The negative spectrum (Fig. 9) contained not only the deprotonated molecular ions and characteristic fragments (formed through loss of N_2), but also Cu clus-

ters, each of which contained two deprotonated inhibitor molecules. The intensities of the signals of the two inhibitors are comparable, which points to the existence of the same surface concentrations; it could therefore be concluded that there was no preferential adsorption of one of the inhibitors. On the one hand this result confirmed the model concept of a "quasi-polymeric chain" of monovalent Cu and deprotonated inhibitor molecules. On the other hand this example demonstrates how sensitive LAMMA is in favorable cases: if a surface concentration of 10^{15} inhibitor molecules per molecular layer and square centimeter is assumed and if one takes into consideration that the layers had a maximum thickness of 5 molecular layers (determined from AES depth profiles), then there were approximately 4×10^9 molecules within the focal point of the laser beam (defocused, $\sim 10 \mu\text{m}$ in diameter). These molecules were detectable as intact molecular ions with an excellent signal-background ratio.

Conclusions

In an industrial environment with a variety of technical products, the organic microprobe capability is the most important feature of LAMMA, as no other method has had this capability so far. Therefore LAMMA has been combined with light microscopy, SEM, and TEM in a micro-analytical laboratory that has proved very effective, as many problems that show the ne-

cessity of organic microanalysis remain after previous light microscopic or SEM investigations.

As far as the other LAMMA applications are concerned, there is some competition with other mass-spectroemtric or surface-sensitive techniques usually used under routine operating conditions. However, these methods may have drawbacks when special problems have to be solved. In such cases the complementary information from a LAMMA experiment, especially the negative mass spectrum, can be very valuable.

References

1. R. Gijbels, "Overview of LAMMS techniques," this volume.
2. H. J. Heinen et al., "LAMMA 1000: A new laser microprobe mass analyzer for bulk samples," *Int. J. Mass Spectrom. Ion Phys.* 47: 19, 1983.
3. H. J. Heinen and R. Holm, "Recent developments with the laser microprobe mass analyzer (LAMMA)," *SEM/1984 III*, 1129.
4. S. B. Thorsteinsson et al., "Crystal-luria and ciprofloxacin: Influence of urinary pH and hydration," *Chemotherapy* 32: 408, 1986.
5. E. Niehuis and A. Benninghoven (in preparation).
6. H. Grafen et al., "Surface- and micro-analytical methods in the investigation of inhibitors," *Werkst. Korros.* 38: 659, 1987.

INVESTIGATIONS ON THE IDENTIFICATION AND DISCRIMINATION OF INDIGO-DYED COTTON FIBERS BY MEANS OF A LASER MICROPROBE MASS ANALYZER

P. F. Schmidt and Bernd Brinkmann

Light microscopical and microspectrophotometric methods are routinely used for the discrimination of colored fibers of textiles. Among the criteria for the identification and discrimination of cotton fibers are dye-stuff, intensity of coloring, morphological characteristics of the fibers and specific fluorescence;^{1,2} but with reference to indigo-dyed cotton fibers (jeans fibers), the application of these methods has shown that jeans fibers of identical coloring are very often indiscernible. The aim of these investigations is to show that laser microprobe mass analysis (LAMMA) can contribute further criteria for a more exact discrimination of indigo-dyed fibers. The LAMMA method is based on the mass spectrometric detection of atomic and molecular ions produced by laser-beam-induced evaporation of fiber matter. The results presented were obtained by investigations with a LAMMA 500.

Identification of the Dye-stuff

LAMMA analyses of differently dyed jeans fibers have shown that LAMMA can identify the specific dye, as can be demonstrated by one typical example. The dye-stuff of a specific jeans fiber can be identified from its spectrum by means of its mass line, $m/e = 263$ (Fig. 1). This mass line indicates the molecule mass line of the dye indigo, $M + H = 263$. The same mass line can be found by the analysis of the dye-stuff indigo as reference. This identification can be the result of one single analysis, carried out within seconds.

Detection of Color Soiling

Due to the high detection sensitivity of LAMMA, even small concentrations of a dye-stuff can be detected. In special cases LAMMA spectra of jeans fibers can show the mass lines of indigo as well as mass lines of unknown origin. Figure 2 shows one example. In this spectrum the mass lines of the unknown dye are labeled with M and indicated by arrows (Fig. 2a). LAMMA investigations applied to other textiles of an accused person demonstrated that spectra from red-dyed cotton fibers of a shirt showed the same mass lines M (Fig. 2b). Later it could be reconstructed that the analyzed jeans fibers originated from jeans trousers that were washed together with the red shirt.

Analogous results can be obtained in the analysis of white fibers, where the spectra can

also show mass lines due to color soiling.

Discrimination of Jeans Fibers by the Detection of a Fabric Softener

The analysis of the fibers of jeans trousers very often show fingerprint spectra of a fabric softener used after washing. Figure 3 shows the spectra of two different fabric softeners, WS 1 and WS 2. The mass lines indicated were used as fingerprints for the identification of the specific fabric softener.

The capability of LAMMA in the discrimination of indigo-dyed jeans fibers by the identification of fabric softeners may be demonstrated by the following case work. During a capital crime jeans fiber were transferred. By microspectrophotometric measurements alone, a similarity in the dye-stuff (indigo) could be determined between jeans fibers of the trousers of a defendant and jeans fibers on the body of the victim. Because the victim also wore indigo-dyed jeans, these fibers were without any significance.

By means of LAMMA the results with reference to the indigo dye-stuff indigo could be ascertained. In Fig. 4 all showed that the jeans fibers on the body of the victim must have originated from two different jeans fabrics: one group of fibers showed the fabric softener WS 1 (Fig. 4a); another, WS 2 (Fig. 4b). The analysis of jeans fibers of the defendant's trousers showed that for these jeans fabric softener WS 1 had been used after washing (Fig. 4c), whereas the jeans trousers of the victim contained fabric softener WS 2.

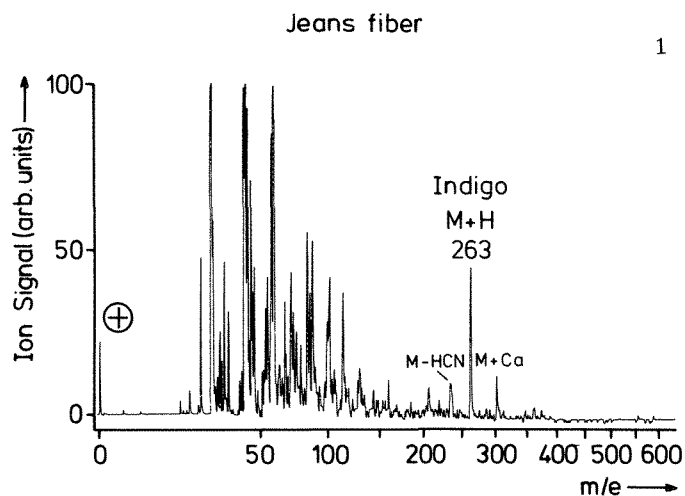
Discussion

The results presented have shown possibilities for the identification and discrimination of indigo-dyed cotton fibers. In general, the detection of the dye indigo presents no difficulties. One advantage of LAMMA is the high detection sensitivity, which enables the analysis of color soiling produced by contamination with dyes from other textiles during a joint washing process. Because fibers with color soiling are very rare, these fibers would have a high specificity.

A further criterion for the discrimination of fibers is given by the adherence of fabric softener. The specificity of fibers with fabric softener depends on the proportion of its distribution with fabric softener in a given area.

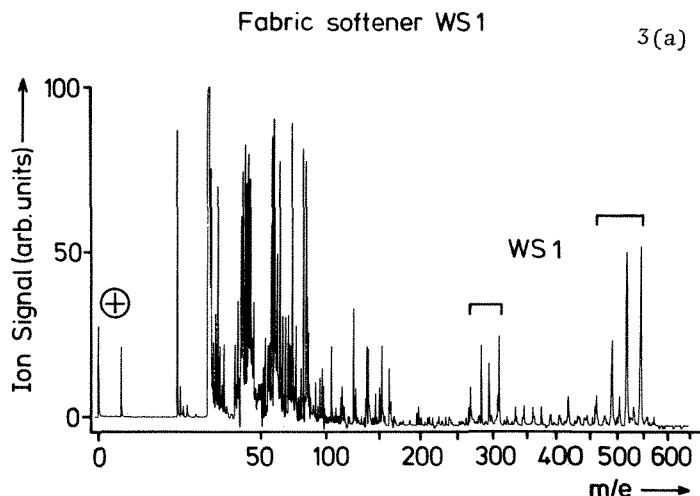
LAMMA analysis takes only milliseconds so that significant results can be obtained within a very short time. Also, the amount

P. F. Schmidt is at the Institut für Medizinische Physik and Bernd Brinkmann is at the Institut für Rechtsmedizin, Universität Münster, Federal Republic of Germany.



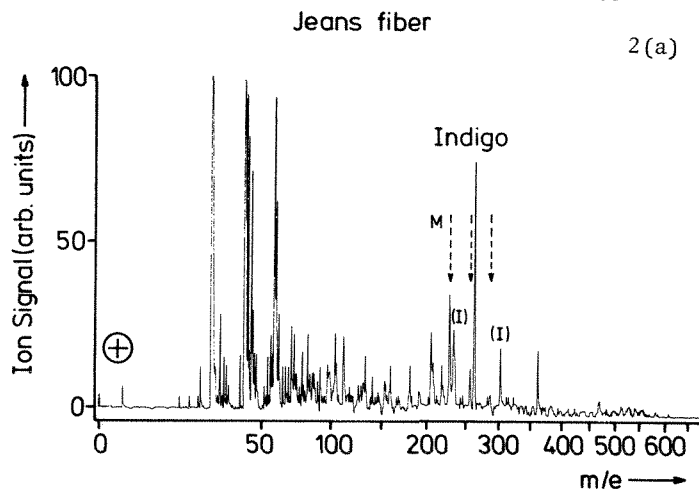
Jeans fiber

1



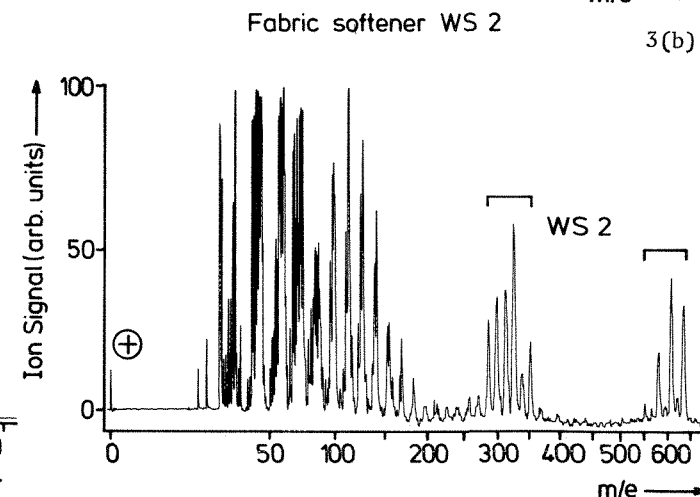
Fabric softener WS1

3(a)



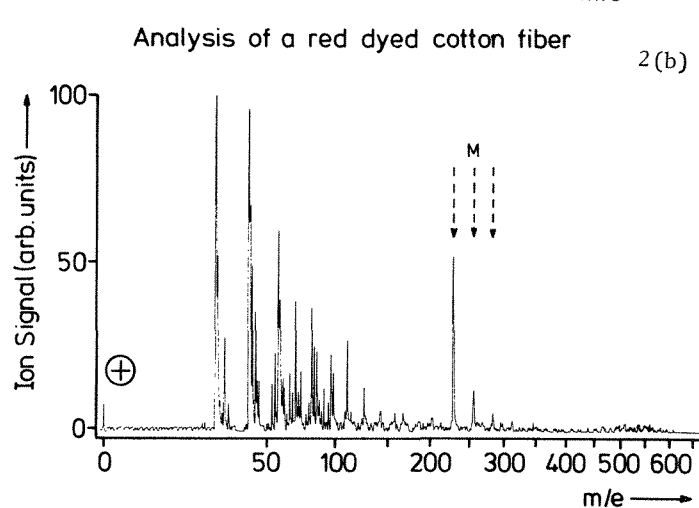
Jeans fiber

2(a)



Fabric softener WS2

3(b)



Analysis of a red dyed cotton fiber

2(b)

FIG. 3.--Spectrum of fabric softeners: (a) WS 1, (b) WS 2.

FIG. 1.--LAMMA analysis of jeans fiber: mass line $m/e = 263$ demonstrates the dye-stuff indigo (molecular weight 262).

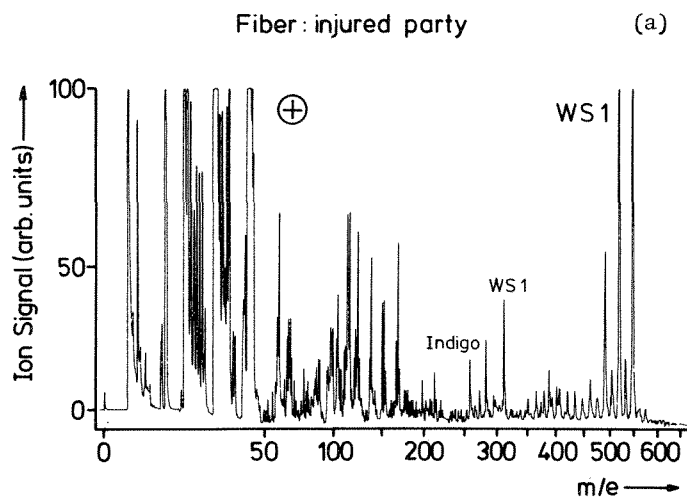
FIG. 2.--(a) LAMMA spectrum of jeans fiber demonstrating mass lines originated by indigo (I) and mass lines of unknown dye-stuff M (arrows); (b) LAMMA spectrum of red-dyed cotton fiber from shirt, demonstrating mass lines of red dye-stuff.

of material necessary for one analysis is of the order of 10^{-13} g. That means that only small areas of a fiber are required for the analyses, so that the rest of the fiber can be used for other investigations.

Normally the fibers are secured by adhesive tapes, so that control measurements of the adhesive are also necessary, but in general no interference of mass lines originating from the adhesive with mass lines of interest are observed. However, the adhesive can influence the intensity of the mass lines because the adhering fabric softener may become partly detached.

Very important is the moment of securing the clothes, which should not be washed between the time of the transfer of fibers and the time the clothes were secured.

To summarize, the analytical information obtained by LAMMA measurements can give additional criteria for the identification and discrimination of indigo-dyed cotton fibers.



References

1. P. Martin, "Möglichkeiten, Grenzen und Wert der vergleichenden Textilanalyse," *Arch. f. Krim.* 161: 47-58, 1978.
2. K. Jenne, "Eine neue rechnergestützte Möglichkeit zur Absicherung des Beweiswertes textiler Faserspuren," *Arch. f. Krim.* 172: 32-40, 1983.

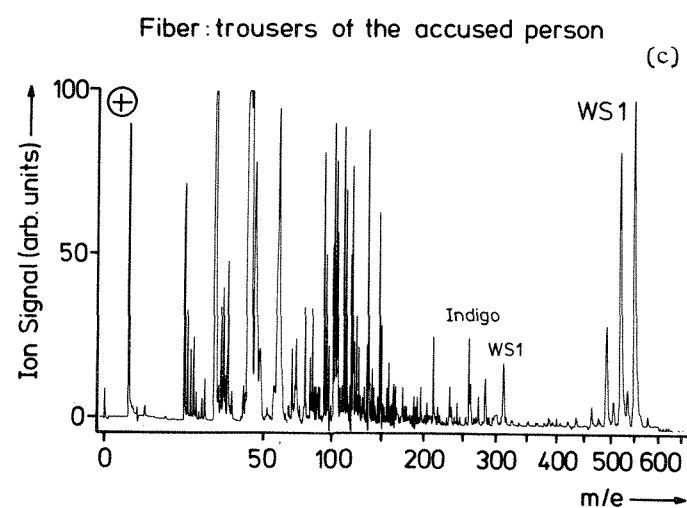
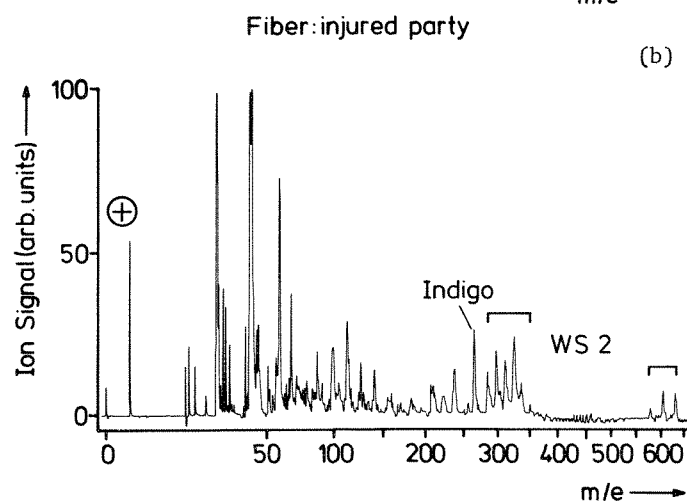


FIG. 4.--Spectrum of jeans fibers, taken from body of victim: (a) one group of jeans fibers contain WS 1; (b) WS 2; (c) spectrum of fiber from jeans trousers of accused person.

LAMMS APPLIED TO PROCESSING PROBLEMS IN THE GLASS INDUSTRY

B. Evans

Surface contamination is one of the major factors that limit the use of glass in many different applications. Control is often vital to economic success in any process and most of the available surface-analytical techniques have been used at one time or another in trying to establish the type and possible sources of contamination on glass surface. Siekhaus has already reported the use of LAMMS to examine the variable laser damage characteristics of polished optical glasses that he was able to attribute to polishing residues remaining on the surface of the glass.¹ However, the ability of the technique to detect both inorganic and organic residues is potentially of great use in sourcing contamination; this note reports some examples of its use in problems associated with glass processing.

Experimental

LAMMS analyses were carried out with a LIMA 4A system (Cambridge Mass Spectrometry Limited, U.K.). The basic system comprises a Q-switched Nd:YAG laser quadrupled in frequency, which is fired as a pulse at the sample. The laser pulse has a power density variable from 0 to 10^{11} W/cm² at 265 nm and can volatilize a cylinder of material 2 μ m in diameter to a depth of 0.1–0.5 μ m. Both positive and negative ions are produced within the plasma; either may be chosen for examination.

Generally, the glass samples examined were analyzed as received or after minimal cleaning to remove loose deposits.

Glass Surfaces

A normal "clean" float glass surface has a distinctive, characteristic spectrum. At high laser energies, the bulk components of the glass are detected; at low laser energies, where the surface zone of the glass is being sampled, one face of the glass shows a very distinctive peak distribution associated with tin. This peak is due to the method of forming the glass, which is floated on the surface of molten tin in the production process.

The negative-ion spectrum of a "clean" glass is also quite distinctive, since a succession of peaks are present that can be attributed to clusters formed by network-forming elements within the glass structure. The presence of the silicate seems to be associated with the

the detection of both SiO₂ (60D) and SiO₃ (76D) with a definite contribution from SiO₃ H (77D), depending on the degree of hydration of the glass surface.

The presence of the higher-order clusters attributed to Si₂O₂ (116D), Si₃O₃ (132D), and Si₂O₅ (136D) may well reflect the bulk structure of the glass, but the most distinctive contributions are from clusters attributable to aluminosilicates at 119D (AlO₂SiO₂) and 179 D [AlO₂(SiO₂)₂]. Alumina is present in such glasses at about one hundredth the concentration of the silica, but it is known to have a dramatic effect on the durability of the glass.

Contaminated Glass Surfaces

The type of contamination found on a flat glass surface very much depends on how it has been formed, transported, handled, and washed. If the glass is washed with dirty water, handled to leave oily fingerprints on the surface, or touched with soiled gloves, the surface becomes contaminated. The contamination is often difficult to remove and may survive a pre-coating cleaning process, with in itself can cause problems. In addition, detergents used in washing machines are sometimes not effectively rinsed off the glass surface and some have proved to be detectable by the LAMMS technique. A wide range of commercial detergents contain phosphates, which form a distinctive contribution to the negative-ion spectrum: peaks are present at 63D (PO₂) and 79D (PO₃). It has been possible to detect the presence of these residual phosphates on the glass surface itself after a cleaning process, within a deposited thin film, and in some circumstances as isolated deposits on the surface where they had formed coating defects and thus corrosion centers in a thin multilayer film. The contamination on the base surface can be confirmed by ESCA analysis, but it is impossible to detect this contamination in the coating by the same technique.

Cationic surfactants are also used within some detergent formulations. Although SSIMS is the preferred method of detecting such residues, tests have shown that residues of cationic materials can be detected on glasses with LAMMA, a result that was supported by spectra obtained on a Fast Atom Beam Time of Flight facility which is present on the same instrument. These residues are difficult to identify and detect by ESCA.

If a glass has had to be cleaned by polishing and the polishing material survives the cleaning process then (as Siekhaus stated) it is possible to detect the presence of and, with

The author is with Pilkington PLC, Pilkington Technology Centre, Hall Lane, Lathom, Lancs., England. This paper is published with the permission of the Directors of Pilkington PLC, and of Dr. A. Ledwith, Director of Group Research.

sufficient patience, the approximate density of such residues on a polished surface. Generally, such levels are not detectable by ESCA and are confirmed with a more detailed analysis by use of an ion microprobe (Cameka 3F).

Most materials that come into contact with the glass are screened to insure that they do not transfer any significant amounts of material to the surface, but some of the subsequent processes (such as coating or silvering) can be sensitive to transferred material. LAMMS, ESCA, and Scanning Electron Microscopy (SEM) are used as tools in this screening process; LAMMS because it complements ESCA in being more sensitive in analyzing inorganic particulates and organic films.

For example, if paper is used as an interleaving material, organic material can transfer to the surface. The positive- and negative-ion spectra from regions on these surfaces produce no obvious contribution from the underlying glass but quite distinctive peaks associated with the organics from the paper. Unfortunately it is not easy to assign these organic peaks directly to one individual component of the paper because of the complex nature of the paper itself, but extensive accelerated testing is used to prepare control samples so that "fingerprints" of control surfaces can be obtained.

Accidental contamination can also occur, for example from paint flakes falling on the glass and being trapped between glass sheets; through rollers that are contaminated with greases or have become worn and degraded; and from welding work carried out near the line or near exposed glass on a building site, which leaves metallic particles on a surface that on weathering lead to a stained glass. Severe staining of this nature can leave a glass with a very distinctive FeO_2 (88D) peak in the negative-ion spectrum of the glass surface.

Again, in most instances, a set of control surfaces deliberately contaminated with material or artificially weathered in a specific manner has been used to provide "fingerprint" spectra against which the spectra from the fult samples are compared. In the future, one would like to foresee the build-up of a library of such fingerprints and of standard compounds so that the chemometric approach may be applied.

Conclusion

The LAMMS technique is very useful in examining surface contamination of glasses, particularly when used in conjunction with other surface-analytical techniques such as SEM, ESCA, Auger, and SIMS. In combination with these techniques, LAMMA allows a better description to be made of the state of the glass surface and of the nature, type, and possible source of both inorganic and organic contaminants on the surface so that contamination can be controlled or removed.

References

1. W. J. Siekhaus, *Proc. Third LAMMA Workshop*, Antwerp, 1986, 181.

APPLICATION OF LAMMS TO LATERAL DIFFUSION IN SEMICONDUCTOR DEVICES

L. A. Heimbrook, K. W. Moyers, and S. J. Hillenius

The evolution of integrated-circuit technology toward devices of finer vertical and lateral dimensions has made their analytical evaluation more difficult. Smaller line dimensions provide higher performance and greater density n+ and p+ channel transistors. The technical problem of maintaining the integrity of n+ and p+ devices as the connecting path becomes shorter must be characterized by both electrical and analytical techniques.

This study applies the technique of LAMMS (Laser Ablation Microprobe Mass Spectroscopy) to the analysis of the lateral diffusion of the dopants As, P, and B through Ta and Co silicides. Electrical data indicate that as the silicide layer between oppositely doped gate structures is shortened, a rapid lateral diffusion path for n and p dopants can form which may counter dope adjacent polysilicon regions. LAMMS was used to analyze the effects of anneal temperature and time on the lateral diffusion of dopants in Ta and Co silicides.

Experimental

A lateral test pattern was designed on 4 and 5 in. wafers including large source regions doped with As, B, or P (10^{19} - 10^{20} atoms/cc) im-

planted into the wafer after patterning. The pattern also consists of device lines 3 μ m wide and 5 to 80 μ m long extending out from the large doped source regions (Fig. 1). The wafers were annealed at temperatures of 700-900 C for 30 to 120 min. In the lateral diffusion experiments over 100 time-of-flight mass spectra are taken of each large source area of a known dopant concentration for a calibrant. Data are then obtained from the 3 μ m runners. The data showing more than 10% variation in laser power were excluded and depth calibration of a known laser power is based on prior measurements.

Results

Figures 2 and 3 show representative data for B lateral diffusion in TaSi₂ and CoSi₂. The data suggest that B lateral diffusion in TaSi₂ is insignificant at LAMMS detection limits, whereas in CoSi₂ the diffusion is much greater at elevated anneal temperatures and times. The lateral diffusion of P and As in CoSi₂ and TaSi₂ was found to be significant at all temperatures and times studied. This lateral diffusion of dopants, if coupled with diffusion into the material, can lead to threshold voltage shifts in n+ and p+ devices.

Conclusions

These data provide information on surface diffusion in semiconductor materials, where

The authors are at AT&T Bell Laboratories, Murray Hill, NJ 07974.

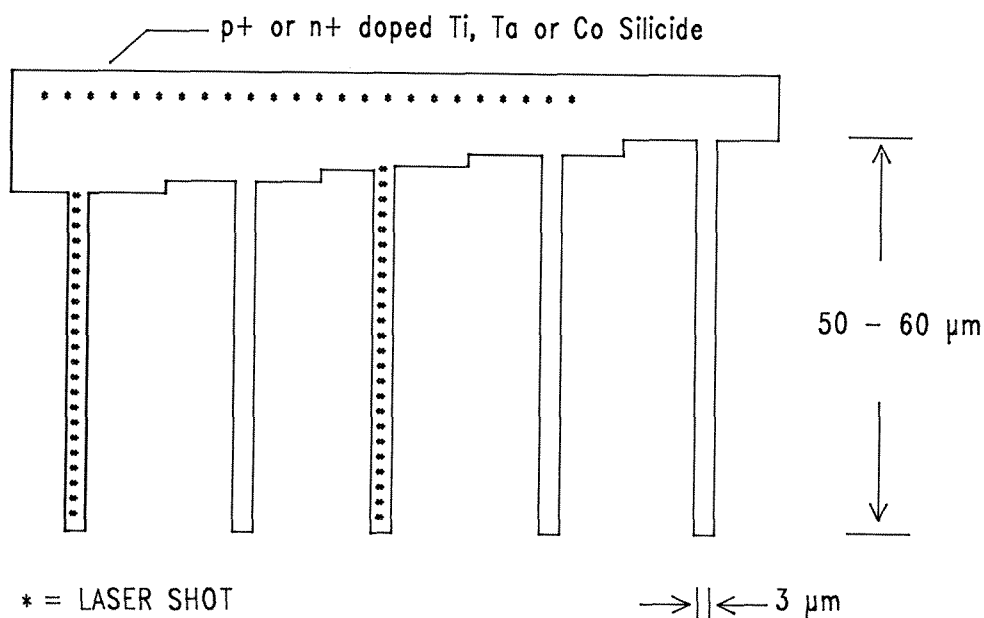


FIG. 1.--Schematic of lateral diffusion test pattern.

The ability to analyze at the dopant level within device dimensions is critical to future device development.

References

1. S. J. Hillenius and W. T. Lynch, *Trans. IEEE ICCD*, 1985, 147.
2. L. A. Heimbrook and K. W. Moyers, *Proc. 35th Nat. AVS Symposium*, 1988.

previously only bulk diffusion could be evaluated. The differences in lateral diffusion of the same dopant in two different silicides is clearly shown in the case of B in TaSi₂ and CoSi₂. The formation of a boride in TaSi₂ limits the extent of the lateral diffusion compared to CoSi₂, where no boride formation occurs and rapid lateral diffusion is detected.

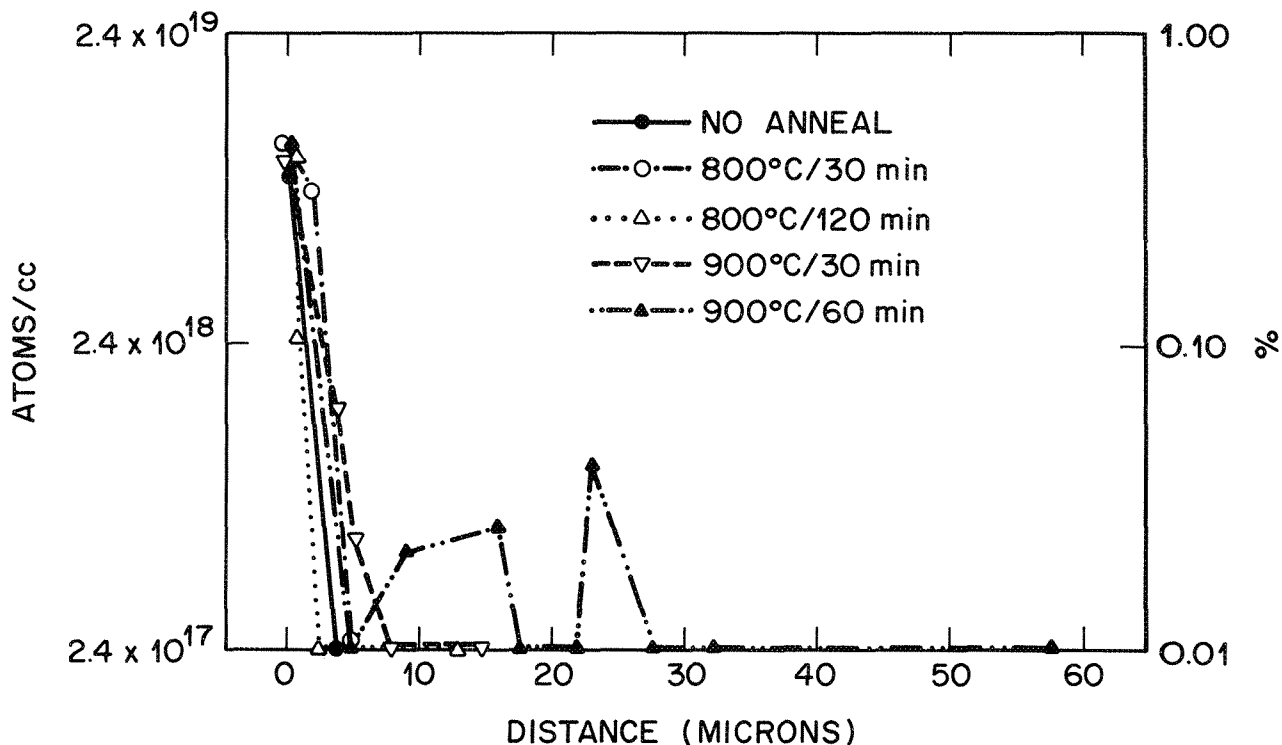


FIG. 2.--Boron signal vs lateral distance down 1 μ m TaSi₂ runner.

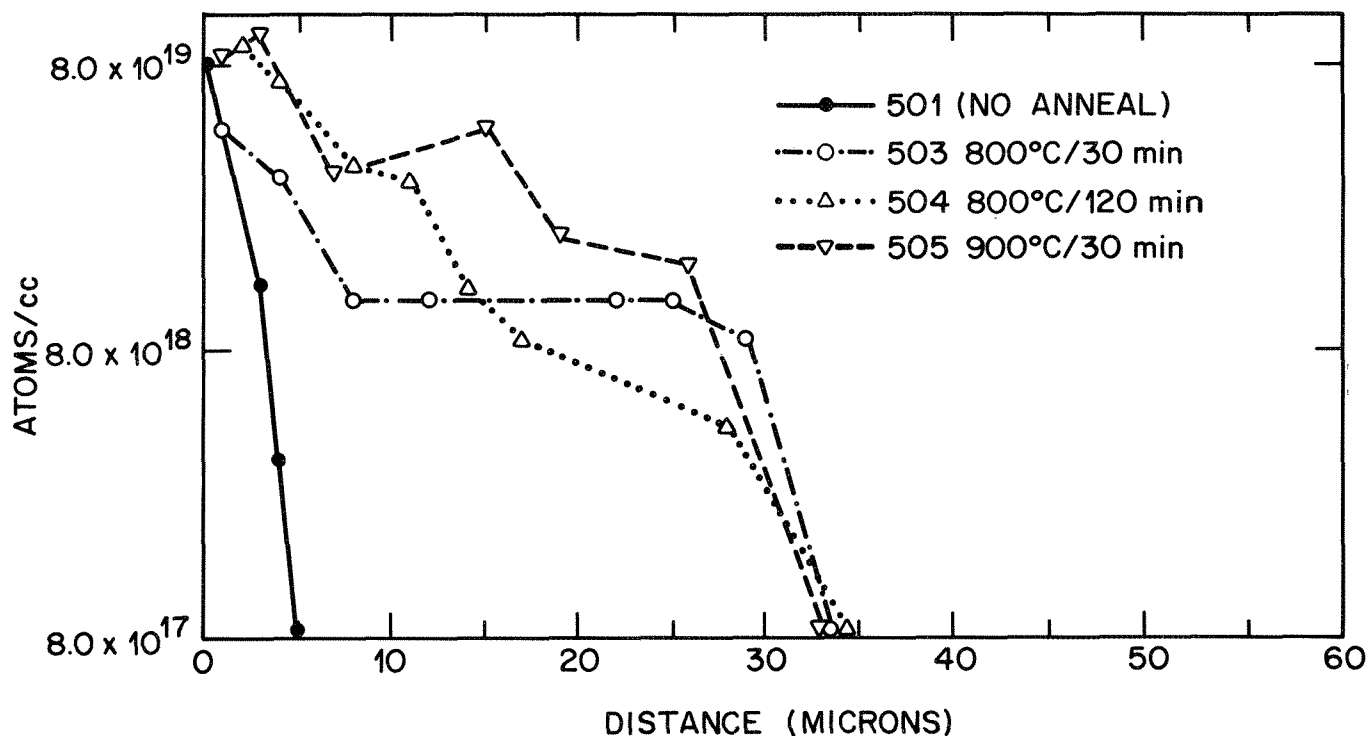


FIG. 3.--Boron signal vs lateral distance down 3 μ m CoSi₂ runner.

DEPTH PROFILING BY LASER MICROPROBE MASS ANALYSIS

Ute Bahr, Michael Karas and Franz Hillenkamp

It is well documented that laser microprobe analysis shows high lateral resolution (down to below 1 μm) but only little is known about the potential of this method in depth profiling of inorganic material. In literature only few results are given showing ablation of at best several monolayers¹⁻³ covering a substrate material. Also, for organic analysis it has been reported that several monolayers can be analyzed without affecting the metal target below.⁴ We report here about depth profiling in bulk inorganic material with depth resolutions in special cases in the subnanometer range.

Experimental

The analyses were performed with a LAMMA 1000® instrument at 266 nm wavelength. A detailed description is given elsewhere.⁵ The irradiances used were between 5×10^{-6} to 5×10^{-7} W/cm². In some cases slightly defocusing the laser spot was necessary for fine tuning of the irradiance. The examples shown in the following are taken for samples supplied from industrial companies for commercial LAMMA analysis.

Results

The first sample to be analyzed was an aluminum target coated with three different layers of photoconducting materials. Data to be controlled by LAMMA depth analysis were as follows: first layer, pure selenium 3-5 μm thick; second layer (about 1 μm), selenium and tellurium; and below a 60 μm layer of selenium, tellurium and arsenic. The spectra were taken at an irradiance of about 5×10^7 W/cm². In Fig. 1(a) the spectrum of the first laser shot shows the isotopic peaks of Se^+ (m/z 74-82), Se_2^+ (m/z 148-164) and Se_3^+ (m/z 222-246). A precise analysis of the isotopic pattern of these species (not shown here) shows a signal at m/z 75, resulting from the monoisotopic arsenic and an enhanced isotopic peak at m/z 155, pointing out a SeAs molecular ion. The spectrum from the second laser shot shows a small peak group around m/z 208 (Fig. 1b); the source of it becomes clear in the next spectrum from the third laser shot. The first layer has been penetrated and tellurium from the second layer with m/z 122-130 for Te^+ and m/z 244-260 for Te_2^+ is registered. The peak group at m/z 202-210 represents a cluster ion of SeTe^+ . The signals from As^+ and SeAs^+ have decreased. With the 8th laser pulse, As^+ has disappeared and the

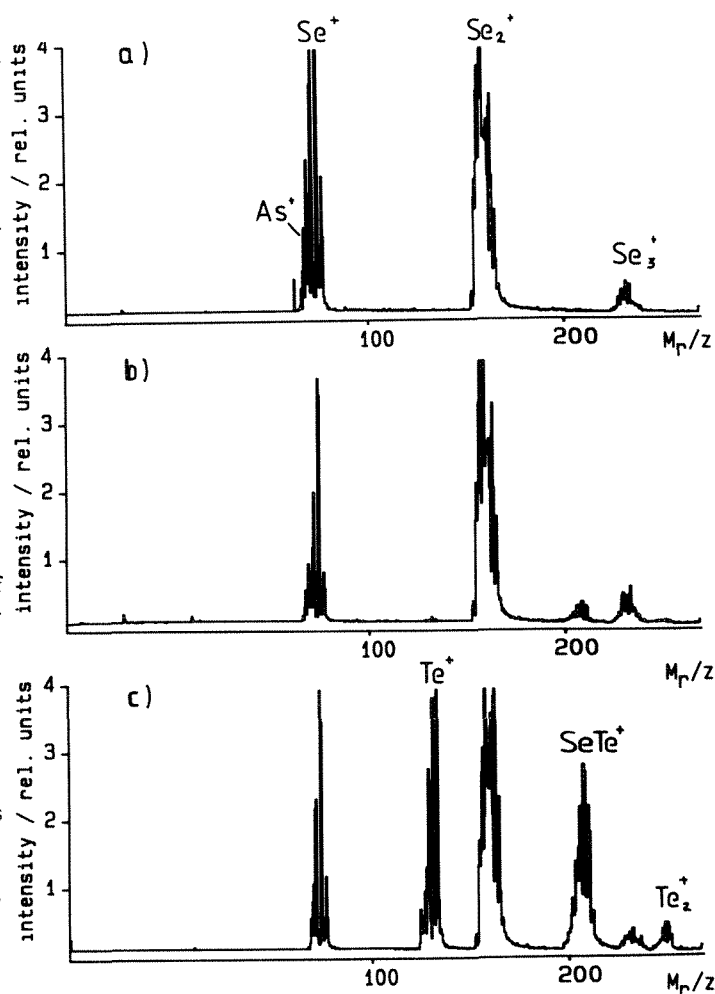


FIG. 1.--LAMMA spectra of semiconductor layers at various depths: (a) spectrum from 1st laser shot, (b) 2nd shot, (c) 3rd shot.

Te^+ signals also decrease, indicating that the ablation front has reached the third layer. With the 10th laser shot, the spectrum shows only signals from selenium. The result of this rough depth profile shows that arsenic is enriched at the surface of the upper selenium layer. The second layer contains selenium and tellurium, as predicted, but has about the same thickness as the first layer; the third layer consists only of selenium--no tellurium and no arsenic was found.

The second example again gives results of a rough depth profile for 1.3 μm copper on a capton foil with a thin interfacial Ni-layer, which acts as adhesion promotor. The spectrum from the first laser shot shows Cu^+ signals accompanied by surface contaminants like Na^+ and K^+ . Spectra from laser shots 2-4 show only copper signals. In the spectrum of the

The authors are at the Institut für Medizinische Physik, Universität Münster, Hüfferstrasse 68, D-4400 Münster, Federal Republic of Germany.

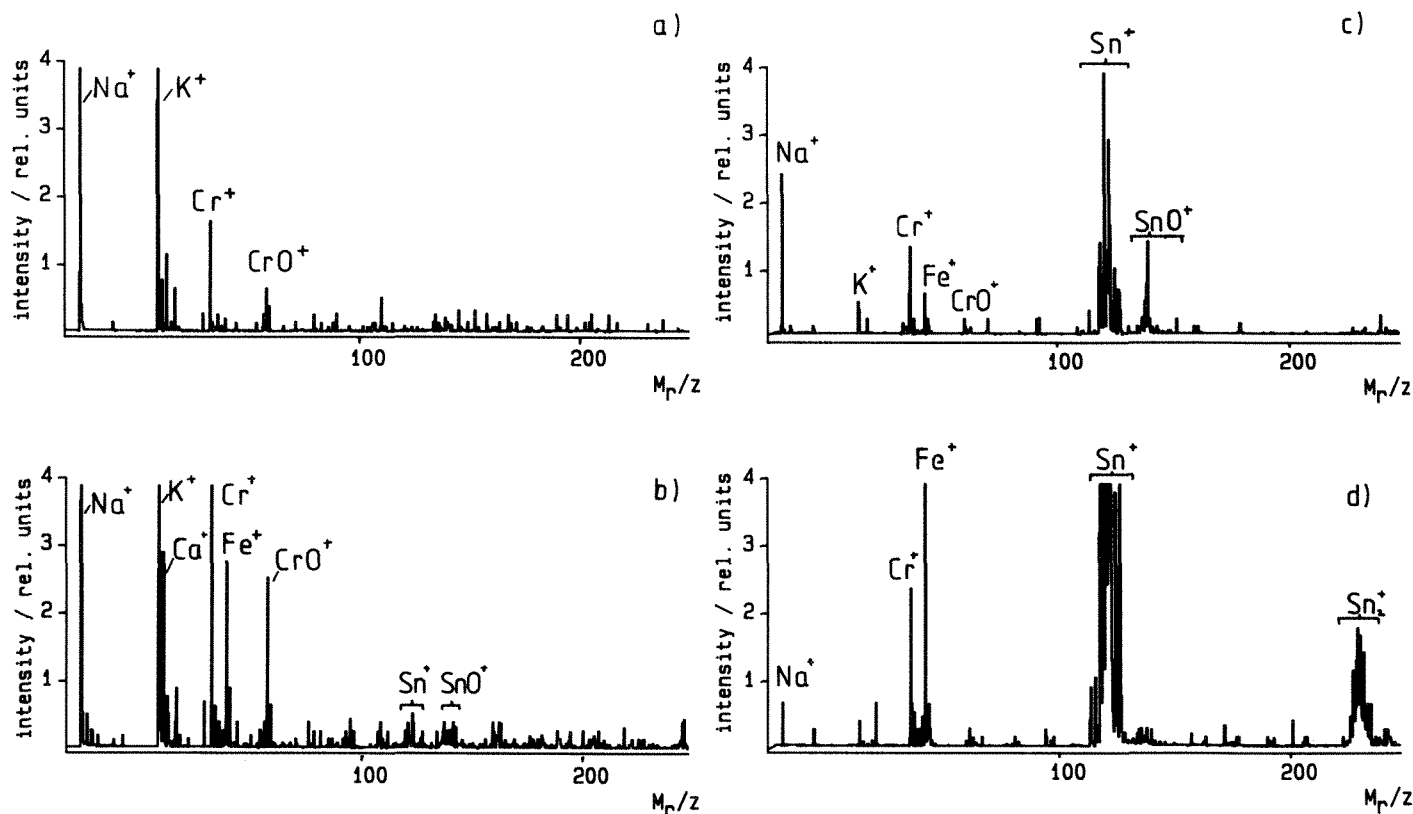


FIG. 2.--LAMMA spectra of passivation layer on tin plate: (a) spectrum from the 1st laser shot, (b) 2nd shot, (c) 3rd shot, (d) 4th shot.

5th laser shot Ni^+ from the interfacial layer is desorbed and not until the 7th laser shot is the pure polymer layer reached. In these examples the minimum depth resolution at low irradiance was below $0.1 \mu\text{m}$. It proves to be of great advantage for routine depth profiling that one can adapt the ablation depth to the problem by varying the irradiance. Thus a complete depth profile for the copper/polymer system was performed within a series of seven laser shots. Example 3 shows the analysis of a passivation layer on tin plate with a 0.5nm chromium oxide layer on top of 2nm SnO_2/SnO covering the tin. Figure 2(a) shows the spectrum from the first laser shot with a very low irradiance of about $7 \times 10^6 \text{ W/cm}^2$. Besides contaminations from the surface, like sodium and potassium, only signals due to chromium and chromium oxide are registered. The fact that no signals from the second layer material are to be seen points out that in this case only a few Ångströms have been ablated. The spectrum from the second shot (Fig. 2b) shows the onset of tin-oxide desorption from the second layer. With the third laser shot (Fig. 2c) intense tin and tin oxide ions are seen, whereas Cr^+ signals decrease. With the next laser shot (Fig. 2d) the tin oxide layer has also been perforated and intense signals from the supporting tin layer, Sn^+ and Sn_2^+ , are registered.

The results presented above show that by variation of the irradiance depth profiling is possible for metallic layers far below $1 \mu\text{m}$; in special cases, as reported for metal oxides, an extremely high depth resolution in the subnano-

meter range is documented.

References

1. H. J. Heinen, S. Meier, H. Vogt, and R. Wechsung, *Int. J. Mass Spectrom. Ion Phys.* 47: 19, 1983.
2. J. C. Ruckman, *3rd Intern. Laser Microprobe Mass Spectrometry Workshop*, Amsterdam, 1986, 165.
3. V. L. Kohler, A. Harris, and E. R. Wallach, *ibid*, 127.
4. F. Hillenkamp, M. Karas, D. Holtkamp, and P. Klüsener, *Int. J. Mass Spectrom. Ion Processes* 69: 265-276, 1986.
5. P. Feigl, B. Schueler, and F. Hillenkamp, *Int. J. Mass Spectrom. Ion Phys.* 47: 15, 1983.

LASER MICROPROBE FTMS AND MATERIAL SCIENCE

M. Pelletier, G. Krier, J. F. Muller, J. Campana, and D. Weil

The laser microprobe provides an important alternative to the ion microprobe for the qualitative analysis of metals, polymers, trace contaminant, and localized distributions of the elements in various matrices. Laser-induced ionization requires a minimum of sample preparation, irradiated areas of about $10\ \mu\text{m}^2$ can be amplified by focusing the laser beam through a special focalization optics, and the amount of energy deposited onto the sample surface can be easily controlled by varying the laser intensity. Because of the wide limits of sample areas (100 to $4\ \mu\text{m}$ diameters) and laser power density (10^6 to $10^{12}\ \text{W}/\text{cm}^2$), two modes of laser-induced ionization were identified by Heinen in 1981: a plasma mode, and a laser-induced desorption (LD). The plasma mode generates atomic and small molecular fragment ions at high-power densities, and the LD mode is used to characterize surface species at low excitation levels and with a minimum degree of dissociation.¹

Instrumentation

All the experiments were performed on a transformed, differentially pumped dual cell, Nicolet Instrument FTMS 2000, which can be called a Laser Microprobe Fourier Transform Mass Spectrometer.² This new apparatus will be described in detail in another communication.³ We may say that we have all the advantages of Fourier Transform Mass Spectrometry, i.e., high resolving power and accurate mass measurements.⁴ This, coupled with a laser microprobe sample system, enables laser-induced ionization experiments.

The laser beam optics have been calculated to obtain at focus a spot size of $3\text{--}4\ \mu\text{m}$ on the target, but for most of our experiments the laser beam was slightly unfocused (crater diameter about $10\ \mu\text{m}$) in order to have an irradiance of about $10^{10}\ \text{W}/\text{cm}^2$, which is high enough to vaporize sufficient material, enabling the analysis of surface contamination.

The viewing system using an inverted Cassegrainian optics design gives a sample visualization with a magnification varying from 60 to $240\times$.

The whole sample surface can be analyzed, as an x,y,z movement is achieved by a micro-animulator or by a tight displacement of the

laser beam.

Experiments

The experiments were done in a dual cell at a magnetic field of 3.181 Tesla, with a source side pressure of about 10^{-8} Torr and an analyzer side pressure of approximately 10^{-9} Torr.

Ionization was performed by an excimer laser charged with a KrF mixture at a 249nm wavelength and an irradiance about $10^{10}\ \text{W}/\text{cm}^2$.

The experimental sequence used for these laser experiments is as follows.

- following the quench events, ions are formed by laser-induced ionization in the source cell
- during the ionization event, the conductance limit is kept at the trap potential (typically 1 or $2\ \text{V}$) to confine the ions in the source side, or contrariwise the conductance limit is grounded to transfer ions in the analyzer side
- a variable delay period follows, during which ion molecule reactions can occur.
- swept frequency ion ejection events can be used to remove major ions and enhance minor ions intensities
- the ions are excited by a swept frequency excitation and the ion image currents are detected, amplified, digitized, and Fourier transformed to produce the mass spectra (Fig. 1).

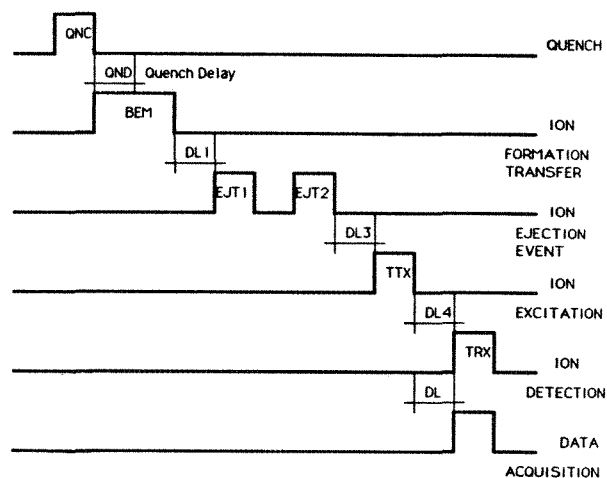


FIG. 1.--Experimental sequence.

Some Results and Discussion

Surface profile analysis of an integrated circuit chip requires high spatial resolution, small laser spot diameters, and accurate sample positioning (Fig. 2). To demonstrate the

M. Pelletier, G. Krier, and J. F. Muller are at LSMCL, Université de Metz, B.P. 794, F-57012 Metz Cédex 1, France; J. Campana and D. Weil are at Nicolet Instrument Corp., Madison, Wis. This work was supported by ANVAR, the Ministère de la Recherche et de l'Enseignement Supérieur, the Ministère de l'Education Nationale, and the Région de Lorraine. M. P. acknowledges the support of his thesis by ELF France.

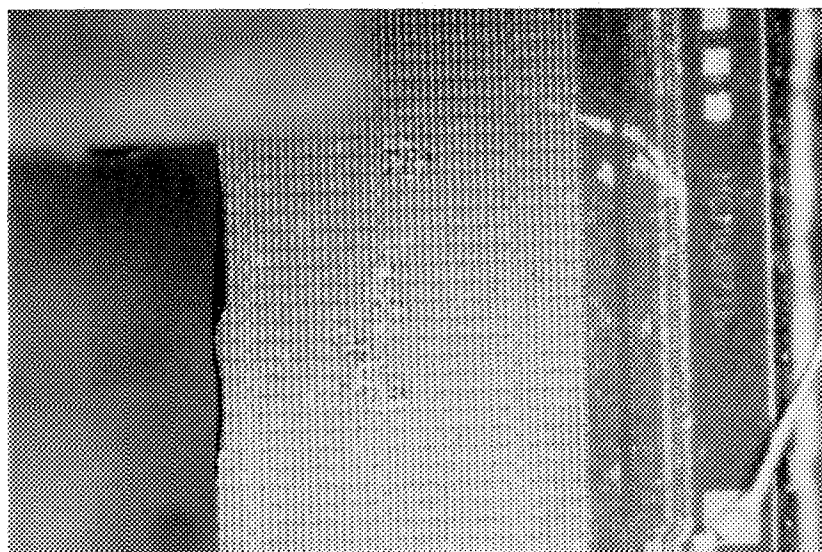


FIG. 2.--Silicon wafer after analysis; $\times 50$ magnification, crater diameter about 10 μm .

TABLE 1.--Results obtained.

	Metallic part	Contact	Ceramic	Wafer
Positive ions	Fig. 3	Fig. 4		
Ejected ions	$\text{Na}^{+*}, \text{K}^{+*}$	$\text{Na}^{+*}, \text{K}^{+*}$	$\text{Na}^{+*}, \text{Al}^{+*}, \text{K}^{+*}$	$\text{Na}^{+*}, \text{K}^{+*}$
Analyzed ions	$\text{Fe}^{+}, \text{Co}^{+}, \text{Ni}^{+},$ $\text{Sn}^{2+}, \text{Sn}^{+}, \text{Au}^{+}$	$\text{Au}^{+}, \text{Au}^{2+}, \dots$ \dots, Au^{8+}	$\text{Al}^{+}, \text{Si}^{+}, \text{Ti}^{+},$ $\text{Cr}^{+}, \text{Zr}^{+}$	$\text{Al}^{+}, \text{Si}^{+}, \text{P}^{+}$ $\text{SiOH}^{+}, \text{Fe}^{+}, \text{SiO}_3^{+}$ $\text{K}_2\text{Cl}^{+*}, \text{Cs}^{+*}$
Negative ions				
Analyzed ions	$\text{CnHm}^{-*}, \text{F}^{-*},$ $\text{Cl}^{-*}, \text{I}^{-*}, \text{Au}^{-}$	$\text{CnHm}^{-*}, \text{F}^{-*},$ $\text{Cl}^{-*}, \text{I}^{-*}, \text{Au}^{-},$ Au^{2-}	$\text{CnHm}^{-*}, \text{F}^{-*},$ $\text{Cl}^{-*}, \text{I}^{-*}, \text{AlO}_2^{-}$	$\text{CnHm}^{-*}, \text{F}^{-*},$ $\text{Cl}^{-*}, \text{I}^{-*}, \text{PO}_2^{-}$ PO_3^{-}

* surface contamination

* element which needs to be ejected to enhance trace element observation

TABLE 2.--Mass accuracy for elimination of mass spectra interferences.

Element	Exact Mass	Measured Mass	Absolute Error ppm
$^{58}\text{Ni}^{+}$	57 934798	57 93476	0.7
$^{116}\text{Sn}^{2+}$	57 950323	57 95035	0.5
$^{59}\text{Co}^{+}$	58 932649	58 93275	1.7
$^{118}\text{Sn}^{2+}$	58 950255	58 95040	2.5
$^{60}\text{Ni}^{+}$	59 930240	59 93020	0.7
$^{120}\text{Sn}^{2+}$	59 950551	59 95060	0.8

Absolute mass error is below 2.5 ppm

Comparison of theoretical and measured isotopic ratios demonstrates that accurate peak heights were obtained with FTMS

FIG. 3.--Positive-ion spectrum of the metallic part.

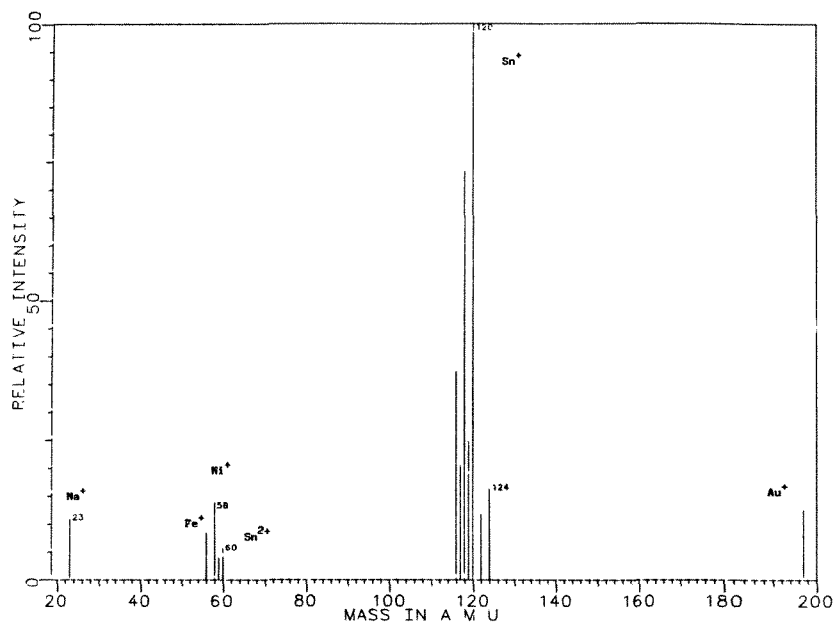


FIG. 4.--Positive-ion spectrum of the contact.

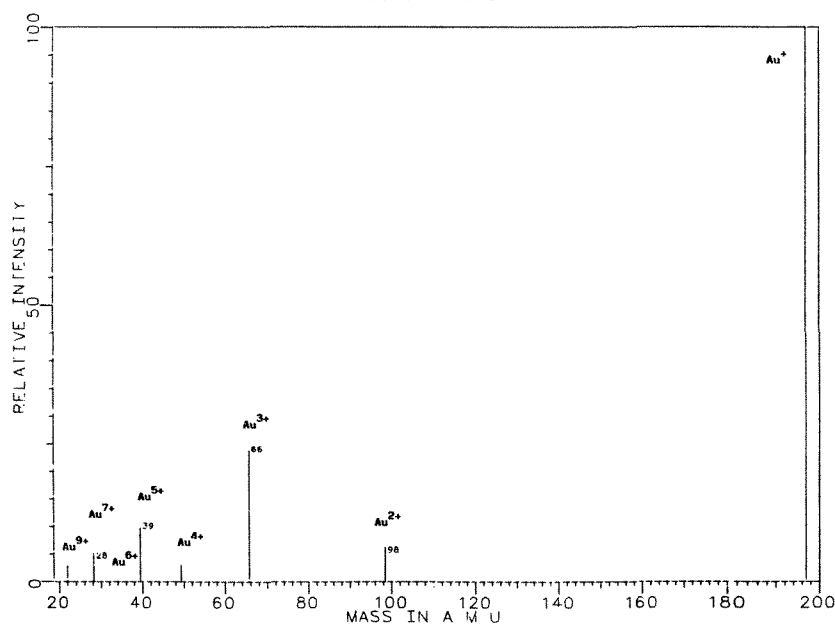
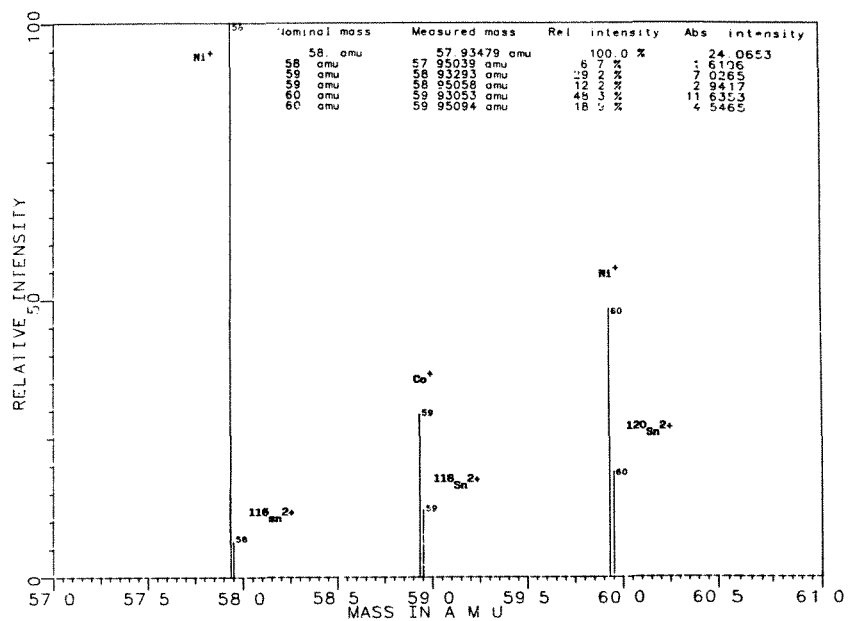


FIG. 5.--Medium-resolution positive-ion spectrum.



usefulness of the laser microprobe FTMS for such applications, positive and negative ion mass spectra were obtained from four separate components of a circuit chip (Table 1).

Metallic part: doubtless made up of tin with some gold, iron, cobalt, and nickel (Figs. 3 and 5)

Contacts: made of gold, which it is not astonishing since gold is the best electrical contact (Fig. 4)

Ceramic substrate: an alumina-based ceramic with some silicon, zirconium, titanium, and chromium oxides (this last gives the ceramic its brown color)

Silicon wafer: contains a film of aluminum and a phosphorous coating

The whole sample surface presents Na^+ , K^+ , and sometimes recombinations such as K_2Cl^+ in positive ions, and Cl^- , F^- , I^- , CnHm^- (carbon clusters) in negative ions. Sodium and potassium cations were certainly due to finger contamination on the surface during handling; that is why those ions were ejected from all positive ions spectra. We have checked that it was a real contamination, by sweeping the surface with multiple laser shots at the same location, to confirm that sodium was only present at the surface. From the negative-ion spectra, it can be said that a fluoro-polymer used during photoablation chip processing may be the source of the fluorine contamination. Compound identification was difficult due to the extensive fragmentation observed even with a defocused laser beam, used to reduce the irradiance. All the spectra were obtained after only one shot in broadband (excitation/detection: 2.6 MHz), which gives enough resolution for spectral interpretation (about 1500 at mass 200). But medium resolution was used to separate mass spectral interferences on the metallic part of the circuitry (Table 2). Doubly charged tin isotopes resulted in doublets at m/z 58, 59, and 60 with nickel and cobalt ions; to resolve them, a 4000 resolving power (easily obtainable with FTMS) is needed. On this sample, the difficulty was not the spectral interpretation nor the use of high resolving power, but only the sample positioning, which was easily achieved with the laser sample microprobe system.

Ultrahigh resolution capability has already been attained and will be presented elsewhere.⁵

Conclusion

The advantages of FTMS for Laser Microprobe Analysis are:

- pulsed technique, excellent with laser-induced ionization
- high mass resolving power
- separation of metal/metal isotopes
- separation of metal/metal oxide isotopes
- separation of singly charged ions from higher-mass doubly charged ions (when operating at high energy values)
- elemental composition information from accurate mass measurements
- entire mass spectrum obtained from a single laser shot

The advantages of Laser Microprobe Analysis are:

- this kind of apparatus provides analytical and imaging capabilities
- spatial resolution, both analytical and viewing, down to 5 μm allows all kinds of samples to be analyzed
- this is a reflection-mode prototype--the laser beam is either focused or defocused and is perpendicular to the surface, so that ions are formed directly in the source cell; there is no information loss with ion transfer

References

1. H. Heinen, "On ion formation in laser desorption mass spectrometry with LAMMA," *Int. J. Mass Spectrom. Ion. Phys.* 38: 309, 1981.
2. M. Pelletier, G. Krier, J. F. Muller, D. Weil, and M. Johnston, "Laser microprobe Fourier transform mass spectrometry," *Rapid Comm. Mass Spectrom.* 2: 146, 1988.
3. J. F. Muller, M. Pelletier, G. Krier, D. Weil, and J. Campana, "A new generation of microprobe: Laser ionization and FT/ICR mass spectrometry,"
4. M. Buchanan, "Fourier transform mass spectrometry," *ACS Symposium Series*, 1987, 359.
5. J. F. Muller, G. Krier, M. Pelletier, D. Weil, and J. Campana, "Laser microprobe Fourier transform mass spectrometry," *Pittsburgh Conf.*, 1989.

SOLID-STATE MASS SPECTROMETRY WITH A LASER MICROPROBE

D. M. Hercules

During the past few years several sources have emerged for obtaining mass spectra of solids: field desorption, fission-fragment desorption, secondary ion mass spectrometry, and laser desorption. Commercially available laser microprobe mass spectrometers present the possibility of a routine tool for obtaining mass spectrometry of solids directly.

A typical example is the LAMMA-1000, which uses a Nd-YAG laser as a source coupled with a time-of-flight mass spectrometer with a mass range from 0 to 200 amu. Although the excitation mechanism is not well understood, ion emission is observed from a variety of organic compounds, including polymers. Laser mass spectra are particularly intriguing because approximately equal intensities of positive and negative ions are obtained. Although power densities of the order of 10^7 - 10^8 W/cm² are used, only moderate fragmentation occurs, even from fairly labile molecules.

The laser microprobe can be used to obtain the mass spectra of many solid materials: simple inorganic and organic compounds, coordination compounds, polymers, and large biochemically important molecules such as vitamin B₁₂. For coordination compounds, results show that decomposition reactions caused by the presence of highly reactive atoms (such as iodine) can dominate the spectrum.

An extensive study has been carried out in which the laser microprobe was used to investigate both simple polymers and complex polymeric materials. Results for acrylic polymers show that spectra can be partitioned between fragmentation of the backbone and the side chain or pendant group. The biomedical polymers Biomer and Avcothane have been studied; fragmentation can be correlated with the polyether backbone and groups used to crosslink the polyether. Selected polymers with no pendant group, such as polyethylene (PE), polytetrafluoroethylene (PTFE), and polyvinyl chloride (PVC), were analyzed for distinct patterns due to the backbone. Two more polymers with distinct differences in sidechain functionality, poly(phenylmethacrylate) and poly(benzylmethacrylate), gave results that were radically different in the positive and negative ion spectra, which could be based on well-known ion stabilities and lead to easy differentiation. Spectra also were observed for polypropylene, polyacrylamide, polystyrene, polycaprolactam (Nylon 6), and polydimethylsiloxane.

Laser mass spectrometry has been investigated as a tool for polyglycol analysis. Accurate M_n values were determined for

polyglycol samples with average molecular weights ≤ 1000 . M_n values derived from LMS data were reproducible to +2% relative standard deviation and consistent with those obtained with field desorption (FD) and electrohydrodynamic ionization (EH). In addition, the relative selectivity of oligomers toward alkali metal ions were determined for PEG and PPG. Selectivity orders and ratios measured by LMS were similar to those obtained from EHMS and solvent extraction data. Therefore, the applicability of LMS for M_n determinations and for probing oligomer-ion interactions for polyglycols has been established.

Laser mass spectrometry was applied to the analysis of poly(fluoroethylenes) for the first time. The polymers investigated ranged from poly(vinyl fluoride) to poly(tetrafluoroethylene). A fragmentation mechanism common to each fluoropolymer yielded structurally relevant ions indicative of the orientation of monomer units within the polymer chain. A unique set of structural fragments distinguishes the positive-ion spectra of each homopolymer, which allows identification. A quantitative study of the structural fragments formed from four poly(vinylidene fluoride) samples allowed determination of percent backward addition of monomer units within each sample. The results compared favorably with those obtained from ¹⁹F NMR spectroscopy. The applicability of LMS to poly(chloroethylene) analysis was also addressed.

The LAMMA 1000 has been automated and programmed to produce ion maps with high lateral resolution. The sample is scanned in an x-y mode and time-of-flight mass spectrometric analysis is performed for each matrix element. A user-selected mass is searched for the maximum intensity, which is density coded and displayed as a four-sided polygon. A matrix consisting of 31 × 31 data points can be completed in 20 min. Ion maps were obtained for control samples consisting of organic dyes deposited on a nitrocellulose substrate with transmission electron microscopy grids as a mask. Results from maps of molecular cations have shown that the maximum lateral resolution obtainable was 2.5 μ m, which was limited by the diameter of the laser beam. Gold and aluminum ion maps were obtained from the analysis of a bonding pad in an integrated circuit, which shows that elemental information can also be obtained. In addition, ion maps were obtained for an inclusion in a coal maceral. The maps showed that the inclusion was composed primarily of iron and sulfur. Organic material was detected in localized areas on the periphery of the inclusion.

The author is at the Department of Chemistry, University of Pittsburgh, Pittsburgh, PA 15260.

Factors affecting the reproducibility of organic laser mass spectrometry have been studied. Laser focus, laser power density, sample preparation method, and chemical effects contribute significantly to the variability of the mass spectra. Defocusing the laser enhances production of structurally significant organic ions. The yield of organic molecular ions is a nonlinear function of power density. The use of a polymer matrix (5% nitrocellulose) for dissolving the analyte(s) was found to be the optimum method of sample preparation. Use of such a polymer matrix, along with internal standards, permitted relative standard deviations of $\pm 15\%$ to be obtained.

It is instructive to contrast the study of polymers by use of the laser microprobe with results obtained by use of time-of-flight secondary-ion mass spectrometry (TOF-SIMS). Secondary ion mass spectra of a poly(dimethylsiloxane), a polyurethane, and polystyrenes were studied. The spectra were obtained by a time-of-flight secondary ion mass spectrometer equipped with a mass-selected primary ion source, an angle- and time-focusing time-of-flight analyzer, and a single-ion-counting detector. Fragmentation in the low-mass range ($m/z < 500$) provided structural information about the repeat unit. Ag^+ and Na^+ cationization of polymer fragments and intact polymer molecules containing large numbers of repeat units in the high-mass range (m/z 500-10 000) allowed identification of the polymers studied. Fragmentation patterns were unique for polymers having different repeat units but equal mass; distinguishing between such polymers was possible. Oligomer distributions for polystyrene standards obtained from the mass spectrum compared well with distributions determined by other techniques (e.g., gel permeation chromatography).

TOF-SIMS has been used for structural characterization and determination of molecular weight distributions of polymers. Structural characterization of polymers is based on fragmentation patterns observed in TOF-SIMS spectra. Molecular weight distributions are based on desorption of intact oligomers. From m/z values of peaks corresponding to intact cationized oligomers and the corresponding intensities, number and weight average molecular weights have been obtained for mixtures and individual standard molecular weight polymers: polystyrenes, polydimethylsiloxanes, polydienes, polyethylene imines, polyethers, etc. ($M_n < 10\,000$). Number average molecular weights determined by TOF-SIMS are within 10% of those determined by gel permeation chromatography.

Two important questions to consider are whether fragmentation and ionization-desorption processes affect molecular-weight distributions determined by TOF-SIMS, and how instrumental parameters influence detection of oligomers. Fragmentation and ionization-desorption will influence a molecular weight distribution if the fragmentation and ionization-desorption probabilities of individual oligomers vary

significantly with oligomer size. To evaluate this, sputtering cross sections of individual oligomers in various molecular weight distributions were determined from semilog plots of intensity vs time. Sputtering cross sections of oligomers of approximately equal sizes are different for different types of polymers, and increase with increasing oligomer molecular weight for the same polymer type. Instrumental resolution and ion detection influence the determination of molecular weight distributions by favoring ions of smaller mass.

TOF-SIMS spectra were obtained for 1mm-thick poly(dimethylsiloxane) and 200 μm -thick films made of Teflon brand fluorocarbon resin in the mass range up to $m/z \leq 4500$. It was found that one could overcome problems arising from charging of the polymers by placing a conducting grid on the polymer surface, keeping the primary ion current low to minimize charge accumulation, and adjusting the energy of the secondary ions. Cationized polymer fragments containing an integral number of repeat units were detected. From the location of a peak and the spacings between consecutive peaks, the mass of the repeat unit of the polymer could be determined. The spectra were also indicative of polymer surface contaminants.

STUDY OF POLYMER DEGRADATION BY LASER MASS SPECTROMETRY

F. P. Scanlan, J. F. Muller, and J. M. Fiquet

Thermal degradation of polymers and the analysis of their pyrolyzates by laser mass spectrometry provides chemical information on the polymer sample.¹⁻³ For the industries that use these materials, the identification of degradation products and a knowledge of the degree of degradation are important aspects; however, results by laser mass spectrometry are scarce. In this study, two types of cation exchange resin, two types of anion exchange resin, and two polymers (polystyrene and polyoxyethylene) were investigated. Laser mass spectrometry was used to characterize the degradation process by following the appearance of polymer degradation products, and in the case of ion exchange resins, their functional group loss.

Experimental

Samples were pyrolyzed in evacuated sealed pyrex tubes placed in an insulated tubular furnace. Pyrolysis experiments were carried out at 200, 250, 300, 350 and 400 C for up to 24 h. The exchange resins were new and untreated. Polystyrene and polyoxyethylene were pure secondary standards.

After pyrolysis the examples were recuperated by use of dichloromethane as solvent and allowed to dry. Analysis of solids was done by the laser microprobe mass analyzer (LAMMA-500 Leybold-Heraeus) and a laser microprobe Fourier transform mass spectrometer (FTMS-2000, Nicolet Instrument Corp.). The LAMMA-500 was operated in the transmission mode with a Nd:YAG ionizing laser wavelength 286.5 or 225.7 nm. Laser energy on sample varied between 2.5 to 3.5 μJ with a laser spot size of 2-5 μm^2 . Spatial resolution is 1 μm . Mass spectrometer resolving power is given as $m/\Delta m = 800$ at m/z 208 for a lead standard, at a 10% valley definition. The FTMS-2000 was operated at an ionizing wavelength 193 nm or 249 nm, spot size of 3-5 μm ; mass spectrometer resolving power can be 10^6 at m/z 131 when operated in heterodyne mode. For our analyses, a resolving power of a few thousand was sufficient.

Two principal laser ionization mechanisms are involved in both instruments. At high laser power density ($\sim 10^{10}$ W/cm²), a plasma formation process takes place. At low power density ($\sim 10^6$

W/cm²), a laser desorption process takes place in which molecules are vaporized into the gas phase. The latter is also considered a "soft" ionization process. The formation of cluster ions is favored by use of a thermal process, and a nonthermal process for molecular or quasimolecular ion formation. Both processes are simply obtained by focusing or defocusing of the laser beam.

Results

The evolution of the degradation process with respect to time and temperature for all samples was shown by the appearance of degradation products in the LAMMA and FTMS mass spectra. Functional group loss was determined for the exchange resin samples. As an example, the loss of the sulfonic -HSO₃ functional group from the polymer chain of a cation exchange resin can clearly be seen by a comparison of the LAMMA spectra of undegraded, slightly degraded, and degraded samples (Fig. 1). In the negative ion spectrum of undegraded resin the molecular ion peak of sulfonated styrene is shown at m/z 184. Carbon and hydrogen cluster ions are found at m/z 's C_nH_m , where $n = 1-10$ and $m = 0-4$, and sulfur-containing ions at m/z 's: 32 S^- , 33 SH^- , 64 (S_2^- or SO_2^-), 80 SO_3^- , and 81 HSO_3^- ; the relative ion intensities of SO_3^- and HSO_3^- are $\sim 80\%$ and 20% , respectively. The negative ion spectrum of slightly degraded resin (200 C/24 h) is the result of 100 accumulated spectra. This spectrum reveals the molecular ion peak at m/z 184, carbon hydrogen clusters C_nH_m , where $n = 2-16$ and $m = 0-2$, at the SO_3^- , HSO_3^- ions. Unlike the mass spectrum of new resin, sulfur at m/z 32 is not found and only a small-intensity sulfur-containing ion at m/z 64 is present. Also, the relative ion intensities of SO_3^- and HSO_3^- are reduced to $\sim 30\%$ and 15% , respectively. The final spectrum presented is also the result of 100 accumulated negative ion spectra. This spectrum is of degraded resin (300 C/24 h). No molecular ion peak at m/z 184 is present, cluster ions of carbon and hydrogen C_nH_m are found where $n = 1-12$ and $m = 0-2$, the relative ion intensities of SO_3^- , HSO_3^- are $\sim 10\%$, and there is no sulfur- or sulfur-containing ion at m/z 64. The degraded resin has lost its -HSO₃ functional group!

Conclusions

The thermal degradation of polymer materials, with respect to pyrolysis times and temperatures, can be followed by laser mass spectrometry (LAMMA and FTMS laser microprobes). Plasma and laser desorption ionization condi-

F. P. Scanlan and J. F. Muller are at the Laboratoire de Spectrométrie de Masse et Chimie Laser, Université de Metz, F-57012 France; J. M. Fiquet is at the Laboratoires Physico-Chimiques, Electricité de France, Carrefour Pleyel, F-93206 St. Denis, Paris, France. FPS gratefully acknowledges the support of Electricité de France in funding his thesis research.

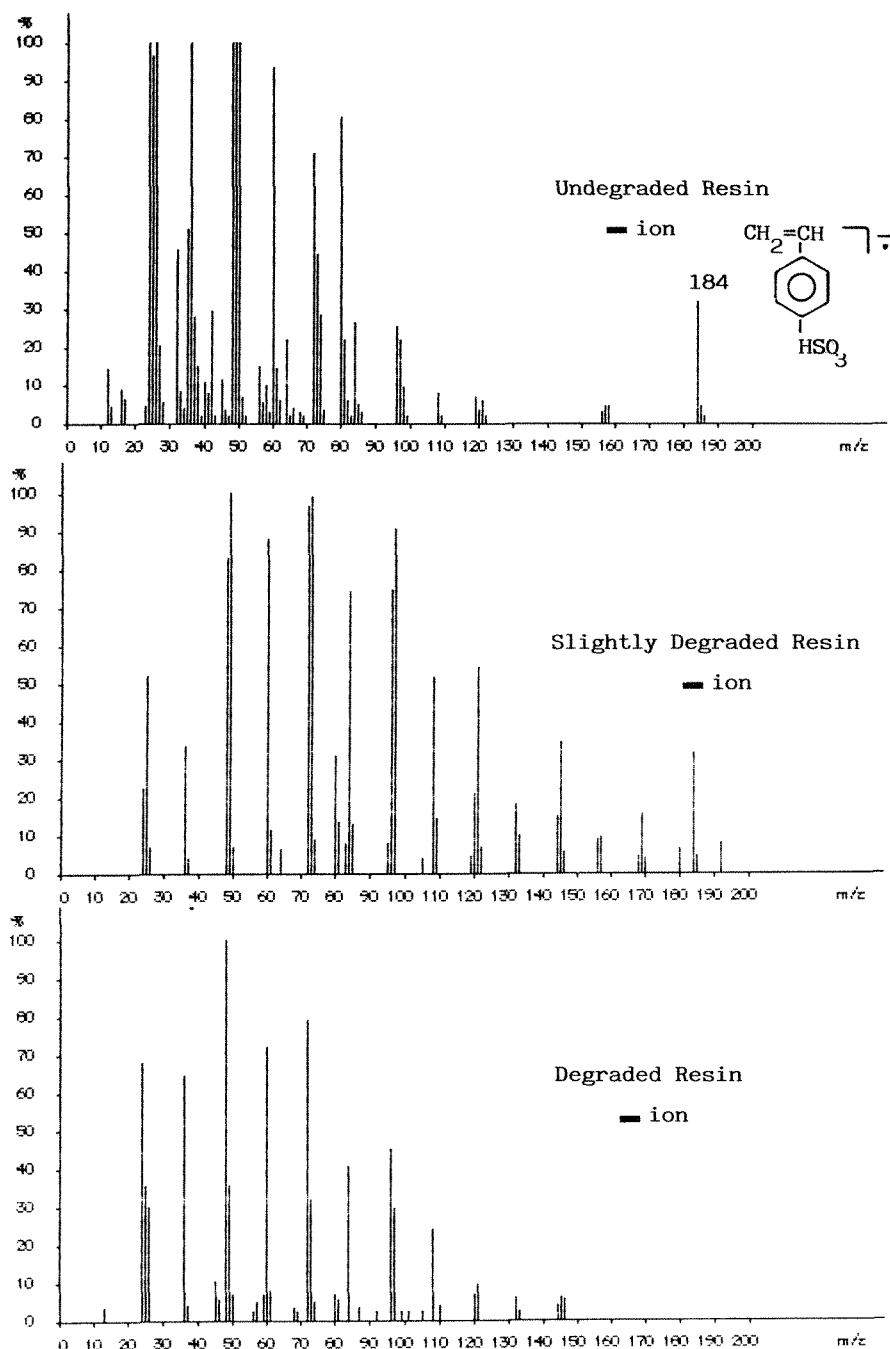


FIG. 1.--LAMMA spectra of undegraded (dried resin), slightly degraded (200 C/24 h) and degraded (350 C/24 h), cation exchange resin ARC 9351 (Duolite Co.), a sulfonated copolymer of styrene-divinylbenzene. Undegraded resin shows molecular ion peak of sulfonated styrene, whereas completely degraded resin shows functional group loss.

tions can be easily obtained by focusing or defocusing of laser beams. These analysis techniques can also be used to identify inorganic and organic degradation products from the direct analysis of the pyrolyzates.

References

1. J. B. Pausch, R. P. Lattimer, and H. L. C. Meuzelaar, "A new look at direct compound analysis using pyrolysis mass spectrometry," *Rubber Chem. Tech.* 56: 1031, 1983.
2. J. Haverkamp and P. G. Kistemaker, "Re-

cent developments in pyrolysis mass spectrometry," *Intern. J. Mass Spectrom. Ion Phys.* 45: 275, 1982.

3. J. A. Gardella Jr., S. W. Graham, and D. M. Hercules, "Structural analysis of polymeric materials by laser desorption mass spectrometry," in C. D. Craver, Ed., *Polymer Characterization*, Washington, D.C.: ACS, 1983, 635.

4. H. J. Heinen, "On ion formation in laser desorption mass spectrometry with LAMMA," *Intern. J. Mass Spectrom. Ion Phys.* 38: 309, 1981.

LASER IONIZATION AND PHOTOABLATION OF POLYMERS WITH LAMMA AND FTMS MICROPROBES

G. Krier, M. Pelletier, J. F. Muller, S. Lazare, V. Granier, and P. Lutgen

Among the numerous applications of laser microprobes, polymer analysis has become important in recent years. These instruments can provide precious information concerning purity and the fragmentation of these products.¹ One must optimize laser conditions such as energy, wavelength, focalization or defocalization, and extraction or trapping of ions, all with respect to the type of phenomena studied. In the first part of this study, a comparison of the repartition of sodium and potassium ions in two polymers (polyethylene terephthalate (PET) and standard Spurr resin²) will be examined with respect to spatial resolution ($\sim 1 \mu\text{m}$), sensitivity, and laser focalization of the LAMMA-500 microprobe.³

The second part of this work concerns the analysis, in reflexion mode, of PET and polystyrene PS by the first Fourier transform microprobe using an excimer laser.⁴ This technique allows for better control of the flux at the level of the impact. Sample ablation carried out by this instrument can be compared with other techniques of polymer photoablation by excimer laser, in widespread use since 1982.⁵ Mass spectrometry can provide precise information on ablation mechanisms due to photodecomposition, for which a better understanding of laser-solid interaction is needed.⁶

Experimental

Two laser microprobes were used. The first is a LAMMA-500 microprobe, in the transmission mode, coupled to a dye laser.⁷ The characteristics of the laser wavefront are shown in Table 1. The time-of-flight mass spectrometer resolution is ~ 800 for m/z 208. Three samples were analyzed by LAMMA: (1) Spurr resin $1 \mu\text{m}$ thick doped with sodium and potassium cryptates with a concentration of 10 mM; (2) polyethylene terephthalate of various thicknesses (1.5 and $12 \mu\text{m}$); (3) polyethylene terephthalate $12 \mu\text{m}$ thick metallized with $\sim 500 \text{ \AA}$ aluminum.

The second instrument is an FTMS microprobe used in bulk-sample analysis in the reflection mode with high resolution ($>100,000$) and high mass accuracy.⁸ The couple excimer laser was

operated at 193 and 249 nm. The laser's energy can be adjusted by use of a series of interchangeable filters. Changing the focalization is done by precise displacement of the telescope lenses. Laser flux can be thus varied from 10 to 10^7 mJ/cm^2 ; that is from 4×10^5 to $4 \times 10^{11} \text{ W/cm}^2$ for a 25 ns laser pulse. Two polymers were analyzed by the FTMS technique: polystyrene and $12 \mu\text{m}$ -thick polyethylene terephthalate.

Results and Discussion

Cation Repartition Study of Na^+ and K^+ in Two Polymers by LAMMA-500. Twenty laser impacts spaced $5 \mu\text{m}$ apart were performed. For each impact, the intensities (in mV) for sodium and potassium are reported in Figs. 1 and 2. The relative variation of these intensities are of the order of 100% for PET, and only 20% for the standard. The difference is even more apparent for the ratio of intensities Na/K, which vary more than 100% and less than 10%. These results can be explained by free migration; that is why Na^+ and K^+ cations are disordered on the surface of PET, whereas they are trapped in the uniformly repartitioned cryptates of the Spurr resin.

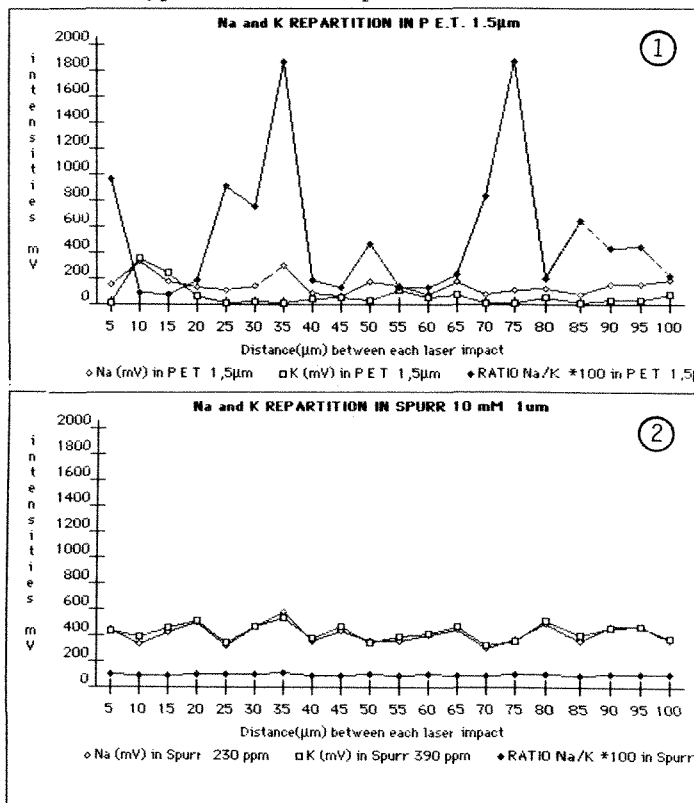


FIG. 1.--Repartition Na/K in PET.
 FIG. 2.--Repartition Na/K in Spurr.

G. Krier, M. Pelletier, and J. F. Muller are at LSMCL, Université de Metz, B.P. 794, F-57012 Metz Cédex 1, France; S. Lazare and V. Granier are at the Université de Bordeaux I, F-33405 Talence, France; P. Lutgen is at Du Pont de Nemours S.A. 2984 Luxembourg. This work was supported by ANVAR, the Ministère de la Recherche et de l'Enseignement Supérieur, the Ministère de l'Education Nationale, and the Région de Lorraine. M.P. acknowledges the financial support of his thesis by ELF France.

TABLE 1.--Laser parameters used with LAMMA.

Wavelength	Energy onto the sample	Pulse duration	Irradiated area	Irradiance	Fluence
286.5nm	3 μ J	10ns	20 μ m ²	1.5E+09W/cm ²	1.5E+04mJ/cm ²
228.8nm	1 μ J	10ns	7 μ m ²	1.4E+09W/cm ²	1.4E+04mJ/cm ²

The LAMMA microprobe's good lateral resolution was used to characterize a metallization defect on the 500Å aluminized surface of 12 μ m-thick PET. It seemed necessary to use ionization at 228.8 nm in order to obtain enough ions from a small surface (7 μ m²); they correspond to the nonmetallized microcircles (Fig. 3). Thus, calcium was significantly detected in these "Milky Way" defects. Ionization at 286.5 nm at the same energy did not give probing results, doubtless because the ionization yield was weak.

Polymer Analysis by the FTMS Microprobe in the Reflection Mode: Comparison with Photoablation. In FTMS the ion intensities are a function of energy and of the excimer laser wavelength used, 193 or 249 nm. For example, with polystyrene to obtain the same base peak intensity (36 arbitrary units), a fluence of 61 000 mJ/cm² at 249 nm is necessary, whereas at 193 nm only 3200 mJ/cm² was needed (Fig. 4). These differences can be compared to the fluence variation of ionization thresholds (that is, minimum fluence necessary to detect a signal in the spectrometer), and the ablation thresholds found in the literature.⁹ The three fluence values are clearly weaker at 193 nm than at 249 nm (Table 2). It is obvious that the ionization yield is more efficient at 193 nm than at 249 nm. This result is explained by a greater gas phase absorption, created by the laser at short wavelengths. Also, above a certain fluence (of the order of 300 mJ/cm²) this gas phase absorbs to the extent of becoming a screen for the solid and the ablation speed for the polymer is reduced, whereas the gas phase absorption at 249 nm is less. Proportionally a lot more neutrals are formed at 249 nm. The same phenomena were observed for PET. Moreover, with an ionization fluence slightly greater than the ionization threshold there are notable differences of intensity levels for certain ions (Fig. 5). An initial analysis showed the characteristic high mass fragments of polymers are more intense at 193 nm whereas the low mass fragments are more intense at 249 nm.

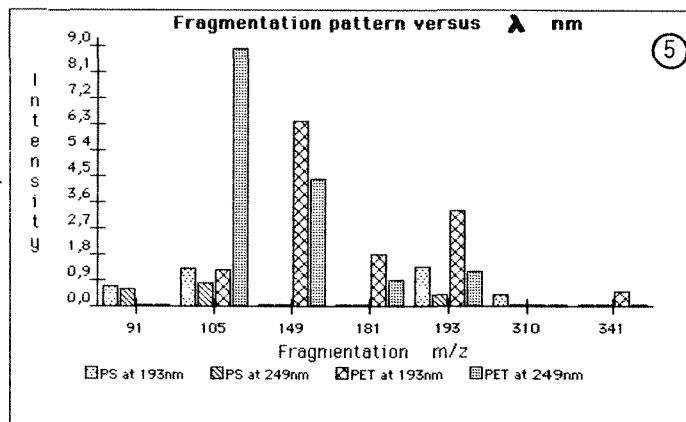
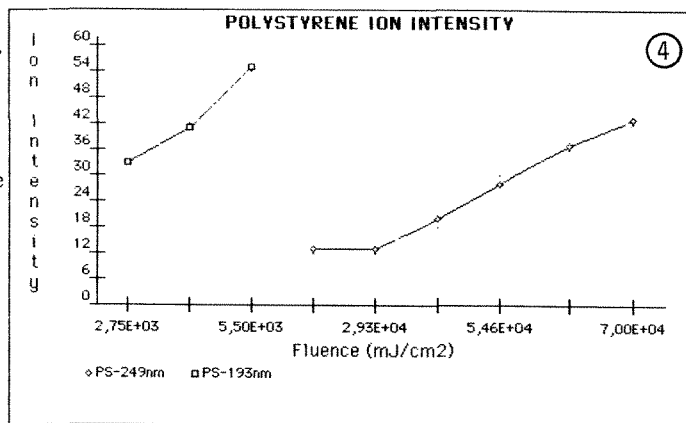
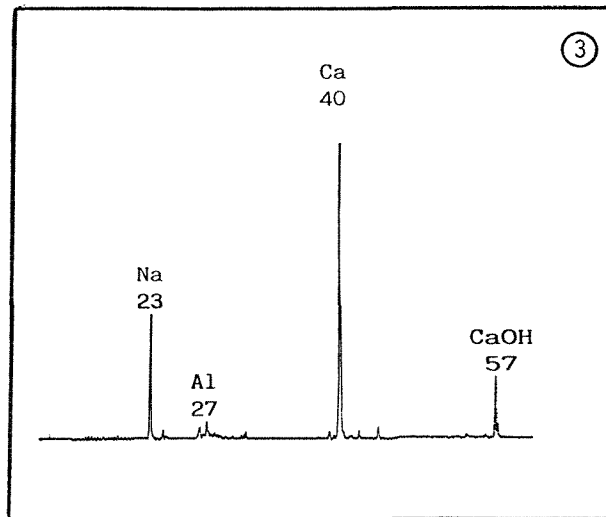


FIG. 3.--Analysis of a "hole" in the Al metallized layer at 228.8 nm.

FIG. 4.--Polystyrene ion intensity.

FIG. 5.--Relative ion intensities of polystyrene and polyethylene terephthalate at 193 and 249 nm.

TABLE 2.--Energy comparisons (mJ/cm²) with respect to wavelength for polystyrene.

Wavelength nm	193	249
Fluence for a given peak base height at 36 (mJ/cm ²)	3200	61000
Fluence Ionization thresholds (mJ/cm ²)	40	400
Fluence Ablation thresholds (mJ/cm ²)	10	60

Conclusion

Good spatial resolution and good sensitivity of the LAMMA microprobe permits the characterization of pinhole defects on polymer surfaces in the form of thin films. Due to its precision in defocalization and tunable laser energy, the FTMS microprobe appears to be a useful tool for ablation control experiments and for the characterization of ions in material profiles. In this study clear ionization differences were shown between 193 and 249 nm. Ionization at 193 nm is more efficient and therefore better adapted for photoablation mechanism studies. In this field the FTMS microprobe will provide more information.

References

1. R. Holm, M. Karas, and H. Vogt, "Polymer investigations with the laser microprobe," *Anal. Chem.* 59: 2, 371, 1987.
2. A. R. Spurr, "A low viscosity epoxy resin embedding medium for electron microscopy," *J. Ultrastructure Res.* 26: 31, 1969.
3. R. Wechsung, F. Hillenkamp, R. Kaufmann, R. Nitsche, E. Unsold, and H. Vogt, "A new laser microprobe mass analyser," *Microscopia Acta Suppl.* 2: 1978.
4. J. F. Muller, G. Krier, M. Pelletier, D. Weil, and J. Campana, "Laser microprobe Fourier transform mass spectrometry," *Pittsburgh Conf.*, 1989; see also the present volume.
5. R. Srinivasan and V. Mayne-Banton, "Self-developing photo-etching of poly(ethylene-terephthalate) films by far ultraviolet excimer laser radiation," *Appl. Phys. Lett.* 41: 576, 1982.
6. S. Lazare and V. Granier, "Ultraviolet laser photoablation of polymers: A review and recent results," *Laser Chem.* 10: 25, 1989.
7. G. Krier, F. Verdun, and J. F. Muller, "Coupling a tunable dye laser to a LAMMA-500 microprobe," *Fresenius Z. anal. Chem.* 322: 379, 1985.
8. M. Pelletier, G. Krier, J. F. Muller, D. Weil, and M. Johnston, "laser Microprobe Fourier Transform Mass Spectrometry," *Rapid Comm. Mass Spectrom.* 2: 146, 1988.
9. S. Lazare and V. Granier, "Excimer laser light induced ablation and reactions at polymer surfaces as measured with a quartz-crystal microbalance," *J. Appl. Phys.* 63: 2110, 1988.

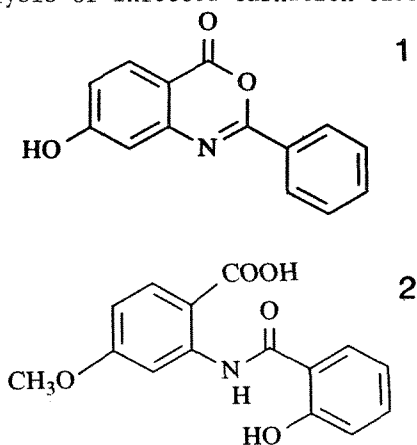
LAMMS: Biomedical & Environmental Applications

IN SITU ANALYSIS OF CARNATION PHYTOALEXINS BY LASER MICROPROBE MASS SPECTROMETRY

Annick Mathey, Luc Van Vaeck, and Pierre Ricci

Phytoalexins are low-molecular-weight (MW) antimicrobial compounds synthesized by and accumulated in plants after exposure to microorganisms.¹ Production and accumulation can be induced by treatment of plant tissues with high-MW cell wall components of pathogenic fungi and bacteria, termed elicitors.² In general, phytoalexins can be extracted and identified, but are not histologically localized by direct methods. To our knowledge, only one attempt has been made on soybean.³

The host-parasite system *Dianthus caryophyllus* L. (carnation) and *Phytophthora parasitica* Dastur (pathogenic fungus) has been extensively studied.⁴ The major phytoalexins are dianthalexin (DX) and methoxydianthramide S (MDS) (Figs. 1 and 2). The fluorescence of the isolated compounds provides the means to guide LMMS analysis of infected carnation tissues.



FIGS. 1 and 2.—Structure of main carnation phytoalexins, DX and MDS.

Experimental

Cuttings of a Sim type Ember variety carnation are dipped in an aqueous solution of elicitor⁴ during three or four days and submitted to light 10h/day. Thick (20–30µm) longitudinal

Author Mathey is with the Department of Plant Pathology, Institut National de la Recherche Agronomique, CRA, F-78026 Versailles CEDEX, France; author Van Vaeck is a Research Associate of the National Science Foundation of Belgium; and author Ricci is with the INRA Station de Pathologie Végétale, B.P. 2078, F-06606 Antibes CEDEX, France. They are indebted to Profs. F. Adams and R. Gijbels (UIA) for encouraging this work; to M. Hauteville (University of Lyon) and M. Ponchet (INRA) for supplying DX and MDS; and to INRA and NFWO for providing financial support.

and cross sections are taken from the elicitor-treated region up to 1 cm with a freezing microtome Reichert Frigocut and observed by fluorescence microscopy. The vascular system consists of partly lignified vessels (Fig. 3). After elicitation, modifications are observed and under UV excitation vessels emit green fluorescence with blue white spots in given points of the lignified parts (Fig. 4). The vessel contents also emit bright fluorescence. These regions are interesting for LMMS analysis. Semi-thin cryosections (0.5 to 1 µm) are made without embedding with an LKB Ultratome, photographed in a fluorescence microscope and in a Philips transmission electron microscope (dark field), and measured with the LAMMA 500. Details on the methods of procedure are available elsewhere.^{5,6}

Results

First pure DX and MDS have been analyzed. Negative LMMS results show deprotonated molecules at m/z 238 for DX and 286 for MDS. Fragmentation is negligible. In the positive mode, there are characteristic fragments serving diagnostic purposes. However, their usefulness depends on the alkali-concentration in the sample. An excess of K^+ suppresses positive organic ion formation.

For LMMS, cross sections of elicitor-treated carnation are more appropriate in view of the surface availability.⁷ All fluorescent spots are investigated in the negative mode and, where possible, in the positive mode. Over 500 spectra have been taken from about 25 sections.

DX is found in the lignified wall of the vessels (Figs. 5 and 6) or in the obstructing inclusions after elicitation. An accompanying product, probably its oxygenated derivative, is usually observed (DXOH?). The lack of a pure reference makes this interpretation tentative. Moreover, the compound has not been identified in the extract of elicited carnation. Longitudinal sections are difficult to analyze because the vessel wall covers the organic target. Hence, inclusions emerging from the vessels after sectioning are analyzed. In general, DX is detected. Otherwise, the covering material has to be perforated first by the laser to permit release of organic ions. The problem is sometimes circumvented by sectioning (dividing the vessel and exposing the contents, Fig. 7). DX is located in the lignified wall of xylem vessels and inside the vessels. The fibrous aspect of the inclusions seems to be due to material from degraded cell walls (Fig. 9). Although pure MDS emits a blue-green fluorescence under UV excitation⁸

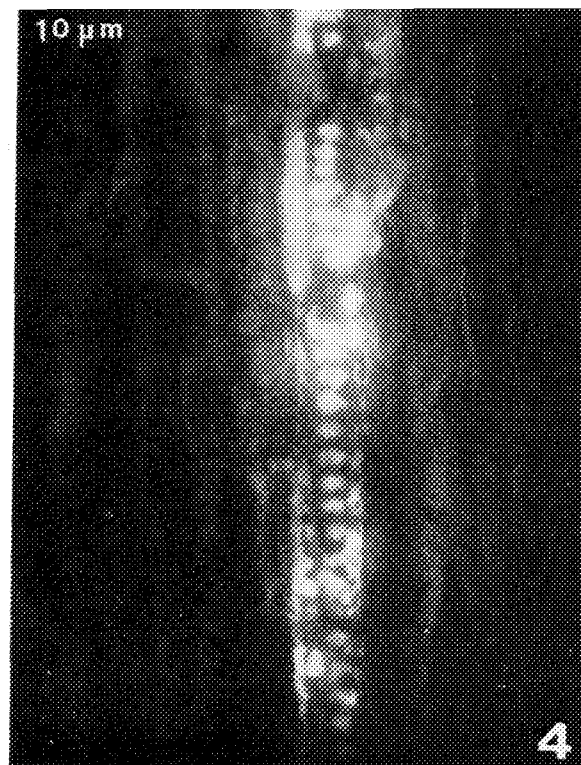
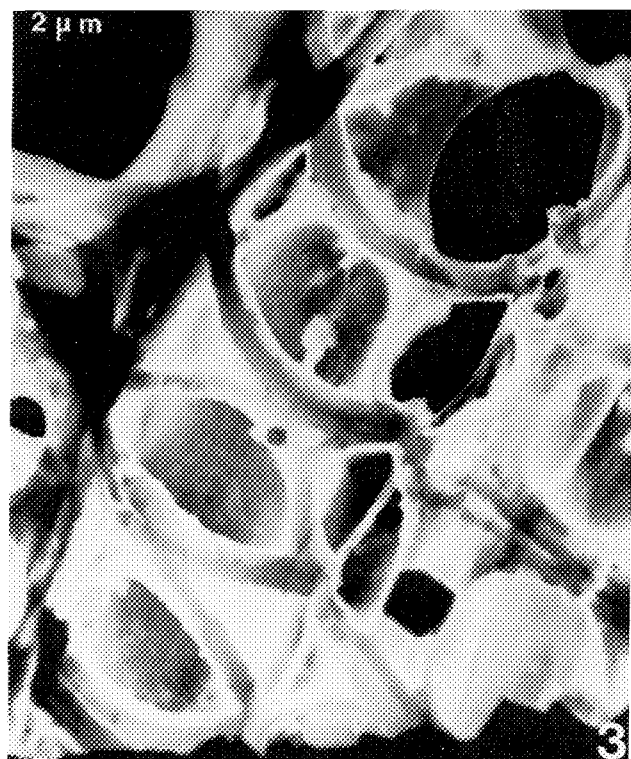


FIG. 3.--TEM dark-field micrograph of semi-thin cryosection of carnation vessels.
FIG. 4.--Fluorescence micrograph of thick cryosection of vessel after elicitation.

and LMMS detection is expected in such regions of elicitor-treated carnation, a prominent signal has been found only once; occasionally a small peak is seen in the presence of DX and its oxygenated analog (Fig. 8).

Extraction and HPLC assay of carnation phytoalexins after elicitation has yielded similar amounts of DX and MDS.⁴ This observation is not confirmed by LMMS. This disagreement can be associated with the K^+ content of the vessel wall. Normally, an ionic form desorbs less easily than the neutral analog. Hence concentration may be underestimated from comparison of the signals at m/z 238 vs 286.

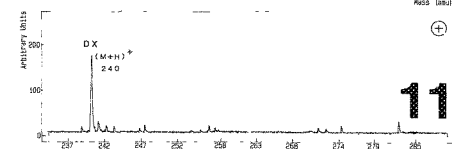
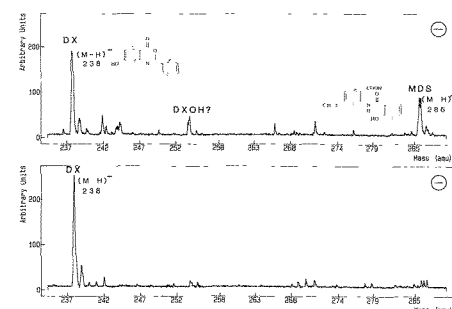
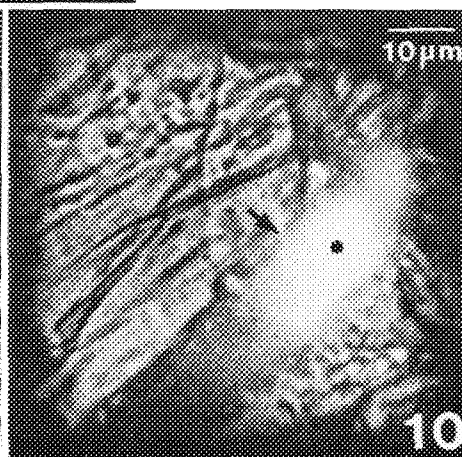
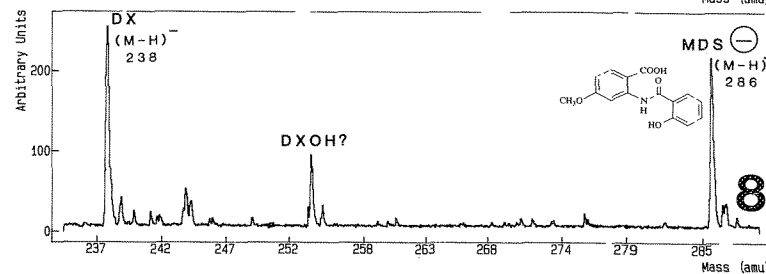
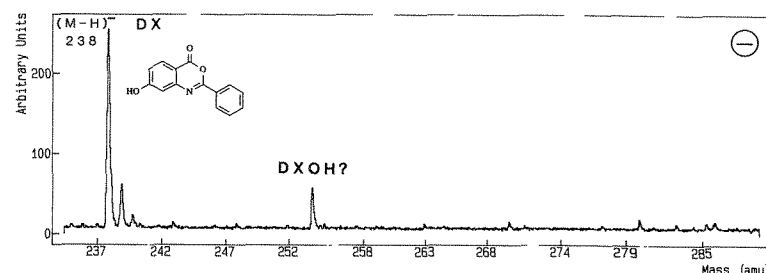
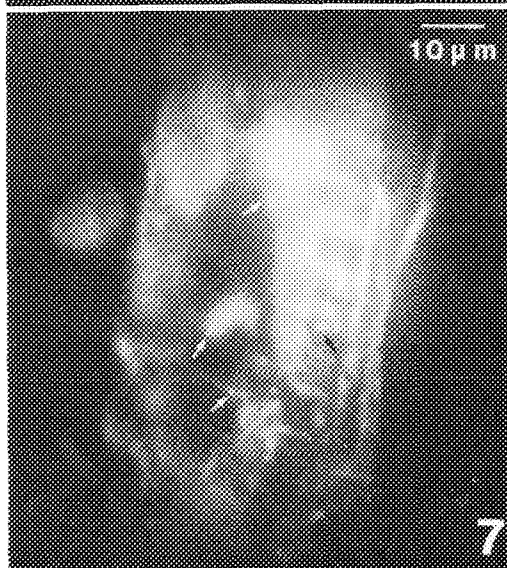
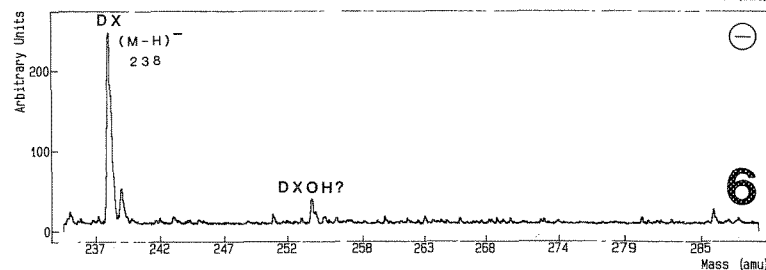
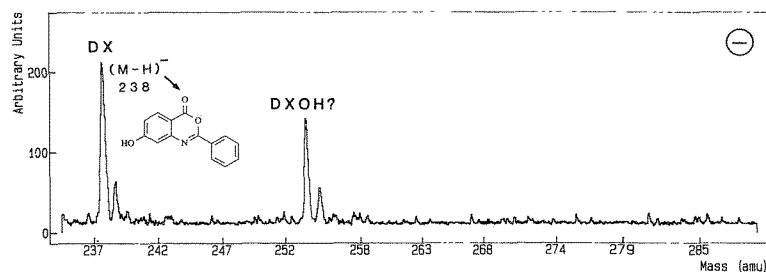
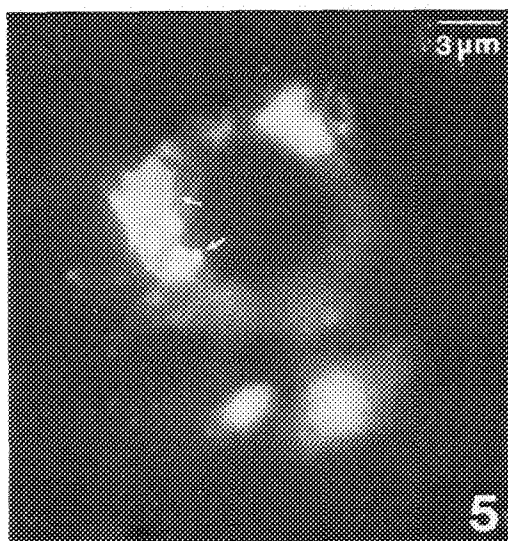
The medullary tissue called parenchyma of elicitor-treated carnation has been also analyzed (Figs. 10 and 11). DX is found in cell walls and cytoplasm. MDS is more rarely detected. Positive spectra show less abundant K^+ concentrations than in the xylem.

Conclusions

The capability of LMMS to detect organic targets in a complex matrix has been exploited to verify the presence of given phytoalexins directly in infected carnation tissues. Analysis is favored by the surface availability and the sensitivity of the product on the one hand, and the size of the local accumulation as well as the possibility of selecting the regions of interest by fluorescence microscopy on the other hand. The results open promising perspectives in plant pathology, e.g., as to flavonoids.

References

1. J. W. Mansfield, "Antimicrobial compounds," in I. Mansfield, Ed., *Biochemical Plant Pathology*, New York: Wiley, 1983- 237.
2. R. N. Goodman, Z. Kiraly, and K. R. Wood, *The Biochemistry and Physiology of Plant Disease*, Columbia, Ms.: University of Missouri Press, 1986.
3. P. Moesta, U. Seydel, B. Lindner, and H. Grisebach, "Detection of glyceollin on the cellular level in infected soybean by laser microprobe mass analysis," *Z. Naturforsch.* 370; 748, 1982.
4. P. Ricci, *Etude des relations hôte-parasite dans l'interaction compatible entre Dianthus caryophyllus L. et Phytophthora parasitica* Dastur: *Nature et intervention d'un mécanisme de défense élicitable*, Ph.D. thesis, No. 3203, University Paris-Sud, Orsay, 1986.
5. A. Mathey, L. Van Vaeck, and W. Steglich, "Investigation of semi-thin cryosections of lichens by laser microprobe mass spectrometry," *Anal. Chim. Acta* 195: 89, 1987.
6. L. Van Vaeck, J. Bennett, W. Lauwers, A. Vertes, and R. Gijbels, "Laser microprobe mass spectrometry: Possibilities and limitations," *Mikrochim. Acta* (in preparation).
7. L. Van Vaeck, P. Van Espen, W. Jacob, R. Gijbels, and W. Cautreels, "In-depth limitation of the LAMMA 500 for the in situ localization of organic compounds in biological embedded tissue samples," *Biomed. Environ. Mass Spectrom.* (in press).
8. M. Ponchet, J. Favre-Bonvin, M. Hauteville, and P. Ricci, "Dianthramides (N-benzoyl and N-paracoumarylanthranilic acid derivatives) from elicited tissues of *Dianthus caryophyllus*," *Phytochemistry* 27: 725, 1988.



FIGS. 5 and 6.--Fluorescence micrograph of semi-thin cryo cross section of vessel after elicitation and corresponding LMMS results.

FIGS. 7 and 8.--Fluorescence micrograph of semi-thin cryo longitudinal section of vessel after elicitation and corresponding LMMS results.

FIG. 9.--TEM dark-field micrograph of semi-thin longitudinal cryosection, showing fibrous content of vessel after elicitation.

FIGS. 10 and 11.--Fluorescence micrograph of parenchyma cell after elicitation and corresponding LMMS results.

PROSPECTS FOR LASER MOLECULAR MICROPROBING

Michael Karas and Franz Hillenkamp

Laser microprobing for biological samples has been so far restricted mainly to elemental analysis. Only in some special cases with high local concentrations or larger organic compounds has a direct molecular analysis^{1,2} been feasible. General biological microanalysis (i.e., the analysis of large biologically active molecules like enzyme proteins directly out of their native surroundings) doubtless constitutes an ultimate goal for laser microprobing. So far, such an analysis was totally out of reach because two important prerequisites were not fulfilled. First, a desorption/ionization technique that can set free and ionize molecules of molecular weights in the 10 or 100 kDa range with high sensitivity was not available; and, second, an adequate detection of such large ions seemed impossible. Recently Ultraviolet Laser Desorption Ionization (UV-LDI) of proteins up to molecular weights of more than 250 000 Da directly out of the condensed phase was demonstrated by the authors using a matrix technique.^{3,4} Such results on protein ion desorption and high mass ion detection will be reported. The possible adaption of matrix desorption technique to biological samples will be discussed.

Experimental

Experiments were done with a LAMMA 1000 microprobe instrument equipped with an ion detection system applying up to 20 keV of postacceleration potential at a separate conversion dynode (Cu-Be Venetian blind) preceding the SEM. Because flight times are larger than 1 ms for masses exceeding 150 000 Da, the transient recorder (LeCroy 9400) was used at a time resolution of 80 ns/channel. Protein/matrix (nicotinic acid) solid layers were prepared on metallic substrates from aqueous solutions by evaporation of the solvent; the total amount of protein was in the sub-pmol range. Microstructural analysis of the desorption sites was done by scanning electron microscopy. The correlation between ion-signal intensities and the amount of ablated material is used to estimate the absolute amount of sample necessary for a protein mass spectrum and thus the sensitivity reached.

Results

Figure 1 shows the matrix UV-LDI spectrum of B-D-galactosidase. Besides singly charged

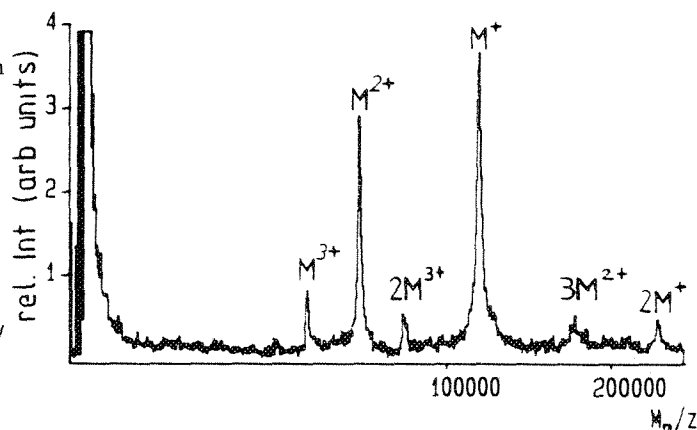


FIG. 1.--Matrix UV-LDI spectrum of G-D-galactosidase, accumulated from 30 single shots; measured molecular weight is 117 130 Da.

molecular ion signals also multiply charged molecular and singly and doubly charged cluster ions show up in the spectrum at lower intensities. Though the mass resolution is less than 100, the accuracy of molecular weight determination is in the 0.1% range. Matrix ions were used for mass calibration. The absolute protein amount of 500 fmol was spread over an area of 5 mm² and only about 10⁻³ mm² of it are irradiated at a typical defocused laser diameter of ca 30 μm. With only 10⁻¹⁷ mol absolute sample amount in the irradiated volume, which is ablated by several successive laser shots under typical irradiances, total sample consumption for a mass spectrum can be estimated to be in the 10⁻¹⁸ mol range. SEM imaging of protein/matrix layers before and after irradiation and the correlation between ablation depths and LDI-spectra justify the above estimates.

The unexpectedly good signal-to-noise ratio of ions even at masses exceeding 100 000 Da and the low absolute sample amount available for a LDI spectrum point to a remarkable detection efficiency, which is not to be expected from the literature^{5,6} for velocities in the range below 10⁴ ms⁻¹.

The signal intensities measured as a function of ion velocity for a variety of different ions in the mass range of 100-170 000 Da suggest that there is a definite dependence of the detection probability on the ion mass, resulting in a much higher overall sensitivity for large ions than anticipated from reports in the literature, even at a conversion potential of only 20 keV as used in the experiments reported here.

The authors are at the Institut für Medizinische Physik, Universität Münster, Hufferstrasse 68, D-4400 Münster, Federal Republic of Germany.

Conclusion

The results document that the mass range for ion production can be extended by matrix UV-LDI to a region covering many biologically relevant macromolecules. Their stability in the millisecond range, prerequisite for ions to be detected in the LAMMA instrument, together with a remarkable sensitivity as well as ion detection efficiency even at masses above 100 000 Da open new perspectives for molecular microprobing of biomacromolecules. If a suitable preparation technique could be found for biological samples, by which the common embedding material such as paraffin or epon could be replaced by a matrix as supportive for the desorption/ionization as is the nicotinic acid used so far in the experiments reported, true molecular microprobing no longer appears to be totally out of reach.

References

1. M. Wink, H. J. Heinen, H. Vogt, and H. M. Schiebel, *Plant Cell Reports* 3: 230, 1984.
2. P. Moesta, U. Seydel, B. Lindner, and H. Grisebach, *Z. Naturforsch.* 37a: 748, 1982.
3. M. Karas and F. Hillenkamp, *Anal. Chem.* 60: 2299, 1988.
4. M. Karas, U. Bahr, A. Ingendoh, and F. Hillenkamp, *Angew. Chem. Int. Ed. Engl.* (in press).
5. R. J. Beuhler, *J. Appl. Phys.* 54: 4118, 1983.
6. A. Hedin, P. Hakansson, and B. U. R. Sundqvist, *Int. J. Mass Spectrom. Ion Proc.* 75: 275, 1987.

LAMMS DETECTION OF DENTAL METALLIC COMPOUNDS IN THE HUMAN ORAL MUCOSA

Peter Rechmann, J. L. Tourmann, and R. L. Kaufmann

Amalgam tattoo of the oral mucosa membrane is a relatively common lesion, with an estimated incidence of 1.4%.¹ Amalgam tattoos usually appear as blue dark lesions, to date considered as not esthetic but innocent (Fig. 1). Amalgam tattoos are generally thought to be the consequence of an accidental implantation of amalgam particles, e.g., by direct penetration of particles into mucosa propelled by high-speed instruments during dental treatment.

With the increasing awareness of the potential chronic toxicology of trace heavy metals it has become necessary to evaluate the fate of such particulated metal inclusions with respect to their local transformations (passive or active). So far, only a few scattered investigations using mainly EDX are found in the literature.²⁻⁴ However, the results are methodologically neither appropriate nor conclusive. From this and other evidence, it is suspected that larger tattoo particles merely undergo passive physico-chemical transformations with preferable mercury leaching out of the alloy, whereas small particles are thought to be taken up for example by macrophages via phagocytosis.

In this study a systematic investigation has been performed in oral mucosa tattoos by means of LAMMS analysis in 17 specimens (16 biopsies, 1 necropsy).

The histological picture of such tattoos is usually rather unspecific, ranging from a virtually unchanged tissue texture to heavy inflammatory reactions. Metal particles are found in nearly every section (at least in the center of the tattoo) ranging in size between the lower limit of the optical resolving power of the UV transmission microscope (0.2 μm) and rather large particles up to several tens of micrometers. The appearance of a typical specimen is shown in Fig. 2.

In 13 of the 16 biopsies particulated inclusions could be identified as being derived from dental amalgams. In the three other samples the tattoos were not related to dental amalgam but obviously originated from a silver cone (2 cases) or an unidentified metal alloy (chromium, molybdenum) in one case. In the necropsy the metallic compounds detectable were identified as parts of a typical gold alloy.

In most of the investigated samples, LAMMS

spectra of the microinclusions revealed--in addition to the leading elements of the alloy--the presence of elements (P, S, Ca, Fe, Se) not known to be contained in the original materials. It is assumed that these elements reflect specific tissue reactions in response to the penetration of metallic microparticles presumably indicative of some kind of an active "detoxification" process.

Materials and Methods

Biopsies were taken under local anesthesia from dark discolored parts of the oral mucosa. Specimens were shock-frozen in supercooled liquid propane and freeze-dried at -80 °C during 72 h. After embedding in Spurr's low-viscosity medium, sections were cut dry (2 μm) and analyzed in a LAMMA 500 instrument, equipped for UV imaging of the unstained sections.⁵

Some of the embedded specimens containing metallic particles exhibited a hitherto unknown "contamination effect" by the metallic elements (see also Kaufmann et al., 4th LAMMS International Workshop). However, this phenomenon did not occur in all specimens; 16 out of 27 samples not infected with this artifact were examined in this investigation.

As a first step during LAMMS analysis a section of each embedded sample was systematically screened for trace elements present anywhere in the tissue. In a second section only the clearly distinguishable particles, visible in the UV microscope of the LAMMA 500, were analyzed (8-15 particles in each specimen). Laser power was set to 100% transmission in order to provide maximal sensitivity with respect to mercury.

The necropsy specimen was taken from a not discolored gingival area opposite of a dental crown made of gold alloy.

Results

An overview of all samples analyzed in this study is given in Table 1.

In the group of the 13 specimens characterized as amalgam tattoos, 119 individual metallic microinclusions were analyzed. In most instances repetitive spectra could be recorded from each particle such that the total number of spectra evaluated amounts to 597. Signal intensities were roughly weighted by distinguishing "trace" signals (near the detection limit), "minor" signals (5-10% full scale) and "major" signals (leading or saturated peaks).

The LAMMS criterion for attributing the origin of a tattoo to amalgam was a mixed population statistics comprising particles of preferably silver or tin signals, or in most

Peter Rechmann is at the ZMK-Klinik of the University of Düsseldorf (School of Dentistry, Department of Oral Surgery and Oral Medicine); J. L. Tourmann and R. L. Kaufmann are at the Institute of Laser Medicine, University of Düsseldorf, Moorenstr. 5, D-4000 Düsseldorf, Federal Republic of Germany. Authors thank the Deutsche Gesellschaft für Zahn-, Mund- und Kieferheilkunde for financial support.

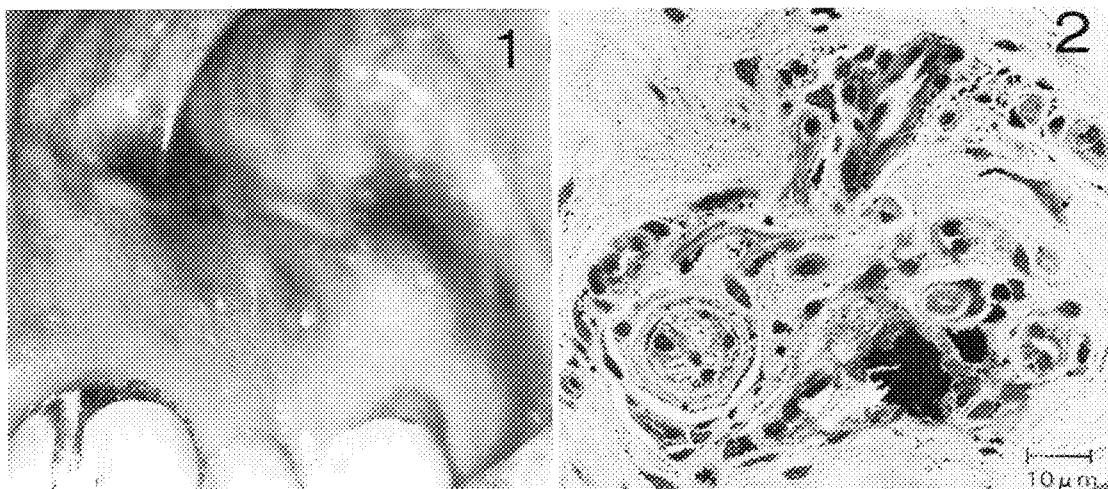


FIG. 1.--Slightly enlarged view of typical amalgam tattoo.

FIG. 2.--Histological section of amalgam tattoo showing metallic particles (toluidin blue staining).

TABLE 1.--Origin of samples and LAMMS signals as related to dental alloy.

Sample	Origin of lesion as revealed by LAMMS analysis	Typical signals related to dental alloy
16 biopsies of tattoo	13 amalgam 2 silver cone 1 unidentified alloy	Ag, Sn, Cu, Hg Ag Cr, Mo
1 necropsy	1 gold alloy	Ag, Pd, Au

instances a combination of both signals. The incidence of the 4 elements copper, silver, tin, and mercury as detected by LAMMS analysis in the metallic tissue inclusions ($n = 597$ spectra out of 119 particles) is demonstrated in Fig. 3, whereas Fig. 4 shows the same kind of statistical evaluation obtained in reference amalgam particles derived from bulk amalgam samples removed from extracted teeth. Comparison of these data reveals a drastically reduced incidence of mercury signals in the metallic tissue inclusions equally affecting the three classes of signal intensities.

A similar but less pronounced reduction of signal intensity refers to the detection of copper, whereas the incidence of Ag and Sn over the three intensity classes remains roughly unchanged. (Whether the slight change of the silver to tin incidence ratio is statistically meaningful cannot be decided at the moment.)

Figure 5 gives a statistical evaluation for the incidence of signals not related to the original alloy but more or less regularly found in the LAMMS spectra recorded in the metallic tissue inclusions. Taking into account only the signal intensities of the "minor" and "major" classification, it appears that 57% of the LAMMS spectra exhibit iron; 57% calcium;

36% sulfur; 28% phosphorus; and most interesting, 17% selenium (with the class of "trace" signals included). A typical spectrum of such an element combination is shown in Fig. 6.

Two of the 16 tattoos, which according to clinical criteria had been classified as typical amalgam tattoos, were found to be unrelated to amalgam by LAMMS analysis since the only element detectable, even in the largest metallic inclusions, was silver, indicating that these two tattoos originated from silver cones typically employed in endodontic surgery.

The remaining case of the investigated tattoos could be identified as being due to an alloy featuring molybdenum and chromium as major components and could not be explained from the known history of the case.

The last case, a necropsy investigated by LAMMS, does not strictly belong into the systematics of this investigation insofar as no recognizable tattoo was present in the area from which the specimen was taken. Nevertheless, LAMMS analysis revealed the presence of a gold alloy (Pd, Ag, Au) most probably originating from a typical dental casting material (Fig. 7). Of particular interest in this case is the presence of lithium detected by the LAMMS analysis.

Discussion

In agreement with earlier results, the investigation confirmed that typical tattoos in the oral mucosa consists of metallic microparticulates^{1,3,6} which in all likelihood were artificially implanted in superficial tissue layers during a dentist's manipulation such as grinding, drilling, or polishing.

It is generally accepted that dental alloys undergo corrosion if exposed to the typical oral environment. However, despite the large body of investigations dealing with this problem, the image of corrosion processes occurring for example in the various amalgams is, up to now, far from being complete and fully understood.

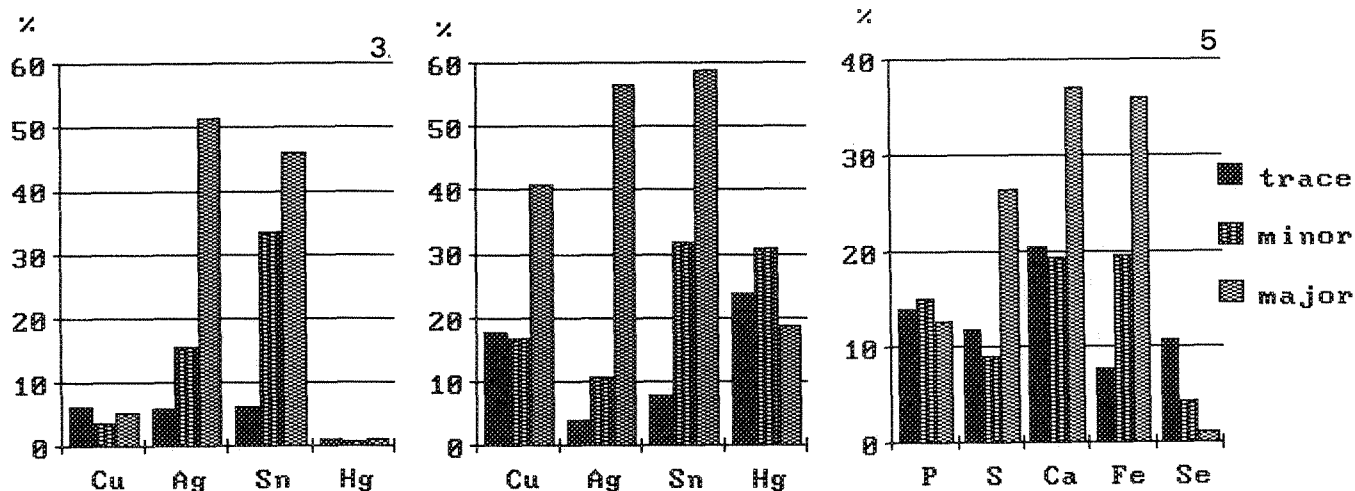


FIG. 3.--Element distribution (in % incidence) of amalgam-related elements in 597 recorded spectra from 119 tattoo particles.

FIG. 4.--Element distribution in amalgam reference sample in % incidence of the analyzed particle population (n = 100).

FIG. 5.--Element distribution (in % incidence) of nonamalgam-related elements in 597 recorded spectra from 119 amalgam tattoo particles.

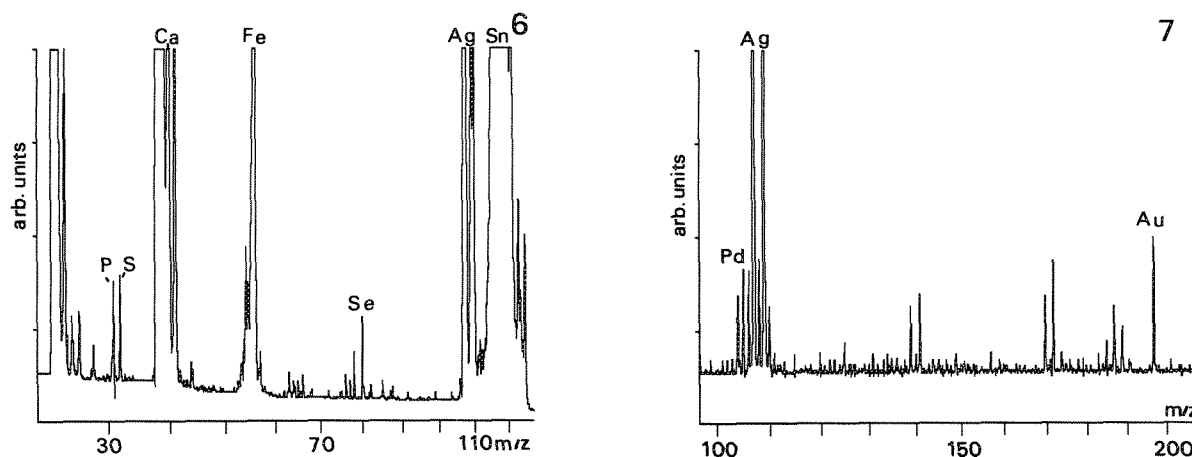


FIG. 6.--Typical LAMMS spectrum demonstrating amalgam-related (Ag, Sn) and nonamalgam-related elements (P, S, Ca, Fe, Se).

FIG. 7.--Spectrum of casting gold alloy as identified by Pd, Ag, Au LAMMS signals in a not discolored gingiva.

Evidence is even less conclusive if one looks at the fate of such alloys implanted in a tissue environment. Such an environment certainly differs in many respects (pH, ionic composition) from the oral milieu. That means that corrosive processes typically seen under saliva exposure are certainly not comparable to what might occur in a tissue environment.

Furthermore, one might expect particles to undergo transformations (if located in a biological active tissue) that are not entirely passive but might be rather the result of active processes in an attempt of the tissue to eliminate and/or "detoxify" the metallic foreign body.

The present investigation can certainly be taken as a piece of evidence that both princi-

ples of transformation do occur. The disappearance of mercury from the tattooing amalgam particulates may be taken as an indicator of an element-selective (corrosive) leaching and agrees with the observation of Cox and Eley, who demonstrated a long-term release of mercury from powdered dental amalgam implanted in guinea pigs.⁷ On the other hand, the accumulation of iron and selenium in combination with sulfur, phosphorus, and calcium are certainly strong indicators for an active metabolic process involved in the process of particle transformation.

In this context we note that a selective association occurs of either iron or selenium with special groups of the metal particles (Fig. 8). Iron was found in 95% of the 130

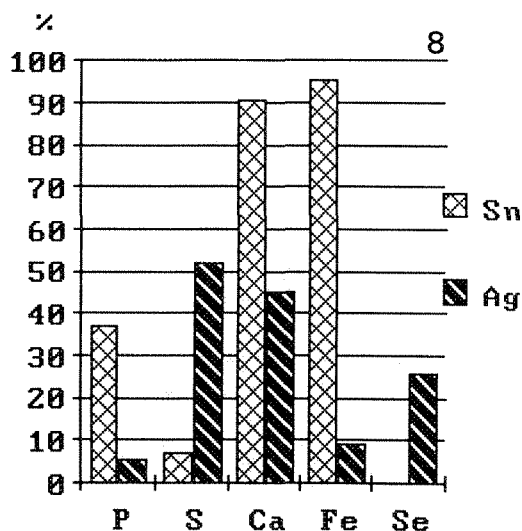


FIG. 8.--Histogram showing the selective association of S and Se to Ag and the association of P and Fe to Sn (standardized to 100% of Sn-dominated spectra and 100% of Ag-dominated spectra, respectively).

spectra (out of the 597 spectra recorded) in which only tin (but not silver) appeared as an amalgam-related signal, but only 9% of the spectra featuring silver (but not tin) as an amalgam-related indicator. On the other hand, selenium occurred exclusively in spectra with silver as the only amalgam-derived compound (26% incidence). A similar unequal distribution was found for phosphorus and sulfur, respectively. Finally, the rather high incidence of calcium associated with both kinds of elements might be at a first suggestive of microcalcification processes occurring around the particles. The latter finding is also consistent with observations made by Harrison et al.³ and McGinnis et al.⁴

Finally, we may dare to speculate that the detection of unusually high sulfur signals in a rather large fraction of the LAMMS-analyzed microinclusions, and even more so, the rather unusual occurrence of selenium have something to do with an accumulation (for example) metallothioneins featuring a large fraction of the sulfhydryl-bearing aminoacid cysteine. Such metallothioneins have been repeatedly mentioned as playing a role in heavy-metal detoxification, although experimental evidence in this respect is still far from being conclusive.⁸

It appears further that in certain enzymatic proteins (e.g., glutathione peroxidase) selenium can replace for sulfur in the cysteine. To what an extent selenium cysteine is present in other cysteine-rich proteins, such as metallothionein, is unknown.⁹

In any case selenium has been known to reduce the toxicity of cadmium and mercury in studies of chronic cadmium/mercury toxicity.¹⁰ Histochemical studies will follow to check for the potential presence of high glutathione peroxidase activities in the investigated samples.

References

1. A. Buchner and L. S. Hansen, "Amalgam pigmentation (amalgam tattoo) of the oral mucosa: A clinicopathologic study of 268 cases," *Oral Surg.* 49: 139, 1980.
2. D. A. Levison, P. R. Crocker, G. Lee, N. A. Shepherd, and A. P. Smith, "Unexpected inorganic elements in oral lesions: Results of x-ray energy spectroscopy (XES) on particulate matter in paraffin sections," *J. Path.* 144: 119, 1984.
3. J. D. Harrison, P. S. A. Rowley, and P. D. Peters, "Amalgam tattoos: Light and electron microscopy and electron-probe microanalysis," *J. Path.* 121: 83, 1977.
4. J. P. McGinnis Jr., J. L. Greer, and D. S. Daniels, "Amalgam tattoo: Report of an unusual clinical presentation and the use of energy dispersive X-ray analysis as an aid to diagnosis," *J. Am. Dent. Ass.* 110: 52, 1985.
5. R. Kaufmann, "Laser microprobe mass analysis (LAMMA): Current state of the art with special emphasis on bio-medical applications," *Microbeam Analysis--1982*, 341.
6. B. Orban, "Discolorations of the oral membrane by metallic foreign bodies," *J. Periodont.* 17: 55, 1946.
7. S. W. Cox and B. M. Eley, "The release, tissue distribution and excretion of mercury from experimental amalgam tattoos," *Br. J. Exper. Pathol.* 67: 925, 1986.
8. H. H. Dieter and J. Abel, "Metallothionein: Biochemie und Hypothesen zur physiologischen Funktion des schwermetallbindenden Proteins," *Biologie in unserer Zeit* 17: 27, 1987.
9. L. Flohé, W. Strassburger, and W. A. Günzel, "Selen in der enzymatischen Katalyse," *Chemie in unserer Zeit* 21: 44, 1987.
10. P. Dürre and J. R. Andreesen, "Die biologische Bedeutung von Selen," *Biologie in unserer Zeit* 16: 12, 1986.

LAMMS STUDIES OF SILICA DUSTS: CHEMICAL CHARACTERIZATION AND CYTOTOXICITY CORRELATION

J. L. Tourmann and R. L. Kaufmann

The pathophysiological mechanisms underlying the induction of coalmine workers disease (pneumoconiosis) are still a matter of debate. Although the predominant role of quartz is widely accepted, there are still conflicting epidemiological and experimental evidences indicating the existence of additional and/or modulating factors determining the degree of pneumotoxicity.¹⁻³ The physico-chemical chemical analysis of coalmine dust samples has been so far entirely based on gross chemical and mineralogical techniques. However, since coalmine dust samples represent a rather heterogeneous mixture (exogen as well as endogen) of particles, a "single-particle approach" appears mandatory for a full characterization of such samples.

Among all techniques of microprobe analysis, LAMMS is at present the only one capable of analyzing, in a reasonable period of time, a large population of individual particles of, say, $N > 500$ to provide meaningful statistical results in the form of "chemical histograms" characterizing the specimens according to selected group parameters. For instance, a dust sample containing 5% of quartz as determined by gross analysis (e.g., IR spectroscopy) can mean that either 5% of particles exclusively consist of quartz (exogen mixture) or, at the other extreme, that all particles have an admixed fraction of 5% quartz each (endogen mixture). From the toxicological point of view, this would probably mean two different situations.

True coalmine dust samples are usually a highly heterogeneous mixture (exogenous and endogenous) of crystalline and probably amorphous mineral compounds with possibly intercorrelated promotive and protective effects (cytotoxic and fibrogenic). Thus studies aiming at a merely monocausal correlation of analytical with toxicological data cannot be expected to yield clearcut and unequivocal information.

It thus appeared necessary to unfold the complexity of the problem by proceeding stepwise in such a way as to delineate subgroups of less complex samples bearing only one known or suspected cytotoxic and/or fibrogenic principle.

The authors are at the Institute of Laser Medicine, University of Düsseldorf, Moorenstr. 5, D-4000 Düsseldorf, Federal Republic of Germany. They thank Prof. Dr. K. Robock (Berbau-Forschung, Essen) and Dr. W. Kriegseis (Institute of Physics I, University of Giessen) for providing the samples and for many fruitful discussions. Authors are also indebted to the Commission of the European Communities and to the Minister für Wirtschaft, Mittelstand und Technologie des Landes Nordrhein-Westfalen for financial support.

Such samples may offer a better chance of establishing clearcut correlations between physico-chemical factors and the biological response. This was the rationale behind the subsequent investigation on various silica dust specimens, all consisting of 84-100% of silica (crystalline or amorphous) that have been shown to exhibit large differences of cytotoxic effects in a macrophage assay.⁴

Ten such samples have been characterized by LAMMS analysis according to a classification scheme centered around three major criteria: (1) the ^{28}Si signal, (2) the ^{27}Al signal and (3) other signals designated individually or in combination as a group indicator called X. Each particle was classified according to the incidence of these three criteria or certain combinations of them so that the entire classification scheme comprised nine groups of particles. The incidence of each group of particles was then correlated with the cytotoxicity data obtained in the same selection of samples.

Experimental; Results

Measurements were performed on the amorphous silica glass Suprasil-W (SUP), the rock crystal KQ BRA I (BRA), and quartz sands of the following geological deposits: Dorentrup (DQ12), Mol (MOL), Hirschau (HIR), Haltern (HAL), Freihung (FRI), Grasleben (GRA), Nemours (NEM), and Gambach (GAM). The gross silica content, the Al-ESCA signal intensity, and the cytotoxic efficacy of these samples are summarized in Table 1.⁴⁻⁶ The cytotoxicity of the samples had been determined in a former investigation by measurement of the TTC (triphenyl tetrazolium chloride) reduction activity of peritoneal macrophages from guinea pigs (incubation time 120 min).⁴ Particle size was below 7 μm with a median between 1 and 2 μm . For LAMMS analysis, particles were deposited by adhesion on a 200-mesh Formvar-coated EM grid. We analyzed 100-130 particles in each sample by means of the LAMMA 500 instrument in the positive-ion mode.

In a first group of LAMMS measurements the recorded spectra were evaluated according to the following scheme:

a. The intensity of each mass signal unequivocally attributed to an element was semi-quantitatively weighted (by normalization to the ^{28}Si signal) into three groups: (1) "trace" (signal amplitude near the detection limit), (2) "minor" (relative intensity comparable to the signals of the ^{29}Si or ^{30}Si isotopes), and (3) "major" (signal reaching the saturation level of the transient recorder).

b. This scheme of evaluation was initially

TABLE 1.--IR quartz content (%), cytotoxicity data (100-TTC.RA in %) and Al-ESCA signal of samples.⁴⁻⁶

SAMPLE	QUARTZ CONTENT (%)	CYTOTOXICITY (%)	Al-ESCA x 10 ⁻²
DQ12	87	97	3.9
SUP	Pure amorphe SiO ₂	94	0
BRA	95.7	94	0
MOL	89.8	90	10
HIR	95.2	82	6.8
HAL	96.8	81	11.9
FRI	88.2	69	9.6
GRA	93	62	--
NEM	84	55	22.2
GAM	84	35	29.4

applied to all mass signals detected (Li, Na, Mg, Al, K, Ca, Ti, Fe, Rb, Zr, Sr, Ba).

All attempts to find a correlation between the incidence of one of these individual elements and the cytotoxicity data failed (with the exception of Al). With respects to the Al-signal, the correlation between the total incidence of Al (trace, minor, and major signals) and the cytotoxicity was negative but rather weak. This result shows that cytotoxicity is determined by a combination of such factors rather than by a single determinant.

One must bear in mind that for Al to occur in natural quartz samples, various mineralogical possibilities exists. It may (1) substitute to a certain extent for tetracoordinated Si in the crystalline lattice of quartz, (2) form aluminosilicates, or (3) be indicative of an heterogeneous structure consisting of quartz and silicates in the same particle.

These different mineralogical manifestations, all characterized by the simultaneous occurrence of Si and Al, most probably represent largely different determinants with respect to cytotoxic and fibrogenic activity. What that means is that one must search for the operational condition in the LAMMA instrument that would allow one to distinguish among the several manifestations. When the LAMMA instrument operated at high laser power (near 100% transmission) it was usually not possible to distinguish between, for example case (2) and (3) (i.e., aluminosilicates and mixed particles). In both cases Al and Si signals usually occurred at roughly the same signal intensity. However, with reduced laser intensity (about 20-30% transmission), such a distinction was easily possible. Under these conditions aluminosilicates showed an Al signal largely exceeding the Si signal, whereas in mixed particles the Si signal kept its leading position but was accompanied by an Al signal of widely varied amplitude.

Thus, the subsequent part of the investigation was entirely carried out at reduced laser power to maintain this important distinction. It was accepted that many of the trace signals related to Li, Rb, Zr, Sr, and Ba as seen under the high laser power condition could no longer

be recorded at the highest possible sensitivity.

In an attempt to reduce the remaining data set further (now comprising Si, Al, Na, Mg, K, Ca, Ti, Fe) in a meaningful manner, the Al and Si signals were evaluated individually, whereas all other signals, alone or in combination, were denoted by the cluster parameter X. Signal intensities of each of these three determinants were again weighted according to "trace," "minor," and "major" (by the notation 0, 1, and 10, respectively). The large number of possible signal combinations was then reduced to nine different clusters which, according to the weight of the Si signal in these clusters, are grouped into three classes (Table 2). Typical spectra representative of these classes are shown in Fig. 1. According to this classification, for example, the reference material SUP counting 100% of class Ia particles can be distinguished from the BRA sample with 54% of group Ia particles but 36% incidence of the "exotic" group 10.0.1 particles (X representing Na).

A synoptic representation of all incidence data as determined according to the above scheme for the eight quartz sands is shown in Fig. 2. Since the samples are numbered in the order of their cytotoxic efficacy (DQ12 is the most and GAM the least toxic specimens) a potential correlation between group incidence and cytotoxicity should manifest itself by a positive or negative slope of the column heights. It is obvious that--with the exception of the IIb-group (Si.Al.X = 10.10.1), which exhibits a negative slope--there is no evident correlation between the incidence of a specific particle group and the cytotoxicity of the specimen.

However, each group represents only a rather small fraction (10-20%) of the total particle population. Thus, it might be justifiable to take data compression one step further, e.g., by summing up the subclasses in each of the three classes as defined in Table 2. This in turn means that now the three remaining classes merely reflect the ratio of the Si to the Al signal. From the histogram alone (Fig. 3) it now appears that the incidence of Si-dominated particles (class I) correlates

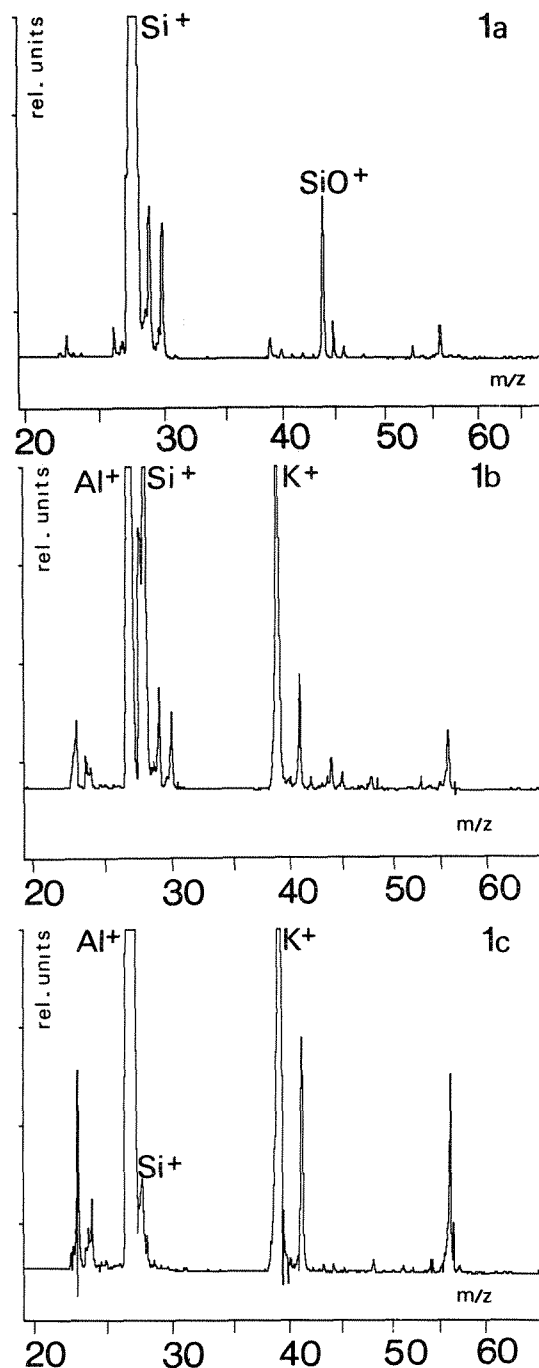


FIG. 1.--Typical LAMMS spectra of (a) group Si.Al.X = 10.0.0, (b) group Si.Al.X = 10.10.10, (c) group Si.Al.X = 1.10.10 of particles.

positively with cytotoxicity, whereas the appearance of Al as major component in the mass spectra (class II and III) exhibits an inverse correlation with the cytotoxic efficacy. Figure 4(a) shows the regression between the incidence of class I particles (Si-dominated particles) and the cytotoxicity, with the correlation coefficient calculated to be $r = +0.88$; whereas Fig. 4(b) shows the regression between the incidence of class II particles and the cytotoxicity with a correlation coefficient $r = -0.82$. These correlations now comprise the data obtained in all 10 investigated samples (eight natural quartz sands, one powdered rock

crystal BRA, and one powdered amorphous silica glass SUP).

Discussion

The results basically support the idea that the cytotoxicity of the investigated samples is primarily determined by the incidence of quartz. It appears, however, that the quartz content as determined by gross analysis (IR spectroscopy) is not nearly as good a cytotoxic parameter as is the incidence of Si-dominated particles (class I particles) as determined by LAMMS analysis (Fig. 5). Whereas the gross content of quartz correlates with only $r = +0.61$ to cytotoxicity, a much better correlation coefficient of $r = +0.88$ has been found in this investigation for the incidence of "pure" quartz particles with cytotoxicity (see also Fig. 4a). This result alone supports the idea that some fraction of the quartz may be toxicologically ineffective because its free surface is not exposed to the biological test system. We suppose that a fraction of the quartz is hidden under a surrounding or covering layer of other mineral components (e.g., clay minerals) for which Al might be a representative indicator as revealed by LAMMS analysis. Thus the problem of cytotoxicity may focus on the question of the free surface quality of such particles, more specifically on the question of how much of the quartz present in a given sample is exposed and freely accessible to the biological system. In this context, a special attention must be paid to the highly cytotoxic DQ12 sample which, for a quartz sand, exhibits an unusual high incidence of class Ia particles (Fig. 2).

If that is so, one would expect that the characterization of the surface contamination by ESCA analysis should give similar results, which has been found to be basically true. In an investigation performed by Kriegseis et al.,^{5,6} the Al signal was recorded to be negatively correlated with cytotoxicity and in good agreement with the incidence of our class II and III particles (Fig. 6). From the present investigation one may further conclude that one can distinguish two types of cytotoxicologically ineffective particles: (1) quartz particles bearing only a superficial layer of protective material (class II) and (2) particles having only a minor fraction of quartz or even none (class III). Both of them are representative for a typical endogen mixture of quartz whereas exogen-mixed quartz particles are revealed by the incidence of class I particles. As to the nature of the quartz protective materials, one may suppose Al-silicates to play the predominant role as shown by elements of cluster X which are typical for such minerals. That does not exclude the possibility that some of those minerals exhibit a cytotoxic effect of their own which, however, remains to be established by toxicological investigations.

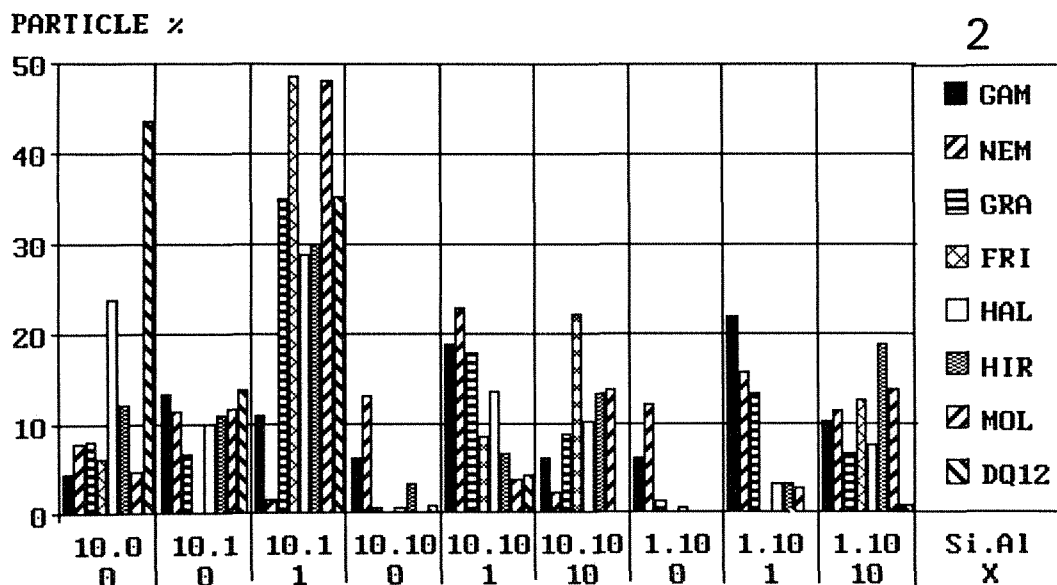


FIG. 2.--Incidence data of nine groups of Si,Al,X combinations for eight quartz sands ordered in sequence of least cytotoxic GAM to most cytotoxic DQ12 sample.

TABLE 2.--Classes and subclasses of Si,Al,X combinations.

	a	b	c
	Si,Al, X	Si,Al, X	Si,Al, X
CLASS I	10. 0. 0	10. 1. 0	10. 1. 1
CLASS II	10.10. 0	10.10. 1	10.10.10
CLASS III	1.10. 0	1.10. 1	1.10.10

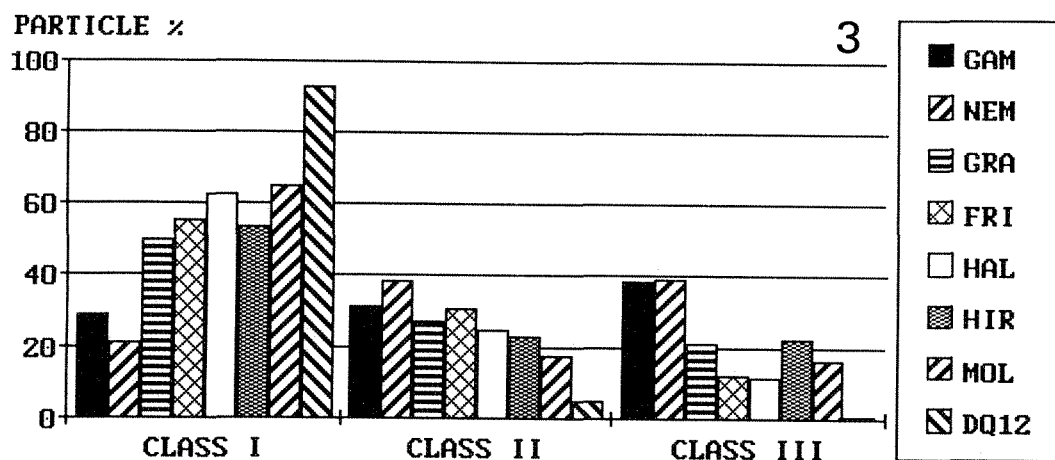


FIG. 3.--Incidence data of three classes of Si,Al,X combinations for eight quartz sands ordered in sequence of least cytotoxic GAM to most cytotoxic DQ12 sample.

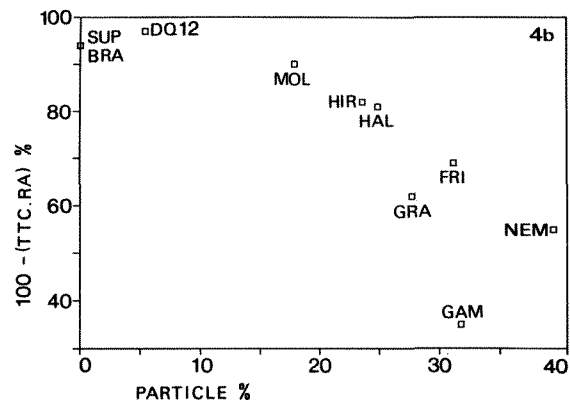
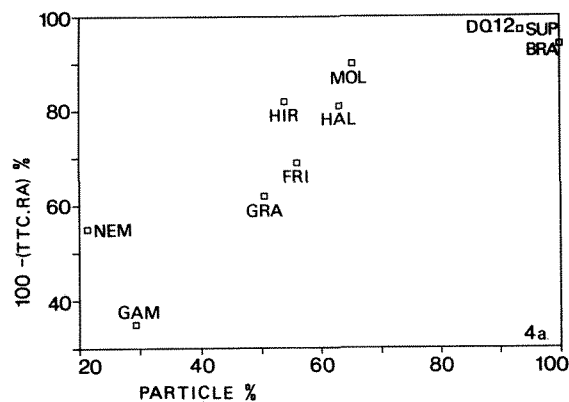


FIG. 4.--Correlation between the cytotoxicity data of ten investigated samples and (a) incidence of class I particles ($r = +0.88$), (b) incidence of class II particles ($r = -0.82$).

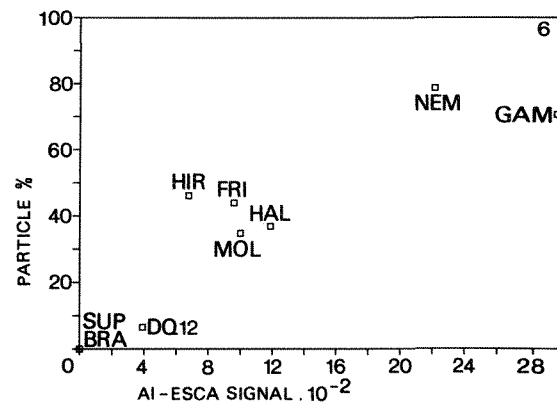
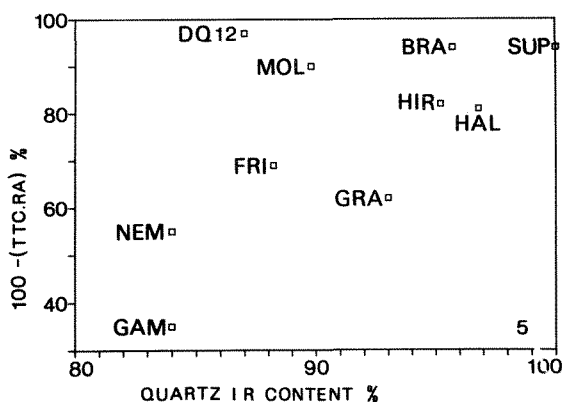


FIG. 5.--Correlation between cytotoxicity data of ten investigated samples and quartz content as determined by IR analysis ($r = +0.61$).

FIG. 6.--Comparison of LAMMS-content of Al as determined by incidence of class II and III particles with Al signal as detected by ESCA analysis.

References

1. J. Bruch et al., *Ergebnisse von Untersuchungen auf dem Gebiet der Staub- und Silikosebekämpfung im Steinkohlenbergbau*, Essen: Glückauf Verlag, 14: 241-255, 1983.
2. J. Bruch et al., *Ergebnisse von Untersuchungen auf dem Gebiet der Staub- und Silikosebekämpfung im Steinkohlenbergbau*, *ibid.*, pp. 265-279.
3. L. Le Bouffant et al., "Effect of impurities and associated minerals on quartz toxicity," *Ann. Occup. Hyg.* 26: 625-634, 1982.
4. K. Robock and W. Klosterkötter, *Ref. 1*, 10: 159-162, 1975.
5. W. Kriegseis et al., *Ref. 1*, 12: 281-299, 1979.
6. W. Kriegseis et al., "Investigations of surface properties of silica dusts with regard to their cytotoxicity," *Ann. Occup. Hyg.* 31: 417-427, 1987.

IN SITU ANALYSIS OF COMPOUNDS SEPARATED BY THIN-LAYER CHROMATOGRAPHY BY LASER MASS SPECTROMETRY

A. J. Kubis, S. K. Viswanadham, A. G. Sharkey, and D. M. Hercules

Mass spectrometric characterization of components separated by thin-layer chromatography involves extracting the separated components from the support followed by mass spectral analysis. In situ analysis directly from thin-layer chromatography (TLC) plates is desirable for faster analysis and to avoid losses during sample preparation. Such in situ analysis was earlier achieved by use of fast atom bombardment and secondary ion mass spectral techniques.^{1,2} These methods have a limited spatial resolution, particularly when a liquid matrix needs to be added to the surface before analysis.

Laser mass spectrometry (LMS) is ideally suited for direct analysis of TLC separated components at high sensitivity and with good spatial resolution, as the laser can be focused to a small spot size (~ 5 mm). In the present communication we report our study of a variety of organic compounds of various functionalities characterized by LMS directly from TLC plates. We further report our results of the TLC-LMS study of mixtures.

The authors are at the Department of Chemistry, University of Pittsburgh, Pittsburgh, PA 15260.

Experimental

Laser mass spectra were obtained with a LAMMA-1000 laser microprobe mass analyzer.³ All the compounds used were commercially obtained and were used as received. The TLC plates used were polyamide A-1700 backed with aluminum (Schleicher and Schuell, Inc.). The samples were prepared by dissolving 0.02 grams of each compound in 30 ml of chloroform. One drop of the solution was then deposited on zinc foil or on a TLC plate. Separation of the mixtures was performed by reported procedures.

Results and Discussion

Sixty organic compounds with different functionalities were studied by LMS both in the positive and negative ion modes. Spectra of the pure compounds were obtained from a metal substrate and from a TLC plate. All the compounds showed $(M + H)^+$ or M^+ in their positive-ion spectra and $(M - H)^-$ in their negative-ion spectra. Spectra obtained from a TLC plate and from zinc substrate were found to be the same both with regard to the observation of molecular species and their intensities. However, spectra obtained from TLC plates needed higher (15–18 μ J) laser energy under focused

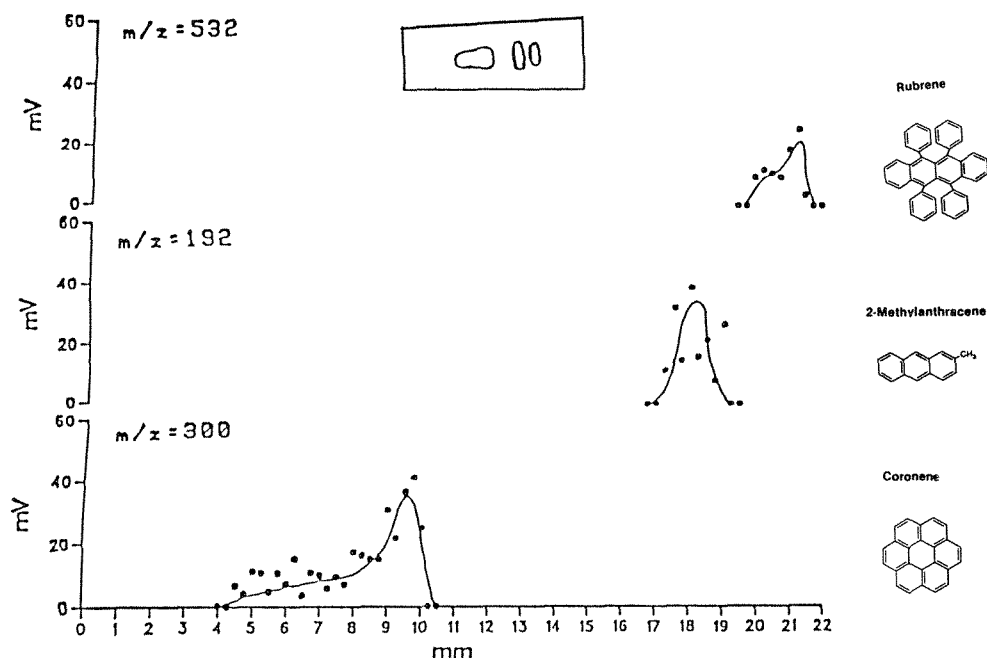


FIG. 1.--TLC-LMS of PAHs rubrene (m/z 532), 2-methylantracene (m/z 192), and coronene (m/z 300): plot of molecular ion intensity vs distance along TLC plate from original spot. Intensity shown on separate scale for each component. Spectra taken at 250 μ m intervals.

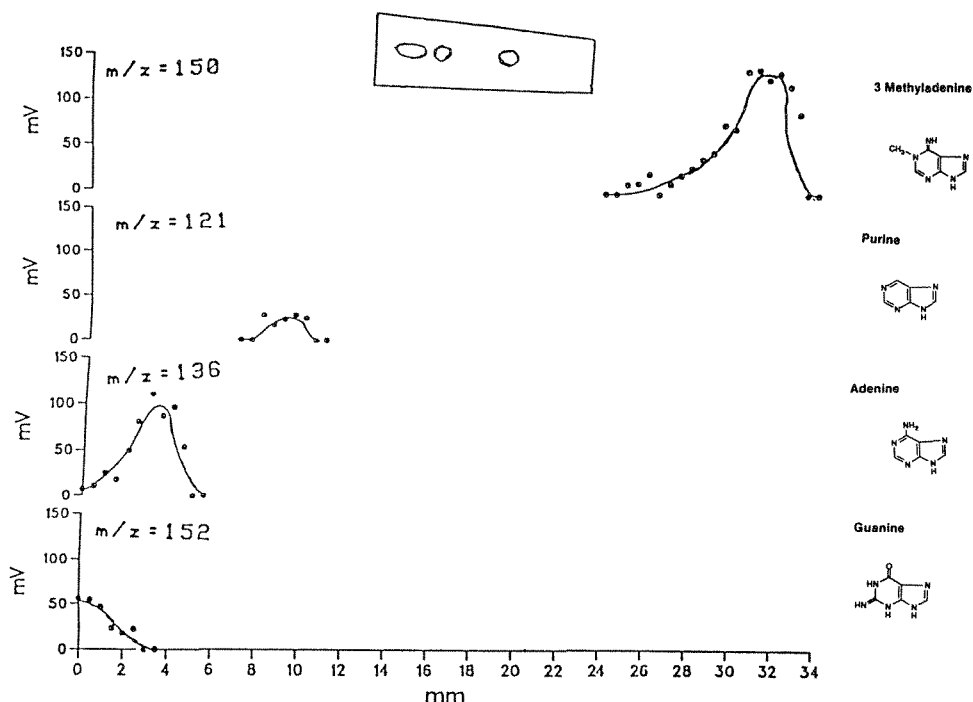


FIG. 2.--TLC-LMS of purine derivatives 3-methyl adenine (m/z 150), purine (m/z 121), adenine (m/z 136), and guanine (m/z 152): plot of molecular ion intensity vs distance along TLC plate from original spot. Spectra taken every 500 μm .

conditions, whereas comparable spectra from zinc could be obtained with lower (2-4 μJ) energy and under defocused conditions (50 μm away from focus). However, reproducible absolute intensities were observed from TLC plates, possibly due to homogeneous dispersed sample.

A mixture of several polycyclic aromatic hydrocarbons (PAHs) and purine derivatives were separated on polyamide plates in two different experiments. The TLC plates were then analyzed by LMS with spectra taken at fixed distances starting from the original sample spot in the direction of solvent front. The total ion current monitored revealed the position of the components. The recorded spectra served to identify the component at each position. Figures 1 and 2 show plots of the intensity of molecular species peak vs distance from the original spot of the mixture for PAHs and purine derivatives, respectively. The R_f values calculated from the LMS data correspond well to those obtained by conventional methods. LMS has the advantage of being able to distinguish between tailing of a single compound and overlapping compounds, as can be seen from the separation observed for adenine and guanine. Greater spatial resolution available in LMS analysis should further aid in defining the

separation and permit mapping⁴ of the presence of any ion or ions in the spectra.

References

1. T. T. Chang, J. O. Lay Jr., and R. J. Francel, *Anal. Chem.* 56: 109, 1984.
2. M. S. Stanley and K. L. Busch, *Anal. Chim. Acta* 194: 199, 1987.
3. H. J. Heinen, S. Meier, H. Vogt, and R. Wechsung, *Int. J. Mass Spectrom. Ion Processes* 47: 19, 1983.
4. Z. A. Wilk and D. M. Hercules, *Anal. Chem.* 59: 1819, 1987.

CHARACTERIZATION OF GRAPHITE FURNACE PRODUCED AEROSOLS BY MICROPROBE MASS SPECTROMETRY

S. Güçer, L. Van Vaeck, and F. Adams

Electrothermal atomic absorption spectrometry (ETAAS) is one of the most widely used methods for trace elemental analysis. Its sensitivity is influenced by matrix suppression and enhancement effects, and there is a distinct need for information on the processes taking place in the graphite furnace during the heating cycle. Current approaches for study rely on spectrometric measurements in the optical path during the atomization and on thermodynamic considerations, but for a safe interpretation these measurements must be backed up by data obtained by other techniques. Previous studies concerned the direct coupling of the graphite furnace with mass spectrometric (gas phase) detectors and the characterization of graphite furnace residues by, for example, differential thermal analysis, x-ray diffraction, x-ray photon spectroscopy, secondary ion mass spectrometry, and electron probe microanalysis (EPMA).

In this work we report on the chemical characterization of the emanating aerosol from the graphite furnace during its heating cycle by laser microprobe mass spectrometry (LMMS) to assist in the interpretation of data obtained by time-resolved molecular absorption measurements of the gas phase within the graphite furnace. We investigated the potential of the approach for tin chloride in the presence of several sulfur-containing salts as a matrix.

Experimental

ETAAS was performed on a Perkin-Elmer 3030 with HGA 500 graphite furnace atomizer. The temperature was programmed from 100 C during 35 s, 800 C (35 s), and 2100 C (5 s), to 2600 C (1 s). Time-resolved signals were calculated from peak height measurements.

The LAMMA 500 was used with a 100MHz LeCroy (TR8818-MM8103/8) transient recorder. Particles were collected on Formvar-coated grids, held at about 5-10 cm above the graphite furnace during 1 to 30 s, depending on the temperature. Smoke formation was monitored to determine suitable sampling periods in order to obtain about 300 isolated ca. 1 µm particles.

Table 1 summarizes the samples studied. Microprobe analysis of the particulates required the introduction in the furnace of concentrated solutions with typically 10 mg/ml of analyte,

i.e., higher by least a factor 1000 than normal working conditions in ETAAS. Atomization in such conditions may be considerably different from the usual analytical situation.¹

Results and Discussion

High power densities as currently applied for inorganic analysis provided complex spectra with insufficient specificity. Hence, the threshold protocol for organic compounds² was followed as it appeared that the spectra obtained were simple and directly related to the chemical composition of the particles.

Reference spectra were recorded from pure products in order to attempt a distinction of the individual particles analyzed on the formvar grids. It appeared that no diagnostic difference was possible in the spectra between SnO and SnO₂; we denote in what follows the oxide species that could be identified by SnO_x. Tin chloride could be easily characterized by the SnCl₂·Cl⁻ anions. Also the SnO_x⁻ ion yield was high and hence the negative ion detection mode became the most suitable to monitor the corresponding mixtures. The identification of SnSO₄ in the possible presence of the likely decomposition products, namely SnO_x, was problematic. A combination of positive and negative mass spectra should be required, but such identification would be hardly reliable for heterogeneous samples, since different microvolumes would be involved.

Figure 1 shows typical negative spectra of SnCl₂ and SnO_x particles in the graphite furnace aerosol. The formation of SnO_x during the atomization of SnCl₂ in the presence of NH₄OH, which is described in the literature,³ could not be confirmed by LMMS.

Reference spectra of sulfur-containing salts (ranging from Na₂S to Na₂SO₄ to Na₂S₂O₇) yielded largely comparable negative ion spectra. The subtle differences in relative abundance of ions at (for example) m/z 32 and 48 vs m/z 64 and 80 had no diagnostic value for mixture analysis. In the positive mode, differentiation was hindered by the predominance of the Na⁺ and Na₂O⁺ signals, which readily overloaded the detector, and a number of salts (e.g., Na₂SO₄, NaHSO₄, and Na₂S₂O₇) became indistinguishable. In contrast, Na₂S was readily characterized by the abundant Na₂S·Na⁺ ions at m/z 101. Also, Na₂S₂O₅ and Na₂SO₃ yielded clearly recognizable spectra with intense peaks at m/z 149 and 165 due to Na₂SO₃·Na⁺ and Na₂SO₄·Na⁺. Finally, LMMS results for pure Na₂S₂O₃ appeared as a superposition of Na₂S and Na₂SO₄. Consequently, speciation capabilities became reduced for mix-

S. Güçer is at the Department of Chemistry, University of İnönü, 44069 Malatya, Turkey; L. Van Vaeck and F. Adams are at the Department of Chemistry, University of Antwerp, B-2610 Wilrijk, Belgium. This work was sponsored by NFWO Belgium and by NATO.

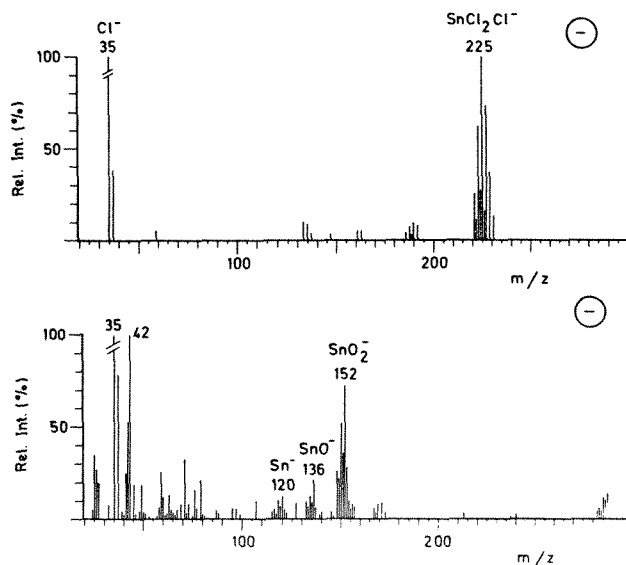


FIG. 1.--LMMS results for graphite furnace produced aerosol from SnCl_2 solution (top) and SnO_2 suspension (bottom).

tures. For instance, a combination of Na_2S and Na_2SO_4 could also easily be confounded with $\text{Na}_2\text{S}_2\text{O}_5$.

Despite the apparent shortcomings in potential of discrimination, we could obtain data that were of considerable use in helping to elucidate the processes going on in the furnace during the heating cycle.

Figures 2 and 3 show two characteristic examples of data obtained. When Na_2SO_4 is injected in the graphite furnace, mass spectra of the aerosol point to a mixture of (pyro)sulfate or sulfite with some amount of sulfide. Hence, graphite furnace heating yields a partial reduction of the sulfate. When Na_2S was injected, particles of three types were encountered: the unmodified salt, a mixture of (pyro)sulfate and sulfite with or without sulfides (Fig. 3).

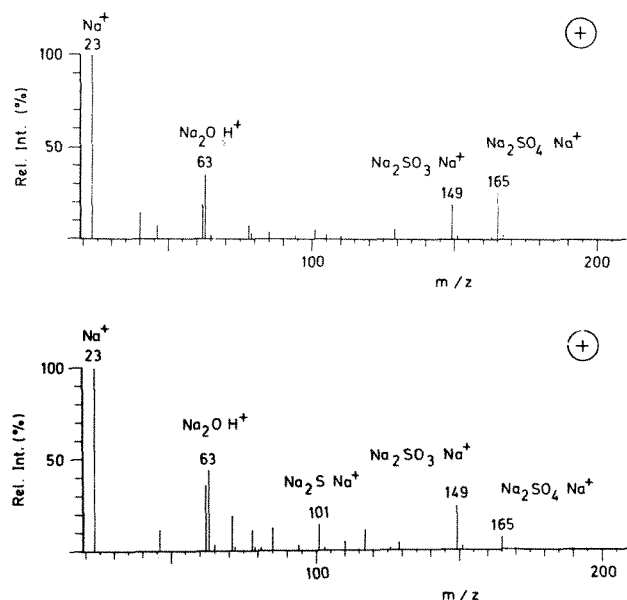


FIG. 2.--LMMS results for aerosol from Na_2SO_4 .

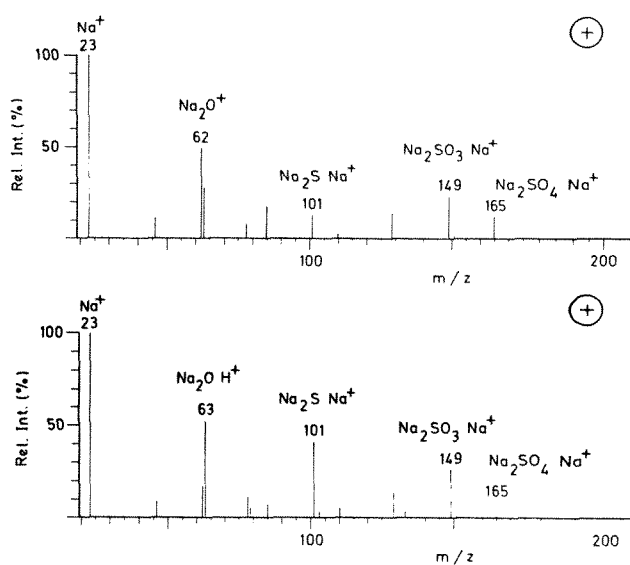


FIG. 3.--LMMS results for aerosol from Na_2S .

Time-resolved background absorption of the type shown in Fig. 4, obtained for SnCl_2 , were measured during the heating cycle. The absorption spectrum obtained at 800 C between 3 and 5 s after the start of the cycle shows a prominent signal between 300 and 350 nm, which can be associated with SnCl_2 from the LMMS measurements. Later in the heating cycle during the first second at 2100 C, absorption becomes related to atomic tin.

A summary of the species identified with LMMS and molecular absorption are given in Table 1. Supporting evidence obtained by EPMA of particles on the graphite furnace is also shown. The background absorption measurements and those obtained with LMMS do not always agree in detail. Despite apparent shortcomings, it can be concluded from this methodological study that the speciation capabilities of LMMS may support assignments of molecular absorption bands. A full report of the results of this study will be published elsewhere.⁴

References

1. R. E. Sturgeon and C. L. Chakrabarti, *Progress Anal. Atom. Spectr.* 1: 157, 1978.
2. L. Van Vaeck, J. Claereboudt, J. De Waele, E. Esmans, and R. Gijbels, *Anal. Chem.* 57: 2944, 1985.
3. E. Lundberg, B. Bergmark, and W. Frech, *Anal. Chem.* 142: 129, 1982.
4. S. Güçer, L. Van Vaeck, and F. Adams, *Spectrochim. Acta B* (submitted).

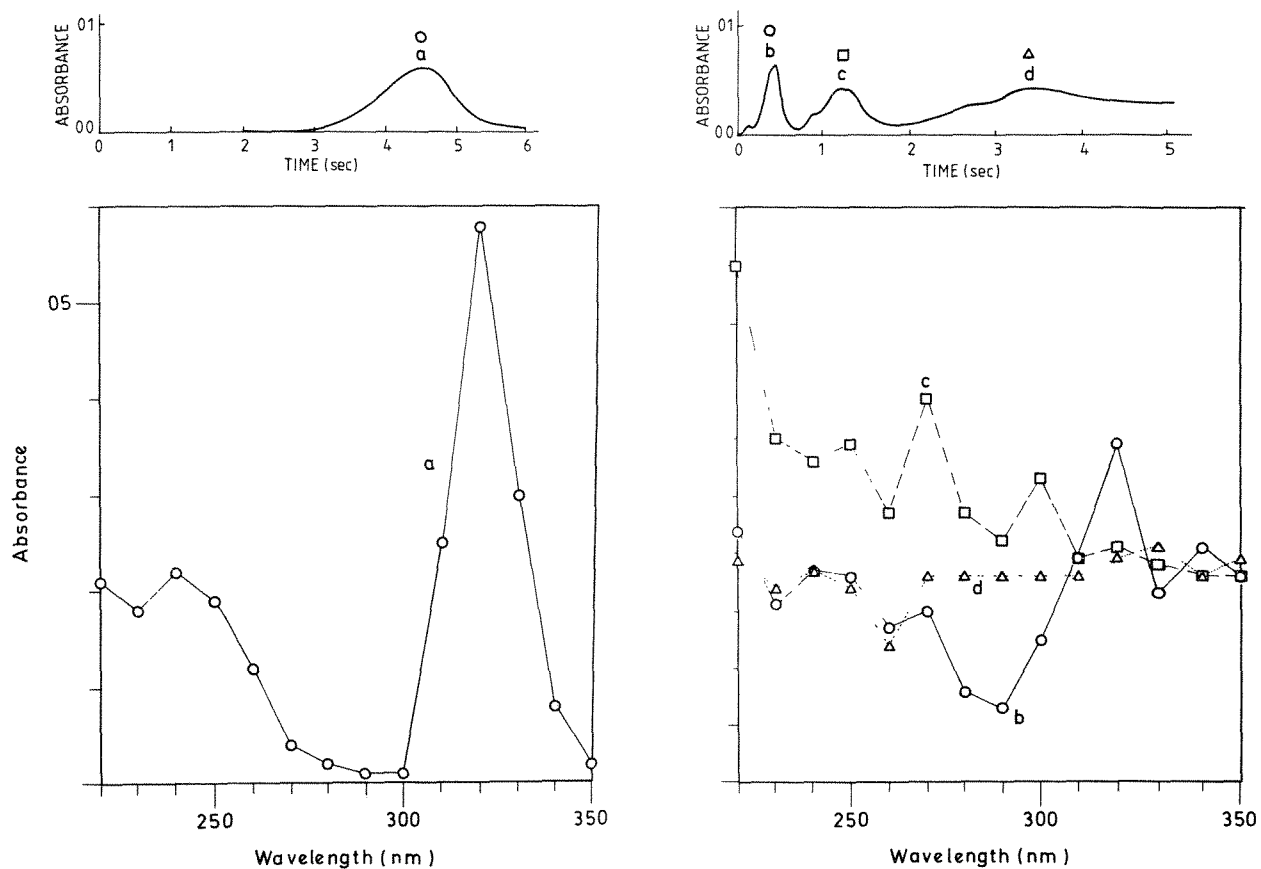


FIG. 4.--Time-resolved absorption spectra for SnCl_2 during (a) ashing and (b-d) atomization step.

TABLE 1.--Survey of experiments and results for ETAAS study of tin and sulfate compounds.

Experimental conditions			Results	
Sample	concentration	temp. (°C)	Aerosol analysis by	
			LMMS	EPMA
SnCl ₂	10,000 ppm Sn in 10 % HCl	800-2100	SnCl ₂	Sn, Cl
SnCl ₂ /NH ₄ OH	10,000 ppm Sn in 10 % NH ₄ OH	800	SnCl ₂	-
SnO ₂	10,000 ppm Sn in H ₂ O suspension	2100	SnO(2)	Sn
Na ₂ SO ₄	20,000 ppm as Na	2100	Na ₂ SO _x ² Na ₂ S ₂ O ₅ or Na ₂ SO ₃	SO _x ³
K ₂ SO ₄	20,000 ppm as K	2100	K ₂ SO _x	SO _x
Na ₂ S	10,000 ppm as Na	2100	Na ₂ S Na ₂ S ₂ O ₅ or Na ₂ S ₂ O ₃	SO _x
SnSO ₄	10,000 ppm as Sn	2100	-	Sn, S
SnCl ₂ in Na ₂ SO ₄	5,000 ppm Sn in 5,000 ppm sulfate	1200	-	Na, Cl Na, Sn, S, Cl
				Sn, SnO(2), SO _x , (?) ⁴ SO _x , SnCl ₂ , (?)

- 1 assignment based on LMMS
2 Na_xSO_x refers to Na₂SO₄, Na₂S₂O₇, etc.
3 SO_x refers to SO₂ or SO₃ bands
4 SO_x refers to unidentified species

MICROANALYTICAL CHARACTERIZATION OF PREBIOLOGICAL COMPONENTS IN INTERPLANETARY DUST

Filippo Radicati di Brozolo, G. P. Meeker, and R. H. Fleming

The elemental, isotopic, textural, and molecular analysis of interplanetary dust particles (IDP) presents a unique opportunity for the study of the origin of prebiological organic molecules in the early solar system and perhaps even in the interstellar medium. Programs are now under way to obtain IDP from low earth orbits and from comet rendezvous missions. The analysis of these pristine materials requires a new level of sophistication in sample handling, preparation, and analysis. We report preliminary results in our development of new microanalytical characterization techniques for the study of prebiological species in pristine interplanetary dust.

Experimental

Particle Embedding. Conventional microtomy procedures involve embedding of samples in organic media. Such media are not suitable for the study of carbon-rich IDP. We have developed a procedure to embed small particles in a nonorganic medium for the preparation of microtome cross sections. The particles are gold coated, embedded in indium, and heated to between 150 and 200 C to form an indium-gold alloy. Cross sections of a small Murchison meteorite matrix particle have been obtained which show the particle to be totally surrounded by AuIn_2 (Fig. 1). This technique was developed under Class 100 clean-room conditions and can be applied without modifications to IDP.

Isotopic Images. We have developed a method for acquiring quantitative isotope ratio images of cross sections of IDP. Hydrogen and deuterium ion images were acquired with a CAMECA IMS-4f ion microanalyzer in raster imaging mode with a Cs^+ primary ion beam. Images of hydrogen and deuterium were alternately acquired and summed to reduce effects of varying ion intensity. The summed deuterium and hydrogen images are shown as Figs 2(a) and (b), respectively. Detector dead-time corrections were made on a pixel-by-pixel basis. The hydrogen-to-deuterium ratio of the epoxy embedding medium serves as the isotope ratio standard in this example. Isotope ratios are shown in Fig. 2(c) as positive deviations (expressed as parts per mil) from the expected values. A nine-by-nine convolution improves the signal-to-noise ratio of the images by a factor of nine. This convolution has little effect on the image lateral resolution, which is determined by the primary

The authors are with Charles Evans & Associates, 301 Chesapeake Drive, Redwood City, CA 94063. Supported by NASA SBIR contract NAS2-12818.

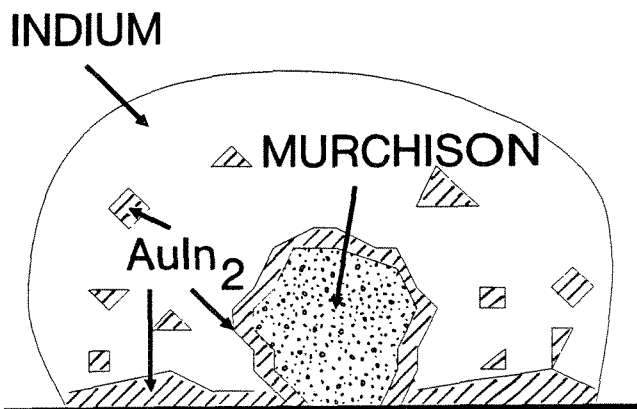


FIG. 1.--Murchison meteorite particle surrounded by AuIn_2 .

ion beam diameter in this analytical mode. Figure 2(d) shows the variation in the deuterium excess along the line shown in Fig. 2(c). Improvements in mass spectrometer vacuum are under way to reduce signals from residual hydrogen.

The deuterium anomalies detected with this technique provide clear evidence for the extraterrestrial origin of the IDP.¹ This is the first example of a direct in situ measurement of inhomogeneous deuterium excess on a micrometer scale.

Organic Microanalysis. Organic microanalytical techniques are critically needed for an understanding of the evolution of organic species in the primitive environment(s) sampled by the IDP. Organic microanalytical techniques available at present lack the lateral resolution or the survey capability needed for the analysis of IDP. We have performed a systematic study of laser desorption and ionization of selected model organic compounds, as well as of fragments of the Murchison meteorite. These analyses were performed by use of both single and double laser configurations of the Cambridge Mass Spectrometry LIMA 2A instrument.

The model compounds selected for this study included tryptophan and proline (aminoacids), urea, glutaric acid, perylene, tetraphenylporphine, bisphenol-A (4,4'-isopropylidenediphenol), a sample of HCN polymer [hereafter indicated as $(\text{HCN})_n$], as well as a matrix sample of the CM meteorite Murchison. Except for the last two, all samples were prepared by dispersing a few milliliters of a dilute solution (~ 0.01 M) onto a clean Si substrate. Some of the samples were also dispersed on metallic substrates, such as high-purity Ag or In. The Murchison and $(\text{HCN})_n$ samples were

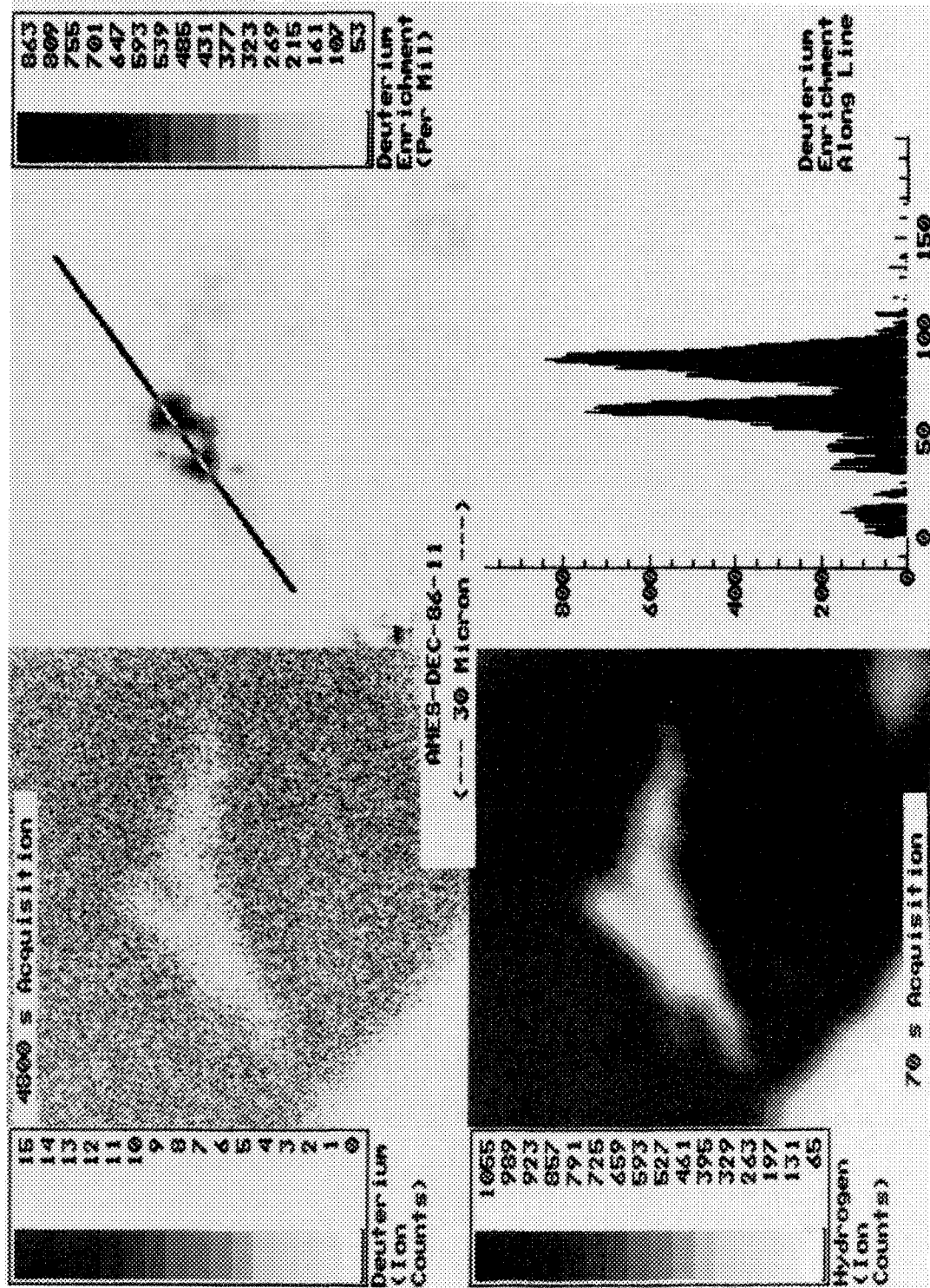


FIG. 2.--(a) Deuterium ion image of Ames-Dec-86-11 thin section; (b) hydrogen ion image of Ames-Dec-86-11 thin section; (c) positive deviation isotope ratio image of Ames-Dec-86-11 thin section; (d) permil deuterium enrichment along line.

prepared by pressing a few micrograms of the solid into an In substrate.

The laser microprobe was operated in two modes, the conventional laser ablation only (LAO) mode and the post-ablation ionization (PAI) mode.² In the first mode, the Nd:YAG laser pulse ($t = 10$ ns, wavelength = 1064 nm or 266 nm) directly produces ionized molecular or fragment species from the sample surface. In the second analytical mode, two Nd:YAG lasers are employed. The first laser pulse ablates neutral and ionized species from the sample surface. The second, frequency quadrupled Nd:YAG laser pulse is fired after a variable delay into the cloud of vaporized neutrals and produces ions via a multiphoton ionization process. The peak post-ionization signal intensities occurred at long delay times between the firing of the two laser pulses, which suggest that the neutral species were ejected from the sample surface at thermal or quasithermal velocities. Figure 3 shows representative mass spectra acquired in this study. Successful identification of molecular or structurally significant ions is achieved for some of the species analyzed. The PAI spectrum of perylene on Ag in Fig. 3 obtained at an ablation wavelength of 1064 nm is particularly interesting because it exhibits minimal fragmentation compared to the other analysis conditions. This observation suggests that the 1064 nm ablation wavelength primarily desorbs intact perylene molecules. The relatively long delay time between the firing of the ablating and ionizing lasers (2.4 μ s and beyond) indicates that these neutral molecules have thermal velocities, consistent with thermal desorption mechanisms.

Conclusions

We have been successful in the embedding of small particles in a metallic medium. These samples can be used for analysis by several microprobe techniques (SIMS, LIMS, EPMA, AES, and SEM). Further experiments are under way to prepare thin sections that can be used for TEM analysis.

The development of a SIMS techniques to obtain digital isotope ratio images has produced the first quantitative measurement of inhomogeneous deuterium excesses in IDP on a micrometer scale. This technique provides the first opportunity for in situ correlation of deuterium excesses with host phase mineralogy in IDP.

Significant progress has been made in the development of laser microprobe techniques that will provide a means of desorbing and ionizing intact molecular species from the carbon-rich portions of IDP.

References

1. K. D. McKeegan, R. M. Walker, and E. Zinner, "Ion microprobe isotopic measurements of individual interplanetary dust particles," *Geochim. Cosmochim. Acta* 49: 1971, 1985.
2. B. Schueler and R. W. Odom, "Nonresonant multiphoton ionization of the neutrals ablated in laser microprobe mass spectrometry analysis

of GaAs and $\text{Hg}_{0.78}\text{Cd}_{0.22}\text{Te}$," *J. Appl. Phys.* 61: 4652, 1987.

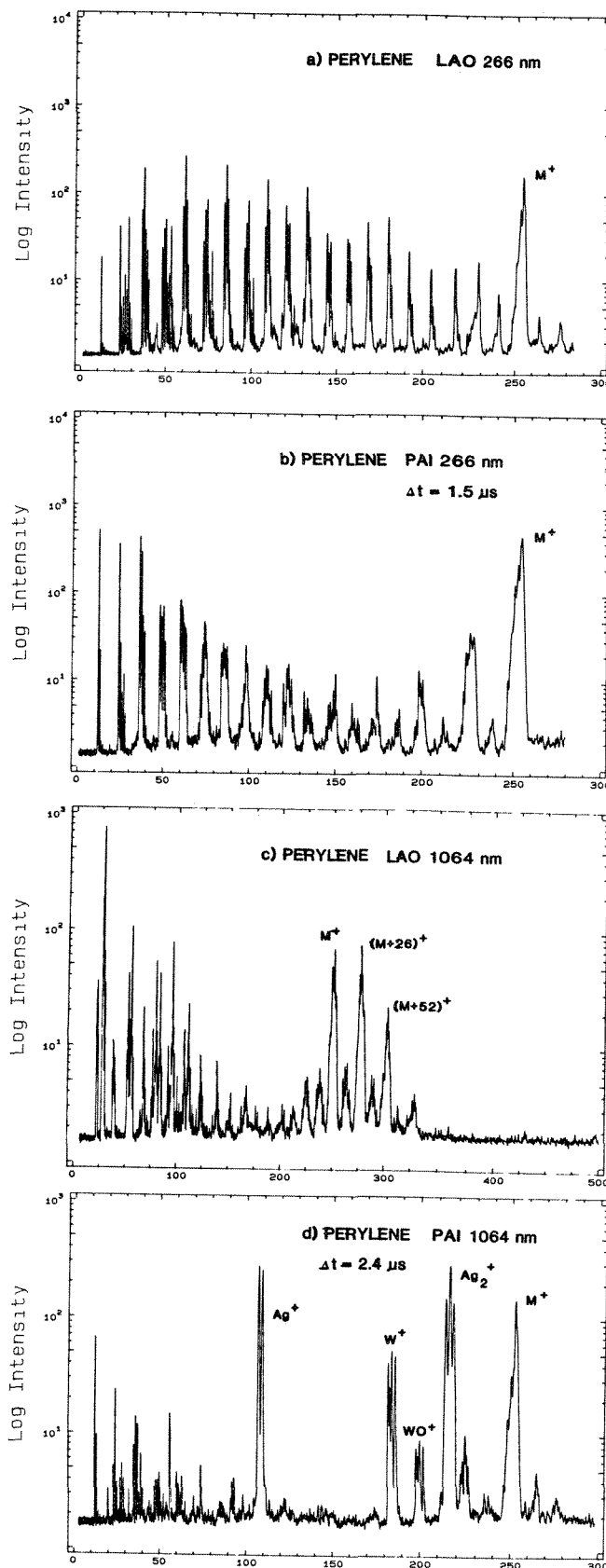


FIG. 3.--Positive-ion LAO and PAI spectra of perylene. Ag and W signals originate from substrate.

LASER MICROPROBE STUDIES OF NEUROPEPTIDES

P. F. Good, J. S. Roboz and D. P. Perl

The laser microprobe mass analyzer has been used primarily for probing microvolumes of tissue sections for their trace-element content. The instrument not only lends itself most readily to the function of elemental analysis, but its mass spectrometric capabilities are equally valuable. Organic molecules when probed in a pure form by LAMMA-500 yield highly reproducible mass spectral patterns, and the possibility of identifying organic molecules in situ by their mass spectral pattern is a concept that deserves intensive investigation. As an experimental model, we have turned our efforts to the identification of the two posterior pituitary neuropeptides oxytocin and vasopressin.

Methods

To establish the ability of the LAMMA-500 to identify the peptides, pure oxytocin (free base formula weight 1007) and arginine vasopressin (free base formula weight 1084) prepared as the acetate salts were obtained from Sigma Chemical Co. Crystals of these compounds were placed on copper formvar-coated grids and inserted on the analytical stage of the LAMMA-500 (Leybold-Heraeus, Cologne, Germany). Mass spectra were produced by the laser focused through a 100× quartz lens at 20-40μJ output energy. Ionic signals were digitized and collected to obtain all masses from 1 through 1300 atomic mass units.

Results

Figure 1 is a representative mass spectrum of atomic masses from 350 to 1300 derived from the oxytocin sample. The spectrum demonstrates prominent peaks at atomic masses 1030 and 1046. These masses correspond to the full molecular ion plus sodium and the full molecular ion plus potassium. Figure 2 is a mass spectrum of atomic masses from 350 to 1300 derived from the arginine-vasopressin sample. This spectrum demonstrates the molecular ion of vasopressin with a sodium adduct at atomic mass 1107 and the molecular ion with a potassium adduct at atomic mass 1123. These peaks are highly reproducible and do not show any high-molecular-weight breakdown products when produced by the lower range of laser energy.

Discussion

We have now made an initial demonstration of mass spectra specific to the two posterior pituitary peptides. These peptides are found in secretory vesicles in combination with a high-molecular-weight peptide, neurophysin, in the posterior pituitary neurosecretory neurons. These two peptides are highly similar: they are nonapeptides with disulfide bonds between cysteines at position one and six, and differ only by two amino acids at position three and eight. Thus the differentiation of the two peptides by mass spectroscopy is a significant step toward identifying these neuropeptides in situ. Further demonstrations of the possibility of identifying oxytocin and vasopressin in situ will require the differentiation of two peptides mixed together and the ability to identify a peptide in the embedment matrix of an epoxy resin used to allow the routine sectioning of histological material for LAMMA analysis. These studies are currently under way.

References

1. P. F. Good and D. P. Perl, "A laser microprobe mass analysis (LAMMA) study of aluminum distribution in the cerebral cortex of dialysis encephalopathy," *J. Neuropath. Exp. Neurol.* 47: 321, 1988.
2. D. T. Krieger, "Brain peptides: What, where, and why?" *Science* 222: 975-985, 1983.
3. D. H. Williams, C. V. Bradley, S. Santikarn, and G. Bojesen, "Fast-atom-bombardment mass spectrometry," *Biochem. J.* 201: 105-117, 1982.
4. A. M. Buko and A. F. Blair, "Peptide studies using a fast atom bombardment high field mass spectrometer and data system: 4. Disulfide-containing peptides," *Biomed. Mass. Spectrom.* 12: 577-585, 1985.
5. E. Denoyer, R. Van Grieken, F. Adams, and D. Natusch, "Laser microprobe mass spectrometry: 1. Basic principles and performance characteristics," *Anal. Chem.* 54: 26-33A, 1982.
6. M. Posthumus, P. Kistemaker, H. Meuzelaar, and M. Ten Noever de Brauw, "Laser desorption-mass spectrometry of polar nonvolatile bio-organic molecules," *Anal. Chem.* 50: 985-991, 1978.
7. D. Hercules, K. Balasubramanian, T. Dang, and C. P. Li, "Laser microprobe mass spectrometry: 2. Applications to structural analysis," *Anal. Chem.* 54: 280-290A, 1982.

The authors are at the Neuropathology Division, Mount Sinai Medical Center, 1 Gustave L. Levy Place, New York, NY 10029-6574.

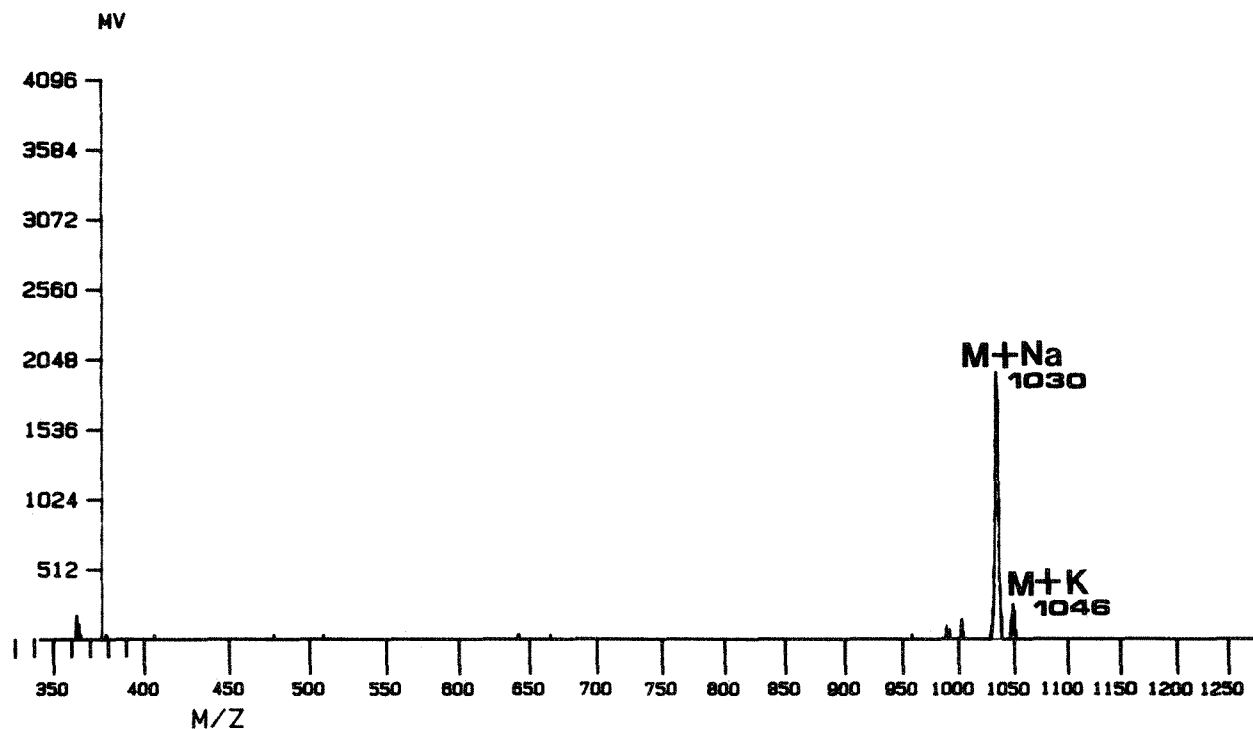


FIG. 1.--Laser mass spectrum of oxytocin (m.w. 1007).

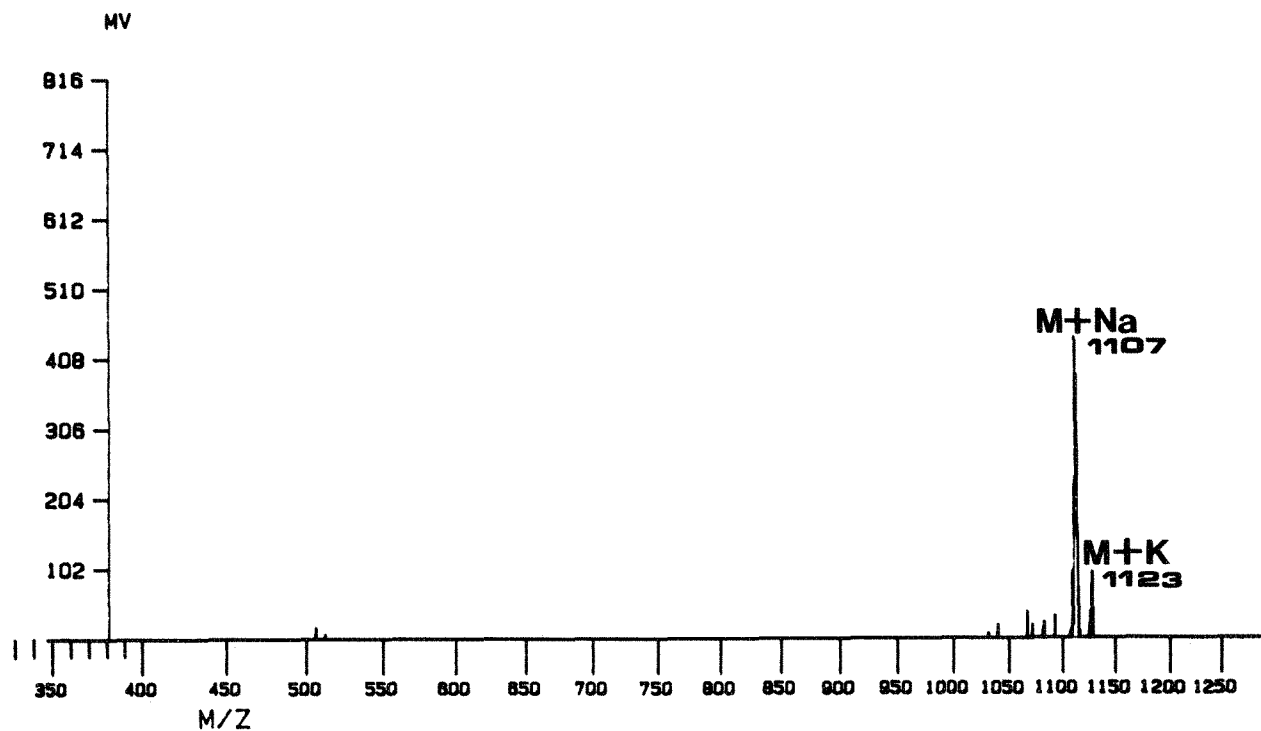


FIG. 2.--Laser mass spectrum of arginine-vasopressin (m.w. 1084).

THE PROBLEM OF VISIBILITY IN NOISY IMAGES

D. S. Bright, E. B. Steel, and D. E. Newbury

A general problem in microscopy is the recognition of low-contrast features in an image in the presence of noise. This situation is often encountered in scanning electron microscopy, where the threshold of visibility is one of the most important yet least appreciated concepts.^{1,2} In many practical applications, the microscopist is confronted with the problem of viewing objects that produce low values of contrast, which pleases the objects near the visibility threshold. An excellent example of such a situation is the imaging of asbestos fibers, which, because of their small dimensions, do not scatter beam electrons efficiently.^{3,4}

The mathematical description of the visibility criterion for scanning electron microscopy is given by the threshold current equation¹

$$i_{th} > \frac{4 \times 10^{-12}}{\epsilon C^2 t_f} \quad (1)$$

The threshold current i_{th} is the amount of beam current that must be supplied to detect a specific level of contrast C arising because of the electron/specimen interaction, in an image of 10^6 picture elements (pixels) recorded in a frame time t_f . The term ϵ combines the efficiencies of signal generation, collection, and detection.

The starting point for the derivation of the threshold equation⁵ is the Rose criterion for the signal-to-noise necessary for small objects to be visible in the presence of noise, which is given in terms of the threshold contrast C_{th} by

$$C_{th} = \frac{\Delta S}{S} > \frac{k\sqrt{n}}{n} \quad (2)$$

where the signal S is related to the number of signal carriers n . Rose stated that, based on experiments with television displays, k "appears to be greater than unity and probably is in the neighborhood of 5." This value of $k = 5$, though not arbitrary, is subject to a number of limitations. In determining the value of k , Rose's experiments only examined a single class of objects (circles), treated only negative objects (black objects on a gray background), used images that had an obvious symmetry and aided the viewer in locating the ap-

parent position of test objects, and defined the visibility limit for small objects that were approximately 1% of the width of the image. The Rose criterion is thus an appropriate choice only for predicting the visibility of fine-scale features in images. Many SEM imaging situations involve objects with shapes that differ radically from the conditions under which the criterion $k = 5$ was determined. In particular, when linear features such as the edges of objects or fibers are examined, and they extend across a significant fraction of the image field, the effect of the contiguity of the pixels is to create a redundancy in the image that renders the feature more readily visible to an observer. In this paper, we have used a series of computer-generated images of fibers to determine an appropriate visibility criterion for fiber-like objects.

Experimental Procedures

The test images were constructed with the LISPIX image processing software described in a previous paper.⁶ The digital images consisted of a random number, selected in the range 0 to 25, of randomly oriented and randomly placed fibers. The fiber dimensions were selected from three size classes, whose characteristics are listed in Table 1. The digital images, with a resolution of 512×512 pixels, were constructed from a two-gray-level image consisting of (1) the fiber gray level F and (2) a background gray level B . For a particular image, F and B were constant. The contrast C of the fibers in each image was given by

$$C = (F - B)/F \quad (3)$$

To simulate real images, each pixel in a particular image that had either B or F as its gray level, was given a new gray level by application of a random Poisson deviate, the mean of the population of which was either B or F , as appropriate. For example, for $F = 100$, $B = 90$, and $C = 0.1$, the pixels within all the fibers had a variance of 100, as defined by a Poisson distribution, whereas all background pixels had a variance of 90. This criterion was chosen on the basis of measurements on real SEM, STEM, and TEM images of asbestos fibers, which revealed intensity distributions of background noise that were indistinguishable from such Poisson distributions. Examples of typical fiber images for $C = 0.2$ and $C = 0.05$ are shown in Fig. 1.

The overall goal of this study was to examine the effects of noise level, object contrast, and object morphology on visibility. A series of images covering a wide range of variance was first examined. A variance level of 100 was chosen for initial experiments because visibility ranged from zero to unity for the

The authors are at the National Institute of Standards and Technology, A121, Gaithersburg, MD 20899. They wish to acknowledge the efforts of their colleagues who evaluated the images to form the database for this study: Joe Bennett, Jack Chang, Peter Chi, Brian Classon, Barry Diamondstone, Bob Fletcher, Greg Gillen, Kurt Heinrich, Diane Johansen, Ryna Marinenko, Bob Myklebust, John Phelps, Cynthia Poston, David Retorick, David Simons, John Small, Craig Stone, Barbara Thorne, Shirley Turner, Rance Velapoldi, and Jennifer Verkouteren.

TABLE 1.

Type	Length (pixels)	Width (pixels)
Short	15-40	1
Long-narrow	41-256	1
Long-wide	41-256	2-9

contrast range of interest, 0.01 to 0.2. This variance is similar to that observed in many live-time SEM images.⁴ An additional experiment was performed on a single test image with a variance of 10 000 to explore the effect of signal-to-noise level.

The measurement procedure consisted of requiring 20 observers to identify the location of fibers in each of 18 images. Observers were classified according to previous microscopy experience: (1) verified asbestos counters,⁷ (2) microscopists, and (3) nonmicroscopists. The digital images were displayed on a video monitor that provided an image edge dimension of 25 cm. Fiber positions were marked with a cursor. Scoring was performed automatically by means of a LISPIX program, which compared true fiber location with the observer's indicated location; a hit was allowed if the marked location was within 1% of the field width (6 pixels) of any pixel on the fiber. Hits, misses, and false hits were recorded.

Results and Discussion

The overall performance of the observers is summarized in Fig. 2, which is a box plot of the fraction of fibers found in each image as a function of contrast. The bottom, middle, and top horizontal lines in each box depict the 25th, 50th, and 75th percentiles, and the extensions show the 10th and 90th percentiles; circles depict individual data points (i.e., one observer's score for one image) that fall outside these limits. It can be seen in Fig. 2 that the 50th percentile for all observers only approached unity (i.e., all fibers found) at the highest contrast tested, $C = 0.2$. For reference, the Rose criterion for this noise level ($\sqrt{n} = 10$, $\Delta S = k\sqrt{n} = 50$) suggests that $C_{th} > 0.5$ for visibility of small objects with dimensions of 1% of the field width. Thus, this experiment suggests an apparent k lower than that of the Rose criterion for the class of objects used in this study, which ranged in size from 3% to 50% of the field width. The results in Fig. 2 clearly demonstrate how dramatically the visibility decreases with the contrast at this noise level. For a contrast of $C = 0.1$, the 50th percentile score fell to a level of only 0.4; i.e., in half of the observer-image cases tested, the observers missed more than 60% of the fibers. Moreover, for $C = 0.1$, no observer ever found more than 65% of the fibers.

In Fig. 3, the results are plotted for short fibers, which more closely approach the small objects of the Rose criterion. Short fibers

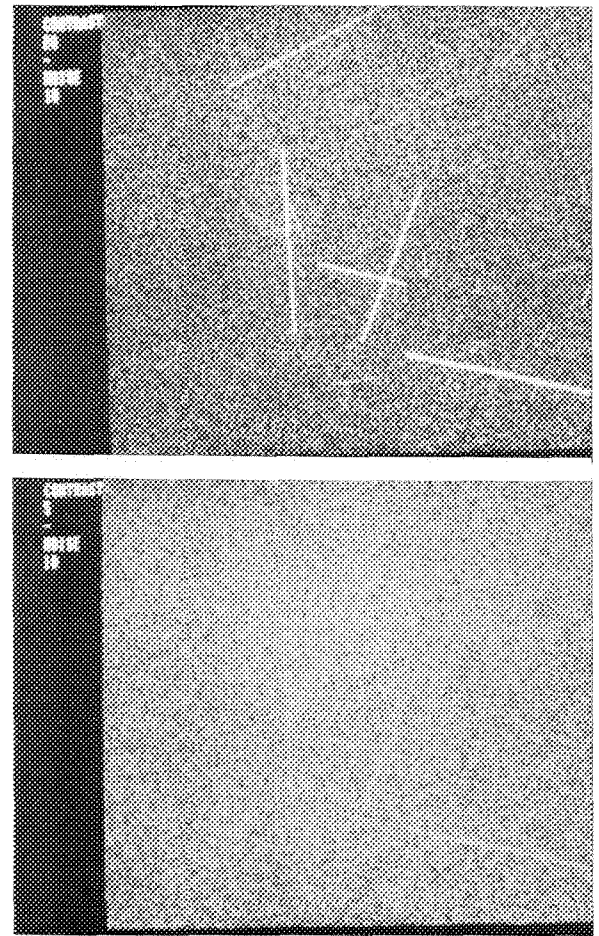


FIG. 1.--Examples of computer-generated fiber images for (a) $C = 0.05$, (b) $C = 0.2$. Same field of fibers is depicted in both images.

are obviously much more difficult to recognize. Even at a contrast of $C = 0.2$, the results for short fibers span the range from complete failure to complete success in locating objects. For these randomly distributed and oriented short fibers, the visibility threshold is clearly tending to higher values of k . To locate the visibility threshold adequately, higher values of contrast will have to be investigated for short fibers.

When the signal level is increased and the relative noise level decreases, the visibility is altered. In Fig. 4, results for images of fibers with $C = 0.05$ and a variance of 100 (i.e., a signal of 100 and a noise level of $\sqrt{n} = 10$, which gives $C_{th} > 0.5$) and a variance of 10 000 ($S = 10\ 000$ and $\sqrt{n} = 100$, which gives $C_{th} > 0.05$) are compared. The observers were highly successful in detecting fibers in the high S/N image, which again confirms a relaxation of the Rose criterion.

The question of false hits is addressed in Fig. 5. It is surprising that the number of false hits is approximately constant regardless of the contrast of the fibers in the image. The number of false hits apparently depends only on the background noise, and the

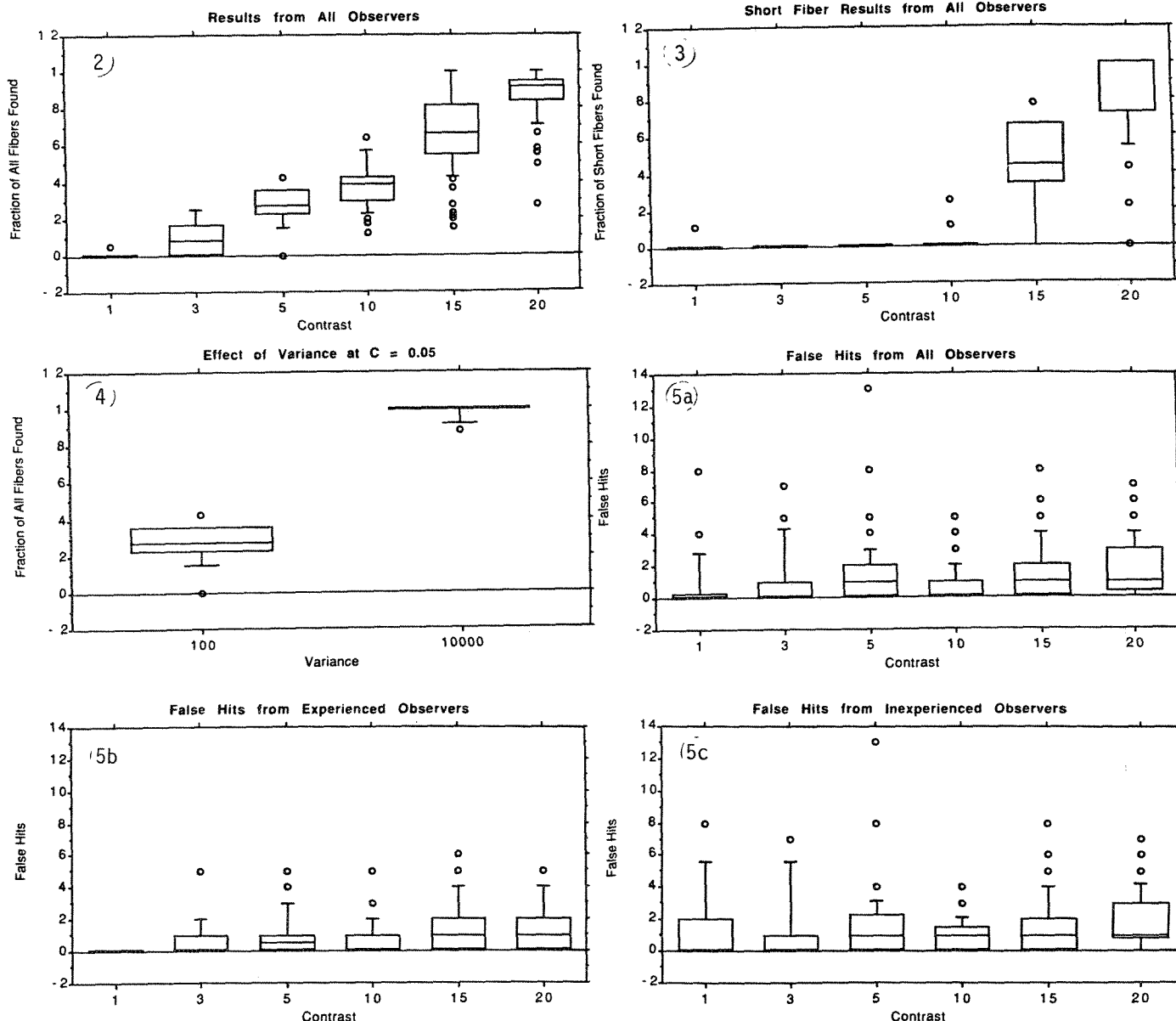


FIG. 2.--Box plot of fraction of all fibers detected in image by observer, taken over complete set of observers, as function of contrast (constant axis is plotted by category rather than linearly). Bottom, middle, and top horizontal lines of box plot represent the 25th, 50th, and 75th percentiles; extensions are 10th and 90th percentiles. Circles are individual observer-image data points that lie outside this range.

FIG. 3.--Box plot of fraction of short fibers detected in image by observer, taken over complete set of observers, as function of contrast.

FIG. 4.--Box plot of fraction of all fibers detected images with $C = 0.05$ by observer, taken over complete set of observers, as function of variance of signal (variance = mean).

FIG. 5.--Detection of false hits as function of contrast: data for (a) all observers; (b) experienced microscopists; (c) nonmicroscopists.

presence of real objects in an image has little effect on the detection of false hits. The only exception to this result was at very low contrast, where the experienced microscopists/asbestos counters found no false hits at the lowest contrast (Fig. 5b), whereas the inexperienced observers found a small number (Fig. 5c). As soon as objects were visible in the field of view, the experienced microscopist began to detect false hits.

Conclusions

The results of this preliminary study clearly reveal the relaxation of the Rose criterion that occurs when linear features such as fibers are viewed near the threshold of visibility. The results suggest that in order to derive an expression for the visibility factor k as a function of fiber length, a more complete examination of both contrast and signal-to-noise ratio will be necessary. The

spread in results observed for the set of observers tested reveals differences in both visual acuity and in individual interpretation which inevitably is encountered in the real world. A robust definition of k will have to include a reasonable statistical criterion for success. In addition, object size, shape, orientation, and signal character (i.e., positive or negative relative to background) must be studied. The eventual product of this study will be to develop standards for image quality which will be applicable to a wide range of imaging problems, both in microscopy and related areas of interest.

References

1. C. Oatley, W. C. Nixon, and R. F. W. Pease, "Scanning electron microscopy," in *Advances in Electronics and Electron Physics*, 1965, 181.
2. J. I. Godstein, D. E. Newbury, P. Echlin, D. C. Joy, C. E. Fiori, and E. Lifshin, *Scanning Electron Microscopy and X-ray Microanalysis*, New York: Plenum, 1981, 172-175.
3. J. A. Small, D. E. Newbury, and R. L. Myklebust, "The visibility of asbestos fibers in the scanning electron microscope," *Microbeam Analysis--1983*, 148.
4. E. B. Steel, "SEM imaging and analysis of submicrometer particles in air and water samples," *Microbeam Analysis--1988*, 466.
5. A. Rose, *Advances in Electronics*, 1948, 131.
6. D. S. Bright, "A LISP-based image analysis system with applications to microscopy," *J. Micros.* 148: 51, 1987.
7. E. B. Steel and J. A. Small, "Accuracy of transmission electron microscopy for the analysis of asbestos in ambient environments," *Anal. Chem.* 57: 209, 1985.

TECHNIQUES FOR 3-D IMAGE PRESENTATION FROM CONFOCAL SCANNING MICROSCOPY

J. J. McCarthy, J. S. Walker, and C. E. Dillon

The development of specialized hardware and software for three-dimensional (3-D) presentation of data has progressed rapidly over the past few years. These advances have been spurred by the availability of faster and much cheaper graphics processors, cheaper memory, and lower-cost high-resolution displays. Most of the attention of developers has focused on the problems presented by the two largest applications for this technology, computer-aided design (CAD) and medical imaging. As the cost of this technology continues to diminish, its application to presentation of image data in microscopy is becoming more common. Adoption of these methods by microscopists has been hindered by the difficulty of image segmentation. Segmentation refers to the process of extracting data specific to the objects of interest from the images of the object. Since microscopy often produces noisy, low-contrast images, accurate segmentation is a key problem. Confocal scanning optical microscopy (CSOM) vastly simplifies the process of acquiring and segmenting 3-D data from a suitable specimen. It does so because a CSOM permits optical rather than physical sectioning of the sample. This simplification has led to the rapid development of techniques for presenting 3-D CSOM data. This paper reviews the fundamentals of 3-D image presentations and discusses their application to CSOM data. A brief description of the principles of CSOM is also presented. The techniques for presentation of 3-D images described here can also be applied to the processing of serial section data from TEM studies and stereo pairs obtained by SEM.

Fundamentals of 3-D Presentations

The basic assumption behind any 3-D presentation is that a computer model of the object(s) of interest can be constructed from the original raw data. The computer model is then used to calculate and draw any 2-D projection of the object selected by the viewer. The first step in model building is the collection of data. Data for the model may be collected in many ways, including manual input of coordinates, contour tracings from a series of photographic or digital images, or by automatic processing of digital images. The second step in model building is segmentation of the data to define only the objects of interest. Accurate segmentation is often the most difficult problem to be solved in preparing a realistic model of the object. It is at this point that gross errors can occur, following the cliché "garbage

in, garbage out." Once the computer model is constructed from the segmented data it can be used to calculate any desired 2-D projection of the object, which can be viewed on the computer display. Two basic approaches have been used to construct computer models: the vector model and the voxel model.

The Vector Model. The most commonly used approach is the vector or "wire-frame" model. In this model, surfaces are first depicted by drawing contours of object perimeters at numerous section planes, which looks much like a model composed of bent wire. The basic assumption of the wire-frame approach is that the surfaces of the object are "known" or at least well behaved so that the space between the wires can be defined as simple surfaces. These surfaces are then represented by a collection of polygons, rendered by the graphics system, which uses a selected viewpoint and includes shading due to light sources, perspective corrections, and depth perception. The vector-model approach has been widely used in CAD and is the approach used in most off-the-shelf graphics systems.

The wires of the wire frame model must be derived from knowledge of the object to be modeled. In the simplest case, vectors are generated from sets of coordinates that are manually input in the proper sequence. The coordinates can be determined from measurements on the actual object or from a reproduction of the object. The vectors have no intensity information about the object, and may be thought of as the contour formed by the intersection of the object surface with a plane. An example of such a process is the tracing of contours from a set of micrographs of serial sections from a TEM study. In TEM, the segmentation of structures in each section is often done manually, but additional processing may be required to register structures from section to section due to distortion from sectioning and other artifacts.

The advantage of the vector model is that it requires a small amount of data compared to that needed to represent all of the actual object. This reduced data set is a key to generating realistic 2-D views quickly enough to allow interactive (1 to 2 s per view) display of the object. The sophistication of the rendering algorithms and the hardware employed affects the system cost and the speed and quality of the final presentation. Typical midrange cost (\$15,000 to 25,000) systems can produce 2000 to 5000 shaded polygons/s. The major disadvantage of the vector model for microscopy data lies in the assumption that the surface between wires is known. In many cases,

The authors are at Tracor Northern, 2551 West Beltline Highway, Middleton, WI 5356202697.

especially biological specimens, this assumption is not justified. However, in the case of reflective surfaces measured in CSOM the assumption of a known surface can often be used. In those cases, the vector model provides excellent presentations.

The Voxel Model. The second approach to model building is the voxel image. In this model, no assumption about the behavior of the surface of the object is made. The computer model of the object is actually a large database that contains all the image data obtained from the specimen. Each individual cell of this database has an intensity value (commonly 8 bits) and is denoted a voxel. Whenever a new view must be presented, each voxel of the entire database is processed to provide the desired 2-D projection.

The advantage of voxel models is the lack of assumptions about the surfaces of the objects being represented, and the ability to visualize all internal structures as recorded, not just as rendered surfaces. This feature is particularly important in the case of noisy data or complex images where several objects of interest are present with nearly the same gray levels in each object. Such noisy, complex images are common in microscopy and make reliable segmentation quite difficult. However, when such data are rendered as a voxel presentation, the human eye and brain can readily segment and interpret the 3-D structures of the object. With proper manipulation tools the observer can select objects from the voxel image for further processing. The major disadvantage of the voxel model is the large number of calculations that must be performed for each new presentation, which has limited the use of voxel presentations to fairly expensive computing platforms in order to approach an interactive display.

Rendering Methods. After an object of interest has been identified in either a vector or voxel model, its surface may be rendered as a 2-D projection. The following steps are followed by most rendering procedures:

1. Each surface of the object is subdivided into a number of polygons using some procedure.
2. A reference point is chosen for the view desired; then each surface is transformed relative to this reference.
3. Depth effects are represented by perspective foreshortening.
4. Hidden surfaces are not displayed.
5. Light sources are reflected on the surfaces possibly with variable shading and shadowing. Depth may be further represented with subdued shading.
6. Jagged edges are smoothed by an anti-aliasing procedure.

A great deal of work has gone into the development of techniques to accomplish the tasks listed above. Several of the more common techniques are described in the following paragraphs and several are illustrated in the examples

Polygon Shading. Computer models of surfaces are rendered as polygons on the display screen. The simplest approach is to divide the surface into polygons in which all pixels have the same intensity. This approach is called flat shading. To achieve a more realistic view, the polygons must be shaded to account for the intensity of the light source and the angle between the source and the surface. The two most commonly used shading algorithms are those of Gouraud¹ and Phong.² Both methods use interpolation techniques to show the effects of shaded intensities in adjacent polygons on the intensity of each pixel in the polygon being rendered. In Gouraud shading, the intensities of interior pixels are interpolated from the intensities found at the adjoining vertices. The intensity at each vertex is proportional to the dot product between the unit vector from the surface and the incident light. The effect is to produce a very smooth gradation from one surface to another. Figure 1 illustrates the improved realism due to Gouraud shading. The surface is a sine function rendered as a wire-frame, flat and Gouraud shaded model.

Phong shading interpolates the angle of the unit vector from the surface for each interior pixel. This method requires that each of these pixels has a more complex intensity calculation than in Gouraud shading. This method provides superior shading in cases where both diffuse (scattered) and specular (direct) reflection must be calculated. The higher realism of the Phong method comes at the price of increased computing time, about five times slower than the Gouraud method.

From the viewer's standpoint, some objects seem to be more realistically rendered by one method than the other. The shading result varies depending on the type of object, the curvature of the surface, the observer's viewpoint, and the direction of illumination. Both methods can, in special cases, produce an optical illusion known as Mach bands. A Mach band is a light or dark band that appears at the juncture of a group of polygons.

Z Buffering. The Z-buffering technique is primarily devised for the purpose of hidden surface removal. The basic method is to calculate the depth of each pixel as part of the other processes of rendering and transfer a pixel to the display only if it covers a previously displayed pixel. Z-buffering algorithms can be implemented in software or hardware, but in either case the technique requires more memory in order to store the additional information about pixel depth. The Z-buffer data can also be used to increase the realism in the rendered image greatly by including depth cueing and transparency effects. Each of these features requires further manipulation of the pixels after the initial shading and depth sorting has been performed. Depth cueing produces a modification to the color or intensity of a pixel based on its z position and shade gradient. Transparency

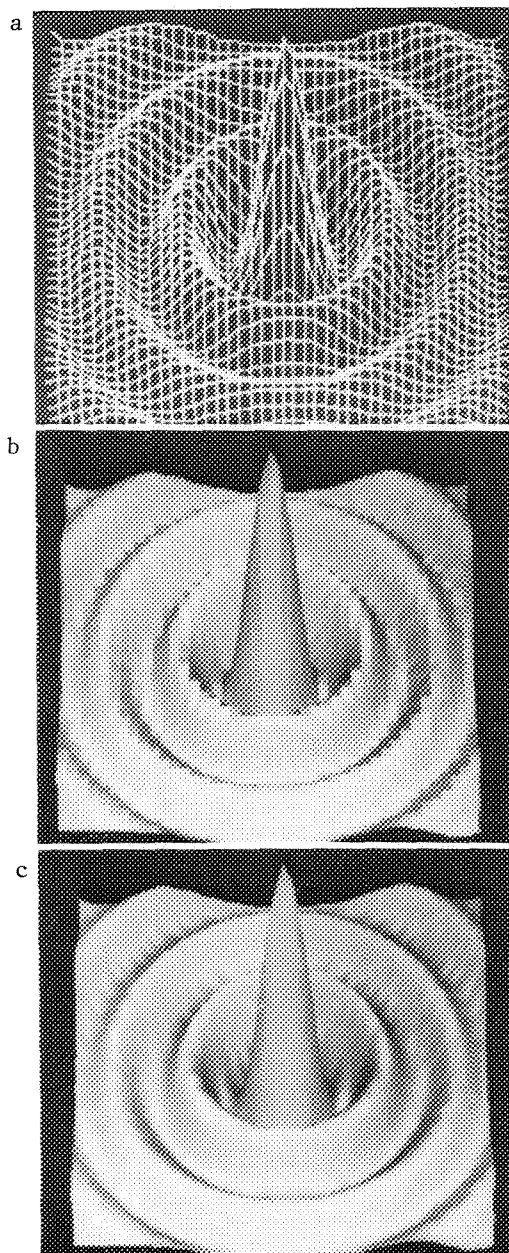


FIG. 1.--Comparison of renderings of sine function: (a) wire grid, (b) flat shaded, (c) Gouraud shaded.

ency is the ability to look at an object "through" another structure that is closer to the viewer. A pixel in front of another which is part of a polygon with a "transparency index" that is nonzero can be looked through for a view of other features that would normally be hidden. These features can be very powerful when one is viewing complex objects, and apply equally well to voxel data and vector models.

Principles of CSOMs

The basic principles of confocal scanning optical microscopy were first described in a patent application by Minsky⁵ and subsequently by various authors.⁴⁻⁷ These concepts will be briefly summarized here to provide a context in

which to discuss the collection and presentation of example 3-D images.

Many of the specimens viewed in reflected light in the optical microscope are either translucent or have no flat surfaces. As a result, even though the specimen is illuminated very brightly at the focal plane of the objective lens, the image contrast is reduced by the light scattered from other surfaces within the specimen. The resulting loss of image detail and poor contrast is particularly evident with unstained live tissue or fluorescent specimens.

This problem is eliminated by use of the principles of confocal scanning. If an aperture is placed in the illuminating beam so that it is imaged in the focused-on plane, and a conjugate aperture is placed in the imaging system before the detector, the scattered, reflected, or fluorescent light from out-of-focus planes is strongly suppressed in the final image. This optical layout and the confocal effect is illustrated in Fig. 2. Combining this principle with any means to scan the specimen in a point-by-point fashion produces a high-resolution, high-contrast image of the thin focused-on layer. By whatever means the scanning is done, the goal is to eliminate scattered, reflected, or fluorescent light from out-of-focus planes. An example of the confocal effect is illustrated in Fig. 3. Figure 3(a) is a photomicrograph of wood fibers in a conventional reflected light microscope, Fig. 3(b) is a similar field in a confocal microscope (tandem scanning microscope). The difference is quite dramatic, and in practical terms the reduced depth of field is the principal benefit of confocal imaging. It is this property that allows collection of image data than can readily be used to examine the three dimensional structure of the specimen. An additional benefit is improved lateral resolution which (in theory) may be as much as 1.4 times better than in a conventional microscope.⁵ This property is being exploited in the area of critical dimension measurements of microstructures.

Collection and 3-D Presentation of CSOM Data. The images presented in the following examples were collected using a Tracor Northern tandem scanning microscope (TSM) controlled by a TN-8502 image processing system. The TSM is a confocal microscope that uses normal illumination sources and is capable of higher than video-rate frame speeds. A more

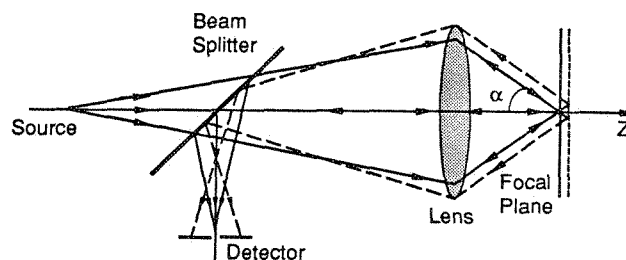


FIG. 2.--Schematic ray diagram of confocal optics.

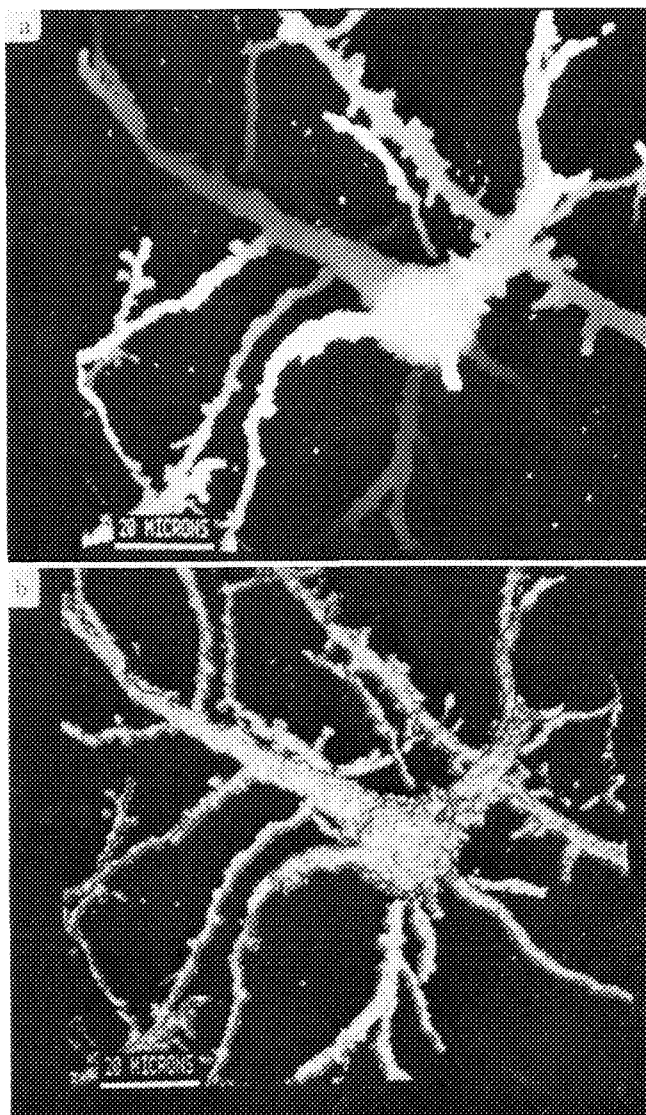


FIG. 5.--Processed images of Purkinje cells from cortex of hamster: (a) depth-coded Zmap image, (b) rendered version of same image (total depth of field is about 25 μm).

general it appears that vector-model rendering may be more appropriate in the study of highly reflective surfaces, and the voxel model is the best suited for viewing complex objects present in a collection of fairly noisy images. The latter case is typical of many studies in microscopy.

For this reason, we can expect additional methods of visualization of voxel data to be developed specifically for the needs of the microscopist.

References

1. H. Gouraud, "Continuous shading of curved surfaces," *IEEE Trans. C-20*: 623-629, 1971.
2. Bui-Tuong Phong, "Illumination for computer-generated pictures," *Comm. ACM* 18: 311-317, 1975.
3. M. Minsky, "Microscopy apparatus," U.S. patent 3 013 467, 1957.
4. M. Petran, M. Hadravsky, M. D. Egger, and R. Galambos, "Tandem-scanning reflected-light microscope," *J. Opt. Soc. Am.* 58: 661-664, 1968.
5. T. Wilson and C. Shepard, *Theory and Practice of Scanning Optical Microscopy*, Orlando, Fla.: Academic Press, 1984.
6. G. J. Brakenhoff, P. Blom, and P. Barends, "Confocal scanning light microscopy with high aperture immersion lenses," *J. Microsc.* 117: 219-232, 1979.
7. M. Petran, M. Hadravsky, and A. Boyde, "The tandem scanning reflected light microscope," *Scanning* 7: 97-108, 1985.
8. J. J. McCarthy and J. S. Walker, "Scanning confocal optical microscopy," *EMSA Bulletin* 18: 2, 1988.
9. N. Aslund et al., "Three-dimensional digital microscopy using the PHOIBOS scanner," *Scanning* 9: 227, 1987.
10. H. T. M. van der Voort et al., "Design and use of a computer-controlled confocal microscope for biological applications," *Scanning* 7: 66, 1985.
11. A. Boyde, "Confocal optical microscopy," *Microscopy and Analysis*, 7-13, Jan. 1988.
12. A. Boyde, "Automated 3-D characterization of osteoclastic resorption lacunae,"

VECTOR IMAGING OF MAGNETIC MICROSTRUCTURE

M. H. Kelley, John Unguris, M. R. Scheinfein,
D. T. Pierce, and R. J. Celotta

An ability to study the properties of microscopic magnetic structures and to investigate magnetic properties with submicron spatial resolution is important both for its fundamental scientific value and its usefulness in applied magnetic technology. As the size of magnetic devices decreases, and the density of recorded information increases, new diagnostic techniques must be developed with which these new magnetic structures and processing techniques can be characterized. Many current techniques for the investigation of magnetic structures suffer either from poor spatial resolution or from the inability clearly to separate contrast due to magnetic structures from that due to topographic or other physical features. We describe a method of magnetic imaging that overcomes many of the difficulties of other current techniques and that allows quantitative analysis at high spatial resolution of the vectorial properties of sample magnetization.

Experimental Method

Magnetization arises from the orientation of the magnetic moments of individual electrons in bulk material. Consequently, the problem of microscopic characterization of magnetic properties can be resolved by measurement of the spin orientation of electrons in a small region of a magnetic solid. The technique described in this work is based on the observation that low-energy secondary electrons produced by high-energy electron bombardment, as in scanning electron microscopy (SEM), retain the spin orientation they had in the bulk.¹ A measurement of the spin polarization of these secondary electrons gives a direct measurement of the magnetization in the small region from which the secondary electrons originate (Fig. 1). The technique of imaging magnetic microstructure through spin analysis of electrons ejected by a focused high-energy electron beam has been called Scanning Electron Microscopy with Polarization Analysis (SEMPA).²⁻⁴

The SEMPA technique has several features that make it an attractive tool for micromagnetic studies. First, the spatial resolution is substantially better than for any other currently available technique for studying bulk specimens. The resolution in SEMPA is the same as in conventional SEM images, with a potential resolution better than 10 nm. Sec-

ond, unlike other methods used to study magnetic microstructure, the magnetic information from SEMPA is essentially independent of, but recorded simultaneously with, the topographic information. This separation makes possible detailed studies of the relationship between physical and magnetic structures. Third, the polarization signal and magnetic contrast are large. The secondary-electron current can typically be 10-50% of the incident electron beam, and typically has a spin polarization between 5% and 30%, depending on the sample. Finally, SEMPA is a surface analytical tool because the secondary electrons have a mean escape depth of only a few nanometers. SEMPA is thus an excellent tool for studies of the magnetic properties of surfaces and thin films.

Our SEMPA apparatus (Fig. 2) has three basic components: the electron microscope, the secondary-electron collection and transport optics, and the spin polarimeter.^{5,6} The SEM is fully ultrahigh-vacuum compatible and is fitted with an ion gun for surface cleaning and an Auger analyzer for surface characterization. A spatial resolution of 40 nm can be achieved with this instrument. The electron optics collect the spin-polarized secondaries emitted from the sample and form them into a beam suitable for use with the spin polarization analyzers.

The two spin analyzers together allow for the determination of all three orthogonal components of the vector magnetization. The first detector, referred to as in-plane in Fig. 2, measures two components, P_x and P_y , in the plane of the sample surface. The second detector, referred to as out-of-plane in Fig. 2, is oriented perpendicular to the in-plane detector and measures both the out-of-plane component P_z and a redundant in-plane component, which provides a diagnostic for the calibration of the two spin analyzers. An electrostatic quarter-spherical switchyard determines which of the two SEMPA detectors is active.

The basis for spin analysis is the scattering of a spin-polarized electron from an atom with large nuclear charge, gold in this case. There is a relativistic effect, the spin-orbit interaction, which causes spin-polarized electrons to be scattered with different probability into two detectors that are symmetrically placed relative to the direction of incidence. This scattering asymmetry is used in spin analyzers to determine the polarization of an incident electron beam.

Our spin analyzer consists of an annular anode that is split into four quadrants, each of which measures the intensity of electrons backscattered from an evaporated gold film and

The authors are at the Center for Atomic, Molecular, and Optical Physics, National Institute of Standards and Technology, Gaithersburg, MD 20899. This work supported in part by the Office of Naval Research.

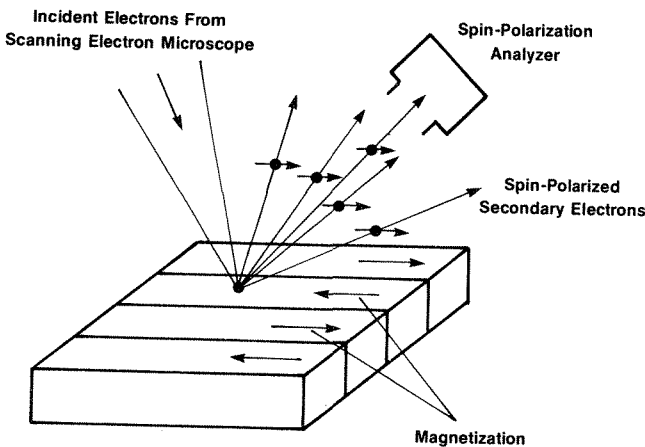
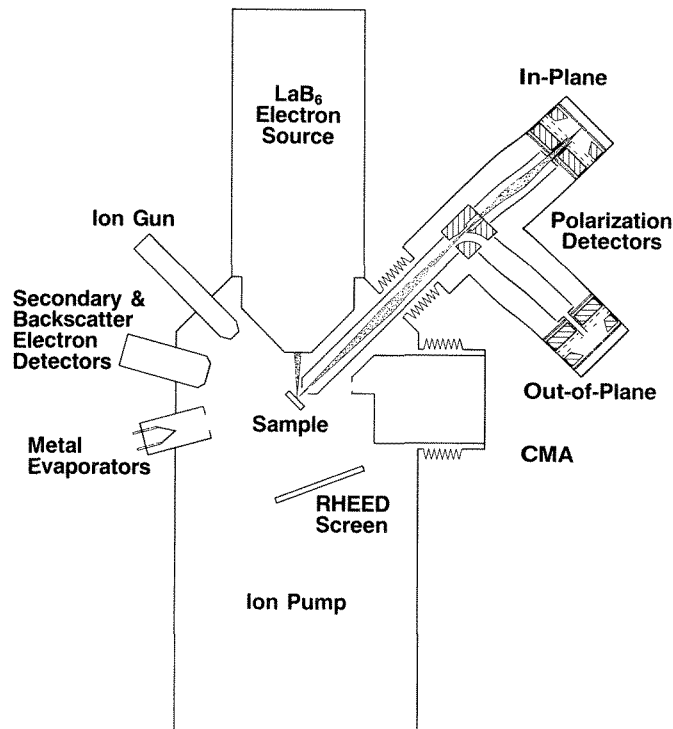


FIG. 1.--Principle of scanning electron microscopy with polarization analysis (SEMPA).
FIG. 2.--Schematic of SEMPA apparatus.



amplified by a microchannel plate multiplier. A pair of opposed quadrants determines one component of the incident spin polarization, say P_x , through the relationship:

$$P_x = \frac{I_a - I_b}{I_a + I_b} \quad (1)$$

where I_a and I_b are the electron fluxes measured by the two quadrants, and S is the analyzing power of the detector. Each SEMPA detector determines two orthogonal components of the spin polarization, and hence of the sample magnetization. The sum of the intensities from any two opposing quadrants is proportional to the total secondary-electron current. As the primary electron beam is rastered over the sample, each detector *simultaneously* measures the conventional secondary-electron image and two images giving the electron spin polarization projected along two perpendicular axes.

A single crystal iron whisker provides a good system for illustrating the SEMPA technique. The magnetic properties of iron single crystals are quite well understood, so the interpretation of the polarization images is straightforward. In particular, for the case of an iron (100) surface, the magnetization is parallel to the surface along one of the two easy magnetization axes. Because there is no out-of-plane component, only data from the in-plane detector are necessary. In addition, the magnitude of the magnetization in ferromagnetic materials is constant and does not depend on the direction. Figure 3 shows both the conventional secondary-electron image and the P_x and P_y polarization components for a small region of the whisker. Several features of these images are particularly noteworthy. First, contrast between the magnetic domains is clearly visible in the polarization images, magnetization in the positive x or y direction (or spin polarization is the negative x or y direction) is indicated by white pixels. The second important feature is the presence of two instrument effects that interfere with accurate polarization measurements. One effect

allows a remnant of the topographic image to be visible in both P_x and P_y . The other contributes a background polarization signal that varies smoothly over the images. Both these experimental artifacts must be corrected by the data analysis. Finally, in the format in which the data are presented in Fig. 3, it is rather difficult to visualize or to interpret quantitatively what is going on in the magnetic structure.

There are thus two areas of immediate interest: (1) what data processing is required to permit quantitative analysis of the polarization images, and (2) how the results should be presented for the most convenient interpretation.

Raw Data Processing

Data processing is required to minimize two basic problems: spurious feedthrough of topographical information into the polarization images, and systematic offsets for zero polarization. Each is caused by a lack of azimuthal symmetry about the detector axis as the electron beam strikes the gold target. Any physical asymmetry causes an artificial asymmetry between the signals collected by opposing pairs of anode quadrants and results in artificial polarization contrast. For example, as the primary electron beam is scanned over the sample, the secondary electron beam may be scanned over the gold target. This feature gives rise to the smoothly varying background in the polarization images. Topographic features appear in the polarization images because the secondary electrons from a surface with topographical structure are not emitted with azimuthal symmetry about the mean surface normal. These systematic effects can be minimized, but not always completely eliminated, by careful adjustment of the secondary electron transport optics. One final instrumental effect, the

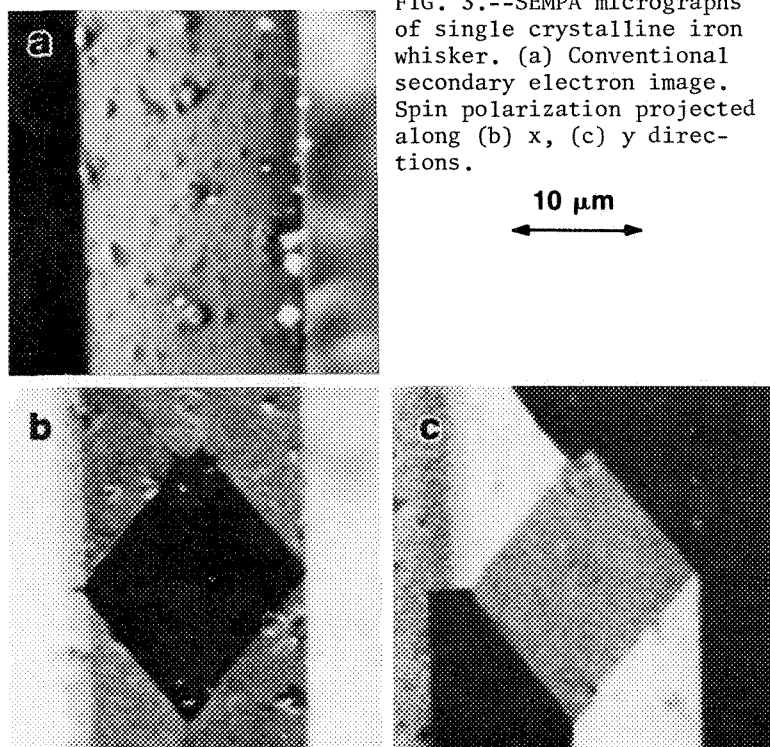


FIG. 3.--SEMPA micrographs of single crystalline iron whisker. (a) Conventional secondary electron image. Spin polarization projected along (b) x, (c) y directions.

overall detection efficiency of individual quadrants, adds a polarization offset that is constant over an entire image.

In practice, one can determine the artificial polarizations very reliably by recording for each image a corresponding image in which the magnetic information is absent, by replacing the gold target in the detector by a graphite target. Carbon atoms have insufficient nuclear charge to generate polarization contrast through the spin-orbit interaction, so that the graphite-scattered images contain only the systematic and artificial asymmetries and can be used to correct the polarization data, apart from the constant overall zero offset.

Graphite background images for the previously shown region of the iron whisker are presented in Fig. 4. The extraneous topographic features are clearly visible. Figure 5 shows the images with the graphite backgrounds subtracted. The smoothly varying background has been removed, along with much of the ex-

traneous structure. The remaining small features are likely real, the result of nonmagnetic contamination of this sample.

There are two principal concerns about the background correction process. First, the noise in the corrected images has increased by roughly $\sqrt{2}$ because the noise in both primary images contributes to the difference image. Second, because the gold-scattered and graphite-scattered images are recorded separately, small drifts in the apparatus can introduce registration problems between the two images. The registration can be adjusted with the image processing software and has so far presented no major difficulties.

At this point, the polarization information is essentially correct as displayed. The remaining problem is that neither the gold-scattered images nor the graphite background images have a well-defined absolute zero of polarization. If the two images have different zero offsets, that difference will appear in the corrected images as well. For the iron whisker images, the correction is straightforward because one has prior knowledge that the magnitude of the polarization is constant across the image. A bias polarization can be determined and subtracted from each image such that the resultant image has maximally uniform polarization magnitude.

For samples where such prior knowledge is not available, the zero bias must be determined in some other manner. Our preferred technique is to record test images of nonmagnetic samples, using both the gold and graphic scattering targets. On the basis of these nonmagnetic data, fine adjustments to the transport optics and detector gains can be made so that the zero bias for the gold-scattered and graphite-scattered images is the same. That done, subtraction of the graphite background also corrects for the zero bias.

Presentation of Results

Thus far, the magnetic information has been presented in terms of the projections of the spin polarization along three orthogonal axes. Because visualization of vector fields is generally difficult, an alternate representation is desirable in which the most important features are clearly emphasized. For the magnetic domains in an iron whisker, and many similar systems, there are two important goals. The first is to determine the direction of the magnetization vector in order to study the relative orientation of adjacent domains. The second is to study the magnitude uniformity of the magnetization independent of its direction. For such studies, it is convenient to present images that correspond to the magnitude and direction of the in-plane spin polarization. These images, referred to as Q_{xy} and D_{xy} , respectively, are related to P_x and P_y by

$$Q_{xy} = \sqrt{P_x^2 + P_y^2}$$

$$(2) \quad D_{xy} = \tan^{-1} \frac{P_x}{P_y} \quad (3)$$

These images for the iron whisker are shown in Fig. 6. It is evident in Fig. 6(a) that the magnitude is essentially constant, with the possible exception of the domain walls where there

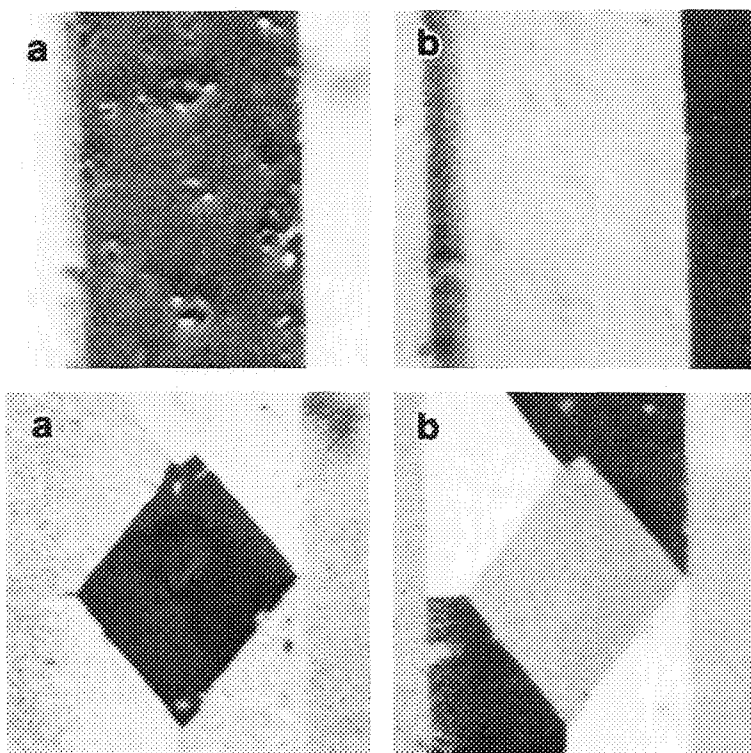


FIG. 4.--Iron whisker. Instrument induced polarization contrast along (a) x, (b) y directions.

FIG. 5.--Iron whisker. (a) x, (b) y components of spin polarization, corrected for instrumental effects.

be verified. The angular difference between the mean polarization directions for adjacent domains can be determined substantially more accurately.

This representation, which is convenient for the two in-plane components, becomes almost essential for the visualization of the vector field in systems where out-of-plane magnetization is also possible. An example of such a system with large out-of-plane magnetization is cobalt. The crystal orientation of the cobalt sample studied was such that the preferred magnetization direction for the bulk was normal to the surface. In order to reduce the magnetic energy at the surface, the magnetic domains break up at the surface in a complex way, but retain a significant out-of-plane component to the magnetization. The in-plane component is constrained by crystal anisotropies to lie primarily along the six crystalline symmetry axes. Images of P_x , P_y , and P_z for the cobalt samples are shown in Fig. 7. The observed vector field is rather complex and difficult to deduce from inspection of these image; the need for a more convenient representation is clearly indicated. As in the previously discussed case of magnetization in iron, the important physical questions concern the uniformity of the in-plane and total polarization magnitudes, the in-plane direction, and the component out-of-plane of the total polarization vector.

In Fig. 8 are shown the images for the in-plane direction and magnitude. Six intensity levels, corresponding to regions polarized primarily along each of the six crystalline axes, are clearly visible in Fig. 8(b). It is also apparent that a gray scale is not the best representation for the angular information. Whenever possible (as in the oral presentation of this work) color can be used to significant advantage for representing the direction information.

The apparent deficit at the domain walls of the in-plane polarization magnitude is very pronounced in Fig. 8(a), and significantly larger than that expected from a consideration of finite resolution effects. This finding seems to indicate a real loss of the in-plane spin polarization at the domain walls. It can be seen from Fig. 7(c) that the in-plane domain walls correspond very well with regions of large positive or large negative out-of-plane polarization.

The picture that emerges from inspection of Figs. 7(c) and 8 is that at domain walls, where the in-plane components of the magnetic vectors from the adjacent domains point toward each other, the composite magnetization is directed into the sample. Where the adjacent in-plane vectors point away from each other, the net magnetization points out of the sample. It is as if underlying bulk domains, which are polarized normal to the surface, act as "sources" or "sinks" of the observed polarization vectors. Further measurements will be required to characterize the magnetic properties of this sample fully.

4 is an apparent drop in polarization. The detailed behavior of magnetization in domain walls is an important topic, but the spatial resolution of the present images is insufficient for quantitative analysis of the walls. One principal effect of finite resolution on the determination of a signed quantity like the spin polarization is to depress the apparent magnitude in regions, such as the domain walls, where the sign changes rapidly. This finite resolution effect can fully account for the deficit observed in Fig. 6(a).

5 In Fig. 6(b) the in-plane spin polarization direction is shown. Dark corresponds to polarization in the +x direction, with increasing angles (in the counterclockwise sense) represented by increasing intensity in the image, until white again corresponds to the +x direction. Arrows in the figure indicate the mean polarization direction for the several domains. The polarization direction can be determined quite well with this technique. A pixel intensity histogram for Fig. 6(b) indicates an approximately Gaussian distribution of angles with a width of about $\pm 10^\circ$ about the mean polarization direction. The width of the mean is indicative of the extent to which the uniformity of spin polarization throughout a domain can

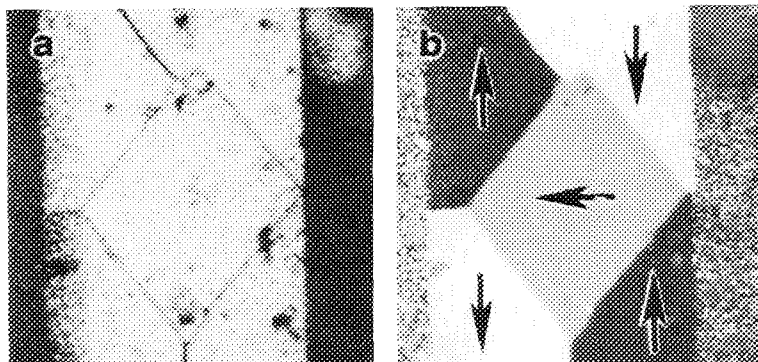
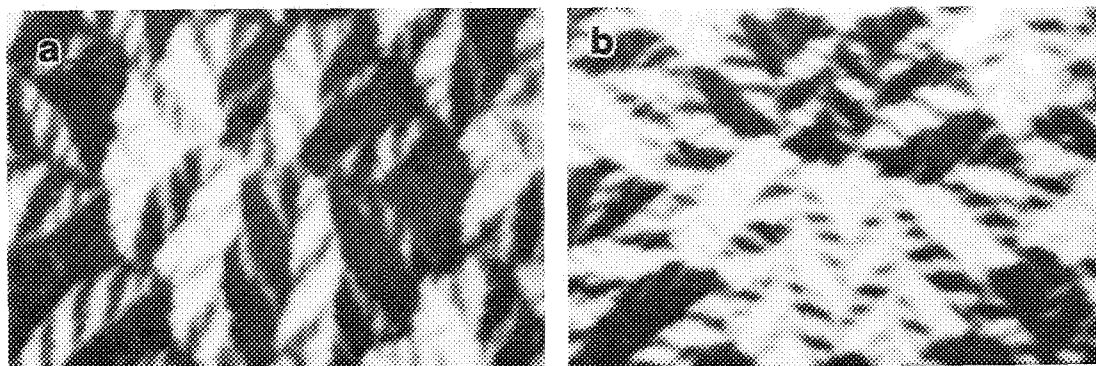
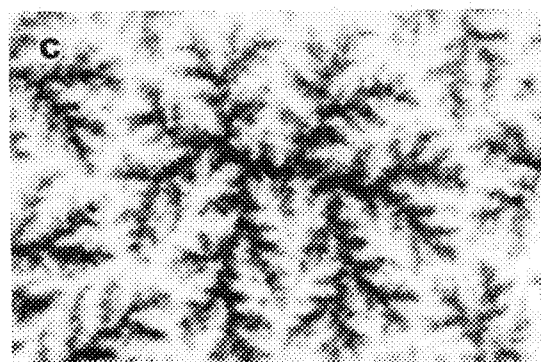


FIG. 6.--Iron whisker. (a) Magnitude, (b) direction of in-plane polarization.



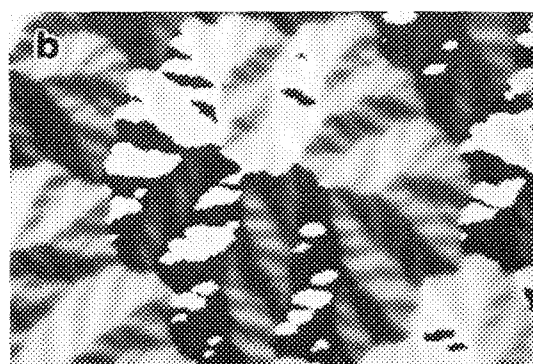
7



5.0 μm

FIG. 7.--SEMPA micrographs for cobalt single crystal. Projections of spin polarization along (a) x, (b) y, (c) z directions.

FIG. 8.--Cobalt single crystal. (a) Magnitude, (b) direction of in-plane polarization.



8

Conclusions

It has been shown in the present work that with adequate data-processing techniques, quantitative studies of vector magnetic properties can be performed. It has further been demonstrated that a judicious choice of data representation can aid enormously in the visualization of the magnetic vector fields.

References

1. D. R. Penn and S. P. Apell, *Phys. Rev. B* 32: 7753, 1985.
2. G. G. Hembree, J. Unguris, R. J. Gelotta,

and D. T. Pierce, *Scanning Microscopy Suppl.* 1: 229, 1987.

3. K. Koike, H. Matsuyama, and K. Hayakawa, *ibid.*, p. 241.

4. R. J. Gelotta and D. T. Pierce, *Science* 234: 249, 1986.

5. J. Unguris, D. T. Pierce, and R. J. Gelotta, *Rev. Sci. Instrum.* 57: 1314, 1986.

6. M. R. Scheinfein, D. T. Pierce, J. Unguris, J. J. McClelland, R. J. Gelotta, and M. H. Kelley, *ibid.*, 60: 1, 1989.

7. J. Kessler, *Polarized Electrons*, Berlin: Springer, 1985.

ELASTIC SCATTERING CROSS SECTION FOR ELECTRON ENERGY ABOVE 1 keV

Zbigniew Czyżewski and D. C. Joy

Monte Carlo simulation requires modeling of two scattering processes: first of the elastic scattering of electrons and second of the inelastic scattering due to collisions with considerable energy losses. The latter is described mostly by the Bethe equation, which provides a well-proven measure of the average rate of energy loss. However, the choice of the elastic scattering formalism should depend on desired results and on the experimental conditions to be modeled.

Monte Carlo Method

The theoretical basis of electron atom interaction was presented a few tens of years ago.¹ It requires the solution of the Dirac equation for a central field for a given potential, which can be done by the partial wave expansion method. The cross section calculated by this method is often called the Mott scattering cross section. There is no analytical formula for the Mott scattering cross section. However, values of this cross section can be calculated numerically for several energy levels and for several dozen values of the scattering angle. Then they can be tabulated and used during a Monte Carlo simulation. Applying the screened Coulomb potential to the Born approximation of the impact problem one obtains the analytical Rutherford scattering formula. It has been widely used for describing elastic scattering of a penetrating electron in solids. However, it has been pointed out that the Rutherford formula is a poor approximation, particularly for heavy atoms.² Direct comparison of Monte Carlo results obtained using both scattering cross sections have so far only been published for gold.³ Reimer et al.² presented Monte Carlo data for the Mott cross section, but their model is based on a plural scattering approximation. Our model for electron scattering is a direct single-step simulation in which the free path resulting from total cross section is used. The path length is assumed to obey an exponential distribution according to the Poisson process for a cascade of scattering events. The energy losses are described by the modified Bethe law.⁴ We used the Mott cross section data after Riley et al.⁵ for scattering angles less than 10° and after Reimer et al.⁶ for greater angles. There are no other published data for energy range 1-30 keV, although there are several Japanese papers on electron scattering using the Mott cross section.⁷ For comparison we used the screened Rutherford

cross section with the usual approximation for the screening parameter.⁶

Results

The values of the backscattering coefficient η obtained by use of the Mott cross section are smaller than those for the Rutherford one (Fig. 1). However, this outcome can be predicted from the total cross section and the average scattering angle--the two most important parameters of the scattering cross section. The energy dependence of the backscattered coefficient as predicted by Mott calculations is in good agreement with experimental data contrary to the Rutherford values. The Mott calculations show a gentle fall in η for gold and a rise in η for Al as the energy is decreased (Fig. 1). Similar curves for the Rutherford cross section predict a significant rise for all elements. A comparison of the total elastic scattering cross section derived from the Mott and the screened Rutherford models shows that the total Rutherford cross section is much larger than the Mott one for energies below 5 keV, except for elements of small atomic number (Fig. 2a, c, e). However, our data of the total Mott cross section are smaller than those presented by Ichimura⁷ but agree well with other data.⁵ This discrepancy is caused by different numerical integration methods for the Dirac equation, as well as by the choice of an atomic potential. It is well known that the screened Rutherford cross section underestimates the scattering probability for low and high scattering angles and overestimates for the intermediate angular range. Nevertheless, the Mott cross section provides smaller values of the average scattering angle θ_v , although for Cu the θ_v values are almost the same (Fig. 2b, d, f). However, the average scattering angle for the Rutherford cross section is a function of the screening parameter. Using more sophisticated formula for screening parameter,³ one obtains somewhat greater values of average scattering angle for

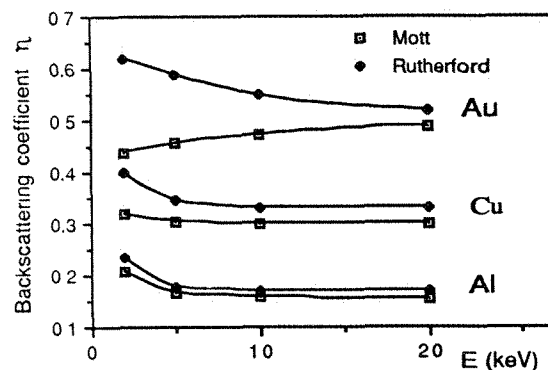


FIG. 1.--Monte Carlo simulation of backscattering coefficient dependence on beam energy from Mott and Rutherford cross sections.

Zbigniew Czyżewski is at the EM facility, University of Tennessee, Knoxville, TN 37996-0810; his permanent address is the Institute of Electronic Technology, Technical University of Wrocław, ul. Janiszewskiego 11, 50-372 Wrocław, Poland. D. C. Joy is at the UT EM facility and at Oak Ridge National Laboratory, Oak Ridge, TN 37831.

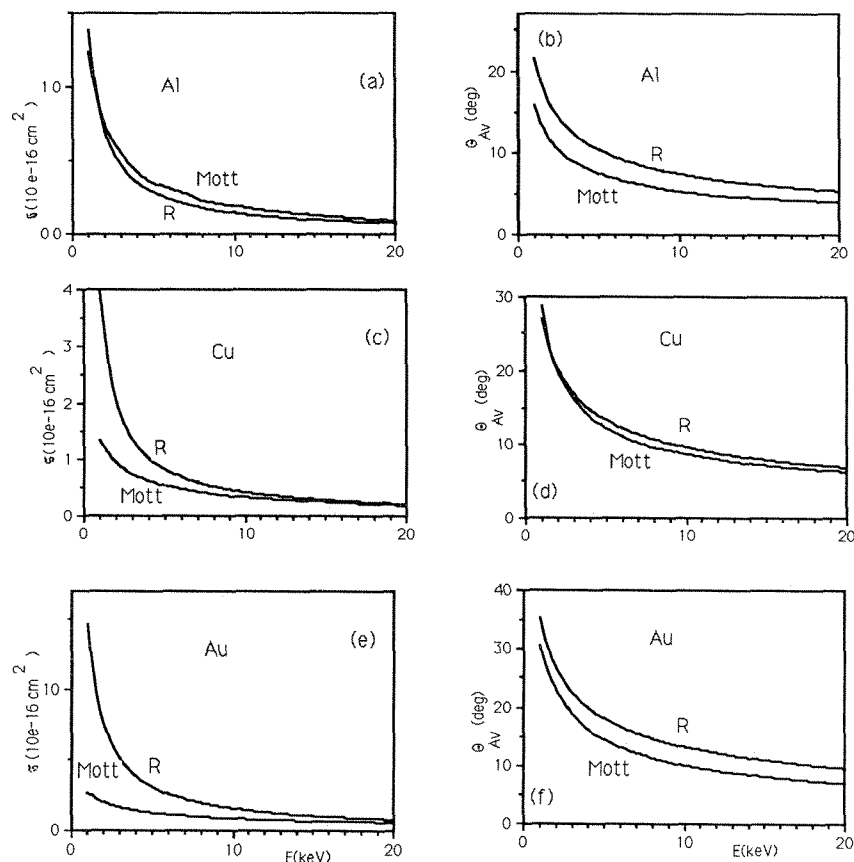


FIG. 2.--Total scattering cross section (a,c,e); average scattering angle (b,d,f); R = Rutherford.

the Rutherford cross section. The backscattered electrons (BSE) energy distribution, energy dissipation, and maximum range curves are affected by the mean free path λ for elastic scattering. The mean free path λ is proportional to the inverse of the total scattering cross section. The maximum range, i.e., the maximum depth of penetrating electrons, depends strictly on the mean free path λ (Fig. 3). Since the λ values for Al for both cross sections are very similar for all energies, the values of maximum range are almost identical for this element. For large values of λ and small values of the average scattering angle θ_V , a typical simulated electron trajectory reaches large depths, and so the energy spectra of backscattered electrons (BSE) simulated by use of the Mott cross section is much smaller for high fractional energies of BSE (Fig. 4) than the corresponding Rutherford data. There are the same reasons of the shift of the energy dissipation curves toward greater depths (Fig. 5). However, for Al these curves are very close to each other. All calculations were performed on an IBM-XT compatible microcomputer equipped with an 8087 math processor using FORTRAN 77. Average simulation time was about 3 s for one trajectory for both scattering cross sections, although the Mott version is somewhat faster than the Rutherford one.

Conclusions

The Rutherford scattering cross section is a good approximation for low-atomic-number elements. The scattering process characteristics are comparable for both cross sections considered for light elements. For higher atomic numbers the Mott cross section is necessary to obtain data that agree with experimental data, especially for low energies. However, for heavy elements (e.g., gold) using the Mott cross section should be obligatory for high energies as well.

References

1. N. R. Mott and H. S. W. Massey, *Theory of Atomic Collision*, Oxford: Oxford University Press, 1965.
2. L. Reimer and E. R. Krefting, "The effect of scattering models on the results of Monte-Carlo calculations," *Use of Monte Carlo Calculations in Electron Probe Microanalysis and Scanning Electron Microscopy*, NBS Special Publication 460: 45, 1976.
3. M. Kotera, K. Murata, and K. Nogami, "Monte Carlo simulation of 1-10 keV electron scattering in a gold target," *J. Appl. Phys.* 52: 997, 1981.
4. D. C. Joy and S. Luo, *Scanning* (in press.)
5. M. C. Riley, C. J. McCallum and F. Biggs, "Theoretical electron-atom elastic scattering cross sections," *Atomic Data and Nuclear Tables* 15: 443, 1975.

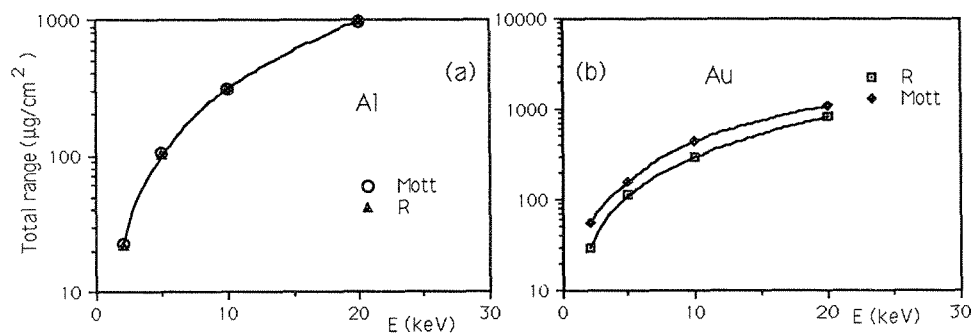


FIG. 3.--Monte Carlo calculations of maximal range for (a) Al, (b) Au for Mott and Rutherford (R) cross sections.

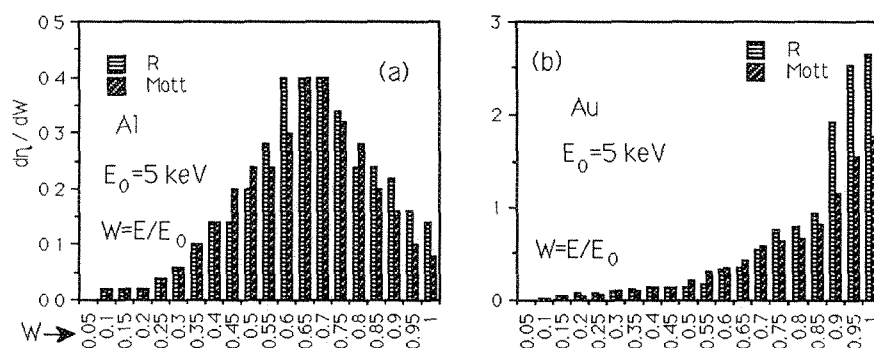


FIG. 4.--Energy distribution of BSE simulated for (a) Al, (b) Au for both cross sections; R = Rutherford.

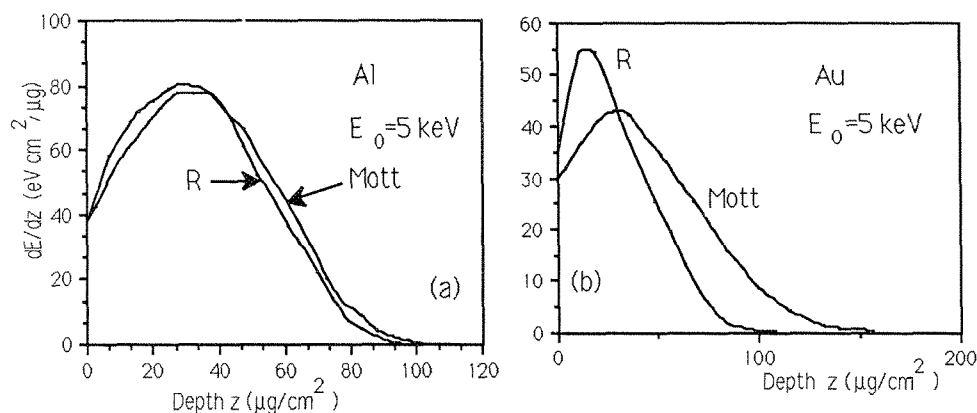


FIG. 5.--Monte Carlo simulation of energy dissipation with depth in bulk target of (a) Al, (b) Au from Mott and Rutherford (R) cross sections.

6. I. Reimer and B. Lodding, "Calculation and tabulation of Mott cross-section for large-angle electron scattering," *Scanning* 6: 128, 1984.

7. S. Ichimura, M. Aramata, and R. Shimizu, "Monte Carlo calculation approach to quantitative Auger electron spectroscopy," *J. Appl. Phys.* 51: 2853, 1980.

AUTOMATED QUALITATIVE ANALYSIS OF AUGER ELECTRON SPECTRA

S. D. Bumgarner, S. K. Hofmeister, D. P. Griffis, and P. E. Russell

The peaks in an Auger spectrum have been traditionally identified by reference to handbooks of standard spectra.¹⁻³ Routine spectral analysis can be made both easier and faster by a computerized routine for automatic identification of Auger peaks. Such automatic peak identification has been successfully applied to x-ray analysis; several software packages are commercially available for this purpose.⁴ However, little has been reported regarding application of automatic peak identification to Auger analysis.

Shaffner in 1980 reported development of software designed to select peaks automatically from derivative Auger spectra,⁵ but identification of the peaks was accomplished subsequently by prompting for operator input of an element atomic number. Frank (1986) reported development of an automated peak selection procedure for undifferentiated Auger spectra;⁶ however, automated identification of the peaks so selected was apparently not a goal.

Automated identification of Auger peaks is complicated by several factors, including shifts in peak positions due to sample charging. Identification is also complicated by variation in peak energies and peak shapes due to chemical effects, since the chemical environment affects the binding energies of the core electrons.⁷

The goal of this research has been to demonstrate the feasibility of automated qualitative analysis of Auger spectral peaks, and to develop algorithms for this purpose. Algorithms for both automatic peak selection and peak identification were developed. These algorithms were applied to spectra acquired from a series of single element standards, and spectra from three multi-element samples.

Peak Selection from Derivative Spectra

Derivative spectra were chosen for analysis, since derivative spectra are commonly used for routine laboratory analysis of solid surfaces.⁸ Shaffner's method for peak selection was used as a starting point; i.e., since each peak in the derivative spectrum consists of a sharp maximum and minimum, a change in slope provides a simple method for selecting peaks from the Auger spectrum. Data points are compared sequentially until an intensity maximum is located. This point is stored, and succeeding data points are compared to locate the corresponding minimum. The minimum is stored in a parallel array. Each maximum-minimum pair represents a

The authors are at the NCSU Department of Materials Engineering, Raleigh, NC 27695-7907. This work was done as part of S. D. Bumgarner's master's thesis. They acknowledge the support of the NCSU Analytical Instrumentation Facility, JEOL USA, Inc., and Dr. A. D. Buonaquisti for his helpful advice.

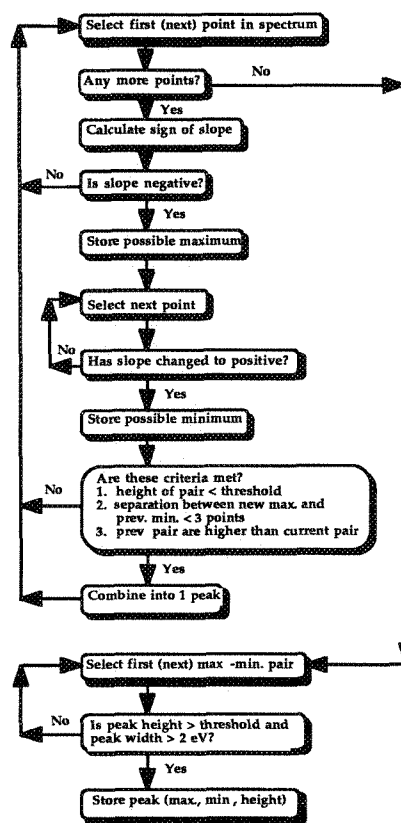


FIG. 1.--Flow diagram for peak selection.

peak. Figure 1 illustrates the logic flow used in peak selection.

There are two points where maximum-minimum pairs (peaks) may be rejected:

(1) During the initial peak detection, sequential maximum-minimum pairs are combined when the height of the second maximum-minimum pair is less than a noise threshold (see below); the two maximum-minimum pairs are separated by fewer than three data points; and the general trend is downward. In this case, the two peaks are treated as a single peak extending from the first maximum to the second minimum. This procedure avoids many instances where a single broad but noisy Auger peak is detected as two or more smaller peaks when noise fluctuations cause a brief reversal in the downward slope.

(2) The initial peak detection produces a list of maximum-minimum pairs including both actual Auger peaks and a large number of peaks due to shot noise. True Auger peaks are selected from this large list on the basis of height and width criteria. Peaks that do not meet minimum height and width criteria may be rejected. Minimum width was chosen as 2 eV. Since the natural linewidth of Auger peaks is of the order of a few electron volts,⁷ this choice helps to eliminate higher-frequency

noise components without eliminating peaks. Minimum height was set by measurement of a noise level during spectrum acquisition.

Since noise represents a statistical variation in an otherwise constant signal intensity, the noise level at a particular energy can be thought of as the average fluctuation in signal intensity at that energy. To acquire a noise level, the Auger signal intensity can be sampled multiple times at each of several energies. If the average signal intensity is calculated at each energy and assumed to represent the true signal intensity at that energy, the average variation from this intensity represents the noise level at that energy. The presence or absence of a peak at the selected energy has no effect on the noise level measured, since the concern is not with absolute signal but with signal fluctuation.

Based on this reasoning, a noise level is now acquired immediately prior to collection of each spectrum. After instrumental parameters for spectrum acquisition are set, the signal intensity is sampled 50 times at each of 10 energies spaced evenly between the initial and final energies selected for the spectrum. These data points are used to calculate a noise level at each energy and to generate a best-fit line representing the noise level vs energy as described above.

This procedure determines the noise level in the absence of signal averaging. Signal averaging can be accounted for if we recall that the signal increases with the number of scans N and the noise increases as the square root of N . Normalization yields

$$\text{Noise} \propto N^{1/2}/N = 1/N^{1/2}$$

To determine what constant value should be multiplied by the noise level to insure detection of Auger peaks and elimination of noise peaks, the following procedure was followed. Spectra were obtained from two samples (one of silicon dioxide, one of a palladium cobalt alloy), with signal averaging over 1 to 40 scans. We first identified the peaks visually, then identified the peaks using the algorithm described above, varying the constant times the noise level until a value K_{th} was found that eliminated all (or nearly all) noise peaks but detected all visible Auger peaks. Where more than one value produced the same results, the smallest value was selected. When K_{th} was plotted against $1/N^{1/2}$, a straight line with slope = 6.81 resulted (Fig. 2). The noise criterion for peak selection was therefore chosen as 6.8 times $1/N^{1/2}$ times the measured noise level. (This is an approximate number; values slightly larger and slightly smaller produce nearly the same results.)

Method for Identifying Peaks

In order to identify the peaks detected from a sample spectrum, a database was established consisting of the energies and intensities of the Auger peaks associated with each

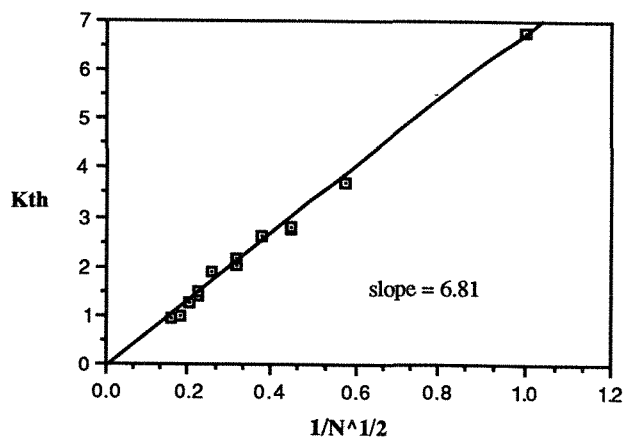


FIG. 2.--Plot used to determine value for noise threshold. K_{th} = empirically determined multiple of measured single-scan noise level that just eliminates noise peaks from signal averaged spectrum; N = number of scans signal averaged.

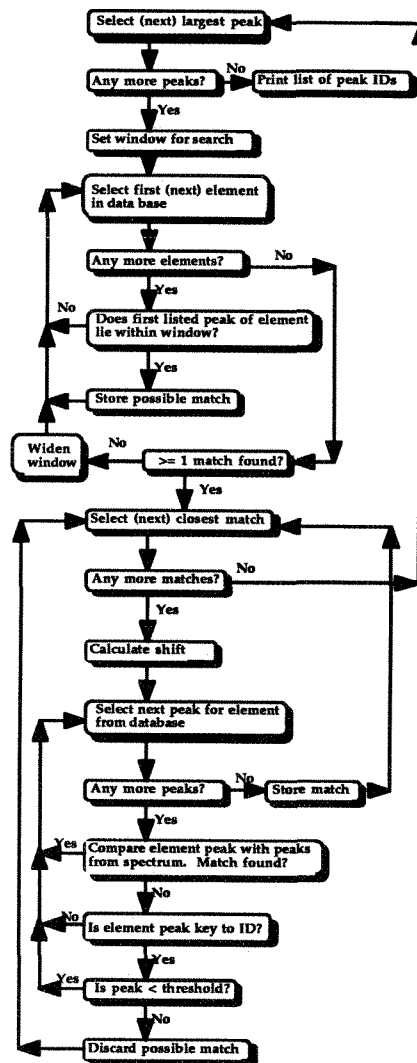


FIG. 3.--Flow diagram for peak identification.

element. Due to the large number of elements with peaks at 40-100 eV, peaks below 100 eV were excluded from this database, since their inclusion would do little to meet the goal of distinguishing between elements. However, that eliminates the possibility of identifying Li in a spectrum, since the only peak from Li falls below 100 eV. We compiled the initial data from the JEOL *Handbook of Auger Electron Spectroscopy*,¹ using the peak energies (at peak minimum) identified in each spectrum, and relative intensities given by the ratios of peak-to-peak heights measured from the spectra. Up to 15 peak energies and intensities were stored for each element, along with a third parameter, the peak "significance," as discussed below.

For each element, a predominant (usually the largest) peak was listed first, followed by all the other peaks in the same transition group (KLL, LMM) in order of decreasing intensity. A flag was inserted to separate the first series from peaks in the second series (if present), which were listed similarly. This is done since the chemical shifts of transitions involving valence levels may differ from the chemical shifts of core level transitions.⁹ The peak significance or key status is simply a flag inserted in the database to identify certain element peaks as key to the identification of that element. The key status of particular element peaks was based on the characteristic appearance of the several spectral series, e.g., the familiar LMM triplet of the transition metals. Although other peaks are present, the presence of only three peaks in this triplet is sufficient to identify the element.⁷ Therefore, only these three peaks are listed as key peaks.

Once a list of peaks from a sample spectrum is obtained, peaks below 100 eV are dropped, and the peaks are sorted by intensity (peak-to-peak height). Figure 3 illustrates the logic flow used for peak identification. The largest peak is examined first. An elemental identification is attempted by a comparison of this peak with the first peak listed for each element in the database. If the peak falls within a specified energy window of the element peak, the element is stored as a possible match.

The use of windows is necessary to allow for the possibility of peak shifts due to charging of the sample or changes in chemical environment. The initial window is set very wide to insure location of all possible matches. Subsequent windows within the same transition group are narrowed but shifted, based on the difference in energy between the originally matched peak and its potential element match (i.e., assuming approximately equal shift). The window is widened again when one is searching for the first element peak of a second transition group, then narrowed again for subsequent peaks. This procedure allows for the possible difference in energy shift due to chemical environment between the less affected inner-shell transitions and the outer or valence-level transitions.

The window size for this search was selected as ± 10 eV for low-energy peaks (< 1000 eV) and

± 15 eV for high-energy peaks (> 1000 eV). These values were chosen based on a review of compilations of Auger chemical shift data found in Refs. 7 and 9. If no possible matches are found, the window is incrementally widened to ± 20 eV.

For each potential match found, the spectral peaks are searched for additional matches with the peaks for that element. The window for comparison is reset to a new value based on the position of the matched spectral peak relative to the first element peak ± 6 eV. This value was empirically chosen to limit the window size and still to allow for variations in the detected peak position due to noise or poor resolution. When an element peak is *not* found, the key status is checked. If the peak is not listed as a key peak, the lack of a match is ignored and the search is continued. If the peak is listed as a key peak, the predicted height of the peak is calculated based on the stored relative intensity value. If the predicted height is less than the measured noise level, it is assumed that the peak would not normally be visible above the noise, and the search is continued. If the elemental peak is listed as a "key" peak *and* is predicted to have a height greater than the measured noise level, but is not found in the spectrum, that element is eliminated as a match. When all key element peaks predicted to have heights greater than the noise level are matched, the element is stored as a positive match.

This procedure is repeated for each peak originally detected in the sample spectrum. The end result is a set of labels attached to each peak representing all the elements "matched" to that peak. There are no restrictions on the number of possible elements matched to a particular peak. For multiple possibilities, the final definitive identification remains in the hands of an experienced operator.

An attempt to distinguish between "good" identifications and "possible" identifications was made, by use of the key status of element peaks described above. If all the key peaks associated with an element are located in the spectrum, the match is considered a good match. If a key peak is not present in the spectrum, and that peak is expected to be visible above the noise, then no match is made. A third possibility is that one or more of the key element peaks is not present in the spectrum, nor is expected to be visible above the noise level based on the stored intensity data. In this case, the match cannot be eliminated, but it is also clearly not as positive as a match for which all key peaks are located. This match is stored with a flag to identify it as less than positive. When element identifications are subsequently plotted with the spectrum, two colors are used to distinguish between these "good" and "possible" matches.

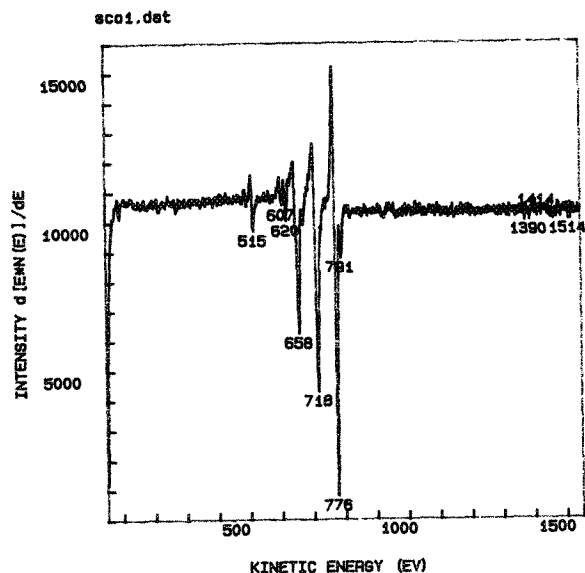


FIG. 4.--Peak selection applied to spectrum taken of cobalt standard.

Experimental Procedure

All spectra were collected with a JEOL JAMP-30 scanning Auger microscope. Programming was done in Microsoft QuickBasic from an IBM PC-AT. Interface hardware between the DEC PDP-11/73 normally used for computer control of the JAMP-30, and the IBM PC-AT, was supplied by JEOL, along with a set of QuickBasic callable routines that permit control from the PC of basic electron column, lock-in amplifier, and cylindrical mirror analyzer (CMA) functions. With them, a program was written to permit selection of instrument parameters and collection of survey spectra from the PC, with signal averaging over a variable number of scans.

Spectra were obtained from a set of 36 UHV standards in order to test the above algorithms. The standards were purchased from Geller Microanalytical Laboratory¹⁰ and consist of 34 different elements plus silicon oxide and silicon nitride. The standards are individually prepared from bulk material, and mounted on a single UHV compatible mount 1 in. in diameter.

Derivative spectra were acquired from each of these standards and used to test the peak detection and identification algorithms. Except where noted, all spectra were acquired with a 10kV electron beam at normal incidence, a beam current of 10^{-8} - 10^{-7} A, with a spot size on the order of 1 μ m, and a modulation voltage of 5 eV peak to peak. Resolution of the CMA was 0.6-0.8%. When cleaning was required, a 3kV argon beam was used for sputter cleaning. All spectra were signal-averaged over 5-15 scans. A noise level was acquired with each spectrum by sampling 50 times at each of ten energies evenly spaced over the energy range selected for acquisition immediately prior to spectrum collection.

Results

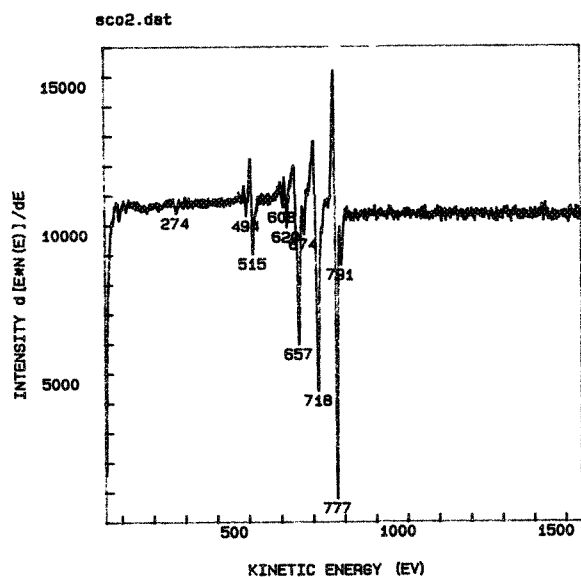
Figure 4 shows an example of peak selection applied to a sample spectrum. Large peaks were found to be consistently identified in every case. Selection of peaks at or near the noise level was only slightly less consistent. In some instances, noise peaks were selected in addition to Auger peaks. Note, for example, the "peaks" at 1390, 1414, and 1514 eV in Fig. 4. These peaks were not present in a second spectrum acquired in the same set, and are apparently due to noise only. Raising the threshold height for peak detection would eliminate these peaks from the list, but would also eliminate any Auger peaks of similar borderline height. In order to maximize sensitivity to Auger peaks, these noise peaks are tolerated. If necessary, any noise peaks detected can be positively identified as such by acquisition of a second spectrum. (Since the noise peaks are randomly located, it would be unlikely for one to appear twice in the same position.)

A second problem in peak identification is misidentification of the exact location of the peak minimum of a broad, noisy peak. This problem arose in only a few instances, but with serious consequences, since its occurrence almost invariably led to misidentification of the element producing the peak.

Figure 5 shows examples of the combined peak selection/peak identification applied to Auger spectra. The major element(s) in each of the 34 standards were consistently identified correctly under resolution and signal-to-noise conditions similar to those shown, except in cases where the shift in peak energies due to sample charging exceeded the width of the search window. Figure 5 shows that multiple identifications of a single peak are common, especially for the smaller peaks of major elements and for minor components/contaminants. The color coding of identifications as "good" or "possible" (shown in the figure as a "?" after possible matches) simplifies decision making somewhat in cases of multiple identification. In most cases, (one of) the "good" id(s) (if any were listed as "good") was consistent with the correct identification based on the known composition of the sample.

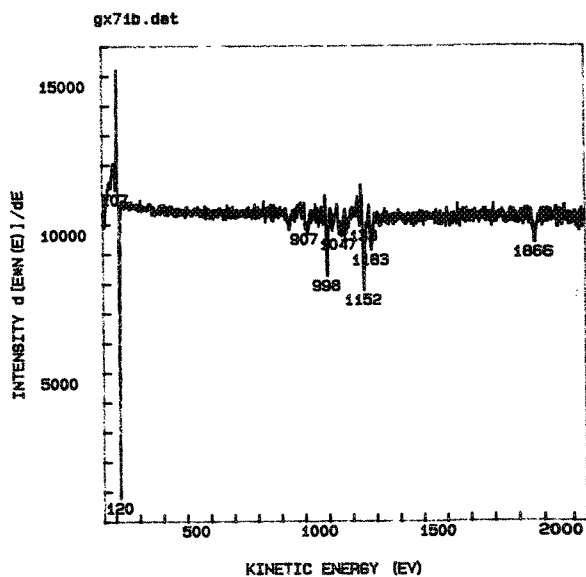
Results for the multi-element samples tested were similar in cases where there was little overlap of peaks. Figure 5(b) is an example. Zinc, germanium, and phosphorus are correctly identified in this spectrum taken from an epitaxial zinc germanium phosphide semiconductor film. Note that several other possibilities are listed, notably magnesium.

Where peak overlaps occurred, identification was found to be less consistent. Figure 5(c) shows a spectrum taken from a silver copper palladium alloy. Silver and copper were identified correctly. Scandium, although not present, is identified since key scandium peaks at 336 and 368 eV match within the window used the observed peaks at 330 and 357 eV. Palladium is identified only as possible by



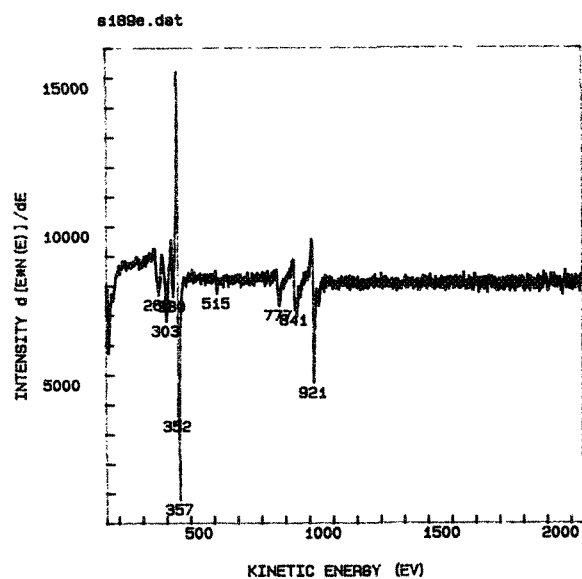
PEAKLIST

1	777	Co	
2	718	Co	La?
3	657	Co	
4	515	O	
5	620	Co	La?
6	791	Co	
7	494	O	
8	674	Co	
9	608	Co	
10	274	C	Ru?



PEAKLIST

1	120	P	Ge	Zn	Rb?	Sr?	Ge?
2	1152	Ge	Mg				
3	998	Zn	Na?				
4	1183	Ge	Mg				
5	1866	P					
6	1047	Ge					
7	1133	Ge	Mg				
8	107	P	Rb?	Se	Sr?		
9	907	Zn					
10	1079	Ge	Ge?				
11	1018	Zn					
12	835	Zn					
13	736	Zn					
14	962	Ge	Na?				
15	951						
16	892						



PEAKLIST

1	352	Ag	
2	921	Cu	
3	357	Ag	Sc
4	303	Ag	Sc
5	330	Pd?	Sc
6	841	Cu	Ni?
7	269	Ag	C
8	777	Cu	Ni?
9	515	I?	O

FIG. 5.--Combined peak selection/peak identification applied to spectra taken of (a) cobalt standard; (b) epitaxial film of zinc germanium phosphide; (c) alloy of silver, copper, and palladium.

the peak at 330 eV. The key palladium peak at 277 eV is obscured by the broad peak at 269 eV. Identification of palladium is uncertain in this case. In the worst case, palladium might not be identified at all.

Conclusions

Rapid automated peak selection from derivative Auger spectra can be successfully achieved. Automated peak identification of nonoverlapped elements present on a sample surface can be achieved with reasonable consistency. Combined peak selection and identification require only seconds to complete. Where peaks overlap, automated peak identification will have to deal with the problem of peak overlaps to produce consistent results.

References

1. T. Sekine, Y. Nagasawa, M. Kudoh, Y. Sakai, A. S. Parkes, J. D. Geller, A. Mogami, and K. Hirata, *Handbook of Auger Electron Spectroscopy*, JEOL, Ltd, 1982.
2. L. E. Davis, N. C. MacDonald, P. W. Palmberg, G. E. Riach, and R. E. Weber, *Handbook of Auger Electron Spectroscopy*, Edina, Minn.: Physical Electronics, 1972.
3. G. E. McGuire, *Auger Electron Spectroscopy Reference Manual*, New York: Plenum Press, 1979.
4. See, for example, Ron Jenkins, R. W. Gould, and Dale Gedcke, *Quantitative X-ray Spectrometry*, New York: Marcel Dekker, 1981.
5. T. J. Shaffner, *SEM/1980* I, 479.
6. Ludek Frank, *Vacuum* 36: 437, 1986.
7. D. Briggs and M. P. Seah, *Practical Surface Analysis by Auger and X-ray Photoelectron Spectroscopy*, New York: Wiley, 1983.
8. M. Thompson, M. D. Baker, A. Christie, and J. F. Tyson, *Auger Electron Spectroscopy*, New York: Wiley, 1985.
9. H. H. Madden, *J. Vac. Sci. Tech.* 18: 677, 1981.
10. Geller Microanalytical Laboratory, 1 Intercontinental Way, Peabody, MA 01960.

COMPUTER SIMULATION OF INITIAL STAGE SINTERING IN TWO-DIMENSIONAL PARTICULATE SYSTEMS

J. H. Chen and P. F. Johnson

Initial-stage sintering and the starting packing geometry prior to the sintering process have been modeled by several authors.¹⁻⁷ Many of the sintering models are based on a simplified packing of monosized spheres. In this paper, computer simulations of random packing and initial-stage sintering based on more realistic packing mechanisms, followed by diffusion-controlled sintering mechanisms, are developed for particles in two dimensions. Particles in the models presented here can have any specified size distribution to approximate the simulated microstructure resulting from "real" sintering conditions. Quantitative properties of the modeled structures are calculated and compared with the values predicted by the theory.

Computer Simulation Procedure

A computer model has been developed to simulate the settling in gravity of particle systems in two dimensions. The resulting compact is used for the later sintering simulation. The basic scheme of the settling procedure is shown in Fig. 1. The motion of a specific particle stops when it reaches a position of local equilibrium—either the system border or the lowest position along the sliding surface of particles. Particles at the bottom of the system hit by an incoming particle can also move horizontally to accommodate the newly arrived particle.

The model incorporates two methods of obtaining green stacks. Particles from a desired size distribution can be first randomly prepacked into the box, with the center positions randomly chosen without intersection with other particles; then the settling model is applied to the prepacked system to simulate a "sedimentation" procedure. Settling starts with the particle that has the lowest central location, then the second lowest particle, and so until all particles are settled. In the second method, particles can fall from the top of the system, with initial positions in the horizontal direction randomly located, which then simulates "filling" the box in a gravity field. The particles in the model can be monosized or randomly chosen from a simulated size distribution, e.g., a log-normal size distribution, or from any specific size distribution. To minimize the effects of the container walls, the system box was chosen with its size at least ten times the size of the largest particle to

The authors are at New York State College of Ceramics at Alfred University, Alfred, NY 14802. This work is currently supported by the Center for Advanced Ceramic Technology at Alfred University.

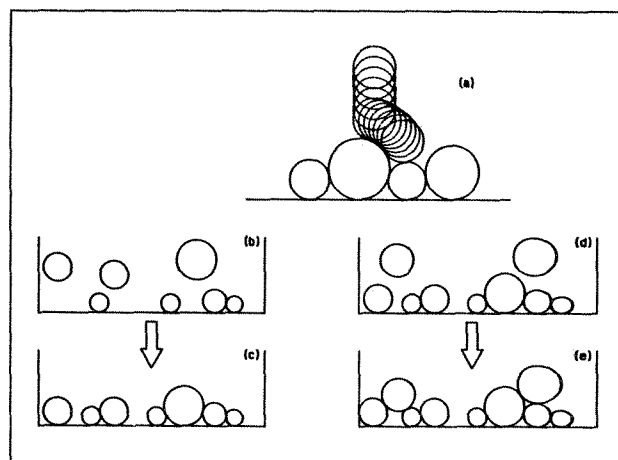


FIG. 1.--Scheme of settling procedure: (a) particles fall in gravity and slide down over surface of particles that have settled; (c), (e) are settled structure resulting from parts (b) and (d), respectively and show adjustment of bottom particles to new incoming particles. to be packed.⁸

The settled structures are characterized by the packing geometry (the sizes and center coordinates of all particles) and the geometry of the pore constructions (the number and identifications of circles forming a closed pore, i.e., excluding all open pores sited around the sides of the box). Quantitative properties of the settled structure, such as porosity, pore-size distribution, randomness of the particle packing, and frequency distribution of the coordination number, are calculated from the geometrical information. To obtain statistical data, each size distribution resource data are run at least ten times, with a different starting random-number generator seed.

To simulate the densification process during initial stage sintering for particle compacts with a size distribution, an extended model based on Coble's two-sphere model⁷ has been developed. Assumptions made are:

- $X/R \ll 1$ (initial stage)
- Volume conservation
- Central-central approach
- Simplified neck-geometry: a straight line
- Mechanism of material transportation: lattice diffusion and/or boundary diffusion (solid-state sintering; densification without rearrangement)

Geometrical notations and the representations of shrinkage due to both diffusion mechanisms are shown in Fig. 2. In a multiparticle system, a further assumption is made that all

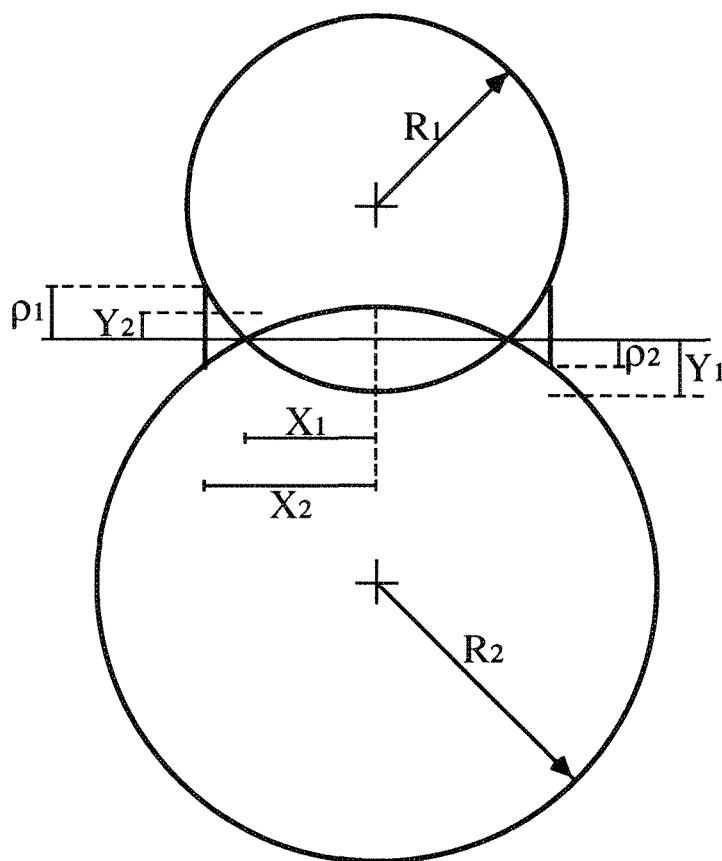


FIG. 2.--Geometrical and diffusion mechanism notations for two-sphere model of initial-stage sintering.

particle centers move together according to the two-sphere model. For simulation purposes, one can accomplish that by increasing the radius of the particles, which produces the same overlap as in the two-sphere model, and a reducing in the size of the "box" by an overall factor to maintain the volume conservation of the particles, after all pairs of particle contacts have been processed.

The sintering simulator can process both diffusion mechanisms individually or together; i.e., either mechanism can contribute to densification alone or both of them contribute to the process alternatively. The nongeometrical constants B and B_b in Fig. 2, which contain material and environment parameters, are hold constant throughout a sintering simulation. The sintering simulator was applied to the structures resulting from the packing simulation with the same densification mechanism and for the same total processing time. During the process, the simulator continuously checks for possible newly formed contacts between particles and initiates shrinkage and neck growth from that point. Time periods between each calculation loop were kept short (a) to minimize the formation of new contacts and (b) so that the evolving microstructure could be evaluated by use of fine time scale (nearly continuously). Geometrical information was recorded and saved after each time step for further analysis.

Volume Conservation :

$$\rho_1 = Y_1 = \frac{X_2^2}{4R_1}$$

$$\rho_2 = Y_2 = \frac{X_1^2}{4R_2}$$

$$X_2 = \sqrt{2} X_1$$

Lattice Diffusion :

$$Y_1 + Y_2 = [Bt(\frac{1}{R_1} + \frac{1}{R_2})]^{1/2} \quad (\text{Eq. 1})$$

$$(B = 8D_L\gamma\Omega/kT)$$

Boundary Diffusion :

$$Y_1 + Y_2 = [B_b t(\frac{1}{R_1} + \frac{1}{R_2})]^{1/2} \quad (\text{Eq. 2})$$

$$(B_b = 12D_b W\gamma\Omega/kT)$$

Where :

D_L : Lattice diffusion coeff.

D_b : Grain-boundary diffusion coeff.

γ : Grain-boundary free energy

Ω : Atomic volume

W : Grain-boundary width

k : Boltzmann's constant

T : Temperature

t : Time

Results

A system with 1181 particles following a simulated log-normal size distribution and another system with 1000 monosized particles were subjected to the "filling box" simulator (particles loaded from the top of the box). The particle size in the monosized system is the same as the geometrical mean size D_g used in the log-normal system (3.0 in units of 0.01 box width). Two resulting compact structures after settling are shown in Figs. 3 and 4. Analysis of the frequency distribution of particle center locations in both X and Y directions shows that the modeled compacts are random packed structures. The pore size distributions of the two structures are shown in Figs. 5 and 6. Mean values and standard deviations of the porosity calculated from ten runs for each size distribution are $(17.6 \pm 1.56)\%$ for log-normal systems and $(16.75 \pm 0.79)\%$ for monosized systems. For two-dimensional monosized random packing, the packing density obtained from the settling model (0.8325) is comparable with the model of relaxation from a defect planar array⁹ (0.824) and from a theoretical calculation¹⁰ (0.82396). Frequency distributions of both the pore and particle

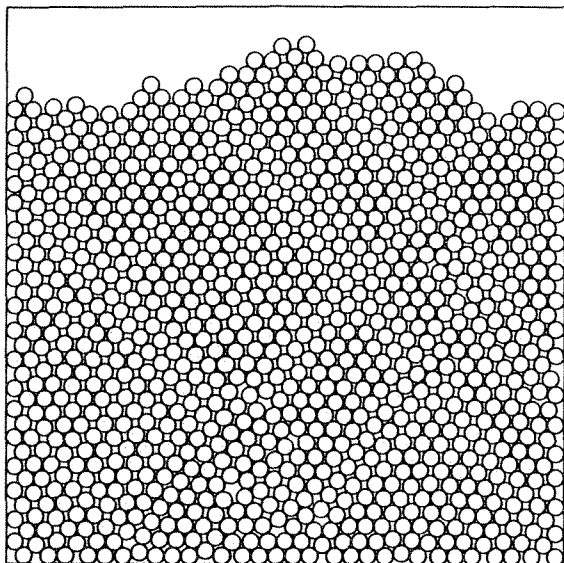


FIG. 3.--Compact structure for monosized particles settled from top of system.

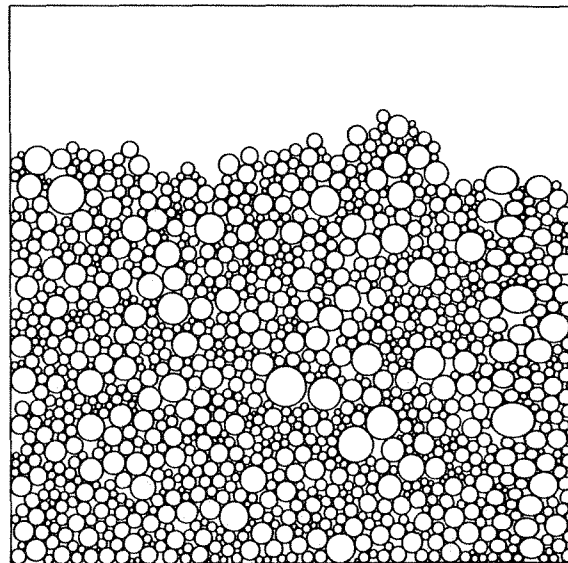


FIG. 4.--Compact structure for particles with log-normal size distribution settled from top of system.

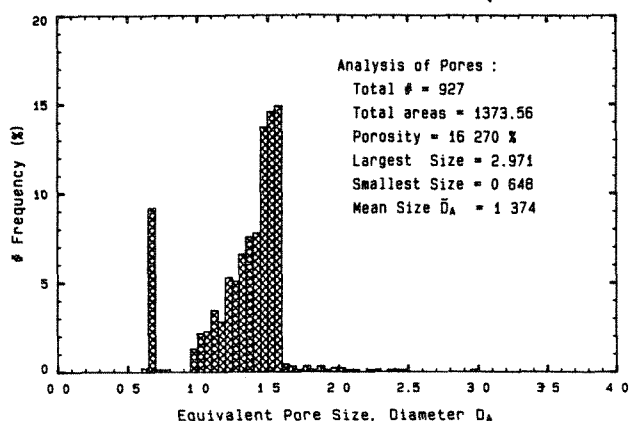


FIG. 5.--Pore-size distribution of monosized structure shown in Fig. 3.

coordination numbers for both settled structures are also reported by the settling simulator.

For the initial-stage sintering simulation, Fig. 7 demonstrates the evolution of the microstructure for a simplified system packed with seven particles. An enlargement of the microstructure near the center of a sintered compact is shown in Fig. 8.

Both systems shown in Figs. 3 and 4 were subjected to the sintering simulator; the rate-controlling mechanism was grain-boundary diffusion ($B_b = \text{constant} \neq 0$, $B = 0$). The structure configurations were recorded at 40 time intervals. The resulting decrease of the porosity during the process for both systems is shown in Fig. 9, which shows that the decrease of the porosity is faster in the log-normal system than in the monosized system. Figure 10 shows a log-log plot of the percent shrinkage with time for both systems. Linear least-square regressions were performed for each data set, with the results also shown in Fig. 10. A straight-line behavior with slope 0.3355

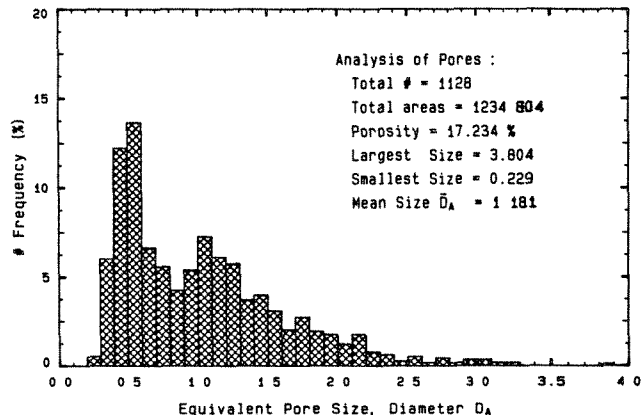


FIG. 6.--Pore-size distribution of structure of log-normal size distribution shown in Fig. 4.

and 0.3336 is found, close to the ideal slope 0.3333 predicted by the two-sphere grain boundary diffusion model (Eq. 2 in Fig. 2). Shrinkage of the log-normal system compacts was found to be larger than the monosized system.

Discussion

Analysis of the distribution of the center locations and comparison of the calculated porosity with values estimated by other two-dimensional monosized models proves that our settling models produce a random packing scheme. The slight lower value of the porosity (16.75% calculated for our compacts, 17.60% from theoretical calculation) may arise from neglecting the open pores around the system box. (A periodic boundary condition would address this discrepancy.) The settling model can also be applied to compacts with a particle-size distribution that better approaches "real" conditions. The higher porosity in the log-normal system results from the open pores

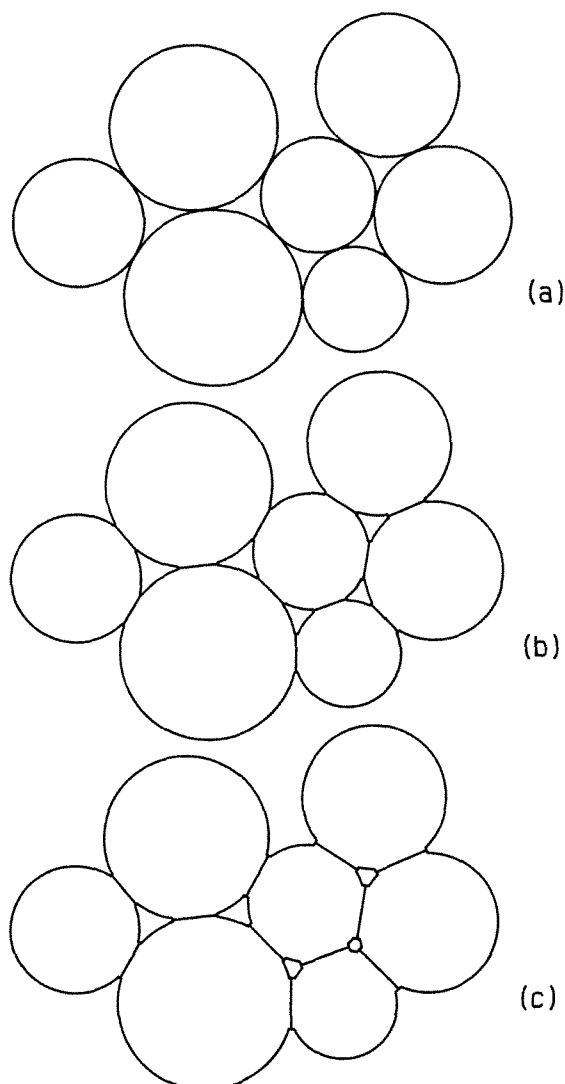


FIG. 7.--Simplified system with seven particles undergoes initial-stage sintering: (a) before sintering; (b),(c) evolving microstructure during initial-stage sintering.

and some large pores formed partly by particles with a coordination number < 3 , which is required for 2-D stability. Neither elastic nor modified elastic recoil has been included in our settling model, which leads to particles in the compact in a very shallow local energy minimum.

The shrinkage of the compacts during simulated initial-stage sintering comes from neck growth with a resulting decrease of pore sizes. The higher shrinkage values and the decrease in porosity in the log-normal system (with a geometrical mean size equal to the particle size in the monosized system) imply that sintering between large and small particles occurs more rapidly than between particles with the mean sizes. This phenomenon can also be predicted from the two-sphere model equations. The fact that the computer-calculated data fall on a straight line in Fig. 10 with a slope that is almost identical with that from the ideal two-sphere model, implies that the algorithm of "increase particle size and reduce box size" is an effective approximation in the simulation work.

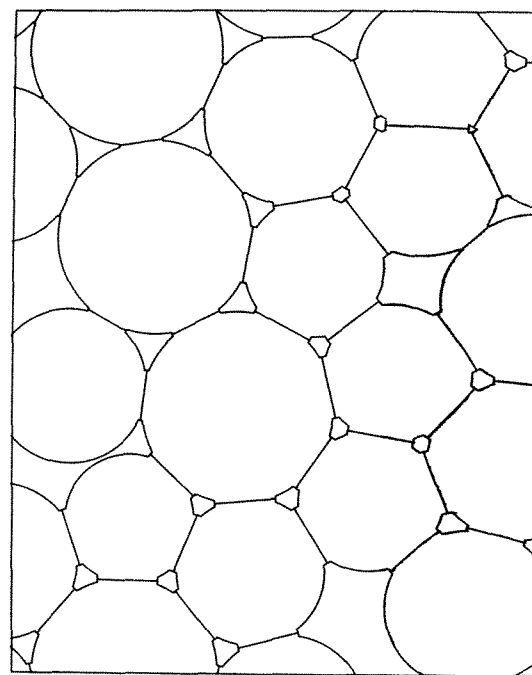


FIG. 8.--Enlarged structure near center of compact showing geometry after sintering.

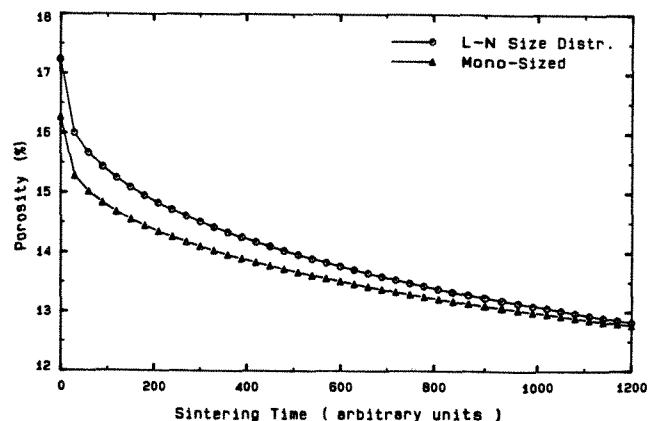


FIG. 9.--Variation of porosity with sintering time for 2-D monosized and log-normal size distribution systems.

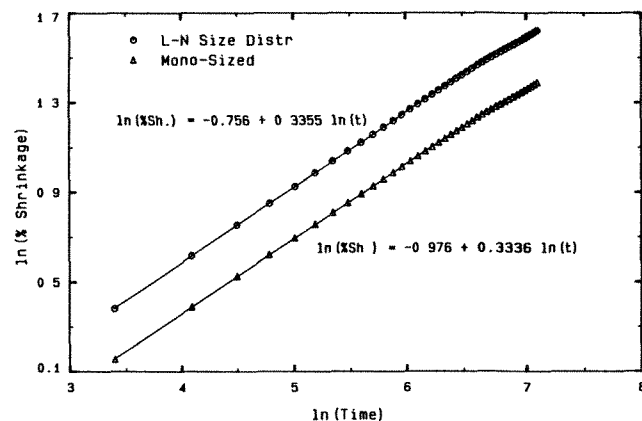


FIG. 10.--Log-log plot of compact shrinkage v. sintering time for 2-D systems with monosized and log-normal particle-size distribution.

Conclusions

Random particle packing and initial-stage sintering models for particle compacts with a size distribution have been developed. The geometric properties and evolution of the microstructure during the processes have been calculated and compared well with those predicted by theory. These models, though limited to two dimensions, can serve as a good tool for the further study on the topological properties, microstructure-properties relationship,¹¹ and simulation of the microstructure evolution during intermediate- and final-stage sintering.

References

1. L. D. Norman et al., *Computer Simulation of Particulate Systems*, U.S. Bureau of Mines, Bull. 658, 1971.
2. R. C. Burk and P. S. Apte, "A packing scheme for real size distribution," *Am. Ceram. Soc. Bull.* 66: 1389-1392, 1985.
3. J. H. Chen and D. R. Dinger, "Computer simulation of random particle packing in a central field," (in preparation).
4. P. Bross and H. E. Exner, "Computer simulation of sintering processes," *Acta Metallurgica* 27: 1013-1020, 1979.
5. T. M. Hare, "Statistics of early sintering and rearrangement by computer simulation," in G. C. Kuczynski, Ed., *Sintering Process*, New York: Plenum Press, 1979.
6. J. W. Ross, W. A. Miller, and G. C. Weathery, "Computer simulation of sintering in powder compacts," *Acta Metallurgica* 30: 203-212, 1982.
7. R. L. Coble, "Effect of particle-size distribution in initial-stage sintering," *J. Am. Ceram. Soc.* 56: 461-466, 1973.
8. R. K. McGeary, "Mechanical packing of spherical particles," *J. Am. Ceram. Soc.* 44: 513-522, 1961.
9. J. W. Ross, M.A.Sc. Thesis, University of Toronto, 1974.
10. R. K. Bordia, "A theoretical analysis of random packing density of mono-sized spheres in two and three dimensions," *Scripta Metall.* 18: 725-730, 1984.
11. M. Lakshminarasimha and P. F. Johnson, "Computer-generated three-dimensional microstructure," *Microbeam Analysis--1987*, 307.

BACKSCATTERED ELECTRON IMAGING OF SUBSURFACE STRUCTURES

Z. J. Radzimski and J. C. Russ

Utilizing the fact that the escape depth of backscattered electrons is related to their energy, one can look inside the material by selecting only those electrons of a certain energy range. We studied this problem both theoretically and experimentally. Monte-Carlo procedures were used to calculate the backscattering fraction from a sample with a buried region of different atomic number. The results were compared with experimental data obtained by use of an energy filter with retarding grid analyzer. Images of subsurface regions were obtained digitally as the difference between two images taken at different suppression voltages.

The backscattered electrons (BSE) in scanning electron microscopy provide complex information about the specimen.¹ They escape from relatively deep volume of the specimen² and consequently carry information about this volume. Since energy loss is continuous along the electron path, the backscattered electrons that penetrate more deeply travel a greater average distance and re-emerge with lower energies. Consequently, the lower-energy BSE carry with them information about deeper subsurface regions in the sample, on the average. In fact, the other side of this phenomenon has been employed by Wells³ in using highly tilted specimen surfaces and imaging of the low-loss BSE to obtain high-resolution images of shallow surface structures.

Since electron scattering is a strong function of atomic number, it would be expected that the total backscattered electron fraction as well as the energy distribution of the BSE would vary with the composition and depth of the region, and that this variation might be used either to measure or to image the structure in depth. The principal uncertainties in this scenario are: (1) the quantitative relationship between the depth in the sample and the contribution to various portions of the BSE energy distribution, (2) the practical problems of measuring the energy distribution and selecting a portion of the energy band for measurement or imaging, and (3) the loss of image resolutions as a function of depth, due to lateral scattering of the electrons. We addressed these problems both theoretically, using Monte-Carlo simulation, and experimentally.

The authors are at the Materials Science and Engineering Department, North Carolina State University, Box 7907, Raleigh, NC 27695. This work was funded by a grant from Amray Corp., Bedford, Mass.

Monte Carlo Simulation

The Monte Carlo program was based on a multiple-scattering model. It allows the user to specify the size and location of a subsurface rectangular prism, and the mean atomic number of that region and of the surrounding sample. The program keeps track of the energy and direction of backscattered electrons. Those that are intercepted by detector(s) positioned by the operator in terms of their size (solid angle) and elevation angle above the specimen are summed to produce an energy spectrum. After verifying that the program produced results in agreement with various published data for electron backscattering from homogeneous specimens, we conducted a series of simulations for the case of a buried prism of gold in a matrix of aluminum, using 20keV electrons. The depth of the top of the gold was varied from 0 to 1 μm and the beam position was moved in steps across the edge of the gold region. As expected, the Monte Carlo results show that the buried gold can be detected in the BSE signal, but that as the depth is increased, the total change in backscattered fraction of electrons decreases. However, when curves for the number of BSE in particular energy bands are plotted, it is evident that the situation is more complex. The contrast (change in intensity across the interface) is maximum for the highest-energy BSE when the junction is at the surface, but as the depth increases, the maximum contrast is found for electrons of progressively lower energy (Fig. 1). A contrast of 50% remains at a depth of 1 μm for electrons in the 5-10keV energy band. Further, there is very little indication of a loss in sharpness of the transition, which corresponds to the resolution of the SEM image.

The test specimen consisted of two pieces of aluminum used to clamp wires of gold and molybdenum (1.2 mm in diameter). The assembly was polished so that the cross sections of the wires were viewed on the exposed surface. This method provided reasonably sharp boundaries between regions of different atomic numbers. In order to correlate the Monte Carlo escape depth of BSE, layers of aluminum were applied to the entire assemblage by evaporation. Total thickness varied up to 1.2 μm . The backscattered electron detector output signal was recorded with the beam positioned over each material, with varying voltage on the suppression grid.

The depth-dependent images were taken with the same test sample coated with an 0.7 μm layer of aluminum. The surface was lightly abraded to produce surface markings, which in the images can be distinguished from the

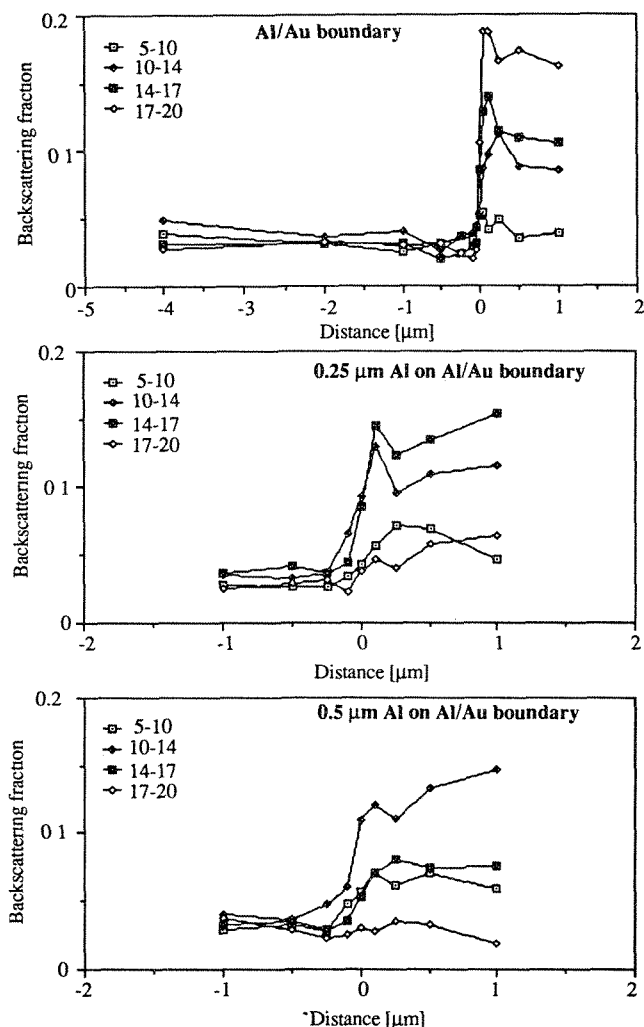


FIG. 1.--Variation of backscattering signal with beam position with respect to edge of Au prism buried in Al matrix, as function of energy band of backscattered electrons (20keV primary beam energy, 0° incident angle); (a) at surface of Al matrix, (b) at $0.25\mu\text{m}$ depth in Al matrix, (c) at $0.5\mu\text{m}$ depth in Al matrix.

subsurface information. A series of images were photographed on regions covering the boundary between the wires and the aluminum block with varying suppression voltages on the grid. In all cases, the beam voltage was 22 keV. The images showing the same Al/Mo boundary with two different suppression voltages are presented in Fig. 2(a) and (b). It is quite clear that in all cases the junction of the aluminum with a heavier metal can be quite sharply imaged under 7000 \AA of aluminum at this accelerating voltage, and that variation of the suppression voltage allows this information to be suppressed so that only the surface markings are seen. A slight increase in image noise was observed at the higher suppression voltages, because fewer electrons reached the detector and the output voltage was lower, requiring

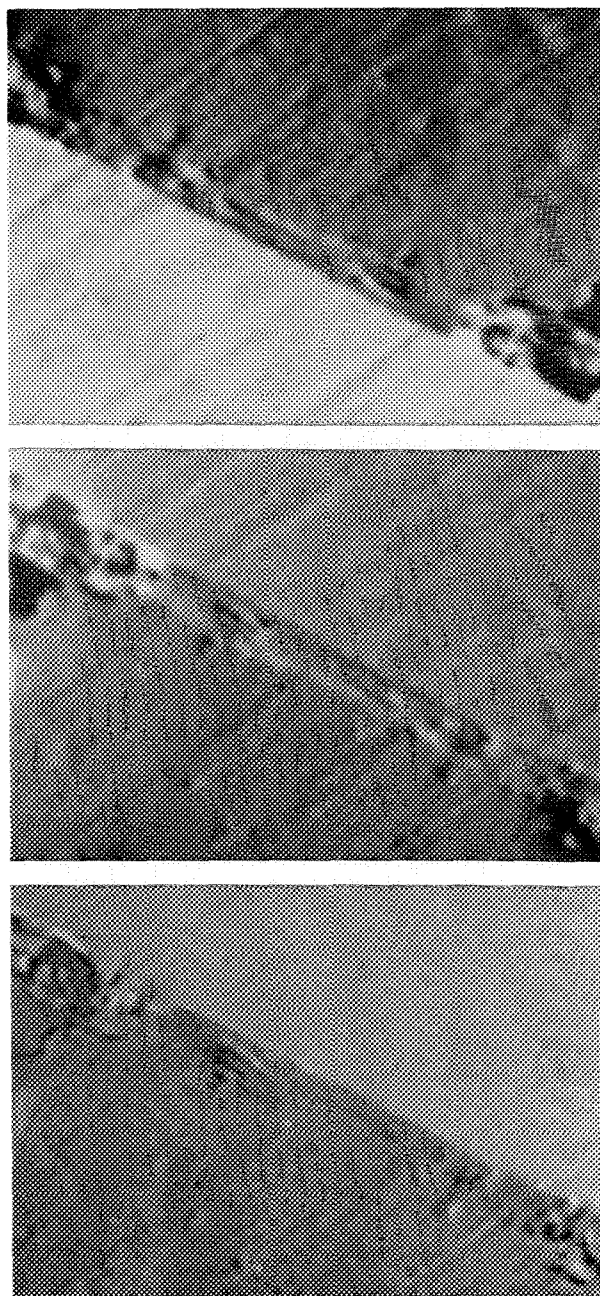


FIG. 2.--BSE images of Al/Au boundary covered with $0.7\mu\text{m}$ -thick Al layer. (a) BSE image without suppression voltage, (b) BSE image with 15 kV suppression voltage, (c) difference of images (a) and (b). (22keV primary beam energy, magnification = 2000.)

more amplification. However, this noise increase had only a small effect on the overall image quality.

In order to see only the subsurface information, it is necessary to image only the electrons with energy corresponding to the region of interest. With the detector in the "integral mode" and responding to all electrons above the threshold energy, this correlation can be accomplished by the difference between two images taken at different threshold energies, as was done (Fig. 2c), by use of

digital image storage, for the pair of images shown in Fig. 2(a) and (b). The images show very clearly that differencing reveals the subsurface contrast and completely or largely eliminates the surface detail (the fine scratches applied to the top of the aluminum coating). This result shows that quite useful resolution of structures rather deep below the surface can be expected.

Conclusions

The use of a suppression grid on the BSE detector in an SEM offers considerable flexibility for imaging of both surface and subsurface structures. Use of a high suppression voltage produces surface image with good resolution (somewhat akin to the Wells low-loss technique, even if the surface is not inclined). Difference images are routinely possible with modern stored-image digital SEMs, and permit imaging of subsurface structures. The ability to sweep the suppression voltage to obtain a BSE energy spectrum may moreover broaden analytical capability in some instances.

References

1. V. N. E. Robinson, *Scanning Microscopy* 1: 107, 1987.
2. H. Niedrig, *J. Appl. Phys.* 53: R15, 1982.
3. O. C. Wells, *Appl. Phys. Lett.* 16: 151, 1970.

AN IN-HOUSE TRAINING PROGRAM FOR THE TEM LABORATORY

J. R. Millette, S. B. Burris, and J. A. Krewer

Staff training is one of the most important aspects of a good quality assurance program. Accreditation programs, such as AIHA and NVLAP, require that laboratory staff meet certain qualifications and that in-house training programs be in place and well documented; however, they offer no guidance on the details of training plans for laboratory or field staff.

A model in-house training program for TEM analysis is presented, along with step-by-step training guidelines. Emphasis is on areas where improperly trained analysts commonly make mistakes, including misidentification or difficult materials and calculation errors. A slide show demonstrating TEM analytical problems is being developed for the presentation.

ASBESTOS ANALYSIS: AN OVERVIEW

E. B. Steel

The accurate analysis of asbestos has become a necessity in a number of health, environmental, regulatory, and research fields. Asbestos is known to cause life-threatening illnesses such as pneumoconiosis and cancer. To protect the health of and determine the risk to employees and the general public, the amount of asbestos in the air and water from industrial and ambient environments has been analyzed for several decades. The advent of the asbestos-abatement industry in the last ten years has placed particular stress on the analysis of asbestos in the materials used in buildings and found in indoor air. The recent characterization of hazardous waste sites, such as some asbestos mines and abandoned manufacturing facilities, has meant that rock, soil, water, and outdoor air samples have to be analyzed. The broad analytical demands over various types of samples that may contain major to trace concentrations and nanograms to grams of asbestos in simple to complex matrices require that the techniques that are used to analyze any given sample be well considered. It is a common problem in asbestos analysis to find that a technique well designed for one purpose is applied inappropriately for another purpose.

Asbestos Analysis

Asbestos analysis may be broken into two basic categories: bulk and filter analysis. Bulk-analysis techniques are applied to materials that are available in approximately gram quantities or larger, such as building materials, soil, and rock samples. Filter analyses are generally for the analysis of minor to trace asbestos components in gases and liquids, such as occupational air samples, abatement clearance air samples, and asbestos contaminants in water and drugs. In any of these analyses, both a qualitative and quantitative analysis must be performed, and the analysis must be specifically tailored to the sample and the reason for the analysis. The different techniques often have quite different qualitative and quantitative capabilities.

Table 1 summarizes the major techniques used for the analysis of asbestos. They include macroscopic analysis that is often performed with the human eye and aided with a low-power or stereo microscope,¹ the polarized light microscope (PLM) method,² the x-ray powder diffraction (XRD) method,² the phase contrast light microscope (PCM) method,³ the scanning electron microscope (SEM) method, and analytical

transmission electron microscope (AEM) methods.⁴⁻⁶ Other less commonly used methods include infrared⁷ and Raman spectrometry,⁸ differential thermal analysis, laser ablation spectrometry,^{9,10} x-ray fluorescence spectrometry, and a variety of physical means such as ashing and chemical dissolution. These less common techniques are useful in samples that have special analytical problems.

Each of these techniques can be useful but each has its limitations. To determine whether a technique is properly applied, we must first consider the general requirements for asbestos analysis.

Qualitative Analysis

A qualitative analysis for asbestos is more difficult than in many other analytical techniques because the definition of asbestos includes both a specific set of minerals *and* a specific morphology or crystal habit.¹¹⁻¹⁴ Simply analyzing for a mineral species *or* a morphology is insufficient for an accurate asbestos analysis. In the general asbestos analysis case, either multiple techniques *or* a single technique that can both identify the mineral species and classify the morphology of materials in a specimen are necessary. Alternately, if one can *assume* an asbestos mineral species *or* an asbestiform morphology from previous knowledge of the specific analyte, it may be possible to use a technique that analyzes only one of the two defining traits (mineral type and morphology) for asbestos.

Asbestos Definitions for Analysis

As noted, the methods that are used to identify asbestos usually have separate morphological and mineralogical definitions. The morphology definitions vary and may make the resulting analyses difficult or impossible to compare. The morphological definitions are not identical in all cases because of analytical limitations and differences in the purpose for which a method is applied. The macroscopic definitions of the extremely fibrous, flexible, weavable bundles or mats that are observed and felt in a hand-size specimens are often lost in the well-dispersed particles observed on the microscope. Each microscopic technique is also limited by image resolution, contrast, magnification, and analytical capability.

Morphology Definitions

Bulk samples have an analytical advantage because they have not been greatly dispersed,

The author is with the National Institute of Standards and Technology, Center for Analytical Chemistry, Gaithersburg, MD 20899.

TABLE 1.--Summary of major analytical methods applied to asbestos.

<u>Method</u>	<u>Sample type</u>	<u>Data</u>	<u>Qualitative information</u>	<u>Units</u>	<u>Limitations</u>	<u>Advantages</u>
Macroscopic	bulk	morphology texture, color	asbestiform morphology ^a	% volume	no mineral-identification	large sample
PLM	bulk	Ref. Index, optical-crystallography morphology	mineral identification ^b asbestiform morphology	% area	fiber size	positive identification
XRD	bulk	d-values/intensities	mineral identification	% weight	no morphology	large sample quantitative
PCM	occupational air filters	morphology	morphology ^c	fibers per unit area	no mineral ident. fiber size	large filter-area cost
SEM	bulk/filters	X-ray spectrometry morphology	partial mineral ident. ^d morphology	fibers per unit area	fiber size no standard sample size variable performance cost	availability
TEM	filters/bulk	X-ray spectrometry electron diffraction morphology	mineral identification morphology	fibers per unit area	sample size cost	positive-identification no fiber size limitation

^a asbestiform morphology means that the full morphology of asbestos can be determined.

^b mineral identification means that sufficient data may be collected to uniquely identify the mineral.

^c morphology means that the morphology is controlled by the method's counting rules and is less specific than asbestiform morphology

^d partial mineral identification means that chemical composition is determined but that this is sometimes insufficient to uniquely identify the mineral.

TABLE 2.--Typical microscope conditions for asbestos analysis of filters.

	TEM	SEM	PCM
Resolution	<1 nm	<10 nm	<.5 μm
Fiber Definition	3:1 aspect ^a 5:1 aspect/>0.5 μm^b	None	3:1 aspect/>5 μm
Illumination	microscope	microprobe	microscope
Image type	true optical	rastered	true optical
Field of View ^c	>5 μm	>5 μm	>200 μm
Contrast ^d Control	diffraction replica thickness	topography atomic number substrate	refractive index
Limited by	analyst	fiber width signal/noise contrast analyst	fiber width resolution analyst
Identification Significance	asbestos	possible asbestos	fiber
Analytical Applications	general filters, trace, Q.C. ^e	Bulk Q.C. PCM Q.C.	known asbestos occupational air- filters

^a EPA TEM provisional methodology

^b EPA asbestos abatement clearance TEM method

^c Approximate diameter of measurement area

^d Fiber width or thickness is a controlling factor in the contrast of all the techniques

^e Q.C. stands for quality control, this is used for verifying the analysis by another technique.

so that many of the properties that are observed macroscopically can be at least in part still observed in a polarized light microscope on friable bulk samples. A morphology definition for asbestos observed by the light microscope in bulk samples has been proposed.^{15,16} This definition states that under the light microscope, the asbestiform habit is generally recognized by the following characteristics:

- (1) mean aspect ratios ranging from 20:1 to 100:1 or higher for fibers longer than 5 μm ;
- (2) very thin fibrils, usually less than 0.5 μm in width;
- (3) two or more of the following: (a) parallel fibers occurring in bundles, (b) fiber bundles displaying splayed ends, (c) fibers in the form of thin needles, (d) matted masses of individual fibers, (e) fibers showing curvature.

This definition is robust, covers the materials sold commercially as asbestos, and eliminates the analytical confusion with samples that contain only nonasbestiform cleavage

fragments, regardless of their mineralogy.

Fiber-on-filter samples are a much more difficult problem because they are generally well dispersed by the gas or liquid medium from which they were taken. The dispersion yields many small thin fibers that do not typically contain the bulk asbestos attributes of curvature, splaying ends, mats, bundles, etc. A simpler morphology definition based on aspect (length-to-width) ratio must thus be used in the filter methods of Table 2, which creates problems in environments where asbestos is a trace component. Since many particles have elongate shapes, a lot of time is spent analyzing nonasbestos particles. A further complication arises in samples that include nonasbestiform cleavage fragments, or a mixture of cleavage fragments and asbestiform fibers of the regulated asbestos minerals: the size distributions and aspect ratios of these particles overlap, so that the microscopist usually cannot distinguish between asbestos and non-asbestos fibers of the same mineral on a

single-fiber basis.

The aspect ratios chosen in the methods are typically 3:1 or 5:1 and have a large overlap with nonasbestiform particles. Choice of a higher aspect ratio would be more selective for asbestos and would eliminate analysis of many nonasbestos particles, but could also eliminate a possibly significant fraction of asbestos fibers. Thus, most methods have opted for low aspect ratios. However, this broad morphology classification can compromise the analysis of asbestos. When amphiboles are being analyzed, these methods are only valid where there is (a) a known amphibole asbestos component in the air and (b) no major source of cleavage fragments of the same mineral. The existence of 3:1 or 5:1 amphibole particles on a filter sample is not sufficient for the analyst to state that asbestos is present.

Mineral Definitions

Several minerals can occur in an asbestiform habit and have been used commercially as asbestos: chrysotile, riebeckite asbestos, grunerite asbestos, tremolite asbestos, actinolite asbestos, and anthophyllite asbestos. The asbestiform varieties of these minerals are regulated by several federal agencies. Chrysotile is a fibrous serpentine mineral.²³ All the other minerals listed are amphiboles, whose nomenclature is defined succinctly by Leake.¹⁷ Other minerals rarely occur in an asbestiform habit, but are not typically used commercially for their asbestos properties and are only rarely found in any measurable quantity. These other materials are not currently regulated.

Mineral Identification

To identify these mineral species unambiguously one must measure properties unique to that mineral, both primary properties such as chemical composition and crystallographic data (symmetry and d-values), and secondary properties such as a combination of optical data including refractive indices at specific crystallographic orientations. There is often interference from other minerals for any single property, so that several properties must be generally measured for a definite mineral identification. Asbestos mineral identification is discussed in detail in number of methods and papers.^{13,18-21} Crystallography, such as used in powder XRD, and molecular spectroscopies, such as infrared and Raman analyses, can uniquely identify the mineral species, if a sufficient number of peaks and intensities are measured. Measurement of electron diffraction at one crystal orientation, as applied in the AEM methods, uniquely identifies only chrysotile. In general, chemical composition is insufficient for a unique identification because various minerals may have the same or similar composition,^{22,23} so that for the electron microscopic identification of amphiboles, both electron diffraction and chemical composition must be analyzed to

provide a unique mineral identification.

Which Technique to Use

With the background provided above, we can now put the various techniques in perspective and define an approach to analysis. Again, it is best to separate the approach into the two major type of asbestos analysis, bulk and filter samples. Only two of the techniques listed in Table 1 (PLM and AEM) give both a unique mineral identification and morphological information necessary for the qualitative identification of asbestos. All the other methods either require supporting data from another procedure or assumptions as to the mineral type or morphology.

Bulk Samples

Of the two methods capable of performing a qualitative analysis, only PLM has a defined method for bulk analysis.² Thus PLM is the technique of choice (and luckily also the most economical). However, the PLM technique has several problems. It requires analysts trained in polarized light microscopy, optical crystallography, and mineralogy and experienced with asbestos analysis. The NIST Bulk Asbestos Accreditation Program has shown that many analysts do not fully understand the use of the polarized light microscope or how to interpret the PLM results. The PLM method also has difficulty with the qualitative analysis of materials that are nonfriable or have well-dispersed thin fibers. The microsampling performed prior to PLM analysis makes the method prone to errors associated with inhomogeneous samples. The PLM method is by nature semiquantitative and cannot yield precise estimates of asbestos concentrations, especially at the lower concentrations, near 1 wt%.

Many of the problems associated with the PLM method can be corrected by supplementing the analysis with quality control checks that employ other techniques. A good macroscopic analysis of the whole sample and a semirandom microsampling system can overcome many homogeneity problems; AEM, XRD, and SEM analyses can aid the qualitative analysis of finely dispersed fibers; XRD is also useful for analysis of nonfriable materials and in more precisely quantifying the asbestos content. The use of PLM as the primary method that is always applied to bulk specimens, with other techniques used as support and quality-control checks for both random and specific types of samples, makes the qualitative analysis of asbestos reliable and economical.

Another, more difficult problem with quantifying the amount of asbestos in a bulk sample has to do with the current practice of quantification based on an estimate of the volume of asbestos in the bulk sample during the macroscopic analysis or an estimate of the area of the asbestos in microsamples on the PLM. Such volume estimates can be reasonable estimators of the weight percent of a phase in a complex assemblage of phases if the densities

of the phases are similar.²⁴ The problem is that there is currently no determination of error or standardization of the volume-estimation technique. This macroscopic method, although valuable semiquantitatively, is a new technique that has not been validated by standards, empirical data, or theory; i.e., how does one estimate volume from a complex, partially fibrous sample? Nor can the macroscopic method distinguish the fibers by mineral type and may miss thin fibers, which leads to incorrect estimates of the asbestos content. Generally, the macroscopic analysis should report the results as "possible" asbestos and should be verified by the PLM method.

The second means of quantifying asbestos by estimating the area in microsamples on the PLM has its own set of problems. Two ways of estimating area are currently employed: (1) point counting and (2) visual estimate. Point counting has an advantage in that it is a standardless technique with defined analysis rules, but it takes a long time to get what is at best a semiquantitative answer. Visual estimation is much faster but can only be employed if the analyst has been trained, through comparison with suitable standards, to make area estimates of fibrous components in morphologically complex matrices. If performed properly both area-estimate techniques should come up with the same asbestos concentration. Yet both area estimates have a major problem: the relative projected area of particles is a function of the relative thickness distributions of the grains. What that means is that area estimates should be made on specimens of equal thickness;²⁴ that is, thick grains should not be compared to thin grains (unfortunately a common occurrence on a typical asbestos sample slide mount). The variation in grain thickness causes the area estimate to be only indirectly related to the weight percent of asbestos in a sample and that area percent changes as a function of the sample manipulation and preparation.

One way of countering some of the weaknesses of the quantitation is to make a semiquantitative estimate of the asbestos content in a sample during both the macroscopic and PLM examination of a sample. The results of each should be consistent, or the causes of any discrepancies should be determined and accounted for in the asbestos-content results. These results will still be semiquantitative and have poor precision at low concentrations of asbestos, but the two estimates will minimize some problems associated with homogeneity and particle size.

A better method for determining the quantity of asbestos in a sample is x-ray powder diffraction. A number of methods exist for quantifying the weight percent of a specific mineral phase in complex samples by XRD, which can measure precision and accuracy and has a sensitivity of approximately 0.5 to 2 wt% for most types of bulk samples. Quantitative XRD has its limitations. It is more time consuming and expensive than PLM, extensive sample pre-

paration is sometimes necessary, and XRD cannot distinguish asbestiform from nonasbestiform particles of the same mineral phase. If XRD is used as a support technique in conjunction with the PLM on samples in which the PLM is quantitatively or qualitatively the weakest (e.g., samples that contain minor to trace quantities of asbestos or nonfriable samples), many of these limitations are minimized.

Filter Techniques

Microscopic techniques can be applied to all type of samples and are not limited to filter materials, but the advantages and limitations of each method are the same as in filter analysis. The microscopic analysis of materials entails several steps: finding the objects of interest, then determining their identity and concentration. Choosing the appropriate microscopic method for the analysis of asbestos entails finding the best technique to accomplish these steps. Reliably finding an object such as an asbestos fiber requires that the fiber be easily visible. Determining its identity requires that enough properties can be measured to identify the object uniquely.

The visibility of an object on the microscope is a function of contrast, signal, noise, size, shape, and the ability and experience of the observer. The contrast, signal, and noise are defined by the sample, sample preparation, and instrument imaging system. The size of the object must be matched to the resolution capability and magnification of the analyzing instrument to produce an image where the object is easily seen. Different observers have different acuities or sensitivities depending on the shape of an object. And different observers, different microscopists, computers, detectors, etc., have differing capabilities of seeing or recognizing objects.

The three techniques used in the analysis of filter materials (AEM, SEM, and PCM) each have quite different mechanisms of image formation. The AEM and PCM have transmission microscope optics where a whole field of view is illuminated and imaged simultaneously; the SEM has a microprobe beam which is rastered over the sample to create a two-dimensional image of the surface of the sample. The AEM and SEM use electron optics for imaging and thus have higher resolution than the light optics on the PCM (Table 2). The use of electrons enable particles to be characterized chemically and crystallographically through x-ray spectroscopy and electron diffraction analysis (Table 1).

Of the three methods, only AEM is capable of the unique identification of the asbestos minerals. Where identification of fibers on filter materials is critical, AEM is thus the only valid method. Identification is necessary whenever the sample is taken in an environment that contains unknown fibrous particulate. AEM is also the only technique that reliably allows observation of the complete asbestos

size distribution. Thus, if the amount of asbestos, without regard to fiber length or width, is desired, only the AEM techniques is capable of analyzing the sample. The very capability of measuring all fibers means that the AEM operates at high magnifications. These high magnifications put practical limits on the amount of sample that can be analyzed by the technique. The AEM is operated at $>10\,000\times$ so that the typically thin (40nm) asbestos fibers can be visualized, and often covers less than 1 part in 10 000 of the area of a filter during a routine analysis. Covering such a small filter area limits the statistical reliability and detection capability of the technique.

The PCM, as used, cannot give any information about the mineral identity of a fiber. That means that any particle meeting the morphology criteria of the method will be counted as asbestos, including gypsum, organic, glass, and other particles. In addition, PCM is limited to fibers more than approximately $0.3\,\mu\text{m}$ wide and does not count complex equant particles composed of asbestos. These size limitations mean that one cannot observe most of the asbestos fibers in a sample by PCM. The PCM method was designed for use in the asbestos workplace, where it was valid to assume that the preponderance of fibers present in the sample are asbestos. In these environments the results of the PCM method were related to the asbestos diseases of the workers. To this day the results of the PCM technique are the only ones to yield a direct relationship to health effect; if used in appropriate circumstances, PCM can be very effective in preventing asbestos-related health problems in asbestos workers. But application of the technique to the general ambient or indoor environment to determine the concentration of asbestos simply generates uninterpretable results.

When performed properly, SEM has the same limitations as AEM, but cannot generally attain its reliability or full capability because the SEM imaging system is much more complex and prone to noise than the AEM. The quality of the SEM image and therefore the visibility of the asbestos fibers is a function of many parameters.^{25,26} Since the visibility of the asbestos fibers on a filter sample is near the limit of the capability of the SEM technique, it would be necessary for each instrument to show routinely, through a rigorous calibration, that the instrument was capable of easily imaging and analyzing asbestos fibers. In addition, the method can only partially identify the fibers as asbestos. SEM is limited to classifying particles by chemical composition, which cannot uniquely identify a mineral species. The capability of SEM falls between AEM and PCM, both in fiber visibility and identification. It is not clear that the SEM serves a useful purpose in the analysis of filters. Unluckily, all these methods report results from an analysis in units of fibers per unit area, which has led to the conclusion that the results should be comparable. Because

of major differences in the counting protocols and the analytical capabilities of the instruments, the results from the SEM, PCM, and AEM are generally not comparable and typically differ by orders of magnitude. Only in a research mode, where many parameters are controlled or held constant, would one expect the results of the methods to be self-consistent; and even then the results would not yield the same numbers. Only if the definition of an asbestos fiber, the fiber size distribution and source of material (dispersed or comminuted), the resolution and imaging mechanism of the instrument, the interfering materials, and the analytical capability of the instruments and methods were the same could one get comparable asbestos concentrations.

Conclusions

The method of choice for the qualitative analysis of asbestos in bulk materials is the polarized light microscope, combined with a thorough macroscopic analysis of every sample. This combination of techniques allows a bulk sample to be adequately defined both morphologically and mineralogically. Quality control checks by other techniques such as XRD, AEM, and SEM are useful in controlling and limiting the errors associated with specific types of samples where the PLM is known to have problems. PLM and macroscopic analysis of bulk samples yield semiquantitative results. To get precise and accurate amounts of asbestos at low concentrations requires the use of other methods such as XRD, ashing, chemical dissolution, weighting, etc.

The method of choice for filter samples is the AEM. It is the only filter analysis method that is capable of unique mineral identification and unlimited morphological characterization. The PCM is useful for relating asbestos aerosol concentrations to health effects, but assumes all fibers to be asbestos and should therefore not be used to determine the quantity of asbestos on a filter. If the quantity of asbestos in a gas or liquid is the desired result, then AEM is the only current technique capable of supplying an answer. If the health effect of a known asbestos aerosol on a worker is the desired result, then the PCM is currently the best method. The SEM gives results that are not completely satisfactory in either case.

References

1. H. W. Berger, L. S. Galowin, J. Horlick, E. B. Steel, and J. R. Verkouteren, *Bulk Asbestos Handbook*, National Voluntary Laboratory Accreditation Program, NISTIR 88-3879, Gaithersburg, Md.: NIST, 1988.
2. U.S. Environmental Protection Agency, *Interim Method for the Determination of Asbestos in Bulk Insulation Samples*, EPA 600/M4-82-020, Research Triangle Park, N.C., 1982.
3. National Institutes of Occupational Safety and Health, Method 7400.

4. U.S. Environmental Protection Agency, *Interim Transmission Electron Microscopy Analytical Methods--Mandatory and Nonmandatory--and Mandatory Section to Determine Completion of Response Actions*, Appendix A to Subpart E, 40 CFR part 763, 30 October 1987.
5. U.S. Environmental Protection Agency, *Draft Provisional Transmission Electron Microscope Method for the Analysis of Asbestos in Air*, Research Triangle Park, N.C., 1988.
6. E. J. Chatfield, R. W. Glass, and M. J. Dillon, *Preparation of Water Samples for Asbestos Fiber Counting by Electron Microscopy*, U.S. Environmental Protection Agency, EPA-600/4-78-011, Athens, Ga., 1978.
7. G. A. Luoma, L. K. Yee, and R. Rowland, "Determination of microgram amounts of asbestos in mixtures by infrared spectroscopy," *Anal. Chem.* 54: 2140-2142, 1982.
8. J. J. Blaha and G. J. Rosasco, "Raman microprobe spectra of individual microcrystals and fibers of talc, tremolite, and related silicate minerals," *Anal. Chem.* 50: 892-896, 1978.
9. J. K. De Waele, F. C. Adams, P. A. Vermeire, and M. Neuberger, "Laser microprobe mass analysis for the identification of asbestos fibers in lung tissue and broncho-aveolar washing fluid," *Mikrochemica Acta* 197-213, 1986.
10. K. R. Spurny and J. Schormann, "Identification of mineral fibers by LAMMA," *Fresenius Z. anal. Chem.* 308: 274-279, 1981.
11. W. J. Campbell, R. L. Blake, L. L. Brown, E. E. Cather, and J. J. Sjoberg, *Selected Silicate Minerals and Their Asbestiform Varieties*, U.S. Bureau of Mines Information Circular 8751, Washington, D.C., 1977.
12. B. Levadie, Ed., *Definition for Asbestos and Other Health-related Silicates*, ASTM 834, Philadelphia, Pa., 1984.
13. C. C. Gravatt, P. D. LeFleur, and K. F. J. Heinrich, Eds., *Proceedings of Workshop on Asbestos: Definitions and Measurement Methods*, National Bureau of Standards Special Publication 506, Gaithersburg, Md., 1978.
14. E. Steel and A. Wylie, "Mineralogical characteristics of asbestos," in P. M. Riordon, Ed., *Geology of Asbestos Deposits*, American Institute of Mining, Metallurgical, and Petroleum Engineers, New York, N.Y., 1981.
15. Ann Wiley (personal communication).
16. ASTM committee D22.05.07 draft, *Standard Method of Testing for Asbestos Containing Materials by Polarized Light Microscopy*.
17. B. Leake, "nomenclature of amphiboles," *Am. Min.* 63: 1023-1052, 1978.
18. P. E. Champness, G. Cliff, and G. W. Lorimer, "The identification of asbestos," *J. Mic.* 108: 231-249, 1976.
19. J. Small and E. Steel, Eds., *Asbestos Standards: Materials and Analytical Methods*, NBS Special Publication 619, NIST, Gaithersburg, Md., 1982.
20. W. C. McCrone, *Asbestos Identification*, McCrone Research Institute, Chicago, 1987.
21. P. A. Russell and A. E. Hutchings, Eds., *Electron Microscopy and X-ray Applications to Environmental and Occupational Health Analysis*, Ann Arbor, Mich.: Ann Arbor Science, 1978.
22. C. S. Hurlbut Jr. and C. Klein, *Manual of Mineralogy*, New York: Wiley, 1977.
23. W. A. Deer, R. A. Howie, and J. Zussman, *Rock-forming Minerals*, London: Longmans, Green and Co., 1967.
24. J. C. Russ, *Practical Stereology*, New York: Plenum Press, 1986.
25. E. B. Steel, "SEM imaging and analysis of submicrometer particles in air and water samples," *Microbeam Analysis--1988*.
26. D. S. Bright, E. B. Steel, and D. E. Newbury, "The problem of visibility in noisy images," in this volume.

COLLECTION, PREPARATION, AND ANALYSIS OF SURFACE SAMPLES

B. H. Clark

Due to the episodic nature of asbestos release, the importance of surface sampling in addition to air sampling has been recognized in the assessment of asbestos-containing buildings. Although methodologies have been published for air sampling and analysis to be followed by all laboratories, a standard operating procedure for surface sample collection, preparation, and analysis has not yet been accepted. This study is concerned with a possible protocol for surface samples that gives reproducible results.

Sampling Procedure

An air sampling pump set at 2 l/min is used to "vacuum" a 1ft² area of the surface for 1 min. A standard air cassette loaded with 0.8µm mixed cellulose ester MCE filter is held at a slight angle to the surface and moved in overlapping, parallel passes across the surface at least twice in different directions. Smaller areas may be sampled as long as the actual area is recorded. Carpets may require aggressive vacuuming in order to pick up the releasable fibers.

Preparation Procedure

The inside of the cassette is rinsed with de-ionized, particle-free water into a container. The filter is removed and sonicated, and the rinse water is added to the sample container. After dilution to 100 ml volume, further sonication, and agitation, a small volume of sample is filtered onto a 47mm, 0.45µm MCE filter. The amount filtered depends upon the amount of material in the sample. When the filter is dry, it is prepared for analysis by the NIOSH 7402 direct preparation method,¹ which consists of collapsing, etching, carbon coating, and dissolving the filter.

Analysis Procedure

The asbestos fiber counting method has been adapted from the AHERA document or from the Yamate Level II analysis.^{2,3} In addition to asbestos structures, other constituents of the dust sample may be identified in an attempt to determine a possible source of the contamination. From this analysis, the concentration of asbestos structures per square foot can be calculated from

$$\text{Concentration} = \frac{SA_{\text{eff}}}{N_{\text{GSO}} A_{\text{GSO}} A_s f}$$

where S is the number of asbestos structures

counted, A_{eff} is the effective area of the sample preparation filter (µm²), N_{GSO} is the average area of one grid square opening (µm²), A_s is the area sampled (ft²), and f is the amount of sample filtered from the total volume of sample. Typical concentration levels found in dust samples analyzed are:

Level	Concentration (structures/ft ²)
Low	5000-1 million
Moderate	1-100 million
High	>100 million

Conclusion

This protocol for surface sampling and analysis is a relatively new method for quantification of asbestos contamination. There are other surface sampling protocols; perhaps a merging of the best parts of various methodologies will provide the most successful approach to this situation.

References

1. J. W. Carter, P. A. Baron, and D. G. Taylor, NIOSH 7402, *NIOSH Manual of Analytical Methods*, 1986, pp. 7402-1 to 7402-7.
2. M. Yamate, S. C. Agarwal, and R. D. Gibbons, *Methodology for the Measurement of Airborne Asbestos Concentrations by Electron Microscopy* (EPA Draft Report), Washington, D.C.: Office Research and Development, U.S. Environmental Protection Agency, Contrast 68-02-3266, 1984.
3. *Federal Register*, 40 CFR Part 763, 30 October 1987.

ON THE CHARACTERIZATION OF ASBESTOS AEROSOLS

K. R. Spurny

Fibrous aerosols, consisting of asbestos, natural, and man-made mineral fibers, whether dispersed in the outdoor and indoor atmosphere or in the workplace environments, are toxic and carcinogenic. Their measurement in air as well as their personal dosimetry are needed.

It has been shown that optical microscopy (OM) is no longer regarded as a suitable procedure for the measurement of fibrous aerosols. The methods of the best available technology are analytical scanning and transmission electron microscopy (ASEM and ATEM). These techniques are to be applied to such measurements. Two available standard reference procedures (VDI, ISO) can be applied to direct evaluation of filter samples. Fibrous aerosols of all particle sizes and types can be quantitatively evaluated and qualitatively identified by combination of these procedures. (ASEM is used as a high-quality screening test.) Concentrations as small as 100 fibers/m³ are measurable.

The health risk can be evaluated by application of toxic and carcinogenic models and by means of "preventive standard limits" (PSL). The PSL proposed for asbestos in the Federal Republic of Germany is 400 fibers L_p ≥ 5 μm per m³. Models for the health risk evaluation which are related to fibers sizes were proposed by Pott. The measured fiber concentrations and sizes are compared with the size-effect model.

The author is at the Fraunhofer-Institut für Umweltchemie und Ökotoxikologie, D-5948 Schmallenberg-Grafschaft, Federal Republic of Germany.

PROCEDURES FOR THE PREPARATION AND ANALYSIS OF BULK ASBESTOS-CONTAINING MATERIALS BY COMPUTER-CONTROLLED SCANNING ELECTRON MICROSCOPY (CCSEM)

L. D. Detter and T. B. Vander Wood

The identification of the origin of asbestos-containing building materials has become a major concern in the economics of asbestos abatement. A wide array of analytical techniques has been applied to building materials to supplement the paper trail leading to the material manufacturer, including electron and optical microscopy for the identification of inorganic components and organic analyses for the identification of surfactants, binders, etc. Scanning electron microscopy combined with energy-dispersive x-ray spectrometry (CCSEM EDS) is currently being investigated and shows great promise for the identification of the inorganic components and the determination of their weight percents. In this method, the sample of interest is pulverized to a fine powder and a representative portion is dispersed on a substrate for mounting in the electron microscope. Under computer control and without operator intervention after the initial set-up, the CCSEM-EDS finds, sizes, and chemically analyzes up to one thousand particles. Each particle can then be assigned to a user-defined material type (e.g., chrysotile, talc, perlite) based on its chemistry, and the weight percent of each type can be calculated. In the present study, recent improvements in sample processing methods are discussed along with a CCSEM-EDS evaluation of a building material (ceiling plaster) of known composition.

The choice of sample pulverization employed greatly influences the CCSEM-EDS data. An ideal sample dispersion would contain particles of similar size and a minimum of particle overlap or agglomeration. The dispersion should also be representative of the parent sample. The first step in our processing procedure involves milling a known weight of material in a freezer mill, followed by suspension in ethanol, which yields a known concentration in suspension. The suspension is homogenized by ultrasonication and an aliquot is filtered through a 0.2 μ m pore size polycarbonate filter. The filter is then washed to remove all acid-soluble components of the building material (the acid-soluble portion is identified in a different procedure) and is mounted on a carbon planchette. A thin carbon layer is applied to the filter to reduce possible charge build up during the CCSEM-EDS analyses.

Once the sample is prepared it is mounted for analysis in our CCSEM (actually a JEOL 733 Superprobe controlled by a Tracor Northern 5500/5600). At present we are using commer-

cially available software to automate the instrument and to process the resulting data. However, advanced software has been developed in-house and should be applied to similar product identification samples in the near future. (For an in-depth discussion of our CCSEM-EDS method, see Ref. 1.)

The CCSEM-EDS results of the ceiling plaster of known composition are shown in Table 1. The first column contains the particle types. The published composition of the ceiling plaster is listed in the second column. The next six columns are CCSEM-EDS results obtained from five different sample pulverization techniques: handground in an agate mortar/pestle; use of a micronizing mill; a pulverizing mill employing a tungsten carbide vial; a freezer mill employing plastic and stainless-steel vials; and a shatterbox with tungsten carbide components. The data in this table illustrate two points. First, the choice of grinding techniques is critical for accurate and reproducible CCSEM-EDS analyses. In this study, the freezer mill was the preferred grinding method. Second, the data indicate that CCSEM-EDS is effective in determining the acid-insoluble composition of building materials, and also illustrate the most difficult problem associated with the method: assignment of particles to the various particle types. Considering the freezer mill data, the most prominent differences between the standard composition and the analytical results are the presence of Si-rich particles that were not listed for the standard composition, and the overestimation of talc. The presence of 9.9% of Si-rich particles may be explained by the presence of a Si-containing acid-soluble material (such as mineral wool) left as a residue after the acid washes. Similarly, the explanation for the overestimated value of talc is not straightforward but is perhaps explained by particle overlap or close association between similar particle types. The weight percents of chrysotile, montmorillonite, and perlite were in close agreement with the building standard's composition. The percentage of the unclassified particles with the freezer mill was 7% of the total number of particles analyzed.

In summary, CCSEM-EDS is an effective method for characterizing asbestos-containing building materials providing adequate care is taken during sample processing and in the definition of particle types.

References

1. L. D. Detter-Hoskin and T. B. Vander Wood, "Procedures for the analysis of bulk

The authors are with McCrone Associates—Atlanta, 1412 Oakbrook Drive, Suite 100, Norcross, GA 30093.

asbestos-containing materials by automated particle analysis," *J. National Asbestos Council* (submitted).

TABLE 1.--CCSEM-EDS data (wt%)^a.

PARTICLE TYPE	BUILDING STANDARD	HANDGROUND AGATE MORTAR/ PESTLE	MCCRONE MICRONIZER CORUNDUM	MCCRONE MICRONIZER CORUNDUM	PULVERIZER TUNGSTEN CARBIDE	SPEX FREEZER MILL/PLASTIC AND STAINLESS	SHATTER BOX TUNGSTEN CARBIDE
Al-Rich (Al ₂ O ₃)	—	0.1	18.4	5.8	0.2	—	0.3
Si-Rich (SiO ₂)	—	1.6	38.0	2.2	10.7	9.9	8.5
Fe-Rich (FeO)	—	0.1	1.0	3.4	0.1	0.3	0.4
Chlorite/ Vermiculite	—	0.1	0.7	1.3	1.4	0.3	1.8
Chrysotile	7.2- 9.3	0.8	1.9	2.7	14.5	5.9	3.3
Talc	7.7-10.3	18.3	10.4	36.6	21.5	18.4	15.7
Montmorillonite/ Bentonite	9.3-16.5	49.1	3.2	3.7	20.9	9.3	19.4
Perlite	56.7-72.1	18.9	23.8	36.7	29.8	55.2	48.4
Kaolin	—	9.0	2.0	6.3	0.9	0.5	2.1
Steels	—	2.1	0.4	1.4	0.1	0.1	0.2
Titanium dioxide	<4.1	—	0.2	—	—	—	—
Number of Non- Integrable	—	7	1	2	3	17	30
Number Unknown (% Unknown)	—	107 (22)	169 (22)	102 (27)	470 (30)	60 (7)	135 (9)
TOTAL NUMBER OF PARTICLES	—	495	808	384	1545	828	1500

a. All the ground samples were acid washed prior to automated analysis.

b. Total weight of sample ground was approximately 0.06g; corundum impactors/plastic vial.

c. Total weight of sample ground was approximately 2 g; corundum impactors/plastic vial.

ASBESTOS ANALYSIS BY POLARIZED LIGHT MICROSCOPY: PROBLEMS AND SUGGESTIONS

R. L. Perkins, B. W. Harvey, and M. E. Beard

Polarized light microscopy (PLM) is the recommended method for analyzing friable bulk materials to determine whether they contain asbestos.^{1,2} An experienced microscopist can detect and identify asbestos fibers at concentrations below 1%. Unfortunately, the experience and skill level represented by the microscopists involved in asbestos analysis vary greatly. This study documents the types of bulk samples that asbestos laboratories have found difficult to analyze and suggests some analytical techniques that could aid the microscopist in identification and quantitation of asbestos in friable bulk materials.

Background

Experience with conducting proficiency testing of asbestos laboratories, both for the U.S. Environmental Protection Agency (EPA) and the U.S. Navy, has indicated some types of materials that cause analytical problems. Eighteen EPA test rounds and 23 Navy test rounds have been conducted. The problems can be summarized as follows:

1. Detection and quantitation of asbestos at low concentrations.
2. Detection and identification of small-fiber asbestos.
3. False positive identification of asbestos substitutes.
4. Incorrect identification of asbestos type(s).
5. Detection, quantitation, and identification of asbestos fibers masked by binders.

Parts a, b, and c of Table 1 illustrate the error rate of participating laboratories in the analysis of samples with the characteristics mentioned above. Approximately one out of ten laboratories could not detect asbestos when present at low (2-3%) concentrations. Depending on the type of sample, 20 to 35% of the laboratories reported false positives for fibrous, nonasbestos materials. Approximately 46% of the laboratories were unable to identify anthophyllite asbestos correctly.

Analytical Techniques

Identification of asbestos by PLM involves a very careful determination of the optical properties of the suspect fibers. Characteristics such as refractive index, pleochroism, birefringence, sign of elongation, morphology,

etc., must be determined to identify asbestos correctly. Several techniques can be used to help the microscopist in analyzing bulk materials. A careful scanning of the material with a simple microscope at low magnification (10-40×) is perhaps the most important step in detecting fibers and also provides (with experience) an opportunity to estimate the relative concentrations of the various sample components visually.

Because many construction materials are heterogeneous, sample homogenization most often facilitates identification and quantitation of fibers. It was found that sample homogenization in a miniblender provided a more even distribution of sample components and was very efficient in the removal of binder material from the fibers.

Suspect fibers are carefully removed from the sample, "teased" if covered with binder or in thick bundles, and mounted in oils with a refractive index above unity on glass slides. Careful PLM analysis, accompanied by the dispersion-staining technique, should make for proper identification of suspect fibers.

Quantitation of asbestos concentration, especially at low levels, is quite difficult for many laboratories. The accuracy of visual estimation depends on the experience of the microscopist. To date, no reference standards are available commercially for use in the training of microscopists. Studies made at the Research Triangle Institute indicate that the technique of point counting makes for much higher precision and accuracy in the quantitation of asbestos.³ Pinch samples of the homogenized sample are permanently mounted on glass slides with either epoxy or commercially available high-dispersion mounting media. A point-counting stage and cross-hair reticle are used and counts are made along longitudinal traverses of the slide. A minimum of 300 points should be counted. This method was tested with prepared reference materials containing known concentrations (by weight) of asbestos and also "real-world" construction materials that had been quantitated by several experienced microscopists using the visual-estimate method. Results show point counting to be a viable method for quantitation of materials.

Conclusions

A well-trained microscopist experienced in asbestos analysis can correctly identify and semi-quantify asbestos even if it is present at low concentrations. PLM remains the most efficient, inexpensive, and quickest method for analysis of friable bulk materials. Nearly

R. L. Perkins and B. W. Harvey are at the Research Triangle Institute, Box 12194, Research Triangle Park, NC 27709-2194; M. E. Beard is with the Environmental Protection Agency, Research Triangle Park, NC 27711.

all errors in analysis may be attributed to improper sample preparation and to microscopists lacking proper training in optical microscopy and/or asbestos analysis.

References

1. *Interim Method for the Determination of Asbestos in Bulk Insulation Samples*, EPA-600/M4-82-020, U.S. Environmental Protection Agency, Research Triangle Park, N.C., 1982.
2. *Bulk Asbestos Handbook*, NISTIR 88-3879, National Voluntary Accreditation Program, National Institute of Standards and Technology, Gaithersburg, Md., 1988.
3. R. L. Perkins, *Development and Evaluation of Polarized Light Microscopy (PLM) for Measuring Low Levels of Asbestos in Bulk Materials*, (EPA Draft), RTI Report 3680-12, Research Triangle Institute, Research Triangle Park, N.C., 1989.

TABLE 1.--Summary of laboratory performance in analysis of (a) samples having low concentrations of asbestos, (b) asbestos substitutes, (c) asbestos type not commonly seen in construction materials.

a. Samples with Low Concentration of Asbestos

Sample Description	Number of Labs Tested		Number of False Negatives		% Error	
	EPA	NAVY	EPA	NAVY	EPA	NAVY
Ceiling tile - 3% Amosite, 85% Mineral wool	1134	91	85	6	7.5	6.6
Ceiling spray - 3% Chrysotile, Calcareous binder	753	---	84	---	11.2	---
Loose-fill insulation, 2% Chrysotile, Mica, Gypsum	616	104	58	48	9.4	46.2

b. Samples Containing Asbestos Substitutes (asbestos-free)

Sample Description	Number of Labs Tested		Number of False Positives		% Error	
	EPA	NAVY	EPA	NAVY	EPA	NAVY
Ceiling spray containing 5% polyethylene fibers	1094	38	350	15	32.0	39.5
Wollastonite (95%+)	616	235	135	45	21.9	19.2

c. Asbestos Sample (Anthophyllite)

Sample Description	Number of Labs Tested		Number of False Negatives and % Error		Number of ID Errors and % Error	
	EPA	NAVY	EPA	NAVY	EPA	NAVY
Anthophyllite (90%+)	518	230	15 2.9%	7 3.0%	247 47.7%	107 45.5%

DEVELOPMENT OF LM/SEM/TEM METHODS FOR THE QUANTITATIVE ANALYSIS OF AIRBORNE GLASS FIBER LEVELS

J. A. Davis and M. R. Kalinowski

Several analytical methods are available for the determination of airborne asbestos fiber concentrations.¹⁻³ These procedures include National Institute of Occupational Safety and Health (NIOSH) methods Nos. 7400⁴ and 7402,⁵ which call for the use of phase-contrast light microscopy (PCLM) and transmission electron microscopy (TEM), respectively. At present, no corresponding scanning electron microscope (SEM) based method is available.

Our laboratory has been involved in the development and implementation of analogous techniques for the quantitative analysis of airborne glass fibers. Many of the approaches investigated were based on published procedures for the examination of asbestos. Our work has shown that these techniques do not necessarily give consistent results for fiberglass. To address this situation, specific new methods were developed in-house. A key goal of this work was the ability to carry out PCLM, SEM, and TEM analyses sequentially on separate sections of the same filter sample. The application of all three techniques was deemed necessary to assess the number and size of any glass fibers that might be missed by a given instrument.

Experimental

All the PCLM work was performed by the NIOSH 7400 method for airborne asbestos. Samples were collected by area or personal air sampling to draw a fixed volume of air through a 25mm-diameter mixed cellulose ester (MCE) filter with a 0.8 μ m pore size. Nominal flow rates and times were 2 l/min for 0.3-12 h, depending on the fiber and dust loadings in the area being sampled. A section of the resultant sample was cut, placed on a glass slide, then optically cleared by exposure to acetone vapors. A refractive index matching fluid, triacetin, and a cover slip were then placed on the filter. Each sample was examined at 400 \times with the aid of a Leitz phase contrast light microscope. Actual fiber dimensions were measured by a Filar digital eyepiece interfaced to a personal computer. Glass and "other" fibers were differentiated on the basis of morphology.

Although several SEM techniques were evaluated, the most reliable approach involved the use of a method modeled after a TEM procedure published by Burdett and Rood.² This approach used a 35% dimethylformamide/15% acetic acid/50% distilled water solution to collapse the filter partially and so to provide a smooth sample that holds the fibers in place. Low-temper-

ature ashing was then employed to remove the uppermost surface of the filter and expose all the collected fibers. The resultant sample was coated with a layer of carbon followed by 60% gold/40% palladium. The SEM analyses were carried out by one of two means. The first approach involved using a JEOL T-300 SEM operated at 1000 \times (to insure the same field of view as the graticule area in the light microscope). Typically, 60-100 photomicrographs were taken on roll film and then printed as approximately 5 \times 7in. prints. Any fibers present were manually measured directly from the photos. The second approach relied on a Cambridge S-90B SEM interfaced to a Quantimet 970 automated image analyzer (AIA). Here the SEM was operated at 1100 \times to provide an image that was then digitized and transferred to the AIA. The actual fiber counts and measurements were then carried out in a semi-automated fashion: an operator pointed out specific features of interest to the instrument, which then made all the necessary measurements.

The TEM sample preparation was performed by Ortiz and Isom's method for asbestos analysis.³ A section of the same MCE filter used for the LM and SEM studies was collapsed by exposure to acetone vapors. The resultant sample was then coated with carbon in a vacuum evaporator. Approximately 2.5 \times 2.5mm portions of the collapsed membrane were placed on 200-mesh Formvar-coated TEM grids that had been placed on 8mm cubes of polyurethane sponge. To dissolve any remaining filter material, these assemblies were then placed in a covered petri dish with a 6mm layer of acetone in the bottom of the container. A Philips 400 TEM was used to examine each grid.

Results

Figure 1 is a PCLM photomicrograph of a glass fiber from a typical sample. The filament is a prominent feature inside the graticule used to define the analysis area. To date, this approach has been applied to over 1300 samples and has been found to offer rapid and reproducible results. Analogous SEM and TEM images are given in Figs. 2 and 3. In both cases, the fibers are readily distinguishable from the filter background. Several air-filter samples have been subjected to parallel studies by PCLM, SEM, and TEM. Table 1 lists measured glass fiber concentration (in fibers per square millimeter of filter area) for samples from a typical series of Owens-Corning Fiberglass insulations. Each of the three techniques used here gives equivalent results,

The authors are with the Owens-Corning Fiberglass Technical Center, Granville, OH 43023.

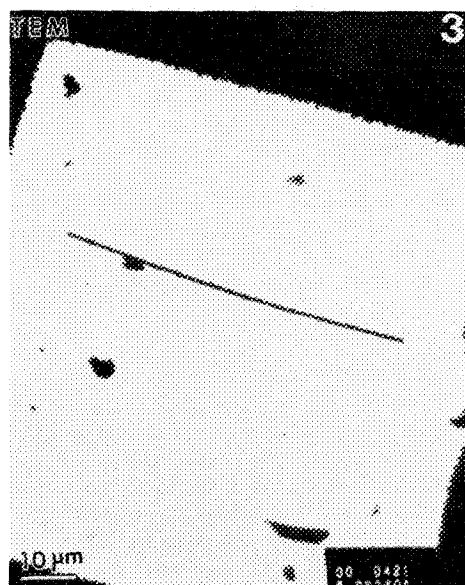
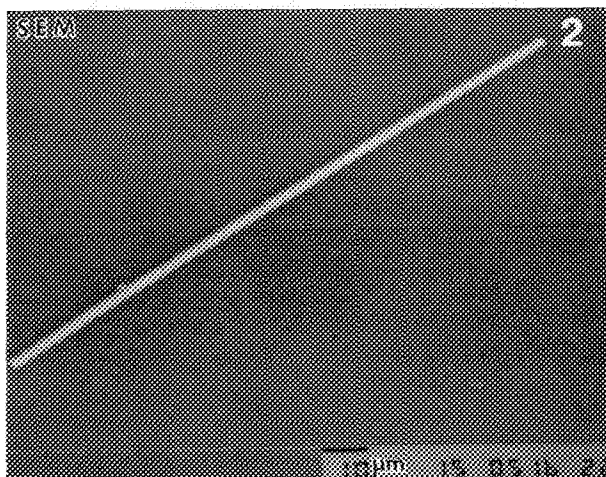
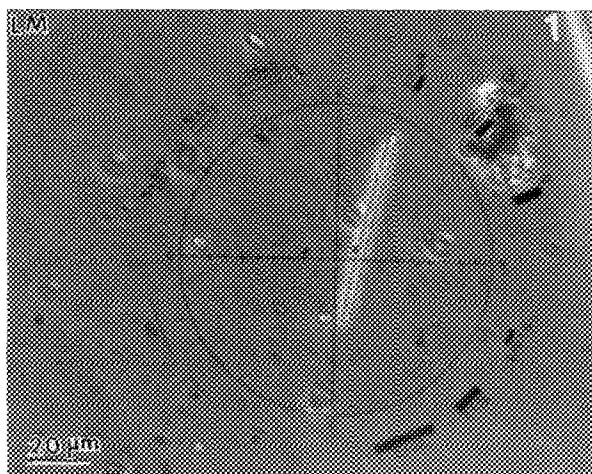


FIG. 1.--Phase contrast light microscope image of glass fiber within area defined by Walton-Beckett graticule.

FIG. 2.--Scanning electron microscope view of glass fiber on surface of collapsed mixed cellulose ester filter.

FIG. 3.--Transmission electron microscope image of glass fiber collected during air sampling.

TABLE 1.--A comparison of PCLM, SEM, and TEM results for airborne glass fibers.

Sample	Measured Fiber Concentrations*		
	PCLM	SEM	TEM
1	18 (9-29)	23 (14-35)	19 (8-39)
2	21 (14-29)	22 (11-38)	22 (7-49)
3	69 (48-89)	52 (37-73)	97 (64-142)

*All results are in fibers/square millimeter of filter area; 95% Poisson confidence levels are given in parentheses.

within the Poisson-distribution counting statistics that govern this type of data. This result is significant because it demonstrates that, unlike the various types of asbestos, LM is fully capable of resolving and counting the range of glass fibers present in these samples.

Conclusions

A series of analytical methods originally intended for the determination of airborne asbestos has been successfully applied to the study of glass fibers. These techniques have been used to examine numerous samples containing glass fibers from products manufactured by Owens-Corning Fiberglas. The resultant data have shown that the three techniques do give statistically equivalent results, contrary to what has been observed for the asbestiform minerals.

References

1. W. C. McCrone, *The Asbestos Particle Atlas*, Ann Arbor, Mich.: Ann Arbor Science Publishers, 1980.
2. G. J. Burdett and A. P. Rood, "Membrane filter, direct transfer technique for the analysis of asbestos fibers or other inorganic particles by TEM," *Environ. Sci. Tech.* 17: 643, 1983.
3. L. W. Ortiz and B. I. Isom, "Transfer technique for electron microscopy of membrane filter samples," *Am. Ind. Hyg. Assoc. J.* 35: 423, 1974.
4. J. W. Carter et al., "No 7400," *NIOSH Manual of Analytical Methods*, Washington, D.C.: 1987.
5. J. W. Carter et al., "No. 7402," *ibid.*

GUIDELINES FOR REFRACTIVE-INDEX MEASUREMENTS OF ASBESTOS

J. R. Verkouteren, J. M. Phelps, and E. B. Steel

Refractive index is one of the primary optical properties used to identify minerals by polarized light microscopy. It is used (in conjunction with the other optical properties of morphology, pleochroism, extinction, birefringence, and sign of elongation) to identify uniquely the type or types of asbestos present in bulk materials.¹ Through our association with the Bulk Asbestos Laboratory Accreditation Program,² we have received requests from hundreds of laboratories for technical assistance in bulk asbestos analysis. Many of these requests are for information on the measurement of refractive index, specifically by the focal screening (dispersion staining) and Becke line techniques. Although many books and articles discuss both techniques, we thought it would be useful to provide a review of the techniques and of their application to asbestos analysis. We have developed Standard Reference Materials (SRMs) of chrysotile, amosite, and crocidolite (SRM1866)³ to serve laboratories as primary calibration standards for the measurement of the optical properties of asbestos, including refractive index. These materials are discussed and used as examples to explain the application of focal screening and the Becke line technique to refractive-index measurement.

Review of Methodology

The refractive index n of a substance varies with wavelength; the effect is referred to as dispersion. In the case of normal dispersion, refractive index decreases with increasing wavelength (Fig. 1). To report the refractive index of any material in a way that allows comparison with other data and other materials, either the dispersion must be numerically described (which requires refractive-index measurements at various wavelengths), or a single wavelength must be chosen as the standard at which to report refractive index. Sodium vapor lamps, which emit monochromatic light with a wavelength of 589.3 nm (a doublet at 589.6 nm and 589.0 nm) are one of the primary light sources used for the measurement of refractive index. As a result, it is the standard convention to report the refractive index at 589.3 nm (n_D).

The authors are at the Center for Analytical Chemistry at the National Institute of Standards and Technology, Gaithersburg, MD 20899. Certain commercial equipment is identified to specify procedures adequately. Such identification does not imply recommendation by the National Institute of Standards and Technology, nor does it imply that this equipment is the best available for this purpose.

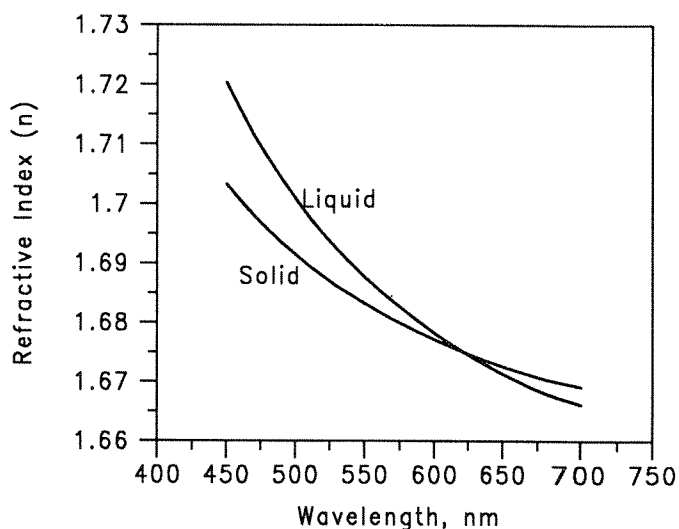


FIG. 1.--Dispersion curves for isotropic solid and liquid showing normal dispersion. Dispersion curves of immersion liquids are typically steeper than those of solids.

The measurement of refractive index by polarized light microscopy is a comparative technique; a solid of unknown refractive index is compared with a liquid of known refractive index. Several techniques have been developed to characterize the degree of match between the two, the most common of which are the observation of relief,⁴⁻⁷ the Becke line technique,⁴⁻⁷ and focal screening (also referred to as dispersion staining).⁸⁻¹⁰ All these techniques are immersion techniques (the solid is immersed in a liquid) and require the use of a light microscope; polarized light is required for the analysis of anisotropic materials (e.g., asbestos).

The relief (edge contrast) of a solid as viewed through the polarized-light microscope depends on the difference in refractive index between the solid and the liquid in which it is immersed. When the two indices are very different, the relief of the solid is high; when they are very close, the relief of the solid is low. Techniques such as oblique illumination are used to enhance the relief of the solid in order to determine more precisely when the refractive index of the solid equals that of the liquid. If monochromatic light is used, the absence of relief is an indication of an exact match in refractive indices at the wavelength of the incident light.

Monochromatic light is not typically used in optical microscopy; the most common illumina-

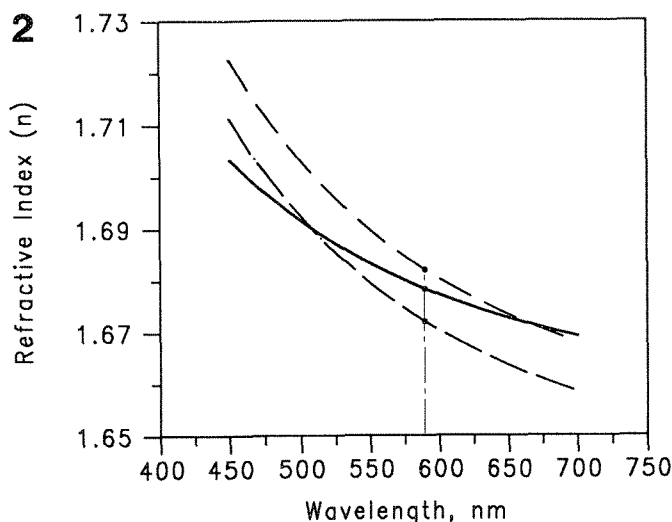
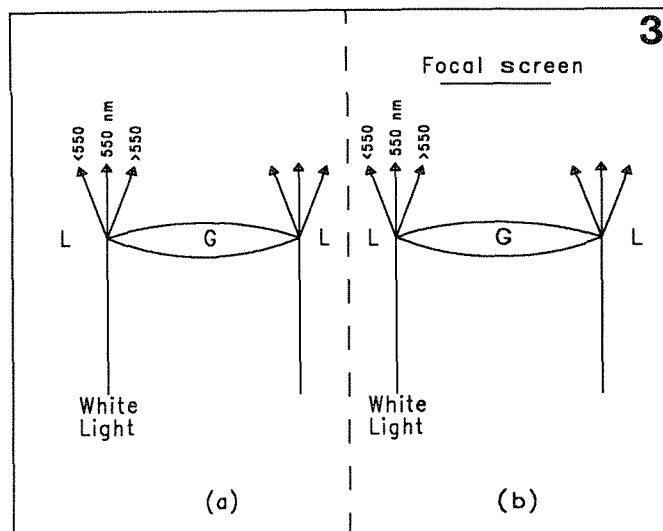


FIG. 2.--Association between liquid-solid refractive-index matches at wavelengths other than 589.3 nm, and differences in n_D . Solid line = solid with $n_D = 1.678$; dashed line = immersion liquid $n_D = 1.674$; dash-dot line = immersion liquid with $n_D = 1.673$. Liquid 1.672 crosses solid dispersion curve at ~ 515 nm (reddish magenta central stop color³); solid $n_D >$ liquid n_D . Liquid 1.682 crosses curve at ~ 665 nm (bright blue-green central stop color³); solid $n_D <$ liquid n_D . FIG. 3.--Origin of Becke-line and focal-screening colors through refraction of light at grain boundaries (adapted from Bloss⁴). Grain (G) and liquid (L) match in refractive index at 550 nm. Light at 550 nm is not refracted; all other wavelengths are refracted either toward grain (wavelengths >550 nm) or toward liquid (wavelengths <550 nm). (a) Becke line technique: all light leaving grain is observed; (b) focal screening technique: some wavelengths are removed by focal screen before reaching observer.

tion is white light (with a blue daylight filter). However, as stated earlier, the refractive index reported for a material is n_D . The Becke-line and focal-screening techniques allow the determination of a wavelength-specific refractive index under white light. The Becke line technique is used to determine the refractive index of the solid at approximately 589.3 nm (n_D); focal screening, at any wavelength in the visible range. If the refractive index is determined at a wavelength other than approximately 589.3 nm, an important point must be remembered: the refractive index of the liquid also varies with wavelength. The Cargille immersion liquids are characterized, following standard convention, by their n_D . If the liquid and solid match at any wavelength other than approximately 589.3 nm, the n_D of the solid is not equal to the n_D of the liquid (i.e., the refractive index as listed on the bottle). If the liquid and solid match at a wavelength below 589.3 nm, the n_D of the solid is greater than the n_D of the liquid; conversely, if the liquid and solid match at a wavelength above 589.3 nm, the n_D of the solid is less than the n_D of the liquid (Fig. 2). (This relationship holds only if the dispersion of the liquid is steeper than the dispersion of the solid, which is the case for the common immersion liquids.)

The Becke-line and focal-screening techniques are very similar; they are simply different ways of viewing the same phenomenon—the refraction of light at grain boundaries. When white light is refracted at the grain boundary, light of one wavelength range is refracted toward the grain and light of a different wavelength range is refracted toward the liquid (Fig. 3), depending on the wavelength at which the grain and liquid



match in refractive index. This process produces lines on the edge of the grain that are colored if the dispersion curve of the liquid and the grain intersect in the visible light range. (The colors of the visible spectrum, and their associated wavelength range, are given in Table 1.) In the case of most asbestos fibers, the entire fiber bundle appears colored because it consists of many fibrils with many edges.

TABLE 1.--Observed color and associated wavelength range.¹¹

Observed color	Wavelength (nm)
Violet	380-450
Blue	450-490
Green	490-560
Yellow	560-590
Orange	590-630
Red	630-760

In the Becke-line technique, all the light leaving the grain boundary is observed, and therefore the colors of the Becke lines are produced by a range of wavelengths. If the grain and liquid match in refractive index at 550 nm, light of all wavelengths above 550 nm is refracted toward the grain and produces a Becke line whose color is a combination of colors from green to red (Fig. 3a). Light of wavelengths below 550 nm is refracted toward the liquid and produces a Becke line whose color is a combination of colors from green to violet. The specific colors associated with different matching wavelengths are given in Bloss⁴ (page 59) and are converted to a dif-

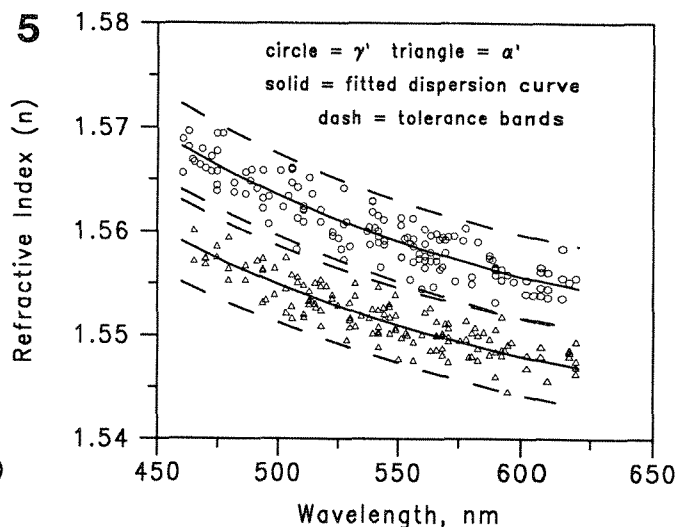
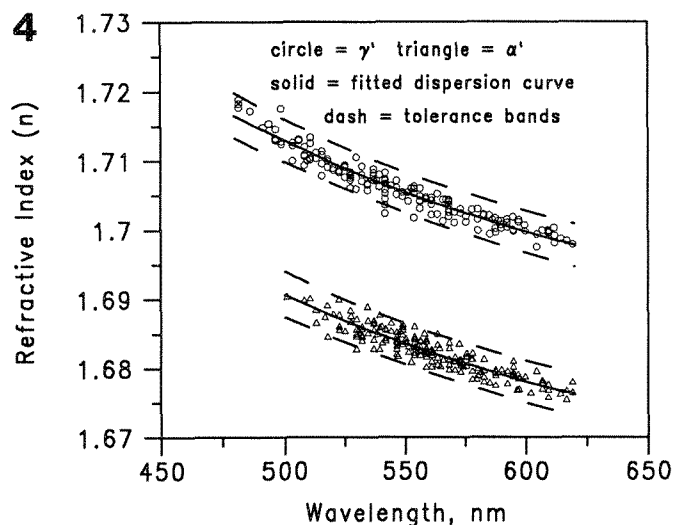


FIG. 4.--Refractive-index measurements of approximately 60 fiber bundles of amosite SRM by double-variation technique; γ' is parallel to fiber length, α' is perpendicular to it. FIG. 5.--Refractive-index measurements of approximately 60 fiber bundles of chrysotile SRM by double-variation technique; γ' is parallel to fiber length, α' is perpendicular to it.

ference in n_p between the grain and the liquid, following the rationale described in Fig. 2. The Becke-line technique requires no special equipment besides the polarized-light microscope, and can be performed in any of the common immersion liquids.

In the focal-screening technique, a screen in the back focal plane of the objective is used to filter out some of the wavelengths from the light leaving the grain boundary (Fig. 3b). An apertural (or annular) screen is used to remove all nonmatching wavelengths; a central screen is used to remove the matching wavelengths. In the case of the apertural screen, the wavelength at which the solid and liquid match in refractive index is determined by conversion of the observed color to its corresponding wavelength, or range of wavelengths (i.e., an observed green color gives a match at 500-520 nm).^{9,10} For the central screen, the observed color is complementary to the color of the wavelength at which the solid and liquid match in refractive index (i.e., an observed reddish-magenta color gives a match at 500-520 nm).^{9,10} The conversion from observed color to corresponding wavelength can be found in references such as Bloss⁹ and McCrone.¹⁰ Focal screening requires a screen or stop in the back focal plane of the objective. It also requires knowledge of the dispersion of the liquid, and, if only one measurement is made at a wavelength other than approximately 589.3 nm, it requires knowledge of the dispersion of the solid. Focal screening can be performed in any immersion liquid; the use of the high-dispersion series is not required in this technique.

Asbestos Standard Reference Materials

Refractive indices were measured at two crystallographic orientations for chrysotile and amosite in SRM 1866; one parallel to the

fiber bundle (γ') and one perpendicular to the fiber bundle (α'). Because individual asbestos crystallites (fibrils) are small compared with the wavelength of light in the visible range, measurements have to be performed on fiber bundles. Because the measurements are done on bundles of fibrils which are oriented randomly about the c-axis (long direction), and which may not be completely parallel to one another, the true α , β , and γ cannot be determined.¹² The convention for reporting the refractive indices of asbestos minerals with parallel extinction is to determine two indices, one parallel to the bundle length and one perpendicular to it. The higher value is reported as γ' and the lower value is reported as α' .

The double-variation technique, which is described in Bloss,⁹ was used to make the refractive-index measurements. This technique involves the variation of the wavelength of the incident light, and variation of the temperature of the immersion liquid. At least 30 individual fiber bundles were measured for each direction of chrysotile and amosite in order to determine any variation within the population.

The results are shown in Figs. 4 and 5. The solid lines in both figures are the dispersion curves calculated by a least-squares fit of the data to a two-term Cauchy equation of the form

$$n(\lambda) = A + (B/\lambda^2)$$

where n = refractive index, λ = wavelength in nm, and A and B are constants. The dashed lines bounding the data are statistical measures of the uncertainty in the data. They represent simultaneous tolerance intervals which cover 95% of the refractive index values at a 95% confidence level. The n_p values for the SRMs are as follows: chrysotile $\alpha' = 1.549 \pm 0.005$, $\gamma' = 1.556 \pm 0.005$; amosite $\alpha' = 1.679 \pm 0.004$, $\gamma' = 1.701 \pm 0.004$. The spread in the data is due to several factors, includ-

ing measurement error and true variation. Identifiable sources of measurement error, such as the calibration of the immersion liquids, the wavelength filter, the temperature, and the analysts, were characterized.

The dispersion of crocidolite was not measured because of crocidolite's strong absorption in the visible range and resultant anomalous dispersion. Near and within an absorption band, the dispersion of a material does not decrease with increasing wavelength in the manner shown in the previous figures, and the refractive index can vary widely within a small range of wavelengths.^{4,5,9} Absorption in the visible also decreases the accuracy and precision of any immersion method,⁵ specifically for refractive-index measurements within the absorption band. However, the observed optical properties, including Becke line and focal-screening colors, are characteristic and can be used to identify crocidolite positively. Becke line and central-stop focal-screening colors for crocidolite in a series of immersion liquids are reported as information values in the certificate for the SRMs.³

Application of Becke-line and Focal-screening Techniques

Measurement of the refractive indices of multiple fiber bundles of the two materials by any appropriate technique should produce values that fall within the tolerance levels of the data (dashed lines in Figs. 4 and 5). The mean of the measurements for any given wavelength should be very close to the fitted value (solid lines in Figs. 4 and 5). Multiple fiber bundles must be analyzed because of the natural variation in the population.

Measurement of the refractive indices of the chrysotile SRM, a subsample of the material is placed in an appropriate immersion liquid, such as a liquid with $n_D = 1.550$. The Becke line colors for the α' direction should indicate a match (orange-yellow and sky-blue (p. 59 of Ref. 4)), whereas the Becke line colors for the γ' direction should indicate that the n_D of the grain is approximately 0.005 higher than the liquid. Different immersion liquids can be used to determine the colors associated with different degrees of match with the liquid.

The n_D of a solid by focal screening can be determined in various ways. If the solid is a complete unknown, then three possible techniques are: (1) change liquids until the focal screening colors indicate a match at approximately 589.3 nm, i.e., $n_D \text{ liquid} = n_D \text{ solid}$; (2) construct dispersion staining curves (which are different from dispersion curves) as described by McCrone,¹⁰ or (3) determine the dispersion curve of the solid for a range of wavelengths that includes 589.3 nm. All three techniques require measurements in more than one liquid. If the solid is not a complete unknown (i.e., its dispersion is characterized), then this information, in combination with one measurement, permits the determination of the n_D of the solid.

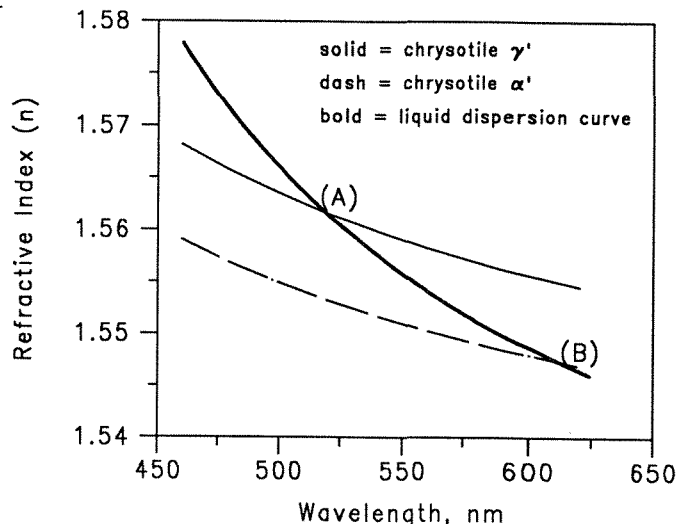


FIG. 6.--Application of focal screening technique for refractive-index measurements of chrysotile SRM. Dispersion curve for immersion liquid with $n_D = 1.550$ intersects chrysotile γ' dispersion curve at approximately 520 nm (A), producing reddish-magenta central stop color; it intersects chrysotile α' dispersion curve at approximately 615 nm (B), producing blue central stop color.

The first technique listed above is straightforward. If the first liquid produces focal screening colors that indicate a match at wavelengths above 589.3 nm, choose a second liquid with a lower n_D (Fig. 2); conversely, if the first liquid produces focal screening colors that indicate a match at wavelengths below 589.3 nm, choose a second liquid with a higher n_D (Fig. 2). The second technique, the use of dispersion staining curves, is described in full in McCrone.¹⁰

The third technique, the construction of the dispersion curve(s) for the solid, requires that the dispersion of the liquid is known. The refractive index of the solid is determined by its intersection with the liquid-dispersion curve; therefore, if the focal screening colors indicate a match at a wavelength other than approximately 589.3 nm, the refractive index of the liquid at that wavelength must be known. Immersion liquids provided by Cargille list the refractive index of the liquid at 656.3 nm (n_C) and 486.1 nm (n_F) in addition to n_D . These data can be plotted and a rough curve drawn between the points, to allow the interpolation of the refractive index of the liquid at any wavelength in the visible range. (Hartmann dispersion paper can be used to produce straight lines, instead of curves, for any material with normal dispersion.) This procedure is done for each liquid used in the determination of the dispersion curve of the solid. Each point on the solid dispersion curve is determined by the intersection with the liquid dispersion curve at the matching wavelength.

In the case of asbestos analysis, the dispersion curves of chrysotile and amosite are characterized, so that the determination of n_D for α' and γ' of chrysotile and amosite requires only one measurement in a liquid of known dispersion. If the refractive index for chrysotile and amosite in any bulk sample, measured at any wavelength, is consistent with the certified value for that wavelength from SRM 1866, then n_D for chrysotile and amosite in the bulk sample is equal to n_D for chrysotile and amosite in the SRM. For example, the matching wavelength for α' of a suspected chrysotile sample in a particular immersion liquid is 460 nm, and the refractive index for the liquid at that wavelength is 1.560. Therefore, the refractive index of α' of the chrysotile sample at 460 nm is 1.560. This value is consistent with the refractive index for the chrysotile SRM α' at 460 nm, which is 1.559 ± 0.004 . Therefore, n_D of chrysotile α' in the sample is equal to n_D of chrysotile in the SRM, which is 1.549 ± 0.005 . If the measured value of either crystallographic direction is not consistent with the certified value, the analyst must consider the fiber an unknown and determine n_D as described earlier for unknown materials.

The SRMs can also be used to help analysts calibrate themselves in the determination of the color (and hence matching wavelengths) of focal-screening and Becke-line colors. Figure 6 shows the dispersion curves of the chrysotile SRM and the dispersion curve for one of the liquids used in our laboratory. The dispersion curve of the liquid intersects the chrysotile γ' dispersion curve at approximately 520 nm (A), and the α' dispersion curve at approximately 615 nm (B). Therefore, the γ' direction should display a reddish-magenta central stop color, and the α' direction should display a blue central stop color.^{9,10} The analyst should determine the wavelength(s) at which their own immersion liquid(s) cross the solid dispersion curve for the SRM, and then use the color-to-wavelength conversion charts given in Bloss⁹ and McCrone,¹⁰ or any other suitable reference, to determine the color associated with the matching wavelength. The SRM should then be placed in that particular immersion liquid, and the focal screening colors observed.

References

1. U.S. Environmental Protection Agency Interim Method of the Determination of Asbestos in Bulk Insulation Samples: Polarized Light Microscopy, 40 CFR ch. 1, pt. 763, Subpt. F, Appendix A, 7/1/87 edition.
2. H. W. Berger et al., NVLAP Bulk Asbestos Handbook, U.S. Department of Commerce, NIST, NISTIR 88-3879.
3. NIST Certificate of Analysis SRM 1866, Office of Standards Reference Materials, NIST, Gaithersburg, Md.
4. F. D. Bloss, *An Introduction to the Methods of Optical Crystallography*, New York: Holt, Rinehart and Winston, 1961.
5. E. E. Wahlstrom, *Optical Crystallography*, New York: Wiley, 1969.
6. P. F. Kerr, *Optical Mineralogy*, New York: McGraw-Hill Book Co., 1959.
7. W. H. Phillips, *Mineral Optics: Principles and Techniques*, San Francisco: W. H. Freeman and Co., 1971.
8. Y. A. Cherkasov, "Application of 'focal screening' to measurement of indices of refraction by the immersion method," *Int. Geol. Rev.* 2: 218-235, 1960.
9. F. D. Bloss, *The Spindle Stage: Principles and Practice*, Cambridge: Cambridge University Press, 1981.
10. W. C. McCrone, *Asbestos Identification*, Chicago: McCrone Research Institute, 1987.
11. *The Science of Color*, Committee on Colorimetry, Optical Society of America, 1963.
12. A. Wylie, "Optical properties of the fibrous amphiboles," *Ann. N.Y. Academy Sci.*, 1979, 611-619.

APPLICATION OF BACKSCATTER KIKUCHI DIFFRACTION FOR PHASE IDENTIFICATION
AND CRYSTAL ORIENTATION MEASUREMENT IN MATERIALS

D. J. Dingley, R. Mackenzie, and K. Baba-Kishi

The first backscatter Kikuchi diffraction patterns recorded directly on photographic film in a scanning electron microscope were obtained in 1981. The considerable detail and wide angular range covered in each pattern suggested an immediate application for phase identification (Fig. 1). On-line orientation measurement and internal strain measurement followed later. Since then further development has been along two lines: (1) the implementation of on-line and off-line computer methods, (2) application to a varied range of materials including metals, ceramics, semiconductors, and minerals, to establish the limitations of the technique.

Origin of Backscatter Kikuchi

The principles of backscatter Kikuchi diffraction (BKD) are somewhat different from those of the more usual diffraction methods. To obtain the patterns the incident beam is focused and held stationary on a selected area of the specimen. Beneath the surface, electrons diverge into the specimen to strike crystal planes at all possible angles of incidence. Some satisfy the Bragg condition for diffraction and pass out of the crystal to form the diffraction pattern. To visualize this process consider a divergent point source of monochromatic radiation emerging from a point close to the specimen surface (Fig. 2). The rays that satisfy the Bragg condition for a particular set of planes are seen to lie on the surface of a cone. The cone axis is normal to the planes and the cone semi-angle is equal to $\pi/2$ minus the Bragg angle. There are in fact two cones for each set of planes, corresponding to diffraction from the upper and lower surfaces of the planes, respectively.

Outside the crystal one images the cones by placing a photographic film or scintillating screen to intercept them. The recorded pattern thus consists of pairs of conic sections (hyperbola), the distribution of which describes the arrangement of crystal planes and the intensities of which are a function of the crystal structure. The basic elements for phase identification and crystal orientation measurement are therefore inherent in the pattern. However, considerable caution has to be exercised in interpretation because of dynamical diffraction effects, geometrical distortion due

to the form of projection, and an angular resolution in the pattern of no better than 0.2° .

In practice the divergent source is of course not monochromatic but contains all electron energies from a few electron volts to the incident beam energy. However, the spread is localized into two regions, one below 100 eV and the other within a few hundreds of eV below the incident beam energy. Only electrons in the latter region contribute to the pattern; all others produce a diffuse background. This spread in energies contributes to the line broadening and is the chief factor limiting the precision of lattice parameter measurements to 1%.

Likewise, the electron source is not an infinitesimal point. It has a radius equal to that of the incident beam plus the radial distance traveled by the electrons before they have lost between 100 to 200 eV of energy; i.e., that energy loss limit above which they no longer contribute significantly to the diffracted intensity. The Bethe equation can be used to calculate this range.⁴ For a material such as copper and for an incident beam energy of 30 keV it is found to be of the order 20 nm. In a standard SEM, fitted with a tungsten filament, the minimum source size under these conditions is therefore typically 50 nm. Patterns have in fact been obtained from single gold particles of this size. However, in a bulk polycrystalline sample the smallest individual grain from which patterns have been obtained is 200 nm.⁵

Experimental

Pattern Detection. The essential SEM specimen chamber geometry is shown in Fig. 3. The specimen is inclined so that the surface normal points 70° from the incident beam direction, which allows the backscattered electrons to scatter forward onto the imaging screen or photographic film positioned vertically 40-50 mm from it. The phosphor is viewed from the rear with a low-light-level television camera system capable of producing a useful image at illumination levels of 10^{-4} lux. This is the light level available on the screen when the SEM is operated under normal conditions of 30 keV accelerating voltage and beam current of 1 nA. The screen is placed close to the specimen to insure a capture angle larger than 50° , though some compromise between closeness and size of screen has been found necessary to avoid interference with the normal specimen stage movements. Both P20 polycrystalline phosphor and YAG single-crystal screens have been tried; the former is preferred because of its better response at low electron energies.

This work was done at the H. H. Wills Physics Laboratory, University of Bristol, Bristol, England BS8 1TL. R. Mackenzie is now at the Clarendon Laboratory, University of Oxford, Parks Road, Oxford; K. Baba-Kishi is now at the Physics Department, University of Essex, Colchester.

Both screen types were coated with 5 nm of aluminum to avoid electrostatic charging.

Direct Recording of Backscatter Kikuchi Patterns on Film. It was noted as early as 1979 that the quality of BKP recorded directly on film was very much better than that observed directly on a phosphor screen even after image processing.¹ A multiplate film camera was thus built to expedite recording of such pictures. The camera was integral with the specimen chamber and held ten cassettes loaded with cut sheet film. A cassette was moved into the record position directly in front of the phosphor screen by sliding it along guide rails with the use of a push rod operating through a vacuum seal. Withdrawal of the cassette automatically loaded the next one onto the guide rails. When in position, the film lay 42 mm from the specimen. The angular range captured by the diffraction patterns was 90° across corners.

Microscope Operation. Apart from the requirement to tilt the specimen toward glancing incidence when obtaining a diffraction pattern, the operational procedures of the SEM were unaltered. It was found convenient to mount the specimen in a special holder so that it was permanently inclined at a tilt angle of 70° to the incident-beam direction. The specimen is then imaged in secondary-electron or backscattered modes as appropriate, though the backscattered signal from such a steeply inclined specimen is often weak. In the latter case the image could be improved by positioning of the backscattered detector in a forward scattering position in front of the specimen. A diffraction pattern is obtained by simple positioning of the incident beam as a stationary probe on the selected area. No other microscope conditions have to be altered. Typical settings for TV imaging are 30 keV operating voltage, 1 nA beam current, 40 nm probe diameter. The settings for direct recording on film are 30 keV operating voltage, 0.5 nA beam current, 20 nm probe diameter, 10 s exposure. These figures relate to a JEOL 840 SEM used with a tungsten filament.

Sample Preparation. One advantage of BKD in the SEM over diffraction methods in the transmission electron microscope is that the patterns can be obtained from bulk samples. Sample preparation is thus in comparison a relatively straightforward procedure and normal metallographic methods can be employed. However, as the patterns originate within 50 nm of the surface, it is necessary to remove any mechanical deformation, oxide films, or contaminants produced during the preparative treatments. A clean surface is essential for high-quality images.

Metals were prepared by standard metallographic procedures with a final polish using 1 µm diamond paste. The samples were then either electrochemically polished, or, for hard materials, mechanically polished further in a colloidal suspension of 20nm-diameter silica particles in an alkaline solution. Semiconduc-

tors were prepared as for metals with a final chemical polish in a suitable reagent. Brittle materials, which included many minerals, were simply fractured and the fresh fracture surface was examined. However, for quantitative work a flat surface was required and was prepared as for metal samples finishing with the colloidal silica solution. In some cases ion beam milling was preferred. It removed any residual mechanical polishing damage and also etched the surface to reveal the microstructure.

Extreme electrostatic charging of insulating materials during examination in the SEM prevented the patterns from being observed. However, the high tilt of the specimen needed for BKD was often found to reduce these effects as did operating at low voltage. Together, this meant that in nearly all cases the diffraction patterns could be observed for at least a limited period. Coating the specimens to avoid charging was not always a viable option as the coating also reduced the pattern contrast. Carbon, aluminum, and titanium coatings were tried.

Techniques

On-line Texture Analysis. Use of the diffraction system for texture analysis has now been applied to cubic, hexagonal, trigonal, and orthorhombic crystals.^{2,6,7} The technique employed is basically the same in each case and requires superimposing a movable cursor generated from a microcomputer onto the TV image of the diffraction pattern (Fig. 4). The cursor is positioned successively at different zone axes in the diffraction pattern such as at A in the figure, which permits their positions in terms of screen coordinates to be measured. From these data the pattern is automatically identified and indexed, and the grain orientation is determined. To carry out the requisite calculations, the positions of the zone axes must be described in terms of vectors drawn from the origin of the diffraction pattern in the specimen, the electron source point, onto the screen.

Three coordinate systems are thus set up, one to define the screen coordinates, one centered at the source point defining the microscope coordinate system, and a third to define the specimen orientation (Fig. 5). We label the screen system XS, YS, ZS; the source system, RX, RY, RZ; and the specimen system, XT, YT, ZT. The origins of the source system and the specimen system coincide. The origin of the screen system is the diffraction pattern center. The projection of the source point onto the screen defines the pattern center: RX, RY, RZ are made parallel to the XYZ specimen shift movements. RY is parallel to the optic axis of the microscope. XT is horizontal in the specimen surface and ZT normal to the specimen surface. With the specimen facing the screen and tilted so that ZT is 20° from the optic axis of the microscope, the relationships between the systems are XT parallel to XR

and XS, YR parallel to YS, and ZM to ZS. ZT lies in the YR-ZR plane inclined 20° above the ZR axis. Experimentally the relationships were determined by calibration.

Calibration is carried out with a silicon single-crystal wafer oriented with [001] normal to its surface, mounted into the microscope on a pretilted holder and rotated so as to face the phosphor screen. The pretilt is 70.5° from the horizontal, which brings the [114] crystal direction (zone axis) normal to the imaging screen. If a cleaved edge of the silicon is placed in the horizontal plane, the (110) crystal plane lies vertically. The position of the [114] zone axis thus defines the pattern center and the line joining the [114] and [111] zone axes defines the vertical axis, i.e., YS and YM. The specimen to film distance d is given by

$$d = R/(\tan \theta)$$

where R is the distance in screen coordinates between the [114] and [111] axes and θ is the angle between them. The pattern center and d together define the position of the origin of the reference and specimen axes systems in terms of screen coordinates. From this information each zone axis located in the diffraction pattern can be redefined in terms of vectors drawn from the origin of the reference system. The arc cosine of the scalar product of two such vectors gives the angle between them. Normally, the indexes of the first zone axis selected are input to the computer. From the measured angle between the two zone axes the indexes of the second axis can then be found by reference to a look-up table of known interzone angles for that particular crystal. In some instances, by locating more than two zone axes, one can identify the crystal indexes of the zone axes without the need to input those of the first zone axis. This identification is achieved by comparing the measured angles with those in the look-up table and interchanging trial indexing until a consistent match is produced. However, because the error in interaxis measurement was no better than 1° , and pairs of interaxis angles are often the same within this limit, unambiguous identification could not always be achieved. The former method is thus preferable.

Having identified two zone axes, one can calculate an orthogonal set of crystal directions by taking successive vector products. Let the two zone axes, in terms of crystal vectors, be denoted by the vectors $M1$ and $M2$, and in terms of vectors referred to the reference coordinate system by $S1$ and $S2$, respectively. The orthogonal set in terms of crystal coordinates is given by $M1$, $M1 \times M2$, $-M1 \times M2 \times M1$. Similarly, in terms of the reference coordinate system, corresponding vectors are $S1$, $S1 \times S2$, $-S1 \times S2 \times S1$. The angles $w1$, $w2$, $w3$, respectively, between these vectors and the screen normal z are then given by the arc cosine of the scalar products $S1 \cdot z$, $S1 \times S2 \cdot z$ and $-S1 \times S2 \times S1 \cdot z$. The vector z has components 0,0,1. The crystallographic vector $A1$ normal to the screen can

then be found by solution of the simultaneous equations $A1 \cdot M1 = \cos w1$, $A1 \cdot M1 \times M2 = \cos w2$, $A1 \cdot M1 \times M2 \times M1 = \cos w3$. Two further orthogonal vectors, the vertical and horizontal screen directions $A2, A3$, are similarly determined. The orientation of the diffraction pattern with respect to the screen is thus established and given by a matrix in which $A1, A2, A3$ are column vectors. The absolute orientation of the grain is then finally obtained by operating on the orientation matrix with a rotation matrix relating the reference coordinate system (which as described above was made parallel to the specimen axes) to the screen orientation.

When determining the orientation of hexagonal crystals an additional procedure is necessary to convert the standard four-index notation for the crystallographic directions into a three-index orthonormal notation.

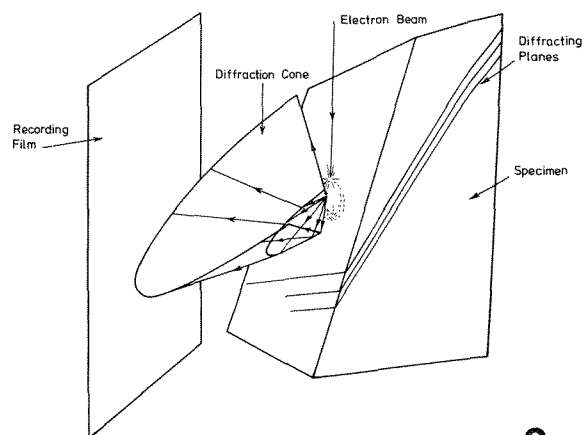
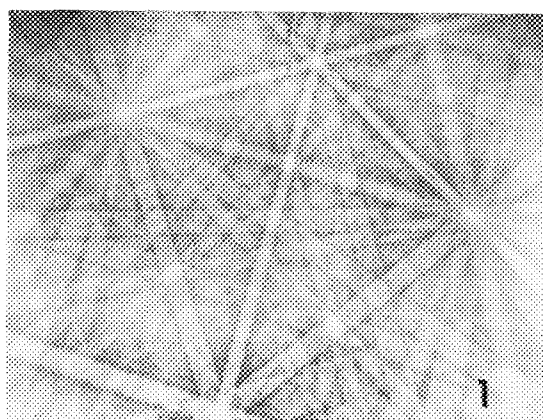
Examples of orientation distributions in copper and stainless steel obtained by this method are shown in Fig. 6.

The principal errors in measurement of the crystal orientation arise from the pixel size of the computer graphics system, nonlinearity of the television camera, and errors in the knowledge of the orientation of the specimen mounted within the microscope.

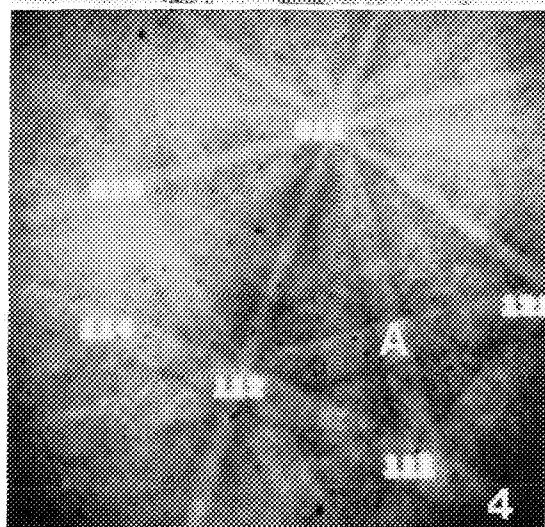
The angular range across one pixel varies according to the location of the pixel with respect to the diffraction pattern center. Close to the center it is 0.23° ; at the periphery of the pattern it is 0.9° . The nonlinearity of pin-cushion distortion of the camera is worst at the edges and can reach a maximum of 5 pixels. Experiment has shown that the sample can be located to within $\pm 1^\circ$ on repeated mountings in the specimen stage. Overall, if only zone axes close to the pattern center are used, the absolute orientation measurement can be within $\pm 1^\circ$. Relative orientation measurements can be obtained to a precision of about half of the above, since the error in location of the specimen in the microscope is eliminated.

Crystal Structure Measurement. The method of directly recording BKP's on film has been used mainly for obtaining point group and space group information. The interpretation of the patterns followed a prescribed routine but was by no means identical in each case. The general principles are outlined here. Details can be found in papers devoted to this aspect of the work.⁸⁻¹⁰

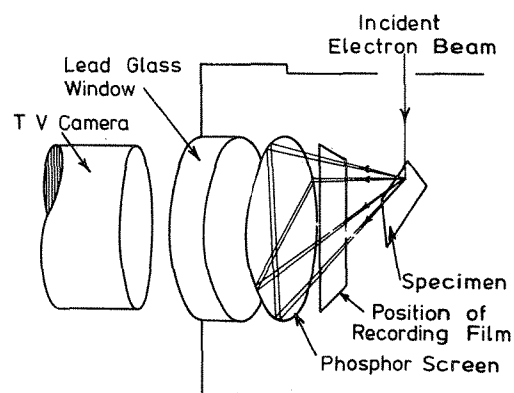
As with orientation determination, the first step was to determine the pattern center and specimen to film distance; the preferred method was again use of a silicon calibration specimen. In this case the pattern was recorded on film and the position of the [114] zone axis, which identified the pattern center as before, was found with respect to two fiducial points. The fiducial points were shadows cast from two pins rigidly fixed to the camera body so that they would always be in the same relative position on each exposure. The calibration diffraction pattern from silicon is



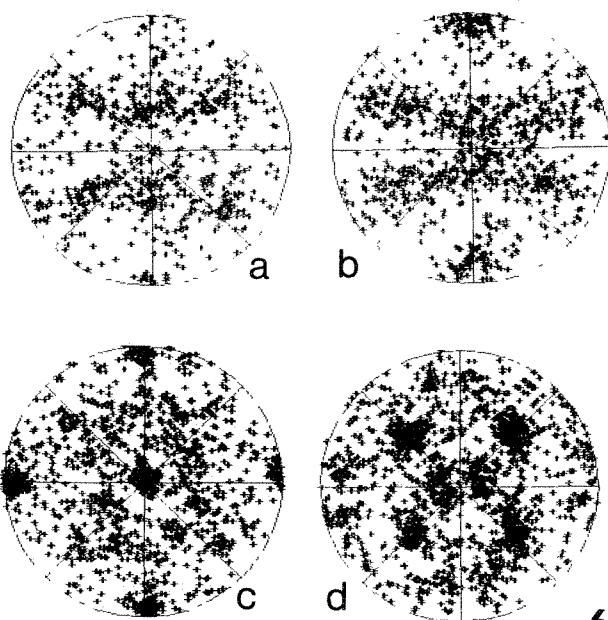
2



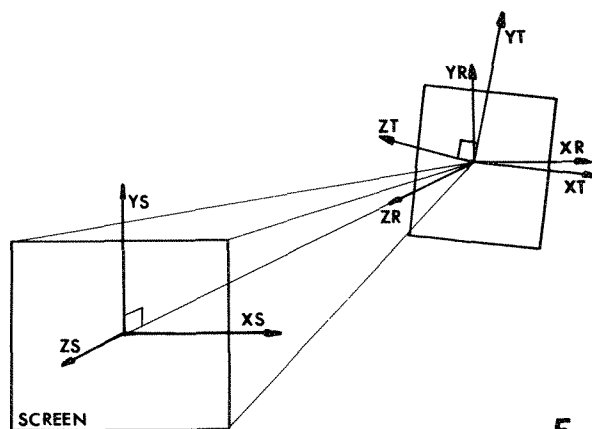
4



3



6



5

FIG. 1.--BKP from GaAs.
 FIG. 2.--Illustration of formation of diffraction cones from point source of divergent beam radiation.
 FIG. 3.--Illustration of specimen, screen, camera arrangement for imaging BKP in an SEM.
 FIG. 4.--Photograph of TV screen with live image of BKP. Pattern has been indexed by computer following orientation determination.
 FIG. 5.--Illustration of coordinate measuring systems for on-line interpretation of BKP.
 FIG. 6.--Stereographic pole figures showing plane orientations in annealed copper and stainless steel: (a) [100] copper, (b) [111] copper, (c) [100] stainless steel, (c) [111] stainless steel.

shown in Fig. 7 and a montage of two diffraction patterns from zinc in Fig. 8. A brief outline of the analysis of the zinc pattern follows to illustrate the method for space group identification. It is conducted as though the structure were unknown.

In the analysis of the pattern it was frequently necessary to measure interzone and interplane angles. This measurement was achieved in the same way as for on-line interpretation of patterns, i.e., by measuring the coordinates of zone axes with respect to the pattern center and transposing them into vector form with reference to a coordinate system located at the point where the pattern originates in the speci-

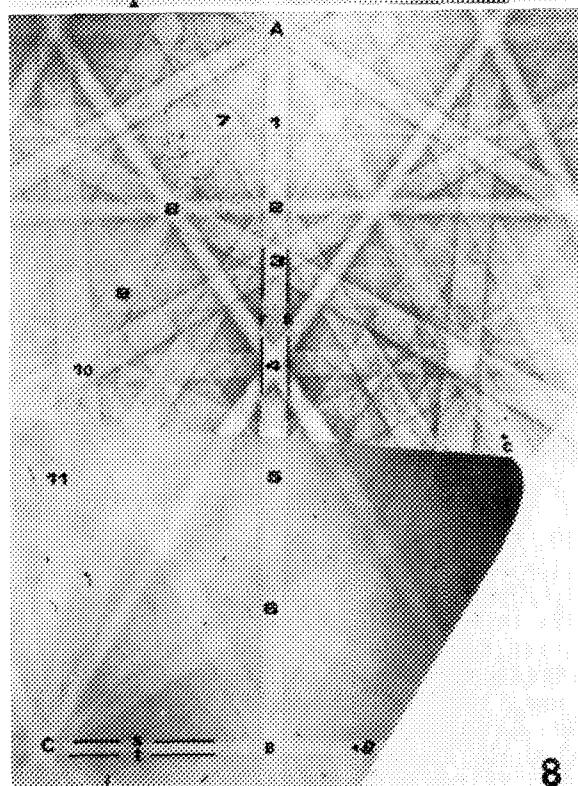
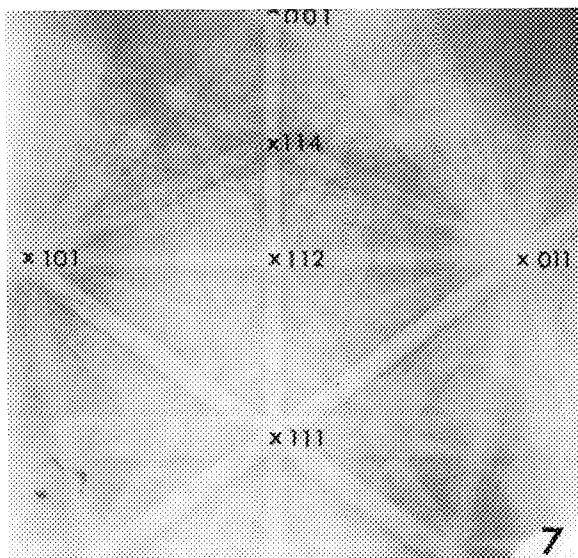


FIG. 7.--BKP from silicon used for calibration purposes.

FIG. 8.--Montage of two BKP from zinc.

men. The interzone angles were obtained from the scalar product of the vectors. The interplane angles were calculated by first obtaining the cross product of two vectors in each plane and then taking the scalar product of the resultants.

The BKP in Fig. 8, with a total angular range of 120° , is a montage of two patterns from a freshly cleaved zinc crystal. To obtain the crystal point group we begin with analysis of the upper half of the montage. The easily recognized prominent zone axis, labeled A, is characterized by the intersection of six mirror planes. The interplane angles were found to be 30° . The zone axis A must therefore be a hexad, so that the only possible point groups are $6mm$ or $6/mmm$. To distinguish between them the Kikuchi band 90° from A and passing through C B was examined and found to be a mirror. Zone axes C and B were diads so that the point group was $6/m\ 2/m\ 2/m$, i.e., $6/mmm$. As zone axes A must have the hexagonal index $[0001]$, zone axes B or C could be either $[1010]$ or $[2110]$. To distinguish between them we note that C has far more Kikuchi bands passing through it than B, which means that there are more low-index planes normal to C. Inspection of a standard stereographic figure shows that if we include all reflections with indexes lower than those given by the condition $h^2 + k^2 + l^2 = 21$, then $[2110]$ has 9 planes normal to it and $[1010]$ has 5. It is likely therefore that zone axis C is $[2110]$. To confirm this result, the interaxis angles between each of the zone axes labeled (1-11) and A were measured and listed as in Table 1. The d-spacings of the Kikuchi lines rs st were next calculated and found to be 0.13 and 0.25 nm, respectively. The Kikuchi line rs was labeled as (1210) so that the calculated lattice parameter a was found to be 0.26 nm. Likewise, st was labeled as (0001) , giving the c parameter as 0.25 nm. The c/a ratio so found was then used to calculate the interaxes angles between zone axes (1-11) and A. The second column of Table 1 shows the values obtained. If the indexing had been correct a direct correspondence between measured and calculated angles would be observed. In this first attempt no correspondence exists. However, a retrieval with st relabeled as (0002) shows good correspondence. We conclude that we have arrived at the correct indexing and that the correct value of the c parameter is 0.5 nm and the c/a ratio 1.92. There are now sufficient data to simulate the diffraction pattern using a suitable computer program. A line-by-line comparison is now carried out and lines present and absent (Table 2). It is seen that the condition for reflections present specifies a primitive Bravais lattice with a c glide parallel to (1100) and a 6 screw axis parallel to $[0001]$. The space group is therefore $p6_3/mmc$.

Similar analyses have been carried out on a large number of crystals taken as specimen samples of the 7 crystal systems and 32 point groups. It was found possible to distinguish

TABLE 1.--Summary of measured and calculated inter-axes angles for zinc between [001] (A) and zone axes X. (drs = 0.13 nm, dst = 0.25 nm, calculated angles.)

zone axes X	Measured angles	rs = (1 $\bar{2}$ 10) st = (0001) c/a=2 5/2 6=0.96	rs = (2 $\bar{4}$ 20) st = (0001) c/a=2 5/5 2=0.48	rs = (1 $\bar{2}$ 10) st = (0002) c/a=5/2=1.92
1	8	{11 8 [10 $\bar{1}$ 5] 14.6 [10 $\bar{1}$ 4]	22 6 [10 $\bar{1}$ 5] 27 5 [10 $\bar{1}$ 4]	6 0 [10 $\bar{1}$ 5] 7 5 [10 $\bar{1}$ 4]
2	15 5	27 5 [10 $\bar{1}$ 2]	46 2 [10 $\bar{1}$ 2]	14 6 [10 $\bar{1}$ 2]
3	20 5	34 8 [20 $\bar{2}$ 3]	54 3 [20 $\bar{2}$ 3]	19 2 [20 $\bar{2}$ 3]
4	27 5	46 2 [10 $\bar{1}$ 1]	64 4 [10 $\bar{1}$ 1]	27 5 [10 $\bar{1}$ 1]
5	39 0	{57 4 [30 $\bar{3}$ 2] 54 3 [40 $\bar{4}$ 3]	73 0 [30 $\bar{3}$ 2] 70 2 [40 $\bar{4}$ 3]	37 0 [30 $\bar{3}$ 2] 34 8 [40 $\bar{4}$ 3]
6	58 5	72 3 [30 $\bar{3}$ 1]	80 9 [30 $\bar{3}$ 1]	57 4 [30 $\bar{3}$ 1]
8	90.0	90 0 [10 $\bar{1}$ 0]	90 0 [10 $\bar{1}$ 0]	90 0 [10 $\bar{1}$ 0]
7	14 0	24 7 [2 $\bar{1}$ 16]	42 6 [2 $\bar{1}$ 16]	13 0 [2 $\bar{1}$ 16]
8	26 0	42 6 [2 $\bar{1}$ 13]	61 4 [2 $\bar{1}$ 13]	24 1 [2 $\bar{1}$ 13]
9	36 0	54 00[2 $\bar{1}$ 12]	70 1 [2 $\bar{1}$ 12]	34 5 [2 $\bar{1}$ 12]
10	44 0	61 44[4 $\bar{2}$ 23]	74 8 [4 $\bar{2}$ 23]	42 6 [4 $\bar{2}$ 23]
11	55 0	70 06[2 $\bar{1}$ 11]	79 7 [2 $\bar{1}$ 11]	54 0 [2 $\bar{1}$ 11]
C	90 0	90.00[2 $\bar{1}$ 10]	90 0 [2 $\bar{1}$ 10]	90 0 [2 $\bar{1}$ 10]

9 of the 11 Laue groups (6mm, 4mm, 3m, 2mm, m, 6, 4, 3, and 2) so that combinations of these groups alone allow us to distinguish a total of 27 of the 32 point groups classes. That leaves 6, 4, 3 1 and 1 as extremely difficult cases. For some classes, although it was possible to identify at least one crystal in the class, other crystals in the same class could not be distinguished. Important examples include crystals of the 111 V and 11 VI compounds. For instance, it was not possible to observe the loss of symmetry of the tetrad axes from 4mm to 2mm in GaAs. However, SbAs, which also has the point group 2mm, could be distinguished. The difficulty with GaAs arises from the closeness in the atomic number of the two elements. For a more detailed discussion of this point the reader is referred to Ref. 11.

The major limitation of the technique is a lack of precision in lattice parameter measurement. Numerous methods of measurement have been attempted based on those developed earlier for divergent beam x-ray diffraction,¹² but the best that could be achieved was 1 part in 300. More routinely a precision of 1 part in 50 was obtained.

Conclusions

The above account has shown that backscatter Kikuchi diffraction provides a versatile tool for crystallographic studies in materials analysis. It has been shown that patterns are easy to obtain and that on-line analysis for texture studies and analysis of directly recorded photographs for structure determination can be accomplished.

TABLE 2.--Observed and absent reflections for zinc.

Class of reflection	Observed reflections	Absent reflections	Conditions for reflection	Cause of Condition
hki 1	1 $\bar{2}$ 12, 1321, 1210, 1011, 1012, 1010, 2020, 1012, 1101, 2203, 1102, 0113, 0112, 0222, 0111, 0221, 0112, 0113	None	all orders	primitive Bravais lattice
h \bar{h} 01	1102, 1101, 2201, 2203, 1102	None	all orders	primitive Bravais lattice
hh2 \bar{h} 1	1120, 1122, 1124	1121	l = 2n	axial glide c parallel to (1100)
0001	0002	0001	l = 2n	6 ₃ screw axis parallel to [0001]

References

1. D. J. Dingley, L. Baker, and L. Hunnings, *Electron Backscattering Patterns from Semiconductor Materials*, Institute of Physics Conf. Series 61: 63, 1981.
2. D. J. Dingley, M. Longden, J. Weinbren, and J. Alderman, "On-line analysis of electron backscatter Kikuchi patterns: 1. Texture analysis of polysilicon," *Scanning* 1: 451, 1987.
3. R. A. D. Mackenzie and D. J. Dingley, "Computer analysis of diffuseness in Kikuchi patterns" (Proc. XIth Int. Cong. on Electron Microscopy), *J. Elect. Microscopy* Supplement 35: 709, 1986.
4. A. E. Bethe, *Physics*, Springer, Berlin: 24: 273, 1933.
5. J. Harase et al., "Study of microtexture using SEM and electron backscattering," *Jap. Inst. of Metals Conf. Series* 62: 502, 1987.
6. D. J. Dingley, "On-line micro texture determination," *Eighth Int. Conf. on Texture of Materials*, Am. Metallurgical Soc., 1987, 189.
7. D. J. Dingley, N. Gravestock, and H. Rothstein, "Texture determination in deformed rocks," *Inst. of Phys. Conf. Series* 90: 139, 1987.
8. D. J. Dingley and K. Baba-Kishi, "Use of electron backscatter patterns for determination of crystal symmetry elements," *Scanning Microscopy* 11: 383, 1986.
9. D. J. Dingley and K. Baba-Kishi, "Extended use of EBSP for crystallography in the SEM," (Proc. XIth Int. Cong. on Elect. Microscopy), *J. Electron Microscopy* Supplement 35: 753, 1986.
10. K. Baba-Kishi and D. J. Dingley, "Application of EBSP to the investigation of nickel sulphide crystals," *ibid.*, p. 741.
11. K. Baba-Kishi and D. J. Dingley, "Backscatter Kikuchi diffraction in the SEM for the identification of crystallographic point groups," *Scanning* (in press).
12. S. Biggin and D. J. Dingley, "A general method for locating the x-ray source point in Kossel diffraction," *J. Appl. Cryst.* 10: 376, 1977.

SURFACE DISPLACEMENT MEASUREMENTS BASED ON DIGITAL IMAGE PROCESSING OF MICROGRAPHS

M. R. James

To investigate a variety of micromechanics problems experimentally, we have developed techniques based on stereoscopic analysis of pairs of optical or SEM micrographs to obtain the surface displacements generated by either mechanical or thermal load.^{1,2} Although stereoscopy is a powerful means to measure the displacements, it suffers from being tedious and providing incomplete data. In this paper we describe a system for measuring these displacements based on digital image cross correlation that overcomes the limitations of stereoscopy. The system is capable of measuring both in-plane and out-of-plane displacements to accuracies approaching 1 nm over submicron spatial regions.

HASMAP

If one micrograph of a surface is taken before a load cycle and the other taken during loading or afterwards, the observed displacement field that differentiates the pair is a direct consequence of the surface deformation. To measure the relative displacements between the two micrographs accurately and conveniently, we have built a digital image processing system nicknamed HASMAP (*High Accuracy Strain MAPper*) as shown in Fig. 1. We achieve our desired spatial resolution by placing micrographs taken before and after deformation on a computer-controlled translation table.

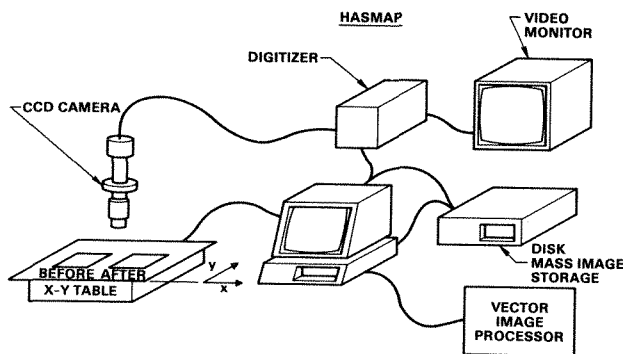


FIG. 1.--Schematic illustration of HASMAP.

The reference micrograph is divided into an array of analysis windows (Fig. 2). A low-power (1-3 \times) lens in front of the video camera magnifies the micrograph so that a typical 512 \times 480 pixel field of view might correspond to approximately a 1 \times 1 cm area on the micrograph (Fig. 2b). The displacement is found

The author is at the Science Center, Rockwell International Corp., Box 1085, Thousand Oaks, CA 91360.

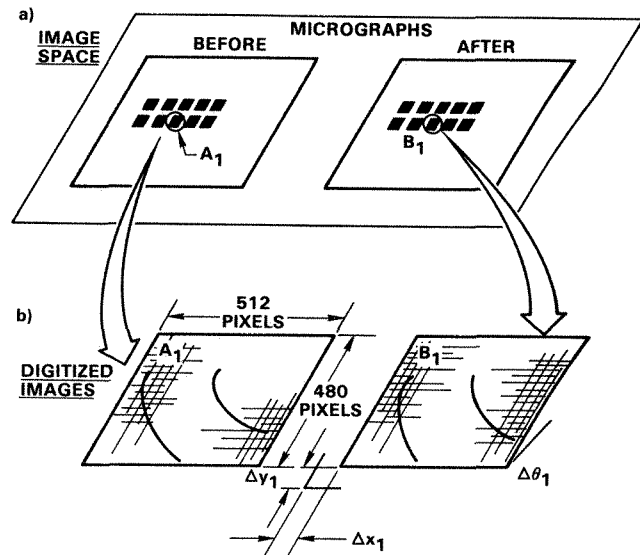


FIG. 2.--(a) Set of windows on equally spaced grid points on reference micrograph to be mapped to corresponding areas in post-deformation view; (b) stored digital images of A_1 and B_1 on which cross correlation is run.

between the image in each window and its twin in the post-deformation micrograph (e.g., A_1 and B_1 in Fig. 2b) by computing the cross correlation function of the two images. The offset of the peak of this function is the displacement estimate. The cross-correlation algorithm used by HASMAP is based on a two-dimensional fast Fourier transform approach as described in Ref. 3. To minimize errors, as close registration of the images as possible must be achieved before the final displacement calculation is made. An iterative scheme is used in which the stage is moved by the calculated displacement until the images in the two windows match so closely that the relative window displacements would not change with further iteration. The displacement can then be determined by the table motion and the residual displacement from the last cross-correlation calculation.

Sources of Error

The final accuracy depends on the precision of the cross-correlation calculation, the stability and accuracy of the translation table, and the quality of the micrographs. These factors have been analyzed in detail in Ref. 3. The largest errors come from recording of the micrographs. Nonuniformity in magnification in the optics of optical microscopes produces distortion unless the micrographs are taken in exactly the same area of the specimen. Careful

attention to focusing variations and phase changes must also be made. Typically, displacement sensitivity of ± 20 nm over $10\mu\text{m}$ areas can be achieved with $500\times$ optical micrographs.

With SEM images, magnification instability and the division of the image into scan lines further degrades accuracy. Small magnification changes easily occur when the sample is taken out of the microscope between the "before" and "after" micrographs are recorded. In situ mechanical loading and thermal heating stages are useful to minimize this error. The useful magnification range is limited by the need to encompass sufficient detail and contrast for the cross-correlation peak to have a good peak-to-background ratio. Typically, $\pm 2\text{ n}$ displacement over $1\mu\text{m}$ regions on the specimen can be obtained with $5000\times$ micrographs.

Out-of-plane Displacements

When the micrographs are recorded by viewing normal to the specimen surface, the in-plane displacements are captured. By comparing micrographs taken of the specimen at a tilt, one obtains a mixture of in-plane and out-of-plane components. Thus, by recording two views of the surface before and after deformation, one can calculate both in- and out-of-plane values.⁴ The large depth of field of the SEM makes this approach especially attractive. Foreshortening of the tilted images can be handled digitally so that displacements can be obtained at the same locations in the tilted and untilted micrographs.

Conclusions

A Fourier transform cross-correlation approach for the calculation of displacements between digitized images coupled with error-minimization procedures allows subpixel displacements to be determined in photographic images. Both orthogonal components of displacements are obtained simultaneously. The data can be obtained over a sufficiently dense pattern so that perspective representations of the deformation can be created by digital warping of the reference image to enhance displacements invisible to the unaided eye, as described in Ref. 3.

References

1. W. L. Morris, R. V. Inman, and M. R. James, "Measurement of fatigue-induced plasticity," *J. Matls. Sci.* 17: 1413, 1982.
2. M. R. James and W. L. Morris, "The effect of microplastic surface deformation on the growth of small fatigue cracks," in R. O. Ritchie and J. Lankford, Eds., *Small Fatigue Cracks*, TMS, 1986, 145.
3. M. R. James, W. L. Morris, and B. N. Cox, "A high-accuracy automated strain field mapper," *Expt. Mech.* (in press).
4. W. L. Morris, R. V. Inman, and B. N. Cox, "Microscopic deformation in a heated unidirectional graphite/epoxy composite," *J. Matls. Sci.* 24: 199, 1989.

MICROMECHANICAL CHARACTERIZATION OF NEAR-SURFACE LAYERS

R. J. Bourcier

This paper reviews several techniques available to the experimenter to characterize the mechanical properties of near-surface layers of engineering materials. The test methods examined are microtensile testing, bulge testing, ultralow-load indentation testing, and microfabricated test structures. The applicability of these techniques and their advantages and difficulties are examined. Special emphasis is given to recent developments in ultralow-load indentation testing and microfabricated structures.

The current high level of interest in the mechanical properties of near-surface layers has been driven largely by three sources. The first is the ongoing search for increased mechanical efficiency, a problem controlled by the wear and friction of contacting materials. The attempt to minimize friction and wear of structural materials has led to the development of a variety of advanced methods to modify the mechanical properties of material surfaces. One of the most effective and promising techniques is ion implantation. A specific example of this technology, which is now seeing engineering application, is the implantation of nitrogen or carbon and titanium into steels.¹⁻³ Such implantation layers are commonly only a few hundred nanometers thick and cannot usually be separated from the underlying material, which presents a difficult problem of how to perform mechanical tests to determine their properties.

In the second case, the application of thin films and ion implantation to the fabrication of microelectronic devices has brought with it another unique set of testing difficulties. In large-scale integrated circuits, implanted layers may again extend only 100 nm or so into the surface of the silicon substrate. Sputtered and evaporated metal films approximately 1 μm thick are deposited onto the surface of these devices to provide electrical interconnects. The successful development of solutions to

problems such as stress voiding of interconnect lines^{4,5} will require careful mechanical characterization of the metal lines and of the semiconducting and dielectric layers that make up an LSI device.

The third case is the very recent development of micromachining technology for sensors and actuators.⁶⁻⁹ This fast-growing technology has introduced the need for test methods to measure the mechanical properties of micromechanical elements lithographically fabricated from silicon. Such measurements are necessary in order to set limits on the mechanical loads that can be expected of these extremely promising small machines.

The mechanical testing of relatively thick films or layers (say, $>5 \mu\text{m}$) is perhaps only slightly more difficult than the testing of bulk materials. Standard techniques such as tensile testing and microhardness testing can be readily applied to such materials. However, for films or layers thinner than 5 nm, testing is much more complex. The possibility of mechanical damage during the handling of very thin films and of very small specimens that have been liberated from their substrate becomes a concern. Sufficient sensitivity in the measurement of loads and displacements is difficult to achieve. This problem is particularly acute in indentation testing, where insufficient resolution makes it impossible to extract film properties from those of the combined film/substrate system. In general, complex measures must be taken to overcome these difficulties.

Very recently, a detailed bibliographic review of the mechanical testing of thin films and near surface layers has appeared.¹⁰ Rather than simply duplicate the bulk of this comprehensive work, the present paper focuses on a discussion of the relative merits and difficulties of the most popular test methods for thin films and ion-implanted surfaces, and provides an introduction to new techniques that show promise to advance the state of micromechanical testing. Ultralow-load indentation techniques and microfabricated test structures receive special emphasis, due to recent developments in the application of both techniques. These developments promise to extend the utility of these techniques to specimens that could not be successfully tested previously, and provide a still wider choice of tools to the experimenter.

Discussion

Microtensile Testing. Microtensile testing is probably the most mature test method considered here.¹¹⁻¹⁴ Conceptually, it is simply a small-scale version of everyday tensile test-

The author is at Sandia National Laboratories, Box 5800, Albuquerque, NM 87185. He should like to acknowledge collaborations and conversations with a number of colleagues. Specifically, the opportunity to work with C. M. Stone, F. G. Yost, A. D. Romig Jr., S. M. Myers, and D. H. Polonis is greatly appreciated. The assistance of D. T. Schmale in the development of our ultralow-load indentation test system and the execution of countless tests is gratefully acknowledged. Also, numerous conversations with W. D. Nix and W. C. Oliver on indentation testing have been very enlightening. This work was supported by the U.S. Department of Energy under contract DE-AC04-76DP00789.

ing used for the examination of bulk material specimens. However, because of the scale of specimen examined, unique problems are introduced into what is, in concept, a very simple test. In a general sense, several of these problems apply to other test techniques to be discussed; they are therefore treated in some detail here.

Specimen fabrication and mounting must be performed with care if meaningful test results are to be obtained--as is obviously true for testing at any scale, but is particularly difficult to achieve for the small, delicate samples with which we are concerned. Separation of the test specimen from its underlying substrate is the first problem to be overcome. Thin-film specimens are commonly deposited onto cleaved rocksalt crystals^{12,15} or mica¹⁶ and then removed. Mounting of the specimen in the load frame must then be addressed. Gripping of specimens has been accomplished by gluing;^{11,12,15} friction;^{13,14,16} or, for extremely delicate samples, van der Waals forces.¹⁷ The technique used must allow the application of sufficient force to deform the specimen gauge section, but not induce enough damage into the grip end so as to precipitate a failure outside the gauge section. Finally, tensile deformation is imposed on the specimen, either by means of a "conventional" mechanical drive system¹³⁻¹⁵ or electromagnetically.^{11,12,16,17} The choice of loading technique can influence the test results. One example is yield phenomena such as load drops, which are not easily captured by a load control test (typically the case for electromagnetic systems).

At first glance, microtensile testing holds the potential to provide a true measure of the mechanical properties of a near-surface layer. Unfortunately, several difficulties have kept the technique from realizing this apparent potential. Above all, the technique is fundamentally limited to thin films that can be removed from their underlying substrate. To meet this criterion, it is frequently necessary to deposit the film to be tested on a substrate other than the one of greatest interest. This choice can influence the resulting microstructure and hence the mechanical properties. Also, because of this constraint, near-surface layers modified by ion implantation or some related technique, which cannot be separated from the underlying substrate, are clearly not amenable to microtensile testing.

In most applications, one is interested in the response of a film while it is attached to a substrate. Removal of the film will relieve any residual stresses the film may contain due to mismatch with the substrate. The resulting strength of the now-unstressed film is different from the strength one would measure for the film in the attached state.

An additional problem that can arise due to residual stresses is that the film may curl when removed from the substrate. Such distortion makes a film more difficult to handle and much more difficult to mount, and obscures measurement of small-strain tensile behavior. As

the film straightens, the load-elongation record of the test reflects the reduced load required to straighten the film instead of stretching it. Thus the test results are colored until the film is fully straightened. As small-strain behavior is the response best examined with microtensile testing, this problem can be particularly vexing.

Another difficulty is that the technique generally requires thin sheet-type specimens whose aspect ratios of width to thickness and length to thickness are very large. Such a configuration leads to a test specimen that is prone to material and/or geometric instabilities and does not provide a good measure of the inherent ductility of the near-surface material. Thin-sheet tensile specimens cannot deform very far under pure uniaxial strain conditions; rather, the specimen localizes deformation into a very narrow region inclined to the tensile axis and deforms to failure under plane-strain conditions.

Also, because the specimens are small or of very large aspect ratio, they tend to be prone to damage during handling prior to the test. For a ductile specimen, this damage generally takes the form of plastic bending, introducing work into the specimen that obscures the actual small-strain behavior of the thin film. For high-strength or brittle specimens, shear banding or cracking may result, degrading the subsequent ductility and strength of the sample.

In addition, both edge preparation¹⁴ and axial alignment¹³ of microtensile test specimens can strongly influence the test results. Poor edge preparation typically leaves geometric defects in the sample that can lead to cracking or tearing. Misalignment introduces a buckling mode into the deformation of the test specimen, results in preferential straining along one edge of the sample, and obscures the true stress-strain response of the entire gauge section.

Bulge Testing. Bulge testing of thin films dates from the same time period as microtensile testing,¹⁸ but the technique has seen less use. As the test is conventionally performed,^{18,22} bulge test films are first deposited on a substrate from which they can be easily removed. Next, they are removed from that substrate, mounted in a test fixture, and pressurized to failure. By monitoring the applied pressure and the displacement of the bulged film, one can obtain a fairly good measure of the biaxial stress-strain response of the material.

One possible advantage of this technique over microtensile testing is that the potential for handling-induced damage is slightly smaller, as higher loads must be applied to deform the relatively wide and approximately square bulge test specimen than in the narrow-gauge section of a microtensile specimen. Also, there is no need to be concerned over alignment of the sample, and specimen edge conditions do not influence test results, since the edge is outside the central section of the stressed specimen.

A drawback to bulge testing is that the test data necessary to calculate fundamental mechanical properties are not easily measured, because strain measurements are not easily made for bulge tests of thin films. The basic difficulty is that any form of contacting displacement probe tends to influence the displacement it attempts to measure. Also, the probe may damage the specimen, causing it to fail prematurely. Optical methods of displacement measurement such as laser interferometry²⁰ may be used to avoid this problem.

Like microtensile testing, bulge testing requires removal of the test specimen from the underlying substrate. However, assuming that the experimental system used can accommodate such a specimen, the near-surface layer to be examined need not be necessarily *completely* separated from the backing material.²³ Instead, it is sufficient if the substrate is etched or milled away from the back to provide a circular film specimen still bonded to the substrate around its circumference. A sample prepared in this manner may be less susceptible to handling-induced damage and may allow the preparation of bulge test specimens from extremely thin films.

As in microtensile testing, one of the biggest problems associated with bulge testing is that the large film area sampled makes the specimens prone to strain localization due to local perturbations in film thickness or properties. Thus, although it is an extremely useful technique for obtaining the average biaxial small-strain response of a thin film, it is somewhat limited for studies of gross plastic flow.

Ultralow-load Indentation. Ultralow-load indentation is at present the most commonly used test method for examining the mechanical behavior of thin films and ion-implanted surfaces. The deformation response of near-surface layers most often of interest to the experimenter is straining due to the application of highly localized forces. As an example, this sort of localized deformation is generally present during sliding friction-plastic flow due to contact of microscopic surface asperities. Such deformation is not very well approximated by the tensile deformation of a large-aspect-ratio liberated thin film. Thus, the local deformation produced in ultralow-load indentation testing can have an advantage over the more global deformation field produced by microtensile or bulge testing.

Ultralow-load indentation tests are relatively simple to perform and can probe extremely thin surface layers (if a state-of-the-art test system is used). In addition, this test technique provides a very useful tool for examining the response of a near-surface layer to very large deformations. Because the indent formed can be extremely small (perhaps 100 nm or so), ultralow-load indentation can serve as a non-destructive screening tool and can be used to determine the effect of sequential modification processes on the mechanical response of a near-surface layer. The material to be tested need

not (and, indeed, in most cases should not) be removed from the underlying substrate, so that the material should not be damaged during handling. That also makes ultralow-load indentation extremely attractive for studies of ion-implanted surface layers. Also, any residual stresses in the near-surface material are not affected, and thus their influence on the mechanical response of the specimen is examined by the test.

In its basic form, ultralow-load indentation testing suffers from the inherent problem that "hardness" is not considered to be a fundamental mechanical property. Rather, it is simply a convenient measure of mechanical integrity. At best, it provides some indication of flow stress that may be useful for comparison with other materials or processes. Analytical models of the indentation test have been able to provide fair correlation between hardness and the compressive flow stress of the material being indented. However, this correlation is not perfect and indeed ultralow-load indentation testing alone cannot hope to measure the complete yield behavior of a material. These problems have limited widespread application of indentation testing for the determination of the mechanical properties of materials. Only recently have techniques been developed that promise to overcome some of these difficulties.

Ultralow-load indentation testing as practiced today is largely a result of the work of Pethica and co-workers.²⁴⁻²⁷ This group worked to develop an extremely sensitive test instrument and proper characterization of the influence of test parameters and indenter configuration on indentation test response. They demonstrated the validity of ultralow-load indentation as a tool to measure the mechanical response of a near-surface layer. Development of the technique has continued²⁸⁻³⁰ and useful methods now exist to calculate additional information about a material from the indentation test. A number of other workers have also played a role in developing highly sensitive test instruments and applying them to the study of material systems not amenable to examination by other methods.³¹⁻³⁹

Indentation tests are not readily interpreted to provide measures of fundamental mechanical properties. Both simple analytical techniques^{40,41} and complex numerical simulations^{42,43} have been used in the attempt to convert hardness values to plastic deformation behavior; neither has proved to be completely successful. Approaching the problem from the opposite direction, Bourcier et al.⁴⁴ showed that indentation load-depth results can be analyzed from the mechanical properties of the material being indented obtained by other mechanical tests. Specifically, it was shown that the load-depth history of indentation tests performed over a wide range of size scales and on a variety of materials could be successfully modeled by uniaxial compression test results as input for a large-strain finite model of a specimen indented by an elastic

indenter. Recently, we have applied this combined experimental/numerical approach to the study of the mechanical response of high-purity aluminum implanted with oxygen ions.⁴⁵ Fully annealed aluminum was implanted to a depth of approximately 500 nm with oxygen levels of 5, 10, and 20 at.%, followed by annealing at 450 and 550 C. Indentation load-depth results obtained with an ultralow-load test system developed at our laboratory³¹ revealed large differences between the responses of the unimplanted and implanted material. However, the resolution of the test system used did not allow us to measure the response of solely the implanted layer; rather, we were sampling the composite response of both the implanted layer and the underlying substrate. In order to determine more clearly the mechanical response of the implanted layer, a large-strain finite-element model of the implanted specimen was constructed. The stress-strain response of the substrate was measured by uniaxial compression testing of annealed samples of the aluminum substrate. Properties of the implanted material in the model were systematically varied until the resulting predicted load-depth response agreed with the experimental results. The strengths calculated in this manner for the implanted material were in good qualitative agreement with calculations based on conventional theories of particle and coherency strengthening in the implanted layer. Although this technique shows promise for the characterization of materials that do not readily lend themselves to any other test method, it is by no means a cure-all. The stress-strain response obtained by this technique (in its current state of development) is not unique. Indeed, what this method actually measures is the flow stress of the implanted layer at some average value of strain characteristic of the indentation test. Such a flow stress could in theory result from any one of an infinite number of combinations of yield strength and plastic stress-strain response. Determination of detailed information about the stress-strain *history* of a modified surface layer requires the use of some other technique.

Microfabricated Test Structures. Progress has been made in the past few years in the development of test methods/specimens for thin films that circumvent the difficulties of the test techniques discussed above. Basically all these approaches involve the fabrication of suspended beam-like microstructures that are either "self-testing" due to residual stresses⁴⁶⁻⁵¹ or gravity⁵² or mechanically deformed by an ultralow-load indentation tester.^{53,54} Several of these new designs are next discussed and compared with earlier techniques.

Simple Beams. The basic technique of measuring the mechanical properties of thin films by use of cantilever beam specimens is about 10 years old. The first work involved inducing resonant frequencies in the beam through the use of an oscillator attached to the substrate.⁵⁵ Recently, ultralow-load indentation test machines have been used to apply mechani-

cal displacements to the cantilever beams.^{56,57} A simple approach to the deformation testing of near-surface layers has recently been developed at Stanford University.^{53,54} It involves the fabrication by silicon micromachining techniques of cantilever microbeams of thin films that have been deposited on a silicon wafer. The beams are deflected in a commercially available ultralow-load indentation test instrument. The technique is most directly applicable to the determination of the elastic response of the test specimen, but may be also used to measure yield strength approximately. However, large-strain plastic deformation cannot be measured by this cantilever beam technique, since interpretation of the very localized bending that occurs in the plastic hinge of the specimen is not currently possible.

A New Microfabricated Test Specimen Design. Very recently, we have started development of a different beam-like specimen design at our laboratory.⁵⁸ The proposed test specimen is shown in Fig. 1. It is a free-standing doubly supported beam with two reduced sections that serve as tensile specimens. The wide center section of the beam serves as the point of contact for a specially fabricated diamond test probe, which displaces the sample into the etched cavity beneath it. Conceptually similar doubly supported beams have previously been fabricated from silicon.⁵⁹⁻⁶¹ It is suggested that the specimen proposed here should be etched from aluminum alloy thin films deposited on oxidized silicon wafers. Other fabrication methods might be employed to examine different film/substrate combinations.

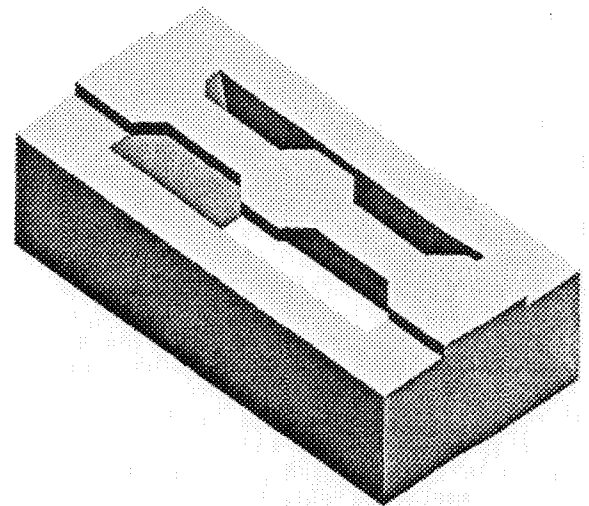


FIG. 1.--Proposed microfabricated test structure currently under study.

In contrast to singly supported cantilever beams, which are best used to measure the elastic response of a surface layer, this kind of specimen may be most suitable for the measure of the plastic deformation of thin films. Large-strain finite-element analysis has been

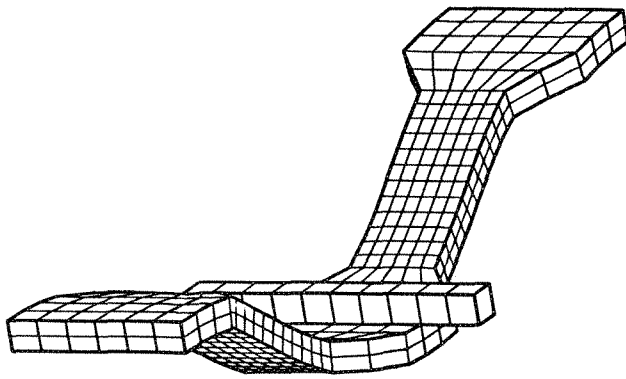


FIG. 2.--Finite element mesh showing predicted deformation of proposed microfabricated test structure.

applied in the design of this specimen. A deformed mesh from one such simulation is shown in Fig. 2. The finite-element calculations predict that this sample will basically bend at the ends of both gauge sections and will simultaneously stretch within the reduced-gauge sections on either side of the diamond probe. The forces required to bend the beam are quite small compared to the forces required to stretch the specimen gauge sections. The resulting force-displacement history predicted by the analysis is thus strongly related to the tensile stress-strain response of the thin film. The analytical results display good resolution of the yield strength of the material and are sensitive to the rate of plastic strain hardening of the film. Through the combined use of experimental testing and numerical modeling of this specimen, we shall be able to determine accurately the tensile stress-strain response of thin-film metallizations. Also, the method may be applicable to creep and stress relaxation testing in load and displacement control, respectively.

Conclusions

A flexible set of tools exists today to examine the mechanical properties of near-surface layers of engineering materials. These test methods vary widely in the specifics of their execution and their resulting strengths and weaknesses. Microtensile testing and bulge testing can provide fine characterization of the global small-strain response of films, but the test specimens are prone to damage and the techniques are not applicable to implanted layers of bulk material. Ultralow-load indentation testing can examine the large-strain response of near-surface layers that remain attached to their substrates, but analysis of the resulting load-depth data is extremely difficult. Microfabricated test structures hold the future promise of providing a wide range of mechanical properties characterization, but as yet have not been fully enough developed for use on a routine basis. No method is available at present that can probe the full range of me-

chanical response for near-surface layers of interest. Rather, investigators must determine which test method(s) best satisfy the goals of their particular investigations.

References

1. "Surface modification of metals by ion beams," in W. A. Grant, R. P. M. Proctor, and J. L. Whitton, Eds., *Mater. Sci. Eng.* 90: 1987.
2. N. Moncoffre, in Ref. A3, pp. 99-109, and references therein.
3. D. M. Follstaedt, *Nucl. Instrum. Meth.* B10/11: 549, 1985, and references therein.
4. F. G. Yost, A. D. Romig Jr., and R. J. Bourcier, *Proc. TMS Fall Meeting*, 1988 (in press).
5. F. G. Yost, A. D. Romig Jr., and R. J. Bourcier, *Stress Driven Diffusive Voiding of Aluminum Conductor Lines: A Model for Time Dependent Failure*, Sandia National Laboratories Report SAND88-0946, August 1988.
6. *Small Machines, Large Opportunities: A Report on the Emerging Field of Microdynamics*, Report of the NSF Workshop on Microelectromechanical Systems Research, AT&T, 1988.
7. L. Csepregi, *Microelectronic Engineering* 3: 221, 1985.
8. G. Kaminsky, *J. Vac. Sci. Technol.* B3: 1015, 1985.
9. K. E. Petersen, *Proc. IEEE* 70: 421, 1982.
10. D. A. Hardwick, *Thin Solid Films* 154: 109-124, 1987.
11. S. S. Brenner, *J. Appl. Phys.* 28: 1023, 1957.
12. C. A. Neugebauer, *J. Appl. Phys.* 31: 1096, 1960.
13. D. Kuhlman-Wilsdorf and K. S. Raghavan, *Rev. Sci. Instrum.* 33: 930, 1962.
14. A. Lawley and S. Schuster, *Rev. Sci. Instrum.* 33: 1178, 1962.
15. J. M. Blakely, *J. Appl. Phys.* 35: 1756, 1964.
16. A. Jankowski and T. Tsakalakos, *J. Appl. Phys.* 57: 1835, 1985.
17. C. G. Andeen, C. W. Hagerling, and R. W. Hoffman, *Proc. 7th Int. Vacuum Congr. and 3rd Int. Conf. on Solid Surfaces*, Vienna, 1977, 1769.
18. J. W. Beams, in C. A. Neugebauer, J. D. Newkirk, and D. A. Vermilyea, Eds., *The Structure and Properties of Thin Films*, New York: Wiley, 1959, 183.
19. W. M. C. Yang, T. Tsakalakos, and J. E. Hilliard, *J. Appl. Phys.* 48: 876, 1977.
20. T. Tsakalakos, *Thin Solid Films* 75: 293, 1981.
21. A. J. Griffin Jr., F. R. Brotzen, and C. F. Dunn, *Thin Solid Films* 150: 237, 1987.
22. F. R. Brotzen, C. T. Rosenmayer, and R. J. Gale, *Thin Solid Films* 166: 291, 1988.
23. R. J. Jaccodine and W. A. Schlegel, *J. Appl. Phys.* 37: 2429, 1966.
24. J. B. Pethica, in V. Ashworth, W. Grant, and R. Proctor, Eds., *Ion Implantation into Metals*, Oxford: Pergamon Press, 1982, 147.
25. J. B. Pethica, R. Hutchings, and W. C. Oliver, *Nucl. Instrum. Methods* 209-210: 995-1000, 1983.

26. J. B. Pethica and W. C. Oliver, in S. T. Picraux and W. J. Choyke, Eds., *Metastable Materials Formation by Ion Implantation*. Amsterdam: Elsevier, 1982, 373-379.
27. W. C. Oliver, R. Hutchings, and J. B. Pethica, *Metall. Trans. A15*: 2221-2229, 1984.
28. M. F. Doerner and W. D. Nix, *J. Mater. Res.* 1: 601, 1986.
29. W. C. Oliver, C. J. McHargue, and S. J. Zinkle, *Thin Solid Films* 153: 185-196, 1987.
30. W. C. Oliver and C. J. McHargue, *Thin Solid Films* 161: 117-122, 1988.
31. D. T. Schmale, R. J. Bourcier, and E. Martinez, *Development of an Ultralow-load microhardness indentation test machine*, Sandia National Laboratories Report SAND86-0509, April 1986.
32. P. E. Wierenga and A. J. J. Franken, *J. Appl. Phys.* 55: 4244, 1984.
33. H. Bangert, A. Wagendristel, and H. Aschinger, *Coll. Polym. Sci.* 259: 238, 1981.
34. M. Nishibori and K. Kinoshita, *Thin Solid Films* 48: 325, 1978.
35. M. Tazaki, M. Nishibori, and K. Kinoshita, *Thin Solid Films* 51: 13, 1978.
36. T. W. Wu, C. Hwang, J. Lo, and P. Alexopoulos, *Thin Solid Films* 166: 299, 1988.
37. S.-P. Hannula, D. Stone, and C.-Y. Li, *1984 MRS Symp. Proc.* vol. 40, Materials Research Society, 1985, 217-224.
38. D. Newey, M. A. Wilkins, and H. M. Pollock, *J. Phys.* E15: 119, 1982.
39. Y. Tsukamoto, H. Yamaguchi, and M. Yanagisawa, *Thin Solid Films* 154: 171, 1987.
40. R. Hill, *The Mathematical Theory of Plasticity*, London: Clarendon, 1950.
41. P. J. Burnett and D. S. Rickerby, *Surface Engineering* 3: 69, 1987.
42. A. Bhattacharya and W. D. Nix, *Int. J. Solids Struct.* 24: 881, 1988.
43. A. G. Tangena and G. A. M. Hurkx, *J. Eng. Mat. Technol.* 108: 230, 1986.
44. R. J. Bourcier, C. M. Stone, and F. G. Yost, *A Numerical and Experimental Study of the Indentation Hardness Test*, Sandia National Laboratories Report SAND85-0486, September 1985.
45. R. J. Bourcier, S. M. Myers, and D. H. Polonis (in preparation).
46. M. Mehregany, R. T. Howe, and S. D. Senturia, *J. Appl. Phys.* 62: 3579, 1987.
47. R. T. Howe and R. S. Muller, *J. Appl. Phys.* 54: 4674, 1983.
48. R. J. Jacodine and W. A. Schlegel, *J. Appl. Phys.* 37: 2429, 1966.
49. S. C. H. Lin and I. Pugacz-Muraszkiewicz, *J. Appl. Phys.* 43: 119, 1972.
50. H. Guckel, T. Randazzo, and D. W. Burns, *J. Appl. Phys.* 57: 1671, 1985.
51. P. G. Borden, *Appl. Phys. Lett.* 36: 829, 1980.
52. R. T. Howe and R. S. Muller, *J. Electrochem. Soc.* 130: 1420, 1983.
53. T. P. Weihs, S. Hong, J. C. Braverman, and W. D. Nix, *J. Mater. Res.* 3: 931-842, 19 .
54. S. Hong, J. C. Braverman, T. P. Weihs, and O. K. Kwon, *MRS Symp. Proc.* 1987, vol. 108.
55. K. E. Petersen and C. R. Guarnieri, *J. Appl. Phys.* 50: 6761-6776, 1979.
56. S. Johansson and J. Å. Schweitz, *J. Appl. Phys.* 63: 4799-4803, 1988.
57. S. Johansson, F. Ericson, and J. Å. Schweitz, *J. Appl. Phys.* 65: 122-128, 1989.
58. R. C. Bourcier (unpublished research).
59. R. T. Howe and R. S. Muller, *Sensors and Actuators* 4: 447-454, 1983.
60. H. Seidel and L. Czepregi, *Sensors and Actuators* 4: 455-463, 1983.
61. Y. Linden, L. Tenerz, J. Tiren, and B. Hok, *Sensors and Actuators* 16: 67-82, 1989.

THE ENVIRONMENTAL SEM: A NEW WAY TO LOOK AT INSULATORS

R. B. Bolon, C. D. Robertson, and Eric Lifshin

Scientific and even nontechnical literature is filled with thousands of scanning electron microscope (SEM) micrographs taken of metals, ceramics, minerals, electronic devices, insects, microrogansisms, and many other types of specimens. This widespread use of the conventional SEM is the result of its ease of operation, high resolution, and large depth of field. However, not all samples are suitable for the conditions imposed by this instrument. For example, insulating specimens have always been something of a challenge because surface charges generated by the impinging electron beam must be continually drained away to prevent distortion of the image. In addition, samples that outgas, evaporate, melt, or decompose under the conditions of operation are generally shunned. To overcome these limitations a new type of SEM, known as the environmental SEM or ESEM, was developed. This paper illustrates a selection of materials applications and special-purpose experiments developed to utilize the unique capabilities of the ESEM.

Specimen charging is usually overcome by vapor deposition of a thin metallic coating on the specimen to provide a conducting path to ground. More recently, the use of field-emission instruments operating at very low voltages, where the secondary-emission coefficient is close to unity, have made it possible to look at insulating samples without metallization. However, if the specimen is insulating and also has a high vapor pressure relative to the 10^{-5} Torr or so required to avoid damaging the electron source and/or secondary-electron detector, neither conventional nor field-emission SEMs can be easily employed. Typical samples excluded by these limitations include ice, liquids, gums, adhesives, and oily materials. In addition, if fresh insulating surfaces are continuously being exposed, as in the case of dynamic fracturing or mechanical deformation experiments on polymers, coating cannot be conveniently used to avoid charging, and conventional SEM use is limited. The ESEM differs from conventional SEM operation in two major ways: (1) the extensive use of differential pumping effectively to isolate the specimen chamber from the rest of the electron optical column during normal operation, and (2) the mode of electron detection.

The authors are at GE Corporate Research and Development Center, Building K-1, Schenectady, NY 12301. They wish to thank Prof. E. M. Schulson at the Thayer School of Engineering, Dartmouth College, for his assistance in the ice fracture studies; D. I. Simpson and R. J. Harniman of ElectroScan for their assistance in the use of the ESEM; and Princeton Gamma-Tech for their helpful cooperation.

By paying special attention to aperture selection and placement it is possible to apply differential pumping so that the sample can be at 25 Torr or higher pressure while the gun is maintained at better than 10^{-5} Torr. Chamber pressures in the range of 0.2-25 Torr or higher are key elements in the charge-neutralization and electron-detection processes. A gas such as water vapor, oxygen, argon, or methane is introduced into the chamber to maintain a selected pressure. A positive bias applied to a detector electrode above the sample attracts the secondary electrons from the sample and accelerates them sufficiently to create a cascade of ion-electron pairs and to yield considerable amplification before they are collected. Although the relative contributions of the various components of the detected signal (i.e., those due to the primary, secondary, and backscattered electrons) are not yet known, it is apparent that the secondary-electron signal is a major component.

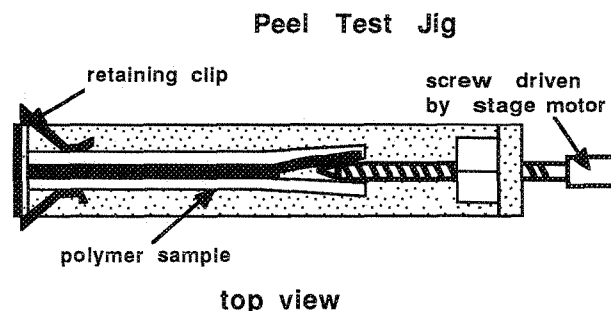
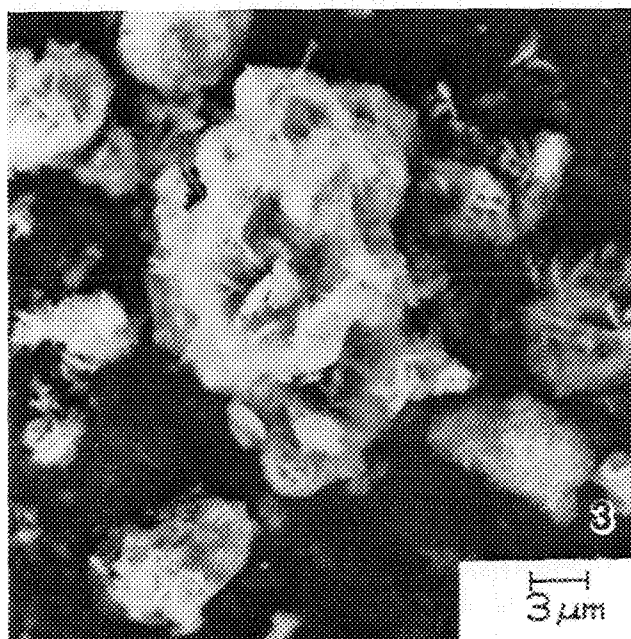
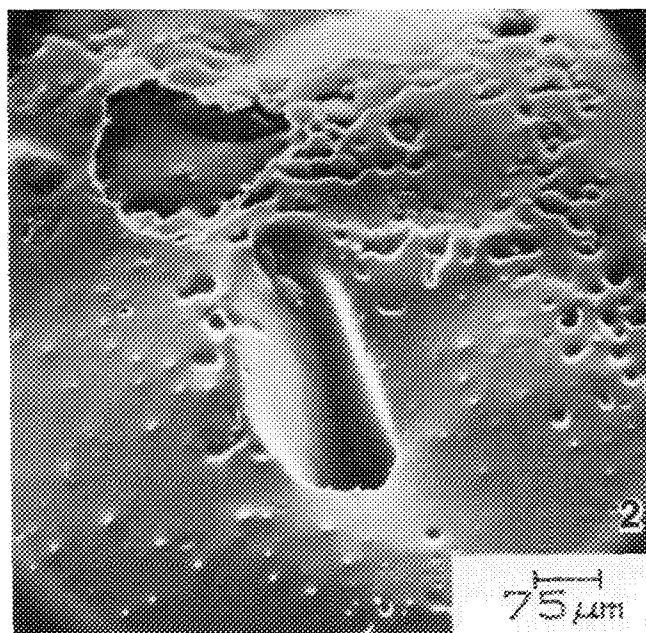
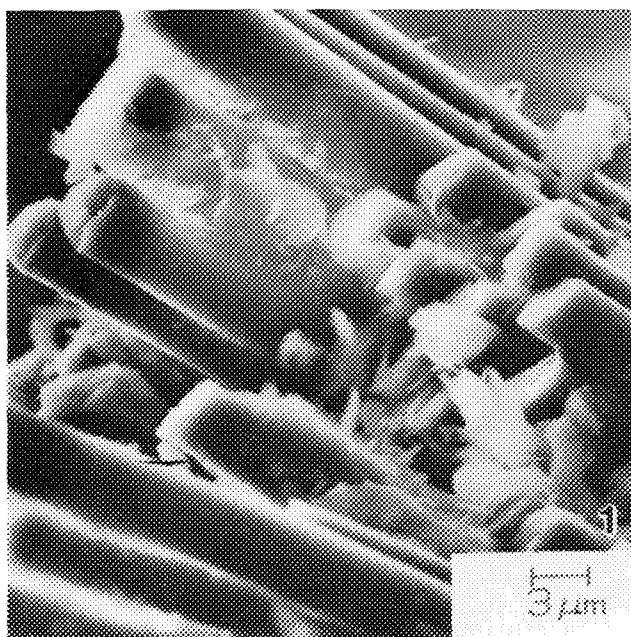
The positive ions migrate to the chamber walls and to the sample, where they contribute to the neutralization of negative surface charges. The bias used is considerably less than that associated with a conventional Everhart-Thornley (ET) detector, which requires a high voltage on the scintillator to generate an adequate signal. The lower bias avoids catastrophic and destructive arcing that would occur with the traditional ET detector.

The many considerations required for constructing and operating the ESEM have been described in an extensive survey by its principal developer, G. D. Danilatos.¹

Experimental Method and Results

The ESEM used in this study was from ElectroScan Corporation, Inc. and was fitted with an Omega EDS detector and System 4 plus analyzer from Princeton Gamma-Tech, Inc. One important reason for examining samples in a gaseous environment is to utilize the surface-charge-neutralization effect of the ions that are generated. Figure 1 is a secondary-electron (SE) image of an uncoated fracture section of a glass-fiber-reinforced epoxy circuit board taken at 20 keV in 3.0 Torr of water vapor. Although a previously fractured sample could have been coated and examined by traditional SEM techniques, it would not be possible to observe and record the changes that occur during dynamic in situ fracture studies, where fresh nonconductive surfaces are continuously being generated.

Ice, an abundant material covering our northern oil fields, is another difficult material to examine in a traditional SEM. Figure 2 is an SE image of a fresh fracture sur-



4

FIG. 1.--Glass fibers in polymer matrix; 20 keV beam, 2.5 Torr of water vapor.
FIG. 2.--Surface of sea-water ice fractured parallel to growth direction showing brine pockets; 20 keV beam, ~ 3.5 Torr of water vapor.
FIG. 3.-- MgCO_3 crystals; 7 keV beam, 4.3 Torr of oxygen.
FIG. 4.--Substage used for dynamic paint peel tests.

face of salt-water ice, revealing pockets of liquid brine. For this experiment a rod of salt-water ice was mounted in a precooled sample holder and then fractured in place by use of the stage motion. This image was recorded at 20 keV in a water-vapor environment of 3.8 Torr pressure. In related studies it was found that inexpensive Peltier thermoelectric heat pumps, obtained from MELCOR,² could lower the temperature of the holder sufficiently to keep the ice frozen.

Figure 3 is an SE image of uncoated magnesium carbonate powder particles. It proved to be difficult to examine this sample with a traditional SEM due to excessive sample charging. Even the usual techniques of preparing sparse dispersions, Au sputter coatings, and use of low

voltages failed to eliminate the problem. Although examination in a 3.8-Torr oxygen environment resulted in a low signal level, there was no problem with charging. The observed structure is different, more "feathery" than that observed on heavily coated samples, suggesting that sample preparation altered the structure.

Understanding of polymer adhesion to polymers or to other materials is of great importance not only to the plastics industry but to many other industries as well. The magnitude of adhesion is often studied by the use of peel tests in which the force required to separate two layers is measured. The ESEM can be used to correlate microscopic phenomena occurring near the peeling boundary with the peel

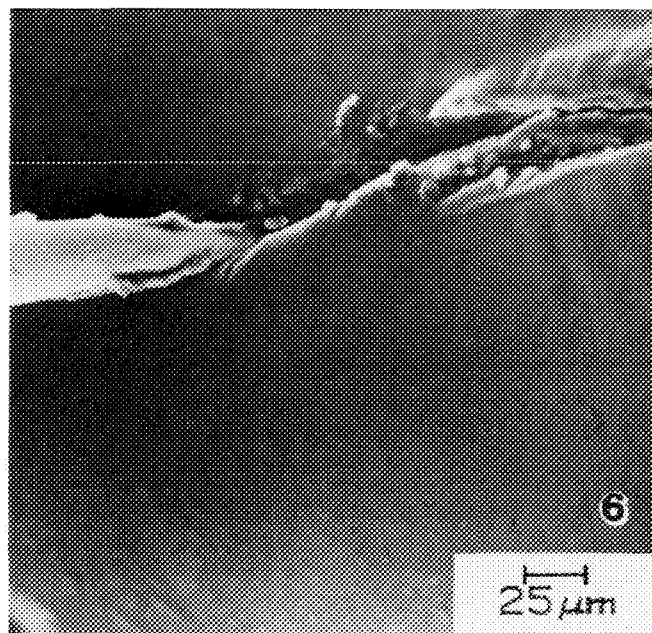
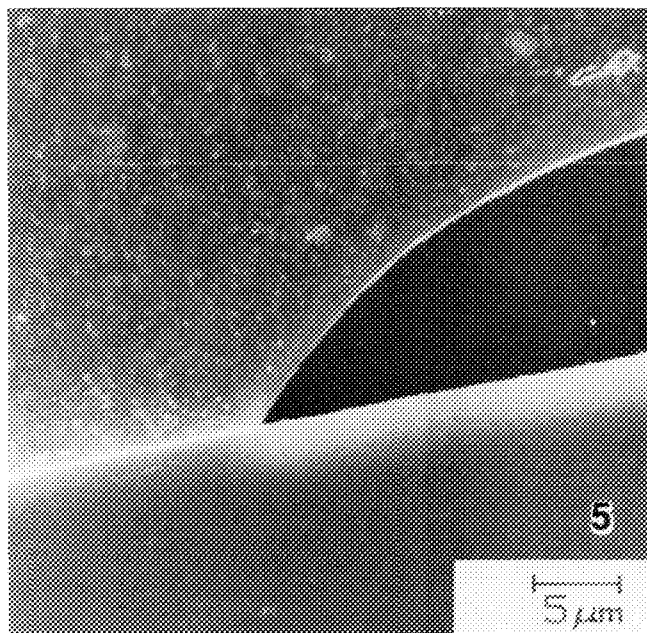


FIG. 5.--Paint peeling off polymer surface; 20 keV beam, 2.5 Torr of water vapor.

FIG. 6.--Needle probing surface of uncured silicone rubber caulk; 20 keV beam, 2.2 Torr of water vapor.

strength. As an example, a layer of paint on an engineering plastic was cross-sectioned by metallography and polished. The specimen was then mounted in a jig as illustrated in Fig. 4 and a pointed screw was driven a distance into the interface to force the bond apart. The crack (Fig. 5) continued to propagate for a considerable time following each advance. The experiment was followed by video recording supplemented by normal micrographs. The dynamics of the "peel" propagation were found to be nonuniform in velocity, degree of plastic deformation, and crack angle. Work is currently under way to develop new mathematical models to describe these observations.

A micromanipulator probe can dynamically deform and expose underlying material, excise particles for identification, and apply or measure electric potentials during observation in the microscope. One example is illustrated in Fig. 6 where the tip of a probe is observed deforming the surface of uncured white bathroom RTV silicone caulk in an effort to develop new methods for characterizing cure dynamics.

One exciting opportunity we are currently evaluating is the ability to perform EDS analysis of small quantities of liquids in conjunction with dynamic reactions. A preliminary example was carried out on copper sulfate in an atmosphere of 7-8 Torr of water vapor. Small particles were placed on an alumina substrate and cooled approximately 10 C with a Peltier thermoelectric heat pump to lower the dew point at the sample and prevent unwanted condensation on the chamber walls. Water condensed on the particles and caused them to dissolve (Fig. 7). The x-ray spectrum from the water droplet is presented in Fig. 8 and shows the presence of copper, sulfur, oxygen, and aluminum. The aluminum is apparently due to

the substrate beneath the drop. With a rise in temperature, the particle recrystallized as shown in Fig. 10, with the corresponding x-ray spectrum presented in Fig. 9. This spectrum shows similar ratios for copper and sulfur but much lower oxygen and no aluminum. Since the chamber pressure was kept constant, the decreased oxygen signal in this spectrum demonstrates that it was primarily due to the water in the droplet. A repetition of this experiment with an iron substrate showed, as expected, that the Fe exchanged for the Cu in the liquid and that the recrystallized material after dehydration was iron sulfate surrounded by thin patches of metallic copper.

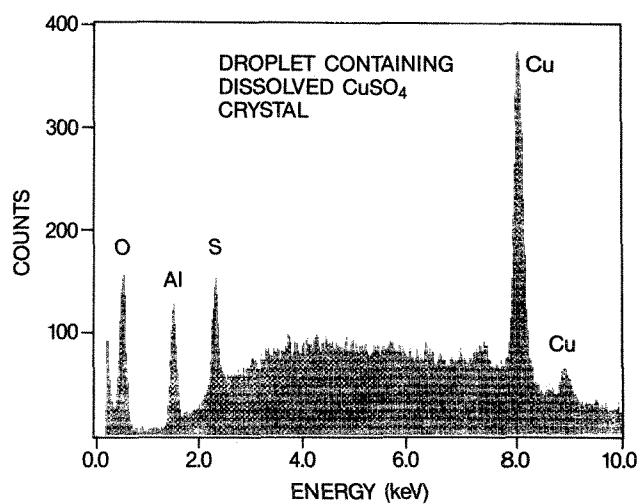
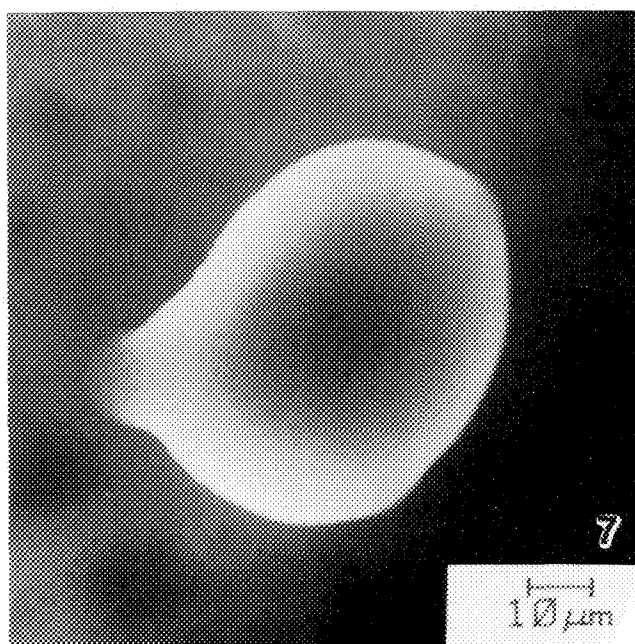
Summary

This evaluation shows that ESEM is a viable technique for examining a variety of materials that either could not be done in a traditional SEM or would require extensive sample preparation. Potentially more important applications involve the ability to study dynamic interactions between the sample and a reactive environment. It will be important to evaluate the effect of the environmental atmosphere on the energy and spatial distribution of x-ray generation as well as subsequent modification of the intensities prior to detection. Additional work is also needed for a better understanding of contrast mechanisms and to relate morphological features of nonsolid samples with their physical or chemical properties.

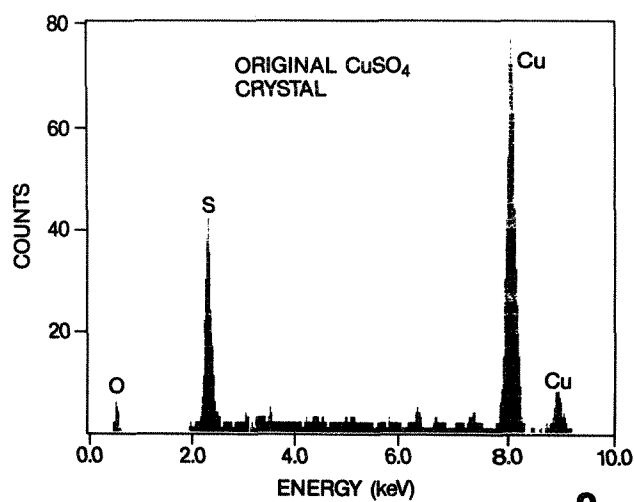
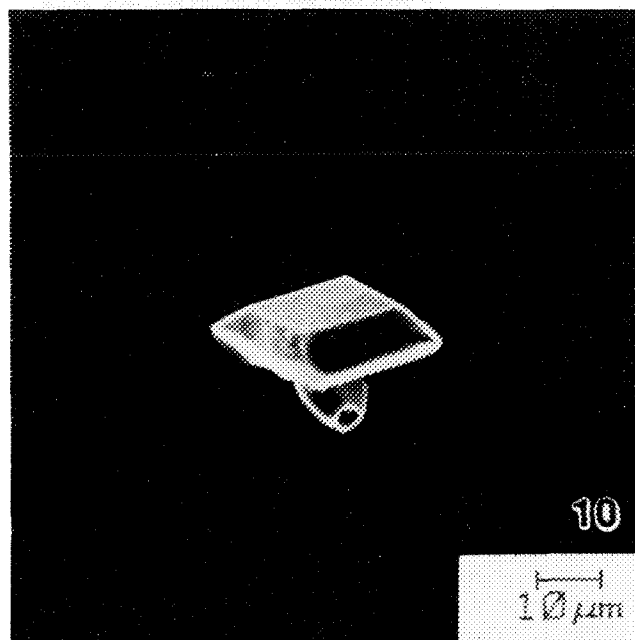
References

1. G. D. Danilatos, "Foundations of environmental scanning electron microscopy," *Advances in Electronics and Electron Physics* 71: 109, 1988.

2. Materials Electronic Products Corporation,
990 Spruce Street, Trenton, NJ 08648.



8



9

FIG. 7.--Drop of water containing dissolved CuSO_4 crystal; 20 keV beam, 7.4 Torr of water vapor.
FIG. 8.--X-ray spectrum of water drop in Fig. 7.
FIG. 9.--X-ray spectrum of crystal in Fig. 10.
FIG. 10.--Recrystallized CuSO_4 on sapphire substrate; 20 keV beam, 4.7 Torr of water vapor.

CHARACTERIZATION OF MICROSTRUCTURAL DEFECTS IN SEMICONDUCTOR SILICON

S. Chevacharoenkul, C. M. Osburn, and G. E. McGuire

In the rapid evolution of integrated circuit technology, we have moved from the VLSI (Very Large Scale Integration) period of the early 1980s, where there are 2^{16} - 2^{21} devices per chip, to the ULSI era of 2^{21} - 2^{26} devices per chip.¹ The reduction of scaling of device dimensions has been the overriding trend in semiconductor technology for the last decade. A common strategy has been to scale each subsequent generation of product by a factor of two in dimension. Initially, constant field scaling was the path taken toward smaller MOS devices.² With this scaling, all device dimensions are reduced by α , which results in a device density per unit area increase of α^2 . The doping density and voltages are reduced by α , and the delay and power-delay product are reduced by α and α^3 , respectively. The total current and current density increase by α .

For several reasons, including the desire for higher performance, constant-voltage scaling was adopted by various groups.^{3,4} With constant-voltage scaling, the power supply is kept constant and device dimensions are reduced by the scaling factor x . The doping in the semiconductor is then adjusted to obtain the desired threshold voltage. Constant-field scaling is used in many processes today, but it does suffer from high field effects and from higher power dissipation. Furthermore, the high doping levels required to produce acceptable electrical designs cause a mobility degradation that counteracts some of the performance advantages of scaling in the first place.

Table 1 gives some of the design parameters of succeeding generations of product which illustrate some of the materials and processing problems associated with achieving higher levels of integration. In general, the challenge is to define small features with the appropriate lithography tools over the surface of a wafer for subsequent etching, deposition, or implantation of device components. These steps are done at the lowest possible temperature in order to minimize secondary reaction,

TABLE 1.--Micron and submicron design parameters.

	2 μ m	1.25-1.5 μ m	1.0 μ m	0.75 μ m	0.5 μ m
Line/space pitch (μ m)	4-5	2.5-3	2	1.5-2	1
Channel length (μ m)	1.8 \pm 0.3	1.3 \pm 0.3	0.9 \pm 0.25	0.7 \pm 0.2	0.40-1
Gate oxide (nm)	40-50	25	20	15	10
Junction depth (μ m)	0.5	0.3	0.25	0.2	0.15
Threshold voltage (v)	1	0.7	0.5	0.4	0.3
Vintage	1980	1984	1988	1992	1996

The authors are at the Microelectronics Center of North Carolina,

diffusion, or precipitation. In order to maintain high yield with high levels of integration, increased emphasis has been placed on the characterization of process-induced defects which may result in device failure. One of the key tools for the evaluation of process or materials-related defects is the transmission electron microscope (TEM). In this paper the application of the TEM in evaluating some of the materials and process related defects associated with the various design parameters is illustrated. Applications which require cross-sectional and plan view micrographs are given.

Experimental

For 0.25 and 0.5 μ m design rules the gate oxide thickness is in the range of 7 and 10 nm, respectively. Thin oxides of this range of thickness become increasingly difficult to grow reproducibly and to characterize by conventional means. Most thickness measurements rely on ellipsometry, which requires knowledge of the correct refractive index of the material under consideration. Cross-sectional TEM has been shown to be a valuable technique for measuring oxide thicknesses and calibrating other measurement tools.⁵ Figure 1 is a cross-sectional TEM micrograph of a thermally grown oxide. At this magnification, it is possible to use the lattice spacing of the rows of silicon atoms, 3.135 Å, as a calibration marker. The oxides measured by TEM then become standards by which ellipsometry, photoelectron spectroscopy, channeling Rutherford backscattering spectroscopy, and other techniques for measuring thin films are calibrated.

Very abrupt junctions are required for ULSI devices. For example, 0.25 μ m devices require 70 nm pn junctions. Control of the initial implant profile has been achieved through the use of molecular ions,⁶ precise orientation of the single crystalline substrate,⁷ and pre-amorphization of the substrate.⁸ Preamorphization of the substrate with a nonelectrically active species such as Si or Ge eliminates channeling. Figure 2 is a cross-sectional TEM micrograph that illustrates the complete amorphization of the outer 97 and 36 nm of a Si wafer for Ge implantation at 85 and 25 keV. Just below the amorphous/crystalline interface, there is a high concentration of Si interstitial atoms produced by the implantation process. When the substrate is annealed to recrystallize the Si and activate the dopant, these interstitial atoms condense, forming monolayer thick disks in the Si matrix. These features are often referred to as end-of-range damage

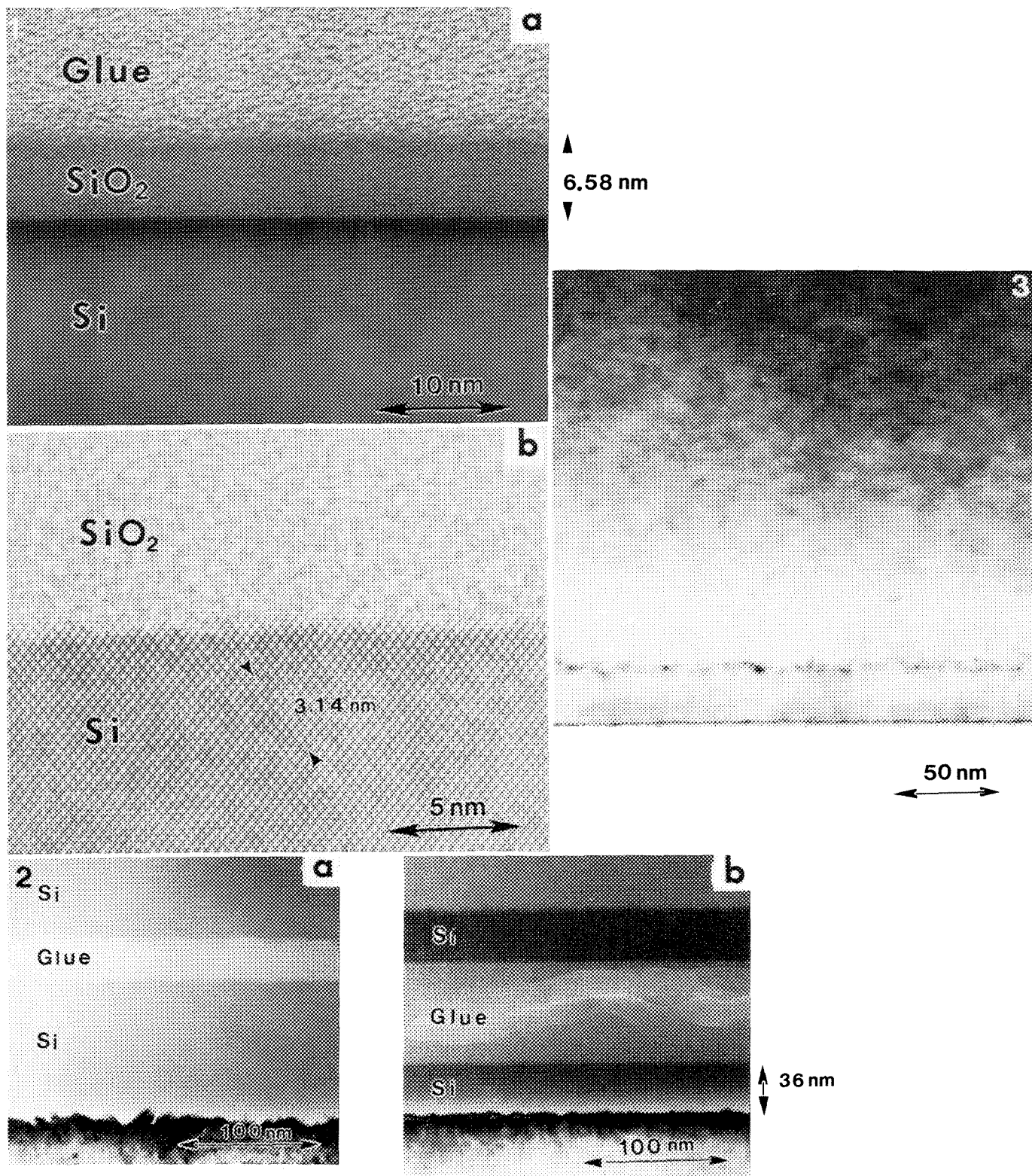


FIG. 1.--(a) Low-magnification TEM image of Si/SiO₂ interface of thermally grown oxide, (b) TEM image of the Si/SiO₂ interface at higher magnification in order to observe Si lattice spacing.
 FIG. 2.--Cross-sectional TEM image of a Si(100) wafer implanted with (a) $10^{15} \text{ cm}^{-2} \text{ Ge}^+$ at 85keV, (b) $4 \times 10^{14} \text{ cm}^{-2}$ at 25keV to produce amorphous layer.
 FIG. 3.--Cross-sectional TEM micrograph of Ge preamorphized wafer after 550 C, 30min furnace anneal, showing recrystallization of amorphous layer and condensation of end-of-range damage.

dislocation loops. They can be seen in Fig. 3 at the original amorphous/crystalline interface.

Low-temperature short-time processes are required to keep the dopant profile shallow. Rapid thermal processing is used to minimize the total thermal budget that devices experience. When preamorphization is used in junction formation, the implantation energy must be adjusted so that the end-of-range defects reside outside the depletion region or completely anneal out. Figure 4 shows a temperature series of Si wafers following Ge preamorphization and BF_2 implantation. In the series (a), (b), and (c) the sample was rapid thermally annealed for 10 s at 750, 850, and 950 C respectively. The plan view TEM micrographs show the evolution of the end-of-range damage from numerous small sites (a), to larger condensed loops (b), to elimination (c). Thus the plan view technique provides information complementary to the cross-section technique in characterizing both the location and amount of damage.

Results and Conclusions

The application of the TEM in evaluating microstructural defects and processing parameters for ULSI devices has been illustrated. The use of both cross-sectional and plan view evaluation has been shown. TEM may be the technique of choice for calibrating other analytical tools for submicron dimensions.

References

1. C. M. Osburn and A. Reisman, "Challenges in advanced semiconductor technology for high-performance and supercomputer applications," *J. Supercomputing* 1: 149, 1987.
2. R. H. Dennard, F. H. Gaensslen, H. N. Yu, V. L. Rideout, E. Basous, and A. R. Leblanc, "Design of ion-implanted MOSFETs with very small physical dimensions," *IEEE J. Solid-State Circuits* SC-9: 256, 1974.
3. J. R. Brews, W. Fichtner, E. H. Nicollian, and S. M. Sze, "Generalized guide for MOSFET miniaturization," *IEEE Electron Device Lett.* EDL-1: 2, 1980.
4. P. K. Chatterjee, W. R. Hunter, T. C. Holloway, and Y. T. Lin, "The impact of scaling laws on the choice of n-channel or p-channel for MOS VLSI," *IEEE Electron Device Lett.* EDL-1: 220, 1980.
5. N. M. Ravindra, J. Narayan, D. Fathy, J. K. Srivastara, and E. A. Irene, "Silicon oxidation and Si-SiO₂ interface thin oxides," *J. Mater. Res.* 2: 216, 1987.
6. D. E. Davies "1-2 keV boron implants into Si," *IEEE Electron Device Lett.* EDL-6: 397, 1985.
7. T. O. Sedwick, *Mater. Res. Soc. Symp. Proc.* 71: 403, 1986.

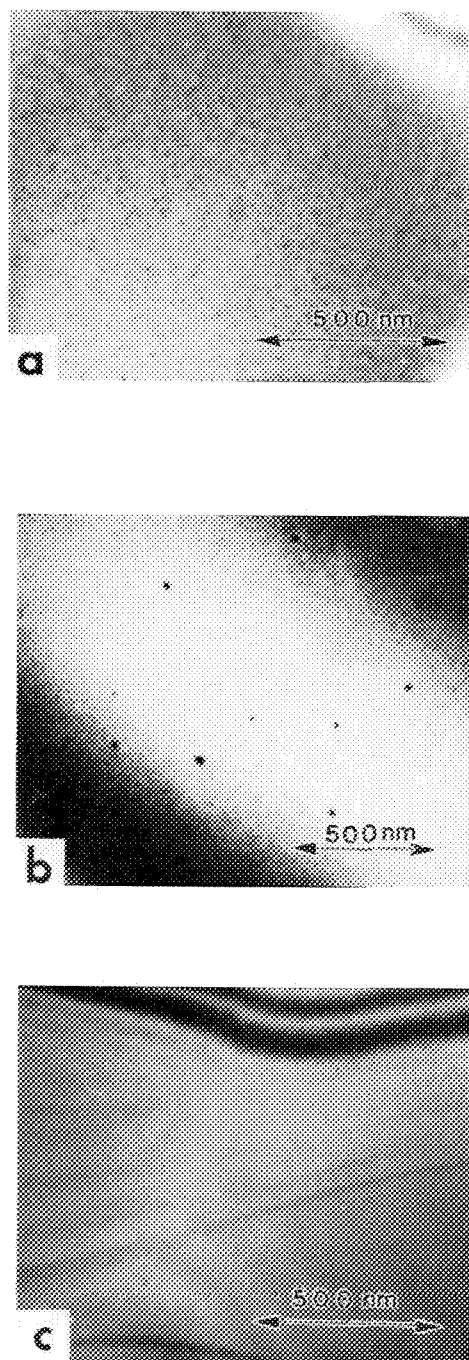


FIG. 4.--Plan-view TEM micrographs of Si(100) samples rapid thermally annealed for 10 s at (a) 750 C, (b) 850 C, (c) 950 C following $25\text{keV } 4 \times 10^{14} \text{ cm}^{-2} \text{ Ge}^+$ implantation plus $8\text{keV } 4 \times 10^{14} \text{ cm}^{-2} \text{ BF}_2^+$ implantation.

LASER BEAM AND ELECTRON BEAM INDUCED CURRENT TECHNIQUES FOR DEFECTS IN Si: A COMPARATIVE STUDY

Z. J. Radzinski, T. Zhou, G. A. Rozgonyi, and P. E. Russell

Charge collection microscopy (CCM), which includes laser beam induced current (LBIC) and electron beam induced current (EBIC), is a very powerful technique for the evaluation of semiconductor materials and devices. In LBIC light quanta from a laser source are absorbed by the semiconductor material, where they generate electron-hole pairs; whereas in EBIC the electron beam in a scanning microscope is used as a source. CCM can be used as a probing method for integrated circuit failure analysis and design verification,^{1,2} and as a materials characterization tool for quantitative measurements of minority carrier lifetime or diffusion length and p-n junction depth.^{3,4} Moreover, CCM may be used for both defect imaging and electrical analysis in semiconductor materials.^{5,6} In the past the EBIC technique has been employed in a wider range of applications; however, LBIC is gaining more and more attention, mainly due to improvements in laser technology. No need for vacuum and the simplicity of operation are major advantages of LBIC over EBIC. One major advantage of EBIC is that one can easily change the analysis excitation depth by changing the energy of the electron beam. One can solve this problem in LBIC by using lasers with different wavelengths, or in the future by using a tunable laser, which will increase the versatility of LBIC and allow in-depth analysis. Also, adjustment of the light-source wavelength may yield LBIC images based on different defect species.⁷ Photo-induced current stimulated with above-bandgap photons is a function of minority carrier lifetime, whereas photo-excitation with below-band gap photons provides a sensitive method of detecting deep states because current is induced only via deep levels.

The imaging of electrically active defects in CCM semiconductor material is possible if defects are located in the range of the depths excited by the probe beam (Fig. 1a). These defects act as recombinations sites and are visible as dark spots or lines, depending on the nature of the defects and the way they propagate through the excited near-surface volume. To image defects located at depths deeper than the excitation volume one can use angle polishing (Fig. 1b), which is commonly used in optical-microscopy defect imaging.⁸ Preparation of a beveled sample allows one to increase the depth

The authors are with North Carolina State University, Department of Materials Science and Engineering, Raleigh, NC 27695-7907. The support of the Center for Advanced Electronic Materials Processing and of Advantest America is gratefully acknowledged.

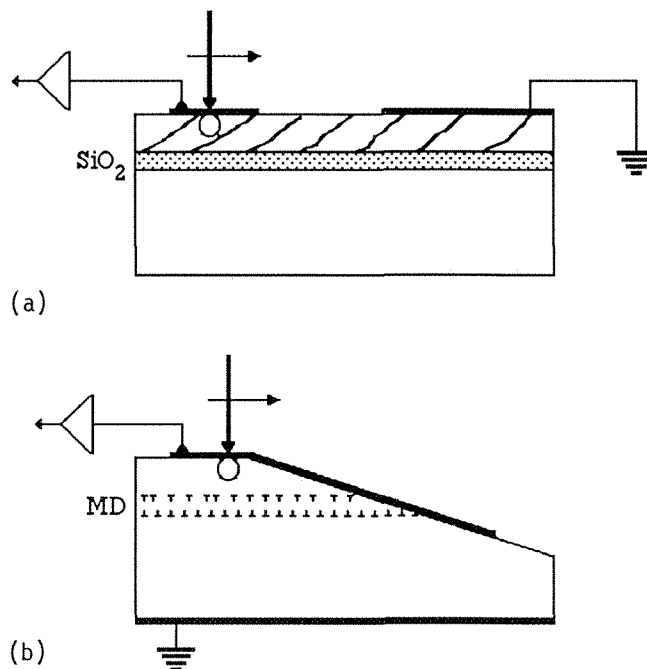


FIG. 1--Schematic diagram of samples used in this work: (a) Silicon on insulator (SiO_2) sample obtained by zone melt recrystallization, (b) extrinsically gettered epitaxial Si with buried misfit dislocations (MD).

range of the technique to reach regions far below the surface.

Experiment

In this work the distribution of electrically active defects in Si epitaxial layers was investigated by both EBIC and LBIC. Preferential chemical etching has also been used to delineate defects emerging at the surface. The investigation was centered on samples with well-determined depth distribution of structural defects. In order to compare the information on depth and resolution of these two techniques, experiments were performed on samples with defects threading to the surface, as well as defects confined to buried interfaces. In the first case a silicon-on-insulator (SOI) structure obtained by zone-melt recrystallization (ZMR) has been used. The SOI structure had a $5\mu\text{m}$ -thick capping layer deposited by chemical vapor epitaxy. The ZMR substrate wafer used in this study was a product of the Kopin Corp. of Taunton, Mass., whereas the epi was deposited at Westinghouse.⁹ The second

structure was an Si(2%Ge) CVD epitaxial structure with defects in the form of misfit dislocation grids confined to two interfacial planes at fixed depths. The dislocations were introduced by incorporation of 2%Ge into 2 μ m-thick Si epitaxial layer. This technique is very effective in proving the electrical properties of devices fabricated in a pure Si capping layer.¹⁰ The capping-layer thickness investigated in this work was 4 μ m. For both LBIC and EBIC studies an evaporated aluminum Schottky contact 1 mm in diameter and 20 nm thick was used. The SOI sample required a large-area ohmic contact to be placed adjacent to the Schottky contact. Figure 1(a) shows the sample structure and contact configuration. Photon and electron beam induced current were measured under zero-bias condition. To obtain precise data on depth information, the experiments were also performed on angle-polished structures in which the Schottky contact was deposited directly on the beveled surface (Fig. 1b).

Threading dislocations emerging from the capping epitaxial layer on the ZMR sample are shown in Fig. 1. The optical micrograph of an etched epi-layer on ZMR wafer (Fig. 2a) shows the characteristic boundaries of high defect density, ($2\text{--}10 \times 10^7 \text{ cm}^{-2}$), separated by 30 to 40 μ m of relatively low-defect material. These boundaries originate during AMR as a result of solid/liquid interface perturbations. The EBIC image in Fig. 2(b) shows a similar defect distribution. It reveals electrically active defects that lie within the 1.5 μ m depth excited by the 15keV electron beam. The characteristic boundaries can be also distinguished in the LBIC image (Fig. 2c), with the volume of

excitation equal to $\sim 1 \mu\text{m}$ for red light. This image is less uniform than the one obtained by EBIC. To understand the difference in image quality one must compare the absorption process occurring with each beam. In charge-collection microscopy the maximum information comes from the local volume or depth at which the maximum energy loss of the penetrating beam occurs. The laser beam losses its energy in an exponential fashion starting at the surface (Fig. 3). The energy loss distribution for electron-beam penetration has a characteristic maximum at a depth approximately equal to $0.4R_{\text{max}}$ (R_{max} = maximum penetration depth) for Si. Therefore, with EBIC surface recombination effects are less important than bulk properties. The opposite occurs with LBIC. However, EBIC and LBIC results from the ZMR sample indicate that device performance and yield would benefit from locating individual devices between the dislocated boundaries. These regions are essentially free of extended defects, whereas the neighboring dislocations should act as efficient gettering centers for metal impurities during subsequent processing steps.

The second sample studied in this work was an extrinsically gettered epitaxial structure containing misfit dislocations.¹⁰ It is useful from the gettering point of view to introduce dislocations close to the active volume of a functioning device. A diagnostic tool is required that can be used to estimate the defect density and dislocation depth, and to verify the confinement of the dislocations to the buried interface. Investigators have successfully used EBIC for this purpose by proving the absence of threading dislocations

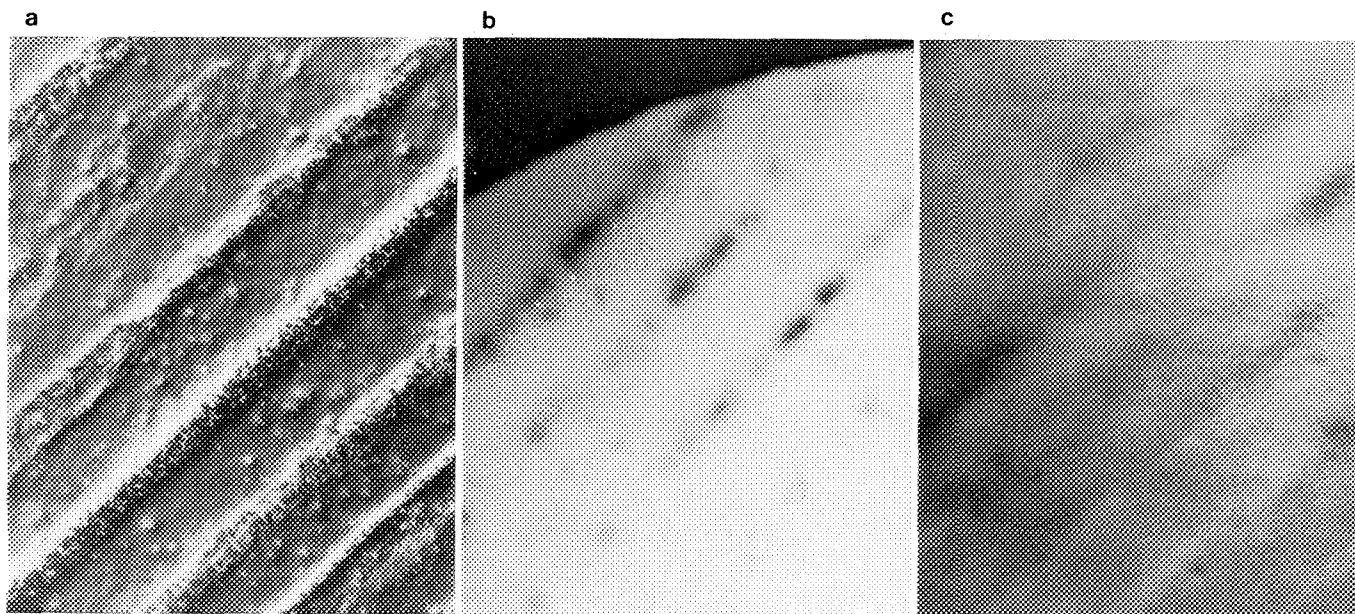


FIG. 2.--Defect distribution in surface layer of ZMR samples obtained by (a) optical micrograph of preferentially etched surface, (b) EBIC image obtained at 15 keV; (c) LBIC image.

25 μm

in the capping layer using a plane-view EBIC image at low (10keV) electron energy. Similar information on depth can be obtained by use of LBIC with a red laser ($\lambda = 0.67 \mu\text{m}$). To estimate quantitatively the dislocation depth it is more appropriate to acquire images from angle-polished surface. An example of such EBIC and LBIC micrographs are shown in Figs. 4(b) and (c), respectively. Both techniques provide essentially the same information about the investigated structure.

Conclusions

In conclusion, the atmospheric ambient of laser microscope and its simple operation make this instrument increasingly attractive for materials studies. We have shown that LBIC can be an useful tool for defect imaging and defect analysis in Si, both at the near-surface region and at buried regions, if it is combined with angle polishing. However, in comparison with EBIC, LBIC images of defects have lower resolution (mainly due to the size of the laser beam in this experiment). Moreover, to improve the LBIC resolution, special care has to be taken in preparation of semitransparent Schottky contacts.

References

1. J. D. Schick, *Scanning Electron Microscopy* 1: 55, 1985.
2. V. Wilke, *Scanning* 7: 88, 1985.
3. H. J. Leamy, *J. Appl. Phys.* 53: R51, 1982.
4. R. G. Lankin and A. E. Dixon, *SPIE*

Scanning Imaging Technology 809: 22, 1987.

5. P. E. Russell and C. R. Herrington, *Microbeam Analysis--1982*, 449.

6. E. M. McCabe, P. D. Pester, and T. Wilson, Ref. 4, p. 29.

7. M. Ogura, K. Sakakue, Y. Tokomaru, *Jpn J. Appl. Phys.* 24: L617, 1985.

8. G. A. Rozgonyi, A. S. M. Salih, Z. J. Radzimski, R. R. Kola, and J. Honeycutt, *J. Crystal Growth* 85: 300, 1987.

9. G. A. Rozgonyi, Z. J. Radzimski, T. Higuchi, B. L. Jiang, D. M. Lee, T. Zhou, D. Schmidt, and J. Blake, *Appl. Phys. Lett.* (in press).

10. A. S. M. Salih, Z. J. Radzimski, J. Honeycutt, and G. A. Rozgonyi, *Appl. Phys. Lett.* 50: 1678, 1987.

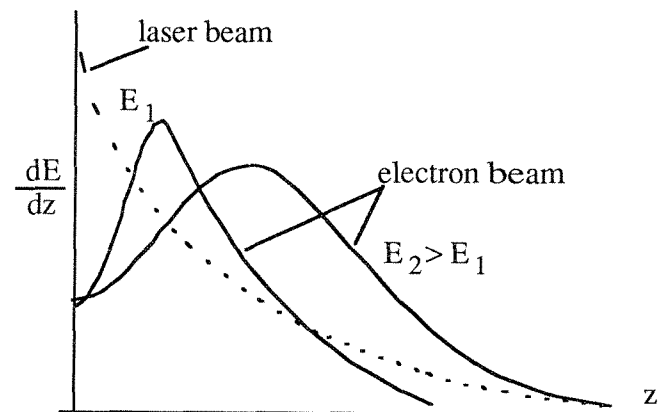


FIG. 3.--Energy loss distribution of laser and electron beam during substrate penetration. E_1 and E_2 are energies of electron beam.

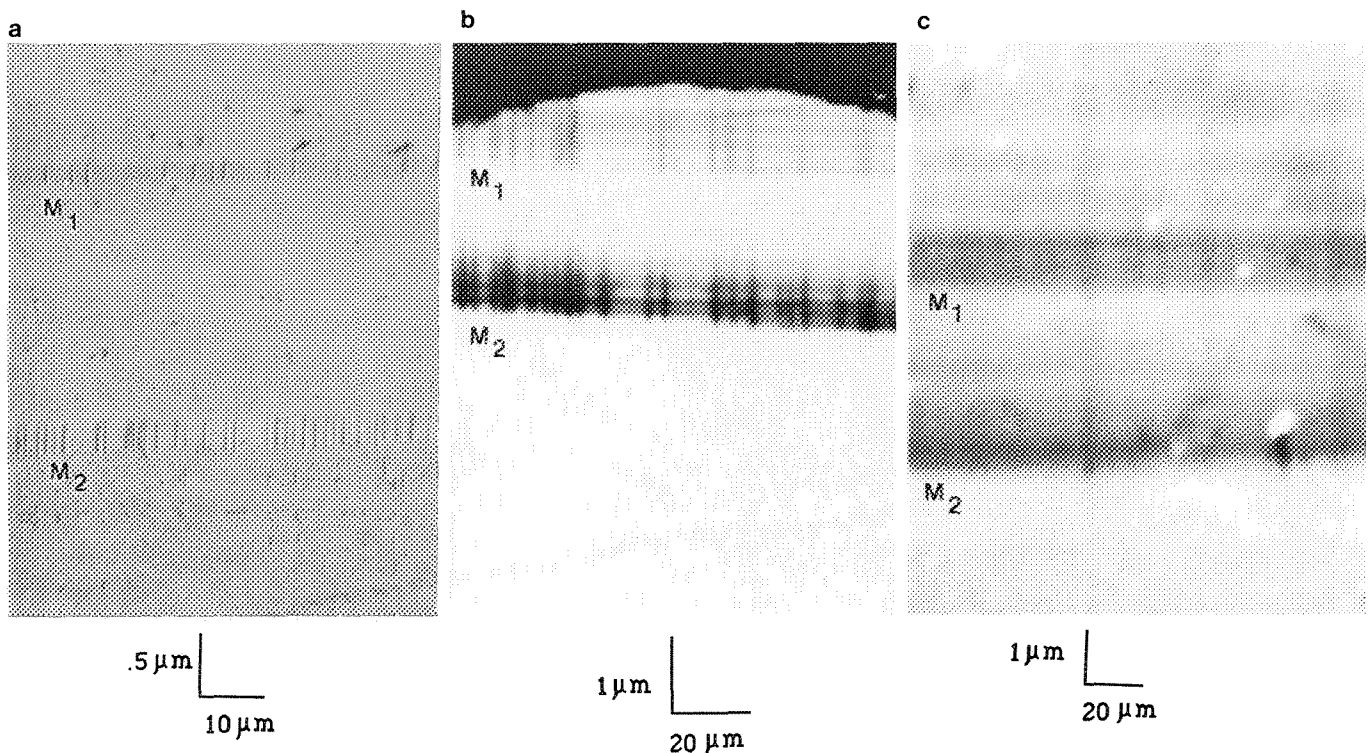


FIG. 4.--Images of buried misfit dislocations in XG silicon obtained on angle polished surface by (a) optical micrograph of preferentially etched ZMR surface, (b) EBIC image obtained at 15 keV, (c) LBIC image. M_1 and M_2 are misfit dislocations at upper and lower interface of Si(2%Ge) layer, respectively.

A NEW METHOD FOR MEASURING THE THICKNESS OF THIN-FILM INSULATORS

S. J. Krause, J. Mohr, G. H. Bernstein, D. K. Ferry, and D. C. Joy

The development of thin-film technologies has created new applications for directing a finely focused high-energy electron beam at a thin film on a bulk substrate, including electron-beam writing of a photoresist on a semiconductor substrate.^{1,2} When an electron beam strikes a bulk insulator, a fixed negative charge may build up and cause charging artifacts, but when an electron beam strikes a thin insulating film on a conducting substrate, charging may or may not occur, depending on the conditions and the nature of the sample. In this paper we describe the conditions for which a new, third "crossover" E3 of accelerating voltage occurs, at which a thin insulating film on a conduction substrate is "dynamically charge balanced." The film is electrically neutral when it is dynamically charge balanced because the charge deposited in the film equals the total yield of electrons exiting from the film. We have studied surface charging effects of a thin film of electron-beam photoresist on a silicon substrate and correlated the relationships between the accelerating voltage and the film thickness, substrate atomic number, and sample tilt. We have also modeled sample-beam interactions with Monte Carlo calculations and shown an excellent correlation between simulated and experimental results. The concepts of "dynamic charge balancing" and the E3 "crossover" of thin-film insulators on conducting substrates should prove useful for measuring film thickness and for determining the thickness limits to avoid negative charging artifacts in imaging or in electron-beam writing.

Background

Charging of a bulk sample can be explained by examining its current balance as given by

$$I_B = I_{SE} + I_{BE} + I_{SP}$$

where I_B is the beam current, I_{SE} is the secondary electron (SE) current, I_{BE} is the back-scattered electron (BE) current, and I_{SP} is the specimen current. The total exit current from the sample surface is $(I_{SE} + I_{BE})$. In a bulk insulator $I_{SP} = 0$, so that a sample charges negatively when $I_B > (I_{SE} + I_{BE})$, positively when $I_B < (I_{SE} + I_{BE})$, and is neutral when $I_B = (I_{SE} + I_{BE})$. Imaging of a bulk polymer or other insulating material by scanning electron mi-

croscopy (SEM) with SE at normal accelerating voltages of 10–25 keV produces a negative surface potential of hundreds of volts because $I_B \gg (I_{SE} + I_{BE})$.³ This potential creates "charging" artifacts in the SE image that can be eliminated by metal coating of the surface so that the difference between I_B and $(I_{SE} + I_{BE})$ is compensated by I_{SP} .^{3,4} At lower voltages, between 0.5 and 1.5 keV, the total electron yield of a material increases until $I_B = (I_{SE} + I_{BE})$ at an accelerating voltage referred to as the second "crossover" E2.^{5–7} This action results in an electrically neutral surface in insulators that makes imaging without charging artifacts possible. At accelerating voltages below E2, $I_B < (I_{SE} + I_{BE})$, but only a small positive potential of a few volts develops because the surface is self-neutralized when some secondary electrons are recaptured by the positive surface potential. The small positive potential does not cause charging artifacts and imaging of an insulator is still possible.⁸ At even lower voltages, in the range from 50 to 150 eV, the total electron yield decreases until a first "crossover" E1 occurs where the surface is also electrically neutral. Curiously, thin films of polymer resist on a semiconductor wafer, when imaged or exposed to an electron beam at higher energies (e.g., 30–100 keV), do not display negative "charging" artifacts, although the voltages are far above E2.⁹ To understand this phenomenon, the charge balance of a thin insulating film on a conducting substrate during exposure to an electron beam must be examined.

Experimental

Polymer films of thicknesses from 0.12 to 5 μm were made by spinning silicon wafers covered with Novolac resin. Films were baked for 30 min at 90 °C and thicknesses were measured with a Dektak profilometer. Samples were examined in a JEOL 840 SEM operated at accelerating voltages between 0.2 and 15 keV with a continuous voltage control. Charging polarity was tested by imaging a sample at a higher magnification, usually 500 \times , then quickly switching to a lower magnification, usually 100 \times . This procedure caused a small charged square from higher magnification to appear in the field of view at lower magnification and persist briefly until the surface static charge field became uniform again. If the charged square was darker than the surrounding area, the surface was positively charged, since some secondary electrons were attracted back to the surface; if it was lighter, the surface was negatively charged, since more secondary electrons were collected from the surface.

The authors are at the Center for Solid State Electronics Research, Arizona State University, Tempe, AZ 85287, except D. C. Joy, who is at the Electron Microscopy Facility, University of Tennessee, Knoxville, TN #7996 and the Metals and Ceramics Division, Oak Ridge National Laboratory, Oak Ridge, TN 37831.

Results

The general trend of surface charging as a function of accelerating voltage was determined by first viewing of a 0.83 μ m photoresist film on silicon in the SEM at a beam current of 1×10^{-9} A with an accelerating voltage beginning at 15 keV. As voltage was reduced, the charged square remained dark until 8.3 keV, when contrast reversed, indicating that surface polarity changed from positive to negative. Voltage was further reduced until, at 0.9 keV, the charged square again reversed contrast and turned dark again, indicating that polarity changed from negative to positive. Further voltage reductions to 0.2 keV caused no other changes.

The interpretation of the data at the lower voltages is fairly normal. The E1 "crossover" was not observed since the lowest available voltage was 0.2 keV, which was too high for E1 of the photoresist. As expected, the sample charged positively in the range from 0.2 to 0.9 keV, which is typical for polymers.⁶ The voltage for the E2 "crossover" occurs at 0.9 keV, which is also typical for polymers.^{9,10} Above E2 negative charging with increasing voltage occurred, as would be expected for a bulk polymer. However, another change in polarity occurs at 8.3 keV to give a new "crossover" E3, which would be unexpected for a bulk polymer but is plausible for a thin insulating film on a conducting substrate. The reasons for the occurrence of E3 will be considered later, along with a simple model to describe and simulate the charge balance of the film.

The effect of film thickness on the E3 "crossover" voltage for a series of films was measured and the results are plotted in Fig. 1. The values of E3 vary continuously for thicknesses from 170 nm to 1400 nm and can be fitted to a relationship such that $(E3)^{1.4}$ is proportional to the thickness. Varying the beam current typically did not change the value of E3, but did cause the persistence time of the charged square to increase with increasing beam current. Surprisingly, tilting the sample up to 40° also did not change E3. However, sputtering a 0.1 μ m gold film on the Si substrate decreased E3 from 11.0 keV to 10.0 keV for a 1.3 μ m polymer thin film on the surface.

Discussion

To the first order, the charge deposited in a solid at a particular depth can be modeled with Monte Carlo calculations by equating the charge to the energy deposited at that depth.¹¹ If we consider this concept with respect to a thin film, we can then say that the fraction of energy F lost by the incident beam current to the film ranges between $0 < F < 1$. We make the first-order assumption that the fractional energy loss by the beam to the thin film equals the total charge lost by a fraction of the beam I_F that is deposited into the film. The charge balance previously discussed can then be modified for the thin film as follows:

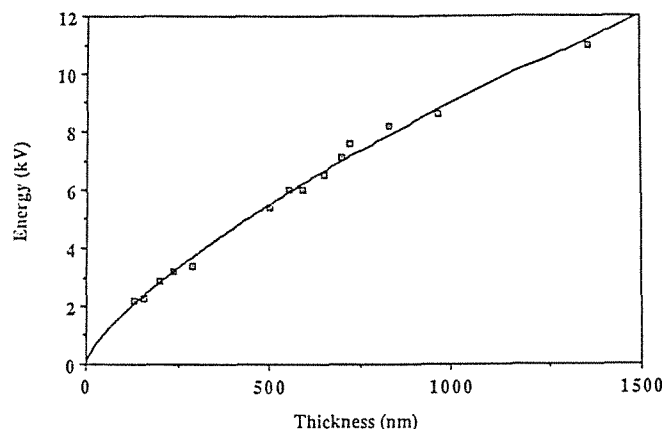


FIG. 1.--Effect of film thickness on beam energy of E3 "crossover" for thin-film photoresist on silicon.

$$I_F = (I_{SE} + I_{BE}) + I_{SP}$$

If the film is a conductor, then I_{SP} (of the film) can maintain neutrality by compensating for changes in I_F , I_{SE} , and I_{BE} as film thickness or accelerating voltage vary. If the film is an insulator, $I_{SP} = 0$ for the film and the film charge balance is generally not 0, but is determined by the relative values of I_F and $(I_{SE} + I_{BE})$. We shall use the term "dynamically charge balanced" to refer to the neutral condition at the E3 "crossover" voltage when $I_F = (I_{SE} + I_{BE})$. The thin insulating film charges negatively when $I_F > (I_{SE} + I_{BE})$ and charges positively when $I_F < (I_{SE} + I_{BE})$. Also, when the sum of $I_F = (I_{SE} + I_{BE})$ changes sign at E3, the surface polarity changes. The current deposited I_F and the exit electron currents $(I_{SE} + I_{BE})$ in the film are shown schematically in Fig. 2(a) and the ratio of $(I_{SE} + I_{BE})$ to I_F is plotted schematically as a function of accelerating voltage in Fig. 2(b). The film behaves as a bulk polymer at lower voltages near E1 and E2, but behaves as a thin film at higher voltages near and above E3, as a larger fraction of the beam current penetrates through the film to be deposited in the substrate. The interaction volumes are shown in Monte Carlo plots for a 0.83 μ m photoresist film on Si in Figs. 3(a), (b), and (c) for energies which are below, at, and above the E3 "crossover" for voltages of 6.0, 8.2, and 10 keV, respectively. These figures show that a larger fraction of charge is deposited in the substrate as the energy increases.

From these concepts, the charge balance on a thin film can be determined by use of Monte Carlo methods to calculate I_F , I_{SE} , and I_{BE} . These calculations take into account interactions of the primary beam with both the thin film and the substrate. The effect of beam energy on the fractional energy deposited F ,

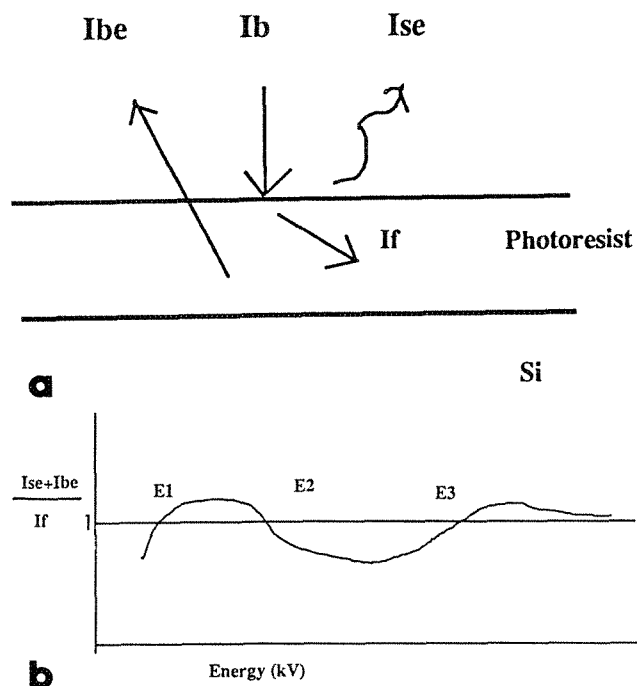


FIG. 2.--Thin-film insulator on conducting substrate showing (a) schematic diagram of electron currents and fractional charge deposition, (b) schematic plot of effect of accelerating voltage on ratio $(I_{SE} + I_{BE})$ to I_F .

total electron yield $(I_{SE} + I_{BE})$, and charge balance have been calculated for a $0.83\mu\text{m}$ -thick photoresist on silicon and are shown in Figs. 4(a), (b), and (c), respectively. Figure 4 shows the film is "dynamically charge balanced" at an E3 "crossover" at 8.2 keV, which agrees with the measured value of 8.3 keV. A unique aspect of the effect of the film-substrate couple on electron yield is that as accelerating voltage increases, a maximum in secondary yield occurs at about 8 keV, as can be inferred from the peak of the total electron yield seen in Fig. 4(b).

Monte Carlo methods were used to calculate the effect of film thickness on the E3 "crossover" and it was found that thickness is proportional to $(E3)^{1.4}$, which is in excellent agreement with the experimental result. This value is similar to, but slightly less than, the $E^{1.7}$ dependence of electron range in a homogeneous bulk sample as specified by the Kanaya—Okayama model.¹² This discrepancy is probably due to the higher atomic number of the silicon substrate compared to the lower atomic number of the thin photoresist film. It has also been shown that a thin *conducting* film on a bulk substrate also experiences brightness changes as a function of accelerating voltage when there is a significant difference in the BE coefficient of the two materials.¹³ In this work the effect of increasing the atomic number of the substrate, as achieved by sputtering $0.1\mu\text{m}$ of gold prior to applying the photoresist to the silicon, resulted in a decrease in E3 from 11.0 to 10.0 deV for a $1.3\mu\text{m}$ -thick photoresist. Monte Carlo methods were used to calculate the

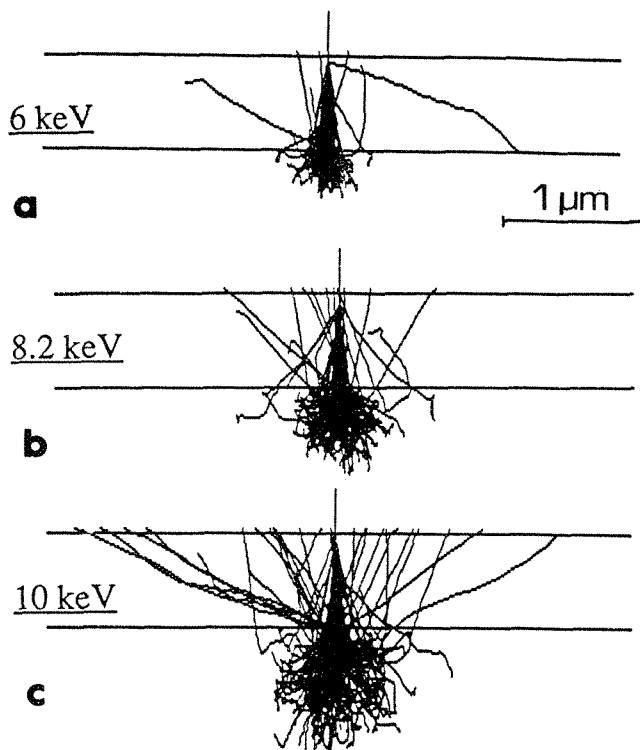


FIG. 3.--Monte Carlo plots for electron penetration in $0.83\mu\text{m}$ -thick photoresist on silicon for accelerating voltages (a) 6.0 keV, (b) 8.2 keV, (c) 10.0 keV.

effect of substrate atomic number for a $0.83\mu\text{m}$ photoresist film and it was found that E3 decreased from 8.3 keV for silicon to 7.9 keV for GaAs to 7.0 keV for Au. The trend for experimental and calculated results agrees and can be explained by the fact that total electron yield increases with a higher-atomic-number substrate because of the higher BE yield plus the higher BE-induced SE yield. The experimental result that tilt, up to 40° , did not affect E3 was somewhat surprising, but was in agreement with Monte Carlo calculations, which also showed no shift in E3 for tilts up to 40° . The constancy of E3 during tilting is due to offsetting factors of increased charge deposition into the film, due in turn to increased path length, which is balanced by increased electron emission from the film.

The general behavior of a thin insulating film is shown in Fig. 5, which schematically plots surface potential as a function of accelerating voltage for the first, second, and third "crossovers" of E1, E2, and E3. The plot shows the regions for which it is possible to use the SEM to image a thin insulating film when the accelerating voltage E is at a value such that $E1 \leq E \leq E2$ or when $E \geq E3$. It shows that it is possible to electron-beam write a polymer resist, which requires complete penetration of the film, when $E \geq E3$. Because E3 is a continuous function of thickness, the E3 value for a given film-substrate couple could be used to measure film thickness. This measurement could be made by a comparison of the E3 value to a calibration curve obtained either from values measured experimentally or

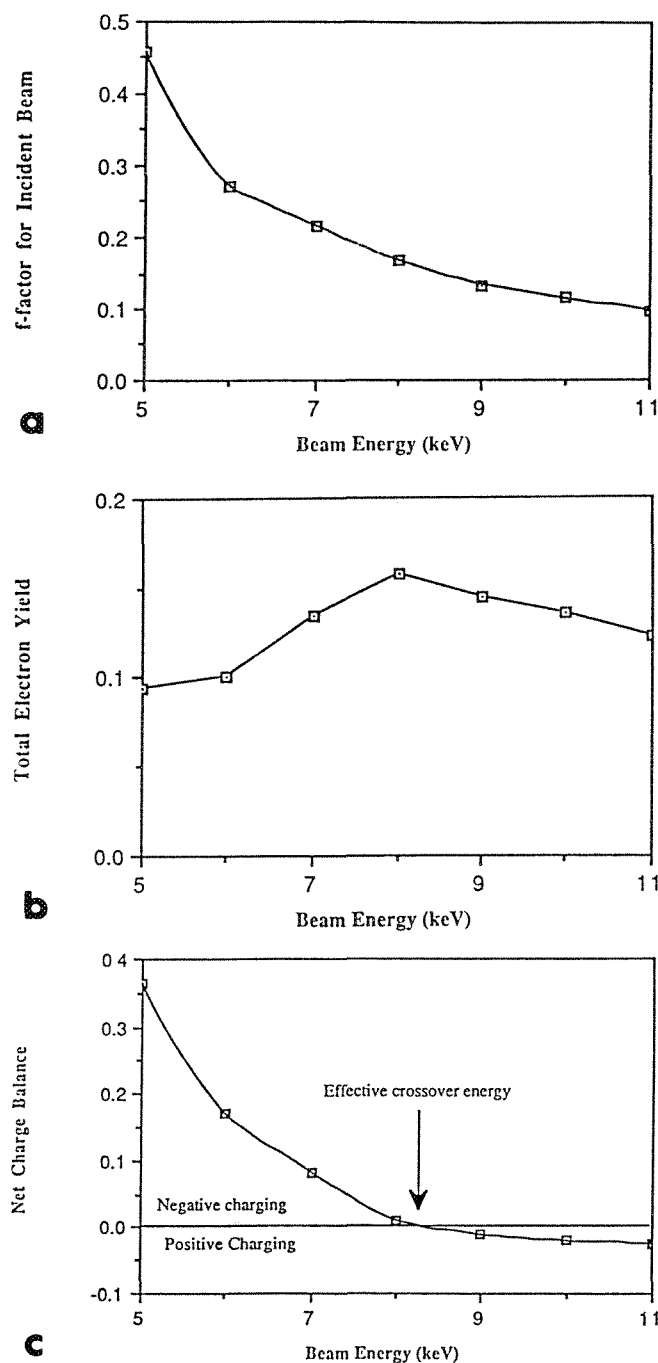


FIG. 4.--Effect of accelerating voltage on (a) fractional energy deposition F , (b) total electron yield ($I_{SE} + I_{BE}$), (c) charge balance for $0.83\mu\text{m}$ -thick photoresist film on silicon substrate.

from values calculated from Monte Carlo methods.

In summary, we have investigated, both experimentally and theoretically, the effects of electron-beam interactions on charge balance for a thin insulating polymer film on a conducting substrate with a SEM and have demonstrated that a new, third "crossover" of accelerating voltage E_3 exists at which the thin film is "dynamically charge balanced." This crossover is

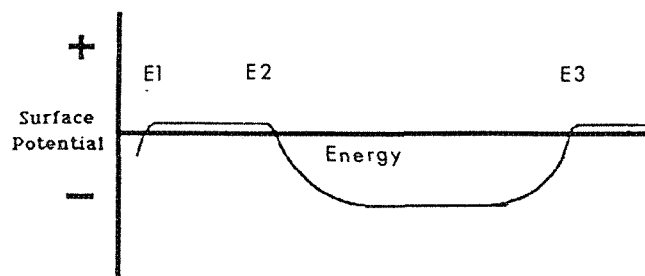


FIG. 5.--Schematic diagram of effect of accelerating voltage on surface polarity for thin-film insulator on conducting substrate showing E_1 , E_2 , and E_3 "crossovers."

due to the fraction of charge deposited in the film being balanced by the electrons exiting from the film. Monte Carlo calculations on the charge balance in the film agree well with the experimental results and show that E_3 is decreased with thinner films and higher-atomic-number substrates, but is unchanged by tilting to 30° . The concepts of "dynamic charge balancing" and the E_3 "crossover" of thin film insulators on conducting substrates should prove useful for measuring film thickness and for determining the thickness limits to avoid negative charging artifacts in imaging or in electron-beam writing.

References

1. J. R. White and E. L. Thomas, *Rubber Chemistry and Technology* 57: 457, 1984.
2. D. C. Joy, *Microelectronic Engineering* 1: 1034, 1983.
3. A. P. Tyutnev, V. S. Sayenko, G. S. Mingaleev, and Y. D. Pozhidayev, *Polymer Science U.S.S.R.* 25: 1206, 1981.
4. J. B. Pawley, *Scanning Electron Microscopy* 1: 153, 1972.
5. O. W. Vaz and S. J. Krause, *Proc. EMSA* 44: 676, 1986.
6. V. K. Berry, *Scanning* 10: 19, 1987.
7. D. B. Holt, M. D. Muir, P. R. Grant, and I. M. Boswarva, *Quantitative Scanning Electron Microscopy*, London: Academic Press, 1974, 117.
8. O. W. Vaz, Master's thesis, Arizona State University, 1986.
9. G. H. Bernstein, Ph.D. dissertation, Arizona State University, 1987.
10. H. Y. Liu, M. P. deGrandpre, and W. E. Feely, *J. Vac. Sci. Technol.* B45: 379, 1988.
11. K. Kanaya and S. Ikayama, *J. Phys.* D5: 43, 1972.
12. D. C. Joy, *J. Microscopy* 147: 51, 1987.
13. D. B. Williams, private communication.

USE OF SEM AND EDS TO MONITOR AND CHARACTERIZE Al/Cu/Si METALLIZATION

R. C. Chapman, W. B. Rogers, and D. G. Thompson

Al/CuSi alloys are commonly used in VLSI metallization. An Al/Cu/Si alloy is the metallization of choice at the Microelectronics Center of North Carolina (MCNC) as well. Because MCNC uses liftoff metal patterning processes, these alloys are typically deposited on wafers through evaporation. In liftoff processing, step coverage must be minimized to assure separation of the metal deposited on a patterned photoresist stencil from that deposited on the substrate. Connection of the two deposited films does not allow proper liftoff. Through evaporation from a single centered crucible, minimal step coverage may be obtained as the vapor stream is virtually normal to the wafer surface.

The evaporated metal consists of an 800nm-thick 4.5wt% Cu/Al film with a 20nm-thick Si cap. The Al and Cu are co-evaporated from a single centered crucible. The Si is subsequently evaporated from a separate centered source. For a 4.5wt% Cu/Al film, it has been found that a 26wt% Cu/Al source material is necessary because of the different vapor pressures of Al and Cu. To maintain the source material concentration at 26wt% Cu, the source must be periodically replenished with an amount of 4.5wt% Cu/Al material equal to the amount that has been evaporated.

After evaporation, the film is annealed in a forming gas at 400 C for 30 min. The purposes of annealing the metal are several. The primary is to increase the conductivity of the metal itself and of the metal-to-silicon contacts; another is to allow the Cu to precipitate at Al grain boundaries to prohibit electromigration of the Al, a phenomenon that can lead to open or short circuits in device metal lines;¹ yet another is to allow the incorporation of Si from the Si cap into the bulk metal. By satisfying the solid solubility of Si in Al, diffusion of Si from the substrate into the overlying metal is inhibited and hence prevents junction spiking, a phenomenon in which the p-n junction is shorted.²

One undesirable effect of the annealing process is hillock formation. A hillock is a protrusion from the metal film caused by the difference in the thermal expansion of the metal layer and the underlying substrate. During annealing of a deposited metal film, the thermal expansion of the metal is greater than in the substrate, which drives the metal into compressive stress. To relieve this stress, a local raised area (i.e., hillock) is formed.³ Hillocks, depending on their size and population, can cause shorting between metal levels in mul-

tilevel metallization processes.

Hillocking lends itself to easy study by scanning electron microscopy (SEM) and x-ray mapping, a form of energy-dispersive spectroscopy (EDS) in which the locations of high concentrations of elements in a film can be determined by correlating electron-beam location to detected characteristic x rays. SEM and EDS are also useful for examining Cu concentrations in evaporated films. In this study, these techniques are used to monitor the Cu concentration in evaporated Al/Cu/Si films showing the effectiveness of source replenishment. SEM and x-ray mapping are used to study the effects of annealing the alloy.

Experimental

Standards were made for quantitative EDS. Rutherford backscattering spectroscopy (RBS) was used to determine actual Cu concentrations. These standards were films of approximately 800 nm Al/Cu deposited onto 0.5mm-thick graphite squares. The source material started as approximately 26wt% Cu/Al. Several runs were made without replenishing the source, which allowed it to deplete. The films obtained from these runs were then measured for Cu content by RBS. EDS spectra of these standards were taken on a JEOL JSM-840 equipped with a KeveX Analyst 8000 EDS system. The electron accelerating voltage was 20 keV, which is sufficient to excite the desired Al K α (1.49 keV) and Cu K α (8.05 keV) lines. These spectra were stored with the RBS-determined Cu concentrations in a library of standards. Using a χ^2 matching routine, the standard spectra are compared for closest fit to that of an unknown using χ^2 minimization. Once a standard spectrum is chosen, the concentration of Al and Cu in the unknown is determined through linear interpolation of the Al and Cu peaks.

Using EDS x-ray mapping on the SEM with the KeveX system and in situ annealing, we viewed the nucleation of Cu and Si in the bulk Al metal. An x-ray map of a $3.5 \times 5 \mu\text{m}$ area was made of an 800nm-thick film of 4.5wt% Cu/Al with a 20nm-thick Si cap evaporated onto a Si substrate. An electron accelerating voltage of 5 keV and a specimen tilt of 50° was used to minimize the number of electrons that reach the substrate and also to accent surface phenomena. A micrograph of the area was taken for future reference. The film was then annealed in situ on a Gatan SEM hot stage for 30 min at approximately 400 C. Another map of the evaporated metal film was obtained and compared to the first. A second micrograph was taken of the area mapped for correlation of defect locations to Cu and Si nucleation sites.

The authors are at the Microelectronics Center of North Carolina, 3021 Cornwallis Road, Research Triangle Park, NC 27709.

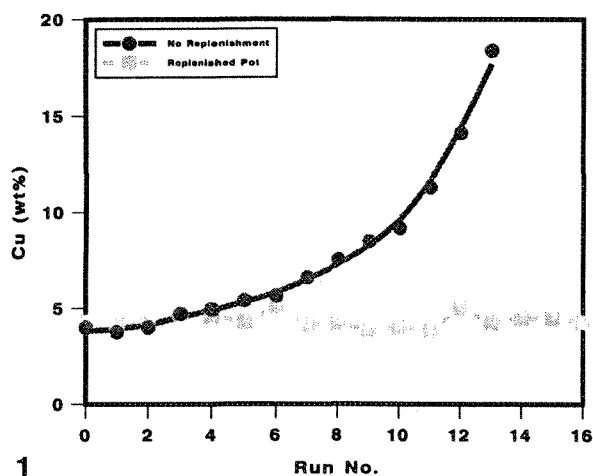
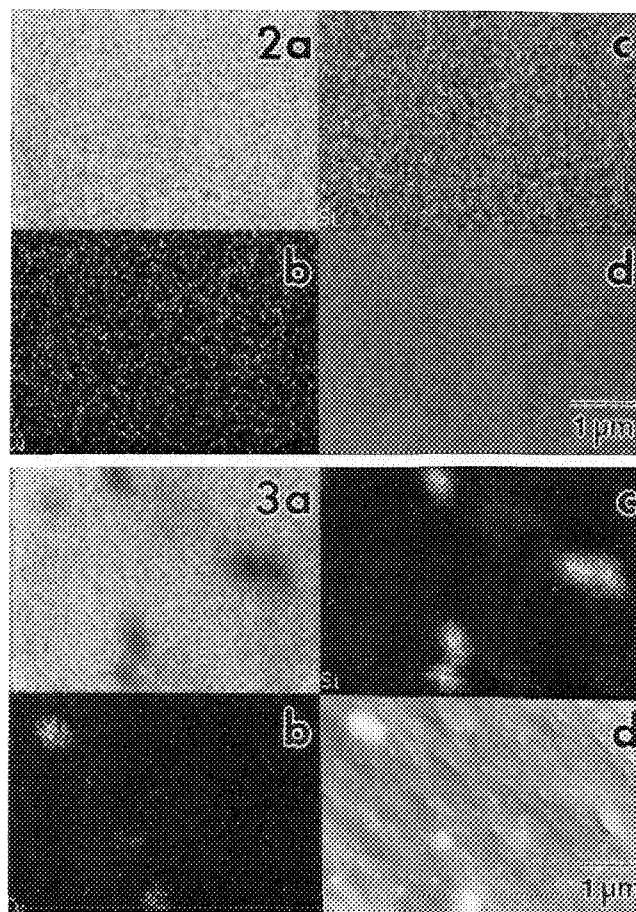


FIG. 1.--Change in Cu concentration in Al/Cu films evaporated from replenished and unreplenished sources.

FIG. 2.--X-ray maps of Al, Cu, and Si in deposited films prior to annealing: (a) Al-K map, (b) Cu-L map, (c) Si-K map, (d) corresponding electron micrograph obtained by Everhart-Thornley detector.

FIG. 3.--X-ray maps of Al, Cu, and Si in the deposited films after annealing: (a) Al-K map, (b) Cu-L map, (c) Si-K map, (d) corresponding electron micrograph obtained by Everhart-Thornley detector.



Results and Conclusions

Figure 1 shows the expected exponential increase in Cu concentration in the film as the source material was depleted to make the Al/Cu standards. Figure 1 also shows that by use of these standards with a χ^2 matching routine for EDS quantitative analysis, subsequent Al/Cu films can be tracked for Cu concentration. All deposited films track closely to the desired 4.5wt% Cu concentration. This finding demonstrates that not only can EDS be used to monitor the Cu content of the films, but also that source replenishment does maintain the Cu concentration within the desired range.

Figures 2 and 3 show the x-ray maps and electron micrographs obtained before and after annealing, respectively. Nucleation of Cu and Si are seen in the once homogeneous films after the anneal. Comparison of the x-ray maps to the micrographs show no apparent correlation between Cu nucleation sites, Si nucleation sites, and defect structures, in particular, hillocks.

References

1. S. C. P. Lim, "Reduction of hillock formation in aluminum thin films," *Semiconductor International*, April 1982, pp. 135-145.
2. S. M. Sze, *VLSI Technology*, New York: McGraw-Hill, 1983, 367.
3. D. S. Herman, M. A. Schuster, and R. M. Gerber, "Hillock growth on vacuum deposited aluminum films," *J. Vacuum Science and Technology* 9: 515-519, 1972.

MATERIALS CHARACTERIZATION OF ALLOYED OHMIC CONTACTS ON GaAs

T. D. Kirkendall and D. B. Wilcox

The long-term failure of GaAs ICs is often due to the degradation of ohmic contacts in Metal-Semiconductor Field Effect Transistors (MESFETs) which are active elements of GaAs Monolithic Microwave Integrated Circuits (MMICs). In this study we investigated the failure mechanisms of ohmic contacts fabricated by alloying and by sintering on GaAs MMICs and identified the physical and chemical qualities that would contribute to both low initial contact resistance and long-term chemical and electrical stability of ohmic contacts.

Technology

At the present time, the most widely used method of fabricating ohmic contacts on n-type GaAs involves the multilayer vacuum deposition of gold, germanium, and nickel. The proportion of Au and Ge is usually chosen to be equivalent to the eutectic composition of 88% Au-12% Ge by weight. Contact areas are usually defined by a mask of photo resist or glass in conjunction with a lift off. A high-temperature (≥ 400 C) furnace exposure in forming gas is used to effect "alloying" between the metals and the semiconductor, and thus achieves low contact resistance. Specific contact resistivities of $\leq 1 \times 10^{-6} \Omega\text{-cm}^2$ are routinely achieved by this method; however, the morphology of such contacts needs further improvements.

This fabrication process has changed little from that originally described 22 years ago by Braslau et al.¹ The current consensus is that the contact is actually made by Ge occupying Ga vacancies in the GaAs lattice. The Ni is associated with the formation of compounds with As and Ge which react with the GaAs and enhance the transport of Ge diffusing in and Ga diffusing out during the alloying.^{2,3} If the alloy time is too long, Au may diffuse into the GaAs, where it acts as an acceptor and may compensate the n layer.^{2,3} Should excess Ni diffuse into the GaAs, it will act as a deep-level trap.⁴ Thus, it is apparent that the fabrication of ohmic contacts is as much an art as a science.

Failure Mechanisms

The degradation of ohmic contacts manifested by increased contact resistance is one major long-term failure mechanism of power MESFETs.^{3,5} Factors that can affect the stability of ohmic contacts are surface damage, traps associated with impurities and defects,⁶ and contamination (including oxides) at the interface.

The authors are at COMSAT Laboratories, Communications Satellite Corp., Clarksburg, MD 20871. Fabrication support by F. R. Phelleps and A. B. Cornfeld is gratefully acknowledged.

In the present study, a comparison is made of the compositional and morphological characteristics of a high temperature furnace alloyed contact (conventional method) vs a rapid thermal alloyed (RTA) contact. Both contacts were made with electron beam evaporated layers of Au (700Å)/Ge (350Å)/Ni (150Å)/Ag (1000Å)/Au (1800Å) in that order on <100> GaAs. The objective of this study was to develop a means of fabricating ohmic contacts that exhibited improved control of alloy depth and long-term reliability. Two contact alloying schemes were evaluated: (a) the conventional high temperature/long-time furnace alloy (>400 C/1 min), and (b) rapid thermal alloy (RTA) of 320 C/5 s and 475 C/4 s. Both alloy processes produced contacts with comparably low contact resistances, yet the bulk metallurgical structure of the two is widely different.

Analytical studies were performed on the two types of contact alloy by use of an innovative method to expose the undersides of the contacts by selective removal of all the GaAs with a backside chemical etch. Shown in Fig. 1 are backscattered electron (BSE) micrographs of the gallium arsenide's eye view of the furnace-alloyed and the rapid-thermal-alloyed contacts. The contrast in the BSE micrographs delineates the various phases and alloy compositions, from the bright areas associated with high gold content to the darkest regions denoting phases rich in nickel. At least three distinct gray levels are discernible to the naked eye. There is a marked difference in roughness and homogeneity of the two contacts. In prior studies by thermal wave microscopy,⁷ the alloy phase segregations were shown to extend throughout the thickness of the metal contact.

Since the gray level in the BSE micrograph is a function of the average atomic number determined by the local composition, an estimate of the areal distribution of a particular compositional phase or alloy can be obtained from a histogram analysis of the BSE image. A digital BSE image is collected in a 512×512 pixel array (Fig. 2a) by a computer-controlled SEM, and is then played back in portions representing user-selected windows of gray levels, such as the three depicted in Figs 2(b), (c), and (d). In this example, the three ranges of gray level (i.e., atomic number) are identified with Au-rich, Ni-rich, all intermediate compositions, respectively. The contact interfacial area of each compositional phase or alloy is easily computed by this analytical scheme and is useful in elucidating the metallurgical role of each phase in effecting good or poor ohmic contact.

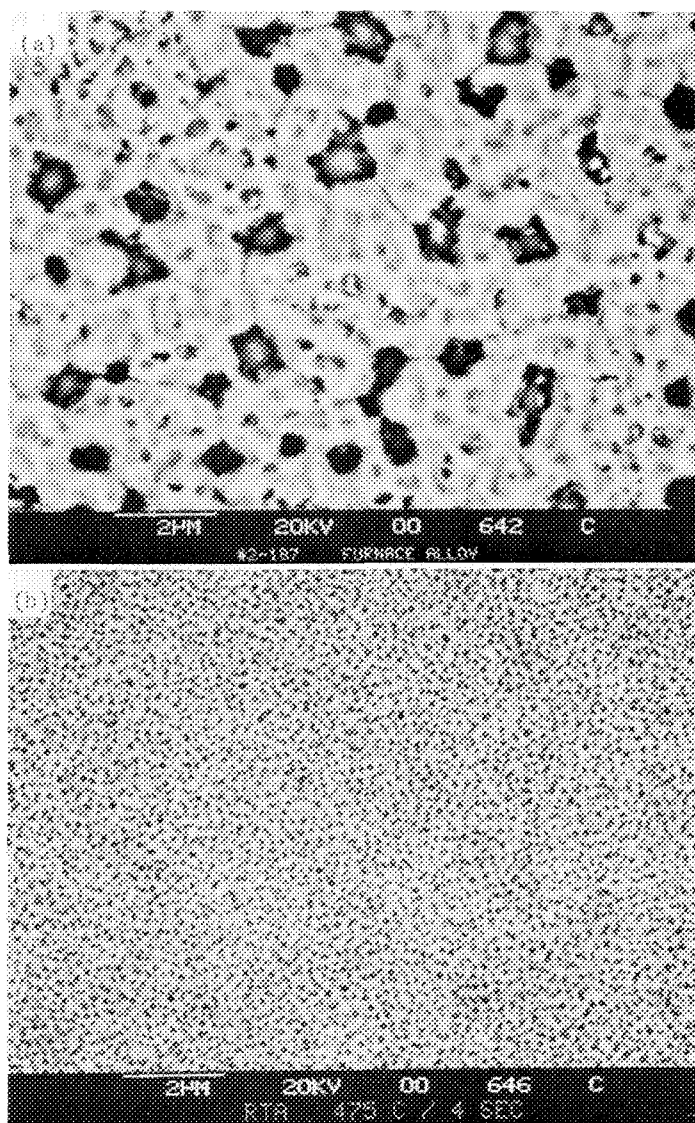


FIG. 1.--BSE micrographs of undersides of two ohmic contacts: (a) conventional furnace alloy, (b) rapid thermal alloy.

Filamentary Diffusion

Power GaAs FETs, operated under short pulse conditions, have been seen to fail due to thermally induced metal intrusion into the GaAs at source and drain contacts.⁸ Irregularities in the ohmic contact/GaAs interface are a probable source of concentrations of hot electrons leading to filamentary metal-GaAs interdiffusion and substrate burnout. By use of the back-etch process to remove GaAs selectively from the underside of ohmic contacts, the presence of gold-gold-rich spikes has been observed to extend thousands of Ångströms beneath the contact interface, well beyond the nominal penetration depth of the contact (Fig. 3). These protrusions occur at random throughout the contact area on power GaAs FETs both on the mesa and on the buffer layer, but the preponderance of spikes occurs on the sloping edges of the mesa delineating the n-doped epi layers and the buffer layer. This configuration indicates that

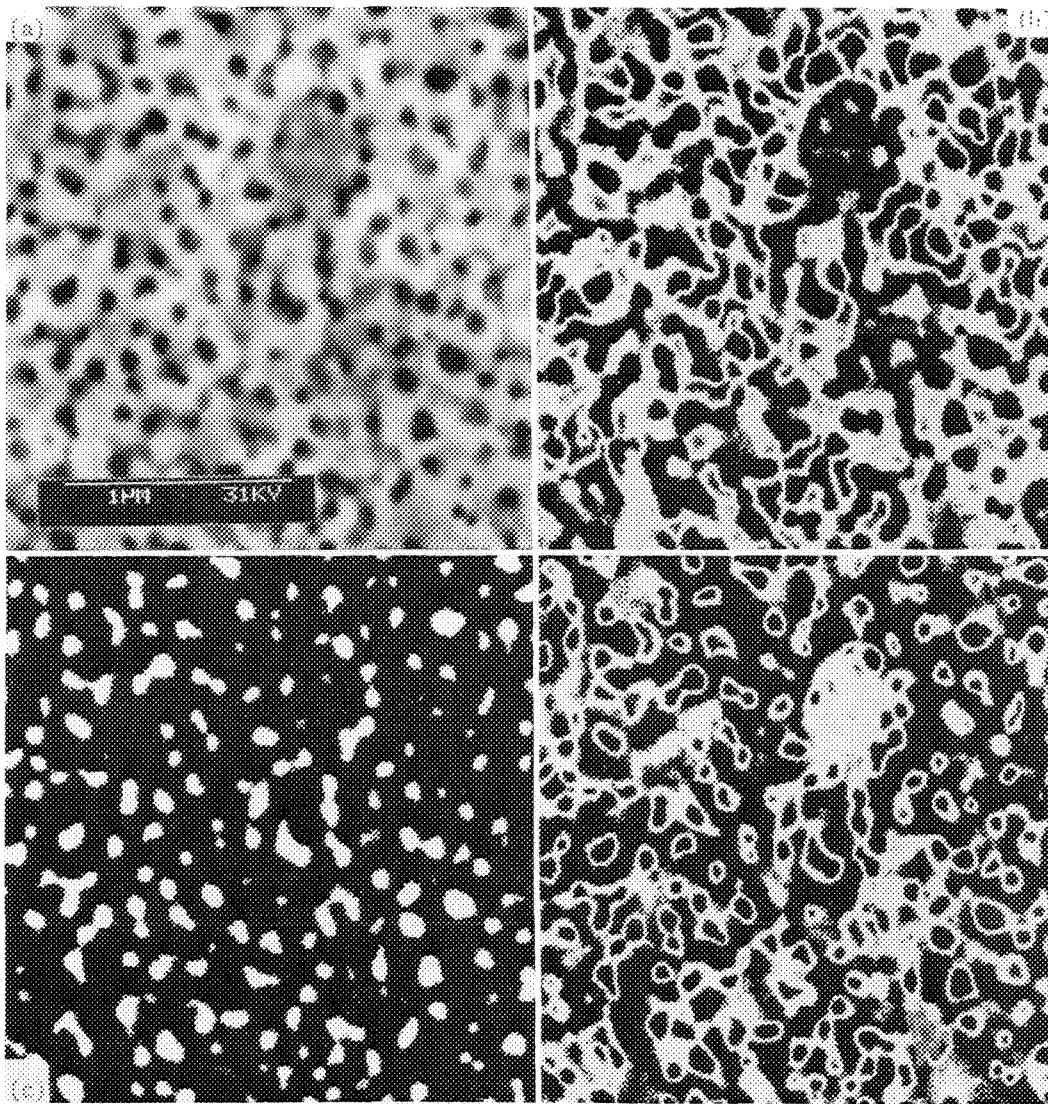
thermally assisted diffusion of Au into GaAs is sensitive to crystal orientation. The RTA fabrication process eliminates these deep gold spikes and produces a more homogeneous interface structure. Accelerated life tests of MESFETs made with the RTA process show predicted mean time to failure $>10^6$ h as required for satellite and other high-reliability applications.

Conclusions

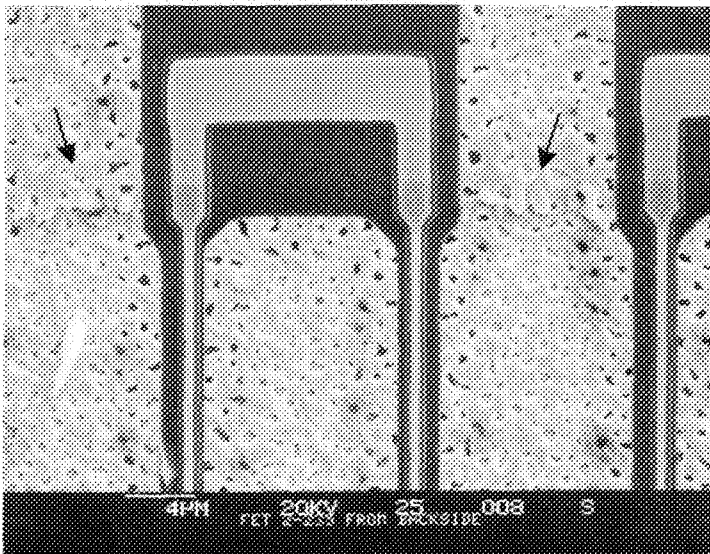
The RTA ohmic contacts exhibited certain preferred morphological and chemical characteristics especially desired for fabricating high-reliability devices: more uniform alloy depth, no spiking of the Au into the semiconductor, less initial lateral diffusion of metals, and lower probability of diffusion induced deep level traps in the vicinity of the contacts. The novel technique of etching away the GaAs is also a useful tool for failure analysis of devices. It allows one to uncover and analyze failure sites beneath ohmic and Schottky contacts in situ and is less destructive than cross sectioning.

References

1. N. Braslau, J. B. Gunn, and J. L. Staples, *Solid-State Electronics* 10: 381, 1967.
2. M. Heiblum, M. I. Nathan, and C. A. Chang, "Characteristics of AuGeNi ohmic contacts to GaAs," *Solid-State Electronics* 25: 3, 185-195, 1982.
3. T. S. Kuan et al., "Electron microscope studies of an alloyed Au/Ni/Au-Ge ohmic contact to GaAs," *J. Appl. Phys.* 54(No. 12): 1983.
4. O. Aina et al., "Low-temperature sintered AuGe/GaAs ohmic contact," *J. Appl. Phys.* 54(No. 1): 1982.
5. K. Togashi, H. Takukuwa, and Y. Kato, "Reliability of low noise microwave HEMTs made by MOCVD," *Microwave J.*, 1987.
6. K. Ohata and M. Ogawa, "Degradation of gold-germanium ohmic contact to n-GaAs," *Reliability Physics Symposium*, 1974.
7. T. D. Kirkendall and T. P. Bammel, "Thermal wave imaging of GaAs material and devices," *J. de Physique* 45: C2-877-880, 1984.
8. W. T. Anderson, F. A. Buot, and A. Christou, "High power pulse reliability of GaAs power FETs," *IEEE/IRPS*, 1986.



2



3

FIG. 2.--Digitized, 512×512 pixel BSE micrographs of rapid thermal alloy contact: (a) original BSE video, (b) high-at.no. Au-rich component, (c) low-at.no. Ni_2GeAs phase, (d) mid-at.no. Ag-rich component.

FIG. 3.--SE micrographs of underside of conventional alloyed ohmic contact exhibiting filamentary diffusion of Au spikes at mesa edge.

ROUTINE ELECTRON MICROPROBE ANALYSIS OF CARBON IN HIGH- T_c SUPERCONDUCTORS: INITIAL RESULTS

R. V. Heyman, D. K. Ross, and Don Elthon

The recent discovery of high-temperature superconductors (HTSC)^{1,2} has led to a worldwide surge of activity to refine and improve these materials. Characterization of the microchemical and microstructural features of HTSC materials is an important step in both understanding the principles of superconductivity and in developing new materials. This laboratory has been involved in routine microanalysis of materials in the Y-Ba-Cu-O system, the Bi-Sr-Ca-Cu-O system, and other related systems. Analyses of these materials, has shown that carbon is a common contaminant in specimens that have been prepared from carbonate starting materials (e.g., BaCO_3 , CaCO_3 , etc.).

Until very recently, measurement of low concentrations of light elements (e.g., C, N, O) required exacting efforts by the electron microprobe operator. Very high sample currents and very long counting times were required. Most intensity ratio correction programs would not work; they either produced results that were obviously wrong or the correction program would not run without major malfunctions. A calibration curve was usually the only reliable method for working with these elements.

Recent development of Layered Synthetic Microstructure (LSM) crystals provide much higher count intensity than previously available. Recent improvements in quantitative analysis intensity ratio correction procedures such as ZAF and $\phi(\rho z)$ combined with improved measurements of critical coefficients (e.g., Henke coefficients³) and refinements in the correction programs themselves have made computer corrections for the light elements possible. By combining these improvements in one system, routine quantitative analysis of carbon has now become both possible and practical.

Experimental

All samples were analyzed on a JEOL JXA-8600 electron microprobe equipped with four wavelength-dispersive spectrometers (WDS) and one energy-dispersive spectrometers (EDS). Two WDS spectrometers are configured for light-element analysis. One light-element spectrometer contains pentaerythritol (PET), thallium acid phthalate (TAP), Layered Dispersive Element-Boron (LDEB) ($2d = 145\text{--}150 \text{ \AA}$)⁴, and Layered

Dispersive Element 1 (LDE1) ($2d = 60 \pm 1 \text{ \AA}$) crystals.⁵ The other light-element spectrometer contains TAP and New Lead Stearate (NSTE) crystals. The other two WDS spectrometers each contain a PET crystal and a lithium fluoride (LIF) crystals. Carbon is usually analyzed with LDE1.

Vacuum in the column region is provided by a water-baffled diffusion pump and mechanical roughing pump providing 4×10^{-6} Torr. The gun chamber may be differentially pumped with a sputter ion pump (SIP) to 8×10^{-7} Torr. A liquid-nitrogen-cooled anticontamination cold finger limits carbon contamination to less than 0.003 wt.%/min when activated. The cold finger has not been used for most routine analyses.

Automation is by Tracor Northern (TN) and consists of a 5600 programmable automation controller module and a TN EDS with 5500 display system coupled to a Digital Equipment Corp. (DEC) 11/73 computer with 3 megabytes of memory. Conversion of instrument-produced intensity ratios into concentrations used the ZAF correction method with Henke et al. coefficients³ as supplied by TN (version 12/L-80).

Carbon's peak position is determined by TN's CALIBRATE routine in their TASK automation program. Background positions are determined by examination of spectrometer scans and confirmed by count intensity measurements at the background positions for all of the elements analyzed (Table 1). Potential peak overlaps of lines from other elements are also identified by this technique. An open detector slit was used.

Usual operating conditions for this instrument for analysis of HTSC materials are 15 kV and 20 nA. These conditions result in a carbon count rate of approximately 1000 counts per second on a graphite standard. A $10\text{-}\mu\text{m}$ -diameter spot size was used, which minimized the effects of surface irregularities, sample heating, and low-order inhomogeneity.

HTSC samples analyzed in this laboratory are usually pressed powder pellets, sintered pressed-powder pellets, or thin films. Both pellet types present several difficulties for carbon analysis. These pellets are friable, fine-grained, and porous. They therefore require vacuum impregnation in a room-temperature self-polymerizing medium so that their surfaces can be polished flat. We are not at present aware of such a medium that is also conductive. Unless the sample is large enough to allow conductive painting of both medium surface and sample edge, vapor deposition of a conductive layer is necessary. We are at present experimenting with Al and Si as conductive

The authors are at the Texas Center for Superconductivity, University of Houston (TCSUH), Houston, TX 77204. Ross and Elthon are also at the UH Department of Geosciences. This material is based on work supported by the UH Texas Center for Superconductivity under prime grant MDA 972-88-G-0002 from DARPA and the State of Texas.

TABLE 1.--Test for interference peak overlaps on carbon: 100s counting time. All standards carbon coated.

Standard	Benitoite	YAG	Olivine	CuFeS ₂	CARBON	ZnS
Peak	2776	2682	2109	2756	89600	3087
+25 mm	1388	1450	1218	1564	3119	1815
-25 mm	1280	1409	1067	1561	1991	1501
Ave Bkg.	1334	1430	1142	1562	2555	1558

TABLE 2.--Analysis of Y-Ba-Cu-O film on silicon substrate. First line for each point is analysis (wt%) with carbon and silicon excluded from ZAF corrections. These 15 points are part of a 24-point scan in which first and last points were determined by operator; all others by computer interpolation.

Pt	Y	Ba	Al	Cu	O	C	Si	Total	Ave.
1	13.69	42.17	.09	27.35	15.24			98.54	
	13.71	42.39	.09	27.50	15.57	1.41	.10	100.78	
2	13.99	41.73	.10	27.71	15.20			98.72	
	14.00	41.94	.10	27.89	15.52	1.37	.06	100.88	
3	14.20	41.65	.11	28.48	15.28			99.72	
	14.22	41.74	.11	28.56	15.46	0.53	.06	100.61	
4	14.32	41.67	.09	28.66	15.60			100.33	
	14.33	41.78	.09	28.75	15.77	.74	.05	101.50	
5	14.11	41.79	.10	28.09	15.23			99.31	
	14.12	41.87	.10	28.15	15.35	.55	.05	100.19	
6	14.19	41.60	.09	27.92	15.41			99.2	
	14.20	41.71	.09	27.99	15.57	.71	.10	100.33	
7	14.09	41.89	.10	27.87	15.06			99.01	
	14.11	41.98	.10	27.94	15.18	.59	.05	99.95	
8	14.10	41.08	.10	28.54	15.49			99.30	
	14.12	41.16	.10	28.59	15.60	.50	.05	100.13	
9	13.95	41.42	.09	28.35	15.31			99.12	
	13.96	41.48	.09	28.40	15.39	.40	.05	99.77	
10	14.11	41.62	.10	27.82	15.45			99.10	
	14.12	41.71	.10	27.88	15.58	.57	.05	100.01	
11	14.01	41.77	.10	28.07	15.25			99.20	
	14.02	41.86	.10	28.14	15.38	.60	.05	100.14	
12	14.02	41.62	.10	28.15	15.54			99.43	
	14.03	41.69	.10	28.20	15.64	.44	.05	100.16	
13	14.15	41.61	.09	28.53	15.33			99.72	
	14.17	41.73	.09	28.62	15.50	.77	.04	100.92	
14	14.03	41.97	.10	28.30	15.48			99.89	
	14.04	42.06	.10	28.37	15.60	.59	.05	100.82	
15	13.90	41.84	.10	28.03	15.20			99.07	99.18
	13.91	41.90	.10	28.08	15.28	.37	.04	99.68	100.07

coating alternatives for the traditional choice of carbon because ZAF cannot correct for an extra thin-film layer of an element being analyzed.

However, thin-film samples do not present these difficulties. At 15 kV accelerating potential, 2 μ m-thick HTSC films are not penetrated by the electron beam. The sample surfaces are generally flat and relatively smooth. These samples can be routinely analyzed without any special sample preparation or conductive coating, and normal ZAF corrections can be used.

ZAF calculations were performed on line for the major elements (e.g., Y, Ba, Cu, and O) and Al. K-ratio values for all the above elements plus Si and C were obtained as output and were manually entered into ZAF corrections later.

Results

An example of results obtained from a Y-Ba-Cu-O thin-film HTSC (nominally 2 μ m thick) deposited on a silicon metal substrate is shown in Table 2. These 15 points are individual analyses obtained along a traverse across the thin-film surface. Peak and background counts are collected for Y, Ba, Cu, O, Si, Al, and C at each point. Silicon is analyzed to check for possible beam penetration into the substrate; Al can sometimes occur as a contaminant from ceramic crucibles used in sample preparation.

Carbon concentrations in Y-Ba-Cu-O and Bi-Sr-Ca-Cu-O HTSC materials prepared with carbonate starting materials is often of the order of 0.5 to several weight percent (Table 2 and our unpublished data). Because the combined ZAF correction factors for C are approximately 2.8 for these compounds, a relatively small measured concentration ratio (k-ratio) of carbon will result in a substantial amount of carbon in the final concentration value. Carbon measurements in HTSC materials consequently require very accurate measurements of the intensity ratios.

Conclusions

Development of LSM crystals capable of producing high count rates from carbon and other light elements and implementation of Henke correction coefficients into vendor-supplied ZAF correction programs have made electron microprobe analysis of these elements routine. These analytical capabilities are necessary for many applications in this laboratory.

References

1. J. G. Bednorz and K. A. Muller, "Possible high T_c superconductivity in the La-Ba-Cu-O system," *Z. Physics* B64: 189, 1986.
2. C. W. Chu et al., "Evidence for superconductivity above 40 K in the La-Ba-Cu-O compound system," *Phys. Rev. Lett.* 58: 405-407, 1987.
3. B. L. Henke et al., *Atomic Data and Nuclear Data Tables* 27: 1-144, 1982.

4. K. Kawabe et al., "Layered synthetic microstructure dispersion elements for electron probe microanalysis of carbon, boron, and beryllium," *Microbeam Analysis--1988*, 341.

5. *X-ray Emission and Absorption Wavelengths and L-Value Tables*, JEOL.

ANALYSIS OF METAL-OPENS FAILURE IN VLSI Al-Si-Cu METALLIZATION

T. E. Rothwell and S. A. Myers

Recently a new failure mechanism has become a concern in VLSI metallization. The presence of slit-like voids, induced by mechanical stress, which cause metal-opens failure has been reported in the literature.¹⁻³ The trend to smaller linewidths in multilevel interconnection systems increases the occurrence of this type of failure, which is linewidth dependent.⁴ This type of failure occurred during high-temperature bias (HTB) stress-testing of a vendor-produced qualification test site. The product under test had two levels of aluminum/silicon/copper metallurgy with a minimum linewidth of 1.5 μm and a 1.3 μm -thick layer of phosphosilicate glass (PSG) as the overlay passivation. This paper describes the analytical techniques used to isolate failures, as well as changes made to the passivation layer which eliminated failures due to metal-opens from later stress testing. The failure locations were isolated by voltage contrast and observed by scanning electron microscopy (SEM). Transmission electron microscopy (TEM) was used to study the grain structure of the metal lines.

Experimental

The test site containing the failures consists of a logic chain with individual data inputs and outputs replicated 36 times on the chip. Each of the chains is connected serially via a scan path. The failures were isolated to one logic chain output by electrical diagnostics on a Takeda tester. Twenty-one failed test-site modules were selected as representative samples for voltage contrast and failure analysis.

Voltage-contrast imaging is an extremely useful technique for isolating integrated circuit failures in the SEM. In voltage-contrast images, regions of a sample at different potentials appear at different brightness levels in the secondary electron (SE) image. This effect occurs because of the differences in the localized electric field strength near areas of different potentials. An area that is negatively biased with respect to ground has a higher average field strength near the detector, the detector efficiency is increased, and the region appears brighter. An area that is positively biased with respect to ground has a lower average field strength, the collection efficiency is lowered, and the region appears darker.⁵

T. E. Rothwell is at IBM-Research Triangle Park, E81/061, Research Triangle Park, NC 27709. S. A. Myers is at National Semiconductor, 2900 Semiconductor Drive, Santa Clara, CA 95051; she was at North Carolina State University when this work was done.

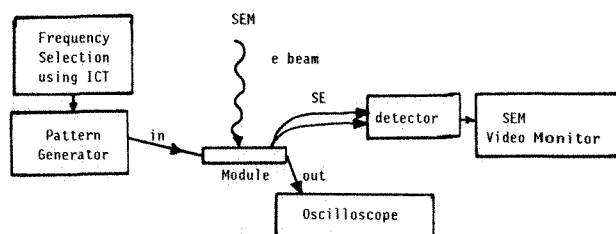


FIG. 1.--Schematic of electron-beam test system.

Voltage coding is a voltage-contrast technique that allows visualization in a SE image of periodic voltage changes in the microsecond range. The effect is achieved by synchronization of the chip's operating frequency with an integer function of the SEM scan rate. Conducting interconnects show alternating light and dark areas when current is flowing; non-functioning regions of the chip appear as normal SE images.

Voltage coding was performed with an Amray 1830/ICT E-beam tester. Accelerating voltages in the range of 1.2-2.5 keV were used; low voltages are necessary to minimize sample charging. The parts were externally driven by a Tektronix 9100 DAS pattern generator to stimulate the scan chain and clock lines; the clock frequency was varied in the ICT tester to maximize the failure visibility. A diagram of the system used for voltage contrast is shown in Fig. 1. Prior to voltage-contrast analysis the majority of the PSG passivation was removed from the chips by reactive ion etching. Figures 2 and 3 show voltage-contrast micrographs containing failure locations.

Once the metal-opens were located by voltage contrast, further preprocessing was required to observe the failure sites in the SEM. The interlevel oxide was removed by a combination of reactive ion etching for bulk removal and wet etching in 7:1 buffered hydrofluoric acid for removal of the remaining oxide film. Once the metal was exposed the failures were visible in the SEM without use of a conductive coating.

Plan view samples of the first-level metallurgy were prepared for examination in the TEM. Small samples were cleaved from chips with both types of passivation layers. The samples were thinned from the backside to a final thickness of 50 μm and mechanically dimpled until they were transparent to white light. The thinned sections were then mounted on copper rings for stability and ion milled at 12 and 5 keV. The foils were examined in a Hitachi H-800 microscope at 200 keV.

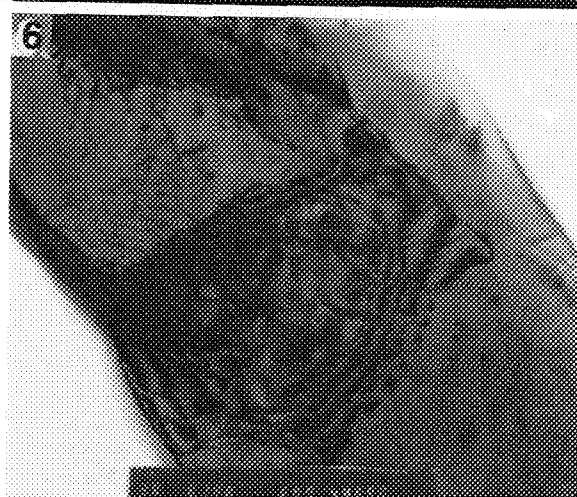
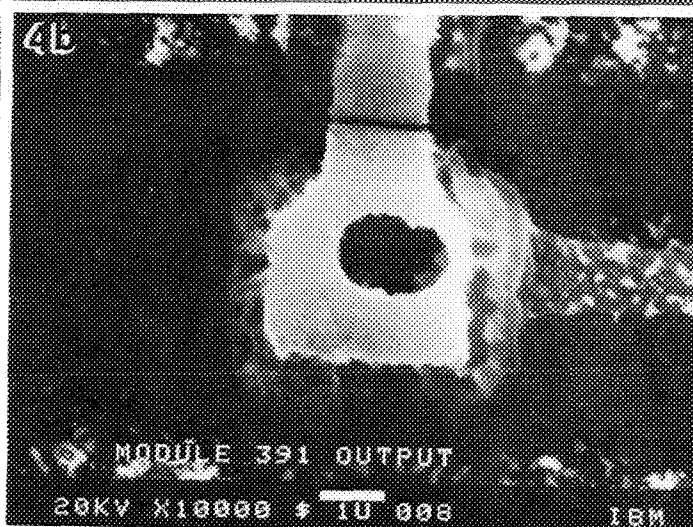
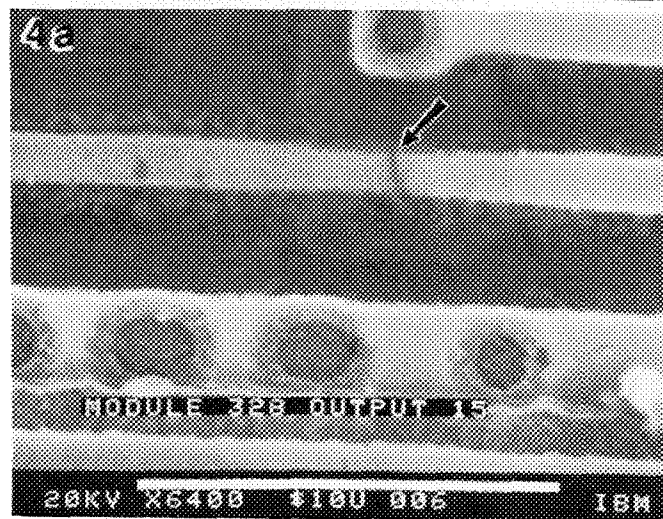
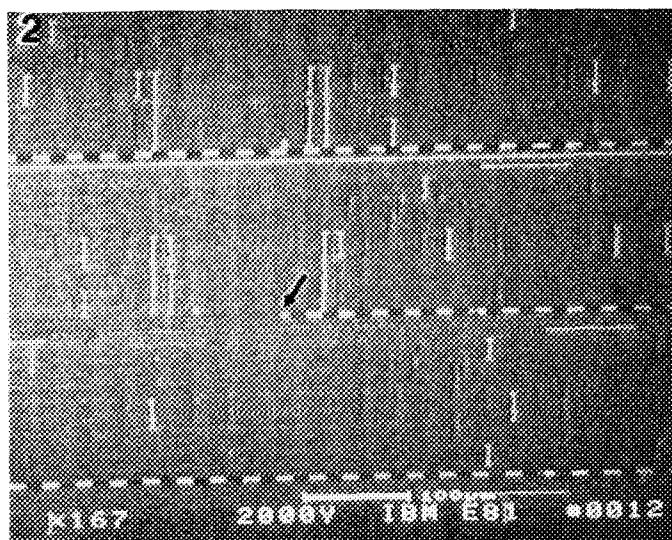


FIG. 2.--Voltage-contrast micrograph of metal-open failure in a first-metal clock line.
 FIG. 3.--Voltage-contrast micrograph of metal-open in a second-metal line.
 FIG. 4.--SEM micrographs of characteristic slit-like cracks in (a) first metal, (b) second metal.
 FIG. 5.--TEM micrograph showing grain structure of Al/Si/Cu interconnection with PSG passivation. Sample was tilted to show features within grains. (40 k \times .)
 FIG. 6.--TEM micrograph showing dislocations generated in grain boundaries of interconnection with PSG passivation. (60 k \times .)

Discussion

Twenty-one failures were selected for isolation by voltage contrast analysis. The failures were divided into the following categories: thirteen verified first-metal (M1) opens, two suspected M1 opens, three verified second-metal (M2) opens, and three unknowns. The unknowns were isolated to a single logic cell where metal opens were not visible. SEM micrographs of both the M1 and M2 fail sites were taken at a high-incidence angle to confirm that the metal step coverage was good and that the lines did not thin at the fail sites. Micrographs of characteristic slit-like cracks in first- and second-level metallurgy are shown in Fig. 4. All but one of the metal-opens seen were the slit-like cracks widely reported in the literature.¹⁻⁴ It has been proposed that this failure mechanism is caused by aluminum atom migration away from a "bamboo" grain boundary. This migration is driven by tensile stress applied by the overlying passivation. The migration is accelerated by temperature.¹ This failure mechanism has been documented as occurring frequently in Al-Si lands; in this case the failing lands contained Al-Si-Cu.

The overlay passivation was changed from 1.3 μm of PSG to a bilevel passivation consisting of 0.4 μm of PSG with 0.9 μm of plasma nitride on top. This overlay reduced the net overlay mechanical stress. In the original HTB test cell 17 modules had failed because of metal-opens by 2000 h of testing. Due to this unexpectedly high level of failures, the stress test was continued and 15 additional failures occurred by the 3000h readout and 20 more failures occurred by the 3700h readout. After the manufacturing process was changed to include the nitride/PSG passivation, no metal opens occurred after 2000 h of HTB testing.

Transmission electron microscopy was performed on interconnections from modules with both types of passivation layers. The "bamboo" grain structure was present throughout the interconnections from samples with both types of passivation. The metallization on the modules with the PSG/nitride passivation had grains with no evidence of necking or thinning of material at the grain boundaries. Figure 5 is a low-magnification micrograph of several grains with the sample tilted to show grain structure within the interconnections. The grain boundary has undergone some thinning. The parallel dislocations and the dislocations which are generated in the grain boundary are shown in more detail in Fig. 6. The presence of dislocations near the grain boundaries supports the proposed mechanism of movement of aluminum away from the grain boundary.

Conclusions

In general, the grains in the sample with PSG passivation (the higher-stress film) had many more dislocations than the sample with PSG/nitride passivation (the lower-stress film). It is possible that the high stress from the PSG passivation layer caused deformation within

the interconnections. These areas look as if they have undergone plastic deformation as indicated by the necking within the grains and the dislocations that have been generated at the grain boundaries.

The primary failure mechanism for these modules was metal-opens. The failure rate difference between the two test cells can be explained by the passivation material dependence of the stress applied to the metal interconnections. This study helped to show that the problem of slit-like voids can be avoided by use of an appropriate overlay passivation. Changing the overlay passivation, which reduced the film stress was shown to be a successful method for reducing failures due to metal-opens in Al-Si-Cu interconnections.

References

1. J. W. McPherson and C. F. Dunn, "A model for stress-induced notching and voiding in very large-scale-integrated Al-Si (1%) metallization," *J. Vac. Sci.* B5: 1321-1325, 1987.
2. C-Y. Li, R. D. Black, and W. R. LaFontaine, "Analysis of thermal stress-induced grain boundary cavitation and notching in narrow Al/Si metallizations," *Appl. Phys. Lett.* 53: 31-33, 1988.
3. N. Owada et al., *Stress Induced Slit-like Void Formation in a Fine Patterned Al-Si Interconnect During Aging Test*, V-MIC, June 1985, 173-179.
4. K. Hinode et al., "Stress-induced grain boundary fractures in Al-Si interconnects," *J. Vac. Sci.* B5: 518-522, 1987.
5. D. E. Newbury et al., *Advanced Scanning Electron Microscopy and X-ray Microanalysis*, New York: Plenum Press, 1986.

THE MICROSTRUCTURE AND INITIAL MAGNETIC PERMEABILITY OF FAST-FIRED MnZn FERRITES

S. G. Cho and P. F. Johnson

Fast firing of electronic ceramics has been studied recently for ferrites and BaTiO₃ ceramics.¹⁻³ Sintering times can be reduced by a factor of 80-1000 relative to conventional sintering while identical magnetic properties are maintained.¹ However, detailed studies of the microstructure of soft ferrites evolved during fast firing have not been made.

The initial magnetic permeability of MnZn ferrite is strongly influenced by composition and microstructure. Zinc depletion (either at the surface or grain boundaries), grain size, distribution of porosity, and the oxidation state of iron are the important factors determining initial magnetic permeability of MnZn ferrites.^{4,5} In this work, stereological studies on the microstructures developed by fast sintering and conventional sintering were made and depletion of zinc from the sample surface was investigated by energy-dispersive spectrometry (EDS).

Experimental

MnZn ferrites with excess Zn were prepared by normal solid-state ceramic techniques. Reagent grade Fe₂O₃, MnCO₃, and ZnO powders were mixed by ball milling and calcined in the air. The powders were calcined at either 900 or 1200 C. Disks and toroids pellets were pressed and sintered by fast firing or conventional firing. Fast firing was conducted by use of a radio-frequency generator and an induction coil. A silicon carbide susceptor was used as a heat source. Conventional sintering was done in a gas-tight tube furnace. Both fast sintering and conventional sintering were conducted in an Ar-2% O₂ gas flow.

Sintered specimens were sectioned, polished, and etched for scanning electron microscopy studies. Average grain size was determined by measurement of the mean linear intercept of the grains.⁶⁻⁷ The volume fractions of intragranular and intergranular porosity were measured separately by the point-count method.⁶ Total grain boundary surface area per unit volume, S_v , was measured by the line intercept method and calculated as $S_v = 2P_L$, where P_L is the number of interceptions of a test line with grain-boundary traces per unit length of the test line. Chemical compositions of surface and bulk area were determined by EDS. EDS spectra from the as-received surfaces and the polished section of the grain inside the sintered specimens were collected and analyzed by means of

TABLE 1.--Characterization of sintered specimen.

Specimen	A	B	C	D
Calcination(°C)	1200	1200	900	900
Sintering	FAST	NORMAL	FAST	NORMAL
Grain size(μm)	15.8	7.0	68.6	257(5.8) ^a
V_p^G (%) ^b	4.0	0.2	5.5	5.6
V_p^{GB} (%) ^b	3.9	9.1	1.9	1.7
V_p^T (%) ^b	7.9	9.3	7.4	7.3
S_v (μm ⁻¹) ^b	0.236	0.542	0.048	0.046
Permeability	3800	3400	5300	5200

^a average grain size of fine grains.

^b V_p^G : intragranular porosity, V_p^{GB} : intergranular porosity, V_p^T : total porosity, S_v : grain boundary surface area per unit volume.

the standardless quantitative analysis program (NOSTD program, Princeton Gamma-Tech, Princeton N.J.).

Results and Discussion

Microstructures of a fast-sintered specimen and a conventionally sintered specimen prepared from the powder calcined at 1200 C are shown in Fig. 1(a) and (b), respectively. High intragranular porosity was found in the fast-fired specimens; typical microstructure with intergranular pores was observed in the conventionally sintered specimen. In spite of their different microstructures, both specimens have similar initial magnetic permeabilities. For a better understanding of the relation between the microstructure and magnetic permeability, stereological microstructure analysis was carried out. Stereological data and initial magnetic permeabilities for the specimens shown in Fig. 1(a) and (b) are summarized in Table 1. The similar magnetic permeabilities of the specimens, which have quite different microstructures, can be explained by use of the extended microstructure analysis data. It is well recognized that the initial magnetic permeability of the soft ferrite increases with the grain size and decreases with the porosity.⁴ Since both grain boundaries and pores--especially intragranular pores--pin domain wall motion, effects of larger grain size (which gives rise to less grain boundary area

The authors are with the College of Ceramics at Alfred University, Alfred, NY 14802. This work is a part of the M.S. thesis of S. G. Cho at Alfred University.

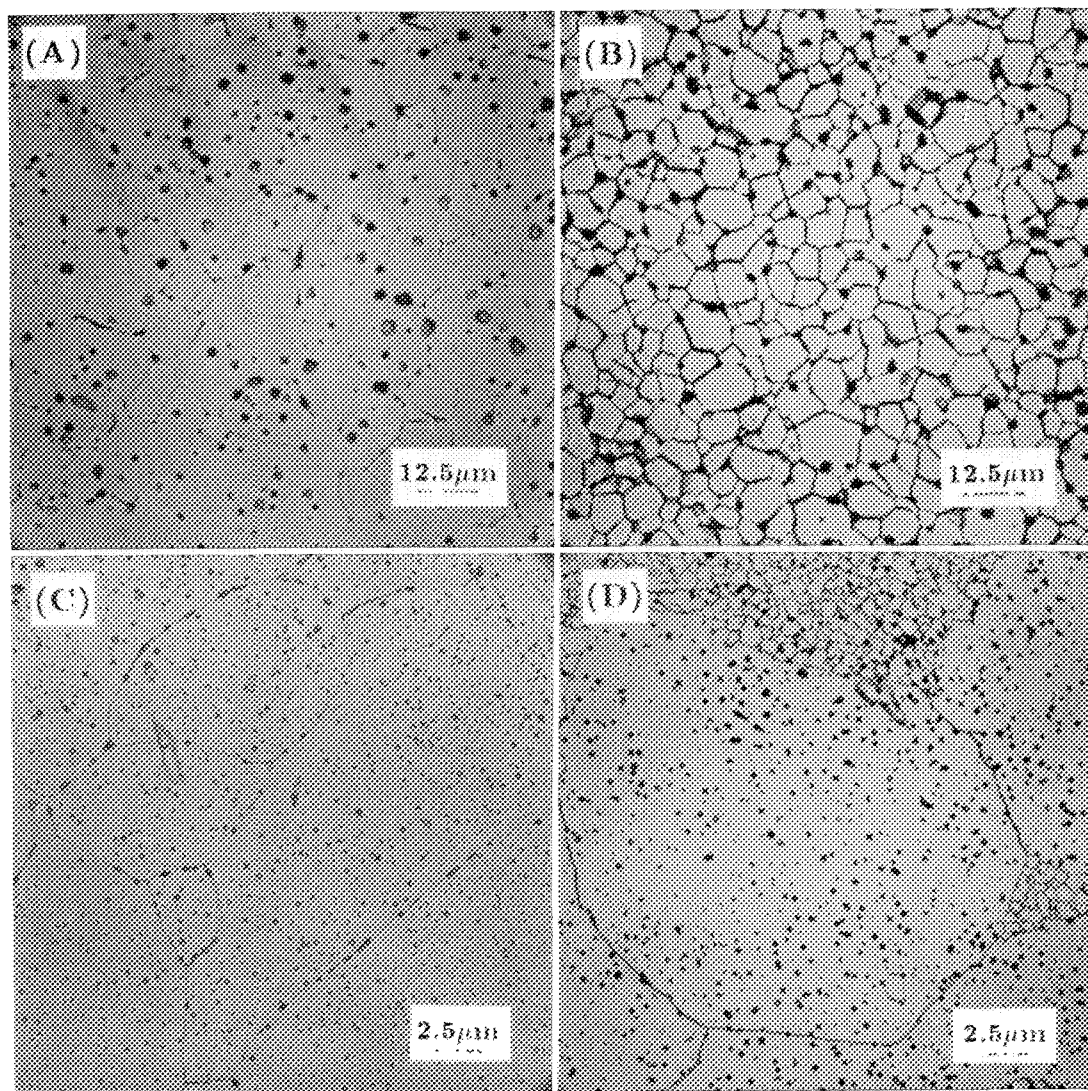


FIG. 1.--Scanning electron micrographs of Mn-Zn ferrites: (a) fast-sintered specimen at 1350 C for 30 min (powder calcined at 1200 C), (b) conventionally sintered specimen at 1300 C for 3 h (same powder as in a), (c) fast-sintered specimen at 1350 C for 30 min (powder calcined at 900 C), (d) conventionally sintered specimen at 1300 C for 3 h (same powder as in c).

per unit volume and high intragranular porosity of fast-fired specimens) compensate each other, and hence result in magnetic permeabilities very similar to those of conventionally sintered specimens with small grain size and intergranular pores.

The specimens prepared from the powder calcined at 900 C have abnormal grains as shown in Fig. 1(c) and (d), irrespective of the sintering methods used. However, conventionally sintered specimens have a duplex structure that was not found in the fast-sintered specimens. Stereological data and initial magnetic permeabilities for the specimens with abnormal grains are also summarized in Table 1. The specimens with abnormal grains showed higher

initial magnetic permeabilities than specimens that consist of relatively small, normal grains. This result agrees with that of Drofenik and Besenicar, who attribute the high permeabilities of the specimens with abnormal grains to low pinning energy of small intragranular pores, ease of accommodation of cylindrical wall bulging, and less grain-boundary-induced stress.⁵ Average grain size generally represents the grain boundary area per unit volume of the specimen, because they are inversely proportional. However, for the specimens with duplex structure, as shown in Fig 1(d), average grain size is hard to measure and often meaningless. Stereological measurements of the grain boundary area per unit vol-

ume S_v has proved to be an excellent tool for these specimens as shown in Table 1. Two different kinds of specimens which consist of abnormal grains have the same magnetic permeabilities, because grain boundary area per unit volume and porosities are about the same.

It was first expected that the fast sintering which exposes the specimens to high temperature for a short time would suppress Zn depletion from the specimen surface. However, as shown in EDS analysis for the surface and bulk of the specimens given in Table 2, the fast-sintered specimens show approximately the same zinc depletion at the surface as conventionally sintered samples, in spite of the short sintering time. The validity of this analysis was examined by a comparison of the results obtained from the bulk of various specimens, where starting composition is maintained throughout the sintering process with the calculated starting composition. As is shown in Table 2, those values agree well with each other.

TABLE 2.--EDS analysis of the surface and bulk of the MnZn ferrites: unit=wt%.

Composition	FAST ^a	NORMAL ^a	BULK ^b	POWDER ^c
Fe	73	73	68	66.7
Mn	16	17	14	14.5
Zn	11	10	18	18.8

^a as received surface of the sintered specimen.

^b polished grain area inside the sintered specimen.

^c calculated from the starting composition.

Conclusion

MnZn ferrites sintered by fast firing show the same initial magnetic permeabilities as those conventionally sintered, although the microstructures are quite different. The extended determination of the two different kinds of porosity improved understanding of the differences. The techniques of quantitative microscopy provide a direct means of understanding the favorable effect of grain size and the adverse effect of intragranular pores on the initial magnetic permeability in MnZn ferrites consisting of normal grain structures. The specimens with abnormal grains show higher initial magnetic permeabilities, even though high intragranular porosities are observed.

References

1. A. Morell and A. Hermosin, *Am. Ceram. Soc. Bull.* 59: 626, 1980.
2. M. P. Harmer and R. J. Brook, *Trans. J. Brit. Ceram. Soc.* 80: 147, 1981.
3. H. Mostaghaci and R. J. Brook, *J. Mater. Sci.* 21: 3575, 1986.
4. B. B. Gbate, in L. M. Levinson and D. C. Hill, Eds., *Advances in Ceramics* 1: 477, 1981.
5. M. Drofenik and S. Besenicar, *Am. Chem. Soc. Bull.* 65: 656, 1986.
6. E. Underwood, *Quantitative Stereology*, Addison-Wesley, 1970, 23.
7. M. I. Mendelson, *J. Am. Ceram. Soc.* 52: 443, 1969.

EXPERIMENTAL LIMITATIONS OF CBED HOLZ LINES FOR COMPOSITIONAL MEASUREMENTS

K. S. Vecchio

Convergent-beam electron diffraction (CBED) can be used to obtain quantitative structural information from crystalline materials with extremely high spatial resolution (<100 nm). One of the most powerful aspects of CBED analyses is the use of higher-order Laue zone (HOLZ) lines for absolute lattice parameter determination and even more accurate determination of relative changes in lattice constants. HOLZ lines, which are seen as sharp black lines within the transmitted disk of a CBED pattern, arise from elastic scattering with reflections that occur in upper Laue zones, well away from the origin. These HOLZ lines are very sensitive to lattice parameter changes because small changes in either lattice parameter or electron wavelength produce large changes in the size of the "g-vectors" responsible for the HOLZ reflection.¹ Since the lattice parameter of a given crystal changes with small changes in chemical composition, even in the absence of any crystal structure changes, HOLZ line analyses offer a unique method to infer compositions of materials.

In order to determine the lattice parameter of a given material, either of two experimental approaches can be employed: (1) a simulation technique in which the position of experimental HOLZ lines is compared with those generated by a computer program, with the position of the HOLZ lines in the simulation derived from kinematical diffraction theory in which only lattice parameter and electron wavelength are allowed to vary; or (2) an experimental technique in which the operating voltage is varied, causing the HOLZ lines to move, until a unique pattern is obtained, whereupon a similar pattern is obtained from a standard material and the difference in voltages between the standard and unknown can be used to determine the change in lattice parameter.^{1,2} For compositional measurements, comparison of the experimentally determined lattice parameter with existing x-ray data for lattice parameter vs composition for the suspect material can be made to infer compositions. Regardless of which technique is used, researchers must use their own judgment to establish the best match for the lattice parameter determined. However, since the choice in lattice parameter is a "judgment call," some range for errors (or the accuracy of the judgment) should be established.

In this paper, we are concerned with determining the experimental accuracy (i.e., a \pm deviation) of HOLZ line analysis for determining chemical compositions.

The author is at the Department of Applied Mechanics and Engineering Sciences, University of California at San Diego, La Jolla, CA 92093.

Experimental Procedure

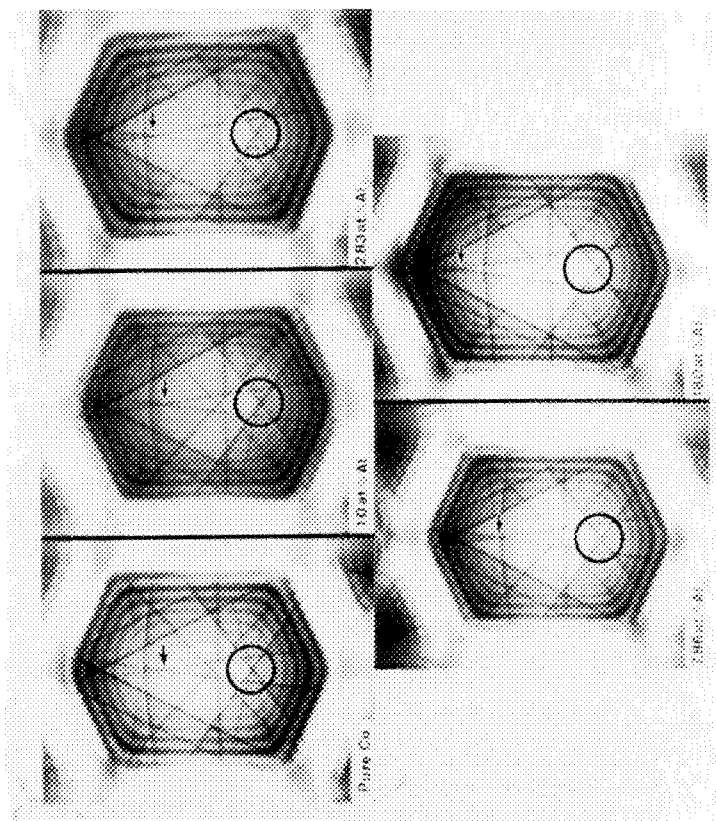
Two different sets of solid-solution alloys were examined in this study. The first set of alloys were Al-rich copper Al-Cu alloys with five different alloys ranging from pure Al to Al-1.48at.%Cu. The second set of alloys were Cu-rich Cu-Al binary alloys ranging from pure Cu to Cu-18.0at.%Al. The composition of each alloy was determined by two different atomic absorption measurements. CBED HOLZ line patterns were obtained from thin-foil samples with either a Philips EM400 AEM or a Philips CM30 AEM. In either case, the results from the same sample were identical for the same microscope conditions, as expected. The Al-rich samples were examined using a liquid-nitrogen cooled holder at -180 C, since HOLZ lines are not visible in Al at room temperature due to thermal vibrations within the lattice.

Results and Discussion

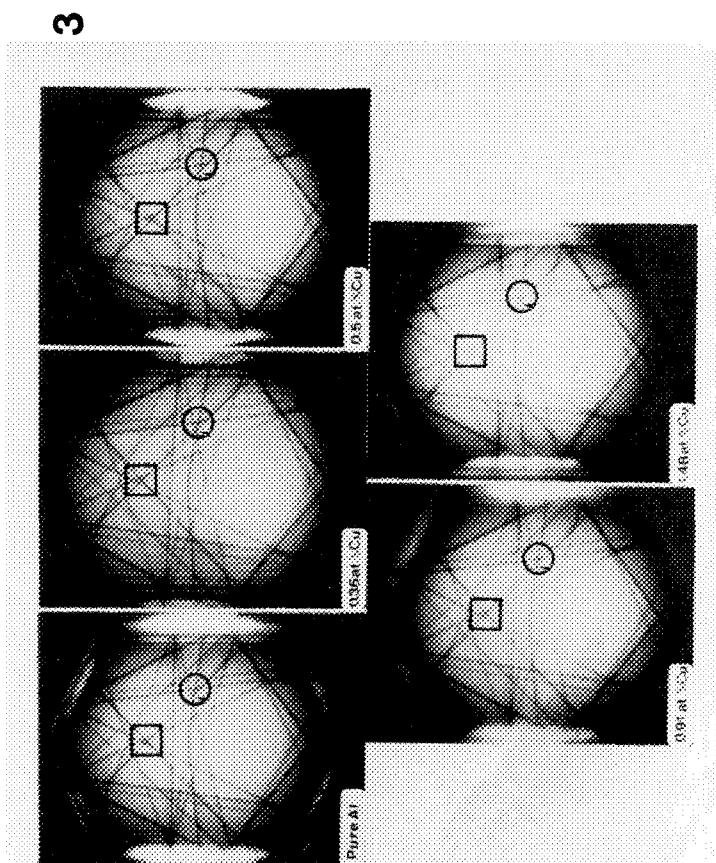
Figure 1 shows a series of HOLZ line patterns within the transmitted disk in the $<114>$ orientation from each of the Cu-rich binary alloys. The first observable change between the HOLZ lines in the pure copper sample and any of the binary samples occurred with the 1.0at.%Al sample, which corresponds to a change in lattice parameter change of approximately 3×10^{-4} or 8.5 parts in 10 000. Figure 2 shows simulated HOLZ line patterns which represent the best matching obtainable for each pattern shown in Fig. 1. Similar results were obtained from HOLZ line analyses along both the $<111>$ and the $<113>$ orientations of the same samples.

When the Al-rich binary alloys were examined, the first identifiable change in HOLZ line positions between the pure Al and any of the binary alloys occurred with the 0.91at.%Cu sample (Fig. 3). The change in lattice parameter, determined from HOLZ line simulations, was approximately 4.4×10^{-4} or 1 part in 1000. Comparison of the Al-rich and Cu-rich sample shows that chemical composition measurements made via the HOLZ line technique can be accurate to approximately 1.0at.% change in composition. This result agrees well with the work of Randle and Ralph,³ in which they demonstrated that the differences of 1.0at.% of Ti could be detected in Ni_3Al .

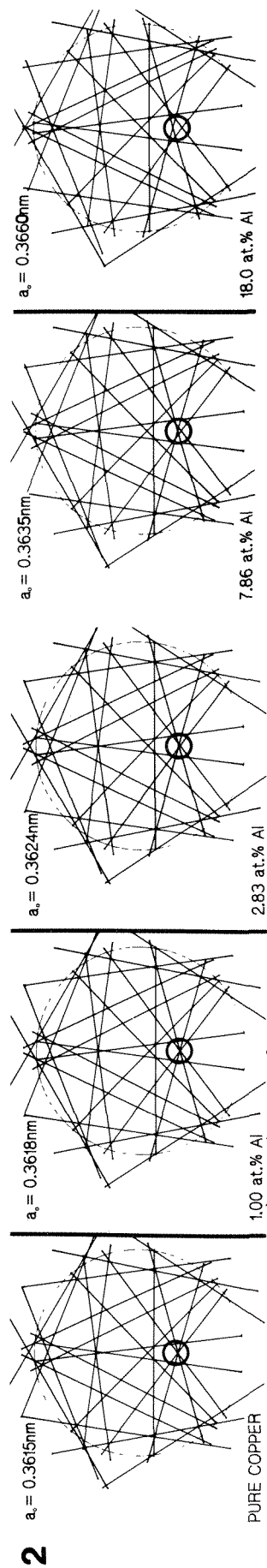
In order to obtain this high degree of accuracy with HOLZ line analyses consistently, several guidelines for deciding which are the best pattern orientations and which HOLZ lines display the greatest sensitivity to changes in either lattice parameter or accelerating voltage should be followed. First, whenever possible the operator should choose an orientation with



1



3



2

FIG. 1.--Series of HOLZ line patterns obtained from five different Cu-Al alloys along the $\langle 114 \rangle$ zone axis orientation. Note shifts in HOLZ lines within black circles and movement of arrowed intersection with changes in composition.
 FIG. 2.--Computer simulations of HOLZ line patterns from Fig. 1. Changes in lattice parameter as small as 3.0×10^{-4} can be detected with simulations.
 FIG. 3.--Series of HOLZ line patterns obtained from five different Al-Cu alloys along $\langle 114 \rangle$ zone axis orientation. Note lack of any significant shifts in HOLZ lines within black circles and black boxes until the 0.91at.%Cu sample. The arrow within circle denotes most obvious change in HOLZ line position.

a single mirror plane in it, such as $\langle 114 \rangle$, $\langle 113 \rangle$, or $\langle 116 \rangle$ in cubic structures. The higher the index for these orientations (for example, $\langle 116 \rangle$ rather than $\langle 113 \rangle$), the greater the sensitivity of the HOLZ lines to shifts in either lattice parameter or voltage. This relationship results from the larger "g-vectors" for the HOLZ reflections responsible for these HOLZ lines. As such, for small changes in lattice parameter, larger displacements of these HOLZ lines along the mirror plane result. Whenever very high-order (3rd order) Laue zones (VHOLZ) lines are visible within the pattern, comparison of the shifts between these so-called VHOLZ lines and lower-order HOLZ lines can yield improved sensitivity, as suggested by Sung.⁴ When the "voltage change" technique is employed exclusively, the choice of an orientation with at least single mirror symmetry or higher, such as $\langle 111 \rangle$ or $\langle 100 \rangle$ in cubic structures, can facilitate the location of a unique and easily recognizable HOLZ line intersection.

If we consider the practical accuracy of these HOLZ line measurements to be 1 part in 1000, then for a 100kV electron beam shifts in HOLZ lines should be observable for changes in accelerating voltage of approximately 0.2 kV. Figure 4 shows one experimental HOLZ line pattern from pure Cu in the $\langle 114 \rangle$ orientation for which the accelerating voltage was varied to produce the unique intersection indicated by the arrow. Figure 4 also contains a series of simulations in which the voltage was changed in 100V steps. The best match of the simulated patterns with the experimental pattern was obtained at 111.50 kV. However, changes in accel-

eration voltage of 100 V do not produce identifiable changes in HOLZ line positions. After changes of 200-300 V, recognizable shifts in HOLZ lines could be seen, which agrees fairly well with the accuracy predicted from the previous experiments.

Conclusions

Using a series of binary alloys, we have shown that an accuracy of approximately 1.0at.% can be obtained for chemical composition measurements made by use of HOLZ line analysis. This level of accuracy would be very difficult to obtain with most other analysis techniques available on a current analytical electron microscope, such as electron energy loss spectroscopy (EELS) or x-ray energy-dispersive spectroscopy (EDS). However, identification of phases with unknown compositions still require the use of these other techniques to identify which elements are present within the phase. The incorporation of VHOLZ lines and use of single mirror orientations have been shown to produce the greatest recognizable sensitivity to HOLZ line shifts.

References

1. P. M. Jones et al., *Proc. Roy. Soc. Lond.* 354A; 197-222, 1977.
2. R. C. Ecob et al., *Phil. Mag.* 44A: 1117-1133.
3. V. Randle and B. Ralph, *J. Micro.* 147A: 305-312, 1987.
4. C. M. Sung, *Proc. 45th Ann. Meet. EMSA*, 1987, 46-47.

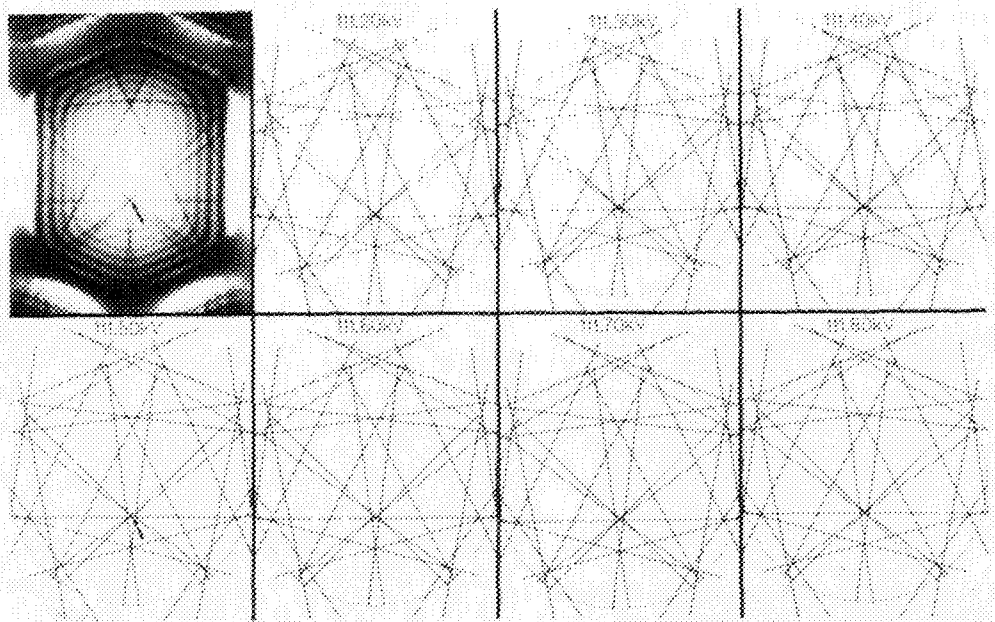


FIG. 4.--Experimental HOLZ line pattern from pure copper along $\langle 114 \rangle$ orientation showing unique HOLZ line intersection at approximately 111 kV; and computer simulations of HOLZ lines in which accelerating voltage was varied by 100 V in each to produce best matching (at 111.50 kV). Little or no significant shifts occur in HOLZ lines for changes of only 100 V.

USING THE (200) THICKNESS CONTOUR TO MEASURE THE Al CONCENTRATION $\text{Al}_x\text{Ga}_{1-x}\text{As-GaAs MQWS STRUCTURES}$

H.-J. Ou, R. W. Glaisher, J. M. Cowley, and H. Morkoç

Many techniques have been used in determining the Al concentration of $\text{Al}_x\text{Ga}_{1-x}\text{As}$ in $\text{Al}_x\text{Ga}_{1-x}\text{As-GaAs MQWS}$ structures, such as Raman spectroscopy, x-ray diffraction, Auger spectroscopy, and photoluminescence.¹⁻³ It has also been suggested that the intensity of the (200) diffraction from $\text{Al}_x\text{Ga}_{1-x}\text{As}$, which is sensitive to its Al content, could be employed in measuring the Al concentration of each $\text{Al}_x\text{Ga}_{1-x}\text{As}$ layer.⁴⁻⁸ A linear relationship between the (200) nanodiffraction intensity and the Al concentration of $\text{Al}_x\text{Ga}_{1-x}\text{As}$ for the region of constant thickness was found to be useful in determining the local Al concentration within the layer of $\text{Al}_x\text{Ga}_{1-x}\text{As}$. In this report, the effects of the Al concentration of $\text{Al}_x\text{Ga}_{1-x}\text{As}$ on its (200) nanodiffraction intensity is studied and a chart of the (200) thickness contour position vs the Al concentration is used for microanalysis, giving the absolute Al concentration for two $\text{Al}_x\text{Ga}_{1-x}\text{As-GaAs MQWS}$ samples.

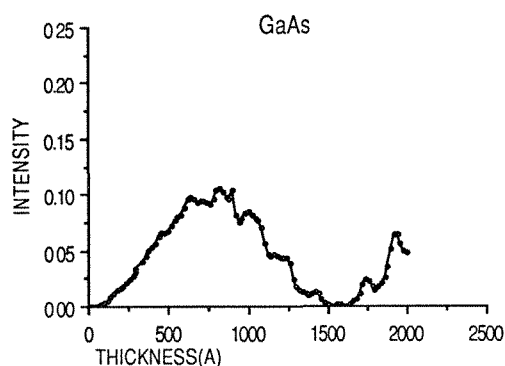
Calculations of the (200) nanodiffraction intensity, by consideration of the dynamic scattering of a 10 Å nano-probe incident electron beam, were done with a modified Ishizuka multislice simulation program. As shown in Fig. 1, the calculated intensity of the (200) nanodiffraction spot from $\text{Al}_x\text{Ga}_{1-x}\text{As}$ grows stronger, but the thickness for the first minimum of the (200) diffraction intensity or the first (200) thickness contour decreases as the Al concentration increases. A chart of the (200) thickness contour position vs Al concentration is shown in Fig. 2. It is immediately evident that the measurement of the (200) thickness contour can be used as a guide for knowing the Al concentration of $\text{Al}_x\text{Ga}_{1-x}\text{As}$. With use of the VG-HB5 scanning transmission electron microscope (STEM), the (200) dark-field STEM image is easy to obtain, since the (200) diffraction spot can be solely detected by a small detector, with the specimen remaining in the [001] on-zone orientation. In the (200) dark-field STEM images, the layer of $\text{Al}_x\text{Ga}_{1-x}\text{As}$ appears in bright contrast and the layer of GaAs is in dark contrast as background.

The authors are at the Department of Physics, Arizona State University, Tempe, AZ 85281, except H. Morkoç, who is at the Coordinated Science Laboratory, University of Illinois, 1101 West Springfield Avenue, Urbana, IL 61801. This study was supported by DOE grant DE-FG02-86 ER 45228 and NSF grants DMR 10238 and DMR 87-18228, was carried out at the ASU Facility for HREM, supported by NSF grant DMR-830651.

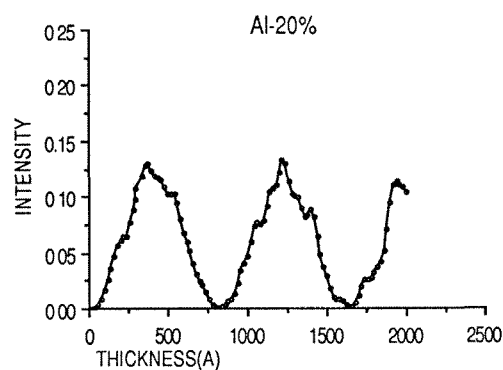
A cleavage specimen is used. The thickness is taken as twice the distance from the edge in the (200) dark-field STEM images.⁹ For $\text{Al}_x\text{Ga}_{1-x}\text{As-GaAs MQWS}$ sample #1, on which 120 periodic layers of 20 Å-thick AlAs and 50 Å-thick GaAs were grown on a GaAs substrate by MBE, the first (200) thickness contour is measured as 320 ± 10 Å for the $\text{Al}_x\text{Ga}_{1-x}\text{As}$ region of bright contrast in the (200) dark-field STEM image of Fig. 3. We see from Fig. 2 that these layers of $\text{Al}_x\text{Ga}_{1-x}\text{As}$ contain $x = 1$. But the measured widths for the layers of $\text{Al}_x\text{Ga}_{1-x}\text{As}$ and GaAs are 15 Å and 55 Å each. We can thus conclude that sample #1 has periodic layers of 15 Å-thick AlAs and 55 Å-thick GaAs and the layer thickness of AlAs is smaller by 5 Å than derived from MBE growth.

The same analysis was carried out on sample #2, which consists of 30 periods of MBE-growth layers of 100 Å-thick $\text{Al}_x\text{Ga}_{1-x}\text{As}$ ($x = 0.3$) and 40 Å-thick GaAs. The first (200) thickness contour measures 800 ± 10 Å for the 100 Å-thick layers of $\text{Al}_x\text{Ga}_{1-x}\text{As}$ in the (200) dark-field STEM image of Fig. 4. The Al concentration for $\text{Al}_x\text{Ga}_{1-x}\text{As}$ of $\text{Al}_x\text{Ga}_{1-x}\text{As-GaAs}$ sample #2 is then found to be $x = 0.26$. The exact layer thickness for either $\text{Al}_x\text{Ga}_{1-x}\text{As}$ or GaAs is the same as proposed by MBE growth, but the Al concentration of $\text{Al}_x\text{Ga}_{1-x}\text{As}$ is 4% less than expected. The brightness change, observed in the direction vertical to the $\text{Al}_x\text{Ga}_{1-x}\text{As}$ layer, is due to the chemical inequivalence of less Al content. This uneven distribution of chemical composition for $\text{Al}_x\text{Ga}_{1-x}\text{As}$ is also believed to be the reason for the modulation of the brightness along the direction of the layer of $\text{Al}_x\text{Ga}_{1-x}\text{As}$. Such composition change is believed to be caused by interruption of growth and/or chemical reactions among the sources of Al, Ga, and As during MBE growth. The progress of this growth study and the measurement of the local Al concentration for the chemical inequivalence region will be reported elsewhere. The layer thickness measured for GaAs is 40 Å, which is the same as expected by MBE. No (200) thickness contours were measured in the GaAs region on either sample; presumably, the Al concentration is less than $x = 0.05$, the detection limit. Also, the nanodiffraction patterns shown in Fig. 5 assure that both samples have good epitaxial growth between $\text{Al}_x\text{Ga}_{1-x}\text{As}$ and GaAs.

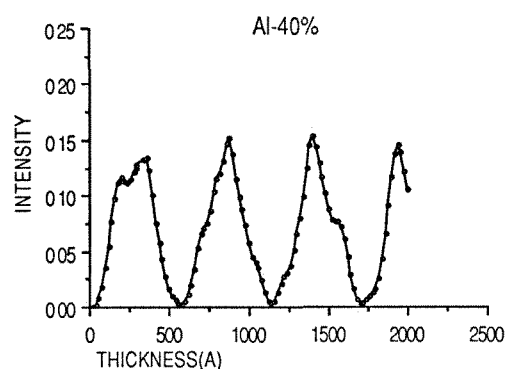
The (200) thickness contour thus is shown to be useful in measuring the Al concentration for $\text{Al}_x\text{Ga}_{1-x}\text{As}$ in the $\text{Al}_x\text{Ga}_{1-x}\text{As-GaAs MQWS}$ sample. The precision of ± 10 Å in the thickness contour measurements suggests that the accuracy for measuring the Al concentration of $\text{Al}_x\text{Ga}_{1-x}\text{As}$ could be as good as ± 0.02 . More use of the



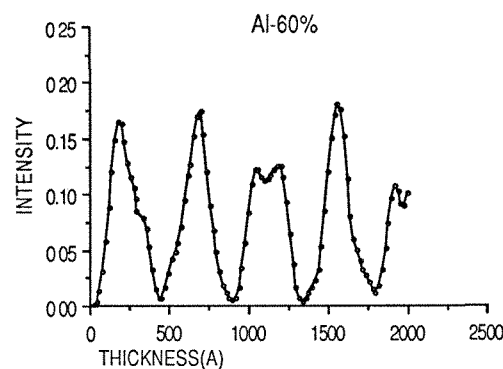
(a)



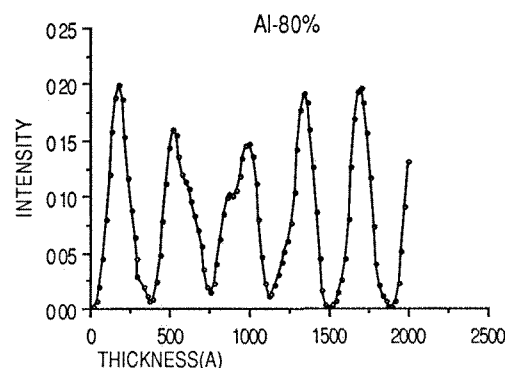
(b)



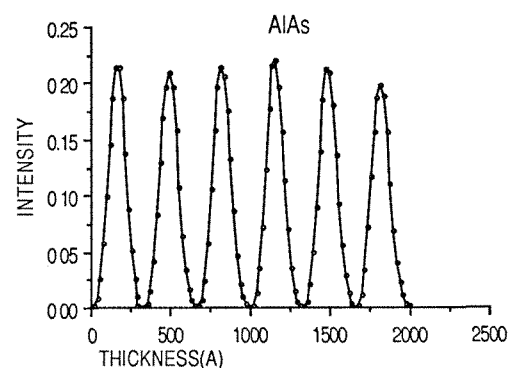
(c)



(d)



(e)



(f)

FIG. 1.--Plot of (200) nanodiffraction intensity vs thickness for $\text{Al}_x\text{Ga}_{1-x}\text{As}$ of x : (a) 0%, (b) 20%, (c) 40%, (d) 60%, (e) 80%, (f) 100%.

(200) dark-field STEM imaging in the study of the growth of good III-V compound electronic materials or devices is being explore.

References

1. B. Deveaud, J. Y. Emergy, A. Chromette, B. Lambert, and M. Caudet, *Appl. Phys. Lett.* 45: 1078, 1984.
2. C. M. Barner, Y. D. Shen, J. S. Kim, G. L. Pearson, W. E. Spicer, J. S. Harris, D. D. Edwall, and R. Sahai, *J. Vac. Sci. Technol.* 14: 985, 1977.

3. P. Parayanthal, F. H. Pollak, and J. M. Woodall, *Appl. Phys. Lett.* 41: 961, 1982.
4. P. M. Petroff, *J. Vac. Sci. Technol.* 14: 973, 1977.
5. C. J. D. Hetherington, J. C. Barry, J. M. Bi, C. J. Humphreys, J. Grange, and G. Wood, *Mat. Res. Soc. Symp. Proc.* 37: 41, 1985.
6. H.-J. Ou, S.-C. Y. Tsen, K. T. Tsen, J. M. Cowley, J. I. Chyi, A. Salvador, and H. Morkoc, *Appl. Phys. Lett.* 54: 1054, 1989.
7. R. W. Glaisher, J. C. Barry, and D. J. Smith, NATO ARW (in press).

8. D. J. Eaglesham, C. J. D. Hetherington, and C. J. Humphreys, *Mat. Res. Soc. Symp. Proc.* 77: 473, 1987.

9. H.-J. Ou, J. M. Cowley, and H. Morkoc, *J. of Appl. Phys.* (in preparation).

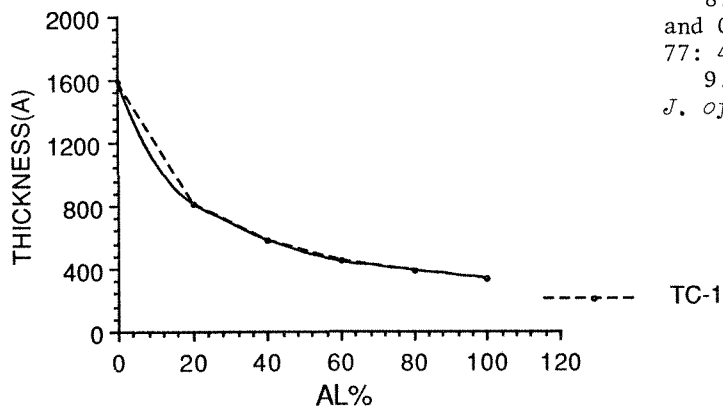


FIG. 2.--First thickness contour vs Al concentrations.

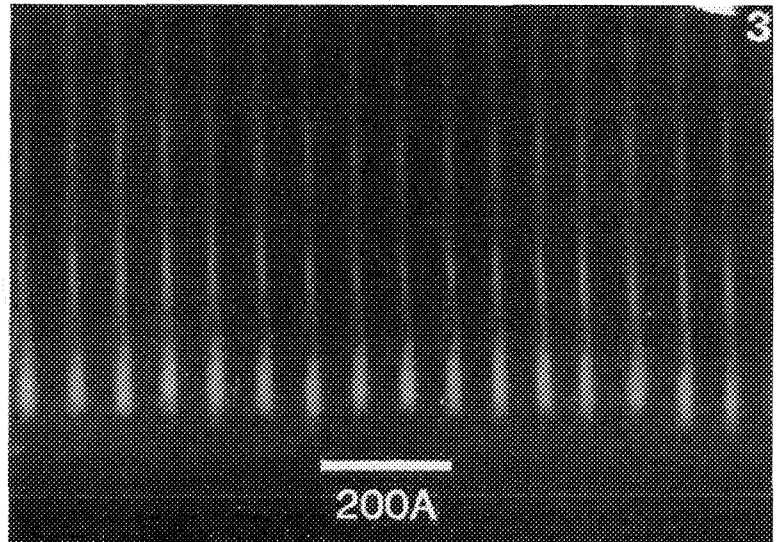


FIG. 3.--(200) dark-field STEM image of $\text{Al}_x\text{Ga}_{1-x}\text{As}$ -GaAs sample #1, which shows layers of 15Å-thick AlAs in bright contrast and 55Å-thick GaAs in dark contrast. Measurement of first thickness contour on AlAs region is 320 ± 5 Å.

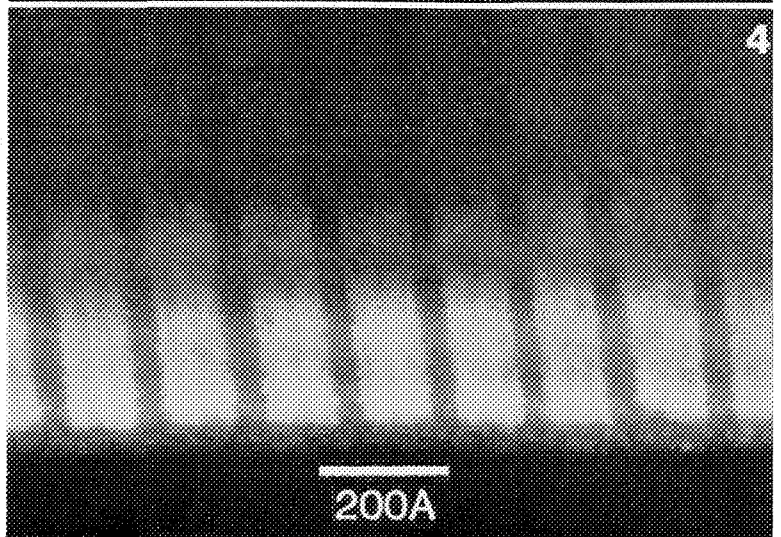
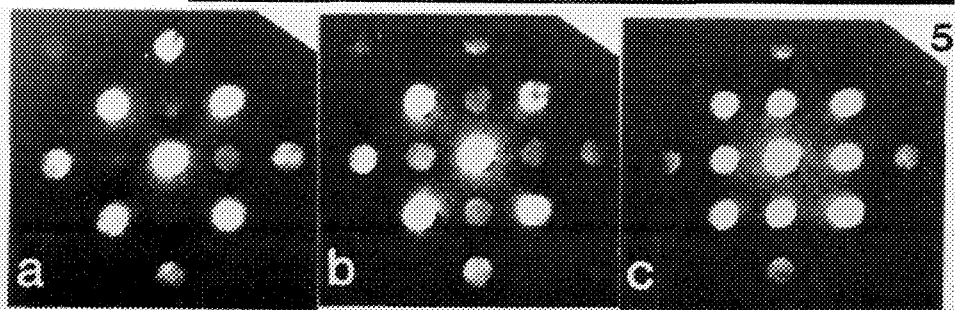


FIG. 4.--(200) dark-field STEM image of sample #2, which shows bright layers of 100Å-thick $\text{Al}_x\text{Ga}_{1-x}\text{As}$ ($x = 0.22 \pm 0.01$) with dark layer of 40Å-thick GaAs in between. First thickness contour of $\text{Al}_x\text{Ga}_{1-x}\text{As}$ layer is 800 ± 5 Å and those two chemical inequivalence regions observed within $\text{Al}_x\text{Ga}_{1-x}\text{As}$ layer are 5 Å in thickness.

FIG. 5.--Nanodiffraction patterns from the regions of (a) GaAs, (b) $\text{Al}_x\text{Ga}_{1-x}\text{As}$ ($x = 0.026$) and (c) AlAs show that these MBE-grown layers of $\text{Al}_x\text{Ga}_{1-x}\text{As}$ -GaAs MQWS are in good epitaxy.



RELIABILITY OF VARIOUS SYMMETRY FEATURES AND PROCEDURES FOR POINT GROUP DETERMINATION OF THIN SPECIMENS BY CBED

J. M. Howe

Convergent-beam electron diffraction (CBED) can be used to determine the point or space group of a sample region that is only a few tens of nanometers across. This makes it a very useful technique in materials research.¹ Although symmetry analysis in a relatively thick sample is usually straightforward, symmetry determination of thin specimens may require caution and considerable judgment.² This paper examines the effect of decreasing specimen thickness on the symmetry features that are present in CBED patterns. A hierarchy of reliability is established for symmetry features and procedures that are used to determine point and space groups.

Experimental

Disks of α -titanium 3 mm in diameter were electropolished in a twin-jet apparatus by use of a 25% $\text{HNO}_3/\text{CH}_3\text{OH}$ solution at -35 C, 50 V, and 50 mA. The CBED experiments were performed on a Philips EM400 fitted with a free-lens control for the second condenser lens. Both 300 and 100 μm condenser lens apertures and 450 and 280 mm camera lengths were used to record the zero-order Laue zone (ZOLZ) and first-order Laue Zone (FOLZ) patterns, respectively. A double-tilt, liquid-nitrogen cold stage (-180 C) was used to reduce contamination on and thermal diffuse scattering in the specimen.

Symmetry Features in a CBED Pattern

A CBED pattern usually contains both two-dimensional and three-dimensional symmetry information.³ Table 1 lists the symmetry features in a CBED pattern and whether they provide two- or three-dimensional crystallographic information. Certain features such as higher-order Laue zone (HOLZ) lines provide three-dimensional symmetry information when they are present. Other features such as Kikuchi lines and the disk pattern can provide two- or three-dimensional information depending on the diffraction conditions. For example, HOLZ Kikuchi lines provide three-dimensional symmetry information when they are present in the CBED pattern. However, when they are absent, the ZOLZ Kikuchi lines provide only two-dimensional information. Similarly, the disk pattern can provide three-dimensional information when the HOLZ disks are visible. Otherwise, the disks provide no more symmetry information than a

TABLE 1.--Symmetry features and their crystallographic information in CBED pattern.

Symmetry feature	Crystallographic information
HOLZ lines	3-dimensional
Kikuchi lines	
HOLZ	3-dimensional
ZOLZ	2-dimensional
Intensity fringes	2-dimensional
Disk pattern	
HOLZ	3-dimensional (with ZOLZ)
ZOLZ	2-dimensional

conventional spot pattern. The intensity (or thickness) fringes within the CBED disks provide only two-dimensional symmetry information, even though their origin is due to dynamical diffraction.

Variation of Symmetry Features with Specimen Thickness

For relatively thin specimens, it is necessary to know how each of the symmetry features in Table 1 changes with specimen thickness and whether or not it displays the correct crystal symmetry. Figures 1(a-c) show a series of three [0001] CBED patterns taken from progressively thinner regions of the α -titanium sample. An enlargement of the ZOLZ in Fig. 1(a) is shown in Fig. 2. The space group of α -titanium is $P6_3/\text{mmc}$ (point group 6/mmm); in a [0001] zone-axis pattern (ZAP) the bright-field (BF), whole-pattern (WP), and projection diffraction (PD) symmetries should all be 6mm.⁴ Examination of the ZOLZ and HOLZ Kikuchi lines and the HOLZ disks in Fig. 1(a) shows that the WP symmetry is 6mm. Additional examination of the intensity fringes in the ZOLZ disks and HOLZ lines in the BF disk in Fig. 2 shows that the PD and BF symmetries are also 6mm. Therefore, all the features in Table 1 display the correct symmetry in this relatively thick area of the sample. Also, the 11 $\bar{2}$ 1 disks (arrows) in the FOLZ in Fig. 1(a) display Gjonnes-Moodie (G-M) lines⁵ since they are forbidden for the space group $P6_3/\text{mmc}$.

In Fig. 1(b), translation of the specimen to a thinner region has eliminated HOLZ lines and HOLZ Kikuchi lines from the pattern, though ZOLZ Kikuchi lines and disks in the ZOLZ and FOLZ are still visible. However, comparison among the Kikuchi lines in Fig. 1(b) shows that their intensity is uneven and that they do not display 6mm symmetry. Therefore, when the Kikuchi lines are included in the WP symmetry in Fig. 1(b), the symmetry is not 6mm (it is actually 2). The enlargement of the ZOLZ disks at this thickness in Fig. 1(d) shows that the

The author is in the Department of Metallurgical Engineering and Materials Science, Carnegie Mellon University, Pittsburgh, PA 15213. This research was supported by NSF under Grant DMR-86 57215.

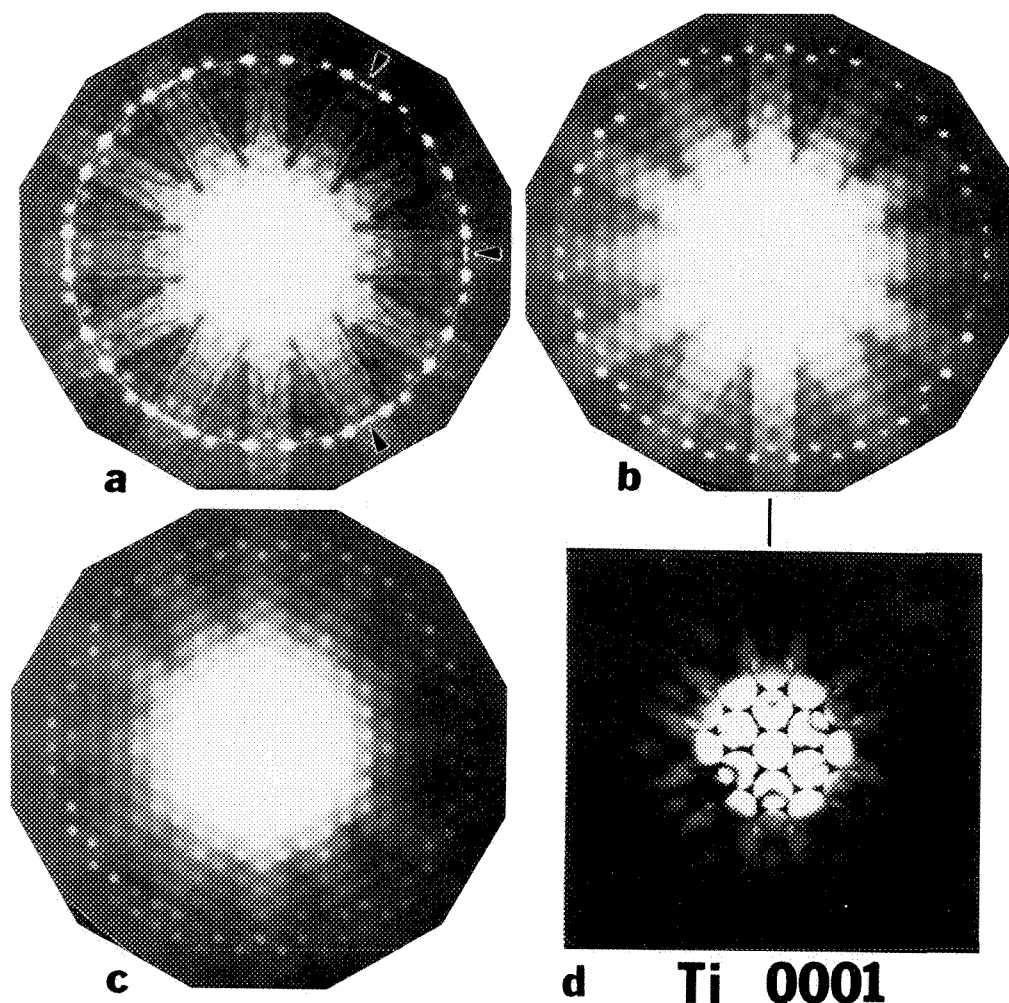


FIG. 1.--CBED patterns of [0001] α -titanium in (a) thick, (b) thin, and (c) very thin regions; (d) enlargement of ZOLZ detail from (b).

intensity fringes in the disks still display 6mm symmetry (although their intensity is also slightly uneven) and that the PD symmetry is still correct. Therefore, the ZOLZ Kikuchi lines appear to be less reliable than the intensity fringes in the ZOLZ disks for providing the correct crystal symmetry, although the latter may also deviate from ideality. The G-M lines in the FOLZ are barely visible in a few of the disks in Fig. 1(b).

A further reduction in specimen thickness eliminates the Kikuchi lines entirely, resulting in the CBED pattern shown in Fig. 1(c). Since the disks in the FOLZ are clearly visible in Fig. 1(c), the pattern displays the correct three-dimensional WP symmetry of the sample, even though only disks are left in the pattern. Therefore, as the specimen thickness decreases, the features in Table 1 gradually disappear in the order that they are listed. That is, HOLZ lines in the BF disk disappear first, Kikuchi lines gradually fade and eventually disappear next, intensity fringes in the ZOLZ disappear last, and the CBED disks in both the ZOLZ and HOLZ remain.

This sequence is further illustrated by the [1 $\bar{1}$ 04] ZAP from α -titanium shown in Fig. 3. In this pattern, the specimen thickness is such that the HOLZ lines are no longer visible in

the BF disk, although ZOLZ Kikuchi lines (arrows) and intensity fringes in the disks (slightly distorted) are still present and indicate that the PD symmetry is 2mm. However, the disks in the FOLZ show that the WP symmetry is m and therefore, that one can determine the PD symmetry and WP symmetry from only the symmetry of the disks in the ZOLZ and FOLZ, without considering either the Kikuchi lines or intensity fringes. Therefore, if there is sufficient high-angle scattering and the disks in HOLZs are visible, determination of the point group of the specimen in very thin regions can be performed reliably by consideration of only the three-dimensional disk pattern. This determination is greatly facilitated by use of a liquid-nitrogen cold stage, which enhances high-angle scattering. Otherwise, the three-dimensional symmetry information provided by HOLZ lines and HOLZ Kikuchi lines appears to be very reliable, whereas two-dimensional information provided by ZOLZ Kikuchi lines and intensity fringes can be quite unreliable.

Reliability of Various Procedures for Determining Symmetry of Thin Specimens by CBED

Several procedures can be used to determine the point group of a specimen by CBED. One of

the earliest procedures was introduced by Buxton et al.⁴ and further refined by Steeds and Vincent.⁶ This method uses the $\pm g$ technique, which compares the detail between opposite ZOLZ disks to test for a center of symmetry.

FIG. 2.--ZOLZ detail corresponding to CBED pattern in Fig. 1(a)

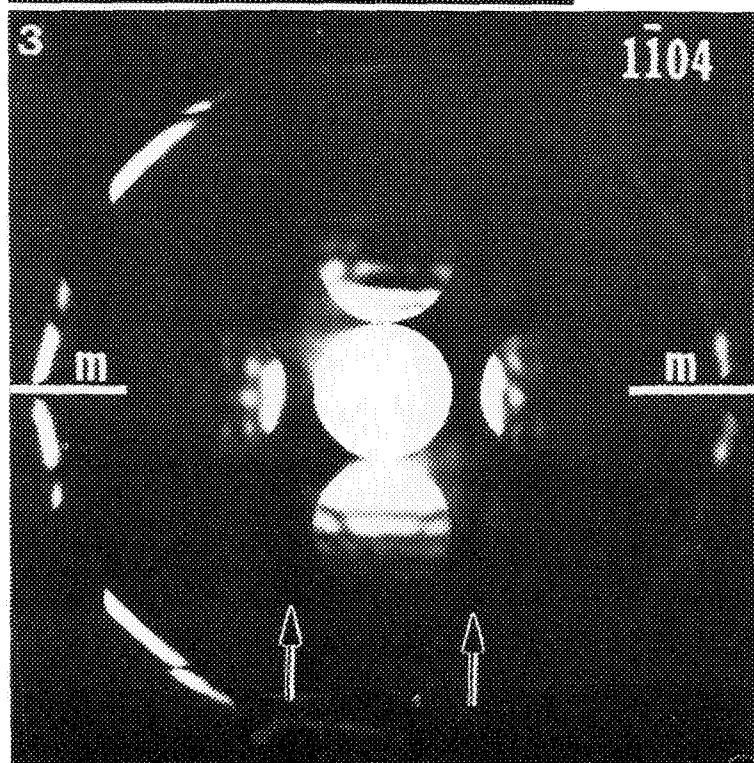
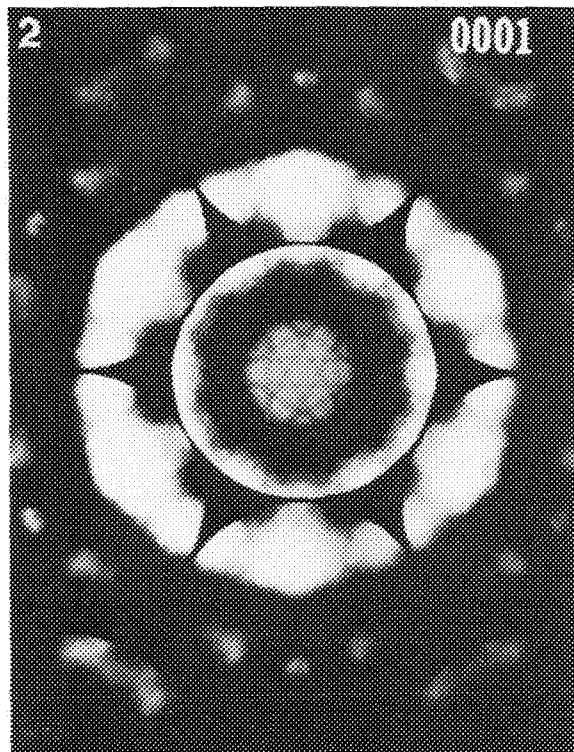


FIG. 3.--CBED pattern of $[1\bar{1}04]$ α -titanium in thin regions.

More recently, Tanaka et al.⁷ have introduced a symmetric many-beam (SMB) method for determining the point group of a specimen. The method is similar to that of Steeds and Vincent⁶ except that under favorable circumstances, the diffraction group and thus the point group can be identified from a single SMB pattern from the figures provided in Tanaka et al.⁷ A third method has been outlined by Loretto⁸ and used extensively by Kaufmann and Fraser.⁹ This method compares the PD and WP symmetries from several different ZAPs to determine the point group. Each of these methods has certain advantages and disadvantages (particularly in the analysis of thin specimens), which are discussed below.

The method used by Loretto⁸ and Kaufmann and Fraser⁹ appears to be the most reliable technique for determining the point group of thin specimens for the following reasons. The method uses the PD and WP symmetries in the CBED pattern, and they can be reliably obtained from the ZOLZ and HOLZ disks in very thin specimens. In addition, several ZAP are usually required to determine the diffraction group, which provides internal consistency in the data. In contrast, the analyses in the previous section showed that symmetry features such as intensity fringes and Kikuchi lines may not yield the correct crystal symmetries for thin specimens. This conclusion is further supported by an earlier investigation¹⁰ which showed that the $\pm g$ test for centrosymmetry can give the wrong result when the sample is thin and no HOLZ lines are present in the BF disk. Such data can complicate the determination of the diffraction group by the technique of Buxton et al.⁴ and Steeds and Vincent.⁶ Although the SMB method appears to be less sensitive to thickness effects, possibly because greater dynamical interaction occurs in a many-beam situation, the intensity fringes in the ZOLZ disks are still quite sensitive to the sample condition for thin specimens and the symmetry may not be correct if HOLZ lines are not present in the SMB pattern. Thus, while these techniques can be simpler because they do not require extensive tilting of the specimen in the microscope, more caution must be used when they are applied to thin specimens.

Conclusions

Higher-order Laue zone lines and HOLZ Kikuchi lines give reliable three-dimensional symmetry information. Intensity fringes and ZOLZ Kikuchi lines appear to be sensitive to sample conditions and may not give accurate symmetry information. Both ZOLZ and HOLZ disk patterns display the correct symmetry for very thin specimens. Use of a liquid-nitrogen cold stage and high-index ZAPs increase

HOLZ interactions, which facilitates analysis of thin specimens. The ZAP method of point group determination may be more reliable than either the $\pm g$ or SMB method for very thin specimens.

References

1. J. A. Eades, M. J. Kaufman, and H. L. Fraser, in *Materials Problem Solving with the Transmission Electron Microscope*, Pittsburgh: Materials Research Society, 1986, 143.
2. J. M. Howe, M. Sarikaya, and R. Gronsky, *Acta Cryst.* A42: 368, 1986.
3. D. B. Williams, *Practical Analytical Electron Microscopy in Materials Science*, Mahwah: Philips Electron Optics Publishing, 1984, 123.
4. B. F. Buxton, J. A. Eades, J. W. Steeds, and G. Rackham, *Philos. Trans. Roy. Soc. London* A281: 171, 1976.
5. J. Gjønnes and A. F. Moodie, *Acta Cryst.* 19: 65, 1965.
6. J. W. Steeds and R. Vincent, *J. Appl. Cryst.* 16: 317, 1983.
7. M. Tanaka, R. Saito, and H. Sekii, *Acta Cryst.* A39: 357, 1983.
8. M. H. Loretto, *Electron Beam Analysis of Materials*, London: Chapman and Hall, 1984, 70.
9. M. J. Kaufman and H. L. Fraser, *Acta Metall.* 33: 191, 1985.
10. J. M. Howe and R. Gronsky, *Ultramicroscopy* 18: 83, 1985.

AEM SPECIMENS: STAYING ONE STEP AHEAD

T. F. Malis

The transformation of transmission to analytical electron microscopy (TEM to AEM) has increased the complexity of specimen preparation because of the differing requirements for both visual and chemical analysis on a growing diversity of materials combinations. Surface phenomena affect AEM data at the low values of specimen thickness preferred for most microanalysis, and thickness variability can produce detrimental effects. This review highlights recent innovations in specimen preparation and presents examples illustrating the need for specimen characterization and maintenance.

Recent Developments in Specimen Preparation

One of the obvious ways of combatting foil thickness in analyzing small second phase particles is to extract them, and a recent review¹ has gone into some detail concerning films other than the standard C for light-element analysis by windowless energy-dispersive x-ray spectroscopy (EDS) or electron energy loss spectroscopy (EELS). A related form of highlighting specific phases has been the use of reactive ion etching to dissolve preferentially the Si_3N_4 matrix in a ceramic matrix composite (CMC), leaving the intergranular Y-Al-Si glassy phase and the SiC reinforcing fiber seemingly unaffected.²

Grinding to produce particulate is a fast and simple means of producing EEL standards from brittle ceramics³ or for AEM of superconducting ceramics;⁴ airborne particulate can be collected by a charged wire method.⁵ The major drawback of particles, unfortunately, is steep thickness gradients.

Electropolishing of self-supporting disks has seen significant upgrading through development of an acid-free electrolyte which has been used in a one-side polishing configuration to thin an impressive number of single and multiphase materials without preferential polishing: Au, Ge, Si, stainless and martensitic steels, V and Zr alloys, and even the 1-2-3 superconducting ceramics.⁶

Advances have been made in ion thinning, including the use of mechanical or chemical dimpling to reduce thinning time, minimize preferential thinning, and even thin to perforation.⁷ Four approaches to the problem of site-specific cross sections for ion thinning

were recently summarized,⁸ including methods that have been used to study steel oxidation⁹ and wear.¹⁰ A different approach to Al oxidation was the drilling of an off-centered 1mm hole in a 3mm disk followed by oxidation, epoxy filling, and ion thinning.¹¹ Another, centered hole-drilling method has been used to construct composite disks for the study of radioactive material so as to minimize x-ray counts.¹² Plan view ion thinning of epitaxial ZnSe on GaAs has been accomplished successfully by photoelectrochemical etching of the GaAs substrate before reactive ion etching of the ZnSe.¹³

The growing problem of differing ion thinning rates for the metal and ceramic phases in metal matrix composites (MMCs) has led to attempts to post-treat the perforated specimen using either chemical polishing or precision ion milling (PIMS) of the thicker phase.¹⁴ Others have combined uniform initial chemical thinning with final jet electropolishing.¹⁵ Encouraging results have been obtained in a recent characterization of an Al-SiC MMC.¹⁶ Figure 1(a) shows that a cluster of SiC particles fell out of a foil in the late stages of thinning, but continued thinning for a few hours led to development of numerous thin areas adjacent to these holes in which metal/ceramic interfaces could be analyzed (Fig. 1b). Figure 1(c) shows another specimen that had produced a large hole with few thin areas. Again, continued thinning for a few hours produced multiple perforations around the rim of the hole, with some thin regions large enough to include entire SiC particles, e.g., the $10 \times 50\mu\text{m}$ particle shown in part in Fig. 4.

Since both electropolished and ion-thinned disk specimens suffer from variable thickness, diamond knife sectioning (ultramicrotomy) has seen growing usage as a complementary preparation technique particularly amenable to AEM by virtue of producing large sections (up to a hundred micrometers square) with uniform, controlled thickness.³ Site-specific sections are generally easier to produce than for ion thinning, particularly for surface or near-surface regions. Thus, impressive longitudinal sectioning of $30\mu\text{m}$ -diameter Al circuit bonding wire has been achieved,¹⁷ as well as both cross sectioning and plan-view serial sectioning of multilayer magnetic recording media.¹⁸ Microtoming largely developed in the area of corrosion research and a recent review of many corrosion applications has been compiled.¹⁹ Two different catalyst studies have noted the benefits of microtoming in obtaining information on both small scale (HREM) structures²⁰ and large-scale particle distributions²¹ more representative than the common method of crushing and dispersion on grids. A method that takes advantage

The author is with the Metals Technology Laboratories, Energy, Mines, and Resources Canada (CANMET), 568 Booth St., Ottawa, Ont., Canada K1A 0G1. The assistance of M. Charest and G. Williams in specimen preparation is gratefully acknowledged.

of the concoidal nature of glass fracture and uses pretreatments to enable stronger glass-epoxy bonding has proved to be a superior method for sectioning of multilayered optical glasses.²²

The relative ease of certain cases of sectioning is demonstrated in Figs. 2 and 3. Figure 2 shows alternate layers of CeO_2 and Cr_2O_3 sputter deposited on Al, then sectioned without any embedding or electroplating (total preparation time of about 1 h). Although substantial distortion of the layers has taken place, segments suitable for detailed imaging and/or AEM remain intact. Reduced preparation time was also significant concerning the BN fibers of Fig. 3, where the goal was to determine whether residual O from the B_2O_3 precursor remained after nitriding. After embedding in epoxy, many sections were produced (Fig. 2a), with the uniform thickness enabling rapid EEL spectral collection and processing (less than two days) and the conclusion that the residual O level was not unduly high (Fig. 2b). Subsequent examination in a Zeiss 902 EELS-imaging TEM showed the O to be very uniformly distributed and not concentrated at the fiber core. A comprehensive review of ultramicrotomy related to materials science is in preparation.²³

AEM Specimen Characterization

As the thickness limitations of EELS (and to a lesser extent, EDS) combine with various surface effects to hinder reliable quantitative analysis, a case can be made for some form of AEM specimen "quality control." EELS is an ideal technique for this task, as it can rapidly monitor either relative or absolute specimen thickness by the log-ratio technique,²⁴ as well as detect and even quantify oxide and/or contaminant layers present.³ The log-ratio method has been found to be linear to thicknesses as low as 10 nm,²⁵ and good agreement for the values of λ (the mean inelastic scattering length needed for absolute thickness determination) has been found.^{24,25} Moreover, the realm of reliable EEL quantification continues to expand regarding confirmation of calculated cross sections and determination of experimental ones.²⁶⁻²⁸ Other microscope modes such as secondary electron (SE) imaging or diffraction techniques can contribute valuable information regarding specimen integrity.

Specimen-related Problems (and a Few Solutions)

There has been debate concerning spurious matrix adhesion to extracted particles, but a consensus seems to be emerging that such pickup can indeed occur and can be distinguished from a genuine presence of matrix elements within the particle only if rigorous replicating procedures are followed, especially with regard to washing.¹ In addition, there is a size limit of 5-10 nm below which it is almost impossible to distinguish between the two effects. Mass loss from small oxides, nitrides, and carbides under certain beam currents continues to be a problem.

Electropolishing artifacts have been known to influence AEM data through such effects as preferential precipitate attack, grain boundary grooving, and enriched surface oxides. The above EELS methodology has been quite useful in characterizing this phenomenon.³ Ion thinning can produce grain boundary grooving as well as Si contamination from diffusion pump oil and significant amorphous surface layers (typically 20-30 nm).²⁹ Ion-induced precipitate alteration has been seen in Al-Li-Cu alloys³⁰ and evidence for heating up to 370 C in Au/Si bilayers,³¹ although data on ferroelectric ceramics indicated heating less than 55 C.³²

A major drawback of variable specimen thickness was found in conducting EDS traces into the SiC particles of the MMC of Fig. 1 to confirm possible Al diffusion.³³ Significant amounts of Al were indeed found extending up to 1 μm into the carbide, but it was noted that the Al profiles from locations with different orientation of the SiC with respect to the x-ray detector showed differing dependencies with distance, indicating possible fluorescence of Al by Si K x rays. EELS showed no detectable Al for the great majority of interfaces or confined to within 50 nm of the interface when it was detected. A similar fluorescence effect has been observed for Y-rich intergranular phases in sintered Si_3N_4 .³⁴ EELS is the only safe technique to use for such material combinations; however, Fig. 4 graphically indicates the thickness limitations imposed on EEL analysis in typical wedge-shaped foils.

Ultramicrotomy may eliminate thickness variability but can present other hazards. Damage, such as the shattering of hard phases (shown for an MnAl_6 intermetallic phase in Fig. 5) can obscure features although it does not necessarily preclude microanalysis or diffraction. Anodic corrosion of the matrix around precipitates caused by the water bath on which the section floats is a problem with Al alloys (Fig. 5) and some other metallic systems. (No practical substitute for water yet exists as a microtoming bath.) A more subtle artifact was observed in the study of the BN fibers (Fig. 3), where a 10nm-thick C layer (Fig. 3b) appeared to have been smeared across the fibers during sectioning, most likely because of the greater elastic response to sectioning of the epoxy relative to the hard fibers.

Figure 6 shows electron beam damage in an intergranular glass phase of ion thinned Si_3N_4 which may have been inhibited by post-thinning phenomena. That is, SE imaging showed the damage blisters to be internal, and sequential EEL analyses indicated no significant mass loss. The C-layer deposited to prevent charging, along with the normal C contamination layer, may actually "seal in" the damage. In view of growing concerns over mass loss from knock-on sputtering in medium voltage AEM³⁵ this effect may be worth investigating. C evaporation has been proposed also as a possible means of preventing contamination cones on electropolished foils,³ but O pickup during C deposition³⁴ is possible.

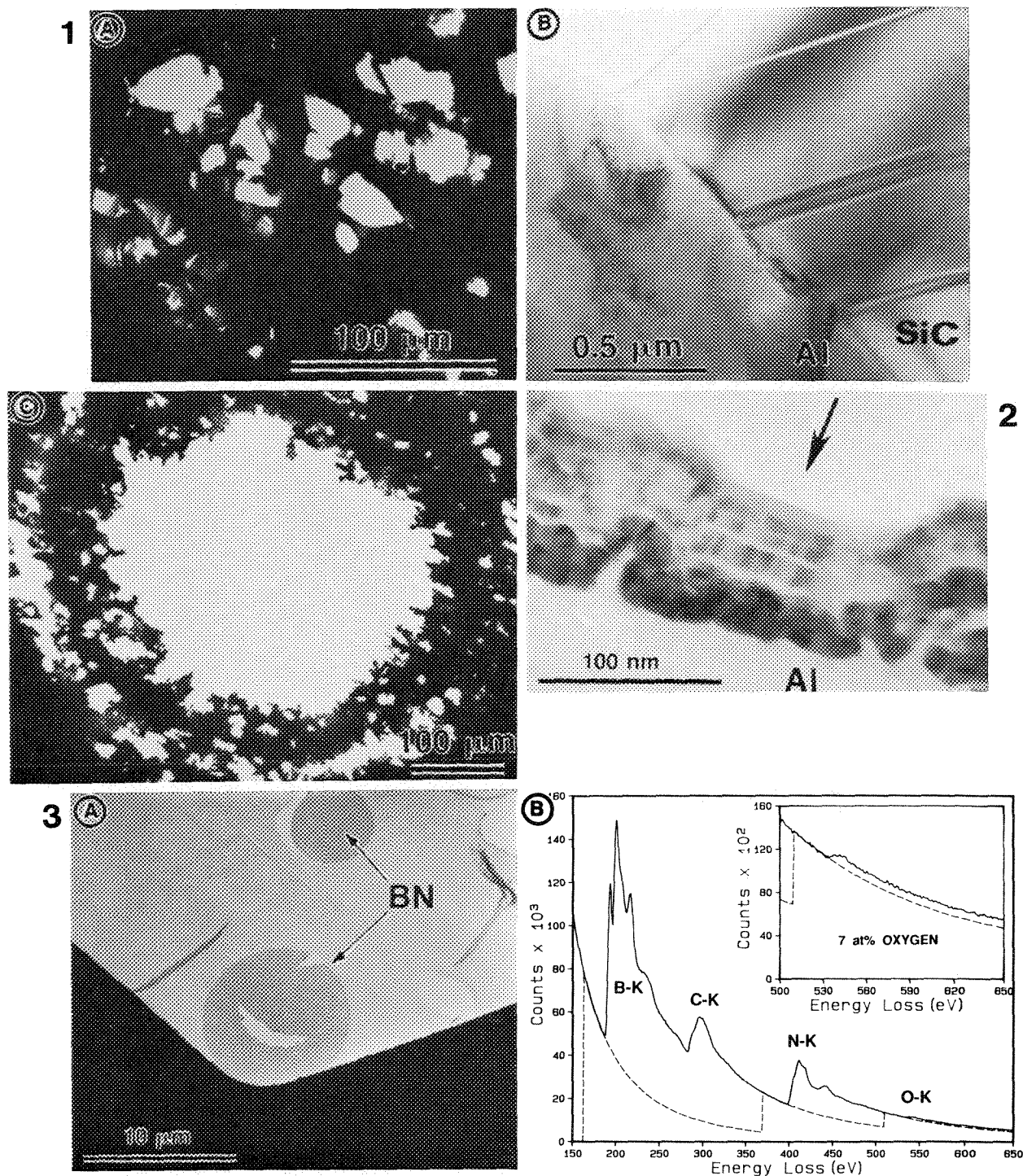


FIG. 1.--(a) Al-SiC thin foil showing particle fallout. (b) Typical Al/SiC interface region. (c) Foil showing "double-hole" effect from continued thinning.
 FIG. 2.--Ultramicrotomed 50nm-thick section of layers of CeO_2 (dark) and Cr_2O_3 (light) deposited on Al. Direction of cut arrowed.
 FIG. 3.--(a) Ultramicrotomed 70nm-thick section of BN fibers in epoxy. (b) EEL spectrum (120 keV, 5.6 mrad collection angle) typical of all fibers.

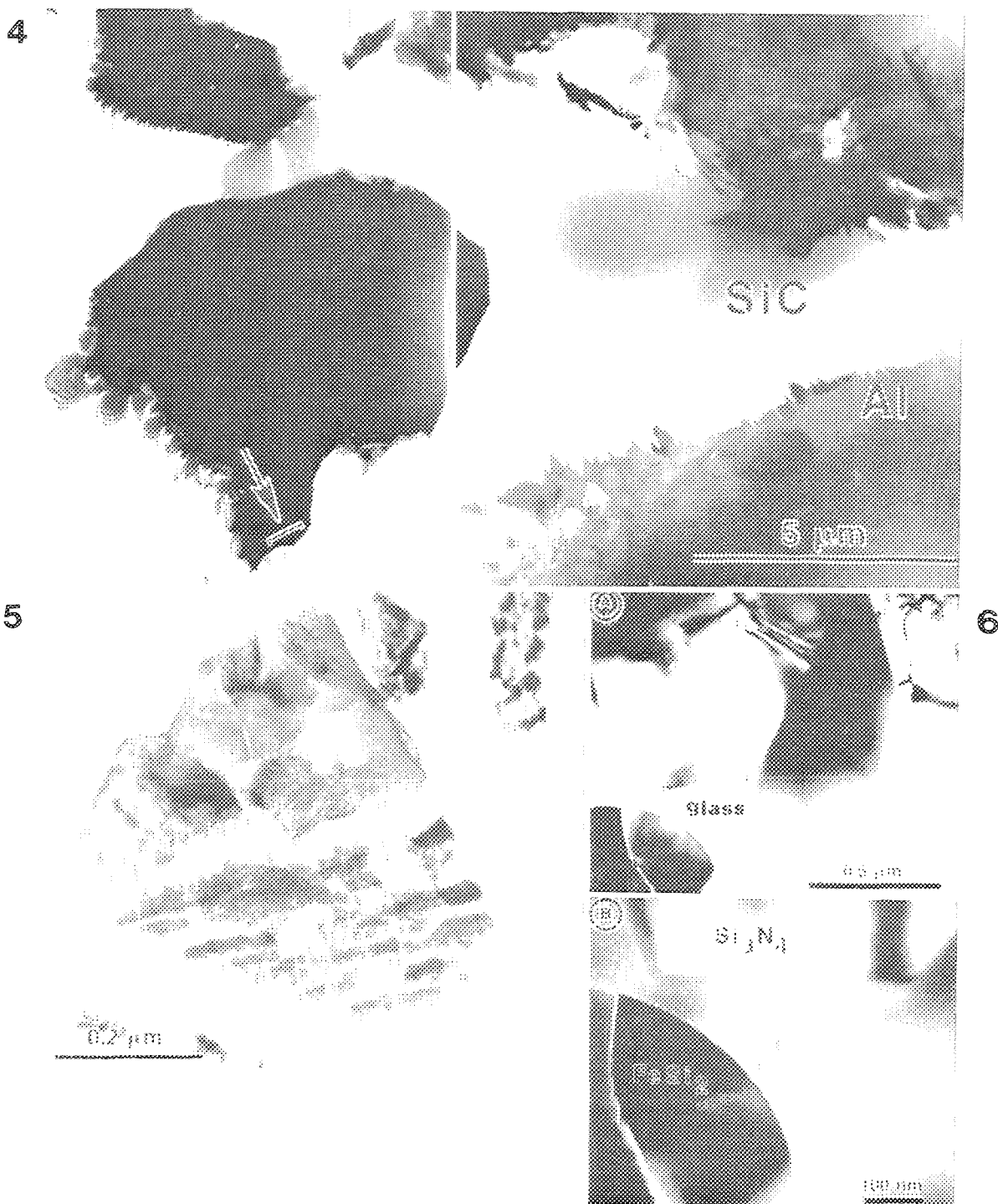


FIG. 4.--Centered dark field of portion of SiC particle with jagged Al/SiC interface. Only portion amenable to EEL analysis is arrowed (over 100 μm of total interface).
 FIG. 5.--Thin section of Al-Mn alloy showing preferential matrix corrosion at particle by microtome water bath.
 FIG. 6.--(a) Intergranular glass phase in Si₃N₄ before microanalysis. (b) Internal damage from focused beam analysis.

Contamination layers on AEM specimens can grow with time, even for clean AEMs (outgassing of storage capsules, dessicator backstreaming from mechanical vacuum pumps, etc.). The effects of such layers may be as subtle as making background fitting of low-loss EELS edges more difficult,³⁴ or as obvious as the reduced image clarity of Fig. 7(a) (due to a 70nm-thick layer). A 5min ion wipe of the pearlitic steel foil (Fig. 7b) was sufficient to restore image quality (and capability of analyzing the overhanging carbides) by removing most of this layer.

The analytical techniques themselves can be adjusted to counter thickness effects. Figure 8 illustrates the decrease in EEL plural scattering for 365nm-thick Si₃N₄ for a smaller collection angle than normal (0.5 vs 5.6 mrad). The decrease is caused by the fact that λ roughly doubles between the two angles,²⁴ similar to the effect of increased keV. Edge visibility (peak/background) is greatly improved, as seen for 280nm-thick BN (Fig. 8b).

New AEM specimen preparation techniques certainly will evolve. Figure 9 (showing a "suspended" grain boundary and a boundary "spike" from the foil edge) shows one such method waiting to be elucidated. A common microalloyed steel had produced a series of "normal" foils, i.e., tending toward preferential polishing at precipitates or grain boundaries, if at all. For no obvious reason one foil in the middle of the series showed the reverse behavior, clear grain interior preferential polishing!

References

1. T. N. Baker and H. S. Ubhi, *AEM Workshop*, EMAG-87, 1988, 135.
2. F. X. Pink and K. J. Ostreicher, *J. EM Techniques* 7: 161, 1987.
3. T. Malis, *AEM Workshop*, EMAG-87, 1988, 127.
4. P. L. Gai, S. E. Male, C. J. Salter, N. J. Long, and E. D. Boyes, *EMAG-87*, 1987, 307.
5. L. M. Brown, J. P. Goff, M. Kalinowski, and D. E. Sheet, *EMAG-87*, 1987, 47.
6. B. J. Kestel, *Ultramicroscopy* 8: 351, 1988.
7. D. G. Ivey and G. R. Piercy, *J. EM Techniques* 8: 233, 1988.
8. S. B. Newcomb, C. S. Baxter, and E. G. Bithell, *EUREM-88* 1: 43, 1988.
9. I. M. Reamey and G. W. Lorimer, *AEM Workshop*, EMAG-87, 1988, 183.
10. M. Rainforth, R. Stevens and J. Nutting, *EUREM-88* 2: 473, 1988.
11. R. C. Dickenson and K. R. Lawless, *Proc. 45 Ann. Meet. EMSA*, 1987, 380.
12. P. K. Rose and J. Rowe, *AEM Workshop*, EMAG-87, 1988, 151.
13. A. C. Wright, T. L. Ng, Z. Zairai, M. E. Pemble, and J. D. Williams, *AEM Workshop*, EMAG-87, 1988, 213.
14. J. C. Walmsley and D. Cherns, *EUREM-88* 2: 439, 1988.
15. M. R. Krishnadev, S. Dionne, K. Tomhanyi, M. C. Chers, and B. Voyzelle, *Microstructural Science*, New York: Elsevier, 1987, 6: 125.
16. L. M. Dignard-Bailey, T. F. Malis, J. D. Boyd, and J. D. Embury, *Int. Symp. Adv. Structural Materials*, Toronto: Pergamon Press, (in press).
17. D. Steele and A. Otto, *EMAG-87*, 1987, 27.
18. D. Steele and A. Rosenfeld, *AEM Workshop*, EMAG-87, 1988, 187.
19. H. Karimzadeh, G. E. Thompson, Y. Yeong, E. Namgoong, S. N. Jones, and G. C. Wood, *EMAG-87*, 1987, 35.
20. A. Legrouiri, T. Baird, and J. R. Fryer, *EMAG-87*, 1987, 31.
21. R. Szymanski and J. Lynch, *EUREM-88* 2: 295, 1988.
22. P. Swab and R. E. Klinger, *Specimen Preparation for TEM of Materials*, Boston: Mat. Res. Soc., 1988, 115: 229.
23. D. Steele, T. Malis, M. D. Ball, and G. E. Thompson, *J. Mat. Sci.* (in preparation).
24. T. Malis, S. C. Cheng, and R. F. Egerton, *J. EM Techniques* 8: 193, 1988.
25. R. W. Carpenter and P. R. T. Jang, *Proc. 44th Ann. Meet. EMSA*, 1986, 718.
26. T. Malis and J. M. Titchmarsh, *EMAG-85*, 1985, 181.
27. T. Malis, K. Rajan, J. M. Titchmarsh, and G. C. Weatherly, *Int. Voltage Microscopy and Its Application to Mat. Sci.*, Philips, 1986, 78.
28. F. Hofer, P. Golob, and A. Brunegger, *AEM Workshop*, EMAG-87, 1988, 119.
29. Y. K. Simpson, C. B. Carter, K. J. Morrissey, P. Angelini, and J. Bentley, *J. Mat. Sci.* 21: 2689, 1986.
30. A. K. Singh, M. A. Imam, and K. Sadanada, *J. EM Techniques* 8: 355, 1988.
31. M. J. Kim and R. W. Carpenter, *Ultramicroscopy* 21: 327, 1987.
32. T. Malis and Herbert Gleiter, *J. Appl. Phys.* 47: 5195, 1976.
33. R. J. Arsenault and C. S. Pande, *Scripta Met.* 18: 1131, 1984.
34. M. M. Chadwick and T. Malis, *Ultramicroscopy* (in press).
35. C. R. Bradley and N. J. Zaluzec, *Ultramicroscopy* (in press).

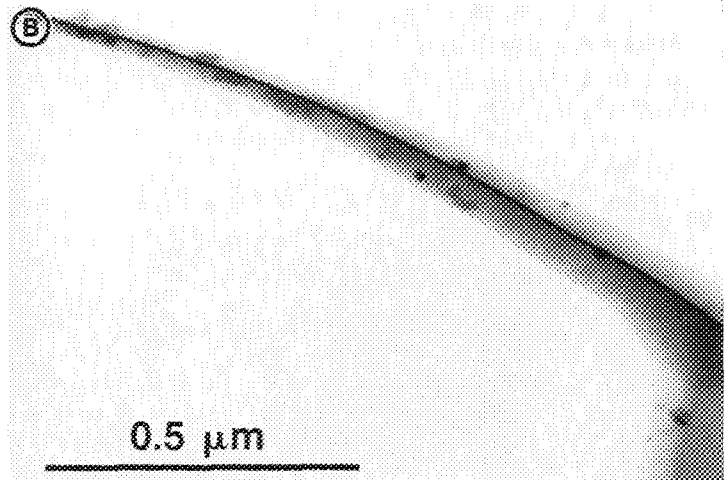
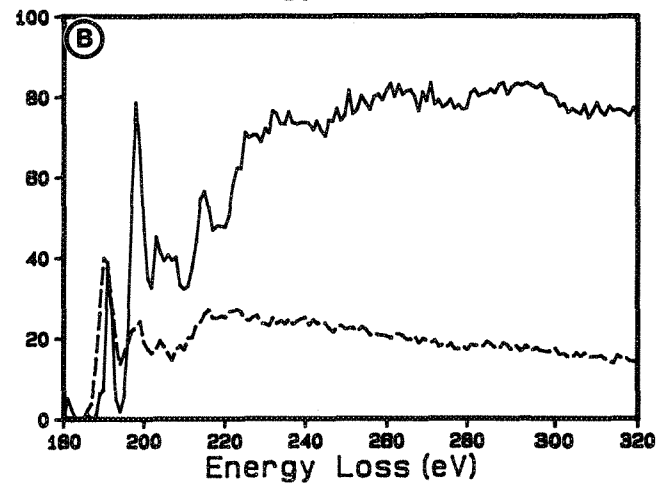
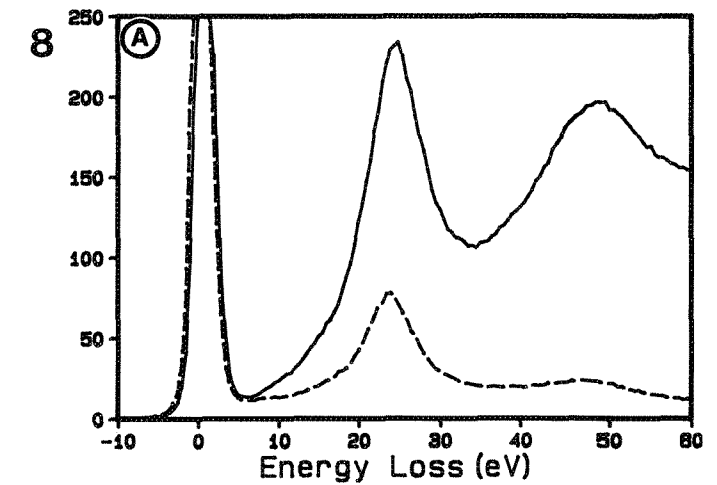
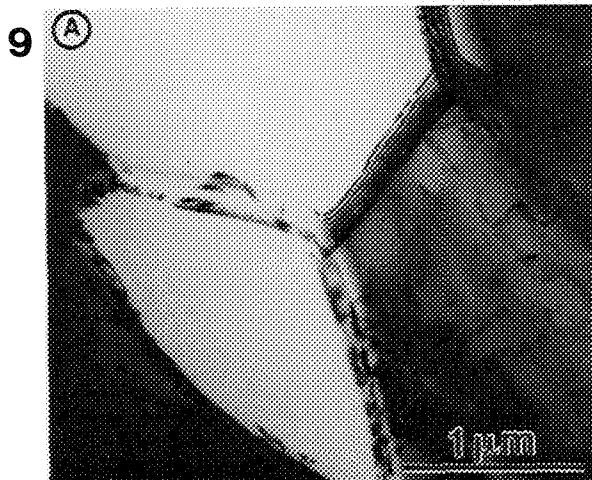
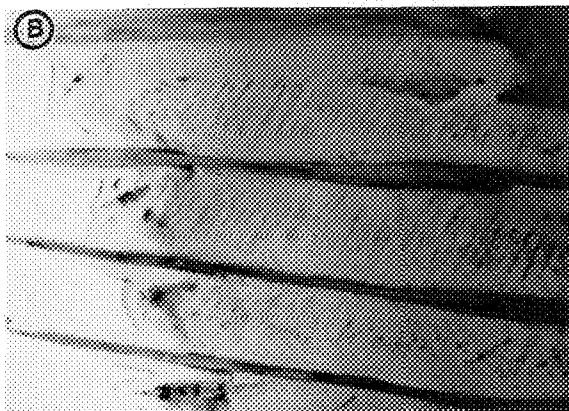
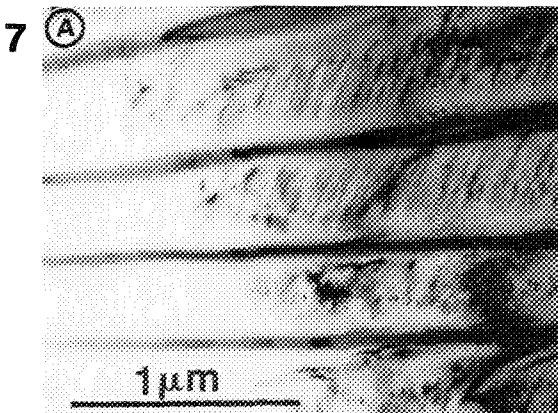


FIG. 7.--(a) Electropolished foil of pearlitic steel obscured by 70 nm of C contamination (as measured by EELS).³ (b) Improvement resulting from 5 min of ion wiping; C layer reduced to 25 nm in this region.

FIG. 8.--(a) Low-loss regions of 120keV EEL spectra from 365nm-thick Si_3N_4 collected at 5.6 mrad (solid) and 0.5 mrad (dashed) showing reduction in plural scattering. (b) Stripped B-K edges for 280nm-thick BN, peak/background 0.07 (5.6 mrad); 0.37 (0.5 mrad).

FIG. 9.--Examples of unusual (and irreproducible) preferential matrix dissolution during electropolishing of common microalloyed steel.

LOSS OF GRAIN-BOUNDARY SEGREGANT DURING ION MILLING

E. A. Kenik

Bismuth segregates to grain boundaries in copper at intermediate temperatures (400–800 C).¹ Currently, x-ray microanalysis is being used to measure the degree of equilibrium segregation as a function of boundary character. As part of that study, transmission electron microscopy specimens were prepared by several techniques in order to select the method that produced optimum specimens. Electropolishing produced specimens of marginal quality because of preferential grain-boundary attack. On the other hand, ion-milling produced good, thin specimens with little or no boundary attack. However, x-ray microanalysis on specimens ion-milled at room temperature indicated no bismuth segregation, whereas analysis on electropolished specimens indicated bismuth segregation. A loss of bismuth from the ion-milled specimens was proposed to result from the high vapor pressure of bismuth at slightly elevated temperatures. The use of a liquid-nitrogen cold stage during ion milling minimizes the loss of bismuth. It is likely that beam heating during ion milling is a contributing factor in this process and must be controlled.

Experimental

A copper-bismuth alloy was prepared by a method similar to that used by Michael and Williams.¹ Bismuth was evaporated to $\sim 0.15 \mu\text{m}$ thickness on both sides of high-purity copper sheet of 0.25 mm thickness. The sheet was annealed in evacuated quartz capsules at 400 C for 16 days to homogenize the material. Scanning electron microscopy (SEM) was used to determine the redistribution of bismuth on the scale of the grain size, $\sim 30 \mu\text{m}$. Specimens for analytical electron microscopy (AEM) were initially prepared by electropolishing. However, preferential etching occurred at the grain boundaries, producing marginal specimens. On the other hand, ion milling with 6kV Ar^+ ions in a Gatan ion miller produced good, thin specimens with little or no boundary attack. Both standard and liquid-nitrogen-cooled specimen stages were used for ion milling.

The author is at the Metals and Ceramics Division, Oak Ridge National Laboratory, Box 2008, Oak Ridge, TN 37831-6376. Research sponsored by the Division of Materials Sciences, U.S. Department of Energy, under contract DE-AC05-84OR21400 with Martin Marietta Energy Systems, Inc. The author is very appreciative of the expertise and assistance of D. C. Joy in the SEM analysis of the bismuth. The useful discussion and review of this manuscript by M. K. Miller, J. M. Vitek, and J. Bentley are also acknowledged.

A Philips EM400T-FEG microscope equipped with an EDAX 9100 analyzer provided high spatial resolution AEM capability. X-ray microanalysis was performed in the scanning transmission electron microscopy mode with a $\sim 2\text{nm}$ -diam. probe on boundaries oriented parallel to the electron beam. Since the Philips EM400T permits direct imaging of the probe, it was possible to avoid aberrated probes and also to measure the probe size and current density by scanning the magnified image of the probe over a $100\mu\text{m}$ entrance aperture to a Gatan 607 electron energy loss spectrometer. Care was taken to minimize the influence of such experimental conditions as hole count,² coherent bremsstrahlung radiation,^{3,4} and electron channeling,⁵ which can have detrimental effects on quantitative analysis. A Gatan liquid-nitrogen-cooled specimen holder was used to minimize contamination under the fine probe, with only a small increase in specimen drift rate. However, the probe could be easily maintained on boundaries by adjustments made on the basis of monitoring the intensities of two reflections in the diffraction pattern, one from each grain. The composition of the excited volume was calculated from the measured Cu $K\alpha$ and Bi $L\alpha$ intensities with the standardless thin-foil approach developed by Zaluzec.⁶

Results

Scanning electron microscopy of the region $\sim 1 \mu\text{m}$ below but parallel to the original surface indicated a nearly continuous film of bismuth $\sim 0.4 \mu\text{m}$ thick at the grain boundaries (Fig. 1a). This film is obviously not equilibrium segregation, but the formation of a second phase, presumably from liquid bismuth attack of grain boundaries during the anneal. However, backscattered electron images from a transverse section of the sheet showed that the continuous film does not extend into the interior of the material, from which specimens for the AEM studies are prepared. Isolated precipitates of essentially pure bismuth were observed at grain boundary triple points throughout the thickness of the sheet (Fig. 1b). Their presence indicates that bismuth has penetrated the entire thickness along the grain boundaries.

Initial x-ray microanalysis performed on the specimens of marginal quality produced by electropolishing indicated bismuth segregation to high-angle grain boundaries and incoherent twin boundaries. No bismuth was detected by x-ray microanalysis of the matrix. No second phase was detected by either imaging or diffraction. Therefore, the bismuth enrichment at boundaries is associated with equilibrium

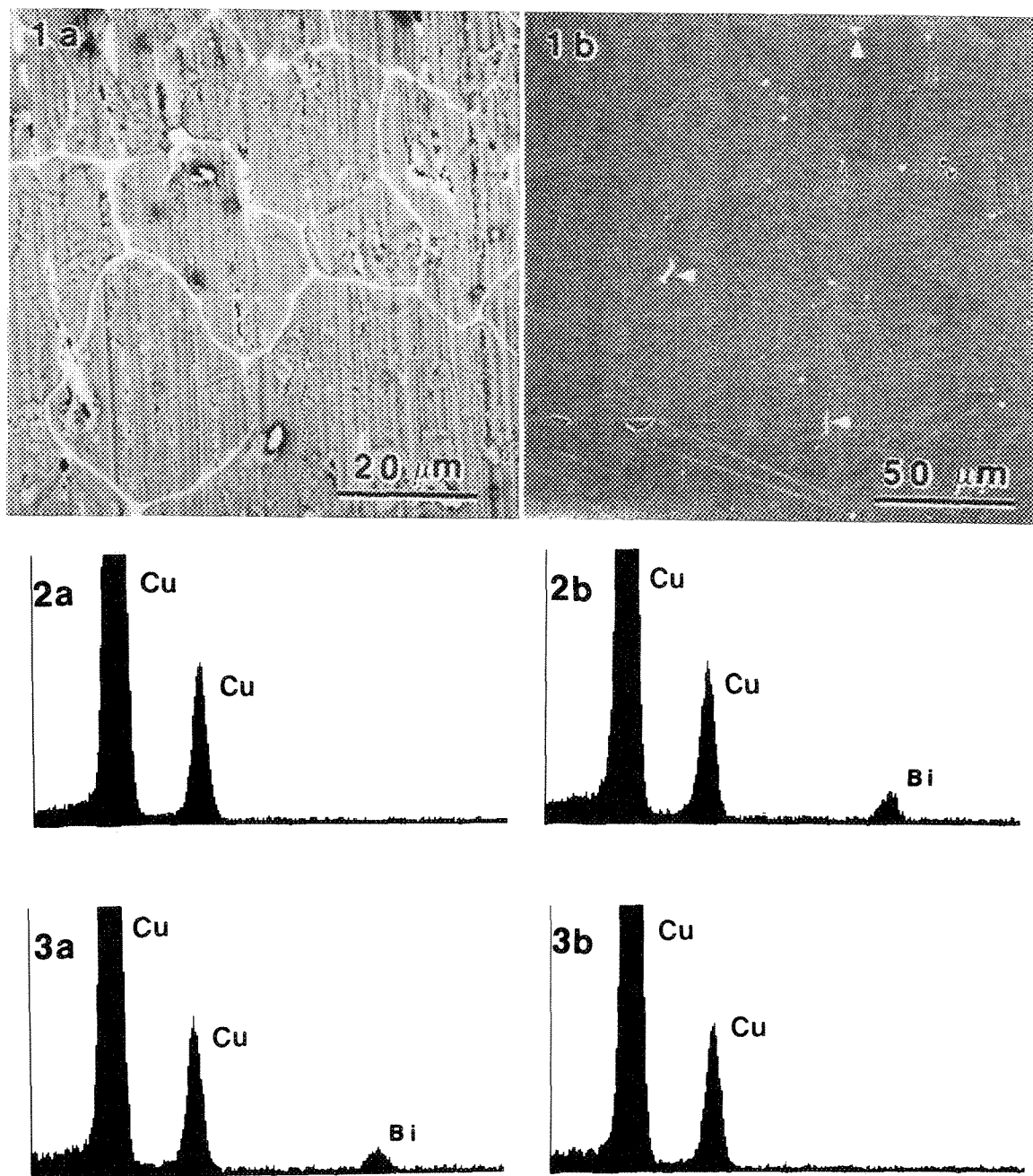


FIG. 1.--Scanning electron micrographs of Cu-Bi alloy. (a) Backscattered electron (BSE) image of region $\sim 1 \mu\text{m}$ below coated surface prepared by mechanical grinding. Continuous film of bismuth $\sim 0.4 \mu\text{m}$ thick revealed at grain boundaries. (b) BSE image of transverse section of sheet indicating isolated precipitates of bismuth at grain boundary triple points (arrowed) and absence of detectable continuous grain boundary film in bulk of specimens.

FIG. 2.--X-ray microanalysis of high-angle grain boundaries in Cu-Bi alloy. (Cu K α peaks are 4 \times full scale.) (a) X-ray spectrum from boundary in specimens ion milled at nominally room temperature. No significant bismuth peaks present. (b) X-ray spectrum from boundary in specimen ion-milled at low temperature. Bismuth content of excited volume ~ 2.8 at.% Bi.

FIG. 3.--X-ray microanalysis of same high-angle grain boundary. (Cu K α peaks are 4 \times full scale.) (a) X-ray spectrum of boundary in specimen prepared by low temperature ion milling. Apparent bismuth content of excited volume ~ 1.9 at.% Bi. (b) X-ray spectrum from same boundary recorded after brief ion-milling under reduced conditions (300 s and 3 kV), at nominally room temperature. No bismuth segregation detected.

segregation. On the other hand, no segregation was indicated by similar analyses on boundaries in ion-milled specimens nominally prepared at room temperature (Fig. 2a). No significant

Bi M or L peaks were detected from the matrix or at grain boundaries in such specimens. At first, this inability to detect bismuth segregation was attributed to the variability of

segregation with boundary character. However, after many boundaries were checked, without any indication of bismuth segregation, it was suspected that the bismuth was being lost from the boundaries during specimen preparation. To test this hypothesis, specimens were ion milled while at cryogenic temperatures. X-ray microanalysis of these specimens indicated the presence of bismuth at various high-angle grain and incoherent twin boundaries. A typical example is given in Fig. 2(b), where the excited volume contains ~ 2.8 at.% Bi. Since the bismuth is concentrated at the grain boundary, the actual bismuth composition at the boundary is significantly higher. Simpson et al.⁷ have shown that a false indication of boundary segregation can result from the preferential collection of one element at surface grooves associated with a boundary. However, x-ray microanalysis of boundaries tilted away from the edge-on configuration has shown that the segregation detected was associated with the boundary plane and not with the intersection of the boundary with the foil surfaces. The measured bismuth segregation was genuine and not a specimen-preparation artifact. Therefore, the absence of detectable bismuth segregation in the specimens ion milled at nominally room temperature must be associated with the loss of bismuth during specimen preparation. Bismuth has a relatively high vapor pressure and may simply be lost by evaporation.

One other test of this proposed loss mechanism was performed. A long, straight high-angle grain boundary was selected in a specimen ion milled at low temperature. The bismuth level in the excited volume was ~ 1.9 at.% Bi for this boundary (Fig. 3a). The same boundary was reexamined after a brief ion milling at nominally room temperature under reduced milling conditions (300 s and 3 kV), which removed ~ 0.5 μm of material. No bismuth segregation was detected (Fig. 3b). As the segregation is expected to be approximately constant along a given boundary, the proposed loss of bismuth from boundaries during nominal room temperature ion milling was confirmed.

The question of beam heating during ion milling is relevant to this problem. Beam heating of 100-150 C has been reported for specimens clamped during milling.⁸ However, it has been shown that specimen temperatures as high as ~ 370 C can be realized for some specimens.⁹ At 370 C, elemental bismuth would be liquid and its vapor pressure would be $\sim 10^{-5}$ Pa ($\sim 10^{-7}$ Torr). That would be sufficient for bismuth to evaporate from the free surface. However, a large portion of the segregated bismuth has been lost from boundaries in regions ~ 50 nm thick. Such loss indicates sufficient mobility of bismuth along boundaries to permit bismuth to diffuse to the free surfaces to be lost. Cooling during ion milling prevents bismuth loss in two ways; it reduces the rate of evaporation at the free surface and reduces diffusion of segregant to the free surface.

Conclusions

The loss of bismuth segregated at high-angle grain and incoherent twin boundaries during nominal room temperature ion milling has been demonstrated. The loss appears to be related to beam heating and the high vapor pressure of bismuth at slightly elevated temperatures. Such high vapor pressures are not uncommon for strong segregants in metallic systems (e.g., As, Cd, S, Sb, and Te). Therefore, care must be taken in specimen preparation for AEM measurement of such segregation. Similar problems may occur in ceramic systems, where greater beam heating is possible.

References

1. J. R. Michael and D. B. Williams, *Metall. Trans.* 15A: 99, 1984.
2. J. Bentley, N. J. Zaluzec, E. A. Kenik, and R. W. Carpenter, "Optimization of an analytical electron microscope for x-ray microanalysis: Instrumental problems," *SEM/1979* II, 581.
3. G. M. Reese, J. C. H. Spence, and N. Yamamoto, *Phil. Mag.* A49: 697, 1984.
4. K. S. Vecchio, *Proc. 43rd Ann. Meet. EMSA*, 1985, 248.
5. J. C. H. Spence and J. Taftø, *J. Microscopy* 130: 147, 1983.
6. N. J. Zaluzec, "Quantitative x-ray microanalysis," in J. J. Hren, J. I. Goldstein, and D. C. Joy, Eds., *Introduction to Analytical Electron Microscopy*, New York: Plenum Press, 1979, 121.
7. Y. K. Simpson, C. B. Carter, K. J. Morrisey, P. Angelini, and J. Bentley, *J. Mater. Sci.* 21: 2680, 1986.
8. D. J. Barber, *J. Mater. Sci.* 5: 1, 1970.
9. M. J. Kim and R. W. Carpenter, *Ultramicroscopy* 21: 327, 1987.

THE EFFECT OF SPECIMEN THICKNESS AND ELECTRON PROBE CHARACTERISTICS ON THE X-RAY SPATIAL RESOLUTION IN THE ANALYTICAL ELECTRON MICROSCOPE

J. R. Michael

The x-ray spatial resolution that may be obtained in the analytical electron microscope (AEM) is a function of the specimen thickness and composition, and of the characteristics of the electron probe (size and current distribution). Due to the importance of the x-ray spatial resolution in microanalysis, many studies have measured the spatial resolution obtained in the AEM for specimens of known thickness. However, in most cases the electron probes used have not been well characterized. Since the probe size has a direct effect on the x-ray spatial resolution, it is important to know the probe size and the current distribution within the probe. It is the purpose of this paper to describe the results of the systematic measurement of the spatial resolution obtained in an AEM equipped with a high-brightness field-emission gun (FEG) electron source and a system to compensate automatically for specimen drift during microanalysis. The experimentally determined spatial resolution is compared with calculated values. Also, the effects of probe size and probe shape are demonstrated.

There have been many studies of the x-ray spatial resolution that may be obtained in the AEM.¹⁻¹⁰ These studies have compared the spatial resolution obtained in the AEM with the various theoretical calculations of beam broadening. Most of these studies have been carried out with transmission/scanning electron microscopes (TEM/STEM) in which the probe size and current distribution have not been well characterized, which leads to large uncertainties in the measurements. Also, in most of the TEM/STEM instruments the electron probe size has been a large fraction of the measured spatial resolution, which makes interpretation of the experimental results difficult due to the need to deconvolute the effects of the initial probe size and the beam broadening. Within the past few years, there have been some studies that demonstrate high-spatial-resolution microanalysis in a range of materials.¹¹⁻¹⁴ These results have been obtained in AEM instruments equipped with FEG electron sources, which produce small electron probes (<2 nm) that contain high currents (>0.1 nA). The high x-ray spatial resolution capability of AEM instruments equipped with FEG electron sources provides an excellent opportunity to measure the beam broadening that occurs in thin specimens, since the contribution of the initial probe size is small due to the small probe size.

Various techniques have been used to measure

the x-ray spatial resolution obtained in the AEM. Some studies have performed point analyses across an interface where there is a discrete change in composition. Due to the beam broadening and the finite probe size, the discrete composition change is degraded into a more gradual change in composition. The spatial resolution is then taken as some fraction of the width of the broadened profile.¹⁵ This is the technique used in this study.

Experimental

The microanalyses were conducted in a Vacuum Generators HB-501 dedicated STEM equipped with a cold FEG electron source operated at 100 kV, and a gun lens. The microscope was equipped with a Link Analytical AN10/95 x-ray system and a Link LZ5 series E windowless x-ray detector. The probe size used was either 1.8 nm full-width at tenth-maximum (FWTM) with 0.8-1.0 nA, or 7.0 nm FWTM with 4.0 nA.^{15,16} The 7.0nm probe has been shown to be spherically aberrated; thus, the probe consists of an intense central region which is surrounded by a low-intensity halo. In order to demonstrate the effects of aperture misalignment, an additional profile was obtained with the beam-defining aperture misaligned. The composition profiles were obtained from specimens with abrupt concentration discontinuities. The chromium composition profiles from which the spatial resolution could be determined were obtained from 40wt%Ni-30wt%Cr-Fe specimens that had been held at 1000 C for 100 h. These specimens consisted of two phases. The matrix phase (γ) contained 25-29wt%Cr and the precipitate phase (α) contained 80-90wt%Cr. The precipitates had long straight interfaces with the matrix, which were ideal for obtaining composition profiles. Figure 1 is a micrograph of the interface region.

The concentration profiles were obtained by stepping the electron probe across / interfaces oriented parallel to the electron beam, a configuration achieved by minimizing the image width of the interface. The Link Analytical system included a software package called Tracking Analyzer, which simplified data acquisition by automatic compensation for specimen drift during microanalysis.^{17,18} The program was initialized by defining the analysis positions on a digitally collected image of the region of interest. The image magnification was 2 000 000 \times in all cases. The computer then controlled the microscope and started the analysis of the defined positions. At intervals of 10 s, the x-ray acquisition was automatically suspended by the computer and an image

The author is at the Homer Research Laboratories, Bethlehem Steel Corp., Bethlehem, PA 18016.

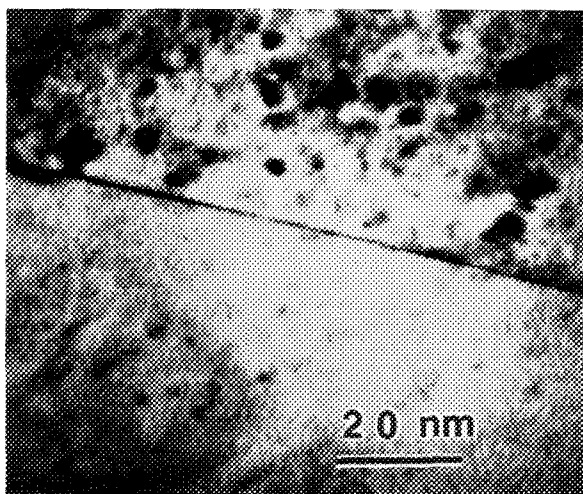


FIG. 1.--STEM bright-field micrograph of interface used for spatial-resolution determination.

was collected. This new image was compared with the previous image to determine the amount and direction of specimen drift that had occurred. The probe was then repositioned to the desired analysis point and x-ray acquisition was resumed. Approximately 1 s was required for each drift correction. This procedure was repeated for each stored analysis point. The x-ray spectra were collected for 60 s of live time. The computer control allows the analysis points to be taken quite closely together with no operator interference. In this case, some points were taken as close together as 0.9 nm.

The Fe, Ni, and Cr x-ray intensities obtained from the x-ray spectra were converted to compositions by use of experimentally determined k-factors. The specimen thicknesses were determined by convergent-beam electron diffraction (CBED) and through the electron energy loss (EELS) log ratio technique.¹⁹ The log ratio technique and the CBED technique differed by a maximum of 10%. The specimen thicknesses were determined to be 55 ± 5 nm, 95 ± 5 nm, 112 ± 5 nm, and 150 ± 5 nm.

In comparing the measured and calculated spatial resolutions, it is important to compare similar fractions of the total electron current. Usually 90% of the incident electrons is used to define the spatial resolution. This fraction may be determined from a composition profile obtained from a step change in composition by measurement of the distance represented by 96% of the total composition change. Alternatively, if Gaussian statistics in the broadened probe are assumed, the 50% resolution [otherwise known as the full-width at half-maximum (FWHM)] may be determined by the distance represented by 76% of the composition change. One can obtain the 90% resolution (equivalent to the FWTM) by multiplying the FWHM by 1.8.¹⁵ This technique was used in this study.

Beam Broadening Calculations

It is generally accepted that the spatial resolution R is made up of some combination of the incident probe size d and the broadening of the probe b as it traverses the specimen. One common definition of R involves the addition of b and d in quadrature⁹:

$$R = (b^2 + d^2)^{1/2} \quad (1)$$

If this calculation is used, it is important that both b and d include the same fraction of the incident electrons. It has been proposed that the full-width at tenth-maximum (FWTM) probe size be used since it includes 90% of the incident electrons, which is the same fraction of the incident electrons that many of the spatial resolution calculations include. The beam broadening (b) may be calculated as:

$$b = 7.21 \times 10^5 (\rho/A)^{1/2} (Z/E)t^{3/2} \quad (2)$$

where ρ , A , and Z are the average density, atomic weight and atomic number of the specimen, respectively; E is the accelerating voltage in eV; and t is the specimen thickness in cm.⁹ This equation is called the single-scattering model and calculates the diameter of a circle at the exit surface of the specimen that contains 90% of the incident electrons. Equation (2) should only be used as a rough estimate of the spatial resolution, since it only describes the beam diameter at the exit surface of the specimen. This diameter will always be the maximum diameter of the electron probe and should overestimate the spatial resolution observed in practice. Although the single-scattering model is relatively simple to apply in practice, it is of limited use as anything more than a rough estimate of the spatial resolution. Also, the single-scattering model (Eq. 2) is only applicable to homogeneous specimens, which are of little interest for x-ray microanalysis.

To overcome the disadvantages of the single-scattering model, the Gaussian beam-broadening models were introduced.^{11,20} These models assume that the current within the initial probe may be represented by a Gaussian distribution, and that this representation remains true as the electron probe traverses the specimen. (This assumption has yet to be proved experimentally.) The Gaussian current distribution within the probe may be easily convoluted with the composition profile that exist in the specimen.^{11,20} The current distribution within the electron probe at any depth in the foil may be described by:

$$I(r,t) = \frac{I_e}{\pi(2\sigma^2 + \beta t^3)} \exp\left(\frac{-r^2}{2\sigma^2 + \beta t^3}\right) \quad (3)$$

where I_e is the total incident current, σ is the standard deviation of the incident probe current distribution, and β is a parameter that describes the amount of broadening that occurs as the probe traverses the specimen. The

TABLE 1.--Comparison of experimental and calculated spatial resolutions.

Specimen Thickness (nm)	Measured Profile Width (nm)	Calculated Profile Width (nm)	$\sqrt{(b^2 + d^2)}$ (nm)	Modified Single-Scattering (nm)
150.	12.0 \pm 0.5	12.0	39.9	13.0
112.	9.0 \pm 0.5	9.0	25.9	8.4
95.	6.6 \pm 0.5	7.2	20.2	6.6
55.	5.2 \pm 0.5	4.1	9.1	2.9

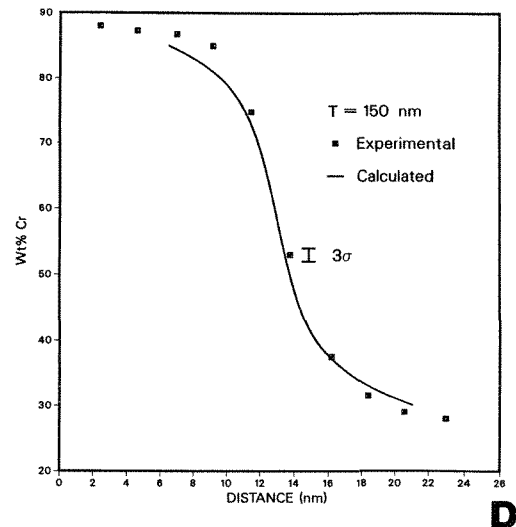
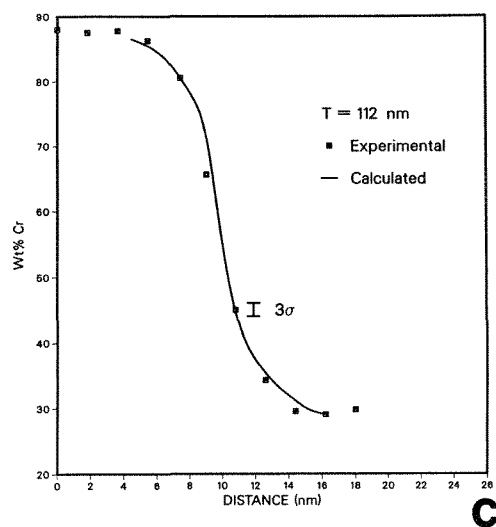
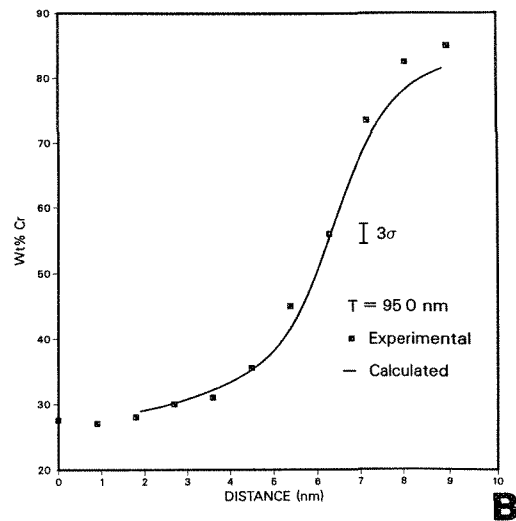
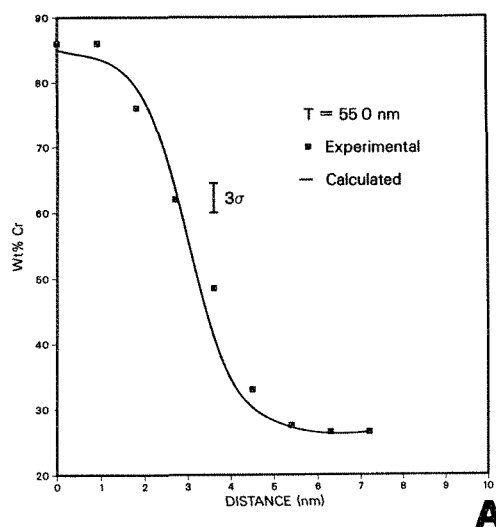


FIG. 2.--Measured and calculated Cr composition profiles obtained with 1.8nm FWTM electron probe in a range of specimen thicknesses: (a) 55 nm, (b) 95 nm, (c) 112 nm, (d) 150 nm.

broadening parameter β is given by²⁰

$$\beta = 500(4Z/E)^2(\rho/A) \quad (4)$$

The convolution of Eq. (3) with the composition profile assumed to exist in the specimen should accurately model the experimentally measured composition profile $C'(x)$ obtained in the AEM. The convolution is expressed mathematically by

$$C'(x) = \int_0^t \int_{-y}^{+y} \int_{-x}^{+x} [I(x,y,t)C(x)]dx dy dt \quad (5)$$

where $I(x,y,t)$ is the intensity distribution within the probe (Eq. 3) and $C(x)$ is the composition profile that is assumed to exist in the specimen. The accurate modeling of experimen-

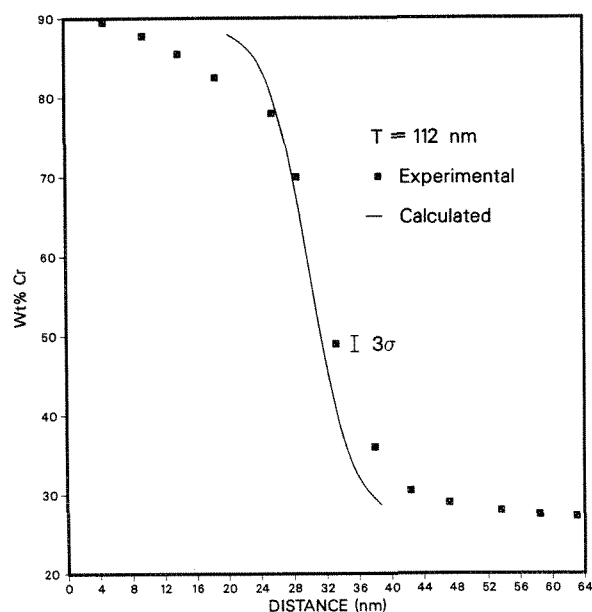


FIG. 3.--Measured and calculated Cr composition profile obtained with 7.0nm FWTM spherically aberrated electron probe.

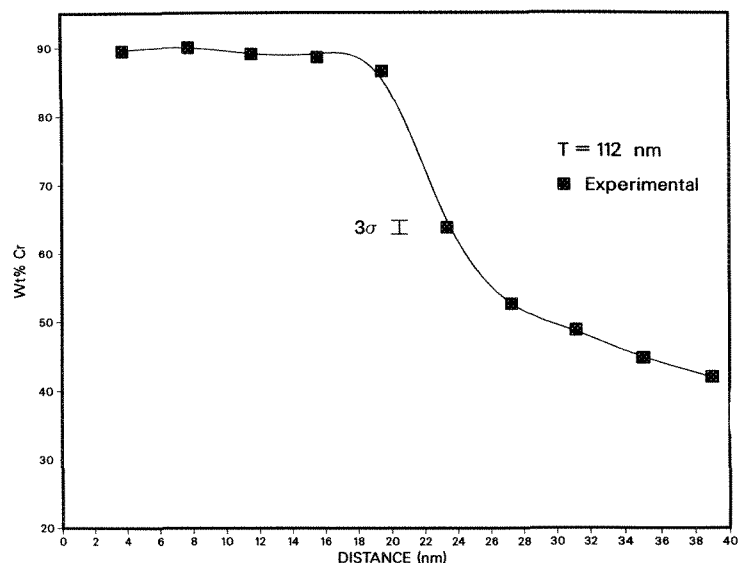


FIG. 4.--Cr composition profile obtained with asymmetric spherically aberrated electron probe.

tal data with this convolution depends on the use of a correctly limited probe to insure that the initial probe current distribution is Gaussian and the correct choice of composition profile.²¹ Since Eq. (5) is difficult or impossible to solve analytically, a computer program has been written that performs the integration and solves for $C'(x)$. This program was used to analyze the composition profiles measured in the analytical electron microscope assuming an atomically sharp step change in composition.

Results and Discussion

Effect of Specimen Thickness. The spatial resolution was determined in four areas, which varied in thickness from 55 to 150 nm. Figure 2 shows the experimental composition profiles obtained in the HB-501 AEM. The error bars represent $\pm 3\sigma$. The error bars are larger for the thinner specimens due to the lower x-ray count rates. Superimposed on each profile are the results of the Gaussian beam-broadening calculations (Eq. 5). In each case, the measured and calculated profiles are in good agreement for all specimen thicknesses studied.

Table 1 is a comparison of the experimental and calculated spatial resolutions. As expected, the width of the profiles shown in Fig. 2 increases as the specimen thickness is increased. The excellent agreement between the experimental results and the results of the Gaussian beam-broadening calculations verifies its applicability to thin foils of medium atomic weight. The spatial resolution calculated by the addition in quadrature of the beam

broadening, as calculated by the single scattering model with the beam size, is also shown in Table 1. It can be immediately seen that the spatial resolution calculated in this manner grossly overestimates the experimentally determined spatial resolution. This overestimate is a result of the single-scattering-model calculation of the diameter of the electron beam at the exit surface of the specimen. The electron probe and thus the x-ray source size will always be smaller than the exit diameter of the electron beam.

The lack of agreement between the single-scattering model and the measured spatial resolution does not mean that the single-scattering model is incorrect. As has been shown previously, the single-scattering model and the Gaussian beam-broadening parameter are nearly identical when expressed in similar form.¹⁵ Therefore, the excellent agreement between the Gaussian beam-broadening calculation and the experimentally determined spatial resolutions indicates that the single-scattering model does accurately represent the diameter of a circle that contains 90% of the incident electrons at the exit surface of the specimen.

The final column of Table 1 shows the results of the spatial resolution calculated by the single-scattering model except that the coefficient of 7.21×10^5 in Eq. (2) has been replaced by 2.35×10^5 . This change results in good agreement between the calculated and measured spatial resolutions of all data except those data obtained from the thinnest region. This agreement shows that the beam broadening does increase as $t^{3/2}$ as predicted by the single-scattering model.

Effect of Probe Characteristics. When too large a beam-defining aperture is used in a probe-forming system, the resulting electron probe consists of an intense central beam surrounded by a low-intensity halo that results from spherical aberration and deviates significantly from a Gaussian distribution.²¹ If the 50 μ m aperture used to obtain Fig. 2 is replaced by a 100 μ m aperture, a spherically aberrated probe results. This probe is also larger than those formed with the smaller aperture, 7.0 nm vs 1.8 nm. Figure 3 shows a profile obtained from the HB-501 AEM by use of a beam-defining aperture that is too large (100 μ m). Superimposed on the profile is the profile calculated from the Gaussian broadening approach with the appropriate probe size. The calculated profile is much narrower than the measured profile. This is a result of the assumption of a Gaussian current distribution in the electron probe. The effect of the spherically aberrated tails on the electron probe may be observed in Fig. 3. The slope of the composition profile seems to decrease more rapidly than it should away from the interface region.

The alignment of the beam-defining aperture controls the symmetry of the electron probe. If the aperture is misaligned, the probe will be markedly asymmetric.²¹ Figure 4 shows a profile obtained with a misaligned beam-defining aperture of the same size as that used in Fig. 3. This profile was obtained from the same specimen region as that shown in Figs. 2(c) and 3. The obvious distortion of the profile indicates the necessity of careful alignment of the beam-defining aperture. The asymmetry of the electron probe results in composition data that are difficult or impossible to interpret.

Conclusions

1. The Gaussian beam-broadening model accurately describes the spatial resolution obtained in the AEM when the initial probe is properly limited by the beam-defining aperture.

2. The single-scattering model grossly overestimates the spatial resolution observed in the AEM, most probably as a result of the single-scattering model's calculation of the beam diameter at the exit surface of the specimen. Replacement of the coefficient of 7.2×10^5 by 2.35×10^5 in the single-scattering model results in good agreement with the experimental data.

3. Beam-defining apertures that are too large result in spherically aberrated probes that cause the measured composition profiles in the AEM to be wider than expected.

4. The misalignment of the beam-defining aperture results in electron probes that are asymmetric, and this asymmetry is apparent in composition profiles obtained with these probes.

References

1. K. E. Easterling, *J. Mater. Sci.* 12: 857, 1977.
2. P. Rao and E. Lifshin, *Microbeam Analysis--1977*, 118.
3. J. I. Goldstein et al., *SEM/1977*, 315.
4. R. Hutchings et al., *Ultramicroscopy* 3: 401, 1979.
5. D. E. Newbury and R. E. Myklebust, *Microbeam Analysis--1980*, 173.
6. G. Cliff and G. W. Lorimer, in *Quantitative Microanalysis with High Spatial Resolution*, London: The Metals Society, 1981, 47.
7. P. Doig and P. E. J. Flewitt, *ibid.*, p. 41.
8. T. A. Stephenson et al., *ibid.*, p. 53.
9. S. J. B. Reed, *Ultramicroscopy* 7: 405, 1982.
10. A. D. Romig et al., *Microbeam Analysis--1982*, 72.
11. E. L. Hall et al., *Phil. Mag.* 43A: 1569, 1981.
12. C. R. M. Grovenor et al., *Phil. Mag.* 50A: 409, 1984.
13. A. J. Garratt-Reed, *SEM/1985*, 21.
14. J. M. Titchmarsh, *Microbeam Analysis--1988*, 65.
15. J. R. Michael and D. B. Williams, *J. Microsc.* 147: 289, 1987.
16. J. R. Michael, *Microbeam Analysis--1988*, 60.
17. S. H. Vale and P. J. Statham, in *Proc. 1986 ICEM*, Kyoto, 1986, 573.
18. S. H. Vale, in *EMAG 1987*, Analytical Electron Microscopy, 15.
19. T. Malis et al., *J. Electron Microscopy Techniques* 8: 193, 1988.
20. P. Doig and P. E. J. Flewitt, *Metall. Trans* 13A: 1397, 1982.
21. G. Cliff and P. B. Kenway, *Microbeam Analysis--1982*, 107.

EFFECT OF FOIL THICKNESS ON QUANTIFICATION OF EDS SPECTRA

J. I. Goldstein and D. B. Williams

X-ray energy-dispersive spectrometry (EDS) in the analytical electron microscope has proved to be a most successful technique because the use of thin foil samples results in two major improvements over the x-ray analysis of thick (bulk) samples in the electron probe microanalyzer (EPMA). First, for the thin sample, the elastic scattering is reduced and so the lateral spatial resolution in the AEM is small ($<0.1 \mu\text{m}$) and is significantly better than in the EPMA ($\sim 1 \mu\text{m}$). Second, the process of quantification of the EDS spectra is much simpler for thin foils than for bulk samples. Therefore, it is clear that the sample thickness is a critical factor in quantitative EDS in the AEM. If the foil thickness approaches the dimension of a bulk sample ($>1 \mu\text{m}$), we lose the advantages outlined above. However, if the sample is made too thin ($<20 \text{ nm}$), then surface effects such as oxidation contamination, preferential leaching, or redeposition of one elemental species could dominate the microanalysis, and the result will not be representative of the bulk.

In this paper we are concerned only with the effect of foil thickness on the quantification of x-ray spectra. Because, at one extreme, a thick foil is equivalent to a bulk sample, we show how the thin-foil quantification procedure is a natural extension and simplification of the well-established procedure for x-ray analysis in the EPMA.

As in the approach outlined by Castaing¹ (for bulk samples), when we analyze thin foils we keep the AEM instrumental settings (kV, beam current, specimen/x-ray spectrometer configuration) constant while the x-ray readings are taken. However, in AEM analyses a particular x-ray line from a specimen is not compared directly with a reference standard of known composition, as in the EPMA. The effects of atomic number Z , absorption A , and fluorescence F (that is, matrix corrections) on the x-ray spectra must also be considered. Because of the thin nature of the sample, a much simpler approach can usually be carried out in the AEM. Although corrections for the effects of Z , A , and F must still be considered, in many circumstances the required correction is much smaller than that required for a bulk sample. As instrumental developments such as high-brightness guns and computerized stage control become available, it will be possible to obtain x-ray data of better quality from the AEM. Therefore

The authors are in the Department of Materials Science and Engineering, Lehigh University, Whitaker Lab #5, Bethlehem, PA 18015. They gratefully acknowledge support of NASA under Grant NAG 9-45.

it will be increasingly important to calculate the corrections more accurately. This paper discusses the most important factor in calculating these corrections, namely the effect of foil thickness t .

The Basic Equations for X-ray Generation

In the x-ray analysis of element A in a bulk or thin specimen containing elements A, B, C, the intensity of the generated primary x-ray emission I_A^{SPEC} from the specimen is given by the expression of Scott and Love²:

$$I_A^{\text{SPEC}} = \phi_A^{\Delta\rho t} \int_0^\infty \phi_A(\rho t) \exp(-\chi\rho t) d\rho t \quad (1)$$

where ρ is the specimen density, $\phi_A^{\Delta\rho t}$ corresponds to the generated x-ray emission in counts per second from element A in an isolated thin film of the specimen of mass thickness $\Delta\rho t$, and $\phi_A(\rho t)$ corresponds to the ratio of the x-ray emission from a layer of element A, of thickness $\Delta\rho t$ at a depth t in the specimen to the x-ray emission from element A in an isolated thin film, of thickness $\Delta\rho t$. The x-ray emission $\phi_A(\rho t)$ is partially absorbed before leaving the specimen. The amount of absorption is calculated by the term

$$\exp(-\chi\rho t) \quad (2)$$

and $\chi = (\mu/\rho)_A^{\text{SPEC}} \csc \alpha$, where $(\mu/\rho)_A^{\text{SPEC}}$ is the mass absorption coefficient for element A in the specimen and α is the x-ray take-off angle, defined as the angle between the sample surface and the axis of the x-ray detector. The total generated intensity, including any fluorescence contributions δ_A , is then

$$I_A^{\text{SPEC}} = \phi_A^{\Delta\rho t} \int_0^\infty \phi_A(\rho t) \exp(-\chi\rho t) d\rho t (1 + \delta_A) \quad (3)$$

The intensity of the generated x-ray emission A from an isolated thin film $\phi_A^{\Delta\rho t}$ in a specimen of mass thickness $\Delta\rho t$ is

$$\phi_A^{\Delta\rho t} = N(\omega_A a_A Q_A / A_A) C_A \Delta\rho t \quad (4)$$

where N is Avogadro's number, A_A is the atomic weight of A, Q_A is the ionization cross section, ω_A is the fluorescence yield for the characteristic K or L lines from element A, C_A is the weight fraction of element A in the specimen, and a_A is the relative transition probability, i.e., the fraction of the total K or L line intensity from element A that is measured as $K\alpha$ or $L\alpha$ radiation.

Equation (4) is applicable to electron-transparent thin films in which electrons lose

only a small fraction of their energy in the film (~ 5 eV/nm). Q_A is considered not to vary significantly with electron-beam energy over the small change in energy that results from passing through a thin foil and must be evaluated at E_0 , the operating voltage of the AEM. Therefore one can obtain the generated x-ray emission intensity for element A in a thin foil sample by substituting Eq. (4) into Eq. (3) and limiting the integral in Eq. (3) to the foil thickness t :

$$I_A^{\text{SPEC}*} = N(\omega_A a_A Q_A / A_A) C_A \Delta \rho t \int_0^t \phi_A(\rho t) \exp(-\chi \rho t) \cdot d\rho t (1 + \delta_A) \quad (5)$$

In bulk specimens, analyzed in the EPMA, the measured intensity of a particular characteristic x-ray line from the specimen is compared with that from a reference standard of known composition, often a pure element. In thin-specimen analysis performed in the AEM, it is difficult to analyze a reference standard of known composition, for two reasons. First, the "ZAF" or the "matrix" corrections are not well developed for bulk sample standards at the high operating voltages (≥ 100 keV) used in the AEM. Second, because of the specimen holder design and the limited volume of the stage region, it is difficult to insert a standard specimen (whether thick or thin) in the AEM and recreate exactly the same analysis conditions as for the unknown sample. The AEM illumination system is not designed to reproduce accurately on the standard sample, the same beam current used for the thin unknown specimen.

The Cliff-Lorimer Ratio Technique for Thin-foil Samples

Cliff and Lorimer,^{3,4} proposed that, if the x-ray intensities (I_A, I_B) of two elements A and B in the same thin specimen can be measured simultaneously, the procedure for obtaining the concentrations of elements A and B can be greatly simplified. Simultaneous measurement of many x-ray lines is routine when using EDS, and the following simple approach has become the standard method for microanalysis of thin foils in the AEM. From Eq. (5) we can take the ratio of generated intensities I_A/I_B , in the specimen as:

$$\frac{I_A^{\text{SPEC}*}}{I_B^{\text{SPEC}*}} = \frac{C_A}{C_B} \cdot \frac{\omega_A a_A Q_A / A_A}{\omega_B a_B Q_B / A_B} \cdot \frac{\int_0^t \phi_A(\rho t) \exp(-\chi \rho t) d\rho t}{\int_0^t \phi_B(\rho t) \exp(-\chi \rho t) d\rho t} \cdot \frac{1 + \delta_A}{1 + \delta_B} \quad (6)$$

The isolated thin-film mass thickness $\Delta \rho t$ drops out in the ratio, so that measurement of $\Delta \rho t$ is not necessary. In this equation, the absorption calculation is carried out from the surface of the specimen, $t = 0$ to the full thickness t of the specimen.

In Eq. (6) we can think of the terms

$$\frac{\omega_A a_A Q_A / A_A}{\omega_B a_B Q_B / A_B} \quad \text{as the atomic-number correction } Z,$$

$$\frac{\int_0^t \phi_A(\rho t) \exp(-\chi \rho t) dt}{\int_0^t \phi_B(\rho t) \exp(-\chi \rho t) dt} \quad \text{as the absorption correction } A, \text{ and}$$

$$\frac{1 + \delta_A}{1 + \delta_B} \quad \text{as the fluorescence correction } F.$$

Both the A and F terms depend critically on the foil thickness.

The measured intensity I_A^{SPEC} from the EDS may be different from the generated intensity $I_A^{\text{SPEC}*}$ because the x rays may be absorbed as they enter the EDS detector in the Be window, Au surface layer, and Si dead layer. We take account of these effects by incorporating a term ϵ that describes the detector efficiency for x rays from elements A and B and thus we can relate the measured intensity I_A^{SPEC} to the generated intensity $I_A^{\text{SPEC}*}$. The ratio of generated intensities in Eq. (6) may be rewritten in terms of the measured intensity ratio:

$$\frac{I_A^{\text{SPEC}}}{I_B^{\text{SPEC}}} = (ZAF) \cdot \frac{\epsilon_A}{\epsilon_B} \cdot \frac{C_A}{C_B} \quad (7)$$

where ϵ (for element A) is given by the expression

$$\epsilon = \{ \exp[-(\mu/\rho)_{\text{Be}}^A \rho_{\text{Be}} t_{\text{Be}} + (\mu/\rho)_{\text{Au}}^A \rho_{\text{Au}} t_{\text{Au}} + (\mu/\rho)_{\text{Si}}^A \rho_{\text{Si}} t_{\text{Si}}] \} \cdot [1 - \exp(-(\mu/\rho)_{\text{Si}}^A \rho_{\text{Si}} t'_{\text{Si}})] \quad (8)$$

where μ/ρ is the mass absorption coefficient of x rays from element A in various detector components comprising the Be window, the Au contact layer, the Si dead layer, and the Si active layer; ρ is the density and t the thickness of the same detector components; and t' is the thickness of the Si active layer. A similar expression can be written for ϵ_B .

As in a bulk specimen the matrix correction or ZAF is a function of the specimen composition, (C_A, C_B, \dots). Since $C_A + C_B + \dots = 1.0$, the composition of each element in the specimen can be calculated by an iterative procedure. This approach contrasts with the ZAF technique for bulk specimens, which does not assume that all the concentrations sum to unity. Therefore the thin specimen analysis

technique depends on the investigator including all elements present in the specimen in the calculation. This reliance on the investigator can lead to problems if certain x rays are too weak to be detected, or too energetic to be stopped by the detector.

If the A and F corrections are negligible and approach unity, the measured intensity ratio of elements A and B in the specimen can be given as:

$$\frac{I_A}{I_B} = (Z) \cdot \frac{\epsilon_A}{\epsilon_B} \cdot \frac{C_A}{C_B} = \frac{\omega_A^a Q_A / A_A}{\omega_B^a Q_B / A_B} \cdot \frac{\epsilon_A}{\epsilon_B} \cdot \frac{C_A}{C_B} \quad (9)$$

In this equation, none of the terms ω , a , Q , A , or ϵ are a function of composition. Therefore

$$\frac{C_A}{C_B} = \frac{1}{Z} \cdot \frac{\epsilon_B}{\epsilon_A} \cdot \frac{I_A}{I_B} = \left[\frac{\omega_B^a Q_B \epsilon_B / A_B}{\omega_A^a Q_A \epsilon_A / A_A} \right] \cdot \frac{I_A}{I_B} \quad (10)$$

The term in the square brackets in Eq. (10) is a constant at a given operating voltage, and is referred to as the k_{AB} factor or Cliff-Lorimer factor. Equation (10) is usually given in a simplified form as

$$\frac{C_A}{C_B} = k_{AB} \cdot \frac{I_A}{I_B} \quad (11)$$

This relationship was applied initially by Cliff and Lorimer⁴ and has gained great popularity because of its simplicity. Obviously, if A or F corrections must be applied, then the complete matrix correction technique in Eq. (7) must be used.

Since atomic number and instrumental factors are well understood, our objective here is to discuss more fully the absorption and fluorescence corrections, since many thin-foil specimens require the full matrix correction. Both these factors depend strongly on the effect of foil thickness. With the increasing availability of 300-400kV AEMs, the ability to see through thicker foils will mean that absorption and fluorescence effects may become more prevalent, if the analyst does not work in the thinnest regions, which are best for microanalysis.

Effect of Foil Thickness-absorption Correction

The absorption correction involves evaluating the expression

$$\int_0^t \phi_A(\rho t) \exp(-\mu/\rho)^A_{\text{SPEC}} \csc \alpha(\rho t) d\rho t \quad (12)$$

for all the elements present in the sample. It is therefore critical to know $\phi_A(\rho t)$ for the thin specimen under investigation. The measurement of $\phi(\rho t)$ curves for bulk specimens is a well-established procedure in the EPMA.⁶ In contrast, only two simplified measurements of $\phi(\rho t)$ have been made for thin specimens.^{7,8} In the work of Stanton et al.,⁷ the tracer

layer $\Delta \rho t$ was placed at the bottom of matrix foils of various thicknesses to measure $\phi(\rho t)$. This was a simplified technique, since it did not account for scattering in the foil below the tracer. In essence, what was measured was $\Delta \phi(\rho t)_{\text{max}}$, not the values of $\phi(\rho t)$ vs t . In these measurements, normal incidence was used and foils were of intermediate atomic number. Tilted specimens and high-atomic-number specimens would allow for more multiple scattering, but were not considered by Stanton et al.⁷

The effects of tilted specimens and high-atomic-number specimens have been studied by Newbury et al.,⁸ both experimentally and by Monte Carlo calculations. Figure 1 shows $\phi(\rho t)$ curves for gold tilted at 45°. The beam energy was 100 keV and the foils were 50, 100, 150, 200, 250 and 300 nm thick. In the thickest specimen $\phi(\rho t)$ increases from 1.2 at the surface to a maximum of 1.5 within the specimen. For specimen thicknesses typically used in the AEM (≤ 100 nm), $\phi(\rho t)$ increases from ~ 1.05 to 1.20. The major points from this work are, first, that $\phi(\rho t)$ in thin films will vary with atomic number, film thickness, tilt, and beam energy; and second, that Monte Carlo techniques can be used to calculate quite reasonable $\phi(\rho t)$ curves for these variables.

Wirmark and Norden⁹ have measured average $\phi_{AV}(\rho t)$ values for Fe in an austenitic stainless steel. They obtained the $\phi_{AV}(\rho t)$ value by dividing the measured x-ray intensity by the sample thickness t_0 at each point of analysis. The data indicated a linear increase in $\phi_{AV}(\rho t)$ with mass thickness, as might be expected, since the amount of elastic single scattering increases with mass thickness. The $\phi_{AV}(\rho t)$ Fe data were also consistent with calculated results of a model for $\phi(\rho t)$ derived by Jones and Loretto¹⁰ based on single-scattering theory. The model of Jones and Loretto gives the depth distribution of x rays $\phi(\rho t)$ from a thin specimen normal to the electron beam as a function of atomic number Z , atomic weight A , specimen thickness t_0 , specimen depth below the surface t , and beam energy E_0 . The relation is:

$$\phi(\rho t) = 1 + [Z^2/E_0^2(A/\rho)] (at_0 + bt)$$

The relevant units are E_0 (eV), A/ρ (cm^3), and t_0 and t (nm). For Si the constants are $a = 7000$ and $b = 16\,000$. The variation, if any, of a and b with atomic number is unknown.

The variation of $\phi(0)$ and $\phi(\rho t)_{\text{max}}$ can be calculated from Eq. (13). These terms represent the values of $\phi(\rho t)$ at the surface and at the bottom of the foil, respectively. Table 1 shows the values of $\phi(0)$ and $\phi(\rho t)_{\text{max}}$ for Si, Ni, and Au at 100 keV and various values of t_{max} . The calculated values of $\phi(\rho t)$ agree quite well with the Monte Carlo calculations for Ni samples with thicknesses of 100 and 350 nm¹¹ and for Au samples 50 and 100 nm thick.⁸ Within the range of typical specimen thicknesses used for x-ray analysis in the AEM at 100 kV, $\phi(\rho t)$ varies no more than 5% relative throughout the film and $\phi(0)$ is no greater than

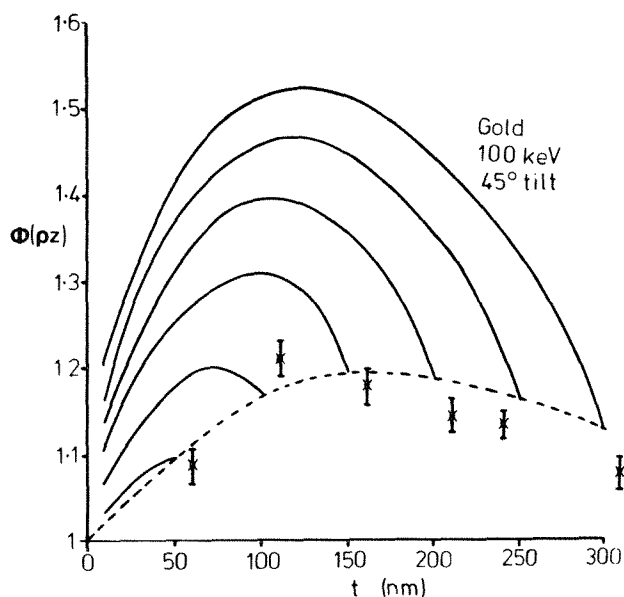


FIG. 1.-- $\phi(\rho t)$ curves for gold foils tilted at 45° . Accelerating voltage, 100 keV; foil thickness, 50, 100, 150, 200, 250, and 300 nm thick.⁸

TABLE 1.--X-ray distribution function at 100 keV vs atomic number and specimen thickness.

Element	Atomic number Z	Foil thickness t(nm)	$\phi(0)$	$\phi(\rho t_{\max})$
Si	14	67	1.0008	1.0025
		335*	1.0038	1.013
Ni	28	25	1.002	1.0068
		100*	1.0083	1.027
		350	1.029	1.096
Au	79	28.5	1.012	1.04
		50*	1.021	1.07
		100	1.04	1.14

*Typical specimen thickness at 100 kV.

1.03. At the current state of the development of x-ray analysis in the AEM one can then assume that x-ray production is essentially uniform throughout the film, and that

$$\phi_A(\rho t) \approx \phi_B(\rho t) \approx 1.0 \quad (14)$$

This assumption was made in the initial approach to the absorption correction by Goldstein et al.,¹² in which the integrals in Eq. (6) were evaluated to give the absorption correction factor A:

$$A = \frac{\mu/\rho_{\text{SPEC}}^A}{\mu/\rho_{\text{SPEC}}^B} \cdot \frac{1 - \exp[-(\mu/\rho)_{\text{SPEC}}^B (\csc \alpha)(\rho t)]}{1 - \exp[-(\mu/\rho)_{\text{SPEC}}^A (\csc \alpha)(\rho t)]} \quad (15)$$

To calculate the absorption correction factor, the values of the mass absorption coefficient μ/ρ the specimen density ρ , and the absorption path length $t(\csc \alpha)$ must be accurately known. Figure 2 shows the geometry of the specimen,

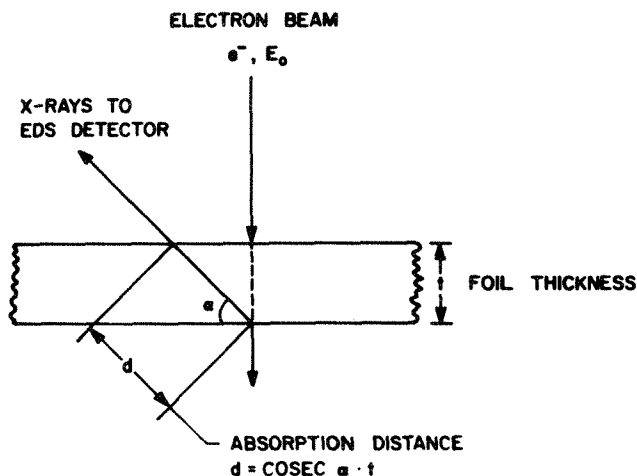


FIG. 2.--Idealized thin-foil geometry in the AEM showing definition of take-off angle α and absorption path length $\csc \alpha \cdot t$.⁵

electron-beam, and EDS detector configuration that must be considered in order to determine the absorption path length.

The absorption correction is usually not applied if A is between 0.97 and 1.03 (a correction $\leq \pm 3\%$ rel.) since some combination of the Z factor, ϵ_A/ϵ_B , and the counting statistics usually result in errors of $\sim \pm 3\%$ rel. However, the specimen thickness at which the A correction must be applied (according to the above 3% criterion) is often much smaller than the specimen thickness obtained as a result of the preparation process. A few examples of calculated thickness for which the A corrections must be made ($A < 0.97$ or > 1.03) are 9nm for Al K α in NiAl, 22nm for P K α in Fe₃P, and 25nm for Mg K α , O K α in MgO. These thicknesses are not often achieved during the specimen preparation process. Also, as already noted, such thin samples may exhibit substantial surface chemical modification and may not be representative of the bulk. As the trend to higher voltage AEMs continues, it will be possible to "see" through thicker samples and perform analyses from thicker areas. Under these circumstances, the "typical" thicknesses in Table 1 will increase by factors of 2-3 and the need for absorption corrections will increase. However, it is also possible that the increased source brightness at 300-400kV and the availability of higher-brightness sources will permit reasonable x-ray emission intensity to be obtained from *thinner* samples than can be analyzed presently at 100 kV. In that case there will be less need for absorption corrections.

The various factors that limit the accuracy of the Absorption correction, mass absorption coefficient, specimen density, absorption path length, and specimen geometry have been discussed by various authors^{5,13} and are not given in this paper. By far the most difficult parameter to measure is the specimen thickness t , which can vary substantially in a wedge-shaped thin foil. Among the methods used to obtain t are contamination-spot separation,¹⁴ the spacing of Kossell-Mollenstedt fringes in convergent-beam electron diffraction

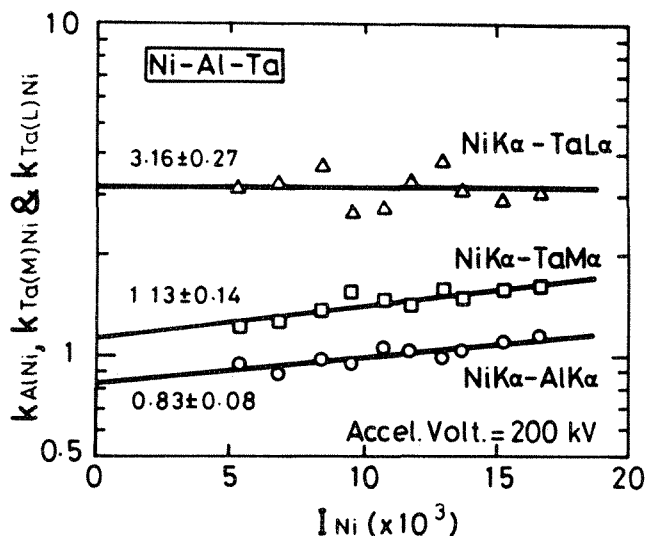


FIG. 3.--Data from Horita et al.,¹⁹ showing intensity ratios from three different Ni-base alloys vs sample thickness. Thickness was measured in terms of Ni K α intensity. By extrapolating to zero Ni intensity, true k_{AB} factor can be obtained. True k_{AB} factor is noted above each set of data. (Courtesy North-Holland Physics Publishing.)

(CBED) patterns,¹⁵ the K to L intensity ratio as a function of t for a given element,¹⁶ the EDS spectrum variation caused by using different tilt angles at the same analysis point,¹⁶ the EELS log-ratio technique,¹⁷ and the standard technique.¹⁸

The popular contamination-spot-separation method unfortunately tends to overestimate the thickness⁷ and may not be available as sample preparation techniques are better controlled and vacuums are improved in the specimen area. The CBED technique is accurate but the required diffraction conditions may not be obtainable at precisely the region of interest. The method involving the K/L ratio is only suitable if both peaks are visible in the x-ray spectrum. Each of the other methods has its own limiting factors.

The standards technique however has clear promise. A thin foil or region of thin foil of known thickness (usually determined by CBED techniques) and of known composition is used to calibrate x-ray intensity in terms of thickness. In this case one usually measures the intensity of the EDS x-ray spectrum is a direct function of thickness until absorption effects become significant. One can therefore use a linear calibration of EDS x-ray intensity vs thickness as calibrated by the standard specimen. A standard that is most useful is a specimen of composition similar to that of the specimen of interest. This technique should be quite useful, as it does not rely on the direct measurement of thickness at each analysis point. However, the technique requires that as measurements of sample and standard are made, the beam current remains constant, which is difficult to achieve in an AEM. As x-ray analysis in the AEM evolves, we expect (1) that feed-

back mechanisms and (2) that on-line probe-current measurements will be available from a Faraday cup in the column below the final probe-limiting aperture.

As CBED techniques become more popular, and computer control of the stage combined with digital imaging becomes available, the possibility of on-line CBED analysis will become a reality. Under those circumstances, this approach will become the accepted on-line method to determine the thickness of crystalline samples.

Figure 3 shows the results of a technique related to the standards method of thickness determination by which the absorption correction can be eliminated.¹⁸⁻²⁰ In this simplification of the x-ray absorption correction, the ratios of I_A/I_B , I_B/I_C , etc. in a homogeneous phase are plotted vs x-ray intensity from one of the elements (e.g., I_A or I_B or ...) that is not absorbed significantly as the specimen increases in thickness. Extrapolation of the nonabsorbed x-ray intensity to zero provides a ratio (I_A/I_B , I_B/I_C , etc.) for which the absorption factor A is 1.0 and therefore I_A/I_B , I_B/I_C equals $k_{AB}C_A/C_B$, $k_{BC}C_B/C_C$, etc. This technique holds great promise. However, it cannot be used in some of the more important analyses, where C_A , C_B . . . and the thickness vary throughout a phase or region of the sample.

The assumption that the specimen is a parallel-sided thin film (Fig. 2) is rarely if ever realized in practical x-ray microanalysis because of the ways in which materials specimens are thinned. Electropolishing and ion-beam thinning both give rise to wedge-shaped specimens, which complicates the analysis considerably. In addition, for multiphase specimens, one must orient the interphase interface parallel to the electron beam and parallel to the EDS detector axis is absorption effects are to be minimized. Specimen geometry effects as outlined above have been described in detail by other authors^{21,22} and are not discussed here.

Effect of Foil Thickness-Fluorescence Correction

X rays produced by electron ionization within the specimen may themselves be sufficiently energetic to excite and ionize other atoms. This effect, known as x-ray fluorescence, is intimately associated with the absorption process, because the primary cause of x-ray absorption is the fluorescence of another x ray.

Equations for the fluorescence factor δ_A have been developed by Philibert and Tixier²³ and Nockolds et al.²⁴ The Nockolds et al. equation for δ_A considers the effect of x-ray generation throughout the foil and is considered more accurate than the equation for δ_A of Philibert and Tixier, who assumed that all x rays originated from the middle of the foil on the beam axis. The equation for δ_A by Nockolds et al.,²⁴ shows that:

$$\delta_A \approx \frac{\rho t}{2} [0.932 - \ln \mu(\rho)]_{\text{SPEC}}^B \rho t \quad (16)$$

As in the absorption correction, the calculation of δ_A depends on the accurate measurement of the foil thickness t . Fortunately the few measurements of δ_A , δ_B in the literature indicate that the F correction is small and not often needed.

Summary

The full quantitative analysis procedure for thin foils is given by Eq. (7), in which the ZAF correction and ϵ_A/ϵ_B must be calculated or measured. We can usually ignore the F correction; the critical factor in applying the A correction is the need either to measure the foil thickness t , or eliminate the A correction by extrapolation methods of the type suggested by Horita et al.,¹⁸⁻²⁰ The standards technique in which the EDS x-ray spectrum intensity is calibrated against standard-thickness specimens holds great promise. This technique may only measure t to an accuracy of $\pm 5\%$ relative, and other prospective methods for t determination are no better. However, the practical effect in terms of errors in the calculated absorption correction A is less than $\pm 1\%$ relative unless the sample is unusually thick or the mass absorption coefficient exceeds $1000 \text{ cm}^2/\text{g}$. Measurement errors in I_A , I_B at the 95% confidence level usually exceed $\pm 2\%$. Therefore one can tolerate the inaccuracy in measured specimen thickness at each point in the analysis and still perform a perfectly acceptable, fully quantitative analysis. The major caveat in suggesting that one can apply the standards technique for specimen thickness, on line, is that the electron-beam current must be measured and held constant as specimen and standard thickness specimens are analyzed. Modern AEM instruments must be designed with this feature in mind.

References

1. R. Castaing, Ph.D. thesis, University of Paris, 1951.
2. V. D. Scott and G. Love, *Quantitative Electron Probe Microanalysis*, Chichester, England: Harwood, 1983, 58.
3. G. Cliff and G. W. Lorimer, *Proc. 5th European Cong. Electron Microscopy*, 1972, 141.
4. G. Cliff and G. W. Lorimer, *J. Microsc.* 103: 203, 1975.
5. J. I. Goldstein, D. B. Williams, G. Cliff, in D. C. Joy, A. D. Romig Jr., and J. I. Goldstein, Eds., *Principles of Analytical Electron Microscopy*, New York: Plenum Press, 1986, 155.
6. J. I. Goldstein, D. E. Newbury, P. Echlin, D. C. Joy, C. E. Fiori, and E. Lifshin, *Scanning Electron Microscopy and X-ray Microanalysis*, New York: Plenum Press, 1981.
7. N. Stenten, Notis, M. R., J. I. Goldstein, and D. B. Williams, in G. W. Lorimer, M. H. Jacobs, and P. Doig, Eds., *Quantitative Microanalysis with High Spatial Resolution*, London: The Metals Society, Book 277, 1981, 35.
8. D. E. Newbury, R. L. Myklebust, A. D. Romig, and K. W. Bieg, *Microbeam Analysis--1983*, 168.
9. G. Wirmark and H. Norden, *J. Microsc.* 128: 167, 1987.
10. I. P. Jones and M. H. Loretto, *J. Microsc.* 124: 3, 1981.
11. D. E. Newbury, private communication in Ref. 5, 1986.
12. J. I. Goldstein, J. L. Costley, G. W. Lorimer, and S. J. B. Read, *SEM/1977 I*, 315.
13. D. B. Williams, *Practical Analytical Microscopy in Materials Science*, Mahwah, N.J.: Electron Optics Publishing Group, 1984.
14. G. W. Lorimer, G. Cliff, and J. N. Clark, in J. A. Venables, Ed., *Developments in Electron Microscopy and Analysis*, London: Academic Press, 1976, 153.
15. P. M. Kelly, A. Jostsons, R. G. Blake, and J. G. Napier, *Phys. Stat. Sol.* 31: 771, 1975.
16. P. L. Morris, M. D. Ball, and P. J. Statham, in T. Mulvey, Ed., *Electron Microscopy and Analysis*, Bristol and London: Institute of Physics, 1979, 413.
17. T. Malis, S. C. Cheng, and R. F. Egerton, *J. Electron Microscopy Technique* 8: 193, 1988.
18. Z. Horita, T. Sano, and M. Nemoto, *J. Microsc.* 143: 215, 1986.
19. Z. Horita, T. Sano, and M. Nemoto, *J. Electron Microsc.* 35: 324, 1986.
20. Z. Horita, T. Sano, and M. Nemoto, *Ultramicroscopy* 21: 271, 1987.
21. D. M. Maher, M. B. Ellington, D. C. Joy, P. H. Schmidt, N. J. Zaluzec, and D. E. Mochel, *Analytical Electron Microscopy--1981*, 29.
22. N. J. Zaluzec, D. M. Maher, and P. E. Mochel, *ibid.*, p. 47.
23. J. Philibert and R. Tixler, in B. M. Siegel and D. R. Beaman, Eds., *Physical Aspects of Electron Microscopy and Microbeam Analysis*, New York: Wiley, 1975, 333.
24. C. Nockolds, M. J. Nasir, G. Cliff, and G. W. Lorimer, in T. Mulvey, Ed., *Electron Microscopy and Analysis*, Bristol and London: Institute of Physics, 1980, 417.

THE HOLE-COUNT TEST REVISITED: EFFECTS OF TEST SPECIMEN THICKNESS

C. E. Lyman, D. W. Ackland, D. B. Williams, and J. I. Goldstein

For historical reasons the hole count, an important performance test for the analytical electron microscope (AEM), is somewhat arbitrary yielding different numbers for different investigators. This was not a problem a decade ago when AEM specimens were often bathed with large fluxes of stray electrons and hard x rays.¹ At that time the presence or absence of a thick Pt second condenser (C2) aperture could be detected by a simple comparison of the x-ray spectrum taken "somewhere in the hole" with a spectrum collected on a "typical thickness" of Mo or Ag foil.²⁻⁴ A high hole count of about 10-20% indicated that the electron column needed modifications; whereas a hole count of 1-2% was accepted for most AEM work. Because quantitative x-ray measurements in the AEM are more precise than 10 years ago, "good" values for the hole count on Ag foils are now well below 1%. The absolute level of the hole count is a function of test specimen atomic number, overall specimen shape, and thin-foil thickness. In order that equivalent results may be obtained for any AEM in any laboratory in the world, this test must become standardized.

The hole-count test we seek must be as simple and as nonsubjective as the graphite 0.344nm lattice-line-resolution test.⁵ This lattice-resolution test spurred manufacturers to improve the image resolution of the TEM significantly in the 1970s and led to the even more stringent resolution tests of today. A similar phenomenon for AEM instruments would be welcome.

The hole-count test can also indicate whether the spurious x-ray signal is generated by high-energy continuum x rays (bremsstrahlung) generated in the electron column (high K-line to L-line ratio) or uncollimated electrons passing through or around the C2 aperture (low K/L ratio).¹⁻⁶ This diagnostic aspect of the hole-count test is useful for the detection and elimination of the sources of hard x rays in in-

termediate-voltage (300-400kV) analytical electron microscopes.

This paper discusses the essential parameters for a standardized test of spurious x rays and proposed a candidate test specimen. This new test specimen reduces the experimental variation in the hole-count test caused by specimen thickness effects.

Standardizing the Hole-count Test

The spurious x rays detected in the hole-count test are caused by hard x rays and/or uncollimated electrons generating x-ray photons from regions of the specimen not directly under the electron beam. The most likely material generating these spurious x rays is the thick rim of the conventional electropolished or ion-milled specimen. To make a precise test for this high-energy bremsstrahlung (if present), the test specimen must generate large numbers of spurious characteristic photons from the thick specimen rim when the beam is placed in the hole. This spurious characteristic x-ray intensity depends on (a) electron optical parameters such as probe current, (b) atomic number of the test specimen, (c) specimen rim thickness, and (d) the shape profile of the thinned area including the size of the hole. Since it is difficult to measure the absolute intensity of x rays detected when the beam is placed in the hole, the hole count is usually expressed as a percentage of the x rays gener-

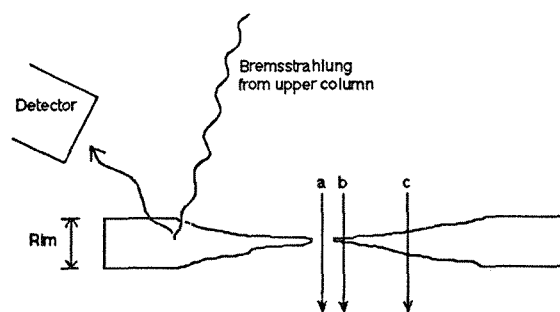


FIG. 1.--Schematic cross-sectional diagram of typical disk-shaped Mo hole-count specimen. Specimen rim provides greatest volume of material for production of spurious x rays by bremsstrahlung from upper column. Mo K-line x-ray intensity collected when beam is in the hole (electron a) is normally ratioed to that from some "typical thickness" of foil. Tests on Mo specimen of this type showed that hole count can be several times larger if x rays generated by electron b are used in this ratio rather than those generated by electron c. (Not drawn to scale.)

The authors are with the Department of Materials Science and Engineering, Lehigh University, Bethlehem, PA 18015. The authors thank the staff of the Electron Optics Group of Philips Electronic Instruments, especially T. Boden, J. Fahy, M. Otten, M. N. Thompson, and J. van der Jeijden, for discussions concerning the universal hole-count test and assistance with some of the data shown. The authors are also grateful to J. R. Michael of Bethlehem Steel Corp. for helpful discussions and for use of the Vacuum Generators HB501. The Cr film on Ag specimen was fabricated and tested by M. Zemyan. The support of DOE through grant DE-FG02-86ER45269 and of NASA through grant NAG 9-45 is gratefully acknowledged.

ated when the beam is placed on the foil itself itself at a "typical specimen thickness." It is this specimen thickness that makes the test arbitrary since this "typical" thickness may vary with each specimen and with each investigator. Thus, the most important variables that must be specified are the thickness of the specimen rim and the specimen thickness used for the "on foil" measurement, as shown in Fig. 1.

Electron Optical Parameters

The reappearance of the hole count as an issue in AEM performance is a consequence of the higher electron accelerating voltages of modern AEMs. Since 300-400kV electrons can generate considerably more high-energy bremsstrahlung (typically 20-200 keV) at the C2 aperture than 100kV electrons, the electron column modifications necessary to produce an adequately low hole count may prove to be more difficult than those employed at 100 kV. At 300-400 kV, hole counts that might appear adequate for AEM analysis of Fe-based samples may indicate serious problems for the analysis of Pt/Al₂O₃ catalyst specimens because high-energy bremsstrahlung excites Pt much more efficiently than Fe.

A major electron-optical parameter to be controlled at any accelerating voltage is the beam current. The hole-count test should be conducted with the same emission current and the same electron probe current each time. One may achieve this by measuring the current before each test with a Faraday cup and a picoammeter. Since many microscopes are not yet equipped with these devices, a secondary measurement such as screen current may be used if properly calibrated by the microscope manufacturer. Although the absolute level of probe current is not very important, this variable must be held constant for comparable tests.

Another important electron-beam parameter is the setting of the first condenser lens. Since the probe will be placed well into the hole, the actual spot size is not important. However, the first condenser lens also governs the extent to which the beam impinges on the second condenser aperture and the liner tube in the upper column. Thus, the real reason that the probe current must be brought to a standard level is to put this lens in a standard condition for the hole-count test.

The hole-count test also assumes that the electron beam is optimally apertured to minimize spherical aberration blurring which causes a broad electron halo around the focused electron probe. This "witches hat" electron distribution results from the use of a C2 aperture that is too large to define the electron probe properly for the chosen setting of the C1 lens.⁷ One effect of this electron tail is the generation of x rays at a distance of several beam diameters away from the nominal position of the beam. Unfortunately, most AEMs have only 3 or 4 positions for C2 apertures, allowing minimal tails at only 3 or 4 C1 settings. In addition, it may not be obvious which C2 aperture to use for the hole-count test since the aperture size

strongly affects the probe current. Thus, since the test should be arranged to generate large numbers of spurious x rays, it is more important to obtain a certain minimum probe current, say at least 0.1 nA, and accept whatever probe size corresponds to this current.

A more stringent test of AEM performance is obtained when the hole-count test is performed near the edge of the hole, say 10 nm into the hole and 10 nm onto the foil. In this case the probe tails, if present, may be sensed.⁸ Correct aperturing at the C2 lens is imperative for adequate performance in this test.

Test Specimen Material

The intensity of a characteristic x-ray line excited by electrons is given by $I_K = i(V - V_K)^{1.67}$, where i is the electron beam current, V is the electron accelerating voltage, and V_K is the excitation potential for the element of the test specimen. However, in most situations encountered with 300-400kV microscopes, the spurious x rays are generated by high-energy bremsstrahlung. For these cases, the intensity of the spurious characteristic x rays follows the mass absorption material. The expression to predict the variation of (μ/ρ) between absorption edges is $(\mu/\rho) \approx Z^4 \lambda^3$, where Z is the atomic number of the absorber (in this case, the test specimen) and λ is the wavelength of the radiation exciting the absorber. For example, under the same test conditions in a Philips EM400T at 120 kV, Ni ($Z = 28$), Mo (42), and Ag (47), thin-foil specimens exhibited K-line hole counts of 3%, 6%, and 9%, respectively. Thus, the test specimen should be made of high- Z material for the generation of a high intensity of spurious characteristic photons at any fluorescing bremsstrahlung wavelength if the bremsstrahlung intensity is significant. This insures that if spurious x rays are generated, the test specimen will allow their detection.

If both a K and an L line from the specimen are to be detected with a Si(Li) EDS detector, the energies of both lines should be within the high-efficiency range for this type of detector: about 2-20 keV. Molybdenum with an L-series at 2.3 keV and a K α line at 17.4 keV is an obvious choice. Mo has the additional advantage that most EDS systems are usually set to the energy range 0-20 keV for normal analysis. One important use of intrinsic Ge detectors in the AEM⁹ may be to determine whether the specimen stage is free of 20-200 keV bremsstrahlung that will fluoresce heavy elements in an analysis sample. These high-energy x rays would not be detected with a Si(Li) detector. Considering the desirability of a single test specimen for both Si(Li) and Ge detectors, the original proposal of silver as a hole-count test specimen still appears attractive,¹ even though the x-ray spectrometer must be operated over the energy range 0-40 keV, which is not normally used for analysis with Si(Li) detectors (Ag L α at 3.0 keV and Ag K α at 22 keV). Intrinsic Ge detectors, with their wider range of efficiency (roughly 2-100

keV), make even higher-atomic-elements suitable as test specimens, such as gold ($M\alpha$ at 2.1 keV; $L\alpha$ at 9.7 keV; and $K\alpha_1$ at 68.7 keV).

Test Specimen Shape

The shape of the test specimen has a significant effect on the efficiency of spurious x-ray generation and is probably responsible for much of the lab-to-lab variation in hole counts. Ideally, the test specimen should have as thick a rim as possible. A thick rim maximized the amount of spurious x rays generated by the high-energy continuum. For Mo specimens with rim thicknesses of 80 and 120 μm , comparable hole counts were found to be 2.6% and 5.9%, respectively (Philips EM400T at 120 kV). Thus, the 100 μm -thick rim typical of an electropolished foil specimen would be more useful than the somewhat thinner rims usually employed for ion-beam-milled specimens in order to reduce milling time.

A specimen of well-controlled shape can be fashioned with standard techniques by cutting disks from 100 μm -thick Mo sheet, dimple grinding (15mm wheel) each side to a few micrometers total thickness, and finally ion-beam milling. But the time and effort to make such specimens and their fragility militate against their widespread acceptance as a standard test specimen.

Even with such a carefully fabricated specimen, the "typical" thin-foil area used to obtain the denominator in the hole-count ratio usually exhibits a range of thicknesses from 50 to 500 nm, depending on the material. With the old hole-count tests, counts on the specimen were collected until 10 000 counts were obtained in the "typical" foil thickness. If the on-foil x-ray count is taken in a thick region of foil, the hole-count ratio will be lower than if it is taken on a thin region. Some method (such as direct thickness measurement or detection of the onset of Kikuchi lines) must be used to indicate a repeatable foil thickness for this test. The alternative to this cumbersome procedure is to use a specimen with a thin foil of constant thickness, as discussed below.

Specimen Environment

Components of the microscope surrounding the specimen also can generate spurious x rays. Many AEMs based on the TEM column have cold fingers and objective aperture mechanisms located within a few millimeters of the specimen which may contribute to the overall extraneous background. Different lens designs also result in different amounts of metal around the specimen. For example, hole counts measured on the same specimen in a symmetrical condenser-objective lens (Philips EM400T) and in an unsymmetrical top entry lens on an inverted column (Vacuum Generators HB-501) were 5.9% and 0.25%, respectively. The low hole count in the VG HB-501 may result partly from the use of a wide second bore for the objective lens (less metal near the specimen).

X-ray Counting Problems

The detection of low x-ray fluxes when the beam is placed in the hole can be difficult with some x-ray spectrometers. For example, if very few x rays are detected when the beam is in the hole, the spectrometer should faithfully record the exact number of photons entering the detector. In some situations, the setting of the fast discriminator or other deadtime circuit parameters can affect the number of x rays apparently detected when the count rate is very low. A standard specimen with the potential for generating large intensities of spurious x rays would relieve this problem.

K- to L-line Ratios from In-hole Spectra

If the K- to L-line intensity ratio from the hole is larger than that obtained when the beam is placed on the specimen, the spurious x rays may be assumed to be generated by high-energy bremsstrahlung. Obviously, it is this component of spurious radiation that is of most concern for 300-400kV instruments. Figure 2 shows an example of this type of analysis for 120 and 300 kV. The 120kV data of AEM #1 show that the K/L ratio in the hole and on the specimen are essentially identical, as might be expected for an electron-generated hole count. The 300kV data show a K/L ratio about 20 times higher for AEM #2 and 4 times higher data for AEM #3. These data indicate that the design of the electron column should be improved at 300 kV to reduce this excessive level of high-energy bremsstrahlung impinging on the specimen.

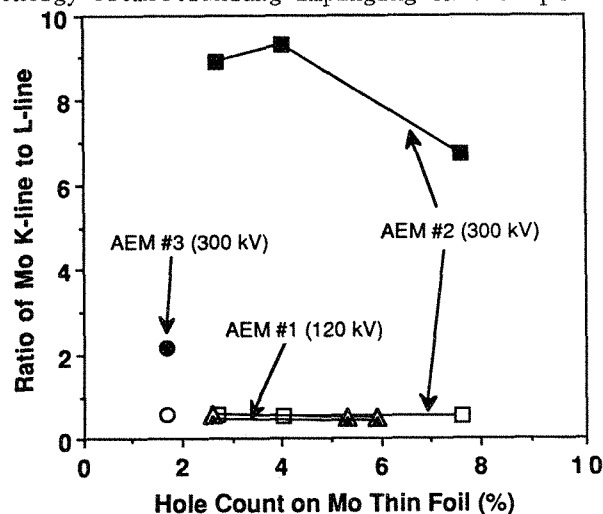


FIG. 2.--Molybdenum K-line to L-line integrated intensity ratios from "in-hole" spectra (solid symbols) and "on-specimen" spectra (open symbols) vs hole count for three AEMs. Higher hole counts for AEM #1 (triangles) and AEM #2 (squares) represent measurements made on thinner regions of foil.

Proposed Test Specimen for Spurious X Rays

Since the main goal of this test specimen is to generate large numbers of spurious photons (when a bremsstrahlung source is present),

there is no reason to employ a specimen of conventional shape. A new hole-count test specimen might consist of an Ag support grid covered with a uniform thickness of Cr sputtered onto a thin film of carbon (Fig. 3). Holes in the Cr film or open-grid squares not covered by Cr may be used to collect the "in-hole" count, and the constant-thickness Cr layer allows a consistent "on-specimen" x-ray intensity measurement.

Preliminary data from a Cr film of unknown thickness on a 400-mesh Ag grid are encouraging. With this specimen in a low-background holder of the Philips EM 430T (200 kV, STEM mode, spot size 3, 0.5 nA probe current, 100s clocktime, 10 000 counts in Cr K α) the ratio (converted to %) of the Ag K α line (FWHM) collected in the hole to the Cr K α line (FWHM) collected on the Cr film ranged from 1.9% to 2.4% and averaged 2.1%. These seven trials included data from three different Cr-covered grid squares and three different open-grid squares. This 24% variation in hole count should be compared with the 100-300% variation in hole count measured when the test was performed with different foil thicknesses in a Mo disk-shaped specimen. The conditions quoted above must not be considered a standard procedure for the new hole-count test. The hole count values measured above with the new test specimen cannot be related to traditional hole count values at the present time. Standard test conditions and acceptable hole count values with this test will emerge in the near future.

The major advantage of this type of specimen is the consistency with which the test can be performed. Since all the thin Cr areas have the same thickness, there should be no significant variability in the test between different operators. This type of specimen should be easy to fabricate in large numbers at reasonable cost.

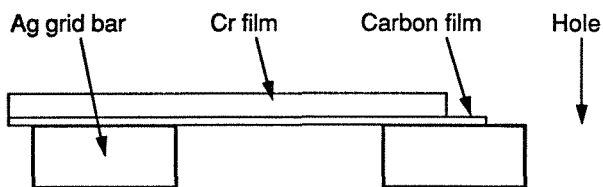


FIG. 3.--Schematic diagram of proposed hole-count test specimen consisting of silver grid supporting thin film of chromium on carbon.

This test specimen has additional advantages in that, once the hole count is determined to be acceptably low, other standardized tests may also be performed on the same specimen. These include tests of Cr peak-to-background,¹⁰ estimated minimum detectability of Cr,¹¹ and comparative x-ray detector collection efficiency.¹²

Spurious X Rays in Relation to Experimental Analysis Data

The above Ag/Cr spurious x-ray test, like the older hole-count test, gives an important figure of merit for an AEM. Of course, the values to be quoted as acceptable for this "Ag/Cr spurious x-ray test" will be different from

those quoted in the old hole-count test. The desired value will again be 0%. Acceptable values for quantitative analysis will depend on the type of sample analyzed. The criterion to be used is whether the characteristic peak of interest, detected when the beam is placed in the hole, is well below the electron-generated background from the analysis area under the beam. This "hole count from the analysis specimen" is a small spectrum related to the average composition of the entire specimen which is added to each individual spectrum taken in regions localized by the focused electron beam. Subtraction of this unwanted signal from the analysis peak is often suggested. However, progress toward use of the AEM as an "electron nanoprobe" for thin specimens, with precision and accuracy approaching that of the "electron microprobe," demands that all extraneous sources of x rays be eliminated at their sources.

Conclusion

A hole-count test specimen consisting of a thin film of chromium over a silver support grid has been shown to have significantly better repeatability than previous specimens used for this test. Whereas the old test was prone to variations both in rim thickness and in the foil thickness selected for the "on-specimen" spectrum, the thicknesses of the Ag grid and the Cr film in this new specimen are nearly constant--eliminating these sources of error. When a standardized test specimen of this type is available in reasonable quantity, further progress can be made toward the reduction of spurious x-ray background in the AEM.

References

1. J. I. Goldstein and D. B. Williams, *SEM/1978 I*, 427.
2. J. Bentley, N. J. Zaluzec, E. A. Kenik, and R. W. Carpenter, *SEM/1979 II*, 581.
3. D. B. Williams and J. I. Goldstein, in *Energy Dispersive X-ray Spectrometry*, NBS Special Publ. 604, U.S. Department of Commerce/NBS, 1981, 341.
4. L. F. Allard and D. F. Blake, *Microbeam Analysis--1982*, 8.
5. R. D. Heidenreich, W. H. Hess, and L. L. Ban, *J. Appl. Cryst.* 1: 1, 1968.
6. D. B. Williams, *Practical Analytical Electron Microscopy in Materials Science*, Mahwah, N.J.: Philips Electron Optics Publishing, 1984, 58.
7. G. Cliff and P. B. Kenway, *Microbeam Analysis--1982*, 107.
8. N. J. Long, described at the 1981 VG Microscopes users' group meeting.
9. E. B. Steel, *Microbeam Analysis--1986*, 439.
10. D. B. Williams and E. B. Steel, *Analytical Electron Microscopy--1987*, 228.
11. C. E. Lyman and J. R. Michael, *Analytical Electron Microscopy--1987*, 231.
12. A. W. Nicholls, *Proc. 46th Ann. Meet. EMSA*, 1988, 672.

QUANTITATIVE THIN FILM X-RAY MICROANALYSIS OF Nb MODIFIED Ti₃Al

A. D. Romig Jr., T. J. Headley, M. J. Carr, and M. J. Cieslak

Advanced titanium-aluminum intermetallic alloys (often simply called titanium aluminides) have certain properties that make them potentially attractive as advanced aerospace alloys.¹ In order to utilize these alloys in engineering applications, it is necessary to process the alloys in a variety of ways including casting, hot forming, and welding. All these processes modify the microstructure of the alloy, which in turn directly influences the properties. The key to optimizing the alloy's properties is to control the microstructure by careful control of the processing parameters. Control of the microstructure requires a thorough understanding of the evolution of the microstructure, including elemental partitioning between the various phases that form in the alloy. Analytical electron microscopy (AEM) is an ideal way to characterize the microstructures on a fine spatial scale. Such high-spatial-resolution microanalysis is required to understand the microstructural evolution in these alloys. In this case, the alloy is an Nb-modified Ti₃Al, and the partitioning behavior of interest is between a variety of ternary phases produced as a function of alloy cooling rate from a single homogeneous high-temperature β phase. The Nb is added to the alloy to enhance its performance, primarily through an improvement in ductility. In this work, the details of the procedure for quantitative analysis of these alloys are presented. The complete details of the phase transformations which occur in this alloy are discussed by Cieslak et al.²

Background

To characterize elemental partitioning between phases quantitatively, the details of the microanalytical technique used to characterize the partitioning must be well understood. In the case of thin-film x-ray microanalysis, what is required is careful attention to the determination of the sensitivity factors used to calculate composition from x-ray intensities; careful examination of the potential for x-ray absorption, which might influence the calculated results; and careful consideration of the impact of x-ray spatial resolution for the analysis. In this paper, all these details are addressed in some depth. The results presented here are then used in the work of Cieslak et al.,² in which the metallurgical details of the study are presented.

Elemental compositions can be determined from

The authors are with Sandia National Laboratories, Albuquerque, NM 87185. The work was supported by the U.S. Department of Energy under contract DE-AC04-76DP00789.

x-ray intensities via the Cliff-Lorimer standardless-ratio technique,³ which is given here by

$$\begin{aligned} C_{\text{Nb}}/C_{\text{Ti}} &= k_{\text{NbTi}} (I_{\text{Nb}}/I_{\text{Ti}}) \\ C_{\text{Al}}/C_{\text{Ti}} &= k_{\text{AlTi}} (I_{\text{Al}}/I_{\text{Ti}}) \\ C_{\text{Ti}} &= C_{\text{Al}} + C_{\text{Nb}} = 1 \end{aligned} \quad (1)$$

where C is composition (wt.%), I is background-corrected x-ray intensity, and k is the sensitivity factor. The values of k can be determined experimentally from standards or calculated from first principles. The value of the sensitivity factors is examined experimentally and by calculation in this paper.

The standardless ratio equations are valid only in the absence of x-ray absorption or fluorescence. To determine if absorption effects are significant, Goldstein et al.⁴ has established the criterion

$$\{0.5 \mu/\rho)^i - \mu/\rho)^j d_\lambda\} < 0.05 \quad (2a)$$

where $(\mu/\rho)^i$ and $(\mu/\rho)^j$ are the mass absorption coefficients of the elements in the specimen (all permutations and combinations of Ti, Al, and Nb must be considered here) and d_λ is the x-ray path length through the specimen en route to the detector. The x-ray path length is defined by the specimen/electron beam/detector geometry and is given by

$$d_\lambda = [\sin \beta / \cos(\theta_e - \beta)] \rho t \quad (2b)$$

where β is the angle between the beam and the foil surface (a complex function of detector azimuthal angle and two specimen tilt axes), θ_e is the detector elevation angle, ρ is the specimen density, and t is the specimen (foil) thickness at the point of analysis. As written, the absorption criterion indicates the thickness at which absorption will alter the quantitation results by 5% (relative).

X-ray spatial resolution can be examined by several techniques. The easiest procedure is to use the single-scattering-model approximation⁴

$$b = 625(Z/E_0)(\rho/A)^{1/2} t^{3/2} \text{ (cm)} \quad (3)$$

where b is the exit beam diameter (cm), Z is atomic number, A is atomic weight, E is the beam energy (keV), ρ is density (g/cm³), and t is thickness (cm). To calculate the diameter of the x-ray generation volume, the beam diameter is added in quadrature to b . To include 90% of the electrons, as in Eq. (3), the beam diameter is $1.82d_p$, where d_p is the full-width-at-half-maximum (FWHM) beam diameter.⁵ The most

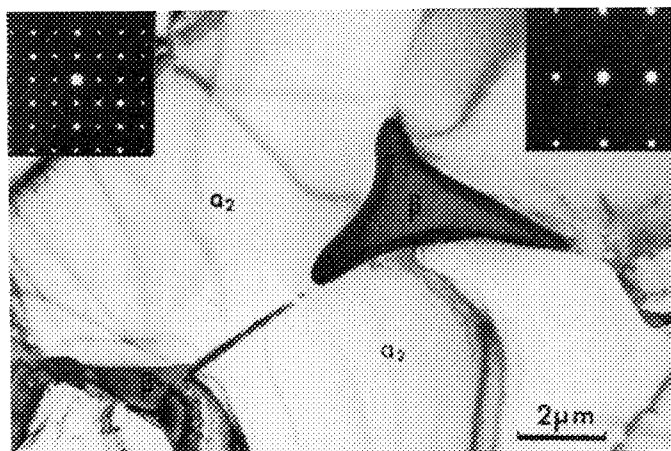


FIG. 1.--TEM bright-field micrograph of Ti-14.8Al-21.3Nb (wt.%). Diffraction pattern inserts show [1120] α_2 zone (left) and [110] β zone (right).

accurate procedure is to use Monte Carlo techniques.⁶ Both procedures are used in the present work and the results are compared.

Experimental

The alloy used in this study contained 63.90Ti-14.80Al-21.30Nb (wt.%), with a few ppm trace levels of Fe (600 ppm), N (60 ppm), and O (600 ppm). The material used in this study was in the form of a hot-rolled sheet and contained a duplex microstructure of the α_2 phase (ordered hexagonal, $D0_{19}$) and β (bcc). As shown in Fig. 1, a bright-field TEM micrograph of the alloy, the matrix is predominately α_2 with β at the grain triple points. The α_2 phase is large enough to determine the composition with the electron probe microanalyzer (EPMA). The composition of the α_2 is 65.4Ti-14.6Al-20.0Nb (wt.%), and the phase is compositionally homogeneous. The α_2 was used as a thin-film standard to determine the Cliff-Lorimer sensitivity factors and to examine absorption effects in the alloy.

Thin foils of the alloy were produced by standard techniques for preparing self-supporting 3mm disk specimens. The foils were thinned to electron transparency by jet polishing of 100 μ m-thick disks in a 5% sulfuric acid in methanol solution at 16 V. The AEM was performed in a JEOL 2000FX (at 200 kV) equipped with a Tracor-Northern 5402 EDS analyzer. The high take-off angle (72°) 7.5 μ m Be window detector was used. The detector had an active area of 30 mm² and was 3 mm thick.

The k-factor determination and absorption experiments were performed in thin areas of the α_2 phase. A series of point analyses was made with a 50nm beam in regions of the foil of various thickness. X-ray intensities were background-corrected and integration was done over the full peak. The thickness of the foil was determined by a variety of techniques, including the contamination-spot technique, the differential x-ray absorption technique, and the integrated

x-ray count rate technique.⁷ A comparison of the thickness determination results will be given later in this paper.

Results and Discussion

Determination of k-factors. Figure 2 shows the k-factor vs thickness. The results are plotted as log k vs t, as suggested by Horita et al.⁸ The Horita analysis is intended to produce the k-factor for an infinitely thin foil, in which any absorption effects are eliminated. The true zero thickness k-factor is given by a least-squares extrapolation to zero thickness. The value of k_{NbTi} is 2.91 ± 0.18 (2σ counting error). In this case, the slope of the k-vs-t curve is zero, indicative of no absorption effect for thicknesses up to 280 nm. The value of k_{AlTi} at zero thickness is 1.07 ± 0.04 (2σ counting error). The change in k_{AlTi} with thickness is slight; it increases about 7.5% over 200 nm. The increase in k_{AlTi} with thickness is just detectable above the noise due to counting statistics.

The k-factors for these elements have also been calculated, by use of the algorithm of Carr and Romig.⁹ The k-factors are calculated from

$$k_{ATi} = [(Q\omega)_A] / [(Q\omega)_A]_{Ti} \times [\epsilon_A / \epsilon_{Ti}] \quad (4)$$

where Q is the ionization cross section, ω is the fluorescence yield, a is the fraction of the K line which is $K\alpha$, A is the atomic weight, and ϵ is the detector efficiency. Here, all k's are referenced to Ti, so Eq. (4) must be written for k_{AlTi} and k_{NbTi} (the subscript A is for Al or Nb).

The cross-section model used is that given by Powell,¹⁰ as modified by Brown.¹¹ The expression is

$$Q = [6.51 \times 10^{-21} / E_c U] n b \ln(cU) \quad (5)$$

where E_c is the critical ionization energy, U is the overvoltage (E_c/E_0 , where E_c is the critical excitation energy and E_0 is still the beam energy), n is 2 for K-shell excitations, and b and c are given by $0.52 + 0.0029Z$ and 1.0, respectively (Z is atomic number).

The fluorescence yield is from Burhop,¹² and given by

$$[\omega / (1 - \omega)]^{1/4} = A + BZ + CZ^3 \quad (6)$$

where A, B, and C are 0.015, 0.0327, and -0.624×10^{-6} , respectively, as given by Bambynek.¹³

The values of a are calculated from the fitted equations of Schreiber and Wims¹⁴ and are 0.882, 0.978, and 0.838 for Ti, Al, and Nb, respectively.

The detector efficiencies are calculated from the absorption of each type of x ray as it passes through the Be window, Au contact film, and Si deadlayer. The efficiency calculation also considers transmission of x rays through the detector. For these calculations, the mass absorption coefficients of Thinh and Leroux¹⁵ are used. The Be window is 7.5 μ m thick and

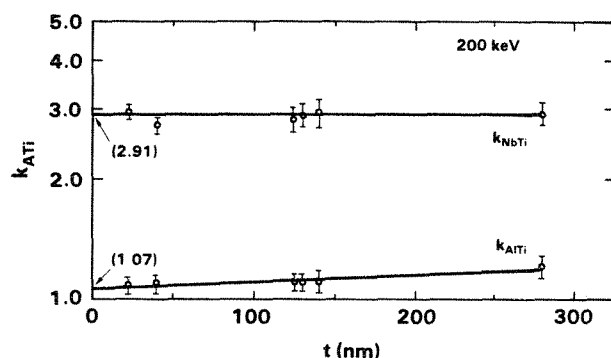


FIG. 2.--Relationships between k_{AlTi} and foil thickness. Extrapolated value to infinitely thin foil is shown at $t = 0$, where $k_{AlTi} = 1.07 \pm 0.04$ and $k_{NbTi} = 2.91 \pm 0.18$ (error from 2σ counting statistics). Error in thickness is approximately 10% relative. Measured k factors are consistent with calculations: $k_{AlTi} = 1.05$ and $k_{NbTi} = 3.07$. Data show absence of absorption for Ti and Nb in alloy and slight (5% at 200 nm) absorption of Al.

the Au film and Si deadlayer are assumed to be 20 nm and 100 nm thick, respectively, as suggested by Zaluzec.¹⁶ As noted, the detector here is 3 mm thick. The calculated detector efficiencies are 0.951, 0.712, and 0.988 for Ti, Al, and Nb, respectively. For a complete description of the detector efficiency calculation, the reader is referred to the paper of Carr and Romig.⁹

With the above formulations and input data, the calculated k -factors are

$$k_{AlTi} = 1.05 \quad \text{and} \quad k_{NbTi} = 3.07$$

These values compare quite favorably to the measured values given above. The calculations match the measured values within the 2 standard deviation counting error.

X-ray Absorption. As shown in Fig. 2, x-ray absorption effects are small. No measurable effect was observed for Nb-Ti and only a small effect for Al-Ti in the ternary alloy. An increase of approximately 7.5% in k_{AlTi} was observed at a thickness of 200 nm. The thicknesses given in Fig. 2 were measured by a variety of techniques, as described by Romig and Carr.⁷ The thicknesses were determined with the contamination-spot technique and by differential x-ray absorption of the Nb K and Nb L lines. (The full details are given in the original references.^{7,17}) The thicknesses determined by each technique agreed within 10-15% relative, with the contamination-spot techniques typically giving slightly larger values. Further, all the thicknesses were self-consistent with the change in x-ray count rate with thickness. (In thin regions of the foil, where single scattering is appropriate, one would expect the count rate to increase linearly with thickness.) Hence, it is reasonable to assume that the reported thicknesses are accurate to at least 10% relative.

Table 1.--Beam spreading as calculated by Eq. (3).

	1 nm	2 nm	5 nm	10 nm	20 nm	50 nm	100 nm
Thickness							
10 nm	10	20	50	10	20	500	100
20 nm	1.2	2.1	5.0	10	20	50	100
50 nm	2.6	3.1	5.5	10	20	50	100
100 nm	6.7	6.9	8.3	12	21	50	100
200 nm	19	19	19	21	28	53	102
500 nm	74	74	74	75	77	89	124

*The diameter encompassing 90% of all the electrons in a Gaussian probe is $1.82 \times \text{FWHM}$. Most instrument manufacturers report FWHM as spot size.

The thin-film criterion at 5% (Eq. 2a) was applied to the data collected from the α_2 phase. With the absorption coefficients of Thinh and Leroux,¹⁵ and the specimen/detector geometry for the 2000FX, the 5% criterion is violated for thickness greater than 160 nm. This calculation is again consistent with the experimental observations.

Other elements, such as Cr and V, have also been considered as alloy additions to Ti_3Al . At the concentration levels used in these alloys (10 to 15 wt.%), absorption effects are similar to those observed in the Nb-modified material. The Cr and V modified alloys violate the thin-film criterion (Eq. 2a) at foil thicknesses of approximately 160 nm.

X-ray Spatial Resolution. X-ray spatial resolution has been examined in this alloy by use of both the simple single-scattering model as given in Eq. (3) and by Monte Carlo modeling.⁶ For foil thicknesses of up to approximately 350 nm, the results of the single-scattering model and the Monte Carlo model are in excellent accord (Table 1). At larger foil thicknesses, the single-scattering model begins to overestimate the beam spreading. However, at these large thicknesses the absorption correction becomes uncertain and reliable quantitative analysis is not possible.

Conclusions

1. Reliable quantitative thin-film x-ray microanalysis is possible on Nb-modified titanium aluminides.

2. At 200 kV, the sensitivity factors for standardless quantification are:

$$\text{Experimental: } k_{AlTi} = 1.07 (\pm 0.04)$$

$$k_{NbTi} = 2.91 (\pm 0.18)$$

$$\text{Calculated: } k_{AlTi} = 1.05$$

$$k_{NbTi} = 3.07$$

3. X-ray absorption is not significant at the 5% level until the foil thickness (with the α_2 composition) exceeds approximately 160 nm. This calculation is consistent with experimental observation, in which the k_{AlTi} was observed to increase by approximately 5% at a thickness of 200 nm.

4. For reasonable foil thicknesses (less than 350 nm), beam spreading can be accurately

calculated by the single-scattering model. Spatial resolution can be calculated by addition of the beam diameter (1.82 FWHM for 90% of electrons) and the spreading factor in quadrature.

References

1. H. A. Lipsitt, in C. C. Koch, Ed., *High Temperature Ordered Intermetallic Alloys*, MRS Symposia Proceedings, Pittsburgh: Materials Research Society, 1984, 351.
2. M. J. Cieslak, T. J. Headley, and W. A. Baeslak III, "Effect of thermal processing on the microstructure of Ti-26Al-11Nb: Applications to fusion welding (submitted to *Metallurgical Transactions*).
3. G. Cliff and G. W. Lorimer, "Quantitative analysis of thin metal foils: The ratio technique," *Proc. 5th European Congress on Electron Microscopy*, 1972, 140.
4. J. I. Goldstein, J. L. Costley, G. W. Lorimer, and S. J. B. Reed, "Quantitative x-ray analysis in the electron microscope," *SEM/1977 I*, 315.
5. A. D. Romig Jr. and M. J. Cieslak, "Solute segregation to phase interfaces and grain boundaries: Studies by analytical electron microscopy and profile deconvolution," *Analytical Electron Microscopy--1977*, 25.
6. D. E. Newbury and R. L. Myklebust, "Monte Carlo electron trajectory simulation of beam spreading in thin foil targets," *Ultramicroscopy* 3: 391, 1979.
7. A. D. Romig Jr. and M. J. Carr, "Thickness and extinction distance measurements in heavy metal thin foils by convergent beam electron diffraction and x-ray absorption," *Analytical Electron Microscopy--1984*, 111.
8. Z. Horita, "An extrapolation method for the determination of Cliff-Lorimer k_{AB} factors at zero foil thickness," *J. Microsc.* 143: 1986, 215.
9. M. J. Carr and A. D. Romig Jr., "Thin foil x-ray microanalysis with the Macintosh," (in preparation).
10. C. J. Powell, "Evaluation of formulas for inner-shell ionization cross-sections," in K. F. J. Heinrich, Ed., *Use of Monte Carlo Calculations in Electron Probe Microanalysis and Scanning Electron Microscopy*, NBS Special Publication 460, 1976, 97.
11. D. B. Brown, in J. W. Robinson, Ed., *Handbook of Spectroscopy*, Cleveland, Ohio: CRC Press, vol. 1, 1974, 248.
12. E. H. S. Burhop, "Le rendement de fluorescence," *J. Phys. Radium* 16: 625, 1955.
13. W. Bambynek et al., "X-ray fluorescence yields, Auger, and Coster-Konig transition probabilities," *Rev. Modern Physics* 44: 716, 1972.
14. T. P. Screiber and A. W. Wims, "Relative intensity factors for K, L, and M shell x-ray lines," *Microbeam Analysis--1981*, 317.
15. T. P. Thinh and J. Leroux, "New basic empirical expression for computing tables of x-ray mass attenuation coefficients," *X-ray Spectrometry* 8: 85, 1979.
16. N. J. Zaluzec, "Quantitative x-ray microanalysis: Instrumental considerations and applications to materials science," in J. J. Hren et al., Eds. *Introduction to Analytical Electron Microscopy*, New York: Plenum Press, 1979, 121.
17. A. D. Romig Jr., "Quantitative x-ray microanalysis of uranium alloys with the analytical electron microscope," *J. Microsc.* 135: 1984, 191.

ANALYTICAL TEM OF YTTRIA-STABILIZED ZIRCONIA WITH SILICATE GRAIN BOUNDARY PHASES

Y. J. Lin, M. L. Mecartney, and Peter Angelini

Yttria partially stabilized zirconia (Y-PSZ) is a ceramic that exhibits a high toughness due to the toughening effect of the tetragonal to monoclinic phase transformation.¹ Typical of many polycrystalline ceramic materials, Y-PSZ usually contains an amorphous silicate grain boundary phase, derived from impurities associated with the raw material or introduced during powder processing. The presence of this grain boundary phase and its composition have been shown to affect microstructural development and the properties of Y-PSZ.^{2,3} A systematic investigation of the significance of the silicate phase composition on the microstructure and composition of the Y-PSZ was reported by Mecartney and Angelini⁴ using analytical transmission electron microscope (TEM) to examine 3 and 8 mol% Y-PSZ with controlled additions of aluminosilicate and borosilicate glasses. To complement to their work, we used analytical TEM to study 4 mol% Y-PSZ doped with similar aluminosilicate and borosilicate grain boundary phases.

Experimental

Co-precipitated zirconia powders containing 4 mol% of yttria were mixed with 5 wt% aluminosilicate or borosilicate glass powders. After sintering at 1400 C for 20 min, these samples were hot isostatic pressed (HIPped) at 1650 C for 100 min in an argon atmosphere at 100 MPa. TEM samples were prepared and investigated with a Philips EM400T at 100 kV with field-emission gun (FEG) and equipped with EDAX 9100 energy-dispersive spectrometer (EDS). EDS spectra were analyzed with NEDQNT program.⁵ A Gatan double tilt cold stage was used to minimize contamination.

Results and Discussion

The microstructure of these materials is typified by extensive grain boundary network and rounded zirconia grains with

a bimodal grain size (Fig. 1). EDS results summarized in Table 1 show that the large zirconia grains contained approximately 7 mol% of yttria, and the small zirconia grains contained about 3 mol% of yttria (Fig. 2). Within the statistical scatter of the data, the partitioned yttria concentrations for aluminosilicate and borosilicate samples were equivalent. These large and small zirconia grains therefore correspond to the cubic and tetragonal phases, respectively, as predicted from the yttria-zirconia phase diagram.⁶ The size difference between the tetragonal and cubic zirconia indicates that the cubic zirconia grew much faster than tetragonal zirconia even in the presence of a completely wetting liquid phase. This phase separation was not obvious for the 3 mol% Y-PSZ in Mecartney and Angelini's work,⁴ although the 3mol% compositions also lies in the two-phase (cubic +tetragonal) region of the phase diagram.

There was also a significant difference in yttria concentration for the grain boundary glasses at room temperature (Fig. 3 and Table 1). The aluminosilicate glassy grain boundary phase contains 7.7 mol% of yttria while the borosilicate glassy grain boundary has little yttria. Since both phase partitioning and grain growth involve the redistribution of yttria among the zirconia grains, there must be some significant solubility of yttria in borosilicate glass at high temperature.

Conclusion

Phase partitioning into large cubic (7 mol%) and small tetragonal (3 mol%) zirconia grains was observed for 4 mol% Y-PSZ with aluminosilicate and borosilicate glassy grain boundary phases. EDS analyses of the grain boundary phases indicate little yttria present in the borosilicate glass but approximately 8 mol% yttria in the aluminosilicate glass. However, the phase partitioning and extensive growth suggest that significant yttria solubility exists at high temperatures.

References

1. T. K. Gupta, in R. C. Bradt, D. P. H. Hasselman and F. F. Lange, Eds., *Fracture Mechanics of Ceramics*, vol. 4, 877-889.
2. M. Ruhle, N. Claussen, and A. H. Heuer, *Advances in Ceramics* 12: 352-370, 1984.
3. E. P. Butler et al., *ibid.*, 12: 572-584, 1984.
4. M. L. Mecartney and P. Angelini, *Proc. Ann. EMSA Meeting* 45: 166, 1987.
5. N. J. Zaluzec, in J. J. Hren, J. I. Goldstein, and D. C. Joy, Eds., *Introduction to Analytical Electron Microscopy*, 1979, 121-167.
6. H. G. Scott, *J. Mat. Sci.* 10:1527. 1974.

Y. J. Lin and M. L. Mecartney are at the Department of Chemical Engineering and Materials Science, University of Minnesota, Minneapolis, MN 55455; P. Angelini is with the Metals and Ceramics Division, Oak Ridge National Laboratory, Oak Ridge, TN 37831-6376. This research was sponsored by the Basic Energy Sciences Division, U.S. Department of Energy, through the SHaRE program under contract DE-AC05-76OR00033 with Oak Ridge Associated Universities; by the Division of Materials Sciences, U.S. Department of Energy, under contract DE-AC05-84OR21400 with Martin Marietta Energy Systems, Inc., and by the Graduate School of University of Minnesota.

EXPERIMENTAL DIFFICULTIES WITH OBTAINING ELECTRICAL PROPERTIES BY SPATIALLY RESOLVED ELECTRON ENERGY LOSS SPECTROSCOPY

P. E. Batson and J. Bruley

The shape of the core absorption edges, on a scale of tens of electron volts, can be explained on the basis of single electron transitions between atomic levels and a free electron continuum.¹ Within a scale of a few electron volts beyond the absorption edge, the bandstructure of the solid needs to be considered. For instance, a very good study of the systematic variation of the transition metals and their oxides has been made.² The question arises whether it is possible to push the analysis further. On a scale of 1-2 eV, variations in the shape of a core absorption ought to reflect variations in the bandstructure that are important to local electrical properties. This is in fact correct.³ Elsewhere in these proceedings,⁴ there is a description of an electron energy loss system that combines a good energy loss resolution (0.35 eV) with a small probe size (0.8 nm). We discuss here some experimental limitations on the use of this system to obtain electrical properties in small areas of silicon and diamond.

Processing of Raw Data to Obtain Uniform Comparisons

The basis of the technique is to measure the shape of a core absorption with sufficient accuracy to detect single electron transitions to unoccupied electronic states near a semiconductor conduction band edge. Transitions to states in the conduction bands produce changes in the absorption edge shape. Transitions to states in the semiconductor gap produce scattering in front of the absorption edge. To obtain small changes in scattering accurately, we must use a systematic method for stripping the edge background. In Fig. 1, we show energy loss results for the Si $L_{2,3}$ absorption edge. We can strip the background off the scattering in the standard way, using a power-law fit to a region below the edge.⁵ In this case, the fit is made only between 90.3 to 93 eV. This extrapolation would not be very good for an elemental analysis that required tens of electron volts of absorption intensity. But in this case we are only interested in a 4eV window about the edge. Under these conditions, we have found that a very good fit of the background can be made with a small window fit. In Fig. 1, we can verify that the real background is adequately approximated up to the absorption edge, even for the narrow fit. Normally, the background fit would be made closer to the edge. Figure 1 includes results

from two acquisitions to show the degree of reproducibility obtainable from different areas. In general, the overall shapes are in agreement. However, small differences are evident and are the subject of this discussion.

In Fig. 2, we show a stripped edge of better quality. Several features are usually seen. At 99.84 eV there is an initial step-like edge. The intensity rises to a small shoulder at 100.2 eV and then rises again to a peak at 101.25 eV. Next, two small peaks appear at 102.6 and 103.2 eV. Some of these features are due to final-state electronic structure. However, some are due to the spin-orbit splitting of the core level. The first difficulty therefore is to separate the $j = 1/2$ and $j = 3/2$ components of the scattering. We can eliminate the $j = 1/2$ part, leaving the $j = 3/2$ component, the $2p^{3/2}$ edge, by a Fourier decomposition method. We construct a "splitting function," consisting of two δ -functions that are separated by the 0.61eV spin-orbit splitting and that have an intensity weighting of two to one, the expected ratio of the populations of the split-core level. We then divide the Fourier components of the data by the Fourier components of the splitting function, and inverse Fourier analyze the result. As shown in Fig. 2, the technique appears to work very well for the bulk silicon, eliminating the doubling of the peaks near 103 eV, and leaving one peak at 102.6 eV. The shape and position of the onset are unchanged; the small shoulder is enhanced; and the 101.25eV peak becomes a sharper peak positioned at 101.0 eV. The figure also shows the positions of the bands for various directions in silicon. We now see clearly that certain features in the Si $2p^{3/2}$ edge align nicely with important positions in the Si bandstructure. If these features move around or change in intensity as the probe is moved, we should be able to infer changes in the bandstructure.

This spin-orbit analysis assumes that we know the splitting and the relative ratio of intensities expected for the two parts. In fact, it has been found that the observed intensity ratio is not always the expected one.² We have observed shape variations at the Si edge that might be attributable to this discrepancy. These variations are subtle and appear for different orientations and surface quality of the Si. At present, we have no systematic study of this possibility. Thus care has to be exercised in applying the Fourier deconvolution technique in the absence of good knowledge of the core-level splitting and intensity ratio.

The authors are at the IBM Thomas J. Watson Research Center, Yorktown Heights, NY 10598.

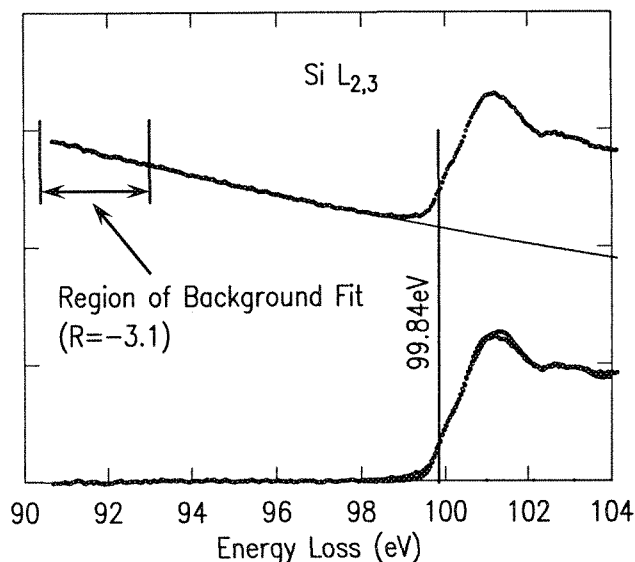


Fig. 1.--Raw data for bulk silicon. Background has been fitted in indicated region and subtracted to show that background extrapolation procedure is quite good over a 10-15eV range.

Variation of Absorption Shape with Specimen Morphology

Given a systematic analysis such as the above, we can now explore the variation in shape as we move the probe around. Figure 3 shows results as a function of thickness in a wedge-shaped specimen. We observe that the shape of the absorption onset changes as the specimen gets thinner. On the extreme edge of the specimen, we observe an SiO_2 spectrum. In the thickest areas, we see a bulk Si result. As the Si thickness approaches 10 nm, determined by analysis of the bulk plasmon multiple scattering, bandstructure-related features disappear. In Fig. 4, a similar situation occurs in thick Si as a function of the lateral distance of the probe to a cleaved surface. In this case, the probe must get very close to the surface--of the order of 1 nm--before the absorption structure disappears.

The results of Fig. 4 seem sensible. When we move the probe to within one or two unit cells at the surface, we expect to see changes in the local bandstructure. However, the changes in Fig. 3 occur when the Si is many unit cells thick. Certainly, high-resolution lattice imaging is routinely possible in specimens of this thickness. In the present case, lattice imaging was successful. In examining various length scales in this problem, it occurs to us that in losing 100eV of energy to the specimen, the 100keV fast electron gives up a well defined amount of momentum in the direction parallel to the electron beam. This momentum transfer defines a length scale of about 7 nm for this problem. In analogy with surface and bulk plasmon scattering,⁶ it is possible for the scattering probability to be affected when the thickness of the specimen becomes comparable to this parallel length

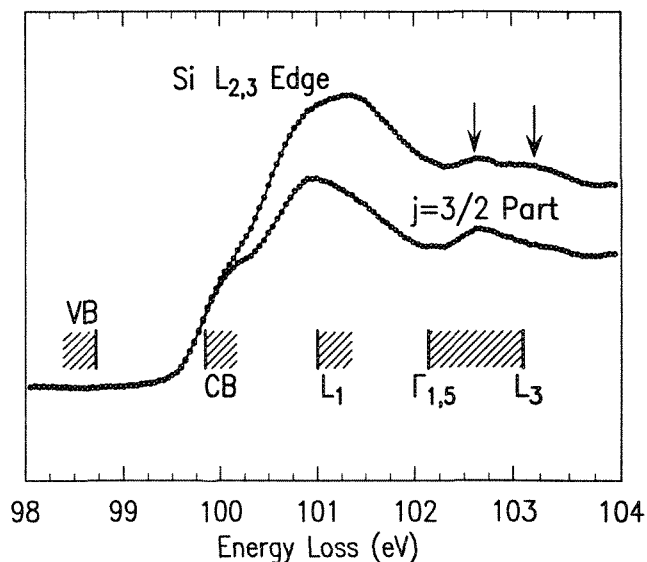


Fig. 2.--Better quality silicon data after background subtraction. It is now necessary to eliminate effects due to spin-orbit splitting of core level. Major band edges and density maxima line up remarkably well with measured data.

scale. It is beyond the scope of this discussion to try to understand this effect further. However, it should be readily apparent that we must be careful with the specimen configuration and thickness when trying to utilize the interpretation of the core-edge to obtain bandstructure information.

Orientation Dependence

Since the information that we are trying to acquire is related to the crystallinity of the solid, we should ask whether the observed structure depends on the crystal orientation with respect to the incident beam. Certainly, in systems with known anisotropy, the shape of the core edge is very sensitive to the crystal orientation. Good examples exist in graphite and boron nitride.⁷ However, we do not expect to see such effects for isotropic systems. In Fig. 5, we show results for silicon in two orientations--one with a $[110]$ axis parallel to the incident beam direction, the other with the $[111]$ axis parallel to the incident beam. The two results have been normalized at 100.0eV--that is, the part of the bandstructure that relates to the band edge. Two differences are then apparent in the results; (1) intensity exists below the onset, in a region corresponding to the Si bandgap, for the $[111]$ orientation; and (2) the intensity in the peaks at 101 and 102.6eV do not match.

As mentioned above, intensity located before the absorption onset is a signature of additional states occurring in the gap of the Si. However, it seems unlikely that this is a bulk effect, because it is not subtle. The ratio of measured intensities within the gap for these two orientations is of the order $5\times$. It seems unlikely that any departure from isotropy

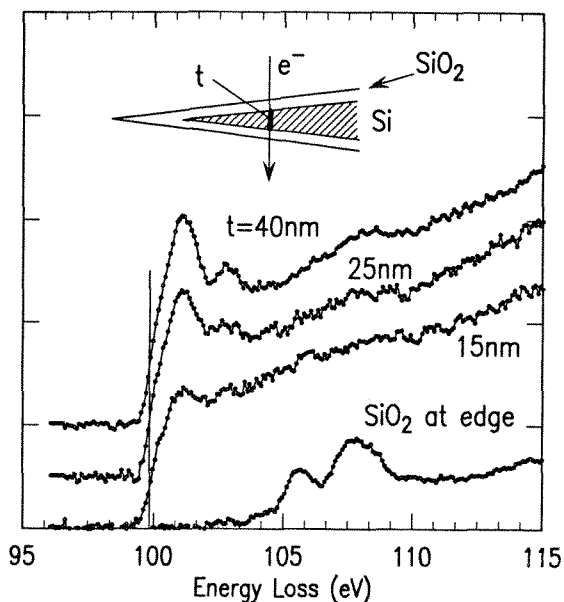


FIG. 3.--Stripped edges for various thicknesses of silicon, obtained by moving the probe toward the edge of a wedge-shaped specimen. At the extreme edge, SiO_2 is present. Well before the edge, the spectrum is significantly modified.

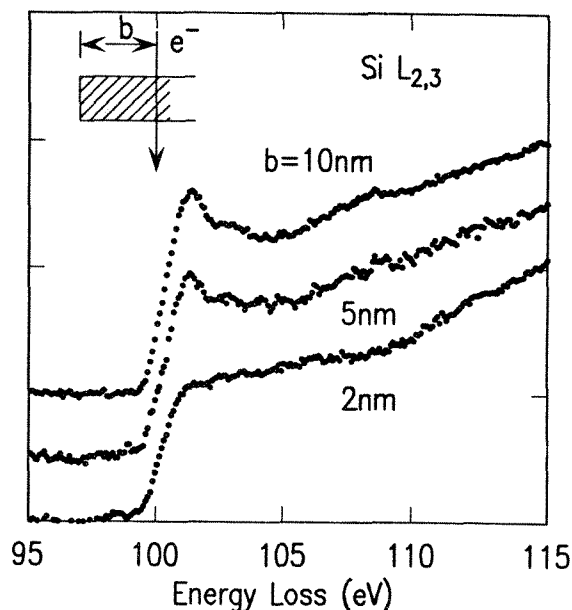


FIG. 4.--Silicon absorption for various distances away from edge of cleaved area. Here, thickness does not change appreciably. Changes in spectrum occur because of close proximity to cleaved edge.

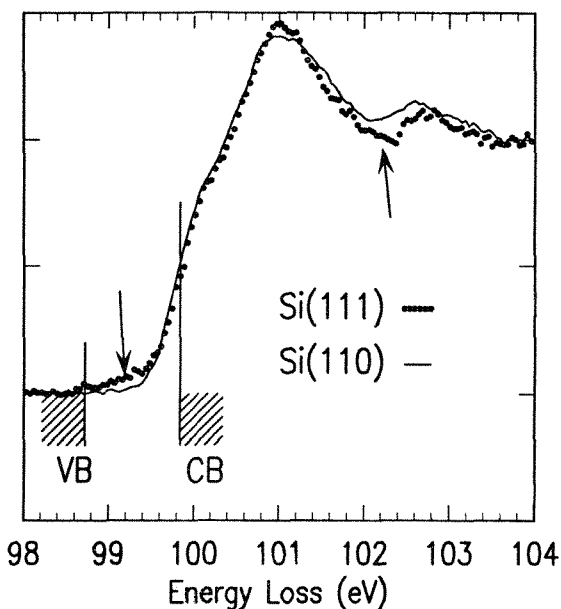


FIG. 5.--Comparison of the Si absorption edge for two orientations. Data are normalized at 99.9 eV to make [100] type scattering equivalent. Two types of differences emerge: (1) scattering at L_1 and L_3 is stronger in the [110] sample, (2) surface-related scattering in Si gap is present in [111] sample.

could be as large as that. We suspect this intensity is due to scattering involving surface states. We remember that the Si [111] surface has many dangling bonds that are

difficult to rearrange to form a noninteracting surface. The [110] surface, on the other hand, can readily reconstruct to satisfy all dangling bonds. Thus, we expect that the [111] oriented sample may show significant scattering to empty surface states located within the Si gap. The results in Fig. 5 are entirely reasonable from this point of view. Differences in intensity above the edge would then be a reflection of the redistribution of the electronic density of states near the surface. Therefore this result is similar to that shown in Fig. 3 and 4 above.

Surface Scattering in Diamond

The results in Fig. 5 are certainly debatable, because the statistical quality of the data is not very good. In diamond, we have much clearer results of a similar behavior. Spectra of the carbon K edge were acquired as a function of thickness in a wedge-shaped sample. The thickness was calibrated with the low-loss multiple scattering. It was found that the intensity of the absorption edge at 288.8 eV was proportional to the thickness of the sample for thin areas. However, most of the intensity below the absorption edge remained relatively constant as the thickness was varied. Two examples of this result are shown in Fig. 6. These data were acquired at constant beam dose, so that they need not be normalized. The background subtraction was the only processing done. It is obvious that the pre-edge structure remains constant in intensity, whereas the absorption onset becomes smaller in the thinner sample. In examining the pre-edge structure in greater detail, we

see that there is a similarity of the shape of the structure to the shape of predicted electronic surface structure in diamond.⁸ We thus are confident, at least in this case, that the structure is surface related.

A Microanalytical Result

Clearly we need to be careful with interpretation of these shape variations until we thoroughly understand the effects due to thickness, orientation, and the surface. At the outset of an experiment, we must characterize the sample, and design the measurements to minimize these problems. Figure 7 shows a recent result⁹ for a single dislocation in Si. The figure shows a comparison of spectra acquired on and off a partial dislocation bounding a stacking fault. The two regions analyzed had the same thicknesses and orientations. They were also close enough for us to assume that they probably had the same amount of surface scattering. There are clear differences between the two spectra. In the context of a recent analysis of the Al/Si(111) interface,³ these differences can be interpreted in the following way. First, intensity below the absorption edge at the dislocation is likely to be due to defect electronic states lying within the Si gap. Second, the Fermi level should be at a position defined by the onset of the in-gap scattering--99.7eV in this case. This is 1.1 eV below the onset of scattering in the bulk--precisely at the valence band edge as indicated in the figure. This result is just what we expect for the p-type material in this experiment. Third, there appears to be a shift of the 102.6eV peak to a

slightly lower energy. If the in-gap states are a result of a distortion of the Si lattice near the dislocation, the conduction band-structure will also be modified. In effect, the spectral density associated with the in-gap states is created at the expense of states lying higher in the Si conduction bands. Recent calculations¹⁰ have shown that the shift of the 102.6eV peak is the most prominent signature of that redistribution of state density.

In conclusion, we are able now to get electronic structure information with a spatial resolution of 1 nm or better. Various effects having to do with the specimen surface, its thickness, and the experimental scattering geometry must be understood and controlled to allow us to interpret this information. However, these effects appear amenable to understanding with proper care. This kind of work thus promises to be a powerful tool to further our understanding of the localized electronic structure of defects and interfaces in device related structures.

References

1. R. D. Leapman, P. Rez, and D. F. Mayers, "K, L, and M shell generalized oscillator strengths and ionization cross sections for fast electron collisions," *J. Chem. Phys.* 72: 1232, 1980.
2. R. D. Leapman, L. A. Grunes, P. L. Fejes, and J. E. Muller, "A study of the $L_{2,3}$ edges in the 3d transition metals and their oxides by electron energy loss spectroscopy," *Phys. Rev. B* 26: 614, 1982.

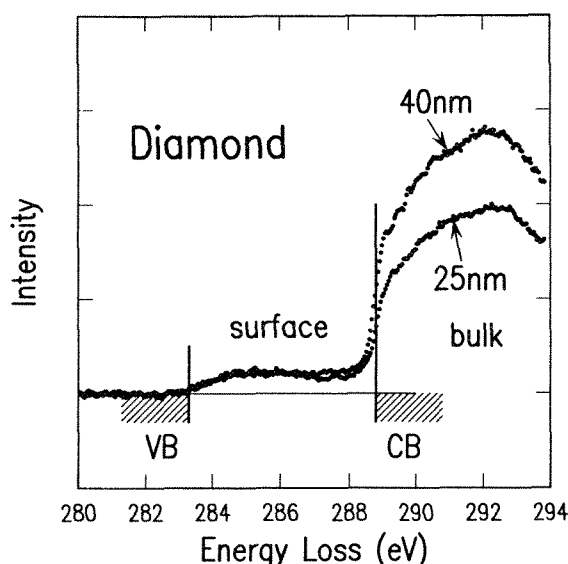


FIG. 6.--Comparison of two carbon K edge spectra taken from different thicknesses of diamond. Scattering below edge corresponds to surface scattering. Surface scattering intensity remains constant; bulk absorption onset decreases for smaller thickness.

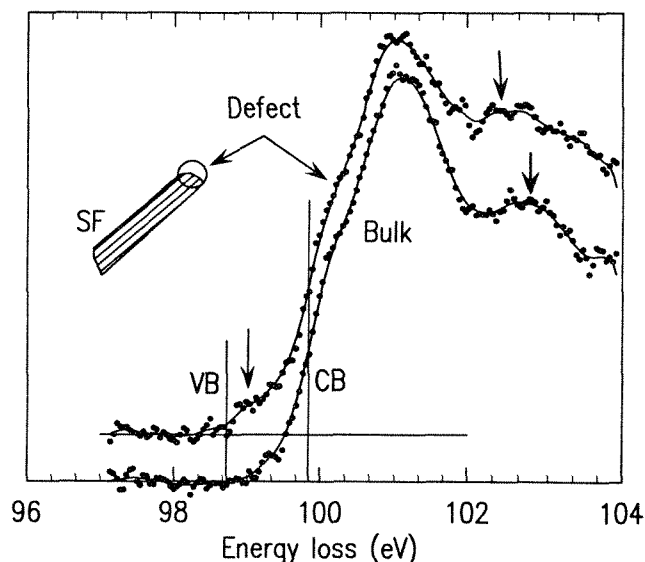


FIG. 7.--Comparison of Si spectra acquired on and near single partial dislocation bounding stacking fault. On dislocation, intensity appears within Si gap and 102.6eV peak shifts to lower energy. Changes can be interpreted in terms of in-gap electronic states near dislocation, accompanied by necessary modification of local Si conduction bandstructure to satisfy density-of-state sum rules.

3. P. E. Batson, "Local electronic structure at the Al/Si(111) interface," *Phys. Rev. Lett.* (submitted).
4. P. E. Batson, "Spatially resolved electron energy loss spectroscopy," this volume.
5. R. F. Egerton, in *Electron Energy Loss Spectroscopy in the Electron Microscope*, New York: Plenum Press, 1986, 258.
6. R. H. Ritchie, "Plasma losses by fast electrons in thin films," *Phys. Rev.* 106: 874, 1957.
7. R. D. Leapman, P. L. Fejes, and J. Silcox, "Orientation dependence of core edges from anisotropic materials determined by inelastic scattering of fast electrons," *Phys. Rev. B* 28: 2361, 1983.
8. J. Bruley (in preparation).
9. P. E. Batson, "High-resolution energy loss spectroscopy," *Ultramicroscopy* (in press).
10. S. G. Louie and M. L. Cohen, "Electronic structure of a metal-semiconductor interface," *Phys. Rev.* 13: 2461, 1976.

QUANTITATIVE MAPPING OF THIN-FILM STEM SAMPLES WITH ENERGY-DISPERSIVE X-RAY SPECTROMETRY

J. F. Konopka

This paper describes one approach to the quantitative interpretation of EDS x-ray maps. Successful methods and problems found in acquiring, processing, and displaying the data are discussed. All work described here was done with the Imagex-II experimental imaging software package, elements of which have been described previously.¹

Acquisition

In ordinary x-ray mapping, it is often sufficient to acquire only a few counts per point to determine whether an element is present or absent. To do meaningful quantitative work, more precision is required. Ideally one would like to get at least the same precision as is obtained in single-point analysis. However, since a measurement of 1000 counts has a standard deviation of 3% and a measurement of even 1000 counts per point per element is unlikely in a STEM, we can see that this precision is not yet attainable; one should endeavor to collect as much data as possible. More data can be obtained by use of higher beam currents, a short time constant in the EDS amplifier, a short sample-to-detector distance, a large area detector, and a longer acquire time. Problems of beam damage and focus limit the usable beam current. Contamination, specimen drift, and operator patience limit the acquire-time of the map. In practice, maps taken in as little as 5-10 min are useful for quantitation. In this procedure, software maps are acquired with the "fast" mapping method. The electron beam makes multiple scans over the sample, integrating the data from each scan at the same point from successive scans. With the use of two acquire groups, this method is 100% efficient. Dwell times at each point are measured as live time. The benefits are that the operator can observe the progress of the whole map from the very start, the decision on total acquire time is postponed until the map is finished, and the mapping can be stopped as soon as some evidence of drift or beam damage appears. Since the beam is constantly scanning (the dwell times per point are typically 1-2 ms), some of the bad effects of electron-beam exposure are mitigated. Improvements in acquisition in the future will most likely come through faster pulse processors and detectors of larger area.

Background Subtraction

Background measurements are a problem because the continuum signal intensity in x-ray spectra is rather low, so that it is difficult

to obtain good precision within the time used to measure the elemental peaks. Initially, one large background window per map was used to measure the background. Fair precision could be obtained, but for low-wt% elements the accuracy was inadequate. Currently multiple windows are allowed. The operator selects the background for each element from a menu just before the data are displayed. This procedure provides better accuracy at the cost of more tedious interaction with the machine. We are now investigating ways of calculating the background at each element given a measurement at one point, as has been suggested for WDX mapping.

Quantitation

The Cliff-Lorimer algorithm is used. This algorithm is simple enough so that an ordinary map can be processed in about 20-30 s. Default k factors are calculated by the method of Schreiber and Wims for oxide or nonoxide samples. Operators may override them and enter their own k factors. The override is often needed for good accuracy as the use of various windows for peak integration affects the k factor. The current version calculates either wt% or atomic%. Accuracy is as good as an analysis done at a single point, mitigated by the poorer precision as described in the acquisition discussion. A characteristic of the Cliff-Lorimer method is that the results are independent of sample thickness. That lets the operator focus exclusively on compositional differences in the sample. In practice, some thickness dependence is visible, as the precision varies with thickness.

Display

One of the biggest problems in this project was how to display the data. In a qualitative map, simple shading and autoscaling of data are sufficient to highlight variations in sample composition, which requires only a small number of gray levels in graphics hardware. Imagex-II uses 30 gray levels for standard map displays. In quantitative mapping, at least 100 levels are desirable and more is better. The range should be 1% to 100% to display simultaneously pure-element regions and trace-element regions. More than 1% precision is useful in calculating the composition of homogeneous areas (described below), even though it exceeds the precision of a single data point. In qualitative mapping, color can be used to relate intensity to composition; in quantitative mapping, the results are less satisfactory. Although the eye can distinguish a large number of colors, the brain cannot easily process so many levels. Qualita-

The author is at Kevex Instruments, 355 Shoreway Road, San Carlos, CA 94070.

Line Scan V02.01

Scan time: 300secs

13-Feb-89 14:14

Smoothing time constant: 1800 milliseconds.

Display is background subtracted.

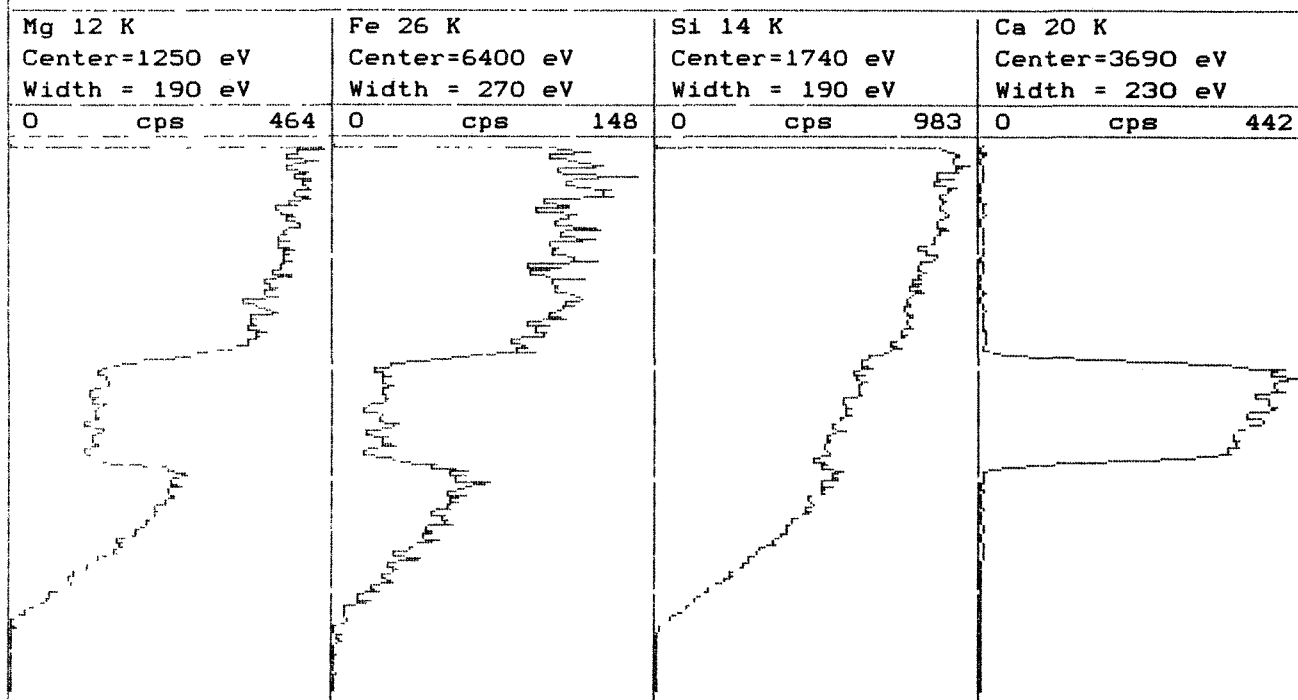


FIG. 1.--Line scan of background-subtracted peak intensities.

tively, we can naturally relate increased composition to increased brightness in an image. Quantitatively, there is no natural mapping between color or brightness and wt%. Red, for example, does not automatically mean 23.0% Si. Even with a key or scale it is difficult to understand a quantitative image with more than five or ten colors--which conflicts with the desire to see up to 100 levels. In Imagex-II two approaches are used. First, in the display, ten color levels are provided. These levels show globally the approximate composition at all points in the map simultaneously, which is useful but too coarse to show small changes in composition. The second method is an octagon-shaped interactive cursor whose size and position are controlled by the operator. It is drawn simultaneously in all displayed maps. Each time the cursor is changed in any way the average value within the cursor is calculated and displayed at the bottom of the screen. This method allows the user to probe about the image and always see unambiguously the composition displayed. Imagex-II uses 240 levels of graphics memory for displaying quantitative maps, so precision is data limited, not hardware limited. A valuable benefit of this method is that the average value calculated over some large number of points is more precise than that of a single point. For a measurement repeated n times the standard deviation of the mean decreases as $1/\sqrt{n}$.⁴

A small cursor 5 points on a side increases the precision by an order of magnitude. Other display modes are being considered. One very promising method is that of concentration-concentration histograms.⁵

Example

An analysis was carried out on a sample of kimberlite. The mineral extracted is orthopyroxene with exsolved lamellae of diopside. The data were taken with a Hitachi H700H STEM and a Kevex Delta III EDS microanalyzer, with the help of Drs. Masao Kitamura and Akira Tsuchiyama of the Department of Geology, Faculty of Science, Kyoto University, Sakyo, Kyoto, 606 Japan. All results reported below are in oxide percent. Figure 1 shows a line scan plot of element intensities. In Fig. 2, data were taken along a line from just below mid-center to the top of the image. These data were collected and plotted with a separate Forth program. The key point is that the variation of x-ray intensity and sample thickness is clearly visible. The larger exsolved lamellae are also clearly indicated.

Figure 2 is a plot of the raw data after background subtraction. Variations in intensity are visible though the sample is homogeneous. Variations in composition are apparent but there is no indication of absolute values.

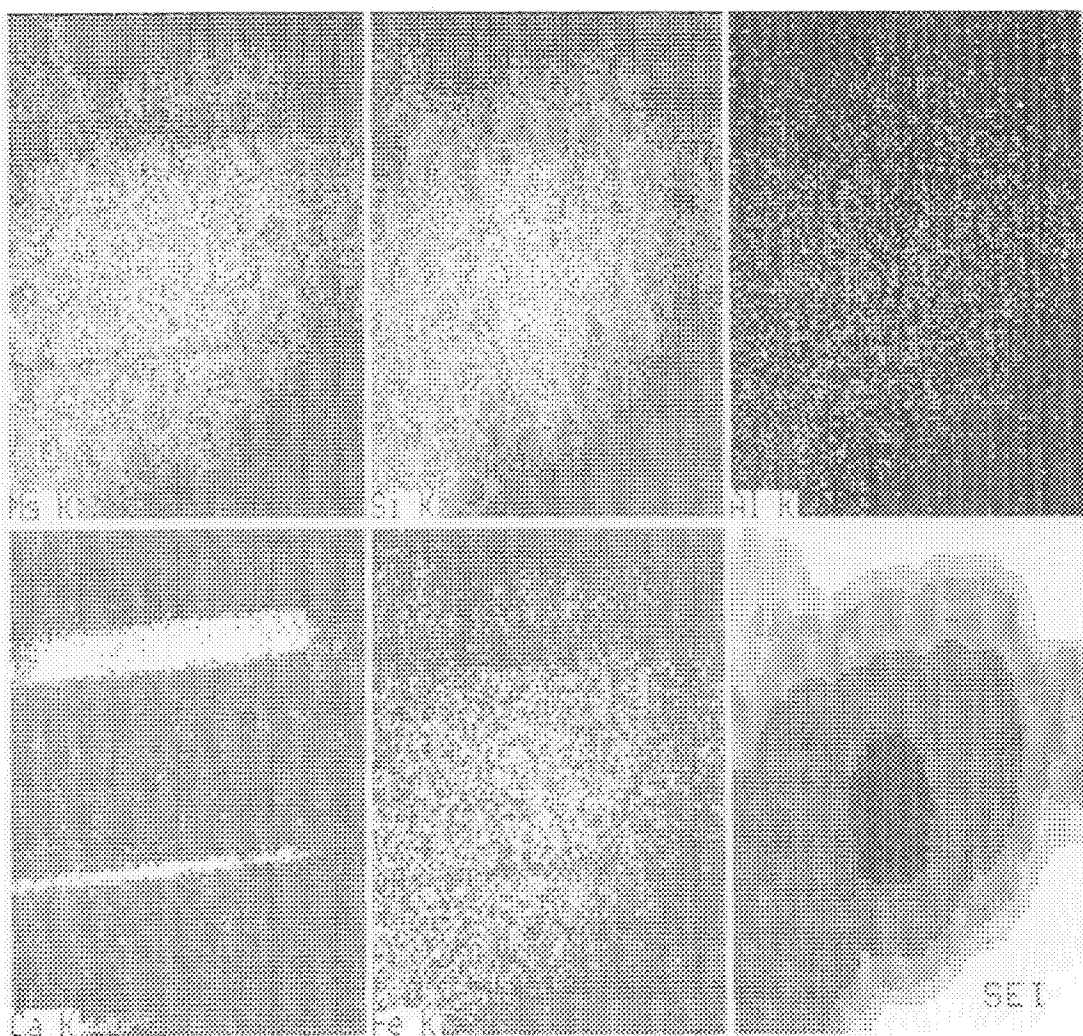


FIG. 2.--X-ray intensity map, background-subtracted peak intensities.

The Ca map shows almost zero Ca outside the lamellae and very high inside the lamellae but there is no indication about actual wt%. A secondary electron image is shown at lower right.

Figure 3 shows the same data as Fig. 2 after quantitation, based on measured k factors available at the time of writing. The composition now seems nearly uniform despite thickness variations. The cursor was expanded to give an average value from a large homogeneous area. We can now see from the scale that Ca is of the order of 40-60% in the lamellae. (The video shows ten composition levels but the plot function can only reproduce five levels.) When the cursor was reduced and placed in the lamellae, the concentration reported was in fact about 45%.

References

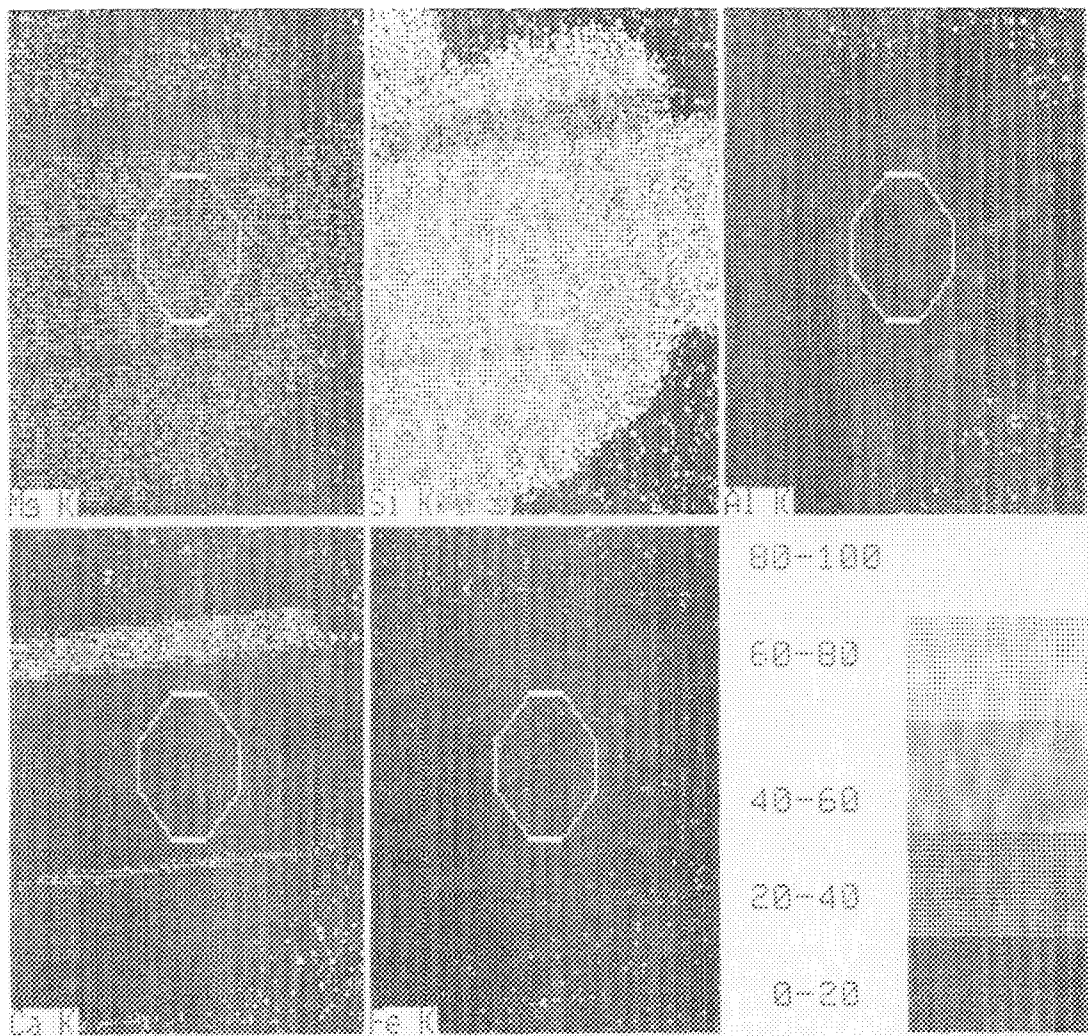
1. J. F. Konopka, "An improved calculator for digital image manipulation," *Microbeam Analysis--1987*, 43.
2. R. L. Myklebust et al., "Background correction in electron microprobe compositional

mapping with wavelength-dispersive x-ray spectrometry," *Microbeam Analysis--1987*, 25.

3. G. Cliff and G. W. Lorimer, "Quantitative analysis of thin metal foils using EMMA--4, the ratio technique," *Proc. 5th European Congress on Electron Microscopy*, Bristol, 1972, 140.

4. S. L. Meyer, *Data Analysis for Scientists and Engineers*, New York: Wiley, 1975, 23.

5. D. S. Bright et al., "Concentration-concentration histograms: Scatter diagrams applied to quantitative compositional maps," *Microbeam Analysis--1988*, 18.



Mg=23% Si=66% Ca=01% Fe=07% Al=03%

FIG. 3.--Quantitative x-ray map. Report is average composition inside cursor.

THE EFFECT OF FAST SECONDARY ELECTRONS ON K_{AB} FACTORS AND SPATIAL RESOLUTION

R. Gauvin and G. L'Espérance

Fast secondary electrons (FSE), which result from inelastic scattering of incident electrons, are known to generate a significant number of x rays for light elements and also to degrade the spatial resolution of x-ray microanalysis in thin foils.¹ A Monte Carlo program simulating the generation of FSE in binary systems has been developed to study the effect of composition on K_{AB} factors and spatial resolution. The effect of accelerating voltage and thickness is also presented. A detailed description of the program will appear elsewhere.²

Description of the Monte Carlo Program

Relativistic Rutherford cross sections are used³ to describe elastic collisions. Each time an elastic collision occurs, the elastic cross sections are weighted with composition and a random number uniformly distributed between zero and one is used to determine which element interacts with the incoming electron. Relativistic Moller cross sections are used⁴ to describe inelastic collisions. Each time a primary electron suffers an inelastic collision, a secondary electron is generated and its trajectory is computed until it escapes the specimen or its energy is smaller than the smallest critical ionization energy E_c .

The energy of the FSE is obtained from

$$R = \frac{\int_{\epsilon_c}^{\epsilon} (d\sigma/d\epsilon)_M d\epsilon}{\int_{\epsilon_c}^{0.5} (d\sigma/d\epsilon)_M d\epsilon} \quad (1)$$

where R is a random number between zero and one, ϵ is the normalized energy of the secondary electron relative to that of the primary electron, $(d\sigma/d\epsilon)_M$ is the differential relativistic Moller cross section, and ϵ_c is the cut-off energy. In our program, a value of 0.01 is used. Sol of Eq. (1) gives

$$R = \frac{\frac{1}{1-\epsilon} - \frac{1}{\epsilon} + \alpha\epsilon + \beta \ln\left(\frac{1-\epsilon}{\epsilon}\right) + \gamma}{\gamma + (\alpha/2)} \quad (2)$$

$$\text{where } \alpha = [\tau/(\tau+1)]^2 \quad (3)$$

$$\beta = (2\tau+1)/(\tau+1)^2 \quad (4)$$

The authors are at the Center for Characterization and Microscopy of Materials (OM)², Ecole Polytechnique de Montréal, C.P. 6079, Succ. "A," Montréal, Canada H3C 3A7. This work was supported by grants from the Natural Sciences and Engineering Research Council of Canada and from Le Fond pour la Formation de Chercheurs et L'Aide à la Recherche of Quebec.

$$\gamma = \frac{1}{\epsilon_c} - \frac{1}{1-\epsilon_c} - \alpha\epsilon_c - \beta \ln\left[\frac{1-\epsilon_c}{\epsilon_c}\right] \quad (5)$$

In Eqs. (3) and (4), $\tau = E_0/511$ (keV) where, E_0 is the energy of the primary electrons. Equation (2) has no analytical solution; solving it requires the use of numerical methods, which are time consuming. As a result, the logarithmic term has been expanded into its Taylor series expansion with the second (and higher) terms neglected. The following equation is then obtained:

$$\epsilon = \frac{\Omega - 2 - \beta + \sqrt{(\Omega - 2 - \beta)^2 + 4(\Omega + \alpha - 2\beta)}}{2(\Omega + \alpha - 2\beta)} \quad (6)$$

$$\text{where } \Omega = R[\gamma + (\alpha/2)] - \gamma \quad (7)$$

Results obtained from Eq. (2) and our approximation are shown in Fig. 1. Our approximation slightly increases the initial energy of FSE. Energy loss is computed for FSE only, from Bethe's relativistic equation.⁵ The angles of deflection and emergence of the primary and FSE electrons are computed from the relativistic expressions of Moller.¹

We are particularly interested in x rays generated by FSE and in their effect on K_{AB} factors, which are defined elsewhere.⁶ We compute the ratio $K^* = K_{AB}(e_p^-)/K_{AB}(e_p^- + e_s^-)$, where the $K_{AB}(e_p^-)$ factor is computed for x rays emitted by the primary electrons; and the $K_{AB}(e_p^- + e_s^-)$ factor, for those emitted by primary and secondary electrons. Then

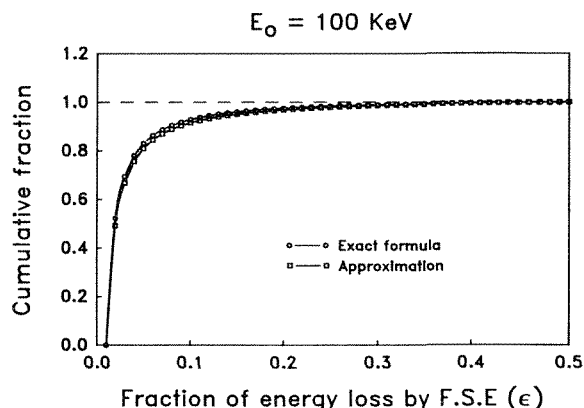


FIG. 1.--Energy distribution of FSE at 100 keV obtained with Eqs. 2 (exact formulation) and 7 (approximation).

$$K^* = \frac{K_{AB}(e_p^-)}{K_{AB}(e_p^- + e_s^-)} = \frac{\Sigma Q_B(E_0) \cdot L_i}{\Sigma Q_A(E_0) \cdot L_i} \cdot \frac{\Sigma Q_A(E_0) \cdot L_i + \Sigma Q_A(E) \cdot LS_i}{\Sigma Q_B(E_0) \cdot L_i + \Sigma Q_B(E) \cdot LS_i} \quad (8)$$

where Q is the ionization cross section, E is the mean energy of the FSE between two collisions separated by a distance LS_i , and L_i is the distance between two collisions for primary electrons. Q is computed from Bethe's relativistic equation with the parameters b_s and c_s measured by Paterson et al.⁷ Since Q should be zero at $U = 1$ ($U = E_0/E_c$), the Bethe expression was modified following Worthington and Tomlin⁸:

$$Q = \frac{6.51 \times 10^{-20} n_s b_s}{E_r E_c} \cdot \left[\ln \frac{E_r/E_c}{(1/C_s) + [1 - (1/C_s)]e^{1-u}} - \ln(1-\beta^2) - \beta^2 \right] \quad (9)$$

where $n_s = 2$ for K lines, β is the ratio of the speed of the electron to the speed of light, and $E_r = mv^2/2$, where m is the rest mass of the electron.

X rays generated by FSE are added in 10 000 boxes 25 Å wide distributed radially as a function of distance from the position of the incident beam. The position of the appropriate box is taken as the mean distance between two successive collisions relative to the origin of the incident electrons. In this way, the diameter corresponding to 90% of the x rays generated by FSE can be computed. When a primary electron is transmitted through the thin film, this electron is summed in the appropriate box corresponding to the radial distance at which it escapes the specimen relative to the origin of the electron beam. In this way, the diameter corresponding to 90% of the transmitted electrons can be computed.

Results

The Monte Carlo code is written in FORTRAN and runs on an IBM 3090 computer with a vector processor. The number of primary electrons simulated was between 200 000 and 5 000 000, yielding 2000 to 14 000 FSE.

Figure 2 shows the ratio K^* as a function of the boron concentration for B-N, B-Fe and B-Nd systems for Kα lines at 100 keV for a 1000 Å-thick foil. The number of x rays generated by the FSE is almost the same for B and N. There is therefore no effect of composition on K_{B-N} factors and the ratio K^* is close to unity. Since FSE do not generate x rays of neodymium and of iron in this case, K_{B-Fe} and K_{B-Nd} are sensitive to boron composition in both systems; the largest differences are 13.2% and 6.7% in B-Fe and B-Nd systems, respectively. It follows that to compute a K_{AB} factor for a system made of a light element and one of a moderate or heavier element, the effects of FSE have to be included. In addition, an exper-

imental K_{AB} factor used to quantify an x-ray analysis in such systems should be obtained from a standard of a composition similar to that of the sample.

Figure 3 shows the effect of thickness on K^* . As the thickness increases, the number of FSE increases and thus the number of B Kα x rays generated by FSE increases. K^* is therefore more sensitive to composition and increases with increasing boron concentration. For Fe Kα x rays, the percentage of x rays generated by FSE was found to be 16.5% at 5000 Å and 5% at 2500 Å for a B-95 wt%Fe alloy. This effect also contributes to increase the sensitivity of the K^* factor to composition. It is advantageous to work at small thicknesses to minimize this effect and that of absorption. In this context, the value of t_c to prevent absorption (computed from the Tixier and Philibert criterion⁹ and the Henke to Ebisu mass absorption coefficients)¹⁰ is equal to 60 Å; even for such a small specimen, 3% of x rays would be generated by FSE.

Since it would be difficult to prepare a foil thinner than 60 Å, the effect of FSE would have to be included to compute K_{AB} factors. In addition, the effect of boron concentration on K^* is significant since usual practical thicknesses range from 500 to 1000 Å. Thus, if experimental K_{AB} factors are to be used, standards of similar composition to that of the sample would have to be used to minimize such an effect.

Figure 4 shows how K^* varies as a function of accelerating voltage. As E_0 increases, the probability for inelastic collisions decreases because the distance between collisions increases for a given thickness. Thus, increasing E_0 decreases the number of FSE, and consequently the effect on the K_{AB} factor decreases.

Figure 5 shows the radial distribution of B Kα x rays generated by FSE and the radial distribution of FSE. The curve of x ray generation of B Kα is similar to a typical $\phi(\rho z)$ curve of x-ray generation in the SEM. Since FSE are emitted almost perpendicularly to the electron beam, this result is not surprising.

Figure 6 shows the diameter of the emission volume corresponding to 90% of the x rays generated by primary and by fast secondary electrons as a function of thickness. It can be seen that FSE considerably decrease the spatial resolution; the best spatial resolution is obtained for the smallest thickness, since the range to escape the specimen is smaller. For B Kα x rays, a linear relationship between the diameter of the volume of emission x rays generated by FSE and sample thickness is observed.

Figure 7 shows the diameter of the volume of emission corresponding to 90% of the x rays generated by the primary and by fast secondary electrons as a function of accelerating voltage for the B Kα line. As E_0 increases, there is a decrease in the number of FSE and thus of the x rays generated by these electrons.

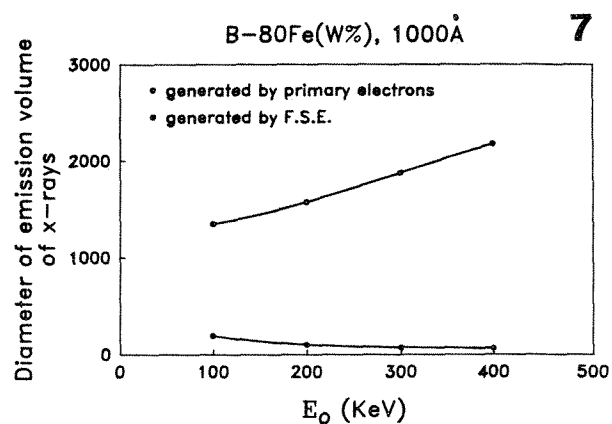
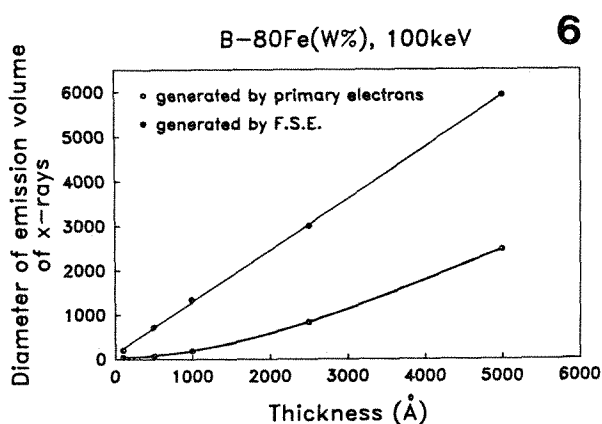
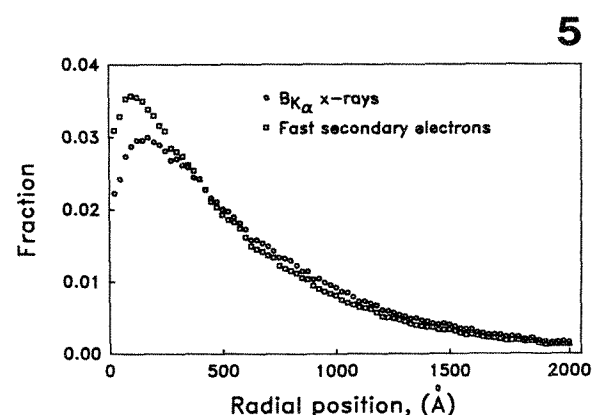
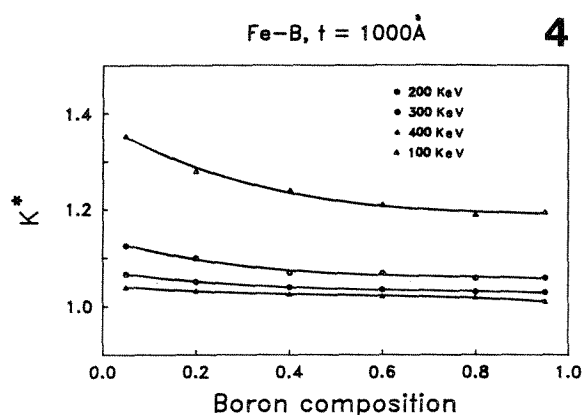
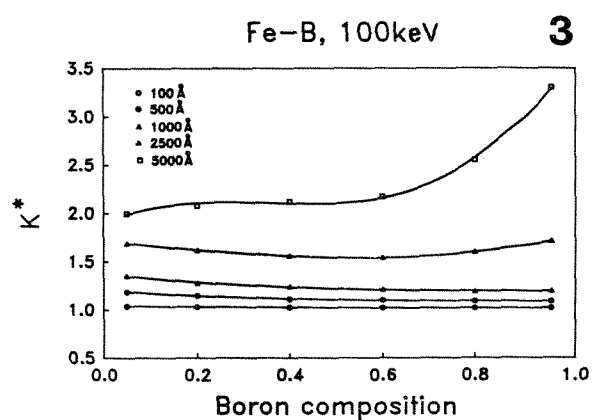
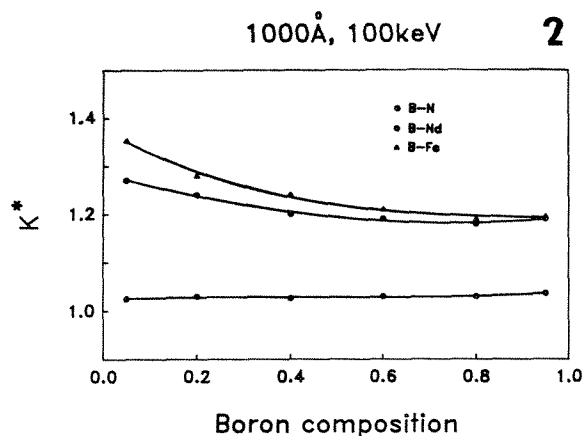


FIG. 2.-- K^* as function of B concentration in B-N, B-Fe, and B-Nd at 100 keV and for 1000Å-thick foil. Density of N has been varied to give value of 2.25 g/cm³ for BN.

FIG. 3.-- K^* as a function of B concentration in the F-FE system for various sample thicknesses. $E_0 = 100$ keV.

FIG. 4.-- K^* as a function of B concentration in the B-Fe system for various accelerating voltages. Sample thickness is fixed at 1000 Å.

FIG. 5.--Radial distribution of FSE and B $K\alpha$ x rays generated by these electrons. B-50wt%Fe, $E_0 = 100$ keV, $t = 1000$ Å.

FIG. 6.--Diameter of emission volume including 90% of x rays generated by primary and by fast secondary electrons as a function of thickness. B-80wt%Fe, $E_0 = 100$ keV.

FIG. 7.--Diameter of emission volume including 90% of x rays generated by primary and fast secondary electrons as a function of accelerating voltage. B-80wt%Fe, $t = 1000$ Å.

However, because the FSE have more energy for high E_0 , their distance between collision increases and the distance they travel in the specimen increases before they can escape from the specimen. Therefore, there is a decrease in the spatial resolution, and since the primary electrons are confined in a smaller volume, this effect is more marked at high E_0 . This relationship can give wrong analysis even if the yield of x rays generated is small.

Conclusions

1. The generation of x rays by FSE for a system with a light element and a medium-to-heavy element has to be included in schemes to compute K_{AB} factors, even for relatively thin samples (500-1000 Å).
2. For K_{AB} factors determined experimentally, the composition of the standards used should be similar to that of the sample analyzed in order to minimize the effect of FSE.
3. FSE also degrade the spatial resolution of x-ray microanalyses, an effect that is larger for thicker samples and for increasing accelerating voltages.

References

1. D. C. Joy, *Analytical Electron Microscopy--1984*, 43.
2. R. Gauvin and G. L'Espérance (in preparation).
3. D. E. Newbury and R. L. Myklebust, *Analytical Electron Microscopy--1981*, 91.
4. K. Murata, D. F. Kyser, and C. H. Ting, *J. Appl. Phys.* 52: 4396, 1981.
5. M. S. Livingston and H. A. Bethe, *Rev. Mod. Physics* 9: 245, 1937.
6. G. Cliff and G. W. Lorimer, *J. Microsc.* 1031: 203-207, 1975.
7. J. H. Paterson, W. A. P. Nicholson, J. N. Chapman, and R. H. Geiss, *Analytical Electron Microscopy--1987*, 96-98.
8. C. R. Worthington and S. G. Tomlin, *Proc. Phys. Soc.* A69: 401, 1956.
9. R. Tixier and J. Philibert, *X-Ray Optics and Microanalysis*, 1969, 180.
10. B. L. Henke and E. S. Ebisu, *Advances in X-Ray Analysis*, New York: Plenum Press, 1974, vol. 17, p. 150.

Scanning Tunneling Microscopy & Related Techniques

STM IMAGING OF BIOLOGICAL STRUCTURE: STATUS AND PROSPECTS

J. A. Panitz

The Scanning Tunneling Microscope (STM), introduced by Binnig and coworkers in 1980, has revolutionized our ability to observe and interpret the structure of extended semiconductor surfaces on an atomic scale.¹⁻³ More recently, the STM has generated considerable excitement as a new imaging modality for visualizing native biological molecules on an atomic scale.⁴ Despite initial optimism for applying this imaging technique to problems in structural biology, progress has been slow and limited by imperfect understanding of the imaging process.⁵ This paper discusses the potential of the STM to visualize native biological structure on an Ångström scale by summarizing a recent review of imaging limitations associated with the poor electrical conductivity, and the large size of many biological objects.⁶

The Scanning Tunneling Microscope

The Scanning Tunneling Microscope (STM) produces a three-dimensional representation of surface morphology by scanning a sharp, needle-like electrode in a raster pattern, several Ångströms above a conducting surface. A bias voltage applied between this electrode (called a *tip*) and the surface causes a tunneling current to flow between them. The tunneling current is monitored during a scan, and a feedback circuit adjusts the vertical position of the tip to keep the current at a constant preset level. The tunneling probability at the surface is mapped by a plot of the position of the tip (X-Y) as a function of tip elevation (Z). A computer can be used to generate a gray-scale image in which tip elevation corresponds to image brightness. Suitable hidden-line and shadowing algorithms can be applied to view the image, in perspective, from any angle. The resulting image corresponds to the real-space morphology of the surface if the tunneling probability faithfully reflects the morphology of the surface. STM imaging can be performed in air or in liquids because tunneling electrons will not ionize molecules in the ambient environment.⁷

Image Resolution

Atomic resolution imaging in the STM requires precise spatial localization of the tunneling current. To a first approximation, image resolution cannot be better than the size of the tip apex. An STM tip is usually prepared by grinding, by cutting, or by etching of a small-diameter wire of an appropriate material. Atom-

ic resolution imaging in the STM presupposes that a tip has at least one stable asperity at its apex that further restricts tunneling to a subnanometer region of its surface during a scan. When the apex of a tip attempts to follow a large change in surface morphology, the relative position of the tunneling asperity and the surface will not necessarily remain constant. Tunneling from a uniquely defined asperity at the apex cannot be guaranteed because it is not possible to preserve the relative orientation of the tip apex and the surface during a scan. If two or more regions of the tip apex contribute to the tunneling current, multiple displaced images of the surface can be recorded in a single STM image.

Abrupt changes in the contour of an extended object are difficult to record in an STM image because the tip has *tunnel vision*. In essence, a tip "sees" only a small, well-defined region of the surface which is opposite the tunneling region at its apex. As a tip encounters an abrupt change in surface elevation during a scan, tunneling is initiated between the tip apex and the closest region on the opposite surface. Since the tunneling current is kept constant by a feedback loop, the elevation of the tip is forced to change as the lateral distance between the tip and the opposite surface decreases. As a result, a continuous movement of the tip toward an object in a lateral direction can be incorrectly recorded as a continuous change in the *local elevation* of the object. If the scan speed is large, the tip may contact or embed itself within the object before it moves above it.

In general, an STM image of a large conducting object resembles the object, but lacks the subtle details that define its true size and shape. The severity of the problem is demonstrated in Fig. 1, which shows an STM image of gold clusters deposited on a gold surface in high vacuum.⁸ Although the clusters have a uniform diameter (~ 2 nm) they do not appear spherical in shape as would be expected from thermodynamic arguments of cluster formation. The clusters in Fig. 1 are elongated in a vertical direction. Individual gold atoms within a cluster are not resolved. Both features are consistent with the imaging distortions discussed above.

Conductivity Limitations

An STM image is produced when a tunneling current flows in an external circuit. Many biological structures of interest are much larger than the nominal separation of the tunneling electrodes ($d \leq 2$ nm). To observe these structures in the STM, electrons must first

The author is at the Department of Physics and Astronomy, The University of New Mexico, Albuquerque, NM 87131.

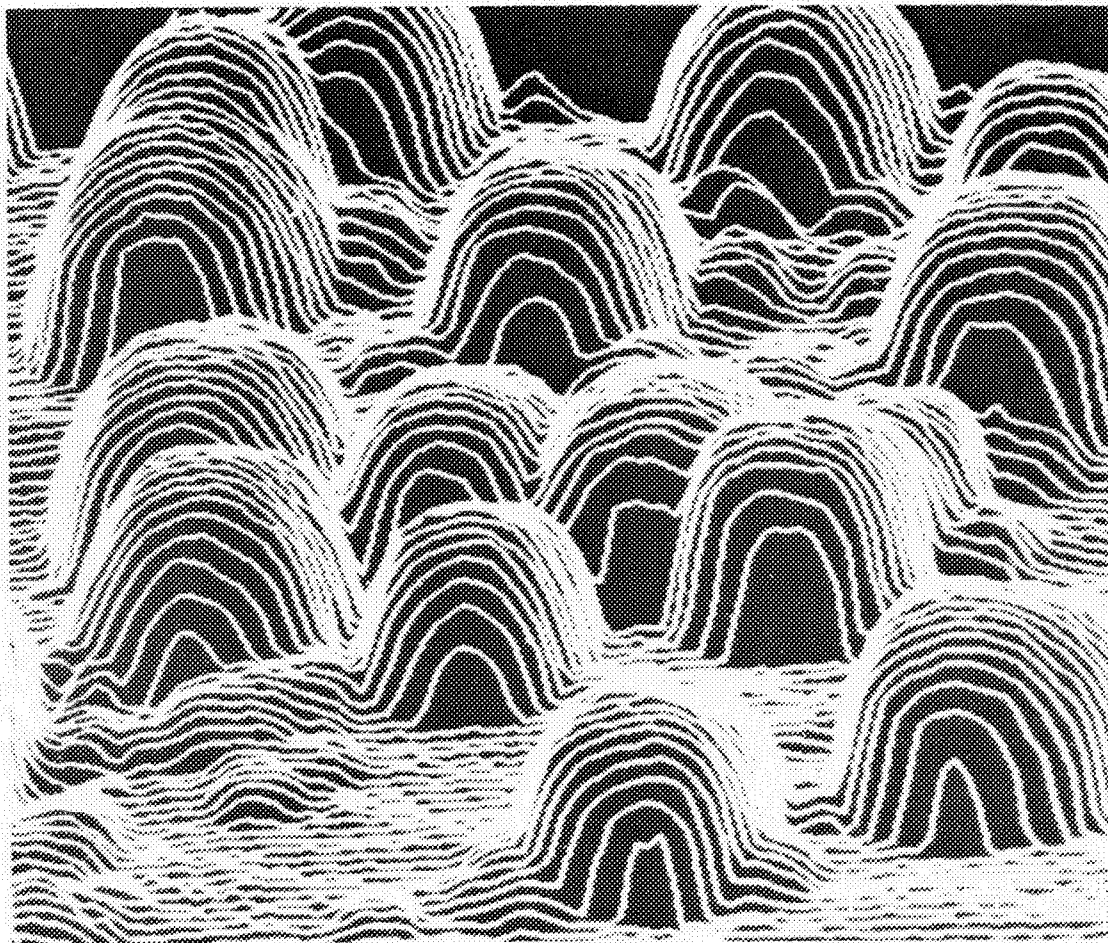


FIG. 1.--Gold clusters deposited on gold surface imaged in STM. Imaged area is 44×44 nm. (Figure courtesy of R. Reifenberger, Purdue University.)

tunnel into the biological structure, then conduct through the bulk of the structure to the substrate below. To observe changes in the morphology of a biological structure as it is scanned, conduction must occur in a time short compared with the time required to scan the smallest feature to be resolved. Although ionic conduction in biological systems is well known, the conduction properties of electrons in biological material is not well documented. At the present time, the only successful STM images of large biological objects have been taken after they had been coated or replicated in metal to circumvent the conductivity problem.

Figure 2 shows an STM image of T7 virus particles deposited on a gold surface.⁹ The virus particles were coated with a thin layer of platinum-carbon, evaporated on the surface at cryogenic temperatures in high vacuum. Figures 2(b) and (c) show TEM images of the same virus deposited on a thin carbon film after rotary shadowing with tungsten. The STM image and the TEM images are similar in appearance, but the STM image lacks the fine detail of its TEM counterparts. For example, STM images do not show the tail of the virus particle, which is clearly delineated in TEM images. STM images of recA-DNA complexes resemble their counterparts in the TEM, but lack expected detail on

an atomic scale.^{10,11} At the present time TEM and STM images of biological objects exhibit a comparable resolution of ~ 1 nm, limited by the inherent imaging constraints of each technique.

DNA Imaging

The first successful tunneling measurements were made in 1961. They used a 1-2nm-thick insulator as a spacer to separate the tunneling electrodes.¹² If an insulating molecule of comparable thickness fills the gap between the tip and the surface in an STM, tunneling should also occur. Native DNA is a suitable candidate for imaging in the STM because it has a nominal diameter of ~ 2 nm. Recently, STM images of uncoated, double-stranded DNA (deposited on graphite) have been obtained in laboratory ambient.¹³ A variation in the pitch of the helix (between 2.7 and 6.3 nm) was extracted from a highly processed image, and was interpreted in terms of surface and dehydration forces, and a possible interaction with ionic species. Unfortunately, STM images are difficult to interpret because contrast is generated by variations in the electron tunneling probability at the surface. The contrast in an STM image actually reflects the local electronic density of states encountered during

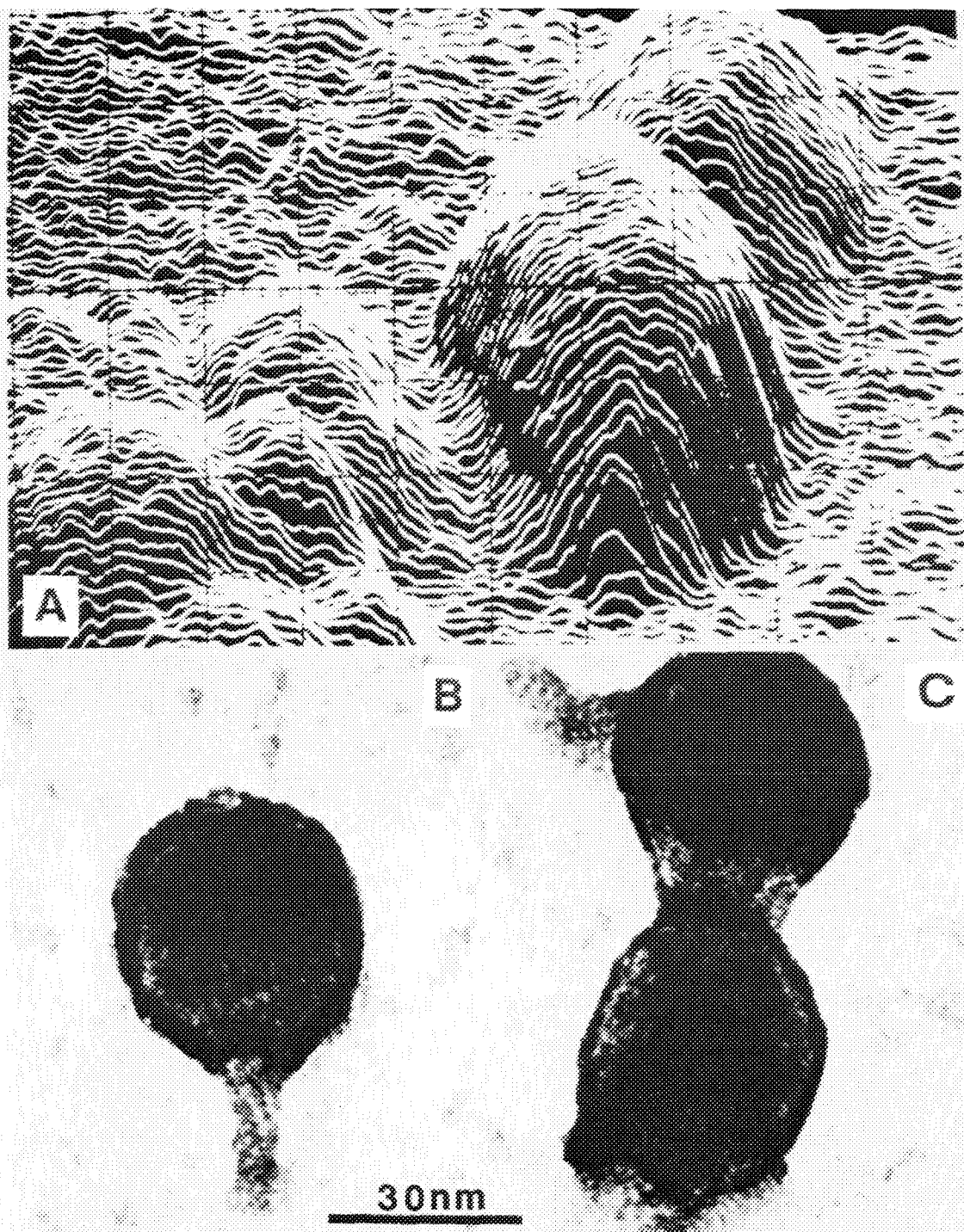


FIG. 2.--Virus particles imaged in STM and in TEM. (a) STM image of T7 virus particles taken in air. Virus particles were deposited on gold surface and coated with thin, platinum-carbon film at cryogenic temperatures. (b)-(c) TEM images of T7 virus particles. Virus particles were deposited on thin carbon film and rotary shadowed with tungsten.

a scan, not necessarily the position of individual atoms or the real-space morphology of an imaged species.

Conclusions

The challenge of biological imaging in the STM is to interpret biological structure correctly in terms of image contrast. Double-blind experiments may be needed to avoid manipulating images to reveal structure that only exists in the mind of the investigator.¹⁴ The problem with image interpretation is underscored by field-electron emission imaging experiments in which tunneling electrons produced "convincing" images of small organic molecules that actually reflected the electronic interaction of the molecules with the surface, and not their real-space morphology.¹⁵ As STM imaging attempts progress, and the tunneling process in biological structures is better understood, the correlation of image contrast with real-space morphology may become routine. Progress will be marked by the use of the STM as a complement to other biochemical, biophysical, and imaging techniques in studies of biological importance.

References

1. G. Binnig, et al., "Surface studies by STM," *Phys. Rev. Letts.* 49: 57, 1982.
2. J. A. Golovchenko, "The tunneling microscope: A new look at the atomic world," *Science* 232: 48, 1986.
3. P. K. Hansma and J. Tersoff, "Scanning tunneling microscopy," *J. Appl. Phys.* 61: R1, 1987.
4. T. P. Beebe et al., "Direct observation of DNA structures with the scanning tunneling microscope," *Science* 243: 370, 1989.
5. P. K. Hansma et al., "Scanning tunneling microscopy and atomic force microscopy application to biology and technology," *Science* 242: 209, 1988.
6. J. A. Panitz, "Scanning tunneling microscopy: Status and prospects for imaging biological structure on an Angstrom scale," in D. L. Stocum, Ed., *The Cellular and Molecular Biology of Pattern Formation*, New York: Oxford (in press).
7. R. Sonnenfeld and P. K. Hansma, "Atomic-resolution microscopy in water," *Science* 232: 11, 1986.
8. T. Castro et al., "Studies of individual nanometer-sized metallic clusters using scanning tunneling microscopy, field emission, and field ion microscopy," *J. Vac. Sci. and Technol.* (in press).
9. R. Garcia et al., "Imaging of metal-coated biological samples by scanning tunneling microscopy," *Ultramicroscopy* (in press).
10. M. Amrein et al., "Scanning tunneling microscopy of recA-DNA complexes coated with a conducting film," *Science* 240: 514, 1988.
11. M. Amrein et al., "Scanning tunneling microscopy of uncoated recA-DNA complexes," *Science* 243: 1708, 1989.
12. J. C. Fisher and I. Giaever, "Tunneling through thin insulating films," *J. Appl. Phys.* 32: 172, 1961.
13. T. P. Beebe et al., "Direct observation of DNA structures with the scanning tunneling microscope," *Science* 243: 370, 1989.
14. J. K. Mackenzie, "Materializing ghosts from random noise," *Micron* 11: 391, 1980.
15. A. J. Melmed and E. W. Müller, "Study of molecular patterns in the field emission microscope," *J. Chem. Phys.* 29: 1037, 1958.

PLATINUM THIN-FILM ROUGHNESS MEASUREMENTS BY SCANNING TUNNELING MICROSCOPY

I. H. Musselman and P. E. Russell

Scanning tunneling microscopy (STM) has been used to characterize the surface roughness of thin Pt films. The deposition of thin metal films, such as Pt, on insulating samples provides a necessary conducting layer for electron tunneling in order to obtain topographic information from these surfaces. However, such thin films must provide a minimal contribution to the structure of the underlying surface of interest. In addition to the use of thin metal films for imaging insulating samples, the characterization of these films by STM can provide an understanding of the film deposition and growth process. This knowledge will in turn aid us in preparing thin films with small grain features suitable for coating specimen surfaces for scanning tunneling microscopy and high-resolution scanning electron microscopy. The results of this study show that thin Pt films deposited on a native silicon oxide have a thickness window for minimum surface roughness, whereas films deposited on atomically flat graphite crystals show no similar trend.

Several groups have studied the structure of thin metal films by scanning tunneling microscopy. Jaklevic et al. have imaged a variety of insulating samples by STM after coating them with thin continuous gold films.¹ They have demonstrated a lateral resolution of $\sim 10 \text{ \AA}$ without the appearance of structure contributed by the Au films for thicknesses ranging from 20 to 100 \AA . Images of 1000 \AA -thick gold films, which have been imaged in air and under paraffin oil, show features $\sim 50 \text{ \AA}$ in height and $\sim 200 \text{ \AA}$ in width.² Garcia et al. proposed a standardization procedure, that of "granular roughness" and "micro-roughness," for the characterization of surface structure in the micrometer and sub-micrometer ranges.³ The roughness of 500 \AA -thick silver films vaporized on fire polished quartz⁴ and of microcrystalline Ag and nanocrystalline silicon surfaces⁵ have been investigated. The surface roughness of single-layer and multilayer x-ray reflecting optics have been studied by STM.⁶ The images obtained from a 1500 \AA -thick Pt single-layer mirror, made by sputtering Pt onto optical glass flats, showed large irregularly shaped hills with lateral

dimensions of 100-1000 \AA . The images typically exhibited an rms roughness of 10 \AA . Ritter et al. have directly observed the nucleation and growth process of adsorbates on Pt (100).⁷ Homogeneous and heterogeneous nucleation were observed for other adsorbates.

In the experiments described below, Pt films of various thicknesses were deposited on (100) single-crystal silicon (0.01 ohm-cm resistivity). (Although Cr and Ta are believed to form thinner continuous films,⁸ unlike Cr and Ta, Pt does not form a native surface oxide which would interfere with electron tunneling in air.) It was desirable to determine which thickness of Pt film contributed least to the surface roughness of the underlying substrate in order to provide guidance for the preparation of thin Pt films on future substrates of this type. However, the silicon substrate could not be imaged by STM because of the presence of a native surface oxide. It was therefore desirable to study a second sample system, that of Pt deposited on highly oriented pyrolytic graphite (HOPG), a conducting substrate. From this sample system, it was possible to assess the contribution of substrate roughness with respect to the roughness of the deposited Pt film. In addition, information could be obtained about the effect that different substrates, such as silicon and HOPG, have on film roughness.

Experimental Section

Sample Preparation. Thin platinum films were made by ion beam sputter deposition using an EM-Microsputter with B12 dual ion guns (Ion Tech Ltd., England). This coating technique has proved to produce films with fine grain structure.^{9,10} The HOPG substrates were prepared using a simple tape-pull cleave technique to expose a flat basal plane. The substrates, Si and HOPG, were secured on a rotating stage such that they uniformly collected the sputtered platinum material without being directly exposed to the plasma. With the exception of deposition time, identical conditions (6 kV ultrapure Ar beam, 0.3 mA each water-cooled gun, vacuum of $\sim 10^{-5}$ Torr) were used to prepare three thicknesses of Pt films; two sets of three films each were prepared on Si substrates and one set on HOPG. The average mass thicknesses of the films were determined to be 25, 50, and 100 \AA by use of an Edwards FTMS Digital Film Thickness Monitor based on a quartz crystal microbalance.

STM Analysis. All images were acquired in air with a Nanoscope 1 (Digital Instruments, Inc.) scanning tunneling microscope with a long-range piezoelectric tube scanner ($X = 300$

The authors are with the Department of Materials Science and Engineering and Precision Engineering Center, North Carolina State University, Raleigh, NC 27695. They gratefully acknowledge the aid of Hoechst Celanese Research Division, especially Linda Sawyer, Rong-Tsang Chen, and Tom Bruno, in providing financial support and supplying the samples for this project. This study was also supported by NSF grant DMR-8657813.

$\text{\AA}/V$, $Y = 270 \text{\AA}/V$, $Z = 100 \text{\AA}/V$). This system was modified to include digital scanning and data acquisition by use of an 80386-based PC/AT computer. Platinum/iridium tips fabricated by simple cutting were used for imaging.

The images were acquired in the constant-current mode at a 2 nA set current with the sample biased positively 20 mV with respect to the tip. Two different areas of 25 and 50 \AA -thick film, as well as the HOPG substrate and three different areas of 100 \AA -thick film were examined. The 25 \AA Pt film deposited on Si in the second sample set was believed to be discontinuous as it was difficult to maintain a constant tunneling current. In addition, electron tunneling on the silicon substrate was prohibitive because of the presence of a thick surface oxide layer. Therefore, images were not acquired from either of these samples.

For each sample area, a large image ($1.6 \times 2.0 \text{ }\mu\text{m}$) was initially obtained in order to choose a $2000 \times 2000 \text{\AA}$ region free from particulate debris from which to obtain the remainder of the images. Within the chosen $2000 \times 2000 \text{\AA}$ region, one $2000 \times 2000 \text{\AA}$ image (101×101 points collected in 20\AA steps) and four $500 \times 500 \text{\AA}$ images (101×101 points collected in 5\AA steps) were acquired after which the $2000 \times 2000 \text{\AA}$ image was reacquired. Images were obtained twice to insure reproducibility. All total, four $2000 \times 2000 \text{\AA}$ and eight $500 \times 500 \text{\AA}$ images were acquired from each area of each sample.

Data Reduction. The surface roughness R_a was computed for each image. Average roughness is defined as the average of the absolute value of the difference between the height of z-position of each experimental data point and the height of the corresponding point determined by fitting a least-squares plane to 1/10 of the data points in the image. A fit to the entire data set did not significantly alter the resulting R_a value.

Results

Image Appearance. The appearances of the images acquired from the Pt thin films are summarized below. For both the 25 and 50 \AA films on Si, the majority of the features observed were approximately 50-250 \AA in diameter and ranging from ~ 5 to 25 \AA in height. Images acquired from the 100 \AA Pt film on Si showed some features similar to those observed in the images acquired from the 25 and 50 \AA films. In addition, areas of larger agglomerates, ~ 200 to 500 \AA in diameter and up to 80 \AA in height, with considerable surface structure were observed.

Images acquired from the HOPG substrate were very smooth. The imaging conditions used in this study to collect data for roughness measurements ($\geq 5 \text{\AA}$ steps between data points and relatively low gain on the feedback loop) precluded the obtaining of atomic resolution. However, an image of freshly cleaved HOPG, obtained with a different STM in our laboratory, is shown in Fig. 1, clearly indicating an atomically smooth structure. A much finer surface

was observed for the 25 and 50 \AA Pt films deposited on HOPG as compared with those deposited on Si. The lateral dimensions of the features were $< 100 \text{\AA}$ and typically $< 20 \text{\AA}$ high. As with the 100 \AA Pt film on Si, larger agglomerates, ~ 200 to 250 \AA in diameter, were observed for the 100 \AA Pt film deposited on HOPG. However, the vertical dimensions of these features were still less than 20 \AA . Examples of images obtained from the 50 \AA Pt films deposited on Si and HOPG are illustrated in Fig. 2.

Intrasample Variation in Roughness. Intra-sample variation in surface roughness refers to observations made among different imaged areas of a given sample. The values of average surface roughness R_a computed separately for the images acquired from each sample area are summarized in Table 1. From these data, intra-sample variation in surface roughness was assessed by applying the Student t-test at the 95% confidence level. Comparisons were made for both image dimensions, i.e., 2000×2000 and $500 \times 500 \text{\AA}$. For each of the three Pt film thicknesses deposited on Si in the first sample set (Table 1a), the Student t-test was able to distinguish among the average surface roughness of the different areas measured. Intuitively, this difference appears to be significant only for the 100 \AA Pt film where the largest difference in surface roughness between area 1 and area 3 may actually represent that contributed by an additional two to three atoms in the vertical dimension. The apparent differences observed for the 25 and 50 \AA films represent less than one and approximately one atom, respectively. For the second set of Pt films deposited on Si (Table 1b), the average surface roughness calculated from the images acquired from two areas of the 50 \AA Pt film were not differentiated at the 95% confidence level. For the 100 \AA Pt film, however, area 1 was distinguished from areas 2 and 3 by a difference of 4 to 6 \AA in the vertical dimension, representing approximately two atomic layers. According to the Student t-test, the areas sampled within each thickness of Pt film deposited on HOPG could not, in general, be differentiated (Table 1c). Any observed differences in roughness, as for example in the $500 \times 500 \text{\AA}$ images for the 25 \AA Pt film and the $2000 \times 2000 \text{\AA}$ images for the 100 \AA Pt film, are not meaningful as they represent that contributed by less than one atom.

Sample-to-sample Variation in Roughness. Although the roughness values are comparable for some areas of different samples as observed in the first sample set (Table 1a), e.g., sample 1 area 1, sample 2 area 2, and sample 3 area 3, a measure of sample-to-sample variation in surface roughness can be obtained by averaging the roughness values for the areas of each sample. The overall average roughnesses of the samples in each set, presented in Table 2, were compared using the Student t-test at the 95% confidence level. With the exception of the $2000 \times 2000 \text{\AA}$ images for the 25 and 100 \AA Pt films in the first sample set, the results indicate that the surface roughness computed for

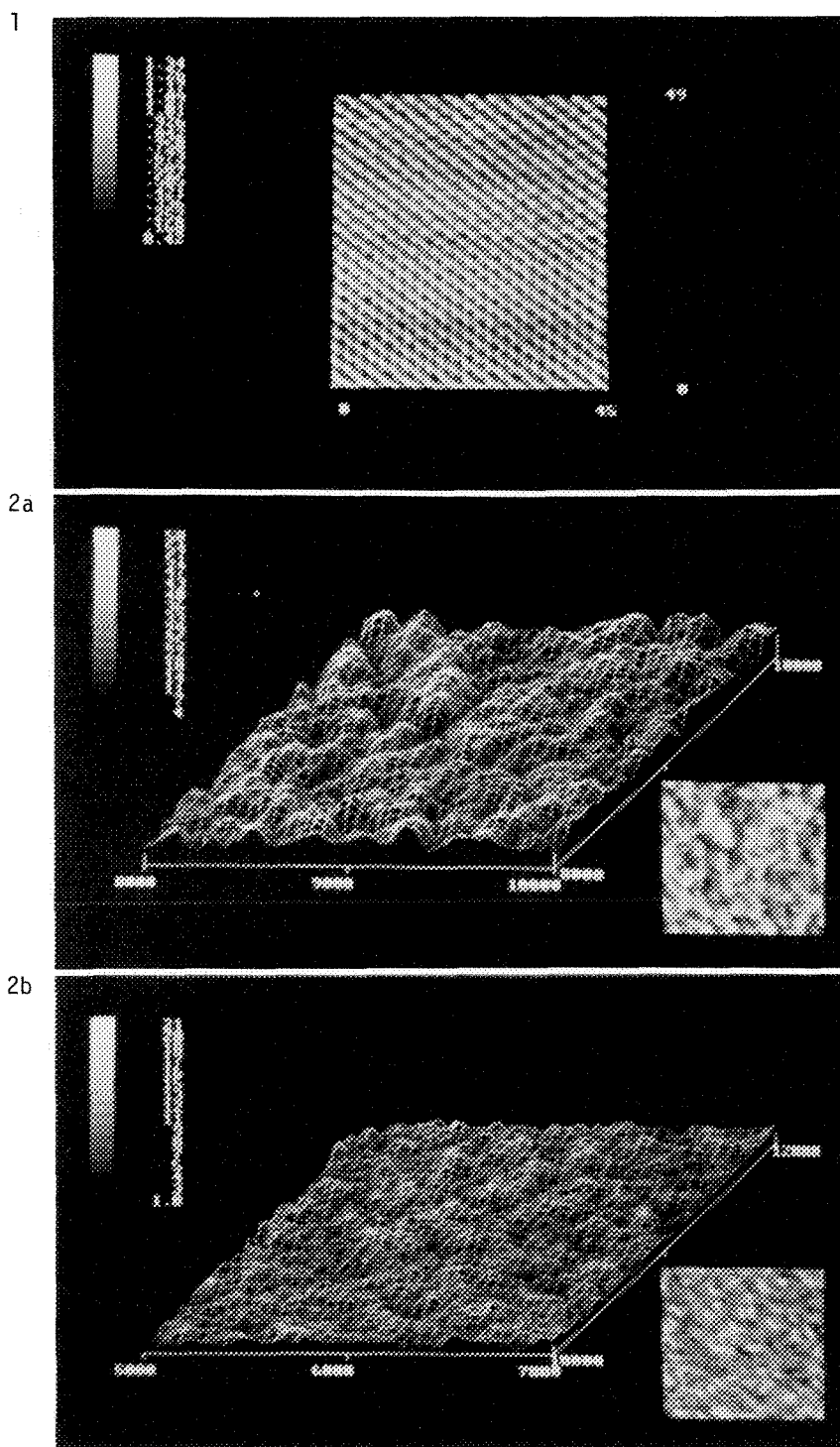


FIG. 1.--STM image ($45 \times 49 \text{ \AA}$) of freshly cleaved highly oriented pyrolytic graphite (HOPG) showing atomically smooth structure. (Courtesy of David Grigg, Precision Engineering Center, North Carolina State University.)

FIG. 2.--(a) STM image ($2000 \times 2000 \text{ \AA}$) acquired from 50 \AA Pt film deposited on silicon substrate. (b) STM image ($2000 \times 2000 \text{ \AA}$) acquired from 50 \AA Pt film deposited on highly oriented pyrolytic graphite (HOPG) substrate.

TABLE 1.--Average surface roughness (\AA). (a) Pt films on Si, first sample set; (b) Pt films on Si, second sample set; (c) Pt films on HOPG.

a				b				c			
Sample	Image Size	N*	R _a	Sample	Image Size	N*	R _a	Sample	Image Size	N*	R _a
#1, 25 Å Pt area 1	2000 X 2000 500 X 500	4	5.4 ± 0.4**	#1, 25 Å Pt	Constant tunneling current could not be maintained. Images were not acquired			#1, substrate area 1	2000 X 2000 500 X 500	4	0.6 ± 0.1**
		8	3.9 ± 0.3								
		8	6.9 ± 0.5	#2, 50 Å Pt area 1	2000 X 2000 500 X 500	4	5.7 ± 2.0**	area 2	2000 X 2000 500 X 500	4	0.8 ± 0.2
		8	6.7 ± 0.7								
#2, 50 Å Pt area 1	2000 X 2000 500 X 500	4	2.2 ± 0.3	area 2	2000 X 2000 500 X 500	4	5.0 ± 1.2	#2, 25 Å Pt area 1	2000 X 2000 500 X 500	4	2.6 ± 0.1
		8	2.2 ± 0.4								
area 2	2000 X 2000 500 X 500	4	5.5 ± 0.5	#3, 100 Å Pt area 1	2000 X 2000 500 X 500	4	10.8 ± 1.7	area 2	2000 X 2000 500 X 500	4	2.3 ± 0.6
		8	4.4 ± 0.2								
#3, 100 Å Pt area 1	2000 X 2000 500 X 500	4	11.4 ± 2.2	area 2	2000 X 2000 500 X 500	4	5.8 ± 1.4	#3, 50 Å Pt area 1	2000 X 2000 500 X 500	4	2.4 ± 0.7
		8	13.6 ± 6.3								
area 2	2000 X 2000 500 X 500	4	8.1 ± 1.0	area 3	2000 X 2000 500 X 500	4	6.8 ± 1.4	area 2	2000 X 2000 500 X 500	4	3.3 ± 0.2
		8	7.0 ± 1.1								
area 3	2000 X 2000 500 X 500	4	5.4 ± 0.3	* N = number of measurements ** 1σ				#4, 100 Å Pt area 1	2000 X 2000 500 X 500	4	2.3 ± 0.2
		8	4.0 ± 0.4								
* N = number of measurements ** 1σ								area 2	2000 X 2000 500 X 500	4	2.8 ± 0.3
								area 3	2000 X 2000 500 X 500	4	2.0 ± 0.2
								* N = number of measurements ** 1σ			

the Pt films deposited on Si, are significantly different as a function of film thickness. For both sets of Pt films deposited on Si, the average surface roughness was least for the 50 \AA film with increasing roughness for the 25 \AA film and a larger increase in roughness for the 100 \AA Pt film. The Pt films of all thicknesses deposited on highly oriented pyrolytic graphite were significantly rougher than the substrate (Table 2). However, no sample-to-sample variation in surface roughness was observed for the 25, 50, and 100 \AA Pt films on HOPG.

From these results, it is clear that the 50 \AA Pt film, as measured by the quartz thickness monitor, deposited on Si, exhibits less roughness than the 25 and 100 \AA Pt films. Therefore, for the deposition of Pt on this particular substrate, there is a window of film thickness over which the films are smoothest. In addition, sample-to-sample variation in surface roughness as a function of Pt film thickness is observed only for the Si substrate. The surface roughness measured for various Pt films deposited on HOPG are indistinguishable. Since identical experimental conditions were used to deposit the Pt films on both substrates, the above results suggest that the substrate has contributed significantly to the quality of the deposited thin film. Notably, the two substrates used in this study are considerably different. The silicon surface oxide is an insulating amorphous film, whereas highly oriented pyrolytic graphite is a single-crystal conductor.

The differences in sample-to-sample variation of Pt film roughness observed for the two substrates can be discussed in terms of a nucleation and growth model described by Peters.⁸ The first phase of film growth, known as "step

TABLE 2.--Average surface roughness of Pt films (\AA).

Sample	Image Size	N*	R_a	
Silicon substrate, first sample set				
#1, 25 Å Pt	2000 X 2000	8	6.2	\pm 0.9*
	500 X 500	16	5.3	\pm 1.6
#2, 50 Å Pt	2000 X 2000	8	3.9	\pm 1.8
	500 X 500	16	3.3	\pm 1.2
#3, 100 Å Pt	2000 X 2000	12	8.3	\pm 2.9
	500 X 500	24	8.2	\pm 5.4
Silicon substrate, second sample set				
#1, 25 Å Pt	Constant tunneling current could not be maintained. Images were not acquired			
#2, 50 Å Pt	2000 X 2000	8	5.3	\pm 1.6
	500 X 500	16	3.5	\pm 0.6
#3, 100 Å Pt	2000 X 2000	12	7.8	\pm 2.6
	500 X 500	24	7.1	\pm 2.9
HOPG substrate				
#1, substrate	2000 X 2000	8	0.7	\pm 0.2
	500 X 500	16	0.7	\pm 0.2
#2, 25 Å Pt	2000 X 2000	8	2.5	\pm 0.5
	500 X 500	16	2.0	\pm 0.3
#3, 50 Å Pt	2000 X 2000	8	2.8	\pm 0.7
	500 X 500	16	2.3	\pm 0.6
#4, 100 Å Pt	2000 X 2000	12	2.4	\pm 0.4
	500 X 500	24	2.3	\pm 0.5

* N = number of measurements

decoration," is characterized by metal atom or cluster nucleation at nucleation sites on the substrate surface. In the second phase, known as "particle decoration," metal atoms add to existing nuclei contributing to aggregate growth. Eventually these aggregates coalesce to produce a continuous film.

The number, location, and size of these

nucleation sites, and the recognition of these sites by other atoms, are a function of the substrate and deposited metal. Metals tend to accumulate at sites of high binding energy but low surface energy. On crystalline materials, these sites correspond to lattice steps whereas for amorphous materials they correspond to elevated fine structures or particles. In the deposition of Au on NaCl, Bassett observed that nuclei form in large numbers along steps.¹¹ However, for parts of the crystal free from steps, the nuclei were randomly dispersed.

Perhaps the observed differences in the roughness of Pt films on silicon and HOPG substrates can be attributed to a difference in the distribution of these nucleation sites. For image acquisition from Pt films on HOPG substrates, sample areas free from atomic steps were deliberately chosen. Therefore, it is likely that random nucleation is occurring leading to the formation of smooth, uniform Pt films which exhibit neither intrasample nor sample-to-sample variation in roughness over a range of film thicknesses. At the other extreme, intrasample and sample-to-sample variations in roughness, which were observed for Pt film deposition on silicon substrates, can be accounted for by the uncontrolled nucleation site distribution on the native silicon oxide.

Conclusions

Scanning tunneling microscopy has been used to study the roughness of thin platinum films of varying thicknesses deposited on two different substrates, silicon and highly oriented pyrolytic graphite. For deposition on silicon (bearing a native oxide), a narrow thickness window exists for the formation of a smooth, continuous film. Within the range of experimental film thicknesses (25 to 100 Å), this window was not present for the HOPG substrate. These differences are attributed to the nucleation and growth differences induced by substrate structure.

In addition to coating insulating samples for STM imaging, thin metal films are often used to coat samples for scanning electron microscopy in order to enhance the contrast of individual surface features and to provide electrical conductivity for nonconducting samples. Scanning tunneling microscopy, with its high lateral and vertical resolution, provides new technology that will be instrumental in understanding the nucleation and growth of ultrathin films to be used for coating specimens for high-resolution scanning electron microscopy and scanning tunneling microscopy.

References

1. R. C. Jaklevic, E. Elie, Weidian Shen, and J. T. Chen, "Application of the scanning tunneling microscope to insulating surfaces," *J. Vac. Sci. Technol.* A6: 448-453, 1988.
2. B. Drake, R. Sonnenfeld, J. Schneir, P. K. Hansma, G. Slough, and R. V. Coleman, "Tunneling microscope for operation in air or fluids," *Rev. Sci. Instrum.* 57: 441-445, 1986.
3. N. Garcia, A. M. Baro, R. Miranda, H. Rohrer, C. Gerber, R. Garcia Cantu, and J. L. Pena, "Surface roughness standards, obtained with the scanning tunneling microscope operated at atmospheric air pressure," *Metrologia* 21: 135-138, 1985.
4. H. Raether, "Roughness on silver films," *Surface Science* 140: 31-36, 1984.
5. J. K. Gimzewski and A. Humbert, "Scanning tunneling microscopy of surface microstructure on rough surfaces," *IBM J. Res. Develop.* 30: 472-477, 1986.
6. M. Green, M. Richter, J. Kortright, T. Barbee, R. Carr, and I. Lindau, "Scanning tunneling microscopy of x-ray optics," *J. Vac. Sci. Technol.* A6: 428-431, 1988.
7. E. Ritter, R. J. Behm, G. Potschke, and J. Wintterlin, "Direct observation of a nucleation and growth process on an atomic scale," *Surface Science* 181: 403-411, 1987.
8. K.-R. Peters, "Metal deposition by high-energy sputtering for high magnification electron microscopy," in J. K. Koehler, Ed., *Advanced Techniques in Biological Electron Microscopy III*, Berlin: Springer-Verlag, 1986, 101-166.
9. T. Sarada, L. C. Sawyer, and M. I. Ostler, "Three dimensional structure of Celgard microporous membranes," *J. Memb. Sci.* 15: 97-113, 1983.
10. C. S. Clay and G. W. Peace, "Ion beam sputtering: An improved method of metal coating SEM samples and shadowing CTEM samples," *J. Microsc.* 123: 25-34, 1981.
11. G. A. Bassett, "A new technique for decoration of cleavage and slip steps on ionic crystal surfaces," *Phil. Mag.* 3: 1042-1045, 1958.

MICRO AND NANOFABRICATION WITH A COMBINED FOCUSED ION BEAM/SCANNING TUNNELING MICROSCOPE

J. G. Pellerin, G. M. Shedd, D. P. Griffis, and P. E. Russell

The focused ion beam (FIB) has exhibited uncommon versatility as a tool for microfabrication. Its small beam diameter enables the FIB to perform micron-scale modifications (e.g., implant ions or remove material) without the need for a mask to protect adjacent regions. The inherent microscopic capability of the FIB can be used to advantage for locating features of interest or to provide in situ visual feedback during microfabrication. The scanning tunneling microscope (STM) is known primarily for its atomic resolution images of surfaces, but it is attracting increasing attention as a possible tool for nanofabrication. We have combined FIB and STM in a system that will allow us to induce surface modifications ranging in size from nanometers to micrometers, and permits us to image regions of from square nanometers to square micrometers.

Background

FIB Micromachining. Many potential applications of the FIB have been demonstrated, including direct-write lithography¹ and ion implantation,² surface chemical analysis techniques,³ source metal droplet deposition,⁴ and submicron-resolution material removal ("micromachining").⁵ All these uses take advantage of high spatial resolution and high current density of the focused ion beam.

Possibly the most highly developed of these applications is micromachining. Micromachining is accomplished by scanning the FIB in a pattern that traces out the desired feature shape. The FIB mills away material at removal rates of from 1 to 10 sputtered atoms per incident ion.

Semiconductor micro- and opto-electronic device developers have used FIB micromachining to make features such as 3-D interconnections, wave guides, laser facets, and mirrors.⁶ Typically, semiconductor laser features are made by anisotropic wet chemical etching or cleaving techniques. Efforts to integrate optoelectronic devices directly into VLSI circuitry may use the FIB because it can address specific locations where laser components are to be machined without affecting the entire wafer.

Before focused-ion-beam micromachining (FIB) can be widely used as a precision fabrication tool, the interaction of the ion beam with the substrate must be understood and controllable.

The authors are at the Precision Engineering Center, North Carolina State University, Raleigh, NC 27695, except author Griffis, who is at the NCSU Analytical Instrumentation Facility. Support from ONR (contract N00014-86-K-0681) and NSF (grant DMR-8657813) is gratefully acknowledged.

Machining conditions should be selected to take advantage of the high material removal rate while maintaining the desired feature profile (i.e., minimizing or controlling redeposition of sputtered material).

At present, information on redeposition during micromachining is derived from cross-sectional SEM of features that have been cleaved. STM could provide detailed cross-sectional profiles without the need for cleaving through small micromachined features (a difficult task). However, it is difficult to locate a micron-sized feature with an STM. By combining the FIB and STM in a single system, it becomes possible either to create the features to be measured close to the STM tip, or to use the FIB imaging capability to guide the STM to the features.

STM Nanofabrication. At an even smaller scale, STM can be used to produce nanometer-scale modifications. The same current-localization phenomena that allow the STM to image with atomic resolution also permit it to function as a high-spatial-resolution probe, capable of influencing a very localized region on a surface. Many fabrication techniques normally associated with lens-focused electron beams can be performed with the STM (e.g., resist exposure and beam-induced deposition).^{7,8} However, since the tunneling electrons possess very low energies (<50 eV), beam damage and proximity effects are effectively eliminated.

STM has exhibited the ability to induce modifications down to the level of individual atoms,⁹ provoking thoughts of genetic surgery, quantum-electronic devices built from individual atoms, or data storage measured in terabytes/cm². If these ideas (and others) are to be realized, however, the control and use of STM as a tool must be more clearly understood than is presently the case.

We plan to study the use of STM for nanomanipulation--to investigate the influence that the STM might exert over nanometer-scale atom clusters. One of our motivations for interfacing STM with a FIB is that in addition to operating as a microscope, the FIB can be used as a source of atom clusters and droplets of liquid metal.⁴ The electrostatic lenses and scanners of the FIB column can be used to focus and deflect the charged clusters and droplets, permitting control of their placement and coverage density on a substrate.

By combining the FIB and STM in a single system we should increase the time efficiency of experiments involving each instrument. The effects of variations in FIB micromachining parameters (e.g., dwell time, current density, beam species) will be studied by in situ STM imaging, and STM nanomanipulation experiments

will be expedited by use of the RIB as a source of nanometer-sized particles.

Equipment

FIB. The FIB column incorporates a liquid metal ion source (LMIS) and an electrostatic optical column. The ions are accelerated to an energy between 0 and 25 keV and focused by a single electrostatic lens. To operate at accelerating voltages below 5 kV, an additional external high voltage power supply is necessary to supply the negative voltages required for beam focusing.

The column is also fitted with a stigmator for beam correction, blanking plates, and an octupole assembly for applying beam position offsets and rastering signals. At 25keV accelerating voltage and 50mm working distance, a 0.2 μ m-diameter beam having a current density of 0.7 A/cm² is attainable. For a 5keV beam at 50mm working distance, the beam diameter increases to 0.75 μ m and current density is reduced to \sim 0.04 A/cm².

Computer Interface. A Macintosh II computer is used to control scanning and blanking of the ion beam and to acquire beam current and secondary electron signals. The input and output hardware to accomplish these tasks is provided by a commercially available data-acquisition board. Two 16-bit D/A converters (100 kHz) send the position offset and scan signal output voltages to the octupole/stigmator deflection controller (OSDC), which generates the 8 octupole beam scanning signals. The software-limited (Z Basic) maximum frame rate is 1 second per 256 \times 256 pixels image. Initial beam focusing is done with 128 \times 128 pixels images at a 4Hz frame rate. Beam blanking is a +5V TTL signal from the computer to the blanking circuit in the OSDC, which in turn applies a 150V potential across two parallel blanking plates in the FIB column.

Beam current, absorbed current, and secondary electron signals are acquired by a 12-bit A/D converter having a 142kHz maximum sampling rate. This signal is used to generate images and can be plotted versus scan distance across an aperture to measure beam diameter.

UHV System. The FIB column is mounted to a UHV system that includes the FIB chamber, a sample introduction chamber, and a third chamber for STM. To reduce vibrations that would interfere with high resolution FIB machining and FIB or STM imaging, the entire vacuum system is rigidly mounted to a vibration isolation table.

The FIB chamber houses the ion gun, an X-Y-Z specimen stage, an ionization pressure gauge, a residual gas analyzer, and a microchannel plate secondary electron detector. The manipulation stage allows sample movement of 1 cm with 20 μ m resolution in the x, y, and z directions. Electrical feedthroughs are included in the stage for beam current and diameter measurements, and for providing electrical connections to the STM. The FIB chamber is connected to a high-voltage ion pump through an isolation gate valve.

The STM chamber is equipped with an ionization gauge and various electrical feedthroughs for the development of UHV STMs. This chamber includes its own sample introduction system, and a wobble-stick manipulator for STM placement and tip exchange.

STM. The STM has been designed around the concept of the STM/FIB interface shown schematically in Fig. 1(a). The most apparent feature of this interface is the high degree of co-linearity of the ion beam and tip axes, achieved by shooting the FIB down the center of the STM tube scanner. This configuration is optimal for STM imaging of FIB-produced particles and micromachined features, and for combined FIB/STM imaging.

The "walking" STM is a variation on tube-in-tube designs that have appeared in the literature.^{10,11} Two piezoelectric tubes of different diameters are attached concentrically to a rigid flange. The inner tube, to which the tip is mounted, operates as a conventional STM tube scanner, scanning the tip parallel to the sample surface (X-Y plane) while moving the tip perpendicular to the surface (Z) to maintain a constant tip-to-sample separation. The removable tip-holder is a plug-shaped piece of insulator that fits inside the inner STM tube, where it rests on the washer-shaped silicon disk that covers the bottom of the tube. A hole drilled through the tip holder (at a 15° angle to the central axis) contains a metal sleeve into which the shank of an STM tip can be placed. The STM tip protrudes beyond the end of the scanning tube, through the hole in the center of the silicon disk. A hole bored down through the center of the tip holder gives the FIB access to the sample and tip.

The outer tube is used for x, y, and z offsets, and the entire double-tube assembly is supported on three spherical feet mounted to its bottom rim. This configuration allows the STM to "walk" by stick-slip motion. If the outer tube is bent slowly to one side, then straightened almost instantaneously, the feet slip relative to their three contact points. This sequence produces a submicron step which is repeated to produce macroscopic motion in the X and Y directions.

By placing the sample on a wedge-shaped sample holder beneath the tip, transverse STM motion toward the uphill part of the wedge reduces the tip-to-sample separation distance. Motion across the wedge's slope (in the x direction) does not change the z height macroscopically, so that coarse x motion is possible without moving of the tip out of the z piezo offset range. The ability of the STM to "walk" increases the area on the sample accessible for imaging without requiring complicated mechanical design. A prototype of this design has successfully approached and imaged (in air) Au on Si, an optical grating, and the highly-oriented pyrolytic graphite lattice shown in Fig. 2.

The STM is designed to sit on top of the standard lin.-diameter sample holders used with the three-axis sample-positioning stage in

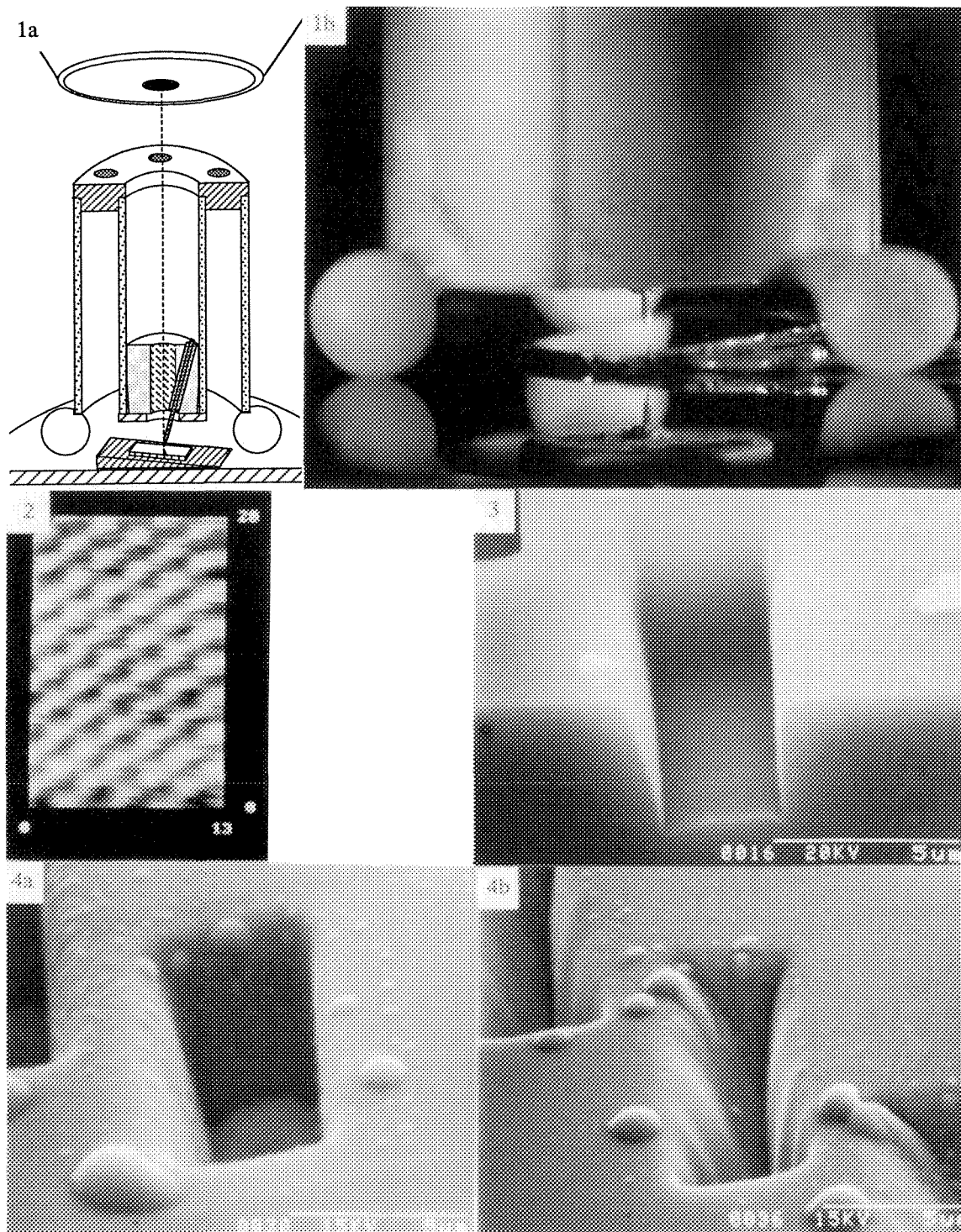


FIG. 1.--(a) Schematic view of STM situated under FIB. STM "walks" by stick-slip motion toward inclined sample to bring tip within range of piezoelectric motion. FIB passes down center of STM tube and tip holder to image tip or to create features to be imaged. (b) Closeup showing feet attached to rim of outer tube. Reflection of tip is seen on sample and on Si wafer used for smooth "walking" surface.

FIG. 2.--Graphite lattice imaged with prototype of "walking" STM.

FIG. 3.--Cross-section SEM view of $4 \times 10 \times 3.5 \mu\text{m}$ rectangular well cut into (100) Si during 15min scan of 25keV, 480pA Ga^+ beam.

FIG. 4.--(a) Well cut in GaAs with 25keV, 490pA Ga^+ beam. Dwell time per pixel, 31 μs ; pattern was repeated 311 times. (b) Same conditions as in 4(a) except dwell time increased to 9.63 ms/pixel and entire frame scanned only once.

the FIB compartment. Transport of the sample holder and STM into the vacuum will be done with the magnetically coupled translator, through the FIB's sample introduction port. Electrical signals will pass to the STM through contacts that will be made when the sample holder is lowered into the securing socket on the stage.

EXPERIMENTAL

FIB Micromachining. To establish the optimal conditions for FIB micromachining, a multiparametric study is being conducted. Beam parameters being examined are beam energy, current, dwell time, and ion species (Ga and Au). Substrate parameters are type of material (Si, GaAs, InP, and Au) and, in the case of Si, crystallographic orientation ((100) and (111)). A $4 \times 10 \mu\text{m}$ rectangular well is used as the test feature.

Maximum sputter yields for the various ion/substrate combinations are determined by machining features using short dwell times and low-beam currents to minimize redeposition. The features are then cleaved and the cross section is viewed by SEM to determine the depth of the feature. The sputter yield is found by the number of ions that impinged during the experiment.

Figure 3 illustrates a cross section of a $4 \times 10 \times 3.5 \mu\text{m}$ rectangular well cut into (100) Si during a 15-min scan of a 25keV, 480pA Ga⁺ beam. Solving for sputter yield gives a value of 2.8 atoms/incident ion. A $4 \times 10 \times 5.8 \mu\text{m}$ rectangular well cut into GaAs with the same beam conditions during a 7-min experiment resulted in a sputter yield of 4 atoms/incident ion.

As stated, the FIB is capable of producing very high current densities focused into a sub-micron beam that permits high-resolution, high-sputter rate milling. However, in actuality, material removal is accompanied by redeposition of sputtered atoms. Redeposition depends on such parameters as beam dwell time and the aspect ratio of the machined features.

For a given total machining time, the dwell time/point is determined by the number of times that the beam is scanned over the feature. For multiple fast raster scans the number of redeposited atoms is less for each scan and they can be removed with subsequent scans. Figure 4(a) shows a feature cut in GaAs with a 25keV, 490pA Ga⁺ beam for a total machining time of 7 min. The dwell time at each point in the raster pattern was 0.031 ms and the pattern was repeated 311 times. For a single slow raster to machine a feature, the beam leaves behind a large number of redeposited atoms that result in a poorly defined feature. The feature in Fig. 4(b) was cut with the same parameters as in Fig. 4(a) except that the dwell time was increased to 9.63 ms/point and the entire frame was scanned only once. The effect of dwell time on the redeposition process is obvious and may greatly influence the functionality of FIB-machined components.

The maximum depth to which a feature may be

machined can be described by a simple cosine distribution of the sputtered atoms. When the feature becomes sufficiently deep so that sputtered atoms cannot escape without striking the sidewalls, appreciable redeposition will occur.

Compositional changes of the substrate are also of importance when FIB micromachining is used for opto- and micro-electronic device fabrication. The incorporation of metal ions from the FIB into the lattice may induce changes in the optical and electronic characteristics of the material. The interaction of the Ga⁺ beam with GaAs and InP substrates has produced interesting artifacts. Figure 4 shows the presence of gallium droplets associated with craters machined in GaAs. Similarly, the formation of an indium crystal at the edge of FIB-machined craters in InP has been observed. It is possible that these artifacts are caused by supersaturation of the compound semiconductor lattice with gallium, or by preferential sputtering of the As and P (in GaAs and InP, respectively).

STM Nanomanipulation. Most of the experimental work associated with the STM nanomanipulation project thus far has involved the testing of the STM design prototype. Measurements with a capacitance gauge and laser interferometer have shown that the STM can "walk" millimeter distances without straying more than 1 μm to either side of the desired path. Step size can vary from tens of nanometers to tenths of micrometers, depending on the magnitude of the applied voltage step and on the frictional properties of the walking surface. Use of the FIB to provide visual feedback of the tip position will make it possible to move the STM from feature to feature.

Gold and graphite were imaged to confirm the STM's imaging capability. Images of the 1.6 μm -period optical disk were used to measure the maximum field of view of the STM scanner. When a scan signal of 260 V was applied to the inner tube, the STM tip traversed a distance of $\sim 4.1 \mu\text{m}$, sufficient for measuring micromachined features. We have also been able to use the outer tube as the Z position transducer when the topography was too rough for the inner tube to accommodate. The STM has thus exhibited the ability to cover a fairly large range of imaging applications in air, and its adaptation for UHV operation is currently under way.

Other preparatory experiments have involved depositing atom clusters onto graphite substrates with the FIB. Thus far we have deposited Ga droplets and succeeded in imaging them with SEM and STM (outside the vacuum chamber). Observed droplet sizes range from tens of nanometers to several micrometers.

Conclusion.

Combining FIB and STM in a single system presents many interesting possibilities for experiments. The capabilities of the FIB and STM are complementary, and each instrument stands to gain from its proximity to the other.

References

1. J. R. A. Cleaver, P. J. Heard, and H. Ahmed, "Scanning ion beam lithography for sub-micron structure fabrication," *SPIE* (Vol. 393: Electron Beam, X-Ray, and Ion Beam Techniques II), 1983, 129.
2. H. Hamadeh, J. C. Corelli, A. J. Steckl, and I. L. Berry, "Focused Ga beam direct implantation for Si device fabrication," *J. Vac. Sci. Technol.* B3: 91, 1985.
3. H. Satoh, M. Owari, and Y. Nihei, "Quantitative analysis by submicron secondary ion mass spectrometry," *J. Vac. Sci. Technol.* B6: 915, 1988.
4. P. Sudraud, G. Ben Assayag, and M. Bon, "Focused ion beam milling, scanning electron microscopy, and focused droplet deposition in a single microcircuit surgery tool," *J. Vac. Sci. Technol.* B6: 234, 1988.
5. H. Yamaguchi, A. Shimase, S. Haraichi, and T. Miyauchi, "Characteristics of silicon removal by a fine focused gallium ion beam," *J. Vac. Sci. Technol.* B3: 71, 1985.
6. J. Puretz, R. K. DeFreez, R. A. Elliot, and J. Orloff, "Focused ion beam micromachined AlGaAs semiconductor laser mirrors," *Electronics Lett.* 22: 700, 1986.
7. M. A. McCord and R. F. W. Pease, "Lift-off metallization using poly(methyl methacrylate) exposed with a scanning tunneling microscope," *J. Vac. Sci. Technol.* B6: 293, 1988.
8. R. M. Silver, E. E. Ehrichs, and A. L. de Lozanne, "Direct writing of submicron metallic features with a scanning tunneling microscope," *Appl. Phys. Lett.* 51: 247, 1987.
9. R. S. Becker, J. A. Golovchenko, and B. S. Swartzentruber, "Atomic-scale surface modification using a tunneling microscope," *Nature* 325: 419, 1987.
10. F. Besenbacher, E. Laegsgaard, K. Mortensen, U. Nielsen, and I. Stensgaard, "Compact, high-stability, 'thimble-size' scanning tunneling microscope," *Rev. Sci. Instrum.* 59: 1035, 1988.
11. J. W. Lydings, S. Skala, J. S. Hubacek, R. Brockenbrough, and G. Gammie, "Variable temperature scanning tunneling microscope," *Rev. Sci. Instrum.* 59: 1897, 1988.

THE NATIONAL INSTITUTE OF STANDARDS AND TECHNOLOGY MOLECULAR MEASURING MACHINE: A LONG-RANGE SCANNING TUNNELING MICROSCOPE FOR DIMENSIONAL METROLOGY

E. Clayton Teague

We have embarked on what we view as a high-risk project to build an ultrahigh-accuracy planar coordinate measuring machine; one that is capable of positioning and measuring to atomic scale accuracies over an area of 25 cm². The design goal is to obtain a point-to-point spatial resolution of 0.1 nm of the distance between any two points within a 50 mm × 50 mm × 100 μm volume, with a net uncertainty for point-to-point measurements of 1.0 nm. Maximum specimen size will be 50 mm × 50 mm × 12 mm.

Three operating modes are planned: large-scale mapping at low resolutions of 1 to 10 μm over areas of 1 to 100 mm²; small-scale mapping at resolutions up to 0.1 nm over areas of 0.01 to 1 μm²; and point-to-point measurements of the distance between two points in one image or between points selected from two macroscopically separated small scale images. Image acquisition size is planned as 1000 × 1000 pixels to be obtained at rates corresponding to probe-specimen speeds up to 1 mm/s. Probes for low-resolution mapping will be confocal optical microscopy or thermal microscopy;¹ for high-resolution mapping, probes will be scanning tunneling or atomic-force microscopy.

These capabilities will in turn enable dimensions of features, angles, straightness, and other geometrical properties of molecular-sized or larger objects to be measured with very high accuracies. The project, which we call the Molecular Measuring Machine (M³) Project, was started about two years ago to address current and anticipated dimensional metrology needs of the large and rapidly growing fields of nanotechnology.

Design Concepts

Several heuristic design concepts have come

The author is at the National Institute of Standards and Technology, Gaithersburg, MD 20899. The current state of development of the Molecular Measuring Machine is the result of major contributions from his colleagues at NIST, Fredric Scire, David Gilsinn, William Penzes, Chris Evans, Robert Polvani, Edward Amatucci, Thomas Wheatley, William Ruff, Brian Scace, Tyler Estler, and Arie Hartman; Robert Hocken (now at University of North Carolina at Charlotte); from colleagues visiting NIST as Guest Scientists: Hans Hansen (LLNL), Miguel Huerta Garnica (CINESTAV-IPN, Mexico), Boyin Lu and Yanshen Xu (Tianjin University, PRC), Xian-Zhang Hu (Tsinghua University, PRC); and fruitful collaboration with Richard Rhorer and his group at LANL, Alex Slocum at MIT; and Zygo Corp. and GCA Corp. under NIST Industrial Research Associateships.

to be widely accepted in the precision engineering community² that we have attempted to incorporate into the design and construction of M³:

Repeatability	Stiff structural loop
Environmental isolation	Kinematic drives
Kinematic mounting	Probe knowledge
Alignment (Abbe) principle	Energy flow analysis
Metrology frame	Error budget
Materials selection	Symmetry

The basic design is to incorporate a tunneling or atomic-force probe into a highly stable mechanical structure with provisions for scanning the probe relative to the specimen in a rastered path. We are not under any illusions that the machine will have motions perfect to within or less than the 0.1 nm design goal resolution. However, every aspect of the machine and system design has been directed at achieving a *repeatability* at or below this value by use of a stiff mechanical structure within an envelope of environmental isolation that provides a stable thermal and mechanical environment for the core structure. If a repeatability at this level can be achieved, then pitch, roll, yaw, and straightness motion errors of the moving machine elements will be measured and built into the control algorithms to correct for the motion errors.

Mechanical Design

A spherical core structure (Fig. 1) was chosen for its high mechanical stiffness and ease of temperature control.³ Even with a 35 cm-diameter hollowed structure of OFHC copper, the first resonance is at about 2000 Hz. OFHC copper was chosen for the core structure material because of its combined reasonable specific stiffness, damping coefficient and excellent thermal properties.⁴ Long-range motion of the probe relative to the specimen is obtained by mounting of the probe assembly and the specimen on separate carriages, which move on crossed linear slideways that are monolithically part of the core mechanical structure. Finite-element analyses⁵ show that static deformations of both the upper and lower slideways due to gravitational loading are less than 1 nm. Probe and specimen carriages are kinematically supported on the slideways with five pads. The materials for the pads and tribological interface at the slideway surface have not been chosen at this time. We are still conducting material stability, machinability, and wear experiments. Motions greater than about 5 μm will be generated by piezoelectric stepping motors for both carriages.

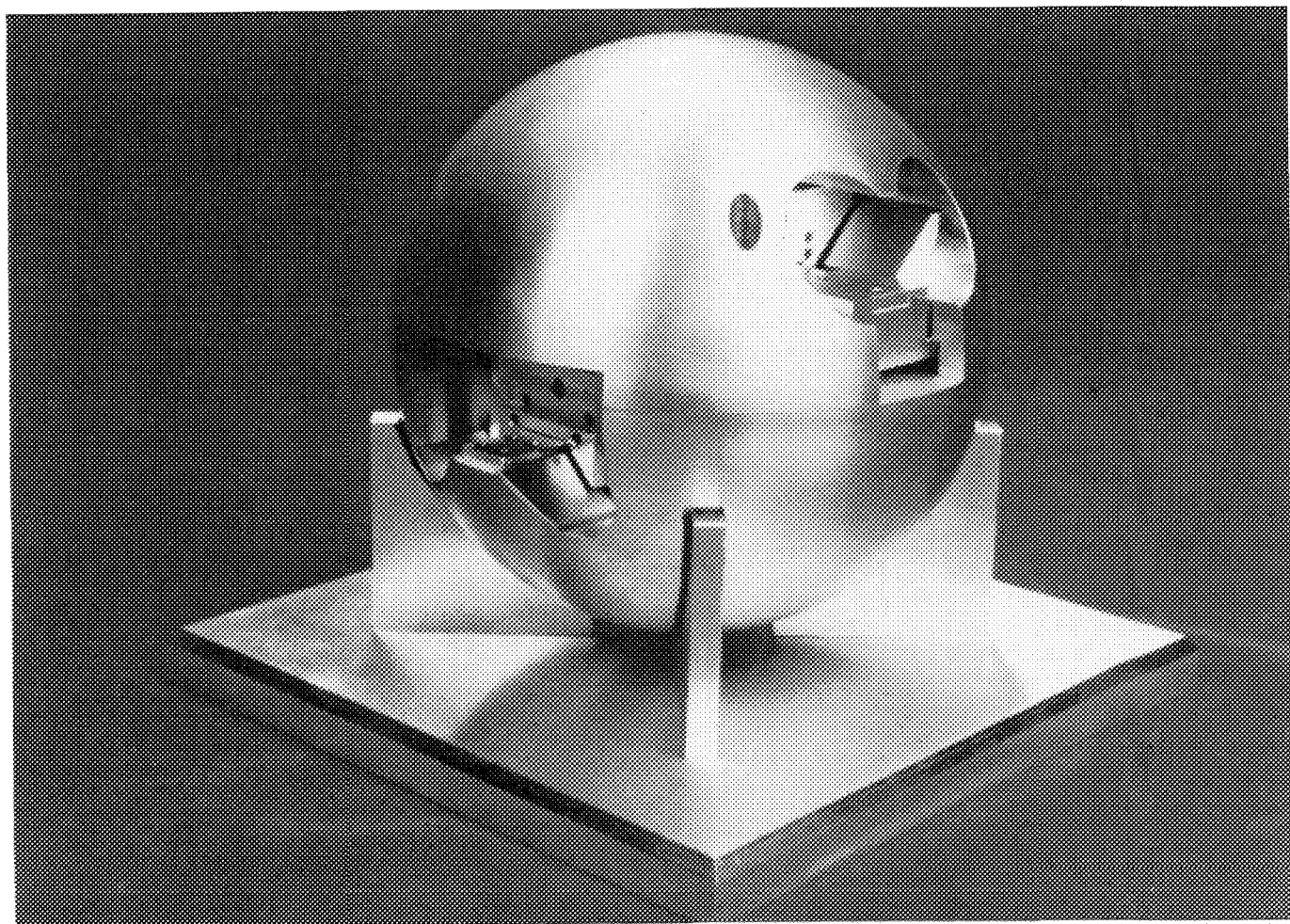


FIG. 1.--Model of NIST M³ core structure. Actual size of the spherical structure in machine is 35 cm in diameter.

Motions smaller than about 5 μm will be generated in secondary carriages supported by and driven relative to the primary carriages by piezoelectric stacks.

The core structure will be operated in a chamber that can be evacuated to pressures as low as 10^{-8} Pa or backfilled with a gas of highly controlled composition (Fig. 2). The cross section of the environmental isolation system (Fig. 2) shows the temperature control shell and two stages of vibration and acoustical isolation for the core structure. Locating the critical measuring volume of the core structure at the center of mass of the vibrationally supported components minimizes any cross coupling between translational and rotational excitations.

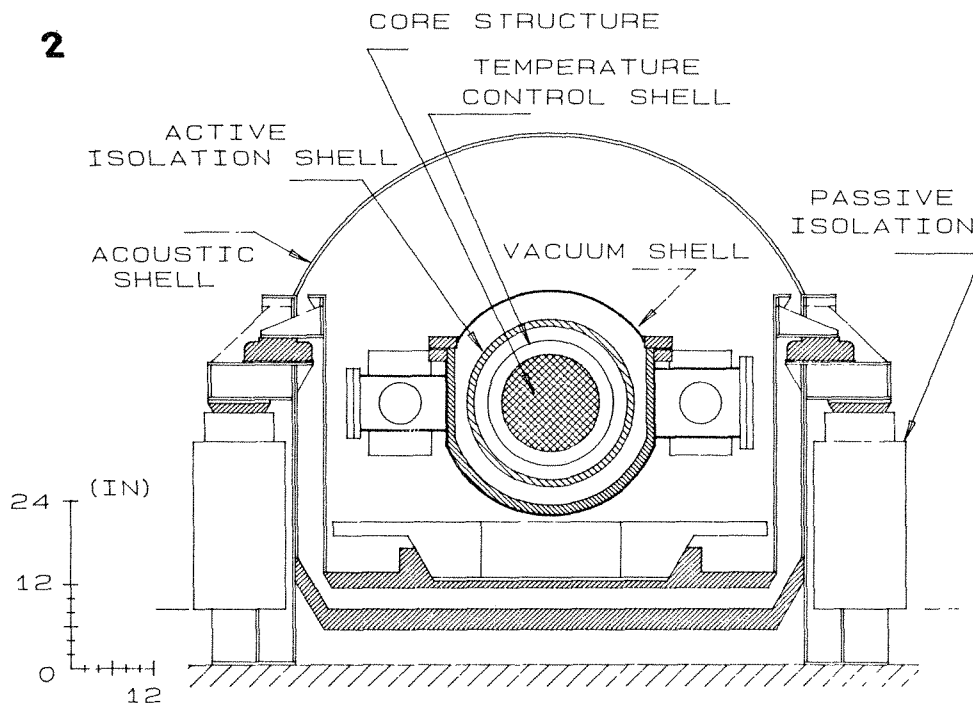
To protect the critical mechanical surfaces of the machine and to provide a clean environment for specimen loading, the machine is being built into a Class 10 clean area. As a final effort to provide a quiet and minimum vibration environment, the clean area is located inside a solid concrete block enclosed room in a basement laboratory.

Metrology System

Relative motion between the probe and specimen will be measured with an ultrahigh resolution heterodyne interferometer with a least count of about 0.075 nm. The interferometer is a four-pass design which gives a $\lambda/8$ displacement resolution. At the helium-neon laser wavelength, the additional subdivision by 1000 to obtain the desired resolution will be obtained electronically. The major barrier to achieving this resolution is the mixing of polarization states in the laser and in the interferometer optics. Careful generation of the two polarization states and characterization of the polarization properties of the interferometer optics should permit the required degree of interpolation. Remnant nonlinearities between measured phase shift and optical path difference in the interferometer should then be repeatable and thus correctable.

The datum for displacement measurements and its integration with the interferometers for the two major axes is shown in Fig. 3. The inside differential interferometer configuration combined with the metrology box enables measurements of probe position relative to a specimen mounted on the metrology box independent

2



3

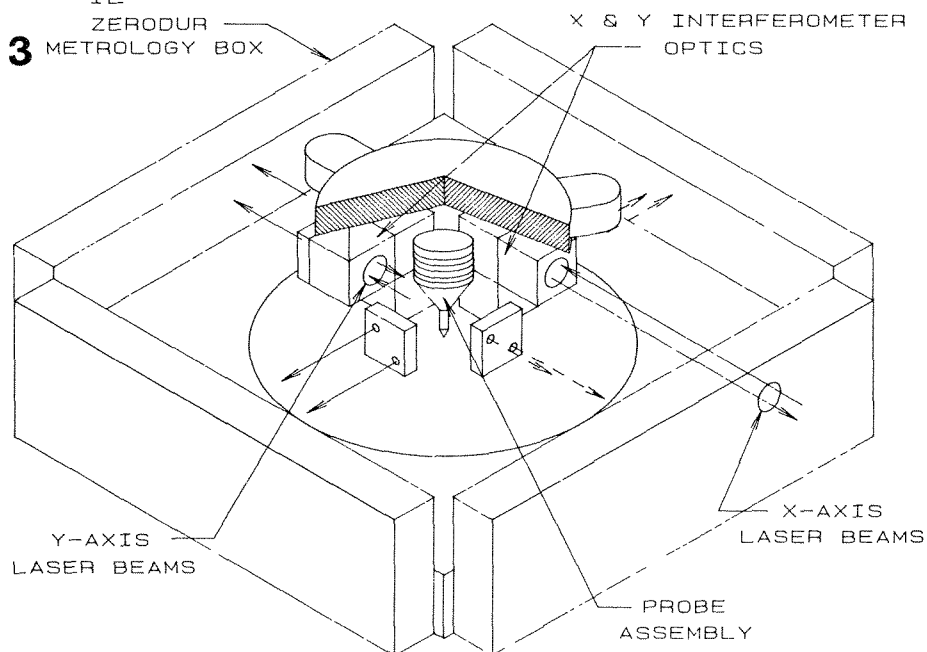


FIG. 2.--Scale cross-section drawing of environmental isolation system for NIST M³.

FIG. 3.--Schematic drawing of metrology reference system and X and Y interferometer arrangement. Interferometer beams for X and Y displacement straddle probe tip to minimize Abbe offset errors.

of other spurious drift or strain generated motions of the core structure or any other part of the machine. Such a design for the datum also provides a metrology frame which is physically comparable to the specimen size, i.e., one that approaches a minimum size.

Status

Currently, many major components of M³ and its support facility have either been procured or built in-house. An initial assembly of the

overall system should be possible in late 1989 or early 1990. We then expect a 12- to 18-month shakedown to bring it to an operational state near the design goals.

References

1. C. C. Williams and H. K. Wickramasinghe, "Thermal and photothermal imaging on a sub 100 nanometer scale," SPIE Vol. 897, Scanning Microscopy Technologies and Applications (1988), E. Clayton Teague, Chair/Ed., p. 129.
2. E. C. Teague and C. Evans, "Patterns for precision instrument design," Tutorial Notes, American Society for Precision Engineering, Raleigh, North Carolina, 1988, 99 pp.
3. E. C. Teague and F. E. Scire, "Spheroids for precision machine structures" (to be published).
4. E. G. Amatucci and E. C. Teague, "Materials selection for precision machines," *Precision Engineering* (submitted).
5. D. E. Gilsinn, H. J. Hansen, Y. Xu, M. Huerta-Garnica, and E. C. Teague, "A comparison of finite-element and analytic calculations of the resonant modes and frequencies of a thick shell sphere," *Proc. Amer. Soc. Prec. Eng.*, Oct. 24-27, 1988; H. J. Hansen, D. E. Gilsinn, and Y. Xu, "Analysis of static and dynamic deformation of the spheroidal core structure of the NIST Molecular Measuring Machine" (to be published).

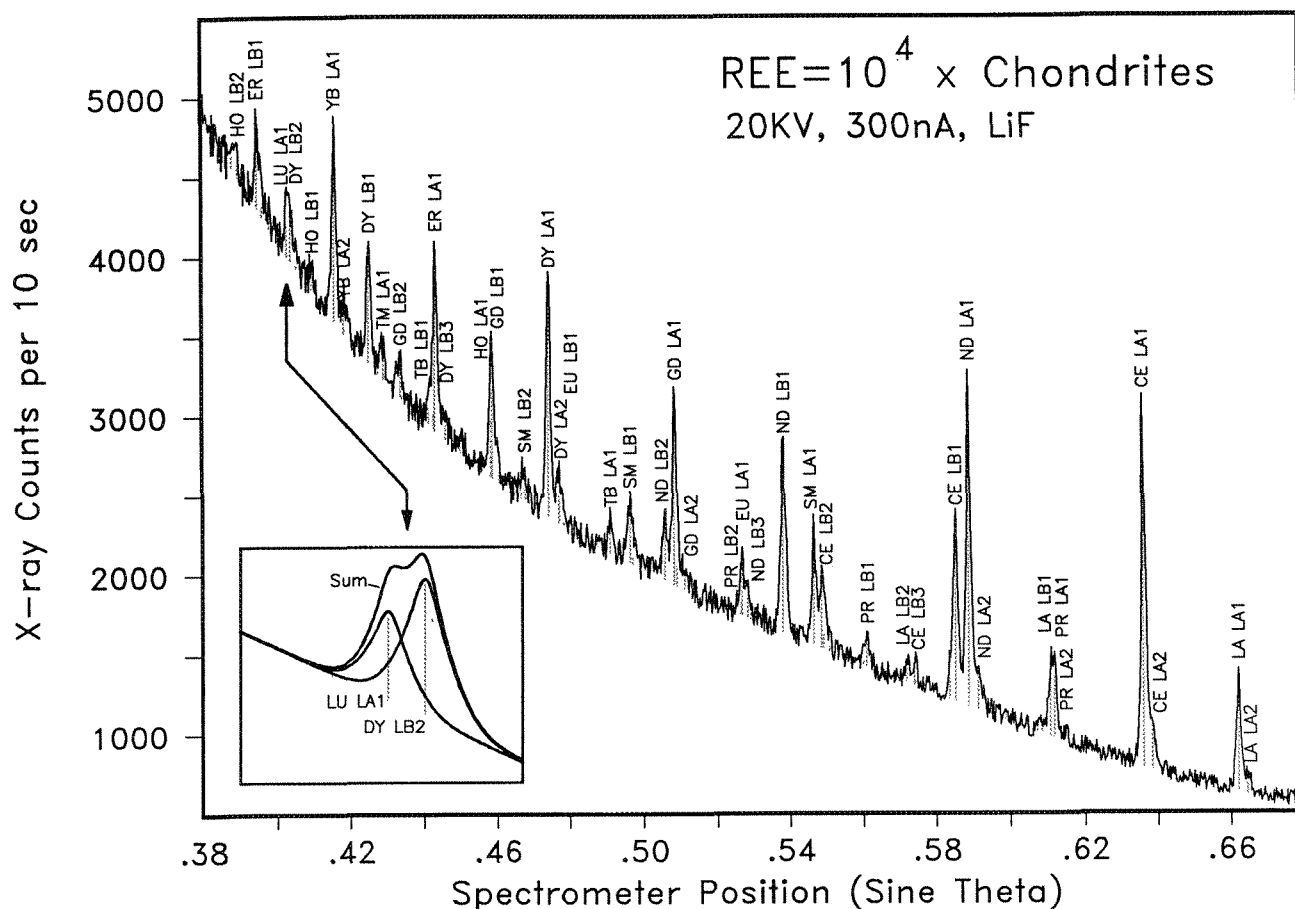


FIG. 1.--Synthetic x-ray spectrum of a hypothetical sample having REE concentrations of 10 000 \times chondrites. Inset shows overlap of Lu La_1 and Dy Lb_2 peaks.

obtaining higher counting rates, but not necessarily higher peak/background ratios.¹⁰ The beam current should be increased to the maximum value consistent with stable operation and tolerable sample damage. In most cases, higher accelerating voltages yield higher precision, but that may not be true for light elements in all matrices. Because of its higher counting rate, a PET crystal generally yields higher precision than LIF, but its lower resolution may cause difficulties with interferences.

In principle, counting time may be increased indefinitely to improve sensitivity. However, in addition to cultural limitations, such as availability of instrument time, etc., long counting times impose a set of technical problems that must be overcome to achieve the highest analytical sensitivity. Most formidable among them are instrument drift and sample damage, leading to variations in x-ray intensity between the measurement of peak and background.

Finally, even when peak and background intensities are measured with very great precision, trace-element analyses may nevertheless suffer from systematic errors in the accuracy of background measurements. The analyst should minimize these errors by using such techniques as careful selection of background positions,

profiling of background regions to check the shape of the background spectra, and making empirical corrections to linear interpolations based on data from a sample with a negligible amount of the analyzed element.

In addition to problems related to the precision and accuracy of intensity measurements, in some cases inaccurate results can arise due to interferences from an adjacent phase with a much higher concentration of the analyzed element than the unknown. We routinely encounter severe difficulties of this sort when measuring trace element partition coefficients of less than 0.01 in experimental charges,⁸ and generally restrict such measurements to spots at least 200 μ m from the adjacent trace element-rich phase.

Simultaneous Measurement of Peak and Background

In the Johnson Space Center Electron Microprobe Laboratory, we have used two different approaches to overcome the above problems and increase analytical sensitivity. One approach is to measure peak and background at the same time on two different spectrometers.¹¹ In this technique, we set one spectrometer at the peak wavelength of the element of interest, and another at a carefully chosen background

wavelength. We measure x-ray intensities for both spectrometers with high precision on a sample (typically natural olivine) known to contain a much lower concentration of the analyzed element than the unknown. Then we measure intensities on the unknown with similar precision. We typically use counting times of hundreds of minutes. The net intensity for the unknown is given by

$$I_{(Net,X)} = I_{(P,X)} - I_{(B,X)} * I_{(P,Ref)} / I_{(B,Ref)}$$

where $I_{(P,X)}$ is the intensity measured with the on-peak spectrometer for the unknown, $I_{(B,X)}$ is the intensity measured with the off-peak spectrometer for the unknown, and $I_{(P,Ref)}$ and $I_{(B,Ref)}$ are the intensities measured for the reference sample. This net intensity is compared with that of a standard in the conventional manner to obtain concentration.

The above technique permits reliable measurements of REE concentrations in the range of a few tens of ppm. Because it does not require spectrometer motion during an analysis, it can be used effectively on older instruments. It overcomes problems with instrument drift over the long counting times required to obtain high precision. Because off-peak and on-peak intensities are measured simultaneously, drift in electron-beam intensity influences x-ray intensities at both wavelengths proportionately, and hence has a negligible effect on net intensity. Likewise, to a first approximation, sample damage or contamination influences off-peak and on-peak measurements proportionately, provided the concentration of the analyzed element does not change significantly during analysis. In contrast to the popular technique of taking the background directly from on-peak measurements for a reference sample with a negligible concentration of the analyzed element, but otherwise similar in composition to the unknown, the above technique is insensitive to small compositional differences, because it determines only the on-peak/off-peak *ratio* from the reference sample, but the absolute level from the unknown itself.

The major limitation of the technique appears to be the difficulty of getting the surfaces of the reference sample and the unknown in precisely the same orientation relative to the beam and the two spectrometers.⁸ Changes in orientation (i.e., take-off angle) as small as a fraction of a degree can significantly affect $I_{(P,Ref)} / I_{(B,Ref)}$. This difficulty leads to an uncertainty of around 20 ppm (2 σ) beyond counting statistics in Nd analyses performed with randomly chosen low-Nd olivines as background reference samples.⁸ This uncertainty, therefore, constitutes the minimum detection limit for Nd obtainable by this technique, regardless of counting time, unless a better way is found to orient the sample surfaces.

Repeated Cyclic Measurement of Peak and Background

The second approach we have used for high-sensitivity analyses involves breaking up the

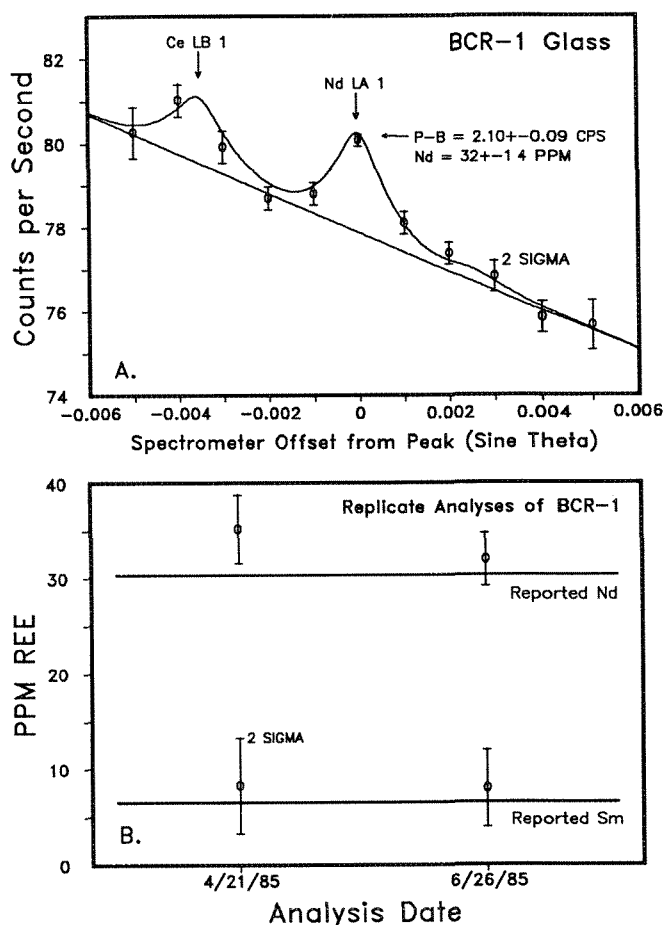


FIG. 2.--Analyses of REE in glass made from standard rock BCR-1. (a) Cyclic profile analysis of Nd. Circles with error bars are actual data. Curve is synthetic spectrum illustrating peak shapes, and shaping proximity of Ce peak. (b) Replicate Sm and Nd analyses of BCR-1, showing analytical reproducibility and agreement with accepted values.

required long counting time into many shorter cycles, during which a spectrometer is alternately moved to the peak and several background positions on either side of the peak.¹² These cycles are repeated until sufficient counts have been accumulated to achieve the desired precision. Backgrounds are determined from these data by use of an iterative procedure, in which intensities measured near the peak are corrected for contributions from the shoulders of the peak according to stripping factors measured on the standard, and are then interpolated to the peak wavelength using a least-squares fitting procedure, in which data collected for different counting times are weighted according to the square root of the counts. This procedure has major advantages over conventional background-measurement techniques. Measurement of intensities in several repeated cycles permits long total counting times, without adverse effects of instrumental drift or sample damage and contamination between peak and background measurements. Cor-

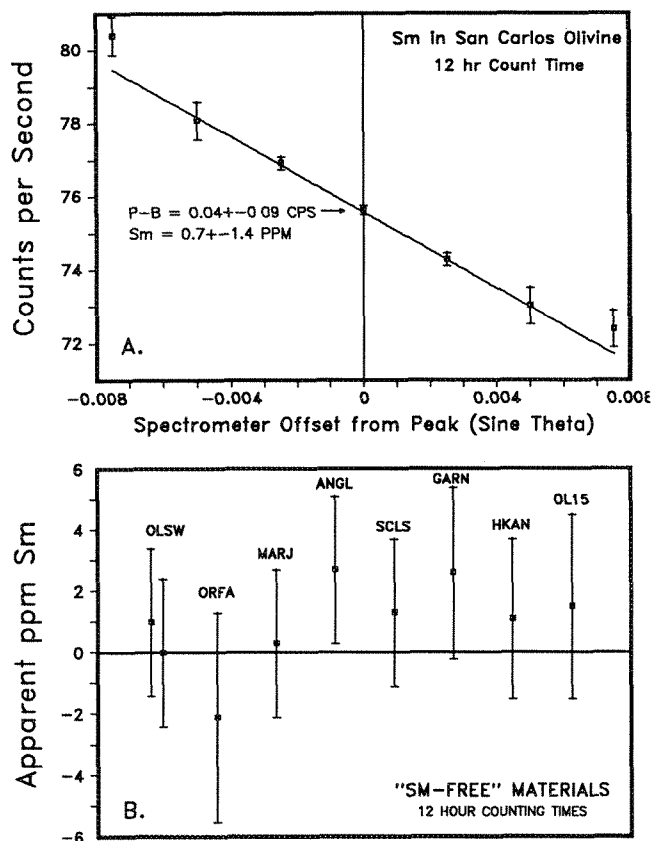


FIG. 3.--Analyses of Sm in samples known to have concentrations below the detection limits. (a) Cyclic profile across Sm peak for San Carlos olivine. Squares with error bars are observed data, and line is interpolated background. Peak intensity is within uncertainty of background. (b) Results of similar analyses for a variety of low-Sm materials.

rection for shoulder contributions permits use of background wavelengths close to the peak, minimizing effects from curvature of the x-ray continuum.

Results for such an analysis of Nd in a fused sample of standard rock BCR-1 are shown in Fig. 2(a). Intensities were measured at the peak wavelength and five locations on either side of the peak, and are shown as circles with error bars. Analyses were done at 30 kV and 300 nA. Total counting time was about 12 h. One curve is a synthetic spectrum, shown to illustrate the peak shapes; the other is the background fit by the procedures described above. This analysis is slightly complicated by interference from the Ce $L\beta_1$ peak, which was removed with stripping factors empirically determined from the Ce standard.¹ BCR-1 contains about 30 ppm Nd. It is clear that the Nd peak is distinctly resolved above background, and that the net Nd peak intensity is determined with a relative precision much better than 10%.

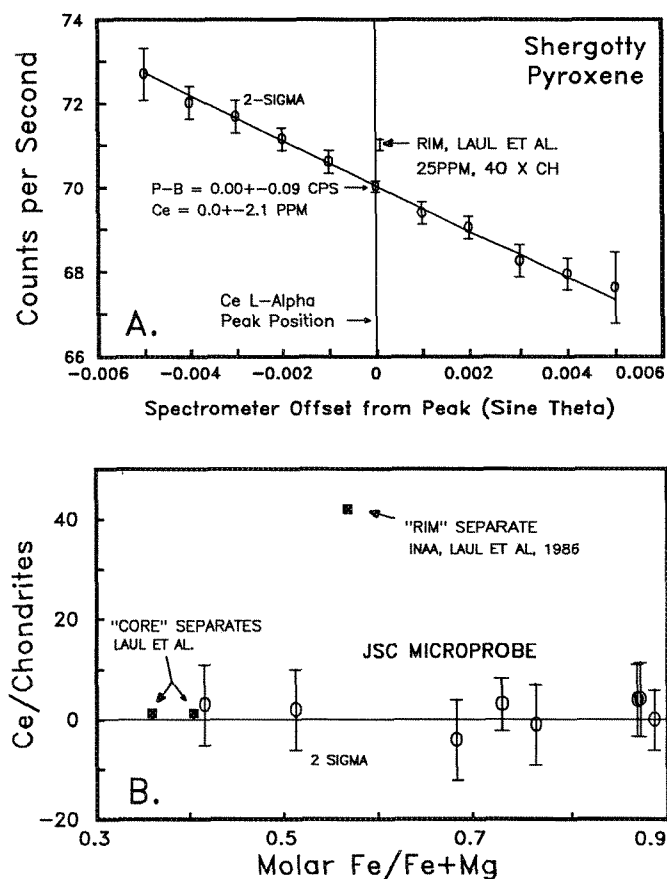


FIG. 4.--Analysis of Ce in pyroxenes from Martian meteorite Shergotty. (a) Profile across Ce peak. Peak intensity is within uncertainty of interpolated background, and is well below that expected for sample with Ce concentrations measured by INAA for bulk pyroxene separate, indicated by error bars marked "Rim." (b) Results of similar analyses for a variety of pyroxene crystals covering the entire observed range of Fe/Mg zoning. Ce contents for all analyzed spots are below detection limits, and well below INAA value for "Rim" separate (square), indicating that LREE-enrichment is carried by contaminating minor phase, rather than being intrinsic to pyroxene.

Replicate analyses of BCR-1 for Nd and Sm on two different dates (Fig. 2b) indicate that results are highly reproducible, and agree well with the accepted values.

In addition to giving the right answer on a standard rock, another important test of a trace-element technique is that it must give the correct result of zero for a sample with concentrations of the analyzed element below the detection limit. Figure 3(a) shows results of a cyclical profiling analysis of Sm in San Carlos olivine, which has less than 1 ppm Sm. The peak intensity is within uncertainty of the interpolated background, and yields an uncertainty (1σ) of 1.4 ppm Sm. In

the analysis of elements such as Sm, for which the background is smooth and well behaved, our procedure routinely yields the "correct" result for samples with negligible Sm content (Fig. 3b), thereby lending considerable credibility to results at the 10-20ppm level.

Application of REE Analysis to the Age of Martian Meteorites

There is a group of meteorites with unusual properties which suggest they formed on Mars.¹³ One of these meteorites, Shergotty, has been the subject of an intense controversy concerning its age and isotopic systematics. Definitive information on these topics would be very valuable in constraining the thermal evolution, and therefore the overall differentiation history of Mars. Unfortunately, the chronology of this sample is complicated by a shock event, which disturbed or reset most isotopic systems.¹⁴ One geochronology group reported a Sm-Nd isochron which they interpreted as indicating a time of crystallization of 350 my.¹⁵ This isochron is based entirely on bulk analysis of different fractions of pyroxene. Several of these fractions have extreme enrichments in light REE (LREE), as demonstrated by both isotopic analyses and neutron activation analysis (NAA).¹⁶ If this enrichment is actually intrinsic to the pyroxene, rather than a minor contaminating phase, it should be detectable by electron microprobe, with the use of the above techniques. If it is not intrinsic to pyroxene, then the isochron probably represents a mixing line or shock-disturbed system, and cannot yield reliable information about the crystallization age.

To investigate this matter, we analyzed Ce in Shergotty pyroxene grains. Data from one such analysis are shown in Fig. 4(a). This analysis shows no detectable Ce. The amount reported in the mineral separate¹⁶ would be easily detectable, as indicated in the figure. Analyses of many different pyroxene grains, covering the entire range of Fe/Mg zoning, indicate that Ce is below detection limits in all cases (Fig. 4b), and well below the concentration reported for "rim cpx" mineral separates.¹⁶ Hence the carrier of the LREE enrichment is not pyroxene, and it is unlikely that the 350my isochron represents the crystallization age of Shergotty.

References

1. M. J. Drake and D. F. Weill, "New rare earth element standards for electron microprobe analysis," *Chemical Geology* 10: 179, 1972.
2. R. Amli and W. Griffen, "Microprobe analysis of minerals using empirical correction factors," *Amer. Mineralogist* 60: 599, 1975.
3. P. L. Roeder, "Electron-microprobe analysis of minerals for rare-earth elements: Use of calculated peak-overlap corrections," *Canadian Mineralogist* 23: 263, 1985.
4. S. E. Haggerty, "The mineral chemistry of new titanates from the Jagerfontein kimberlite, South Africa: Implications for metasomatism in the upper mantle," *Geochimica et Cosmochimica Acta* 47: 1833, 1983.
5. R. A. Exley, "Micro-probe studies of REE-rich accessory minerals: Implications for Skye granite petrogenesis and REE mobility in hydrothermal systems," *Earth and Planetary Science Letters* 48: 97, 1980.
6. R. A. Exley and J. V. Smith, "The role of apatite in mantle enrichment processes and in the petrogenesis of some alkali basalt suites," *Geochimica et Cosmochimica Acta* 46: 1375, 1982.
7. A. P. Jones and P. J. Wyllie, "Minor elements: An electron-probe study," *Earth and Planetary Science Letters* 69: 128, 1984.
8. G. McKay, "Crystal/liquid partitioning of REE in basaltic systems: Extreme fractionation of REE in olivine," *Geochimica et Cosmochimica Acta* 50: 69, 1986.
9. G. McKay, J. Wagstaff, and S.-R. Yang, "Clinopyroxene REE distribution coefficients for shergottites: The REE content of the Shergotty melt," *Geochimica et Cosmochimica Acta* 50: 927, 1986.
10. T. N. Solberg, "Electron microprobe trace element analysis," *Microbeam Analysis--1988*, 485.
11. G. McKay and R. Seymour, "Electron microprobe analysis of trace elements in minerals at 10 ppm concentrations," *Microbeam Analysis--1982*, 431.
12. G. McKay, J. Wagstaff, and S.-R. Yang, "Zirconium, hafnium, and rare earth element partition coefficients for ilmenite and other minerals in high-Ti lunar mare basalts: An experimental study," *Proc. Sixteenth Lunar and Planetary Science Conference, Part 2, J. Geophysical Res.* 91: D229, 1986.
13. H. Y. McSween, "SNC meteorites: Clues to Martian petrologic evolution?," *Rev. Geophysics* 23: 391, 1985.
14. L. Nyquist, B. Bansal, H. Wiesmann, C. Shih, G. McKay, and D. Bogard, "Rb-Sr age of the Shergotty achondrite and implications for metamorphic resetting of isochron ages," *Geochimica et Cosmochimica Acta* 43: 1057, 1979.
15. E. Jagoutz and H. Wanke, "Sr and Nd isotopic systematics of Shergotty meteorite," *Geochimica et Cosmochimica Acta* 50: 939, 1986.
16. J. C. Laul, M. Smith, H. Wanke, E. Jagoutz, G. Dreibus, H. Palme, R. Spettel, A. Burghelle, M. Lipschutz, and R. Verkoeteren, "Chemical systematics of the Shergotty meteorite and the composition of its parent body (Mars)," *Geochimica et Cosmochimica Acta* 50: 909, 1986.

R. V. Fodor, D. P. Malta, G. R. Bauer, and R. S. Jacobs

Concentrations of rare-earth elements (REE) in Hawaiian basaltic rocks have been one of the main geochemical characteristics used over the past ten years to construct models for petrogenesis of Hawaiian tholeiitic and alkalic basalts (see, for example, Refs. 1-4). Studies of hundreds of Hawaiian basalts have documented that when REE abundances are normalized to chondritic meteorite values, the light REE (LREE)--La, Ce, and Nd--are enriched by factors of 20 to 40 over chondritic values; and that heavy REE (HREE)--Yb and Lu--abundances are about 5 to 12 times those of chondrites (Fig. 1). By determining the absolute amounts of REE in any particular basalt and applying those values to the coefficients for partitioning among various silicate phases and liquids, geochemists can model and interpret the mineralogical characteristics and melting processes of the mantle whence basalts are derived.¹⁻⁴

Only a few samples of basalt from the eight major Hawaiian islands have been noted for anomalously high REE concentrations, several times greater than in rocks having otherwise comparable compositions. These samples also have anomalously high yttrium abundances, where Y apparently behaves like a HREE. For example, Roden et al.⁵ report a tholeiitic basalt from the Koolau range of Oahu to have $La_n = 140$ and $Y = 61$ ppm (n means normalized to chondrites; typical Y for Hawaiian basalt is 20 to 35 ppm); Clague⁶ found REE-enriched basalts on Molokai; and Fodor et al.⁷ report basalt from Kahoolawe anomalously high in REE and Y (Fig. 1). The importance of these observations lies in understanding whether they represent, among other possibilities, unusual mantle source material for basalt, an ability for REE and Y to concentrate during melting of typical Hawaiian mantle, magma contamination by assimilation, or vapor-phase concentration of REE, Y during eruption and cooling, or whether the REE, Y concentrations are secondary due to weathering.

Before any of these possibilities can be evaluated, one must establish exactly where and how the anomalously high REE and Y are

R. V. Fodor is at the Department of Marine, Earth, and Atmospheric Sciences, and D. P. Malta is at the Department of Materials Science and Engineering, North Carolina State University, Raleigh, NC 27695; G. R. Bauer is at the Honolulu Board of Water Supply, Hawaii 96832, and collected Kahoolawe samples with assistance from the U.S. Navy Pacific Fleet; and R. S. Jacobs is at Bass Enterprises Production, Ft. Worth, TX 76102, and did the microprobe analyses for part of his Master's degree research at NCSU. Instrumentation was supported in part by NSF grants EAR83-02737 and OCE85-09894, and by a North Carolina Board of Science and Technology grant to R. V. Fodor.

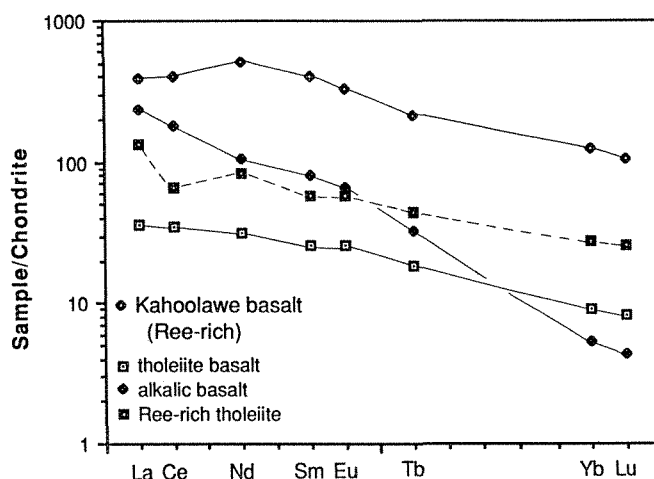


FIG. 1.--Chondrite-normalized rare-earth element concentrations for Hawaiian basalts. Representative tholeiitic and alkalic basalt and REE-rich tholeiitic basalt from Koolau Range, Oahu, Hawaii.⁵ Kahoolawe basalt is host for rare-earth phosphate of this study.⁷ (F. A. Frey, MIT, provided the REE data for this rock.)

contained in the basalts. Examination by polarizing microscope proved to be unequal to the task. To achieve documentation, we therefore chose REE, Y-rich alkalic basalt from Moaula vent on Kahoolawe Island (Fig. 1) for exploration by electron microprobe and scanning electron microscopy (SEM). Our examinations revealed that a groundmass phosphate mineral not known or expected to occur in basaltic rocks is the host for the abundant REE and Y.

Analytical Approach

The electron microprobe used in the Department of Marine, Earth, and Atmospheric Sciences at North Carolina State University is a manually operated ARL-EMX. It has three spectrometers and is interfaced with an Apple II computer for data reduction. Operating conditions were 15 kV accelerating voltage and 0.015 μ A sample current. Matrix corrections were made according to Bence and Albee,⁸ and intra-REE overlapping wavelengths were corrected (e.g., $La L\beta_1$ enhancing $Pr L\alpha_1$).

We located the REE, Y-bearing areas on polished thin sections by setting spectrometers to L wavelengths for La and Y, and then moving the sample under the electron beam until high La and Y concentrations were detected. Five to ten such areas of about $10 \times 40 \mu$ m were noted in three 1-in.-diameter thin sections of the Moaula vent basalt analyzed. REE analyses were made against REE standards⁹; P and F values were determined with the Smithsonian Institution reference apatite. Counting times

were 10 s per point, averaged over 10 points per grain. Backgrounds were the average of two off-peak settings.

The SEM was a JEOL JSM-840 at the Microelectronics Center of North Carolina. It is equipped with a Kevex 8000 microanalyzer and an energy-dispersive x-ray detector. SEM analyses were done on a rock chip cut by saw to yield a flat surface. The surface was gently buffed with #600 grit paper and carbon coated for a reconnaissance survey in the electron microprobe to locate REE,Y-bearing areas before SEM.

Analytical Results

The phosphate phase containing the REE and Y is randomly located in the basalt groundmass of plagioclase, olivine, clinopyroxene, Fe-Ti oxides, apatite, and minor amounts of phlogopite. The SEM x-ray map in Fig. 2 for the simultaneous data collection of P, Y, La, and Ce illustrates the subrounded outline of one of these REE,Y phosphate concentrations. Figure 3 shows a series of secondary-electron images of this area. Although the material appears polycrystalline, comprised of many elongate grains, we cannot be certain of that from the imagery acquired. The x-ray spectrum from a point on the surface in Fig. 3 shows K peaks for P, Ca, and Si, and L peaks for Y (the $L\beta_1$ line is incorporated under the P peak), La, Ce, and Nd (Fig. 4).

Table 1 lists the analysis by electron microprobe. The summation is low probably because the mineral was not analyzed for all REE likely to be present (e.g., Tb, Dy, and Yb), and possibly due to water content. The high amounts of La, Ce, and Nd, and the P_2O_5 of 29 wt% yield a composition similar to the relatively common REE-phosphate monazite (Table 1). However, distinctive are the relatively high amount of Y and lower LREE than usually present in monazite. In this regard, the composition is closer to that of the REE,Y hydrated phosphate rhabdophane, but differs from rhabdophane by the high (0.9 wt%) F content (Table 1). Fluorine may actually be present in rhabdophane, but is not reported as having been determined.

The REE pattern of the new phosphate resembles that of monazite in relative LREE contents, but is notably higher in middle-REE (Fig. 5). The REE pattern differs from that for rhabdophane by relatively higher Pr and middle-REE contents. However, as pointed out by Bowles and Morgan,¹⁰ the proportions of individual REE in rhabdophane probably depend on environment, where the structure accommodates the predominant REE available.

Discussion and Conclusions

Electron microprobe and SEM analyses document the occurrence of a REE- and Y-bearing phosphate previously unreported in Hawaiian basalts. Its composition does not specifically resemble known REE,Y-bearing phosphates¹¹ but comes close to that of rhabdophane. Also, its occurrence in the basalt resembles that noted by

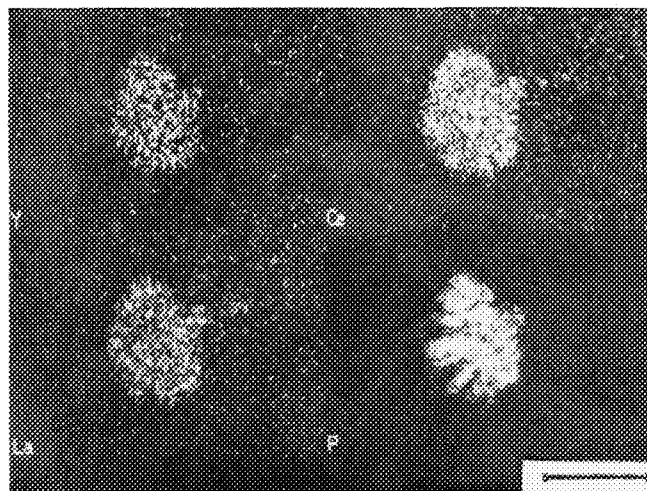


FIG. 2.--SEM x-ray map of REE- and Y-bearing phosphate in a Kahoolawe basalt. Dwell time was 50 ms. Accelerating voltage was 25 kV. K lines for P; L lines for Y, La, and Ce. Scale bar equals 40 μ m.

TABLE 1.-- Composition in wt% for a new REE,Y-bearing phosphate from Hawaiian basalt compared to compositions for monazite and rhabdophane.

	New phosphate	Monazite ^a	Rhabdophane ^b
SiO ₂	1.3	0.68	
TiO ₂	0.20		
Al ₂ O ₃	0.19		
FeO	0.48		0.35
CaO	0.95		0.26
K ₂ O	0.10		
P ₂ O ₅	29.4	28.66	28.59
F	0.9		
Cl	0.10		
ZrO ₂	0.25		
SrO	<0.01		
La ₂ O ₃	6.8	11.05	12.19
Ce ₂ O ₃	16.1	32.19	11.85
Pr ₂ O ₃	3.1	5.71	1.02
Nd ₂ O ₃	14.1	17.73	21.18
Sm ₂ O ₃	6.5	2.61	3.49
EuO	2.3		1.78
Gd ₂ O ₃	5.3	0.75	3.24
Tb ₂ O ₃			0.34
Dy ₂ O ₃		0.27	1.69
Ho ₂ O ₃		0.16	0.40
Er ₂ O ₃		0.07	1.12
Tm ₂ O ₃			0.51
Yb ₂ O ₃		0.10	0.40
Y ₂ O ₃	7.6	0.96	4.02
Sum	95.57		
- 0 \pm F	-0.38		
Total	95.19	100.94	92.43

^aRef. 14, Table 9.

^bRef. 10; see also Refs. 11, 12.

Open places in analyses indicate element not determined. PHA used for F analysis to eliminate P interference.

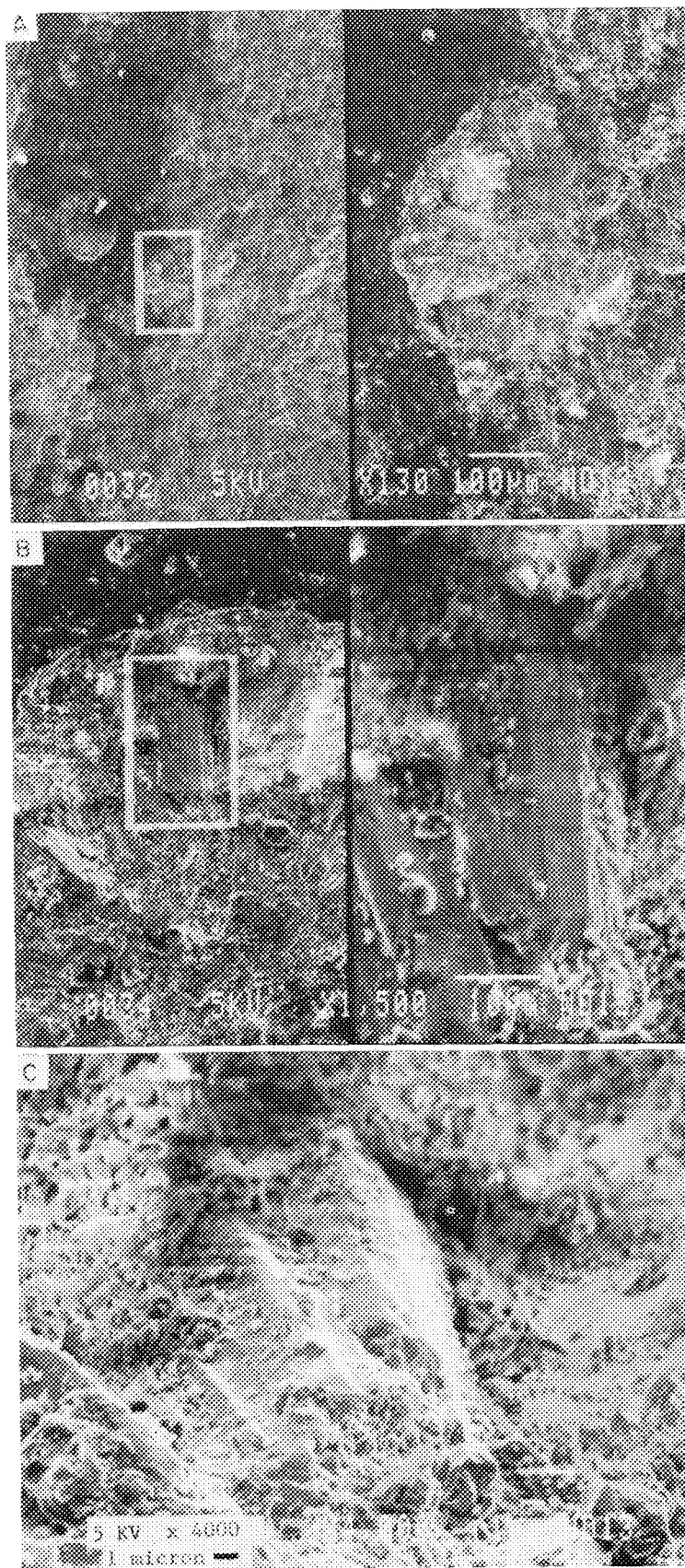


FIG. 3.--Secondary-electron images of REE- and Y-bearing phosphate in Kahoolawe basalt. All images are from same area as in Fig. 2. Images (a) and (b) were taken at 0° tilt, (c) from about 45° tilt. Scale bars in (a) and (b) refer to left-side images only.

Adams¹² for rhabdophane in a mineralized zone (supergene) in Idaho as aggregates of intergrown crystals in spheroidal forms less than 20 μm in diameter. Based on its subrounded occurrence in the basalt groundmass, this new phosphate could represent precipitation from vapor or fluid permeating the basaltic magma while in a shallow reservoir, or during eruption and cooling on the surface. The source of such REE,Y concentrates migrating in Hawaiian magmatic plumbing systems is unknown. However, the mobility of REE and Y is most likely facilitated by complexing with Cl and F¹³ in magma systems --and F appears to be part of the rhabdophane-like phosphate (Table 1).

References

1. W. P. Leeman, A. V. Murali, M.-S. Ma, and R. A. Schmitt, "Mineral constitution of mantle source regions for Hawaiian basalts: Rare earth element evidence for mantle heterogeneity," *Bull. Oregon Dept. Geol. Mineral. Ind.* 96: 169, 1977.
2. D. A. Clague and F. A. Frey, "Petrology and trace element geochemistry of the Honolulu volcanics, Oahu: Implications for the oceanic mantle below Hawaii," *J. Petrol.* 23: 447, 1982.
3. C.-Y. Chen and F. A. Frey, "Trace element and isotopic geochemistry of lavas from Haleakala volcano, East Maui, Hawaii: Implications for the origin of Hawaiian basalts," *J. Geophys. Res.* 80: 8743.
4. F. A. Frey and M. F. Roden, "The mantle source for the Hawaiian Islands: Constraints from the lavas and ultramafic inclusions," in M. A. Menzies and C. J. Hawkesworth, Eds., *Mantle Metasomatism*, New York: Academic Press, 1987, 423.
5. M. F. Roden, F. A. Frey, and D. A. Clague, "Geochemistry of tholeiitic and alkalic lavas from the Koolau Range, Oahu, Hawaii: Implications for Hawaiian volcanism," *Earth Planet. Sci. Lett.* 69: 141.
6. D. A. Clague, "Petrology of West Molokai volcano," *Geol. Soc. Amer. Prog. (Abstracts)* 19: 366, 1987.
7. R. V. Fodor, G. R. Bauer, R. S. Jacobs, and T. J. Bornhorst, "Kahoolawe Island, Hawaii: Tholeiitic, alkalic, and unusual hydrothermal (?) 'enrichment' characteristics," *J. Volcan. Geotherm. Res.* 31: 171, 1987.
8. A. E. Bence and A. L. Albee, "Empirical correction factors for the electron microanalysis of silicates and oxides," *J. Geol.* 76: 382, 1968.
9. M. J. Drake and D. F. Weill, "New rare-earth element standards for electron microprobe analysis," *Chem. Geol.* 10: 179, 1972.
10. J. F. W. Bowles and D. J. Morgan, "The composition of rhabdophane," *Mineral. Mag.* 48: 146, 1984.
11. J. D. Nriagu, "Phosphate minerals:

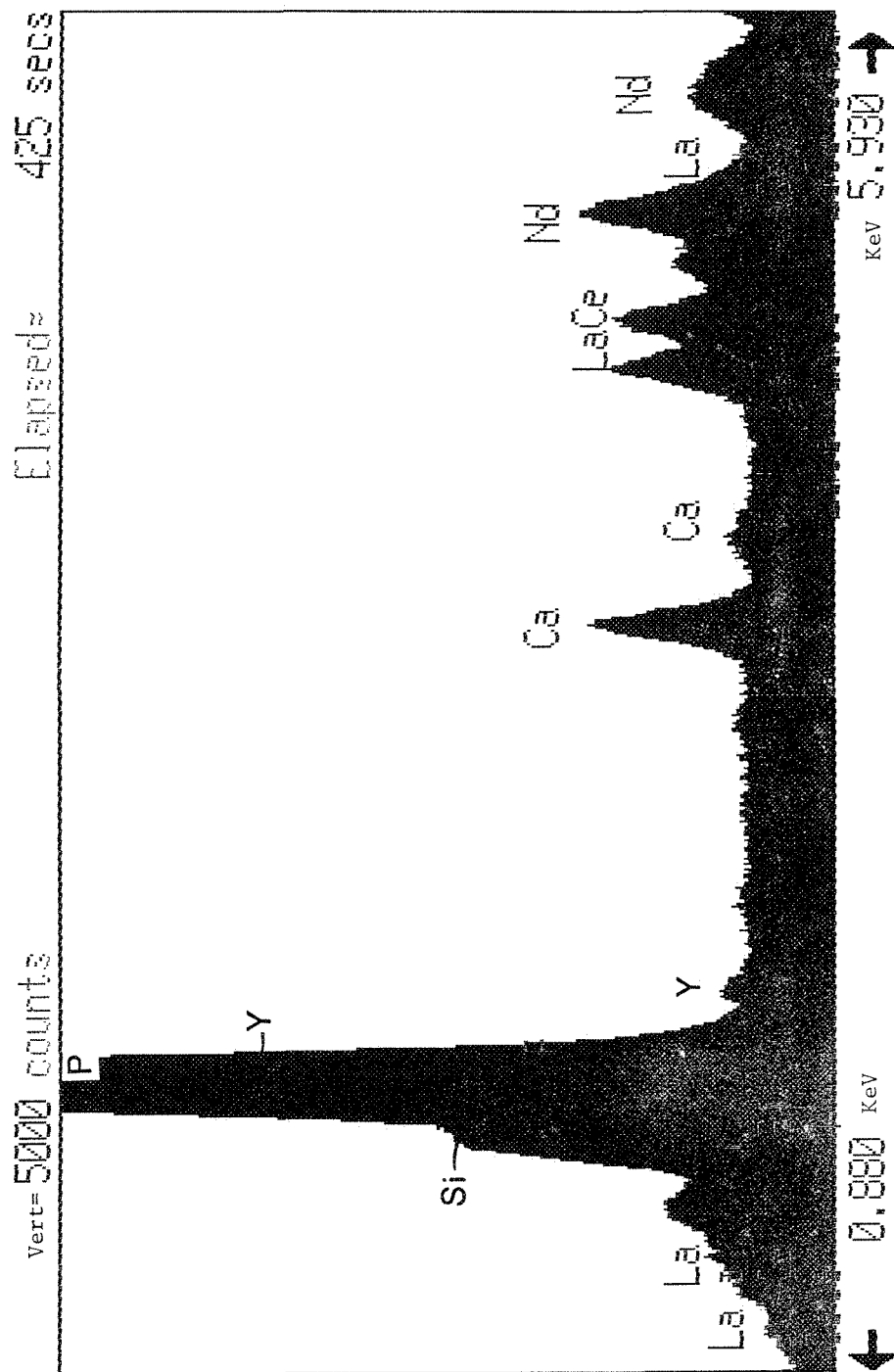


FIG. 4.--Energy-dispersive x-ray spectrum of REE- and Y-bearing phosphate illustrated in Fig. 3. Y $L\beta_1$ peak blends with P $K\alpha_{1,2}$ peak.

Their properties and general modes of occurrence," in J. O. Nriagu and P. B. Moore, Eds., *Phosphate Minerals*, New York: Springer, 1984, 1.

12. J. W. Adams, "Rhabdophane from a rare-earth occurrence, Valley County, Idaho," U.S. Geol. Surv. Prof. Paper 600B, 1968, B48.

13. S. E. Humphris, "The mobility of the rare earth elements in the crust," in P. Henderson, Ed., *Rare Earth Element Geochemistry*, Amsterdam, New York: Elsevier, 1984, 317.

14. W. P. Nash, "Phosphate minerals in terrestrial igneous and metamorphic rocks," in Ref. 11, p. 215.

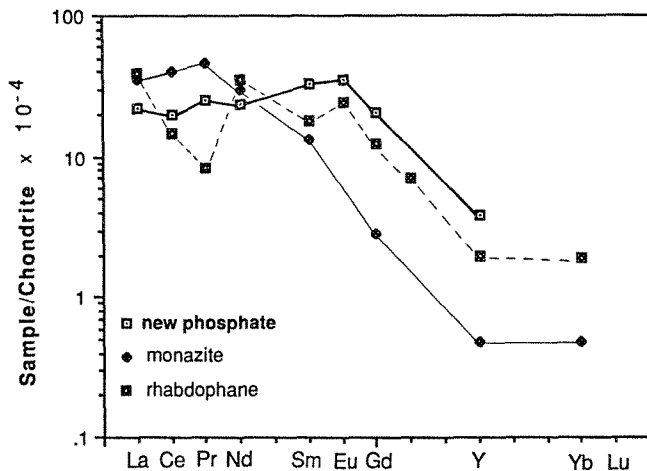


FIG. 5. Chondrite-normalized REE pattern for new phosphate in Kahoolawe Island basalt, compared to patterns for monazite and rhabdophane; compositions in Table 1.

IDENTIFICATION OF RARE EARTH AND YTTRIUM MINERALS USING THE MinIdent DATABASE

Dorian G. W. Smith

The last decade has seen renewed interest in yttrium and the rare-earth elements (REE) as their industrial potential in such areas as superconductors, ceramics, and nuclear-waste disposal systems has grown. Exploration for rare-metal deposits has been very active and their investigation has inevitably led quickly to the use of microbeam techniques to examine the constituent minerals and their textural relationships. Among the most intractable have been minerals containing essential, or at least significant, concentrations of Y and REE. Although certain well-known REE minerals have often been recognized, many others have been doubtless passed over simply because investigators have been unable to make identification from available data.

Because they frequently contain significant quantities of Th and U, REE minerals are commonly metamict. Thus the techniques of powder diffraction, employed so commonly in mineral identification, are useful only after heat treatment (see, for example, Ref. 1). Then it is often found that a mineral is to be reconstituted into two or more phases, rather than the original mineral that crystallized. In this situation, quantitative electron microprobe analysis and recognition of the original phase on the basis of composition of the metamict mineral becomes even more important.

Accurate determination of REE concentrations in situ by use of the electron microprobe is one of the more difficult tasks facing a microanalyst. Papers in these proceedings may discuss in detail many problems that present themselves. They include severe peak overlaps and the determination of background beneath the crowded peaks of the complex L spectra normally used in analysis. The sheer number of measurements of peak and background intensities required to determine accurately 14 REE, Y, and the many other elements commonly present (the total may often exceed 30) poses additional problems, as do ubiquitous inhomogeneities and the common instability of REE minerals beneath an electron beam. Correction of data for matrix effects, and the unusual self-absorption phenomena that can seriously affect measurements of M-line intensities, are yet other problems that must be dealt with, as are inherent restrictions on the number of elements that can be corrected simultaneously in many software packages. Requirements for satisfactory

standardization must also be faced.

Even when all these problems have been resolved, the difficulties of mineral identification may remain. At present the literature includes over 140 named mineral species containing *essential* REE plus another 20 or so that have been recognized but remain as yet unnamed. If we include minerals that may contain appreciable amounts of REE that, however, are not essential to their definition, the total is several hundred.

MinIdent

Normally, a well-trained mineralogist is likely to recognize a handful of these species. Most microanalysts will recognize less. Nor should the importance of mineral identification be underestimated. It is the key to unlocking all the information previously gathered for that natural compound and is often a shortcut to determining the most successful methods of treatment, beneficiation, etc. The present paper shows how the MinIdent² computer software and the database it uses can be employed to assist an investigator in obtaining either a rapid identification or at least reducing possible identities from several hundred to a handful.

MinIdent can use two different procedures as an aid to identification. In the first, MATCH, data for an unknown are compared to corresponding data in the database for all minerals. If the input values for the unknown do not lie within the range stored for a particular mineral, that mineral is not considered further. In the second procedure, IDENTIFY, no minerals are dropped from consideration but "demerit points" are assigned according to the size of the mismatch between the data for an unknown and that in the database. Up to 20 minerals having the lowest "demerit points" may then be listed. In applying these two procedures, MATCH is normally employed first to reduce the list of possibilities from nearly 4600 to a 100 or so. To do that, compositional data (and/or other properties) are input with wide error limits—limits that will embrace any possible uncertainties in data for the unknown and also allow for the fact that data in the database may not necessarily include the full range of values that can exist in nature. Only major element concentrations are included at this stage. Minor elements may be peculiar to a particular unknown and hence might cause rejection of a mineral that in every other respect is a good "fit." Once possibilities have been reduced in this way, the most precise data available for all elements (and other properties) are entered and

The author is at the Department of Geology, University of Alberta, Edmonton, Alberta, Canada T6G 2E3. This work was supported financially by Grant A4254 from the Natural Sciences and Engineering Research Council of Canada.

TABLE 1.--Analytical data.

	"euxenite"	monazite	allanite	U,Nb-oxide [†]
U308	22.7	0 0	0 0	28.2*
Th02	6.0	8 6	0.0	
Y203	18.9	0 0	0.0	
Nb205	26.9	0.0		47.8
Ta203	0.4	0 0		
Ti02	19.7	0 0	1.4	4.2
Fe0	1.9	0.3**	17.0**	7.6
Ca0	0.3	0.6	10.8	5.7
La203	0.0	13.8	8.3	
Ce203	0.0	27.5	11.3	3.3
Pr203	0.3	6.1	2.7	
Nd203	0.3	10.3	2.1	
Sm203	0.4	1.9	0.33	
Eu0	0.1	1.0	0.16	
Gd203	1.3	3.4	0.0	
Tb203	0.4	0.2		
Ho203	1.4	0.2		
Er203	2.4	0.0		
Dy203	3.9			
P205		25.9		
Al203			14.9	
Si02			29.5	3.2
TOTAL	107.3	99.8	99.89	100.0
MinIdent 1st choice:				
	polycrase-(Y) monazite-(Ce) allanite-(Ce) ashanite			

[†] Analyst: R. Pinckston, U of Alberta; * UO₂; ** Fe₂O₃.

the procedure IDENTIFY AND is invoked to determine the *most* likely identities. (The AND following IDENTIFY limits the list of minerals considered to that produced by MATCH.)

Analytical Data

Table 1 shows compositions of three Y and REE minerals, published recently in these proceedings.³ The minerals were identified as euxenite, monazite, and allanite--REE minerals that are relatively common, but not easily identified without previous familiarity or the aid of accurate compositional information. In fact, all the names were incomplete. According to rules recently adopted by the International Mineralogical Association and its Commission on New Minerals and Mineral Names, all Y and REE minerals should be followed by an identifier indicating which of these elements is dominant in that species.⁴ For example, allanite-(Ce), allanite-(La) and allanite-(Y) are isostructural minerals with similar but distinct compositions and with optical and physical properties that vary somewhat. This scheme brings order to a nomenclature that had grown chaotic. The data actually entered into the program are shown in Table 2.

Results

The mineral euxenite-(Y)--the Y indicates that yttrium is dominant--has the formula (Y,Ca,Ce,U,Th)(Nb,Ta,Ti)O₆ and forms a series with the mineral polycrase-(Y) (Y,Ca,Ce,U,Th)(Ti,Nb,Ta)O₆, in which Ti is dominant over Nb; the reverse is the case in euxenite-(Y). According to the formula calcu-

TABLE 2.--MinIdent data entry for "euxenite," monazite, allanite, and U,Nb-oxide.

```

"EUXENITE" DATA
unknown|w Nb205=17-37|w Ti02=10-30|w Y203=9-29|save|match
unknown edit|w=null|w U308=22.7|w Th02=6|w Y203=18.9|w Nb205=26.9
w Ta205=0.4|w Ti02=19.7|w Fe0=1.9|w Dy203=3.9|w Er203=2.4|w Ho203=1.4
save|identify and
tab name unk TM w O w Nb w Ti w Ta w U w Th w Y w Dy w Er w Ho w Fe
MONAZITE DATA
unknown|w P205=16-36|w Ce203=17-38|save|match
unknown edit|w=null|w Th02=8.6|w Ca0=0.6|w La203=13.8|w Eu0=1
w Ce203=27.5|w Pr203=6.1|w Nd203=10.3|w Sm203=1.9|w Gd203=3.4
w P205=25.9|save|identify and
tab name unk TM w O w P w La w Ce w Pr w Nd w Sm w Eu w Gd w Dy w Th
ALLANITE DATA
unknown|w Si02=20-40|w Al203=5-25|w Fe203=7-27|w Ca0=1-21|w Ce203=1-21
save|match
unknown edit|w=null|w Si02=29.5|w Al203=14.9|w Ca0=10.8|w Ce203=11.3
w La203=8.3|w Pr203=2.7|w Nd203=2.1|w Sm203=0.33|Ti02=1.4|save|
identify and
tab name unk TM w O w Si w Al w Ca w Ce w La w Pr w Nd w Sm w Eu w Ti
U,Nb-OXIDE DATA
unknown|w UO2=18-38|w Nb205=33-63|save|match
unknown edit|w=null|w UO2=28.2|w Nb205=47.8|w Ti02=4.2|w Fe0=7.6
w Ca0=5.7|w Ce203=3.3|w Si02=3.2|save|identify and
tab name unk TM w O w U w Nb w Ti w Fe w Ca w Ce formula

```

lated by Knowles,³ the mineral is close to the center of the series, but just on the polycrase-(Y) side. This also becomes apparent when the data are processed through MinIdent (Table 2). Polycrase-(Y) and euxenite-(Y) both appear in the list of minerals, but the former has a slightly better total matching index ("TM"). Table 3 also shows that the monazite is easily identified as monazite-(Ce), clearly a better match than monazite-(Nd). The processing of the allanite data (Table 3) shows that the mineral should be termed allanite-(Ce).

Finally, semiquantitative data are also presented in Table 1 for an unidentified U,Nb-oxide from the Thor Lake rare-metals deposit.⁵ This mineral contains Ce as a significant but probably nonessential constituent, i.e., its presence might be common but not likely to be the dominant element in a particular structural site. In such a case the Y or REE symbols should *not* be appended to the mineral name, since it might be entirely possible to have examples of this mineral that contain little or no Ce. Table 3 shows possible identities obtained by processing of the data through MinIdent. Note that Ce was not in the initial data entered for the MATCH procedure. A sufficient reduction in possibilities could be obtained by use of only the major elements Nb and U. In fact, because of the scarcity of really accurate REE data, it is often best to exclude these elements from MATCH unless they are present in very high concentrations, and even then they should be used only with very generous error limits. The complete analytical data are of course introduced before the

Record: 2645 ASHANITE species of OXIDES										00:01:46FEB 9, 1989		
Formula: (Nb,Ta,U,Fe,Mn)408												
Symmetry: Orthorhombic					Space Group: Pcan[60]			JCPDS: 33-0660		Dispersion:		
Type: OXIDES			Year First Described: 1980			Samples: 1		Generals: 1		Total Samples: 1		
El	Wt Min	Wt Ave	Wt Max	Std Dev	At Prop	Coord	a	b	c	Alpha	Beta	Gamma
Nb	0 000	25 697	74 382		1 573		5 869	4 873	5 216	90.000	90 000	90 000
O	11.850	22 510	36 807		8 000*							
U	0 000	20 191	88 150		0 482							
Ta	0 000	19 172	84 973		0.602		n(alpha)	n(beta)	n(gamm)	Density	VHN	MOH
Fe	0 000	6 413	63 574		0 653		2 310	2 350	2 400	6.6	570.0	5.8
Mn	0 000	6.018	63 193		0 623					6.61	710 5	6 2
										6.61	851.0	6.6
							R(470)	R(546)	R(589)	R(650)	2V(gam)	OAP
							11 4				70 0	
							11 45	10 9	10 8	10 6	73 0	
							11.5				75.0	
							C(alpha)	C(beta)	C(gamm)	d-vals		
							L Br Rd		D Br Rd	2 95		
										3 65		
										2 54		
										2 51		
										2 38		
11.85 100.0 411.078 11.933												
Sources: Amer. Min. v.66, p.217;												
Collection number(s):												
Polymorphs:												
Remarks: Dark in colour with brownish streak Lustre is submetallic to pitch-like and the fracture subconchoidal An infrared spectrum is available in the original literature The mineral is a Nb-analogue of ixiolite. 1.40% undifferentiated RE2O3 also reported in only analysis.												
Occurrence: In the central part of a pegmatite in an albitized two-mica granite Assoc with Ta-rich columbite, Th-rich monazite and ishikawaite.												
Location(s): Altai Mts., N.W. China.												

FIG. 1.--Compiled ashanite data.

TABLE 3.--MinIdent output.

EUXENITE RESULTS												
Name	TM	O	Nb	Ti	Ta	U	Th	Y	Dy	Er	Ho	Fe
unidentified sample		25 4	18 616	11 692	0 324	19 057	5 22	14 734	3 364	2 078	1 21	1 462
		25.913	18.992	11.928	0.331	19.442	5.326	15.031	3.432	2.12	1.234	1.492
POLYCRASE-(Y)	75 5	26 566	15 465	14 285	5 288	7 749	3 098	13 235	1 613	1 582	0 428	1 41
EUXENITE-(Y)	75 2	28 324	27 033	8 242	3 78	7 582	2 027	13 734	1 18	0 924		4 379
UM1926-O1	52 5	25 383	28 118	19 925	35 725			12 327		19 053		
PISEKITE	49 6	25 137	28 661	2 518	5 651	8 815	1 845	7 334				2 021
AESCHYNITE-(Y)	41 0	26 196	17 005	16 171	3 57	2 423	5 618	8 779	2 63	1 619	0 506	1 811
UM1930-O1	36 5	28 206	28 933	2 572	5 954	10 658	1 389	13 89				4 092
MURATAITE	30 1	25 378	6 597	22 703				9 497	1 899	2 702	0 498	3 397
BETAFITE-SUBGROUP	24 0	29 798	23 05	8 822	4 172	13 062	0 943	4 962	0 017			2 336
PYROCHLORE-SUBGROUP	19 5	29 712	36 757	2 366	4.557	6 285	0 475	3 735	0 334	0 205		1 649
NIOBO-AESCHYNITE-(Y)	14.5	23.853	27.197	11.451	6.779	0.339	9.465	3.481	0.862	0.331	0.0	0.745
MONAZITE RESULTS												
Name	TM	O	P	La	Ce	Pr	Nd	Sm	Eu	Gd	Dy	Th
unidentified sample		24 778	11 19	11 649	23 244	5 16	8 742	1 622	0 896	2 92		7 482
		25.279	11.416	11.885	23.713	5.264	8.919	1.655	0.914	2.979		7.633
MONAZITE-(CE)	87 0	27 347	12 828	13 463	24 691	2 657	10 331	1 867	0 33	0 986	0 713	0 985
MONAZITE-(ND)	74 3	26 923	12 477	6 184	16 71	3 652	21 821	6 129	0 788	2 392	0 523	0 773
CERPHOSPHORHUTTONITE	59 2	27 564	4 364	3 846	10 117	1 256	4 835	1 026				35 644
RHADOOPHANE-(CE)	54 0	28 543	10 31	13 881	26 999	1 668	3 589	0 052		0 069	0 0	1 538
BELOVITE	46 1	29 601	12 604	5 756	9 605	1 923	4 818					
UM1983-17	28 0	37 414	10 118	32 016	32 116							37 418
BROCKITE	13.0	32.92	10.78	0.418	2.006	0.017	1.303	0.621	0.259	0.859	0.558	37.525
ALLANITE RESULTS												
Name	TM	O	Si	Al	Ca	Ce	La	Pr	Nd	Sm	Eu	Ti
unidentified sample		29 68	13 652	7 807	7 642	9 551	7 006	2 284	1 782	0 282		0 831
		30.279	13.927	7.965	7.796	9.744	7.148	2.33	1.818	0.287		0.848
ALLANITE-(CE)	73 3	37 072	16 271	8 587	9 593	7 969	4 098	0 498	1 799	0 223	0 083	0 407
ALLANITE-(Y)	56 4	39 254	15 495	10 368	9 676	1 59	0 662	0 393	2 185	1 248		0 118
ALLANITE-(LA)	54 1	36 742	14 299	8 515	6 505	7 232	9 713	0 0	0 0	0 0		0 46
TRITOMITE-(Y)	48.8	39.517	11.584	2.001	7.163	3.196	0.731	0.628	2.709	1.05		0.276
U,Nb-OXIDE RESULTS												
Name	TM	O	U	Nb	Ti	Fe	Ca	Ce	Formula			
unidentified sample		24 666	24 61	33 08	2 493	5 848	4 033	2 789				
		25.164	25.107	33.748	2.543	5.967	4.115	2.846				
ASHANITE	73 4	22 51	20 191	25 697		6 413			(Nb,Ta,U,Fe,Mn)408			
PISEKITE	73 4	25 137	8 815	28 661	2 518	2 021	2 001	2 489	(Y,Ce,Ca,As,Fe,U)(Nb,Ti,Ta)(O,OH)			
PYROCHLORE-SUBGROUP	56 3	29 712	6 285	36 757	2 366	1 649	2 322	1 111	N/A			
PETSCHEKITE	54 3	21 386	35 701	25 305		7 079	0 35		U4+Fe2+(Nb,Ta)208			
UM1930-O1	53 2	28 206	10 658	28 933	2 572	4 092	3 016	0 265	(Ca,Pb,Y,U)(Nb,Ta,Ti,Fe3+)206			
PLUMBOBETAFITE	34 6	24 848	12 925	21 642	7 973	0 797	1 508	2 408	(Pb,U,Ca)(Nb,Ti)206(OH,F)			
SAMARSKITE-(Y)	27 7	26 132	10 883	25 651	1 572	6 106	0 581	1 312	(Y,Ce,U,Fe3+)3(Nb,Ta,Ti)5016			
ISHIKAWAITE	23.4	22.763	19.801	23.133	0.622	7.812	1.06	0.748	(U,Fe,Y,Ca)(Nb,Ta)04			

IDENTIFY AND procedure is invoked.

Figure 1 shows a compilation of data stored in the database for the mineral aphanite, which is one of the two minerals that are most similar to our unidentified U,Nb-oxide. Such records give the average and in some cases a range of values for a substantial number of properties. They also summarize geological situations in which a mineral has been found previously, provide localities for samples used in the database, and perhaps most important, give the corresponding references, which allow the user to trace literature sources. Many data for REE minerals appear in non-English language (particularly Russian) literature. Whenever possible references are given to translations of such articles, or at least to English-language abstracts.

An entry "UM1930-01" appears in the list of "identified" minerals in Fig. 1. This designation stands for an Unnamed Mineral reported first in 1930; it was probably the first entered into the database for that year. At present more than 600 such minerals are included in MinIdent. Unnamed minerals, scattered widely throughout the literature, are particularly difficult to trace. Only a few (now incomplete) compilations have appeared.⁶⁻⁷ The compilation in MinIdent includes unnamed minerals for which solid, compositional, optical, or other physical data are available. Possibly new species described only in vague terms such as hand-specimen color, habit, and other nondefinitive physical characteristics have been excluded. In addition, when an unnamed mineral is subsequently named, the UM... listing is removed in favor of the new correct name, and a note drawing attention to this substitution is included in the *Remarks* field for the new species.

Two other features of MinIdent are noteworthy in connection with applications to REE minerals. The SYNONYM list provides information (including references) for mineral names that are either synonymous with other, preferred names, or that simply designate *varieties* of true species. The same facility is used to provide a message (and reference) when a request is made concerning a discredited mineral name. The SUBSET facility allows a user to create a list of minerals from within the database and then consider only that subset when using procedures such as MATCH and IDENTIFY. Since the size of database that must then be searched is greatly reduced, significant economies in processing time result. This could be particularly significant if MinIdent were to be used in an automated mode in conjunction with a digital imaging package.

Conclusions

Notwithstanding the success demonstrated in the distinction of various REE minerals, there is a great paucity of good, accurate data for many of the minerals. Early wet chemical analyses seldom distinguished the individual REE, and later microprobe analyses may suffer from

all the difficulties noted at the beginning of this paper. As new and better data are added, so the ability of the MinIdent software to discriminate among possible REE minerals will improve further.

References

1. J. Lima de Faria, "Identification of metamict minerals by X-ray powder photographs," in Junta de Investigações do ultramar: Estudos, ensaios e documentos No. 112, Lisbon, Portugal, 1964 (74 pp. plus tables).
2. D. G. W. Smith and D. P. Leibovitz, "MinIdent: A data base for minerals and a computer program for their identification," *Can. Mineralogist* 24: 695, 1986.
3. C. Knowles and T. H. Kiilsgaard, "Rare earth minerals in black sands of the Big Meadow deposit, Idaho," *Microbeam Analysis--1988*, 483.
4. P. Bayliss and A. A. Levinson, "A system of nomenclature for rare-earth mineral species: Revision and extension," *Amer. Mineralogist* 73: 422, 1988.
5. D. L. Trueman, J. C. Pedersen, L. de St. Jorre, and D. G. W. Smith, "The Thor Lake rare-metal deposits, Northwest territories," in J. P. Taylor and D. Strong, Eds., *Recent Advances in the Geology of Granite-related Mineral Deposits*, Can. Inst. Mining & Metallurgy, Sp. vol. 39, 1988, 280.
6. M. H. Hey, *An Index of Mineral Species and Varieties Arranged Chemically*, London: British Museum of Natural History, 1962 (728 pp.).
7. M. H. Hey, *Appendix to the Second Edition of an Index of Mineral Species and Varieties Arranged Chemically*, London: British Museum of Natural History, 1963 (135 pp.).

SEM ANALYSIS OF ROCK VARNISH CHEMISTRY: A GEOMORPHIC AGE DISCRIMINATOR

C. D. Harrington and Robert Raymond Jr.

Rock varnish, a manganese- and iron-rich coating commonly found on rock surfaces in arid and semiarid regions, has long been of interest as a potential age indicator. Rock varnish has been shown to be an effective medium for dating of geomorphic surfaces over a time range of several thousand to over a million years, by use of a ratio among minor cations $[(K + Ca)/Ti]$ for the total volume of rock varnish.¹ We have recently developed a technique using the scanning electron microscope (SEM) equipped with an energy-dispersive x-ray analyzer (EDAX) to analyze the chemistry of rock varnish.² This technique has several advantages over the earlier cation ratio technique.

Methodology

Our SEM procedure utilizes two 0.5cm-thick disks made from circular cores drilled through the varnish and rock substrate on each varnished clast. The rock substrate is ground parallel to the varnish surface and the disks from each varnished clast are mounted on a glass slide and carbon coated for SEM analysis. We analyze the rock varnish on 8 to 10 rock clasts (16 to 20 disks) for each geomorphic surface being dated. For SEM analysis we use a takeoff angle of 40° and a counting time of 100 s. To assure a steady beam current, dead time is held between 15 and 25%. All data are obtained with a Tracor standardless program in which x-ray peak intensities are ZAF (factors for atomic number, absorbance, and fluorescence) corrected before elemental weight % are calculated. Elemental weight % are recorded for four major (Si, Al, Fe, and Mn) and seven minor (Mg, Ca, K, Ti, P, S, and Cr) varnish constituents.

The bulk chemistry of the varnish on each disk, which has a surface area of about 4 cm², is obtained by SEM-EDAX. Relative abundance of elements are based on relative x-ray peak intensities. Although absolute concentrations of individual elements may not be determined with great accuracy due to microrelief on the varnish surface, ratios of elements have a high degree of accuracy. Before the varnish is analyzed, several analyses are obtained of exposed rock substrate where the varnish has been chipped during coring. Elements that are either of markedly greater or of very low abundance when compared to the varnish chemistry are noted.

In analyzing rock varnish we use a small SEM

magnification ($\sim 30\times$) in order to include the maximum area of varnish in each analysis. Six sites are analyzed on each disk to produce an integrated analysis of the entire disk surface. We initially use a low electron accelerating potential (10 kV) and then progressively increase the voltage in 5kV increments while analyzing the same sample area, so that greater depth penetrations into progressively older varnish are achieved. In varnish analyses, quantities of Ti, Mn, and Fe gradually increase as varnish is penetrated (voltage is increased), reach a maximum when older varnish is included, and then decrease with increasing voltage where substrates are deficient in these elements. The quantity of K and/or Ca may decrease with depth in the near-surface varnish and rapidly increase when substrates high in K or Ca are penetrated. Thus, in varnish analyses, the varnish cation ratio $[(K + Ca)/Ti]$ decreases to a minimum value at some depth in the varnish and then, for substrates rich in K and/or Ca, gradually increases with increasing penetration. The cation ratio minima occur below the voltage at which elements absent in the varnish, but abundant in the rock substrate, appear in the analysis; and at (or just below) the voltage level at which Mn and/or Fe maxima are obtained. It is this minimum cation ratio we select for a site analysis. The cation ratio for each disk is calculated from the five lowest site ratios. A cation ratio for each rock sample is calculated by averaging of the two disk ratios. The cation ratio for a geomorphic surface or deposit is calculated from the average of the 8-10 rock cation ratios. Thus, the cation ratio for a surface combines 80 to 100 analyses.

In this paper, polished sections across the varnish/substrate interface are used to show relationships between varnish occurrence and substrate morphology, and between the chemistries of varnishes and substrates. Due to the high absorption coefficients of Mn and Fe for Ca, K, and Ti x rays, such comparisons could not be shown on planar surfaces of samples on which VCR analyses have been made.

Comparison of SEM and Earlier Technique

The SEM technique differs from and has a number of advantages over the earlier method described by Dorn¹ to calculate cation ratios. The earlier method entails extraction of the varnish from the rock substrate by scraping with a tungsten-carbide needle under 40 \times magnification and analyzing the scrapings by proton-induced x-ray emission (PIXE).

Rock varnish coatings are commonly a few to

The authors are in the Earth and Space Sciences Division, Los Alamos National Laboratory, Los Alamos, NM 87545. Supported by the U.S. Department of Energy.

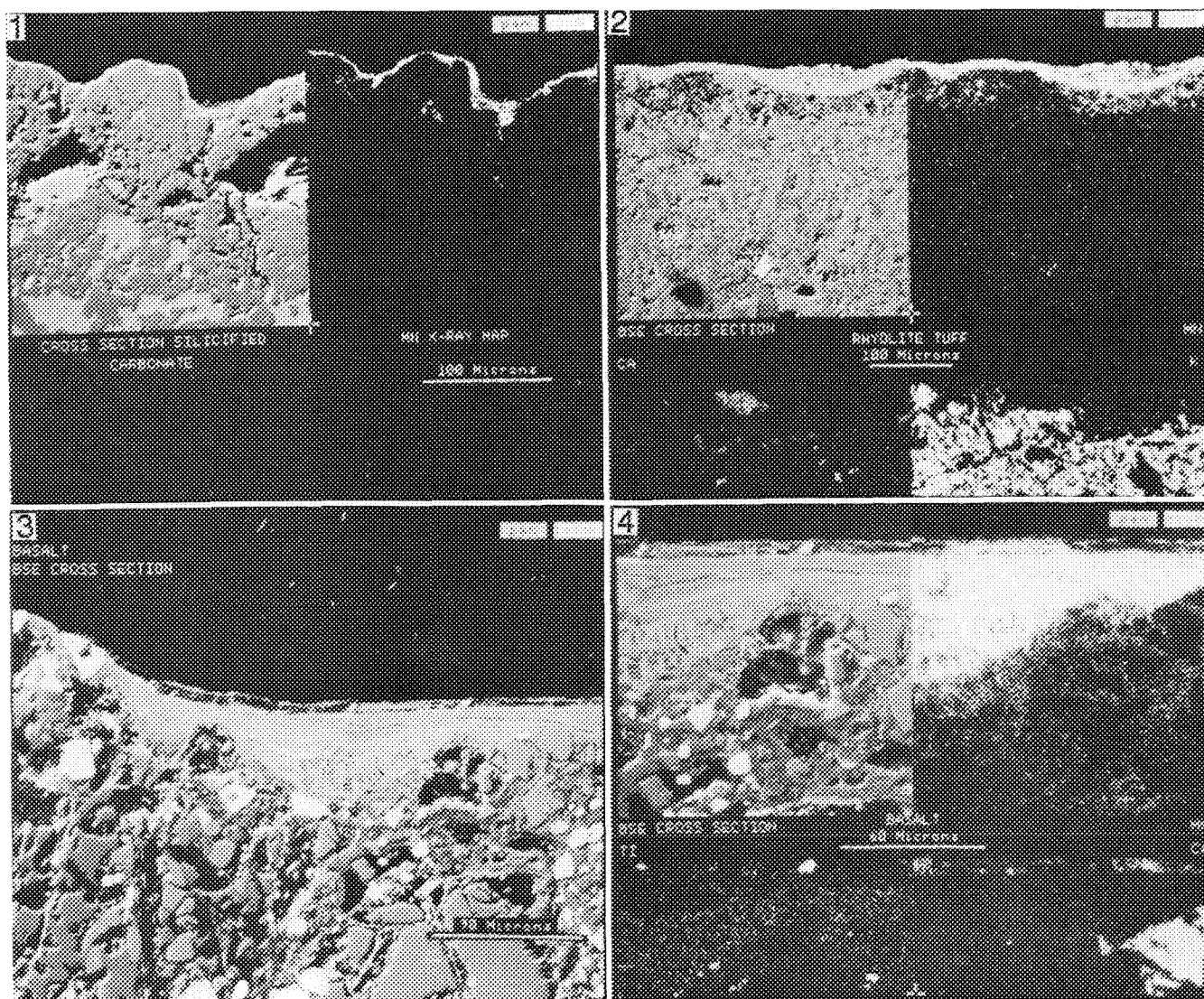


FIG. 1.--Backscattered electron (BSE) image and Mn x-ray map of polished cross section of silicified carbonate showing continuity of thin rock varnish coat over substrate with great micro-roughness due to the substrate's mineralogy.

FIG. 2.--BSE image and Mn, Ca, and K x-ray maps of polished cross section of rhyolite tuff. Two areas of substrate most vulnerable to removal during scraping of rock varnish host Ca- and K-rich feldspar grains.

FIG. 3.--BSE image of polished cross section of basalt showing small depression infilled with rock varnish. Within upper layers of infilling is detritus horizon that has been bound in place by overlying Mn-rich rock varnish.

FIG. 4.--BSE image and Mn, Ti, and Ca x-ray maps of area of Fig. 3 magnified to show presence of Ti-rich (titanomagnetite) and Ca-rich (probably feldspar) material in detritus horizon that is incorporated in rock varnish.

a few tens of micrometers thick and are best formed on fine-grained rocks such as basalt, tuff, sandstone, and chert that may contain a surface microroughness (Fig. 1). With the SEM technique, once a complete varnish coat has been accreted, substrate surface microroughness does not significantly affect calculated cation ratios³ and major topographic irregularities can be avoided by use of slightly higher magnification and changes in location of sites for analysis. In addition, topographic irregularities on the varnish/substrate interface do not

pose a serious problem in analysis as the varnish thickness determines at what voltage the cation ratio is obtained. It is difficult or impossible to scrape such irregular varnish or rock surfaces so as to remove only the varnish without incorporating a substantial quantity of powdered rock material that may contain high concentrations of Ca, K, or Ti (Fig. 2). With the SEM, we analyze the varnish in situ, avoiding problems inherent in attempting to remove the varnish from the substrate.

Other major advantages of the SEM technique

lie in the procedure of SEM analysis. The most significant among them is the ability to examine the variation in varnish chemistry across a disk or from disk to disk as the sample is being analyzed. Thus, areas of anomalous chemistry may be avoided and analyses of those areas discarded. For example, major depositional events within a geomorphic area can result in varnish surfaces becoming covered with eolian detritus. Such mineral detritus tends to be concentrated in depressions on horizontal rock surfaces. If eolian detritus withstands winnowing and erosional processes long enough, varnish accretion binds or buries these externally derived mineral grains and a record of the event is retained within the layers of rock varnish (Figs. 3 and 4). If this eolian detritus is rich in Ca, K or Ti (Fig. 4) and the mineral grains remain bound into the varnish, areas of the varnish where the detrital concentrations occur yield anomalous cation ratios that may significantly alter the cation ratio calculated for the rock clast and thus for the geomorphic surface being dated. Such anomalous results would be readily apparent where the SEM technique is used because of the variability between detritus-rich and detritus-poor areas; anomalous areas can then be discarded prior to calculation of the VCR for the clast. The scraping method, in contrast, extracts varnish from the substrate without knowledge of the variation in chemistry within the sample. Detrital concentrations such as above cannot be avoided and are likely to be incorporated into the final sample to be analyzed. Furthermore, preparing a varnish sample for PIXE analysis requires combining varnish from several clasts to form one sample of great enough bulk. Such mixing makes recognition of chemically anomalous areas of varnish much more difficult and destroys the ability to cross-check duplicate samples as is done in the SEM method.

In some examples, Ba has been found to be heterogeneously distributed as a minor varnish constituent. Because both the SEM and PIXE rely on EDAX analysis there exists in either method a problem of interference (overlap) of Ba L and M Peaks with the K and L peaks of Ti. Anomalous Ba occurrence could cause anomalously low cation ratios. PIXE analysis may use the correct proportions of the five Ba L peaks and the imperfect overlap of one of those L peaks with Ti K α peak to deconvolute the effect of Ba occurrence on measured Ti content. In the SEM technique, Ba occurrence can be recognized in a relative sense by examination of the EDAX spectra during analysis for the Ba M β line and, when present, the analysis can be disregarded in cation ratio calculations. In addition, we have the capability of using wavelength-dispersive analysis to distinguish Ba and Ti for samples where Ba is pervasive. This capability allows an evaluation of the degree and distribution of Ba occurrence within varnishes and also permits calculation of cation ratios for varnish samples in which Ba occurs.

Finally, varnish is not removed from its substrate for SEM analysis, as it must be for PIXE analysis. If an SEM-EDAX analysis yields an anomalous result, the specific site on the disk may be examined to determine the cause of the anomaly and, if warranted, the cation ratio determined at that site can be disregarded in the calculation of the cation ratio for the disk. Furthermore, chemical inhomogeneities can be examined across an entire disk. If a PIXE analysis is anomalous, the original varnish surface cannot be reexamined, and a substitute sample must be studied.

Summary

SEM combined with EDAX offers a new method by which to analyze the chemistry of rock varnish. The SEM analytic technique for determining rock varnish cation ratios to date geomorphic surfaces has several advantages over previously published cation-ratio dating techniques:

1. SEM analysis is done in situ and may be performed on thin or thick varnish coats; microrelief on substrates is not problematic.
2. Site-by-site analysis allows recognition and exclusion of chemical inhomogeneities in calculated cation ratios.
3. The SEM technique is nondestructive of varnish surfaces, which permits reexamination of anomalous results if warranted.

References

1. R. I. Dorn, "Cation-ratio dating: A new rock varnish age determination technique," *Quaternary Res.* 20: 49, 1983.
2. C. D. Harrington and J. W. Whitney, "Scanning electron microscope method for rock-varnish dating," *Geology* 15: 967, 1987.
3. R. Raymond Jr. and C. D. Harrington, "Lithologic controls on rock varnish as determined with SEM," (this volume).

A NEW TECHNIQUE UTILIZING SCANNING ELECTRON MICROSCOPY AT LOW TEMPERATURE AND VOLTAGE TO ANALYZE NATIVE-STATE RESERVOIR ROCKS

C. J. Stuart, L. C. Liang, and J. B. Toney

A new technique has been developed to allow direct imaging of native-state petroleum reservoir rocks using the scanning electron microscope (SEM) in a low-voltage mode combined with a solid-state cryosystem. SEM investigation of native-state reservoir rock samples is important because it enables direct visualization of (1) the fluid distributions in the pore system; (2) clays in their natural hydrated states; (3) the native mineralogy; and (4) combined effects on the reservoir's wettability and permeability. The new technique uses low-voltage SEM to image the uncoated surface of the wet sample, and the cryostage to control the vapor pressure of the fluid phase while imaging. A differentially pumped environmental chamber is not required with this approach.

This technique utilizes a solid-state thermoelectric device (TED) to achieve the required sample cooling. The TED operates on the Peltier principle permitting the surface of the TED to reach temperatures as low as 110 C below its reference temperature. A sample stage is refitted with a TED substage. The sample is fixed to the substage so that it is in direct thermal contact with the TED. The TED is then biased to provide the cooling necessary to minimize vaporization of interstitial fluids.

Sandstone samples were used for the preliminary trials. Pieces of the sample were placed in a vacuum and a 2% KCl solution was imbibed into the pore structure of the rock. The vacuum-imbibition technique assured that brine was in the pore system of the rock simulating a "native-state" rock. A representative chip was taken from the rock and mounted in an aluminum sample cup with silver paint. The sample cup was epoxied to the TED device and thermocouples were attached to both the sample surface and the substage. The apparatus was then placed in an ISI WB-6 SEM, the sample cooled and the vacuum system engaged. The uncoated sample was examined using a LaB₆ gun at 1.5 kV, in secondary-electron mode, with a vacuum of approximately 10^{-6} Torr.

This technique provides quick analysis, requires no sample preparation, and permits the visualization of "native-state" core with minimal sample preparation artifacts. The rock/fluid interactions were observed along with clays in their hydrated states. Crude oil was also imaged on an unconsolidated sand pack.

This technique shows a great promise for the observation of fluid distributions, clay interactions wettability, and permeability of the "native-state" reservoir rock.

Authors are at ARCO Oil and Gas Co., 2300 W. Plano Parkway, Plano, TX 75075. They wish to express appreciation to T. J. Rohrer, Austin, Tex., for his assistance in design and integration of the cooling apparatus to the SEM.

LITHOLOGIC CONTROLS ON ROCK VARNISH FORMATION AS DETERMINED BY SEM

Robert Raymond Jr. and C. D. Harrington

Rock varnish is a ubiquitous, manganese- and iron-rich coating found on rock exposures in arid and semiarid regions. Recent work has demonstrated the potential for using rock varnish to date geomorphic surfaces semi-quantitatively.¹⁻³ Such dating relies on ratios of minor elements in the varnish $[(Ca + K)/Ti]$ calculated for a specific geographic area. However, although cation-ratio dating has been shown to work empirically, relationships between varnish mineralogies, varnish element contents, varnish diagenesis, and mechanism of varnish formation are not yet understood. In addition, it is not clear what effect these various varnish attributes have on the elemental ratios used in rock varnish dating. We do know, however, that the mineralogy, texture, and morphology of substrate lithologies may greatly affect initial varnish accretion. Understanding this effect may help to clarify uncertainties that now exist in the empirical varnish cation-ratio (VCR) dating technique.

Methodology

Samples of rock varnish were collected from geomorphic surfaces along Lake Mead in southern Nevada, and from surfaces in proximity to Las Vegas Wash, a tributary to Lake Mead. Samples were collected as whole varnish-coated surface clasts or as chips of varnished rock, broken from the surface clasts or outcrops of rock. To prevent collection of anomalous varnish, care was taken to avoid samples adjacent to lichens and other vegetation and to varnish formed along cracks or on rock surfaces in contact with soil. Samples were selected to represent variable lithologies with the most mature (darkest, thickest, and most complete coating) varnish development on the surface being sampled.

Although rock varnish may be composed of as much as 70% clay minerals, its distribution on rock surfaces can be best defined by the presence of Mn and Fe oxides, particularly when the underlying substrate is deficient in Mn and/or Fe. The distribution of Mn and Fe, and therefore of rock varnish, can be determined by use of energy-dispersive x-ray analysis. Excitation of substrate elements is avoided during VCR dating of varnish surfaces by use of the scanning electron microscope (SEM) technique.³ However, the relationship between varnish ac-

cretion and substrate mineralogy can best be seen during SEM analysis by use of accelerating voltages that completely penetrate varnishes. All elements comprising the varnish are then excited, and in rocks that are Mn or Fe poor, or in which the Fe is contained in specific minerals, it is possible to decipher the relative thickness of varnish coat by relative intensities of Mn and Fe x-ray maps.

Varnish distribution was studied with an ISI DS-130 SEM both across clast surfaces and on polished thin sections made perpendicular to the varnish/substrate interface. Samples were carbon coated prior to analysis. Back-scattered secondary-electron (BSE) images were digitally acquired on a 512×512 pixel array. X-ray maps were collected on a 256×256 pixel array with an acquisition time of 0.03 s/pixel.

Results

Rock varnish deposition, whether by inorganic or biogeochemical processes, occurs initially in depressions on a rock surface. These are the areas where water accumulates first and evaporates last, depositing previously soluble Mn and Fe compounds during evaporation. In hand specimens, such preferential deposition of varnish delineates troughs on a rock surface by the occurrence of thicker, smoother, and darker varnish. On a finer scale, small depressions on rock surfaces may be preferentially filled during initial varnish accretion when lateral coating is incomplete. In Fig. 1, a small depression on a basalt surface approximately 2 mm across shows preferential varnish deposition relative to areas with greater relief on either side of the depression. On a much finer scale small depressions $<50 \mu\text{m}$ across have been preferentially filled between quartz (SiO_2) grains located on the surface of a quartz-rich siltstone (Fig. 2).

When rock varnish deposition has been minimal and varnish covers a substrate surface incompletely, an opportunity exists to investigate whether there is any preferential accretion of rock varnish on specific areas of a substrate as a result of chemical affinities that might exist between rock varnish and different phases comprising the substrate. Figures 3 and 4 are BSE images of a planar view and a cross section of a quartz-rich siltstone with respective Mn and Si x-ray maps. Figure 3 appears to show an inverse relationship between the very irregular varnish (Mn) occurrence and Si occurrence. However, comparison of Mn distribution to Si distribution in Fig. 4 demonstrates that the relationship seen in

The authors are in the Geology and Geochemistry Group, Los Alamos National Laboratory, Los Alamos, NM 87545. Supported by the Department of Energy, contract W-7405-ENG-36, under the auspices of Dr. G. A. Kolstad, Office of Basic Energy Sciences.

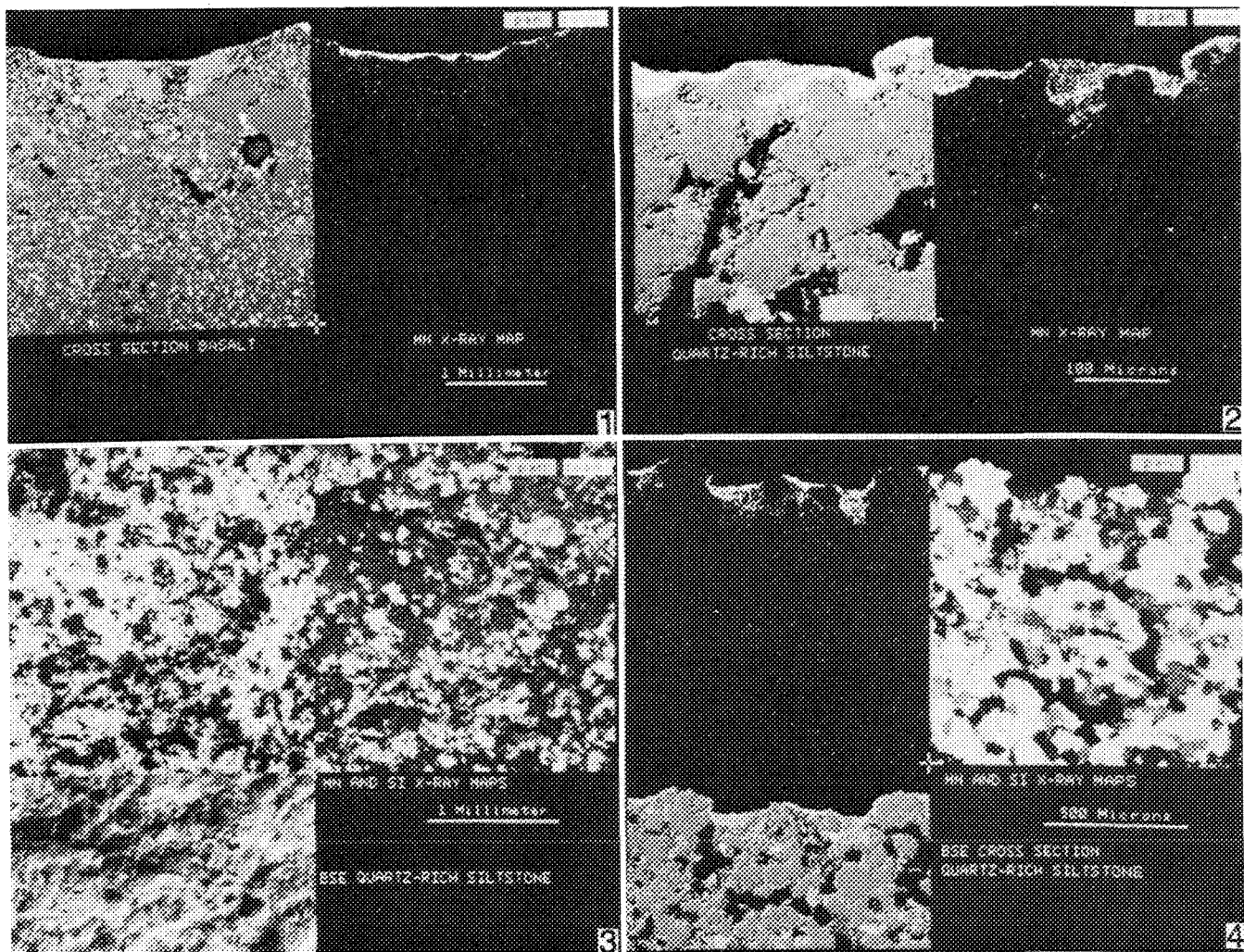


FIG. 1.--BSE image and Mn x-ray map of polished cross section of basalt.

FIG. 2.--BSE image and Mn x-ray map of polished cross section of quartz-rich siltstone.

FIG. 3.--Mn x-ray map, Si x-ray map, and BSE image of planar view of quartz-rich siltstone having discontinuous varnish coat.

FIG. 4.--Mn x-ray map, Si x-ray map and BSE image of cross section of quartz-rich siltstone shown in Fig. 3.

Fig. 3 results from a lack of accretion of varnish on the quartz grains with greatest relief. Quartz grains with less relief and areas between quartz grains having the least relief have been covered by initial varnish deposition. In this particular case the siltstone had been cemented with a carbonate cement (CaCO_3) which has been preferentially eroded from the surface by weathering prior to varnish accretion. Rather than an inverse relationship between quartz occurrence and varnish deposition, a direct relationship exists between varnish deposition and the mineralogy of the substrate most susceptible to weathering, the carbonate cement. The initial size of varnish accretion zones is controlled by the grain size of the substrate lithology.

In Figs. 5 and 6, a similar type of relationship is shown between varnish occurrence and mineralogy for an amphibolite substrate. In this case, the inverse relationship appears

to be strongest between the occurrence of varnish as defined by the Mn x-ray map and the minerals containing the greatest Ca and Si concentrations, specifically quartz (SiO_2) and amphibole, e.g., $\text{Ca}_2\text{Mg}_5\text{Si}_8\text{O}_{22}(\text{OH})_2$ (Fig. 5). However, as can be seen in Fig. 6, varnish accretion is not controlled by substrate mineralogy but by the relief superimposed on the rock following weathering. The grains with the most relief, whether quartz or amphibole, tend to have the least varnish accretion. In this instance, unlike in Fig. 4, accretion zones that result from weathering of the surface are not controlled by mineralogic grain size. However, they are controlled by the overall fabric of the metamorphic rock, the schistosity of which can be seen trending from the lower left to the upper right of all images in Fig. 5.

Although the substrate in Fig. 5 contains a mineral rich in Ca, Ca x rays are essentially

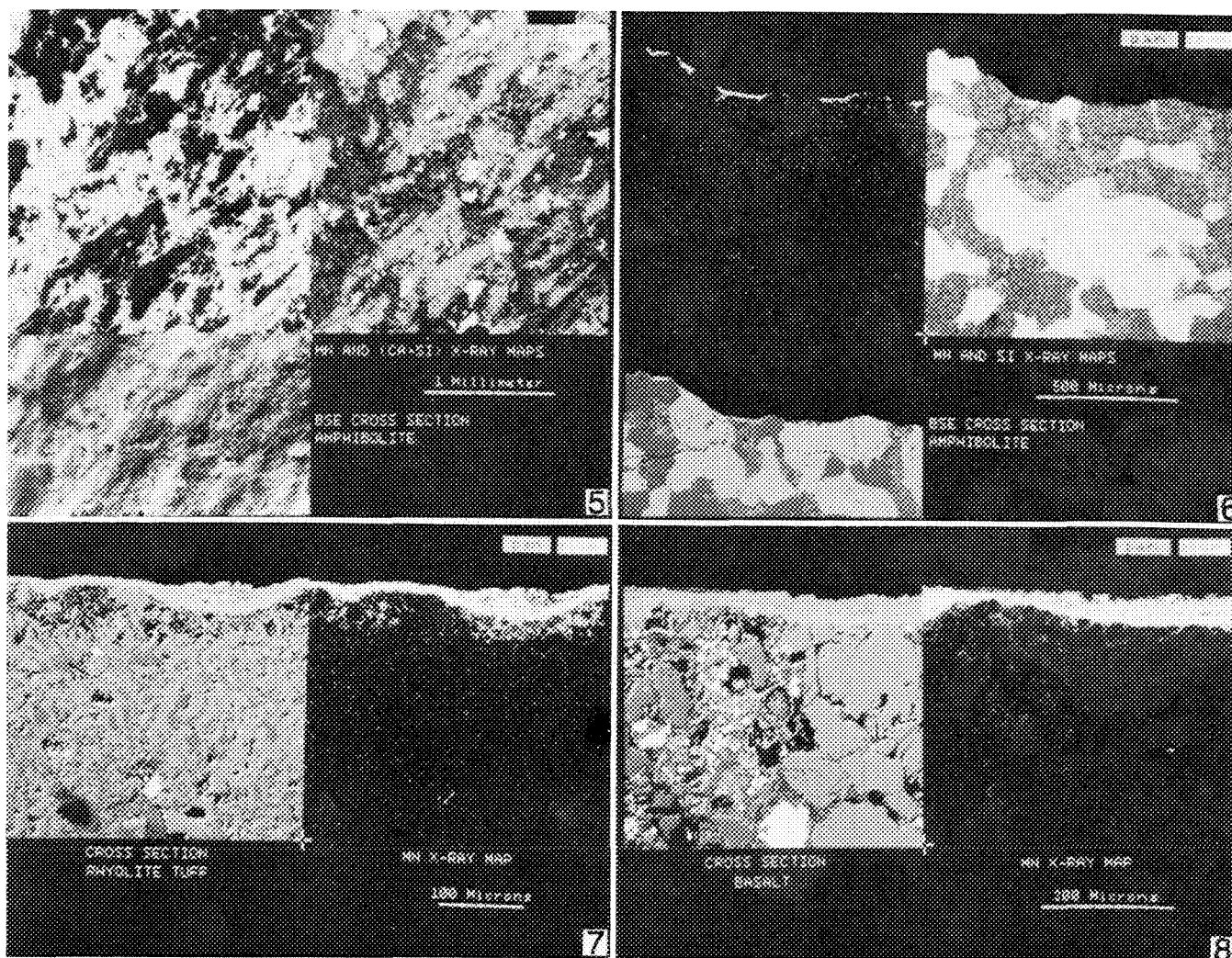


FIG. 5.--Mn x-ray map, [Ca + Si] x-ray map, and BSE image of planar view of amphibolite having discontinuous varnish coat.

FIG. 6.--Mn x-ray map, Si x-ray map, and BSE image of cross section of amphibolite shown in Fig. 5.

FIG. 7.--BSE image and Mn x-ray map of basalt with continuous varnish coat.

FIG. 8.--BSE image and Mn x-ray map of rhyolite tuff with continuous varnish coat.

nonexistent where the substrate is overlaid by even a thin coat of varnish, partly because the electron beam cannot penetrate completely through the varnish coat, and partly because of the very high coefficient of absorption of Mn and Fe of the Ca x rays traveling from the substrate to the surface. With complete varnish coats of greater thickness (Figs. 7 and 8) the surface microroughness noted in Figs. 2-6 no longer affects calculated VCRs.

Discussion

Various rock types develop fractured or weathered surfaces that relate to the grain size, mineralogy, and texture of the rock. Rock varnish accretes to surface areas that represent depressions relative to immediately adjacent substrate, whether on a micrometer or centimeter scale. Rock varnish deposition appears to be little affected directly by the chemistry of substrate mineralogy. However,

weathering and erosion, resulting in pitting of a mineral surface or the total removal of a mineral, provides environments for rock varnish deposition.

When performing VCR dating on a variety of lithologies, one should consider the mineralogic content of the substrate and the relative resistance of these minerals to weathering. The occurrence of resistant minerals comprising topographic highs with chemical compositions rich in Ca, K, or Ti cause anomalous results in VCRs. However, knowledge of such possible anomalies permits the choice of lithologies with little problem of substrate interference or consideration of the potential for such interference when one is analyzing VCRs on rocks containing minerals with high Ca, K, or Ti contents. Large uncertainties in previous duplicate VCR analyses on some varnish surfaces may be the result of thin varnish coats overlying irregular substrates contain-

ing such high Ca, K, or Ti contents. Once varnish coats attain substantial thickness, interference from substrate chemistry appears to be negligible.

References

1. R. I. Dorn, "Cation-ratio dating: A new rock varnish age determination technique," *Quaternary Res.* 20: 49, 1983.
2. C. D. Harrington and J. W. Whitney, "Scanning electron microscope method for rock-varnish dating," *Geology* 15: 967, 1987.
3. C. D. Harrington and R. Raymond Jr., "SEM analysis of rock varnish chemistry: A geomorphic age discriminator," (this volume).

RAMAN SPECTROSCOPY OF ZEOLITES: CHARACTERIZATION OF NATURAL ZEOLITES WITH THE LASER RAMAN MICROPROBE

C. L. Knight, M. A. Williamson, and R. J. Bodnar

Raman spectra were collected from 14 natural zeolites (Table 1) as part of an ongoing project to provide a basis for identification of zeolites and to accumulate data for theoretical interpretations. Spectral features observed for these zeolites occur primarily in the $<600\text{ cm}^{-1}$ structurally sensitive region of the spectrum, facilitating identification of these zeolites on a structural basis. Although apparent relationships between zeolite structure and Raman spectra have been noted for some zeolites in prior studies, to the authors' knowledge there has been no comprehensive evaluation of this relationship to date.

TABLE 1.--Names, average chemical compositions, symmetry, and catalog numbers of zeolite minerals surveyed in this study. Specimens belong to the Geological Sciences Museum at VPI&SU, and the Geology Department of Radford University.

Zeolite	Typical unit-cell formula	Crystal system	Catalog No
Analcime	$\text{Na}_{16}(\text{Al}_{16}\text{Si}_{32}\text{O}_{96}) \cdot 16\text{H}_2\text{O}$	cubic	B393
Phillipsite	$(\text{Na},\text{K})_{10}(\text{Al}_{10}\text{Si}_{22}\text{O}_{62}) \cdot 20\text{H}_2\text{O}$	orthorhombic	B216
Harmotome	$\text{Ba}_2(\text{Al}_4\text{Si}_{12}\text{O}_{32}) \cdot 12\text{H}_2\text{O}$	orthorhombic	M1207
Chabazite	$(\text{Na}_2,\text{Ca})_6(\text{Al}_{12}\text{Si}_{24}\text{O}_{72}) \cdot 40\text{H}_2\text{O}$	trigonal	B267
Gmelinite	$\text{Na}_8(\text{Al}_8\text{Si}_{16}\text{O}_{48}) \cdot 24\text{H}_2\text{O}$	hexagonal	64
Faujasite	$\text{Na}_{58}(\text{Al}_{58}\text{Si}_{134}\text{O}_{384}) \cdot 240\text{H}_2\text{O}$	cubic	1646
Heulandite	$\text{Ca}_4(\text{Al}_8\text{Si}_{28}\text{O}_{72}) \cdot 24\text{H}_2\text{O}$	monoclinic	1607
Stilbite	$\text{Ca}_4(\text{Al}_8\text{Si}_{28}\text{O}_{72}) \cdot 28\text{H}_2\text{O}$	monoclinic	150*
Natrolite	$\text{Na}_{16}(\text{Al}_{16}\text{Si}_{24}\text{O}_{80}) \cdot 16\text{H}_2\text{O}$	orthorhombic	B208
Mesolite	$\text{Na}_{16}\text{Ca}_{16}(\text{Al}_{48}\text{Si}_{72}\text{O}_{240}) \cdot 64\text{H}_2\text{O}$	orthorhombic	D13
Scolecite	$\text{Ca}_8(\text{Al}_{16}\text{Si}_{24}\text{O}_{80}) \cdot 24\text{H}_2\text{O}$	monoclinic	1619
Thomsonite	$\text{Na}_4\text{Ca}_8(\text{Al}_{20}\text{Si}_{20}\text{O}_{80}) \cdot 24\text{H}_2\text{O}$	orthorhombic	1609
Mordenite	$\text{Na}_8(\text{Al}_8\text{Si}_{40}\text{O}_{96}) \cdot 24\text{H}_2\text{O}$	orthorhombic	1614
Epistilbite	$\text{Ca}_3(\text{Al}_6\text{Si}_{18}\text{O}_{48}) \cdot 18\text{H}_2\text{O}$	monoclinic	70

Experimental Methods

Raman spectra are collected with an Instruments SA Ramanor U-1000 laser Raman spectrometer.

C. L. Knight and R. J. Bodnar are with the Vibrational Spectroscopy Lab, and all three are with the Department of Geological Sciences, Virginia Polytechnic Institute and State University, Blacksburg, VA 24061. They wish to express their gratitude to the Geological Sciences Museum, VPI&SU, Blacksburg, Va., and the Geology Department of Radford University, Radford, Va., for the loan of zeolite specimens, and to Sharon Chiang for her drafting expertise.

ter coupled with an Olympus BH-2 optical microscope. The light source, a Spectra Physics model 2016 5W argon laser, is tuned to the argon green line at 514.5 nm with a power of 100 mW measured as the beam enters the microscope. Laser light is sent through the $100\times$ objective (numerical aperture 0.95) of the microscope and onto the sample surface with a laser spot $<1\text{ }\mu\text{m}$ in diameter. Raman scattered light is collected from a sample volume of a few cubic micrometers, which permits data collection on single crystals as small as $4\text{ }\mu\text{m}$ in diameter. The Raman signal is collected through the $100\times$ objective in a 180° collection geometry and passed through the entrance slits (all slits open to $300\text{ }\mu\text{m}$) into the 1m -focal-length double monochromators of the U-1000 spectrometer. The holographic gratings within the spectrometer are controlled by a dedicated IBM-AT personal computer and the ISA Prism software package, and are stepped in 2 cm^{-1} increments. Photon counts are accumulated by an RCA photomultiplier tube for 10 s at each step over the spectral range $100\text{--}1500\text{ cm}^{-1}$. Data are stored and displayed by the computer. When feasible, spectra are taken from different crystallographic orientations on the same crystal in order to obtain reference spectra that can be compared with those of nonisotropic samples of unknown orientation. The laser Raman microprobe has distinct advantages over its macro-oriented predecessors in this type of study. The Raman microprobe can collect these data in a completely nondestructive manner on samples as small as a few cubic micrometers, with a greater signal-to-noise ratio, and can do so in situ with little or no sample preparation.¹ These qualities allow Raman microspectroscopy to be easily combined with other microbeam techniques in the study of zeolites (see Williamson et al., in this volume) or other minerals.

Discussion

As can be seen in Fig. 1, the Raman bands observed for zeolites in this study are almost completely restricted to the $<600\text{ cm}^{-1}$ structurally sensitive region of the spectrum. This restriction implies that differences seen in the spectra of these aluminosilicate framework minerals can be related to differences in their structure. Indeed, these zeolites can be separated into different structural groups sharing common secondary building units (SBUs) that correlate with groupings based on similar Raman spectral signatures (Table 2). However, any band assignments in this region are empirical by nature as the state of theoretical

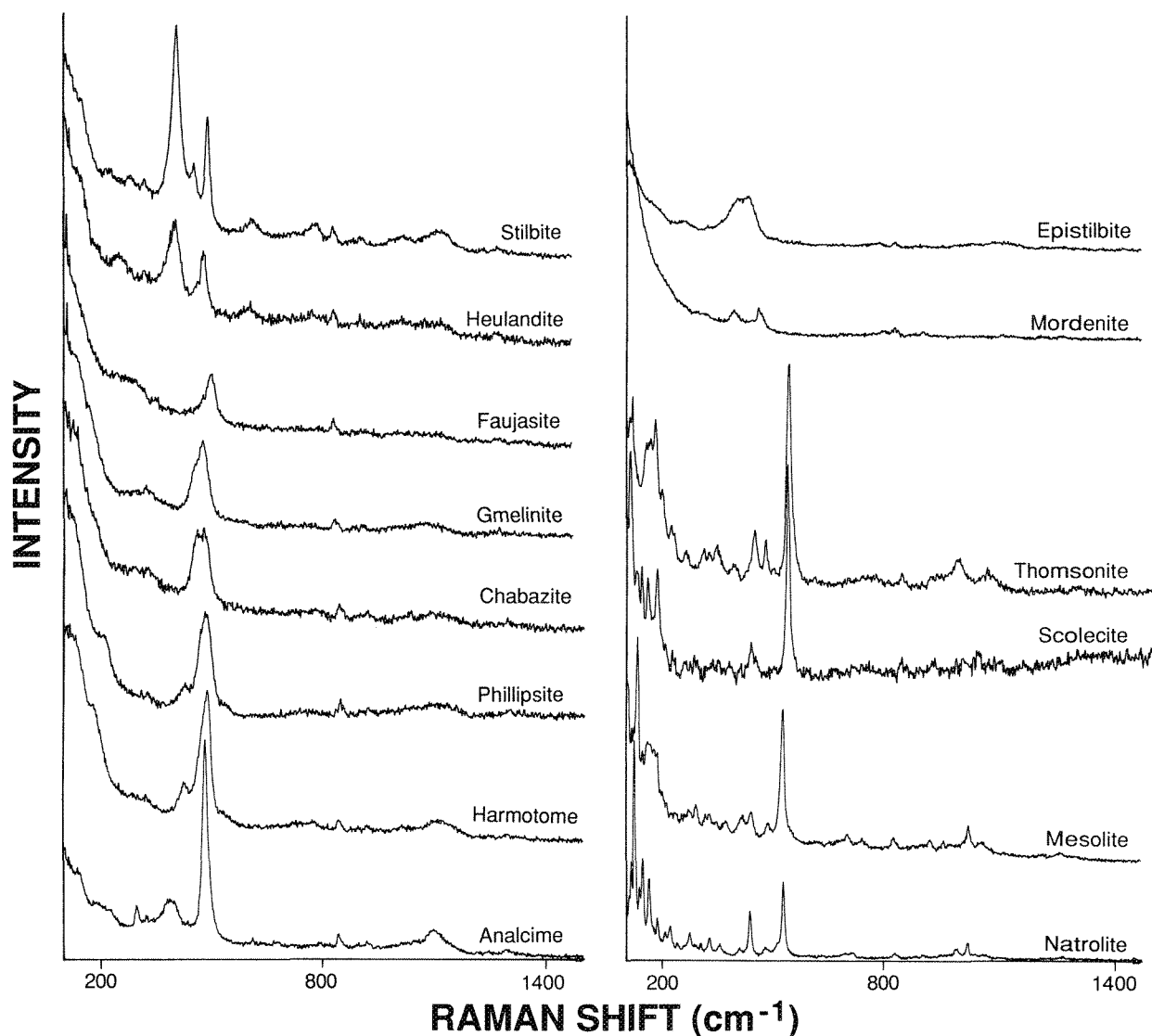


FIG. 1.--Raman spectra of several natural zeolites over 100-1500cm⁻¹ range.

TABLE 2.--Structural group, space group, and characteristic observed Raman frequencies for several natural zeolites.

SBU	Space group	Mineral	Characteristic Raman frequencies (cm ⁻¹)					
S4R	Ia3d	Analcime	389m	482vs				
	P2 ₁ /m	Phillipsite	424m	479vs				
	P2 ₁ /m	Harmotome	426m	483vs				
D6R	R3m	Chabazite	322w	468s				
	P6 ₃ /mmc	Gmelinite	324w	473s				
	Fd3m	Faujasite	322w	505s				
4-4-1	Cm	Heulandite	405vs	484s	614m			
	F2/m	Stilbite	410vs	496s	618m			
4-1	Fdd2	Natrolite	123vs	145s	163s	443s	534s	
	Fdd2	Mesolite	130vs	162m	186m	448m	534vs	
	Cc	Scolecite	111vs	142s	158s	436m	536vs	
5-1	Pnn2	Thomsonite	116s	156m	180s	446m	539vs	
	Cmcm	Mordenite	398m	468m				
	C2/m	Epistilbite	408m	436m				

prediction of the Raman activity of zeolites has barely begun to progress beyond isolated TO₄ band assignments.²

Analcime, harmotome, and phillipsite are structurally composed of single rings of four tetrahedra (S4R) and share a common spectral signature of a very strong band centered at 480 cm⁻¹ accompanied by a lesser peak or shoulder at 425 cm⁻¹ (389 cm⁻¹ for analcime). Based on the work of Galeener on silicate-ring vibrations in this structurally sensitive region, one may assign the 480cm⁻¹ band to a planar 4-fold ring stretch in which the vibration is a result of a breathing motion of the oxygen atoms in the planar rings.³ Among these three spectra, it is interesting to note the sharpness of the 480cm⁻¹ peak in analcime (space group Ia3d), and the relative broadening of this peak in the lower-symmetry members of this structural group, harmotome and phillipsite (space group P2₁/m). The position of the lower frequency peak at 389 cm⁻¹ in analcime as compared to the 425cm⁻¹ peak of harmotome and phillipsite serves to distinguish

analcime from the other members of its group. Harmotome and phillipsite, which share a common structure, have nearly identical Raman spectra, and cannot reliably be distinguished from each other.

Chabazite, gmelinite, and faujasite, structurally characterized by double six-membered rings of tetrahedra (D6R) linked by S4R, are spectrally identified by a broad band (or grouping of bands) centered in the range of 470-510 cm^{-1} assigned to 6-fold and 4-fold ring stretching,¹⁻³ accompanied by a small, broad peak centered at 323 cm^{-1} which is tentatively ascribed to 6-fold ring stretching based upon the inverse relationship between ring size and stretching-mode frequency observed by Galeener.³ As seen in Fig. 1, the strong bands shift to higher frequencies and become sharper with increasing symmetry within this group: the band centered at 468 cm^{-1} in chabazite (space group $R\bar{3}m$) shifts to 473 cm^{-1} in gmelinite (space group $P6_3/mmc$) and to 505 cm^{-1} in faujasite (space group $Fd\bar{3}m$).

Zeolite species structurally characterized by the "stilbite unit" (4-4-1) can be distinguished from other structural groups by the presence of two strong bands at 410 cm^{-1} and 496 cm^{-1} for stilbite (space group $F2/m$) and 405 cm^{-1} and 484 cm^{-1} for heulandite (space group Cm), and a third, weak band at $\sim 615 \text{ cm}^{-1}$ for both minerals.

The natrolite structural group, typically fibrous minerals comprised of chains of tetrahedra (4-1), is the most Raman active group among the natural zeolites. All members of this group exhibit several strong, sharp peaks. Most prominent characteristic of the group are (1) a very strong peak in the range of 110-130 cm^{-1} , (2) a grouping of strong peaks in the range of 145-185 cm^{-1} , and (3) a moderate peak and strong peak at 443 cm^{-1} and 534 cm^{-1} , respectively, for natrolite (space group $Fdd2$), 448 cm^{-1} and 534 cm^{-1} for mesolite (space group $Fdd2$), 436 cm^{-1} and 536 cm^{-1} for scolecite (space group Cc), and 446 cm^{-1} and 539 cm^{-1} for thomsonite (space group $Pnn2$).

The Raman spectra of mordenite and epistilbite, structurally composed of 5-membered rings of tetrahedra with an additional single tetrahedron (5-1), display two moderate peaks. Epistilbite (space group $C2/m$) displays a broad feature in which at least two peaks are discernible at 408 cm^{-1} and 436 cm^{-1} . The higher-symmetry mordenite (space group $Cmcm$) displays two moderate peaks at 398 cm^{-1} and 468 cm^{-1} . The $\sim 400 \text{ cm}^{-1}$ band in each case is assigned to a 5-fold ring stretch.⁵ Although the Raman spectrum of mordenite is very similar in shape and position of the two main peaks to that of heulandite, the mordenite spectrum lacks the 615 cm^{-1} peak characteristic of the stilbite group. Likewise, the spectrum of epistilbite resembles that of chabazite in the D6R group. However, the peaks for epistilbite occur at lower frequencies than the comparable peaks of chabazite or any other member of the D6R group.

All spectra contain a band at $\sim 845 \text{ cm}^{-1}$, which has been assigned to silicon-nonbonded

oxygens at the crystal surface, and nearly all display features in the 950-1250 cm^{-1} range ascribed to the zeolite- Si-O-Al -chain asymmetric stretching modes.^{2,6}

Conclusions

Raman spectra of the 14 natural zeolites examined permit their classification by structural group based on SBU type and, in most cases, by individual mineral name. Although relationships can be seen between zeolite structure and Raman spectra, the lack of theoretical interpretation of this low-frequency region places severe restrictions on the interpretation of the spectral features. It is hoped that continuing data collection in this field will provide impetus for further development of theoretical models.

References

1. F. Adar, "Developments in Raman microanalysis," *Microbeam Analysis--1981*.
2. A. Miecznikowski and J. Hanuza, "Application of the long chain approach to the structure and vibrational spectra of X and Y zeolites," *Zeolites* 5: 188, 1985.
3. F. L. Galeener, "Planar rings in glasses," *Sol. St. Comm.* 44: 7, 1037-1040, 1982.
4. P. K. Dutta, D. C. Shieh, and M. Puri, "Synthesis and structure of zeolite ZSM-5: A Raman spectroscopic study," *J. Phys. Chem.* 91: 4329, 1987.
5. P. K. Dutta and D. C. Shieh, "Crystallization of zeolite A: A spectroscopic study," *J. Phys. Chem.* 90: 11, 2331, 1986.

CHARACTERIZATION OF AUTHIGENIC ZEOLITE PHASES IN VAPOR-DOMINATED HYDROTHERMAL SYSTEMS WITH MICRO-RAMAN SPECTROSCOPY

M. A. Williamson and C. L. Knight

The employment of nondestructive analytical techniques to determine the chemical composition of solid, gaseous, and liquid materials has received ever increasing attention in the geological sciences. With respect to hydrothermal systems, in situ characterization of micron-sized occurrences of alteration products from hydrothermal systems is both difficult and increasingly important. The Raman microprobe is well suited for such analyses. The examination and identification of very tiny authigenically formed phases (e.g., zeolites) in intimate association with host material is possible. Hence, a detailed examination might be carried out of the mineral-mineral interactions that accompany the transfer of mass in a thermal gradient. The purpose of this communication is to report on continuing efforts to identify the alteration minerals produced by an experiment to simulate mass-transfer processes in a thermal gradient. Efforts to date have identified the presence of faujasite, stilbite, and feldspar as authigenic minerals. Zeolite growth was observed to be most commonly associated with a feldspar substrate, which suggests that an epitaxial nucleation may be an important factor in localizing zeolite formation.

Mass transport in a thermal gradient is a significant source of geochemical differentiation in the earth. The coupling of heat and mass flow in a liquid + vapor system in near-surface rocks is a common process in present-day vapor-dominated hydrothermal systems or some of their ancient counterparts, epithermal gold deposits. Placement of high-level radioactive waste canisters in the partly saturated tuffs of Yucca Mountain, Nev. will result in a steep thermal gradient and possibly an analog of these natural processes.

Vapor-dominated geothermal systems are found in areas of high heat flow in rocks where the groundwater recharge is generally exceeded by the heat-driven discharge to surfacial environments. Under these conditions, a vapor zone develops where the interstitial spaces of the rock are filled with both vapor and liquid water, in proportions governed by a complex interplay of heat flux, mass flux, and rock per-

meability.¹ These systems are divided into two geochemical zones: a boiling and a condensation zone. Boiling of slightly alkaline, dilute chloride solutions in the liquid-dominated portion of the system will produce, in the absence of sulfur species, a CO₂-rich vapor phase that travels upward and laterally until it condenses. Assuming that the condensate does not react with the oxidizing shallow seated groundwater, a slightly acidic bicarbonate solution results, producing mild alteration conditions. Consequently, efforts in the VPI&SU Department of Geological Sciences have resulted in the design of an experiment to simulate the coupled heat and mass flow in a vapor-dominated system composed of Yucca Mountain tuffs.

A Vertical Thermal Gradient Experiment (VTGE), designed and operated at VPI&SU, duplicates the heat source (waste canisters) at the base of a column of tuff and imitates a zone of conductive cooling through an impermeable, confining material (Fig. 1).² As condensed, mildly acidic solutions trickle downward, they react with tuff grains used as the charge in the apparatus, leaching alkali and alkaline earth elements and silica. Subsequent refluxing of these solutions acts to produce supersaturated conditions with respect to amorphous silica, clays, and zeolites, which are precipitated in the liquid dominated portion of the system. Reported here is a method to identify the authigenic zeolite phases produced in this experiment. It is expected that this technique will be quite useful for identifying similar phases formed in natural systems.

Experimental

Nonlithophysal tuff from the Topopah Springs member of the Yucca Mountain tuffs of Nev. was crushed and sieved to a size fraction less than 2 mm. Fine-grained material was then washed from the surfaces of the grains with successive washings of 400cm³ portions of the solids by stirring into 1500 cm³ of distilled-deionized water, in a column 18 cm high. The agitated mixture was allowed to settle for 1 min and the suspended fines were decanted. Three washings were used for each 400cm³ portion of crushed and sieved tuff. Following drying at 100 C, secondary electron microscopic (SEM) examination of the unreacted material indicated that fines had been effectively removed. Permeability and porosity determination were made on the material of 0.0385 cm-sec⁻¹ and 45%, respectively.

Initially, 80% of the pore volume of the 3700cm³ run solids was filled with deionized water. The apparatus was run for 31 days. At

The authors are with the Department of Geological Sciences, Virginia Polytechnic Institute and State University, Blacksburg, VA 24061. Thanks are due J. D. Rimstidt and R. J. Bodnar for helpful review and comment. Funding for this work was provided in part by a grant from Mifflin and Associates, Inc., Las Vegas, Nev., to J. D. Rimstidt, and NSF grant EAR-8657778 to R. J. Bodnar.

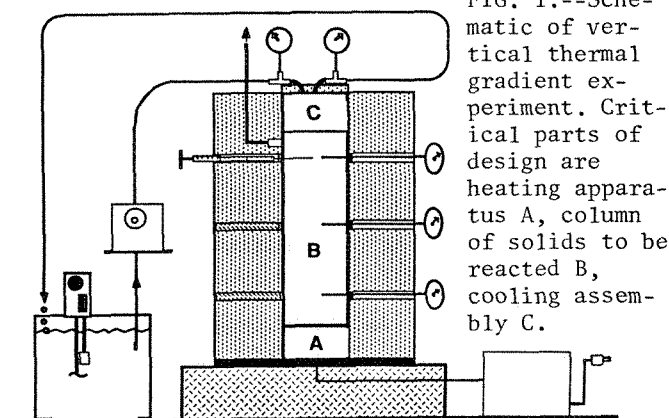


FIG. 1.--Schematic of vertical thermal gradient experiment. Critical parts of design are heating apparatus A, column of solids to be reacted B, cooling assembly C.

the termination of the run, the column of reacted tuff (4×21 in.) was sectioned into seven 3 in parcels and dried at room temperature.

Tuff grains from all seven sampling zones were mounted for SEM analysis. Raman spectra were obtained for mineral grains observed to be growing on the surface of the reacted tuff with an Instruments SA Raman spectroscopy system. This system was comprised of a Jorbin Yvon model U100 optical bench interfaced to an Olympus BH-2 microscope equipped with $100\times$ objective. Excitation was achieved with a Spectra-Physics model 2016 argon laser, tuned to the 514.5nm line, at 100 mW to the microscope. A dedicated IBM AT was employed for instrument control and data acquisition via Instruments SA supplied software routines.

Raman spectra for the authigenic grains were recorded from 100 to 1500 Rcm^{-1} , where Rcm^{-1} indicates the Raman shift frequency. Scans were produced by stepping 2 Rcm^{-1} and counting for 2 s at each step. As the scattering cross section for zeolites is very low, a spectral addition of five scans was used, which resulted in optimal signal-to-noise ratios and the most reproducible spectral results.

Results and Discussion

All reacted tuff sections were examined by SEM. Iron hydroxides and amorphous silica coatings were noted to be ubiquitous throughout, with the formation of micron-sized single-crystal alteration products in the lowest section. Examination of the lowest section of the column of reacted tuff revealed the occurrence of phases not observed prior to reaction. Amorphous silica and platy clay-like materials were noted, in addition to well-developed crystalline materials whose habit suggested a zeolite mineral. The appearance of one of the alteration products (Fig. 2) markedly resembled the fibrous habit of stilbite ($(\text{NaCa}_2)[\text{Al}_5\text{Si}_{13}\text{O}_{36}]\cdot 16\text{H}_2\text{O}$). Although the likely identity of this material was developed with SEM, that alone was not conclusive; nor could the precipitation site be evaluated by this approach.

Grains mounted on the stage of the Instruments SA micro-Raman system provided informa-

tion not obtainable by SEM examination. Edges of reacted tuff grains were illuminated with transmitted light, which threw the authigenic mineral grains into sharp relief. Grains were observed to be transparent to partially clouded and ranged in size from <0.5 to $5\text{ }\mu\text{m}$. Often the grains possessed a "sheaf-of-wheat" shape in cross section, such that the direction of elongation was perpendicular to the surface on which they were observed to occur. The spatial relationship between these elongate grains and the surface of the mount was considered to be indicative of the authigenic nature of the grains. In the overwhelming majority of the occurrences, the authigenic phases were noted on a translucent substrate that regularly displayed two cleavages and fluid inclusions.

A Raman spectrum was recorded for one particularly well-developed grain about $3\text{ }\mu\text{m}$ in size and is displayed in Fig. 3(a). Well-resolved peaks at 414 , 480 , and 514 cm^{-1} were noted, with minor signals slightly exceeding noise levels between 200 and 400 cm^{-1} . The deflection at 514 cm^{-1} was thought to be representative of feldspar. Numerous Raman spectra for feldspars recorded at this laboratory have consistently shown this peak as a characteristic feature of feldspar minerals, regardless of specific composition. A spectrum of plagioclase is shown in Fig. 3(d) and is typical of all feldspars we have observed. Indeed, comparison of the Raman spectrum for the substrate mineral (Fig. 3b) with that of plagioclase shows an almost identical match for shift frequencies of 159 , 282 , 476 , and 514 cm^{-1} . We conclude that presence of the 514 cm^{-1} band in the authigenic mineral spectrum is representative of "contamination" by the substrate mineral. This is not a surprising result as the analytical volume of excitation by the laser source would likely extend to some degree beyond that defined by the micron-sized mineral grain. Thus, the signal observed in the spectrum of the authigenic grain is attributed to feldspar.

Remaining signals at 414 and 480 cm^{-1} correlate well with frequencies observed for zeolites of Group 7, where the group labeling is consistent with that denoted by Mumpton in 1977.³ This group, the clinoptilolite group, includes stilbite (see Knight et al., this volume). The correlation of the strongest spectrum signal at 414 cm^{-1} with 410 cm^{-1} noted in stilbite is good (Fig. 3c). The primary spectral deflection at 405 cm^{-1} for clinoptilolite and heulandite does not support these choices for the identity of the authigenic grain. Inspection of the spectrum for stilbite reveals fine structure at 458 cm^{-1} that is not observed for experimental-run products. The low signal-to-noise (S/N) ratio of the run product spectrum compared to the far greater S/N of the standard is thought to be responsible for the lack of detection of this minor peak. From our experience, with respect to natural zeolite minerals, the position of the most intense band in the spectrum

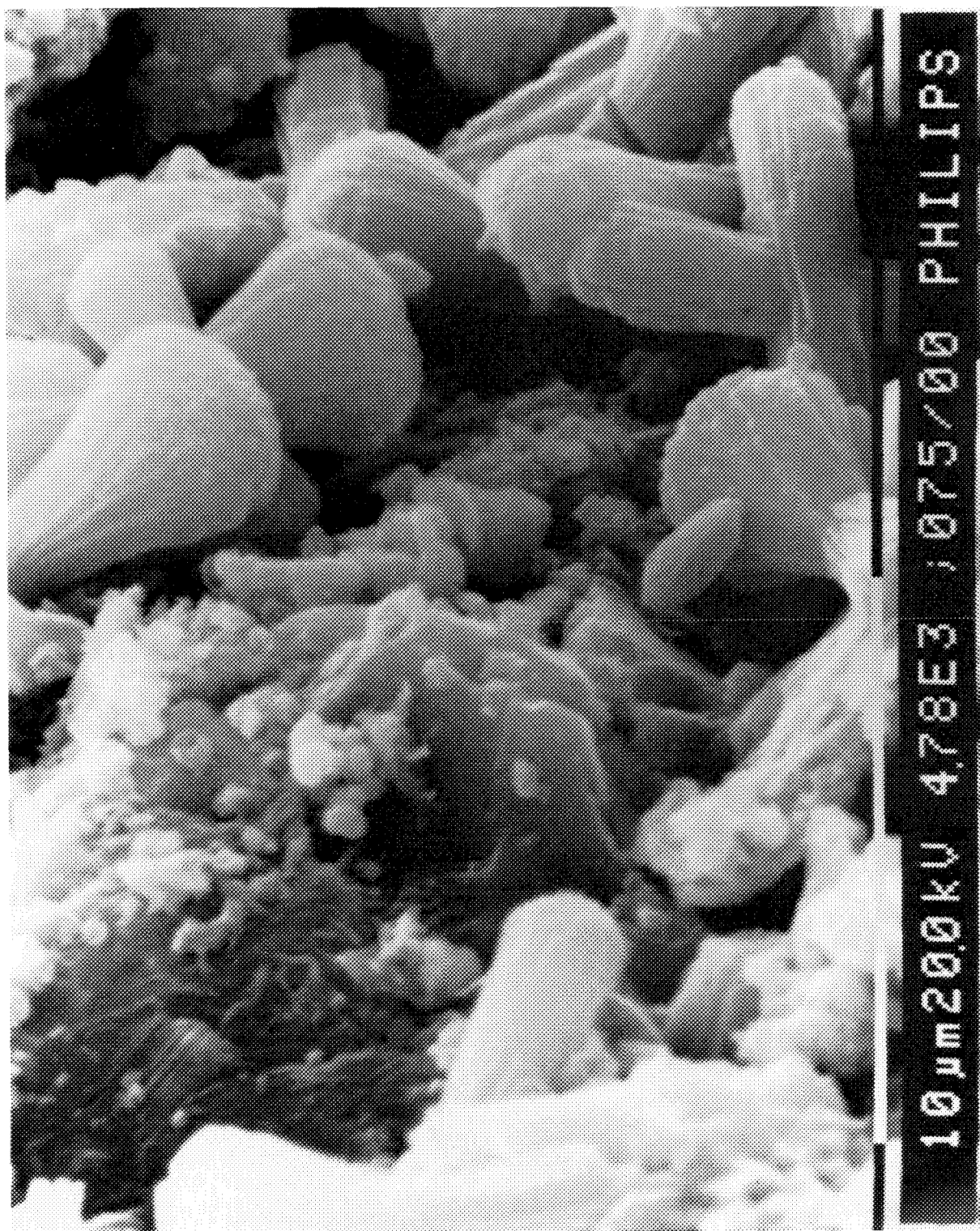


FIG. 2.--SEM photograph of crystalline authigenic mineral phases observed on surface of Yucca Mountain, Nev., tuff grains following exposure to vertical thermal gradient.

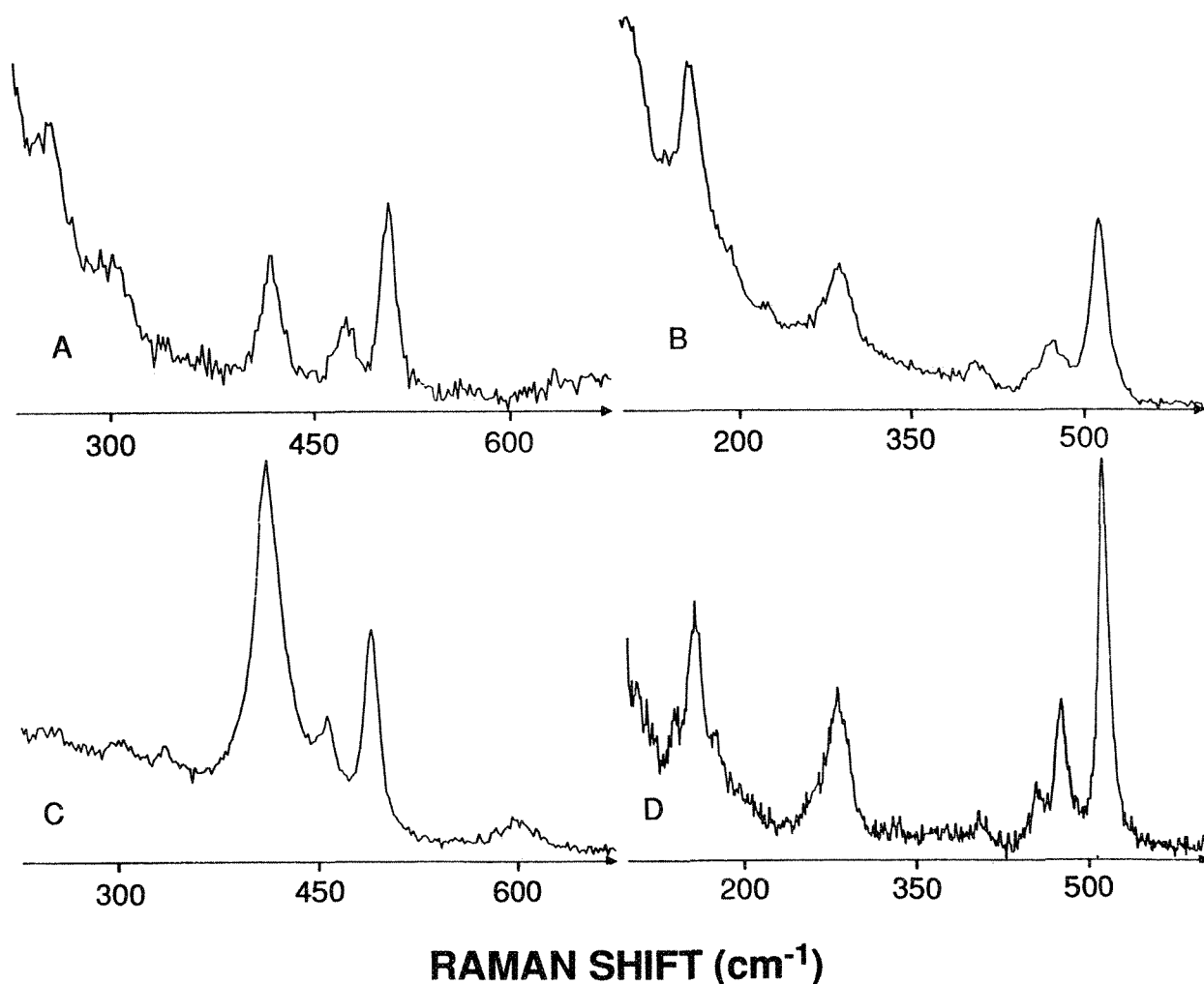


FIG. 3.--Raman spectra of (a) authigenic mineral grain, (b) substrate on which (a) formed, (c) stilbite, (d) plagioclase.

is the most useful in determining its identity; and when this factor is coupled with SEM crystal habit observation and reactor thermal conditions that are in agreement with observed formation of stilbite in Iceland,⁴ we conclude that authigenic mineral grain is stilbite. However, the displacement of the authigenic 480cm^{-1} peak relative to the determined 496cm^{-1} for stilbite is not clearly understood at this time. The role of cations held in pore spaces is not certain and is currently under investigation. It is worth noting that initial SEM observation of crystal habit is nicely complemented by the structural information provided by Raman microprobe analysis. Use of Raman spectroscopy revealed vibrational frequencies for the material not in complete agreement with those observed for museum samples of stilbite and is therefore more specific in its analysis than SEM or electron microprobe.

A particularly large, well-developed authigenic grain was observed and noted to be particularly elongate ($2 \times 6\text{ }\mu\text{m}$), oriented so that the direction of elongation was perpendicular to the substrate surface. Examination of the

grain (Fig. 4a) yielded conclusive results. The occurrence of a very sharp band at 506cm^{-1} coupled with a second minor deflection at 844cm^{-1} indicated the occurrence of a group 4 zeolite. The Raman spectra for minerals of this group (chabazite, faujasite, and gmelinite) are easily resolved based on the observed direct relationship between degree of symmetry and frequency position of the $460\text{--}529\text{cm}^{-1}$ deflection (Knight et al., this volume). The position of a strong band at 506cm^{-1} compared to 505cm^{-1} for faujasite (Fig. 4b), coupled with the modest signal at 844cm^{-1} , is definitive in identifying this anolyte as faujasite $((\text{Na}_2\text{Ca})[\text{Al}_2\text{Si}_4\text{O}_{12}] \cdot 8\text{H}_2\text{O})$. Examination of the substrate on which this material formed produced another spectrum of a feldspar mineral. A spectrum of this mineral is not reproduced here, as it is very similar to that shown in Fig. 3(d).

In addition to identifying feldspar as the endogenic substrate for authigenic zeolite formation, numerous occurrences of authigenic feldspar were noted. Feldspar produced during the experimental run was typically

small ($2 \times 2 \mu\text{m}$) relative to the feldspar that acted as a substrate ($15 \times 15 \mu\text{m}$), but produced Raman spectra similar to Fig. 3(d). Authigenic varieties were nearly equiangular compared to the more elongate forms of zeolites described above.

Conclusions

In situ characterization of zeolite alteration minerals as products in a hydrothermally altered geologic material is possible with micro-Raman spectroscopic techniques. The ability to evaluate the nature of the substrate on which such minerals precipitated is also possible and may provide insight into control mechanisms for zeolite formation in these environments. The specific structural information that is obtainable with micro-Raman spectroscopy enables a more reliable identification of alteration minerals and can be used to complement either SEM or electron microprobe analyses. Zeolite alteration minerals identified for Yucca Mountain, Nev., tuffs exposed to a vertical thermal gradient include faujasite and a group 7 zeolite here identified as stilbite. Zeolite growth was most commonly associated with feldspars, which suggests that epitaxial nucleation may be an important factor in localizing authigenic zeolite formation.

Raman microspectroscopy promises to be a useful technique for the identification of alteration minerals in a hydrothermal environment. Qualitative description of authigenic phases with this technique will be a solid complement to SEM and electron microprobe analysis and will yield structural information of great value.

References

1. J. Cline, R. J. Bodnar, and J. D. Rimstidt, "Quantitative evaluation of quartz transport and deposition in boiling solutions: Application to epithermal gold deposits," *Geol. Soc. America* (Abstracts with Programs) 19: 621, 1987.
2. W. Newcomb and J. D. Rimstidt, "An experiment to simulate mass transport near the Yucca Mountain high level radioactive waste repository," *ibid.* 20: A278, 1988.
3. F. A. Mumpton, *Mineralogy and Geology of Natural Zeolites*, Washington, D.C.: Mineralogical Society of America, 1977.
4. H. Kristmannsdottir and J. Tomasson, "Zeolite zones in geothermal area in Iceland," in L. B. Sand and F. A. Mumpton, Eds., *Natural Zeolites*, Oxford: Pergamon Press, 1978.

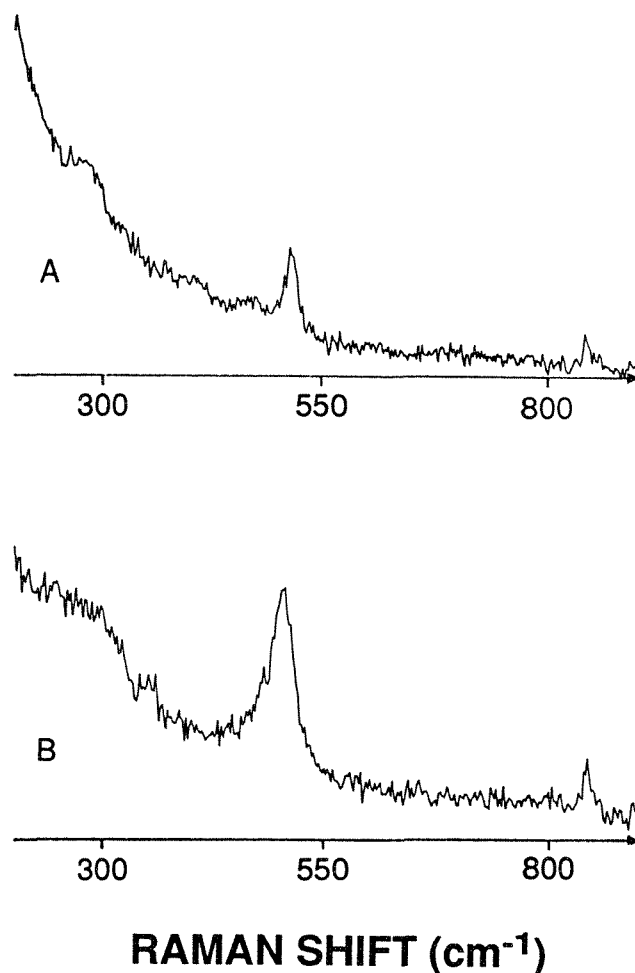


FIG. 4.--Raman spectra of (a) authigenic mineral grain, (b) faujasite.

FOURIER-TRANSFORM INFRARED (FTIR) MICROSCOPY OF INDIVIDUAL PETROLEUM FLUID INCLUSIONS IN GEOLOGICAL SAMPLES

M. R. O'Grady, R. J. Bodnar, J. W. Hellge, C. M. Conroy, L. T. Taylor, and C. L. Knight

Petroleum-filled fluid inclusions trapped in minerals from the sedimentary environment provide direct evidence for the migration of petroleum through the rocks at some unknown time in the geologic past. The migration and maturation history of the oils may be inferred and used subsequently to develop an exploration model for economic oil occurrences if temporal and spatial variations in compositions of petroleum inclusions are known. Fourier Transform Infrared (FTIR) microspectrometry is ideal for determining compositions of individual petroleum fluid inclusions, as many important petroleum components exhibit characteristic infrared absorption bands. In addition, the technique permits rapid and nondestructive analysis. We have used FTIR microspectrometry to analyze petroleum fluid inclusions in halite obtained from well cuttings and have compared these results with analyses of bulk oil samples obtained from the same wells to confirm that the bulk oil samples have preferentially lost carbon dioxide, methane, and aromatic components as a result of decompression during and following sampling.

When a crystal grows in the presence of a fluid phase, some of the fluid is trapped as imperfections in the growing crystal to form fluid inclusions.¹ These *primary* fluid inclusions, trapped during initial growth of the host mineral phase, provide a microsample of the fluid from which the mineral precipitated. The composition of the fluid in the inclusion and the temperature and pressure (depth) at which the mineral and inclusion formed can be determined by standard microchemical and microthermometric techniques. Occasionally, a second immiscible fluid present during crystal growth may be trapped as inclusions. Although these inclusions exhibit petrographic characteristics of primary inclusions and were trapped during growth of the crystal, they do not represent the fluid from which the bulk of the mineral was precipitating. Petroleum fluid inclusions trapped along growth surfaces in minerals that were being precipitated from an aqueous brine are an example of this type of inclusion.

If the host mineral fractures at some time

after its formation, small amounts of fluid surrounding the crystal may enter the fracture and be trapped as *secondary* fluid inclusions as the fracture heals. These inclusions provide a sample of the fluid that bathed the crystal at some time after its formation. Secondary inclusions may be trapped hundreds of millions of years later, and might contain fluids significantly different from those from which the crystal originally precipitated. Petroleum inclusions trapped along fractures in quartz grains in a sandstone are an example of secondary inclusions formed long after the host quartz grains.

Fluid inclusions provide one of the best tools available for determining the physical and chemical conditions attending a variety of geologic processes. In recent years, the use of fluid inclusion techniques to study mineral diagenesis and petroleum generation and migration in sedimentary basins has become common. Primary aqueous fluid inclusions in overgrowths on detrital grains, in cements in clastic rocks, and in fracture-filling minerals can provide valuable information on the P-T conditions of mineral formation, as well as compositions of diagenetic fluids.

Petroleum inclusions are often found coexisting with aqueous inclusions in cements and fracture-filling minerals from sedimentary basins. The presence of hydrocarbon (petroleum) inclusions provides definitive evidence that petroleum has migrated through the rock at some time in the past. By relating the paragenesis of the oil inclusions to other structural and chemical features, the timing of oil migration relative to these events may be determined, and microthermometric data obtained from coexisting aqueous and petroleum fluid inclusions may be used to determine the temperature and pressure conditions of oil migration.^{2,3}

Generally, hydrocarbon inclusions are recognized based on their color in plain, transmitted light. Whereas aqueous inclusions are almost always clear and colorless, the oil inclusions are often a dull yellow to orange to dark brown color in plain (white) transmitted light and are readily distinguished from their aqueous counterparts. Occasionally very small and/or flat petroleum inclusions are clear and colorless and indistinguishable from simple aqueous inclusions in plain, transmitted light. These clear, colorless oil inclusions are easily distinguished from similar appear-

M. R. O'Grady, J. W. Hellge, C. M. Conroy, and L. T. Taylor are at the Department of Chemistry, and R. J. Bodnar and C. L. Knight, at the Vibrational Spectroscopy Laboratory, Department of Geological Sciences, Virginia Polytechnic Institute & State University, Blacksburg, VA 24061. This work was supported in part by National Science Foundation Grant EAR 8657778 to RJB.

Comparison of spectra obtained from three bulk oil samples (Fig. 2b-d) with the inclusion spectrum (Fig. 2a) shows several obvious differences. Absorption bands at 2337 and 1300 cm^{-1} are absent in the bulk oil spectra; they correspond to CO_2 as described above and to CH_4 , respectively. The absence of absorptions above 3000 cm^{-1} reflects the lack of aromatic components and methane. The absence of an aromatic component is supported by the fact that the bulk oil samples do *not* fluoresce under UV illumination. These differences are consistent with the loss of the more volatile components CO_2 , CH_4 , and aromatics during decompression and sampling as the oil approaches the surface. Also note that oil 3 shows a small but recognizable absorbance at $\sim 1700 \text{ cm}^{-1}$, attributed to carbonyl stretch, which suggests that the oil may have been oxidized by interaction with oxygenated groundwaters or rocks in the reservoir.

Conclusions

FTIR microspectrometry provides a rapid, nondestructive technique for the analysis of petroleum fluid inclusions in natural mineral samples. Halite is the ideal host mineral phase for FTIR microspectrometry analysis of petroleum fluid inclusions because of its transparency over the mid-infrared range. Fluorite is transparent over most of the same range, whereas quartz and calcite exhibit only limited "windows" in the range of interest, which limits the amount of information potentially available from oil inclusions in these two minerals.

Compared to petroleum inclusions, bulk oil samples obtained from the same wells have preferentially lost the lighter hydrocarbon components methane and carbon dioxide, as well as the important aromatic components. Thus, when using data obtained from bulk oil samples to determine compositions of oils from which PVT properties are to be calculated, one must estimate the amount and nature of the lost light components and add these components back into the bulk composition for a closer representation of the composition of the oil in the inclusion. Comparison of FTIR spectra of inclusions with spectra for different bulk oil samples from the same well or reservoir can provide constraints on the maturation and fluid flow history of petroleum in the reservoir.

References

1. E. Roedder, "Fluid inclusions," *Mineralogical Soc. Am. Reviews in Mineralogy* 12: 644, 1984.
2. K. L. Aulstead and R. J. Spencer, "Diagenesis of the Keg river Formation, Northwestern Alberta: Fluid inclusion evidence," *Canadian Petroleum Geology* 33: 167-183, 1985.
3. W. Narr and R. C. Burrus, "Origin of reservoir fractures in Little Knife Field, North Dakota," *AAPG Bulletin* 68: 1087-1100, 1984.
4. R. J. Bodnar, "Fluid inclusion evidence for the physical and chemical conditions of petroleum generation in the Miocene Monterey Formation of California, USA," *European Conference on Research on Fluid Inclusions* (Abstracts with Program, in press).
5. O. A. Barres et al., "Application of micro-FT-IR spectroscopy to individual hydrocarbon fluid inclusion analysis," *Applied Spectros.* 41: 1000-1008, 1987.
6. N. Dahan and R. Couty, "Emploi de la microspectroscopie infrarouge dans l'étude des inclusions d'hydrocarbures contenues dans une fluorine: Effet d'un chauffage sous pression (400°C-400 bars)," *Compte. Rend. Acad. Sci. (Paris)* 135: Ser. II, 687-689, 1987.
7. M. R. O'Grady et al., "Fourier Transform Infrared Microprobe (FTIRM) analysis of petroleum fluid inclusions," *Pan American Conference on Research on Fluid Inclusions* (Program and Abstracts) 2: 50, 1989.
8. J. Pironon and O. Barres, "Microspectrometric analyses of synthetic and natural hydrocarbon fluid inclusions (UV fluorescence, Raman, FT-infrared)," *ibid.* 2: 71, 1989.
9. B. Wopenka, J. D. Pasteris, and J. J. Freeman, "Analysis of individual fluid inclusions by micro-FTIR and micro-Raman spectroscopy: Advantages and disadvantages," *ibid.* 2: 71, 1989.

ANALYSIS OF FLUID INCLUSIONS IN OCEANIC ROCKS BY LASER RAMAN MICROPROBE TECHNIQUES

D. A. Vanko and C. L. Knight

Fluid inclusions in oceanic rocks are studied in a variety of ways, including observation of phase changes during controlled heating and freezing on a microscope stage and during crushing. We have used laser Raman spectroscopy by laser Raman microprobe (LRM) to help characterize nondestructively the presence and distribution of Raman-active chemical species in these fluid inclusions.

Many rocks that are dredged, drilled, or otherwise sampled from the ocean floor have been exposed at some time in their history to hydrothermal fluids,¹ the result of which is a metamorphism of the rocks characterized by corrosion of primary magmatic minerals and replacement by new minerals. In some cases, hydrothermal fluid flow through the rocks is effected along a system of interconnected fractures; the evidence is that some fractures are subsequently "fossilized" by getting infilled with new minerals. In both cases, whether new minerals replace old ones or grow in a fracture, primary fluids may be trapped as microscopic inclusions.² The analysis of these fluid inclusions yields information on the physical and chemical conditions that were in effect during the hydrothermal activity.

Two major reservoirs are available for supplying hydrothermal fluids in an oceanic setting: the seawater reservoir and the reservoir of trace volatiles resident in the earth's upper mantle. The seawater reservoir is well characterized and of relatively constant starting composition. In a neovolcanic portion of the seafloor, cold seawater invades the newly formed and fractured oceanic crust. It is heated by conduction and begins to react with the volcanic rocks, primarily oxidizing them and exchanging cationic species such as Mg^{++} for Ca^{++} and Na^{+} . As the fluid continues to heat and penetrates further, it reacts more vigorously with the oceanic rocks and leaches trace metals. At some region deep in the crust (estimated to be around 2 km), the hydrothermal fluid attains such buoyancy that it flows convectively upwards, to emerge at the seafloor as a hydrothermal hot spring. Observed temperatures of hot springs in the deep sea are typically 250-350 C, with boiling in-

hibited by the large ambient hydrostatic pressure. Upon quenching at the seafloor by the cold ocean, the hydrothermal fluid becomes saturated in minerals that were soluble at temperature, and large chimney structures bearing metal sulfides are constructed.

In contrast to seawater-derived hydrothermal fluids, mantle-derived fluids owe their origin to concentration of magmatic volatiles during the crystallization of primary magma deep in the crust. The volatiles commonly thought to be important are H_2O , CO_2 , and lesser amounts of H_2 , CO , CH_4 , Cl , F , and H_2S . Also in contrast to the seawater hydrothermal systems, magmatic volatiles are thought to be much more restricted in volume and distribution.

The detection of traces of gases that are characteristic for magmatic volatiles is one means to classify natural oceanic fluid inclusions as being part of a magmatic rather than a seawater hydrothermal system. This information is important especially for fluids in deep crustal oceanic rocks (gabbros, diabase), as the nature of deep crustal fluids (more than about 2 km deep) is controversial. LRM is a quick and nondestructive means to test for the presence and relative abundance of "magmatic" gases, because CO_2 , CH_4 , CO , H_2 , and H_2S are Raman active.

Methods

Fluid inclusions are analyzed with an Instruments S.A. Ramanour U-1000 microprobe equipped with a double-monochromator spectrometer, an Olympus BH-2 microscope, and a Spectraphysics Model 2016 5W Ar laser. Sample preparation consists of slicing the inclusion-bearing rocks into thin wafers, typically 0.05-0.10 mm thick, and polishing both sides with 1 μ m diamond paste. The resulting wafers are transparent and can be examined in plane-polarized and doubly polarized transmitted light to locate appropriate fluid inclusions. These inclusions are individually relocated in transmitted light on the microscope stage of the LRM, and then irradiated with the 514.5nm laser light, which is focused through the light microscope optics onto the inclusion. Backscattered light is then collected through the microscope optics and directed into the spectrometer for analysis.

Results

Fluid inclusions in quartz veins of seawater-type hydrothermal origin consistently test negative for the presence of Raman-active gases such as CO_2 , CH_4 , and H_2S , even for vapor-rich inclusions that formed from a two-

D. A. Banko is at the Department of Geology, Georgia State University, Atlanta, GA 30303; C. L. Knight is at the Department of Geological Sciences, Virginia Polytechnic Institute & State University, Blacksburg, VA 24061. Supported by NSF grant EAR-8607139 to R. J. Bodnar, Virginia Tech, to whom we acknowledge thanks. Also supported by Georgia State University Research Grant 89060 and NSF grant OCE-8710717 to D.A.V.

01V22DC.S00

REGION: 2

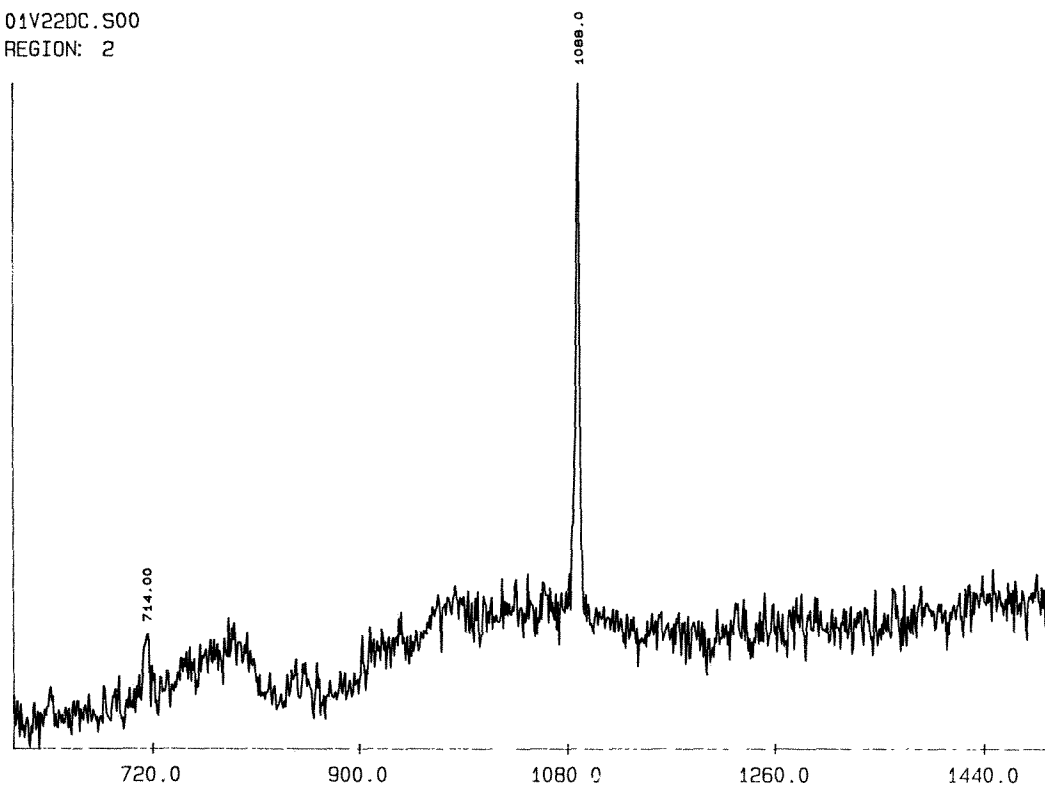


FIG. 1.--Raman spectrum for small birefringent daughter crystal in fluid inclusion in primary plagioclase, identified as carbonate (probably calcite) because of sharp strong symmetric stretch mode at 1088 cm^{-1} , and weaker in-plane bend mode at 714 cm^{-1} .⁴

01V584A.S00

REGION: 1

CTS/SEC X10E3

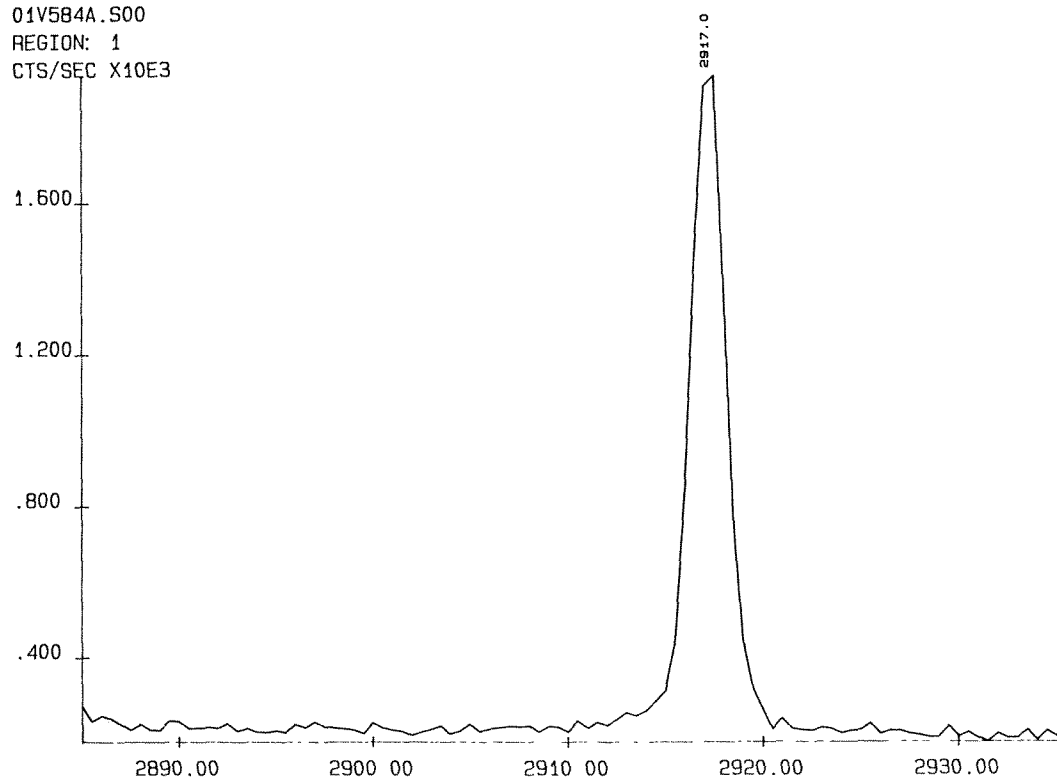


FIGURE 2.--Raman spectrum for fluid inclusion in quartz showing methane peak at 2917 cm^{-1} .

phase (boiling) hydrothermal system. In the latter case, had gases been present in minute quantities, they would be expected to fractionate strongly to the vapor phase and be detected in vapor-rich inclusions. The fact that gases are undetected is consistent with analyses of actual deep-sea hot spring fluids, which are modified seawater solutions. Typically, they contain H_2 and CH_4 in the range 10^{-5} to 10^{-4} mol/kg and CO_2 around 10^{-3} mol/kg.³ Such small amounts of gas are three to four orders of magnitude below the detection limit of LRM (detection limits are about 1 mole %, or 5×10^{-1} mol/kg for CO_2 or CH_4).

Some fluid inclusions in magmatic and metamorphic minerals in oceanic gabbros contain detectable gases interpreted to be of magmatic origin. Gabbros from the Indian Ocean 12 million years old, drilled at Site 735B of the Ocean Drilling Program, contain aqueous fluid inclusions in primary and secondary plagioclase, primary quartz, and secondary hornblende. Many inclusions of the earliest generations contain daughter crystals (Fig. 1). The fluids in primary plagioclase and quartz expand on crushing owing to the presence of compressed gases, but crushing is destructive and cannot reveal the type of gas present. LRM analyses of these inclusions consistently reveals the presence of methane, but no other common gases (Fig. 2). Identification of methane is supported by cooling experiments, where a clathrate is observed that dissociates at temperatures up to +24 C. Methane clathrate is the only common one to remain stable up to such a high temperature.

Fluid inclusions in vein diopside from the same drillhole were analyzed by LRM and found to be devoid of detectable methane or other common gases. This result suggests that diopside-bearing veins are related to a seawater-type hydrothermal system instead of a magmatic-volatile system.

In conclusion, the LRM technique is useful for detecting in fluid inclusions gases that originate as magmatic volatiles. This technique enables petrologic features associated with the inclusions to be recognized as either magmatic or seawater-derived hydrothermal. As a result the origin and evolution of ocean crustal fluids, which are so important in several processes such as metal sulfide deposition, can be inferred.

References

1. P. A. Rona, "Hydrothermal mineralization at oceanic ridges," *Canadian Mineralogist* 26: 431-465, 1988.
2. Edwin Roedder, *Fluid Inclusions*, Reviews in Mineralogy, Mineralogical Society of America, vol. 12, 1984.
3. W. C. Evans, L. D. White, and J. B. Rapp, "Geochemistry of some gases in hydrothermal fluids from the Southern Juan de Fuca Ridge," *J. Geophys. Res.* 93: 15305-15313, 1988.
4. W. D. Bischoff, S. K. Sharma, and F. T. Mackenzie, "Carbonate ion disorder in synthetic

and biogenic magnesian calcites: A Raman spectra study," *Am. Mineralogist* 70: 581-589, 1985.

Secondary Ion Mass Spectroscopy

ADVANCED IMAGING AND ANALYSIS TECHNIQUES WITH A SCANNING ION MICROPROBE

J. M. Chabala, R. Levi-Setti, and Y. L. Wang

The principles and mechanics of imaging microanalysis with scanning ion microprobes have been extensively discussed for over two decades. In 1967 Liebl described the first scanning ion microprobe system that utilized secondary ion mass spectrometry (SIMS, magnetic sector) for materials analysis.¹ The lateral resolution of this pioneering instrument was less than 1.6 μm —comparable to the resolution of several commercial direct imaging and scanning ion microscopes currently available. Following this invention, numerous improvements in source brightness,² image resolution,³ and SIMS sensitivity were achieved. The theoretical foundation of lateral image resolution attainable with these machines, which depends strongly on SIMS signal statistics, has been explored.⁴⁻⁵

Although it is a mature field, advances in scanning ion microanalysis continue to occur. In this essay, we report several technologies recently developed at the University of Chicago—Enrico Fermi Institute Focused Ion Beam Facility that have been applied to our high-lateral-resolution analytical scanning ion microprobe (UC SIM). We demonstrate an efficient method to obtain parallel mass-resolved images when using an RF quadrupole mass spectrometer, and describe a mass peak switching procedure that is useful for depth profiling. We describe directed-probe vector scan modes that often hold advantages over conventional raster-scan analysis. Finally, we outline several development programs, near fruition, that should further improve the analytical capabilities of this instrument. A companion article in this volume by our group, "The use of focused heavy ion beams for submicrometer imaging microanalysis," discusses applications of conventional high-resolution SIMS imaging.

Overview: The UC Scanning Ion Microprobe

We assume that the reader is familiar with

The authors are at the Enrico Fermi Institute and Department of Physics, The University of Chicago, 5640 S. Ellis Ave., Chicago, IL 60637. They acknowledge the service of the James Franck Institute Electronics Facility at the University of Chicago. The ALi alloy example was obtained as part of a collaboration with D. B. Williams (Lehigh University) and D. E. Newbury (NIST). They thank their collaborators at Ilford Ltd and Ilford AG for encouraging them to present the photoemulsion example in this context. This material is based on work supported by the National Science Foundation under grant DMR 861224, by the University of Chicago Materials Research Laboratories, and by a grant from Ilford, Ltd.

the basic design of the University of Chicago Scanning Ion Microprobe. For details, refer to our second article in this volume, mentioned above, which contains a diagram indicating the relationships between the functional components of this instrument; or consult Refs. 3, 5, and 6. Several features of the UC SIM are relevant to the present discussion.

1. The primary ion optical column generates a beam of heavy ions, typically Ga^+ , that can be focused to a spot less than 20 nm in diameter.³ This diameter, defining the best image resolution possible with the UC SIM, matches the practical limit imposed by the lateral spread of the bombarding-ion-induced collisional cascade⁷ and by considerations of secondary ion signal statistics.⁵ Even if some lateral resolution (edge definition) must be sacrificed, as occurs when our parallel mass-resolved imaging scheme is employed, image resolution can still be 100 nm or better.

2. The SIMS system consists of an RF quadrupole mass spectrometer integrated with ion collection and transport optics. The detection efficiency of this system ($\sim 0.2\%$) compares favorably with that of similarly configured instruments. As a result of this good efficiency, the probe can be manipulated rapidly over a sample surface without forfeiting meaningful signal statistics.

3. The probe can be scanned either by dedicated X-Y (square) raster electronics or by a programmable (68020 microprocessor-based) pattern generator,⁸ which is in turn controlled by a digital image processor⁸ fully interfaced to the microprobe SIMS system, as described below. The first scan method (dedicated raster electronics) has been used successfully since the first operation of the UC SIM. With use of the image processor scan control, more sophisticated analytical imaging is possible.

4. We have recently supplemented the RF quadrupole spectrometer⁹ with a custom-designed mass peak switcher. When appropriate trigger signals have been received, the peak switcher, using CMOS technology integrated circuit switches, rapidly tunes the spectrometer through a sequence of up to four mass-to-charge ratios. (More ratios can be implemented with minimal recirculating.) The masses to be analyzed are readily selected with four calibrated potentiometers. The spectrometer can readjust to filter a different ion species in a time estimated to be less than 5 μs . However, the minimal effective switch time is dictated by the transit time for ions through the quadrupole.⁶ This time varies, of course, according to ion energy and $(\text{mass})^{1/2}$; in general, ions require no longer than 100 μs to

traverse the quadrupole in our system. During this effective switch time, the SIMS signal can be automatically quenched by a gating procedure or by beam blanking. The switch interval is so short that quenching is usually unnecessary.

It is significant that the mass peak switching hardware installed in the UC SIM is not hampered by hysteresis delays that occur during the tuning of single-focus magnetic sector spectrometers. Time of flight¹⁰ and multiple focus magnetic¹¹ spectrometers permit true parallel mass (several masses at one time) SIMS. The microsecond-period mass switching SIMS system described here comes close to this ideal.

Parallel Mass-resolved Imaging

Given the mass peak switching capability introduced above, several parallel mass-resolved imaging procedures could be adopted. As a further restriction, we require that each set of parallel SIMS images (maps) be derived from the *same surface layers*. If SIMS maps are sequentially acquired by multiple scans, as is the conventional methodology, each noncontemporaneous map is a record of a possibly changed environment at a different eroded depth. Furthermore, in order to minimize the consumption of material by erosion, it is desirable to obtain multimass distributions in the same time as is necessary to acquire a single-mass map (for the UC SIM, ≤ 524 s). Finally, the secondary ion signal per probe raster position must be the same as that for a single-mass map, otherwise the reduced signal statistics (and therefore image resolution) could nullify any gain earned by peak switching.

Figure 1 describes the mass peak switching protocol we use for two-mass parallel imaging. The field of view is encompassed by 512×512 or 1024×1024 probe raster positions, as for single-mass imaging. The spectrometer is set to transmit either M_1 or M_2 for each odd or even numbered line, respectively. The spectrometer mass tuning is changed only once per line; consequently, the SIMS "dead time," the switching time during which the SIMS signal is quenched, is low. The SIMS signal, in the form of digital pulses from a channel electron multiplier operated in pulse-detection mode, is stored directly in arrays of memory in the image processor. Because no intervening image conversions are necessary (for example, no video cameras or resistive anode detectors are used), no degradation of SIMS data integrity can occur. Within the image processor, the two interlaced maps are stripped apart and separately displayed (Fig. 1), a process that requires a fraction of a second. To aid interpretation, the two maps can be color-coded and superimposed, either during the image accumulation scan or afterward.

In theory, following this exercise the image resolution (edge definition) of edges lying parallel to the x axis is larger by a factor ≤ 2 times than that of edges lying parallel to the y axis, i.e., vertical lines are "sharper"

PARALLEL MASS-RESOLVED IMAGING

Rapid Mass Peak Switching (< 0.1 ms)
Using an RF Quadrupole Spectrometer

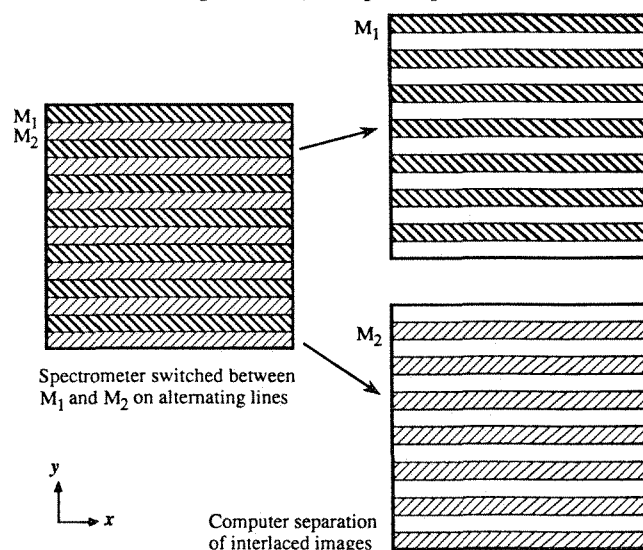


FIG. 1.--Schematic illustration of two-mass parallel SIMS imaging scheme employed in UC scanning ion microprobe system.

than horizontal ones.⁵ In practice, this compromise is not important, as illustrated by the two pairs of parallel mass-resolved images in Fig. 2. These images have not been doctored by any image-processing techniques such as edge enhancement. The first two images are concurrently acquired $^7\text{Li}^+$ (Fig. 2a) and $^{27}\text{Al}^+$ (Fig. 2b) maps of the clean surface of an Al 0.24wt%Li alloy. The scale bars within these maps correspond to $1 \mu\text{m}$. Large rounded zones devoid of Li but still rich in Al, as well as myriad submicrometer details, are evident. Under the experimental conditions of this measurement (512×512 probe settings, 35mm FWHM probe diameter), one computes comparable resolutions along the x and y axes (vertical edge definition ~ 45 nm, horizontal ~ 55 nm), which can be confirmed by direct measurements of the images.

Figures 2(c) and (d) show maps resulting from one scan of a spread of cubic monosize silver bromide photocrystals with buried iodide.¹² Submicrometer-size emulsion crystals, of which this is an example, often exhibit large sputtering yields and are prone to amorphization if they receive large ion doses/time. For such samples, recourse to parallel mass imaging is necessary. Comparison with sequentially acquired single-mass maps of the same material, as shown in "The use of focused heavy ion beams for submicrometer imaging microanalysis" (this volume), reveals no apparent loss in image quality, even for the low-signal-statistics $^{127}\text{I}^+$ map (Fig. 2d).

Three- and four-mass parallel imaging is performed according to the plans shown in Fig. 3. Two methods for four-mass imaging have been explored. In the second (lower right, Fig. 3), each horizontal line is scanned twice

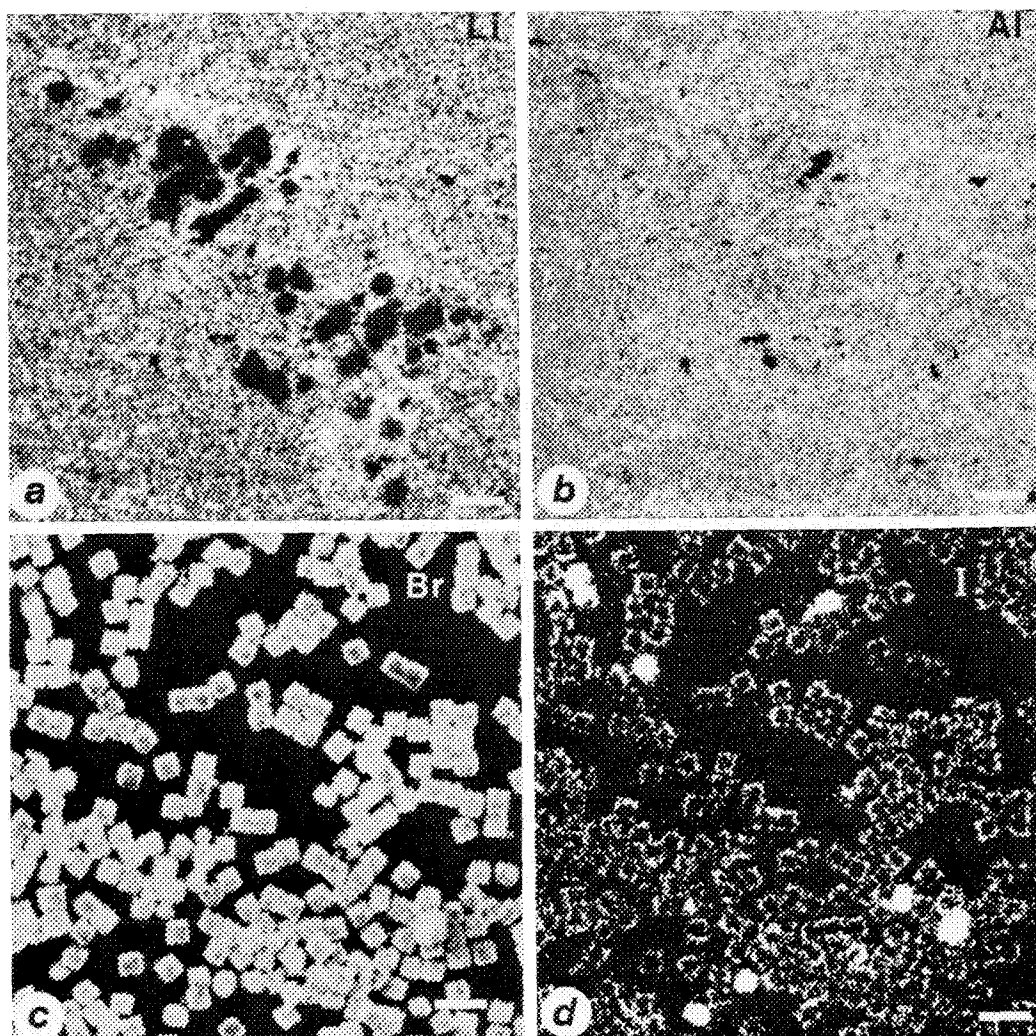


FIG. 2.--Examples of parallel mass-resolved imaging with the UC SIM. Concurrently acquired maps of clean surface of Al 0.24wt% Li alloy for (a) $^7\text{Li}^+$, (b) $^{27}\text{Al}^+$. Scale bar = 1 μm . Concurrently acquired maps of a spread of cubic monosize AgBr photoemulsion with buried I shell¹² for (c) $^{79}\text{Br}^-$, (d) $^{127}\text{I}^-$. (For comparison, see Fig. 4 in "The use of focused heavy ion beams for submicrometer imaging microanalysis," this volume.) Scale bar = 2 μm .

before moving to the next line: during the first pass, the odd-numbered probe positions, corresponding to one mass, are scanned; during the second pass, the interleaved even-numbered positions are scanned with a different mass tuning. This scan format reduces the SIMS dead time. Specimen drift, if any, is irrelevant during the short time required for two line passes.

Three-dimensional multimass volume reconstruction (3D imaging) can be profitably performed with these parallel mass imaging procedures, even for delicate objects (for example, photocrystals). Nonimaging multimass depth profiling is also facilitated. We have used these techniques for several studies, the results of which are being prepared for publication. We claim no novelty as to these capabilities, only assert that they are powerful tools when used in conjunction with a high-resolution imaging microprobe.

Vector Scan Microanalysis

There are several situations in which it is necessary to avoid scanning over features within a field of view. To determine the compositional mass spectrum of regions within a larger area, for example submicrometer-scale intraboundary phases in ceramics and alloys, these regions must be scanned while their surroundings are excluded. Alternatively, islands of surface contamination, frequently dust or oxide deposits, must be avoided in order to obtain reliable assays of surface composition. The sputter redeposition of material between adjacent areas, as occurs during conventional raster scans, can deleteriously affect quantitative measurements of surface features.¹³ In response to these requirements and concerns, among others, we have devised directed-probe vector scan microanalysis techniques in which the probe is scanned in arbitrarily defined patterns over a sample.

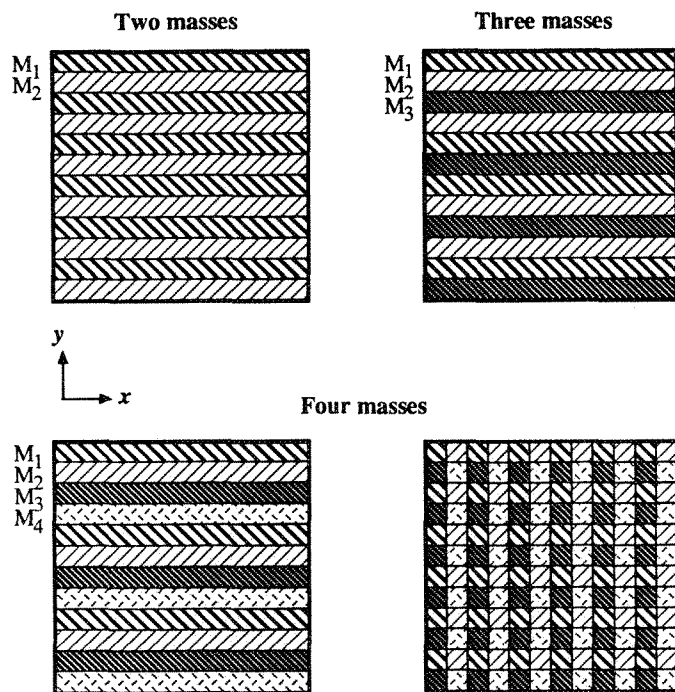


FIG. 3.--Details of multimass parallel SIMS imaging strategies employed in UC scanning ion microprobe system.

As a first step, a secondary ion or topographic micrograph is acquired and stored in the image processor; in order to minimize sputter redeposition, the accumulation time for this image is made as short as possible. This orientational image serves to locate precisely the items that are to be examined in more detail. Areas of interest are selected either manually with a mouse cursor or automatically according to any of a number of discrimination criteria (e.g., feature intensity, size, shape, or orientation). The image processor then generates a set of templates that defines the probe positions over which the beam will be preferentially scanned. Additional variables (time per probe position, number of scan loops) are set at this point. Finally, the computer reprograms the pattern generator, instructing it to guide (vector scan) the probe over the chosen features. If necessary, the beam is blanked while it is directed between widely separated points. During scanning, mass spectra, multimass depth profiles, or SIMS images of the selected areas are obtained.

We have used this capability for a number of studies. In Ref. 14 we report an analysis of electronic microstructures where vector scan microanalysis was essential, enabling us to determine separately the composition of circuit metallizations and the substrate without sputter redeposition cross-contamination. We now routinely employ this technique for numerous biological and materials science applications.

Future Work and Final Remarks

We have instituted several technical development programs, nearing completion, that should strongly enhance the analytical performance of the UC scanning ion microprobe.

1. We are completing pattern-generator software routines conceived to improve the reliability of mass spectrum and depth profile data. Judicious combination of signal gating with unconventional scan patterns should make it possible to eliminate the problems of crater edge effects from these measurements. For one routine, an old method recently promoted by Perkin Elmer,¹⁵ the probe is repeatedly scanned in a converging square spiral, first bombarding the crater edges, the interior areas. Properly gated in a simple manner, the SIMS signal is derived only from central regions of the crater.

2. A long-anticipated cryogenic sample stage is in the final stages of machining. This regulated liquid-nitrogen-temperature stage will enable many biological studies (e.g., analysis of frozen hydrated tissue) and materials science studies (e.g., SIMS measurements of high-temperature superconductors while they are in the superconducting phase).

3. We are replacing the 2MHz 8-bit Z80-based microprocessor currently governing the microprobe optics system with a 15.7MHz 32-bit 86030 computer (Macintosh IIX). We expect concomitant improvements in system speed, reliability, and capability. Already, mass spectra and depth profiles are collected by this new computer, facilitating data analysis, display, and intercomputer communication.

The parallel-mass-imaging system described here is, we believe, a revolutionary improvement in the analytical capabilities of the UC scanning ion microprobe. We are only beginning to explore the many interdisciplinary applications of this system. We look forward to presenting some of these results, as well as additional information about the other programs described here, at the 1990 MAS conference.

References

1. H. Liebl, "Ion microprobe mass analyzer," *J. Appl. Phys.* 38: 5277-5283, 1967.
2. For a recent review of high brightness liquid metal ion sources, see P. D. Prewett and E. M. Kellogg, "Liquid metal ion sources for FIB microfabrication systems: Recent advances," *Nucl. Instr. Methods Phys. Res.* B6: 135-142, 1985.
3. R. Levi-Setti, G. Crow, and Y. L. Wang, "Progress in high resolution scanning ion microscopy and secondary ion mass spectrometry imaging microanalysis," *SEM/1985 II*, 535-551.
4. F. G. Rüdener, W. Steiger, and H. W. Werner, "Quantitative evaluation of secondary-ion micrographs," *Mikrochimica Acta Suppl.* 8: 59-69, 1979.
5. J. M. Chabala, R. Levi-Setti, and Y. L. Wang, "Practical resolution limits of imaging microanalysis with a scanning ion microprobe," *Appl. Surf. Sci.* 32: 10-32, 1988.
6. R. Levi-Setti, Y. L. Wang, and G. Crows, "High spatial resolution SIMS with the UC-HRL scanning ion microprobe," *J. Physique* 45: C9-195-205, 1984.

7. J. P. Biersack, "Computer simulations of sputtering," *Nucl. Instr. Methods Phys. Res.* B27: 21-36, 1987.
8. Kontron Bildanalyse GMBH, Eching/Munich, Federal Republic of Germany.
9. Extranuclear 324-9, Pittsburgh, Pa.
10. A. R. Waugh, D. J. Fathers, and D. R. Kingman, "Development of an imaging time-of-flight SIMS instrument," *Microbeam Analysis--1986*, 82-84.
11. Y. Nihei, H. Satoh, S. Tatsuzawa, and M. Owari, "High spatial resolution secondary ion mass spectrometry with parallel detection system," *J. Vac. Sci. Tech.* A5: 1254-1257, 1987.
12. T. Maternaghan, C. Falder, R. Levi-Setti, and J. M. Chabala, "Elemental mapping of silver halide emulsion microcrystals by high resolution imaging SIMS," *J. Imaging Science* (in preparation).
13. F. G. Rüdener and W. Steiger, "Sputter redeposition as a limit to spatially three-dimensional SIMS microanalysis," *Ultramicroscopy* 24: 115-124, 1988.
14. R. Levi-Setti, J. M. Chabala, P. Halle-got, and Y. L. Wang, "Chemical characterization of electronic microstructures with sub-100 nm lateral resolution," *Microcircuit Engineering* 88 (in press).
15. S. M. Daiser, C. Scholze, and J. L. Maul, "The checkerboard technique: An essential progress in SIMS data acquisition and evaluation," *Nucl. Instr. Methods Phys. Res.* B35: 544-549, 1988.

INTERPRETATION OF SECONDARY ION MASS SPECTROMETRY (SIMS) SPECTRA BY LINEAR PROGRAMMING TECHNIQUES

T. B. Vander Wood and Christine Bowers

Chemical analysis of complex materials often involves the acquisition of some type of spectrum, followed by deconvolution of the spectrum in order to determine the composition of the sample. The procedure, which takes several forms, is essentially the solution of a set of simultaneous equations constructed from the unique spectra of the anticipated constituents of the material and is commonly known as "peak stripping"¹ or "spectral subtraction."²

In secondary ion mass spectrometry (SIMS) a sample is separated into ions composed of single atoms or simple atomic clusters, and the relative number of ions at each mass is measured. Figure 1 shows a typical SIMS spectrum in the mass range 201-211 amu for the mineral zircon, from which we would like to extract the $^{207}\text{Pb}/^{206}\text{Pb}$ ratio in order to determine the age of the mineral. Unfortunately, a simple ratio of the ions present at masses 207 and 206 does not give the desired result because ions other than those of lead are known to occur at these masses. These "interference" species are ubiquitous in low-resolution SIMS spectra. Instruments capable of high resolution³ can considerably reduce or even eliminate such interferences. However, the majority of SIMS instruments currently in use do not possess this capability, so that spectrum deconvolution is necessary. These interferences also occur at other masses, but always in constant ratios across masses. In principle, therefore, measurement of ion intensities at other masses should allow corrections for interferences at masses 206 and 207. In practice, 11 ions are known to occur in this region, and their distribution over the mass range 201 to 211⁴ is shown in Table 1. This system of equations makes up a determinate 11×11 matrix, which is most easily solved for repetitive cases by a single inversion of the matrix, which exchanges input and output variables followed by input of the ions counted at each mass. The results of this inversion are shown as Table 2, and this matrix can be used to calculate the relative intensities of all the contributing species from the measured ion intensities.

The above data treatment contains a large assumption--that all the species contributing to the ion intensities are accounted for. If other species are present, the species concentrations calculated from the inverted matrix will be wrong, and there will be no indication that things have gone awry.

There is an alternative method of data reduction that allows for the possibility that unknown interferences are present in the data, and also gives an indication of the size and nature of the interferences as well as the robustness of the resulting solution. By setting up the matrix in Table 1 as constraints that require all peak intensities to be less than the measured peak intensities and constructing an objective function which maximizes the intensities of the known species, one can construct a linear programming problem. Table 3 is the resulting solution, which indicates the calculated species intensities and "leftover intensities" (slack/surplus variable), which suggest the presence or absence of unanticipated interferences.

The lead 207/206 ratio calculated from the linear programming solution ($^{207}\text{Pb}/^{206}\text{Pb}$) is 0.2193. The solution resulting from matrix inversion is 0.2086 with a 2σ uncertainty of 0.0045. The difference in the two solutions is significant. Where does this difference arise? Examination of the slack variables indicates a small proportion of excess counts at masses 201 ($S1/201 = 0.008$), 202 ($S2/202 = 0.006$), and 209 ($S9/209 = 0.024$). But the most significant slack variable by far occurs at mass 205, with $S5/205 = 0.93$. Clearly, there is a contribution at mass 205 that has not been included in the matrix used to reduce the data, and examination of Table 2 indicates that the ratio of ^{207}Pb to ^{206}Pb is sensitive to the count rate at 205.

Included in the linear-programming solution is a sensitivity analysis; the results for this problem are also shown in Table 3. For each peak, a range of values is calculated that indicates the minimum and maximum values of the count rate at each mass that would still yield the same species intensities. In this example, the very limited range in the count rate at mass 203 suggests that the solution is very sensitive to mass 203 and that experimental conditions should be adjusted to minimize uncertainty in the count rate at this mass. The sensitivity analysis operates within the constraints defined by the model and does not evaluate the validity of these constraints. The results of the sensitivity analysis are most useful in the evaluation and choice of experimental parameters such as counting time.

To summarize, the application of linear programming techniques to this particular data set yields a $^{207}\text{Pb}/^{206}\text{Pb}$ ratio that is significantly different from the ratio obtained by matrix inversion. In addition, the large slack variable calculated by linear

The authors are with McCrone Associates-Atlanta, 1412 Oakbrook Drive, Suite 100, Norcross, GA 30093.

TABLE 1.--Relative abundances of some species in the mass region 204-211⁴ present in the secondary ion signal of zircon. Read by columns, the entries indicate the relative intensities of a given species at various masses. (²H, ³H are ignored.)

	HfNa ⁺	Zr ₂ O ⁺	Zr ₂ OH ⁺	SiHf ⁺	HfO ₂ ⁺	HfO ₂ H ⁺	Zr ₂ Si ⁺	²⁰⁴ Pb ⁺	²⁰⁶ Pb ⁺	²⁰⁷ Pb ⁺	²⁰⁸ Pb ⁺
201	.2710	.0391	.2080	0	0	0	0	0	0	0	0
202	.1380	.0886	.0391	.0017	0	0	0	0	0	0	0
203	.3520	.0064	.0886	0	0	0	0	0	0	0	0
204	0	.0400	.0064	.0475	0	0	0	1	0	0	0
205	0	0	.0400	.1721	0	0	0	0	0	0	0
206	0	.0098	0	.2600	.0018	0	0	0	1	0	0
207	0	0	.0098	.1454	0	.0018	0	0	0	1	0
208	0	.0007	0	.3416	.0513	0	.2443	0	0	0	1
209	0	0	.0007	.0208	.1843	.0512	.1190	0	0	0	0
210	0	0	0	.0108	.2702	.1843	.1874	0	0	0	0
211	0	0	0	0	.1384	.2702	.0478	0	0	0	0

TABLE 2.--Correction matrix used in calculating species distributions in zircon secondary ion signals.

	201	202	203	204	205	206	207	208	209	210	211
HfNa ⁺	-1.8145	0.508	4.0387	0	-.0067	0	0	0	0	0	0
Zr ₂ O ⁺	-.3350	11.7484	-4.3480	0	-.1113	0	0	0	0	0	0
Zr ₂ OH ⁺	7.2347	-2.8675	-4.4457	0	.0297	0	0	0	0	0	0
SiHf ⁺	-1.6815	.6644	1.0340	0	5.8037	0	0	0	0	0	0
HfO ₂ ⁺	.6647	-.2626	-.4087	0	-2.2941	0	0	0	30.1067	-21.38	8.8802
HfO ₂ H ⁺	-.2277	.0899	.1400	0	.7858	0	0	0	-9.3724	5.5138	1.7160
Zr ₂ Si ⁺	-.6375	.2519	.3921	0	2.2005	0	0	0	-34.19	30.744	-14.49
²⁰⁴ Pb ⁺	.0470	-.4831	.1533	1	-.2714	0	0	0	0	0	0
²⁰⁶ Pb ⁺	.4391	-.2873	-.2254	0	-1.5038	1	0	0	-.0539	.0383	-.0159
²⁰⁷ Pb ⁺	.1740	-.0686	-.1070	0	-.8456	0	1	0	.0168	-.0098	-.0031
²⁰⁸ Pb ⁺	.6963	-.2842	-.4246	0	-2.4023	0	0	1	6.8085	-6.4139	3.0847

programming for mass 205 indicates that a significant interference species has not been recognized. The solution obtained by matrix inversion contains no indication of an undefined interference species. Adoption of linear programming techniques, which allow the constraints to be formulated as inequalities, provides a means to evaluate these assumptions through inspection of the slack variables. Furthermore, sensitivity analysis is a valuable guide for a SIMS operator in the evaluation and adjustment of the analytical parameters in order to produce a statistically sound analysis.

References

1. T. B. Vander Wood and R. N. Clayton, "Ion-microprobe determined lead isotope

ratios in zircons from the Abitibi greenstone belt," *J. Geology* 93: 545, 1982.

2. W. Steiger and F. G. Ruedenauer, "A computer program for peak identification in secondary ion mass spectra," *Vacuum* 25: 409, 1975.

3. D. O. Froude et al., "Ion microprobe identification of 4,100-4,200 Myr-old terrestrial zircons," *Nature* 304: 616, 1983.

4. N. W. Holden and F. W. Walker, *Chart of the Nuclides*, Schenectady, N.Y.: General Electric Co., 1972.

TABLE 3.--Solution to sample linear-programming problem for lead 206 and lead 207 relative concentrations in zircon.

SOLUTION TO LINEAR PROGRAM

Original Variable	Value	Slack/Surplus Variable	Value
HfNa	0.00000	S1	28.04616
ZrO	90092.03100	S2	49.89825
ZrOH	49.78543	S3	0.00000
SiHf	0.00000	S4	0.00000
Hf	18592.52340	S5	29.00858
HfOH	1699.68689	S6	0.00000
ZrSi	5555.21530	S7	0.00000
O4Pb	0.00000	S8	0.00000
O6Pb	795.63153	S9	102.26828
O7Pb	174.45267	S10	0.00000
O8Pb	0.000	S11	0.00000

Objective Value: P=116959.33600

RIGHTHAND SIDE Sensitivity Analysis

CONSTRAINT NO.	LOWER LIMIT	ORIGINAL VALUE	UPPER LIMIT
1	3532.95	3561.00	NONE
2	7984.10	8034.00	NONE
3	576.64	581.00	593.17
4	3207.05	3604.00	3627.00
5	1.99	31.00	NONE
6	816.37	1712.00	NONE
7	3.55	178.00	NONE
8	1677.70	2374.00	6578.64
9	4174.73	4277.00	NONE
10	3713.81	6378.00	6486.56
11	3072.27	3298.00	7203.94

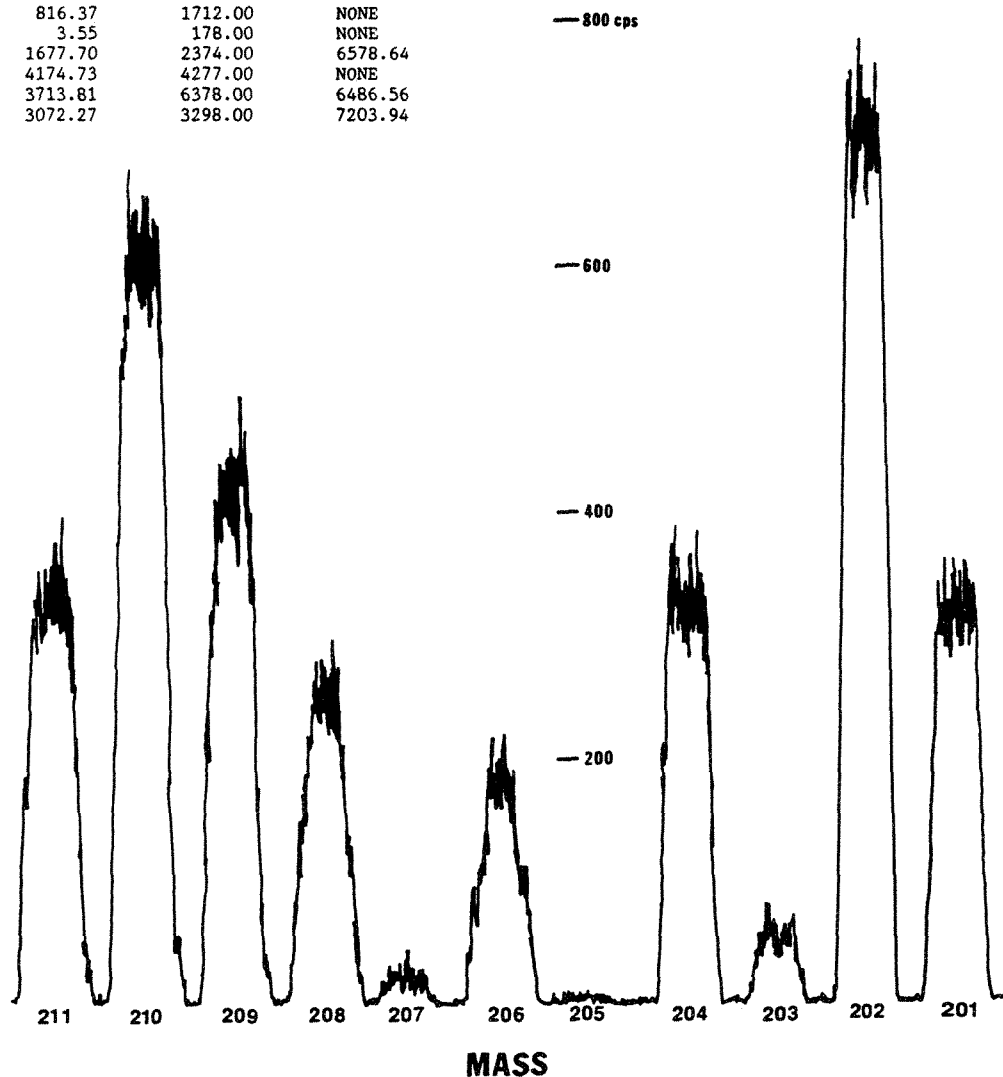


FIG. 1.--Typical mass spectrum in lead region for zircon.

ASPECTS OF QUANTIFICATION OF ION MICROSCOPE IMAGES RECORDED WITH A CAMERA-BASED DETECTION SYSTEM

F. P. Michiels, W. K. Vanhoolst, P. E. Van Espen, and F. C. Adams

The interest in quantitative lateral analysis with both ion microscopes and ion microprobes is increasing rapidly. The present paper describes the quantification of ion microscope images recorded by a camera-based detection system and evaluates the results obtained on steel and aluminum standard reference materials, based on the sensitivity factor (SF) and the matrix ion species ratio (MISR) method.¹

Experimental

The ion images were recorded with a CAMECA IMS 3-f, equipped with a high-sensitivity camera (MTI 66-SIT). Image processing was performed with a KONTRON image processing system and a MicroVAX II with user-developed software.

Method

The influence of the different components of the image formation system (microchannel plate, fluorescent screen, camera) on analytically important parameters such as linearity of the response, shading, and background was investigated.

The SF and the MISR method were evaluated with steel and aluminum standard reference materials, measured under O_2^+ and Ar^+ bombardment, respectively. The conversion of a gray-value image to a concentration image was done in two steps: (1) conversion of the gray-value image to a counts per second image and (2) the conversion of the counts per second image to a concentration image.

The first conversion is straightforward if all analytical parameters and their influence on the resulting gray value are known. This is a huge task, which may be circumvented by equating the integrated gray-value image to the secondary-ion current, as measured by an electron multiplier. This is a legitimate procedure, since it was experimentally verified that the relation between the gray value and the secondary ion current is linear.

By combination of images recorded during various integration times, the dynamic range can be extended appreciably. Figure 1(a) shows a 45ppm Mn image in brass. As the background is about 2000 times lower than the maximum Mn intensity, the dynamic range was compressed by use of a logarithmic scale in order to be able to display it as an 8-bit deep image. The

physical relevance of this image is demonstrated by the complementarity with the Cu (matrix) image in Fig. 1(b), in which differences in intensity depend on crystallographic contrast.

Two standard quantification methods were used to convert the counts-per-second images to concentration images. In the SF method, the Fe^+ was used as a reference image; in the MISR method, the AlO^+/Al_2^+ intensity ratio image was used as the MISR. The calculations were performed on a MicroVAX, which automatically performs the whole procedure, from the input of raw image information to the composition of an extended dynamic range image and the calculation of a concentration image. Figure 2 shows a few examples.

Results and Discussion

Since no suitable reference techniques were available to evaluate the accuracy of the localized quantification, the mean concentrations in the image and the certified concentrations were compared. Table 1 summarizes the results. Mean relative errors of 17 and 22% were obtained for the MISR and the SF method, respectively. This is a satisfactory agreement, since the heterogeneity of the elements contributes significantly to the residual error, as can be seen from column 3 of Table 1. Although the data do not actually prove the accuracy of the concentration maps, the agreement suggests that the methods described are successful. The advantage of the MISR method is that the sensitivity maps are not necessarily uniform over the whole image, and that it may correct for difference in oxygen concentration. If O_2^+ is used, the SF method is probably less susceptible to errors introduced by local variations in matrix composition (inclusions).²

References

1. J. Ganjei, D. Leta, and G. Morrison, *Anal. Chem.* 50: 285, 1978.
2. F. Michiels and F. Adams, *J. Analytical Atomic Spectrometry* 2: 773, 1987.

The authors are at the University of Antwerp, Universiteitsplein 1, B-2610 Wilrijk, Belgium. F. P. M. is indebted to the Belgium National Science Fund for a position as a research assistant.

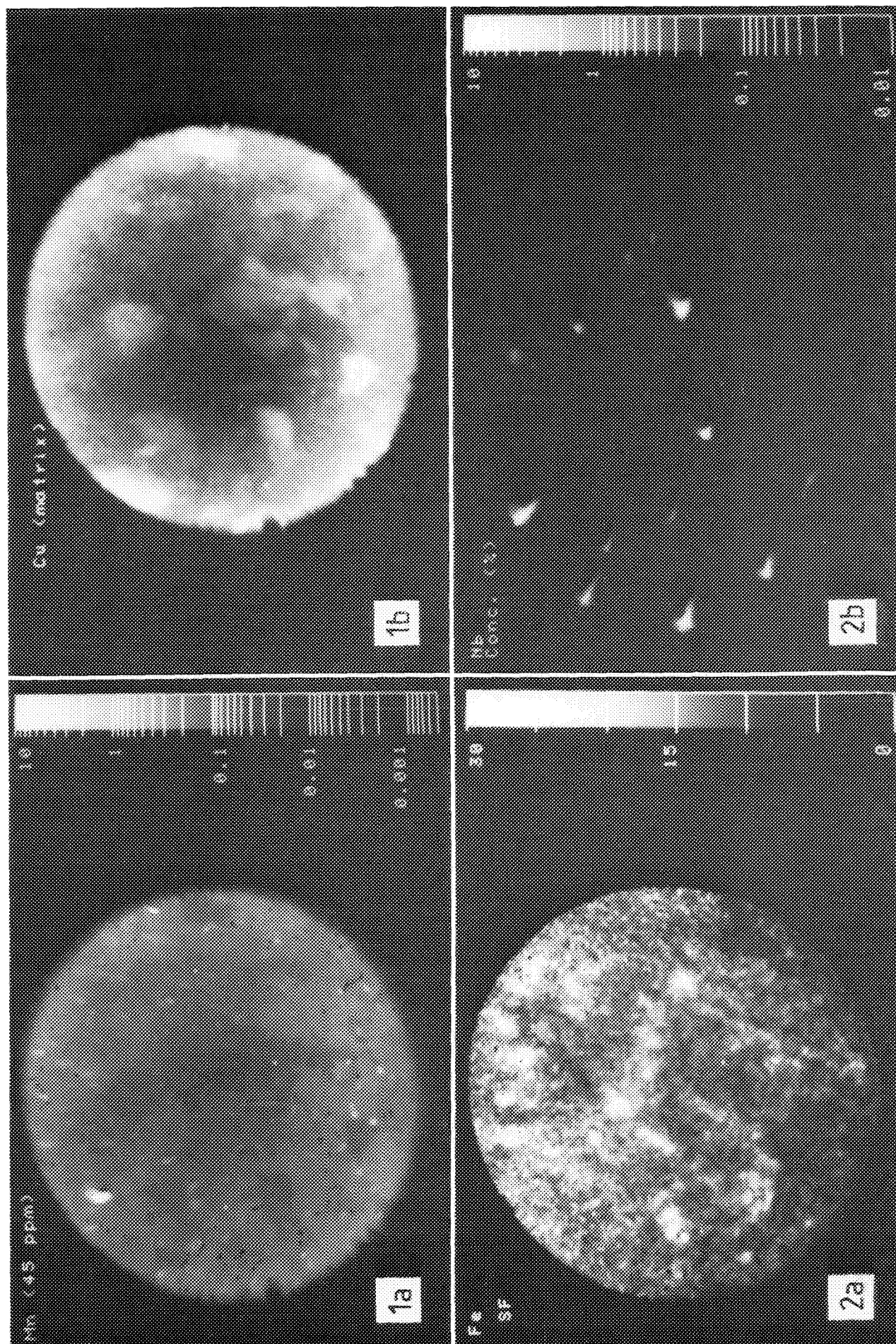


FIG. 1.--(a) Logarithmic intensity map of 45ppm Mn in brass (arbitrary units); (b) Cu ion image (diameter 150 μm).
 FIG. 2.--(a) SF map of Fe in aluminum, calculated by MISR method; (b) concentration map for Nb in steel, obtained by SF method.

TABLE 1.--Comparison of the experimental and the certified concentrations for the SF and the MISR method.

SF METHOD				MISR METHOD		
Element	cert. (a) conc.	exp. (a) conc.	estimated heterogeneity (%)	Element	cert. (a) conc.	exp. (a) conc.
Mn	1.50	1.56	6	Mn	0.31	0.30
Si	0.74	0.38	60	Si	0.30	0.29
Cu	0.09	0.15	14	Cu	7.10	5.7
Ti	0.050	0.040	7	Ti	0.0030	0.0052
Ni	0.32	0.33	9	Mg	0.15	0.14
Cr	1.31	1.61	9	Pb	0.35	0.35
V	0.31	0.39	11	Fe	0.35	0.31
Mo	0.030	0.027	5			
Nb	0.049	0.045	4			
B	0.0009	0.0007	3			
Zr	0.049	0.047	16			

(a) in weight percent.

A HIGH-SENSITIVITY, HIGH-DYNAMIC-RANGE SIMS DIGITAL IMAGE ACQUISITION AND PROCESSING SYSTEM

J. L. Hunter Jr., S. F. Corcoran, R. W. Linton, and D. P. Griffis

Since the first application of digital imaging techniques for the acquisition and manipulation of ion micrographs¹ by secondary ion mass spectrometry (SIMS) with stigmatic imaging instruments (i.e., Cameca IMS-300, IMS-3f, and IMS-4f), many advances have been made in digital imaging hardware and software. These advances include utilization of resistive anode encoders for direct digital acquisition of very-low-intensity signals,² and the development of hardware and software for automated acquisition of high-dynamic-range image depth profiles using digital camera-based systems.³ In addition, over the past few years, the PC-compatible computers, particularly the PC-AT compatible class machines, have seen increased analytical laboratory usage for instrument control and data processing. The considerable computing power of these inexpensive machines is enhanced by the wide availability of hardware and software products. In order to take advantage of these features, we have recently completed development in our laboratory of a PC-AT based control system for the IMS-3f.⁴ This paper describes the next stage of development for this control system, the addition of a PC-AT controlled digital imaging capability using a charge coupled device (CCD) detector. The resulting system optimizes the control of both the IMS-3f and the image acquisition and processing system from a single computer.

Hardware

Our previous custom imaging system⁵ suffered from three significant limitations: (1) eight-bit image storage, which limited single image dynamic range; (2) the use of a charge injection device camera with relatively poor sensitivity and noise characteristics; (3) incompatibility with most commercially available hardware. These deficiencies are addressed by the following selection criteria for the new imaging system:

1. Compatibility with existing IMS-3f control hardware and software (Hewlett-Packard Vectra PC/AT compatible).
2. Sixteen-bit dynamic range frame stores.
3. Video rate data manipulation for post-

J. L. Hunter, S. F. Corcoran, and D. P. Griffis are at the Analytical Instrumentation Facility, Box 7916, North Carolina State University, Raleigh, NC 27695; J. L. Hunter and S. F. Corcoran are also at the Department of Chemistry, University of North Carolina, Chapel Hill, NC 26599-3290, as is R. W. Linton. This work was supported by the Analytical Instrumentation Facility, Materials Science and Engineering, North Carolina State University.

acquisition image processing.

4. Large library of software routines for image acquisition and processing functions.

5. Low noise, high sensitivity, integrating charge coupled device (CCD) camera.

The imaging system developed in our laboratory which meets the above criteria consists of three major components: (1) CCD camera; (2) image acquisition and frame store system; and (3) computer control and data storage system. A block diagram of the integrated system is shown in Fig. 1. These subsystems are described below.

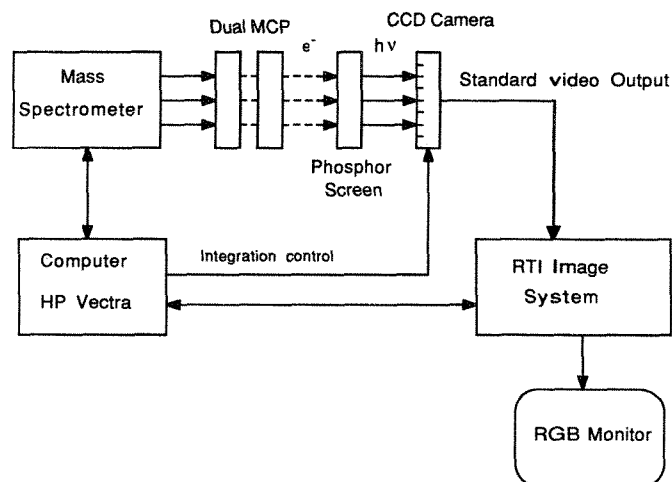


FIG. 1.--PC-AT camera based ion imaging system for the Cameca IMS-3f ion imaging system.

Camera

In the IMS-3f incoming secondary ions are converted to electrons at the first stage of a dual micro-channel plate (DMCP); these electrons are then converted to light at the phosphor screen of the IMS-3f and the light level is recorded by a CCD camera (Fig. 1). The camera chosen for acquisition of ion images from the IMS-3f phosphor screen is a Pulnix TM-840N integrating CCD camera. This camera overcomes the major limitations of our previous camera, a General Electric TN2500 charge injection device (CID) camera. The TN2500 suffered from poor signal-to-noise ratio due to image array readout noise, poor light sensitivity (1.0 lux faceplate illumination), and high dark current limiting integration to 2 s. The new generation TM-840N CCD camera has significantly lower readout noise, higher sensitivity (0.15 lux faceplate illumination), and a Peltier cooling block to decrease dark

current allowing integration times from 16 ms to more than 5 s. The increased sensitivity allows single-ion impacts on the DMCP to be detected by this camera based system.

Image Acquisition and Frame Store System

Recognition Technology Inc. (RTI) imaging system was chosen. The RTI system is a stand-alone image acquisition and processing system controlled by PC/AT compatible computers through a multibus interface. Pixel values stored in the digital frame stores appear directly on the PC memory (memory mapped) which allows processing of these pixel values in the computer memory without the need to transfer from or to the digital storage units on the RTI system. The RTI imaging system consists of three main components (Fig. 2): the analog subsystem (AS), the pipelined pixel Processor (PPL), and the digital storage units (DSU). A brief description of each of these components and its function is given below:

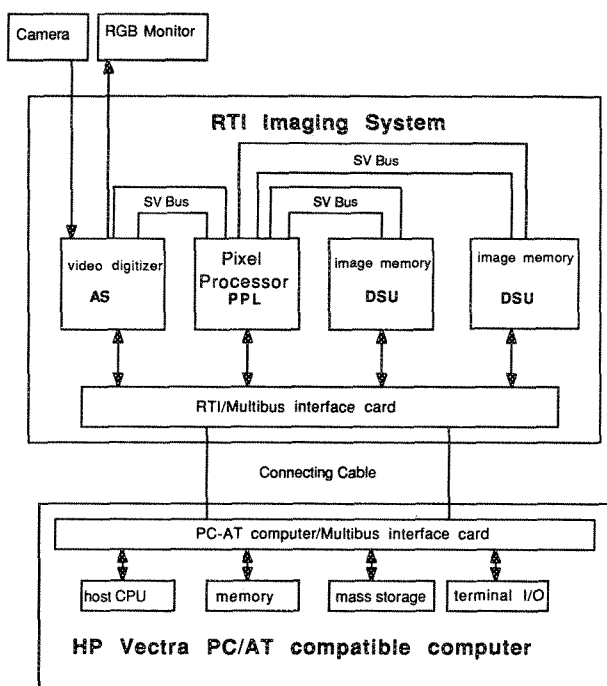


FIG. 2.--Interactions of major components of ion imaging system.

Analog Subsystem (AS). The AS converts the incoming analog signal from the camera to digital signal for storage in the frame stores. It features are 8-bit analog/digital (A/D) resolution with a 10MHz A/D conversion rate for 512×512 images; inputs for RS-170, RS-330, or RS-343 cameras; IEEE 796 or multibus interface, programmable gain and offset; software programmable real time input and output transformation tables; three 8-bit outputs (typically RGB) for display of 256 gray levels or 512 colors simultaneously from a palette of over 16 million.

Pipelined Pixel Processor (PPL) Sybsystem. The PPL is a high-speed pipelined pixel proces-

sor used for real time (1/30 s) data manipulations including convolutions and frame operations. Its features are: 10MHz processing speed with four pipeline channels yielding an effective speed of 40 million pixel operations per second; source selection for each of the four pipeline channels and output data selection to all of the digital storage units; 16-bit arithmetic/logic operation and 16-bit shifter/rotator; frame by frame, and frame by constant arithmetic operations; real time (1/30 s) convolution with user-definable convolution kernels for image enhancement and processing.

Digital Storage Units (DSU) Subsystem. The digital storage units retain the pixel values and make these values available to the PPL. However, the pixel values also appear directly on the PC-AT memory which allows for fast image storage and processing from the PC. Some features of our system as configured are: ten $512 \times 512 \times 8$ -bit frames stores capable of being used as five $512 \times 512 \times 16$ -bit frame stores; a ninth bit for graphic overlays on image data without changing the image data; and the availability of pan and scroll on a per pixel basis.

Computer Control and Data Storage System. The computer controlling both the IMS-3f and the imaging system is a PC-AT compatible Hewlett-Packard Vectra. The IMS-3f control hardware and software has been described previously.⁴ The imaging system is interfaced to the computer via a 16-bit PC bus to multibus interface card. (Additional interface cards were purchased and placed in other PC-AT compatibles in our laboratory to allow shifting of the control of the RTI imaging system to these computers for the off-line processing.) Since 512×512 pixels \times 16-bit depth images require approximately 500K bytes of data storage, an Iomega two drive, 20 Mbyte removable Bernoulli cartridge disk drive was chosen for mass storage. This system permits massive on-line data storage, since as soon as one disk is full, storage can be switched to the second disk and the first disk can be replaced. A listing of image storage times is included in Table 1.

TABLE 1.--Performance characteristics for a 256K image ($512 \times 512 \times 8$ bits).

Function	Time (s)
Read and display image from Bernoulli	2.5
Write image to Bernoulli	5.0
Add/subtract/multiply two images	1/30
Image convolution with kernel	1/30
Generate histogram of 256K pixels (8-bit image)	1/30
Zoom a 256×256 image to 512×512	1/30
Acquire $512 \times 512 \times 8$ -bit image	1/30
Acquire $512 \times 512 \times 16$ -bit image	255/30

Image Acquisition and Processing Software.

The software is a combination of routines written at the Analytical Instrumentation Facility (AIF) at NCSU and library routines that come with RTI system. All routines are written in C language and compiled by use of Microsoft C version 5.10. The menu system, which allows efficient selection and combination of the above routines, is written in Microsoft Quick BASIC version 4.0.

The HP Vectra controls both the operation of the Cameca IMS-3f and the RTI imaging system. A software package was written in our laboratory that integrates instrument control functions of the IMS-3f with image acquisition by the RTI system. This feature allows user control of all instrument parameters and image acquisition functions from a single computer. The user may change masses, secondary voltage offset, and a number of other instrument functions while operating the image acquisition system. Routines have been written for automated image depth profiling (IDP) with the IMS-3f based on the former image acquisition system.^{3,5} Images may be stored and retrieved from either the computer hard disk or secondary storage system (e.g., Iomega 20MB Bernoulli disk subsystem). CCD camera operations such as integration time and number of frames acquired can be controlled from the instrument control computer. Routines have been written to assure the optimum dynamic range for each image acquired. This system can acquire an 8- or 16-bit background-subtracted image and store it on disk for processing at a later time.

Since the RTI/PC-AT imaging system can be used for acquisition and processing of images acquired from other sources such as light microscopy (LM), scanning electron microscopy (SEM), scanning tunneling microscopy (STM), and scanning Auger microscopy (SAM), a universal image file format for analytical instrumentation (UIFFAI) was developed in our laboratory. This format allows images from the various techniques (along with their associated acquisition parameters) to be stored on disk and manipulated with the same image-processing software. The user can then correlate image data from the various image sources since, all images are on the same storage medium with the same file format with sufficient information for quantitative processing. The common format eliminates the need for file-format-conversion programs.

Software for Post-acquisition Image Processing

Images stored on a secondary storage device may be processed off line by means of software written for post-acquisition image processing. These routines allow processing of both 8- and 16-bit image data. Some useful features include:

- Cursor for line scans
- Image smoothing of 512 512 (Table 1)
- Image by image, and image by constant arithmetic operations (Table 1)
- Edge enhancement processing routines

- Edge extraction processing routines
- Fast histogram calculation on user definable area of interest (Table 1)
- Tools for binary image overlays for image correlations
- Contrast enhancement of image features by means of histogram equalization and related techniques
- Three-dimensional image reconstruction from image depth profile data
- Image zoom (Table 1)
- Calculation of local area depth profile data
- Summation of pixels in user-definable areas of interest for quantitative work
- Display of 16-bit images by logarithmic mapping to the 8-bit display

In conclusion, this work describes the hardware and software as well as some of the capabilities of the integrated image acquisition and processing system developed in our laboratory for SIMS. The PC-AT controlled imaging system can also be used, with only minor alterations to the hardware and software, for acquisition of images from other analytical instruments (e.g., LM, SEM, STM, SAM) and so permits correlative microscopy. Work is currently under way to expand the use of the system to STM and SAM.

References

1. J. D. Fassett, J. R. Roth, G. H. Morrison, *Anal. Chem.* 49: 2322, 1977.
2. R. W. Odom, B. K. Furman, C. A. Evans Jr., C. E. Bryson, W. A. Peterson, M. A. Kelly, and D. H. Wayne, *Anal. Chem.* 55: 574, 1983.
3. S. R. Bryan, R. W. Linton, and D. P. Griffis, "An automated method for high dynamic range secondary ion image depth profiling," *J. Vac. Sci. Technol.* A4: 2317, 1986.
4. S. F. Corcoran, W. S. Woodward, R. W. Linton, and D. P. Griffis, "A PC based interface for the Cameca IMS-3f," *Microbeam Analysis --1988*, 111.
5. S. R. Bryan, W. S. Woodward, D. P. Griffis, and R. W. Linton, "A microcomputer based digital imaging system for ion microanalysis," *J. Microsc.* 138: 15, 1985.

DETERMINATION OF URANIUM AND THORIUM IN OYSTER TISSUE BY ISOTOPE DILUTION: SECONDARY ION MASS SPECTROMETRY

D. S. Simons, J. D. Fassett, and W. R. Kelly

Secondary ion mass spectrometry (SIMS) is a sensitive and isotopically selective method for the direct analysis of solid material. The high sensitivity of SIMS for most elements is commonly exploited in the trace analysis of dopants and impurities in semiconductor matrices where detection limits are often at sub- $\mu\text{g/g}$ and sometimes sub-ng/g levels.¹ The high absolute sensitivity is also used to advantage in the analysis of minor-to-trace level constituents in individual micrometer sized particles.² The isotopic ratio measurement capability of SIMS under sample-limited conditions has also been assessed.³ With these powerful features available it would seem natural to explore the use of SIMS as an isotope ratio measurement method for isotope dilution mass spectrometry (IDMS), especially for those elements for which the traditional measurement method--thermal ionization mass spectrometry (TIMS)--is limited by low sensitivity. It is therefore surprising that only a few preliminary investigations of IDMS-SIMS have been described to date.⁴⁻⁷

The fundamentals of IDMS are well established.⁸ It is a "definitive" method in that it relies on internal standardization to achieve highly accurate and precise results. Briefly, a known weight of a sample is completely dissolved and a measured amount of a spike of the element of interest (usually enriched in a stable isotope with minor natural abundance or in a long-lived radioactive nuclide) is added to, and equilibrated with, the sample solution. After this point the loss of material has no effect on the concentration determination as long as the chemical blank is negligible.⁹ The element is then purified and concentrated, and the ratio between the spike isotope and the major natural isotope in the element-spike mixture is measured by mass spectrometry. From this ratio, from the known ratio of the same isotopes in the original sample and in the spike, and from the weight of sample and spike, the original concentration of the element in the sample can be calculated.

We have undertaken a comparison between secondary ion mass spectrometry and thermal ioniza-

tion mass spectrometry for the concentration measurement of uranium and thorium by isotope dilution mass spectrometry. These particular elements were chosen because the chemical procedures for their separation and measurement by TIMS are already established and they can provide a baseline against which the SIMS measurements are compared. The sample chosen for this comparison was SRM 1566a, freeze-dried oyster tissue.

Experimental

Chemistry. The chemical procedure for the separation of U has been described previously.^{10,11} Minor modifications have been made to enable the separation of both U and Th from the matrix and from each other in high yields and purity. NIST high-purity acids were used in all chemical separations and NIST sub-boiling quartz-distilled water was used for dilution of these acids.

One-gram samples from each bottle of oyster tissue were placed in glass weighing bottles and dried over $\text{Mg}(\text{ClO}_4)_2$ for 48 h under laboratory vacuum. Between 0.1 and 0.2 g of the dried samples were weighed into Teflon beakers. Ten-mL of concentrated nitric acid was added to the 50mL beakers followed by the addition of the powdered sample. Approximately 0.5 g of the ^{230}Th spike solution (concentration ~ 220 picomoles/g) and 1 g of the ^{233}U spike solution (concentration ~ 44 picomoles/g) were added to each beaker. The beakers were covered with quartz covers and refluxed on a hot plate for 12-16 h until dry. The residues were treated with 10 mL of nitric and 0.5 mL of perchloric acids and refluxed again until the brown solutions became clear, at which point the covers were removed and the samples taken to dryness. The residues were white or yellow in color and dissolved readily in 1 mL of 8N HNO_3 . The samples were heated to dryness again in an effort to fume off as much perchloric acid as possible.

The residues were dissolved in 1 mL of 8N HNO_3 and added to an 8×0.5 cm quartz column containing anion exchange resin in the nitrate form. The U and Th are held on the column under these conditions. The column was washed with 1 mL of 8N HNO_3 and the U was eluted with 15 mL of 8N HNO_3 followed by the elution of the Th fraction with 10 mL of 0.1N HNO_3 . The U fraction was converted to the chloride form by the addition of a few drops of concentrated HCl and heating to dryness. The residue was dissolved in 0.5 mL of 9N HCl and added to a 2×0.2 cm quartz column containing anion resin in the chloride form. The column was washed with

The authors are with the Center for Analytical Chemistry, National Institute of Standards and Technology, Gaithersburg, MD 20899. Certain commercial equipment, instruments, or materials are identified in this paper to specify adequately the experimental procedure. Such identification does not imply recommendation or endorsement by NIST, nor does it imply that the material or equipment identified are necessarily the best available for the purpose.

1 mL of 9N HCl and the U eluted with 3 mL of 0.1N HNO₃.

Thermal Ionization Mass Spectrometry. The purified U and Th fractions were dissolved in a drop of HNO₃. A small drop of water was added and the total sample was dried on a rhenium V-shaped filament. The basic thermal ionization procedure for U using ion-counting detection and ²³³U spike has been documented previously.¹⁰⁻¹¹ However, both Th and U were determined in one mass spectrometric run for each sample and as a result a number of changes were made to the standard procedure. First, the rhenium filaments used in the analysis were much more rigorously outgassed. The Th content of the filaments was higher and more variable than the U content. Extended heating was done to "clean up" the filaments. Thorium is much less efficiently ionized than U and is desorbed at a higher temperature. After U ratio measurements were completed, the temperature was taken to 1750 C and the mass range from m/z 229-232 was scanned to assess the background. Ratio measurements of ²³⁰Th/²³²Th were taken at 1775 C and 1825 C. Although the absolute Th signal could be increased greatly by an increase in the temperature above 2000 C, the background from the filament increased disproportionately at the higher temperatures.

SIMS Sample Preparation. All manipulation and loading of samples were performed in Class 100 clean air hoods. A polished, 25mm-diameter pyrolytic graphite planchet that fits into the SIMS sample holder was the substrate used for drying the SIMS sample solutions. A separate substrate was used for each element. In the case of uranium, the substrate was scribed into octants with a clean stainless-steel scalpel. The four solutions (three samples and one blank) were loaded on alternate octants with clean glass pipettes while the substrate sat under a heat lamp. In the case of thorium, the substrate was scribed into quadrants and the solutions were delivered to the surface by use of a 5μL Teflon-tipped micropipette. The size of the surface area covered was determined by the size of the drop delivered. Since the glass pipettes had a variable tip diameter and a haphazard delivery mechanism, the U deposits were broad and diffuse. The drops spread out over an area as large as 5 mm and were highly irregular in some cases. The residual salt tended to concentrate at the edges of the dried drop. Thus, the micropipette was tried in an attempt to alleviate this problem and make the dried deposits more reproducible. In fact, 0.5μL subdrops could be delivered to the surface, and the deposit could be limited to roughly the diameter of the Teflon tip, about 1 mm. The fact that the delivery process had to be repeated to deliver the entire sample did broaden the area in most cases. However, the deposit was limited to a circular area roughly 2 mm in diameter in the case of Th, a considerable improvement over that achieved for U.

TABLE 1.--Mass of uranium and thorium on planchets (ignoring losses in chemical separation).

Sample	Uranium		Thorium	
	Natural	Spike	Natural	Spike
OT-1	1.3 ng	0.9 ng	0.43 ng	2.2 ng
OT-2	13.	2.9	2.1	6.3
OT-3	23.	8.6	6.1	20.
Blank	5 pg	50 pg	22 pg	40 pg

Table 1 summarizes the maximum amount of material loaded for the SIMS analyses. The natural content of the original samples was determined from the spike-to-sample ratios that were measured. The yield of the chemical separation is not 100% (typically 80% for U)¹⁰, so that the actual amount deposited on the planchet should be reduced by this unknown factor. The sample sizes ranged over about an order of magnitude, or 2-3 orders of magnitude if blanks are included.

SIMS Ratio Measurements. All SIMS measurements were made with a Cameca IMS-3f Ion Microanalyzer.¹² The samples were sputtered by a primary beam of O₂⁺ ions with an impact energy of 8 keV and a current of 1-2 μA. The beam was raster-scanned over an area of 250 × 250 μm. A mass scan was taken before each sample was measured to estimate the background in the U/Th mass region of the mass spectrometer. A sample voltage offset of 10-20 V was applied so as to transmit atomic ions preferentially with respect to molecular ions, and thus to reduce the spectral background. Positive secondary ions of U⁺ or Th⁺ were detected. Signal levels of 10³-10⁴ counts per second for the most abundant isotope were used for ratio measurements, except in the case of the blanks where the signals were lower by a factor of 10.

Figure 1 shows a mass spectral scan of the actinide region from a graphite planchet in a location where no sample had been deposited. The background signals produced by molecular ions are typically less than a few counts per second. Figure 2 shows the mass spectrum in the uranium region from the uranium fraction of sample OT-3. The peaks are well resolved and the spectral background is low, as evidenced by the lack of signal at m/z 236 and 237, where no uranium isotopes or hydride ions are expected. The spectrum of a thorium deposit from sample OT-2 is displayed in Fig. 3. The spectral background seen at m/z 226-229 is well below 1% of the thorium isotopic peaks. The uranium was not completely separated from the thorium in the chemical procedure, as indicated by the significant ²³³U peak in Fig. 3, but that presents no difficulty for the thorium ratio measurement. A spectral plot of the uranium blank deposit is given in Fig. 4. In this case less than 5 pg of ²³⁸U was deposited and the molecular ion background could be as

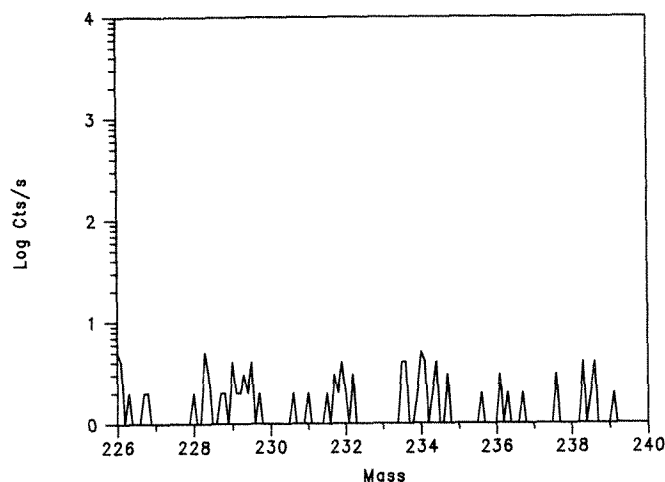


FIG. 1.--SIMS mass spectral scan of actinide region from clean area of graphite platchet.

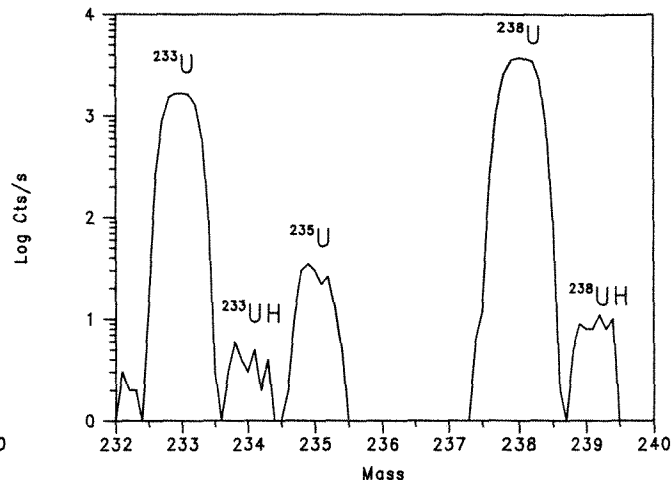


FIG. 2.--SIMS mass spectrum of uranium isotopes from uranium sample OT-3.

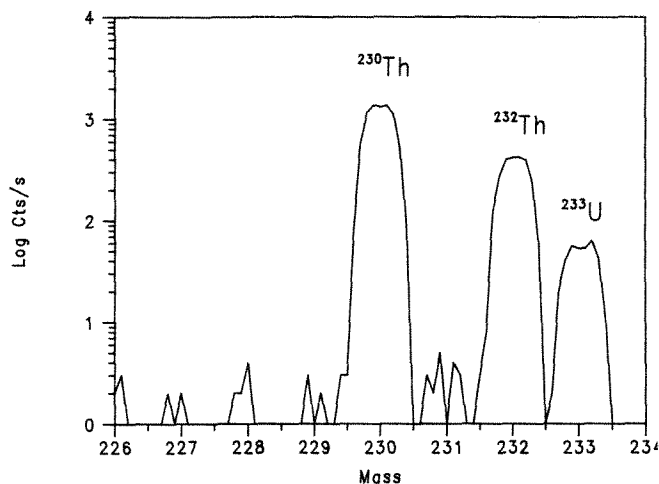


FIG. 3.--SIMS mass spectrum of thorium isotopes from thorium sample OT-2.

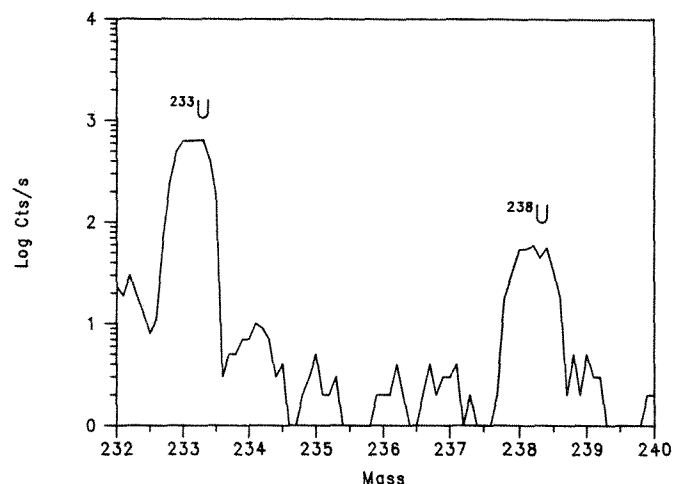


FIG. 4.--SIMS mass spectrum of uranium isotopes from uranium blank deposit.

high as 5% of the ^{238}U signal. The relative contribution of the background could probably be reduced by use of a larger value of sample voltage offset if higher accuracy were required for this amount of sample.

Three or four independent isotope ratio measurements were made from different regions of each dried deposit. In no case did this procedure come close to exhausting the available material. A summary of the results is given in Table 2. The variance in the ratio measurement for a set of ratios on a single analysis spot did not significantly exceed that expected from counting statistics. However, the spot-to-spot variability was larger than would be expected from counting statistics alone for most of the samples. The standard deviation of the mean among spots for each sample is included in the data of Table 2 and ranges from 0.07 to 0.3% relative for U and 0.13 to 0.5% relative for Th, excluding the blanks.

An estimate of the instrumental isotopic discrimination was made by internal normalization to the $^{235}\text{U}/^{238}\text{U}$ ratio, which is assumed

TABLE 2.--Summary of results: SIMS isotope ratio measurements.

Uranium:

Sample	$^{233}/^{238}$ measured	Uncert. σ_m	N	$^{233}/^{238}$ bias cor.	Uncert. σ_m
OT-1	0.7241	0.0005	3	0.712	0.006
OT-2	0.2277	0.0007	3	0.224	0.002
OT-3	0.3778	0.0005	3	0.372	0.003
Blank	10.44	0.10	4	10.3	0.13

Thorium:

Sample	$^{230}/^{232}$ measured	Uncert. σ_m	N	$^{230}/^{232}$ bias cor.	Uncert. σ_m
OT-1	4.825	0.011	4	4.793	0.019
OT-2	2.825	0.014	5	2.806	0.016
OT-3	3.721	0.005	3	3.697	0.013
Blank	1.910	0.012	3	1.897	0.013

TABLE 3.--Comparative results between SIMS and TIMS.

Uranium:

Sample	SIMS 233/238	Rel.Meas. Uncert.	TIMS 233/238	Rel.Meas. Uncert.	Difference Abs.	Rel.
OT-1	0.712	0.07%	0.7045	0.18%	-0.0075	-1.0%
OT-3	0.372	0.14%	0.3758	0.22%	+0.0038	+1.0%

Thorium:

Sample	SIMS 230/232	Rel.Meas. Uncert.	TIMS 230/232	Rel.Meas. Uncert.	Difference Abs.	Rel.
OT-1	4.793	0.22%	4.789	0.08%	-0.004	- 08%
OT-3	3.697	0.13%	3.682	0.10%	-0.015	-.41%

to be natural (0.00725). This correction of $1.67\% \pm 0.83\%$ for the $^{233}\text{U}/^{238}\text{U}$ ratio was applied to the measured ratio. The factor determined for U was also applied to the Th ratio measurements, but in this case it was $0.66\% \pm 0.33\%$ for the 2 mass unit difference between the Th isotopes. The uncertainty for mass bias was added in quadrature with the measurement uncertainty for an overall estimate of ratio measurement uncertainty.

There was no difficulty in achieving adequate signal levels for all samples and blanks. In fact, there was no correlation between the measurement precision and amount of

sample loaded. The only cases in which a systematic error is likely to occur is in the ratio measurement of the blanks, where the background from molecular ions is several percent of the actinide peaks. The uncertainty in the concentration determinations from this source is much smaller than the variation among blanks in the procedure.

Comparative Results

We have a direct comparison of ratios for only two samples of U and Th because one of the TIMS samples, containing both U and Th, was lost during loading. This accident was caused by the more extensive heating applied to the filaments to reduce the Th background. The filaments were very much more brittle than normal, and one broke while a sample was being loaded. Comparative results for the remaining two samples are shown in Table 3. The measurement uncertainty indicated for SIMS is the relative standard deviation of the mean for spot-to-spot measurement. The measurement uncertainty indicated for TIMS is the relative standard deviation of the mean among ratio sets taken at different times during the same run. The agreement between the two mass spectrometric methods is about 1% or better, even for the OT-1 sample for which the smallest amounts of U and Th were loaded for SIMS.

The final results for the concentration determinations of all samples are shown in Table 4. The problem of blank control is illustrated by the disagreement between the Th results for samples OT-1 and OT-3. Although the SIMS and TIMS isotopic ratio measurements agree to better than 1% for these samples, the concentration determinations differ by about 25%. This result suggests that sample OT-3 was contaminated before it was split for the isotopic measurements. This contamination could have occurred in the chemical processing, or it could have been adventitious contamination of the oyster tissue source material. The Th blank values are also informative, pointing to a significant filament blank for Th by TIMS. The U blank values are consistent for the two methods, indicating that this blank is introduced during chemical dissolution and purification processes.

Conclusions

We have demonstrated that the isotopic ratio measurement capability of SIMS is comparable to that of thermal ionization for nanogram quantities of uranium and thorium. It appears that SIMS is capable of achieving lower loading blanks for thorium compared to TIMS. For subnanogram quantities of material this difference would be significant. However, at the present time the chemical blank for thorium is highly variable, and that variability limits the capability to analyze for thorium at the sub-ng/g level by IDMS by use of either the SIMS or the TIMS technique.

TABLE 4.--Isotope dilution results, all samples.

	Uranium (ng/g)		Thorium (ng/g)	
	SIMS	TIMS	SIMS	TIMS
OT-1	128.2	129.6	33.3	33.3
OT-2	130.0	-	35.6	-
OT-3	130.9	129.6	42.2	42.4
OT-5	-	130.0	-	32.7
OT-6	-	128.8	-	33.8
Blank-1	10.0 pg	-	43 pg	-
Blank-2	-	9.7 pg	-	176 pg

References

1. A. Benninghoven, F. G. Rüdenauer, and H. W. Werner, *Secondary Ion Mass Spectrometry*, New York: Wiley, 1987, 787-792.
2. J. A. McHugh and J. F. Stevens, "Elemental analysis of single micrometer-sized particles by ion microprobe mass spectrometry," *Anal. Chem.* 44: 2187, 1972.
3. D. S. Simons, "Single particle standards for isotopic measurements of uranium by secondary ion mass spectrometry," *J. Trace Microprobe Tech.* 4: 185, 1986.
4. W. H. Christie, R. E. Eby, R. J. Warmack,

and Larry Landau, "Determination of boron and lithium in nuclear materials by secondary ion mass spectrometry," *Anal. Chem.* 53: 13, 1981.

5. C. J. Allègre and J. M. Luck, "¹⁸⁷Re-¹⁸⁷Os systematics in meteorites and cosmochemical consequences," *Nature* 302: 130, 1983.

6. R. W. Odom, Gayle Lux, R. H. Fleming, P. K. Chu, I. C. Niemeyer, and R. J. Blattner, "Quantitative trace element analysis of microdroplet residues by secondary ion mass spectrometry," *Anal. Chem.* 60: 2070, 1988.

7. A. Prinzhofer, C. J. Allègre, and A. Pierre, "Improvement of the analytical technique LIDIA (large isotope dilution ion probe analyses)," *Chemical Geology* 70: 178, 1988.

8. K. G. Heumann, "Isotope dilution mass spectrometry," in F. Adams, R. Gijbels, and R. Van Grieken, Eds., *Inorganic Mass Spectrometry*, New York: Wiley, 1988, 301-376.

9. W. R. Kelly and S. A. Hotes, "Importance of chemical blanks and chemical yields in accurate trace chemical analysis," *J. Res. Nat. Bur. Stds.* 93: 228, 1988.

10. W. R. Kelly and J. D. Fassett, "Determination of picogram quantities of uranium in biological tissues by isotope dilution thermal ionization mass spectrometry with ion counting detection," *Anal. Chem.* 55: 1040, 1983.

11. W. R. Kelly, J. D. Fassett, and S. A. Hotes, "Determination of picogram quantities of uranium in human urine by thermal ionization mass spectrometry," *Health Phys.* 52: 331, 1987.

12. M. Lepareur, "Le micro-analyseur ionique de seconde génération Cameca modèle 3F," *Revue Technique Thomson-CSF* 12: 225, 1980.

CHARACTERIZATION OF A FAST ATOM SOURCE FOR SECONDARY ION MASS SPECTROMETRY

S. Corcoran, N. Parikh, D. P. Griffis, and R. W. Linton

This paper reports on the methodology used in an effort to characterize a FAB source developed for the Cameca IMS-3f based on the design of Degreve and Lang.¹ This work was undertaken in an attempt to provide information about a primary-beam source whose characteristics were unknown. Conventional methods for primary-current measurement by use of a Faraday cup are not possible with a neutral primary beam. At best, an order-of-magnitude estimate can be obtained by a comparison of the secondary-ion signals from the same species in both the FAB and conventional SIMS modes.¹ This method is not rigorous, since it does not correct for the variations of sputter yield and ionization probability with incident angle and energy. Another complication is the chemical enhancement of secondary-ion yields by oxygen adsorbed onto the sample surface from the residual vacuum in the IMS-3f. Since UHV conditions are not attainable with our IMS-3f (analysis chamber pressure is typically 1×10^{-8} Torr), this enhancement effect can be especially significant when the sputter rate is low, as is the case in all "static" SIMS experiments. Therefore, an alternative method of dose determination was used. A series of experiments were performed with the FAB source used for on-line implantation of Si wafers. Rutherford backscattering spectroscopy (RBS) was used to determine the total dose of the neutral primary beam in the implanted regions. SIMS was used to depth profile the implanted atoms, in an attempt to reveal information about the energy distribution of the implanted neutral atoms.

Experimental

The FAB source was installed on a Cameca IMS-3f secondary ion mass spectrometer. The FAB source consists of a collision cell placed along the optical axis of the primary ion column¹ inside of an existing tube, which is accessed through an existing flange. As described below, there are various differences compared to the original Degreve and Lang¹ de-

S. F. Corcoran and D. P. Griffis are at the Analytical Instrumentation Facility, Box 7916, North Carolina State University, Raleigh, NC 27695-7916; S. F. Corcoran is also at the Department of Chemistry, CB 3290, University of North Carolina, Chapel Hill, NC 27599-3290, as is R. W. Linton. N. Parikh is at the Department of Physics and Astronomy, CB 3255, University of North Carolina, Chapel Hill, NC 27599-3255. This work was supported by the Analytical Instrumentation Facility, Department of Materials Science and Engineering, North Carolina State University.

sign: collision-cell dimensions and composition, primary-column optics, and differential pumping capabilities. The collision gas is introduced to the cell via an external leak valve. When the high-energy primary ions (5-15 keV) enter the collision cell they encounter the low-energy collision gas atoms present and undergo gas-phase charge exchange.² The result of this interaction is a beam of energetic neutral particles whose energy is similar to that of the incoming ion beam. The ions that pass through the cell without being neutralized are deflected into a Faraday cup by electrostatic deflection plates, so that the neutral component of the beam is allowed to impinge upon the sample. The end of the collision cell is located ~30 cm from the sample. In order to reduce the potential for background contamination, the collision cell was fabricated from Ta since the beam-limiting apertures in the primary column are also made of Ta. In order to decrease the pressure in the primary analysis chamber, a

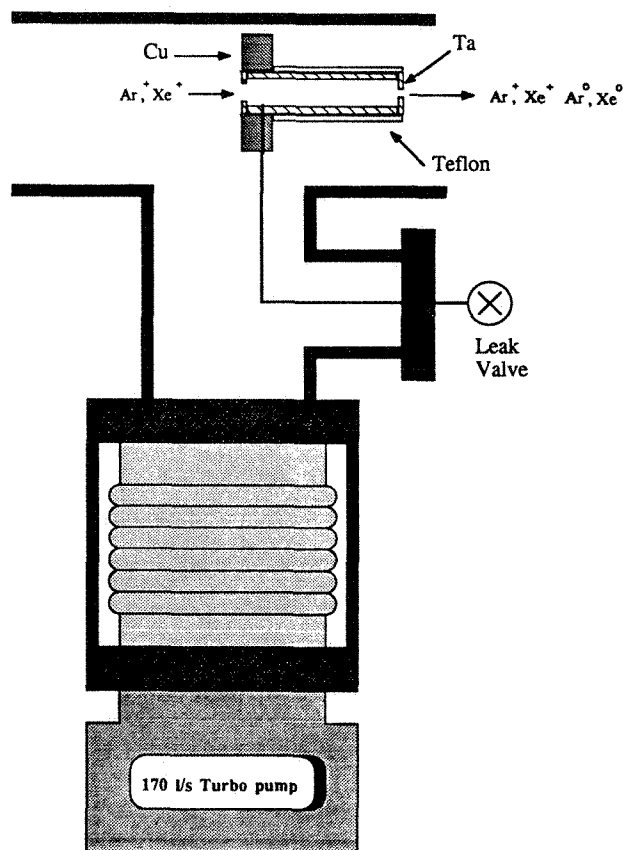


FIG. 1.--Schematic of FAB source collision cell assembly.

150 l/s turbomolecular pump has been added to the primary column. The addition of this pump aids in the differential pumping of the primary column, thereby reducing losses in primary beam intensity by inelastic scattering events. To enhance the differential pumping of the collision gas, the entrance aperture to the collision cell was made slightly larger than the exit aperture (1.5 cm vs 1.0 cm). A diagram of the current hardware configuration is given in Fig. 1.

In this experiment, a 4in. Si <100> wafer was cut into several 1 × 2cm sections, dipped into dilute HF to remove any residual surface oxide, rinsed with de-ionized water, and dried in air allowing the formation of a reproducible native surface oxide. The samples were then loaded into a sample holder assembly for subsequent neutral-beam implantation. A 10keV Ar⁺ beam was generated from a duoplasmatron ion source on the IMS-3f. The flow rate of the collision gas was adjusted until the pressure in the analysis chamber was 2 × 10⁻⁷ Torr. This was determined to be an optimum pressure for our system, as further increases in leak rate resulted in the loss of primary-beam intensity. The primary current was adjusted to the appropriate value and the collision cell was then pressurized with Ar gas. The beam was aligned in the primary column by maximization of the secondary-ion current measured by the electron multiplier detector.

All neutral implants and subsequent SIMS analyses were performed on the Cameca IMS-3f. All sputtered crater depths were determined by stylus profilometry with a Tencor Alpha-Step 200. The RBS analysis was performed on the Van de Graaff research accelerator located at the University of North Carolina, Chapel Hill. RBS analyses of the implanted samples were performed with 2MeV He⁺ ions incident normal to the sample surface. Since the implanted area on the samples was smaller than the size of the He⁺ beam, a film of mylar with a small hole cut to the size of the implanted area (~2 mm) in the center was placed over the samples. The mylar was confirmed to be free of Ar and any heavy impurities.

Results

Prior to implantation, calculations of the dose rate based on first principles were carried out in order to estimate implanted doses. The beam diameter was estimated to be ~2 mm from profilometry of a sputtered Si surface. From the shape of sputtered craters previously acquired, the beam-current density profile was known to be quite uniform over ~1 mm ± 20%). It was assumed that the neutralization efficiency for Ar was ~35%¹ and the implanted area was 4 × 10⁻² cm² (for a 2mm beam diameter). Given 100nA primary current, the neutral dose rate should be ~3.3 × 10¹⁴ atoms cm²/min. A series of three Si samples were implanted for 3, 6, and 9 min giving estimated doses of 1 × 10¹⁵, 2 × 10¹⁵, and 3 × 10¹⁵ atoms/cm², respectively. Figure 2 shows the RBS spectrum of

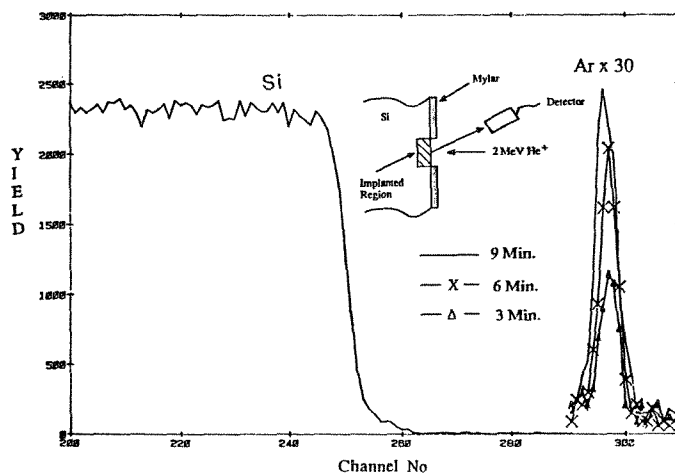


FIG. 2.--RBS spectra of Ar⁰ implanted Si. Implantation times 3, 6, and 9 min. Insert is schematic target detector set-up.

the three Ar⁰ implanted samples. The insert in Fig. 2 is a schematic of the RBS experimental set-up. The Ar peak increases with exposure time to the fast atom beam. The areal densities of Ar were calculated from³

$$(N_t)_{Ar} = \frac{A_{Ar}}{H_{Si}} \frac{\sigma_{Si}(E_0)}{\sigma_{Ar}(E_0)} \frac{\xi}{[\epsilon_0]_{Si}} \quad (1)$$

where A_{Ar} is the number of counts under the Ar peak, H_{Si} is the height of the Si (counts) at the surface, $\sigma_{Si}(E_0)$ and $\sigma_{Ar}(E_0)$ are the back-scattering cross sections of Si and Ar at incident energy E_0 , ξ is the energy width per channel, and $[\epsilon_0]_{Si}$ is the stopping-cross-section factor for He in Si. Values for the calculated doses are given in Table 1. The RBS results provide an accurate measure of the Ar dose actually incident on the sample. This relationship assumes that implanted atoms are not being sputtered off by the incident Ar beam. At the calculated doses of $<1 \times 10^{16}$ atoms/cm² the extent to which sputtering removes near-surface implanted Ar should be negligible. This assumption is probably not valid at high doses ($>1 \times 10^{16}$), since high doses would lead to the removal of at least several surface monolayers and the potential removal of implanted Ar. It is interesting that the values in Table 1 agree within a factor of 3 with the values calculated from first principles. However, a clear linear relationship between implantation time and the areal density determined by RBS is not evident. This deviation may be due in part to the fact that the beam was turned off and on by the coarse switching of the primary magnet. Because of hysteresis the magnet does not return to the same value upon resetting. In an effort to reduce the effects of primary-beam sputtering and eliminate the contribution by primary-magnet hysteresis, the implantation experiment was repeated with a lower Ar primary-beam current (10 nA corrected) and physical blanking "off" of the neutral beam by a Ta beam stop. The implanta-

TABLE 1.--Ar areal densities, N_{Ar} (atoms/cm²), determined for 10keV Ar implanted Si. Primary-ion current, 100 nA.

TABLE 2.--As in Table 1, for 20 nA.

Sample	N_{Ar}	Sample	N_{Ar}
Ar ⁺ Si, 3 min	3.1E15	Ar ⁺ Si, 6 min	7.0E14
Ar ⁺ Si, 6 min	4.4E15	Ar ⁺ Si, 12 min	1.6E15
Ar ⁺ Si, 9 min	9.9E15	Ar ⁺ Si, 24 min	2.8E15

tion times were 6, 12, and 24 min. First-principle calculations estimate that the neutral beam dose rate should be $\sim 7 \times 10^{13}$ atoms/cm² per min, which gives implanted doses of 4.2×10^{14} , 8.4×10^{14} , and 1.7×10^{15} . The Ar areal densities determined by RBS for 6, 12, and 24 min were 7.0×10^{14} , 1.6×10^{15} , and 2.8×10^{15} , respectively (Table 2). The predicted doses and those determined by RBS agree within a factor of 2. The relationship between the implantation time and measured areal density also appears more linear when the Ta aperture is used to block the Ar beam.

Of additional concern is the energy distribution of the neutral beam, which can be especially important in analytical applications where the primary-beam energy and its energy spread can have a significant impact on FAB-SIMS studies. SIMS was used to obtain depth profiles of the implanted Ar⁰. For the quantitative SIMS analysis of Ar implanted Si, a Cs⁺ primary beam was used to produce sputtered (CsAr)⁺ cluster ions whose yield has been shown by Ray et al. to be proportional to the concentration of the Ar present in the sample.⁴ This SIMS method provides the high sensitivity and depth resolution required for the analysis of shallow implants without the use of excessive primary-current densities and corresponding high sputter rates required to measure Ar⁺ directly. Quantification of the Ar is inherently difficult at a depth less than 55 Å (the implant depth of 5.5 keV Cs⁺ under these conditions) due to the possible effects of ion yield transients.^{5,6} In an attempt to resolve the near-surface details, a Si sample was presputtered with 2×10^{17} 5.5 keV Cs⁺ ions prior to Ar⁰ implantation. The Cs presputter, Ar⁰ implantation and subsequent SIMS analysis were all done in situ without removing the sample from the high vacuum (1×10^{-8} Torr) of the Cameca sample chamber. Although the presence of Cs could change the stopping power of the Si in the near surface region, this approach will nevertheless avoid some of the potential ion yield transient effects. The presputtering should also render the near surface region of the Si amorphous. Figure 3 is a plot of intensity vs depth for a typical 10 keV Ar⁰ implanted sample presputtered with Cs. The peak of the Ar distribution is approximately 110 Å, which is in close agreement with the value of 120 Å calculated for 10keV Ar⁺ from standard implantation theory developed by Lindhard, Scharff, and Schiott (LSS).⁷

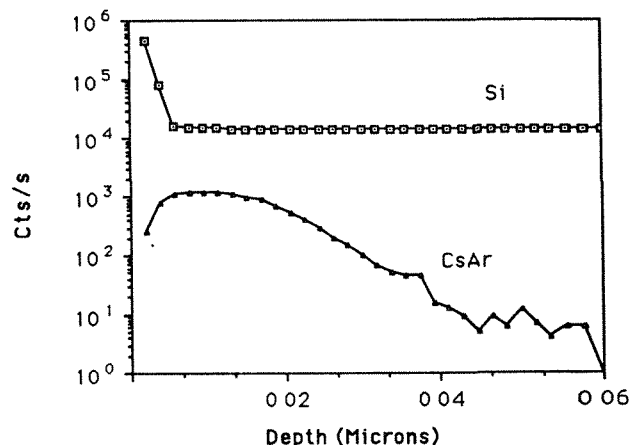


FIG. 3.--Raw data for SIMS depth profile of (CsAr)⁺ in Cs presputtered Si.

Summary

The analytical utility of this FAB source for the Cameca IMS-3f has been increased by the accurate characterization of the primary dose and energy under a set of standard conditions. For Ar⁰, under the conditions we have chosen, the RBS indicates a dose rate of $\sim 1 \times 10^{14}$ atoms/cm²/min at 20nA primary-ion current. The reproducibility of the primary-neutral-beam characteristics needs to be determined by evaluation of the FAB source on different occasions. Based on the RBS results presented, the neutral-beam flux of Ar⁰ was estimated within a factor of 2 on two different occasions. Performing RBS analysis on a daily basis in order to determine the absolute neutral flux is impractical. A more practical approach would be to depth profile a shallow multilayer structure with Ar⁰ to establish a sputtering rate that could be converted to a current density by comparison with an Ar⁺ profile. Rigorous determination by this method would involve sputter yield correction for incident primary-beam angle. With this information, SIMS experiments that require controlled primary-beam doses may not be conducted. The direct imaging capabilities of the Cameca IMS-3f permit secondary ion imaging in the FAB mode, as shown previously.^{1,8}

References

1. F. Degreve and J. M. Lang, *Surf. Interface Anal.* 7: 117, 1985.
2. F. M. Devienne and J. C. Roustan, CRAS (Paris), 276, 1973.
3. W. K. Chu, J. W. Mayer, and M. A. Nicolet in *Backscattering Spectroscopy*, New York: Academic Press, 1978.
4. M. A. Ray, J. E. Baker, C. M. Loxton, and J. E. Greene, *J. Vac. Sci. Technol.* A6: 44, 1988.
5. S. R. Bryan, R. W. Linton, and D. P. Griffis, *J. Vac. Sci. Technol.* A5: 9, 1987.
6. K. Wittmaak, *Int. J. Mass Spectrom. Ion Phys.* 17: 39, 1975.
7. J. F. Gibbons, W. S. Johnson, and S. W. Mylroie in *Projected Range Statistics*,

Stroudsburg, Pa.: Dowde, Hutchinson, and Ross, 1975.

8. R. W. Linton, I. H. Musselman, J. T. Rickman, J. O. Mullis, J. L. Hunter, S. F. Corcoran, and D. P. Griffis, *Secondary Ion Mass Spectrometry: SIMS VI*, New York: Wiley, 1988, 569.

AUTHOR INDEX

A

Abo-Namous, S. A., 239
 Abraham, J. L., 55
 Ackland, D. W., 507
 Adams, F. C., 594
 Adams, F., 366
 Adar, F., 159
 Anderhalt, R. W., 249
 Andrews, S. B., 85
 Angelini, P., 515
 Arlinghous, H. F., 180
 Armstrong, D. A., 131

B

Baba-Kishi, K., 435
 Bahr, U., 337
 Balazs, L., 273
 Barbour, J. C., 196
 Barckhaus, R., 50
 Bastin, G. F., 207
 Batson, P. E., 5, 518
 Batstone, J. L., 11
 Bauer, G. R., 554
 Baxter, C. S., 264
 Beard, M. E., 425
 Becker, C. H., 281
 Bernstein, G. H., 459
 Blackburn, D. H., 254
 Bodnar, R. J., 571, 579
 Bolon, R. B., 449
 Bond, M., 122
 Boore, V., 211
 Bostrom, T. E., 233
 Bourcier, R. J., 443
 Bowers, C., 591
 Brenna, J. T., 306
 Bright, D. S., 377
 Brinkmann, B., 330
 Bruley, J., 518
 Bryan, S. R., 323
 Buchanan, J. W., 63
 Buchanan, R. A., 129
 Bumgarner, S. D., 399
 Bunn, R. D., 127
 Burchette, J. L., Jr., 45
 Burris, S. B., 413
 Burrus, R. C., 173

C

Campana, J., 311, 339
 Cantello, H., 65
 Cantino, M. E., 73, 94
 Carl, R. T., 163

Carlson, D., 173
 Carney, M., 119
 Carr, M. J., 511
 Celotta, R. J., 391
 Chabala, J. M., 17, 586
 Chapman, R. C., 463
 Chen, J. H., 405
 Chen, R.-T., 535
 Chen, S. W., 73
 Chevacharoenkul, S., 453
 Cho, S. G., 474
 Cieslak, M. J., 511
 Clark, B. H., 421
 Cohen, B. J., 65
 Conroy, C. M., 579
 Corcoran, S. F., 597
 Corcoran, S., 605
 Cowley, J. M., 480
 Crabos, M., 65
 Currie, L. A., 303
 Czyzewski, Z., 396

D

Darmon, L. S., 166
 Das, K., 171
 Davis, J. A., 427
 Detter, L. D., 423
 Dillon, C. E., 381
 Dingle, T., 319
 Dingley, D. J., 435
 Doyle, B. L., 196
 Dreyfus, R. W., 261
 Dunlap, J. R., 127

E

Echlin, P., 79
 Eichberg, J., 26
 Elthon, D., 468
 Enloe, W. S., 148
 Evans, B., 333

F

Fassett, J. D., 600
 Ferry, D. K., 459
 Fiori, C. E., 219, 236
 Fleming, R. H., 370
 Fletcher, R. A., 303
 Fodor, R. V., 554
 Foster, M. C., 137
 Franz, H. E., 107
 Furuya, K., 301

G

Gauvin, R., 527
 Giardini-Guidoni, A., 299

Gijbels, R., xviii, 273
 Ging, T., 173
 Girod, C., 17
 Glaisher, R. W., 480
 Goldstein, J. I., 501, 507
 Golijanin, D. M., 125, 186
 Good, P. F., 43, 373
 Gordon, B. M., 191
 Granier, V., 347
 Griffiths, D. P., 399, 540, 597, 605
 Griffiths, B. W., 319
 Grupp, C. T., 107
 Gucer, S., 366

H

Hallegot, P., 17
 Hanson, A. L., 191
 Harrington, C. D., 563, 567
 Harrington, P. B., 283
 Harvey, B. W., 425
 Havrilla, G. J., 323
 Hawkey, L. A., 97
 Hayashi, Y., 301
 Headley, T. J., 511
 Heijligers, H. J. M., 207
 Heimbrook, L. A., 335
 Heinrich, K. F. J., 242
 Hellgeth, J. R., 579
 Hercules, D. M., 297, 343, 364
 Heyman, R. V., 468
 Hillenius, S. J., 335
 Hillenkamp, F., 277, 337, 353
 Hillier, J., 1
 Hochella, M. F., 281
 Hoffmeister, S., 399
 Holm, R., 325
 Holtkamp, D., 325
 Housden, J., 269
 Howe, J. M., 483
 Humphreys, T. P., 171
 Hunter, J. L., 45
 Hunter, J. L., Jr., 597
 Hutt, K. W., 269

I

Ingram, P., 69, 97, 119
 Ino, Y., 301
 Isenberg, G., 117
 Ishimori, A., 317
 Izutsu, K. T., 73

J

Jacobs, R. S., 554
 James, M. R., 441

Jaraki, A.-R., 122
 Johnson, D. E., 73, 94
 Johnson, P. F., 405, 474
 Jones, K. W., 191
 Joy, D. C., 127, 129, 131, 396, 459
 Juhasz, P., 273

K

Kalinowski, M. R., 427
 Karas, M., 337, 353
 Kaufmann, R. L., 35, 355, 359
 Kayton, R. J., 73
 Kelley, M. H., 391
 Kellogg, G. L., 201
 Kelly, W. R., 600
 Kenik, E. A., 493
 Kikuchi, T., 301
 Kinne, R. K. H., 107
 Kirk, R. G., 31
 Kirkendall, T. D., 465
 Klintworth, G. K., 60
 Knight, C. L., 571, 574, 579, 583
 Konopka, J. F., 523
 Kopf, D. A., 97
 Krause, S. J., 459
 Krewer, J. A., 413
 Krier, G., 311, 339, 347
 Kubis, A. J., 364
 Kusy, R. P., 63

L

Lazare, S., 347
 Leake, J. A., 264
 Leapman, R. D., 85, 89
 Lechene, C.,
 Lee, J. J., 45
 Lee, P., 31
 LeFurgey, A., 69, 97, 119
 Lehman, J., 119
 Lehner, S., 135
 L'Esperance, G., 527
 Levi-Setti, R., 17, 586
 Liang, L. C., 566
 Lieberman, M., 119
 Lifshin, E., 243, 449
 Lin, Y. J., 515
 Lindner, B., 286
 Lineman, D. N., 297
 Linton, R. W., 45, 293, 597, 605
 LoPachin, R. M., 26
 LoPachin, V. R., 26
 Lowery, J., 26
 Lus, S., 127
 Lutgen, P., 347
 Lyman, C. E., 507

M

McCarthy, J. J., 381
 Mackenzie, R., 435
 McGuire, G. E., 453
 McKay, G., 247, 549
 Malis, T. S., 487
 Malta, D. P., 554
 Mandel, L. J., 69
 Marinenko, R. B., 254, 257
 Mathey, A., 350
 Matthews, L. J., 264
 McCartney, M. L., 515
 Meeker, G. P., 370
 Mele, A., 299
 Michael, J. R., 496
 Michiels, F. P., 594
 Millette, J. R., 413
 Mogro-Campero, A., 243
 Mohr, J., 459
 Morkoc, H., 480
 Morris, M. D., 146
 Moyers, K. W., 335
 Muller, J. F., 311, 339, 347
 Musselman, I. H., 293, 535
 Musselman, R. L., 151
 Myers, S., 471
 Myklebust, R. L., 219, 223

N

Nemanich, R. J., 141, 171
 Newbury, D. E., 216, 257, 377
 Nicholas, M., 323
 Nockolds, C. E., 233

O

Odom, R. W., 283
 O'Grady, M. R., 579
 Osburn, C. M., 453
 Ou, H. J., 480
 Oxborne, M. P., 75

P

Packwood, R., 211
 Paesler, M. A., 148
 Panitz, J., 531
 Parikh, N. R., 171, 605
 Pavenstadt-Grupp, I., 107
 Pellerin, J., 540
 Pelletier, M., 311, 339, 347
 Peluso, L. A., 243
 Perkins, R. L., 425
 Perl, D. P., 43, 373
 Phelps, J. M., 433
 Pierce, D. L., 166
 Pierce, D. T., 391
 Posthill, J. B., 171

Pounds, J. G., 191
 Pruett, J. G., 323

R

Radicati di Brozolo, F., 283, 370
 Radzimski, Z. J., 410, 456
 Raymond, R., Jr., 563, 567
 Reasor, M. K. J., 31
 Rechmann, P., 35, 355
 Reffner, J. A., 167
 Retorick, D. R., 254
 Ricci, P., 350
 Rivers, M. L., 191
 Ro, C.-U., 293
 Robers, W. B., 463
 Robertson, C. D., 449
 Roboz, J. S., 373
 Roggli, V. L., 57
 Romans, G. M., 23
 Romig, A. D., Jr., 511
 Roomans, G. M., 103, 105
 Ross, D. K., 468
 Rothwell, T., 471
 Rozgonyi, G. A., 456
 Russ, J. C., 176, 410
 Russell, P. E., 399, 456, 535, 540

S

Sandborg, A. O., 249
 Sanfilippo, A. P., 45
 Saubermann, A. J., 26, 112
 Scanlan, F. P., 345
 Scheinfein, M. R., 391
 Schidlovsky, G., 191
 Schmidt, P. F., 50, 330
 Schmitt, H. W., 180
 Schnatz, H., 35
 Sharkey, A. G., 297, 364
 Shedd, G., 540
 Shelburne, J. D., 45
 Shire, N. J., 254
 Shou, T., 456
 Simons, D. S., 600
 Small, J. A., 223, 254
 Smith, D. G. W., 559
 Smith, J. V., 191
 Spanne, P., 191
 Sparks, R. G., 148
 Spencer, A. J., 75, 103
 Spurny, K. R., 422
 Steel, E. B., 216, 377, 414, 433
 Stephen, J., 75
 Strain, J. J., 97
 Stranges, D., 299
 Stuart, C. J., 566
 Sukow, C. A., 171

Sun, S., 125, 186
 Sutton, S. R., 191
 Swyt, C. R., 89, 236
 Sydel, U., 286

T

Taylor, L. T., 579
 Teague, E. C., 545
 Teghil, R., 299
 Thomas, S., 211
 Thompson, D. G., 463
 Thompson, S. P., 319
 Thonnard, N., 180
 Tingle, T. N., 281
 Toney, J. B., 566
 Tormey, J. McD., 115
 Tourmann, J. L., 35, 355, 359
 Treado, P. J., 146
 Tsugoshi, T., 301
 Turner, L., 243

U

Unguris, J., 391

V

Vander Wood, T. B., 423, 591
 Van Espen, P. E., 594
 Vanhoolst, W. K., 594
 Vanko, D. A., 583
 Van Vaeck, L., xviii, 350, 366
 Vecchio, K. S., 477
 Verkouteren, J. R., 433
 Vertes, A., 273
 Viswanadham, S. K., 297, 364
 Voorhees, K. J., 283
 Voyksner, R. E., 45

W

Wagstaff, J., 247
 Walker, J. S., 381
 Wallach, E. R., 269
 Walsh, L. G., 115
 Wang, Y. L., 17
 Warley, A., 118
 Weil, D., 311, 339
 Weinlaender, M., 159
 Wells, O. C., 227
 Wendt-Gallitelli, M. F., 117
 Wilcox, D. B., 465
 Wilkinson, L. E., 73
 Williams, D. B., 501, 507
 Williamson, M. A., 571
 Williamson, M., 574
 Winterberg, B., 50
 Wittry, D. B., 125, 186
 Wong, J. G., 94
 Wurster, R., 135

Y

Yamamoto, T., 317
 Yang, V., 247
 Yang, Y. L., 586

Z

Zglinicki, T. von, 103, 105
 Zhang, X., 129
 Zierold, K., 109
 Zumkley, H., 50